SCHOLARLY PUBLICATIONS

A CURRENT AWARENESS BULLETIN
OF RESEARCH OUTPUT

@DTU

(64th Edition)

APRIL, 2018

BY: CENTRAL LIBRARY

DELHI TECHNOLOGICAL UNIVERSITY
(FORMERLY *DELHI COLLEGE OF ENGINEERING)*
GOVT. OF N.C.T. OF DELHI
SHAHBAD DAULATPUR, MAIN BAWANA ROAD
DELHI 110042

PREFACE

This is the **Sixty Fourth** Issue of Current Awareness Bulletin started by Delhi Technological University, Central Library. The aim of the bulletin is to compile, preserve and disseminate information published by the faculty, students and alumni for mutual benefits. The bulletin also aims to propagate the intellectual contribution of Delhi Technological University (DTU) as a whole to the academia.

The bulletin contains information resources available in the internet in the form of articles, reports, presentations published in international journals, websites, etc. by the faculty and students of DTU. The publications of faculty and student which are not covered in this bulletin may be because of the reason that the full text either was not accessible or could not be searched by the search engine used by the library for this purpose.

The learned faculty and students are requested to provide their uncovered publications to the library either through email or in CD, etc. to make the bulletin more comprehensive.

This issue contains the information published during **April, 2018**. The arrangement of the contents is alphabetical. The full text of the article which is either subscribed by the university or available in the web is provided in this bulletin.

Central Library

CONTENTS

1. A comprehensive power-flow model of multi-terminal PWM based VSCHVDC systems with DC voltage droop control, ***6.1.Shagufta Khan*** and ***3.Suman Bhowmick***, Electrical, DTU

2. A High Linearity and Low Noise Shunt Resistive Feedback UWB LNA, ***6.Aditi*** and ***3.Malti Bansal***, Electronics & Communication, DTU

3. A high-Q floating active inductor using 130 nm BiCMOS technology and its application in IF band pass filter, ***7.1.Divyesh Sachan***, Manish Goswami and Prasanna Kumar Misra, Electronics and Communication, DTU

4. A Review of Particle Swarm Optimization, ***3.N. K. Jain***, ***3.Uma Nangia*** and ***6.Jyoti Jain***, Electrical, DTU

5. A Review on Research Aspects and Trends in Micro-Electrical Discharge Machining (Micro-EDM), Shrikant Vidya, P. Mathiyalagan and ***3.Reeta Wattal***, Mech, DTU

6. A Study on the Application of Turbo Expansion in Light Duty Gasoline and Diesel Engines: A Review, ***6.Satvik Jain***, ***Rahul Fageria***, ***6.Srishti Mishra***, ***6.Adeel Ahmad*** and ***3.Naveen Kumar***, Mechanical, DTU

7. ALTERNATIVE REFRIGERANTS FOR HCFC 22-A REVIEW, S.K.Kalla, ***3.B.B. Arora*** and J.A. Usmani, Mechanical, DTU

8. Ambient Air Quality Status in Noamundi Iron Ore Mines, Jharkhand (India): A Case Study, ***6.Amit Krishan***, Ankita Srivastava and ***3.Rajeev Kumar Mishra***, Envt, DTU

9. Biofunctionalized tungsten trioxide-reduced graphene oxide nanocomposites for sensitive electrochemical immunosensing of cardiac biomarker, ***6.Deepika Sandil***, ***6.Saurabh Srivastava***, ***3.B.D. Malhotra, 3.S.C. Sharma***, ***3.Nitin K. Puri***, Physics and Biotechnology, DTU

10. COMMON FAILURES IN GAS TURBINE BLADE A CRITICAL REVIEW, ***3.Sushila Rani***, Mechanical, DTU

11. Compact Modeling of Drain Current, Charges, and Capacitances in Long-Channel Gate-All-Around Negative Capacitance MFIS Transistor, Amol D. Gaidhane, ***8.1.Girish Pahwa***, Amit Verma and Yogesh Singh Chauhan, ECE, DTU

12. COMPARISON OF SCOUR AROUND DIFFERENT SHAPES OF GROYNES IN OPEN CHANNEL, ***6.Thangamani Vijaya Kumar***, ***7.Devesh Tyagi***, ***7.Lokesh Aggarwal*** and ***3.Munendra Kumar***, Civil, DTU

13. Copy-Move Forgery Detection Techniques: A Literature Survey, ***3.Ritu Agarwal*** and ***7.B.N. Deepankan***, Information Technology, DTU

14. Decoupled Active and Reactive Power Predictive Control for PV Applications using a Grid-tied Quasi-Z-Source Inverter, ***6.Sarthak Jain***, Mohammad B. Shadmand and Robert S. Balog, Electrical, DTU

15. Design and Optimization of Composite Horizontal Axis Wind Turbine (Hawt) Blade, ***8.Rohan Brella***, ***8.Mayank Sehgal***, and ***3.Naveen Kumar***, Mechanical, DTU

16. Design, Analysis, and Comparison of LNA topologies for IEEE 802.15.4 Zigbee Standard, ***8.Aditi*** and ***3.Malti Bansal***, Electronics & Communication, DTU

17. Design, development and characterization of MEMS Silicon diaphragm Force sensor, Rajesh Kumar, Shanay Rab, B. D. Pant and ***3.S Maji***, Mechanical, DTU

18. Economic Load Dispatch Using Adaptive Social Acceleration Constant Based Particle Swarm Optimization, ***3.N. K. Jain***, ***3.Uma Nangia*** and ***6.Jyoti Jain***, Electrical, DTU

19. Effect of hybrid wire EDM conditions on generation of residual stresses in machining of HCHCr D2 tool steel under ultrasonic vibration, Sanjay Kumar, Sandeep Grover and ***3.R. S. Walia***, Mechanical, Production and Industrial and Automation, DTU

20. Electrochemical studies of novel olivine-layered (LiFePO4-Li2MnO3) dual composite as an alternative cathode material for lithium-ion batteries, ***6.Rakesh Saroha***, ***3.Amrish K. Panwar***, Anurag Gaur, Yogesh Sharma, ***6.Vinay Kumar*** & ***3.Pawan K. Tyagi***, Applied Physics, DTU

21. Electrophoretically deposited nanostructured PdO thin film for room temperature amperometric H2 sensing, ***6.Kamal Arora*** and ***3.Nitin K. Puri***, Applied Physics, DTU

22. Ellipsoidal all-dielectric Fano resonant core-shell metamaterials, ***6.Reena Reena***, ***3.Yogita Kalra*** and ***6.Ajeet Kumar***, applied Physics, DTU

23. Evolution and thermodynamics of new holographic dark energy with bulk viscosity in modified f(R, T) gravity, ***3.C. P. Singh*** and ***6.Milan Srivastava***, Mathematics, DTU

24. Factors affecting the remanucaturing of a product, ***3.Saurabh Agrawal***, Mech, DTU

25. Gate Metal Engineered Heterojunction DGTFETs for Superior Analog Performance and Enhanced Device Reliability, ***6.Jaya Madan***, ***8.Skanda Shekhar*** and ***3.Rishu Chaujar***, Physics, DTU

26. Generation of high power sub millimeter radiation using free electron laser, ***6.J Panwar***, ***3.S C Sharma***, ***6.P Malik***, ***6.M Yadav*** and ***3.R Sharma***, Physics, DTU

27. Irreversibility analysis of three stage vapour compression refrigeration systems with flash-intercooler using eco-friendly new refrigerants (R134a, R1234yf, R1234ze, R227ea and R245fa), ***3.R.S. Mishra***, Mechanical, DTU

28. Irreversibility analysis of Two and three stage vapour compression refrigeration systems with multi evaporators and flash-intercooler using new ecofriendly refrigerants (R227ea, R236fa, R245fa, R1234yf, R1234ze) for replacing R134a, ***3.R.S. Mishra***, Mechanical, DTU

29. MODAL ANALYSIS OF CANTILEVER BEAM TO DETECT FAILURE ZONE, ***3.Sushila Rani***, Mechanical, DTU

30. Modelling the effects of nitrogen doping on the carbon nanofiber growth via catalytic plasma-enhanced chemical vapour deposition process, ***6.Ravi Gupta*** and ***3.Suresh C. Sharma***, Physics, DTU

31. Multi-Metal Citrate Complex, ***3.Anil Kumar***, Applied Chemistry, DTU

32. Numerical analysis of THz radiation wave using upper hybrid wave wiggler, ***6.Pratibha Malik***, ***3.Suresh C. Sharma***, ***6.Jyotsna Panwar*** and ***3.Rinku Sharma***, Applied Physics, DTU

33. Pentavariate Vmin Analysis of a Subthreshold 10T SRAM Bit Cell With Variation Tolerant Write and Divided Bit-Line Read, Shourya Gupta, ***6.Kirti Gupta*** and ***3.Neeta Pandey***, Electronics and communication, DTU

34. Performance Analysis of 4 Stroke Compression Ignition Engine by Using Diesel and Biodiesel Blend of Hingot Oil, Mr. Akash Singh Raikwar, Mr. Amit Agarwal and Dr. ***3.Amit Pal,*** Mechanical. DTU

35. Performance analysis of solar parabolic trough collectors driven combined supercritical CO2 and organic Rankine cycle, ***6.Harwinder Singh*** and ***3.R.S. Mishra***, Mechanical, Production & Industrial, Automobile, DTU

36. PL approximation of DBPSK in DF-based cooperative FSO network with pointing error, Deepti Agarwal, Ankur Bansal and ***7.1.Ashwni Kumar***, ECE, DTU

37. Programmable gain amplifier using operational floating current conveyors, ***6.Prateek Pahalwan***, ***6.Prateek Tripathi***, ***6.Prashant Gola***, ***3.Neeta Pandey*** and ***3.Deva Nand***, Electronics and Communication, DTU

38. Recent Developments in Corrole Synthesis, ***3.Anil Kumar***, Applied Chemistry,, DTU

39. SentiMozart: Music Generation based on Emotions, ***6.Rishi Madhok***, Shivali Goel and ***6.Shweta Garg***, Computer Science, DTU

40. Spectroscopic studies of Dy3+ doped Borate Glasses for Cool White Light Generation, ***6.Sumandeep Kaur***, ***6.Amit K.Vishwakarma***, ***6.Nisha Deopa***, ***6.Aman Prasad***, ***3.M. Jayasimhadri*** and ***3.A.S. Rao***, Applied Physics, DTU

41. Stabilization and Protection of Biomaterial through Biomineralization via Surface Interaction: An Astrobiological Approach, Preeti Bhatt, Chandra Kala Pant, Pramod Pandey, Yogesh Pandey, Satish Chandra Sati, ***3.Mohan Singh Mehata***, Applied Physics, DTU

42. STATISTICAL ANALYSIS OF RESERVOIR INDUCED SEISMICITY AT A RESERVOIR SITE, ***3.Munendra Kumar***, ***3.T. Vijaya Kumar*** and ***6.Saurabh Sah***, Civil, DTU

43. Structural physical approximation for the realization of the optimal singlet fraction with two measurements, ***6.Satyabrata Adhikari***, Physics, DTU

44. STUDY OF REDUCING WASTAGE OF WATER IN HOUSEHOLD USING FOOT TAP, ***3.Munendra Kumar*** and ***7.Dharmender Tiwari***, Civil, DTU

45. Study of Starting Friction during the Running of Plain Journal Bearing under Hydrodynamic Lubrication Regime, ***6.Vipin Kumar Sharma***, ***3.Ramesh Chandra Singh*** and ***3.Rajiv Chaudhary***, Mechanical, DTU

46. STUDY OF THE IMPACT OF INCLINATION ON SCOURING AROUND THE BRIDGE PIER, ***3.Munendra Kumar***, Civil, DTU

47. Sustainable development of groundwater: A case study of Begamganj block in Bina River Basin of Madhya Pradesh, India., ***6.Sushant Kumar***, ***3.A.K.Sahu***, ***3.Munendra Kumar***, M.K. Choudhary and T.R.Nayak, Civil, DTU

48. Tb3+ and Eu3+ Doped Zinc Phosphate Glasses for Solid State Lighting Applications, ***6.Kaushal Jha***, ***6.Amit K Vishwakarma***, ***3.M. Jayasimhadri***, D. Haranath and Kiwan Jang, Applied Physics, DTU

49. Thermal performance of combined cycle power plant with solar reheating and regeneration using ecofriendly organic fluids, ***3.Radhey Shyam Mishra***, Mech, DTU

50. Thermodynamic performance analysis of two stage vapour compression refrigeration systems with flash-intercooler using eco-friendly new refrigerants (R134a, R1234yf, R1234ze, R227ea and R152a), ***3.R.S. Mishra***, Mechanical, DTU

51. Tunable Single and Double Emission Semiconductor Nanocrystal Quantum Dots: A Multianalyte Sensor, ***6.R. K. Ratnesh*** and ***3.Mohan Singh Mehata***, Applied Physics, DTU

52. TWITTER SENTIMENT ANALYSIS AND TEXT MINING IN R, Rishabh Nigam and ***7.1.Nidhi Sengar***, IT, DTU

1. *Chancellor*

2. *Pro Vice Chancellor*	***2.1.*** *Ex Pro Vice Chancellor*
3. *Faculty*	***3.1.*** *Ex Faculty*
4. *Teaching-cum-Research Fellow*	***4.1.****Asst. Librarian*
5. *Alumni*	
6. *Research Scholar*	***6.1.*** *Ex Research Scholar*
7. *PG Scholar*	***7.1.*** *Ex PG Scholar*
8. *Undergraduate Student*	***8.1.*** *Ex Undergraduate Student*

Electrical Power and Energy Systems 102 (2018) 71–83

Contents lists available at ScienceDirect

Electrical Power and Energy Systems

journal homepage: www.elsevier.com/locate/ijepes

A comprehensive power-flow model of multi-terminal PWM based VSC-HVDC systems with DC voltage droop control

Shagufta Khan*, Suman Bhowmick

Department of Electrical Engineering, Delhi Technological University, Delhi 110042, India

ARTICLE INFO

Keywords:
Droop control
MTDC
VSC

ABSTRACT

This paper presents power-flow models of AC power systems integrated with voltage-sourced converter (VSC) based multi-terminal high voltage direct current (MTDC) grids. Pulse-width modulation (PWM) control is employed for the VSCs. In the proposed approach, the VSC modulation indices are considered as unknowns. For control of the MTDC grid, DC voltage droop control has been implemented. The proposed method includes both linear and nonlinear voltage droop characteristics. Converter losses are included in the proposed model. Depending upon the terminal end line active power specifications of the VSCs, two different voltage droop control models have been developed. The convergence properties in the proposed approach are found to be independent of the MTDC grid location, its topology, the MTDC control strategy employed and the operating point specification. Numerous case studies are carried out by applying different control modes to multiple topologies of MTDC grids embedded in the IEEE-300 bus test system. For all the case studies, the power-flow algorithms were implemented with MATLAB. In all occurrences, a mismatch error tolerance of 10^{-10} p.u. was selected. The results validate the proposed work.

1. Introduction

In recent years, the demand for electrical energy around the world has risen exponentially. Due to this, the capacities of power transmission networks across the globe need to be augmented. VSC based high-voltage DC (HVDC) links help in promoting this cause. Unlike AC transmission, the length of a HVDC link is unaffected by stability considerations. VSC based HVDC transmission systems enhance system reliability by facilitating interconnection of asynchronous AC grids. They can also be used to improve the network capacity by integrating offshore wind farms with AC grids. Modern VSC-HVDC grids employ IGBTs with PWM control technique. HVDC links using PWM controlled VSCs have the advantage of rapid and independent controllability of active as well as reactive powers, along with compact and inexpensive AC filters [1–8].

Compared to a HVDC link between two-terminals, a MTDC grid is able to exploit the benefits of VSC-HVDC technology in a superior way. Moreover, sources of renewable energy can be easily integrated with a MTDC system, as and when the need arises. A meshed MTDC grid linking offshore wind farms and three asynchronous AC grids of the European Network of Transmission System Operators for Electricity (ENTSO-E) is being envisaged in the North Sea region [9,10].

In a MTDC grid, the VSCs can be connected in a back-to-back (BTB) or a point-to-point (PTP) disposition, depending on whether they are placed nearby or are at distant locations, respectively [11]. The PTP connection is common to most of the MTDC systems in operation, wherein DC links or cables are used to connect the DC terminals.

For proper MTDC operation, DC voltage control is an essential requirement. In this respect, several DC voltage control techniques have been envisaged. Among these, DC slack bus control (familiar as master–slave control) and distributed voltage droop control have been the more popular ones.

In DC slack bus control [11–14], the voltage of one DC terminal is maintained constant. It is known as the DC slack bus and it sustains the power balance of the DC grid. The converter which controls its DC side voltage is known as the master converter. The rest of the converters (also known as slave converters) regulate their power flow. The main disadvantage of this control scheme is the DC grid instability following a failure of the master converter.

The above problem can be tackled by ensuring that individual converters take part in the DC voltage regulation scheme by adjusting their active power flow in response to changes in the DC voltage with the operating point, known as DC voltage droop control [15–23]. For MTDC systems, different types of DC voltage droop control have been envisaged to ensure proper sharing based on the converter ratings. These include voltage-power (V-P) droop and voltage-current (V-I)

* Corresponding author.
E-mail addresses: khan.shagufta7@gmail.com (S. Khan), suman.bhowmick@dce.ac.in (S. Bhowmick).

https://doi.org/10.1016/j.ijepes.2018.04.019
Received 26 September 2017; Received in revised form 7 February 2018; Accepted 17 April 2018
0142-0615/ © 2018 Elsevier Ltd. All rights reserved.

droop.

Now, for planning, operation and control of interconnected AC-MTDC systems, their power-flow models are required. [11–14,21,22] present some comprehensive power-flow models of integrated AC-DC systems. However, most of the current research works do not address the following issues:

(1) Development of a unified approach for the power-flow modeling of integrated AC-MTDC grids incorporating DC voltage droop control. In this respect, although [22] presents the power-flow modeling of AC-MTDC grids incorporating voltage droop control, the convergence properties of the unified AC/DC Newton-Raphson algorithm is lost because of the choice of sequential iterative algorithm.
(2) The VSC modulation index 'm' is not considered as an unknown. For VSC applications, 'm' is a crucial parameter. Typically, $0 < m \leqslant 1$. [6] reports some of the factors that put a cap on the lower and upper bounds of 'm'.

This paper presents a unified approach for the power-flow modeling of AC-MTDC grids. As against most of the research works published in this area, 'm' is considered as an unknown and can be obtained directly, from the power-flow solution. Realistic MTDC grid control strategies like DC voltage droop control can be implemented in the model.

The paper is organized as follows: In Section 2, the modeling of a hybrid AC-MTDC system is presented. DC voltage droop control is presented in Section 3. Section 4 and 5 detail two different models of integrated AC-MTDC grids employing voltage droop control. The case studies and results are presented in Section 6. The conclusions are presented in Section 7.

Throughout this paper, regular and bold quantities are used to represent scalar variables and complex variables as well as matrices, respectively. All the transmission lines are represented by their equivalent-pi models.

2. Modeling of AC-MTDC systems

Fig. 1 shows an AC power system network comprising 'n' buses, integrated with a MTDC grid. The MTDC grid constitutes 'q' VSCs.

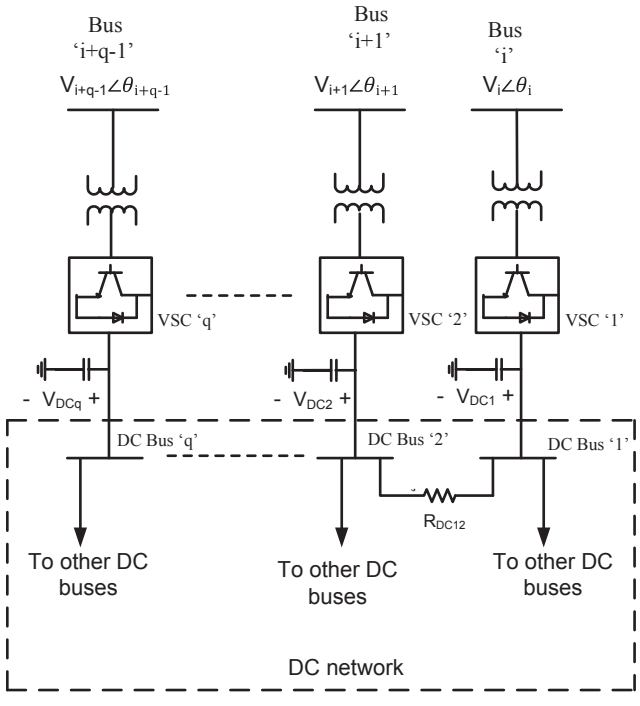

Fig. 1. Schematic diagram of AC-MTDC system.

Converter transformers are used to interconnect the VSCs with their AC terminal buses. For generalization, it is assumed that the AC buses connected to the 'q' VSCs are numbered as 'i', '(i + 1)', and so on, up to '(i + q-1)'. On their DC sides, the 'q' VSCs follow a PTP connection. Fig. 2 shows the equivalent circuit for the network shown in Fig. 1.

In Fig. 2, 'q' fundamental frequency, positive sequence voltage sources pertaining to the 'q' VSCs are shown. Now, let R_{sha} and X_{sha} be the resistance and the leakage reactance of the a^{th} ($1 \leq a \leq q$) converter transformer, respectively. Also, let $\mathbf{y_{sha}} = \mathbf{1/Z_{sha}}$, where $\mathbf{Z_{sha}} = R_{sha} + jX_{sha}$. Therefore, from Fig. 2, the current in the link (not shown) connecting the a^{th} VSC and its AC terminal bus is

$$\mathbf{I_{sha}} = \mathbf{y_{sha}}(\mathbf{V_{sha}} - \mathbf{V_{i+a-1}}) \tag{1}$$

In Eq. (1), $\mathbf{V_{ha}}$ is the voltage phasor pertaining to the a^{th} VSC. Also, in Eq. (1), $\mathbf{V_{sha}} = V_{sha}\angle\theta_{sha} = m_a c V_{DCa}\angle\theta_{sha}$ where 'm_a' is the VSC modulation index. The constant 'c' is representative of the VSC architecture [4].

Now, from Fig. 1, at the AC bus '(i + a-1)' pertaining to the a^{th} VSC, it can be shown that the net active and reactive power injections are

$$P_{i+a-1} = \sum_{k=1}^{n} V_{i+a-1}V_k Y_{(i+a-1)k}\cos[\theta_{i+a-1} - \theta_k - \phi_{(i+a-1)k}] - m_a c V_{DCa} V_{i+a-1} y_{sha}\cos(\theta_{i+a-1} - \theta_{sha} - \phi_{sha}) \tag{2}$$

$$Q_{i+a-1} = \sum_{k=1}^{n} V_{i+a-1}V_k Y_{(i+a-1)k}\sin[\theta_{i+a-1} - \theta_k - \phi_{(i+a-1)k}] - m_a c V_{DCa} V_{i+a-1} y_{sha}\sin(\theta_{i+a-1} - \theta_{sha} - \phi_{sha}) \tag{3}$$

where 'ϕ_{sha}' is the phase angle of $\mathbf{y_{sha}}$.

In a similar manner, from Fig. 2, it can be shown that the line active and reactive power flows pertaining to the a^{th} VSC are given as follows:

$$P_{sha} = \mathrm{Re}[\mathbf{V_{i+a-1}}\mathbf{I_{sha}^*}] = m_a c V_{DCa} V_{i+a-1} y_{sha}\cos(\theta_{i+a-1} - \theta_{sha} - \phi_{sha}) - V_{i+a-1}^2 y_{sha}\cos\phi_{sha} \tag{4}$$

$$Q_{sha} = m_a c V_{DCa} V_{i+a-1} y_{sha}\sin(\theta_{i+a-1} - \theta_{sha} - \phi_{sha}) + V_{i+a-1}^2 y_{sha}\sin\phi_{sha} \tag{5}$$

Again from Fig. 2, in the MTDC grid, the net injected current at the u^{th} ($1 \leq u \leq q$) DC node is given as,

$$I_{DCu} = \sum_{v=1}^{q} Y_{DCuv} V_{DCv} \tag{6}$$

where $Y_{DCuv} = -\frac{1}{R_{DCuv}}$, where '$R_{DCuv}$' is the resistance of the interconnection between DC buses 'u' and 'v'.

Now, for the a^{th} VSC, the converter losses are [13,23,24].

$$P_{lossa} = a_1 + b_1 I_{sha} + c_1 I_{sha}^2 \tag{7}$$

where 'a_1' indicates the VSC losses at no load, 'b_1' and 'c_1' are constants representative of the linear and quadratic dependency of the VSC losses on the converter current magnitude (I_{sha}), respectively.

Also, from Fig. 2, by virtue of the power balance at its AC and DC sides,

$$\mathrm{Re}(\mathbf{V_{sha}}\mathbf{I_{sha}^*}) + \sum_{v=1}^{q} V_{DCa} I_{DCa} = -P_{lossa}$$

Substituting Eqs. (1), (6) and (7) in the above equation, we get, for the a^{th} VSC,

$$(m_a c V_{DCa})^2 y_{sha}\cos\phi_{sha} - m_a c V_{DCa} V_{i+a-1} y_{sha}\cos(\theta_{sha} - \theta_{i+a-1} - \phi_{sha}) + \sum_{v=1}^{q} V_{DCa} V_{DCv} Y_{DCav} + P_{lossa} = 0$$

$$\text{or,} \quad f_{1a} = 0 \quad \forall\, a, 1 \leqslant a \leqslant q \tag{8}$$

where

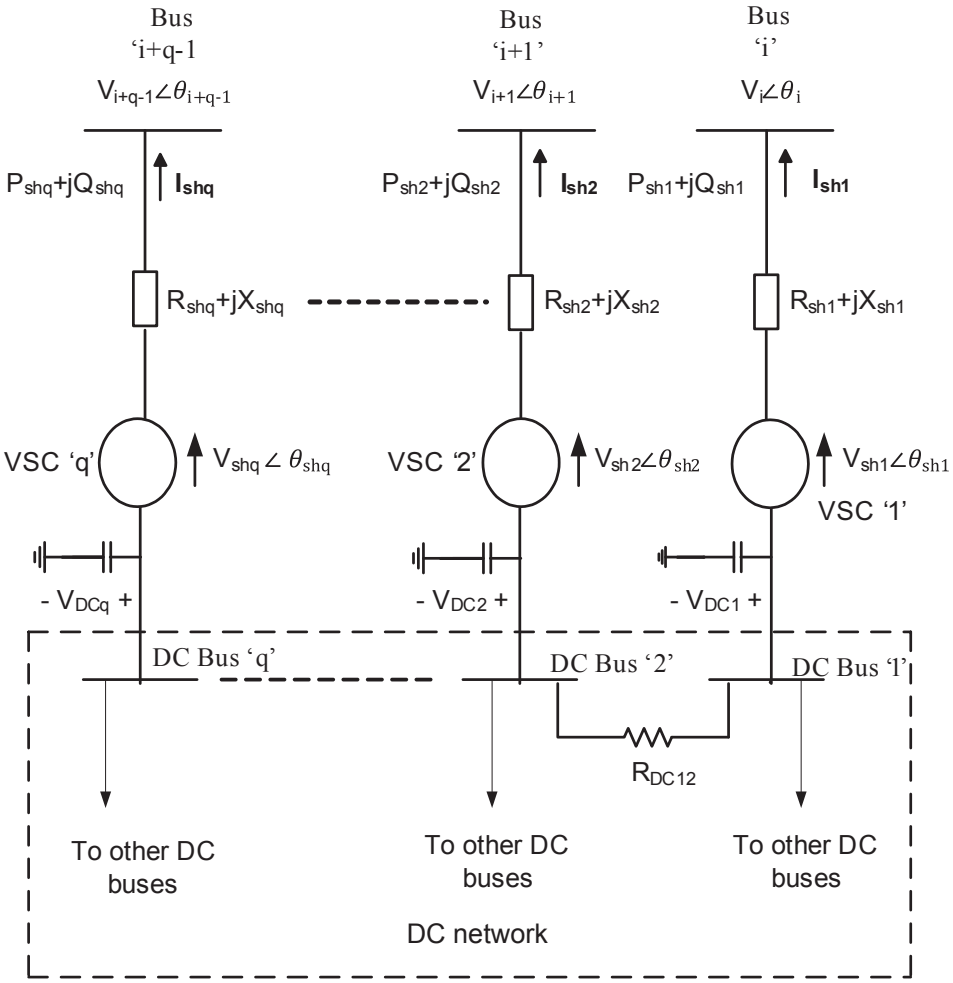

Fig. 2. Equivalent circuit of AC-MTDC system.

$$f_{1a} = (m_a c V_{DCa})^2 y_{sha}\cos\phi_{sha} - m_a c V_{DCa} V_{i+a-1} y_{sha}\cos(\theta_{sha} - \theta_{i+a-1} - \phi_{sha}) + \sum_{v=1}^{q} V_{DCa} V_{DCv} Y_{DCav} + P_{lossa}$$

Eq. (8) represents 'q' independent equations (for 'q' VSCs).

Now, in the AC-MTDC system {Fig. 2)} with 'q' VSCs, it is important to note that not more than '(q-1)' line active power flows {Eq. (4)} can be specified.

If it is assumed that VSC 1 controls its DC side voltage 'V_{DC1}' i.e. DC slack bus control is employed for DC terminal 1, then, for the rest of the '(q-1)' VSCs controlling the line active power flows, we get,

$$P_{sha}^{sp} - P_{sha}^{cal} = 0 \quad \forall\, a,\ 2 \leqslant a \leqslant q \tag{9}$$

In a similar manner, for the line reactive power flows,

$$Q_{sha}^{sp} - Q_{sha}^{cal} = 0 \quad \forall\, a,\ 1 \leqslant a \leqslant q \tag{10}$$

Thus, we get '(2q-1)' independent equations.

Instead of PQ control mode, if a VSC operates in the PV one, Eq. (10) changes to:

$$V_{i+a-1}^{sp} - V_{i+a-1}^{cal} = 0 \quad \forall\, a,\ 1 \leqslant a \leqslant q \tag{11}$$

In Eqs. (9)–(11), V_{i+a-1}^{sp}, P_{sha}^{sp} and Q_{sha}^{sp} are specified values while V_{i+a-1}^{cal}, P_{sha}^{cal} and Q_{sha}^{cal} are calculated values {using Eqs. (4) and (5)}.

3. DC voltage droop control in MTDC systems

In DC voltage droop control [15–23], multiple converters participate in the DC voltage control scheme. Both linear and nonlinear DC voltage droop characteristics are elaborated below.

(1) Voltage-Power (V-P) droop

If the ath VSC follows a linear V-P droop characteristic, its rectifying power can be expressed as,

$$P_{DCa} = R_a(V_{DCa}^{*} - V_{DCa}) + P_{DCa}^{*} \tag{12}$$

where 'V_{DCa}^{*}' and 'P_{DCa}^{*}' represent the DC voltage and power references of its droop characteristics and 'R_a' is the droop control gain.

(2) Voltage-Current (V-I) droop

If the ath VSC follows a linear V-I droop characteristic; the net DC current injection at its terminal can be expressed as,

$$I_{DCa} = R_a(V_{DCa}^{*} - V_{DCa}) + I_{DCa}^{*} \tag{13}$$

where 'I_{DCa}^{*}' and 'V_{DCa}^{*}' are the DC current and voltage references of its droop line and 'R_a' is the droop control gain.

Thus, the rectifying power of the VSC can be expressed as,

$$P_{DCa} = V_{DCa}[R_a(V_{DCa}^{*} - V_{DCa}) + I_{DCa}^{*}] \tag{14}$$

Fig. 3 depicts linear V-P and V-I droop characteristics for any arbitrary VSC 'a'.

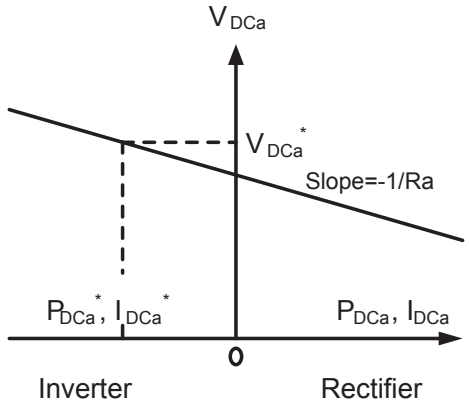

Fig. 3. Linear Voltage Droop Characteristic of the a[th] VSC.

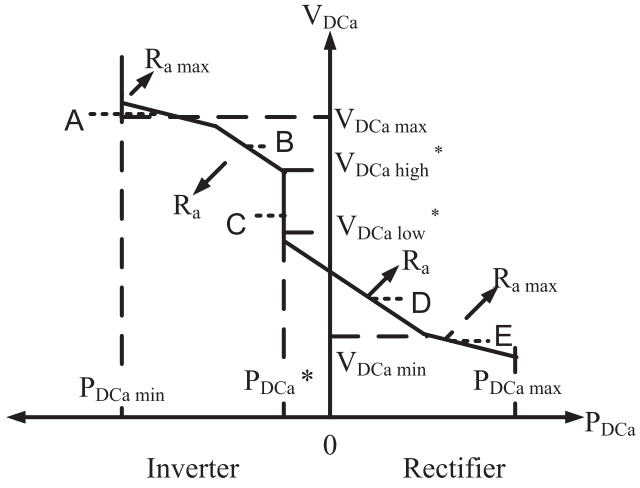

Fig. 4. Nonlinear Voltage Droop Characteristic of the a[th] VSC.

3.1. Computation of 'V^*_{DCa}' and 'P^*_{DCa}'

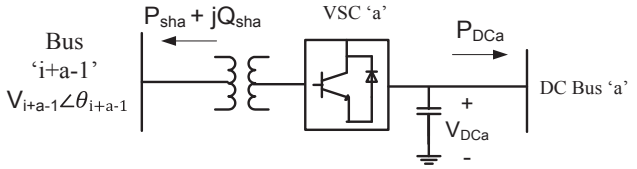

Fig. 5. Power flows for the a[th] VSC connected to its AC bus '(i + a-1)'

The values of the DC voltage and power references 'V^*_{DCa}', 'P^*_{DCa}' and 'I^*_{DCa}' in Eqs. (12) and (13) for all the 'q' converters are either pre specified or obtained from a DC power-flow. If DC slack bus control is adopted, then, by convention, the voltage 'V^*_{DC1}' (of DC terminal 1) is specified and it does not operate on droop control. This problem can be circumvented if the average voltage of all the 'q' DC terminals 'V^*_{DCav}' is specified instead of 'V^*_{DC1}' [22]. In that case, the DC power-flow equations are as follows:

Solve $\mathbf{V^*_{DC}}$ specified $\mathbf{P^*_{DC}}$ and V^*_{DCav}

$\mathbf{V^*_{DC}} = [V^*_{DC1}...V^*_{DCq}]^T$, $\mathbf{P^*_{DC}} = [P^*_{DC2}...P^*_{DCq}]^T$.

Subsequently, P^*_{DC1} and 'I^*_{DCa}' ($1 \le a \le q$) can be computed.

(3) Voltage-Power (V-P) droop with dead-band

In practical DC grids, the droop characteristics are combinations of multiple linear or nonlinear functions of the DC voltage. Fig. 4 shows a typical nonlinear voltage droop characteristics with dead-band and voltage limits. If the a[th] VSC follows a nonlinear droop characteristic as shown in Fig. 4, the converters operate in constant power control mode when DC voltage is maintained between '$V^*_{DCa\,high}$' and '$V^*_{DCa\,low}$'. When the DC voltage lies outside the dead-band zone, the DC terminal follows the linear V-P characteristic. Again, beyond a threshold DC voltage, the droop control gain increases ($R_{a\,max}$) to maintain the DC voltage within an acceptable limit for the stability of the DC grid.

The composite droop characteristic is shown in Fig. 4 and can be expressed as

$$P_{DCa} = R_{amax}(V_{DCamax} - V_{DCa}) + [R_a(V^*_{DCahigh} - V_{DCamax}) + P^*_{DCa}] \quad \text{for } V_{DCa} \geqslant V_{DCamax} \tag{15}$$

$$= R_a(V^*_{DCahigh} - V_{DCa}) + P^*_{DCa} \quad \text{for } V^*_{DCahigh} < V_{DCa} < V_{DCamax} \tag{16}$$

$$= 0.\,(V^*_{DCahigh} - V_{DCa}) + P^*_{DCa} \quad \text{for } V^*_{DCalow} \leqslant V_{DCa} \leqslant V^*_{DCahigh} \tag{17}$$

$$= R_a(V^*_{DCalow} - V_{DCa}) + P^*_{DCa} \quad \text{for } V^*_{DCamin} < V_{DCa} < V^*_{DCalow} \tag{18}$$

$$= R_{amax}(V_{DCamin} - V_{DCa}) + [R_a(V^*_{DCalow} - V_{DCamin}) + P^*_{DCa}] \quad \text{for } V_{DCa} \leqslant V_{DCamin} \tag{19}$$

In this scheme, the droop control gains can be specified according to the rating of the converters to share the additional power.

4. Modeling of AC-MTDC systems with DC voltage droop control (Model 'A')

Let us assume now that all the 'q' VSCs in the AC-MTDC system shown in Fig. 2 operate on droop control. To simplify matters, let all the 'q' VSCs follow linear V-P droops. Then, for the a[th] VSC ($1 \leqslant a \leqslant q$), from Eqs. (6) and (12), we have,

$$\sum_{v=1}^{q} V_{DCa}V_{DCv}Y_{DCav} = P_{DCa} = R_a(V^*_{DCa} - V_{DCa}) + P^*_{DCa}$$

$$\text{or,} \quad \sum_{v=1}^{q} V_{DCa}V_{DCv}Y_{DCav} + R_aV_{DCa} - R_aV^*_{DCa} - P^*_{DCa} = 0 \tag{20}$$

Let us assume that,

$$f_{2a} = \sum_{v=1}^{q} V_{DCa}V_{DCv}Y_{DCav} + R_aV_{DCa} - R_aV^*_{DCa} - P^*_{DCa} = 0 \tag{21}$$

The Eq. (21) can also be written as,

$f_{2a} = 0 \quad \forall\, a, \quad 1 \leqslant a \leqslant q$

Eq. (21) represents 'q' independent equations for the 'q' VSCs.

Now, two distinctly different models can be realized depending on whether the values of 'V^*_{DCa}' and 'P^*_{DCa}' are specified or not. These are elaborated below.

4.1. Model 'A': Values of '$\mathbf{V^*_{DCa}}$' and '$\mathbf{P^*_{DCa}}$' are known apriori

In some models [22], the values of 'V^*_{DCa}' and 'P^*_{DCa}' for all the 'q' converters are pre-specified, having been obtained from a DC power-flow, or otherwise. In such cases, the 'q' independent droop equations represented by Eq. (21) are sufficient to compute the values of the DC bus voltages 'V_{DCa}' directly, and subsequently, the DC bus power injections 'P_{DCa}'($1 \leqslant a \leqslant q$). Once '$P_{DCa}$' are known, for the AC-MTDC power-flow, the active powers 'P_{sha}' {Eq. (9)} in the lines joining the '(q-1)' VSCs to their corresponding AC buses cannot be specified, as this would be tantamount to knowing the losses in the converter transformers, prior to the power-flow. This is detailed in Fig. 5. This is not in line with practical considerations which are targeted to maintain a specified 'P_{sha}'. This is a major drawback of the model.

Now, under the presumption that in the AC system with 'n' buses, the first 'p' buses are voltage controlled and bus '1' is the slack bus, the

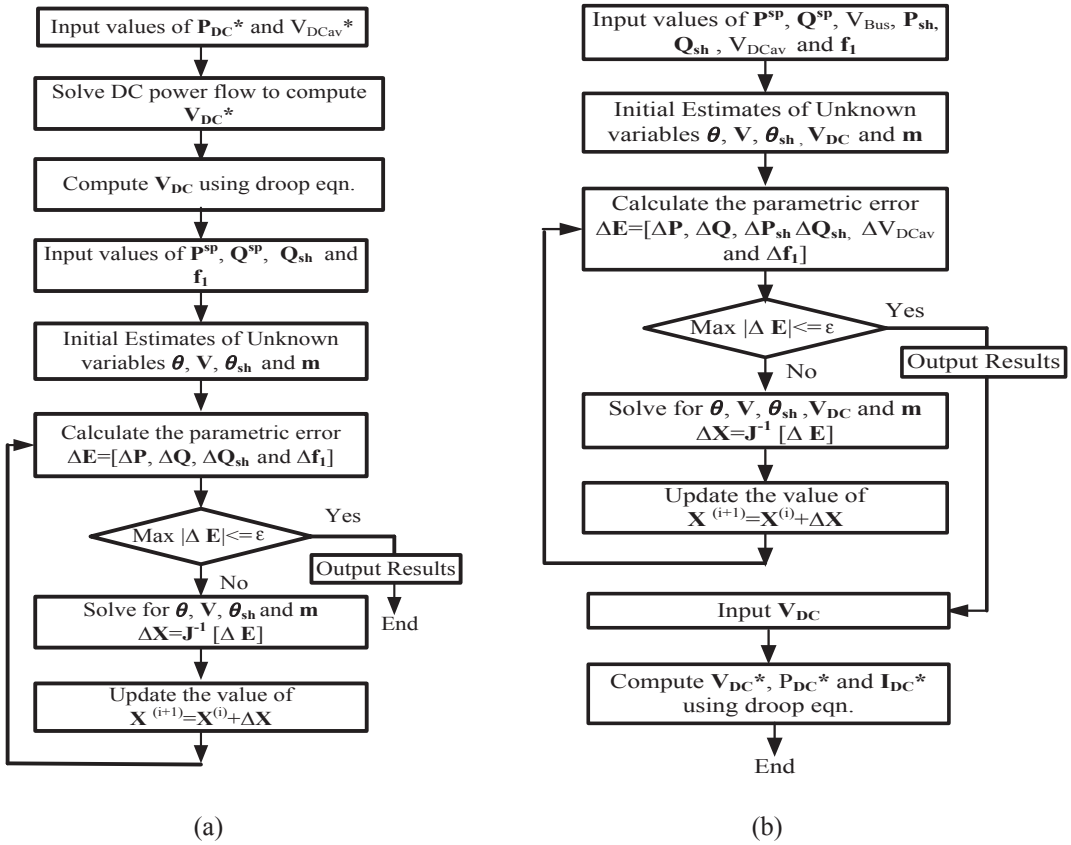

Fig. 6. Flow charts of the proposed approach with. (a) Model A. (b) Model B.

Table 1
First AC-MTDC case study (slack bus control).

Base case power-flow (IN = 6 and PT = 0.56); $\mathbf{V_{268}}$ = 0.9684∠−21.01; $\mathbf{V_{272}}$ = 0.9811∠−19.46; $\mathbf{V_{273}}$ = 1.0058∠−17.47		
Given quantities	Solution	
	AC Buses	VSC
V_{DC1} = 3; Q_{sh1} = 0.35; Q_{sh2} = 0.1; Q_{sh3} = 0.09; P_{sh2} = 0.3; P_{sh3} = 0.4;	$\mathbf{V_{268}}$ = 1.0052∠−48.6890; $\mathbf{V_{272}}$ = 1.0174∠−39.7899; $\mathbf{V_{273}}$ = 1.0316∠−3.5159; DC Power Converter loss (%) IN = 6; PT = 1.11;	θ_{sh1} = −53.3432; θ_{sh2} = −38.1517; θ_{sh3} = −1.3870; m_1 = 0.9830; m_2 = 0.9702; m_3 = 0.9834; V_{DC2} = 2.9970; V_{DC3} = 2.9955; P_{DC1} = 0.4520; P_{DC2} = −0.0857; P_{DC3} = −0.3656; P_{loss1} = 1.73; P_{loss2} = 1.23; P_{loss3} = 1.28;

unified AC-MTDC power-flow problem corresponding to model 'A' is of the form:

Compute: θ, **V**, **X**
Given: **P**, **Q**, **R**

with

$$\theta = [\theta_2 ... \theta_n]^T, \quad \mathbf{V} = [V_{p+1} ... V_n]^T, \quad \boldsymbol{\theta_{sh}} = [\theta_{sh1} ... \theta_{shq}]^T, \quad \mathbf{m} = [m_1 ... m_q]^T, \quad \mathbf{X} = [\boldsymbol{\theta}_{sh}^T \mathbf{m}^T]^T$$

$$\mathbf{P} = [P_2 ... P_n]^T, \quad \mathbf{Q} = [Q_{p+1} ... Q_n]^T, \quad \mathbf{Q_{sh}} = [Q_{sh1} ... Q_{shq}],$$

$$\mathbf{f_1} = [f_{11} ... f_{1q}], \quad \mathbf{R} = [\mathbf{Q_{sh}} \mathbf{f_1}]^T$$

For the above model, it is assumed that all the 'q' VSCs control their line reactive power flows.

The Newton power flow equation is

$$\mathbf{J}[\Delta\theta^T \Delta\mathbf{V}^T \Delta\boldsymbol{\theta}_{sh}^T \Delta\mathbf{m}^T]^T = [\Delta\mathbf{P}^T \Delta\mathbf{Q}^T \Delta\mathbf{R}^T]^T \quad (22)$$

where **J** is the power-flow Jacobian.

In Eq. (22), 'Δ**P**', 'Δ**Q**' and 'Δ**R**' represent the mismatch vectors while $\Delta\theta$, Δ**V**,$\Delta\boldsymbol{\theta}_{sh}$ and Δ**m** represent the correction vectors. It may be noted that if a VSC operates in the PV control mode (instead of PQ), the voltage magnitude of its AC terminal bus will be a specified quantity instead of the line reactive power flow and the Jacobian matrix **J** needs to be appropriately modified. It can be observed that 'V_{DCa}' ($1 \leqslant a \leqslant q$) can be solved using Eq. (20), independent of the AC-MTDC power-flow {Eq. (22)}, if 'V^*_{DCa}' and 'P^*_{DCa}' are known.

After all the unknowns are solved, the line active power-flows 'P_{sha}' can be computed {using Eq. (4)}.

Thus, to summarize, Model 'A' addresses the problem "given the DC voltage and power (or current) references of the VSC droop lines and

Table 2
First AC-MTDC case study (Droop model 'A').

DC (3-terminal) power-flow

Given quantities	Solution
V^*_{DCav} = 3; P^*_{DC2} = 0.2; P^*_{DC3} = 0.3;	DC power-flow converged in three iterations V^*_{DC1} = 2.9972; V^*_{DC2} = 3.0011; V^*_{DC3} = 3.0017; P^*_{DC1} = −0.4993; I^*_{DC3} = 0.0999; IN = 3; PT = 0.024;

Computation of V_{DC} from droop equations

Given quantities	Solution
V^*_{DC1} = 2.9972; V^*_{DC2} = 3.0011; V^*_{DC3} = 3.0017; P^*_{DC1} = − 0.4993; P^*_{DC2} = 0.2; I^*_{DC3} = 0.0999; R_1 = 20; R_2 = 15; R_3 = 10;	V_{DC1} = 2.9972; V_{DC2} = 3.0011; V_{DC3} = 3.0017; IN = 4; PT = 0.076;

AC-MTDC power-flow with droop control
(VSCs connected to AC buses 268, 272 and 273)

Given quantities	Solution	
	AC buses	VSC
V_{DC1}= 2.9972; V_{DC2}= 3.0011; V_{DC3}= 3.0017; Q_{sh1}= -0.07; Q_{sh2}= -0.06; Q_{sh3} =-0.08;	$\mathbf{V_{268}}$ = 0.8959∠−7.624; $\mathbf{V_{272}}$ = 0.8975∠−11.0284 $\mathbf{V_{273}}$ = 0.9562∠−30.7860; $\mathbf{P_{sh2}}$ = **−0. 2121**; $\mathbf{P_{sh3}}$ = **−0. 3126**; DC Power Converter loss (%) IN = 6; PT = 1.17;	θ_{sh1} = −4.1328; m_1 = 0.8402; θ_{sh2} = −12.5438; m_2 = 0.8396; $\theta_{\mathbf{sh3}}$ = −32.7574; m_3 = 0.8933; P_{DC1} = −0.4993; P_{DC2} = 0.2; P_{DC3} = 0.3; P_{loss1} = 1.39; P_{loss2} = 1.2; P_{loss3} = 1.25;

Table 3
Second AC-MTDC case study (Droop model 'B').

AC-MTDC power-flow with droop control
(VSCs connected to AC buses 268, 272 and 273)

Given quantities	Solution	
	AC buses	VSC
V_{DCav}= 3.0; P_{sh2} =0.3; P_{sh3}= 0.4; Q_{sh1}= 0.35; Q_{sh2}= 0.1; Q_{sh3}= 0.09;	θ_{268} = −40.6354; θ_{272} = −33.5968; θ_{273} = −3.1191; V_{268} = 1.0860; V_{272} = 1.0919; V_{273} =1.0332; DC Power Converter loss (%) IN = 6; PT = 1.26;	θ_{sh1} = −44.1554; m_1 = 1.0542; V_{DC1} = 3.0040; θ_{sh2} = −32.1725; m_2 = 1.0392; V_{DC2} = 2.9983; $\theta_{\mathbf{sh3}}$ = −0.9967; m_3 = 0.9841; V_{DC3} = 2.9977; P_{DC1} = 0.7268; P_{DC2} = −0.3123; P_{DC3} = −0.4130; P_{loss1} = 1.57; P_{loss2} = 1.22 ; P_{loss3} = 1.29;

Computation of references V^*_{DC} from droop equations

V_{DC1} = 3.0040; V_{DC2} = 2.9983; V_{DC3} = 2.9977; R_1 = 20; R_2 = 15; R_3 = 10;	V^*_{DC1} = 3.004; V^*_{DC2} = 2.9983; V^*_{DC3} = 2.9977; IN = 4; PT = 0.074;

the target line reactive power flows, what should be the line active power flow values ?"

5. Modeling of AC-MTDC systems with DC voltage droop control (Model 'B')

5.1. Model 'B': Values of '$\mathbf{V^*_{DCa}}$' and '$\mathbf{P^*_{DCa}}$' are not known apriori

If the DC voltage ('V^*_{DCa}') and power ('P^*_{DCa}') references of the 'q' VSCs are not known, the DC bus voltages 'V_{DCa}' and hence the DC bus power injections 'P_{DCa}' ($1 \leqslant a \leqslant q$) cannot be computed independently {using Eq. (21)}. This enables the line active power-flow values 'P_{sha}' to be specified control objectives {Fig. 5}, which is in line with practical MTDC control. This is an advantage over model 'A'.

For the above modeling strategy, the unified AC-MTDC power-flow problem is of the form:

Compute: θ, **V**, **X**
Given: **P**, **Q**, **R**

with

$\theta = [\theta_2 ... \theta_n]^T$, $\mathbf{V} = [V_{p+1} ... V_n]^T$, $\theta_{\mathbf{sh}} = [\theta_{sh1} ... \theta_{shq}]^T$, $\mathbf{m} = [m_1 ... m_q]^{\mathbf{T}}$ and

Table 4
Third AC-MTDC case study (non-linear Droop).

DC power-flow

Given quantities	Solution
$V^*_{DCav} = 3$; $P^*_{DC2} = 0.3$; $P^*_{DC3} = 0.2$;	$V^*_{DC1} = 2.9972$; $V^*_{DC2} = 3.0017$; $V^*_{DC3} = 3.0011$; $P^*_{DC1} = -0.4993$; $I^*_{DC3} = 0.0666$; IN = 3; PT = 0.02;

Computation of V_{DC} from droop equations

Given quantities		Solution
$V^*_{DC1} = 2.9972$; $V^*_{DC2} = 3.0017$; $V^*_{DC3} = 3.0011$; $P^*_{DC1} = -0.4993$; $P^*_{DC2} = 0.3$; $I^*_{DC3} = 0.0666$; $V_{DCmax} = 3.014$; $V^*_{DChigh} = 3.008$; $V^*_{DClow} = 3.002$; $V_{DCmin} = 3$; $R_1 = 20$; $R_2 = 15$; $R_3 = 10$; $R_{max} = 30$;		$V_{DC1} = 2.9973$; $V_{DC2} = 3.0018$; $V_{DC3} = 3.0012$; $P_{DC1} = -0.5007$; $P_{DC2} = 0.3035$; $P_{DC3} = 0.1979$;
Converter	Control Mode	IN = 4; PT = 0.05;
1	V-P droop	
2	V-P droop with dead-band	
3	V-I droop	

AC-MTDC power-flow with nonlinear voltage droop control with dead band and limits (VSCs connected to AC buses 268, 272 and 273)

Given quantities	Solution	
	AC buses	VSC
$V_{DC1} = 2.9973$; $V_{DC2} = 3.0018$; $V_{DC3} = 3.0012$; $Q_{sh1} = 0.04$; $Q_{sh2} = 0.06$; $Q_{sh3} = 0.07$;	$\mathbf{V_{268}} = 1.0649\angle -12.3463$; $\mathbf{V_{272}} = 1.0580\angle -15.0685$; $\mathbf{V_{273}} = 1.0118\angle -25.5816$; $\mathbf{P_{sh2}} = \mathbf{-0.3159}$; $\mathbf{P_{sh3}} = \mathbf{-0.2098}$; Converter loss (%) $P_{loss1} = 1.33$; $P_{loss2} = 1.23$; $P_{loss3} = 1.19$; IN = 6; PT = 0.91;	$\theta_{sh1} = -12.3463$; $\theta_{sh2} = -15.0685$; $\theta_{sh3} = -25.5816$; $m_1 = 1.0098$; $m_2 = 1.0024$; $m_3 = 0.9601$;

$$\mathbf{V_{DC}} = [V_{DC1}...V_{DCq}]^{\mathbf{T}}$$

$$\mathbf{X} = [\theta^{\mathbf{T}}_{\mathbf{sh}}\ \mathbf{m^T}\ \mathbf{V^T_{DC}}]^{\mathbf{T}}$$

$$\mathbf{P} = [P_2...P_n]^T, \quad \mathbf{Q} = [Q_{p+1}...Q_n]^T,$$

$$\mathbf{P_{sh}} = [P_{sh2}...P_{shq}], \quad \mathbf{Q_{sh}} = [Q_{sh1}...Q_{shq}], \quad \mathbf{f}_1 = [f_{11}...f_{1q}] \quad \text{and} \quad \mathbf{R} = [\mathbf{P_{sh}}\mathbf{Q_{sh}}V_{DCav}\mathbf{f}_1]^T$$

For this model, it is assumed that VSC 1 controls the average voltage 'V_{DCav}' of all the 'q' DC terminals while the other '(q-1)' VSCs control their line active power flows. It is again assumed that all the 'q' VSCs control their line reactive power flows.

It may be noted that if a VSC operates in the PV control mode (instead of PQ), the Jacobian matrix **J** needs to be appropriately modified.

The unified AC-MTDC power flow equation is

$$\mathbf{J}[\Delta\theta^{\mathbf{T}}\ \Delta\mathbf{V}^{\mathbf{T}}\ \Delta\theta^{\mathbf{T}}_{\mathbf{sh}}\ \Delta\mathbf{m}^{\mathbf{T}}\ \Delta\mathbf{V}^{\mathbf{T}}_{\mathbf{DC}}]^{\mathbf{T}} = [\Delta\mathbf{P}^{\mathbf{T}}\ \Delta\mathbf{Q}^{\mathbf{T}}\ \Delta\mathbf{R}^{\mathbf{T}}]^{\mathbf{T}} \tag{23}$$

where **J** is the power-flow Jacobian.Fig. 6(a) and (b) depict the flow charts of the proposed approach for droop control models 'A' and 'B' respectively.

If a VSC operates in the PV control mode (instead of PQ), the Jacobian matrix **J** {in Eq. (23)} needs to be appropriately modified.

It is important to note that subsequent to 'V_{DCa}' ($1 \leqslant a \leqslant q$) being obtained from the AC-MTDC power-flow {Eq. (23)}, 'P_{DCa}' ($1 \leqslant a \leqslant q$) is computed. Thereafter, the DC voltage ('V^*_{DCa}') references of the 'q' VSC droop lines can be computed from the droop equations {Eq. (24)}, as given below.

Eq. (12) can be written as,

$$\sum_{v=1}^{q} V^*_{DCa}V^*_{DCv}Y_{DCav} + R_aV^*_{DCa} - R_aV_{DCa} - P_{DCa} = 0 \tag{24}$$

After 'V^*_{DCg}' ($1 \leqslant g \leqslant q$) are computed, the power ('P^*_{DCg}') or the current ('I^*_{DCg}') references are also computed.

Thus, to summarize, Model 'B' addresses the problem "given the target line active and reactive power flows, what should be the voltage and power references of the VSC droop lines?"

6. Case studies and results

For validation of the above model, a large number of studies were executed by employing diverse DC voltage control strategies on MTDC grids with different topologies embedded within the IEEE 300-bus network [25]. In all the occurrences, the VSC constant was selected as $c = \frac{1}{2\sqrt{2}}$ [4]. Also, for all the VSC coupling transformers, $R_{sha} = 0.001$ p.u. and $X_{sha} = 0.1$ p.u. ($\forall$ a, $1 \leqslant a \leqslant q$). The converter loss constants 'a_1', 'b_1' and 'c_1' are chosen as 0.011, 0.003 and 0.0043, respectively [23]. 'IN' and 'PT' denote the iteration number and the processing time in seconds, pertaining to a 1.99 GHz Dell PC. In all the results given in Tables 1–7, values of bus voltages, powers, currents and droop control gains are denoted in p.u. while phase angles are denoted in degrees.

6.1. IEEE-300 bus system integrated with three terminal DC network

For the above AC-DC hybrid system, four case studies are carried out.

Table 5
Fourth AC-MTDC case study (Droop model 'A').

Base case power-flow (IN = 6 and PT = 0.56);
$\mathbf{V_{266}}$ = 1.0114∠−11.2446; $\mathbf{V_{268}}$ = 0.9684∠−21.0123; $\mathbf{V_{270}}$ = 1.0114∠−11.3193;
$\mathbf{V_{271}}$ = 0.9978∠−17.6745; $\mathbf{V_{272}}$ = 0.9811∠−19.4562; $\mathbf{V_{273}}$ = 1.0058∠−17.4683;
$\mathbf{V_{275}}$ = 0.9654∠−23.3051;
$\mathbf{V_{291}}$ = 0.964∠−21.1093;

DC (3-terminal) power-flow

Given quantities	Solution
V^*_{DCav} = 3; P^*_{DC2} = −0.2118; P^*_{DC3} = −0.3124; P^*_{DC4} = −0.2621; P^*_{DC5} = −0.2621; P^*_{DC6} = −0.2621; P^*_{DC7} = −0.2119; P^*_{DC8} = −0.3627;	DC power-flow converged in three iterations V^*_{DC1} = 3.0523; V^*_{DC2} = 3.0031; V^*_{DC3} = 2.9710; V^*_{DC4} = 2.9530; V^*_{DC5} = 3.0480; V^*_{DC6} = 3.0305; V^*_{DC7} = 2.9837; V^*_{DC8} = 2.9583; P^*_{DC1} = 1.9246; P^*_{DC2} = −0.2118; P^*_{DC3} = −0.3124; P^*_{DC4} = −0.2621; I^*_{DC5} = −0.0860; I^*_{DC6} = −0.0865; I^*_{DC7} = −0.0710; I^*_{DC8} = −0.1226; IN = 4; PT = 0.0187;

Computation of V_{DC} from droop equations

Given quantities	Solution
DC power-flow converged in three iterations V^*_{DC1} = 3.0523; V^*_{DC2} = 3.0031; V^*_{DC3} = 2.9710; V^*_{DC4} = 2.9530; V^*_{DC5} = 3.0480; V^*_{DC6} = 3.0305; V^*_{DC7} = 2.9837; V^*_{DC8} = 2.9583; P^*_{DC1} = 1.9246; P^*_{DC2} = −0.2118; P^*_{DC3} = −0.3124; P^*_{DC4} = −0.2621; I^*_{DC5} = −0.0860; I^*_{DC6} = −0.0865; I^*_{DC7} = −0.0710; I^*_{DC8} = −0.1226; R_1 = 20; R_2 = 15; R_3 = 10; R_4 = 20; R_5 = 15; R_6 = 10; R_7 = 20; R_8 = 15;	V_{DC1} = 3.0523; V_{DC2} = 3.0031; V_{DC3} = 2.9710; V_{DC4} = 2.9530; V_{DC5} = 3.0480; V_{DC6} = 3.0305; V_{DC7} = 2.9837; V_{DC8} = 2.9583; IN = 4; PT = 0.077;

AC-MTDC power-flow with droop control
(VSCs connected to AC buses 266, 268, 270, 271, 272, 273, 275 and 291)

Given quantities	Solution	
	AC buses	VSC
V_{DC1} = 3.0523; V_{DC2} = 3.0031; V_{DC3} = 2.9710; V_{DC4} = 2.9530; V_{DC5} = 3.0480; V_{DC6} = 3.0305; V_{DC7} = 2.9837; V_{DC8} = 2.9583; Q_{sh1}= 0.08; Q_{sh2}= 0.02; Q_{sh3} =0.08; Q_{sh4}= 0.03; Q_{sh5}= 0.02; Q_{sh6} =0.08; Q_{sh7}= 0.02; Q_{sh8}= 0.01;	$\mathbf{V_{266}}$ = 1.0085∠−11.9694; $\mathbf{V_{268}}$ = 0.9908∠15.3893; $\mathbf{V_{270}}$ = 1.0092∠−11.9907; $\mathbf{V_{271}}$ = 0.9770∠9.0723; $\mathbf{V_{272}}$ = 0.9900∠13.9005; $\mathbf{V_{273}}$ = 1.0204∠−2.1020; $\mathbf{V_{275}}$ = 0.9662∠32.6953; $\mathbf{V_{291}}$ = 1.0126∠16.5262; $\mathbf{P_{sh2}}$ = **0. 2**; $\mathbf{P_{sh3}}$ = **0. 3**; $\mathbf{P_{sh4}}$ = **0. 25**; $\mathbf{P_{sh5}}$ = **0. 25**; $\mathbf{P_{sh6}}$ = **0. 25**; $\mathbf{P_{sh7}}$ = **0. 2**; $\mathbf{P_{sh8}}$ = **0. 35**; DC Power P_{DC1} = 1.9246; P_{DC2} = −0.2118; P_{DC3} = −0.3124; P_{DC4} = −0.2621; P_{DC5} = −0.2621; P_{DC6} = −0.2621; P_{DC7} = −0.2119; P_{DC8} = −0.3627; Converter loss (%) P_{loss1} = 3.3134; P_{loss2} = 1.1785; P_{loss3} = 1.2330; P_{loss4} = 1.2059; P_{loss5} = 1.2036; P_{loss6} = 1.2056; P_{loss7} = 1.1810; P_{loss8} = 1.2552; IN = 6; PT = 1.033;	θ_{sh1} = −22.8271; θ_{sh2} = 16.5524; θ_{sh3} = −10.3216; θ_{sh4} = 10.5657; θ_{sh5} = 15.3572; θ_{sh6} = −0.7418; θ_{sh7} = 33.9189; θ_{sh8} = 18.4781; m_1 = 0.9572; m_2 = 0.9355; m_3 = 0.9690; m_4 = 0.9392; m_5 = 0.9210; m_6 = 0.9601; m_7 = 0.9183; m_8 = 0.9700;

The first one corresponds to the DC slack bus model. The second and third ones pertain to linear droop Models 'A' and 'B'. The fourth case study corresponds to nonlinear droop (dead-band) model. For all the four case studies, it is assumed that between any two DC terminals 'u' and 'v', R_{DCuv} = 0.05 p.u. [23].

6.1.1. Case study I: DC voltage slack bus control

For this case study, at the outset, the base case power-flow (in the absence of any MTDC grid) is executed. The results are given in Table 1 (row 1). Then a 3-terminal MTDC grid is integrated with the 300-bus network at AC buses '268', '272' and '273'The converter connected to AC bus '268'operates as a master converter while the converters connected to AC buses '272' and '273' operate as slave converters. Both the slave converters operate in PQ control mode. The specified quantities are shown in first column of Table 1. The power flow solution is shown in second and third columns of Table 1.

Table 6
Fifth AC-MTDC case study (Droop model 'B').

AC-MTDC power-flow with droop control (VSCs connected to AC buses 266, 268, 270, 271, 272, 273, 275 and 291)		
Given quantities	Solution	
	AC buses	VSC
V_{DCav}= 3.0; P_{sh2} = 0.2; P_{sh3} = 0.3; P_{sh4} = 0.25; P_{sh5} = 0.25; P_{sh6} = 0.25; P_{sh7} = 0.2; P_{sh8} = 0.35; Q_{sh1}= 0.08; Q_{sh2}= 0.02; Q_{sh3} =0.08; Q_{sh4}= 0.03; Q_{sh5}= 0.02; Q_{sh6} =0.08; Q_{sh7}= 0.02; Q_{sh8}= 0.01;	$\mathbf{V_{266}}$ = 1.0085∠−11.9694; $\mathbf{V_{268}}$ = 0.9908∠15.3901; $\mathbf{V_{270}}$ = 1.0092∠−11.9907; $\mathbf{V_{271}}$ = 0.9770∠9.0731; $\mathbf{V_{272}}$ = 0.9900∠13.9013; $\mathbf{V_{273}}$ = 1.0204∠−2.1024; $\mathbf{V_{275}}$ = 0.9662∠32.6812; $\mathbf{V_{291}}$ = 1.0126∠16.527; DC Power Converter loss (%) IN = 6; PT = 1.14;	$\theta_{\mathbf{sh1}}$ = −22.8272; $\theta_{\mathbf{sh2}}$ = 16.5535; $\theta_{\mathbf{sh3}}$ = −10.3214; $\theta_{\mathbf{sh4}}$ = 10.5667; $\theta_{\mathbf{sh5}}$ = 15.3581; $\theta_{\mathbf{sh6}}$ = −0.7421; $\theta_{\mathbf{sh7}}$ = 33.9042; $\theta_{\mathbf{sh8}}$ = 18.4787; m_1 = 0.9572; m_2 = 0.9355; m_3 = 0.9690; m_4 = 0.9392; m_5 = 0.9210; m_6 = 0.9601; m_7 = 0.9184; m_8 = 0.9700; V_{DC1} = 3.0523; V_{DC2} = 3.0031; V_{DC3} = 2.9710; V_{DC4} = 2.9530; V_{DC5} = 3.0480; V_{DC6} = 3.0305; V_{DC7} = 2.9837; V_{DC8} = 2.9583; P_{DC1} = 1.9246; P_{DC2} = −0.2118; P_{DC3} = −0.3124; P_{DC4} = −0.2621; P_{DC5} = −0.2621; P_{DC6} = −0.2621; P_{DC7} = −0.2119; P_{DC8} = −0.3627; P_{loss1} = 3.3135; P_{loss2} = 1.1786; P_{loss3} = 1.2330; P_{loss4} = 1.2059; P_{loss5} = 1.2036; P_{loss6} = 1.2056; P_{loss7} = 1.180; P_{loss8} = 1.2551;
Computation of references V^*_{DC} from droop equations		
V_{DC1} = 3.0523; V_{DC2} = 3.0031; V_{DC3} = 2.9710; V_{DC4} = 2.9530; V_{DC5} = 3.0480; V_{DC6} = 3.0305; V_{DC7} = 2.9837; V_{DC8} = 2.9583; R_1 = 20; R_2 = 15; R_3 = 10; R_4 = 20; R_5 = 15; R_6 = 10; R_7 = 20; R_8 = 15;		V^*_{DC1} = 3.0523; V^*_{DC2} = 3.0031; V^*_{DC3} = 2.9710; V^*_{DC4} = 2.9530; V^*_{DC5} = 3.0480; V^*_{DC6} = 3.0305; V^*_{DC7} = 2.9837; V^*_{DC8} = 2.9583; IN = 4; PT = 1.08;

6.1.2. Case study II: DC voltage linear droop control (Model 'A')

For this case study, at the outset, a 3-terminal MTDC grid is integrated with the 300-bus network at AC buses '268', '272' and '273'. While the VSCs having interconnections with AC buses '268' and '272' follow linear V-P droop characteristics, the VSC interconnected with AC bus '273' operates on a linear V-I droop characteristic. The droop control gains of VSCs 1, 2 and 3 are set to 20, 15 and 10, respectively [18–20,22].

Next, a DC power-flow is carried out to obtain the voltage ('V^*_{DCa}'), power ('P^*_{DCa}') and current ('I^*_{DCa}') references ($1 \leqslant a \leqslant 3$) for the droop lines of the VSCs. The results are given in Table 2 (row 3).

Thereafter, the DC voltages {'V_{DCa}'($1 \leqslant a \leqslant 3$)} are computed from the voltage ('V^*_{DCa}'), power ('P^*_{DCa}') and current ('I^*_{DCa}') references using the droop equations {Eq. (15)}. The results are given in Table 2 (row 6).

After obtaining 'V_{DCa}', the AC-MTDC power-flow is executed. The results are given in Table 2 (row 9). The computed values of the active power flows in the (two) lines ('P_{sh2}' and 'P_{sh3}') are shown in bold in Table 2 (row 9). Thus, the line active power-flows are not controllable, unlike the line reactive powers (which are specified). This is a major drawback of model 'A'.

First row of Tables 1 and 2 show that for both the base case and the AC-MTDC power-flow with droop model 'A', 'IN' remains same. But 'PT' is more in the latter case as the number of variables rise.

6.1.3. Case study III: DC voltage linear droop control (Model 'B')

The 3-terminal MTDC grid is again integrated with the AC system at buses '268', '272' and '273'. This study is similar to case study II (model 'A'), except that the line active power-flows (except one) are specified. This is an advantage of model 'B'. The results of the AC-MTDC power-flow are given in Table 3 (row 3).

Subsequent to the AC-MTDC power-flow, using the values of 'V_{DCa}' ($1 \leqslant a \leqslant 3$) obtained (and hence, '$P_{DCa}$' and '$I_{DCa}$'), the DC voltage ('$V^*_{DCa}$') and thereafter, the power ('P^*_{DCa}') and current ('I^*_{DCa}') references for the droop lines of the VSCs are computed using the droop equations {Eq. (19)}. The results are given in Table 3 (row 5).

6.1.4. Case study IV: DC voltage nonlinear droop control (dead-band)

This study is similar to the study of Table 2, except that the VSC connected to AC bus '272' follows nonlinear (dead-band) droop characteristics. The results are shown in Table 4. It is observed that the VSC connected to AC bus '272' is operating at point 'D' of the nonlinear droop characteristics shown in Fig. 4.

From Tables 1–4, it can be observed that 'IN' remains same for slack bus model, linear (Models 'A' and 'B') and nonlinear models. This demonstrates the robustness of the proposed algorithm.

The convergence features of all the five power-flow cases relevant to first row of Table 1, third row of Table 1, Table 2, Table 3 and Table 4, are presented in Fig. 7, respectively. From Fig. 7, it is noticed that the AC-MTDC model shows quadratic convergence characteristics similar to the base case. This validates the proposed method.

6.2. IEEE-300 bus system integrated with eight terminal DC network

For this hybrid AC-DC system, a practical, eight terminal DC network was considered, as reported in [23]. Three case studies were considered, corresponding to linear droop Models 'A', 'B' and nonlinear

Table 7
Sixth AC-MTDC case study (non-linear Droop).

DC power-flow

Given quantities	Solution
$V^*_{DCav} = 3$; $P^*_{DC2} = -0.24$; $P^*_{DC3} = -0.1$; $P^*_{DC4} = -0.2$; $P^*_{DC5} = -0.2621$; $P^*_{DC6} = -0.2621$; $P^*_{DC7} = -0.2119$; $P^*_{DC8} = -0.3627$;	$V^*_{DC1} = 3.0425$; $V^*_{DC2} = 3.0016$; $V^*_{DC3} = 2.9779$; $V^*_{DC4} = 2.9625$; $V^*_{DC5} = 3.0381$; $V^*_{DC6} = 3.0240$; $V^*_{DC7} = 2.9869$; $V^*_{DC8} = 2.9665$; $P^*_{DC1} = 1.6648$; $I^*_{DC3} = -0.0336$; $I^*_{DC4} = -0.0675$; $I^*_{DC5} = -0.0863$; $I^*_{DC6} = -0.0867$; $I^*_{DC7} = -0.0709$; $I^*_{DC8} = -0.1223$; IN = 4; PT = 0.06;

Computation of V_{DC} from droop equations

Given quantities		Solution
$V^*_{DC1} = 3.0425$; $V^*_{DC2} = 3.0016$; $V^*_{DC3} = 2.9779$; $V^*_{DC4} = 2.9625$; $V^*_{DC5} = 3.0381$; $V^*_{DC6} = 3.0240$; $V^*_{DC7} = 2.9869$; $V^*_{DC8} = 2.9665$; $P^*_{DC1} = 1.6648$; $P^*_{DC2} = -0.2400$; $I^*_{DC3} = -0.0336$; $I^*_{DC4} = -0.0675$; $I^*_{DC5} = -0.0863$; $I^*_{DC6} = -0.0867$; $I^*_{DC7} = 3.014$; $V^*_{DChigh} = 3.008$; $= -0.0709$; $I^*_{DC8} = -0.1223$; V_{DCmax} $V^*_{DClow} = 3.002$; $V_{DCmin} = 3$; $R_1 = 20$; $R_2 = 15$; $R_3 = 10$; $R_4 = 20$; $R_5 = 15$; $R_6 = 10$; $R_7 = 20$; $R_8 = 15$; $R_{max} = 30$;		$V_{DC1} = 3.0425$; $V_{DC2} = 3.0017$; $V_{DC3} = 2.9779$; $V_{DC4} = 2.9625$; $V_{DC5} = 3.0382$; $V_{DC6} = 3.0241$; $V_{DC7} = 2.9869$; $V_{DC8} = 2.9665$; $P_{DC1} = 1.6644$; $P_{DC2} = -0.2348$; $P_{DC3} = -0.1005$; $P_{DC4} = -0.2002$; $P_{DC5} = -0.2627$; $P_{DC6} = -0.2632$; $P_{DC7} = -0.2138$; $P_{DC8} = -0.3630$; IN = 4; PT = 0.08;
Converter	Control Mode	
1	V-P droop	
2	V-P droop with dead-band	
3, 4, 5, 6, 7 and 8	V-I droop	

AC-MTDC power-flow with nonlinear voltage droop control with dead band and limits
(VSCs connected to AC buses 266, 268, 270, 271, 272, 273, 275 and 291)

Given quantities	Solution	
	AC buses	VSC
$V_{DC1} = 3.0425$; $V_{DC2} = 3.0017$; $V_{DC3} = 2.9779$; $V_{DC4} = 2.9625$; $V_{DC5} = 3.0382$; $V_{DC6} = 3.0241$; $V_{DC7} = 2.9869$; $V_{DC8} = 2.9665$; $Q_{sh1} = 0.08$; $Q_{sh2} = 0.02$; $Q_{sh3} = 0.08$; $Q_{sh4} = 0.03$; $Q_{sh5} = 0.02$; $Q_{sh6} = 0.08$; $Q_{sh7} = 0.02$; $Q_{sh8} = 0.01$;	$\mathbf{V_{266}} = 1.0091\angle -11.8974$; $\mathbf{V_{268}} = 0.9967\angle 14.5325$; $\mathbf{V_{270}} = 1.0096\angle -11.9597$; $\mathbf{V_{271}} = 0.9821\angle 7.9444$; $\mathbf{V_{272}} = 0.9953\angle 12.8969$; $\mathbf{V_{273}} = 1.0205\angle -1.9418$; $\mathbf{V_{275}} = 0.9625\angle 33.4340$; $\mathbf{V_{291}} = 1.0185\angle 15.6574$; $\mathbf{P_{sh2}} = \mathbf{0.2228}$; $\mathbf{P_{sh3}} = \mathbf{0.0891}$; $\mathbf{P_{sh4}} = \mathbf{0.1884}$; $\mathbf{P_{sh5}} = \mathbf{0.2506}$; $\mathbf{P_{sh6}} = \mathbf{0.2511}$; $\mathbf{P_{sh7}} = \mathbf{0.2020}$; $\mathbf{P_{sh8}} = \mathbf{0.3504}$;	$\theta_{sh1} = -21.2972$; $\theta_{sh2} = 15.8135$; $\theta_{sh3} = -11.4673$; $\theta_{sh4} = 9.0581$; $\theta_{sh5} = 14.3416$; $\theta_{sh6} = -0.5757$; $\theta_{sh7} = 34.6786$; $\theta_{sh8} = 17.5890$; $m_1 = 0.9568$; $m_2 = 0.9415$; $m_3 = 0.9666$; $m_4 = 0.9409$; $m_5 = 0.9290$; $m_6 = 0.9623$; $m_7 = 0.9138$; $m_8 = 0.9729$;
	Converter loss (%) $P_{loss1} = 2.82$; $P_{loss2} = 1.19$; $P_{loss3} = 1.14$; $P_{loss4} = 1.17$; $P_{loss5} = 1.2$; $P_{loss6} = 1.21$; $P_{loss7} = 1.18$; $P_{loss8} = 1.25$; IN = 6; PT = 1.2;	

droop model.

Case study V: DC voltage droop control (Model 'A'): For this study, first, the base case power-flow (in the absence of any MTDC grid) is executed. The results are given in Table 4 (row 1). Then an eight-terminal DC grid is integrated with the 300-bus network at AC buses '266', '268', '270', '271', '272', '273', '275' and '291'. While the four VSCs having interconnections with AC buses '266', '268', '270' and '271' follow linear V-P droop characteristics, the VSCs interconnected with AC buses '272', '273', '275' and '291' operate on linear V-I droop characteristics.

Subsequently, a DC power-flow is carried out to obtain the voltage ('V^*_{DCa}'), power ('P^*_{DCa}') and current ('I^*_{DCa}') references ($1 \leqslant a \leqslant 8$) for the droop lines of the VSCs. The results are given in Table 4 (row 4).

Next, the DC voltages {'V_{DCa}'($1 \leqslant a \leqslant 8$)} are computed from the voltage ('V^*_{DCa}'), power ('P^*_{DCa}') and current ('I^*_{DCa}') references using the droop equations {Eq. (15)}. The results are given in Table 4 (row 7).

After obtaining 'V_{DCa}', the AC-MTDC power-flow is executed. The results are given in Table 4 (row 10). The computed values of the active power flows in the lines ('P_{sh2}', 'P_{sh3}', 'P_{sh4}', 'P_{sh5}', 'P_{sh6}', 'P_{sh7}' and 'P_{sh8}') are shown in bold in Table 4 (row 10). Table 4 shows that for both the base

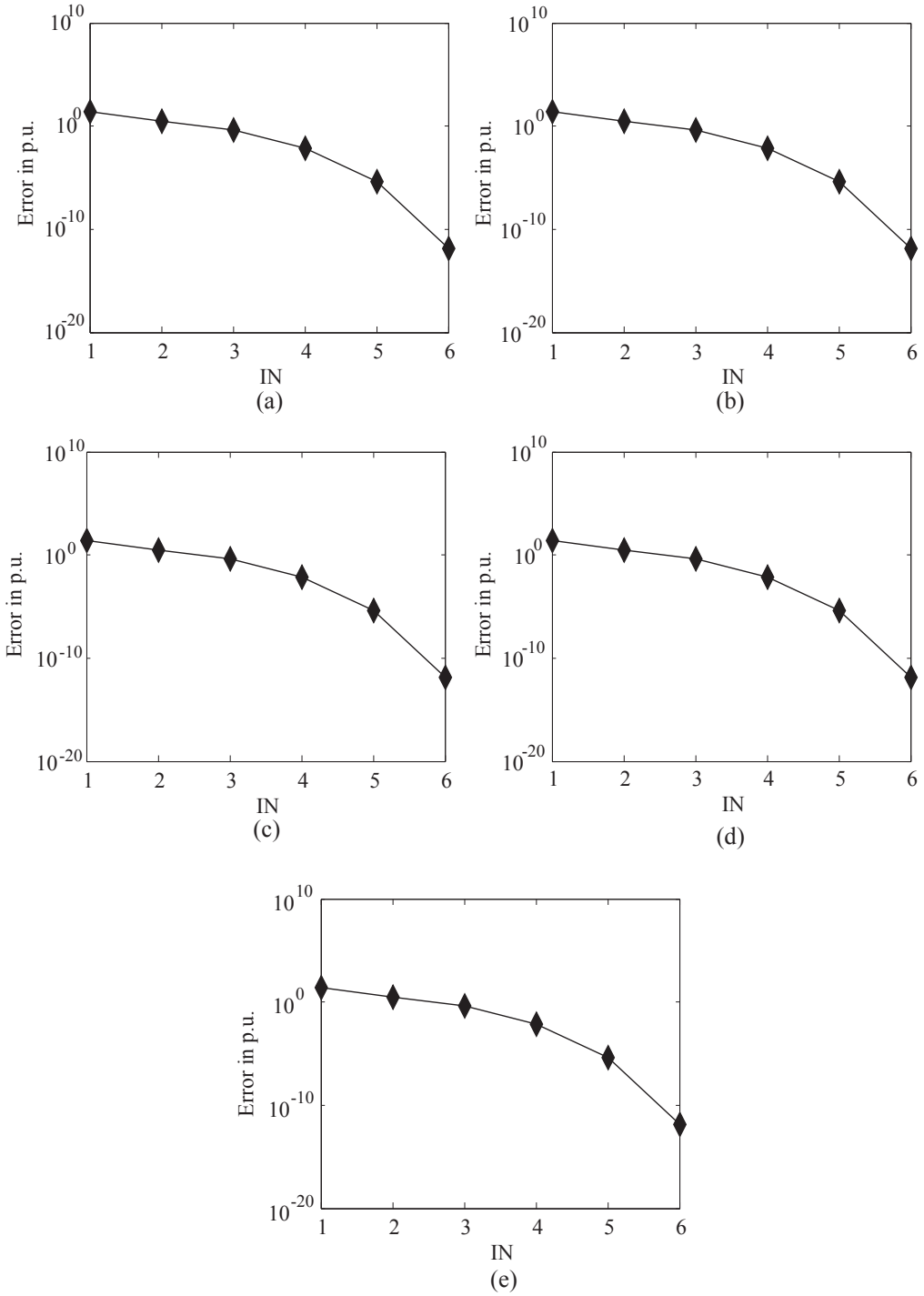

(a) base case (Table 1 row 1), (b) slack bus model (Table 1 row 3), (c) linear droop model 'A' (Table 2 row 9), (d) linear droop model 'B' (Table 3 row 3), (e) nonlinear (dead-band) droop model (Table 4 row 10)

Fig. 7. Convergence features of different case studies.

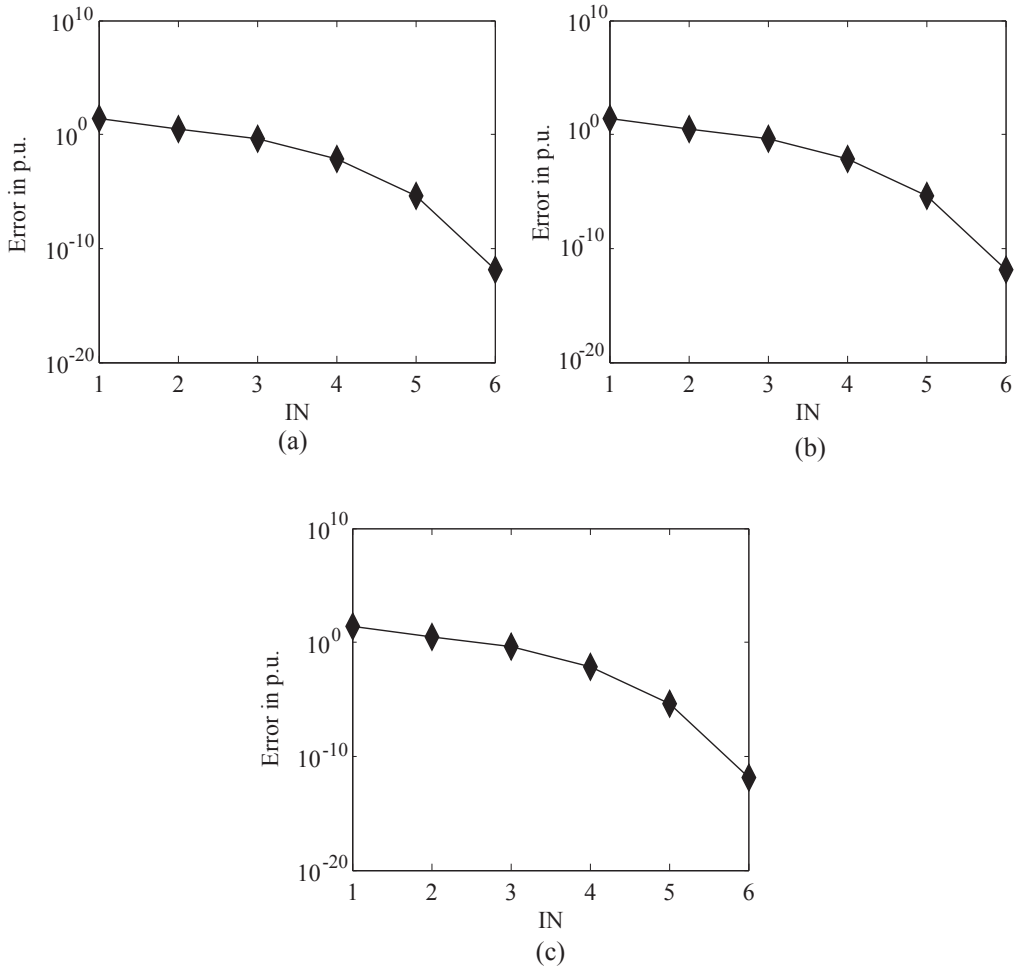

(a) linear droop model 'A' (Table 5 row 9), (b) linear droop model 'B' (Table 6 row 3), (c) nonlinear droop model (Table 7 row 10

Fig. 8. Convergence features of different case studies.

case and the AC-MTDC power-flow with droop model 'A', 'IN' remains same. Thus, the convergence of the proposed method is independent of the topology of the DC network.

6.2.1. Case study VI: DC voltage droop control (Model 'B')

This study is similar to case study IV (model 'A'), except that the line active power-flows (except one) are now specified. The results of the AC-MTDC power-flow are given in Table 5 (row 3). From Tables 4 and 5, it can be observed that 'IN' does not change. Thus, the proposed method is independent of the HVDC control strategy employed.

Subsequent to the AC-MTDC power-flow, using the values of 'V_{DCa}' ($1 \leqslant a \leqslant 8$) obtained (and hence, '$P_{DCa}$' and '$I_{DCa}$'), the DC voltage ('$V^{*}_{DCa}$') and thereafter, the power ('P^{*}_{DCa}') and current ('I^{*}_{DCa}') references for the droop lines of the VSCs are computed using the droop equations {Eq. (19)}. The results are given in Table 5 (row 5).

6.2.2. Case study VII: DC voltage nonlinear droop control (dead-band)

This study is similar to the study of Table 5, except that the VSC connected to AC bus '266' follows VP linear droop characteristics, the VSC connected to AC bus '268' follows VP nonlinear (dead-band) droop characteristics. The other VSCs connected to AC buses '270', '271', '272', '273', '275' and '291' operate in VI linear droop characteristics. The results are shown in Table 7.

From Table 7, It is observed that the VSC connected to AC bus '268' operate at point 'D' of the nonlinear droop characteristics shown in Fig. 4.

From Tables 1–7, it is observed that in all the studies (base case, DC slack bus control, linear droop model 'A' and model 'B' and nonlinear (dead-band) model), 'IN' remains same. Thus, 'IN' is independent of the MTDC grid location, its topology, the DC grid control strategy employed and the operating conditions. This is also reiterated by the similarity of convergence features obtained for case studies IV and V and given in Fig. 8.

Table 8 compares the proposed method with some of the published ones.

7. Conclusions

In this paper, a comprehensive approach for the development of power-flow models of integrated AC-MTDC systems is proposed. Three terminal and eight terminal MTDC grids are embedded within the IEEE 300-bus network for power flow analysis. In this work, the modulation indices and the DC side voltages of the VSCs are obtained directly from the power-flow solution. The MTDC grid control techniques employ both classical methods like DC slack bus control as well as modern ones like DC voltage droop control. Based on the specifications of the line active powers at the terminal ends of the VSCs, two different AC-MTDC power-flow 'A' and 'B' have been developed. It is observed that unlike model 'A', model 'B' facilitates the specification of both line end active and reactive power-flows. Numerous case studies were carried out with different topologies of MTDC grids integrated with the IEEE 300-bus test system. It is observed that the convergence characteristics of the

Table 8
A comparison of the proposed approach with some of the published works.

Ref No.	Tolerance (p.u)	No. of buses		IN	PT (sec)
		AC	DC		
[13]	10^{-6}	9	4	6	0.2
		32	4	7	0.45
[22]	10^{-8}	29	5	Min:3 Max:15	Min:0.37 Max:0.99
[26]	10^{-6}	9	2	3	0.27
	10^{-8}	57	7	4	0.28
Proposed approach	10^{-10}	300	NIL	6	0.56 (Base case)
			3 DC slack bus model	6	1.11 (AC-DC)
			3 (linear droop Model A)	3	0.024 (DC)
				4	0.076 (Droop)
				6	1.17 (AC-DC)
			3 (linear droop Model B)	4	0.074 (Droop)
				6	1.26 (AC-DC)
			3 Nonlinear droop model (dead-band)	3	0.02 (DC)
				4	0.05 (droop)
				6	1.19 (AC-DC)
			8 (droop Model A)	4	0.018 (DC)
				4	0.077 (Droop)
				6	1.033 (AC-DC)
			8 (droop Model B)	4	1.08 (Droop)
				6	1.14 (AC-DC)
			8 Nonlinear droop model (dead-band)	4	0.06 (DC)
				4	0.08 (droop)
				6	1.2 (AC-DC)

proposed method are independent of the MTDC grid location, its topology, the DC grid control technique employed and the operating conditions. A comparison of all the case studies with previously published works is also presented. The results validate the model.

Appendix A. Supplementary material

Supplementary data associated with this article can be found, in the online version, at http://dx.doi.org/10.1016/j.ijepes.2018.04.019.

References

[1] Arrillaga J, Liu YH, Watson NR. Flexible power transmission: The HVDC options. John Wiley & Sons Ltd; 2007.
[2] Sood VK. HVDC and FACTS controllers – applications of static converters in power systems. Kluwer; 2004.
[3] Acha E, Agelidis VG, Lara OA, Miller TJE. Power electronic control in electrical systems. Butterworth: Newnes; 2002.
[4] Padiyar KR. HVDC power transmission systems. 2nd ed. New Age International Publishers; 2012.
[5] Kothari DP, Nagrath IJ. Modern power system analysis. 4th ed. New Delhi: Tata McGraw Hill; 2011.
[6] Yazdani A, Iravani R. Voltage-sourced converters in power systems: modeling, control and applications. Wiley-IEEE Press; 2010. p. 171.
[7] Flourentzou N, Agelidis GV, Demetriades GD. VSC-Based HVDC power transmission systems: an overview. IEEE Trans Power Electron 2009;24(3):592–602.
[8] Asplund G. Application of HVDC light to power system enhancement. Proc IEEE PES winter meeting; 2000.
[9] Blau J. Europe plans a north sea grid. IEEE spectrum; 2010. p. 12–13.
[10] Haileselassie MT, Uhlen K. Power system security in a meshed north sea HVDC grid. IEEE Proc, invited paper, vol. 101, No. 4, 2013. p. 978–90.
[11] Zhang XP. Voltage-sourced converter-based HVDC Models for power flow analysis. IEEE Trans Power Syst 2004;19(4):1877–84.
[12] Camacho AC, Tortelli LO, Acha E, Fuerte-Esquivel RC. Inclusion of a high voltage DC voltage source converter model in a Newton Raphson power flow algorithm. Proc Inst Elect Eng, Gen, Trans Distr 2003;150(6): 691–6.
[13] Baradar M, Ghandhari M. A multi-option unified power flow approach for hybrid AC/DC grids incorporating multi-terminal VSC-HVDC. IEEE Trans Power Syst 2013;28(3):2376–83.
[14] Gengyin L, Ming Z, Jie H, Guangkai L, Haifeng L. Power flow calculation of power systems incorporating VSC-HVDC. Proc Int Conf power system technology (Power Con), vol. 2; 2004. p. 1562–6.
[15] Dierckxsens, C. VSC MTDC systems with distributed slack bus. M.S. thesis, Leuven., Belgium: Katholieke Univ.; 2010.
[16] Chaudhuri NR, Chaudhuri B, Majumdar R, Yazdani A. Multi-terminal direct current grids modelling analysis and control. Wiley: IEEE Press; 2014.
[17] Rouzbehi K, Miranian A, Candela JI, Luna A, Rodriguez P. A generalised voltage droop strategy for control of muti-terminal DC grids. IEEE Trans Ind Applns 2015;51(1):607–18.
[18] Khalik ASA, Massoud AM, Elserougi AA, Ahmed S. Optimum power transmission based droop control design for multi-terminal HVDC of offshore wind farms. IEEE Trans Power Sys 2013;28(3):3401–9.
[19] Bellmunt OG, Liang J, Ekanayake J, Jenkins N. Methodology for droop control dynamic analysis of multiterminal VSC-HVDC grids for offshore wind farms. IEEE Trans Power Delivery 2011;26(4):2476–85.
[20] Zhao X, Li K. Droop setting design for multi-terminal HVDC grids considering voltage deviation impacts. Electr Power Syst Res 2015;123:67–75.
[21] Hertem JDV, Belmans R. VSC MTDC systems with a distributed DC voltage control-a power flow approach. IEEE Trondheim Power Tech 2011:1–6.
[22] Wang W, Barnes M. Power flow algorithms for multi-terminal VSC-HVDC with droop control. IEEE Trans Power Syst 2014;29(4):1721–30.
[23] Cao J, Du W, Wang HF. Minimization of transmission loss in meshed AC/DC grids with VSC-MTDC networks. IEEE Trans Power Syst 2013;28(3):3047–55.
[24] Daelemans G. VSC-HVDC in meshed networks, M. Eng. Thesis, Leuven, Belgium: Katholieke Universiteit Leuven; 2008.
[25] http://www.ee.washington.edu/research/pstca.
[26] Lei J, An T, Du Z, Yuan Z. A general unified AC/DC power flow algorithm with MTDC. IEEE Trans Power Syst 2017;32(4):2837–45.

2017 Conference on Information and Communication Technology (CICT'17)

A High Linearity and Low Noise Shunt Resistive Feedback UWB LNA

Aditi, Malti Bansal
Department of Electronics & Communication Engineering, Delhi Technological University (DTU),
Delhi-110042, India
(maltibansal@gmail.com)

***Abstract*— A shunt resistive feedback CMOS low noise amplifier (LNA) using a pi-matching network has been designed in this paper using 0.13µm CMOS technology for applications in ultra-wideband (UWB) systems. Minimum simulated noise figure is of 1.811 dB value and the maximum linearity of 3 dBm with moderate gain of 11.0037 dB is achieved simultaneously, when operated at 1.2 V power supply, with a 3-dB bandwidth ranging from 3.1 GHz to 10.6 GHz.**

Keywords*— Advanced Design Simulation (ADS) Software, Low Noise Amplifier (LNA), Wideband, Complementary MOSFET (CMOS), Common Source (CS), Common Gate (CG), Noise Figure (NF), Resistive Feedback.

I. INTRODUCTION

The Federal Communication Commission (FCC) in US has approved the ultra-wide band (UWB) in the range of 3.1-10.6 GHz, for use for commercial applications recently [1]. For wireless communication, significant interest has been developed in Ultra-wideband (UWB) technology as it provides, over a wide frequency band spectrum, transmission of data at very low power, high data rate and low cost [2]. It is envisioned that in the ultra-wide band technology, wireless connections will be all home and office cable networks, by featuring hundreds of megabits per seconds. So, this technology is being applied in sensor networks, wireless personal area networks, imaging systems, etc. Since, it relays data within area by providing cost effective, power efficient and large bandwidth circuits, it is specifically most suitable for short-range radios and wireless personal area networks. The multiband OFDM and the direct sequence (DS) are the two ultra-wide band technology approaches, of which, in multiband OFDM, 3.1-10.6 GHz spectrum is divided into 528MHz sub-bands and to transmit data at high data rate (480 Mb/s), OFDM (Orthogonal Frequency Division Multiplexing) is employed while in the direct sequence technique, the 3.1-10.6 GHz spectrum is covered in pulses. Low noise amplifier is required by both the techniques [3] and is the first block of the receiver as it comes directly after the antenna. However, several challenges such as low noise figure (to increase receiver sensitivity), low power consumption (to increase battery life), 50 Ω wide-band input impedance matching (the input matching network is present to ideal resistance of 50 Ω so that the input return loss or input reflection coefficient (S_{11}) is minimum without additional noise introduction.), high gain, etc. are encountered in the designing of low noise amplifier for ultra-wide band, so designing of low noise amplifier is not an easy job. Hence, to achieve desired parameters, many topologies have been explored and developed to design ultra-wide band CMOS low noise amplifier in the recent years, of which inductively degenerated common source low noise amplifier, common gate low noise amplifier and common source resistive feedback low noise amplifier are the popular low noise topologies. The first stage of all the low noise amplifier structures is either common source or common gate configuration but in wide band applications common gate low noise amplifier is preferred over common source inductively degenerated low noise amplifier because common gate low noise amplifier has low power consumption, high linearity, high reverse transmission and good wideband input impedance matching due to low quality factor of input resonant matching network [4],[5]. But it also has high noise figure i.e., poor noise performance. So, common source resistive feedback is an alternative as it provides input impedance matching for broad-band. But it is difficult to achieve input matching, low noise figure and low power consumption simultaneously [6],[7]. The proposed common-source cascode amplifier using shunt feedback topology is shown in Figure 1.

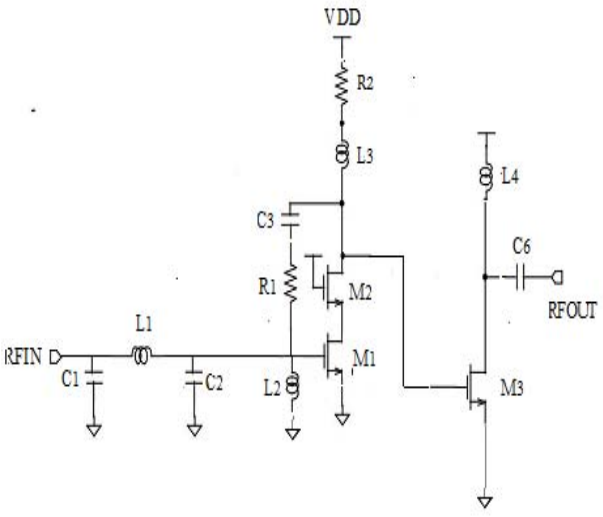

Fig. 1 Proposed Common Source Shunt Resistive Feedback UWB LNA

In general, linearity and gain are two different poles and to balance them is difficult because while improving gain,

978-1-5386-1866-0/17/$31.00 ©2017 IEEE

linearity gets degraded and vice versa. So, pi-matching is used to enhance the forward gain of LNA, by providing additional degree of freedom [8].

II. CIRCUIT DESIGN

The proposed low noise amplifier topology's schematic is shown in Figure 2. One common source transistor and other following common gate transistor, connected in cascode configuration, are present in the first stage of the low noise amplifier. The common source load impedance can be approximated to input impedance which is parallel to parasitic capacitance and the common source stage's gain is not large. Cascoded topology is used because it has negligible Miller effect on M_1 transistor. Here, R_1 and C_3 are used as the feedback resistor and the blocking capacitor respectively. The feedback resistor is in shunt configuration so as to obtain negative feedback and also for broadband matching of input. The negative feedback improves the stability factor and hence, unconditional stability is provided by the amplifier and gain sensitivity of the amplifier is reduced. L_3 and R_2 in series act as loading elements of the cascode stage. For further extending the bandwidth and for achieving high gain, the second stage is is used which is a source follower stage. Pi-matching network is formed by L_1, C_1 and C_2 at input for improvising linearity of the circuit. Furthermore, it also helps to achieve input impedance matching. Since, this is a very simple low noise amplifier topology, therefore, it is suitable for low cost LNA applications (ideally).

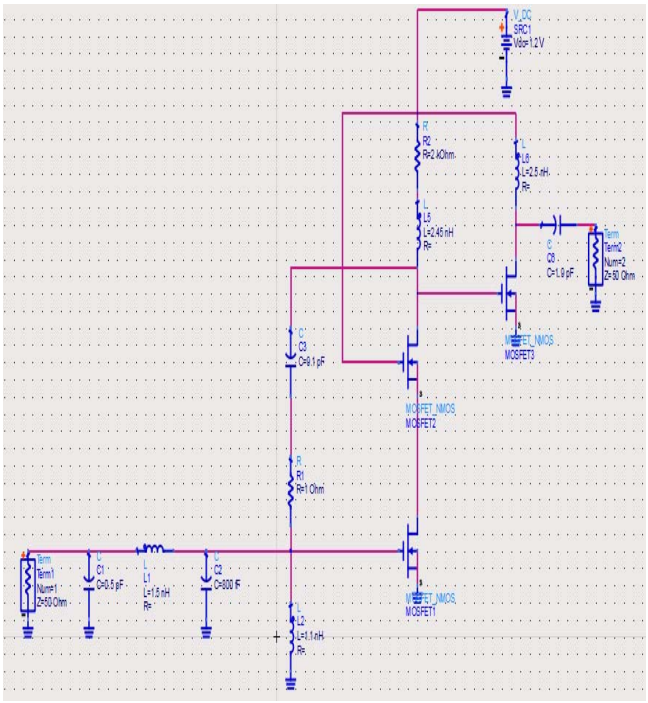

Fig 2. Schematic of Common Source shunt resistive feedback UWB LNA

III. SIMULATION AND RESULTS

The proposed LNA has been designed in a 0.13µm CMOS process and the simulations of the designed LNA were performed using ADS. The circuit operates at 1.2 V power supply. In Figure 3, the input reflection coefficient (S_{11}) is shown and in Figure 5, the power gain (S_{21}) is shown. The circuit has maximum power gain of 11.037 dB over 3.1-10.6 GHz frequency range. The reverse isolation (S_{12}) is shown in Figure 4. The measured reverse isolation is from -14.265 dB to -31.897 dB in the range from 3.1-10.6 GHz. The output reflection coefficient (S_{22}) is shown in Figure 6 and is less than -10 dB. The noise figure of proposed low noise amplifier, shown in Figure 7, is about 1.811 dB. The simulated third order intercept point (IIP3) result for UWB LNA is shown in Figure 8, and IIP3 of 3 dBm is obtained. From the result, it can be concluded that good value of gain and high linearity with low noise figure have been achieved. The simulated amplifier's characteristics summary is presented in Table I. From Table I, compared with other LNA's, the performance of our proposed CMOS LNA is much better as it has the best reported value of noise figure and linearity, in both 0.18µm and 0.13µm technology, in the range of 3.1-10.6 GHz.

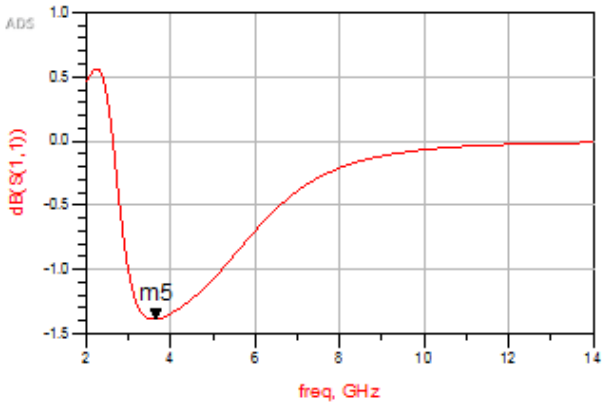

Fig. 3 Input Reflection Coefficient (S_{11})

S_{11} is input reflection coefficient or input return loss. In order to measure S_{11}, a signal is injected at input port and its reflected signal is measured. In this case, no signal is injected into output port. So, it represents the measure of matching of the input impedance to the reference impedance. For 3.1-10.6 GHz frequency range, the S_{11} parameter obtained is -1.390 dB, as shown in Figure 3.

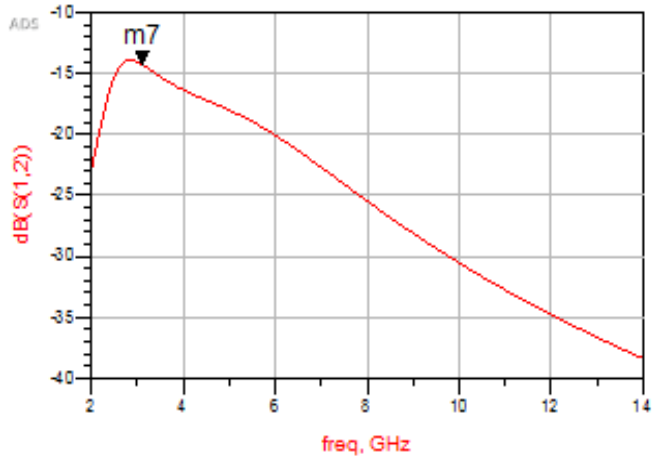

Fig. 4 Reverse Gain/ Reverse Isolation (S_{12})

S_{12} is reverse transmission coefficient or reverse isolation as it measures how much the input signal is reflected back. In S_{12}, a signal is injected into output port, and signal power leaving port is measured. For 3.1-10.6 GHz, the minimum value of S_{12} is less than -10 dB, i.e., -14.265 dB, as shown in Figure 4.

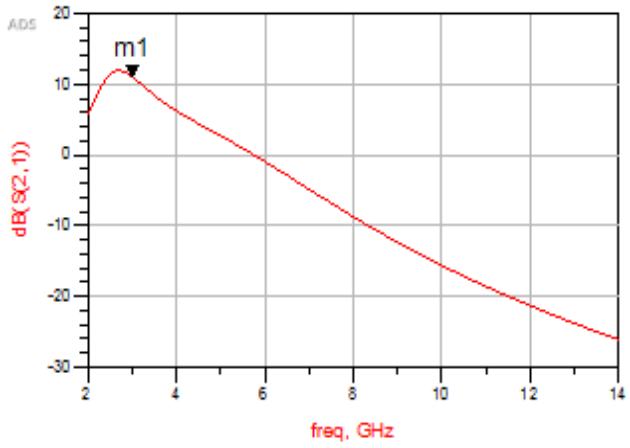

Fig. 5 Forward Gain (S_{21})

S_{21} is forward transmission coefficient or forward gain. If S_{21} is to be measured, a signal is injected at the input port, and the resulting signal power exiting output port is measured. It measures how well the signal goes from input to output. For 3.1-10.6 GHz, the value of maximum gain obtained is 11.037 dB, as shown in Figure 5.

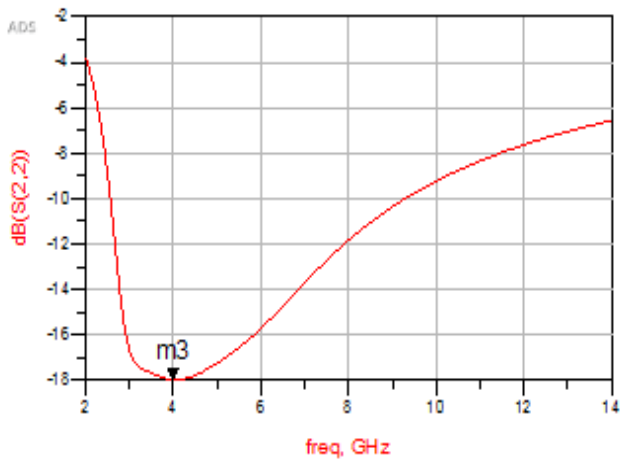

Fig. 6 Output Reflection Coefficient (S_{22})

S_{22} is output reflection coefficient or output return loss. For S_{22} measurement, a signal at output port is injected and its reflected signal is measured. So, it represents the measure of matching of the output impedance to load impedance. For 3.1-10.6 GHz, the S_{22} is less than -10 dB, i.e., -17.980 dB, as shown in Figure 6.

Fig. 7 Noise Figure (NF)

The noise performance of device at high frequency is indicated by noise figure. Noise figure is a figure-of-merit, the amount of excess noise present in a system is described by it. The system impairments resulting from the noise can be reduced by minimizing the noise in the system. The minimum noise figure of 1.811 dB has been obtained for 3.1-10.6 GHz, as shown in Figure 7.

Fig. 8 IIP3

LNA along with amplification of signal and good noise performance, should be linear, even when the signal is strong. Hence, during designing of LNA, linearity is an important consideration. The third order intercept point (IIP3) is the most typical measure of linearity [9]. The value of third order intercept point is 3 dBm as shown in Figure 8, showing that the LNA achieves good gain and noise performance without affecting its linearity. In fact, the linearity of the LNA is quite high.

TABLE I COMPARISON OF DIFFERENT CMOS LNAS

PARAMETER	[10]	[11]	[12]	This work
Frequency (GHz)	3.1-10.6	3.1-10.6	3.1-10.6	3.1-10.6
Technology (µm)	0.18	0.13	0.13	0.13
Supply (V)	0.8	1.2	1.2	1.2
Gain (dB)	13.1	15.1	13	11.037
Noise Figure (dB)	3.25	2.1	2.9	1.811
IIP3 (dBm)	-16.2	-8.5	-4.8	3

From the table I, it can be concluded that for the range of frequency from 3.1-10.6 GHz, at 0.13µm technology, operating at 1.2 V, compared to other LNAs, the designed LNA has least noise figure (of value 1.811 dB) and maximum linearity (value 3 dBm), with a good value of gain (11.037 dB). So, our designed LNA, in terms of linearity and noise, is much better as compared to other reported LNAs for 3.1-10.6 GHz frequency range.

IV. CONCLUSION

The design for an UWB LNA based on a simple resistive shunt feedback technique is reported in this paper, that can perform well over the entire range of 3.1-10.6 GHz i.e., in ultra-wide band. More importantly, decent gain, low noise figure and good IIP3 is achieved simultaneously over ultra-wide bandwidths using a relatively simple resistive shunt feedback topology for LNA at 1.2V power supply. Because of the simplicity in the design, it is possible to achieve low noise figure and high linearity; and most importantly, provides an alternative as well as attractive design to realize high performance and low-cost CMOS UWB receivers and systems.

ACKNOWLEDGMENT

One of the authors (Aditi) acknowledges the fellowship support she is receiving from Delhi Technological University (DTU), for carrying out this work, as a part of her Master of Technology Thesis work in the domain of Microwave and Optical Communication. She also acknowledges the guidance support from her thesis mentor, Dr. Malti Bansal, Assistant Professor, Department of Electronics and Communication Engineering, DTU, for carrying out this research work.

REFERENCES

[1] FCC, "Revision of Part 15 of the Commission's Rules Regarding Ultra-Wideband Transmission Systems," *First Report and Order*, ET Docket 98-153, FCC 02-8, adopted/released Feb. 14/Apr. 22, 2002.

[2] W. Hirt, "Ultra-Wideband Radio Technology: Overview and Future Research," *Comp. Commun*unications, vol. 26, no. 1, pp. 46–52, Jan. 2003

[3] X. Guan, C. Huynh and C. Nguyen, "Design of a 0.18-µm CMOS resistive shunt feedback low-noise amplifier for 3.1–10.6-GHz UWB receivers," *2011 Proceedings of International Conference on Infrared, Millimeter, and Terahertz Waves*, Houston, TX, pp. 1-2.

[4] A. Ismail and A. A. Abidi, "A 3-10-GHz low-noise amplifier with wideband LC-ladder matching network," in *IEEE Journal of Solid-State Circuits*, vol. 39, no. 12, pp. 2269-2277, Dec. 2004.

[5] A. Valdes-Garcia, C. Mishra, F. Bahmani, J. Silva-Martinez and E. Sanchez-Sinencio, "An 11-Band 3.4 to 10.3 GHz MB-OFDM UWB Receiver in 0.25µm SiGe BiCMOS," *2006 Symposium on VLSI Circuits, 2006. Digest of Technical Papers*, Honolulu, HI, 2006, pp. 206-207.

[6] R. Gharpurey, "A broadband low-noise front-end amplifier for ultra wideband in 0.13-µm CMOS," in *IEEE Journal of Solid-State Circuits*, vol. 40, no. 9, pp. 1983-1986, Sept. 2005.

[7] Shih-Chih Chen, Ruey-Lue Wang, Ming-Lung Kung and Hsiang-Chen Kuo, "An Integrated CMOS Low Noise Amplifier for 3-5 GHz UWB Applications," *2005 Proceedings of IEEE Conference on Electron Devices and Solid-State Circuits*, 2005, pp. 225-228.

[8] T. T. N. Tran, C. C. Boon, M. A. Do and K. S. Yeo, "A 2.4 GHz ultra low-power high gain LNA utilizing π-match and capacitive feedback input network," *2011 Proceedings of IEEE 54th International Midwest Symposium on Circuits and Systems (MWSCAS)*, Seoul, 2011, pp. 1-4.

[9] M. Muhamad, N. Soin, H. Ramiah, N. M. Noh and W. K. Chong, "Design of CMOS differential LNA at 2.4GHz," *2013 Proceedings of IEEE International Conference of Electron Devices and Solid-state Circuits, Hong Kong*, 2013, pp. 1-2

[10] Z. Hong-min, Z. Ying, Y. Ying and D. Ke-ke, "Analysis and design of a 3.1–10.6 GHz wideband low-noise amplifier using resistive feedback," *2016 Proceedings of IEEE International Conference on Ubiquitous Wireless Broadband (ICUWB)*, Nanjing, 2016, pp. 1-3.

[11] M. T. Reiha, J. R. Long and J. J. Pekarik, "A 1.2 V reactive-feedback 3.1-10.6 GHz ultrawideband low-noise amplifier in 0.13µm CMOS," *IEEE Radio Frequency Integrated Circuits (RFIC) Symposium, 2006*, San Francisco, CA, 2006, pp. 4.

[12] A. Visweswaran and W. A. Serdijn, "A low power UWB-LNA using active dual loop negative feedback in CMOS 0.13µm," *2009 Proceedings of IEEE International Symposium on Circuits and Systems*, Taipei, 2009, pp. 225-228.

Analog Integrated Circuits and Signal Processing
https://doi.org/10.1007/s10470-018-1196-3

A high-Q floating active inductor using 130 nm BiCMOS technology and its application in IF band pass filter

Divyesh Sachan[1] · Manish Goswami[1] · Prasanna Kumar Misra[1]

Received: 18 November 2017 / Revised: 11 April 2018 / Accepted: 20 April 2018
© Springer Science+Business Media, LLC, part of Springer Nature 2018

Abstract
In this work, the performance of floating active inductor is studied using 130 nm BiCMOS technology. A new design of floating type active inductor based on gyrator-C topology using MOSFETs and npn SiGe HBTs has been proposed. The quality factor, power consumption, noise figure, S11 and inductance value of the proposed design have been obtained and results are compared. The tradeoff between design parameters are discussed and optimal values of design components are found. The maximum value of quality factor obtained is 300 with inductive bandwidth of 0.32–2.65 GHz and power consumption of 269 μW. The design was also used in IF band pass filter for receiver applications and performance is studied in terms of gain, 1 dB compression point and IIP3. From the study, it has been observed that proposed floating type active inductor can be used in high performance RF applications compared to the applications that uses passive inductor.

Keywords Active inductor · Band pass filter · Quality factor · RF · BiCMOS

1 Introduction

The active inductors have been the popular choice in RF circuit designs as compared to the passive inductor [1–3]. High quality passive devices in RF CMOS technology are needed for designing high performance radio frequency integrated circuits and inductors are essential component for designing filters, low noise amplifiers (LNA), voltage controlled oscillators (VCO), etc. The performance of all aforementioned circuits largely depends on the quality of inductors. For a passive inductor, obtaining high quality factor at minimal area has been a challenging task due to the technological limitations. Therefore, interests have been developed towards active inductors that offers relatively better quality factor at minimal area compared to the passive inductor. Among active inductors there are two possible designs that are grounded inductor and floating inductor. The performance of these active inductors can be improved by using heterojunction bipolar transistor (HBT) since this device offers wide range of transconductance values compared to the MOSFETs. In recent years, active inductors based on gyrator-C topology are actively used in RF components like LNA [4, 5], VCO [6], filter [7–13] and high-speed VCSEL driver [14].

In the gyrator-C based active inductors, the high value of inductance can be obtained by optimizing the size of the transistors as compared to the passive inductors [1, 15]. For the same inductance value, active inductors perform better in terms of quality factor, chip area as compared to spiral passive inductors. The high performance values obtained in the design are attributed to high value to transconductance offered by npn SiGe HBTs. The IHP 130 nm BiCMOS technology was used to take advantage of both MOSFETs and HBTs in the design. In Sect. 2, the design of the floating active inductor is discussed followed by results and discussion in Sect. 3. In Sect. 4, application of proposed floating active inductor in IF BPF is discussed and results are compared with state of the art designs.

2 Design of floating active inductor

Floating active inductors (AI) are considered better than Grounded AI due to their versatile usage. Floating AIs have twice the voltage swing compared to their counterpart [1] and it can be used in the place of spiral inductors.

✉ Divyesh Sachan
divyeshsachan@gmail.com

[1] Indian Institute of Information Technology, Allahabad, India

Published online: 27 April 2018

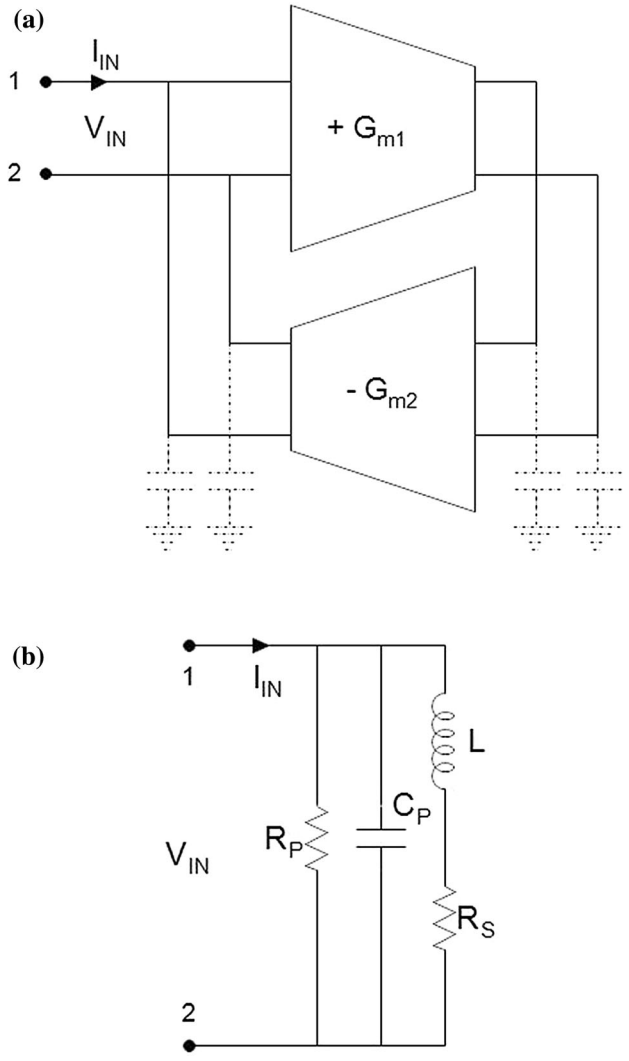

Fig. 1 Lossy gyrator-c floating active inductor. **a** Model. **b** Equivalent

Grounded AIs have limited application since it can only be used as an inductor in the circuits where one of inductor terminal is at ground potential. The differential transconductors used in floating AIs effectively rejects signal noise and disturbance and hence it can be used in the circuits where analog and digital components are fabricated in single substrate [1, 16, 17]. Figure 1(a, b) shows block diagram and equivalent circuit of floating AI respectively.

The expression for inductance (L) and port impedance (Z_{in}) of active inductor shown in Fig. 1 are reported in [1] as,

$$L = \frac{C_1/2}{Gm_1 Gm_2} \tag{1}$$

$$Z_{in} = \left(\frac{Rs}{CpL}\right)\left(\frac{s\frac{L}{Rs}+1}{s^2 + s\left(\frac{1}{RpCp}+\frac{Rs}{L}\right)+\frac{Rp+Rs}{RpCpL}}\right) \tag{2}$$

The quality factor (Q) of lossy gyrator-C AI can be written as [1]

$$Q = \frac{\mathrm{Im}[Z]}{\mathrm{Re}[Z]} \tag{3}$$

The expression of quality factor (Q) in terms of equivalent circuit components can be evaluated from Eqs. (2) and (3) as

$$Q = \left(\frac{\omega L}{Rs}\right)\left(\frac{Rp}{Rp + Rs\left\{1+\left(\frac{\omega L}{Rs}\right)^2\right\}}\right)\left[1 - \frac{Rs^2 Cp}{L} - \omega^2 LCp\right] \tag{4}$$

The schematic of proposed floating AI and its equivalent small signal model is shown in Fig. 2(a, b) respectively which uses MOSFETs along with npn SiGe HBTs. In this design, a common emitter amplifier is used as negative trans-conductance unit and a NMOS (Q1 and Q8) are used as positive trans-conductance unit. Q2, Q3 and Q9, Q10 constitute a common emitter amplifier. Q6 and Q13 acts as a resistance which boosts the quality factor. Q4, Q5 and Q11, Q12 generates reference current to bias Q13 and Q6 respectively. The value of trans-conductance of Q1, Q2, Q8, Q9 along with capacitance at node 1 and 2 plays most crucial role in this design. The value of trans-conductance of HBT (Q1 and Q8) are higher than the MOSFETs. So, this design offers better inductive bandwidth compared to the designs those only uses MOSFETs. Also series resistance associated with the inductor is inversely proportional to product of trans-conductance of Q1, Q2 and Q8, Q9, and as a result quality factor of the design has been improved. Use of resistive feedback (Q6 and Q13) has improved the quality factor of the design further by a large factor. Due to Q6 and Q13, series resistance decreases and equivalent inductance increases [2]. Therefore, the quality factor improves in consequence. The value of Vdd and Vss used in the design is + 0.75 and − 0.75 V respectively.

From the small signal model of proposed design shown Fig. 2(b), the impedance of floating AI at input port Z_{in} can be approximated as

$$Z(S) = \frac{N(S)}{D(S)} \tag{5}$$

and

$$\begin{aligned} N(S) = {} & g_3 g_6 g_{m6} + g_3 g_6 g_{o6} + g_4 g_5 g_{m13} + g_4 g_5 g_{o13} \\ & + S\big(C_{gs6} g_3 g_6 - C_{gs6} g_3 g_{o6} + C_{gs6} g_6 g_{o6} \\ & - C_{gs6} g_{o6} g_{m3} + C_{gs13} g_4 g_5 - C_{gs13} g_4 g_{o13} \\ & + C_{gs13} g_5 g_{o13} - C_{gs13} g_{o5} g_{m10}\big) \end{aligned}$$

$$
\begin{aligned}
D(S) = S^2\big(&C_{gs6}C_1g_3g_6 - C_{gs6}C_1g_3g_{o6} + C_{gs6}C_1g_6g_{o6}\\
&-C_{gs6}C_1g_{o6}g_{m3} + C_{gs13}C_2g_4g_5\\
&- C_{gs13}C_2g_4g_{o13} + C_{gs13}C_2g_5g_{o13} - C_{gs13}C_2g_{o13}g_{m10}\big)\\
&+S\big(C_{gs6}g_3g_1g_6 - C_{gs6}g_3g_1g_{o6} + C_1g_3g_6g_{o6}\\
&+C_{gs6}g_1g_6g_{o6} + C_{gs6}g_3g_6g_{m1}\\
&- C_{gs6}g_3g_{o6}g_{m1} + C_{gs6}g_6g_{o6}g_{m1} - C_{gs6}g_{o6}g_{m1}g_{m2}\\
&- C_{gs6}g_1g_{o6}g_{m3} - C_{gs6}g_{o6}g_{m1}g_{m3} + C_1g_3g_6g_{m6}\\
&+ C_{gs13}g_4g_2g_5 - C_{gs13}g_4g_2g_{o13} + C_2g_4g_5g_{o13}\\
&+ C_{gs13}g_2g_5g_{o13} + C_{gs13}g_4g_5g_{m8} - C_{gs13}g_4g_{o13}g_{m8}\\
&+ C_{gs13}g_5g_{o13}g_{m8} - C_{gs13}g_{o13}g_{m8}g_{m9} - C_{gs13}g_2g_{o13}g_{m10}\\
&-C_{gs13}g_{o13}g_{m8}g_{m10} + C_2g_4g_5g_{m13}\big)\\
&+ g_3g_1g_6g_{o6} + g_3g_6g_{o6}g_{m1} + g_6g_{o6}g_{m1}g_{m2} + g_3g_1g_6g_{m6}\\
&+ g_3g_6g_{m1}g_{m6} + g_4g_1g_5g_{o13} + g_4g_5g_{o13}g_{m8}\\
&+ g_5g_{o13}g_{m8}g_{m9} + g_{10}g_2g_5g_{m13} + g_4g_5g_{m8}g_{m13}
\end{aligned}
$$

where gm_i, Cgs_i and g_{oi} are the transconductance, gate capacitance, and output conductance of transistor M_i as shown in Fig. 2(a). C_i and g_i are total parasitic capacitance and conductance at node *i*. The term *i* can be replaced with respective node number as shown in Fig. 2(a).

The quality factor and inductance of the FAI can be calculated by

$$Q = \frac{\text{Imag }\{Z\}}{\text{Real}\{Z\}} = \left|\frac{BC - AD}{AC + BD}\right| \tag{6}$$

$$L = \frac{\text{Imag}\{Z\}}{\omega} = \frac{BC - AD}{\omega} \tag{7}$$

where

$$A = g_3g_6g_{m6} + g_3g_6g_{o6} + g_4g_5g_{m13} + g_4g_5g_{o13}$$

$$
\begin{aligned}
B = \big(&C_{gs6}g_3g_6 - C_{gs6}g_3g_{o6} + C_{gs6}g_6g_{o6} - C_{gs6}g_{o6}g_{m3}\\
&+C_{gs13}g_4g_5 - C_{gs13}g_4g_{o13} + C_{gs13}g_5g_{o13}\\
&-C_{gs13}g_{o5}g_{m10}\big)\omega
\end{aligned}
$$

$$
\begin{aligned}
C = &g_3g_1g_6g_{o6} + g_3g_6g_{o6}g_{m1} + g_6g_{o6}g_{m1}g_{m2} + g_3g_1g_6g_{m6}\\
&+ g_3g_6g_{m1}g_{m6} + g_4g_1g_5g_{o13} + g_4g_5g_{o13}g_{m8}\\
&+ g_5g_{o13}g_{m8}g_{m9} + g_{10}g_2g_5g_{m13} + g_4g_5g_{m8}g_{m13}\\
&- \big(C_{gs6}C_1g_3g_6 - C_{gs6}C_1g_3g_{o6} + C_{gs6}C_1g_6g_{o6}\\
&-C_{gs6}C_1g_{o6}g_{m3} + C_{gs13}C_2g_4g_5\\
&- C_{gs13}C_2g_4g_{o13} + C_{gs13}C_2g_5g_{o13} - C_{gs13}C_2g_{o13}g_{m10}\big)\omega^2
\end{aligned}
$$

$$
\begin{aligned}
D = &C_{gs6}g_3g_1g_6 - C_{gs6}g_3g_1g_{o6} + C_1g_3g_6g_{o6}\\
&+ C_{gs6}g_1g_6g_{o6} + C_{gs6}g_3g_6g_{m1} - C_{gs6}g_3g_{o6}g_{m1}\\
&+ C_{gs6}g_6g_{o6}g_{m1} - C_{gs6}g_{o6}g_{m1}g_{m2} - C_{gs6}g_1g_{o6}g_{m3}\\
&- C_{gs6}g_{o6}g_{m1}g_{m3} + C_1g_3g_6g_{m6} + C_{gs13}g_4g_2g_5\\
&- C_{gs13}g_4g_2g_{o13} + C_2g_4g_5g_{o13} + C_{gs13}g_2g_5g_{o13}\\
&+ C_{gs13}g_4g_5g_{m8} - C_{gs13}g_4g_{o13}g_{m8} + C_{gs13}g_5g_{o13}g_{m8}\\
&- C_{gs13}g_{o13}g_{m8}g_{m9} - C_{gs13}g_2g_{o13}g_{m10}\\
&- C_{gs13}g_{o13}g_{m8}g_{m10} + C_2g_4g_5g_{m13}
\end{aligned}
$$

Noise model of [18, 19] has been used to analyse the noise performance of proposed floating AI. An individual MOSFET which has mainly two noise sources, i.e. channel induced noise and gate induced noise and can be expressed as

$$\frac{\overline{i_{\text{nd}i}^2}}{\Delta f} = 4kT\gamma g_{d0i} + \frac{K_F g_{mi}^2}{C_{ox}L_{eff}^2 f^{EF}} \tag{8}$$

and

$$\frac{\overline{i_{\text{ng}i}^2}}{\Delta f} = 4kT\delta\frac{\omega^2 C_{gsi}^2}{5g_{d0i}} \tag{9}$$

where $i = 1, 3, 4, \ldots 7, 9, 10, \ldots 14$, k is Boltzmann's constant, γ and δ are technology dependant constant, T is absolute temperature in Kelvin, g_{d0i} is drain conductance for transistor M_i at zero V_{DS}. The surplus term in Eq. (8) is added as per BSIM4 model [20] for flicker noise source. As per model, C_{ox} is gate oxide capacitance, L_{eff} is effective gate length, EF is flicker noise's frequency exponent, K_F is flicker noise coefficient. PSD of noise voltage source can be represented in terms of noise current source [21] as

$$\frac{\overline{v_{\text{nd,g}}^2}}{\Delta f} = \frac{\frac{\overline{i_{\text{nd,g}}^2}}{\Delta f}}{g_m^2} \tag{10}$$

Consequently, when referred to input terminal of AI, the expression (8) and (9) can be written in terms of noise voltage for MOSFET as

$$\frac{\overline{v_{\text{nd}i}^2}}{\Delta f} = \frac{4kT\gamma g_{d0i}}{g_{mi}^2} + \frac{K_F}{C_{ox}L_{eff}^2 f^{EF}} \tag{11}$$

$$\frac{\overline{v_{\text{ng}i}^2}}{\Delta f} = \frac{4kT\delta}{5g_{d0i}} \tag{12}$$

In HBT, the main sources of noise are, thermal noise of base spreading resistance r_b, shot noise, flicker or 1/f noise of base current I_B, shot noise of collector current I_C [19]. The expression for equivalent noise current and voltage for HBT can be expressed as

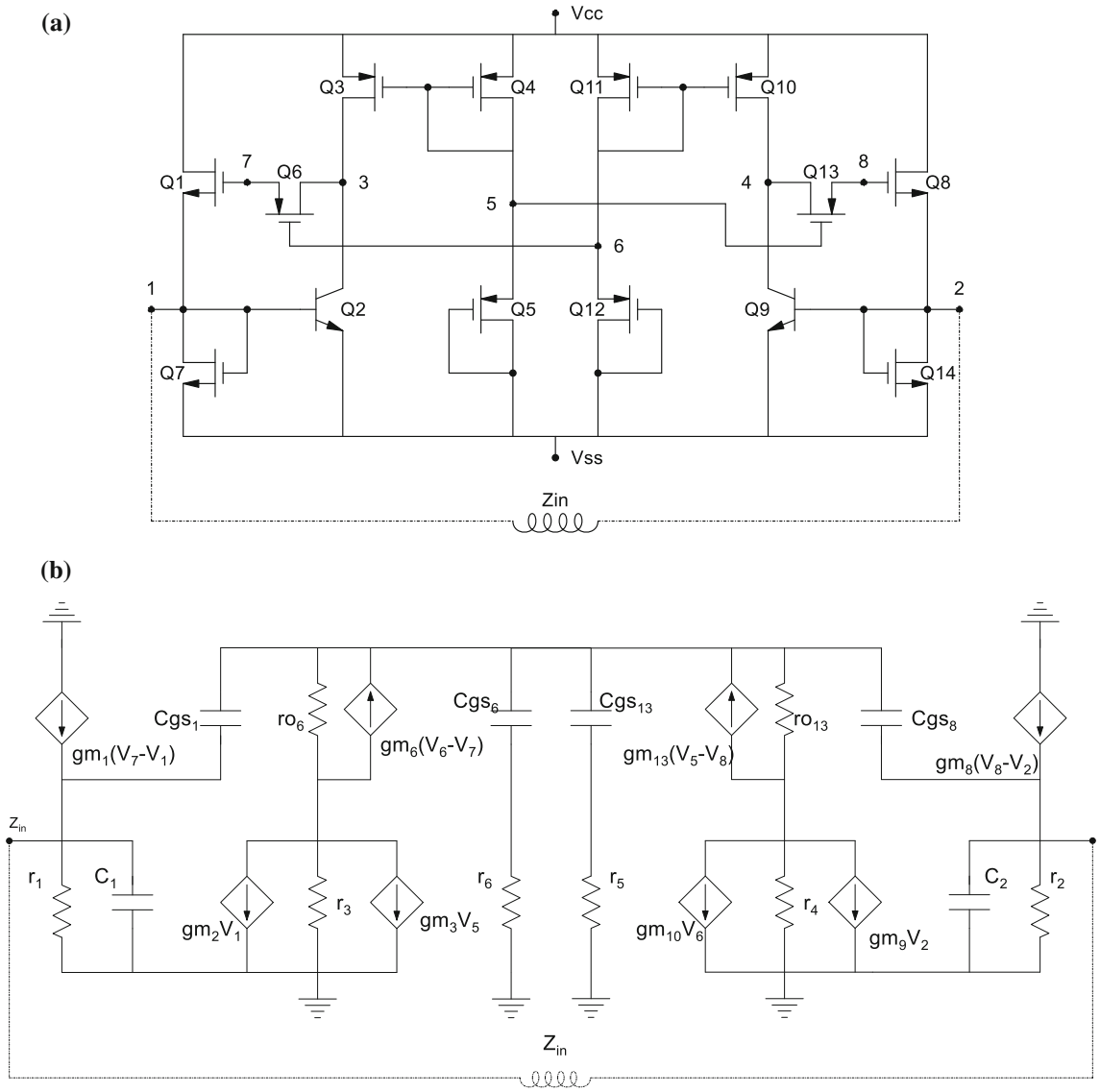

Fig. 2 Design of proposed floating AI. **a** Schematic. **b** Small signal equivalent model

$$\frac{\overline{i_n^2}}{\Delta f} = 2qI_B + \frac{K_F I_B^{\alpha}}{f^{EF}} + \frac{2qI_C}{\beta^2} \tag{13}$$

$$\frac{\overline{v_n^2}}{\Delta f} = 4kTr_b + \left(2qI_B + \frac{K_F I_B^{\alpha}}{f^{EF}}\right) r_b^2 + 2qI_C \left(\frac{r_b}{\beta} + \frac{V_T}{I_C}\right)^2 \tag{14}$$

where β is common emitter current gain and V_T is 25 mV.From (11), (12) and (14), the total noise contributed by all the transistors of floating AI can be written as

$$\frac{\overline{V_{total}^2}}{\Delta f} = \sum_{i=1, i\neq 2,8}^{14} \left(\frac{\overline{V_{ngi}^2}}{\Delta f}\right) + \sum_{i=1, i\neq 2,8}^{14} \left(\frac{\overline{V_{ndi}^2}}{\Delta f}\right) + \sum_{i=2,8} \left(\frac{\overline{V_{ni}^2}}{\Delta f}\right) \tag{15}$$

3 Results and discussion

The performance of proposed AI has been analysed using IHP 130 nm BiCMOS technology using Cadence Spectre after including post layout parasitics and components. The aspect ratio of transistor used in design are listed in

Table 1 Aspect ratio of transistors used in design

Transistor name	Transistor size
Q1, Q8	3μ/130n
Q2, Q9	NA
Q3, Q10	450n/130n
Q4, Q6, Q7, Q11, Q13, Q14	150n/130n
Q5, Q12	1.5μ/130n

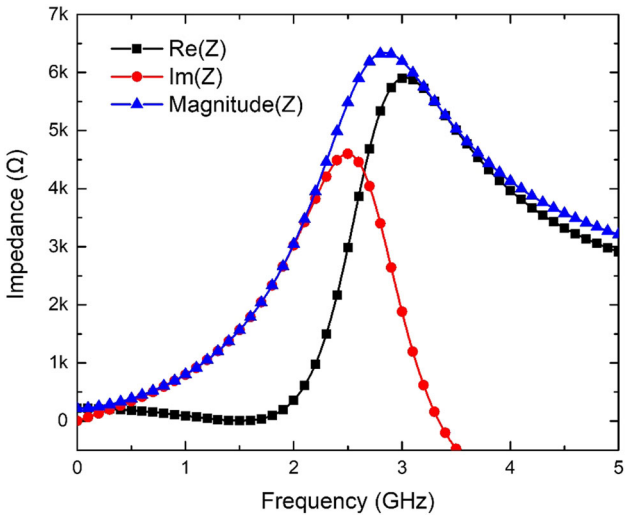

Fig. 3 Impedance of floating AI

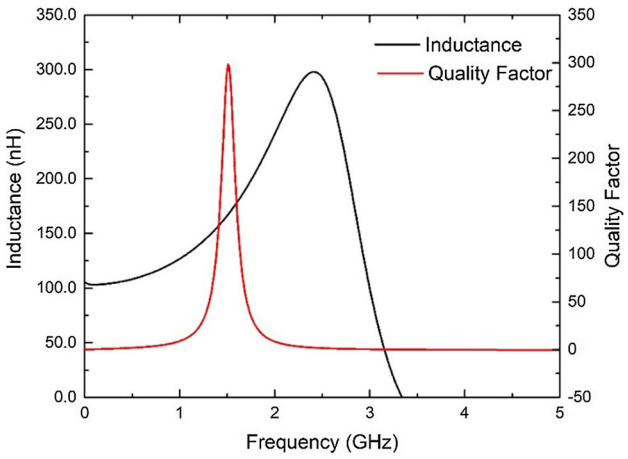

Fig. 4 Inductance and quality factor of floating AI

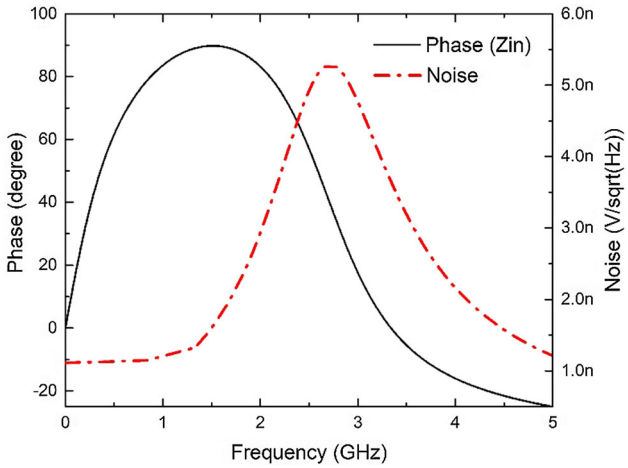

Fig. 5 Zin phase and noise output of floating AI

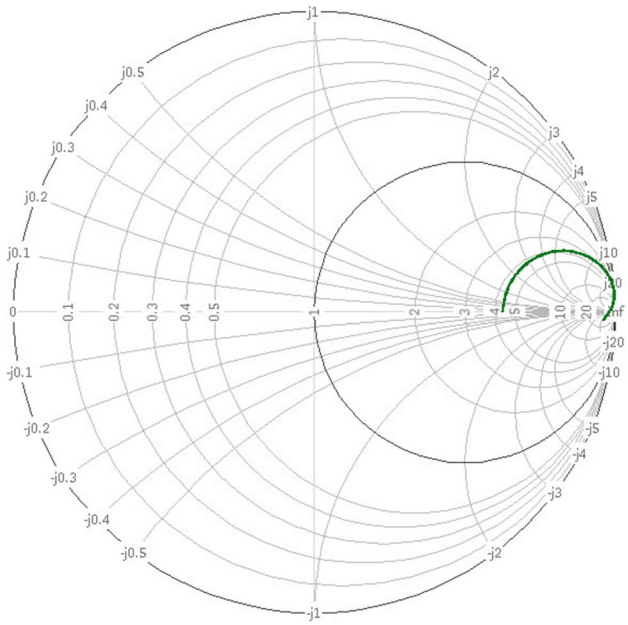

Fig. 6 S11 Smith chart of floating AI

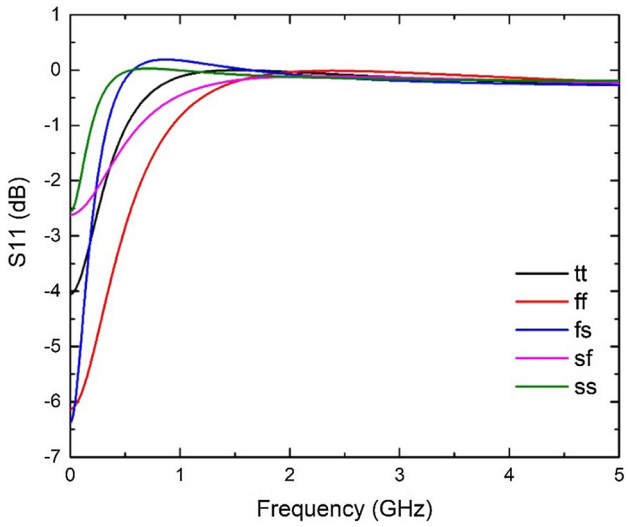

Fig. 7 S11 corner analysis of floating AI

Table 1. The reference current of circuit is kept at 15.4 μA and total current drawn by circuit is 179 μA. Total power consumption of the circuit is 269 μW. From the study, the parameters such as input impedance, S11, noise figure, bandwidth, inductance, noise voltage and quality factor are analysed. It has been observed that the increase in value of quality factor decreases bandwidth which is also discussed in [3].

Port impedance of proposed floating AI is shown in Fig. 3. It has been observed that the operating frequency of proposed design is between 322 MHz to 2.65 GHz. The maximum value of quality factor Q_{max} (300) is obtained at

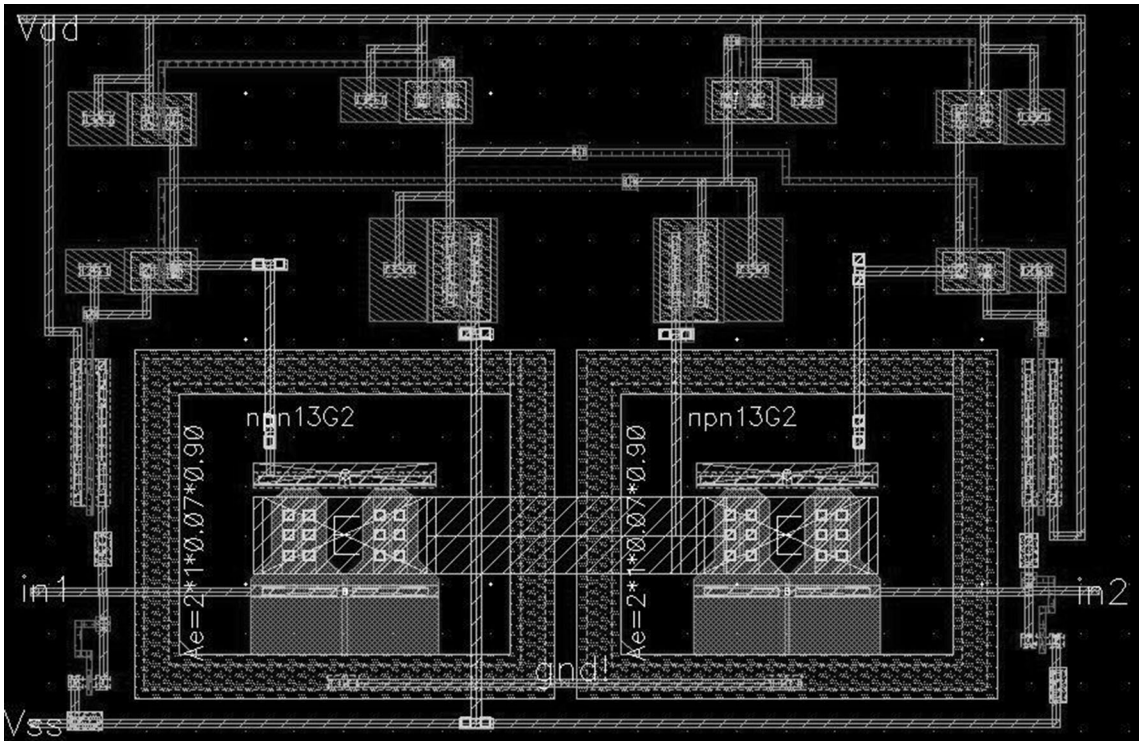

Fig. 8 Layout of floating AI

Table 2 Comparison of performance parameters with other floating active inductors

Parameter	[15]	[22]	[23]	[24]	[25]	Proposed AI
Process (nm)	800	180	Discrete	180	130	130 BiCMOS
Inductive BW (GHz)	1.06	4	0.430	0.1–6.2	3.5	0.32–2.65
Q factor (max)	350	68	700	567@1 GHz	38.8	300@1.5 GHz
L (nH)	294–394	33	230	6–284	1.9	100.5–301.5
Area (μm^2)	–	810	–	934	2600	330
Power (mW)	8.6	3.6	40	2	6.4	0.269

frequency of 1.51 GHz as shown in Fig. 4. The minimum and maximum value of inductance obtained within inductive bandwidth is 100.5 to 301.5 nH respectively. The phase response and noise voltage is shown in Fig. 5. The noise voltage of AI varies from 1.12 to 5.28 $nV/\sqrt{Hz}$ and noise figure at Q_{max} frequency 1.51 GHz is 11.2 dB and it varies in the range of 10.9–11.3 dB for the entire inductive bandwidth range of 0.32–2.65 GHz. From the smith chart shown in Fig. 6, S11 is observed almost at its peak at frequency of 1.51 GHz.

Process voltage and temperature (PVT) variation analysis has been performed to study the robustness of the circuit. Variation range of inductive bandwidth, maximum quality factor Q_{max} and inductance L has been recorded by varying temperature from 0 to 75 °C and supply voltage by ± 10%. From the variation results, bottom and supreme inductive bandwidth obtained is 0.28 and 2.97 GHz respectively, Q_{max} varies in the range of 245–364. Correspondingly, minimum and maximum value of inductance L varies from 76.4 to 121.6 nH and 279.3–386.8 nH respectively during entire inductive bandwidth range. Post layout corner analysis of all 5 usual process corners (ff-fast fast, fs-fast slow, sf-slow fast, ss-slow slow and tt-typical typical) is also carried out to study variation of performance parameters due to process inaccuracies. During the analysis worst case has been observed when transistors have fast slow (fs) process corner as shown in Fig. 7.

The layout of proposed design is shown in Fig. 8. Total area occupied by the design is 22 × 14.7 µm. Comparison of performance parameters with existing floating AIs are shown in Table 2.

4 Application of floating active inductor in IF BPF

Active inductors has an advantage of small chip area as compared to passive spiral inductors and floating AI it can be used anywhere in the design in place of spiral inductors. Most common use of AIs in RF application includes voltage controlled oscillators (VCO) and RF filters. Few architecture of RF systems are homodyne, heterodyne and Zero-IF receivers. Low-IF receivers which offer high selectivity and high integration level are also popular in RF system applications to overcome the issues like high DC offset, gain phase mismatch between I/Q signals [26]. Floating type active inductors can be employed by LNA, VCO and filters blocks in low-IF receiver chain and these blocks needs critical attention in the design. A typical IF receiver chain with IF-filter is shown in Fig. 9. Low pass filter is common choice for these type of receivers. However, LC band pass filters employing active inductor can also be incorporated in these receivers because of high quality factor and inductance range offered by active inductors. Further, LC band pass filter is also a good choice for low-IF receivers due to higher selectivity. A simple 2nd order IF BPF with high quality factor has been designed as shown in Fig. 10 with a center frequency of 1 GHz. The center frequency can be easily tuned from 500 MHz to 1.5 GHz by varying value of capacitor in LC tank.

The gain response of 2nd order BPF using floating AI tuned at centre frequency of 1 GHz is compared with spiral inductor as shown in Fig. 11. It is observed that gain of BPF using proposed AI is steeper than gain of BPF using passive spiral inductor. Linearity and bias condition of the BPF has been investigated by 1 dB compression point (P_{1dB}) and Third Order Intercept Point (IIP3) simulation. The point where output power is compressed by 1 dB is known as P_{1dB} and it is a good measure to know the bias point of the circuit. The circuit must be biased below P_{1dB} to operate in linear region. The harmonics produced by mixer are easily filtered by the IF filter. However, multiple closed frequency components either sum or difference frequencies which are also known as intermodulation product within the operating bandwidth of the filter cannot be filtered out. These intermodulation products surge at the rate of 3 times of input signal and can increase more than input signal at some point. The point where third order intermodulation product signal equals input signal is known as IIP3. Higher values of intercept output power results in better linearity. Two tone signal of 1 and 1.1 GHz are injected to verify the linearity of BPF using P_{1dB} and IIP3. 1 dB compression point of BPF is − 0.38 dBm as shown in Fig. 12. IIP3 value of 7.2 dBm is attained for the BPF as shown in Fig. 13 with reference to 50 Ω source. The W/L of transistors used in floating AI are picked optimally for all transistors to function in their optimum operating point. The higher values of P_{1dB} and IIP3 is attributed to the finest bias condition of the floating AI along with the use of HBT's in the circuit which offers better transconductance as compared to MOSFET's. The performance comparison of BPF using proposed AI with existing BPFs using AIs are listed in Table 3.

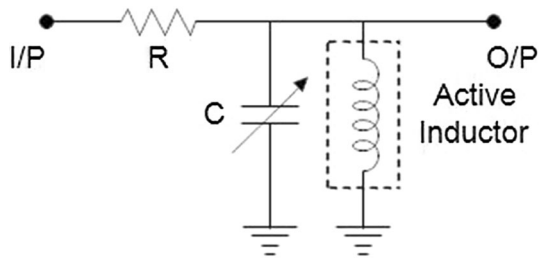

Fig. 10 Simple LC band pass filter using active inductor

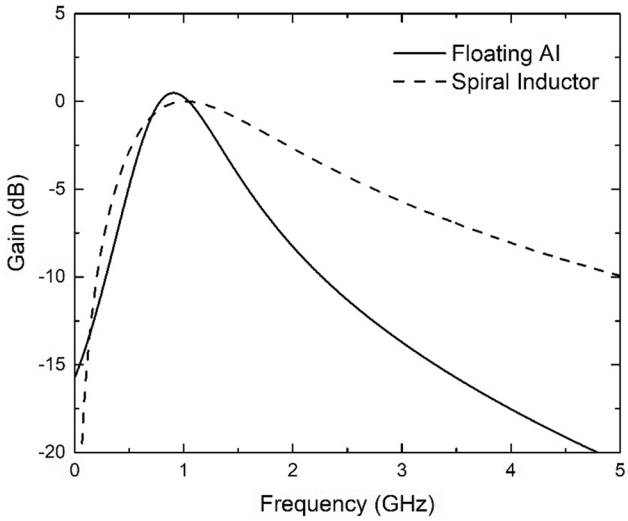

Fig. 11 Gain response of IF-BPF using proposed floating AI

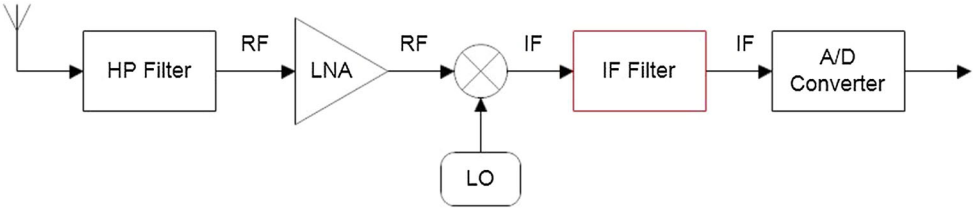

Fig. 9 Schematic of IF receiver

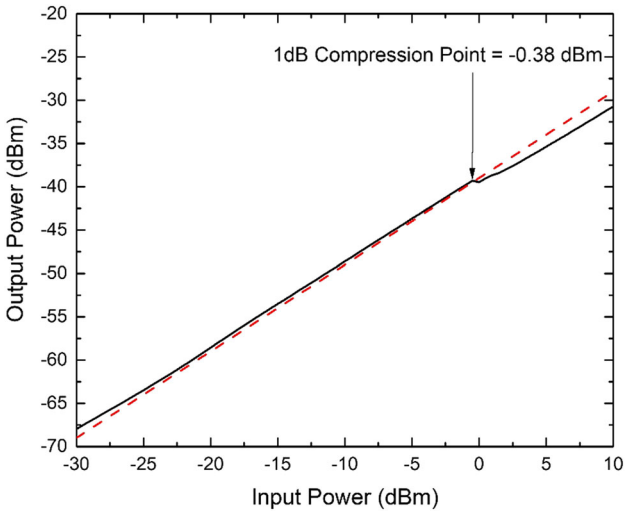

Fig. 12 1 dB compression point of IF-BPF using proposed floating AI

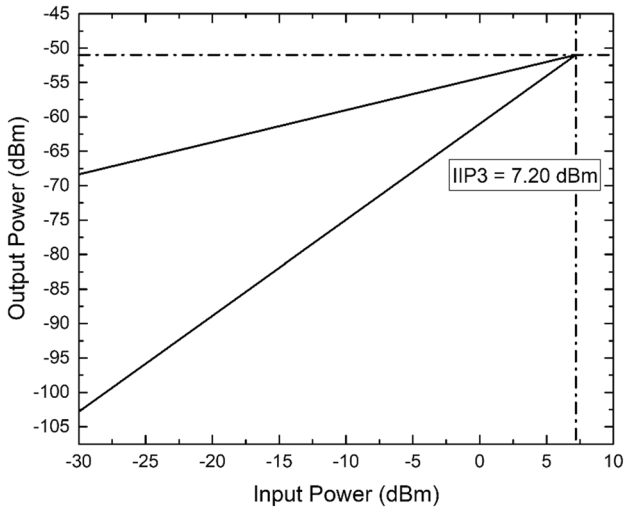

Fig. 13 IIP3 of IF-BPF using proposed floating AI

5 Conclusion

The floating active inductor has been designed using 130 nm BiCMOS technology. It has been observed that proposed design is good choice for RF system applications considering high value of quality factor, inductance and inductive bandwidth. The performance is attributed to high value of transconductance of the HBTs used in the design. A tradeoff between inductance and quality factor is observed. Maximum quality factor of 300 and inductance range of 100.5–301.5 nH is obtained in the inductive bandwidth of 0.32–2.65 GHz. The dimension of the transistors are critical and have been optimized in order to achieve appropriate value of inductance, quality factor and inductive bandwidth. Further, proposed design has been used in band pass filter and performance of LC BPF is investigated in terms of gain, 1 dB compression point and IIP3. The performance parameters of LC BPF using proposed active inductor are found much better than passive spiral inductor. It has been observed that proposed floating AI can be a widely used as an inductor component in RF applications including Low IF architecture based receivers.

References

1. Yuan, F. (2008). *CMOS active inductors and transformers: Principle, implementation, and applications, chap. 2*. New York, US: Springer. ISBN 978-0-387-76477-1.
2. Hsiao, C. C., Kuo, C. W., Ho, C. C., & Chan, Y. J. (2002). Improved quality-factor of 0.18 μm CMOS active inductor by a feedback resistance design. *IEEE Microwave and Wireless Components Letters, 12*(12), 467–469.
3. Xiao, H., Schaumann, R., Daasch, W. R., Wong, P. K., & Pejcinovic, B. (2004). A radio-frequency CMOS active inductor and its application in designing high-Q filters. In *IEEE proceedings of the international symposium on circuits and systems* (pp. 197–200).
4. Kia, H. B. (2014). Adaptive CMOS LNA using highly tunable active inductor. In *IEEE 22nd Iranian conference on electrical engineering (ICEE)* (pp. 1–6).
5. Kia, H. B., A'ain, A. K., Grout, I., & Kamisian, I. (2013). A reconfigurable low-noise amplifier using a tunable active inductor

Table 3 Comparison of performance parameters of BPF using proposed active inductors

Parameter	[7]	[8]	[9]	[10]	[11]	Proposed
Tech. (nm)	90	180	180	500	350	130
Filter Order	2	2	5	6	2	2
Supply Voltage	1.2	1.8	1.8	2.5	2.7	1.5
Centre Freq. (GHz)	3.46	0.5–2	3.45–3.6	0.07	0.4–1.1	0.5–1.5
Q Factor (Max.)	120	–	540	350	40	300
Inductance (nH)	165–530	0.5–4	3.2	–	–	100.5–301.5
P_{1dB} (dBm)	–	–	–	− 42.5	–	− 0.38
IIP3 (dBm)	− 10.29	–	− 2.4	− 10	− 15	7.2

for multistandard receivers. *Circuits, Systems, and Signal Processing, 32*(3), 979–992.
6. Cheng, K. H., Hung, C. L., Gong, C. S. A., Liu, J. C., Jiang, B. Q., & Sun, S. Y. (2014). A 0.9-to 8-GHz VCO with a differential active inductor for multistandard wireline SerDes. *IEEE Transactions on Circuits and Systems II: Express Briefs, 61*(8), 559–563.
7. Krishnamurthy, S. V., El-Sankary, K., & El-Masry, E. (2010). Noise-cancelling CMOS active inductor and its application in RF band-pass filter design. *International Journal of Microwave Science and Technology, 2010,* 1–8.
8. Heydarzadeh, S., & Torkzadeh, P. (2013). 1 GHz CMOS band-pass filter design using an active inductor and capacitor. *American Journal of Electrical and Electronics Engineering, 1,* 37–41.
9. Liang, K. H., Ho, C. C., Kuo, C. W., & Chan, Y. J. (2005). CMOS RF band-pass filter design using the high quality active inductor. *IEICE Transactions on Electronics, E88-C,* 2372–2375.
10. Choi, Y. W., & Luong, H. C. (2001). A high-Q and wide-dynamic-range 70-MHz CMOS bandpass filter for wireless receivers. *IEEE Transactions on Circuits and System II: Analog and Digital Signal Processing, 48*(5), 433–440.
11. Wu, Y., Ding, X., Ismail, M., & Olsson, H. (2003). RF band pass filter design based on active inductors. *IEEE Transactions on Circuits and Systems II, 50*(12), 942–949.
12. Kumar, V., Mehra, R., Majumder, D., Khanna, S., Prasad, S., & Islam, A. (2018). Process and voltage variation-aware design and analysis of active grounded inductor-based bandpass filter. In P. K. Sa, M. N. Sahoo, M. Murugappan, Y. Wu, & B. Majhi (Eds.), *Progress in intelligent computing techniques: Theory, practice, and applications* (pp. 309–315). Singapore: Springer. ISBN 978-981-10-3372-8.
13. Pantoli, L., Stornelli, V., & Leuzzi, G. (2016). A low-voltage low-power 0.25 μm integrated single transistor active inductor-based filter. *Analog Integrated Circuits and Signal Processing, 87*(3), 463–469.
14. Fu-Tian, L., Datao, G., Suen, H., Chonghan, L., Tiankuan, L., Da-Shung, S., et al. (2013). Active inductor shunt peaking in high-speed VCSEL driver design. *Chinese Physics C, 37*(11), 116101.
15. Thanachayanont, A., & Payne, A. (2000). CMOS floating active inductor and its applications to bandpass filter and oscillator designs. *IEE Proceedings Circuits, Devices and Systems, 147*(1), 42–48.
16. Kumar, R., Sachan, D., Yadav, S. S., Sihara, A. K., & Misra P. K. (2017). Design of active inductor at 2.4 GHz frequency using 180 nm CMOS technology. In *International conference on electrical, computer and electronics (UPCON)*, IEEE Uttar Pradesh Section, India.
17. Zito, D., Pepe, D., & Fonte, A. (2015). High-frequency CMOS active inductor: Design methodology and noise analysis. *IEEE Transactions on Very Large Scale Integration (VLSI) Systems, 23*(6), 1123–1136.
18. Van Der Ziel, A. (1986). *Noise in solid state devices and circuits*. New York: Wiley. ISBN 0471832340.
19. Wilamowski, B. M., & Erwin, J. D. (2011). *Fundamentals of industrial electronics, chap. 11* (2nd ed.). Boca Raton: CRC Press, Taylor and Francis Group. ISBN 9781138074392.
20. Liu, W., & Hu, C. (2011). *BSIM4 and MOSFET modeling For IC simulation*. Singapore: World Scientific. ISBN 978-981-256-863-2.
21. Galup-Montoro, C., & Schneider, M. C. (2007). *MOSFET modeling for circuit analysis and design*. Singapore: World Scientific. ISBN 978-981-256-810-6.
22. Lai, Q. T., & Mao, J. F. (2010). A new floating active inductor using resistive feedback technique. In *IEEE MTT-S international microwave symposium digest (MTT), Anaheim, CA* (pp. 1748–1751).
23. Branchi, P., Pantoli, L., Stornelli, V., & Leuzzi, G. (2015). RF and microwave high-Q floating active inductor design and implementation. *International Journal of Circuit Theory and Applications, 43,* 1095–1104.
24. Momen, H. G., Yazgi, M., Kopru, R., & Saatlo, A. N. (2016). Design of a new low loss fully CMOS tunable floating active inductor. *Analog Integrated Circuits and Signal Processing, 89*(3), 727–737.
25. Ahmed, A., & Wight, J. (2010). 6.7 GHz high-Q active inductor design using parasitic cancellation with process variation control. *Electronics Letters, 46*(7), 486–487.
26. Crols, J., & Steyaert, M. S. J. (1998). Low-IF topologies for high-performance analog front ends of fully integrated receivers. *IEEE Transactions on Circuit and Systems-II: Analog and Digital Signal Processing, 45*(3), 269–282.

Divyesh Sachan received his B.Tech. from UPTU, Lucknow in 2008 and M.Tech. from Delhi Technological University, Delhi in 2014. During 2008–2012, he worked as a C&I Engineer at BHEL. He is currently working towards his Ph.D. degree in Electronics and Communication Enginering at the IIIT Allahabad. His research areas are mixed signal design, analog circuit design, digital design and signal processing.

Dr. Manish Goswami received his Ph.D. degree from B.I.T. Mesra, Ranchi in 2012. He has held short-term position at Atlaz Digital Pvt. Ltd Mumbai as Assistant Engineer R&D and worked as a lecturer at J.E.C.R.C. Jaipur till 2005 and B.I.T. Mesra till 2008. He is currently holding Associate Professorship at IIIT-Allahabad. His research interest includes Analog and Mixed Signal VLSI design circuits, Low power VLSI circuit design.

Dr. Prasanna Kumar Misra was born in Berhampur, India, in 1983. He received B.E. from National Institute of Science and Technology, Berhampur in 2005 and Ph.D. from IIT Kanpur in 2014. Since June 2014 he is working as a faculty member in the department of Electronics and Communication Engineering at IIIT Allahabad. His research interests are semiconductor device design and Analog/RF integrated circuit design.

J. Inst. Eng. India Ser. B
https://doi.org/10.1007/s40031-018-0323-y

REVIEW PAPER

A Review of Particle Swarm Optimization

N. K. Jain[1] · Uma Nangia[1] · Jyoti Jain[1]

Received: 21 June 2016 / Accepted: 6 March 2018
© The Institution of Engineers (India) 2018

Abstract This paper presents an overview of the research progress in Particle Swarm Optimization (PSO) during 1995–2017. Fifty two papers have been reviewed. They have been categorized into nine categories based on various aspects. This technique has attracted many researchers because of its simplicity which led to many improvements and modifications of the basic PSO. Some researchers carried out the hybridization of PSO with other evolutionary techniques. This paper discusses the progress of PSO, its improvements, modifications and applications.

Keywords Iteration · Optimization · Particles · PSO

Introduction

Particle Swarm Optimization (PSO) was introduced in 1995 for solving non-linear functions [1]. It is simpler than other Evolutionary techniques as it requires only the specification of the problem and a few parameters to solve it. For this reason and to identify the untouched areas of research about PSO, this paper has been compiled. This paper presents an overview of research work concerning PSO. The research papers concerning PSO have been considered from 1995 to 2017.

The papers have been categorized depending upon the aspects of PSO explored as follows:

1. Review Papers
2. Acceleration Coefficients (C_p, C_g) and IW
3. Stopping Criterion
4. Applications of PSO
5. Comparison of various types of PSO
6. Hybridization of PSO with other Optimization techniques
7. Multiobjective Optimization using PSO
8. Modified PSO
9. Velocity Upgradation

PSO Algorithm

PSO is a population based self-adaptive, stochastic optimization technique. The PSO begins by creating the initial particles, and assigning them initial velocities. It evaluates the objective function at each particle location, and determines the best function value and the best location. It chooses new velocities, based on the current velocity, the particles' individual best locations, and the best locations of their neighbors. It then iteratively updates the particle locations (the new location is the old one plus the velocity, modified to keep particles within bounds), velocities, and neighbors. Iterations proceed until the algorithm reaches a stopping criterion.

In an n-dimensional search space, position and velocity of particle j is represented by vectors $X_j = (X_{j1}, X_{j2},\ldots X_{jn})$ and $V_j = (V_{j1}, V_{j2},\ldots V_{jn})$ respectively. Let X_{pbest} and X_{gbest} be the personal best position of particle j and global best position of group. The modified velocity and position of each particle can be calculated using current velocity and distance from X_{pbest} and X_{gbest} as follows:

✉ Jyoti Jain
jyotijain_in@yahoo.com

[1] Electrical Engineering Department, Delhi Technological University, Delhi 110042, India

Published online: 30 March 2018

$$V_{ij}^{k+1} = V_{ij}^{k} + C_p r_p \left(X_{pbestij}^{k} - X_{ij}^{k}\right) + C_g r_g \left(X_{gbesti}^{k} - X_{ij}^{k}\right)$$
$$\text{i} = 1, 2 \ldots \text{N} \quad j = 1, 2 \ldots \text{p} \tag{1}$$

where,

k	Iteration Count.
V_{ij}^{k+1}	Velocity of j^{th} particle of i^{th} variable at $k + 1^{th}$ iteration.
X_{ij}^{k}	Value of position of j^{th} particle of i^{th} variable at k^{th} iteration.
C_p, C_g	Cognitive and social acceleration coefficients.
N	Total number of variables.
$X_{pbestij}^{k}$	Personal best position of jth particle of i^{th} variable at k^{th} iteration.
X_{gbesti}^{k}	Global best value of i^{th} variable until k^{th} iteration.
r_p, r_g	Separately generated uniformly distributed random numbers.

Velocities are updated by Eq. (1) and position of each particle is updated by Eq. (2)

$$X_{ij}^{k+1} = X_{ij}^{k} + V_{ij}^{k+1} \quad \text{i} = 1, 2 \ldots \text{N} \quad \text{j} = 1, 2, \ldots \text{p} \tag{2}$$

To increase the convergence rate of PSO, the inertia weight is proposed in the velocity Eq. (1). By using inertia weight, the suggested particle velocity will be changed to

$$V_{ij}^{k+1} = W * V_{ij}^{k} + C_p r_p \left(X_{pbestij}^{k} - X_{ij}^{k}\right) + C_g r_g \left(X_{gbesti}^{k} - X_{ij}^{k}\right)$$
$$\text{i} = 1, 2 \ldots \text{N} \quad \text{j} = 1, 2 \ldots \text{p} \tag{3}$$

where, W is the Inertia Weight.

The algorithm is shown in flow chart as shown in Fig. 1.

The papers under various categories are discussed below:

1. Review Papers

The concept of PSO was implemented on non-linear benchmark function. The relationship of PSO was presented with A-life (Artifical life) as well as Genetic Algorithm.

Four review papers have been published so far. Parsopoulas and Vrahatis [2] published a review paper covering research papers up to 2002, discussing ability of PSO for multiobjective, mini-max, integer programming etc. Kameyama [3] have covered papers from 1995 to 2008, and discuss the progress of PSO, modifications in the basic PSO for improving exploitation and exploration.

Floudas and Gounaris [4] presented progress in global optimization during 1998–2008. The area of twice continually differentiable non-linear optimization, optimization with differentiable algebraic models, semi- infinite programming, optimization with grey box/nonfactorable models and bi-level nonlinear optimization were covered. Zhang et al. [5] provided advances with PSO, including its modifications, population topology, hybridization, extensions (to multiobjective, constrained, discrete, and binary optimization), theoretical analysis and parallel implementation mainly during 2010–2014.

2. Acceleration Coefficients (C_p, C_g) and IW

You et al. [6] proposed an adaptive weight PSO with constriction factor to overcome the problem of premature convergence. The value of inertia weight is set according to changes in the value of objective function.

Bansal et al. [7] studied 15 popular inertia weight strategies. They found Chaotic IW to be the best for better accuracy and random IW for efficiency.

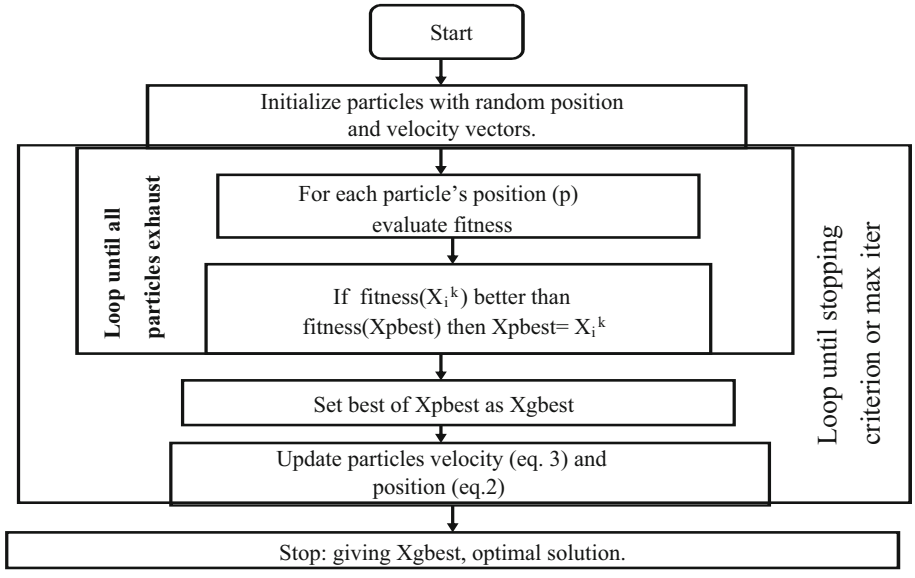

Fig. 1 Flow chart of PSO algorithm

Bonyadi and Michalewicz [8] investigated the movement patterns of a particle in the PSO algorithm. The Movement patterns were characterized on the basis of correlation between positions generated by particles and its range of movement.

3. Stopping Criterion:

Zielinski and Laum [9] evaluated various stopping criteria on the basis of movements made by the particles, improvements based criteria and distribution based criterion for a constrained single—objective PSO algorithm.

4. Applications of PSO:

A number of papers have been published on applications of PSO.

Engineering Applications

Wu et al. [10]. suggested various application of PSO in the field of Railway for scheduling, active controls, and network layout planning. In scheduling applications, PSO was used to find the optimal schedules. Al Rashidi and El-Hawary [11] suggested the application of PSO in solving optimization problems in the area of electric power systems. Jain et al. [12] applied PSO to multiobjective economic load dispatch problem considering various objectives. PSO has also been implemented for Optimal power flow [13, 14], load flow [15, 16], and optimum design of PID controller in AVR system [17], power loss minimization [18] etc. Nimtawat and Nanakom [19], suggested a PSO algorithm for beam-slab layout design of rectangular floor. Mac et al. [20] proposed a novel hierarchical global path planning method for mobile robots in cluttered environments using PSO.

Islam et al. [21] suggested a time-varying transfer function in the BPSO, namely TVT-BPSO, for systematic analysis of its exploration and exploitation capability. Suresha et al. [22] implemented PSO to predict the length of stay of patient in hospital and found PSO to be better than BP for prediction.

Other Applications

PSO has been implemented for various applications. Some of these are Source Seeking Problem [23] Elevator Door System [24], Quad Assignment Problem [25], Equipment Possession Quantity [26], Job Shop Scheduling Problem [27] etc.

5. Comparison of various type of PSO

Bhushan and Pillai [28] compared PSO and firefly algorithm (FFA). Ten standard nonlinear functions were chosen. Elapsed time and mean value of the function were evaluated for PSO and FFA. The mean value of function and elapsed time were found to be much smaller than FFA.

Angleline [29] attempted particle selection with PSO on four test functions and claimed that his method offered same improvement in performances in respect of some functions but not all functions.

6. Hybridization of PSO with other optimization techniques

Many researchers have attempt to Hybridize PSO with various other techniques and claimed improvements from performance point of view.

Chen and Peng [30] proposed a new hybrid methodology called PSO with recombination and dynamic linkage discovery (PSO-RDL) and implemented on four benchmark functions and a real world power system problem of Economic Dispatch. Authors found its performance to be comparable to that of classical EP, Fast EP(FEP), modified EP, improved FEP, as well as modified PSO(MPSO). Jiao et al. [31] have developed Elite particles swarm optimization with mutation to avoid local convergence. In this method bad particles were replaced by elite particles and to avoid local convergence mutation has been used.

Other hybrid algorithms reported are hybridized simplex method with PSO [32], combined mutative scale chaos [33] and mutation in PSO [34].

7. Multiobjective optimization using PSO

Multiobjective approach to optimization has been attempted through PSO using Discrete multiobjective PSO [35], a competitive co-operative and co-evolutionary approach [36], and vector evaluated PSO [37]. In all these papers the result have been discussed qualitatively.

8. Modified PSO

Many modifications have followed the original algorithm, like Memory Enhanced PSO [38], Predator–Prey PSO [39] There are newer variants like: CLPSO [40], SLPSO [41] and OLPSO [42] which do not require parameter tuning. These algorithms, unlike previously mentioned variants, have a structure entirely different from the PSO. They make use of the current information and usually do not include the previous iterations information.

Schutte and Groenwold [43] studied the variants of PSO algorithms and applied to Dixan-Szego test set. Liu and Wang [44] introduced Evolutionary game (EGPSO) in which the behavior of particles are modelled using Replicator dynamics and multi-start technique.

Hossen et al. [45] also tried an adaptive PSO based on behavior of spider.

Benmessabel and Touahria [46] illustrated the effect of excluding the redundant particle from current iteration. Jii

and Wangi [47] combined PSO with gradient method, which avoids immature convergence.

Beheshti et al. [48] proposed binary accelerated PSO using two parameters that is no. of generations and population size. Rios and Sahinidis [49] presented a review of derivative free algorithms including PSO for constrained problems. Chen et al. [50] presented an organizational adjustment PSO based particle filter (OAPSO-PF) algorithm which allowed the particles to adopt to environment and reach the global optimum.

9. Velocity Upgradation:

Arasomwan and Adewumi [51] tried a PSO which upgrades the velocities based on Euclidean distance between particles. Baiquan et al. [52] have suggested a control system based strategy for speed and position formulas of PSO, which resulted in improvement in speed of convergence as well as premature convergence.

Conclusions

PSO has attracted many researchers from mathematical point of view. But, from application point of view, only a few researchers have developed their efforts. So there is a lot of scope of research work from application point of view.

The various aspects of PSO which need further exploration are the following:

1 Recombination and linkages discovery in PSO.
2 Elite particles, mutation and engineered crossover have potential to add to the efficiency and reliability of PSO.
3 Investigations on multistart techniques to avoid premature terminations.
4 For repetitive problems as is the case in practical field, PSO parameters need be tuned keeping in view the constraints on independent variables of the problems.
5 In multiobjective optimization we need various solutions (noninferior solutions) rather than one (optimum) solution. In other techniques dealing with multiobjective optimization, the problem is to be solved many times in order to achieve noninferior set. However, PSO starts with a number of points and, therefore, may be capable of identifying noninferior set in a single run. This aspect is under investigation of authors.

References

1. J. Kennedy, R. Eberhart, Particle swarm optimization, in *Proceedings of IEEE International Conference on Neural Networks (Perth, Australia)* (IEEE Service Center, Piscataway, NJ, 1995), pp. 1942–1948
2. K.E. Parsopoulos, M.N. Vrahatis, Recent approaches to global optimization problems through particle swarm optimization. J. Nat. Comput. **1**, 235–306 (2002)
3. K. Kameyama, Particle swarm optimization—a survey. Inst. Electron. Inf. Commun. Eng. **E92-D**, 1354–1361 (2009)
4. C.A. Floudas, C.E. Gounaris, A review of recent advances in global optimization. J. Global Optim. **45**, 3–38 (2009)
5. Y. Zhang, S. Wang, G. Ji, A comprehensive survey on particle swarm optimization algorithm and its applications, published in Hindawi, Math. Probl. Eng. 2015, 1–38 (2015)
6. Z. You, W. Chen, X. Nan, Adaptive weight Particle Swarm Optimization Algorithm with Constriction factor, in *Proceedings of International Conference of Information Science and Management Engineering* (2010), pp. 245–248. https://doi.org/10.1109/isme.2010.234
7. J.C. Bansal, P.K. Singh, M. Saraswat, A. Verma, S.S. Jadon, A. Abraham, Inertia weight strategies in particle swarm optimization, in *2011 Third World Congress on Nature and Biologically inspired Computing* (IEEE, 2011), pp. 633–640, 978-1-4577-1124-4/11/©
8. M.R. Bonyadi, Z. Michalewicz, Impacts of coefficients on movement patterns in the particle swarm optimization algorithm. IEEE Trans. Evolut. Comput. **21**(3), 378–390 (2017)
9. K. Zielinski, R. Laum, Stopping criteria for a constrained single-objective particle swarm optimization algorithm. Informatica **31**, 51–54 (2007)
10. Q. Wu, C. Cole, T. McSweeng, Applications of particle swarm optimization in the railway domain. Int. J. Rail Transp. **4**(3), 167–190 (2016)
11. M.R. Al Rashidi, M.E. El-Hawary, A survey of particle swarm optimization applications in electric power systems. IEEE Trans. Evolut. Comput. **13**(4), 913–918 (2016)
12. N.K. Jain, U. Nangia, A. Jain, PSO for multiobjective economic load dispatch (MELD) for minimizing generation cost and transmission losses. J. Inst. Eng. (India) Ser. B **97**(2), 185–191 (2016)
13. M.A. Abido, Optimal power flow using particle swarm optimization. Int. J. Electr. Power Energy Syst. **24**(7), 563–571 (2002)
14. R.-H. Liang, R.-H. Liang, Y.-T. Chen, W.-T. Tseng, Optimal power flow by a fuzzy based hybrid particle swarm optimization approach. Electr. Power Syst. Res. **81**(7), 1466–1474 (2011)
15. C.P. Salomon, G. Lambert-Torres, H.G. Martins, C. Ferreira, C.I.A., Costa Load flow computation via particle swarm optimization, in *9th IEEE/IAS International Conference on Industry Applications (INDUSCON)* (2010), 8–10 Nov 2010, pp. 1–6
16. P. Acharjee, S.K. Goswami, Chaotic particle swarm optimization based reliable algorithm to overcome the limitations of conventional power flow methods, in *Power Systems Conference and Exposition, 2009. PSCE '09. IEEE/PES*, 15–18 March 2009, pp. 1–7
17. Z.L. Gaing, A particle swarm optimization approach for optimum design of PID controller in AVR system. IEEE Trans. Energy Convers. **19**(2), 384–391 (2004)
18. H. YapJcJ, N. Çetinkaya, An improved particle swarm optimization algorithm using eagle strategy for power loss minimization. Math. Probl. Eng. (2017). https://doi.org/10.1155/2017/1063045. **(Article ID 1063045)**
19. A. Nimtawat, P. Nanakom, Simple particle swarm optimization for solving beam-slab layout design problems. Elsevier **14**, 1392–1398 (2011)
20. T.T. Mac, C. Copot, D.T. Tran, R. De Keyser, A hierarchical global path planning approach for mobile robots based on multi-

objective particle swarm optimization. Appl. Soft Comput. **59**, 68–76 (2017)
21. M.J. Islam, X. Li, Y. Mei, A time-varying transfer function for balancing the exploration and exploitation ability of a binary PSO. Appl. Soft Comput. **59**, 182–196 (2017)
22. A. Suresha, K.V. Harisha, N. Radhika, Particle swarm optimization over back propagation neural network for length of stay prediction. Procedia Comput. Sci. **46**, 268–275 (2015)
23. R. Zoi, V. Kalivarapu, E. Winer, J. Oliver, S. Bhattacharya, Particle swarm optimization based source seeking. IEEE Trans. Autom. Sci. Eng. **12**(3), 865–875 (2015)
24. P. Wen, M. Zhi, G. Zhang, S. Li, Fault prediction of elevator door system based on PSO-BP neural network, Scientific Research Publishing, Engineering **8**, 761–766 (2016). ISSN Online: 1947-394X, ISSN Print: 1947-3931
25. T. Gong, A.L. Tuson, Particle swarm optimization for quadratic assignment problems—a forma analysis approach. Int. J. Comput. Intell. Res. **2**, 1–9 (2007)
26. Z. Liu, R. Zhao, Equipment possession quantity modelling and particle swarm optimization, in *Proceedings of Third IEEE International Conference on Genetic Evolutionary Computing* (2009), pp. 628–632. https://doi.org/10.1109/wgec
27. J.-Q. Li, Q.-K. Pank, B.-X. Jia, Y.-T. Wang, A hybrid particle swarm optimization and tabu search algorithm for flexible job-shop scheduling problem. Int. J. Comput. Theory Eng. **2**(2), 1793–8201 (2010)
28. B. Bhushan, S.S. Pillai, Particle swarm optimization and firefly algorithm: performance analysis, in *2013 3rd IEEE International Advance Computing Conference (IACC)* (IEEE, 2013), pp. 746–751, 978-1-4673-4529-3/12
29. P.J. Angeline, Using Selection to Improve Particle Swarm Optimization (Natural Selection Inc, Vestal) (1998), pp. 84–89
30. Y.-P. Chen, W.-C. Peng, Particle swarm optimization with recombination and dynamic linkage discovery. IEEE Trans. Syst. Man Cybern. Part B Cybern. **37**(6), 1460–1470 (2007)
31. W. Jaio, G. Liu, D. Liu, Elite particle swarm optimization with mutation, in *2008 Asia simulation Conference—Proceedings of IEEE 7th International Conference on Systems Simulation and Scientific Computing* (2008), pp. 800–803
32. S. Song, Shujun et al., Improved particle swarm cooperative optimization algorithm based on chaos & simplex method, in *Proceedings o f Second IEEE International Workshop on Education Technology and Computer Science* (2010). https://doi.org/10.1109/etcs.2010.235.10
33. M. Chen, T. Wang, J. Feng, Y.-Y. Tang, L.-X. Zhao, A hybrid particle swarm optimization improved by mutative scale chaos algorithm, in *Fourth International Conference on Computational and information Sciences* (IEEE, 2012), pp. 321–324, 978-0-7695-4789-3/12 ©. https://doi.org/10.1109/iccis.2012.19
34. J. Liu, B. Zhu, The application of particle swarm optimization algorithm in the extremum optimization of nonlinear function, in *12th IEEE International Conference on Computer and Information Technology* (IEEE, 2012), pp. 286–289,978-0-7695-4858-6/12 ©. https://doi.org/10.1109/cit.2012.74
35. A.M. Sharaf, A.A.A. Ei-Gammal, *A Novel Discrete Multi-objective Particle Swarm Optimization (MOPSO) of Optimal Shunt Power Filter* (IEEE, 2009), 978-1-4244-3811-2/09
36. C.K. Goh, K.C. Tan, D.S. Liu, S.C. Chaim, A competitive and cooperative co-evolutionary approach to multi-objective particle swarm optimization algorithm design. Eur. J. Oper. Res. **202**, 42–54 (2010)
37. K.R. Harrison, B. Ombuki-Berman, A.P. Engelbrecht, Knowledge Transfer Strategies for Vector Evaluated Particle Swarm Optimization. Technical Report (Brock University, 2012)
38. M. Benedetti, A. Massa, Memory enhanced PSO-based optimization approach for smart antennas control in complex interference scenarios. IEEE Trans. Antennas Prop. Mag. **56**(7), 1939–1947 (2008)
39. H. Duan, P. Li, Y. Yu, A predator-prey Particle swarm optimization approach to multiple UCAV air combat modeled by dynamic game theory. IEEE/CAA J. Autom. Sin. **2**(1), 11–18 (2015)
40. J.J. Liang, A.K. Qin, P.N. Suganthan, S. Baskar, Comprehensive learning particle swarm optimizer for global optimization of multimodal functions. IEEE Trans. Evolut. Comput. **10**(3), 281–295 (2006)
41. C. Li, S. Yang, T.T. Nguyen, A self-learning particle swarm optimizer for global optimization problems. IEEE Trans. Syst. Man Cybern. Part B Cybern. **42**(3), 627–646 (2012)
42. Z.-H. Zhan, J. Zhang, Y. Li, Y.-H. Shi, Orthogonal learning particle swarm optimization. IEEE Trans. Evolut. Comput. **15**(6), 832–847 (2011)
43. J.F. Schutteand, A.A. Groenwold, A study of global optimization using particle swarms. J. Glob. Optim. **31**, 93–108 (2005)
44. W.-B. Liu, X.-J. Wang, An evolutionary game based particle swarm optimization algorithm. J. Comput. Appl. Math. **214**, 30–35 (2008)
45. S. Hossen, F. Rabbi, M. Rahman, Adaptive particle swarm optimization (APSO) for multimodal function optimization. Int. J. Eng. Technol. **1**(3), 98–103 (2009)
46. B. Benmessahel, M. Touahria, An improved combinatorial particle swarm optimization algorithm to database verticle partition. J. Emerg. Trends Comput. Inf. Sci. **2**(3), 130–135 (2010), ISSN 2079-8407
47. W. Jii, K. Wangi, An improved particle swarm optimization algorithm, in 2011 *International Conference on Computer Science and Network Technology* (IEEE, 2011), pp. 585–589, 978-1-4577-1587-7111/$26.00 ©
48. Z. Beheshti, S.M. Shamsuddin, S.S. Yuhaniz, Binary accelerated particle swarm algorithm (BAPSA) for discrete optimization problems. J. Glob. Optim. **57**, 549–573 (2013). https://doi.org/10.1007/s10898-012-0006-1
49. L.M. Rios, N.V. Sahinidis, Derivative-free optimization: a review of algorithms and comparison of software implementations. J. Glob. Optim. **56**, 1247–1293 (2013). https://doi.org/10.1007/s10898-012-9951-y
50. Z. Chen, Y. Bo, P. Wu, W. Zhou, A new particle filter based on organizational adjustment particle swarm optimization. Appl. Math. Inf. Sci. **7**(1), 179–186 (2013)
51. M.A. Arasomwan, A.O. Adewumi, *An Adaptive Velocity Particle Swarm Optimization for High-Dimensional Function Optimization Congress on Evolutionary Computation, June 20–23, Cancún, México* (IEEE, 2013)
52. L. Baiqum, G. Gaiquin, L. Zeyu, The block diagram method for designing the particle swarm optimization. J. Glob. Optim. **52**(689), 710 (2012)

International Journal of Engineering Technology Science and Research
IJETSR
www.ijetsr.com
ISSN 2394 – 3386
Volume 5, Issue 3
March 2018

A Review on Research Aspects and Trends in Micro-Electrical Discharge Machining (Micro-EDM)

Shrikant Vidya
Galgotias University, Uttar Pradesh
P. Mathiyalagan
Galgotias University, Uttar Pradesh
Reeta Wattal
Delhi Technological University, New Delhi

ABSTRACT

Miniaturization of parts and components play an important role in the development of today's and future's sophisticated technology in various fields. With the increasing demand for micro parts and structures in many industries like electronic, medical, aerospace etc. and also with rapid developments in micro-electro-mechanical systems (MEMS), micro manufacturing techniques for producing these parts become increasingly important. In this respect, Micro-EDM process has helped a lot to obtain higher accuracy and precision in manufacturing. It's a contactless machining process. Any conductive material with a low machinability can be machined by this process at micro-level with a higher production rate, dimensional and geometrical accuracy and economy. By virtue of inherent micro-to-nano-meter range material removal ability, various non-traditional machining processes such as Electrical Discharge Machining (EDM), Ultrasonic Machining (USM), Electro-Chemical Machining (ECM) and laser machining have come as a handy tool for micro-machining with EDM being the most prominent among them due to its capability of producing micro-features. The review begins with the introduction to Micro-EDM and its principle, followed by the variants of Micro-EDM. The different aspects and research trends and developments in Micro-EDM have been also discussed in this review.

KEYWORDS

Micro-EDM, Micro-machining, Material Removal Rate, Micro-ED-Milling.

1. INTRODUCTION

Micro Electrical Discharge Machining (micro-EDM) is a derived form of EDM, which is generally used to manufacture micro and miniature parts and components by using the conventional electrical discharge machining principles.

Micro-EDM is a material removal process employing discharges between a work piece and a micro size electrode that are submerged in dielectric fluid. Discharges occur when the electric field between the electrode and work piece exceeds a critical value and the dielectric breaks down. Either increasing the electric potential or reducing the separation distance between the electrode and work piece may cause the field to exceed the critical value. Charging and discharging the capacitor in a RC circuit governs the potential difference, while electronics control the separation distance by monitoring feed rate and short circuits. Energy from each discharge melts a microscopic amount of material, which is subsequently washed away after the voltage drops and the discharge collapses.

The main differences of micro-EDM from conventional EDM are being in the type of pulse generator, the resolution of the X-, Y- and Z- axes movement, and the size of the tool used. In micro-EDM; pulse generator produces very small pulses within pulse duration of a few micro seconds or nano seconds. Because of this reason, micro-EDM utilizes low discharge energies (~10^{-9}-10^{-5} joules) to remove small volumes (~0.05-500 μm^3) of material [1].

International Journal of Engineering Technology Science and Research
IJETSR
www.ijetsr.com
ISSN 2394 – 3386
Volume 5, Issue 3
March 2018

The most important factor which makes micro-EDM very important in micromachining is its machining ability on any type of conductive and semi-conductive materials with high surface accuracy irrespective of material hardness. It is preferred especially for the machining of difficult-to-cut material due to its high efficiency and precision. Small volumetric material removal of micro-EDM provides substantial opportunities for manufacturing of micro-dies and micro-structure such as micro holes, micro slot, and micro gears etc.

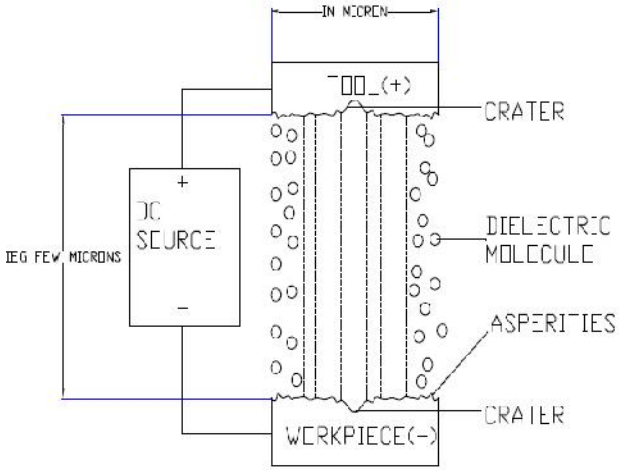

Fig.1: Schematic diagram of Micro-EDM

Although micro-EDM is a very efficient process in micro hole machining and having many advantages, it has also some disadvantages. One of them is that it is a rather slow machining process; the other is that while the work piece electrode is being machined, the tool electrode also wears at a rather significant rate. This tool-wear leads to shape inaccuracies. Another drawback is the formation of a heat affected layer on the machined surface. Since it is impossible to remove all the molten part of the work piece, a thin layer of molten material remains on the work piece surface, which re-solidifies during cooling [2].

Another significant point of micro-EDM is the inverted polarity of the tool electrode. Due to polarity effect in conventional EDM with long pulse duration, the tool electrode is usually charged as anode to increase material removal rate and to reduce electrode wear. At short pulse durations as used in micro-EDM, this effect is reversed. Therefore, in micro-EDM, the tool electrode is usually charged as cathode [3].

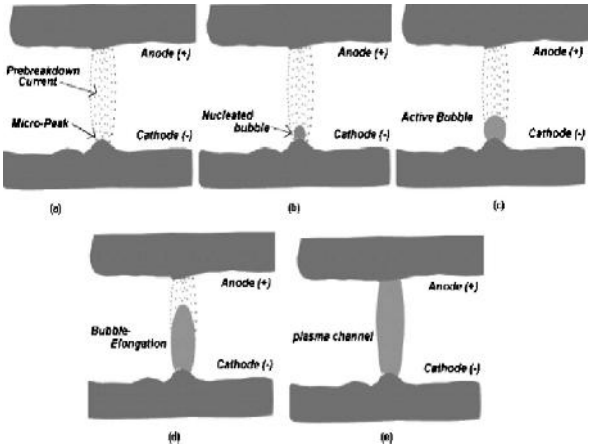

Fig.2 [4]: Proposed model of breakdown phase. (a) Emission of pre-breakdown current and heating at micro peaks. (b) Bubble nucleation at micro-peak. (c) Reaching electron impact criteria at bubble interface. (d) Bubble elongation towards anode. (e) Bubble abridged the inter-electrode gap and fully developed plasma channel at the end of the breakdown phase [5].

International Journal of Engineering Technology Science and Research
IJETSR
www.ijetsr.com
ISSN 2394 – 3386
Volume 5, Issue 3
March 2018

2. VARIANTS OF MICRO-EDM

Micro-EDM can be used as variant machining processes:-

Micro-ED drilling, Micro-ED milling, Micro-ED die sinking, Micro-ED contouring, Micro-ED dressing, and Micro wire electrical discharge grinding (micro-WEDG). All of these processes are integrated in a today's sophisticated micro-EDM machines.

(a) Micro-EDM drilling: -In this process, micro-electrodes (of diameters down to 5–10μm) are used to 'drill' micro-holes in the work piece.

Application: injection nozzles.

(b) Micro-EDM milling (Trajectory EDM):-Here, micro-electrodes (of diameters down to 5–10 μm) are employed to produce 3D cavities by adopting a movement strategy similar to that in conventional milling.

Application: micro-injection molds, embossing or coining tools.

(c) Die-sinking micro-EDM:-Here, an electrode with micro-features is employed to produce its mirror image in the work piece.

Application: Replication molds, embossing tools.

(d) Micro-WEDG: -Wire-Electric Discharge Grinding (WEDG) [6] is a prerequisite machining for drilling micro-holes and milling micro-cavities with micro-EDM technology.

WEDG is used to prepare smaller size tool down to Ø10 μm by using electrical discharge machining principle with reverse polarity. Smaller size tool is prepared from larger tools.

This process can be divided into two steps. At first step, the diameter of larger tool is reduced to nearly the desired smaller diameter by rough machining. At second step, the roughly machined tool diameter is reduced to the desired diameter by using finish machining parameters.

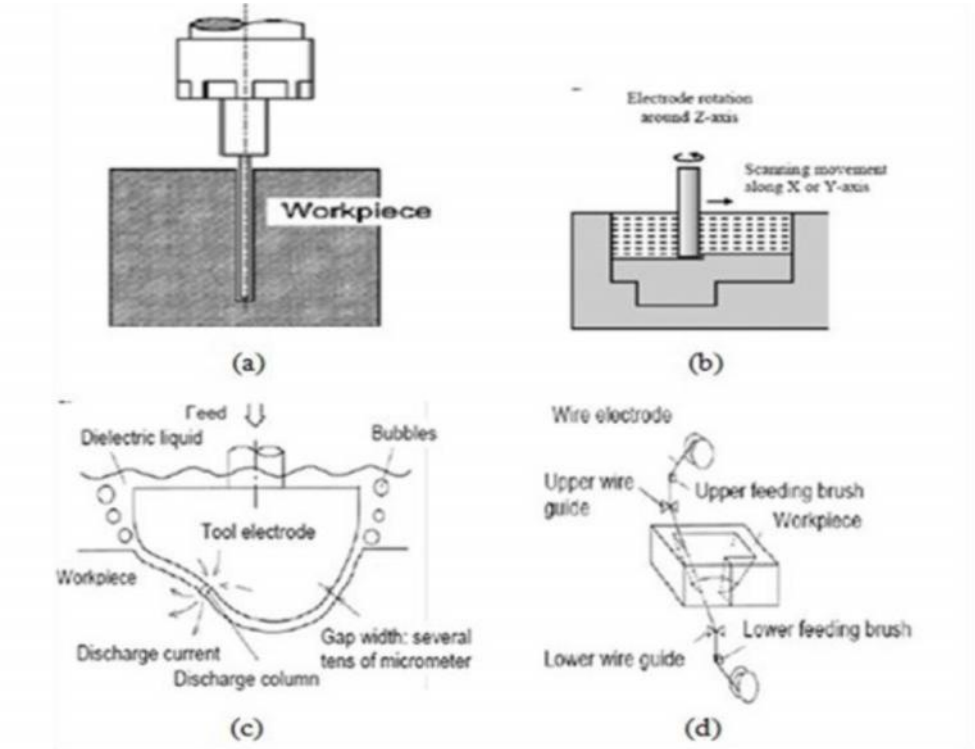

Fig.3: Variants of Micro-EDM: (a) Micro-EDM Drilling [7] (b) Micro-EDM Milling [8] (c) Die-sinking micro-EDM [9] (d) Micro-WEDG [9]

International Journal of Engineering Technology Science and Research
IJETSR
www.ijetsr.com
ISSN 2394 – 3386
Volume 5, Issue 3
March 2018

An overview of the capabilities of different types of micro-EDM is provided in Table 1.

Table 1: Overview of the micro-EDM varieties [2]

Micro-EDM variant	*Geometric complexity*	*Minimum feature size (µm)*	*Maximum aspect ratio*	*Surface quality Ra (mm)*
Drilling	2D	5	~ 25	0.05–0.3
Die-sinking	3D	~ 20	~ 15	0.05-0.3
Milling	3D	~ 20	~ 10	0.5-1
WEDM	2.5 D	~ 30	~ 100	0.1–0.2
WEDG	Axis-sym.	3	30	0.8

3. RESEARCH ASPECTS, TRENDS AMD DEVELOPMENTS IN MICRO-EDM

Material Removal Mechanism

Han et al. [10] developed a new transistor-type isopulse generator for micro-EDM. Their experiments showed that the transistor type isopulse generator is suitable for micro-EDM. Their experimental results revealed that the transistor-type pulse train generator is unsuitable for micro-EDM due to its low removal rate. The removal rate of the transistor-type isopulse generator is two or three times higher than that of the traditional RC pulse generator.

Wong et al. [11] investigated the micro-EDM material removal characteristics using single RC-pulse discharges. It was reported that the estimated erosion efficiency of material removal at low-energy (<50µJ) discharges is found to be seven to eight times higher than that at higher-energy discharges. They observed that the volume and size of the micro craters are more consistent at lower energy discharge than at higher energy discharges. A single-discharge erosion RC circuit with dc voltage power supply (0-300V) was developed.

Valentincic et al. [12] presented experimental results on observing the material removal rate (MRR) in dependence of alternating machining parameters and thus various discharge energies. They applied relatively low discharge energies as used in micro-EDM and relatively high as used in conventional EDM. Copper rods were used as electrodes. MRR of anode and cathode was measured. According to the results presented, the following conclusions were drawn:

- Measuring of MRR results in micro-EDM is rather difficult due to really low MRR. To reduce disturbances in weighting of the electrodes, the experiments have to last for a long time and thus they are time consuming. Alternative method for MRR measuring should be applied.
- When both anode and cathode materials are copper, anode has higher MRR in the case of low discharge energy values whereas in the case of conventional EDM higher MRR is noticed on cathode. This could be due to different phenomena in material removal mechanism, but it is also possible due to the effect of longer discharge time.
- Thus, additional research should be carried out in order to investigate influences of individual machining parameters on the material removal in micro-EDM process.

Yang et al. [13] simulated the forming process of discharge craters in three dimensions and was analyzed material removal mechanism in micro-EDM using Molecular Dynamics (MD). It was found that material removal mechanism in EDM can be explained in two ways; one by vaporization and the other by the bubble explosion of superheated metals. It was also found that the metal removal efficiency is 0.02–0.05, leaving most of the melted pool resolidified. In addition, authors also investigated the influence of power density on the removal process and reported that as the power density increases, the diameter and depth of the melted area increase, as does the metal removal efficiency. In this study, the forming mechanism of the bulge around

discharge craters was also analyzed, and it was found that bulge is formed due to two mechanisms. The first is the shearing flow of the molten material caused by the extremely high pressure in the superheated material, and the second is the accumulation of the ejected material on the bulge formed by the first forming mechanism. It was also concluded that existence of micro pores in the work piece material increases the depth of the discharge crater and melted area, thereby increasing the machining surface roughness. Simulation of the distribution of removed materials in the gap showed that some part of the removed material becomes debris ejected from the gap, while another part settles on the surface of the opposite electrode, and the last part returns to the surface of the electrode from which it was ejected.

Roy et al. [14] studied the debris and craters formed in micro-EDM by ultra short pulsed low energy electric discharge and analyzed the debris size, shape, and microstructure phases. Micrographs of debris produced at low energy (2.8-78 μ J) discharge shown less number of spherical particles dispersed in large number of non-spherical particles. They reported that the spherical particles are smooth individual balls and the non-spherical particles are in the form of lumps, consisting of large number of smaller particles having a common matrix. Few of them are in the form of curled thin strips. It was found that the microstructures of non-spherical particles resemble to that of sintered particles, and at high energy discharge debris appears to be solidified. The SEM/EDS analysis showed that material erosion at cathode work piece (hot die steel – ASTM H11) is more than at anode (tungsten carbide) tool electrode. The precise examinations of debris and sub-surface damage at crater showed material phase transitions in the molten regions and it was confirmed that material evaporation due to overheating is not found to be predominant in μ-EDM. Instead significant presence of non-spherical particles particularly at low voltage, shorter pulse on time discharge confirmed the influence of thermal spalling effect. It was also concluded that the presence of curved debris with perforated edges might be attributed to certain degrees of deformation.

Yeo et al. [15] proposed an electro-thermal model to estimate the geometrical dimensions of micro-crater. The model predicted the temperature distribution on the work piece as a result of single discharges in micro-EDM using voltage, current and pulse-on-time as input parameter during material removal. It was assumed that the entire superheated area is ejected from the work piece surface while only a small fraction of the molten area is expelled. For verification purposes, single discharge experiments using RC pulse generator were performed with pure tungsten as the electrode and AISI4140 alloy steel as the work piece. It was concluded that electric energy, spark gap and discharge time have a significant influence on the performance of the micro-EDM process.

Plasma Characteristics

Natsu et al. [16] measured the apparent temperature distribution in EDM arc plasma using spectroscopic analysis and compared it with the true temperature in arc plasma, calculated with Abel's inversion. After further investigation of influences of machining conditions on the temperature distribution and deionization time, it was concluded that the highest plasma temperature during discharge exists at the centre of arc plasma and ranges from 4000K to 8000 K, depending on machining conditions. They reported that higher plasma temperature is obtained by a thinner electrode, greater gap distance and higher discharge current. The greater is the discharge current, the greater the plasma diameter will be. It was found that the plasma deionizes faster when the gap distance is narrow.

Naga*hanumaiah et al. [17]* presented the spectroscopic measurement of temperature and electron density in the micro-EDM process. Authors studied the effects of voltage, current, spark gap and electrode size on the plasma characteristics. It was found that the average plasma temperature and electron density are 6170 K and respectively, with a coupling parameter of0.475. The low-energy discharge plasma produced in micro-EDM process is more a non-ideal plasma with a higher electron density and lower temperature than high-energy discharge plasma produced in conventional EDM. The inter particle distance in the micro-EDM plasma was found almost equal to the Debye length and hence existence of only one electron in the Debye sphere. It was reported that there is significant electrostatic interactions between the charged particles. Authors also reported that the electrode size and spark gap play a major role in determining the plasma characteristics in micro-

EDM. Smaller electrode size and larger spark gaps produce higher plasma temperature and electron density. This study may contribute in modelling of temperature evolution at the electrode surface and the mode of material erosion.

Process Performance and Optimization

Bigot et al. [18] proposed a method for the simple calculation of volumetric wear ratio is proposed based only on the geometrical information obtained and stated the influence of various factors contributing to micro electrode wear during the EDM process. EDM drilling and EDM milling were regarded as entities for the investigation. Their objective was to investigate the suitability of electrode wear compensation methods, during the micro EDM process. Electrode shape deformation and random variation of the volumetric wear are stated as the main factors affecting the applicability of wear compensation methods and as an indicator for the achievable accuracy with the micro EDM process. Finally, the following conclusions have been made:

- Understanding the electrode wear process and influencing factors is the key to more accurate and more reliable micro EDM process. Any electrode wear compensation methods should take into account the variation of volumetric wear ratio in order to insure that the required tolerances can be achieved.
- Variations of the wear ratio brought by uncontrolled factors are not negligible.
- The measured wear ratio does not appear to be constant, which does not always allow for the use of compensation method that relies on such assumption.
- When EDM machining of soft materials like brass and aluminium is to be done, machining strategies that insure good flushing should be used, for instance in a layer by layer machining. In the situation where flushing becomes an issue, for example when drilling small holes, steel would be a preferred solution because it is less affected by the flushing conditions.
- When using any new combination of electrode/Work piece materials and for any new diameter of electrode, similar tests should be conducted on the machine in order to measure the wear ratio and assess its repeatability. This should facilitate the choice of compensation method and allow for the production of accurate micro cavities. Further research will concentrate on testing a bigger variety of materials including variety of grain structures and investigation on inter grain boundaries.

Pham et al. (2007) [19] investigated the electrode wear during micro-electrical discharge drilling with micro rod and micro tube electrodes, shown in Figure 4. They reported that wear measurement increasing dramatically after a certain depth while rod electrode is used. This is mainly expected due to deteriorated flushing conditions. Good flushing should be enabled to avoid from side sparking on the electrode. However, tubular electrode is more stabilize in deep depth when comparing to the rod electrode.

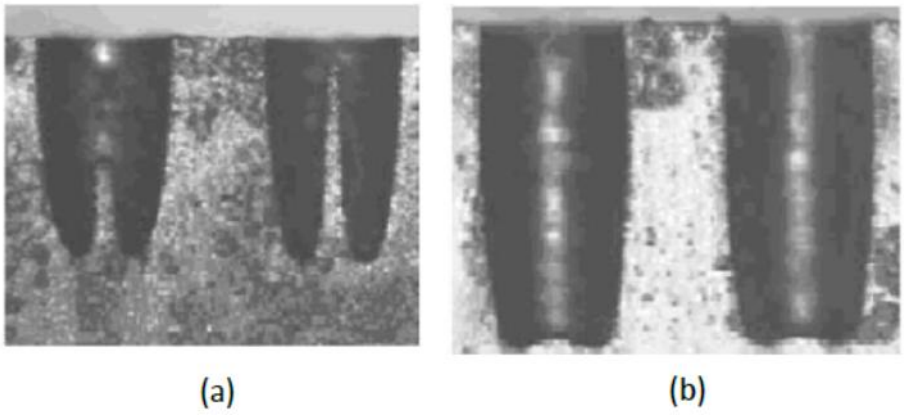

Fig. 4: Shape of micro-hole by (a) tubular electrode (b) rod electrode [18]

Kibria et al. [20] established and analyzed the micro-EDM performance characteristics such as MRR, TWR, overcut, diametral variance at entry and exit hole and surface integrity during machining of Ti-6Al-4V super alloy for the study of influence of different pure and boron carbide(B_4C) mixed kerosene and deionized water dielectrics. The experimental results revealed that MRR and TWR are higher using deionized water than kerosene due to formation of TiO_2 layer on work piece surface in case of deionized water which melts at lower discharge energy compared to TiC formed in case of kerosene. When B_4C mixed deionized water is used as dielectric, MRR is found to be increased whereas TWR decreases when B_4C mixed kerosene is used as dielectric. After analysis with SEM micrographs, the thickness of white layer is found to be less when deionized water is used as dielectric in comparison with kerosene. Overcut is directly proportional to the value of discharge energy in case of deionized water and inversely proportional in case of kerosene. So, the accuracy of the micro hole is higher at lower peak current and pulse-on-time using deionized water and at higher peak current and pulse-on-time using kerosene. B_4C mixed dielectrics show larger overcut as compared to both pure dielectric. The topography of inner machined surface is smooth in case of pure as well as additive mixed deionized water as compared to pure and additive mixed kerosene. Pure deionized water results in excellent machining efficiency than kerosene as well as B_4C mixed dielectrics. Also, B_4C mixed dielectrics results in more machining time as compared to pure dielectrics.

Jahan et al. [21] revealed that micro-EDM is an effective method of machining the extremely hard and brittle material such as Tungsten Carbide (WC). This study investigated the influence of major operating parameters on the performance of micro-EDM of WC with focus in obtaining quality micro-holes in both transistor and RC-type generators. Experimental investigations have been conducted with view of obtaining high-quality micro-holes in WC with small spark gap, better dimensional accuracy, good surface finish and circularity. In micro-EDM, the fabrication of micro-parts requires minimization of the pulse energy supplied into the gap which can be fulfilled using the RC-generator. It is observed that the RC-generator can produce better quality micro-holes in WC, with rim free of burr-like recast layer, good dimensional accuracy and fine circularity. Moreover, the smaller debris formed due to low discharge energy in RC-type micro-EDM can be easily flushed away from the machined area resulting in surface free of burr and re-solidified molten metal.

Paul et al. [22] explained the experimental results on dry-micro-EDM machining and oil-micro-EDM machining of γ-Titanium Aluminide alloy using 200μm steel electrode. They investigated influences of process variables i.e. open circuit voltage, discharge capacitance, pulse frequency and pulse-on-time and optimal conditions for minimum overcut on crater dimensions using ANOVA test. Overcut was measured from optical microscope images using Image Analyzer software. A regression model was developed to correlate the effect of discharge energy and spark on time on overcut. Based on the results, the following conclusions were noted:

- Micro-EDM in dry conditions can be effectively used for micro machining of γ-Titanium Aluminide alloy. The high heat and fire resistance property of this alloy prevents arcing issues during shot circuiting with low energy discharge. No deformation appeared in the work material.
- For precision machining i.e. smaller overcut dimensions of crater, lower energy is desirable, whereas MRR is low in these conditions.
- For the purpose of optimization of process variables, ANOVA test was performed that highlights that circuit capacitance of RC pulse generator contributes significantly in the accuracy of machining i.e. overcut of craters.
- For given micro-EDM process parameters the crater depth formation by a single discharge in the absence of dielectric liquid (dry-micro- EDM) is relatively small, compared to machining in presence of dielectric oil. At the same time electrostatic force induced between the tool and work piece is considerably small in dry machining.
- It has been observed that at the same set of discharge energy and spark on time the overcut was more in oil medium and also from experiments and FESEM micrographs it was evident that machining speed was also higher in oil medium compared to that in air medium. So for precision machining air medium is preferable at the cost of machining time.

Rasheed et al. [23] stated that while micro-EDM machining of Ni-Ti Shape Memory Alloy, Tungsten electrode is recommended for better surface roughness and Brass electrode for better MRR. In this study, the Taguchi design approach was employed to investigate the micro-EDM parameters to achieve the highest MRR, good surface quality, and low TWR. Dimensional accuracy of produced micro holes was observed from the SEM images. Based on the investigations, it was concluded that:

- Capacitance is the most influencing factor on MRR, TWR and Surface Roughness. MRR increases with increase in capacitance and discharge voltage for both tungsten and brass electrodes, but adversely affects the surface quality due to increase in crater size on the drilled surface.
- Electrical and thermal properties of electrode as well as work piece material also affect the performances.
- TWR is less in the tungsten electrode as compared to the brass electrode. So, Tungsten electrode is recommended for better surface roughness and Brass electrode for better MRR.

Somashekhar et al. [24] have reported on the development of modelling and optimization for micro-EDM process. Artificial neural network (ANN) is used to analyze the material removal of μ-EDM to establish the parameter optimization model. A feed forward neural network with back propagation algorithm is trained to optimize the number of neurons and number of hidden layers to predict a better material removal rate. A neural network model is developed using MATLAB programming, and the trained neural network is simulated. When experimental and network model results are compared for the performance considered, it is observed that the developed model is within the limits of agreeable error. Then, genetic algorithms (GA) have been employed to determine optimum process parameters for any desired output value of machining characteristics. This well-trained neural network model is shown to be effective in estimating the MRR and is improved using optimized machining parameters.

Sundaram et al. [25] presented an investigation on the optimization of machining parameters on the MRR and TW in ultrasonic assisted micro-EDM by introducing ultrasonic vibration to the work piece. Deep hole drilling was conducted on A2 tool steel work piece using tungsten electrode. The significance of the parameters on MRR and TW was determined using ANOVA and the results were confirmed experimentally at 95% confidence level. Based on analysis, it was found that ultrasonic vibration at 60% of the peak power with capacitance of 3300 PF is significant for the best MRR and the tool wear increases with the increasing machining time.

Karthikeyan et al. [26] analyzed the physical behavior of micro -EDM-milling process on the basis of channel shape, form, and surface quality. It was concluded that the tool rotatory motion plays a significant role in determining the amount of redeposition on the micro channel surface and analyzed the shape of micro channels for different speed and feed directions through experiments. It was reported that redeposition does not take place on the surface of tool due to centrifugal force.

Vidya et al. [27] studied the effects of five different cavities: circular, triangular, square, channel, and cross channel (square pillars) on the machining performance of micro-EDM-milling have been studied by analyzing dimensional accuracy, surface integrity, profile error, and formation of recast layers. The results highlight significant shape effect on machining performance in micro-EDM-milling. Circular holes machined by die sinking are found to be more accurate, and square shaped pillars machined in two settings by generating cross channels at 90 deg have poor dimensional control. On the other hand, triangular cavities have the highest surface finish and profile uniformity compared to other shapes. The microscopic study in scanning electron microscopy (SEM) reveals significant variations in globule formation, recast layer deposition, flow of eroded molten metal, and final shape of cavities, which are found to be dependent of tool rotation.

4. CONCLUSIONS AND FUTURE SCOPE

In summary, studies over material removal mechanism, plasma characteristics and parametric optimization describe the basic phenomenon of micro-EDM. These results provide a platform to investigate the physics on micro scale and for complex 3D microstructures further.

After going through the recent past research works as well as the problematic areas of different micro-EDM processes, it is quite evident that the study of in depth characteristics of micro-EDM is still unexplored and required further research and most of experiments have been performed over circular micro holes.

With rapid developments in electronic, micro-electro-mechanical systems (MEMS), aerospace etc. , micro manufacturing techniques for producing complex and 3D microstructures become important demanding fine fabrication tolerances and improved surface integrity.

In this world of high precision micro machining, there exists a need to develop the methodology and instruments used for measurements and analysis.

5. REFERENCES

[1] Moylan, S. P., Chandrasekar, S., and Benavides, G. L., 2005, "High-Speed Micro-Electro-Discharge Machining", Sandia National Laboratories, Sandia Report No. SAND-2005-5023.
[2] Masuzawa T., 2000, "State of the art of micromachining", Ann. CIRP 49 pp. 473-488.
[3] Uhlmann E., Piltz S., Doll U., 2005, "Machining of micro/miniature dies and moulds by electrical discharge machining-Recent development", Journal of Materials Processing Technology, 167 pp.488-493.
[4] Muralidhara, Vasa N. J., Singaperumal , "A piezoactuated tool feed mechanism for micro EDM" , Precision Engineering and Instrumentation Lab .International Journal of Machine Tools & Manufacture.
[5] Dhanik S., Joshi S.S., 2005, "Modelling of a Single Resistance Capacitance Pulse Discharge in Micro-Electro Discharge Machining", Journal of Manufacturing Science and Engineering 127, pp.759-767.
[6] Masuzawa T., Fujimoto M., Kobayashi K., 1985, "Wire electro-discharge grinding for micromachining", Ann. CIRP 34 pp.431-434.
[7] Lim H.S., Wong Y.S., Rahman M., Lee E.M. K. 2003 "A study on the machining of high-aspect ratio micro-structures using micro-EDM", Journal of Materials Processing Technology140 pp.318–325.
[8] Bleys P., Kruth J.P., Lauwers B., 2004, "Sensing and compensation of tool wear in milling EDM", Journal of Materials Processing Technology, 149 pp.139–146 .
[9] Kunieda M., Lauwers B., Rajurkar K.P., Schumacher B.M., 2005, "Advancing EDM through fundamental insight into the process", Annals of the CIRP 54 pp.599–622 .
[10] Han F., Chen L., Yu D., Zhou X., 2007, "Basic study on pulse generator for micro-EDM", Int. J. Adv. Manuf. Tech. 33 pp.474-479.
[11] Wang Z.L., J.Z. Cui J.Z., X.F. Liu X.F., Zhao W.S., 2004, "Mechanism of Electrode Material Removal in Short Pulse Time Electric Discharge Machining" ,Materials Science Forum Vols. 471-472 pp.784-789.
[12] Valentincic J., Sabotin I., Junkar M. "Investigation of tool ware ratio in micro and conventional EDM".
[13] Yang X., Guo J., Chen X., Kunieda M., 2011, "Molecular dynamics simulation of the material removal mechanism in micro-EDM", Precision Engineering 35 pp. 51–57.
[14] Roy S., Nagahanumaiah, Roy H., Ghosh D., 2009, "Characterization of debris produced in micro-EDM", International Conference on Multi Material Micro Manufacture (4M-ICOMM), Germany, September 22-23.
[15] Yeo S.H., Kurnia W., Tan P.C., 2007, "Electro-thermal modelling of anode and cathode in micro-EDM", J. Phys. D: Appl. Phys. 40 pp.2513–2521.
[16] Natsu W., Shimoyamada M., Kunieda M., 2006, "Study on Expansion Process of EDM Arc Plasma", JSME Int. J., Series C, Vol.49, No.2.
[17] Nagahanumaiah, Janakarajan, R., Glumak, N., Kapoor, S. G., and DeVor, R. E., 2009, "Characterization of Plasma in Micro-EDM Discharge Using Optical Spectroscopy," J. Manuf. Processes, 11(2), pp. 82–87.
[18] Bigot S., Ivanov A., Popov K., 2005, "A study of the micro EDM electrode wear", Proceedings of the 1st International Conference on Multi-Material Micro Manufacture (4M), Karlsruhe, Germany, pp. 355-358.
[19] Pham D.T., Ivanov A., Bigot S., Popov K., Dimov S., 2007, "An investigation of tube and rod electrode wear in micro EDM drilling", Int. J. Adv. Manuf. Tech. 33 pp.103-109.
[20] Kibria G., Sarkar B.R., Pradhan B.B., 2010, "Comparative study of different dielectrics for micro-EDM performance during microhole machining of Ti-6Al-4V alloy", Int. J. Adv. Manuf. Tech.48 pp.557-570.
[21] Jahan M.P., Wong Y.S., Rahman M., 2009, "A study on the quality micro-hole machining of tungsten carbide by micro-EDM process using transistor and RC-type pulse generator", Journal of materials processing technology 209 pp.1706–1716 .

[22] Paul G., Roy S., Sarkar S., Nagahanumaiah, Mitra S., 2013, "Investigations on influence of process variables on crater dimensions in micro-EDM of γ-titanium aluminide alloy in dry and oil dielectric media". Int J Adv Manuf Technol 65: pp.1009–1017.
[23] Rasheed M.S., Al-Ahmari A.M., El-Tamimi A.M, Abidi M.H., 2012, "Analysis of influence of micro-EDM parameters on MRR, TWR and Ra in machining Ni-Ti Shape Memory Alloy", IJRTE, Vol.1.
[24] Somashekhar K.P., Ramachandran N., Mathew J., 2010, "Optimization of material removal rate in Micro-EDM using artificial neural network and genetic algorithm", Materials and Manufacturing Processes 25 pp. 467-475.
[25] Sundaram M.M., Pavalarajan G.B., Rajurkar K.P., 2008, "A Study on process parameters of Ultrasonic Assisted micro-EDM based on Taguchi method", JMEPEG 17 pp.210-215.
[26] Karthikeyan, G., Garg, A. K., Ramkumar, J., and Dhamodaran, S., 2012, "A Microscopic Investigation of Machining Behaviour in l-ED-Milling Process," J. Manuf. Processes, 14(3), pp. 297–306.
[27] Vidya S, Barman S, Chebolu A, et al. Effects of different cavity geometries on machining performance in microelectrical discharge milling. J Micro Nano-Manuf 2015; 3(1): 011007.

ResearchGate

See discussions, stats, and author profiles for this publication at:
https://www.researchgate.net/publication/324197825

A Study on the Application of Turbo Expansion in Light Duty Gasoline and Diesel Engines: A Review

Article · April 2018
DOI: 10.4271/2018-01-0051

CITATIONS
0

READS
12

5 authors, including:

Naveen Kumar
Delhi Technological University
115 PUBLICATIONS **878** CITATIONS
SEE PROFILE

Some of the authors of this publication are also working on these related projects:

Production of Biodiesel from Tree borne oil. View project

Engine design optimization View project

All content following this page was uploaded by Naveen Kumar on 08 April 2018.

The user has requested enhancement of the downloaded file.

Downloaded from SAE International by Naveen Kumar, Sunday, April 08, 2018

2018-01-0051 Published 03 Apr 2018

A Study on the Application of Turbo Expansion in Light Duty Gasoline and Diesel Engines: A Review

Satvik Jain, Rahul Fageria, Srishti Mishra, Adeel Ahmad, and Naveen Kumar Delhi Technological University

Citation: Jain, S., Fageria, R., Mishra, S., Ahmad, A. et al., "A Study on the Application of Turbo Expansion in Light Duty Gasoline and Diesel Engines: A Review," SAE Technical Paper 2018-01-0051, 2018, doi:10.4271/2018-01-0051.

Abstract

Turboexpansion is a concept which is aimed at reducing the fuel consumption of pressure-charged combustion engines by providing over-cooled air to the engine prior to its induction in the combustion chamber. The performance of the engine is dependent on intake charge density which is preferred to be high at reduced charge air temperature. This becomes achievable through a cooling system known as a turbo expander which expands a high-pressure gas to produce work that is usually employed to drive a compressor. Though, initially used for the purpose of refrigeration in industries, for the past few decades various researches have proved its efficiency in internal combustion engines. In gasoline engines, it is usually employed to extend the knock limit and reduce carbon emissions. Also, an extension to the knock limit allows several improvements in parameters such as increased specific output, an increase in compression ratio and a reduction in the fuel consumption of the engine. Without its application in gasoline engines, the engine must operate at lower compression ratio in order to prevent knock. When applied to the diesel engines, it has been found to be effective in lowering the nitrous oxide levels which is central to the formation of ground-level ozone which is associated with hazardous health effects. In addition to that, it also reduces the peak combustion temperature as in the case of the gasoline engine. This paper aims to review advantageous and disadvantageous effects as well as results of the application of turbo expansion in light-duty gasoline and diesel engines.

Introduction

Today automobile manufacturers assimilate the importance of lower emissions and decreased fuel consumption of the vehicles. It is well known that human activities are substantially increasing greenhouse gas concentrations resulting in a warming of the Earth's surface. Transportation system represents 20 to 25% of the CO2 in the atmosphere and this share tends to increase [1]. Furthermore, the theory of Peak Oil [2] predicts the point at which demand becomes greater than the supply. Oil is a finite energy source and the dependence on it will need to shift towards cleaner and renewable energies due to availability and monetary reasons. One of the ways to decrease automobile's share in degrading environment is the use of superchargers and turbochargers. Turbochargers are more efficient than superchargers and widely used in diesel engines. They recover exhaust heat which otherwise would remain unexploited. Heat recovery is considered a significant area with large potential for improving fuel efficiency in automobiles. The energy rejected as waste heat accounts for 35% in the exhaust system and 30% via engine cooling [3]. Even in gasoline engines, turbocharging helps to reduce fuel consumption and CO_2 emission [4, 5]. The reduction in fuel consumption is more than 10% in running conditions close to best efficiency areas [6, 7, 8]. Turbocharger design is the key used to calculate the optimum solution for minimum fuel consumption and maximum transient response in combination with satisfying the constraints such as maximum turbine temperature, turbocharger rotational speed, compressor surge limit, maximum combustion pressures and knock limit [9, 10]. However, in spark ignition engine turbocharging is limited due to knocking phenomenon which is autoignition of air-fuel mixture. High temperature due to the compression of air through the compressor is at the origin of all these problems. In order to decrease charged air temperature, experiments such as using water vapor or ethanol in the combustion chamber have been performed [11]. Traditionally in a turbocharged engine to lower the air temperature before it reaches the intake manifold, an intercooler is used to remove some of the heat added at the compression stage. However, it is not practically reasonable to have an intercooler that reduces the charge air temperature to the atmospheric temperature. The intercooler functioning and limitations are discussed under next heading. Therefore to facilitate the decrease in charge air temperature there is an addition of an expansion device between the intercooler and the intake manifold. Since turbocharging is applied to a downsized engine, effects of a turboexpander are studied in light-duty engine.

The system studied in this paper is one which extracts waste heat from the compressed charge air using an air expander to facilitate further decrease of charge air temperature. The cooling capacity of the system is used to lower the temperature of the charge air intake to increase density. The

© 2018 SAE International. All Rights Reserved.

Downloaded from SAE International by Naveen Kumar, Sunday, April 08, 2018

concept of turbo expansion was developed in the mid-20th century and has seen much advancement in recent years.

Intercooler

The Intercooler is a heat exchanger with the sole purpose of lowering the temperature of compressed air charge as much as possible before reaching the intake manifold. Passing charge through an intercooler reduces its temperature, allowing a greater volume of air to be admitted to an engine. Intercoolers have a key role in controlling the cylinder combustion temperature in a turbocharged engine. The effectiveness of an intercooler is a measure of how much heat is extracted from the charged air as compared to how much is added by the compressor [12]. Mathematically, effectiveness is defined as

$$E_{ic} = \frac{T_{co} - T_{io}}{T_{co} - T_a}$$

where

T_{co} = Compressor outlet temperature
T_{io} = Intercooler inlet temperature
T_a = Ambient air temperature

Naser et al. [13] through their own programme code in MATLAB presented the effect of the intercooler (as a heat exchange device air-to-liquid with three different sizes and overall heat transfer coefficient and one base) at a multi-cylinder engine performance for operation at a constant speed of 1600 RPM. They presented the simulation predictions of temperature and pressure in the cylinder for three types of intercoolers. Also, they presented the pressure and temperature in the intake, exhaust manifold and, other performance. From the experimental data, the authors concluded that the maximum temperature in engine cylinder was decreasing from 1665.6 K at S.U = 1000 to 1659.2 K at S.U = 1600 where S is surface area heat exchange and U is heat transfer coefficient. Also, intercooler performance was increased by increasing the design parameters. Intercooler effectiveness was 0.92 at S.U = 1000 and 0.98 at S.U = 1600. Similarly, Canli et al. [14] also studied the intercooler's effect on power output of an internal combustion engine. In their study, a diesel engine was considered and it was evaluated whether it was equipped with either a turbocharger or both a turbocharger and a super intercooler. Using thermodynamics laws and expressions, the power output of the engine was analytically examined by changing intercooler's features such as pressure drop values and engine revolution at full load. Results were presented and interpreted as power (kW) and downsizing of the engine volume values (m^3). In their study, Canli et al. concluded that engine power can be increased to 154% by ideal intercooler while single turbocharger without intercooler can only increase 65% engine power output. Through these researches, one can conclude the necessity of an intercooler and the importance of its purpose.

In actual practice, the effectiveness cannot reach 100% and can only reach 70-75% in case of an air-to-air intercooler and 80-85% in case of an air-to-water intercooler. Therefore, it is no possible to reduce the temperature of charge air below ambient temperature or temperature of coolant in case of air-to-liquid intercooler. The advantages of turbocharging and limitations of intercooler explain the need for a permanent solution in the form of turboexpander.

Turboexpansion

Overcoming the limitations of an intercooler, using expansion cooling right before the entry of charge air into the intake manifold, the temperature of charge can be theoretically brought down to less than ambient temperature. The benefits of a turbocharged engine can be summarized using the following power equation [15],

$$P = \frac{n_f\, n_v N\, V_d Q_{HV} \rho_{a,i} \left(\frac{F}{A}\right)}{2}$$

where

P = power generated
n_f = fuel conversion efficiency
n_v = volumetric efficiency
N = speed of engine
V_d = engine displacement
Q_{HV} = fuel heating value
$\rho_{a,i}$ = intake manifold air density
(F/A) = fuel air ratio

Therefore, according to this equation the intake manifold density is directly proportional to intake manifold density. The intake manifold air density $\rho_{a,i}$ will increase when air is compressed before entering the combustion chamber. However, density is not only dependent on the pressure but also temperature [16]. The turbocharger compressor increases pressure, therefore increases density. The higher temperature that results from the compression, however decreases density as shown in the following equation

$$\rho_{a,i} = 2.7 \frac{P_{a,i}}{T_{a,i}}$$

where

$\rho_{a,i}$ = intake manifold air density
$P_{a,i}$ = intake manifold pressure
$T_{a,i}$ = intake manifold temperature

The key principle is to achieve increased intake charge density in combination with reduced charge air temperature to offer benefits in respect of detonation and thermal loading, with control over combustion rates and in-cylinder pressures. Therefore, by extracting energy from the pressurized charge air, its temperature can be lowered. Since this temperature is before compression, it is known as Start of compression temperature (SOCT). It results in a lowered end of compression temperature (EOCT) for a given compression ratio. As said earlier, it is achieved by passing the gas flow through an air expander and the energy extracted from the charged air at this point can be used to produce useful work.

It is also worth noting that if at this point temperature is not lowered, it results in retarding of spark. It has been proven

© 2018 SAE International. All Rights Reserved.

Downloaded from SAE International by Naveen Kumar, Sunday, April 08, 2018

by Russ [17] that ignition retard has two drawbacks, one is the loss of efficiency resulting in fuel economy penalty and the second is that spark retard increases cycle-to-cycle Indicative Mean Effective Pressure cycle fluctuations increases engine roughness.

A simple turboexpander configuration and its T-s diagram [18] is shown below.

It can be seen from Figure 2 that air is compressed isentropically from points 1 to 2′. Heat is rejected at constant pressure to point 3′, from where it is expanded isentropically to the desired engine inlet conditions at point 4. The real process is represented by points 1 to 4.

It should be understood that this diagram represents ideal processes and not the losses present during real conditions.

The three configurations of turboexpander system showing the components and the gas flow direction are shown below.

In this configuration, exhaust gas from the exhaust manifold is used to drive a turbine which transmits this spin through a shaft to a compressor which compresses the intake air. The compressed air passes through an intercooler which is a heat exchanger and reduces the charge air temperature.

FIGURE 1 Turboexpander configuration [18]

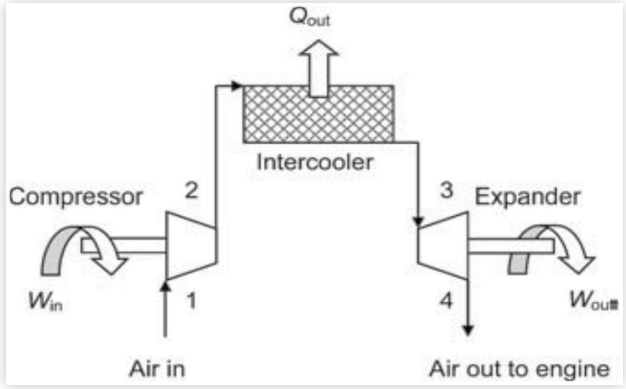

© SAE International

FIGURE 2 T-s diagram for intake charge conditioning system [18]

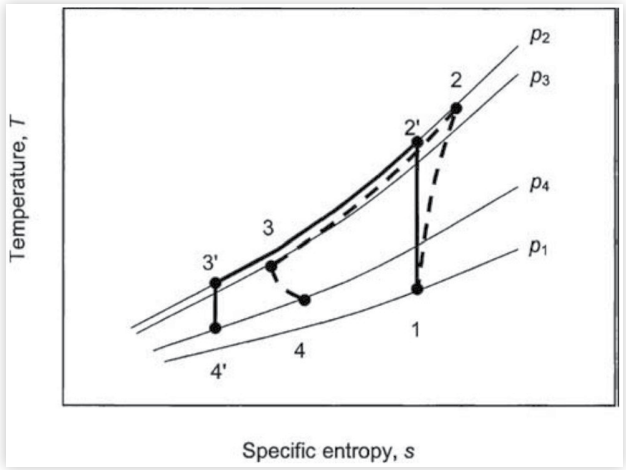

© SAE International

FIGURE 3 Turboexpander configuration with single compression

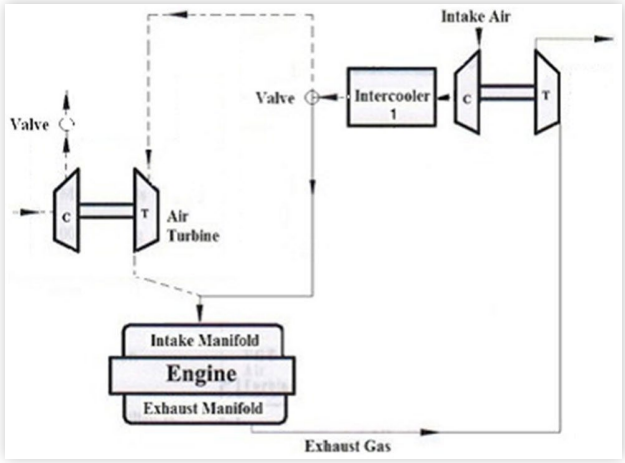

© SAE International

To further reduce its temperature it is passed through an air turbine which expands charge air below ambient temperature and the energy extracted can be used further.

In this configuration, the compressor can be equipped with a valve that would regulate the flow of air from ambient and back to ambient. This variation in the flow valve can regulate the expansion of the air by allowing more or less work to be extracted from it. This cooled air can then be fed to the intake manifold and finally to the combustion chamber. The main difference between the exhaust turbine and expander (air turbine) is their purpose. The purpose of exhaust gas driven turbine is to extract useful energy from the hot gases and as a consequence, the exhaust gas temperature decreases. The purpose of air turbine is to decrease the charged air temperature and as a consequence, useful work is extracted.

The second configuration is shown in Figure 4.

In this configuration air after being cooled from intercooler 1, passes through a compressor driven by an air turbine which itself is driven by charge air, both compressed and cooled for the second time. This configuration is expected to

FIGURE 4 Turboexpander configuration having double compression

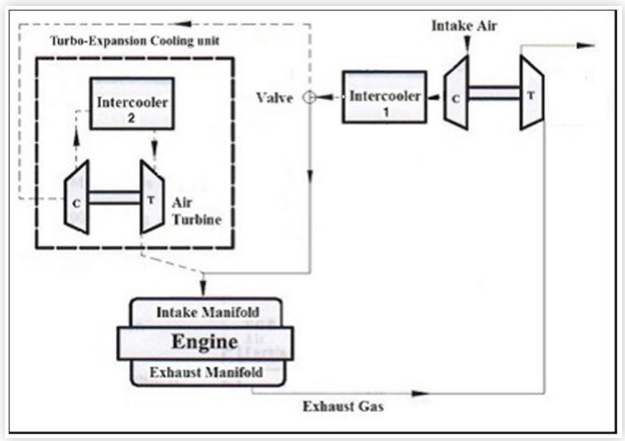

© SAE International

© 2018 SAE International. All Rights Reserved.

Downloaded from SAE International by Naveen Kumar, Sunday, April 08, 2018

FIGURE 5 Turboexpander configuration by Shi [19].

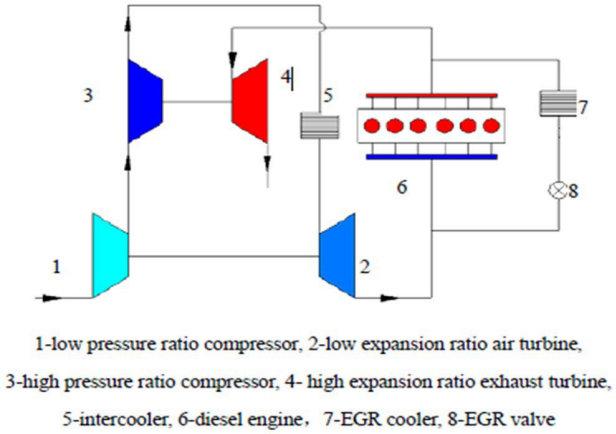

© SAE International

be used on commercial vehicles. Since this configuration includes two sets of intercoolers and turbochargers, it is thus an expensive one.

The third configuration has been proposed by Shi [19] and simulated on a diesel engine is shown in Figure 5.

The difference between Figure 4 and Figure 5 is that there is only one intercooler in Figure 5 and the low pressure ratio compressor works as the first stage of the turbocharging system. As the low pressure ratio compressor works as a power absorber of the air turbine, its pressure ratio and temperature rise are rather less than that of the other. So it seems unnecessary to employ an intercooler between the two compressors. The working principle of the system is similarly such that exhaust gas from the engine with high pressure and temperature expands through gas turbine 4 which drives the high pressure compressor 3. Compressed air from the high pressure compressor with high pressure and temperature goes through the intercooler 5 and transfer its heat to the cooling air, and then expands in the air turbine 2 driving the low pressure compressor 1 with its thermal energy, so as to reach further lower temperature. As a result, the air with lower temperature and pressure, and big enough density enters engine 6.In this configuration, there is no valves and pipes and has to be modified to be used for commercial purposes. There are several other configurations also proposed by Wang [20] in his patent for low temperature air cooling through turboexpansion.

History of Turboexpansion

The first published text that introduces the idea of expanding internal combustion charged air is from 1959. In that publication, William R. Crooks [29] evaluated various systems of combustion air conditioning, with a special highlight on expansion cooling of air by making use of the surplus of energy from the turbo-supercharging system. In 1961, Crooks filed a patent [30] and in this invention, the power generated by the expansion turbine was used to power a centrifugal Freon compressor. In 1966, Helmich published a paper showing the successful development and application of the design covered in Crooks' patent [31]. The benefits of an increase in power and decrease in fuel consumption were also proven. But the refrigeration system was so big that it had to be installed outside the building containing the engine.

In 1975, Charles E. McInerney filed a patent with the US patent office [32]. In McInerney invention, there was no refrigeration cycle and it was the first attempt at a smaller setup that could eventually be applied to automotive. The power recovered from the expansion was used to power a fan blowing on the intercooler to maximize the heat rejection at that stage. He claimed that recent exhaust pollution control devices were designed to reduce the production of carbon monoxide and hydrocarbons by increasing the operating temperature of the engine. This resulted in a grater completion of combustion of the fuel but produced more oxides of nitrogen.

In 1991, Roy C. Meyer and S. M. Shahed presented a turbo-cooling system in which two-stage compression and intercooler is used [33]. Through the use of the Joule-Thompson effect, compressed and cooled charged air is expanded before reaching the intake manifold. The positive work extracted from the expansion is used in the first stage compression process. It was shown that the concept would be feasible using a basic thermodynamic model. More specifically, it was revealed that a minimum intercooler effectiveness of 55% was required.

In 1992, Harry A. Cikanek and Vemulapalli D. N. Rao filed a patent with the US patent office [34]. Their invention is very similar to that of Meyer & Shahed except that Cikanek & Rao made use of a refrigeration cycle. The compressor for the refrigerating fluid is driven by one of the turbines already in use by the charged air system. The refrigerating system's evaporating coils are placed in close proximity or inside the intake manifold to further reduce the intake temperature. The goal of this invention was to reduce emission in diesel powered vehicles.

In 2003, J. W. G. Turner, R. J. Pearson, and M. D. Bassett performed an initial study on Turbo-Expansion [35]. Reducing inlet air temperature in order to increase the compression ratio and go beyond the limits set by engine knock along fuel economy was the objective. They also focused on engine downsizing. The reduction in vehicle size and mass would also help achieve their goals. Running the downsized engines at higher brake mean effective pressure (BMEP) would also contribute, since brake specific fuel consumption (BSFC) is improved due to the reduction of throttling loss. The authors also pointed out that the basic idea of Turbo-Expansion was similar to an aircraft air conditioning system and has been used for years. In addition to simulations, they collected data based on a test rig equipped with a positive displacement screw expander. It was concluded that Turbo-Expansion could improve power and fuel economy.

In 2004, the first law of thermodynamic model used to characterize the performance of the Turbo-Expansion concept [18]. The model was verified against experimental testing data collected by Turner et al. [35] and the effects of the compressor, expander and intercooler effectiveness variation were quantified. It was shown that the intercooler effectiveness was the most critical parameter which has already been discussed in the intercooler section. The authors concluded that the constant mass flow rate thermodynamic analysis of the system was valuable as a test for the viability of the concept. The next step would be the engine simulation at constant BMEP. Then

© 2018 SAE International. All Rights Reserved.

Downloaded from SAE International by Naveen Kumar, Sunday, April 08, 2018

Turner published a review of various technologies for fuel economy improvement in gasoline engines and discussed how they interacted [36]. Then the NOMAD development engine was built to investigate the concept and other technologies.

In 2005, the presented their dynamometer testing results of the NOMAD engine [26] which did not prove the feasibility of the cooling system. It was concluded that the efficiency of the components used on the NOMAD engine was not able to deliver significant temperature reduction. The reductions were so minimal that even convection heat transfer from the engine compartment could offset any benefit. It was proposed that research concentrating on the improvement of expanders and intercoolers could help make the Turbo-Expansion a reality. Notice that the water-cooled intercooler used was set to maximum performance, which corresponds to an effectiveness of 96%. Although the results were unsatisfactory, the model developed led to some interest in pursuing a single-cylinder study [37]. The capability of Turbo-Expansion to extend the knock limit was proven based on experimental data. It is important to understand that although successful results were obtained with the single cylinder engine, the externally conditioned air was used with the plenum charge air temperature as the control variable. Taitt and Turner also published in 2006 [38], the work performed as a continuation of their publication in 2004. The results of their improved thermodynamic model, new engine cycle simulations, combustion and knock modeling showed an improvement in engine break specific fuel consumption based on Turbo-Expansion. If a constant value of 0.8 was used for the effectiveness or efficiency of all components, the benefits were greatly reduced due to heat transfer between the expander and the manifold. A second explanation was based on the amount of residual gases left in the cylinder after the exhaust stroke. It was proposed that the use of a mechanically driven compressor, a supercharger, could help reduce the backpressure, therefore helping with residual gas reduction.

In 2006, Whelan's research [39] on a gasoline turbocharged engine showed promising result and encouraged the use of turboexpander. The results showed an increase in power and boost pressure along with decreased intake temperature with no fuel consumption penalty. The author also suggested the use of turboexpander for ease of use for EGR operations in light and medium duty diesel vehicles.

In 2006, a publication by Dr. Lin-Shu Wang and Shiyou Yang [40] focused on the simulation of an air conditioning system for a turbocharged engine, using a VGT as the exhaust turbine. Notice here VGT is not used as expansion turbine for turboexpander. Part of the compressed air is expanded and used as a heat exchanger cooling medium in a second intercooler before being compressed again to use the expansion energy and finally be rejected in the atmosphere.

The other part of the charged air exchanges heat with ambient at a primary intercooler and with the expanded air at the secondary intercooler before reaching the intake manifold. The expander, which is a turbocharger turbine along with its compressor and the secondary intercooler, form the turbo-cool unit. The author concluded that the VGT turbocharger and turbo-cool are indispensable to each other and that the resulting temperatures could be below ambient. Improved brake mean effective pressure and lower break specific fuel consumption were also reported. Then, Dr. Wang et al. filed a patent in 2006 [20] in which several ways were presented for turbocooling. It was claimed that Engine operates according to a turbo-cooling process that uses exhaust-gas expansion in a turbine to achieve a higher effective expansion ratio. Excess power from higher exhaust-gas expansion through a turbine is used for conditioning intake charge-air for the purpose of engine-loss reduction. Moreover, apart from diesel and gasoline engines, these designs were claimed to be used on HCCI engines as well. Based on one of these designs, simulation work [24] was done on a gasoline engine and improvement in torque and fuel efficiency could be seen evidently.

In 2010, Whelan published a paper [42] in which a project named ACCESS was pursued by the author. The key objectives of the ACCESS project were the design, testing, and validation of a turbo-expander, suitable for application to a down-sized automotive engine. These focused on the possibility of applying current turbocharger designs and manufacturing methods to a turboexpander. The issue was the design of a high-efficiency, low-cost, turbine and housing to replace the existing turbine. The author studied that turbocharger's turbines are designed for operation at high gas temperatures and have other constraints which trade off efficiency with a number of vehicle operational requirements. But, the turbo-expander turbine does not have these constraints, so its design can be optimized for efficiency. The results were obtained using both simulation and experimental verification on a highly boosted gasoline engine. An increased efficiency of cold air turbine with respect to an existing turbocharger turbine was reported with simulated and experimental data being in close proximity.

In 2010, being inspired by works of Whelan, Shi [19] derived his design from Whelan's turboexpander design [39] as shown in Figure 5.Then the author simulated his design on a diesel engine equipped with EGR and showed decreased NO_x emissions accompanied by increased BSFC. As Whelan proposed, the authors found out that EGR operation was easier with use of turboexpander.

In 2012, Kitanović [43] simulated a spark ignition engine with the concept of turboexpansion but their results too were disappointing. They concluded that if instead of a VGT turbocharged engine, they would have taken a wastegate equipped turbocharged engine, the benefits of the turbo-expansion system would have been greater because of increased back-pressure caused by fractional exhaust flow.

In 2014, Romangoli along with Turner [28], used supercharger as an expander but only to be disappointed by the decreased isentropic efficiency of the supercharger. They then concluded that supercharger cannot be used as expander but reported that small amount of power can be extracted from supercharger when used as expander which was not surprising.

In 2014, Hu [44] researched on net fuel efficiency benefit from the turboexpansion concept using a super-turbo twin-charger 1-D simulation model. The author switched between compressor and expander mode of the supercharger and thus, the supercharger could provide the boost at low engine speed whilst behaving like a turbine presenting an indirect means to recover exhaust gas energy at high engine speed and meanwhile reducing the intake temperature. Similar to Romangoli [28], they also concluded that due to poor efficiency of the

© 2018 SAE International. All Rights Reserved.

Downloaded from SAE International by Naveen Kumar, Sunday, April 08, 2018

supercharger as expander turbine, there was no increase in fuel efficiency.

Study of Effects of Turboexpansion

The positive effects of turboexpansion cooling on various engine parameters are.

Compression Ratio

Compression ratio of a gasoline engine is limited due to knocking of engine as told earlier and for a diesel engine the reason seems to be the availability of material and the cost of material that is why for a naturally aspirated diesel engine compression ratio of 25:1 has been achieved. Diesel engine combustion generates large amounts of NOx because of the high flame temperature in the presence of abundant oxygen and nitrogen [21, 22].Compression ratio also acts a limiting factor for a turbocharged engine. Now, because the inlet charge has been cooled, the turbocharging limit or rather the compression ratio can be further increased.

Fuel Efficiency

The mathematical relation between compression ratio and efficiency for gasoline engine is

$$\eta_f = 1 - \frac{1}{r^{\gamma-1}}$$

where

η = efficiency
r = compression ratio
γ = ratio of specific heat at constant pressure to specific heat at constant volume

For diesel engine efficiency is given by

$$\eta_f = 1 - \frac{1}{r^{\gamma-1}}\left(\frac{\rho^{\gamma}-1}{\gamma(\rho-1)}\right)$$

where

ρ = cut-off ratio

The efficiency of both engines depends on compression ratio and when the compression ratio increases the efficiency also increases. Hence, when efficiency increases more power is produced from the same amount of fuel and fuel efficiency of engine increases. The increase of compression ratio also results in engine downsizing.

Emissions

In addition to reducing fuel costs, the Turbo-Expansion concept will help lessen pollutant formation. This will be possible for two reasons. Primarily, the objective of the concept is to reduce temperature of the charged air. Secondly, adding more fuel to absorb some of the heat in the combustion chamber will no longer be necessary. A controlled fuel/air equivalence ratio results in reduced emissions since more pollutant is formed with a richer air fuel mixture. When talking about emissions, the concerned products are carbon monoxide (CO), hydrocarbons (HC) nitric oxide (NO) and nitrogen dioxide (NO_2). NO and NO_2 are generally combined and called NOx. According to John B. Heywood [15], these products are formed at high temperature during the different phases of the engine cycle. During combustion phase of engine's cycle, the in cylinder temperature is the highest. During combustion, NO is formed around the spark plug, behind the flame propagating through the chamber, where the high-temperature burnt gas is present. The higher the temperature, the more NO is formed. Within that same region, CO is also formed when there is more fuel than oxygen as compared to the amount expected from a balanced chemical equation. Therefore, the richer the mixture, the more CO is produced as a result of the incomplete reaction which should have resulted in the production of CO_2 instead. Finally, HC production is observed at different phases but the main source is the extra fuel in the combustion chamber. Ultimately, the expansion of the charged air before it reaches the combustion chamber will be the source of an overall drop in temperature across the engine cycle, which will result in emission control and render the necessity of adding fuel to the mixture obsolete. CO and NO production will drop with the temperature. A leaner air mixture will control the formation of CO and HC.

Performance

As already told that power of engine depends on air intake density and air intake density depends on air intake temperature, therefore increasing charge air density increases power of engine. Also, power depends on efficiency as explained an earlier, therefore efficiency increase also increases the power of the engine. As fuel used will be leaner, the air fuel ratio will increase thus increasing power. Lastly, this concept will also allow higher boost pressures. This concludes the expected advantages of the turboexpansion cooling system but to what degree these advantages are achieved will be discussed later.

Turbine (Air Expander)

Turbine, being the most important component of the Turboexpansion cooling system (TCS) and its varied use by different authors is the reason why it has been given a separate section. Different authors have used and different types of turbines to test its effects on turboexpansion cooling. Authors have also proposed different types of turbine due to their advantages. The reason being, the air is expanded through it and the temperature lowered depends on the isentropic efficiency of the turbine. Two main turbine parameters are used to help determine the turbine characteristics. First, the turbine exducer bore diameter which can be measured. The exducer is the area where the exhaust gas exits the turbine. The second aspect is the A/R ratio. This ratio is defined as the cross-section area A of a turbine flow path over its distance from the center (i.e. its radius, R). This ratio is kept constant and affects the speed at which exhaust gas impact the turbine wheel. This results in more or less torque being applied to the compressor. From experiments [12], is has been proven that a small A/R

© 2018 SAE International. All Rights Reserved.

Downloaded from SAE International by Naveen Kumar, Sunday, April 08, 2018

ratio provides more low-speed response and a larger one provides more top end power. With few assumption, temperature drop through expander turbine can be found out using some equations [23]. The equation is

$$\Delta T_t = \frac{T_{t1} * \eta_t * Y_t}{1 + Y_t}$$

where

ΔT_t = temperature difference through the turbine
T_{t1} = Inlet temperature of gas
η_t = isentropic efficiency of turbine
Y_t = air calculation constant for turbine, it is calculated through pressure ratio of the turbine

Generally, a wastegated turbine is used. The wastegated turbine has an internal flap, a valve that opens when there is a need to bypass the turbine blades. A Variable geometry turbines (VGT) has also been used by the author [24] to be used as an expander. The configuration remains the same as Figure 4 but the air turbine is replaced by a VGT. They are equipped with a mechanism that adjusts the angle of the turbine vanes so that the torque transmitted to the turbo shaft is greater at low engine RPM. This mechanism can be controlled pneumatically or/and electronically. The use of VGT is extensively done in diesel engine turbocharging. Cheong et al. [25] studied the effect of variable geometry turbocharger on HSDI diesel engine and compared it to mechanically adjusted wastegate turbine to find that low-speed torque can be increased by 44% at maximum. Turner et al. [26] used an Opcon Twin-Screw Expander in a turbo-cooling system for an SI engine, in order to decrease the intake temperature to extend the knock limit. Oscarsson [27] studied that by adding a Twin Screw Expander, 30-35% of the compressor input power can be recovered and the power output and the size and weight of the compressor drive motor reduced accordingly. Shi [19] has done extensive research which designing the geometry of air turbine, It has also been proposed to use supercharger as the expander. The researchers [28] presented a new use of an Eaton supercharger and showed that the device could be used as an expander in the series, turbo-super arrangement if it were possible to change the drive ratio. However, operating as an expander, the supercharger could only deliver isentropic efficiencies between 40-50%. Turbine should be selected according to its use as there is no simple equation to find the right one. Inlet temperature and pressure are two of the few things which should be considered before choosing the right turbine.

Study of Experimental Results

The primary reason why turboexpansion cooling was pursued in the 2000s in gasoline engine was due to increased efficiency and fuel efficiency. Similarly, for diesel engines researchers sought decreased NO_x emissions and easy realization of EGR. Therefore, this section reports the simulated and experimental results of negative and positive effects of turboexpander on gasoline engine as well as diesel engine on various parameters to study how much these expectations were met.

Intake Temperature

The turboexpander reduces the intake charge air temperature and thus the temperature should be significantly decreased if the system has to be proved successful. However, Kitanović [43] in his research studied effects of turboexpansion using exhaust turbine with three different effective diameters using a VGT over a wide range of engine RPM concluded that the maximum cooling provided was at 4000 rpm of a minimal 12 ° C. The reason concluded was the increase mass of residual gas left in combustion chamber and rise in temperature at high RPM was due to drop in isentropic efficiency of turbocharger compressor. But Taitt [38] used a NOMAD engine in which very little valve timing overlap (1.5°) was done. This timing overlap was used to minimize residual exhaust gas fraction in the intake charge normally associated with high pre-turbine exhaust back pressure and thus high exhaust–inlet pressure differential. But even after this full beneficial effect of the charge-air conditioner system was not realized because of increase in charge-air temperature (approximately 80 °C) between the expander outlet and the cylinder. Then Wang [40] differentiated between intake temperature of a turbocharged engine and a turbocooled engine at different RPM at different loads and found intake temperature differences increases with increase in RPM at increasing load conditions. He also concluded that The resulting temperature of the TurboCool conditioned charge air is around or even below ambient air temperature Similarly, Turner [37] found temperature reduction of 40 ° C to 20 ° C at 1.6 kg/m^3 density point and a temperature reduction of 30 to 20° at 1.8 kg/m^3 and these results were obtained when externally conditioned air was used with the plenum charge air temperature as the control variable. Whelan [39] in his research paper reported that for the Baseline engine, the manifold temperature was near 50 °C at 110 kW, rising to over 65 °C at 150 kW and after applying turboexpander (TCS), the manifold temperature was constant at 30 °C. 35 °C maximum reduction was obtained and lead to good results. Figure 6 shows the intake manifold temperature of Whelan's research.

Hu [44] in this paper reported that his turboexpansion concept using a super-turbo twin-charger showed a decrease of average intake temperature from 324.42 K to 321.95 K when compared to the original turboexpansion concept. These

FIGURE 6 Intake Manifold Temperature [39]

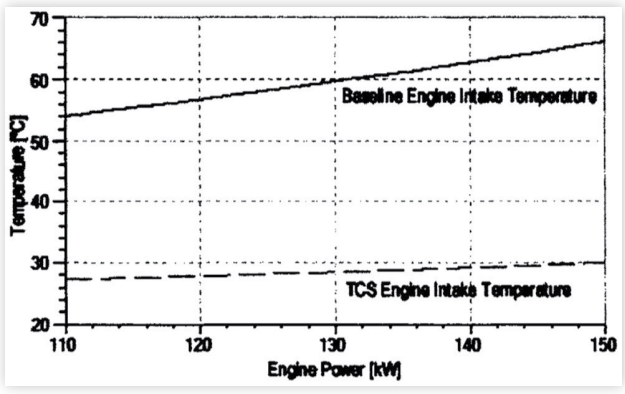

© SAE International

© 2018 SAE International. All Rights Reserved.

Downloaded from SAE International by Naveen Kumar, Sunday, April 08, 2018

FIGURE 7 Intake manifold temperature drop [19] in diesel engine

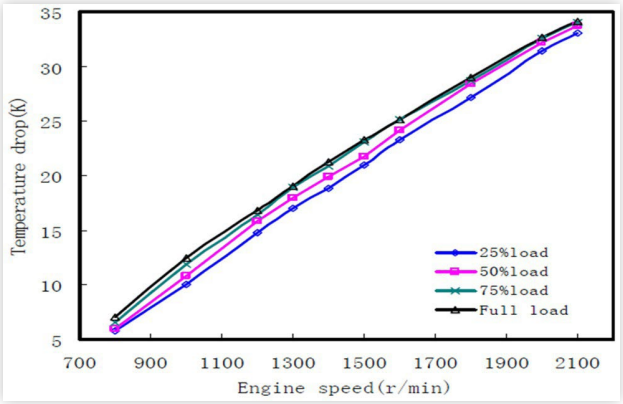

© SAE International

results were achieved when the original simulated results were extrapolated. Original results showed no decrease in intake temperature. The reason was the poor isentropic efficiency of supercharging working as an expander.

In a diesel engine, Shi [19] reported temperature drops which increased with increase in engine speed which further increases at increased load as shown in Figure 7. The author concluded that reduction in intake temperature was achieved due high isentropic efficiency of the air turbine. At 1500 r/min, the intake air temperature is about 20 K lower than the base engine.

Performance

Whelan [39] showed that for a given power, the turboexpander intake pressure is lower and the exhaust pressure higher than the Baseline engine. The greater pressure difference increases pumping work as can be seen in Figure 8.

At 150 kW, the Turboexpander (TCS) main turbine power is approximately 50% greater than the Baseline indicating the source of additional energy required to maintain low intake air temperatures. The pumping loss varied from under 5 kW to over 10 kW at increased engine power. Nonetheless, Whelan concluded that, on a downsized gasoline engine, turbo-expansion has quantified differences in the boosting system characteristics between TCS and standard turbocharging as power levels increase. Hu [44] also found out that his turboexpansion idea increased pumping loss from 2.192 bar in original turboexpansion to 2.310 bar and the increase was also found in his extrapolated results. Due to the same reason, Turner [37] also found no significant increase in BMEP. Kitanović [43] also reported maximum improvement in brake thermal efficiency of 1.8 percent at 4500 RPM. Taitt [38], reported that at 10:1 compression ratio, a charge-air conditioner system operating with an expander pressure ratio of 1.2 could offer a net power improvement of 6.5 percent over a conventional pressures charging and intercooling system with no expander and this result was obtained under unachievable constrains.

On the other hand, in Wang's simulated study [40] it can be seen that at 100 per cent load the power of the Turbo-Cool turbocharged SI engine can be increased by 20.3, 22.6, 23.0,

FIGURE 8 Pumping power of turbine and engine [39]

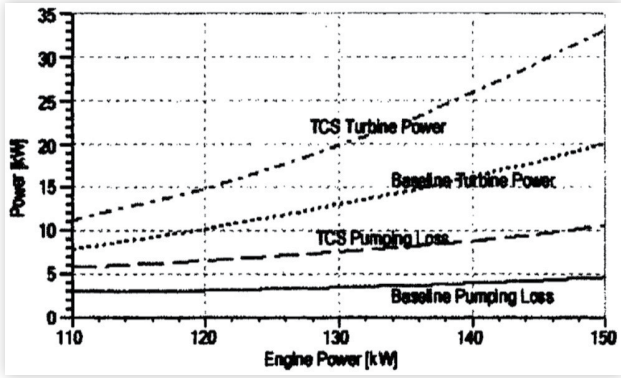

© SAE International

and 31 percent relative to the baseline turbocharged gasoline engine at 6000, 5000, 4000, and 3000 r/min and can be increased by 110.6, 100.4, 96.0, and 150.8 percent relative to the naturally aspirated gasoline engine at 6000, 5000, 4000, and 3000 r/min respectively. Similarly in Yang's simulated study [41] with Wang, using VGT as exhaust and air turbine, power can be increased by 22.1%, 26.3%, 36.0%, 70.9% and 54.5% relative to baseline turbocharged gasoline engine at 6000 rpm, 5000 rpm, 4000 rpm, 3000 rpm, 2000 rpm respectively. Wang's [40] reported an increase in BMEP and power can be seen in Figure 9.

FIGURE 9 Increase in BMEP and power at 100% load [40].

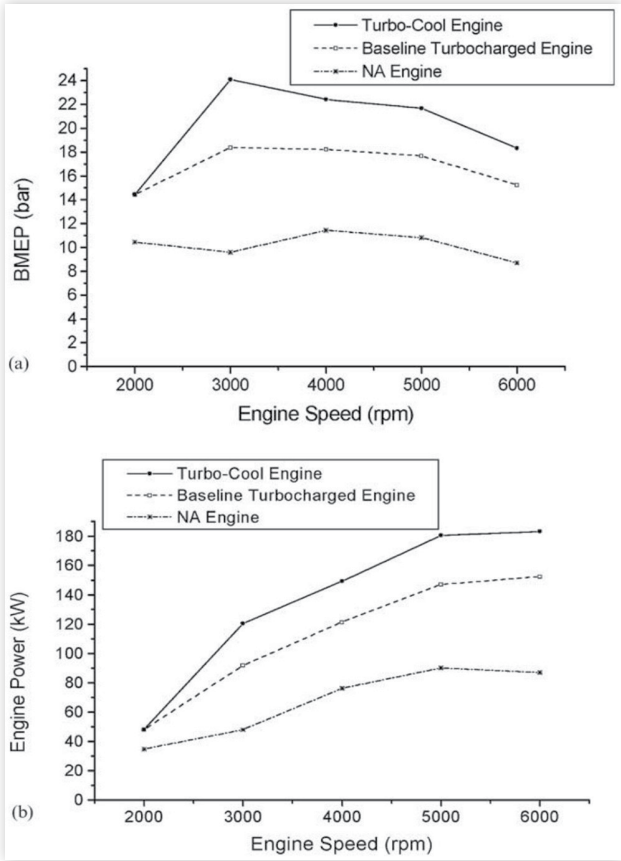

© SAE International

© 2018 SAE International. All Rights Reserved.

Downloaded from SAE International by Naveen Kumar, Sunday, April 08, 2018

FIGURE 10 Engine power output [19]

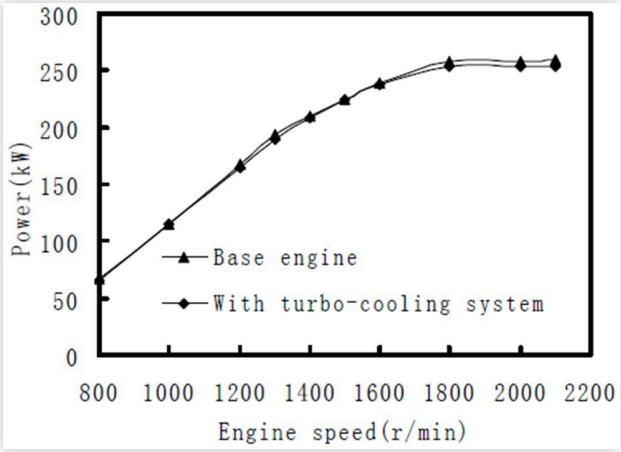

© SAE International

FIGURE 11 BSFC comparison at 50% load.

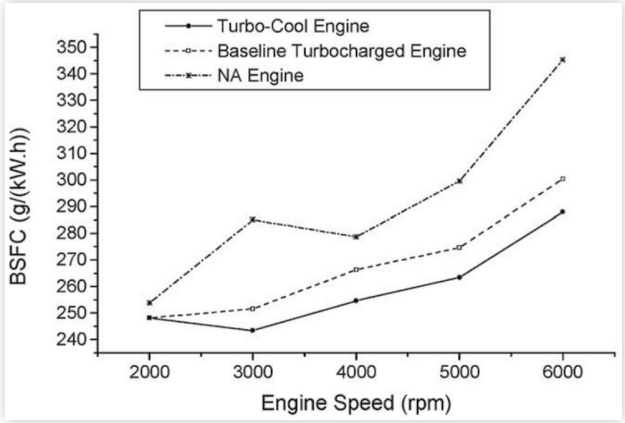

© SAE International

Shi [19] in simulating turboexpansion in diesel engine found out no increase in power. Rather, at high engine speed, the power decreased as can be seen in Figure 10.

The authors reported that because the compression and expansion processes of fluid in the air turbocharger were not completely isentropic, there must be some loss in thermal energy, which makes the engine power decrease a little.

Fuel Efficiency

Turner [37] using a single cylinder gasoline engine found no significant reduction in BSFC. Whelan [39] found an increase in BSFC after application of turboexpander of 16 g/kWh. This is due to pumping losses as explained earlier and as the air temperature is increased, when the fuel is injected, more fuel will evaporate in the intake port and less on the engine structure, and so a greater charge-cooling effect will be offset by the effect of a reduction in combustion efficiency caused by the retarded ignition timing. Taitt [38] reported a reduction in BSFC of 1.5% through an increase of half a ratio of compression ratio. This was achieved with intercooler, compressor and expander efficiencies of 0.8.Hu [44] reported an increase in BSFC from 258.66 to 259.59 g/kWh and reasoned it with poor the isentropic efficiency of a supercharger, pumping loss and an ironic increase in intake temperature.

Wang [40] reported BSFC can be decreased by an average value of 13% at 50% load relative to the naturally aspirated SI engine as seen in Figure 11 and Yang [41] reported BSFC can be decreased by 10.2% relative to the naturally aspirated SI engine at 100% load condition.

In diesel engine, Shi [19] reported BSFC increase up to 5% and the Figure 12 compares BSFC increase with a turbocharged diesel engine.

Emissions

Emissions have only been studied in diesel engine and Shi [19] reported a decrease of 15% in the amount of NO_x as seen in Figure 13.

FIGURE 12 BSCF increase in diesel engine [19]

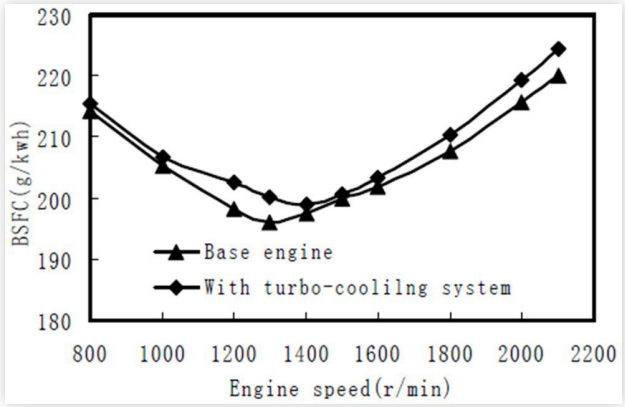

© SAE International

FIGURE 13 NO_x emission in diesel engine [19].

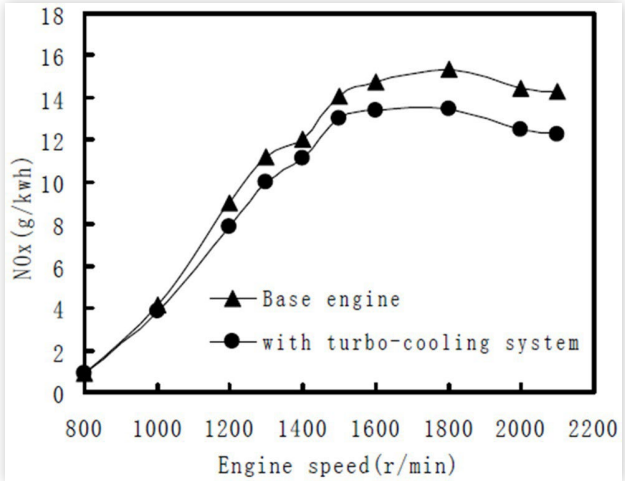

© SAE International

© 2018 SAE International. All Rights Reserved.

Downloaded from SAE International by Naveen Kumar, Sunday, April 08, 2018

Conclusions

This paper reviews the results of using turboexpansion for cooling charge air in gasoline and diesel engine on parameters, namely intake temperature, performance, fuel efficiency and emissions. As seen from the comparison, experimental results show that turboexpansion fulfills the principle the purpose of reducing intake temperature; its effects cannot be seen on the remaining parameters to a great extent because it incorporates energy losses and limitations of its components add to these losses. These losses account for the limitations in its applications. A large amount of practical research has been done on it but only a few shows positive results. The simulation work performed by certain authors also shows positive results. There is no doubt that turboexpansion has potential, but it needs further research in the area of turbine efficiency.

The reason why it has been pursued as a research topic by researchers worldwide is its potential to reduce fuel consumption and emissions and increase the efficiency of an engine. Its effects were first discovered in the 1950s and the researchers worldwide have come a long way to increase the effectiveness of turboexpansion. Although other methods to reduce charge air temperature have been proposed and researched, turboexpansion proves to be a permanent and economical solution. In gasoline engines this concept proves to decrease fuel consumption and in diesel engine it proves to decrease emissions apart from other already discussed benefits. In diesel engines, it is also reported to ease EGR realization.

However, the benefits of turbocharging are not limited to gasoline and diesel engine. Authors have discussed the possibilities of using this concept on HCCI engine as well. This area requires research and further study.

Whelan [42] has already produced a high performance, high-efficiency turboexpander which is derived from a mass-production turbocharger. Therefore, turboexpansion can truly be referred to as the technology of near future in the automotive industry because of the inherent benefits it presents. The number of automobiles is increasing at an incredible rate and the demand for increased performance is undying. Turboexpansion promises to reduce the consumption of fuels by increasing charge density. It claims in minimizing the damage to the environment by reducing the emissions while providing increased power and efficiency. Further research to decrease pumping losses can boost confidence in this technology.

This concept faces some stumbling blocks in form of its effectiveness and designs. This is an exciting technology in the field of automotive engineering, which when supported thoroughly by economic means and exhaustively by intellectual means will pave the path towards an efficient and clean means of transportation.

References

1. Leduc, P., Dubar, B., and Ranini, A., "Downsizing of Gasoline Engine: An Efficient Way to Reduce CO2 Emissions," *Oil &Gas Science and Technology* 58:115-127, 2003.
2. Danny Harvey, L.D., "Energy Efficiency and the Demand for Energy Services," Earthscan, 2010.
3. Krothapalli, A. and Greska, B., "Concentrated Solar Thermal Power," 2010. http://esc.fsu.edu/documents/CSP/Krothapalli%20Article.pdf.
4. Kasseris, E. and Heywood, J., "Comparative Analysis of Automotive Powertrain Choices for the Next 25 Years," SAE Technical Paper 2007-01-1605, 2007, doi:10.4271/2007-01-1605.
5. Schulte, H. and Wirth, M., "Internal Combustion Engines for the Future," Ford Motor Company.
6. Petitjean, D., Bernardini, L., Middlemass, C., and Shahed, S., "Advanced Gasoline Engine Turbocharging Technology for Fuel Economy Improvements," SAE Technical Paper 2004-01-0988, 2004, doi:10.4271/2004-01-0988.
7. Lake, T., Stokes, J., Murphy, R., Osborne, R. et al., "Turbocharging Concepts for Downsized DI Gasoline Engines," SAE Technical Paper 2004-01-0036, 2004, doi:10.4271/2004-01-0036.
8. Lecointe, B. and Monnier, G., "Downsizing a Gasoline Engine Using Turbocharging with Direct Injection," SAE Technical Paper 2003-01-0542, 2003, doi:10.4271/2003-01-0542.
9. Albrecht, A., Knop, V., and Corde, G., "Observer Design for Downsized Gasoline Engine Control Using 1D Engine Simulation," *Oil & Gas Science and Technology* 61:165-179, 2006.
10. Korakianitis, T. and Sadoi, T., "Turbocharger-Design Effects on Gasoline Engine Performance," *Journal of Engineering for Gas Turbines and Power* 127:525-530, 2005.
11. Bromberg, L., Cohn, D.R., and Heywood, J.B., "Calculations of Knock Suppression in Highly Turbocharged Gasoline/Ethanol Engines Using Direct Injection," MIT Laboratory for Energy and the Environment Report LFEE 2006-001.
12. Bell, C., "Maximum Boost: Designing, Testing, and Installing Turbocharger Systems, Bentley, 1997.
13. Naser, B.L., Baxhaku, B.I., and Lajqi, S.B., "Effect of Intercooler on Turbocharged Diesel Engine Performance," *13th International Research/Expert Conference, Trends in the Development of Machinery and Associated Technology*, Hammamet, Tunisia, October 2009.
14. Canli, E., Darici, S. and Ozgoren, M., "Intercooler Effect on Conventional Supercharging Systems," *International Scientific Conference*, Gabrovo, November 19-20, 2010.
15. Heywood, J.B., "*Internal Combustion Engines Fundamentals*," (McGraw Hill, 1988).
16. Crooks, W.R., "Combustion Air Conditioning Boosts Output 50 Per Cent," *CIMAC* 15:475-494, 1959.
17. Russ, S., Lavoie, G., and Dai, W., "SI Engine Operation with Retarded Ignition: Part 1 – Cyclic Variations," SAE Technical Paper 1999-01-3506, 1999, doi:10.4271/1999-01-3506.
18. Taitt, D.W., Garner, C.P., Swain, E. et al., "An Automotive Engine Charge-Air Intake Conditioner System: Thermodynamic Analysis of Performance Characteristics," *Proceedings of the Institution of Mechanical Engineers, Part D: Journal of Automobile Engineering* 219(3):389-404, 2005.
19. Proc. ASME. 44007, *Volume 5: Industrial and Cogeneration; Microturbines and Small Turbomachinery; Oil and Gas Applications; Wind Turbine Technology*, 447-457, October 10, 2010, asmecp002010044007000447000001, doi:10.1115/gt2010-22868.

© 2018 SAE International. All Rights Reserved.

Downloaded from SAE International by Naveen Kumar, Sunday, April 08, 2018

20. Wang, L.-S. and Yang, S., "Turbocharged Intercooled Engine Utilizating the Turbo-Cool Principle and Method for Operating the Same," U.S. Patent, 2007/0033939A1.
21. Zelenka, P., Aufinger, H., Reczek, W. et al., "Cooled EGR – a Key Technology for Future Efficient HD Diesels," SAE Technical Paper 980190, 1998, doi:10.4271/980190.
22. Kreso, A., Johnson, J., Gratz, L., Bagley, S. et al., "A Study of the Effects of Exhaust Gas Recirculation on Heavy-Duty Diesel Engine Emissions," SAE Technical Paper 981422, 1998, doi:10.4271/981422.
23. Whalley, P.B., "*Basic Engineering Thermodynamics*," (Oxford University Press, 1992).
24. Yang, S. and Wang, L., "Modeling of two Charge-Air Cooling Turbo-Charging Systems for Spark Ignition Engines," *SAE Int. J. Fuels Lubr.* 1(1):1195-1205, 2009, doi:10.4271/2008-01-1702.
25. Cheong, J., Cho, S., and Kim, C., "Effect of Variable Geometry Turbocharger on HSDI Diesel Engine," *Seoul 2000 FISITA World Automotive Congress*, 2000.
26. Turner, J., Pearson, R., Bassett, M., Blundell, D. et al., "The Turboexpansion Concept – Initial Dynamometer Results," SAE Technical Paper 2005-01-1853, 2005, doi:10.4271/2005-01-1853.
27. Oscarsson, J., "Power Recovery by a Twin Screw Expander in a Fuel Cell Application," SAE Technical Paper 2003-01-0411, 2003, doi:10.4271/2003-01-0411.
28. Copeland, C., Romagnoli, A., Wan-Salim, W.B. et al., "Assessment of the Supercharging Boosting Component for Heavily Downsized Gasoline Engines," in *IMechE Conference Transactions*, 2014.
29. Crooks, W.R., "Combustion Air Conditioning Boosts 50 Percent," *CIMAC 1959 a15*, 475, 1955.
30. Crooks, W.R., "Method and Apparatus for Refrigerating Combustion Air for Internal Combustion Engine," U.S. Patent 3,141,293, 1964.
31. Helmich, M.J., "Development of Combustion Air Refrigeration System Enabling Reliable Operation at 220 Psi Bmep for a Large Four-Cycle Spark Ignited Gas Engine (ASME 66-DGPE-7)," 1966.
32. McInerney, C.E., "Turbocharged Engine after Cooling System and Method," The Garrett Corporation, U.S. Patent 4010613 A, 1975.
33. Meyer, R. and Shahed, S., "An Intake Charge Cooling System for Application to Diesel, Gasoline and Natural Gas Engines," SAE Technical Paper 910420, 1991, doi:10.4271/910420.
34. Cikanek, H.A. and Rao, V.D.N., Diesel Engine Turbo-Expander, Ford Motor Company, US Patent 5,269,143, 1993.
35. Turner, J., Pearson, R., Bassett, M., and Oscarsson, J., "Performance and Fuel Economy Enhancement of Pressure Charged SI Engines through Turboexpansion – an Initial Study," SAE Technical Paper 2003-01-0401, 2003, doi:10.4271/2003-01-0401.
36. Turner, J.W.G., Pearson, R.J., and Kenchington, S.A., "Concepts for Improved Fuel Economy from Gasoline Engines," *Int. J. Engine Res.*6, 2004.
37. Turner, J.W.G., Pearson, R.J., Milovanovic, N., and Taitt, D.W., "Extending the Knock Limit of a Turbocharged Gasoline Engine via Turboexpansion, *8th Conference on Turbochargers and Turbocharging*, May 2006.
38. Taitt, D.W., Garner, C.P., Swain, E. et al., "An Automotive Engine Charge-Air Intake Conditioner System: Analysis of Fuel Economy Benefits in a Gasoline Application," *Proceedings of the Institution of Mechanical Engineers, Part D: Journal of Automobile Engineering* 220(9):1293-1307, 2006, September 1, 2006, doi:10.1243/09544070JAUTO94.
39. Whelan, C.D. and Richards, R.A., "Turbo-Cooling Applied to Light Duty Vehicle Engines," *IMechE 8th Conference on Turbochargers and Turbocharging*, May 2006.
40. Wang, L.-S. and Yang, S., "Turbo-Cool Turbocharging System for Spark Ignition Engines," *Proceedings of the Institution of Mechanical Engineers, Part D: Journal of Automobile Engineering* 220, 2006, doi:10.1243/09544070JAUTO172.
41. Yang, S. and Wang, L., "Modeling of Two Charge-Air Cooling Turbo-Charging Systems for Spark Ignition Engines," *SAE Int. J. Fuels Lubr.* 1(1):1195-1205, 2009, doi:10.4271/2008-01-1702.
42. Whelan, C., Richards, R., Spence, S., Young, A., "Design and Development of a Turbo-Expander for Charge Air Cooling," in *Proceedings of IMechE 9th International Conference on Turbochargers and Turbocharging*, London, 2010, 459-470, C1302-037.
43. Kitanović, M., "A Simulation Study of the Effects of Turbo-Expansion Concept Implementation on Combustion and Gas-Exchange Processes of a 1.4 l Spark-Ignition Engine," in *MVM2012-026, International Congress Motor Vehicles & Motors 2012 (MVM 2012).*
44. Hu, B., Copeland, C., Brace, C., Akehurst, S. et al., "A New Turboexpansion Concept in a Twin-Charged Engine System," SAE Technical Paper 2014-01-2596, 2014, doi:10.4271/2014-01-2596.

Contact Information

Phone Number: +91-8800841827
satvik2794@gmail.com

Abbreviations

VGT - Variable Geometry turbocharger

HCCI - Homogeneous Charge Compression Ignition

EGR - Exhaust Gas Recirculation

BMEP - Brake Mean Effective Pressure

BSFC - Brake Specific Fuel Consumption

All rights reserved. No part of this publication may be reproduced, stored in a retrieval system, or transmitted, in any form or by any means, electronic, mechanical, photocopying, recording, or otherwise, without the prior written permission of the copyright holder.

Positions and opinions advanced in this paper are those of the author(s) and not necessarily those of SAE International. The author is solely responsible for the content of the paper.

ISSN 0148-7191

View publication stats

Journal of Thermal Engineering, Vol. 4, No. 3, pp. 1998-2017, April, 2018
Yildiz Technical University Press, Istanbul, Turkey

ALTERNATIVE REFRIGERANTS FOR HCFC 22—A REVIEW

S.K. Kalla[1,*], B.B. Arora[2], J.A. Usmani[3]

ABSTRACT

The aim of this paper is to determine the best available alternative which could replace existing refrigerant R22, with minimum or no changes in the air conditioning system. For this purpose, both the theoretical as well as experimental studies done in this area of research have been reviewed. The most popular HFC, R410A is having lower critical temperature, which restricts its usage in compression based systems working at higher condensing temperatures whereas for R407C, a change to synthetic lubricant is required and HC-290 is flammable. It is suggested that until the safety issue of use of hydrocarbon refrigerants in quantities exceeding 500gm is resolved, we should go for those mixtures of HFCs and HCs for which TEWI index is the lowest.

Keywords: *HCFC, R22, Refrigerant, Alternative, HFC, HC, TEWI*

INTRODUCTION

R22 has extensively been used in applications like air conditioning, heat pumps, deep freezers and bottle coolers. Since R22 is ozone depleting, it is presently being replaced by HFCs (hydroflorocarbons) like R407C and R410A. As per Kyoto protocol, use of substances having high global warming potential (GWP) like HFCs have to be avoided in the long-term perspective. This underlies the need of searching an alternative refrigerant that is not only having a zero ODP but also possessing a low GWP. Hence extensive research is going on across the globe to find a viable alternative to R22.

Poggi et al. [1] reviewed the efforts to reduce the refrigerant charge in refrigeration systems and concluded that the technical options favorable to charge reduction are (i) the use of refrigerating systems with secondary refrigeration rather than direct refrigeration, (ii) the use of direct expansion fed evaporators rather than flooded evaporators, (iii) the use of hydrocarbon, ammonia or CO_2 like refrigerant, and (iv) the use of compact exchangers.

In a similar work, Palm [2] surveyed the use of hydrocarbons insmall air conditioning systems of 0.5 to 3.2 kW and reported that a minimum room area of $15m^2$ is prescribed for a unit with 300 g charge. During production, extra care is taken for leak detection. The systems are found to have 5–10% higher efficiency than with HFC.In another review by Calm [3], it was reported that in contrast to R-410A, R-32 avoids the sharp performance decline at higher ambient temperatures and offer both higher seasonal efficiencies and much lower GWPs . It is, however, marginally flammable.

In a review on recent developments in new refrigerant mixtures for vapor compression-based refrigeration, air-conditioning and heat pump units by Mohanraj et al. [4], it was concluded that HC refrigerant mixtures are identified as a long-term alternative to phase out the existing halogenated refrigerants in the vapor compression-based systems.

Environmental effect of using a refrigerant in refrigeration and air conditioning systems is assessed by an indicator known as TEWI (total equivalent warming impact). The method of calculating TEWI is available (AIRAH, 2012). Sarbu [5] based on the TEWI (total equivalent warming impact) index variation grouped possible substitutes for refrigerant R22 into three categories: a) with deviations of 2% (R417A, R407C, R427A, and R424A); b) with deviations of 30-45% (R134A, R410A, R290, R600A, and R152A); and c) with deviations of 50-70% (R507, R404A, R428A, and R422A). For substitutes involved in the b) and c) groups, their use is not recommended because the plant will operate with a significant decrease of refrigeration power. The use of such substitutes is possible only if some changes in the components of the installation are made.

This paper was recommended for publication in revised form by Regional Editor Somchai Wongwises
[1]Research Scholar, Department of Mechanical Engineering,Jamia MilliaIslamiaUniversity,New Delhi, INDIA
[2]Department of Mechanical Engineering, Delhi Technological University,New Delhi, INDIA
[3] Department of Mechanical Engineering, Jamia MilliaIslamiaUniversity,New Delhi, INDIA
**E-mail address: skkalla@yahoo.com*
Manuscript Received 22 July 2016, Accepted 26 March 2017

In order to have an idea of latest scenario in the worldwide efforts for searching an alternative to R22, this paper reviews the studies (theoretical as well as experimental) that have been done so far in order to find an alternative refrigerant that could replace R22.

ALTERNATIVES AVAILABLE

Hydrochlorofluorocarbons (HFCs)

R407C (Ternary mixture of R32/R125/R134a) and R410A (Binary mixture of R32/R125) fall under this category. These are refrigerants containing Hydrogen, Fluorine, and Carbon. Therefore they do not contain any ozone depleting Chlorine. Besides containing no ozone depleting elements, they usually have an even lower global warming potential than HCFCs.

Hydrocarbons (HCs)

R290 (C_3H_8, propane) and propylene (R1270) belong to this category. Several hydrocarbons have excellent thermodynamic properties and can be used as refrigerants. The ODP of hydrocarbons is zero, while their GWP is very small. The main concerns that most of the hydrocarbons are flammable.

Refrigerant Mixtures

R422A (R125/R134A/R600A), R417A (R125/R134A/R600) andR433A (30% propylene and 70%propane) fall under this group. Blends or mixtures are used either to obtain different desired properties such as bubble point temperature, oil solubility, flammability, as drop-in-substitutes for older refrigerants that are no longer produced, etc. by combining different fluids or to obtain variable temperature refrigeration.

Other Natural Refrigerants

CO_2 (R744) and NH_3 (R717) belong to this category. Ammonia is an environmentally safe but toxic working fluid which is attracting renewed attention. It possesses the most advantageous thermodynamic and thermophysical properties needed for refrigeration. Carbon dioxide is an excellent refrigerant when both heating and cooling are desired. Also, it is not preferable for use in tropical countries such as India due to the high ambient temperatures which result in high condensing pressures.

COMPARATIVE STUDY OF HFCs, HCs, REFRIGERANT MIXTURES AND NATURAL REFRIGERANTS IN COMPARISON WITH R22

After a thorough review of the literature on using alternative refrigerants for R22 in window air conditioning system, the findings have been summarised in Table 1.

Table 1. Summary of literature survey

YEAR	AUTHOR	TOPIC	REFRI-GERANT	PARAMETER	CONCLUSION
1996	Lampugnani and Zgliczynski	R290 as a Substitute of R502 and R22 in Commercial Refrigeration and Air Conditioning	R290	Materials compatibility, oil solubility, operating temperature	The hermetic compressors, designed for use with R22, while operating with propane show a strong benefit in terms of general reliability, due to the lower bearing loads and the lower thermal level. It has a positive influence on the risk associated to the use of flammable refrigerants.
1997	Bensafiet al	Experimental evaluation of some proposed R22 alternatives in chillers and unitary a/c equipment	R407c	Capacity and efficiency	Marginal degradation in capacity & EER compared to R22

Table 1. Summary of literature survey

YEAR	AUTHOR	TOPIC	REFRI-GERANT	PARAMETER	CONCLUSION
1996	Lampugnani and Zgliczynski	R290 as a Substitute of R502 and R22 in Commercial Refrigeration and Air Conditioning	R290	Materials compatibility, oil solubility, operating temperature	The hermetic compressors, designed for use with R22, while operating with propane show a strong benefit in terms of general reliability, due to the lower bearing loads and the lower thermal level. It has a positive influence on the risk associated to the use of flammable refrigerants.
1997	Bensafi et al	Experimental evaluation of some proposed R22 alternatives in chillers and unitary a/c equipment	R407c	Capacity and efficiency	Marginal degradation in capacity & EER compared to R22
2001	Wang et al	Rationally based model for evaluating the optimal refrigerant mass charge in refrigerating machines	R410A	COP, cooling capacity, compressor work	In the early stage of refrigerant charge process, a sharp rise of COP is observed. The COP reaches an optimal value for a specified refrigerant charge and shows a slight drop for a further increase of refrigerant charge.
2004	Roberts and Chambers	Energy Saving Refrigerant Blends Comprising R125, R134a, R600 or R600a	R417A & Blend 79(R125/ R134a/ R600a (85.1%/11. 5%/3.4%))	Energy efficiency, GWP	R417A has been demonstrated as suitable for the full temperature range of applications from air conditioning to low temperature supermarket rack systems with no problems experienced through lack of capacity but in every case energy savings were experienced. Blend 79 has been demonstrated to be suitable for use as a replacement for the HCFC based R502 replacements without the need for system or oil changes and to replace R22 with minimal changes to the expansion valves.
2005	Devotta et al	Performance assessment of HC-290 as a drop-in substitute to HCFC-22 in a window air conditioner	Propane	COP, Discharge pressure, cooling capacity, energy consumption	Cooling capacity of HC-290 was lower in the range 6.6– 9.7%. Energy consumption with HC-290 was lower in the range 12.4–13.5%. Discharge pressures of HC-290 were lower in the range 13.7–18.2%.

Table 1. Summary of literature survey

2005	Devotta et al	Performance assessment of HCFC-22 window air conditioner retrofitted with R-407C	R407C	Cooling capacity, coefficient of performance, power consumption, discharge pressure	Cooling capacity of R-407C was lower in the range 2.1–7.9%. Power consumption with R-407C was higher in the range 6–7%. Discharge pressures of R-407C were higher in the range 11–13%.
2008	Chen and Yu	Performance of a new refrigeration cycle using refrigerant mixture R32/R134a for residential air-conditioner applications	Mixture R32/R134a	COP, volumetric refrigerating capacity	In the conventional refrigeration cycle (CRC), the mixture R32/R134a has a close performance to that is obtainable with pure refrigerant R22. However, the mixture R32/R134a in the NRC (new refrigeration cycle) will result in a better performance. The maximal COP can be improved in a range of 8–9% over that of the CRC, and the volumetric refrigerating capacity can be approximately increased by 9.5%.
2009	Mohanraj	Environment friendly alternatives to halogenated refrigerants—A review	R407C and R410A	GWP, ODP	The choice of alternative to R22 in air conditioning applications is R407C and R410 which are available in the Indian market
2011	Bolaji	Performance investigation of ozone-friendly R404A and R507 refrigerants as alternatives to R22 in a window air-conditioner	R404A and R507	Pressure ratio, discharge temperature, compressor power and energy consumption, refrigeration capacity, coefficient of performance	The average discharge temp obtained using R507 and R404A were 4.2% and 15.3% higher than that of R22, respectively The lowest compressor power and energy consumption were obtained from R507 retrofitted system. The average refrigeration capacities of R507 and R404A were 4.7% higher and 8.4% lower than that of R22, respectively. Average COP of R507 increased by 10.6% and that of R404A reduced by 16.0% with respect to that of R22.

Table 1. Summary of literature survey

2011	Chinnaraj et al	Influence of Electronic Expansion Valve on the Performance of Small Window Air Conditioner Retrofitted With R407c and R290	R407C and R290	Degree of superheat, COP	The electronic expansion valve shows good overall performances comparing the capillary tube system. The coefficient of performance of R290 is the maximum among the three refrigerants tested
2012	Wu et al	Study of R161 Refrigerant for Residential Air conditioning Applications	R161	Cooling capacity, COP, Discharge temperature	Cooling capacity reduced 7.6% 2. cooling EER increased 6.1% Refrigerant optimized charge reduced 43% compared to R22. R161 has lower discharge temperature
2013	Padmanab-han & Palanisamy	Exergy efficiency and irreversibility comparison of R22, R134a, R290 and R407C to replace R22 in an air conditioning system	R134a, R290 and R407C	Exergy efficiency, irreversibility	The refrigerant R290 is the best performer among candidate refrigerants but it suffers from flammability. Thus, R407C can considerably be used to replace R22.
2014	Ramu et al.	Energy Performance Assessment of R32/R125/R600a Mixtures as Possible Alternatives to R22 in Compression Refrigeration Systems	R32/R125/ R600a (in the ratio of 0.4:0.4:0.2, by mass)	Coefficient of performance (COP), compressor power consumption, compressor discharge temperature and volumetric cooling capacity (VCC). Total equivalent global warming impact (TEGWI)	1. VCC of new refrigerant mixture is closer to R22 2. COP of the mixture was found to be lower by about 16-20% 3. Compressor discharge temp of the new refrigerant mixture was observed to be 6-11^{o}C lower 3. TEGWI of new refrigerant mixture was found to be higher than that of R22 by about 20%
2014	Samuel et al	An Experimental Investigation and Performance Evaluation of 1.5 TR Window Air-Conditioner by Using R22, R407C and R410A by Varying the Capillary Pitch	R407C and R410A	COP, compressor power, heat rejection ratio	R410A with a capillary pitch of 18mm gave the best Coefficient of performance to retrofit an window air conditioner working on R22.

Hydro-Fluorocarbons (HFCs)

Based on Evaporator Temperature

Below -30º Carora et al. [6] performed a theoretical analysis of a vapour compression refrigeration system with R-407C and R-410A using Engineering Equation Solver software for evaporator temperatures between −38°C to 7°C and concluded that COP and exergetic efficiency for R-22 were higher in comparison to R-407C and R-410A. DuPont [7] in their technical information paper tested the performance of R422A at an evaporator temperature of -35ºC in a low temperature direct expansion refrigeration system and found discharge temperature to be lower by 8K and COP higher by 16% as compared to R22. Menlik et al. [8] theoretically analysed the performance (in terms of energy and exergy aspects) of a vapour compression refrigeration system working with R22 and its alternatives R407C and R410A. It was reported that R407C has higher COP, less EDR and higher exergetic efficiency than R410A. With increase in subcooling/superheating temperature, COP of R22, R407C and R410A increase. R407C has 10% higher exergetic efficiency than R410A between 20°C and 35°C dead state temperature.

Between -30º C to 0º C, Klein et al. [9] theoretically studied a vapour compression refrigeration system operating at an evaporating temperature of -20ºC and reported that liquid-suction heat exchangers that have a minimal pressure loss on the low pressure side are useful for systems using R507A, R134A, R12, R404A, R290, R407C, R600, and R410A. Grace and Tassou [10] simulated the performance of R407C, R134A, R404A and R507A in a liquid chiller and their results showed that for typical air-conditioning applications, R407C is the preferred alternative to R22, with Rl34A being an option at lower evaporating temperatures, although this would require a replacement compressor in order to produce comparable cooling capacities. R407C has a high glide temperature which can lead to composition changes after leakage and may require some valve adjustment.

In a theoretical analysis conducted with R134a, R404A, R407C, R410A, and R507 and three natural refrigerants at evaporating temperatures ranging from –30ºC to 10ºC, it was reported that for air conditioning and heat pumps, R407C, R410A, R134A exhibit excellent performance, and could be proposed to replace R22 in these applications (Boumaza [11]). In related work, Rani and Balachander [12] simulated the performance of an R22 system working with R407C by using MATLAB software. It has been reported that performance degradation shall be minimized by selecting a slightly higher condensation temp for R407C (than R22), without changing mass flow rate. Jia [13] in a study done at an evaporating temperature of -4ºC suggested that R404A and R410A represent a good balance of system performance, product safety and environmental impact. In an experimental assessment with R422D as an alternative to R22 in walk-in air cooler, it has been reported that COP of R422D was lower than that of R22 (Aprea et al. [14]). In an experimental study, Han et al. [15] concluded that in a small scale refrigeration system using HFC-161, it was possible to achieve higher COP by 15–25% than HFC-410A and HFC-32. In another work, Padmanabhan &Palanisamy [16] tested the refrigerants R134A, R290 and R407C in the VCRS of an air conditioner and reported that the refrigerant R290 was the best performer among candidate refrigerants but it suffered from flammability. Thus, R407C could considerably be used to replace R22. Similarly, Bolaji et al. [17] (2014) theoretically assessed the performance of R432A and R433A in a VCRS at an evaporating temperature of -30 to 10ºC and reported that the average COPs obtained for R432A and R433A were lower by only 4.5 and 5.4%, respectively, than those of R22. La Rocca et al. [18] investigated R413A, R417A, R422A and R422D in a low-temperature refrigerating unit to replace R22 and reported that COP was lower for all the replacement fluids showing inferior energy efficiency and higher energy consumption.

Between 0º C to 15º C, Hewitt & McMullan [19] studied the performance of HFC R407C in a R22 compressor and reported deterioration in performance with decreasing evaporator temperature compared to that of R22. Johansson &Lundqvist [20] performed simulation as well as field tests in chillers at an evaporating temperature of 6ºC working with R134A, Propane, R404A, R407C and lsceon 59 refrigerants. It was reported that to make the system perform its best with lsceon 59 the area used for subcooling had to be larger than when R22 were used. With other substitutes, like R134A, a smaller subcooling area gave the maximum performance of the system. Devotta et al. [21] in their simulation study assessed the performance of a VCRS at an evaporating temperature of 7.2ºC using CYCLE_D software working with HFC-134A, HC-290, R-407C, R-410A, and three blends of HFC-32, HFC-134A and HFC-125. Their results reported that R-407C is mainly used for retrofitting whereas R-410A is the next popular choice for new systems. Johansson &Lundqvist [22] reported that R407C is

suitable for retrofitting whereas R410A could be used for new air conditioners. Calm &Domanski [23] suggested that R410A is the leading replacement for redesigned window air conditioners. Horuz [24] studied the alternatives for R22 and concluded that possible alternatives for R22 are R407C, R410A and R410B. Chen and Yu [25] theoretically analysed the performance of a residential air-conditioner (at evaporating temperature of 5°C) working with mixture R32/R134a. It was reported that the mixture R32/R134A in the NRC (new refrigeration cycle) will result in an improved COP in a range of 8–9% over that of the CRC (conventional refrigeration cycle), and the volumetric refrigerating capacity can be approximately increased by 9.5%. Allgood [26] suggested in an ASHRAE report that R422D suited to supermarket application whereas R410A/R407C suited to air conditioning. Emerson Network Power [27] in their technical note reported that R410A and R407C offer equivalent performance and higher capacity alternatives to R22. Currently R410A is being used extensively for most new, small residential air-cooled systems. Honeywell [28] in their study suggested that for unitary air conditioning, R407C and R410A are environmentally safer alternatives. Department for Environment, Food and Rural Affairs, UK [29] reported that for larger industrial refrigeration and air-conditioning systems ammonia is a well-established refrigerant which can provide a high efficiency system. For very small systems hydrocarbons such as iso-butane have become well established whereas CO_2 has been used successfully in small systems, in larger commercial refrigeration systems and in some industrial applications. BITZER [30] reported that R407C is short term substitution for R22 as performance & efficiency are very similar. R410A has 50% higher volumetric cooling capacity but a proportional rise in system pressure whereas R438A was designed for higher critical temperature for hot climate areas. Bolaji [31] has experimentally evaluated the performance of a split-air-conditioner (at evaporator temperatures between 2°C to 12ºC) working with R410A and R417A as an alternative to R22. His results reported that the average COP with R417A and R410A were found to be 2.9% higher and 8.4% lower, respectively, than that with R22.

Based on Cooling Capacity

Up to 3.5 kW capacity, Vjacheslav et al. [32] theoretically assessed the performance of a 3 kW air conditioner working with R410A and reported that in the early stage of refrigerant charge process, a sharp rise of COP is observed. The COP reaches an optimal value for a specified refrigerant charge and shows a slight drop for a further increase of refrigerant charge. Aprea and Renno [33] experimentally assessed the performance of a 1.6 kW experimental vapour compression refrigeration plant, applied to a commercially available cold store working with R417A. It was reported that the percentage difference between the COP of the fluids experimentally tested is, on average, about 15%. Moreover, the exergy destroyed in the plant components when R417A is used as working fluid is, on average, about 14% higher than the exergy destroyed with R22. Spatz & Motta [34] theoretically analysed the performance of a 0.5 kW walk-in cooler working with 404A, R-410A and R-290 and concluded that environmentally acceptable alternative is R-410A. Chen [35] performed a simulation study of split-type residential air conditioner of 3.55kW capacity using Genesym software working with R410A. It was reported that adoption of R410A could be helpful for air conditioner to decrease their heat exchanger size or improve their operation efficiency for power saving. Similarly, Mohanraj et.al. [36] reviewed the performance of environment friendly refrigerants for room air conditioners and concluded that the choice of alternative to R22 in air conditioning applications is R407C and R410 which are available in the Indian market. Wang et al. [37] experimentally studied the performance of a process cooling system at -15ºC working with HFC-404A. Their results indicated that retrofitted system using HFC-404A refrigerant can achieve similar cooling performance as the HCFC-22 system in addition to the temperature control accuracy for process cooler requirement. In an experimental study on residential air conditioner of 3.5 kW capacity using R161, it was concluded that the cooling capacity reduced 7.6%, cooling EER increased 6.1%, refrigerant optimized charge reduced 43% compared to R22 and R161 had lower discharge temperature (Wu et al. [38]). Aprea et al. [39] tested the performance of a walk-in cooler working with R422D and their results reported that COP of R422D is 20% lower than that of R22. Furthermore, for plant whose condenser is air cooled, R422D could lead to increase the fan speed or to adopt bigger blowers.

3.5 kW to 7 kW capacity, Bensafi et al. [40] tested the performance of a room air conditioner of 6 kW capacity working with HFC R407C and reported marginal degradation in capacity & EER compared to R22. Aprea & Greco [41] have experimentally investigated the performance with HFC 407C in a 5 kW vapour compression plant to replace R22. Their results reported that in order to increase the overall performance of the vapour compression plant working with R407C, the evaporator and the compressor must be optimized. In a

similar work, the performance of a window air conditioner of 5.13 kW capacity working with R407C was experimentally assessed and it was reported that the cooling capacity of R-407C was lower in the range 2.1–7.9%, power consumption with R-407C was higher in the range 6–7% and discharge pressures of R-407C were higher in the range 11–13% (Devotta et al. [42]). Bolaji [43] experimentally assessed the performance of a window air-conditioner of 3.86 kW capacity working with R404A and R507. It was concluded that R507 can be used successfully as a retrofitting refrigerant in existing window air-conditioners originally designed to use R22. Samuel et al. [44] experimentally assessed the performance of a 5.27 kW window air-conditioner working with R407C and R410A. Their results indicated that R410A with a capillary pitch of 18mm gave the best Coefficient of performance to retrofit a window air conditioner working on R22.

Above 7 kW capacity, Payne & Domanski [45] have experimentally evaluated the performance of a 9.5 kW split air-conditioning system working with R410A as an alternative. Their results reported that while capacities of both systems were approximately equal at the 35.0°C rating point, at the 54.4°C outdoor temperature the R410A capacity was 9% below that of R22. For the same test points, the R410A COP was 4% and 15% lower than the R22 COP, respectively. In another experimental study on 11 kW walk-in refrigeration system working with R-290, R-404A and R-410A, it was reported that R-410A has less or equivalent environmental impact as compared to R-290 when safety (toxicity and flammability), environmental impact (climate change), cost and performance (capacity and COP) are considered (Hwang [46]). Kulcar et al. [47](2010) theoretically analysed the performance of a 215 kW cooling system for preparing chilled water working with R407C. Their results concluded that by using refrigerant R407C, the consumption of electrical energy needed for the running of compressors is reduced, thus helping to keep our environment cleaner. In a similar study, Rocca &Panno [48] tested R22, R417A, R422A and R422D in a 25 kW vapour compression refrigerating unit and their results showed that despite the case of substitution and the advantage of being able to continue to use mineral oil as a lubricant in the compressor, the performance with the new tested fluids did not result as efficient as when using R22. Rocca et al. [49] compared the performance of a 25 kW refrigerating plant working with R417A, R407CandR404A. They reported that substituting a pure HCFC fluid such as R22 is disadvantageous since the different replacement fluids give a less satisfactory rendering due to their particular thermophysical properties in a system sized for the given original fluid. TEWI increment may be far more damaging than the low ODP of the original fluid. Jain et al. [50] theoretically assessed the performance of a 66.67kW VCRS using R134A/R410A/R407C/M20 and their results indicated that R407C can be a potential HFC refrigerant replacement for new and existing systems presently using R22 with minimum investment and efforts. Qureshi and Zubair [51] theoretically assessed the performance of a 100 kW VCRS working with R134A, R410A, R407C/ R717, R404A, R290 by using EES software. Their results indicated that considering R134A, R410A and R407C from a first law standpoint, the COP indicates that R134a always performs better unless only the evaporator is being fouled. Volumetric efficiency of R410A remained the highest.

Based on Changes in Components of the System

Lee et al. [52] experimentally evaluated the performance of a 100 kW commercial screw chiller with shell-and-tube heat exchangers working with R407C. They reported that the cooling capacity decreases by 10–20% and the COP by 20–30% depending on the temperature condition as compared to R22. Aprea et al. [53] experimented with R417A, R507 and R407C in a vapour compression refrigeration plant subjected to a commercially available cold store. During their experimentation, the operating temperatures were maintained at 32 and 10ºC (condenser temperature) and 5, 0, -5, -10 and -15ºC (evaporator temperature). It has been reported that by using the R407C, it is possible an average electric energy consumption about 12% smaller when an inverter is employed to control the compressor refrigeration capacity instead of the thermostatic control which imposes on/off cycles on the compressor, working at the nominal frequency of 50 Hz. Llopis [54] experimentally assessed the performance of a double-stage vapour compression plant driven by a compound compressor working with HFC-422A and the HFC-417B. It was reported that there is a reduction in cooling capacity and in COP with regard to the HCFC-22 operation. In a related work, a 1 kW VCRS with two-stage and intercooler was theoretically investigated by using Solkane software working with R507, R407C and R404A. The results indicated that COP and exergy efficiency of the system using R407C is better than the other refrigerants. Subiantoro and Ooi [55] theoretically analysed the performance of a 5.27 kW medium scale air conditioning system working with CO2, R134A, NH3, R32, R404A, R1234yf, R410A, R407C and R438A. It was reported that the use of expanders in commercial refrigeration systems not only reduces the environmental impact of the

systems, but also has practical payback periods for both the conventional and especially, the transcritical CO2 systems.

Performance Comparison

The coefficient of performance comparison (COP) of R407C and R410A with respect to R22 has been shown in Figure 1 (Menlik et. al. [8]) whereas the variation of exergetic efficiency with condenser temperature is shown in Figure 2 (Menlik et al. [8]).

Hydrocarbons (HCs)

Based on evaporator temperature

Below -30º C Jürgensen [56] in his study for commercial refrigerated appliances suggested that the energy efficiency and reliability of the appliance using R290 is expected to be equivalent to or better than that of equipment using R22. Because R290 has no ODP and a very low GWP, assuming that R290 has the same energy efficiency as R22, the environmental impact is reduced. Saleh and Wendland [57] simulated the performance of a vapour compression refrigeration system at an evaporating temperature of -40°C and a condensing temperature of 30°C working with propane and propylene. Their results showed that propane and propylene are alternative for R22.

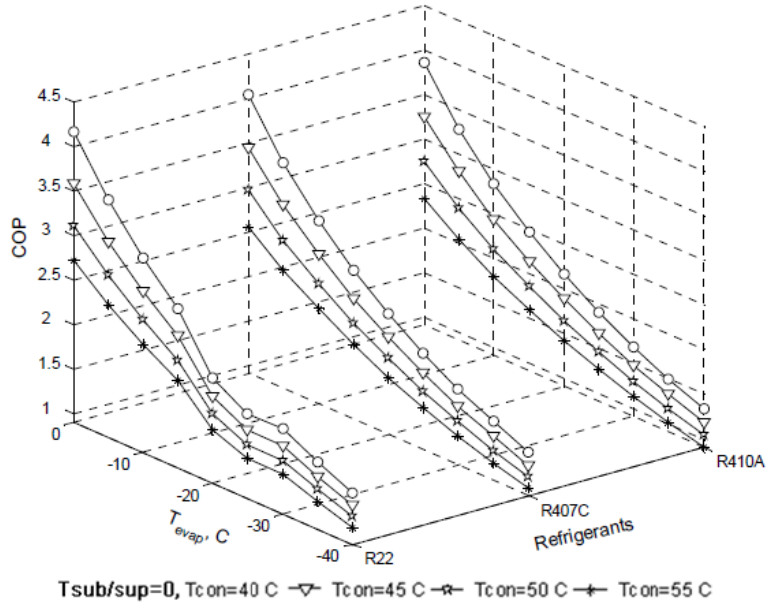

Figure 1. Comparison of COP of R22, R407C and R410A with evaporator temperature at different condenser temperatures [8]

Between -30º C to 10º CGranryd [58] comprehensively reviewed the performance of hydrocarbons as refrigerants in various applications and suggested that commercial "hydrocarbon chillers" are available on the market for low temperature applications (-35ºC) as well as for comfort cooling (+6ºC) and for heat pumps. Copetti et al. [59] theoretically analysed the performance of Propane and Isobutane in a 1kW refrigeration system at an evaporation temperature between -20°C to 10°C and condenser temperature of 40°C. Their results concluded that the hydrocarbon presenting better performance for R22 substitution, in the range of temperatures analyzed, was R600a. The propane presents for the same range of temperature a slightly inferior performance. In a related work, Park & Jung [60] tested the performance of R290 and R1270 in a 3.5 kW heat pump bench tester and their results concluded that COPs of R290 and R1270 are up to 12% higher than those of R22. These hydrocarbons provide good performance with reasonable energy savings without any environmental problems. In a similar work, Bayrakci and Ozgur [61] studied the performance of a 1kW VCRS at an evaporating temp of -25 to 0°C and a condensing temperature of 30 to 50°C working with R1270, R600, R600a and R290. Their results showed that in the point of view of energy and exergy efficiency, the best alternative refrigerant is R1270

for R22 and R134a. Differences of coefficient of cooling performance values of these refrigerants are quite small. Park et al. [62] experimentally investigated the performance of R170/R1270 mixture (R170 varied from 0 to 10% with an interval of 2%) as alternatives to R22 in a 3.5 kW heat pump bench tester. They reported that pure propylene and R170/R1270 mixture are good long-term candidates to replace R22 in residential air conditioners and heat pumps from the viewpoint of energy efficiency and greenhouse warming. Dalkilic & Wongwises [63] theoretically predicted the performance of a VCRS at a condensation temperature of 50 °C using different refrigerant blends R-290/R-1270 (20/80), R-290/R-1270 (50/50), R-290/R-1270 (60/40), R-290/R-1270 (80/20), R-290/R-152A (60/40), R-32/R-134A (30/70) (the refrigerant mixture blending being on mass basis). It has been reported that the refrigerant blend of HC290/HC1270 (20/80 by wt. %) is found to be the most suitable alternative among refrigerants tested for R22. Boumaza [64] simulated the performance of VCRS using refrigerant R290, R600A and R717 as alternatives to R22. It was revealed that the examined new refrigerants show varying performance, depending on the evaporator temperatures, but in every case, the condenser temperature seems to have an important impact on the performance of the cycle. Wan et al [65] reported that residential air-conditioner with HC-290 will produce more environmental benefits compared with HFC-410A, due to a high reduction of greenhouse gas emissions which slows down global warming. Farraj et al. [66] experimentally compared the performance of R22 and Liquefied Petroleum Gas Mixture (LPGM) of 30 % propane, R-290 and 70 % butane, R-600, (weight ratio) in a one ton split air conditioning unit (A/C) powered by solar energy. Their results showed that although systems using LPGM had lower COP and lower capacity than those using R-22, the first systems had the advantages of higher refrigeration effect, lower mass flow rate, lower energy consumption and lower compressor exit temperature. Prapainop and Suen [67] investigated the performance of some common refrigerants, including R22, following two approaches of refrigerant comparison for retrofit replacement. Using both the methods of full simulation as well as refrigerant thermo-physical properties and cycle performance analysis, it was concluded that in general the full simulation results agree well with the experimental results. Bolaji and Huan [68] analysed the performance characteristics of a vapour compression refrigeration system at -20º C evaporating temperature working with three hydrocarbons R290, R600A and R1270. Their results indicated that the degree of sub-cooling greatly increased the coefficient of performance and it had positive effects on the refrigerating capacity. Bolaji [69] theoretically assessed the performance of a VCRS at an evaporating temp of -20 °C and a condensing temperature of 40 °C working with the refrigerants R432A and R433A. It was reported that the two alternative refrigerants, consistently exhibited better performance than R22 in sub-cooling heat exchanger refrigeration system.

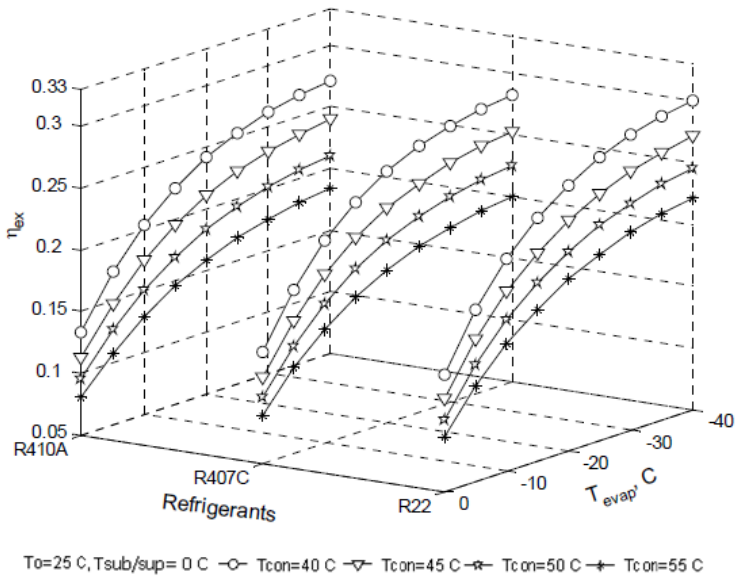

Figure 2. Effect of condenser temperature on exergetic efficiency [8]

Based on Cooling Capacity

Up to 3.5 kW capacity Lampugnani and Zgliczynski [70] investigated R290 as an alternative for R22 in a 1.8 kW air conditioner. Their results revealed that the hermetic compressors, designed for use with R22, while

operating with propane show a strong benefit in terms of general reliability, due to the lower bearing loads and the lower thermal level. It has a positive influence on the risk associated to the use of flammable refrigerants. Zaghdoudi [71] simulated the performance of a 2.63 kW residential air conditioner using refrigerants R134A, R290, R600, R404A, R407A, R407B, R407C, 407D, R410A, R410B, and R417A as alternatives to R22. R290 was identified as the best candidate for R22.

3.5 kW to 7 kW capacity Devotta et al. [72] experimentally investigated the performance of propane as alternative to R22 in a 5.13 kW window air conditioner at an evaporating temperature of 7.4°C and a condensing temperature of 35°C. Their results showed that cooling capacity of HC-290 was lower in the range 6.6– 9.7% but energy consumption with HC-290 was lower in the range 12.4–13.5%. Discharge pressures of HC-290 were lower in the range 13.7–18.2%. Al-Joudi & Al-Amir [73] have studied the performance (both theoretically and experimentally) of a split type air conditioner of 2 TR working with refrigerants R290, R407C and R410A. It was reported that R290 is the better replacement for R22 when the air conditioning system works under high ambient temperature. R407C has the closest performance to R22, followed by R410A.

Above 7 kW capacity Agrawal et al. [74] simulated the performance of a 28.64 kW bulk milk cooler using refrigerants R1270 and R32/R152 as alternatives to R22. R1270 was identified as best choice for replacing R22 with zero ODP and negligible GWP. Out of four mixtures, R32/R152 is best with zero ODP and low GWP. Zakrzewski & Łokietek [75] compared the performance of a 25 kW heat pump working with R22 and its alternatives (R41, R152A, R218, R227ea, RC318, R600A, R290, and R1270). They suggested that despite their good properties for air conditioning, wider use of R600A, R152A, R290, and R1270 is limited because of their high combustibility.

Based on Changes in Components of the System

Chinnaraj et al. [76] experimented with R407C and R290 in a 3.5 kW window air conditioner. It has been reported that the electronic expansion valve shows good overall performances comparing the capillary tube system. The coefficient of performance of R290 is the maximum among the three refrigerants tested. Cheng et al. [77] experimentally investigated the performance of R32 and R290 as alternatives to R22 in a 2.9 kW small split household air conditioner with 5 mm finned tube heat exchanger. Their results showed that COP of R32 and R290 were 26.8% and 20.4% higher than R22 and 7.3% and 2.1% higher than R410A. The systems with R290 and R32 have huge difference of capacities to that with R22 and R410A. In consideration of charge amount, R290 could be considered as the most superior alternative refrigerant in air conditioners with the small finned tube heat exchanger. Padalkar et al. [78] experimentally studied the performance and flammability of R290 in split air conditioners with nominal cooling capacities up to 5.1 kW. Their results concluded that with PFC (parallel flow condenser), HC-290 gave highest EER of 3.7 which was 37% higher than that of HCFC-22. The lowest HC-290 charge used in test was 340 g which is well below LFL (lower flammability limit).

Performance Comparison

Figure 3 shows the variation of COP of HC 290 with evaporation as well as condenser temperature in comparison with R22 (Boumaza [64]). Figure 4 depicts the COP and volumetric refrigerating capacity (VRC) of R290 and other alternative refrigerants relative to R22 (Saleh and Wendland [57]).

Refrigerant Mixtures

Domanski and Didion [79] suggested a semi-theoretical model for residential heat pumps working with R32/125 (60/40), R32/125/134A/290 (20/55/20/5), R32/125/134A (10/70/20) and (30/10/60), R290, R32/227ea (35/65), R32/134A (25/75) and (30/70), and R134A (the refrigerant mixture blending being on mass basis). Their results indicated that higher pressure fluids demonstrated a higher volumetric capacity and a lower COP. A strong exception was the high-glide R32/227ea mixture, of which the performance was penalized by use of pure cross-flow heat exchangers. Using the llsl-hx may be warranted for some of the candidate fluids. Devotta [80] studied the performance of a propane and butane mixture in a heat pump and reported some improvement in COP at the cost of risk of flammability. In a similar study, Chang et al. [81] assessed the performance of propane/isobutane/butane/propylene/propane, isobutane mix/propane, butane mix in a heat pump and concluded that the capacity and COP of R1270 are slightly greater than that of R22, which is an indication of a possible alternative for air conditioning and heat pumping applications. The COP of hydrocarbon mixtures for the cooling condition is higher than that of R22 for a wide range of the mixture compositions. Jung et al. [82]analysed the

performance of 14 refrigerant mixtures composed of R32, R125, R134A, R152A, R290 (propane) and R1270 (propylene) and reported that 26% R32 / 14% R125 / 60% R134A (the refrigerant mixture blending being on mass basis), has better performance than R407C. COPs of the binary mixtures composed of R32 and R134A are 7% higher and their capacities are similar to those of HCFC22. Both COP and capacity of the binary azeotrope of R290 and R134a are 3-5% higher than those of HCFC22.

Roberts and Chambers [83] experimented with R417A & Blend 79(R125/R134A/R600A (85.1%/11.5%/3.4%)) in an air conditioner (the refrigerant mixture blending being on mass basis). During their experimentation, the operating temperatures were maintained at 56°C, 48 to 50ºC & 58C (condenser temperature) and 5, 10.8 & -2°C (evaporator temperature). It has been reported that R417A is suitable for air conditioning with no problems experienced through lack of capacity, but energy savings were experienced. Blend 79 has been demonstrated to be suitable for use as a replacement for R22 with minimal changes to the expansion valves. Arcaklioglu [84] compared the performance of R32/R134A-25/75, R32/R134A-30/70, R32/R125/R134A-30/10/60, R290/R134A-46/54, 32/R125/R290/R134A-20/55/5/20, R32/R125-50/50, R32/R125/R134A-10/70/20 and R22 in a compression-based refrigeration system (the refrigerant mixture blending being on mass basis). It was reported that for R22, R32/R125/R134A (32.5/5/62.5) mixture provides 0.8% better COP.

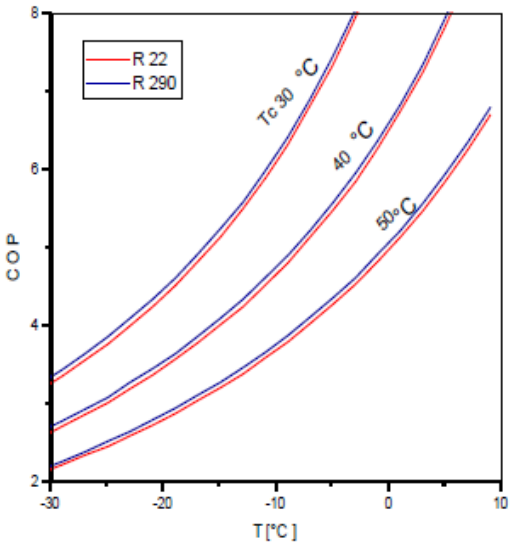

Figure 3. Variation of the Coefficient of performance with respect to Tev and Tcond, for HC 290 and R22 [64]

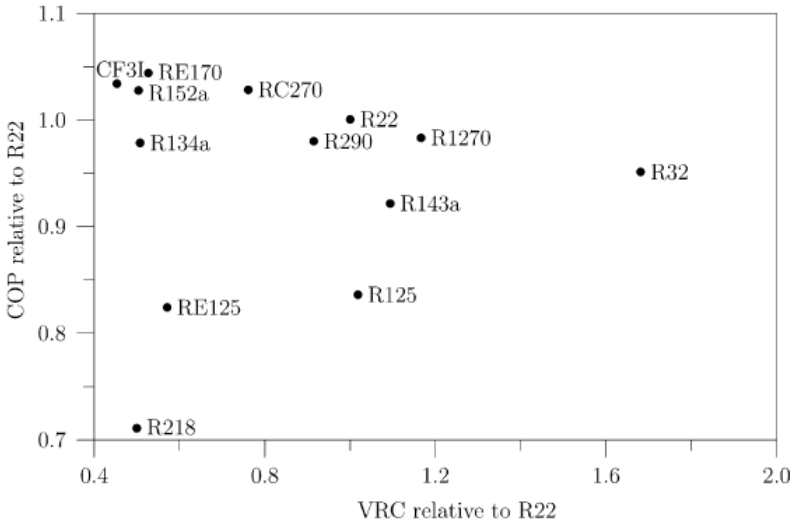

Figure 4. COP and VRC of alternative refrigerants relative to R22 [57]

Park et al. [85] have conducted an experimental investigation in R22-based air-conditioners and heat pumps working with propylene, propane and seven mixtures composed of propylene, propane, HFC152A, and dimethyl ether as alternatives. It has been reported that COP of these mixtures is up to 5.7% higher than that of R22. Propane showed an 11.5% reduction in capacity while most of the fluids had a similar capacity to that of R22. The compressor-discharge temperatures were reduced by 11–17ºC and the amount of charge was reduced by up to 55% as compared to HCFC22. Park et al. [86] experimentally studied the thermodynamic performance of R433A (30% propylene and 70% propane) as alternative for R22 in air-conditioners and heat pumps (the refrigerant mixture blending being on mass basis). The results reported in their study are compared in Table 2. It is found that the COP of R433A is 4.9–7.6% higher and the capacity of R433A is 1.0–5.5% lower. The compressor discharge temp of R433A is 22.6–27.9ºC lower while the amount of charge for R433A is 57.0–57.7% lower.

In another experimental study, Park et al. [87] also compared the performance of R432A in a heat pump bench tester and concluded that the COP of R432A is 8.5–8.7% higher than that of R22 and the capacity of R432A is 1.9–6.4% higher than that of R22. The compressor discharge temp of R432A is 14.1–17.3ºC lower than that of R22 whereas the amount of charge for R432A is 50% lower than that of R22 due to its low density. Cleland et al. [88] conducted experimental studies on an on-farm milk cooling working with Care-50 [a mixture of propane (R-290) and ethane (R-170)] as an alternative to R22. It was reported that Care-50 reduced energy use by 6–8% and had similar system cooling capacity relative to HCFC-22. The small charge means that hydrocarbons could meet standards for safe use of refrigerants.

Allgood & Lawson [89] experimented with R438A in existing refrigeration & air conditioning systems and reported that compared to R22, similar cooling performance & energy efficiency were achieved. Lower discharge temperature and similar evaporator & condenser pressure were observed with no change of lubricant during retrofit. BOCK Compressors [90] tested R422D (MO29), R417A (MO59) and R438A (MO99) in their compressors and found that among the three alternative refrigerants, the compression temperature was the lowest for R417A; R438A had the highest refrigerating capacity while R417A had the highest energy efficiency, in comparison to R22. Lopez [91] reported that R434A is the only possible direct solution on the market for the range of temperatures in air conditioning while emphasizing to use this refrigerant with adjustable expansion devices in order to set the correct superheat.

Cabello et al. [92] conducted experimental studies on single-stage vapour compression refrigeration plant working with drop-in fluids R417B and R422A and long-term substitute R404A. Their results showed that use of IHX allows the drop-in fluids to approximate the energy performance of R22, especially in the case of R417B. Ramu et al. [93] investigated a new mixtureR32/R125/R600A (in the ratio of 0.4:0.4:0.2, by mass) as an alternative for R22 in an air conditioner. Their results revealed that VCC of new refrigerant mixture is closer to R22 and COP of the mixture was found to be lower by about 16-20%. The compressor discharge temperature of the new refrigerant mixture was observed to be 6-11ºC lower and TEGWI of new refrigerant mixture was found to be higher than that of R22 by about 20%. Dalkilic et al. [94] theoretically analysed the performance of various alternative refrigerants in a shell and tube condenser at an evaporating temp of -10 °C and a condensing temperature of 35 to 55°C.

Table 2. Test results for HCFC22 and R433A under air-conditioning condition [86]

Refrigerants	COP	Diff in COP (%)	Q_e (W)	Diff in Q_c (%)	W (W)	Diff in W (%)	PR	T_{dis} (ºC)	Charge (g)
HCFC22	3.41		3734		1096		2.99	84.7	1300
R433A	3.67	7.6	3527	-5.5	960	-12.4	2.52	62.1	550

The results showed that the refrigerant mixture of R290/R600, R152a/R125/R32 and R32/R134a were the most proper replacement refrigerant among the alternatives. Figure 5 compares the saturation pressure vs temperature of R422D and R22 (Aprea et al. [39]). Figure 6 shows the variation of COP of R422D with refrigeration duty in comparison to R22 (Aprea et al. [39]).

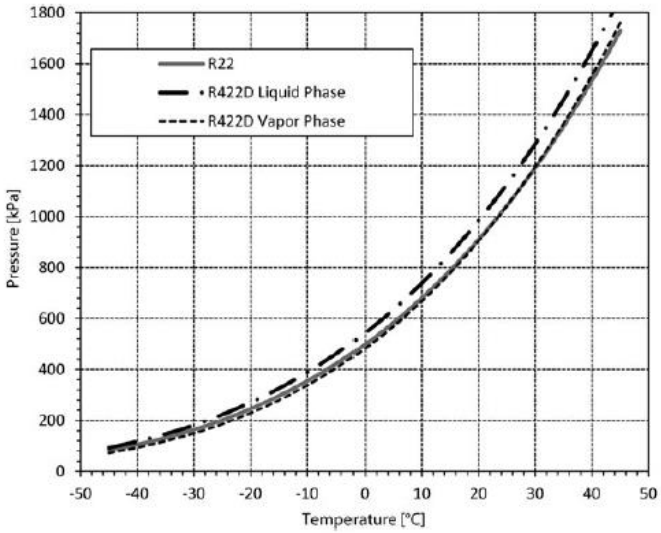

Figure 5. Comparison of saturation pressure vs. temperature of R422D and R22 [39]

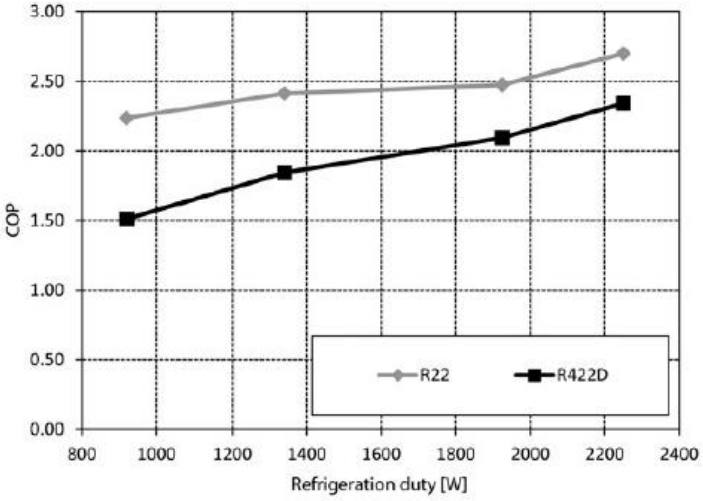

Figure 6. Comparison of COP vs. refrigeration duty for R22 and R422D [39]

Other Refrigerants

Lorentzen [95] in a study on vapour compression refrigeration system suggested that, in the conventional refrigeration and heat pump domain three refrigerants will be sufficient to satisfy normal requirements: NH_3, R290 & CO_2. McMullan [96] reported that due to the failure to find single fluid replacement fluids in most applications, the potential role for fluid mixtures and natural refrigerants like NH_3, HCs &CO_2, has had to be re-examined. Tao et al. [97] tested the performance of CO_2 in a transcritical CO_2 system at evaporating temperature of 10 to 14°C and their results showed that CO2 has zero ODP, negligible GWP and very low cost. So, CO_2 is an excellent alternative to the traditional refrigerants. The average relative exergy losses in gas cooler and expansion valve are the dominant exergy losses in the transcritical CO_2 residential air-conditioning system. Benhadid-Dib &Benzaoui [98] reported that there is merit of redeploying natural refrigerants as an alternative solution to replace halogenated refrigerants. Sarbu&Valea [99] suggested that a possible solution is the use of inorganic refrigerants (NH_3, CO_2) and hydrocarbon refrigerants (propane, isobutene, ethylene, propylene) in air conditioning. Because the hydrocarbon refrigerant presents a high risk of flammability and explosion, these substances will not be often used as refrigerants comparative with CO_2 or NH_3.

Figure 7 depicts the variation of the volumetric refrigerating capacity of R717 and R22 with respect to evaporator temperature and condenser temperature. Figure 8 shows the variation of COP of NH_3 (R717) with evaporator temperature as well as condenser temperature in comparison with R22 (Boumaza [64]).

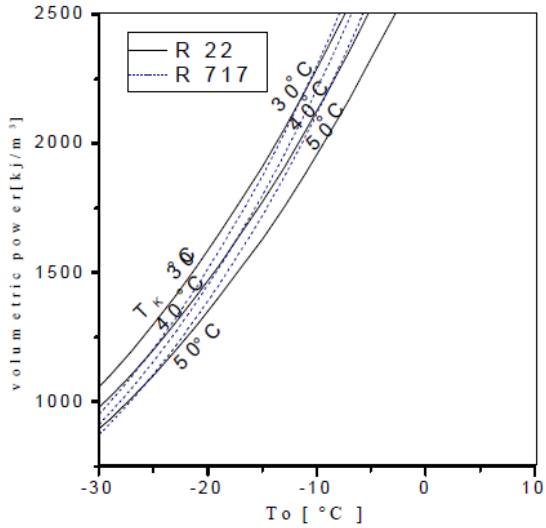

Figure 7. Variation of the volumetric refrigerating capacity of R717 andR22 with respect to T_0 (evaporator temperature) and T_c (condenser temperature) [64]

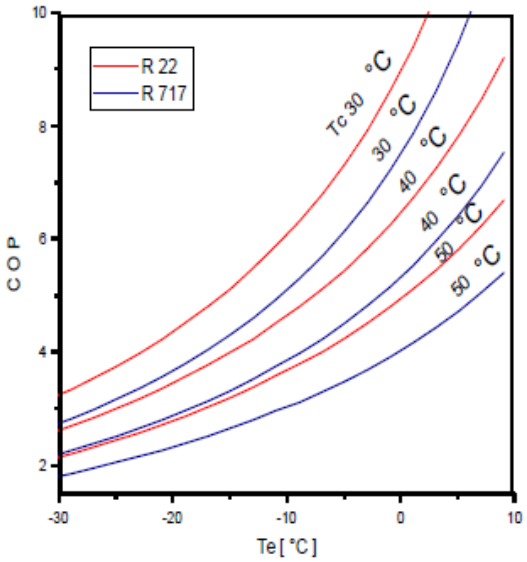

Figure 8. Variation of the Coefficient of performance with respect to T_e (evaporator temperature) and T_c (condenser temperature), for R717 and R22 [64]

RESULTS AND DISCUSSION

HFCs that replaced CFCs in the last decade have high GWP and need to be eventually phased out. Environment friendly natural refrigerants such as ammonia, carbon dioxide, hydrocarbons have specific practical deficiencies that limit their universal use. Thus, there are no refrigerants in the horizon that completely meet the safety, stability, energy efficiency and environmental friendliness. The refrigerants HC290 and HC1270 seem to be the most near to R22 in terms of their thermodynamic performance. Although easily available and having low cost, they have the drawback of being flammable as both belong to ASHRAE safety group A3. The next available choice is the HFCs. The drawback of HFCs is that they have high GWP. R407C has GWP of 1700 whereas that of R410A is 2000. The third option is to use natural refrigerants NH_3 (R717) and CO_2 (R744). The drawback of using CO_2 is that it necessitates high pressures in the system and NH_3 is toxic and flammable in nature. This narrows down the choice of alternative refrigerant of R22 to a mixture of HFCs and HCs which are mixed in such a ratio that GWP is kept to a minimum, flammability is within accepted limits and the refrigerant mixture is miscible in the conventional cheap lubricant i.e. mineral oil.

CONCLUDING REMARKS

Alternatives for R22 in air-conditioning can be grouped into four types: HFC, HC, other natural substances and refrigerant mixtures. The most popular HFC, R410A is having lower critical temperature, which restricts its usage in compression-based systems working at higher condensing temperatures. Whereas for R407C, a change to synthetic lubricant is required and HC-290 is flammable. The conventional CO_2 systems require high power consumption and lose capacity at high temperature. NH_3 has high toxicity and high initial costs. In view of the above it is suggested that until the safety issue of use of hydrocarbon refrigerants in quantities exceeding 500gm is resolved, we should go for those mixtures of HFCs and HCs for which TEWI index is the lowest.

NOMENCLATURE

HCFC Hydrochloroflurocarbon
ODP Ozone depleting potential
HC Hydrocarbon
COP Coefficient of performance
EDR Exergy destruction ratio
VCRS Vapour compression refrigeration system
EER Energy efficiency ratio

REFERENCES

[1] Poggi, F., Macchi-Tejeda, H., Leducq, D., & Bontemps, A. (2008). Refrigerant charge in refrigerating systems and strategies of charge reduction. International Journal of Refrigeration, 31(3), 353-370.
[2] Palm, B. (2008). Hydrocarbons as refrigerants in small heat pump and refrigeration systems–a review. International journal of refrigeration, 31(4), 552-563.
[3] Calm, J. M. (2008). The next generation of refrigerants–Historical review, considerations, and outlook. international Journal of Refrigeration, 31(7), 1123-1133.
[4] Mohanraj, M., Muraleedharan, C., & Jayaraj, S. (2011). A review on recent developments in new refrigerant mixtures for vapour compression-based refrigeration, air-conditioning and heat pump units. International journal of energy research, 35(8), 647-669.
[5] Sarbu, I. (2014). A review on substitution strategy of non-ecological refrigerants from vapour compression-based refrigeration, air-conditioning and heat pump systems. International Journal of Refrigeration, 46, 123-141.
[6] Arora, A., Arora, B. B., Pathak, B. D., & Sachdev, H. L. (2007). Exergy analysis of a vapour compression refrigeration system with R-22, R-407C and R-410A. International journal of Exergy, 4(4), 441-454.
[7] Du Pont (accessed Jan 14, 2015). http://www.isceon.com/uk
[8] Menlik, T., Demircioğlu, A., & Özkaya, M. G. (2013). Energy and exergy analysis of R22 and its alternatives in a vapour compression refrigeration system. International Journal of Exergy, 12(1), 11-30.
[9] Klein, S. A., Reindl, D. T., & Brownell, K. (2000). Refrigeration system performance using liquid-suction heat exchangers. International Journal of Refrigeration, 23(8), 588-596.
[10] Grace, I. N. & Tassou, S. A. (2000). In Simulation of the performance of alternative refrigerants in liquid chillers, International Refrigeration and Air Conditioning Conference Paper 513.
[11] Boumaza, M. M. (2007). A numerical Investigation and Comparison of Chlorines Compounds Refrigerants and their Potential Substitutes Operating at High Ambient Temperature Case for the Replacement of R22. Final Research Report.
[12] Rani, T. U., & Balachander, P. (2008). Numerical simulation of fin and tube condenser in a R22 system charged with R407C.
[13] Jia, S. (2009). Evaluation of HCFC alternative refrigerants. Heatcraft Worldwide Refrigeration.
[14] Aprea, C., Maiorino, A., & Mastrullo, R. (2011). Change in energy performance as a result of a R422D retrofit: An experimental analysis for a vapor compression refrigeration plant for a walk-in cooler. Applied energy, 88(12), 4742-4748.
[15] Han, X. H., Qiu, Y., Li, P., Xu, Y. J., Wang, Q., & Chen, G. M. (2012). Cycle performance studies on HFC-161 in a small-scale refrigeration system as an alternative refrigerant to HFC-410A. Energy and Buildings, 44, 33-38.
[16] Padmanabhan, V. M. V., & Palanisamy, S. K. (2013). Exergy efficiency and irreversibility comparison of R22, R134a, R290 and R407C to replace R22 in an air conditioning system. Journal of Mechanical Science and Technology, 27(3), 917-926.
[17] Bolaji, B. O., Abiala, I. O., Ismaila, S. O., & Borokinni, F. O. (2014). A theoretical comparison of two eco-friendly refrigerants as alternatives to r22 using a simple vapour compression refrigeration system. Transactions of FAMENA, 38(3), 59-70.

[18] La Rocca, A., La Rocca, V., Messineo, A., & Panno, D. (2014). Use of HFC fluids as suitable replacements in low-temperature refrigeration plants. Journal of Engineering and Applied Sciences, 9(1, Gennaio 2014), 74-79.
[19] Hewitt, N. J., & McMullan, J. T. (1997). The replacement of CFCs in refrigeration equipment by environmentally benign alternatives. Applied thermal engineering, 17(8-10), 955-972.
[20] Johansson, A., & Lundqvist, P. (1998). Optimal distribution of Condenser area for Retrofits. International Refrigeration and Air Conditioning Conference.
[21] Devotta, S., Waghmare, A. V., Sawant, N. N., & Domkundwar, B. M. (2001). Alternatives to HCFC-22 for air conditioners. Applied Thermal Engineering, 21(6), 703-715.
[22] Johansson, A., & Lundqvist, P. (2003). Replacement of R22 in existing installations: experiences from the Swedish phase out. Royal Institute of Technology, Department of Energy Technology, Stockholm, Sweden.
[23] Calm, J. M., & Domanski, P. A. (2004). R-22 replacement status. ASHRAE journal, 46(8), 29.
[24] Horuz, I. (2004). Ozone-depleting substances, phase-out program and alternatives. International communications in heat and mass transfer, 31(4), 607-618.
[25 Chen, J., & Yu, J. (2008). Performance of a new refrigeration cycle using refrigerant mixture R32/R134a for residential air-conditioner applications. Energy and Buildings, 40(11), 2022-2027.
[26] Allgood, C. (2008). Refrigeration Regulations, Outlook, Transitions & Alternatives. ASHRAE Meeting 11 November.
[27] Emerson Network Power (2009). Comparing R407C and R410A as Alternatives for R22. http:/www. EmersonNetworkPower.com.
[28] Honeywell (accessed Jan 14, 2015). http//www.genetron.com
[29] Department for Environment, Food and Rural Affairs, UK, (2012). Guidance: F Gas and Ozone Regulations.
[30] Bitzer (accessed Jan 14, 2015). http://www.bitzer.de
[31] Bolaji, B. O. (2012). Performance of A R22 split-air-conditioner when retrofitted with ozone friendly refrigerants (R410A and R417A). Journal of Energy in Southern Africa, 23(3), 16-22.
[32] Vjacheslav, N., Rozhentsev, A., & Wang, C. C. (2001). Rationally based model for evaluating the optimal refrigerant mass charge in refrigerating machines. Energy Conversion and Management, 42(18), 2083-2095.
[33] Aprea, C., & Renno, C. (2004). Experimental comparison of R22 with R417A performance in a vapour compression refrigeration plant subjected to a cold store. Energy conversion and management, 45(11-12), 1807-1819.
[34] Spatz, M. W., & Motta, S. F. Y. (2004). An evaluation of options for replacing HCFC-22 in medium temperature refrigeration systems. International Journal of Refrigeration, 27(5), 475-483.
[35] Chen, W. (2008). A comparative study on the performance and environmental characteristics of R410A and R22 residential air conditioners. Applied thermal engineering, 28(1), 1-7.
[36] Mohanraj, M., Jayaraj, S., & Muraleedharan, C. (2009). Environment friendly alternatives to halogenated refrigerants—A review. International Journal of Greenhouse Gas Control, 3(1), 108-119.
[37] Wang, F. J., Tsai, K. I., Wang, Y. J., & Lee, H. C. (2011). Experimental investigation of a process cooling system retrofitted with HFC-404A refrigerant for precise manufacturing application. Journal of Mechanical Science and Technology, 25(2), 495-501.
[38] Wu, Y., Liang, X., Tu, X., & Zhuang, R. (2012). Study of R161 refrigerant for residential air-conditioning applications. International Refrigeration and Air Conditioning Conference Paper 1189.
[39] Aprea, C., Maiorino, A., & Mastrullo, R. (2012). Exergy analysis of a cooling system: experimental investigation on the consequences of the retrofit of R22 with R422D. International Journal of Low-Carbon Technologies, 9(1), 71-79.
[40] Bensafi, A., Mondot, M., & Durier, F.F. (1997). Experimental evaluation of some proposed R22 alternatives in chillers and unitary A/C equipment. Clima. Centre Technique des Industries Aérauliques et Thermiques (CETIAT), France.
[41] Aprea, C., & Greco, A. (2002). An exergetic analysis of R22 substitution. Applied Thermal Engineering, 22(13), 1455-1469.
[42] Devotta, S., Padalkar, A. S., & Sane, N. K. (2005). Performance assessment of HCFC-22 window air conditioner retrofitted with R-407C. Applied Thermal Engineering, 25(17-18), 2937-2949.
[43] Bolaji, B. O. (2011). Performance investigation of ozone-friendly R404A and R507 refrigerants as alternatives to R22 in a window air-conditioner. Energy and Buildings, 43(11), 3139-3143.
[44] Samuel, K. J., Govindarajulu, K., & Edison, G. (2014). An Experimental Investigation and Performance Evaluation of 1.5 TR Window Air-Conditioner by Using R22 R407C and R410A by Varying the Capillary Pitch. World Applied Sciences Journal, 29(11), 1468-1472.
[45] Payne, W. V., & Domanski, P. A. (2002). A comparison of an R22 and an R410a air conditioner operating at high ambient temperatures. National Institute of Standards and Technology Building Environment Division: Thermal Machinery Group Gaithersburg, Maryland, USA.

[46] Hwang, Y., Jin, D. H., & Radermacher, R. (2007). Comparison of R-290 and two HFC blends for walk-in refrigeration systems. International Journal of Refrigeration, 30(4), 633-641.
[47] Kulcar, B., Goricanec, D., & Krope, J. (2010). Economy of replacing a refrigerant in a cooling system for preparing chilled water. international journal of refrigeration, 33(5), 989-994.
[48] La Rocca, V., & Panno, G. (2011). Experimental performance evaluation of a vapour compression refrigerating plant when replacing R22 with alternative refrigerants. Applied energy, 88(8), 2809-2815.
[49] La Rocca, V., Messineo, A., & Panno, D. (2011, June). An experimental study of a refrigerating plant when replacing R22 with HFCs refrigerants. In XIV European Conference "The Latest Technologies in Air Conditioning and Refrigeration Industry". IT.
[50] Jain, V., Kachhwaha, S. S., & Mishra, R. S. (2011). Comparative performance study of vapour compression refrigeration system with R22/R134a/R410A/R407C/M20. International journal of energy and environment, 2(2), 297-310.
[51] Qureshi, B. A., & Zubair, S. M. (2011). Performance degradation of a vapor compression refrigeration system under fouled conditions. International Journal of Refrigeration, 34(4), 1016-1027.
[52] Lee, D. Y., Ahn, Y., Kim, Y., Chang, Y. S., & Nam, L. (2002). Experimental investigation on the drop-in performance of R407C as a substitute for R22 in a screw chiller with shell-and-tube heat exchangers. International journal of refrigeration, 25(5), 575-585.
[53] Aprea, C., Mastrullo, R., Renno, C., & Vanoli, G. P. (2004). An evaluation of R22 substitutes performances regulating continuously the compressor refrigeration capacity. Applied Thermal Engineering, 24(1), 127-139.
[54] Llopis, R., Cabello, R., Sánchez, D., Torrella, E., Patiño, J., & Sánchez, J. G. (2011). Experimental evaluation of HCFC-22 replacement by the drop-in fluids HFC-422A and HFC-417B for low temperature refrigeration applications. Applied Thermal Engineering, 31(6-7), 1323-1331.
[55] Subiantoro, A., & Ooi, K. T. (2013). Economic analysis of the application of expanders in medium scale air-conditioners with conventional refrigerants, R1234yf and CO2. international journal of refrigeration, 36(5), 1472-1482.
[56] Jürgensen, H. (2016). Propane as R22-Replacement in Commercial Appliances. Danfoss Compressors GmbH.
[57] Saleh, B., & Wendland, M. (2006). Screening of pure fluids as alternative refrigerants. International journal of refrigeration, 29(2), 260-269.
[58] Granryd, E. (2001). Hydrocarbons as refrigerants—an overview. International journal of refrigeration, 24(1), 15-24.
[59] Copetti, J. B., Macagnan, M. H., Geyer, M., & Oliveski, R. C. (2005). The use of hydrocarbons propane and isobutane in refrigeration systems. In 18 th International Congress of mechanical Engineering-COBEM.
[60] Park, K. J., & Jung, D. (2008). Performance of R290 and R1270 for R22 applications with evaporator and condenser temperature variation. Journal of Mechanical Science and Technology, 22(3), 532-537.
[61] Bayrakçi, H. C., & Özgür, A. E. (2009). Energy and exergy analysis of vapor compression refrigeration system using pure hydrocarbon refrigerants. International Journal of Energy Research, 33(12), 1070-1075.
[62] Park, K. J., Lee, Y., & Jung, D. (2010). Performance of R170/R1270 mixture under air-conditioning and heat pumping conditions. Journal of mechanical science and technology, 24(4), 879-885.
[63] Dalkilic, A. S., & Wongwises, S. (2010). A performance comparison of vapour-compression refrigeration system using various alternative refrigerants. International Communications in Heat and Mass Transfer, 37(9), 1340-1349.
[64] Boumaza, M. (2010). Performances assessment of natural refrigerants as substitutes to CFC and HCFC in hot climate. Int. J. of Thermal & Environmental Engineering, 1(2), 125-130.
[65] Wan, T., Dou, Y., Wang, L., Yang, L., Zhou, X., Wan, D., & Hu, J. (2011). Environmental benefits for phase-out HCFC-22 in the residential air-conditioner sector in China. Advances in Climate Change Research, 2(2), 86-92.
[66] Farraj, A., Mallouh, M. A., Kalendar, A. R., & Al-Rzaq, A. (2012). Experimental Study of Solar Powered Air Conditioning Unit Using Drop–In Hydro Carbon Mixture to Replace R-22. JJMIE, 6(1).
[67] Prapainop, R. & Suen, K.O. (2012). Simulation of potential refrigerants for retrofit replacement. ARPN Journal of Engineering & Applied Science, 7(9), 1146-1151.
[68] Bolaji, B. O., & Huan, Z. (2012). Comparative analysis of the performance of hydrocarbon refrigerants with R22 in a sub-cooling heat exchanger refrigeration system. Proceedings of the Institution of Mechanical Engineers, Part A: Journal of Power and Energy, 226(7), 882-891.
[69] Bolaji, B. (2014). Influence of sub-cooling on the energy performance of two ecofriendly R22 alternative refrigerants. Journal of Science and Technology (Ghana), 34(2), 73-83.
[70] Lampugnani, G., & Zgliczynski, M. (1996). R290 as a Substitute of R502 and R22 in Commercial Refrigeration and Air Conditioning, International Compressor Engineering Conference Paper 1087.

[71] Zaghdoudi, M. C., Maalej, S., Saad, Y., & Bouchaala, M. (2010). A comparative study on the performance and environmental characteristics of alternatives to R22 in residential air conditioners for Tunisian market. Journal of Environmental Science and Engineering, 4(12).
[72] Devotta, S., Padalkar, A. S., & Sane, N. K. (2005). Performance assessment of HC-290 as a drop-in substitute to HCFC-22 in a window air conditioner. International Journal of Refrigeration, 28(4), 594-604.
[73] Lect, K., & Al-Amir, Q. (2014). Performance evaluation of small scale air-conditioning system using R22 and alternative refrigerants. Journal of Engineering, 20(1).
[74] Agrawal, A. B., Dave, R. K., & Shrivastava, V. (2009). Replacing harmful refrigerant R22 in a bulk milk cooler. Indian Journal of Science and Technology, 2(9), 51-58.
[75] Zakrzewski, B., & Łokietek, T. (2010). Assessing the applicability of new refrigerants in marine cooling systems. Polish Maritime Research, 17(2), 55-59.
[76] Chinnaraj, C., Govindarajan, P., & Vijayan, R. (2011). Influence of electronic expansion valve on the performance of small window air conditioner retrofitted with R407C and R290. Thermal Science, 15(suppl. 2), 327-339.
[77] Cheng, S., Wang, S., & Liu, Z. (2014). Cycle performance of alternative refrigerants for domestic air-conditioning system based on a small finned tube heat exchanger. Applied thermal engineering, 64(1-2), 83-92.
[78] Padalkar, A. S., Mali, K. V., & Devotta, S. (2014). Simulated and experimental performance of split packaged air conditioner using refrigerant HC-290 as a substitute for HCFC-22. Applied Thermal Engineering, 62(1), 277-284.
[79] Domanski, P. A., & Didion, D. A. (1993). Theoretical evaluation of R22 and R502 alternatives (No. DOE/CE/23810-7). Air-Conditioning and Refrigeration Technology Inst., Inc., Arlington, VA (United States); National Inst. of Standards and Technology (NEL), Gaithersburg, MD (United States). Building Environment Div.
[80] Devotta, S. (1995). Alternative heat pump working fluids to CFCs. Heat Recovery Systems and CHP, 15(3), 273-279.
[81] Chang, Y. S., Kim, M. S., & Ro, S. T. (2000). Performance and heat transfer characteristics of hydrocarbon refrigerants in a heat pump system. International journal of refrigeration, 23(3), 232-242.
[82] Jung, D., Song, Y., & Park, B. (2000). Performance des mélanges de frigorigènes utilisés pour remplacer le HCFC22. International Journal of Refrigeration, 23(6), 466-474.
[83] Roberts, N. A., & Chambers, O. R. (2004). Energy saving refrigerant blends comprising R125, R134a, R600 or R600a. International Refrigeration and Air Conditioning Conference Paper 632.
[84] Arcaklıoğlu, E., Çavuşoğlu, A., & Erişen, A. (2006). Thermodynamic analysis of refrigerant mixtures for possible replacements for CFCs by an algorithm compiling property data. Applied Thermal Engineering, 26(4), 430-439.
[85] Park, K. J., Seo, T., & Jung, D. (2007). Performance of alternative refrigerants for residential air-conditioning applications. Applied energy, 84(10), 985-991.
[86] Park, K. J., Shim, Y. B., & Jung, D. (2008). Performance of R433A for replacing HCFC22 used in residential air-conditioners and heat pumps. Applied Energy, 85(9), 896-900.
[87] Park, K. J., Shim, Y. B., & Jung, D. (2009). Experimental performance of R432A to replace R22 in residential air-conditioners and heat pumps. Applied Thermal Engineering, 29(2-3), 597-600.
[88] Cleland, D. J., Keedwell, R. W., & Adams, S. R. (2009). Use of hydrocarbons as drop-in replacements for HCFC-22 in on-farm milk cooling equipment. international journal of refrigeration, 32(6), 1403-1411.
[89] Allgood, C. C., & Lawson, C. C. (2010). Performance of R-438A in R-22 refrigeration and air conditioning systems. International Refrigeration and Air Conditioning Conference at Purdue, July 12-15.
[90] Bock Compressors, (accessed Jan 20, 2015). www.bock.de
[91] Lopez, D.L.G. (2010). The replacement of R-22. Gas Technical Department of Gas Servei S.A.
[92] Cabello, R., Torrella, E., Llopis, R., Sánchez, D., & Larumbe, J. A. (2013). Energy influence of the IHX with R22 drop-in and long-term substitutes in refrigeration plants. Applied Thermal Engineering, 50(1), 260-267.
[93] Ramu, N. S., Kumar, P. S., & Mohanraj, M. (2014). Energy performance assessment of R32/R125/R600a mixtures as possible alternatives to R22 in compression refrigeration systems. International Journal of Mechanical and Mechatronics Engineering IJMME–IJENS, 14(02), 12-22.
[94] Dalkilic, A. S., Mahian, O., & Wongwises, S. (2014). Selection of the most suitable refrigerant for a shell and tube condenser. Heat and Mass Transfer, 50(2), 183-197.
[95] Lorentzen, G. (1995). The use of natural refrigerants: a complete solution to the CFC/HCFC predicament. International journal of refrigeration, 18(3), 190-197.
[96] McMullan, J. T. (2002). Refrigeration and the environment—issues and strategies for the future. International Journal of Refrigeration, 25(1), 89-99.
[97] Tao, Y. B., He, Y. L., & Tao, W. Q. (2010). Exergetic analysis of transcritical CO2 residential air-conditioning system based on experimental data. Applied Energy, 87(10), 3065-3072.

[98] Benhadid-Dib, S., & Benzaoui, A. (2012). Refrigerants and their environmental impact Substitution of hydro chlorofluorocarbon HCFC and HFC hydro fluorocarbon. Search for an adequate refrigerant. Energy Procedia, 18, 807-816.
[99] Sarbu, I., & Valea, E. S. Ecological refrigerants used in refrigeration, air-conditioning and heat pump systems. Proceedings of the 2014International Conference on Power Systems, Energy, Environment.

International Conference on Recent Innovations in Science and Engineering
Buddha Institute of Technology, Gida, Gorakhpur (India) (ICRISE-18)
1st-2nd April 2018 www.conferenceworld.in ISBN : 978-93-87793-15-6

Ambient Air Quality Status in Noamundi Iron Ore Mines, Jharkhand (India): A Case Study

Amit Krishan[1, 2], Ankita Srivastava[3] , Rajeev Kumar Mishra[1]

[1]*Department of Environmental Engineering, Delhi Technological University, Delhi, (India)*

[2]*Department of Civil Engineering,*

G. L. Bajaj Institute of Technology and Management, Greater Noida (UP), (India)

[3]*Department of Environmental Science and Engineering,*

Indian Institute of Technology (Indian School of Mines), Dhanbad, Jharkhand, (India)

ABSTRACT

Noamundi iron ore mine is one of the ten captive mines of Tata Iron Steel Co. Ltd. It is one of the oldest and largest open cast mines in the country. Mining activities are inherently disruptive to the environment. Due to unsuitable and inefficient working practices during mining causes environmental deterioration. The current work has been carried out to assess the ambient air quality in the open cast iron ore mines in the Noamundi of Jharkhand, India. For the decision makers it has been an important task to keep the air quality within acceptable limit. In the present study monitoring and analysis of SO_2, NO_2, PM_{10} and $PM_{2.5}$ have been carried out. The AQI was also calculated using IND-AQI specified by CPCB and it was based on the dose-response relationship of various pollutants. The monitoring result illustrates that particulate materials were the major pollutants to be concerned in mining areas but all the four parameters was well below the maximum allowed limit of National Ambient Air Quality Standards (NAAQS) for different areas. The overall AQI was found to fall under the category of good.

Keywords: AQI, Iron ore mine, Mining, NAAQS, Open cast mine

I. INTRODUCTION

The air we breathe is a mixture of gases and small solid and liquid particles from both the natural sources and human activities. Presence of substances up to that level which could damage the health of humans and animals, or could harm plants and materials causes air pollution. These substances are called air pollutants and can be either particles, liquids or gaseous in nature [1]. Now days it has become an important task for decision makers to keep the air quality within acceptable limit [2].

Mining is a vital industry for the industrial and economic growth of any country. The development of infrastructure and core sector is directly linked to the increased production of minerals, like coal for the power sector, iron ore for steel sector, limestone for cement for housing and infrastructure development. With

increased industrialization, urbanization and other developmental activities; there is a greater need for increased production of minerals.

Mining activities are inherently disruptive to the environment. The environmental degradation caused by mining activities occurs mainly due to lack of appropriate working practices. The magnitude of impact on air quality depends upon the types of mineral being mined, methods, scale and concentration of mining activities [3]. Open-cast mining is more deteriorating to air quality than underground mining. In the last few decades, this problem has been further provoked with the introduction of mechanized mining techniques and heavy earth moving equipment [4] [5]. Major sources of atmospheric emissions from open-cast mining activity include land clearing, removal of overburden, and vehicular movement on the haul roads, excavation, loading and unloading of ore materials as well as overburden.

Air quality monitoring and assessment are required to prevent and minimize the fall of air quality due to mining and other anthropogenic activities. The existing evaluation and assessment of air quality in India are based totally on the compliance of calculated concentration levels of pollutants with the National Ambient Air Quality Standards (NAAQS) [6]. This approach is used to maintain the desired quality of the ambient atmosphere, the concentration level of pollutants found below the NAAQS are fair and acceptable air quality, but sometimes the concentrations are adequately high to cause serious environmental and health problems.

The use of standards is important in administrating and enforcing the desired policy, but there is not a complete tool for evaluating the environmental quality [6]. The requirement to quantify air quality and follow the evolution of pollution has led to a huge quantity of Air Quality Indices, giving an idea of the state of pollution in a day [7]. Air Quality Indices are also of specific significance because; air pollution monitoring data are generally complex and not understandable to the general public. The huge data habitually do not communicate the air quality grade to the scientific community, policymakers and the general public in a uncomplicated and clear-cut manner. This problem can be addressed by determining the Air Quality Index (AQI) of a given area using environmental synthetic indices to review complex situations in a single figure, allowing for comparisons in time and in space [8].

Keeping the aforesaid problems in mind, the current work has been carried out with the objectives of ambient air quality assessment in the open cast iron ore mines in the Noamundi of Jharkhand, India.

II. MATERIALS AND METHODS

2.1. Study Area

Noamundi is one of the oldest and largest open cast mines in the country. It is one of the ten captive mines of Tata Iron Steel Co. Ltd. Noamundi is a census town in Pashchimi Singhbhum district in the Indian state of Jharkhand. It is also an administrative block. It is a small mining town located close to the Odisha border. It lies near to Jamshedpur and 64 km from Chaibasa. The deposit was discovered in the year 1917. The mining was started in the year 1925, however fully fledged mining operations commenced from the year 1926. Legend has it that when the first iron ore explorers came to this region, they were amazed to find the local tribal population

(Adivasis) using iron axes. When the explorers asked the tribals where they had found the ore, they pointed to a hill nearby and called it Noamundi, which literally means 'that hill' in their language. The mine passed through phases of manual, semi mechanized and highly mechanized mining. It is one of the earliest mines in India to convince and execute comprehensive ecology promotion programme. The drive included a unique and first slime dam in the country, large scale afforestation in lease hold and surrounding areas and dust suppressing facilities for arresting air pollution. The major produce of this mine is iron ore including blue dust.

2.2. Geology and Geography

Noamundi is located at 22.15°N 85.53°E. It has an average elevation of 487 metres. Noamundi is located in the heart of Saranda forest, which is the densest deciduous forest of Asia. 'Saranda' in the local tribal language means 'The land of 700 hills'. The administrative boundary of the Saranda reserve forest, however, lies a few kilometres away. Along with dense forest cover, Noamundi is highly resourceful region. The formation containing iron ore deposits belongs to the late Archean iron ore series. These deposits have been formed under marine conditions. The origin of iron seems to be weathering of continental rocks under reducing atmospheric conditions which were prevalent during the early Archean age. It consists of an undulating surface with steep to a gentle slope and reddish yellow to the chocolate colour soil.

2.3. Meteorology

The climate of the area is dry tropical. There are four seasons during the year, i.e., (i) Summer season (March to May), (ii) Rainy season (June to September), (iii) Autumn season (October to November), and (iv) Winter season (December to February). During summer months temperature goes up to 47^0 C and in winter it falls to as low as 10^0 C. Annual mean maximum and minimum temperatures are 33.2^0 C and 20.5^0 C respectively. The wind speed (km/h) and direction were monitored during the winter season in order to find the maximum impact of air qualities and its averages values was calculated for three significant ranges in all direction. It was observed during the study that the prevailing wind direction at that time was northwest.

2.4. Study Sites

Total four monitoring sites were selected for the present study. The first sampling site was at the side of the Primary crusher (N – 1) situated at 600 meter RL. The main source of pollution at primary crusher was basically vehicular pollution and pollution caused by the dumping of ore throughout the day and night. The second sampling site was near rakes in Bottom Bin (N – 2). The main source of pollution was basically vehicular pollution, pollution due to movement of locomotors, due to loading and dumping of processed ore throughout the day and night. The third sampling site was at the gate of GM's office (N – 3). The main source of pollution at GM's office is basically two wheelers and four wheelers vehicles throughout the day, one of the main places of the Noamundi. The fourth sampling site was Near Hospital (N – 4) where pollution level is almost very low,

posse's forest and vegetation covers. The main source of pollution at hospital premises is two wheelers, three wheelers and four wheelers vehicles throughout the day.

2.5. Monitoring and Analysis

The samples of SO_2, NO_2, PM_{10} and $PM_{2.5}$ were collected at all the four sites namely Primary crusher, Bottom Bin, GM's office and Near Hospital. The monitoring was conducted for 24 hrs at four different sites for 2 days per week for four weeks. The concentration of NO_2 was measured with the standard method of Modified Jacobs- Hochheiser method (1958), SO_2 was measured by Modified West and Geake method (1956). SO_2 and NO_2 samples were collected by aspirating air through measured volume (25 ml) of 0.04 M potassium tetra chloro mercurate (K_2HgCl_4:TCM) and a mixture of sodium hydroxide and sodium arsenite (NaOH + Na_2AsO_2), respectively at a flow rate of 2 l/min for 24 hr. The collected samples were transferred to pre-washed polypropylene bottles, and preserved in the refrigerator and analysed colorimetrically at 548 nm for SO_2 and 540 nm for NO_2. The apparatus was kept at a height of 2 m from the surface of the ground.

PM_{10} and $PM_{2.5}$ samples were collected on Whatman GF/A and Teflon (Millipore) filter papers by Respirable Dust Sampler (APM 460DX, Envirotech, New Delhi) and Wins-Anderson impactor (APM 550, Envirotech, New Delhi) with the sharper cut point of 10 µm and 2.5 µm, respectively. The Respirable Dust Sampler and Wins-Anderson impactor were operated at flow rates of 1.0 m^3/min and 16.671 m^3/min (or 1 m^3/hr), respectively.

All the filter papers were pre-weighed on a Metler analytical weighing balance before the sampling and desiccated for 24 hr. To avoid the contamination, the conditioned and weighed filter papers were placed in filter holder cassette ($PM_{2.5}$) and zip lock polybag (PM_{10}) and were taken to the field for sampling. Before loading the filter papers on the samplers, initial volume and timer readings were noted for $PM_{2.5}$ and the manometer reading for PM_{10} sampler. Then the filter papers were loaded on respective samplers and screwed properly before starting the samplers. After sampling, the loaded filter of $PM_{2.5}$ was removed with forceps and placed in a cassette and wrapped with aluminium foil. Similarly, the PM_{10} filter paper was wrapped in aluminum foil and placed back in zip lock polybag and both the filter papers were brought back to the laboratory. In the laboratory, filter papers were conditioned and weighed again to determine the mass concentration of the PM_{10} and $PM_{2.5}$. The weighed filter papers were preserved in the freezer until further chemical analysis.

2.6. Air Quality Index (AQI)

Air Quality Index (AQI) is a tool, introduced by Environmental Protection agency (EPA) in USA to measure the levels of pollution due to major air pollutants. An AQI is defined as an overall scheme that transforms weighted values of individual air pollution related parameters into a single number or set of numbers [9]. In the present study the AQI was calculated using IND-AQI specified by Central Pollution Control Board, New Delhi (CPCB). The index has been developed based on the dose-response relationship of various pollutants. AQI concept transforms weighted values of individual air pollutants into a single number or set of numbers which may be

widely used for air quality communication and decision making. This IND-AQI has 6 categories and presented in table 1.

The AQI method involves formation of sub-indices for each pollutant and aggregation of sub-indices. It has been developed on the dose-response relationship of various pollutants [10]. The table 1 shows the Linear segmented relationship for sub-index values and the corresponding pollutant concentrations that are calibrated to Indian conditions.

The mathematical equation for calculating sub-indices is as follows:

$$I_P = \left(\frac{I_{HI} - I_{LO}}{B_{PHI} - B_{PLO}} X \left(C_P - B_{PLO} \right) \right) + I_{LO}$$

Where: I_P is AQI for pollutant "P" (Rounded to the nearest integer),

C_P the actual ambient concentration of pollutant "P",

B_{PHI} the upper end breakpoint concentration that is greater than or equal to C_P,

B_{PLO} the lower end breakpoint concentration that is less than or equal to C_P,

I_{LO} the sub index or AQI value corresponding to B_{PLO},

I_{HI} the sub index or AQI value corresponding to B_{PHI}

TABLE 1. Various Categories of IND-AQI and Break Points of Various Pollutants (National Air Quality Index, CPCB, October 2014), (Units: µg/m^3)

AQI Category	Range	PM_{10} (24hr)	$PM_{2.5}$ (24hr)	SO_2 (24hr)	NO_2 (24hr)
Good	0-50	0-50	0-30	0-40	0-40
Satisfactory	51-100	51-100	31-60	41-80	41-80
Moderately Polluted	101-200	101-250	61-90	81-380	81-180
Poor	201-300	251-350	91-120	381-800	181-280
Very Poor	301-400	351-430	121-250	801-1600	281-400
Severe	401-500	>430	>250	>1600	>400

III. RESULTS AND DISCUSSION

To evaluate the air quality condition of the study area, the CPCB guidelines for sampling and measurement of ambient air quality parameters were followed. For $PM_{2.5}$, PM_{10}, SO_2 and NO_2, NAAQS, 2009 [11] were followed. The NAAQS for $PM_{2.5}$, PM_{10}, SO_2 and NO_2, in the Noamundi iron ore mine is depicted in Table 2.

TABLE 2. Concentration levels of $PM_{2.5}$, PM_{10}, SO_2 and NO_2 in the Noamundi iron ore mine and NAAQS

Location	Primary Crusher (N-1)	Bottom Bin (N-2)	G.M's Office (N-3)	Near Hospital (N-4)	NAAQS

$PM_{2.5}$	29.38	28.38	15.25	9.9	60
PM_{10}	49.5	49	35.38	25	100
SO_2	9.61	9.53	8.6	8.28	80
NO_2	9.84	9.74	8.66	8.45	80

3.1. Site-specific variations

The monitoring results illustrate that particulate materials were the major pollutants to be concerned in mining areas. The ambient air concentration of PM_{10} concentrations at the monitoring station was well below the maximum allowed limit of National Ambient Air Quality Standards (NAAQS) for different areas. It ranged from 37.00 to 59.00 µg/m^3, 39.00 to 57.00 µg/m^3, 28.00 to 42.00 µg/m^3 and 19.00 to 31.00 µg/m^3 at site N-1, N-2, N-3 and N-4 respectively (Figure 1). Further, it was observed that average concentrations of $PM_{2.5}$ ranged from 18.00 to 39.00 µg/m^3, 19.00 to 36.00 µg/m^3, 9.00 to 21.00 µg/m^3 and 9.00 to 11.00 µg/m^3 at site N-1, N-2, N-3 and N-4 correspondingly (Figure 2). Highest value of PM_{10} and $PM_{2.5}$ was attained at the Primary crusher (N – 1), while lowest value was attained at Near Hospital (N – 4).

The high concentration of PM_{10} at Primary crusher (N – 1) and Bottom Bin (N – 2) was mainly due to different mining activities as well as running of vehicles on the unpaved road including abrasion of road materials, tires and brake linings as well as re-suspension of soil material because of traffic induced turbulence [12] [13]. The sources of $PM_{2.5}$ have generally been confined to movement of vehicle on paved/unpaved roads, vehicular exhaust (diesel based), mining activities particularly drilling, blasting and crushing of rocks. The release inventory indicates that heavy duty diesel trucks were accountable for majority of the exhaust particulate matter [14].

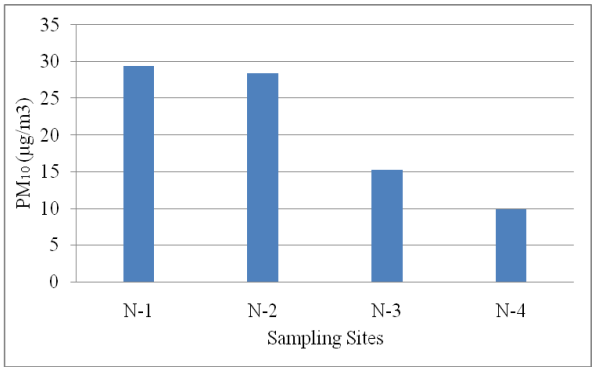

Fig. 1. Variation in the concentration PM_{10} at sampling sites

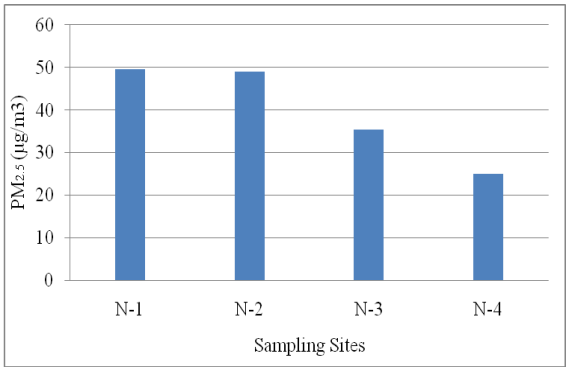

Fig. 2. Variation in the concentration $PM_{2.5}$ at sampling sites

According to the present study, NO_2 and SO_2 concentrations at the monitoring station were well below the maximum allowed limit of National Ambient Air Quality Standards (NAAQS) for different areas. The concentration of NO_2 ranged from 9.30 to 10.30 µg/m^3, 9.30 to 10.20 µg/m^3, 8.30 to 9.00 µg/m^3 and 8.10 to 8.70 µg/m^3 at site N-1, N-2, N-3 and N-4 respectively (Figure 3). The concentration of SO_2 ranged between 9.10 to10

µg/m^3, 9.10 to 9.90 µg/m^3, 8.20 to 9.10 µg/m^3 and 7.90 to 8.60 µg/m^{3}at site N-1, N-2, N-3 and N-4 respectively (Figure 4).

The main sources of NO_2 in mining rejoin are vehicular exhaust, blasting operations, etc. During combustion process (at high temperature) atmospheric nitrogen combines with oxygen to form NO_2 which is aggravated when engine is diesel operated. According to tunnel studies while comparing to gasoline vehicles diesel engine produce five times the amount of NO_X per mass of fuel burned [15].

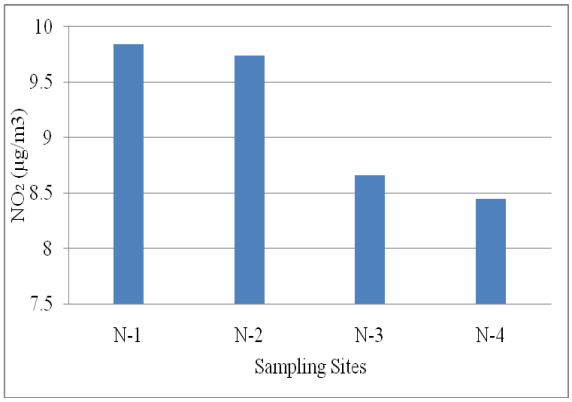

Fig. 3. Variation in the concentration NO_2 at sampling sites

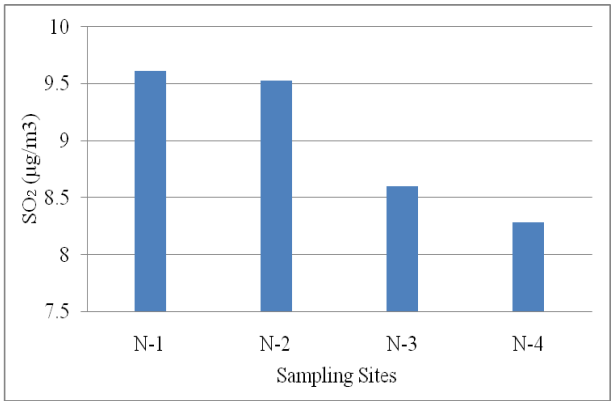

Fig. 4. Variation in the concentration SO_2 at sampling sites

3.2. Results of AQI

Data obtained from monitoring of ambient air at four different sites is used to calculate the sub- indices for critical parameters. The calculated AQI values for 24 hourly averages SO_2 and NO_2 concentrations are categorized as good during the study period at all the four sites. The AQI values calculated for $PM_{2.5}$ showed G.M's Office (N-3) and Near Hospital (N-4) under good category but Primary Crusher (N-1) and Bottom Bin (N-2) under satisfactory category in case of PM_{10} the calculated AQI values varied 25 to 50 µg/m^3 at four different sites which lies under good category. The overall air quality was evaluated using AQIs. The AQIs were estimated for criteria pollutants SO_2, NO_2, PM_{10} and $PM_{2.5}$ using IND-AQI procedure. The overall AQI was found to fall under the good category.

TABLE 3. AQI and Sub- indices at different sampling sites

Location	Primary Crusher (N-1)	Bottom Bin (N-2)	G.M's Office (N-3)	Near Hospital (N-4)
$PM_{2.5}$	49	47	25	17
PM_{10}	50	49	35	25
SO_2	12	12	11	10
NO_2	12	12	11	11
AQI	50	49	35	25

3.3. Air pollution control equipments and prevention techniques

As mechanized open cast iron ore mines are becoming larger, deeper and more capital intensive, resulting in environmental pollution. Continuing efforts has been made to improve ambient air quality condition upon the open cast mining activities. A management strategy was formulated for effective control of air pollution at source and other mitigative measures including green belt design have also been devised for sensitive areas [16]. Some pollution prevention measures and techniques were employed like mobile water sprinkler, fixed water sprinkler, dry fog system at primary crusher, dust extractor at primary crusher, wet drilling, addition of dust suppresscent in sprinkling water, wet processing of iron ore and transportation by conveyors.

IV. CONCLUSION

Open-cast mining is more deteriorating to air quality than underground mining. To assess the environmental impact of different mining activities, SO_2, NO_2, PM_{10} and $PM_{2.5}$ were measured at all the four sites namely Primary crusher, Bottom Bin, GM's office and Near Hospital. The analysis result illustrates particulate materials as the major pollutants to be concerned in mining areas. The ambient air concentration of PM_{10} concentrations at the monitoring station was well below the maximum allowed limit of National Ambient Air Quality Standards (NAAQS) for different areas. Highest value of PM_{10} and $PM_{2.5}$ was observed at the Primary crusher (N – 1), while lowest value was found at Near Hospital (N – 4). According to the present study, NO_2 and SO_2 concentrations at the monitoring station were well below the maximum allowed limit of National Ambient Air Quality Standards (NAAQS) for different areas. The calculated AQI values for SO_2 and NO_2 concentrations are categorized as good during the study period at all the four sites. The AQI values calculated for $PM_{2.5}$ showed under good category for two points but under satisfactory category for the other 2 points. In case of PM_{10}, the calculated AQI value lies under good category. The overall AQI was found to fall under the category of good. Many measures and management strategies were formulated for effective control of air pollution at source.

REFERENCES

[1] A. Masitah, H. Zaini and K. L. See, PM_{10} and Total suspended particulates (TSP) measurements in various power stations, *The Malayasian Journal of Analytical Sciences, 11(1),* 2007, 255-261.

[2] P. V. Mukunda Rao, V. Hima Bindu, G. Sagareshwar, J. Indracanti and Y. Anjaneyulu, Assessment of ambient air quality in the rapidly industrially growing Hyderabad urban environment, 2003.

[3] TERI, Area wide environmental quality management (AEQM) plan for the mining belt of Goa, Directorate of Planning statistics and Evaluation - Government of Goa, Goa, 1997.

[4] G. Singh and P. K. Sharma, Ambient air quality status in certain coal mining areas of Raniganj coalfield, *Energy Environment Monitor., 7(2),* 1991, 56-65.

[5] P. K. Sharma and G. Singh, Distribution of suspended particulate matter with trace element composition and apportionment of possible sources in the Raniganj Coalfields, India, *Env. Monit. Asses., 22,* 1992, 237-244.

[6] G. Singh, An index to measure depreciation in air quality in some coal mining areas of Korba industrial belt of Chhattisgarh, India, *Env. Monit. Asses., 122,* 2006, 309-317.

[7] D. Shooter and P. Brimblecombe, Air quality indexing, *International Journal of Environment Pollution, 36,* 2009, 305-323.

[8] F. Bruno and D. Cocchi, Recovering information from synthetic air quality indices, *Environmental Geology, 18,* 2007, 345–359.

[9] M. Sharma, Interpretation of air quality data using an air quality index for the city of Kanpur, India, *Journal of Environmental Engineering and Science, 2,* 2003, 453–462.

[10] M. Prakash and J. K. Bassin, Analysis Of Ambient Air Quality Using Air Quality Index – A Case Study, *International Journal of Advanced Engineering Technology, 1,* 2010, 106-114.

[11] NAAQS, National Ambient Air Quality Standard, India, prescribed by Central Pollution Control Board on 18 November, 2009.

[12] I. Barmapadimos, M. Nufer , D. C. Oderbolz, J. Keller, S. Aksoyoglu, C. Hueglin, U. Baltensperger and A. S. H. Prevot, The weekly cycle of ambient concentration and traffic emission of coarse (PM_{10} to $PM_{2.5}$) atmospheric particles. *Atmospheric Environment, 45,* 2011, 4580-4590.

[13] N. Bukowiecki, P. Lienemann, M. Hill, M. Furger, A. Richard, F. Amato, A. S. H. Prevot, U. Baltenspurger, B. Buchmann, and R. Gehrig, PM_{10} emission factors for non-exhaust particles generated by road traffic in an urban street canyon and along a freeway in Switzerland. *Atmospheric Environment, 44,* 2010, 2330-2340.

[14] R. F. Sawyer, R. A. Harley, S. H. Cadle, J. M. Norbeck, R. Slott and H. A. Bravo, Mobile sources critical review: 1998 NARSTO assessment. *Atmospheric Environment, 34,* 2010, 2161-2181.

[15] W. T. Kirchstetter, H. A. Miguel and A. R. Harley, On road comparison of exhaust emission from gasoline and diesel engines. In: Proceedings of the Eighth CRC On-road Vehicle Emission Workshop, 1998, April 20-22,San Diego, CA.

[16] R. Trivedi, M. K. Chakrabotry and B. K. Tewary, Dust dispersion modeling using fugitive dust model at an opencast coal project of Western Coalfields Limited, India, *Journal of scientific and Industrial research, 68,* 2009, 71-78.

Accepted Manuscript

Biofunctionalized tungsten trioxide-reduced graphene oxide nanocomposites for sensitive electrochemical immunosensing of cardiac biomarker

Deepika Sandil, Saurabh Srivastava, B.D. Malhotra, S.C. Sharma, Nitin K. Puri

PII: S0925-8388(18)31627-X

DOI: 10.1016/j.jallcom.2018.04.293

Reference: JALCOM 45931

To appear in: *Journal of Alloys and Compounds*

Received Date: 12 February 2018

Revised Date: 14 April 2018

Accepted Date: 26 April 2018

Please cite this article as: D. Sandil, S. Srivastava, B.D. Malhotra, S.C. Sharma, N.K. Puri, Biofunctionalized tungsten trioxide-reduced graphene oxide nanocomposites for sensitive electrochemical immunosensing of cardiac biomarker, *Journal of Alloys and Compounds* (2018), doi: 10.1016/j.jallcom.2018.04.293.

This is a PDF file of an unedited manuscript that has been accepted for publication. As a service to our customers we are providing this early version of the manuscript. The manuscript will undergo copyediting, typesetting, and review of the resulting proof before it is published in its final form. Please note that during the production process errors may be discovered which could affect the content, and all legal disclaimers that apply to the journal pertain.

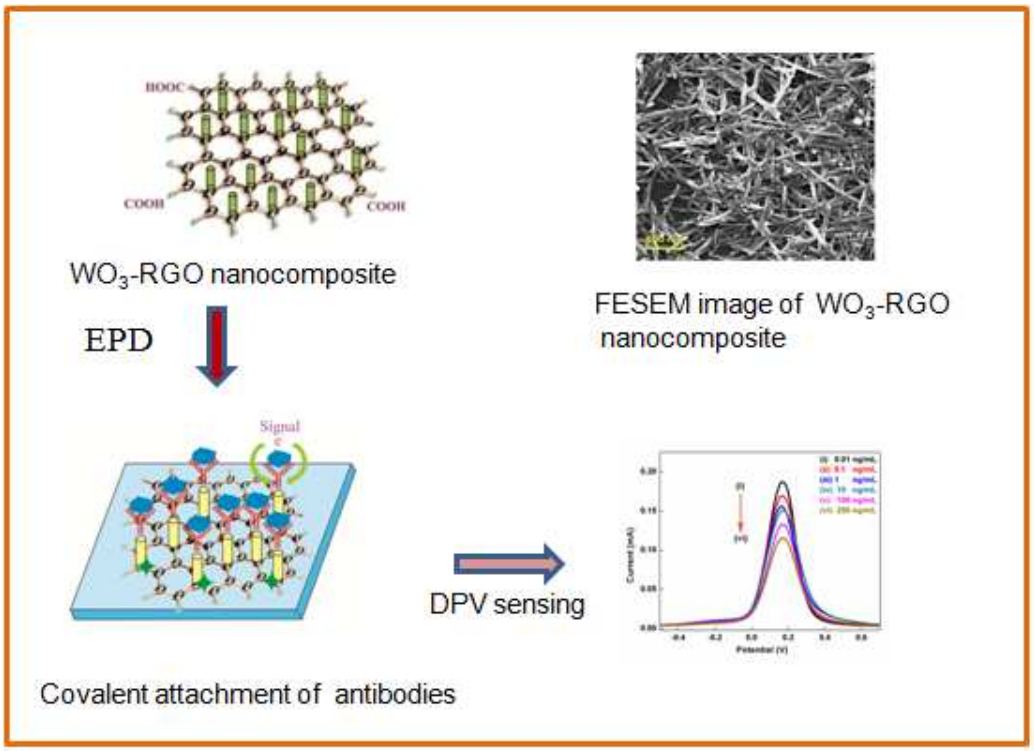

The proposed WO_3-RGO nanocomposite based immunosensor exhibited a high sensitivity and much broader detection range for cTnI cardiac biomarker

ACCEPTED MANUSCRIPT

ACCEPTED MANUSCRIPT

Biofunctionalized tungsten trioxide-reduced graphene oxide nanocomposites for sensitive electrochemical immunosensing of cardiac biomarker

Deepika Sandil[a,b], Saurabh Srivastava[a], B.D. Malhotra[c], S.C. Sharma[a], Nitin K. Puri[a,*]

[a]*Advanced Sensor Laboratory, Department of Applied Physics, Delhi Technological University, Delhi 110042, India*
[b]*Department of Applied Physics, Bhagwan Parshuram Institute of Technology, Delhi 110089, India*
[c] *Department of Biotechnology, Delhi Technological University, Main Bawana Road, Delhi 110042, India*

Abstract:

We demonstrate the fabrication of a facile and efficient biosensing platform for electrochemical detection of human cardiac biomarker Troponin I (cTnI) using Tungsten trioxide-reduced graphene oxide (WO_3-RGO) nanocomposite as a matrix. The *in-situ* hydrothermal method was employed for the synthesis of the WO_3-RGO nanocomposite. Raman spectroscopy, X-ray diffraction (XRD), high- resolution transmission electron microscopy (HRTEM) and field emission scanning electron microscopy (FE-SEM) were employed to investigate structural and morphological behavior. The WO_3-RGO nanocomposite was further functionalized with 3-aminopropyl tri-ethoxy saline (APTES) for the activation of amino groups ($–NH_2$) that can covalently bind to the antibodies of cTnI. This immunosensor was further studied using contact angle measurement, Fourier transform infrared spectroscopy (FT-IR) and electrochemical techniques. The synergistic behavior between RGO and WO_3 nanorods has allowed the immunosensor to exhibit enhanced heterogeneous electron transfer rate constant (K_o=2.4 $\times 10^{-4}$ cms^{-1}) resulting in improved biosensor efficiency. The immuno-sensor exhibit good sensitivity as 58.24 $\mu A/cm^2$ per decade in an extended linear detection range 0.01- 250 ng/mL with the stability up to 30 days. Besides this, the fabricated immuno-sensor exhibits good reproducibility and excellent selectivity towards the detection of the cTnI biomarker. Furthermore, the validation of immunosensor with cardiac patient samples demonstrates the clinical application of this nano-biosensing platform for the detection of other biomarkers too.

Keywords: Reduced graphene oxide, Tungsten trioxide, Cardiac biomarker Troponin I, electrochemical biosensor

**Corresponding author:*
E-mail addresses: nitinkumarpuri@dtu.ac.in, nitin.phy@dce.edu, nitinpuri2002@yahoo.co.in (Nitin K. Puri),

1. Introduction

Cardiovascular disease (CVD), a heart and blood vessel disease has become the primary cause of morbidity and mortality across the world. Among different CVDs, Myocardial Infarction (MI), an acute coronary syndrome (ACS) cause adverse cardiac injury in the myocardium such as irreversible damage to tissues. Electrocardiogram (ECG) currently preferred for the measurement and diagnosis of cardiac injuries. However, ECG has some limitations and sensitivity issues which suggests for an alternative approach for the diagnosis purpose[1]. Hence, a sensitive and rapid diagnosis is crucial for the early prognosis of Myocardial Infarction (MI). In clinical research, cardiac biomarkers play an important role in understanding and identification of myocardial infarction concerning other cardiac diseases, which might help in the diagnosis of CVD. Currently, creatine Kinas-MB, myoglobin and cardiac troponin (cTnT and cTnI) considered as remarkable MI diagnostic biomarkers. Among these, cardiac troponin I (cTnI) had highest cardio-specificity and considered as a principal diagnostic biomarker for MI [2]. Cardiac troponin I is a protein found in cardiac muscles and is made up of 209 amino acid residues with a molecular weight as 22.5kDa [3]. After myocardial infarction, the systemic blood concentration of this protein rises and remains elevated for 8-10 days, hence serving longer window of detection for MI. The level of cTnI in normal blood serum is below 0.6 ng/ml which could potentially rise to 1-4 ng/ml at the onset of AMI. It can increase up to 100 ng/ml or more within 3-6 hours and remains elevated for 5-9 days. For the detection of cTnI many conventional methods such as fluoro-immunoassay, enzyme-linked immunosorbent assay (ELISA), radioimmunoassay and spectrophotometric methods have been used. However, these assays are time-consuming, expensive, laborious and demands small volume of blood for testing [4-5]. Thus for the safe and rapid diagnosis of the AMI, biosensors can be used as a faster and cheaper means for its detection. Among different biosensors, electrochemical biosensors based on immuno-chemical reactions such as specific antibody-antigen interaction considered as the most sensitive detection tool due to its precise measurement, fast driven analysis and simple preparation[6-7] . Also, they allow automation, miniaturization, development of disposable devices and require very small sample volumes[8-11]. While fabricating an electrochemical immunosensor, biomolecular immobilization is a crucial step to achieve efficient performance. For the successful antibody immobilization, an ideal immunosensor should permit high loading and retain its biological activity for the long term. Nanomaterials in this context can be preferred

as a substantial matrix for the immobilization of antibodies [12]. A lot of nanomaterials such as gold, metals, carbon and metal oxides with variable morphology have been utilized to fabricate the biosensing platform owing to their distinctive physiochemical features, good biocompatibility, and large electro-active surface[13]. Among different nanomaterials, nanostructured metal oxides exhibit good catalytic properties, high electron –transfer kinetics and firmed adsorption capability that can provide appropriate microenvironments for the immobilization of biomolecule. Tungsten trioxide nanostructures (n-WO_3) have been considered as a promising material as an immobilized matrix because of its enhanced catalytic activity, chemical stability, simple synthesis and strong adherence to the substrate[14].

The incorporation of semiconducting materials such as carbon nanotubes and graphene with the nanostructured metal oxides provide improved biosensing characteristics [15]. In this context, graphene or chemically reduced graphene oxide (RGO) considered as promising supportive matrix [16]. RGO, an array of carbon atoms are covalently connected via sp^2 bonds to form a two-dimensional honeycomb sheet that contributes toward its exceptional properties such as good electrical conductivity, large surface area, and high electrochemical activity[17].

Herein, we report the synthesis of a WO_3-RGO nanocomposite with simultaneous reduction of GO. And for the first time, the synthesized nanocomposite has been utilized as an immobilized matrix for the fabrication of a facile and label-free electrochemical immuno-sensor for the detection of a cardiac biomarker cTnI. Further, EDC-NHS chemistry was employed for the activation of carboxyl groups of an antibody of cardiac troponin I. The proposed mechanism delivers improved sensitivity, wide detection range, and good stability.

2. Experimental section

2.1 Synthesis of WO_3-RGO nanocomposite and functionalization of electrodes

WO_3-RGO nanocomposite was synthesized by employing the In-situ hydrothermal method. In brief, a defined amount of as-synthesized graphene oxide (GO) [See Supplementary information sheet] was dispersed in 20 mL of DI water and kept for half an hour ultrasonication. Then, 0.1 M of $NaWO_4.2H_2O$ and 0.225g of NaCl were added to the resultant dispersed solution and kept on stirring for one hour. The pH value of the resultant suspension was adjusted to 2 using HCl

solution. After this, the suspension was transferred to 50 mL Teflon –lined stainless steel autoclave and placed in a hot air oven at temperature 180 °C for 24 hours. Latterly, the autoclave was cooled naturally to the room temperature, and the sample was collected through multiple washing with deionized water and ethanol followed by drying at 70 °C.

The as-synthesized WO_3-RGO nanocomposite was further functionalized with APTES for providing active amino groups (-NH_2) that can covalently bind to the antibodies. Electrophoretic deposition technique (EPD) was used for deposition of APTES functionalized WO_3-RGO nanocomposite thin films on the pre-hydrolyzed ITO electrode at optimized potential 45V for 90 seconds. The fabricated APTES/WO_3-RGO nanocomposite/ITO electrodes were washed with DI water and dried at room temperature.

2.2 Fabrication of the immuno-electrode

Subsequently, the cTnI antibodies were covalently attached to the APTES/WO_3-RGO nanocomposite/ITO electrode using EDC-NHS chemistry. A fresh stock solution (50 μg/mL) of anti-cTnI was prepared in phosphate buffer solution (PBS, pH= 7.4). Prior to immobilization, the carboxyl groups present in antibodies were activated by using EDC-NHS chemistry. EDC (0.2 M) worked as a coupling agent and NHS (0.05 M) as an activator. 15 μL of anti-cTnI was mixed with 7.5 μL of 0.2 M EDC and 7.5 μL of 0.05 M NHS. Subsequently, this solution (30 μL) was uniformly spread onto APTES/WO_3-RGO nanocomposite/ITO electrode by drop-casting. The electrode was kept in a humid chamber at room temperature followed by washing with PBS to remove any unbound antibody molecules. Lastly, ethanolamine (EA) solution (0.1 mg/mL) was used for blocking the non-specific active sites present on the electrode. The fabricated EA/anti-cTnI/APTES/WO_3-RGO nanocomposite/ITO immunoelectrode was washed with PBS solution and stored at 4°C when not in use.

2.3 Electrochemical measurement procedure:

The electrochemical measurements such as electrochemical impedance spectroscopy (EIS) and differential pulse voltammetry (DPV) were performed using an electrochemical Autolab Potentiostat (Netherlands) employing a three-electrode system that consists of the fabricated immuno-electrode as the working electrode, platinum (Pt) as the counter electrode and Ag/AgCl as the reference electrode. The phosphate buffer saline (PBS, 50mM, pH 7.4) containing 5mM

$[Fe(CN)_6]^{3-/4-}$ as redox couple was used for all the electrochemical measurements. The impedance spectrum was measured in the frequency range of 10^5 to 10^{-1} Hz at a biasing potential of 10 mV. The Nyquist plot was studied in which X-axis and Y-axis represent the real part, and the imaginary part of the impedance and the curve consists of the semi-circle and the straight line. The straight line at low frequency signifies the diffusion process whereas the semicircle at high frequency signifies the charge transfer resistance (R_{CT}). For the differential pulse voltammetry measurements, the response was measured at the scan rate of 50 mV/sec in the potential range of -0.8 to 0.8 V.

A step-wise fabrication process of EA/anti-cTnI/APTES/WO_3-RGO nanocomposite/ITO immunoelectrode is shown in Scheme 1.

3. Results and Discussion

3.1 Crystallographic and Morphological studies

The crystallinity and phase purity analysis of RGO and RGO-WO_3 nanocomposite was examined by powder X-ray diffractometer (XRD) in the range of 5°- 80°. The XRD spectrum of graphene oxide (GO) shown in Fig. 1a exhibits a characteristic peak at 11.7° corresponding to (002) plane (d_{002} = 7.5 A°), which shifts to 23.4° in the XRD spectrum of RGO (d_{002} =3.79 A°) (Fig. 1b). The reduction in the interplanar spacing of RGO as compared to GO is due to the removal of the oxide groups that allow graphene sheets to be tightly packed. The XRD pattern of synthesized RGO-WO_3 nanocomposite (Fig. 1c) shows strong diffraction peaks at 2θ = 14.3°and 28.1° corresponding to (100) and (200) planes respectively. The other peaks are seen at 34.2°, 37°, 44.8°, 49.6°, 52.2° and 59.01° are indexed to (111), (210), (002), (220), (310) and (400) crystal lattice planes, respectively. All these planes are well matched with a hexagonal WO_3 crystal structure (JCPDF 75-2187) without the presence of any undesired phases. The intense high peaks of the nanocomposite indicate good crystallinity of the structure. Additionally, no peak emerges at around $2\theta = 23.4^0$ in the XRD spectrum of the nanocomposite, suggesting that the RGO sheets are homogeneously dispersed in the nanocomposite. The average crystallite size of WO_3 nanorods in nanocomposite was found to be 32 nm using Debye-Scherrer's equation

The morphological and structural analysis of the synthesized WO_3 NRs and RGO-WO_3 nanocomposite have been studied using field-emission scanning electron microscopy (FE-SEM) and Transmission electron microscopy (TEM), respectively, shown in Fig. 2. From Fig. 2.a, it

can be seen that the proposed hydrothermal synthesis route has obtained a uniform 1-D nanostructure of WO_3 NRs with a smooth surface and exist in the form of bundles with an average diameter as 54 nm. The average size of the nanorods as estimated by FESEM is in close agreement with the TEM image of the WO_3 NRs (Inset, Fig. 2a). However, in the *in-situ* grown RGO-WO_3 nanocomposite, the RGO affects the width and uniformity of the 1-D structure as can be observed by comparing Fig. 2a and 2b. Instead of bundles, monodispersed WO_3 NRs was observed in this case. Also, the WO_3 NRs are visible on the surface of the graphene sheets while some of these are found to be trapped between the RGO sheets.

3.2 Spectroscopic studies

The grafting of the WO_3-RGO nanocomposite surface through the APTES and antibody immobilization was investigated by studying FT-IR spectrum of the WO_3–RGO nanocomposite, APTES/ WO_3-RGO nanocomposite, and anti-cTnI/APTES/ WO_3-RGO nanocomposite [Fig. 3(a)]. The FT-IR spectrum of WO_3-RGO nanocomposite (curve (i)) exhibits the two distinctive peaks at 1205 cm^{-1} and at 1724 cm^{-1} which can ascribe to C–OH stretching vibrations of a hydroxyl group and C=O stretching vibration of carboxylic /carbonyl groups respectively present in RGO. The peaks observed at 962 cm^{-1} and 1610 cm^{-1} represents the C–H stretching vibrations and aromatic C=C stretching vibrations, whereas the characteristic peaks of WO_3 seen at 1410 cm^{-1} and 766 cm^{-1} correspond to W–O and W–O–W stretching vibration of the bridging O_2 [18]. The peaks at 3440 cm^{-1} and 1623 cm^{-1} in curve (ii) can be ascribed to asymmetric (N–H) stretching and bending of the NH_2 present in the APTES revealing that APTES has been successfully grafted on the WO_3-RGO nanocomposite surface [19]. The 1408 cm^{-1} peak corresponds to bending vibrations (Si–CH_2) present in APTES. The intensities of IR peaks are found to be suppressed after immobilization of antibody onto the APTES/WO_3-RGO nanocomposite/ITO (curve (iii)). The appearance of the additional band at 3462 cm^{-1}, 1636 cm^{-1} and 705 cm^{-1} indicate the presence of N–H stretching of the amide A, amide I and amide IV, respectively, confirming the successful binding of antibody onto APTES/WO_3-RGO nanocomposite/ITO electrode [20].

The Raman spectroscopy has also investigated the interaction between WO3 NRs and RGO sheets. Fig.3 (b) represents the Raman spectra of RGO, WO_3 NRs and WO_3-RGO nanocomposite obtained in the range of 200 cm^{-1} to 3000 cm^{-1}. The Raman spectra of RGO

(curve (i)) indicates well-defined peaks at 1349 cm^{-1} and at 1598 cm^{-1} respectively that can be attributed to the presence of characteristic D-band and G-band in RGO. The intense peaks centered at 813 cm^{-1}, 760 cm^{-1} and 933 cm^{-1} (curve (ii)) indicate stretching vibrations of W– O, W–O–W, and W=O respectively. Whereas, peaks observed at 242 cm^{-1} and 329 cm^{-1} can be assigned to the bending vibration of O–W–O [21]. It is noteworthy that the peaks observed in WO_3 NRs are shifted and broaden in case of WO_3-RGO nanocomposite composites (curve (iii)) along with the presence of D and G band. The observed change can be attributed to the formation of C–O–W bonds during the hydrothermal treatment, which further confirms the decoration of WO_3 NRs on the RGO sheets surface.

3.3 Contact angle measurement studies

The investigation of the hydrophilic and hydrophobic character of the WO_3-RGO nanocomposite/ITO electrode has been done using contact angle measurement. The static sessile drop method has been employed to determine the contact angle of the electrode at different stages of surface modification. For the study of drop image, an image analysis system is used to calculate the contact angle (θ) value from the shape of the drop. The initial contact angle value of the hydrolyzed ITO glass electrode (66.54°) [Fig. 4(a)] is found to decrease to 31.50° [Fig. 4(b)] on the deposition of WO_3-RGO nanocomposite film due to the presence of oxygenated hydrophilic groups like -OH and -COOH in the WO_3-RGO nanocomposite matrix. However, after functionalization with APTES, the contact angle is found to increase to ~ 37° [Fig. 4(c)]. This increase of contact angle value indicates the presence of hydrophobic alkyl chains in APTES molecules which imparts a more hydrophobic character to the surface of the matrix. Finally, after covalent immobilization of antibody molecules on the functionalized surface, the contact angle value decreased to 6.03° [Fig. 4(d)] showing the hydrophilicity nature of the antibody molecules. Thus, the successful immobilization of antibody over the functionalized matrix APTES/WO_3-RGO nanocomposite was accomplished.

3.4 Electrochemical characterization

The electrochemical properties of WO_3NRs and in-situ grown WO_3-RGO nanocomposite have been investigated by electrochemical impedance spectroscopy (EIS) studies conducted in the frequency range of 10^5 to 10^{-1} Hz at a biasing potential of 10 mV. The electrochemical

system has modeled with an equivalent circuit (Randles circuit) comprising of solution resistance (Rs), charge transfer resistance (R_{CT}), Warburg impedance (W) and double layer capacitance (C_{DL}). The diameter of the semi-circle as shown in the Nyquist plot (Fig.5a) measures the magnitude of charge transfer resistance R_{CT} that depends on the dielectric characteristics at the electrode/electrolyte interface [22]. All these studies have been done using software Nova provided with the Autolab system. The charge transfer resistance value measured for WO_3-RGO nanocomposite (R_{CT} = 887 Ω) is small as compared to that of WO_3 NRs (R_{CT} =1350 Ω). This decrease in resistance can be attributed to the excellent electrical conductivity of the RGO in the nanocomposite matrix that enhances the electron transfer kinetics at the electrode and solution interface.

The heterogeneous electron transfer rate constant (k_o) of the WO_3 NRs/ITO and WO`$_3$-RGO nanocomposite has been calculated using equation (1)

$$K_o = \frac{RT}{n^2 F^2 A R_{CT} S} \quad (1)$$

Where R represents as the gas constant, T as absolute temperature (K), F as the Faraday constant, A as the specific electrode area (cm^2), S as the bulk concentration of redox probe (mol cm^{-3}) and n as the number of transferred electrons per molecule of the redox probe. The K_o value of the WO_3-RGO nanocomposite has been estimated as 2.54×10^{-4} cm s^{-1} which is better than that of the WO_3 NRs (1.8×10^{-4} cm s^{-1}). This indicated that the WO_3-RGO nanocomposite exhibits faster charge transfer property as compared to that of WO_3 NRs and can give a superior analytical performance in electrochemical biosensing device.

Further, the electrochemical impedance spectra (EIS) obtained for different modified electrodes is shown in Fig.5(b). The maximum R_{CT} value is found for WO_3 NRs as 1.35 KΩ. However, the significant reduction in the R_{CT} value is observed in the case of the WO_3-RGO nanocomposite (887 Ω). This can be ascribed to the enhanced electrochemical conductivity of the RGO in the nanocomposite matrix. After antibody immobilization, the functionalized matrix (anti-cTnI/APTES/RGO-WO_3NRs/ITO) exhibited a higher R_{CT} (905 Ω) as compared to WO_3-RGO nanocomposite which shows the insulating nature of the antibody molecules. Lastly, after attachment of ethanolamine (EA) which covers most of the non-specific active sites of the immunoelectrode surface, the charge transfer process is again hindered, resulting in a higher R_{CT} (1.6 KΩ) of the EA/anti-cTnI/APTES/WO3-RGO nanocomposite electrode.

3.5 Electrochemical sensing studies

The variation in the response current of the immunoelectrode as a function of cTnI concentration (0.01ng/mL to 250 ng/mL) was studied using differential pulse voltammetry (DPV) technique (Fig. 6a). The response study was carried out in phosphate buffer saline (PBS, 50mM, pH 7.4) containing 5mM $[Fe(CN)_6]^{3-/4-}$ as redox coupling agent. For each measurement, 20μL of diluted antigen was added into the electrochemical cell with 10 minutes of incubation. The response graph shows that the magnitude of the peak current decreases with the increase in cTnI concentration in the detection range 0.01-250 ng/mL. This decrease in response current attribute towards the formation of electrically insulating antigen-antibody complexes produced from the specific interaction of cardiac troponin I antigen and its antibody that might have blocked the electron transfer via $[Fe(CN)_6]^{3-/4-}$ [23]. In Fig. 6(b), calibration plot was obtained between response peak current and different cTnI concentration. It was observed that the DPV peak current varies linearly with a logarithmic cTnI concentration in the linearity range of 0.01 – 250 ng/mL, obeying equation (2).

$$I = 0.1587\ (mA) - 0.01456\ (mA) * log[cTnI\ concentration\ (ng\ mL^{-1})] \qquad (2)$$

The sensitivity of 58.24 μA/cm^{2}per decade is estimated from the slope of the calibration curve with regression coefficient as 0.989. Further, this immunosensor can detect cTnI concentration as low as 0.01 ng/mL. A control experiment (inset, Fig. 6 (b)) was performed in the presence of cTnI concentrations (0.01- 250 ng/mL), to check for any non-specific adsorption of the antigen molecule to the electrode surface in the absence of antibodies. However, no remarkable change was observed in the current response revealing that cTnI antigen specifically interacts with the EA/anti-cTnI/APTES/WO3-RGO nanocomposite/ITO immunoelectrode.

The reproducibility of the EA/anti-cTnI/APTES/WO_3-RGO nanocomposite/ITO immunosensor was examined by measuring the DPV current response in the presence of cTnI (0.01 ng/mL) on four independently fabricated immunoelectrode prepared under identical conditions (Fig. 7(a). The relative standard deviation (RSD) was studied to evaluate the reproducibility of the electrodes. It was found that the immunoelectrode shows good

reproducibility for four different electrodes with low value of RSD of 4.36% with an average current of 200 μA. The low value of RSD obtained for each electrode comes within the acceptable error range under the tested conditions, suggesting a good reproducibility.

For a clinical purpose, a sensor must possess high specificity for the target biomolecule compared to other interfering protein biomarkers present in the blood serum. Hence, the specificity of the fabricated immunosensor was evaluated using different interferents such as Carcinoembryonic antigen (CEA), Cytokeratin-19 antigen (CYFRA), endotheline one protein (ET), C-reactive protein (CRP) and Myoglobin (Mb) as shown in Fig. 7(b).The magnitude of DPV current response for the EA/anti-cTnI/APTES/WO_3-RGO nanocomposite/ITO immunoelectrode (shown as blank in fig. 7(b)) has been observed as 0.209 mA. After that, the current response of the immunoelectrode has been taken in the presence of above interferents each of concentration 5ng/mL with 10 minutes incubation. Although we observed some signal variation, there was no prominent alteration in the current response in the presence of each interferent as compared to the blank electrode. However, on the addition of cTnI protein, a remarkable reduction of current was observed. This specificity of the immunoelectrode can be attributed to the fact that all other protein biomarkers could not able to bind with anti-cTnI antibody functionalized on the APTES/RGO-WO_3 nanocomposite surface.

Further, for clinical application, the developed immunosensor was utilized to measure cTnI concentration in human serum obtained from pathology laboratory (Dr. Lal path lab, Rohini, Delhi). The DPV current response is recorded for four different real samples and those for standard samples of the same concentrations. The results are shown in Fig. 7(c) reveals a low RSD value for the current responses obtained for real and standard samples. This indicates that the developed detection strategy might be preliminarily applicable for the determination of cTnI in human serum for routine clinical diagnosis.

The shelf life of the proposed immunosensor was also monitored by measuring DPV current response in the presence of 0.01 ng/mL cTnI with a regular interval of 1 week. The immunoelectrode retains its activity up to four weeks with the decrease in current as 8% when stored in refrigerated conditions at 4^0C, implying that cTnI antibody has been immobilized on APTES/WO_3-RGO nanocomposite/ITO matrix with its bioactivity well preserved. A comparative analysis of presently fabricated immunoelectrode with previously reported electrode

materials has shown in Table 1. The proposed WO_3-RGO nanocomposite based immunosensor exhibits improved linearity and sensitivity as compared to these methods.

4. Conclusions

In summary, a hydrothermally synthesized tungsten trioxide-reduced graphene oxide (WO_3-RGO) nanocomposite based electrochemical immunosensor was fabricated for the cardiac biomarker detection. A thin film of APTES/WO_3-RGO nanocomposite/ITO was obtained using electrophoretic deposition technique, followed by covalent immobilization of antibody of cTnI for the label-free electrochemical detection of cTnI using DPV technique. The heterogeneous electron transfer kinetics of WO_3-RGO nanocomposite found to be superior as compared to that of bare WO_3 resulting in the high performance of the immunosensor. The electrochemical measurements showed that the proposed immunosensor exhibit a good sensitivity of 58.24 $\mu A/cm^2$ per decade in a wide detection range of 0.01 – 250 ng/mL. This superior performance can be attributed to: (i) strong covalent coupling of antibody molecules to WO_3-RGO nanocomposite matrix through APTES which leads to the high stability of the device, (ii) large oxygen moieties present in WO_3 leading to increased antibody loading capacity resulting in wider detection range and lastly, (iii) strong synergistic effect between WO_3-RGO nanocomposite that has enhanced the electron transfer kinetics. The study of real sample analysis has also revealed an excellent correlation between the current response of standard and real samples of cardiac troponin I (cTnI). Thus all these features is responsible for high sensing performance of the proposed electrochemical immunosensor.

.Conflicts of interest

There are no conflicts to declare.

Acknowledgements

The authors thank Prof. Yogesh Singh, Vice-chancellor, Delhi Technology University, Delhi, India for providing the research facilities. The financial support received from IUAC sponsored project *(Grant No. IUAC/XIII.7/UFR-56324)*, Department of Atomic Energy -Board

of Research in Nuclear Sciences *(DAE-BRNS)*, India and Department of Science and Technology, India *(Grant No. IFA14-MS-34)* are gratefully acknowledged.

Table 1: Comparative analysis of fabricated immunosensor for the detection of cardiac biomarker troponin I along with those reported in the literature

Sensing platform	**Detection technique**	**Detection range**	**Sensitivity (S)**	**Detection limit**	**Stability**	**Reference**
Conducting paper	CV	1-100ng/ mL	$5.5\mu A/ngmL^{1}cm^{-2}$	-	-	[24]
Porous GO/GCE	EIS	0.1-10 ng/mL	-	0.07 ng/mL	-	[25]
Pt/Graphene sheet/GCE	EIS	0.01-10 ng/mL	80 Ω cm^2 per decade	4.2 pg/mL	-	[26]
Au/GO/GCE	Amperometric	0.05-3.0 ng/mL -	-	0.05 ng/mL	30 days	[27]
APTES/WO_3-RGO nanocomposite	**DPV**	**0.01-250 ng/mL**	**58.24μA/cm^2per decade**	**0.01 ng/mL**	**30 days**	**Present work**

ACCEPTED MANUSCRIPT

ACCEPTED MANUSCRIPT

References

[1] M. Fathil, M.M. Arshad, S.C. Gopinath, U. Hashim, R. Adzhri, R. Ayub, A. Ruslinda, A. Azman, M. Zaki, T.-H. Tang, Diagnostics on acute myocardial infarction: Cardiac troponin biomarkers, Biosensors and Bioelectronics, 70 (2015) 209-220.
[2] X. Han, S. Li, Z. Peng, A.M. Othman, R. Leblanc, Recent Development of Cardiac Troponin I Detection, ACS Sensors, 1 (2016) 106-114.
[3] F.S. Apple, P.O. Collinson, I.T.F.o.C.A.o.C. Biomarkers, Analytical characteristics of high-sensitivity cardiac troponin assays, Clinical chemistry, 58 (2012) 54-61.
[4] A.S. Ahammad, Y.-H. Choi, K. Koh, J.-H. Kim, J.-J. Lee, M. Lee, Electrochemical detection of cardiac biomarker troponin I at gold nanoparticle-modified ITO electrode by using open circuit potential, Int. J. Electrochem. Sci, 6 (2011) 1906-1916.
[5] Y. Lin, Q. Zhou, D. Tang, R. Niessner, D. Knopp, Signal-on photoelectrochemical immunoassay for aflatoxin B1 based on enzymatic product-etching MnO2 nanosheets for dissociation of carbon dots, Analytical chemistry, 89 (2017) 5637-5645.
[6] K. Zhang, S. Lv, Z. Lin, D. Tang, CdS: Mn quantum dot-functionalized gC 3 N 4 nanohybrids as signal-generation tags for photoelectrochemical immunoassay of prostate specific antigen coupling DNAzyme concatamer with enzymatic biocatalytic precipitation, Biosensors and Bioelectronics, 95 (2017) 34-40.
[7] Z. Qiu, J. Shu, D. Tang, Near-Infrared-to-Ultraviolet Light-Mediated Photoelectrochemical Aptasensing Platform for Cancer Biomarker Based on Core–Shell NaYF4: Yb, Tm@ TiO2 Upconversion Microrods, Analytical chemistry, 90 (2017) 1021-1028.
[8] G. Liu, Y. Lin, Nanomaterial labels in electrochemical immunosensors and immunoassays, Talanta, 74 (2007) 308-317.
[9] Q. Xiang, The Development and Application of Electrochemical Biosensor, in: International Conference on Information and Management Engineering, Springer, 2011, pp. 215-220.
[10] J. Shu, D. Tang, Current Advances in Quantum-Dots-Based Photoelectrochemical Immunoassays, Chemistry–An Asian Journal, 12 (2017) 2780-2789.
[11] J. Shu, Z. Qiu, S. Lv, K. Zhang, D. Tang, Plasmonic Enhancement Coupling with Defect-Engineered TiO2–x: A Mode for Sensitive Photoelectrochemical Biosensing, Analytical chemistry, 90 (2018) 2425-2429.
[12] P.R. Solanki, A. Kaushik, V.V. Agrawal, B.D. Malhotra, Nanostructured metal oxide-based biosensors, NPG Asia Materials, 3 (2011) 17.
[13] Z. Qiu, J. Shu, D. Tang, Bioresponsive release system for visual fluorescence detection of carcinoembryonic antigen from mesoporous silica nanocontainers mediated optical color on quantum dot-enzyme-impregnated paper, Analytical chemistry, 89 (2017) 5152-5160.
[14] L. Santos, C.M. Silveira, E. Elangovan, J.P. Neto, D. Nunes, L. Pereira, R. Martins, J. Viegas, J.J. Moura, S. Todorovic, Synthesis of WO 3 nanoparticles for biosensing applications, Sensors and Actuators B: Chemical, 223 (2016) 186-194.
[15] C. Hu, T. Lu, F. Chen, R. Zhang, A brief review of graphene–metal oxide composites synthesis and applications in photocatalysis, Journal of the Chinese Advanced Materials Society, 1 (2013) 21-39.
[16] L. Fu, T. Xia, Y. Zheng, J. Yang, A. Wang, Z. Wang, Preparation of WO 3-reduced graphene oxide nanocomposites with enhanced photocatalytic property, Ceramics International, 41 (2015) 5903-5908.
[17] Q. Zhou, Y. Lin, K. Zhang, M. Li, D. Tang, Reduced graphene oxide/BiFeO3 nanohybrids-based signal-on photoelectrochemical sensing system for prostate-specific antigen detection coupling with magnetic microfluidic device, Biosensors and Bioelectronics, 101 (2018) 146-152.

ACCEPTED MANUSCRIPT

[18] X. An, C.Y. Jimmy, Y. Wang, Y. Hu, X. Yu, G. Zhang, WO 3 nanorods/graphene nanocomposites for high-efficiency visible-light-driven photocatalysis and NO 2 gas sensing, Journal of Materials Chemistry, 22 (2012) 8525-8531.
[19] A. Radu, G. Truica, R. Penu, V. Moroeanu, S.C. Litescu, Use of the Fourier transform infrared spectroscopy in characterization of specific samples, UPB Scientific Bulletin B: Chemical and Materials Science, 74 (2012) 137-148.
[20] M.A. Ali, C. Singh, K. Mondal, S. Srivastava, A. Sharma, B.D. Malhotra, Mesoporous Few-Layer Graphene Platform for Affinity Biosensing Application, ACS applied materials & interfaces, 8 (2016) 7646-7656.
[21] C.I. Vargas-Consuelos, K. Seo, M. Camacho-López, O.A. Graeve, Correlation between particle size and Raman vibrations in WO3 Powders, The Journal of Physical Chemistry C, 118 (2014) 9531-9537.
[22] M. Cell, Electrochemical Impedance Spectroscopy (EIS): A Powerful and Cost-Effective Tool for Fuel Cell Diagnostics.
[23] S. Kumar, J.G. Sharma, S. Maji, B.D. Malhotra, Nanostructured zirconia decorated reduced graphene oxide based efficient biosensing platform for non-invasive oral cancer detection, Biosensors and Bioelectronics, 78 (2016) 497-504.
[24] K.K. Jagadeesan, S. Kumar, G. Sumana, Application of conducting paper for selective detection of troponin, Electrochemistry Communications, 20 (2012) 71-74.
[25] S.H. Kazemi, E. Ghodsi, S. Abdollahi, S. Nadri, Porous graphene oxide nanostructure as an excellent scaffold for label-free electrochemical biosensor: Detection of cardiac troponin I, Materials Science and Engineering: C, 69 (2016) 447-452.
[26] S. Singal, A.K. Srivastava, A.M. Biradar, A. Mulchandani, Pt nanoparticles-chemical vapor deposited graphene composite based immunosensor for the detection of human cardiac troponin I, Sensors and Actuators B: Chemical, 205 (2014) 363-370.
[27] G. Liu, M. Qi, Y. Zhang, C. Cao, E.M. Goldys, Nanocomposites of gold nanoparticles and graphene oxide towards an stable label-free electrochemical immunosensor for detection of cardiac marker troponin-I, Analytica chimica acta, 909 (2016) 1-8.

ACCEPTED MANUSCRIPT

Figure captions

Scheme 1: Fabrication of anti-cTnI/APTES/WO_3-RGO nanocomposite/ITO based immunosensor for cTnI detection.

Fig.1 XRD pattern of (a) GO (b) RGO and (c) WO_3-RGO nanocomposite composite.

Fig. 2 (a) FESEM image of WO_3 NRs, inset TEM image of WO_3 NRs and (b) FESEM image of WO3-RGO nanocomposite composite.

Fig. 3 (a) FT-IR spectra of (i) WO_3-RGO nanocomposite, (ii) APTES/WO_3-RGO nanocomposite and (iii) anti-cTnI/APTES/WO_3-RGO nanocomposite and (b) Raman spectra of (i) RGO, (ii) WO_3 NRs and (iii) WO_3-RGO nanocomposite.

Fig. 4 Contact angle measurement of (a) hydrolyzed ITO glass, (b) WO_3-RGO nanocomposite/ITO, (c) APTES/WO_3-RGO nanocomposite/ITO and (d) anti-cTnI/APTES/WO_3-RGO nanocomposite/ITO

Fig.5 Electrochemical impedance spectroscopy (EIS) of (a) WO_3 NRs/ITO and WO_3-RGO nanocomposite/ITO electrodes (Inset: Randles circuit) and (b) EIS spectra of different modified electrodes in PBS solution (50mM, pH 7.4)containing 5mM $[Fe(CN)_6]^{3-/4-}$

Fig. 6 (a) The differential pulse voltammetry (DPV) responses of the EA/anti-cTnI/APTES/WO_3-RGO nanocomposite/ITO immunoelectrode obtained as a function of cTnI concentrations (0.01-250 ng/mL) and (b) Calibration plot between the DPV peak current and the logarithm of cTnI concentrations (0.01-250 ng/mL); inset : control study.

Fig. 7 (a) Electrochemical current response of different EA/anti-cTnI/APTES/WO_3-RGO nanocomposite/ITO immunoelectrode fabricated under identical condition with cTnI (0.01 ng/mL), (b) Electrochemical current response of the immunoelectrode in the presence of different interferent (c) Real sample analysis study and (d) Shelf life studies of EA/anti-cTnI/APTES/WO_3-RGO nanocomposite/ITO immunoelectrode.

ACCEPTED MANUSCRIPT

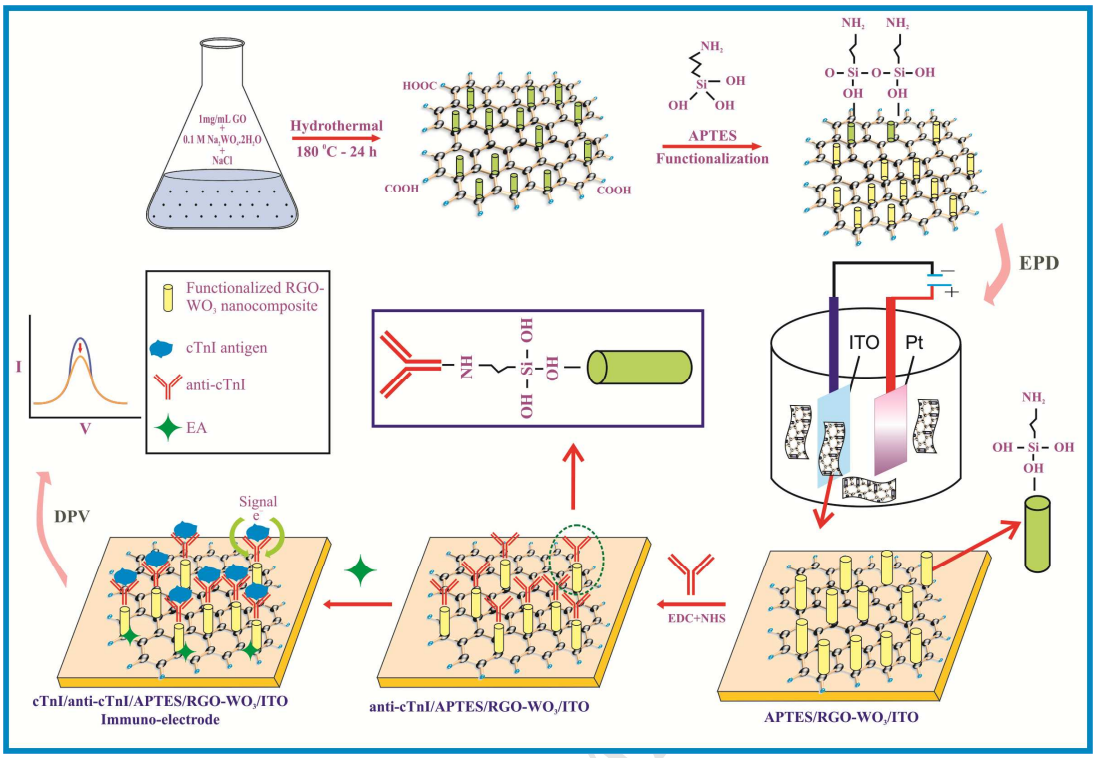

Scheme 1: Fabrication of anti-cTnI/APTES/WO_3-RGO nanocomposite/ITO based immunosensor for cTnI detection.

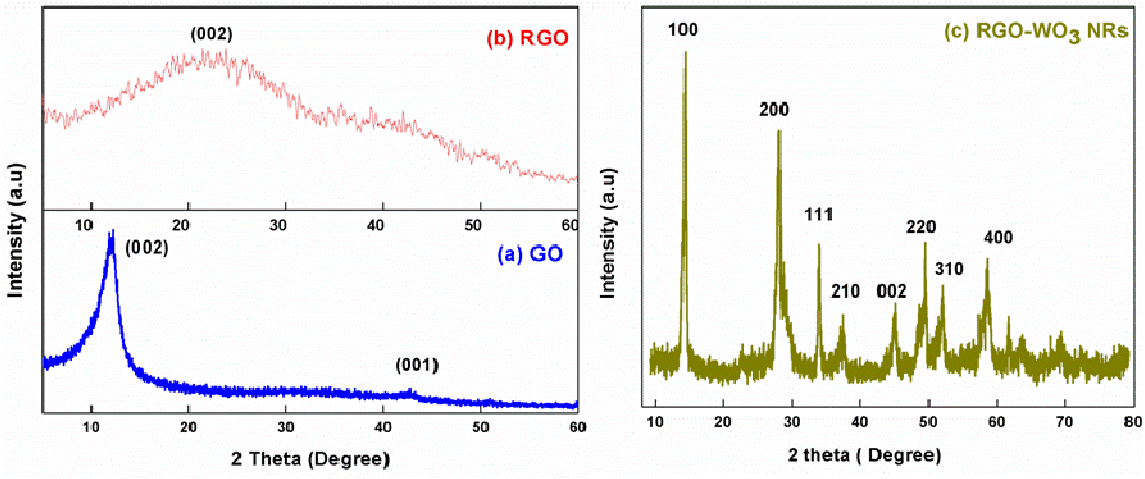

Fig.1 XRD pattern of (a) GO (b) RGO and (c) WO_3-RGO nanocomposite.

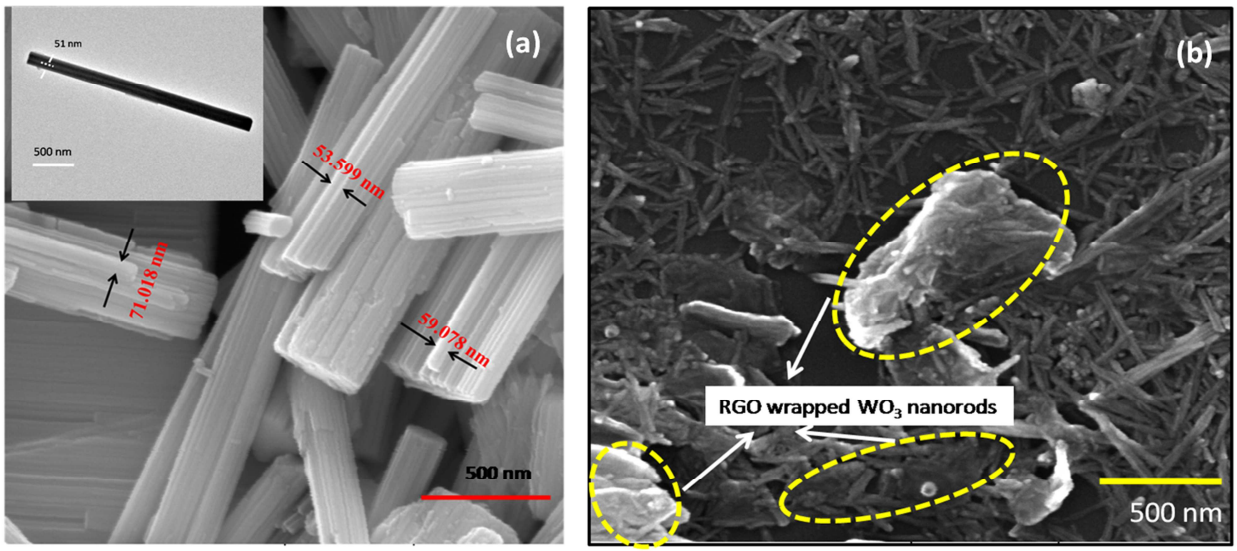

Fig. 2 (a) FESEM image of WO_3 NRs, inset TEM image of WO_3 NRs and (b) FESEM image of WO_3-RGO nanocomposite.

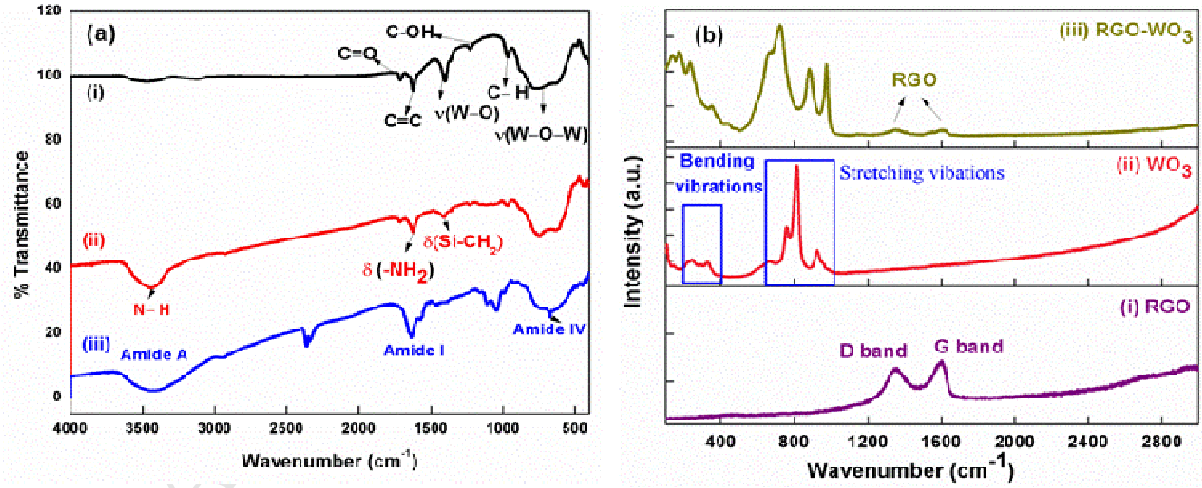

Fig. 3 (a) FT-IR spectra of (i) WO_3-RGO nanocomposite, (ii) APTES/WO_3-RGO nanocomposite and (iii) anti-cTnI/APTES/WO_3-RGO nanocomposite and (b) Raman spectra of (i) RGO, (ii) WO_3 NRs and (iii) WO_3-RGO nanocomposite.

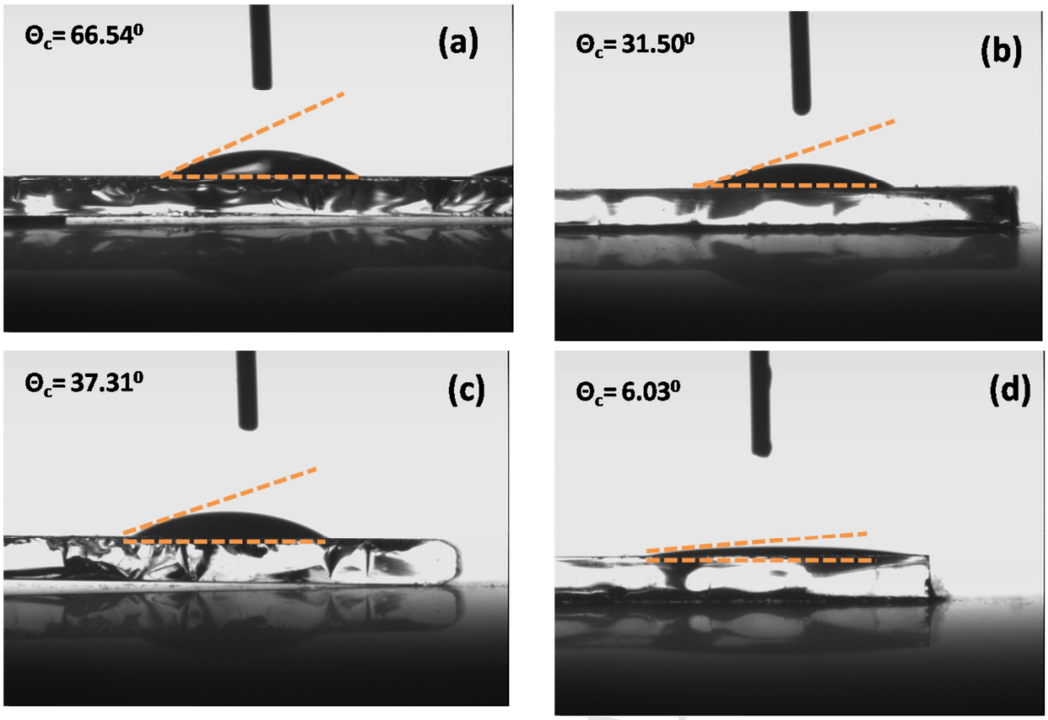

Fig. 4 Contact angle measurement of (a) hydrolyzed ITO glass, (b) WO_3-RGO nanocomposite/ITO, (c) APTES/WO_3-RGO nanocomposite/ITO and (d) anti-cTnI/APTES/WO_3-RGO nanocomposite/ITO

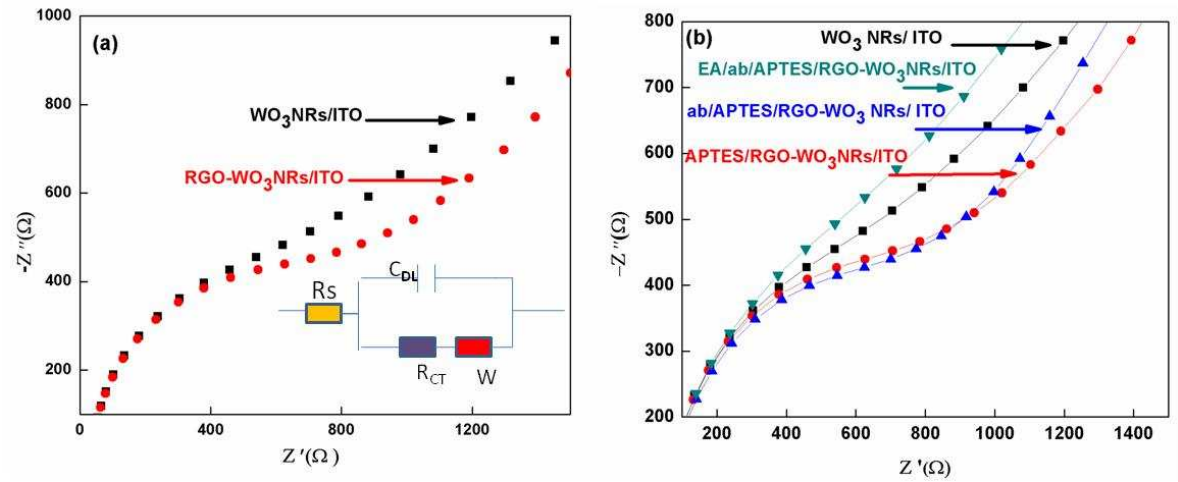

Fig.5 Electrochemical impedance spectroscopy (EIS) of (a) WO_3 NRs/ITO and WO_3-RGO nanocomposite/ITO electrodes (Inset: Randles circuit) and (b) EIS spectra of different modified electrodes in PBS solution (50mM, pH 7.4)containing 5mM $[Fe(CN)_6]^{3-/4-}$

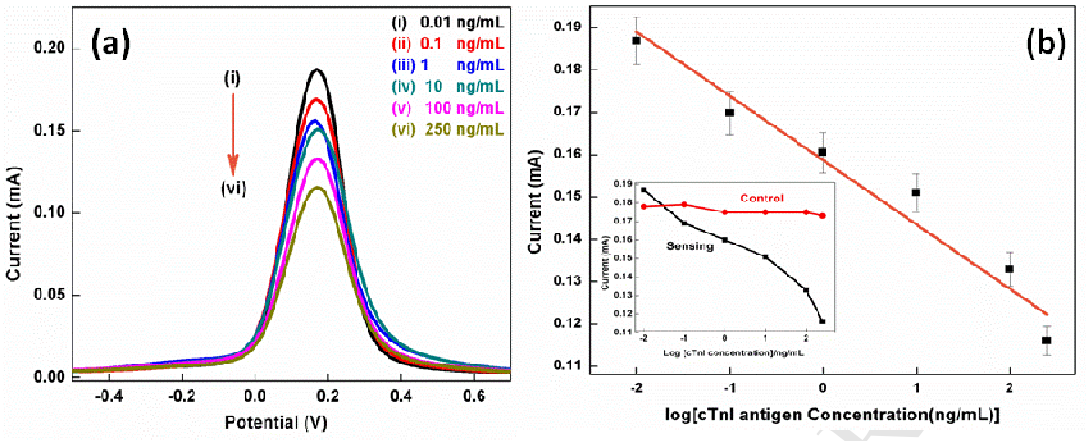

Fig. 6 (a) The differential pulse voltammetry (DPV) responses of the EA/anti-cTnI/APTES/WO_3-RGO nanocomposite/ITO immunoelectrode obtained as a function of cTnI concentrations (0.01-250 ng/mL) and (b) Calibration plot between the DPV peak current and the logarithm of cTnI concentrations (0.01-250 ng/mL); inset : control study.

ACCEPTED MANUSCRIPT

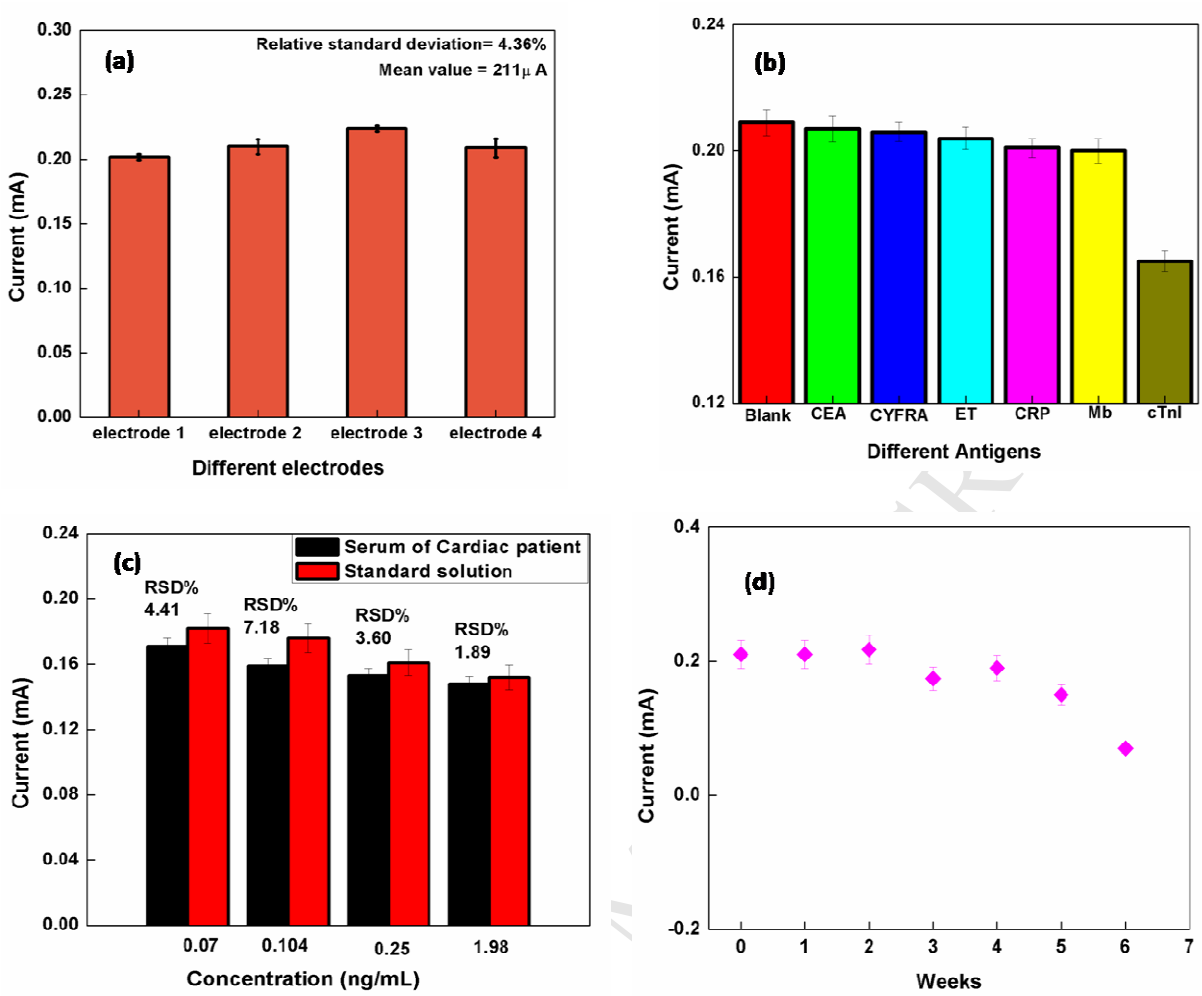

Fig. 7 (a) Electrochemical current response of different EA/anti-cTnI/APTES/WO_3-RGO nanocomposite/ITO immunoelectrode fabricated under identical condition with cTnI (0.01 ng/mL), (b) Electrochemical current response of the immunoelectrode in the presence of different interferents, (c) Real sample analysis study and (d) Shelf life studies of EA/anti-cTnI/APTES/WO_3-RGO nanocomposite/ITO immunoelectrode.

Highlights:

1. APTES functionalized WO_3-RGO nanocomposite was used as a matrix for cardiac detection cTnI.
2. The in-situ grown WO_3-RGO nanocomposite improves the biosensor efficiency.
3. The matrix yields enhanced heterogeneous electron transfer rate ($K_O = 2.4 \times 10^{-4}$ cms^{-1}).
4. The proposed WO_3-RGO nanocomposite based biosensor exhibits great sensitivity as 58.24 $\mu A/cm^2$ per decade and long stability.

ACCEPTED MANUSCRIPT

RESEARCHERID
THOMSON REUTERS

[Rani*, 7(3): March, 2018]
IC™ Value: 3.00

ISSN: 2277-9655
Impact Factor: 5.164
CODEN: IJESS7

IJESRT

INTERNATIONAL JOURNAL OF ENGINEERING SCIENCES & RESEARCH TECHNOLOGY

COMMON FAILURES IN GAS TURBINE BLADE: A CRITICAL REVIEW

Dr. Sushila Rani*

* Assistant Professor, Mechanical Engineering Department, Delhi Technological University, New Delhi, India

DOI: 10.5281/zenodo.1207072

ABSTRACT

Almost all commercial electrical power on earth is generated with a turbine, driven either by wind, water, steam or burning gas. Turbine blades are subjected to very strenuous environments inside a gas turbine. They face high temperatures, high stresses, and a potentially high vibration environment. All these factors can lead to blade failure, resulting in catastrophic failure of turbine. In the event of turbine blade failure, turbine does not work and this leads to shutdown of power plant from one to four weeks or longer, depending on the extent of the damage and the procedure used to make the machine operational again, which results in economic loss and service to mankind also stops. For each day of a forced outage, a utility could lose hundreds of thousands of dollars in electrical power.

The external and internal surface damages include corrosion, oxidation, crack formation, erosion, foreign object damage and fretting. The internal damage of microstructure include γ' phase, $CoNi_3$ [(Al, Ti)] phase aging (rafting), grain growth, brittle phases formation, carbides precipitation, creep and grain boundary void formation. These damages produce dimensional change which results in increase in operational stress that leads to deterioration in turbine efficiency. The deterioration of blade material is related to the high gas temperature, high steady state load levels (centrifugal load) and high thermal transient load (trips, start-ups, start downs). In this research, a review of common failures due to metallurgical defects found in gas turbine discussed is presented.

KEYWORDS: Turbine blade, corrosion, fretting fatigue, High cycle fatigue, Overheating

I. INTRODUCTION

A study was conducted by *Blotch (1982)* for gas turbine failures and concluded that turbine blades and rotor component contributed to 28 percent of primary causes of gas turbine failures, whereas 18 percent is due to faults in turbine nozzles and stationary parts. Another study was done by *Dundas (1994)* for gas turbine losses and observed that creep, high cycle fatigue (HCF) and turbine blade cooling related failures added 62% of the total damage costs for gas turbines. In the year 1992, another study was conducted by Scientific Advisory Board (SAB) of the United States Air Force and it was concluded that high cycle fatigue (HCF) is the single biggest cause of turbine engine failures (*Ritchie et al., 1999*). The degree of blade material deterioration for individual blade differs and it depends on several factors such as total service time, operational conditions, manufacturing process and history of turbine. The common failures found in gas turbine blades due to metallurgical defects are discussed and illustrated.

II. CORROSION

For more than 80 years, corrosion failure of machine components and structures has been studied. From the study, it is observed that maximum outages in the gas turbine power plants are due to corrosion fatigue failure of turbine blades. Many researchers have done metallographic and fractrographic analysis of failed turbine blades and concluded that chemicals compounds such as oxide, chromium sulfide and complex sulfides play significant role in reducing fatigue strength of turbine blades.

Gladys et al., (1999) have investigated a rotor blade made of Ni based super-alloy (AMS 5704) having wear resistant Cr-Ni coating. They have observed deposition of hard catalyst on the shroud and concluded that the blade failure occur due to erosion and high temperature sulfidation corrosion. *Eliaz et al., (2002)* have studied macroscopic and microscopic characteristics of Type I (HTHC-high temperature hot corrosion) and Type II

ISSN: 2277-9655
Impact Factor: 5.164
CODEN: IJESS7

(LTHC-low temperature hot corrosion). They have described different practical approaches to minimize hot corrosion. *Khajavi et al., (2004)* have discussed different types of hot corrosion, i.e. HTHC (High temperature hot corrosion), LTHC (Low temperature hot corrosion) and transition type, and investigated a first stage blade of a GE-F5 gas turbine. They have concluded that the blade has failed by both types of hot corrosion but HTHC was dominant. *Gallardo et al., (2002)* have investigated a gas turbine blade made of nickel super-alloy CMSX-4. They have observed that at high temperature, coating on the surface deteriorated due to wear. The unprotected surfaces suffered with high temperature hot corrosion (HTHC). *Attarian et al., (2013)* have collected a gas turbine blade made of IN738LC nickel base super-alloy, which was failed after rendering service for 1500 hours. They have found that the blade failure took place by dissolving the γ' in matrix due to exposure of high temperature and pressure. *Das et al., (2003)* have investigated a stainless steel turbine blade of a 220 MW thermal power plant. They have observed several pits on the surface and the presence of chloride salt in these pits was responsible for crack initiation by crevice corrosion and concluded that the blade failed due to corrosion –fatigue mechanism. *Xie et al., (2006)* have investigated the premature tip cracking of the high pressure first stage gas turbine blade. They have found that the premature crack was due to corrosive/oxidative service environment and high thermal stresses. They concluded that coating having both oxidation and abrasion resistance should be applied in blade tip to avoid the problem. *Bhagi et al., (2013)* have studied a fractured low pressure 110 MW steam turbine blade made of chrome alloy X20Cr13. They have found the oxides of silicate and sodium on fractured surface, which leads to the formation of corrosion pits and concluded that the blade failed due to corrosion fatigue. *Patil et al., (2007)* has investigated a failed second stage gas turbine blade made of nickel based super-alloy IN738LC. They have found that crack initiated at the leading edge due to hot corrosion and propagated by fatigue mechanism finally resulting in complete fracture of the turbine blade.

Corrosion is reduced to great extent by providing coatings on surface of turbine blade and proper cleaning of cooling holes. Secondly, proper selection of alloy element for manufacturing of turbine blades is a major concern; the material must be corrosion resistant. *Nicholls et al., (2002)* have studied smart lay coatings and described that the smartcoat design consists of a MCrAlY base, first enriched in chromium and then aluminium. At high temperature, the coating oxidised to form protective aluminium rich surface layer, which provided reisistance to high temperature oxidation and Type I hot corrosion. The coating also had an intermediate chromium rich interlayer, which permitted the formation of chromia healing areas of Type II corrosion damage. *Strawbridge et al., (1997)* have studied the oxidation behaviour of air plasma sprayed NiCrAlY coatings at 1200^0C in 1 atm air. They have observed that a protective alumina layer developed during the early stages, but this layer broke away after prolonged exposure. Turbine blades are normally protected with sophisticated coatings, usually based on chromium and aluminum, but often containing exotic elements such as Yttrium and Platinum group metals to provide resistance to corrosion and oxidation while in service *(Carter, (2005)).*

III. FATIGUE

Turbine blades are most susceptible to crack formation in regions of contact surfaces, which are exposed to both centrifugal loading and oscillatory vibrations. These mating component are failed due to fretting fatigue. Fretting fatigue results in an increase in tensile and shear stress at the contact surface, which leads to crack initiation and its propagation till failed completely. At elevated temperatures, fatigue cracks have been observed to initiate from grain boundaries, slip bands, pores, twin boundaries or due to cracking of inclusions/precipitates. The majority of turbine failure includes fatigue leading to crack initiation and propagation. The operating conditions of high rotational speed at elevated temperature, corrosion, erosion and oxidation accelerates fatigue failure.

Pang et al., (2007) have performed an assessment for finding the effects of microstructure and operating parameters on fatigue crack initiation and short crack growth in powder metallurgy (PM) nickel-based super-alloys, at room temperature and at 650 °C. They revealed that, at room temperature, fatigue cracks were observed to initiate from both porosity and slip bands and at 650 °C, only porosity dominated for the initiation of fatigue crack and no slip-band initiation observed. *Mazur et al., (2009)* have evaluated a last stage, AISI 420 stainless steel blade (L-0) of 28MW geothermal turbine and concluded that blade failure initiation and propagation was due to a high cycle fatigue mechanism, which got accelerated to a high degree by corrosion/ erosion processes that occurred in the blade trailing edge zone. *Kim et al., (2011)* have investigated a fourth stage blade of a 500 MW steam turbine to evaluate a crack found on the leading edge vane and observed that the condenser tube had leakage through which the seawater entered resulting in the induction of corrosion pits. These corrosion pits acted as a notch for stress concentration and facilitated crack initiation under cycling

loading conditions. The crack propagated inwards by fatigue mechanism due to vibration of blade. *Barella et al., (2011)* have investigated a third stage turbine blade of 150MW thermal power plant, made of nickel-based super-alloy IN738 which failed after rendering service of 22,400 hrs. They have concluded that the blade failed due to fretting fatigue mechanism. *Poblano-salas et al., (2011)* have studied a steam turbine blade made up of stainless steel having a crack on the airfoil. They have observed that the fractured surface contained a section of lacing bar and concluded that the airfoil failure took place due to deficient brazing process employed for bonding the component to the lacing bar at the last stage of the turbine. SEM evaluation revealed that crack propagation was due to fatigue mechanism. *Kubiak et al., (2006)* have investigated a first stage gas turbine blade of 150MW turbine that was failed suddenly due to high vibrations. They have concluded that the low cycle fatigue mechanism generated a crack in the securing pin hole located at the root of the blade and it propagated by excessive thermal stresses inside the body of the blade. The crack started from the pin hole below the blade platform – this meant that the fault was associated with faults in the cooling system. They have suggested modifying the gas heater and the rotor air cooling system to prevent accumulation of the condensate in the gas heater and avoid corrosion of inner surfaces of the pipes using different materials and/or coatings. *Liacy et al., (2011)* have investigated a first stage blade of 85 MW gas turbine made of Ni base super-alloy Udimet 520 having MCrAlY coating. They have revealed that the formation of a continuous net of carbides on grain boundaries reduced the toughness of the alloy and resulted in a brittle inter-granular fracture.

Farhangi et al., (2007) have analyzed a 32 MW second stage turbine blade of a thermal power plant, made of nickel based super-alloy Udimet 500 which failed after rendering service of 50,000 hrs. They have found debris on the contact surfaces of fir tree root and concluded that the blade was failed due to fretting fatigue. *Mazur et al., (2005)* have investigated a 70 MW first stage gas turbine blade made of nickel based super-alloy IN738LC which failed after rendering service of 24,000 hrs. They have observed cracks in the cooling holes at 0.4mm depth, which penetrated the coating and substrate at high stressed areas of airfoil. They have concluded that the crack initiation and propagation occurred due to fatigue/ creep mechanism at high temperature. They have suggested that the cooling system should be improved to increase the life of blade. *Maktouf et al., (2015)* have analyzed a first stage compressor blade of a gas turbine generator in a gas treatment plant. They have observed that the cracks are initiated at internal metallurgical anomaly region near the airfoil leading edge and propagated towards mid chord of airfoil till failed completely with high cycle fatigue mechanism. *Poursaeidi et al., (2008)* have investigated a failed second stage gas turbine blade made up of nickel based super-alloy IN738LC. They have concluded that the crack was initiated due to hot corrosion at the leading edge and propagated by fatigue till the blade fractured completely. *Lee et al., (2011)* have investigated first stage compressor blades of J85 military aircraft engine made of Ti-6Al-4V, found cracked on blade tangs. They have concluded that the crack is initiated due to fretting wear on the pinhole surface of the tang and propagated by fatigue mechanism induced from centrifugal load and vibration.

Shot peening and ultrasonic impact treatment (UIT) methods are used for treating fretting fatigue. These methods induce compressive stresses under the surface to increase the fatigue strength *(Barella et al., 2011).* UIT method removes tensile stresses to a great extent. More recently, it has been demonstrated that other surface treatment approaches, such as laser shock processing (LSP) can have a beneficial effect on fretting fatigue performance.

IV. OVERHEATING

The surface degradation of turbine blade by the formation of needle separation topologically closed packed phase (TCP) occurs due to overheating. This structural instability of the alloy results in decrease in strength and ductility of alloy *(Rybhino et al., 2012). Tawancy et al., (2009)* have examined the first stage turbine blades and vanes and concluded that the failure of both components took place due to overheating. Overheating promoted creep, resulting in inter-granular cracking that shortened the fatigue life of blades and vanes. *Vardar et al., (2007)* have investigated a 40 MW gas turbine blade made of Udimet 500. They have observed continuous film of carbides in grain boundaries, which was formed by the transformation of MC type of carbides to M_6C type of carbides due to high temperature. *Kargarnejad et al., (2012)* have analyzed a first stage blade of 3MW gas turbine, made of nickel based alloy Nimonic 80A. They have observed that the blade lost coating at high temperature and concluded that the blade was failed due to oxidation, corrosion, erosion and inters diffusion of coating substrate, which resulted in the degradation of base alloy.

V. CONCLUSIONS

ISSN: 2277-9655
Impact Factor: 5.164
CODEN: IJESS7

Based on the literature and studies reported above, following conclusions are drawn:

1. The external and internal surface damages include corrosion, oxidation, crack formation, erosion, foreign object damage and fretting. The internal damage of microstructure include γ' phase, $CoNi_3$ [(Al, Ti)] phase aging (rafting), grain growth, brittle phases formation, carbides precipitation, creep and grain boundary void formation.
2. It is concluded that maximum outages in the gas turbine power plants are due to corrosion fatigue failure of turbine blades. It is concluded that chemicals compounds such as oxide, chromium sulfide and complex sulfides play significant role in reducing fatigue strength of turbine blades.
3. Fretting fatigue results in an increase in tensile and shear stress at the contact surface, which leads to crack initiation and its propagation till the turbine blade failed completely.
4. The majority of turbine failure includes fatigue leading to crack initiation and propagation. . At elevated temperatures, fatigue cracks have been observed to initiate from grain boundaries, slip bands, pores, twin boundaries or due to cracking of inclusions/precipitates.
5. The surface degradation of turbine blade by the formation of needle separation topologically closed packed phase (TCP) occurs due to overheating. This structural instability of the blade alloy results in decrease in strength and ductility of blade alloy.

VI. REFERENCES

[1] Bloch H. P., "Improving machinery reliability in process plants", Houston, Texas: Gulf Publishing", Vol. 1, third edition, 1982.
[2] Dundas R. E., "A statistical study of gas turbine losses and analysis of causes and optimum methods of prevention", ASME paper number: 94-GT-279, 1994.
[3] Ritchie R.O., Boyce B.L., Campbell J.P., Roder O., Thompson A.W., Milligan W.W., "Thresholds for High-cycle Fatigue in a Turbine Engine Ti–6Al–4V alloy", INTERNATIONAL JOURNAL OF FATIGUE, Vol. 21, pp. 653–662, 1999.
[4] Gladys N., Laura V., "Analysis of rotor blade failure due to high temperature corrosion/erosion", SURFACE AND COATINGS TECHNOLOGY, Vol. 120, pp. 145-150, 1999.
[5] Eliaz N., Shemesh G., Latanision R.M., "Hot corrosion in gas turbine component", ENGINEERING FAILURE ANALYSIS, Vol. 9, pp. 31-43, 2002.
[6] Khajavi M.R., Shariat M.H., "Failure of first stage turbine blades", ENGINEERING FAILURE ANALYSIS, Vol. 11, pp. 589-597, 2004.
[7] Gallardo J.M., Rodriguez J.A., Herrera E.J.,"Failure of gas turbine blades", WEAR, Vol. 252, pp. 264-268, 2002.
[8] Attarian M., Khoshmanesh R., Natesh S., Davami P., "Micro-structural evaluation and fracture mechanism of failed IN738LC gas turbine blade", Case Studies in ENGINEERING FAILURE ANALYSIS, Vol. 1, pp. 85-94, 2013.
[9] Das G., Chowdhury S.G., Ray A.K., Das S.K., Bhattacharya D.K., " Turbine blade failure in a thermal power plant", ENGINEERING FAILURE ANALYSIS, Vol. 10, pp. 85-91, 2003.
[10] Xie Y, Wang M, Zhang G., "Analysis of super alloy turbine blade tip cracking during service", ENGINEERING FAILURE ANALYSIS, Vol. 13, pp. 1429-1436 2006.
[11] Bhagi L, Rastogi V, Gupta P., " Fractographic investigations of the failure of L-1 low pressure steam turbine blade", CASE STUDIES ENGINEERING FAILURE ANALYSIS, Vol. 1, 2013.
[12] Patil A.A, shirsat U.M., "Study of failure analysis of gas turbine blade", IOSR JOURNAL OF ENGINEERING, ISBN: 2878-8719, pp.37-43, 2010.
[13] Nicholls JR., "Smart overlay coating: concepts and practice", JOURNAL OF SURFACE COATING TECHNOLOGY, Vol. 149, pp. 236–44, 2002.
[14] Strawbridge A, Evans HE, Ponton CB., "Spallation of oxide scales from NiCrAlY Overlay coatings", MATERIAL SCIENCE FORUM, Vol. 251, pp. 365–372, 1997.
[15] Carter T.J., "Common failures in gas turbine blades", ENGINEERING FAILURE ANALYSIS, Vol. 12 No. 2, pp. 237-247, 2005.
[16] Pang H.T., Reed P.A.S., "Microstructure effects on high temperature fatigue crack initiation and short crack growth in turbine disc nickel-base super-alloy Udimet 720 Li", MATERIALS SCIENCE AND ENGINEERING, Vol. 448, pp. 67-79, 2007.
[17] Mazur Z., Illescas R.G., Calderon J.P., "Last stage blades failure analysis of a 28 MW geo-thermal turbine", ENGINEERING FAILURE ANALYSIS, Vol. 16, pp.1020-1032, 2009.

ISSN: 2277-9655
Impact Factor: 5.164
CODEN: IJESS7

[18] Kim H., "Crack evaluation of the fourth stage blade in a low –pressure steam turbine", ENGINEERING FAILURE ANALYSIS, Vol. 18, pp. 907–913, 2011.
[19] Barella S., Boniardi M., Cincera S., Pellin P., Degive X., Gijbels S., "Failure analysis of a third stage gas turbine blade", ENGINEERING FAILURE ANALYSIS, Vol. 18, pp.386-393, 2011.
[20] Poblano-Salas C.A., Sanchez J.D.O., Jimenez J.C.S., "Failure analysis of an AISI 410 stainless steel airfoil in a steam turbine", ENGINEERING FAILURE ANALYSIS, Vol. 18, pp. 68-74, 2011.
[21] Kubaik J., Urquiza G., Rodriguez J.A., Gonzalez G., Rosales I., Castillo G., Nebradt J., "Failure analysis of the 150MW gas turbine blades", ENGINEERING FAILURE ANALYSIS, Vol. 16, pp. 1794-1804, 2006.
[22] Liacy H.M., Abouali S., Garakani M.A., "Failure analysis of a first stage gas turbine blade", ENGINEERING FAILURE ANALYSIS, Vol. 18, pp. 517-522, 2011.
[23] Farhangi H., Moghadam A.A.F., "Fractographic investigation of the failure of second stage gas turbine blades", Proceedings of 8th International Fracture Conference; Istanbul/TURKEY, pp. 577-584, November 2007.
[24] Mazur Z, Ramirez A, Amezcua C. A., "Failure analysis of a gas turbine blade made of Inconel 738LC alloy", ENGINEERING FAILURE ANALYSIS, Vol. 12, pp. 474–86, 2005.
[25] Mktouf W., Sai K., "An investigation of premature fatigue failures of gas turbine blade", ENGINEERING FAILURE ANALYSIS, Vol. 8, pp.89-101, 2015.
[26] Poursaeidi E., Aieneravaie M., Mohammadi M.R., "Failure analysis of a second stage blade in a gas turbine engine", ENGINEERING FAILURE ANALYSIS, Vol. 15, pp. 1111-1129, 2008.
[27] Lee B.K., Suh J., Lee H., Kim T., "Investigations on fretting fatigue in aircraft engine compressor blade", ENGINEERING FAILURE ANALYSIS, Vol. 18, pp. 1900-1908, 2011.
[28] Rybhino A. I., Gestov L.B., Mozhaiskaya N.V., "Operation experience with cast rotor blades made of Russian alloys in stationary gas turbines", THERMAL ENGG., Vol. 59, No. 3, pp. 242–249, 2012.
[29] Tawancy HM, Hadhrami LM., "Degradation of turbine blades and vanes by overheating in a power plant", ENGINEERING FAILURE ANALYSIS, Vol. 16, pp. 273–280, 2009.
[30] Vardar N., Ekerim NA., "Failure analysis of gas turbine blade in a thermal power plant", ENGINEERING FAILURE ANALYSIS, Vol. 14, pp. 743–749, 2007.
[31] Kargarnejad S., Djavanroodi F., "Failure assessment of Nimonic 80A gas turbine blade", ENGINEERING FAILURE ANALYSIS, Vol. 26, pp. 211-219, 2012.

CITE AN ARTICLE

Rani, S., Dr. (n.d.). COMMON FAILURES IN GAS TURBINE BLADE: A CRITICAL REVIEW. *INTERNATIONAL JOURNAL OF ENGINEERING SCIENCES & RESEARCH TECHNOLOGY*, *7*(3), 799-803.

This article has been accepted for inclusion in a future issue of this journal. Content is final as presented, with the exception of pagination.

Compact Modeling of Drain Current, Charges, and Capacitances in Long-Channel Gate-All-Around Negative Capacitance MFIS Transistor

Amol D. Gaidhane, *Student Member, IEEE*, Girish Pahwa, *Student Member, IEEE*, Amit Verma, *Member, IEEE*, and Yogesh Singh Chauhan, *Senior Member, IEEE*

***Abstract*— In this paper, we present a surface potential-based explicit continuous model for a metal-ferroelectric-insulator-semiconductor (MFIS) type gate-all-around negative capacitance transistor (GAA-NCFET). Unlike previously reported models, an explicit formulation to calculate the electrical characteristics of GAA-NCFET is proposed. Our model includes the radial dependence of the electric field in the ferroelectric, ignored in the previous works and accurately captures ferroelectric material parameter variations in the nonhysteretic regime. In contrast to bulk NCFETs, GAA-NCFET characteristics show different bias dependence due to the absence of bulk charge. We also present analytical expressions for the terminal charges which are essential to obtain the trans-capacitances for transient simulations. We find that, compared with conventional MOSFETs, the gate charge saturates to a different fraction of its maximum value. Furthermore, the modeling of quantum mechanical effect and overlap capacitances in an MFIS NCFET structure is discussed. Finally, the proposed model has been implemented in Verilog-A and tested for the transient response of ring oscillator in a commercial circuit simulator.**

***Index Terms*— Ferroelectric, fin field effect transistor (FinFET), GAA-NCFET, metal-ferroelectric-insulator-semiconductor (MFIS), nanowire, negative capacitance, overlap capacitance, quantum mechanical effect (QME).**

I. Introduction

NEGATIVE capacitance field-effect transistor (NCFET) is a promising device for low-power applications which exploits the negative capacitance behavior of a ferroelectric material present in the gate stack to enhance surface potential compared to the conventional MOSFETs [1], [2]. Experimental studies on NCFETs have shown steep subthreshold characteristics [subthreshold swing (SS) < 60 mV/dec] and high ON currents [3], [4]. Recent simulation studies of SRAM and nonvolatile memory designs using NCFETs have also shown promising results [5], [6]. Furthermore, gate-all-around (GAA) architecture is being considered as a potential candidate for future CMOS generations which offers excellent immunity to short channel effects because of its superior electrostatic control which improves drain induced barrier lowering, SS, and I_{ON}/I_{OFF} [7], [8]. Experimental and numerical studies of GAA-FET-based CMOS circuits show better OFF-state device performance, lower circuit delays, and faster switching compared with fin field effect transistor (FinFET) [9], [10]. In this paper, we investigate the case of GAA-NCFET which utilizes the combined advantages of negative capacitance effect and the GAA architecture.

In order to design circuits using NCFETs, there is a strong need to develop fast and physically accurate compact models. Compact models for bulk NCFET and NC-FinFET have already been developed [11], [12]. However, the reported analytical models for GAA-NCFETs have expressed the drain current in implicit forms [13], [14]. These implicit equations are solved using numerical methods, which require a large number of iterations. This approach is computationally inefficient for circuit-level simulations.

In this paper, we have developed a long-channel core model for an undoped cylindrical metal-ferroelectric-insulator-semiconductor (MFIS) GAA-NCFET that uses a computationally efficient approach by solving the intermediate steps explicitly. We have also derived analytical expressions for the terminal charges which are essential for ac and transient circuit simulations. The model has been implemented in Verilog-A code and tested for the transient response of a ring oscillator (RO). Second-order issues such as polarization damping effect in the ferroelectric material [15], [16], short-channel effects, and so on [17] are not considered in this paper to focus on the effects of negative capacitance only.

II. Model Development

A cylindrical MFIS GAA-NCFET and its cross-sectional view are schematically shown in Fig. 1. GAA-NCFET consists

Manuscript received November 16, 2017; revised January 29, 2018 and February 20, 2018; accepted March 1, 2018. This work was supported in part by the Department of Science and Technology, Science and Engineering Research Board, Government of India and in part by Semiconductor Research Corporation. The review of this paper was arranged by Editor B. Iñiguez. *(Corresponding author: Amol D. Gaidhane.)*

The authors are with the Department of Electrical Engineering, IIT Kanpur, Kanpur 208016, India (e-mail: amold@iitk.ac.in; chauhan@iitk.ac.in).

Color versions of one or more of the figures in this paper are available online at http://ieeexplore.ieee.org.

Digital Object Identifier 10.1109/TED.2018.2813059

0018-9383 © 2018 IEEE. Personal use is permitted, but republication/redistribution requires IEEE permission.
See http://www.ieee.org/publications_standards/publications/rights/index.html for more information.

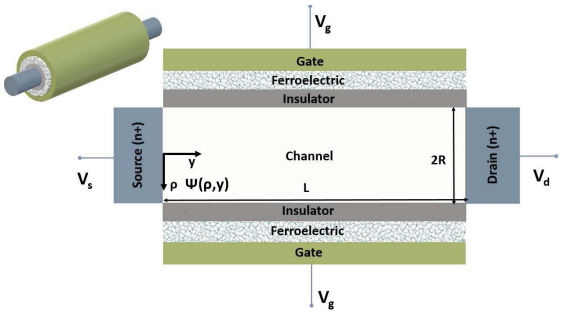

Fig. 1. Cylindrical MFIS-type GAA-NCFET and its cross-sectional view.

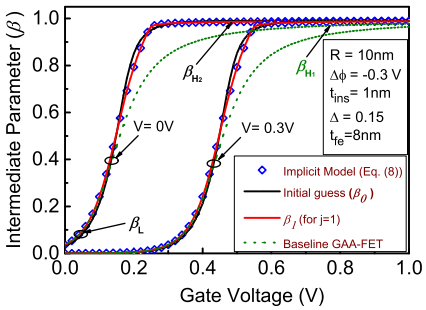

Fig. 2. Intermediate parameter (β) versus gate voltage (V_g) for two different electron quasi fermi potentials (V). The steep characteristics of β near transition region for GAA-NCFET compared to baseline GAA-FET appear due to negative capacitance phenomenon which entails surface potential amplification and steeper subthreshold characteristics of drain current. We consider SiO_2 as the insulator material throughout this paper.

of extra ferroelectric layer in between metal and insulator layers compared with baseline GAA-FET. Another structure that has been widely used for NCFET demonstration contains a metal layer between the ferroelectric and the insulator (metal-ferroelectric-metal-insulator-semiconductor (MFMIS) FET). It has been recently shown that the presence of this metal floating gate may hamper the negative capacitance effect if the ferroelectric is leaky [18]. It can also cause other issues such as threshold voltage variation in the presence of charge trapping and detrapping in the metal [19]. Therefore, the MFIS structure instead of the MFMIS structure has been considered in this paper.

Under the gradual channel approximation, the potential $\psi(\rho)$ of a surrounded gate FET can be expressed as [20], [21]

$$\psi(\rho) = V - \frac{2kT}{q}\ln\left[\frac{R}{2L_{\mathrm{Di}}\beta}\left(1-\frac{\beta^2\rho^2}{R^2}\right)\right] \tag{1}$$

where q is the electronic charge, k is Boltzmann's constant, V is the electron quasi-fermi potential which is assumed to be a constant along the ρ-direction, R is the radius of the cylindrical channel, $L_{\mathrm{Di}} = (2\varepsilon_{\mathrm{si}}kT/q^2\, n_i)^{1/2}$ is the intrinsic Debye length, $\varepsilon_{\mathrm{si}}$ is the permittivity of silicon, n_i is the intrinsic carrier density, and β is a dimensionless intermediate parameter which is a function of gate voltage V_g and V as described later in this section.

In the steady state, voltage across the ferroelectric layer, V_{fe}, in terms of mobile charge density, Q, can be expressed using Landau–Devonshire theory as [22]

$$V_{\mathrm{fe}} = a_0 Q + b_0 Q^3 \tag{2}$$

where the coefficients a_0 and b_0 are related to the Landau parameters (a and b) of the ferroelectric material for a cylindrical gate, derived from (38) in the Appendix as

$$a_0 = 2aR\ln[1 + t_{\mathrm{fe}}/(R + t_{\mathrm{ins}})] \tag{3}$$

$$b_0 = 2bR^3[1/(R + t_{\mathrm{ins}})^2 - 1/(R + t_{\mathrm{ins}} + t_{\mathrm{fe}})^2] \tag{4}$$

where t_{fe} is the ferroelectric thickness and t_{ins} is the thickness of intermediate insulator layer. Note that a_0 and b_0 are also functions of R and t_{ins} in addition to t_{fe}, which stems from the radial dependence of the electric field in the ferroelectric layer, not considered in the earlier models [13], [14]. Throughout this paper, we have assumed ferroelectric material parameters $a = -3 \times 10^9$ m/F and $b = 6 \times 10^{11}$ m^5/C^{2}F [12] with the corresponding coercive field $E_c = 1.15$ MV/cm and remnant polarization $P_r = 5$ μC/cm^2, which are close to Al doped HfO_2 ferroelectric parameters [23]. From the voltage balance condition, we get

$$V_g - V_{\mathrm{ins}} - \Delta\phi - \psi_s = a_0 Q + b_0 Q^3 \tag{5}$$

where V_{ins} is the voltage across an intermediate insulator layer, $\Delta\phi$ is the work function difference between the gate electrode and the semiconductor, and ψ_s is the surface potential at $\rho = R$. The V_{ins} can be expressed as $V_{\mathrm{ins}} = Q/C_{\mathrm{ins}}$, where $C_{\mathrm{ins}} = \varepsilon_{\mathrm{ins}}/(R\ln(1 + t_{\mathrm{ins}}/R))$ is the capacitance and $\varepsilon_{\mathrm{ins}}$ is the permittivity of an intermediate insulator layer. After substituting V_{ins} in (5), we get

$$V_g - \Delta\phi - \psi_s = (a_0 + 1/C_{\mathrm{ins}})Q + b_0 Q^3 \tag{6}$$

From Gauss's law, magnitude of the total mobile charge density can be determined using (1)

$$Q = \varepsilon_{\mathrm{si}}\left(\frac{d\psi}{d\rho}\right)\Big|_{\rho=R} = \left(\frac{2\varepsilon_{\mathrm{si}}}{R}\right)\left(\frac{2kT}{q}\right)\left(\frac{\beta^2}{1-\beta^2}\right). \tag{7}$$

Substituting Q in (6) gives an implicit equation in β as

$$\ln(\beta) - \ln(1-\beta^2) + m\left(\frac{\beta^2}{1-\beta^2}\right) + n\left(\frac{\beta^2}{1-\beta^2}\right)^3 - G = 0 \tag{8}$$

where $m = (a_0 + 1/C_{\mathrm{ins}})(2\varepsilon_{\mathrm{si}}/R)$, $n = b_0(2\varepsilon_{\mathrm{si}}/R)^3(2kT/q)^2$ and $G = q(V_g - \Delta\phi - V)/(2kT) - \ln(2L_{\mathrm{Di}}/R)$. As the surface potential, drain current, and terminal charges are all expressed in terms of β, it must be solved explicitly to enable faster circuit simulations. Explicit solution of β is calculated using the following steps.

1) We need to choose initial guess such that it appropriately takes into account all the geometrical and material parameter variations of GAA-NCFET. We calculate the initial guess by considering the asymptotic behavior of β. Lower values of gate voltage imply a smaller β (see Fig. 2) for which the first term in the left-hand side (LHS) of (8) [$\ln(\beta)$] dominates. Therefore, β follows an exponential behavior with the gate voltage, the lower asymptotic value of β is expressed as

$$\beta_L = \exp(G). \tag{9}$$

However, for higher values of gate voltages, β is also high, and therefore, either the third or the fourth term

This article has been accepted for inclusion in a future issue of this journal. Content is final as presented, with the exception of pagination.

in LHS of (8) becomes dominant, depending upon the coefficients a_0 and b_0. Whenever the third term dominates (for small values of a_0 and b_0), the higher asymptotic value of β is given as

$$\beta_{H_1} = [G_0/(m + G_0)]^{1/2}. \tag{10}$$

On the other hand, when the fourth term dominates (for large values of a_0 and b_0), the higher asymptote of β is given as

$$\beta_{H_2} = \left[G_0^{1/3}/(n^{1/3} + {G_0}^{1/3})\right]^{1/2}. \tag{11}$$

Note that we have used $G_0 = G + \ln(2L_{\rm Di}/R) + qV/2kT$ in the place of G in β_{H_1} and β_{H_2} expressions. For $V_g < (2kT/q)\ln(2L_{\rm Di}/R) + \Delta\phi + V$, G becomes negative leading to imaginary values of β_H. To avoid this issue, we have shifted the original G by $\ln(2L_{\rm Di}/R) + qV/2kT$ which does not affect the value of β much in the strong inversion region. The final expression of β_H is now obtained by taking minimum of β_{H_1} and β_{H_2}

$$\beta_H = \beta_{H_1} - 0.5\left(\beta_{H_{12d}} + \sqrt{{\beta_{H_{12d}}}^2 + 4\Delta\beta_{H_1}}\right) \tag{12}$$

where $\beta_{H_{12d}} = \beta_{H_1} - \beta_{H_2} - \Delta$ and Δ is a smoothing parameter. Finally, to join the lower (β_L) and higher (β_H) asymptotic values obtained in (9) and (12), we again use the same minimum function described earlier. The value of $\beta = \beta_0$ thus obtained is very close to the actual value as shown in Fig. 2 for two different values of V. The obtained value of β ranges from 0 to 1 as shown in Fig. 2.

2) To further improve the initial guess, especially in the transition region, we modify the initial guess with a second-order correction term as [20]

$$\beta_j = \beta_{j-1} - \frac{p(\beta_{j-1})}{p'(\beta_{j-1})}\left(1 - \frac{p(\beta_{j-1})p''(\beta_{j-1}}{2p'(\beta_{j-1})^2}\right)^{-1} \tag{13}$$

where j denotes the iteration number and $p(\beta)$ is LHS of (8) and $p'(\beta)$, $p''(\beta)$ are the first- and second-order derivatives of $p(\beta)$, respectively. Using the above-mentioned formulation, convergence to accurate solution can be achieved with only one or two iterations for a wide range of geometrical and material parameters. As shown in Fig. 2, β_1 for $j = 1$ matches very well with the actual value of β obtained from numerical solution of (8) using large number of iterations, which we refer as an implicit model. β for the GAA-NCFET shows steep characteristics near the transition region compared to the baseline GAA-FET due to a negative capacitance phenomenon which leads to surface potential amplification and as we will see later, steeper subthreshold characteristics of drain current.

Fig. 3(a) shows the variation of surface potential (ψ_s) and voltage amplification factor (A_V) at the source side with the gate voltage for different ferroelectric thicknesses. Increase in ψ_s and the peak value of A_V with $t_{\rm fe}$ result from an improved capacitance matching of the ferroelectric and the internal

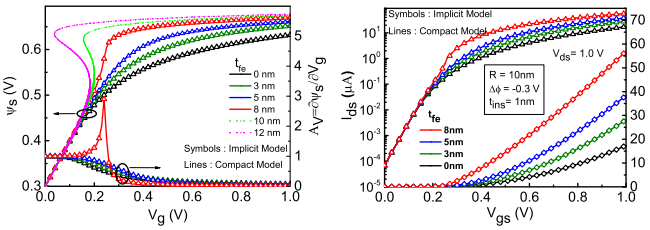

Fig. 3. (a) Surface potential (left y-axis) and the corresponding amplification factor (right y-axis) at the source side ($V = 0$) as a function of V_g for different $t_{\rm fe}$. Further increase in $t_{\rm fe}$ leads to hysteresis (multiple ψ_S solution for given V_g) in the characteristics as shown by the dashed lines. (b) $I_{\rm ds}$–$V_{\rm gs}$ for different $t_{\rm fe}$ in linear (right y-axis) and in log (left y-axis) scale. $L = 1$ μm and $\mu = 300$ cm^2/Vs are used to obtain drain current characteristics.

FET capacitances [3], [24]. For the ferroelectric material and geometrical parameters used for GAA-NCFET, the surface potential exhibits nonhysteretic behavior up to $t_{\rm fe} = 8$ nm for which it provides maximum voltage amplification. Note that the surface potential for $t_{\rm fe} = 10$ and 12 nm in Fig. 3(a) is obtained using implicit formulation. The explicit model presented in this section is valid for nonhysteretic regime only which is actually going to be the operating regime for the low-power logic applications.

A. Channel Current

For easier calculations of the drain current and the terminal charges of the GAA-NCFET, we will express all the subsequent equations in terms of α, where $\alpha = 1 - \beta^2$. Using (7), the total mobile charge density in terms of α is now expressed as

$$Q = (2\varepsilon_{\rm si}/R)(2kT/q)[(1 - \alpha)/\alpha]. \tag{14}$$

In order to obtain the drain current, we assume the gradual channel approximation and the total drain current is expressed with the drift-diffusion formulation as [25]

$$I_{ds} = (2\pi R)\mu Q dV/dy \tag{15}$$

where μ is the effective mobility of mobile carriers. Integrating (15) with respect to y and using current continuity in the channel gives

$$I_{ds} = \mu\frac{2\pi R}{L}\int_{V_s}^{V_d} Q(V)dV = \mu\frac{2\pi R}{L}\int_{\alpha_s}^{\alpha_d} Q(\alpha)\frac{dV}{d\alpha}d\alpha \tag{16}$$

where L denotes the channel length, α_s and α_d correspond to source side ($V = 0$) and drain side ($V = V_{\rm ds}$), respectively. $dV/d\alpha$ is obtained using (8) as

$$dV/d\alpha = (kT/q)[1/(1 - \alpha) + 2/\alpha + 2m/\alpha^2 + 6n(1 - \alpha)^2/\alpha^4]. \tag{17}$$

Integrating the expression in (16), we get

$$I_{ds} = \frac{8\pi\varepsilon_{\rm si}\mu}{L}\left(\frac{kT}{q}\right)^2[f(\alpha_d) - f(\alpha_s)] \tag{18}$$

where $f(\alpha)$ is given as

$$f(\alpha)=-\frac{2}{\alpha}-\ln(\alpha)+m\left(-\frac{1}{\alpha^2}+\frac{2}{\alpha}\right)+n\left(\frac{6}{\alpha}-\frac{9}{\alpha^2}+\frac{6}{\alpha^3}-\frac{3}{2\alpha^4}\right). \tag{19}$$

B. Terminal Charges

The analytical expression for terminal charges associated with gate, source, and drain terminals are essential for the calculation of trans-capacitances and for ac/transient circuit simulations. The gate charge can be computed directly by integrating the inversion charge density along the channel as

$$\begin{aligned} Q_g &= 2\pi R\int_0^L Q(y)\,dy = (2\pi R)^2\frac{\mu}{I_{ds}}\int_{\alpha_s}^{\alpha_d} Q^2(\alpha)\frac{dV}{d\alpha}d\alpha \\ &= 8\pi\varepsilon_{\rm si}L(kT/q)[g(\alpha_d)-g(\alpha_s)]/[f(\alpha_d)-f(\alpha_s)] \end{aligned} \tag{20}$$

where $g(\alpha_s)$ and $g(\alpha_d)$ are obtained from (21), as shown at the bottom of this page.

On the account of current continuity in the channel, current at any point y must be equal to the drain side current. Using this fact and (18) lead to

$$y/L=[f(\alpha)-f(\alpha_s)]/[f(\alpha_d)-f(\alpha_s)]. \tag{22}$$

Now, the drain and source terminal charges can be computed using Ward–Dutton charge partition scheme [26] as

$$Q_d = 8\pi\varepsilon_{\rm si}L\frac{kT}{q}W_{\rm sd}$$

and

$$Q_s = 8\pi\varepsilon_{\rm si}L\frac{kT}{q}W_{ds} \tag{23}$$

where

$$W_{ij}=\frac{f(\alpha_i)[g(\alpha_j)-g(\alpha_i)]+[h(\alpha_j)-h(\alpha_i)]}{[f(\alpha_j)-f(\alpha_i)]^2} \tag{24}$$

where i and j denote s/d and $h(\alpha_i)$ and $h(\alpha_j)$ are calculated using (25), as shown at the bottom of this page. The above-mentioned analytical expressions for the terminal charges take $0/0$ form for $V_{\rm ds}=0$ V. For $V_{\rm ds}=0$ V, an inversion charge density at every point in the channel remains the same and equal to the source side charge density. Thus, $Q(y)$ in (20) can be taken out of the integration. Substituting $Q(y)$ for source side from (14) then leads to the following expressions for the terminal charges:

$$Q_g=-2Q_s=-2Q_d=8\pi\varepsilon_{\rm si}L(kT/q)[(1-\alpha_s)/\alpha_s]. \tag{26}$$

All the nine capacitances can now be calculated using analytical expressions of the terminal charges.

III. Results and Discussion

A. Drain Current

In order to validate the compact model, we compare the electrical characteristics obtained by calculating α_s and α_d numerically and using our explicit modeling approach. We have implemented our model in Verilog-A to obtain these characteristics. Fig. 3(b) shows $I_{\rm ds}-V_{\rm gs}$ characteristic for different $t_{\rm fe}$. It shows a lower SS and higher ON current compared to baseline GAA-FET. Both of these quantities improve with increase in $t_{\rm fe}$, showing optimum values for $t_{\rm fe}=8$ nm without entering the hysteresis region. Moreover, the GAA-NCFET exhibits approximately the same OFF-state current as the baseline GAA-FET, unlike the bulk NCFET which has been shown to exhibit a higher OFF-state current compared to bulk MOSFET [11]. The absence of bulk charge in undoped/lightly doped body of GAA-NCFET and a very small inversion charge in the subthreshold regime lead to a negligible voltage drop across the ferroelectric-oxide stack as evident from (6). Thus, $\psi_s\approx V_g-\Delta\phi$ that results in approximately the same OFF currents irrespective of the values of $t_{\rm fe}$ and $t_{\rm ins}$ [21], [27]. Fig. 4(a) and (b) compare the $I_{\rm ds}-V_{\rm gs}$ and transconductance (g_m) characteristics of the GAA-NCFET for optimum $t_{\rm fe}=8$ nm with the baseline GAA-FET ($t_{\rm fe}=0$ nm) for $V_{\rm ds}=50$ mV and $V_{\rm ds}=1.0$ V. Interestingly, g_m exhibits different behaviors in the linear ($V_{\rm ds}=50$ mV) and saturation ($V_{\rm ds}=1$ V) regions as shown in Fig. 4(b). To analyze the transconductance characteristics, we calculate g_m using (18) and (14) in terms of source ($Q|_{y=0}$) and drain ($Q|_{y=L}$) end mobile charge density as

$$g_m=\mu\frac{8\pi\varepsilon_{\rm si}}{L}\frac{kT}{q}\left(\frac{1}{\alpha_s}-\frac{1}{\alpha_d}\right)=2\pi R\frac{\mu}{L}(Q|_{y=0}-Q|_{y=L}). \tag{27}$$

g_m depends on the difference between mobile charge densities at the source and drain ends. For $V_{\rm ds}=1.0$ V, channel near the drain end gets pinched off resulting in $Q|_{y=L}\approx 0$. Now, since $Q|_{y=0}$ continues its increasing behavior with $V_{\rm gs}$,

$$g(\alpha)=-\frac{1}{\alpha^2}+\frac{3}{\alpha}+\ln(\alpha)+m\left(-\frac{2}{3\alpha^3}+\frac{2}{\alpha^2}-\frac{2}{\alpha}\right)+n\left(-\frac{6}{5\alpha^5}+\frac{6}{\alpha^4}-\frac{12}{\alpha^3}+\frac{12}{\alpha^2}-\frac{6}{\alpha}\right) \tag{21}$$

$$\begin{aligned} h(\alpha) =& -\frac{4}{3\alpha^3}+\frac{5}{2\alpha^2}+\frac{1}{\alpha}-\frac{\ln(\alpha)}{\alpha^2}+\frac{3\ln(\alpha)}{\alpha}+\frac{\ln^2(\alpha)}{2}-m\left(\frac{3}{2\alpha^4}-\frac{43}{9\alpha^3}+\frac{9}{2\alpha^2}+\frac{2-6\alpha+6\alpha^2}{3\alpha^3}\ln(\alpha)\right) \\ &-n\left[\left(\frac{6}{\alpha}-\frac{12}{\alpha^2}+\frac{12}{\alpha^3}-\frac{6}{\alpha^4}+\frac{6}{5\alpha^5}\right)\ln(\alpha)+\frac{27}{2\alpha^2}-\frac{27}{\alpha^3}+\frac{207}{8\alpha^4}-\frac{633}{50\alpha^5}+\frac{5}{2\alpha^6}\right]-m^2\left(\frac{2}{5\alpha^5}-\frac{2}{\alpha^4}+\frac{10}{3\alpha^3}-\frac{2}{\alpha^2}\right) \\ &-n^2\left(-\frac{18}{\alpha^2}+\frac{66}{\alpha^3}-\frac{117}{\alpha^4}+\frac{621}{5\alpha^5}-\frac{84}{\alpha^6}+\frac{36}{\alpha^7}-\frac{9}{\alpha^8}+\frac{1}{\alpha^9}\right)-mn\left(-\frac{12}{\alpha^2}+\frac{32}{\alpha^3}-\frac{39}{\alpha^4}+\frac{129}{5\alpha^5}-\frac{9}{\alpha^6}+\frac{9}{7\alpha^7}\right) \end{aligned} \tag{25}$$

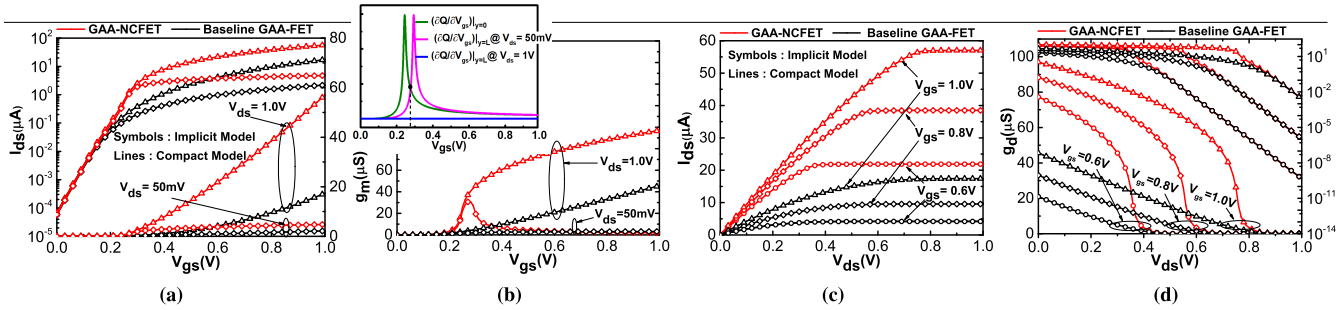

Fig. 4. (a) I_{ds}–V_{gs} of GAA-NCFET and baseline GAA-FET for $V_{ds} = 50$ mV and $V_{ds} = 1.0$ V in linear (right y-axis) and in log (left y-axis) scale. (b) Transconductance (g_m) versus V_{gs}. Inset: capacitance densities at the source ($y = 0$) and drain ($y = L$) end versus gate voltage for $V_{ds} = 50$ mV and $V_{ds} = 1.0$ V. The point is marked for $V_{ds} = 50$ mV, where both end capacitance densities are equal, the peak in g_m is occurred for this corresponding value of V_{gs}. (c) I_{ds}–V_{ds} of GAA-NCFET and baseline GAA-FET for different V_{gs} values. I_{ds} saturates approximately at the same V_{ds} value as that of baseline GAA-FET unlike the case of bulk NCFET in which it saturates at a higher drain voltage than the baseline bulk MOSFET. (d) Output Conductance g_d. We have assumed that $\mu = 300$ cm^2/Vs, $\Delta\phi = -0.3$ V, $L = 1$ μm, $t_{fe} = 8$ nm, $R = 10$ nm, and $t_{ins} = 1$ nm to obtain the characteristics GAA-NCFET.

so does g_m. However, for $V_{ds} = 50$ mV, g_m exhibits a peak and decreases afterward with V_{gs}. To understand this behavior, we differentiate (27) to get

$$\frac{dg_m}{dV_{gs}} = 2\pi R\frac{\mu}{L}\left[\left.\frac{\partial Q}{\partial V_{gs}}\right|_{y=0} - \left.\frac{\partial Q}{\partial V_{gs}}\right|_{y=L}\right] \tag{28}$$

where $(\partial Q/\partial V_{gs})|_{y=0}$ and $(\partial Q/\partial V_{gs})|_{y=L}$ are the gate capacitance densities at the source and drain ends, respectively, which are shown in Fig. 4(b) (inset). The peak in g_m occurs at that value of V_{gs}, where $\left.(\partial Q/\partial V_{gs})\right|_{y=0} = \left.(\partial Q/\partial V_{gs})\right|_{y=L}$. For higher V_{gs} values, $\left.(\partial Q/\partial V_{gs})\right|_{y=L} > \left.(\partial Q/\partial V_{gs})\right|_{y=0}$, and therefore, g_m starts to decrease. However, there is no decreasing trend in g_m for $V_{ds} = 1.0$ V, as $\left.(\partial Q/\partial V_{gs})\right|_{y=L} < \left.(\partial Q/\partial V_{gs})\right|_{y=0}$ for all V_{gs} values.

Fig. 4(c) and (d) shows $I_{ds} - V_{ds}$ and g_d characteristics of GAA-NCFET and GAA-FET, respectively. The drain current for GAA-NCFET saturates at the same drain saturation voltage (V_{dsat}) as that of GAA-FET. In the saturation region, charge density at the drain side is approximately zero which implies $\beta_d \approx 0$ from (7). For these very small values of β_d, only the first term in LHS of (8) ($\ln(\beta_d)$) dominates, and hence, (8) reduces to

$$\ln(\beta_d) \approx (q/2kT)(V_{gs} - \Delta\phi - V_{dsat}) - \ln(2L_{Di}/R). \tag{29}$$

Equation (29) is independent of the ferroelectric material parameters which results in the same V_{dsat} expression as for GAA-FET. In fact, V_{dsat} of NCFET and the corresponding baseline FET will always be the same (for any long-channel geometry: GAA, FinFET or double gate, and so on) when the body is undoped. In general, the V_{dsat} value can be evaluated by applying the voltage balance condition at the drain end where the only difference between NCFET and baseline FET comes through the ferroelectric voltage drop term V_{fe} (zero for baseline FET). V_{fe} is a function of only the gate charge density which is equal to the mobile charge density (Q) for an undoped body. As Q is negligible for the pinched-off condition, V_{dsat} is governed by the same equation for both the NCFET and baseline FET since V_{fe} becomes zero. This is in contrast with the behavior of bulk NCFET in which the addition of ferroelectric material lowers its threshold

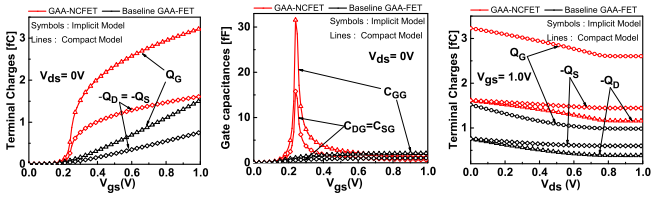

Fig. 5. (a) Comparison of GAA-NCFET and baseline GAA-FET for (a) variation of gate, drain, and source terminal charges with V_{gs} at $V_{ds} = 0$ V, (b) corresponding gate voltage-related capacitances at $V_{ds} = 0$ V, and (c) terminal charges versus drain voltage at $V_{gs} = 1.0$ V. In the saturation region, $Q_g \simeq 4Q_{g0}/5$ for GAA-NCFET, in contrast to the conventional approximation of $Q_g \simeq 2Q_{g0}/3$ for GAA-FET and bulk MOSFET, where Q_{g0} is the maximum value of gate terminal charge at $V_{ds} = 0$ V.

voltage compared to baseline MOSFET (due to the presence of bulk charges $V_{fe} \neq 0$), resulting in a higher drain saturation voltage [11].

In the ON-state, the saturation value of the drain current (I_{dsat}) for GAA-NCFET shows a bias dependence different from GAA-FET. In this case, α_s and α_d are close to 0 and 1, respectively. Using these approximations in (18), I_{dsat} can be expressed as

$$I_{dsat} \approx -(8\pi\varepsilon_{si}\mu/L)(kT/q)^2 f(\alpha_s) \tag{30}$$

where $f(\alpha_s) \approx -3n/2\alpha_s^4$ from (19) and $\alpha_s \approx (n/G)^{1/3}$ from (8). Thus, for GAA-NCFET, $I_{dsat} \propto (V_{dsat})^{4/3}$ in contrast to $I_{dsat} \propto (V_{dsat})^2$ for the conventional long-channel FETs.

B. Terminal Charges and Capacitances

The variations of gate, drain, and source terminal charges and the corresponding capacitances with V_{gs} for $V_{ds} = 0$ V are shown in Fig. 5(a) and (b), respectively. The source and the drain terminal charges are identical due to the existence of symmetry at $V_s = V_d$. In the case of GAA-NCFET, in the low V_{gs} window, the polarization value of ferroelectric dipoles is also low. Thus, all of them lie in the negative capacitance zone that boosts the gate terminal charge (Q_g) and effectively increases the gate-related capacitances (C_{gg}, C_{sg}, and C_{dg}). However, as V_{gs} is increased further, the increase in Q_g becomes rather gradual as the dipoles

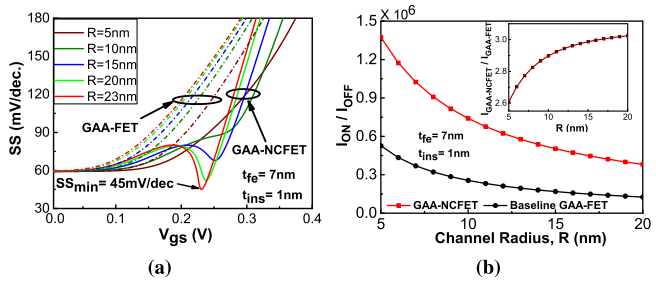

Fig. 6. (a) SS versus gate voltage for different channel radii for GAA-NCFET (solid lines) and GAA-FET (dashed lines). $SS_{\min}$ decreases as R increases for the same t_{fe}. (b) Comparison of I_{ON}/I_{OFF} ratio of the GAA-NCFET and the GAA-FET as a function of the channel radius. Inset: variation of the ON currents ratio of GAA-NCFET and GAA-FET with channel radius.

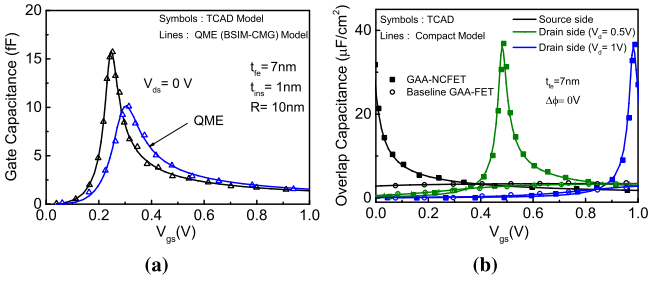

Fig. 7. (a) Gate capacitance of GAA-NCFET with and without QME at $V_{ds} = 0$ V. The QME effectively diminishes the benefits achievable from NC effect. (b) Comparison of overlap capacitances between the baseline GAA-FET and GAA-NCFET at the source and drain side.

enter the positive capacitance zone, which leads to decrease in C_{gg}, C_{sg}, and C_{dg}. Fig. 5(c) shows the terminal charges as a function of V_{ds} for $V_{gs} = 1$ V. In the strong inversion region, $\alpha_s = 1 - \beta_s{}^2$ becomes very small [as $\beta_s \approx 1$ (see Fig. 2)]. For $V_{ds} = 0$, terminal charges are maximum and their expressions for both the GAA-NCFET and GAA-FET can be approximated as $Q_{g0} = -2Q_{s0} = -2Q_{d0} \simeq 8\pi\varepsilon_{si}LkT/q\alpha_s$. Since α_s of GAA-NCFET is smaller than GAA-FET, its Q_{g0} value is higher. As V_{ds} is increased, terminal charges decrease and saturate at high V_{ds}. In the saturation region, $\alpha_d \approx 1$, and after considering only the dominant terms in (20), the expression of Q_g simplifies to $Q_g \simeq 4\ Q_{g0}/5$ for GAA-NCFET. This is in contrast to the conventional approximation of $Q_g \simeq 2\ Q_{g0}/3$ for GAA-FET and bulk MOSFET [25], [28], [29]. However, partitioning of charges in this region remains the same for both the FETs, given by $Q_s \simeq -6Q_g/10$ and $Q_d \simeq -4Q_g/10$.

C. Radius Dependence

Fig. 6(a) shows the SS characteristics for different channel radii with $t_{fe} = 7$ nm. Since the coefficients a_0 and b_0 are functions of the channel radius, it also plays an important role in the ferroelectric capacitance tuning. An increase in R increases the values of a_0 and b_0 which improves the matching of the ferroelectric and internal GAA-FET capacitances. Therefore, the minimum SS ($SS_{\min}$) and the ON-current of GAA-NCFET improve with the increase in R as shown in Fig. 6(a) and Fig. 6(b) (inset). A large R (>23 nm) can also produce a hysteresis in the $I_{ds} - V_{gs}$ characteristics. The I_{ON}/I_{OFF} ratio decreases with R for both the GAA-NCFET and GAA-FET as shown in Fig. 6(b). I_{OFF} is proportional to cross-sectional area of the channel (volume inversion effect), and I_{ON} is proportional to the perimeter of the channel (surface inversion effect) [21], thus the I_{ON}/I_{OFF} ratio is inversely proportional to R for both FETs. GAA-NCFET exhibits the higher I_{ON}/I_{OFF} ratio for all values of R because of its high ON-current.

D. Quantum Mechanical Effect

The quantum mechanical effect (QME) in a transistor is significant where the transverse field is the highest, i.e., near the source end [25]. Therefore, for compact model, we only consider QME at the source end which is a standard approach followed in Berkeley short-channel IGFET model (BSIM) models [17]. Since the impact of drain bias near the source is negligible in our long channel structure, the capacitance divider formed of ferroelectric capacitance (C_{fe}) and internal FET (C_{int}) capacitance at this end remain unaffected by it. Thus, we can model QME in C_{int} similar to the case of regular GAAFETs (i.e., assuming $V_{ds} = 0$ V) and simply add the C_{fe} in series with it. We utilize the charge centroid model of QME from BSIM-common multi-gate [17]. Thus, the total gate capacitance C_{gg} is obtained by self-consistently solving the internal FET equations including QME with L–K equation of ferroelectric. Moreover, as $V_{ds} = 0$ V is assumed, the MFIS structure considered in our paper behaves similar to the MFMIS structure [11]. Therefore, for model validation, the same TCAD approach as in the case of MFMIS NCFET can be used for MFIS NCFET too [24], [30]. The gate capacitances with and without including QME are shown in Fig. 7(a) and are validated with the gate capacitance obtained from Sentaurus TCAD for the MFMIS structure at $V_{ds} = 0$ V. The C_{gg} can be written in terms of C_{int} and C_{fe} as

$$C_{gg} = (|C_{fe}|C_{int})/(|C_{fe}| - C_{int}). \tag{31}$$

QME results in an increase in the effective oxide thickness of the internal FET causing a reduction in C_{int} which in turn disturbs the capacitance matching between C_{int} and C_{fe}. This leads to a reduction in C_{gg} as shown in Fig. 7(a).

E. Overlap Capacitance

For modeling of overlap capacitances, we have considered the overlap regions at the source and drain ends as MFMIS capacitors, as there will be a negligible voltage drop across these regions. We have obtained the overlap charge densities by simulating MFMIS capacitors via coupling the internal FET electrostatics simulated in Sentaurus TCAD to the L–K equation of ferroelectric in a self-consistent manner [24], [30] for the model validation. The overlap charge densities are then modeled as follows.

1) We assume that the overlap region is fully depleted when the internal gate voltage (V_{int}) of the MFMIS structure is close to zero or negative (note that overlap regions have n-type doping). The overlap depletion charge density in this case is given as

$$Q_{dep} = (qN_DV)/A \tag{32}$$

where N_D is the doping concentration of source/drain region, $V = \pi R^2 L_{\rm ov}, A = 2\pi R L_{\rm ov}$, and $L_{\rm ov}$ are the volume, area, and length of the overlap region, respectively.

2) When $V_{\rm int}$ is more positive, the accumulation charge density in the overlap region is proportional to the difference between the internal gate voltage ($V_{{\rm int}_{s/d}}$) at source and drain sides and source and drain voltages ($V_{s/d}$) which is modeled as

$$Q_{\rm acc} = -C_{\rm ins}[(V_{\rm int})_{s/d} - V_{s/d}] \tag{33}$$

where $C_{\rm ins}$ is the insulator capacitance. Finally, the gate overlap charge density $Q_{\rm ov}$ is modeled by connecting the charge densities in the above-mentioned two extreme cases, i.e., $Q_{\rm dep}$ (in depletion) and $Q_{\rm acc}$ (in accumulation) using the following smoothing function:

$$Q_{\rm ov} = -0.5\left[Q_{\rm acc} + Q_{\rm dep} - \sqrt{(Q_{\rm acc} - Q_{\rm dep})^2 + 4\delta}\right] \tag{34}$$

where δ is a smoothing parameter. $Q_{\rm ov}$ in (34) is a direct function of $V_{\rm int}$. To obtain $Q_{\rm ov}$ for a given external gate bias V_g, (34) is solved self-consistently with L–K model in Verilog-A code. The overlap capacitances $(C_{\rm ov})_{s/d} = \partial(Q_{\rm ov})_{s/d}/\partial V_g$ obtained from the model at the source and drain sides are shown in Fig. 7(b) and also validated with the TCAD simulations. $C_{\rm ov}$ exhibits a peak in a region where negative ferroelectric capacitance matches closely with the baseline overlap capacitance. As the internal gate is not present in the MFIS structure, the overlap and fringing capacitances have only a local impact at the source and drain side which does not affect internal FET capacitance much in a long channel structure. On the contrary, in MFMIS structure, due to the presence of internal metal gate the parasitic capacitances directly add up to the internal FET capacitance which strongly affects capacitance matching between the internal FET and the ferroelectric layer along the channel [31]. However, for short-channel structures, the parasitic capacitances can have a considerable impact even in the case of MFIS NCFET [12].

F. Transient Analysis of Ring Oscillator

We test the transient capability of our compact model by simulating a 17-stage RO built using complementary GAA-NCFETs (NC-RO) and also compare its transient response with the reference RO (Ref-RO) built using the corresponding GAA-FETs in Fig. 8(a). As shown in Fig. 8(a), NC-RO performs faster than Ref-RO for $V_{\rm dd} = 0.6$ V. Fig. 8(b) compares the propagation delay per stage ($\tau_{\rm pd}$) of the two ROs as a function of supply voltage. NC-RO shows $\approx$ 30 % reduction in the propagation delay at $V_{\rm dd} = 0.6$ V and $\approx$110 mV reduction in $V_{\rm dd}$ at the same propagation delay, compared with Ref-RO. The better performance of NC-RO is observed because of GAA-NCFET's higher ON-current than GAA-FET. However, for very low-supply voltages (say $V_{\rm dd} < 0.35$ V), the delay improvement over Ref-RO becomes less due to sharp rise in the gate capacitance in this regime [see Fig. 5(b)].

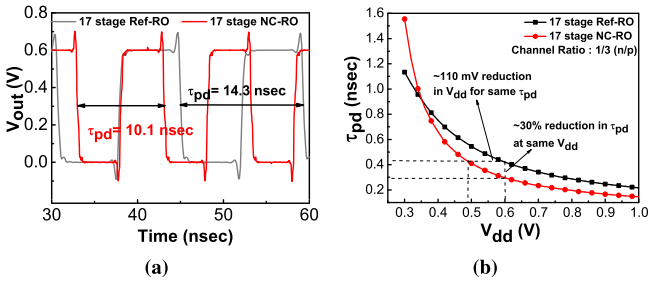

Fig. 8. (a) Simulated transient response comparison of a 17-stage RO at $V_{\rm dd} = 0.6$ V. (b) Propagation delay per stage as a function of supply voltage. Mobility of electrons and holes assumed in the drain current calculation are 300 and 100 cm^2/Vs, respectively. To compensate low value of hole mobility, we have assumed three nanowire channels for p-FETs. The device parameters used for GAA-NCFET are $t_{\rm fe} = 8$ nm, $t_{\rm ins} = 1$ nm, $R = 10$ nm, and $\Delta\phi = -0.3$ V.

IV. Conclusion

We have presented a Verilog-A implementable surface potential-based core model of long channel MFIS-GAA-NCFET including the radial dependence of electric field in the ferroelectric layer. Analytical expressions for the drain current and the terminal charges have been derived in terms of intermediate parameters which are evaluated using a computationally efficient algorithm. We have also analyzed the electrical characteristics of GAA-NCFET. A distinctive feature of GAA-NCFET compared to bulk-NCFET is that the addition of ferroelectric layer in the gate stack does not change its OFF-current and the drain saturation voltage because of the absence of bulk charges. In comparison to GAA-FET, the saturation current is proportional to $(V_{\rm dsat})^{4/3}$. Moreover, for high drain biases, the gate terminal charge for GAA-NCFET is found to saturate to (4/5) of the maximum value (at $V_{\rm ds} = 0$) in contrast to conventional devices for which it saturates to (2/3) of the maximum value. The QME degrades the performance of NCFETs by affecting the capacitance matching between the internal FET and ferroelectric layer, whereas the overlap and fringing capacitances will have local effect in long-channel MFIS structure in contrast to the MFMIS structure. The robustness of the model for transient simulations is demonstrated by simulating an RO circuit. The GAA-NCFET performs faster than GAA-FET for higher $V_{\rm dd}$. However, for low supply voltages, the performance improvement in the propagation delay is impeded by a large rise in the gate capacitance. It is worth mentioning here that the damping effect of the ferroelectric material of GAA-NCFET which we have neglected in this paper will influence the maximum speed of the circuit and can be a topic of future research.

Appendix

Poisson's equation in the cylindrical coordinate is given as

$$(1/\rho)\partial(\rho D(\rho))/\partial\rho = 0 \tag{35}$$

This article has been accepted for inclusion in a future issue of this journal. Content is final as presented, with the exception of pagination.

where $D(\rho)$ is the radial component of displacement vector. First, D at the boundary between the ferroelectric and intermediate insulator layer is calculated by integrating (35) from $\rho = R$ to $\rho = R + t_{\text{ins}}$ as

$$D|_{R+t_{\text{ins}}} = [R/(R + t_{\text{ins}})]D|_R \tag{36}$$

where $D|_{R+t_{\text{ins}}}$ is the displacement vector at $\rho = R + t_{\text{ins}}$ and $D|_R$ is the displacement vector at $\rho = R$ which is equal to $-Q$ (mobile charge density). Now, we can calculate the $D(\rho)$ in the ferroelectric layer by integrating (35) from $\rho = R + t_{\text{ins}}$ to ρ, which gives

$$D(\rho) = [(R + t_{\text{ins}})/\rho]D|_{R+t_{\text{ins}}} = -RQ/\rho. \tag{37}$$

Finally, the voltage across ferroelectric layer (V_{fe}) is calculated using Landau–Devonshire theory [22] as

$$V_{\text{fe}} = \int_{R+t_{\text{ins}}}^{R+t_{\text{ins}}+t_{\text{fe}}} -E(\rho)d\rho = \int_{R+t_{\text{ins}}}^{R+t_{\text{ins}}+t_{\text{fe}}} -[2aP(\rho) + 4bP(\rho)^3]d\rho$$

where $E(\rho)$ and $P(\rho)$ are the electric field and the polarization in the ferroelectric layer, respectively. $P(\rho)$ in the ferroelectric can be approximated as $P(\rho) = D(\rho) - \varepsilon_0 E \approx D(\rho)$ (for small voltages considered in this paper), which yields

$$V_{\text{fe}} = \int_{R+t_{\text{ins}}}^{R+t_{\text{ins}}+t_{\text{fe}}} -[2aD(\rho) + 4bD(\rho)^3]d\rho. \tag{38}$$

By solving (38), we get V_{fe} in terms of Q as given in (2).

References

[1] S. Salahuddin and S. Datta, "Use of negative capacitance to provide voltage amplification for low power nanoscale devices," *Nano Lett.*, vol. 8, no. 2, pp. 405–410, 2007.

[2] A. Rusu, G. A. Salvatore, D. Jiménez, and A. M. Ionescu, "Metal-Ferroelectric-Meta-Oxide-semiconductor field effect transistor with sub-60mV/decade subthreshold swing and internal voltage amplification," in *IEDM Tech. Dig.*, Dec. 2010, pp. 16.3.1–16.3.4.

[3] A. Khan, C. Yeung, C. Hu, and S. Salahuddin, "Ferroelectric negative capacitance MOSFET: Capacitance tuning and antiferroelectric operation," in *IEDM Tech. Dig.*, Dec. 2011, pp. 11.3.1–11.3.4.

[4] K. S. Lee *et al.*, "Sub-60mV-swing negative-capacitance FinFET without hysteresis," in *IEDM Tech. Dig.*, Dec. 2015, pp. 22.6.1–22.6.4.

[5] T. Dutta, G. Pahwa, A. R. Trivedi, S. Sinha, A. Agarwal, and Y. S. Chauhan, "Performance evaluation of 7-nm node negative capacitance FinFET-based SRAM," *IEEE Electron Device Lett.*, vol. 38, no. 8, pp. 1161–1164, Aug. 2017.

[6] X. Li *et al.*, "Enabling energy-efficient nonvolatile computing with negative capacitance FET," *IEEE Trans. Electron Devices*, vol. 64, no. 8, pp. 3452–3458, Aug. 2017.

[7] I. Lauer *et al.*, "Si nanowire CMOS fabricated with minimal deviation from RMG FinFET technology showing record performance," in *Proc. Symp. VLSI Technol. (VLSI Technol.)*, Jun. 2015, pp. T140–T141.

[8] S.-G. Hur *et al.*, "A practical Si nanowire technology with nanowire-on-insulator structure for beyond 10 nm logic technologies," in *IEDM Tech. Dig.*, Dec. 2013, pp. 26.5.1–26.5.4.

[9] S. Bangsaruntip *et al.*, "Gate-all-around silicon nanowire 25-stage CMOS ring oscillators with diameter down to 3 nm," in *Proc. Symp. VLSI Technol.*, Jun. 2010, pp. 21–22.

[10] K. Nayak *et al.*, "CMOS logic device and circuit performance of Si gate all around nanowire MOSFET," *IEEE Trans. Electron Devices*, vol. 61, no. 9, pp. 3066–3074, Sep. 2014.

[11] G. Pahwa, T. Dutta, A. Agarwal, and Y. S. Chauhan, "Compact model for ferroelectric negative capacitance transistor with MFIS structure," *IEEE Trans. Electron Devices*, vol. 64, no. 3, pp. 1366–1374, Mar. 2017.

[12] J. P. Duarte *et al.*, "Compact models of negative-capacitance FinFETs: Lumped and distributed charge models," in *IEDM Tech. Dig.*, Dec. 2016, pp. 30.5.1–30.5.4.

[13] Y. G. Xiao *et al.*, "Simulation of electrical characteristics in negative capacitance surrounding-gate ferroelectric field-effect transistors," *Appl. Phys. Lett.*, vol. 101, no. 25, p. 253511, 2012.

[14] C. Jiang, R. Liang, J. Wang, and J. Xu, "Analytical drain current model for long-channel gate-all-around negative capacitance transistors with a metal–ferroelectric–insulator–semiconductor structure," *Jpn. J. Appl. Phys.*, vol. 55, no. 2, p. 024201, 2016.

[15] Z. C. Yuan *et al.*, "Switching-speed limitations of ferroelectric negative-capacitance FETs," *IEEE Trans. Electron Devices*, vol. 63, no. 10, pp. 4046–4052, Apr. 2016.

[16] M. Kobayashi, N. Ueyama, K. Jang, and T. Hiramoto, "Experimental study on polarization-limited operation speed of negative capacitance FET with ferroelectric HfO_2," in *IEDM Tech. Dig.*, Dec. 2016, pp. 12.3.1–12.3.4.

[17] Y. S. Chauhan *et al.*, *FinFET Modeling for IC Simulation and Design: Using the BSIM-CMG Standard*. San Francisco, CA, USA: Academic, 2015.

[18] A. I. Khan, U. Radhakrishna, K. Chatterjee, S. Salahuddin, and D. A. Antoniadis, "Negative capacitance behavior in a leaky ferroelectric," *IEEE Trans. Electron Devices*, vol. 63, no. 11, pp. 4416–4422, Nov. 2016.

[19] Z. Dong and J. Guo, "A simple model of negative capacitance FET with electrostatic short channel effects," *IEEE Trans. Electron Devices*, vol. 64, no. 7, pp. 2927–2934, Jul. 2017.

[20] B. Yu, H. Lu, M. Liu, and Y. Taur, "Explicit continuous models for double-gate and surrounding-gate MOSFETs," *IEEE Trans. Electron Devices*, vol. 54, no. 10, pp. 2715–2722, Oct. 2007.

[21] D. Jiménez *et al.*, "Continuous analytic I-V model for surrounding-gate MOSFETs," *IEEE Electron Device Lett.*, vol. 25, no. 8, pp. 571–573, Aug. 2004.

[22] A. F. Devonshire, "XCVI. Theory of barium titanate," *London, Edinburgh, Dublin Philos. Mag. J. Sci.*, vol. 40, no. 309, pp. 1040–1063, 1949.

[23] S. Mueller *et al.*, "Incipient ferroelectricity in al-doped HfO_2 thin films," *Adv. Funct. Mater.*, vol. 22, no. 11, pp. 2412–2417, 2012.

[24] G. Pahwa *et al.*, "Analysis and compact modeling of negative capacitance transistor with high ON-current and negative output differential resistance—Part I: Model description," *IEEE Trans. Electron Devices*, vol. 63, no. 12, pp. 4981–4985, Dec. 2016.

[25] Y. Tsividis and C. McAndrew, *Operation and Modeling of the MOS Transistor*. New York, NY, USA: Oxford Univ. Press, 2011.

[26] D. E. Ward and R. W. Dutton, "A charge-oriented model for MOS transistor capacitances," *IEEE J. Solid-State Circuits*, vol. 13, no. 5, pp. 703–708, Oct. 1978.

[27] Y. Taur, "An analytical solution to a double-gate MOSFET with undoped body," *IEEE Electron Device Lett.*, vol. 21, no. 5, pp. 245–247, May 2000.

[28] B. Yu, W. Y. Lu, H. Lu, and Y. Taur, "Analytic charge model for surrounding-gate MOSFETs," *IEEE Trans. Electron Devices*, vol. 54, no. 3, pp. 492–496, Mar. 2007.

[29] Y. S. Chauhan *et al.*, "BSIM6: Analog and RF compact model for bulk MOSFET," *IEEE Trans. Electron Devices*, vol. 61, no. 2, pp. 234–244, Feb. 2014.

[30] G. Pahwa *et al.*, "Analysis and compact modeling of negative capacitance transistor with high ON-current and negative output differential resistance—Part II: Model validation," *IEEE Trans. Electron Devices*, vol. 63, no. 12, pp. 4986–4992, Dec. 2016.

[31] S. Khandelwal, J. P. Duarte, A. I. Khan, S. Salahuddin, and C. Hu, "Impact of parasitic capacitance and ferroelectric parameters on negative capacitance FinFET characteristics," *IEEE Electron Device Lett.*, vol. 38, no. 1, pp. 142–144, Jan. 2017.

Amol D. Gaidhane (S'16) received the M.Tech. degree in VLSI from the Center for VLSI and Nanotechnology, Visvesvaraya National Institute of Technology, Nagpur, India, in 2016. He is currently pursuing the Ph.D. degree with IIT Kanpur, Kanpur, India.

His current research interests include simulation, modeling, and fabrication of negative capacitance transistors.

This article has been accepted for inclusion in a future issue of this journal. Content is final as presented, with the exception of pagination.

Girish Pahwa (S'16) received the B.Tech. degree in electronics and communication engineering from Delhi Technological University, Delhi, India, in 2014. He is currently pursuing the Ph.D. degree with IIT Kanpur, Kanpur, India.

His current research interests include physics and modeling of negative capacitance transistors.

Amit Verma (M'18) received the Integrated M.Tech. degree in engineering physics from IIT (BHU) Varanasi, Varanasi, India, in 2010, and the Ph.D. degree in electrical engineering from the University of Notre Dame, Notre Dame, IN, USA, in 2015.

He held a post-doctoral position with Cornell University, Ithaca, NY, USA. He is currently an Assistant Professor with the Department of Electrical Engineering, IIT Kanpur, Kanpur, India.

Yogesh Singh Chauhan (SM'12) was with IBM, Bengaluru, India, from 2007 to 2010. From 2010 to 2012, he was with the University of California Berkeley, Berkeley, CA, USA. He is currently an Associate Professor with IIT Kanpur, Kanpur, India.

Dr. Chauhan is the Editor of the IEEE TRANSACTIONS ON ELECTRON DEVICES and an EDS Distinguished Lecturer.

International Journal of Recent Trends in Engineering & Research
ISSN (ONLINE) : 2455 – 1457
IMPACT FACTOR : 4.101

COMPARISON OF SCOUR AROUND DIFFERENT SHAPES OF GROYNES IN OPEN CHANNEL

Thangamani Vijaya Kumar[1], Devesh Tyagi[2], Lokesh Aggarwal[3], Munendra Kumar[4]

[1,2,3,4] *Department of Civil Engineering, Delhi Technological University, Delhi*

Abstract : Groynes are the simplest form of river training structures that are placed laterally to the flow direction and used for diverting the flow away or towards the banks. In India different shapes of groynes are used as per the necessity and desired outcome. It is a question of great value that, in given conditions which shape of groyne would be more suitable under the possible conditions of emergency? In this study the scour variation and bed variation with different shapes of groynes was investigated using experimental works. Equilibrium of bed variation in both spur dikes and difference and similarities of the pattern of scour hole formation was also identified and it is concluded that T-shaped groynes are more stable and safe in terms of scour formation. It is also found that the flow diverting capabilities of a T-shaped groyne is far more better than a straight groyne in given conditions of channel. However it is easier to construct a straight groyne and they are the most economical and easy one to design in practical world. By using the suitable contraction ratio(length of spur/width of channel) and spur ratio or contraction ratio(spacing/length) desired outputs can be obtained. In this study contraction ratio of 0.39 and spur ratio of 5 was used.

Keywords: Sediment erosion and deposition, scour, T-shaped groynes, Straight groynes

I. INTRODUCTION

Groynes are the hydraulic structures extending outward from the river bank in the lateral direction to the flow for the purpose of diverting the flow away or towards the bank to protect it. Sometimes they are provided with an inclination in order to divert the high velocity flow away from the bank so that there is minimized erosion of the bank, availability of navigable depth in the channel and increased sediment deposition near the bank of the river. Different shapes of groynes are available with their individual advantages and disadvantages. The obstruction produced by the groynes generates a complicated system of vortices which is the main cause of the scour. Basically scour is of two types (i) General scour; which include the removal of sediments from the bed without any obstruction. (ii) Local scour; which is defined as the removal of bed material from the bed around any obstruction like spur dike, piers, abutment due to the erosive action of water. This local scour makes the hydraulic structures unstable and leads to destructive consequences. Therefore, understanding the mechanism and characteristics as well as investigating flow pattern and scour around groynes are crucial. Various studies has been conducted to understand the basic scour affecting parameters and their respective variations with the geometry of groynes, but still no specific conclusion is available about the variation of scour with shapes of spur dikes. Different shapes of groynes results in different scour formations which are not acceptable from stability point of view of hydraulic structures. Speaking of groynes geometrical variations there are various shapes available such as straight, T shaped, L-shaped , hockey shaped etc. Till now the main focus was emphasized upon the straight groynes with different arrangement. It was observed from design point of view, straight groynes are the first choice of designers but every situation demands a

different solution.Therefore T-shaped groynes are more in use despite of their complex design and possible variations. In this study the formation of scour around two types of spur dikes with different shapes of head was investigated using experimental works. Two studies were conducted; first with straight groynes and second one with T-head groynes. Bed variation in both the runs was observed and differences and similarities of the pattern of scour hole was investigated. Finally an in-depth discussion about the formation of the scour and the deposition of the sediment around these two types of spur dikes was studied in order to evaluate the performance of both the spur dikes. Main aspects of this study was to highlight the factors, that controlling the bank erosion, better navigability and improving biodiversity since these are being directly affected by the shape of groyne's head. Using a series of T-head groynes would be an advantage as compared to the straight ones.

II. LITERATURE REVIEW

Mushtaq Ahamad, 1951 carried out number of tests on a model for more than one spur dike for bank protection of the river Satluj and from a series of experiments he concluded that, the optimum ratio(spacing of spur/legth of spur) for maximum bank protection should be less than or equal to 5.[1]

Garg et al,1980 found that where more than one spurs are constructed, spacing between them being was to be decided according to the angle of the spur and curvature of the flow. The spacing of such spur was proposed around 3 to 4 times their length.[2]

Shafaie et al,2008 performed an experiment to study the effect of minor spur dike on the scouring around the first spur dike in the gravel bed. Three different lengths of minor spur dike were considered with three different flow depths in the gravel bed. Minor spur dike was installed at the upstream of main spur dikes in three different spacings.They concluded that scouring was reduced when a minor spur dike was used as compared to unprotected spur dikes. Scour rate was also reduced from 33% to 10% reaching to its maximum value when the length of minor spur dike was half the length of first spur dike.[3]

M..Ghodsian et al,2010 conducted experimental investigations to analyze the shape effects on bed shear stress distribution around a straight and T-shaped spur dike. It was found that in the straight type, the region of shear stress amplification was adjacent to the upstream part of the separated shear layer whereas in T-shape this region it is shifted towards the centerline and is 35% less than that of straight one. High shear region was confined to a smaller region and is more uniform than straight groynes.[4]

Mohammed Alauddin et al,2011 investigated the response of channel against different configuration of groynes and found that the semi permeable groyne with a slight alignment towards downstream, minimized the strong return currents and the relative aspect ratio could be increased. Morever, the maintenance of these groynes is expected to be lower than that for the conventional ones, Which only added to the sustainability of the concept of inducing permeability to the groynes.[5]

M.Vaghefi et al,2012 performed experimental investigations on scour around a T-shaped spur dike in a channel bend. It was stated that when the spur dike was inclined at an angle of 30° to 45°, the height of sediment deposition ridge is higher than when the spur dike is located at sections 60° to 75°. Any change in the position of the spur dike toward the downstream portion of the bend increases the scour depth.[6]
Roger A. Kuhnle et al, 2012 carried out work on local scour around the spur dike aligned at 45°, 90°, and 135° and compared the result with the equation proposed by the Melville (1992).

@IJRTER-2018, All Rights Reserved

$$\frac{d_s}{y_\infty} = 2K_M\eta^{(1-\delta)} \qquad (1)$$

After experiment it was concluded that the scour hole was more concentrated in the 90° spur whereas it was more elongated in the case of 45° and 135°. More elongation was seen in 45° case near the wall of the flume.[7]

Kedar sharma and Pranab K. Mohapatra,2012 carried out work on separation zone in flow past a spur dike in a rigid bed meandering channel. Straight groyne was placed in meandering channel one by one on left as well as on the right bank moving in the downstream direction. Separation zone increased when moving in the downstream direction. Less separation zone was observed when groyne was placed at left bank.[8]

Saleh.I.Khassaf, Alaa Mhseen Dawood,2013 performed an experiment to compute the depth of local scour around groynes by using the spacing between the groynes as a countermeasure. Uniform cohesionless sand was used as bed material and it was observed that increasing the distance between the groynes leads to increase in depth of the scour of about 20%.[9]

Hamid Shamloo et al,2014 compares the result of numerical simulation of the angle of groyne installation on separation zone with the experimental data of the Yeo et al (2005). A total of 69 experiments were done by Yeo et al with the variation of groyne length, angle of installation and degree of permeability. The Centre of smallest eddy was at a distance equal to length of groyne whereas, the Centre of largest eddy was at a distance equal to six times the length of groyne. The separation zone for the impermeable groyne was 12 times the groyne length for groyne of length 0.3m. Incidence angle calculated of the separation zone by numerical simulation was 4.78 degree whereas through experiment it was 5 degree.[10]

Salamatian et al,2016 investigated the flow pattern and stress distribution around spur dikes located in ninety degree bend using 2D velocity meter. Experiment was done by locating the spur dikes at a spacing of 5° around ninety degree bend as (30, 35, 40, 45, 50, 55, 60, 65, 70, 75 degrees). Maximum scouring was observed in the case of 75 degree bend. Separation zone increased by increasing the distance of spur dike along the bend.[11]

Bateni et al,2017 performed an experiment to investigate the flow pattern around repelling and attracting T-head spur dikes on a flat bed. It was concluded that downflow velocity and length of the separation zone are more significant for attractive spur dikes than for repelling spur dikes. Maximum longitudinal component of velocity vector occurred at tip of the spur dike. Maximum shear stress was observed at the wing of the spur dike and this increase in shear stress around the spur dike are due to increased flow velocity and turbulence.[12]

Vijaya Kumar and Lokesh Aggarwal,2018 investigated and compared the scouring around impermeable straight groynes aligned at different angles. Groynes were installed at 45°,90° and 135° to the wall of the channel. It is concluded that scouring depth increases with increase in velocity and follows a decreasing trend along the downstream direction of the channel.[13]

@IJRTER-2018, All Rights Reserved

Vijaya Kumar and Devesh Tyagi,2018 performed experimental studies on scouring around T-head groynes in open channel. Three different configurations of flanges were used. It was observed that symmetric T-head groynes are more efficient in scour prevention and control as compared to the other forms of T-head groynes. Symmetry in flange should be preferred over the upstream and downstream shift in the flange.[14]

III. PRESENT STUDY

In this study scouring pattern for straight and T-shaped groynes was analyzed and compared in an open channel. This experiment focuses only upon measuring the local scouring around the groynes and analyzing these scouring patterns for the different shape of groynes under the similar fluvial conditions. Further it was also tried to understand the deposition mechanism of the bed material around the groynes to provide the suitable navigable depth in the channel. Both categories of groynes were tested at the same location and similar spacings without any inclination in the upstream or downstream direction of the flow.

IV. GROYNES MODELS USED

Fig.1 T-head groyne (TG) used in the study with total length of 12.5(all units in cm)

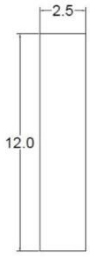

Fig.2 Straight groyne (SG) used in the study (all units in cm)

@IJRTER-2018, All Rights Reserved

Fig.3 Flow around T-shaped groynes (TG)

V. EXPERIMENTAL SETUP

All the experiments were conducted in the hydraulics laboratory of Delhi Technological University. A tiltable flume 8m long,0.40m deep and 0.32m wide was used as channel section which comprised a pumping system to recirculate the water through the channel. Flume includes a central part made up of acrylic glass sheet to observe the flow and the changes in bed profiles of the channel section. Groynes were made of wood and it was made sure that there is no change in geometrical features of the groynes after the submergence in water. Two models of spur dikes were used with a variation in their head only. Spacing between the groynes were kept constant except in the first groyne as the major effect of scouring is observed at the first groyne itself. Pointer gauge with an accuracy of 0.01% was mounted on a trolley which was attached to the flume. With the help of the trolly the pointer gauge which is movable in both directions and this was used to measure the depth of sand bed, scour around the groynes and depth of the flow. Groynes models were made of wood and a uniform sediment bed of 5cm thickness was provided in the flume. Sand bed was provided for total of 6.3m distance in the flume which started from the head gate along the flow direction. First groyne was installed at 2.5m from the head gate to allow the flow to be in regime condition initially. Spacing of 0.6m was provided in between the groynes so that erosive and deposition of sediment can be allowed. Scouring was also measured at a point 1.32m upstream of the first spur dike so that the erosive action of free flow can also be analyzed.

VI. EXPERIMENTAL PROCEDURE

Firstly, uniformity of sand bed was ensured by a wooden plank and groynes were installed at suitable locations with the help of tape and it was ensure that they do not fail during the test run. Fluid was allowed to flow in the flume from recirculation tank through centrifugal pump so as to drain the bed.

Sand bed readings were taken at the head, downstream and upstream side around the groynes. Two points were chosen (A) at 1.2m distance from the head gate and (B) after the last groyne so as to observe the scouring due to turbulence flow at (A) and deposition at (B) in the downstream direction. Main spur

dike was installed at a distance of 2.8m from the head gate so as to reduce the effect of turbulence on the scouring. Flow depth was maintained in the flume with the help of tail gate.

Pressure difference was measured with the help of tilting flume lodger at the head/tip of every groyne to maintain accuracy in measuring the discharge. Pressure difference was calculated at critical points in the channel and at the locations of groynes from which velocity and discharge at those points were calculated.

$$\frac{p_1}{\rho g} + \frac{{v_1}^2}{2g} + z_1 = \frac{p_2}{\rho g} + \frac{{v_2}^2}{2g} + z_2 \qquad (2)$$

Bernouli's equation was used to find out the velocity and further the discharge from the pressure readings.

$$Discharge = Area * velocity$$

Area is flow depth * width of the flume. Width of the flume is constant (30cm) so by varying the depth of the flow velocity can be varied.
Test run of 45 minutes for each type of groynes were made and the scour depth was measured. Shape of the scour hole, elongation and deposition in between the groynes were also analyzed. To cut out any possibility of error three runs were made for both type of groynes and average values were taken.

VII. SEDIMENT USED

Locally available sand was used as the bed material to imitate the alluvial channel. Before using the sand in the flume it was made sure that it is free from any impurities and air lumps by coarse sieving. Fine sieving was done to calculate the mean size of the particles which is 0.215mm with the geometric standard deviation of 2.625. Sieve analysis data of sand is shown in figure.4.

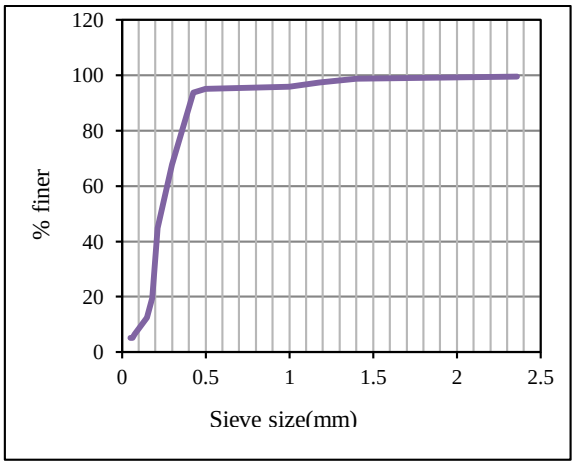

Fig.4 Sieve analysis of sand used as a bed material

VIII. FLOW CONDITIONS

Experimental runs were performed in a uniform flow conditions and a smooth entry of flow into the channel was ensured by adjusting a suitable floating wooden plank at the entrance of flow into the channel. This way the turbulence was prevented to hit the bed material. Any unwanted erosion in the

channel was minimized by keeping the flow below the incipient condition by physical observation of the regime of channel bed.The flow was kept uniform and subcritical with the help of flow controlling valves provided with pumping set. A horizontal channel was ensured by controlling the longitudinal slope and channel bed was levelled with a horizontal plank so that the bed material remains uniformly distributed throughout the channel.

IX. RESULTS AND DISCUSSION

Scour depth for both shapes of groynes was calculated and their respective erosion rate was found to be influenced by the flow rate.

Scour depth Variation

Test Run-1: T-shaped groynes (TG)

It is evident from the Figure.5 that for T-shaped groynes,the scour depth increases initially and reaches a maximum value and then starts decreasing, reaching its minimum value towards the end of the channel while the velocity follows a decreasing trend throughout the channel. Obstruction effects are minimum in the channel and scour occurs maximum in the latter stages of the channel.

Table.1 Observation table for T-shaped groynes(TG)

	Flow depth (cm)	Velocity (m/s)	Discharge (l/s)	Scour depth (cm)
TG_1	7.5	0.54	12.96	0.9
TG_2	7.8	0.53	13.2	1.6
TG_3	7.7	0.525	13.03	1.7
TG_4	8.7	0.52	14.8	1.2
TG_5	7.9	0.517	13.06	1

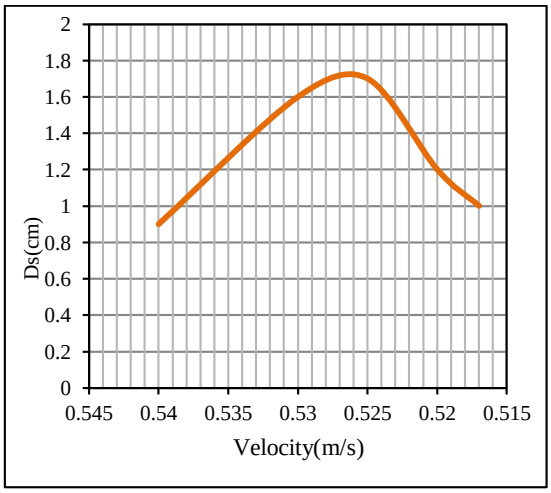

Fig.5 Variation of scour depth with velocity for T-shaped groynes(TG)

Fig.6 *Scour around T-shaped groyne (TG)*

Fig.7 *Sand bed after test run for T-shaped groynes(TG)*

Test Run-2: Straight groynes (SG)

From figure.8 it is concluded that for straight groynes the scour depth follows a decreasing trend along the flow in the downstream direction. Velocity also decreases as the flow reaches the end of the channel. It is observed that the scour depth is considerably large in the upstream portion of the channel and in the downstream portion of the channel it decreases.

@IJRTER-2018, All Rights Reserved

Table.2 *Observation table for straight groynes(SG)*

	Flow depth (cm)	Velocity (m/s)	Discharge (l/s)	Scour depth (cm)
SG_1	5.7	0.525	7.34	2.4
SG_2	5.7	0.517	9.42	2.23
SG_3	5.3	0.514	8.71	2.1
SG_4	4.3	0.512	7.21	1.8
SG_5	6.6	0.5	11.02	1.4

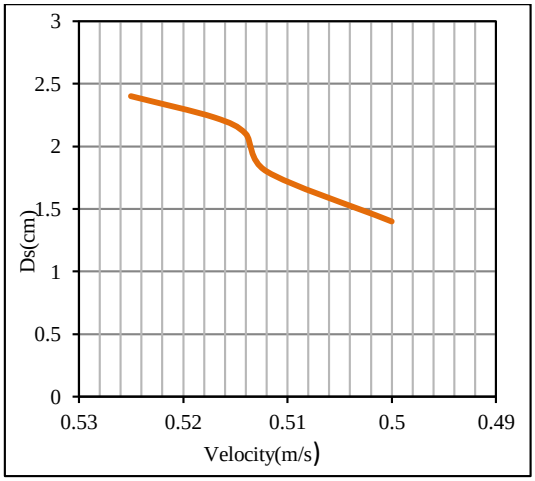

Fig.8 Variation of scour depth with velocity for straight groynes(SG)

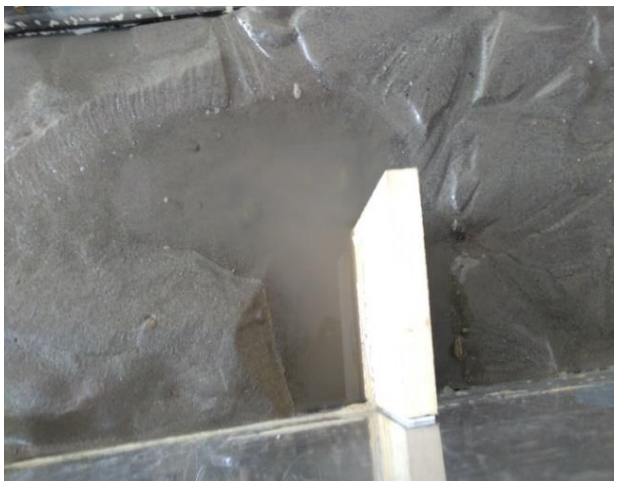

Fig.9 Scour around straight groyne (SG)

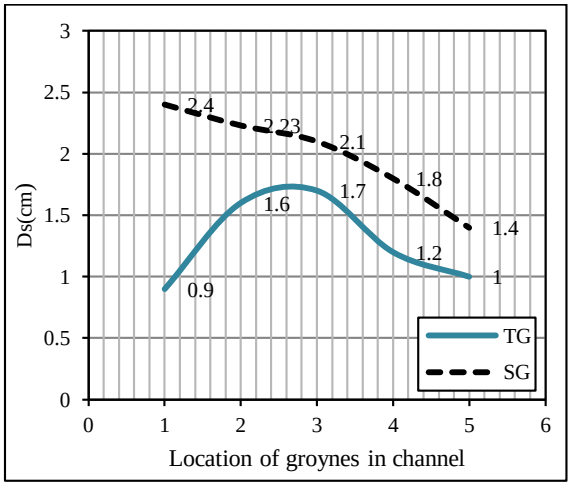

Fig.10 Variation of scour depth along the channel for both groynes

Comparing the scour depth for both groynes as shown in figure.10 it is seen that T-shaped groynes are more safe as compared to straight groynes throughout the channel. Scour depth for straight groynes follows a decreasing trend along the channel whereas for T-head groyne it increases in the initial reaches of the channel and after reaching a maximum value it starts decreasing to its minimum value in the end of the channel. One important thing that is observed is that, the scour for a straight groynes is always greater than that of T-shaped groyne at every location which makes it less stable than T-shaped in terms of protection against scouring and stability of structures.

X. CONCLUSION

T-shaped groynes are more efficient than straight groynes in scour protection and reducing the failures of hydraulic structres. It is to be noted that scour is deeper for straight groynes as compared to T-shaped groynes. For straight groynes the scour reduces along the flow towards the downstream direction. For T-shaped groynes it increases initially and then decreases after attaining its maximum value while moving towards the downstream direction. Series of straight groynes is useful in stabilizing the bed against scour and by using the T-head groynes scouring can further be reduced upto its minimum value. Straight groynes are useful for economical protection of structure whereas T-head groynes proves to be a bit costlier but gives more stability in protection against scour.

Where important hydraulic structures are to be protected ,T-shaped groynes are recommended and straight groynes should be used where deflecting and diverting of the flow is the only concern.

NOMENCLATURES

TG: T-shaped groynes
SG: Straight groynes
Ds: Scour depth
p: Pressure (kg/cm^2)
v: Velocity(m/s)
ρ: Mass density of water (kg/m^3)
g: Acceleration due to gravity(m/s^2)

@IJRTER-2018, All Rights Reserved

REFERENCES

I. M.Ahamad,1951 study of bank protection on Satluj river.International journal of advanced engineering research and studies, E-ISSN2249-8974
II. Garg.et.al,1980 study of groynes on the basis of their angle of inclination and curvature of flow.International journal of advanced engineering research and studies. E-ISSN2249-8974
III. A.Shafaie,A.Ardeshir,S.M.Sadat M.Saneie. The effect of minor spur dike on scouring at the first spur dike in the gravel bed. Fourth International Conference on scour and erosion,2008
IV. A.Safarzadeh, S.A.A.Salehi Neyshabouri and M.Ghodsian. Experimental study of head shape effects on shear stress distribution around a single groyne,2010. ISBN-978-3-939230-00-7
V. M.Alauddin, T.Tashiro, T.Tsujimoto. Experimental investigation of channel responses against different configurations of groynes,Advances in River Engineering,JSCE 2011
VI. M.Vaghefi,M.Ghodsian,S.Ali.Akbar.Salehi Neyshabouri. Study on scour around T-shaped groynes in a channel bend,ASCE 2012.
VII. Roger.A.Kuhnle et al. "Local Scour associated with angled spur dikes". Journal of Hydraulics Engineering,2012.
VIII. Kedar Sharma and Pranab Mohapatra. Separation zone in flow past a spur dike on rigid bed meandering channel. Journal of Hydraulic Engineering , ASCE-2012
IX. S.I.Khassaf, A.M.dawood. Development of clear water scour formula around groynes, International journal of modern engineering research,2013 pp-2083-2088
X. Hamid Shamloo et al, Numerical simulation of angle of installation of groyne on the separation zone length behind it. Jounal of River Engineering,2014
XI. S.A.Salamatian et al, Flow pattern and stress distribution around three spur dikes in 90° channel bend. International journal of engineering and technology,2016
XII. A.M. Najafabadi and M.M.Bateni. Investigation of flow pattern around repelling and attracting groyne on flat bed, Journal of Fundamental and Applied Sciences,2017. ISSN 1112-9867
XIII. Vijaya Kumar and Lokesh Aggarwal. Estimation and comparison of depth of scouring around straight partially submerged impermeable groynes aligned at different angles. IJWRE eISSN :2456-1606, Vol-4:Isue1,2018
XIV. Vijaya Kumar and Devesh Tyagi. Experimental study on scour around T-head groynes in open channel. IJWRE eISSN :2456-1606, Vol-4:Issue 1,2018

@IJRTER-2018, All Rights Reserved

International Journal of Engineering Technology Science and Research
IJETSR
www.ijetsr.com
ISSN 2394 – 3386
Volume 5, Issue 3
March 2018

Copy-Move Forgery Detection Techniques: A Literature Survey

Ritu Agarwal
Delhi Technological University
B.N. Deepankan
Delhi Technological University

ABSTRACT

Digital images have become a major part of our lives, as most of us post our everyday lifestyle to social media such as Twitter, Facebook, Instagram etc. Hence, it increases the usability of the image editing software and filters. So it has become a difficult task to determine an original image or a forged image. There are many types of image forgery but we're focusing on Copy-Move forgery which is the most common type of image forgery, where one region of the image is copied and pasted to another region of the image such that it depicts as an original image. This paper provides a literature survey of different copy-move forgery detection techniques.

KEYWORDS

Image forgery, copy-move forgery, Image forgery detection

INTRODUCTION

Since every information we get in our daily routine has been in a digital form with increasing technological advancement, it has brought a major issue of security. With the latest development of powerful algorithms and technology for manipulating digital images has made a very difficult task for determining a genuine image.The Digital image can be manipulated using many techniques and software like transformation, scaling, filtering, cropping, blurring, photoshop, coral draw, and others. Image forgery has indeed become a major challenge for institutions as well as individuals. The verification of digital image is necessary for many applications.

Digital Image forgery can be detected using two different approaches. These are active approach and Passive approach. The active approach is of two types, one is watermarking and another is steganography. The basic idea of watermarking is to embed some information in digital images so that it cannot be misused or owned by others and to check the authenticity of the message. Steganography is the technique to hide a message within a digital image, to protect the privacy of the data.

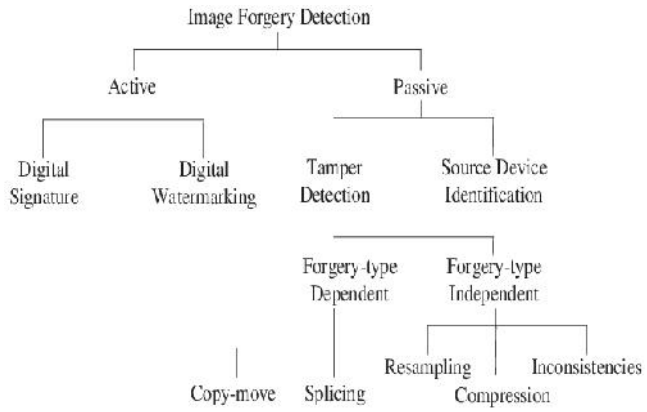

Fig 1: Classification of different types of Image forgery

International Journal of Engineering Technology Science and Research
IJETSR
www.ijetsr.com
ISSN 2394 – 3386
Volume 5, Issue 3
March 2018

The Passive approach doesn't require any prior information about the image as it can examine the image for any traces of manipulation during the preprocessing step. With the help of different image forgery detection techniques the forged area, location and the amount of forgery can be detected. It includes copy-move forgery and image splicing and they also help to detect the operations that occur, like rotation scaling, blurring, etc. Figure 1 [1] gives a complete classification of different types of image forgery.

TYPES OF IMAGE FORGERY

COPY-MOVE FORGERY

Copy-move forgery or Cloning, in which one region of the image is being copied and pasted into another region of the same image such that it depicts as an original image [2]. Since, the part of the image being copied is from the same image it has the sametexture, noise, and color as rest of the image which makes it difficult to determine if it an original image or a forged image. Thiskind of image forgeryis common nowadays, as it can use for the altercations on the image related to crime evidence, magazines etc. Many methods have been developed for the detection of this forgery which involves extracting features or dividing the image into blocks, which we will present in the next section.

(a) **(b)**

Fig 2: (a) Original Image (b) Forged Image

IMAGE SPLICING

In Image splicing, multiple images are merged together to create a fake scene. Image splicing can easily be detected by looking at the boundaries of the image as it contains different image regions and they all have a different texture, color, and noise which can easily be detected. Several algorithms such as [3], [4] which effectively detect the image splicing forgery have been developed.

(a) **(b)**

Fig 3: (a) Spliced image (b) Original Image

International Journal of Engineering Technology Science and Research
IJETSR
www.ijetsr.com
ISSN 2394 – 3386
Volume 5, Issue 3
March 2018

LITERATURE SURVEY ON FORGERY DETECTION TECHNIQUES

The following steps are common in the algorithms for the detection of the tampered region.

1. A forged color image of size P x Q is changed into grayscale or it is used as it is as per the algorithm.
2. **Block-based methods.** Some algorithms involve separating an image into blocks by sliding a small window over the image. Then applying the forgery detection algorithm over those blocks.
3. **Keypoint based methods.** There are several algorithms by which features are extracted which will be described later in this paper, which extracts the points which make the image unique. If an image is being forged then that image contain similar feature points. These features are stored as a feature vector or in a matrix depending on the algorithm.
4. Then, for the matchingprocess, these feature vectors may be arranged using sorting techniques such as lexicographic sorting, nearest neighbor etc.
5. Some morphological operations are applied so that it can detect the forged region.

In [5] presented a hybrid approach which involves 2D-DWT and SVD. It is fast, efficient and accurate for tampering detection. In this approach, a color image is provided for the possible detection of forgery. Then, B, G and R channels are extracted and 2D-DWT is applied to each channel and approximated coefficient are extracted for further processing. These approximated coefficients are separated by sliding a window of size b x b which separate them into coinciding blocks. The dimension of each block is reduced by applying SVD. These R, G and B channel blocks are stored in a row matrix. From the row, matrix separates the non-overlapping blocks and compute the Euclidian distance between them and if it is more than the threshold Ct than it is considered as a candidate block. The distance between these candidate blocks and the coinciding blocks is calculated, a threshold Cd is selected if the computed distance is below than Cd then it is considered to be forged.[6] developed a new algorithm in order to account for low contrast segments in a forged image. It is a combination of DCT with PCA. First, PCA is applied to the image from which important features are extracted. Afterward, a window of size a xa is slid over the image to separate the image into coinciding blocks. Local contrast for each block is calculated, those blocks which exceeded the fixed contrast are kept. 2D-DCT is applied to each block and local feature matrix is extracted. This feature matrix is lexicographically sorted, and autocorrelation is evaluated. If the autocorrelation exceeds a threshold than those blocks are considered to be duplicates.[7] proposedan approach using discrete wavelet transform (DWT), in this approach consider a grayscale image or convert a color image into a grayscale image. Then, DWT transform is applied to the converted image and it divides the image into sub-images, these sub-images are labeled as LL^1, LH^1, HL^1, and HH^1. A block of size b x b is slid over these sub-images from LL to HH. DWT transform is calculated and stored in a lexicographical manner in the matrix. Normalized shift vector is calculated for the matched pairs and it is compared with the user-defined threshold to determine if the region is being copied.[8] usesa hybrid approach which involves DWT with DCT. In this approach consider a grayscale image or convert a color image into a grayscale image and apply DWT to divide the image into sub-images. Slide a window of size n x n over those sub-images resulting in K blocks. DCT is applied on the rows of the blocks to reduce the vector length and a matrix is formed H. The matrix is lexicographically sorted and Normalized shift vector is calculated for the matched pairs and it is compared with the user-defined threshold to determine if the region is being copied.In [9] approach Dyadic Wavelet Transform is used i.e. DyWT. Apply DyWT on the image to get LL^2 and HH^2 sub-bands. Analyze the pattern for each segment, and calculate the Euclidean between the pair of patterns. Check if the distance is less than the threshold T. If yes, then that region is marked as forged.[10] has proposed an approach which involves SURF and DyWT, which is identical to SURF and DWT [11] but DyWT is used as DWT is not shift-invariant. In this approach DyWT is performed into an image which divides the image into sub-images, key points and features are extracted by applying SURF. Feature descriptor vector of SURF is obtained and determine the similar feature descriptors. Finally, mark the forged regions.

[12] proposed a keypoint technique by using SIFT. SIFT involves four major step first, Scaled spaced extrema detection which finds the interest points using Laplacian of Gaussian (LOG). Second, key points are selected based on the measures of their stability. Third, Depending on the scale, a neighborhood point is chosen around the keypoint location. Then for that region, the gradient magnitude and direction is calculated. Fourth, a 16x16 neighborhood is selected near the key point and it is separated into 16 sub-blocks of 4x4 size. Then, the Key point between similar imageis matched.In [13] presented an algorithm for tampering detection using SVD. A small window of size A x A is slid over the input image to separate the image into overlapping blocks. SVD is applied to these separated blocks to obtain feature vectors, sort them and store it in the matrix. k-d tree is constructed using the feature vectors and it is searched for similar blocks. The matched blocks satisfying a threshold t will be labeledas suspected regions and these suspected regions are merged together to determine the tampered region.[14] proposed an algorithm involving local binary pattern and neighborhood clustering. In this algorithm the colored image is separated into R, B and G color components and these components are divided into blocks. LBP histogram is extracted for each component and calculate the distance between blocks using histogram for every component. Then, sort the block-pairs according to the minimum distance and keep only the shortest one-fourth of the total. Extract block pairs which are common in the three components, if duplicates were found then create sub-blocks using clustering and should a visual result.[15] proposed an algorithm for both keypoint regions and smooth regions. Initially, Simple Linear Iterative Clustering [16] is applied to the image to separate the image into different blocks. Then SIFT is used to extract a key point from each block, the number of key points in a region is divided by the total number of pixels in that region to determine if it is a smooth region or a key point region. If it is detected as a key point region then the duplicate part is marked by using multiple keypoint matching [17] and RANSAC [18] is used to filter outliers. If it is a smooth region then Zernike moments [19] is used to detect the copied part.[20] presented an approach using SWT and SVD. Initially, thecolored image is changed into grayscale and SWT is applied to separate the image into sub-bands LL1, LH1, HL1, and HH1. Then, the LL1 band is separated into coinciding blocks since LL1 gives the smoothest version of the image. SVD is used to extract a feature of the image and store it in a matrix, this feature matrix is lexicographically sorted. Check for similar features and calculate the Euclidian distance between then and store it in list L. The block pairs in list L are compared with threshold value T_s which is the minimum distance between duplicated regions. If it any block pair distance is more than T_s it is considered as a forged region.[21] proposed an algorithm which uses 2D-DCT and SVD. First, the image is separated into coinciding blocks of equal size. 2D-DCT is applied to each block and DCT quantized coefficients are obtained. SVD is applied to extract features on each quantized block and stored in a lexicographically order in a matrix. Euclidian distance is calculated between matched pairs and compared with a threshold. After removing the disturbed matching output image is obtained containing marked forged region.[22] presented an algorithm using non-negative matrix factorization in which we normalize the original input image, then a block of size B x B is slid over the normalized image to divide the image into overlapping blocks. NMF is applied to each block for feature extraction and it is lexicographically stored in a matrix. Then the hamming distance between two similar matrices is calculated and matched with the threshold T. If it is less than the threshold T, then it is considered as similar blocks and clustered together according to their displacements. Those blocks are marked as a duplicate region.[23] presenteda robust and efficient technique in which it involves a block of size a x ais slid over the image to separate it into coinciding blocks, and seven characteristic features are calculated for each block C_j (j=1,2,3…7) where C_1, C_2,and C_3red, green and blue components. C_4, C_5, C_6, and C_7 are the characteristics feature of Y channel which is a combination of R, G and B. These characteristic features are stored in a vector V for each block separately and saved in an array A. The array A is lexicographically sorted and similarity is calculated between two vectors if it is greater than a threshold L it is recorded. A histogram is prepared with the recorded vectors, greater than threshold L and choose the main vector, d if any vector differs too much from d, it is discarded and remaining vectors are put in a binary image with the forged region set to white and rest of the region is set to black.

CONCLUSION

Copy-move forgery has a huge impact on our day to day life. Efficient and viable algorithms are necessary to detect the forged region. In this paper, we have discussed different types of image forgery. Steps that should be followed to detect the copy-move forgery. A detailed description of algorithms used to detect copy-move forgeries while some algorithms are not very effective to detect the forged region and others have the major problems which requires the computational time to be reduced, increase the accuracy, robustness against various geometric transformations. But some algorithm have achieved the mentioned goals up to certain extent like the algorithm which detects the forgery in both key point region and the smooth region is considered the best among the discussed methods. Also in future, there is a need to develop a robust and effective algorithm to detect Imageforgery.

REFERENCES

[1] Jung, Ki-Hyun. (2016). Block-Based Authentication Scheme for Forgery Attacks on Digital Images. Advanced Science Letters. 22. 2583-2587. 10.1166/asl.2016.7784.
[2] N. Kanagavalli and L. Latha, "A survey of copy-move image forgery detection techniques," 2017 International Conference on Inventive Systems and Control (ICISC), Coimbatore, 2017, pp. 1-6.
[3] A. A. Alahmadi, M. Hussain, H. Aboalsamh, G. Muhammad and G. Bebis, "Splicing image forgery detection based on DCT and Local Binary Pattern," 2013 IEEE Global Conference on Signal and Information Processing, Austin, TX, 2013, pp. 253-256.
[4] F. Hakimi, M. Hariri, and F. GharehBaghi, "Image splicing forgery detection using local binary pattern and discrete wavelet transform," 2015 2nd International Conference on Knowledge-Based Engineering and Innovation (KBEI), Tehran, 2015, pp. 1074-1077.
[5] Kaushik, Rajeev, Bajaj, Rakesh Kumar, Mathew, Jimson, “On Image Forgery Detection Using Two Dimensional Discrete Cosine Transform and Statistical Moments,” 2015 Proceedings of the 4th International Conference on Eco-friendly Computing and Communication Systems, 2015, SN 1877-0509.
[6] A. Hilal, T. Hamzeh and S. Chantaf, "Copy-move forgery detection using principal component analysis and discrete cosine transform," 2017 Sensors Networks Smart and Emerging Technologies (SENSET), Beirut, 2017, pp. 1-4.
[7] M. F. Hashmi, A. R. Hambarde and A. G. Keskar, "Copy move forgery detection using DWT and SIFT features," 2013 13th International Conference on Intelligent Systems Design and Applications, Bangi, 2013, pp. 188-193.
[8] M. Ghorbani, M. Firouzmand, and A. Faraahi, "DWT-DCT (QCD) based copy-move image forgery detection," 2011 18th International Conference on Systems, Signals, and Image Processing, Sarajevo, 2011, pp. 1-4.
[9] N. Muhammad, M. Hussain, G. Muhammad and G. Bebis, "Copy-Move Forgery Detection Using Dyadic Wavelet Transform," 2011 Eighth International Conference Computer Graphics, Imaging and Visualization, Singapore, 2011, pp. 103-108.
[10] M. F. Hashmi, V. Anandand A. G. Keskar, "A copy-move image forgery detection based on speeded up robust feature transform and Wavelet Transforms," 2014 International Conference on Computer and Communication Technology (ICCCT), Allahabad, 2014, pp. 147-152.
[11] Alamro, Loai&Yusoff, Nooraini. (2017). Copy-move forgery detection using integrated DWT and SURF. Journal of Telecommunication, Electronic and Computer Engineering (JTEC). 9. 67-71.
[12] S. Prasad and B. Ramkumar, "Passive copy-move forgery detection using SIFT, HOG and SURF features," 2016 IEEE International Conference on Recent Trends in Electronics, Information & Communication Technology (RTEICT), Bangalore, 2016, pp. 706-710.
[13] T. Zhang and R. d. Wang, "Copy-Move Forgery Detection Based on SVD in Digital Image," 2009 2nd International Congress on Image and Signal Processing, Tianjin, 2009, pp. 1-5.
[14] M. AlSawadi, G. Muhammad, M. Hussain and G. Bebis, "Copy-Move Image Forgery Detection Using Local Binary Pattern and Neighborhood Clustering," 2013 European Modelling Symposium, Manchester, 2013, pp. 249-254.
[15] M. R. Resmi and S. Vishnukumar, "A novel segmentation based copy-move forgery detection in digital images," 2017 International Conference on Networks & Advances in Computational Technologies (NetACT), Thiruvananthapuram, 2017, pp. 346-350.
[16] M. K. S. Varma, N. K. K. Rao, K. K. Raju, and G. P. S. Varma, "Pixel-Based Classification Using Support Vector Machine Classifier," 2016 IEEE 6th International Conference on Advanced Computing (IACC), Bhimavaram, 2016, pp. 51-55.

[17] S. Debbarma, A. B. Singh and K. M. Singh, "Keypoints based copy-move forgery detection of digital images," 2014 International Conference on Informatics, Electronics & Vision (ICIEV), Dhaka, 2014, pp. 1-5.
[18] M. M. Isaac and M. Wilscy, "A key point based copy-move forgery detection using HOG features," 2016 International Conference on Circuit, Power and Computing Technologies (ICCPCT), Nagercoil, 2016, pp. 1-6.
[19] RyuSJ., Lee MJ., Lee HK. (2010) Detection of Copy-Rotate-Move Forgery Using Zernike Moments. In: Böhme R., Fong P.W.L., Safavi-Naini R. (eds) Information Hiding. IH 2010. Lecture Notes in Computer Science, vol 6387. Springer, Berlin, Heidelberg.
[20] R. Dixit, R. Naskarand S. Mishra, "Blur-invariant copy-move forgery detection technique with improved detection accuracy utilizing SWT-SVD," in IET Image Processing, vol. 11, no. 5, pp. 301-309, 5 2017.
[21] H. Moradi-Gharghani and M. Nasri, "A new block-based copy-move forgery detection method in digital images," 2016 International Conference on Communication and Signal Processing (ICCSP), Melmaruvathur, 2016, pp. 1208-1212.
[22] H. Yao, T. Qiao, Z. Tang, Y. Zhao and H. Mao, "Detecting Copy-Move Forgery Using Non-negative Matrix Factorization," 2011 Third International Conference on Multimedia Information Networking and Security, Shanghai, 2011, pp. 591-594.
[23] Weiqi Luo, Jiwu Huang and GuopingQiu, "Robust Detection of Region-Duplication Forgery in Digital Image," 18th International Conference on Pattern Recognition (ICPR'06), Hong Kong, 2006, pp. 746-749.

This article has been accepted for publication in a future issue of this journal, but has not been fully edited. Content may change prior to final publication. Citation information: DOI 10.1109/JESTPE.2018.2823904, IEEE Journal of Emerging and Selected Topics in Power Electronics

Decoupled Active and Reactive Power Predictive Control for PV Applications using a Grid-tied Quasi-Z-Source Inverter

Sarthak Jain, *Student Member*, *IEEE*, Mohammad B. Shadmand, *Member, IEEE*, and Robert S. Balog, *Senior Member*, *IEEE*

***Abstract*— This paper proposes a predictive power control algorithm that decouples active and reactive power for grid integration of photovoltaic (PV) systems using a quasi-Z-source inverter (qZSI). This is important to meet the emerging smart inverter requirements for grid interconnection. The proposed controller uses model predictive control (MPC) framework to ensure that the maximum available power is harvested from the PV array and that the active and reactive power injected into the grid is controlled to compensate reactive power required by local loads and as need to ensure stable operation of the grid at the point of common coupling (PCC). Thus, a power electronics interface (PEI) is proposed to integrate the PV array to the grid and to work as a reactive power compensator simultaneously. A robust technique is proposed to regulate the impedance network voltage and current according to the maximum operating point of PV panels and grid voltage/current requirements. The proposed controller features a simple structure suitable for practical implementation, fast dynamic response under changing sky condition, and negligible tracking error in steady state for decoupled active and reactive power control in a typical distributed generation (DG) systems. The performance of the proposed controller is verified experimentally; the grid-side power quality analysis is provided and evaluated according to IEEE-519 standard.**

***Index Terms*—Impedance source inverter, model predictive control, reactive power compensation, grid-tied inverter, PV system**

I. INTRODUCTION

Growth in the energy demand coupled with aging infrastructure and increasing concern over environmental impact is driving the development of Distributed Generation (DG) systems that support Renewable Energy Sources (RES) like solar, wind, thermoelectric, fuel cell etc. Increases in cell efficiency and reduction in total system costs, including ease of installation, has made photovoltaic energy systems not only affordable, but in some markets cheaper than energy from conventional sources [1, 2]. However, PV cells produce low, direct-current (DC) voltage as compared with the high-voltage alternating current (AC) grid and thus require power electronics for step-up, dc/ac conversion and maximum power point tracking (MPPT) for efficient operation. This generally requires multiple power converter stages to accomplish. Many of the common PV inverter topologies are two-staged with an energy buffer, such as dc-link capacitor [3]. The first stage performs MPPT, boosts the PV voltage and transfer the PV power to the energy buffer, the energy buffer is followed by second inverter stage to connect the system to the utility grid [4]. This two-staged system configuration decreases the efficiency as well as the dynamic response of the system with respect to both changes in environmental conditions and grid perturbations. In addition, the inverter is being required to provide smart-grid interface and enhanced inverter functionality. Thus, the ideal DG based power electronics interface needs a single conversion stage for high efficiency, a comprehensive and robust controller for grid interaction, and multiple modes to accomplish the PV-side and grid-side control.

Several techniques have been proposed for single stage grid connection of the PV in which the inverter performs both MPPT and inversion functions [3]. However, as these topologies are either voltage sourced or current sourced inverters, they are limited to only buck or boost operation of the PV source voltage respectively [5]. The Z-source inverter (ZSI) and quasi-Z-source inverter (qZSI) have been extensively studied for PV applications due to their capability of both buck/boost operation of DC input voltage by coupling an impedance network between power source and the inverter bridge [6-9]. ZSI/qZSI incorporates an overlap-mode switching state (commonly called *shoot through*) in which both switches of a bridge phase leg are purposely turned on which results in the boosting of the input voltage controlled by the amount of time in this overlap state (shoot through time) [10]. In comparison with traditional two stage PV energy harvesting systems which require DC/DC stage for boosting/MPPT and DC/AC stage for inversion, ZSI/qZSI can provide a more efficient, reliable, and cost-effective solution with just a single stage conversion and reduced number of active switches [5, 11]. These properties make ZSI/qZSI suitable for renewable energy sources (RES) to overcome the limitations of VSI/CSI topologies [7]. Expanding the advantages of the ZSI, the qZSI has continuous input current [11] which can eliminate problems with electro-magnetic interference (EMI), leakage/ground currents and can significantly increase PV life span and energy harvest [12-15]. In addition, the voltage across one of the two capacitors in the impedance network is lower than the other capacitor, thus supporting a lower rating capacitor which can reduce the cost, which isn't the case in ZSI [16]. Accordingly,

This publication was made possible by NPRP grant # 7-299-2-124 and NPRP-EP grant # X-033-2-007 from the Qatar National Research Fund (a member of Qatar Foundation). The statements made herein are solely the responsibility of the authors.

M. B. Shadmand is with the Department Electrical & Computer Engineering at Kansas State University, Manhattan, KS (email: mohamadshadmand@gmail.com). S. Jain and R. S. Balog are with the Department of Electrical and Computer Engineering at Texas A&M University, College Station, TX (emails: jainsarthak2091@gmail.com, robert.balog@ieee.org).

2168-6777 (c) 2018 IEEE. Personal use is permitted, but republication/redistribution requires IEEE permission. See http://www.ieee.org/publications_standards/publications/rights/index.html for more information.

This article has been accepted for publication in a future issue of this journal, but has not been fully edited. Content may change prior to final publication. Citation information: DOI 10.1109/JESTPE.2018.2823904, IEEE Journal of Emerging and Selected Topics in Power Electronics

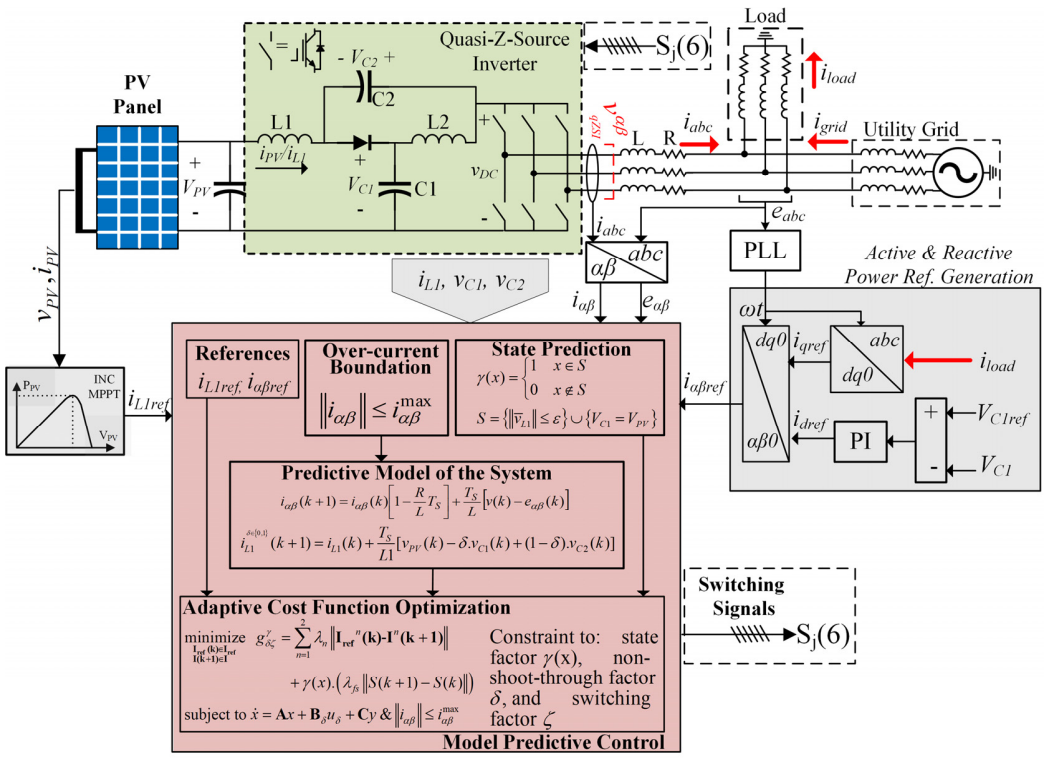

Fig. 1. Proposed power electronics interface system overview.

the voltage fed qZSI proposed in [17] is used for the proposed PV energy harvesting unit with reactive power compensation in this paper.

Due to the increasing penetration of low-power inverters into the grid distribution system, jurisdictions are developing codes and standards to maintain grid stability particularly during the transient or abnormal conditions [18, 19]. Apart from just working under MPPT conditions, RES based distributed generation (DG) systems are mandated by grid codes to have a precise and independent control over reactive power [20] and hence provide ancillary support to grid for voltage regulation at the local bus as well to maintain the overall stability of the grid [21].

The addition of the impedance network and overlap mode in the inverter of the qZSI complicates the traditional control and requires a complex modulator with multi/nested loop control system [11] to control the capacitor voltage, input inductor current along with the injected grid current [11]. Hence, for conventional control, separate control loops are required for grid integration and other mandated objectives, which could result in slow dynamic response/lower bandwidth and highly complex control design. Instead, model predictive control (MPC) is well suited to handle this multi-control objective task.

With the rapid advancements of fast and efficient digital signal processors, MPC is becoming increasingly popular for power electronics applications [22-24]. Among the two control types of MPC [25], finite set MPC has been extensively used due to its simplicity in which switching states are directly estimated and controlled without needing a modulator to create the switching signals. Also, for complex non-linear systems, MPC has been proven to be an effective solution over conventional multi/nested loop compensators which have complex structure and multi-variable tuning [11]. MPC offers various advantages like fast dynamic response, incorporation of non-linear control variables in a straightforward manner and possible implementation of conventional nested loop structure in a single loop [25-28]. Classical controller requires multi-loop variable tuning, more complex PWM modulator design and provides less modularity in the qZSI thus the advantages of the MPC controller can be seen more in qZSI application. qZSI unlike conventional VSI requires multiple objectives like input inductor current, capacitor voltage, output grid current etc. to be handled simultaneously thus require nested loop control. The presented algorithm provides a different approach to decrease the computational complexity of the control along with maintaining the various parameter control quality with minimal control effort. It eliminates the PWM modulator which is a major challenge in ZSI/qZSI system due to proper shoot-through insertion requirement [26], which requires complex logic to incorporate the shoot through state with precise timing control.

Therefore, the above-mentioned advantages motivated many researchers to focus on implementing model predictive controlled qZSI for wide range of applications. In [11], direct predictive control is used for qZSI for an off-grid system with RL load. The presented control calculated the references based on the known values of the load parameters, which is practically not the case. Also, the grid connection capability and control testing was not shown which is necessary for DG systems. The system proposed in [29] shows Z-source grid-tied PV inverter where grid synchronization is done using a simple boost pulse width modulation (PWM) strategy. In [30], MPC for direct power control is developed for off-grid systems. The system in [30] does not cover the grid integration and the system shown was for constant DC input but not for a PV source. The intermittent nature of PV can effectively change the dynamic behavior of the system. The modeling and control of qZSI for

2168-6777 (c) 2018 IEEE. Personal use is permitted, but republication/redistribution requires IEEE permission. See http://www.ieee.org/publications_standards/publications/rights/index.html for more information.

This article has been accepted for publication in a future issue of this journal, but has not been fully edited. Content may change prior to final publication. Citation information: DOI 10.1109/JESTPE.2018.2823904, IEEE Journal of Emerging and Selected Topics in Power Electronics

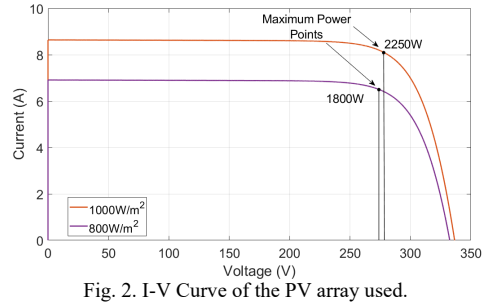

Fig. 2. I-V Curve of the PV array used.

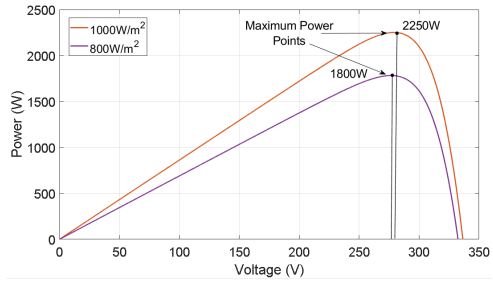

Fig. 3. P-V Curve of the PV array used

grid-connected PV system is developed in [7] by using conventional multi-loop classical control system suffering from low bandwidth and slow response. In addition, none of the above-mentioned literature discusses the problem of independent power control of qZSI for grid integration of PV systems that can simultaneously compensate the reactive power required by the grid as an ancillary service that can be provided by DG systems to main utility grid [20].

This paper proposes a control algorithm for grid-tied qZSI PV system with decoupled active and reactive power control along with energy-loss optimization per switching cycle based on MPC framework. Thus, the presented power electronics interface (PEI) can simultaneously inject the maximum harvested power to the grid and work as a reactive power compensator providing the ancillary services to the grid. The following list summarizes the contributions of the paper:

1. Active/Reactive power decoupled control with their exact reference generation for MPC.
2. Reactive power compensation at point of common coupling (PCC) using the proposed PV energy harvesting system.
3. Incorporate minimum energy controller by minimizing the switching events per cycle, thus optimizing the average switching frequency and as a result minimizing the switching losses.
4. An adaptive cost function is proposed to prioritize the active/reactive power control and power quality over the switching event minimization during dynamic changes in the system. The dynamic changes could be due to change in ambient conditions of the PV or change in the reactive power requirement at the PCC.
5. The cost function proposed in the system only uses two parameters apart from switching event minimization formulation as opposed to three parameters in conventional PEI control making it simpler to tune weight factors and reduce design complexity.

With the increased small-scale penetration of RES into the grid, the proposed PEI based-qZSI shows the promising application in highly efficient future microgrid architectures. The presented system decouples the DC bus controller from MPC using a low bandwidth PI control which performs majorly two functions, i.e., to decouple power and provide a low bandwidth, less complex DC bus controller, thereby reducing the computation burden of computing predictive values V_{C1} by solving higher order equations. This allows user to run the rest of the algorithm at higher rate thereby achieving high quality current waveforms along with low tracking error.

The decoupling and independent reference generation for active and reactive current at AC side allows more robust and modular control in context of the grid codes needs to be followed any PEI interfaced with the grid. The active/reactive power can be easily modified based on low voltage ride through (LVRT) [20] conditions like grid voltage support, load reactive power compensation, etc.

II. System Modeling

Fig. 1 shows the complete power stage with an overview of the control system adopted in this paper. Power stage includes PV array connected to qZSI with an input capacitor to stabilize the input voltage. PV module Suntech STP250-20/Wd is used to create a PV array by connecting 9 panels in series for the experiments in this paper. The I-V and P-V characteristic curves of the array shown in Fig. 2 and Fig. 3 respectively for solar irradiance levels of 1000 W/m^2 and 800 W/m^2. Then, the qZSI is tied to 3-phase grid at PCC through a first order R-L filter. The PCC is feeding some passive load demanding both active and reactive power. The three-phase grid is assumed to have impedance to test the system model for more practical and accurate scenario. The control system shown can be divided into two parts for easier understanding, named, *reference generation* based on the active and reactive power to be supplied by qZSI and *predictive control* to achieve the referenced parameters. The active power reference to be supplied by the qZSI to the PCC is generated through MPPT algorithm and reactive power reference can be generated through various ways. Reactive power demand of the system can be catered based on the load reactive power demand, which is adopted in this paper or through droop control/low-voltage ride through strategies proposed in various literature [20]. The algorithm proposed in the system can be adapted for any of the above-mentioned reactive power injection strategies based on the needs. The following sub-sections explain the modeling of the qZSI and its dynamic behavior for devising the discrete equations for MPC.

A. Quasi-Z-Source Inverter Modeling

Fig. 1 shows the PV sourced qZSI with predictive control of active and reactive power in decoupled manner. Fig. 4 shows qZSI equivalent circuit during active and shoot through state based on δ, where δ represents active state and shoot through state when its value is 1 and 0 respectively. The qZSI is analyzed in both active states and shoot through states separately to develop system equations which are required for designing MPC framework. The full switching period of the qZSI bridge is considered to be T ($T = T_1 + T_o$), active state

2168-6777 (c) 2018 IEEE. Personal use is permitted, but republication/redistribution requires IEEE permission. See http://www.ieee.org/publications_standards/publications/rights/index.html for more information.

This article has been accepted for publication in a future issue of this journal, but has not been fully edited. Content may change prior to final publication. Citation information: DOI 10.1109/JESTPE.2018.2823904, IEEE Journal of Emerging and Selected Topics in Power Electronics

time to be T_1, shoot through state time to be T_o and shoot through duty ratio D as T_o/T. From Fig. 1 and Fig. 4, state space model can be determined as (1), (2) and (3):

$$\begin{bmatrix} \dot{i}_{l1} \\ \dot{i}_{\alpha} \\ \dot{i}_{\beta} \end{bmatrix} = \begin{bmatrix} 0 & 0 & 0 \\ 0 & \frac{-R}{L} & 0 \\ 0 & 0 & \frac{-R}{L} \end{bmatrix} \begin{bmatrix} i_{L1} \\ i_{\alpha} \\ i_{\beta} \end{bmatrix} + \begin{bmatrix} \frac{-1}{L1} & 0 & 0 \\ 0 & \frac{-1}{L} & 0 \\ 0 & 0 & \frac{-1}{L} \end{bmatrix} \begin{bmatrix} v_{C1} \\ e_{\alpha} \\ e_{\beta} \end{bmatrix} + \begin{bmatrix} \frac{1}{L1} & 0 & 0 \\ 0 & \frac{1}{L} & 0 \\ 0 & 0 & \frac{1}{L} \end{bmatrix} \begin{bmatrix} v_{PV} \\ v^{\alpha}_{qZSI} \\ v^{\beta}_{qZSI} \end{bmatrix} \quad (1)$$

$$\begin{bmatrix} \dot{i}_{l1} \\ \dot{i}_{\alpha} \\ \dot{i}_{\beta} \end{bmatrix} = \begin{bmatrix} 0 & 0 & 0 \\ 0 & \frac{-R}{L} & 0 \\ 0 & 0 & \frac{-R}{L} \end{bmatrix} \begin{bmatrix} i_{L1} \\ i_{\alpha} \\ i_{\beta} \end{bmatrix} + \begin{bmatrix} \frac{1}{L1} & 0 & 0 \\ 0 & \frac{-1}{L} & 0 \\ 0 & 0 & \frac{-1}{L} \end{bmatrix} \begin{bmatrix} v_{C2} \\ e_{\alpha} \\ e_{\beta} \end{bmatrix} + \begin{bmatrix} \frac{1}{L1} & 0 & 0 \\ 0 & \frac{1}{L} & 0 \\ 0 & 0 & \frac{1}{L} \end{bmatrix} \begin{bmatrix} v_{PV} \\ v^{\alpha}_{qZSI} \\ v^{\beta}_{qZSI} \end{bmatrix} \quad (2)$$

$$\overline{v}_{L1} = \frac{T_o(V_{C2} + V_{PV}) + T_1(V_{PV} - V_{C1})}{T} \quad (3)$$

The equations (1)-(2) are written in standard form as, $\dot{x} = \mathbf{A}x + \mathbf{B}_{\delta}u_{\delta} + \mathbf{C}y$. The parameters for active state (δ=*1*) and shoot-through state (δ=*0*) as A, B_0, B_1 and C where B_0 is for shoot-through states and B_1 for active states matrices are as follows:

$$\mathbf{A} = \begin{bmatrix} 0 & 0 & 0 \\ 0 & \frac{-R}{L} & 0 \\ 0 & 0 & \frac{-R}{L} \end{bmatrix} \quad \mathbf{B}_0 = \begin{bmatrix} \frac{-1}{L1} & 0 & 0 \\ 0 & \frac{-1}{L} & 0 \\ 0 & 0 & \frac{-1}{L} \end{bmatrix}$$

$$\mathbf{B}_1 = \begin{bmatrix} \frac{1}{L1} & 0 & 0 \\ 0 & \frac{1}{L} & 0 \\ 0 & 0 & \frac{1}{L} \end{bmatrix} \quad \mathbf{C} = \begin{bmatrix} \frac{1}{L1} & 0 & 0 \\ 0 & \frac{1}{L} & 0 \\ 0 & 0 & \frac{1}{L} \end{bmatrix}$$

where the state vector is $x = \begin{bmatrix} i_{L1} & i_{\alpha} & i_{\beta} \end{bmatrix}^T$, the input vector is $u_0 = \begin{bmatrix} v_{C2} & e_{\alpha} & e_{\beta} \end{bmatrix}^T$ and $u_1 = \begin{bmatrix} v_{C1} & e_{\alpha} & e_{\beta} \end{bmatrix}^T$ for shoot through and active state respectively. Control output vector is $y = \begin{bmatrix} v_{PV} & v^{\alpha}_{qZSI} & v^{\beta}_{qZSI} \end{bmatrix}^T$ where v_{PV} is the instantaneous PV voltage, v^{α}_{qZSI} and v^{β}_{qZSI} as the instantaneous bridge output voltage vector in α and β frame. Using state-space averaging, inductor voltage

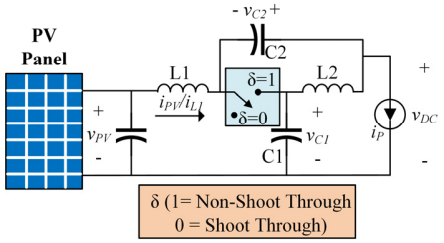

Fig. 4. qZSI equivalent circuit in Non-Shoot through (δ=1) and Shoot through state (δ=0)

in (1)-(2) can be simplified over the complete switching cycle T in terms of D (shoot through duty ratio) and (1-D) as active state duty ratio which results in average voltage given by (3). The average inductor (L1) voltage (3) will be zero in case of steady state operation and this technique will be used later to detect the state (transient or steady state) of the system and develop an adaptive MPC cost function to prioritize the control and provide fast dynamic performance. It is worth mentioning that, the proposed method only uses L1 voltage for the state (transient or steady state) detection to reduce the computation and redundancy; the detail of this state detection technique is explained in section III. D.

B. Filter-grid Interface Modeling

In the proposed PEI, qZSI is connected to the grid through L filter with equivalent loss resistance of R. This paper doesn't deal with the filter dynamics and its effects on the system, thus a simple R-L filter is chosen for reduced complexity, although, the system can be extended to the higher order filters like LCL or LLCL with proper modifications in the presented control and careful design of the filter [31-34]. The behavior of the system at the inverter-grid junction (PCC) is described as:

$$v^{abc}_{qZSI} = Ri_{abc} + L\frac{di_{abc}}{dt} + e_{abc} \quad (4)$$

Here, v^{abc}_{qZSI} is the present output voltage vector of qZSI, i_{abc} is the injected current into system through R-L filter and e_{abc} is the instantaneous PCC voltage. The grid voltage has been measured at the PCC. All the three phase vectors can be represented as $\boldsymbol{\xi}_{\mathbf{abc}} = \begin{bmatrix} \xi_a & \xi_b & \xi_c \end{bmatrix}^T$. The system is further analyzed in $\alpha\beta$ complex frame for MPC framework (Section III.B) to reduce the number of equations from 3 to 1 complex equation. The time domain system model in $\alpha\beta$ frame can be transformed using $\boldsymbol{\xi}_{\boldsymbol{\alpha\beta}} = \mathbf{K}\boldsymbol{\xi}_{\mathbf{abc}}$, where **K** is Clarke's transformation matrix.

$$v^{\alpha\beta}_{qZSI} = Ri_{\alpha\beta} + L\frac{di_{\alpha\beta}}{dt} + e_{\alpha\beta} \quad (5)$$

Here, each quantity with $\alpha\beta$ is taken in complex form as $x_{\alpha\beta} = x_{\alpha} + jx_{\beta}$.

III. Control Design with Predictive Model

The control design for the system shown in Fig. 1 can be divided into six parts: (A) reference generation for MPC, (B) predictive model of the qZSI and its grid interface, (C) optimal control effort, (D) system state determination for adaptive cost function implementation, (E) cost function formulation and minimization, and (F) Lyapunov stability analysis of the

2168-6777 (c) 2018 IEEE. Personal use is permitted, but republication/redistribution requires IEEE permission. See http://www.ieee.org/publications_standards/publications/rights/index.html for more information.

This article has been accepted for publication in a future issue of this journal, but has not been fully edited. Content may change prior to final publication. Citation information: DOI 10.1109/JESTPE.2018.2823904, IEEE Journal of Emerging and Selected Topics in Power Electronics

system. All these parts will be explained separately in detail in the following sub-sections.

A. Reference Generation for MPC

Overview block diagram of reference generation is shown in Fig. 1. As discussed in introduction (Section. I), qZSI control requires multiple quantities to be controlled simultaneously. In general, for a qZSI, v_{C1}, i_{L1} and i_{abc} is controlled [11], however, the proposed algorithm does not include V_{C1} in the cost function thus providing a simpler multi-objective predictive controller and easier weight function tuning. A PI controller is used for the regulation of $V_{C1.}$ DC bus voltage reference tells the PI controller about the amount of current need to be extracted from the bus which converts into the real power on the AC side. Here, decoupled active/reactive power controller is proposed which requires the independent control of both the power or their power components i.e. i_d and i_q. MPC is used to achieve the reference value of the currents on the AC side and the DC side only. PI is used to provide the $i_{d,ref}$ as explained and is combined with the $i_{q,ref}$ to make the total AC currents needs to be injected by the qZSI on the AC side. This way a decoupled control is achieved which is not possible if we include the V_{C1} in the MPC itself as it will try to achieve the different AC current form and won't have any i_q component. Thus, using PI module allows us to realize a decoupled power control, less complex MPC while maintaining high quality current controller, easy tuning of the system and less computation time for the system.

The reference for V_{C1} is considered to be 600V [35, 36] which is more than the double of the considered utility grid having 208 V_{RMS}(L-L) to transfer active power easily [37] and also to compensate high reactive power demand. The reference value for V_{C1} can be altered based on the system requirements for active and reactive power.

The Conventional Incremental and Conductance (INC) [38] algorithm is used to generate PV current reference, which is the $i_{L1,ref}$ in steady state due to charge balance on the input capacitor shown in Fig. 1. An input capacitor is used with PV to eliminate the ripple current from PV, which can eliminate the voltage ripple and provide voltage stability at the input and does not change the DC component of PV current, $i_{PV,ref}$ from $i_{L1ref,}$. In addition, the i_q part is presented as general parameter and left on reader to decide its source as it can be based on different goals. For example, in current paper, i_q has been generated to make the grid work at unity power factor thus compensating for all the reactive power required at the PCC by local load. User can extend this methodology and use latest grid codes, LVRT requirements etc. to find the reactive power (i_q) reference needs to be injected into the grid. The i_{qref} (reactive power component) is generated based on the reactive power requirement of the grid which can be either estimated based on the connected load by sensing the load reactive current component (i_{qload}) as adopted in this paper and shown in Fig. 1 or by providing the Q_{ref} through different ways mentioned in the *Introduction* section of this paper. After finding i_d and i_q, they are converted into $\alpha\beta$ stationary frame using PLL. In ideal system, we can directly convert the i_{L1ref} to the output i_{abcref} using output voltage as the losses are considered zero and grid voltage is stiff. But, here the PI module is used which can cater for the losses in the whole system making it more practical and robust as compared with the previous presented work in which the references are generated assuming zero losses in conversion. The zero-loss consideration can also lead to system instability due to power mismatching at input/output ports. The two references, i_{L1ref} and $i_{\alpha\beta ref}$ are then fed to the MPC block for further processing and switching signal generation. The MPC block is executed at fixed sampling time of T_s and estimates the appropriate switching vector for $k+N$ sampling interval, where in this paper one step prediction ($N=1$) is used. Thus, the whole control is analyzed as two independent systems like in the two-stage grid connected system with DC side MPPT being the first stage and inverter side doing grid synchronizations being second, although, here both are used to control the single inverter bridge unit.

B. Predictive Model of the System

Predictive model of the system is determined by discretizing continuous time domain equations explained in Section II. Sampling frequency is chosen high enough to have an accurate prediction while meeting the hardware processor capability to execute the control loop efficiently for experimental implementation. With sufficiently high sampling frequency, the system can be approximated using forward Euler method as explained in [39]. This sub-section develops the predictive model equations for the qZSI-filter-grid interface and the impedance network inductor (L1) current at PV side of qZSI.

The $i_{\alpha\beta}$ current predictive model is developed by considering qZSI output voltage vector as $v_{qZSI}^{\alpha\beta}$ which is interfaced with grid having voltage of $e_{\alpha\beta}$ at PCC through R-L filter. The continuous time system mode given by (5) is discretized and used to predict the $i_{\alpha\beta}$ current using forward Euler method as:

$$i_{\alpha\beta}(k+1) = i_{\alpha\beta}(k)\left[1-\frac{R}{L}T_S\right] + \frac{T_S}{L}(v_{qZSI}^{\alpha\beta}(k) - e_{\alpha\beta}(k)) \quad (6)$$

where, k is the present sampling instant and k+1 is the predicted sample one step ahead in horizon of time. All the parameters are defined in $\alpha\beta$ complex frame of reference converting three equations to *one complex equation*.

To predict the future values of inductor current (i_{L1}), both shoot-through and active state model equations given by (1) and (2) are used. Using the voltage-current relationship for an inductor and discretizing it using forward Euler method, with mathematical re-arrangements, the inductor ($L1$) predicted current can be determined by:

$$i_{L1}^{\delta\in\{0,1\}}(k+1) = i_{L1}(k) + \frac{T_S}{L1}\left[v_{PV}(k) - \delta.v_{C1}(k) + (1-\delta).v_{C2}(k)\right] \quad (7)$$

where $i_{L1}(k+1)$ is the predicted value of inductor current and δ is active state indicator as described in Section II.A.

C. Optimal Control Effort: Minimizing the Energy-loss per Switching Event

Switching frequency is a critical parameter that influences the switching losses of the converter. IGBTs are extensively used for grid-tied inverters applications due to their high voltage rating and low conduction losses as compared to the same rated Si-MOSFETs. However, IGBT has switching frequency limitation and generally, they are restricted to approximately maximum value of 20~30 kHz. Thus, an effective controller should minimize the switching frequency while maintaining the quality of power injection to the system.

2168-6777 (c) 2018 IEEE. Personal use is permitted, but republication/redistribution requires IEEE permission. See http://www.ieee.org/publications_standards/publications/rights/index.html for more information.

This article has been accepted for publication in a future issue of this journal, but has not been fully edited. Content may change prior to final publication. Citation information: DOI 10.1109/JESTPE.2018.2823904, IEEE Journal of Emerging and Selected Topics in Power Electronics

The proposed algorithm accounts for extra term in cost function, which minimizes the switching changes per switching event thus achieving a minimum energy controller. The switch state change from instant k to k+1 is formulated as:

$$\Delta S(k+1) = S(k+1) - S(k) \tag{8}$$

where S(k) and S(k+1) are the current switching vector and the switching vector to be applied to qZSI at instant (k+1). To achieve a minimum energy controller, the following penalty function is added to the MPC cost function:

$$g_{fs} = \lambda_{fs} \left\| \Delta S(k+1) \right\| \tag{9}$$

By minimizing (9) with weight factor of λ_{fs}, the average energy loss per switching cycle will be reduced.

D. System State Determination

The determinations of the system state are done based on the estimated input inductor (L1) voltage by MPC, the average voltage value of the inductor is computed for every switching cycle (T) based on (3). The MPC algorithm is running at a constant sampling frequency of f_s generating a switching vector every T_s second. The proposed algorithm will count the number of sample (T_s) time (N_1) for which the output vector is in shoot-through (S_9) and number of sample time (N_2) output vector is in active (non-shoot through) state ($S_j \mid j \in [1,8], j \in \mathbb{Z}$) before going into shoot through again. There is a possibility of the qZSI to operate without going in shoot through state, which is only possible when v_{PV} is equal to v_{C1} in (3). The time periods used in (3) can be estimated using the following integers:

$$T_o = N_1 T_S, T_1 = N_2 T_S \Rightarrow T = (N_1 + N_2) T_S \tag{10}$$

There are two possible scenarios of the operation of the qZSI:

1) If N1≠0, meaning the qZSI is boosting the input voltage PV by employing shoot-through state during its operation. In this scenario, the average voltage of the inductor given by equation (3) will be used to determine the state of the system. Time periods T_o, T_1 and T calculated by using equation (10) will be used to balance the inductor volt-sec which should balance in steady state and should be equal to a small value of voltage drop across its ESR only. If volt-sec doesn't balance, that means system is in transient mode and changing the inductor current.
2) If N1=0, qZSI is not boosting the input PV voltage and thus, is not employing shoot through states during its operation. During this case, the capacitor C1 voltage will be equal to the input PV voltage.

TABLE I: SWITCHING TABLE

Switching State	S_1	S_2	S_3	S_4	S_5	S_6	Voltage Magnitude	Angle
000	0	1	0	1	0	1	0	0
100	1	0	0	1	0	1	$\frac{2}{3}V_{DC}$	0
110	1	0	1	0	0	1	$\frac{2}{3}V_{DC}$	$\frac{\pi}{3}$
010	0	1	1	0	0	1	$\frac{2}{3}V_{DC}$	$\frac{2\pi}{3}$
011	0	1	1	0	1	0	$\frac{2}{3}V_{DC}$	π
001	0	1	0	1	1	0	$\frac{2}{3}V_{DC}$	$\frac{4\pi}{3}$
101	1	0	0	1	1	0	$\frac{2}{3}V_{DC}$	$\frac{5\pi}{3}$
111	1	0	1	0	1	0	0	0
S9 (Shoot Through)	1	1	1	1	1	1	0	0

Statement (11) estimates system state factor $\gamma(x)$ by returning 1 (steady state) if the equation is true, 0 otherwise (transient):

$$\gamma(x) = \begin{cases} 1 & x \in S \\ 0 & x \notin S \end{cases} \qquad S = \left\{ \left\| \bar{v}_{L1} \right\| \le \varepsilon \right\} \cup \left\{ V_{C1} = V_{PV} \right\} \tag{11}$$

$\bar{v}_{L1}$ is the average value of inductor voltage from (3) and V_{C1} and V_{PV} are the average values of capacitor C1 voltage and input PV voltage over one switching cycle. ε is the error tolerance for $\bar{v}_{L1}$ as in practical cases, there would be a small DC component of voltage across the inductor due to its ESR. This error tolerance is an important property, as $\bar{v}_{L1}$ will never be zero in any practical case.

The final task of the proposed controller is the over-current protection. The proposed MPC cost function is subject to the constraint given by (12) which bound the output current within a predefined limit:

$$\left\| i_{\alpha\beta} \right\| \le i_{\alpha\beta}^{\max} \quad \text{where } i_{\alpha\beta}^{\max} \in \mathbb{R}^+ \tag{12}$$

The inverter current is constrained by this bound in the optimization of the cost function. This also enforces inverter over-current protection and avoids large inrush current during grid faults and supports LVRT [40]. The bound value $i_{\alpha\beta}^{\max}$ can be set around 90% of the rating of the semiconductor devices used giving a proper headroom to compensate for the various parametric variations in the devices due to heating, ageing etc.

E. Cost Function Computation

In this paper, the cost function computation and minimization is done based on the current state of the system, i.e. transient or steady state. To provide maximum dynamic response while maintaining the lower switching frequency, the system ignores the switching loss optimization during transients to achieve the reference values faster after which the control is switched to work optimally reducing switching effort and energy-loss per switching event. The general form of the cost function is given by (13) with its matrices in Table. II.

$$\begin{aligned} \underset{\substack{\mathbf{I_{ref}(k)} \in \mathbf{I_{ref}} \\ \mathbf{I(k+1)} \in \mathbf{I}}}{\text{minimize}} \quad & g_{\delta\zeta}^{\gamma} = \sum_{n=1}^{2} \lambda_n \left\| \mathbf{I_{ref}}^n\mathbf{(k)} - \mathbf{I}^n\mathbf{(k+1)} \right\| \\ & \qquad + \gamma(x).\left(\lambda_{fs} \left\| S(k+1) - S(k) \right\| \right) \\ \text{subject to } & \dot{x} = \mathbf{A}x + \mathbf{B}_\delta u_\delta + \mathbf{C}y \\ & \left\| i_{\alpha\beta} \right\| \le i_{\alpha\beta}^{\max} \\ & \gamma(x) \in \{0,1\}, \delta \in [0,1], \zeta \in [1,9] \ \ \& \ \ \delta, \zeta \in \mathbb{Z} \end{aligned} \tag{13}$$

Here, the cost function is divided into two parts: major system control objectives and auxiliary minimization of energy loss per switching event. The cost function is minimized based on the system equations developed earlier. In addition, the output current protection is considered while minimizing the cost

2168-6777 (c) 2018 IEEE. Personal use is permitted, but republication/redistribution requires IEEE permission. See http://www.ieee.org/publications_standards/publications/rights/index.html for more information.

This article has been accepted for publication in a future issue of this journal, but has not been fully edited. Content may change prior to final publication. Citation information: DOI 10.1109/JESTPE.2018.2823904, IEEE Journal of Emerging and Selected Topics in Power Electronics

Algorithm 1: Proposed MPC Algorithm

1: *function* PredictiveControl() *sampling* at T_s
Input: $i_{L1}(k)$, $v_{C1}(k)$, $v_{C2}(k)$, $i_{abc,ref}(k)$, $i_{abc}(k)$, $e_{abc}(k)$, $v_{PV}(k)$
Initialization: $N_1, N_2 = 0$
2: *Conversion* from *abc* to *αβ* frame
$x_{\alpha\beta,} = \mathbf{K}x_{abc,} \,|\, x \in \{e_{abc}, i_{abc}, i_{abc,ref}\}$
3: *Loop-1:* State Prediction
Count N_1, number of times output of MPC is shoot-through consecutively.
Count N_2, number of times output of MPC is non-shoot through state between two shoot-through states.
$\gamma(x) \Leftarrow$ Compute from (3), (10), and (11)
4: *Loop-2:* Predictive Control & Cost function Computation
for $i = 0,\ldots,8$:
grid prediction model:
$i_{\alpha\beta}(k+1)_{(i)} \Leftarrow$ Compute from (6) $\forall\ S_j$
subject to ζ
qZSI Predictive model:
$i_{L1}(k+1)_{(i)} \Leftarrow$ Compute from (7) $\forall\ S_j$
subject to δ, ζ
Compute $g^{\gamma}_{\delta\zeta}(i) = g_{\delta\zeta}(i) + g^{\gamma}_{fs}(i)$ **from** (13)
subject to $\dot{x} = \mathbf{A}x + \mathbf{B}_{\delta}u_{\delta} + \mathbf{C}y$
$\left\|i_{\alpha\beta}\right\| \le i^{\max}_{\alpha\beta}$
with constraint of *state factor (γ(x)), non-shoot through indicator (δ), and switching factor (ζ).*
end for
5: *Loop-3:* Cost function minimization
$g_{\min} \Leftarrow \infty, i_{\min} \Leftarrow 0$
for i=0,…,8
if $g^{\gamma}_{\delta\zeta}(i) \le g_{\min,} then$
$g_{\min} \Leftarrow g^{\gamma}_{\delta\zeta}(i), i_{\min} \Leftarrow i$
end if
end for
6: *Return switching state*
Return $\mathbf{S}_i$ (switching state corresponding to ***i***, generating minimum error)
end function

functions. The cost function is adaptive in a sense that it is constrained by $\gamma(x), \delta$, and ζ.

The proposed predictive controller Algorithm. 1 is executed for the number of possible voltage vector states shown in Table. I for the inverter, in this case 9 vectors are obtained including 6 active states, 2 null states and 1 equivalent shoot through state. The prediction of the variable is done for each possible voltage vector state between two switching instants and the cost function (13) is calculated for each voltage vector. The voltage vector generating minimum value of $g^{\gamma}_{\delta\zeta}$ is applied to the inverter. There is no analytical approach to finding the weighing factors which are usually done empirically [39]. The previous systems proposed in literature generally employ more than 3 weighting factors which can make the tuning a complex task hence this problem is eliminated in the presented control. The tuning of factors is done in a way to ensure the stability of the system. Giving the preference to i_{L1} over $i_{\alpha\beta}$ as i_{L1} is the deciding factor for $i_{\alpha\beta}$ and if the change in $i_{\alpha\beta}$ is done faster than the i_{L1}, it can lead to stability issues of the V_{C1} due to extra demand of current on AC side. Also, rather than treating i_{α} and i_{β} as two different cost functions as in conventional MPC for grid-tied inverters [41, 42], in this paper, the proposed controller used the complex notation of the variable.

TABLE II: COST FUNCTION PARAMETERS

n	$\mathbf{I_{ref}}^{n}(\mathbf{k})$	$\mathbf{I}^{n}(\mathbf{k+1})$
1	$i^{\delta}_{L1ref}(k)$	$i_{L1}(k+1)$
2	$i^{\zeta}_{\alpha\beta ref}(k)$	$i_{\alpha\beta}(k+1)$

F. Lyapunov Stability Analysis of the System

System stability is analyzed using Lyapunov stability criterion. The future actual votage vector $v^{\alpha\beta,opt}_{qZSI}(k+1)$ required for perfect tracking can be represented as:

$$v^{\alpha\beta}_{qZSI}(k+1) = v^{\alpha\beta,opt}_{qZSI}(k+1) + \phi(k+1) \tag{14}$$

where, $v^{\alpha\beta}_{qZSI}(k+1)$ shows the converter output voltage vector based on 9 switching states, $v^{\alpha\beta,opt}_{qZSI}(k+1)$ is the optimum voltage vector that can make the current error in next sampling insatnt to zero and $\phi(k+1)$ represents the quantization error in the voltage vectors, here, $\left\|\phi(k+1)\right\| \le l$ and $l \in \mathbb{R}^{+}$.

Since, $v^{\alpha\beta}_{qZSI}(k+1)$ is bounded and is in finite sets, the hysteresis bounds of width $\phi(k+1)$ are also bounded, thus the existence of *'l'* is guaranteed. Taking control parameters defined above, $i_{\alpha\beta-error}$ can be defined as:

$$i_{\alpha\beta-error} = i_{\alpha\beta}(k+1) - i_{\alpha\beta-ref}(k+1) \tag{15}$$

From equation (6),

$$\begin{aligned} i_{\alpha\beta-error}(k+1) &= i_{\alpha\beta}(k)\left[1 - \frac{R}{L}T_S\right] \\ &+ \frac{T_S}{L}(v^{\alpha\beta}_{qZSI}(k) - e_{\alpha\beta}(k)) - i_{\alpha\beta-ref}(k+1) \end{aligned} \tag{16}$$

The goal of the control function is to reduce tracking error $i_{\alpha\beta-error}$ asymptotically to zero or a very small error tolerance value ε. The lyuponav function $L(k)$ is defined as:

$$L(i_{\alpha\beta-error}) = \frac{1}{2}\left[i_{\alpha\beta-error}(k)\right]^{T}\left[i_{\alpha\beta-error}(k)\right] \tag{17}$$

Using (16), the rate of change of lyuponav function can be defined as:

$$\begin{aligned} &\Delta L(i_{\alpha\beta-error}) = L(i_{\alpha\beta-error}(k+1)) - L(i_{\alpha\beta-error}(k)) \\ &\Delta L(i_{\alpha\beta-error}) = \\ &\frac{1}{2}\left[i_{\alpha\beta}(k)\left[1 - \frac{R}{L}T_S\right] + \frac{T_S}{L}(v^{\alpha\beta}_{qZSI}(k) + \phi(k+1) - e_{\alpha\beta}(k)) - i_{\alpha\beta-ref}(k+1)\right]^{T} \\ &\left[i_{\alpha\beta}(k)\left[1 - \frac{R}{L}T_S\right] + \frac{T_S}{L}(v^{\alpha\beta}_{qZSI}(k) + \phi(k+1) - e_{\alpha\beta}(k)) - i_{\alpha\beta-ref}(k+1)\right] \\ &-\frac{1}{2}\left[i_{\alpha\beta-error}(k)\right]^{T}\left[i_{\alpha\beta-error}(k)\right] \end{aligned} \tag{18}$$

2168-6777 (c) 2018 IEEE. Personal use is permitted, but republication/redistribution requires IEEE permission. See http://www.ieee.org/publications_standards/publications/rights/index.html for more information.

This article has been accepted for publication in a future issue of this journal, but has not been fully edited. Content may change prior to final publication. Citation information: DOI 10.1109/JESTPE.2018.2823904, IEEE Journal of Emerging and Selected Topics in Power Electronics

According to lyuponav theorem, for convergence of $i_{\alpha\beta-error}$ to zero and for system to be stable, the rate of change of lyuponav function $\Delta L(i_{\alpha\beta-error})$ should be always negative, thus, $i_{\alpha\beta-error} \to 0$, $iff\ \Delta L(i_{\alpha\beta-error}) < 0$. The discrete future voltage vector which ensure the negative rate of change of $\Delta L(i_{\alpha\beta-error})$ is given by:

$$v_{qZSI}^{\alpha\beta} = \frac{L}{T_S} i_{\alpha\beta}(k+1) + i_{\alpha\beta}(k)\left[R - \frac{L}{T_S}\right] + e_{\alpha\beta} \tag{19}$$

For lyuponav stability, system should follow the following criteria:

$$\begin{aligned} &L(i_{\alpha\beta-error}(k)) \geq C_1 \left|i_{\alpha\beta-error}(k)\right|^{\sigma}, \forall i_{\alpha\beta-error}(k) \in \Upsilon \\ &L(i_{\alpha\beta-error}(k)) \geq C_2 \left|i_{\alpha\beta-error}(k)\right|^{\sigma}, \forall i_{\alpha\beta-error}(k) \in \Gamma \\ &L(i_{\alpha\beta-error}(k+1)) - L(i_{\alpha\beta-error}(k)) < -C_3 \left|i_{\alpha\beta-error}(k)\right|^{\sigma} + C_4 \\ &C_1, C_2, C_3, C_4 \in \mathbb{R}^+, \sigma \geq 1 \\ &\Upsilon \in \mathbb{R}^+, \Gamma \subset \Upsilon \end{aligned} \tag{20}$$

Substituting (19) in (18)

$$\Delta L(k) \leq \frac{1}{2}\left(\frac{T_S}{L}\right)^2 l^2 - \frac{1}{2}\left[i_{\alpha\beta-error}(k)\right]^T \left[i_{\alpha\beta-error}(k)\right] \tag{21}$$

Also, the current vector converges to compact given by equation (22)

$$\Omega = \left\{ \left\| i_{\alpha\beta-error}(k) \right\| \left\| i_{\alpha\beta-error}(k) \right\| \leq \frac{T_S}{L} l \right\} \tag{22}$$

From (20),

$$C_1 = C_2 = 1$$

$$C_3 = \frac{1}{2}, C_4 = \frac{1}{2}\left(\frac{L}{T_s}\right)^2 l^2$$

Therefore, all the signals will be bounded and will satisfy the Lyapunov stability criterion.

IV. Results and Discussions

The proposed system and controller is verified experimentally using dSPACE-DS1007 platform. The performance of the proposed PEI is evaluated for the following criteria: solar irradiance variation and reactive power compensation of the passive load connected at the PCC. The system is analyzed independently at the PV side for its MPP tracking performance by the system while simultaneously controlling the reactive power injection into the grid and their dynamic response on controlled parameters. Table. III shows the parameters of the system and Table. IV shows the controller parameters. The results are verified for above criteria and are shown in Fig. 5-Fig. 12. This section has been further divided for a clear overview as, A) PV side dynamics, B) Grid side dynamics, C) Parameter variation effect, and D) Proposed controller performance comparison.

TABLE III: System Parameters

Parameters	Values
V_{abc}	208VRMS (L-L)
Frequency	60Hz
PV MPP @ STC	2250W
V_{MP}	276.3V
I_{MP}	8.15A
RL Filter	1.5mH-0.01Ω
L1and L2	1mH
C1 and C2	1000μF

TABLE IV: Controller Parameters

Parameters	Values
Weight Factor i_{L1}	1
Weight Factor $i\alpha\beta$	0.25
Weight Factor for fs	0.02
Sampling Time (T_s)	100kHz
Average Switching frequency	22kHz

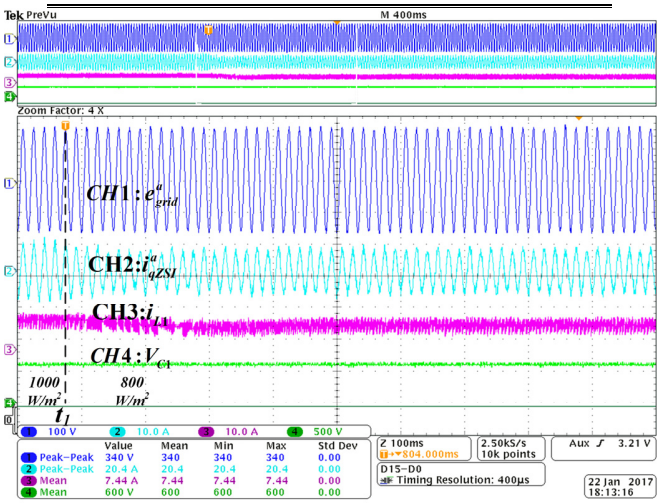

Fig. 5 The solar insolation changes from 1000W/m² to 800W/m². The step change in active power reference from the MPPT algorithm occurs at t_1. e^a_{grid} is the PCC voltage, i^a_{qZSI} is the phase a current fed by qZSI to PCC, il_1 is the qZSI input inductor current, and Vc1 is the qZSI C1 voltage.

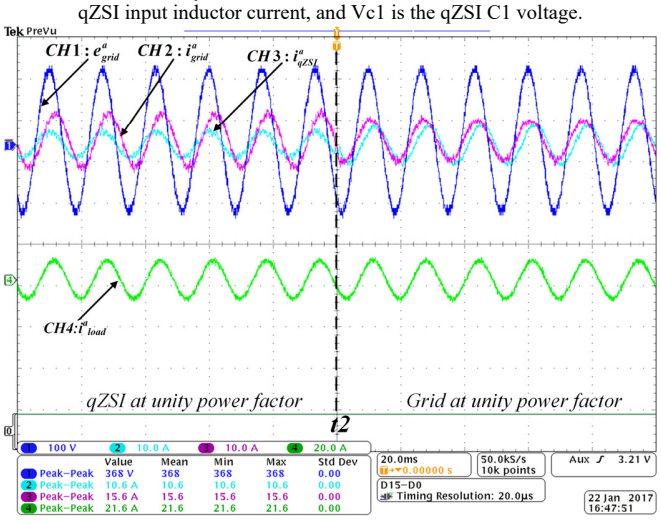

Fig. 6 Reactive power compensation by qZSI: grid current, grid voltage, inductive load current, and qZSI current waveforms before and after triggering the reactive power compensation.

2168-6777 (c) 2018 IEEE. Personal use is permitted, but republication/redistribution requires IEEE permission. See http://www.ieee.org/publications_standards/publications/rights/index.html for more information.

This article has been accepted for publication in a future issue of this journal, but has not been fully edited. Content may change prior to final publication. Citation information: DOI 10.1109/JESTPE.2018.2823904, IEEE Journal of Emerging and Selected Topics in Power Electronics

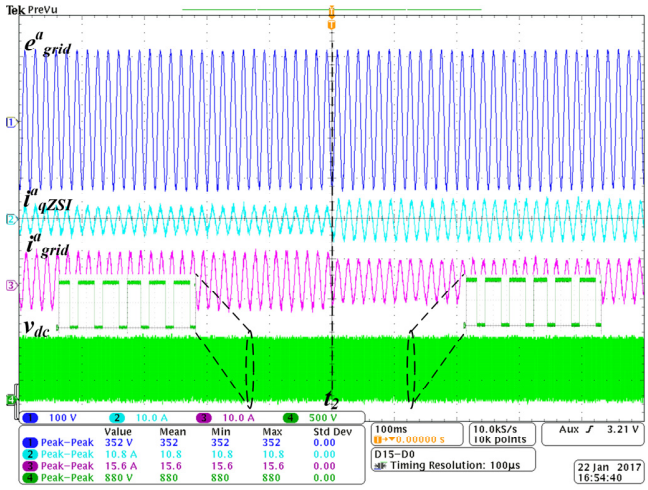

Fig. 7 Effect of triggering the reactive power compensation at t_2 by qZSI on DC-link voltage, grid current, and qZSI current. e^a_{grid} is the PCC voltage, i^a_{qZSI} is the phase a current fed by qZSI to PCC, i^a_{grid} is the grid current, and v_{dc} is the qZSI DC link pulsating voltage demonstrating boosting operation.

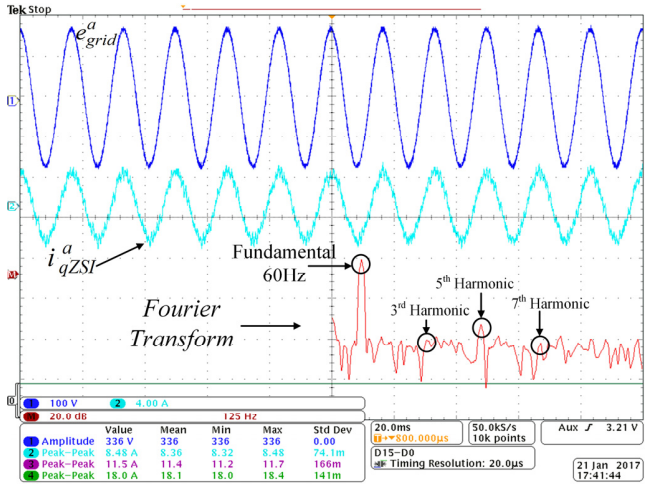

Fig. 8 Injected qZSI current and its FFT analysis.

A. PV Side dynamics

Fig. 5 shows the DC side parameters of the qZSI during the transient operation of the system. A step change is applied to solar irradiance level decreasing the irradiance from 1000W/m2 to 800W/m2, which is followed by the fall in i_{L1} as shown in Fig. 5. The V_{C1} was constantly maintained at 600V during the transient operation showing the dynamic performance and effectiveness of the control. The e_a and i_a are shown to be in-phase showing the active power injection by the qZSI. In this, qZSI is only catering the active power of the load by pushing the maximum available power from the PV.

B. Grid Side dynamics

Fig. 6 shows the reactive power compensation for the local loads shown in Fig. 1. The system is commanded to change the operation from lagging power factor to unity power factor at grid side by compensating the reactive power of the load by qZSI. During this time, qZSI will partially behave as STACOM. This paper adopts conventional load reactive power compensation method to show the effectiveness of the control. In Fig. 6, before instant t_2, the reactive power command was 0, thus all the reactive power is supplied by the grid and can be

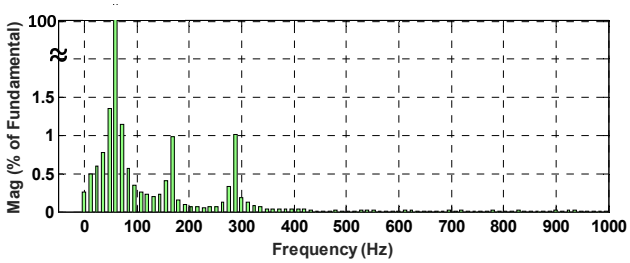

FIG. 9 Detailed FFT analysis

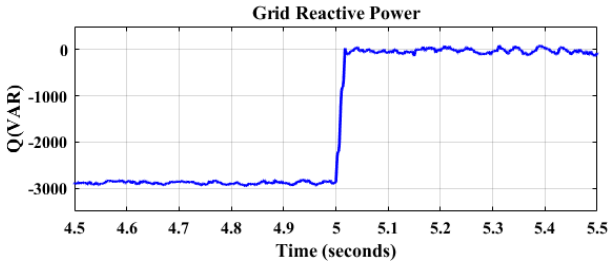

Fig. 10 Dynamic response of the grid reactive power to reactive power compensation by the qZSI.

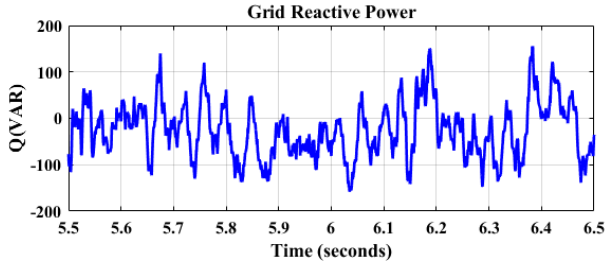

Fig. 11 Grid reactive power ripple after compensation by qZSI.

seen as grid current is leading the voltage and qZSI is operating at the unity power factor. At instant t_2, the reactive power is commanded to make the grid at unity power factor as in conventional STATCOMs, thus making grid at unity power factor and qZSI at leading. The reactive power demand of 750VAR has been compensated by the qZSI along with the PV MPP of 2.25kW.

Fig. 7 shows the DC link of qZSI, grid voltage, qZSI injected current and grid current for reactive power compensation, which was elaborated in Fig. 6. The pulsating DC link shows the boosting operation. The system followed the command without any DC link voltage spike. This ensures the system dynamic performance as well as current bound limits of the system. Current is limited within bounds eliminating the sudden spikes in the voltages which can result in damaging of semi-conductor devices. Also, the zoomed in DC link voltage before and after the reactive power commend verifies that the control maintains the same boosting ratio confirming that the system is maintaining MPP tracking independent of the reactive power injection. Fig. 8 shows the Fast Fourier Transform (FFT) of the injected qZSI currents. As seen, the system has high fundamental peak with all the harmonics distributed over the band. This is due to the variable switching frequency of the MPC. This is advantageous as the distribution of harmonics reduced the individual 3rd, 5th and 7th harmonic magnitude and provide low (3.2%) Total Harmonics Distortion (THD) current, which is within IEEE-519 standards [43]. The detailed FFT

2168-6777 (c) 2018 IEEE. Personal use is permitted, but republication/redistribution requires IEEE permission. See http://www.ieee.org/publications_standards/publications/rights/index.html for more information.

This article has been accepted for publication in a future issue of this journal, but has not been fully edited. Content may change prior to final publication. Citation information: DOI 10.1109/JESTPE.2018.2823904, IEEE Journal of Emerging and Selected Topics in Power Electronics

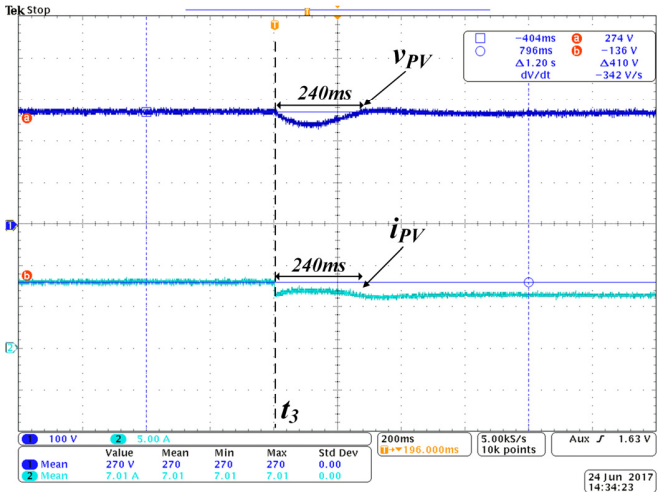

Fig. 12 Irradiance step change at t_3 from 1000W/m^2 to 800W/m^2.

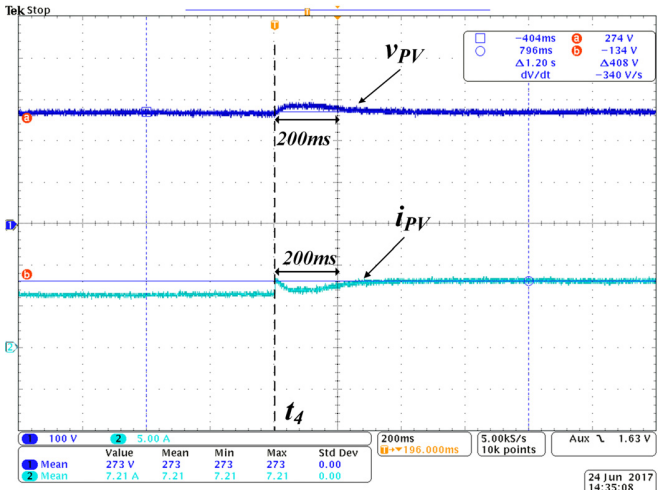

Fig. 13 Irradiance step change at t_4 from 800W/m^2 to 1000W/m^2.

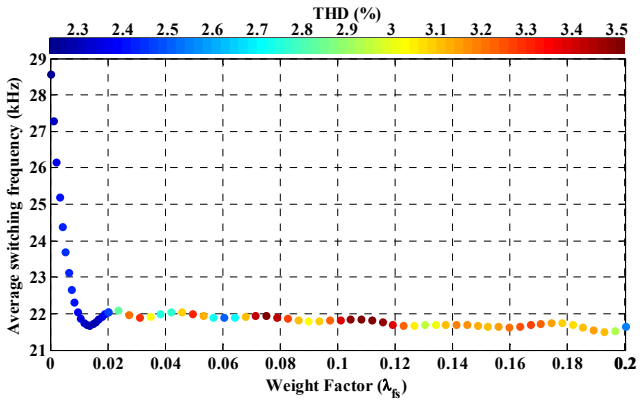

Fig. 14 Variation of switching frequency and THD with respect to weight factor of g_{fs}^{γ}.

TABLE V: PV MPP EFFICIENCY

IRRADIANCE (W/m^2)	PV MPP TRACKING EFFICIENCY (%)	RIPPLE (%)
1000	99.14	0.632
900	98.11	0.3735
800	98.165	0.6735

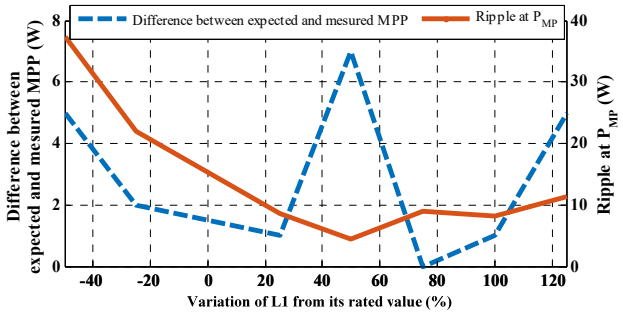

Fig. 15 Variation of L1 from its nominal model and its effect on MPP tracking at irradiance of 1000W/m^2.

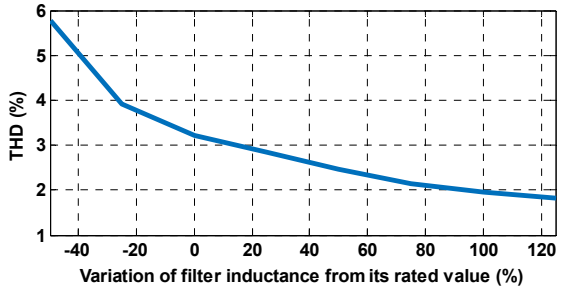

Fig. 16 Variation of filter inductance from its nominal model and its effect on THD at irradiance of 1000W/m^2.

waveform is shown in Fig. 9 to confirm the low THD of 3.2% which can be verified by looking at the harmonics percentages.

Fig. 10 shows the response of the grid to the reactive power compensation by the qZSI triggered at t=5sec and Fig. 11 shows the grid reactive power ripple and tracking error in steady state. Fig. 10 shows the fast-dynamic response of the system to the commanded reactive power and reach the steady state in less than 20ms, which is nearly one AC cycle of the grid. Fig.12 and Fig. 13 shows the performance of the MPPT and the current controller on V_{PV} and I_{PV} during positive (800W/m^2 to 1000W/m^2) and negative (1000W/m^2 to 800W/m^2) irradiance transients.

It can be seen from both the Fig. 12 and Fig. 13, that the PV voltage remains almost constant whereas the PV current has changed to track the MPP. The above-mentioned figures also demonstrate the speed at which the MPP is being tracked. During negative transient at t_3, Fig. 12, the sudden power decrease leads to voltage dip (undershoot) at the DC bus of around 80V. After the transient, the system recovered within 240ms and reached the previous voltage value as well as new MPP current of 6.15A with the MPP efficacy of 98.165%. During positive step at t_4 in Fig. 13, the overshoot is around 20V which is significantly lower than the undershoot as expected because at this point the extracted power is less than PV MPP. Therefore, system recovered in 200ms to the new MPP with the MPP current as 8.1A tracking MPP with an efficacy of 99.14%.

C. *Parameter Variations effect*

Fig. 14 shows the effect of optimal control effort on the system parameters like average switching frequency and THD of the injected current. The graph shows the variation of average switching frequency with weight factor λ_{fs}. The THD is represented by the color variation on the scattered points. The THD of the injected current is low at high switching frequency

2168-6777 (c) 2018 IEEE. Personal use is permitted, but republication/redistribution requires IEEE permission. See http://www.ieee.org/publications_standards/publications/rights/index.html for more information.

This article has been accepted for publication in a future issue of this journal, but has not been fully edited. Content may change prior to final publication. Citation information: DOI 10.1109/JESTPE.2018.2823904, IEEE Journal of Emerging and Selected Topics in Power Electronics

as expected for low weight factors. The increase in weight factor decrease the frequency significantly in started showing the effect of the optimal control effort for minimizing the energy-losses per switching event.

Table. V Shows the MPP tracking efficiency of the system for various irradiance values and the corresponding power ripple. The overall system efficiency was found to be 85.6% at STC condition. The system maintained a good tracking accuracy and negligible power ripple of less than 1% for every irradiance. On the scale of 2.25kW, the power ripple is negligible and doesn't effect the system. In addition to test the MPC robustness with the parameter variation, both the parameters used in MPC are varied without changing the MPC algorithm and their corresponding affect on controller perfromance on MPP tracking, MPP ripple and maintaining low THD is analyzed. Fig. 15 and Fig. 16 shows the variation of input inductor L1 and filter inductor L variation respectively.

Fig. 15 shows the variation of L1 from -50% to 125% its rated value, and the PV MPP efficiency along with PV MPP ripples is measured. It is found that, the difference between the expected MPP and the measured is less than 8W for the whole L1 variation range which is 0.35% of the rated L1 MPP value. Further, the ripple at any variation point is within 2% of the maximum power at STC. Fig. 16 shows the same variation of filter inductance from -50% to 125% of its rated value and its affect on the THD value of the injected current. The THD value is in compliance and is 5.7% for the -50% variation in inductance.

The above analysis confirms the robustness of the controller on the model parameter variation of the system. Also, the effect of V_{C1} on the system will be negligible, as it is not included in the MPC algorithm to compute future values which require exact values. This is another advantage of using PI controller for the V_{C1} which automatically compensate for the variation of C1 and have negligible effect on the performance of the system.

D. Proposed Controller Dynamic Performance Analysis and Comparison

Fig. 17 shows the imported oscilloscope data of measured PCC voltage along with the grid current to clearly demonstrate the reactive power compensation and unity power factor operation. At t2, reactive power compensation is turned off as marked on Fig. 17. Lines have been marked before and after t2 to show the out of phase and in phase nature of the current to further verify the unity power operation after t2. Also, settling time has been marked showing the controller response time of less than one power cycle to achieve the compensation. The fast response shows the effectiveness of proposed control scheme.

Fig. 18 and Fig. 19 shows the tracking performance of active and reactive power for the experiment of Fig. 6 at time t2. Fig. 18 shows the tracking performance of the reactive power compensation. Reactive power compensation was triggered at 0.5sec. The system followed the reference and was able to track the reference under 250ms as can be verified from the Fig. 18. Similarly, Fig. 19 shows the tracking performance of the active power reference for the experiment of Fig. 5 at time t1 in the revised manuscript. For this, PV irradiance have been stepped to decrease the active power input to the system

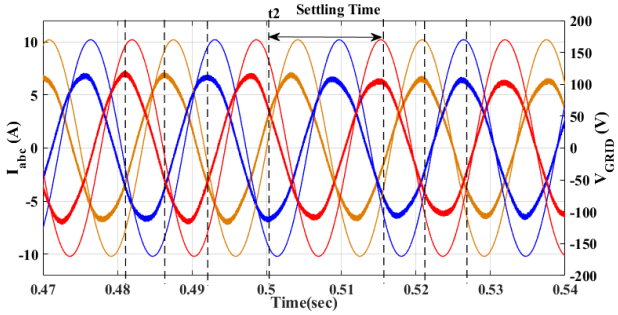

Fig. 17 Dynamic response of the grid reactive power to reactive power compensation by the qZSI.

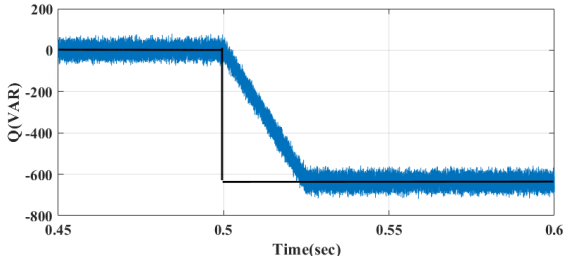

Fig. 18 Step response of reactive power compensation

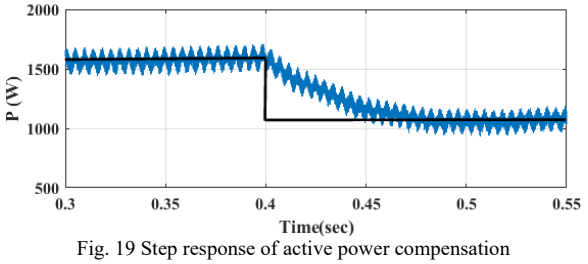

Fig. 19 Step response of active power compensation

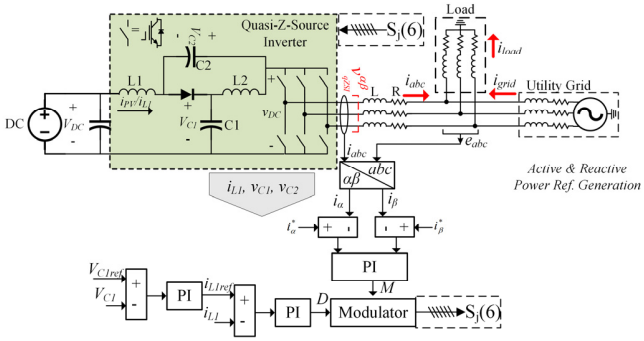

Fig. 20 Classical PI controller approach for the qZSI under study.

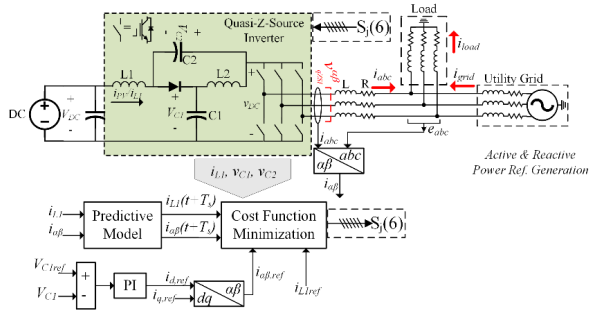

Fig. 21 The proposed control scheme based on MPC for qZSI with advance functionality.

which is followed by the MPPT and MPC controller which consequently reduce the active power injection into the grid. Further the performance comparison between classical

2168-6777 (c) 2018 IEEE. Personal use is permitted, but republication/redistribution requires IEEE permission. See http://www.ieee.org/publications_standards/publications/rights/index.html for more information.

This article has been accepted for publication in a future issue of this journal, but has not been fully edited. Content may change prior to final publication. Citation information: DOI 10.1109/JESTPE.2018.2823904, IEEE Journal of Emerging and Selected Topics in Power Electronics

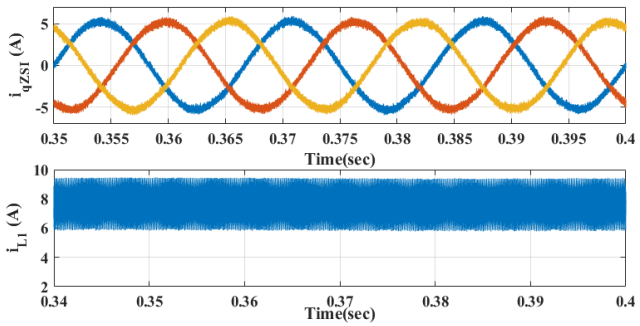

Fig. 22 Classical control-based response.

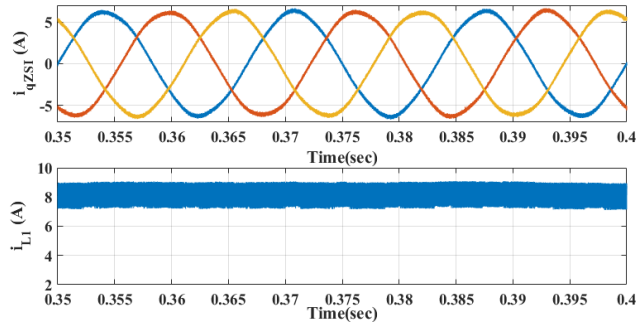

Fig. 23 MPC based control response.

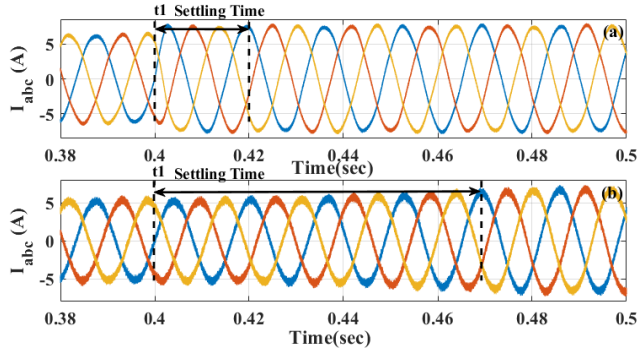

Fig. 24 (a) MPC, (b) classical based control response to step change in reactive power compensation.

controller and propose MPC based controller is performed. Fig. 20 shows the general classical controller and Fig. 21 shows the control block diagram of the proposed controller. In this analysis, the PI controller gains for conventional method are designed using the well-known Ziegler-Nichols method which is basically evaluates the step response of the system for determination of the gains, this technique is widely used in industry.

The structure of the proposed model based predictive controller differs from the PI based controller since there is no modulator and no cascaded liner controller which are challenging to tune and are not robust to grid abnormalities for the application in this paper. In the proposed system a single cost function is utilized for optimal actuation. Thus, it is easier to design since there are no cascaded modules as in classical linear controllers that must be tuned simultaneously to achieve smooth dynamic response and negligible active and reactive power tracking error in steady state operation.

Fig. 22 shows the output current and input inductor current using classical controller and Fig. 23 shows the same parameters using the MPC based controller. As can be observed the proposed controller has lower current ripple at both AC side and DC side input inductor. This is since MPC is hysteresis type of controller and can instantaneously follow the reference by applying the appropriate voltage vectors and thus, can achieve very small current ripples. Further, both the system has been compared for the step response for the reactive power compensation at t1. Fig. 24 shows the response comparison. Fig. 24 (a) shows the MPC response and Fig. 24(b) shows the classical control response. As can be observed, the MPC was able to respond within single cycle to achieve the reference whereas classical control took around 2-3 cycles.

V. Conclusion

A grid-tied PEI using qZSI for PV applications is developed based on MPC framework. The system is analyzed for PV application as Distributed Generation unit along with ancillary service requirement by the grid at PCC. The proposed control accurately generates the references of the variables to be controlled. A PI module is used to regulate the DC bus voltage and the conventional Incremental & Conductance algorithm for PV MPP current (I_{MP}) generation reference. Finally, the qZSI predictive model is used to generate the voltage vector and switching pulses for the qZSI leading to the lowest error between the predictive and reference values. The system also tackles the problem of overcurrent during grid faults and provide cycle by cycle overcurrent protection which is constraint to optimize the cost function. Further, a minimum energy controller is also included in the algorithm to minimize the switching effort to go from one voltage vector to another, thus, aims on reducing the switching losses. The system was first designed, simulated, and finally tested experimentally using dSpace-1007. The system was capable of tracking and delivering maximum power from PV with fast tracking dynamics along with independent reactive power compensation for the load/grid connected at the PCC. The system could condition the grid by supplying the required reactive power thus making grid operate at unity power factor.

References

[1] Z. Moradi-Shahrbabak, A. Tabesh, and G. R. Yousefi, "Economical Design of Utility-Scale Photovoltaic Power Plants With Optimum Availability," *IEEE Trans. on Ind. Elect.,* vol. 61, pp. 3399-3406, 2014.

[2] H. Long, M. Eghlimi, and Z. Zhang, "Configuration Optimization and Analysis of a Large Scale PV/Wind System," *IEEE Trans. on Sust. Energy,* vol. 8, pp. 84-93, 2017.

[3] S. B. Kjaer, J. K. Pedersen, and F. Blaabjerg, "A review of single-phase grid-connected inverters for photovoltaic modules," *IEEE Trans. on Ind. App.,* vol. 41, pp. 1292-1306, 2005.

[4] Y. Liu, B. Ge, H. Abu-Rub, and F. Z. Peng, "Control System Design of Battery-Assisted Quasi-Z-Source Inverter for Grid-Tie Photovoltaic Power Generation," *IEEE Trans. on Sust. Energy,* vol. 4, pp. 994-1001, 2013.

[5] M. Shen, A. Joseph, J. Wang, F. Z. Peng, and D. J. Adams, "Comparison of Traditional Inverters and Z -Source Inverter for Fuel Cell Vehicles," *IEEE Trans. on Pow. Elect.,* vol. 22, pp. 1453-1463, 2007.

[6] P. Fang Zheng, "Z-source inverter," *IEEE Trans. on Ind. App.,* vol. 39, pp. 504-510, 2003.

[7] Y. Li, S. Jiang, J. G. Cintron-Rivera, and F. Z. Peng, "Modeling and Control of Quasi-Z-Source Inverter for Distributed Generation Applications," *IEEE Trans. on Ind. Elect.,* vol. 60, pp. 1532-1541, 2013.

[8] D. Sun, B. Ge, W. Liang, H. Abu-Rub, and F. Z. Peng, "An Energy Stored Quasi-Z-Source Cascade Multilevel Inverter-Based Photovoltaic Power

2168-6777 (c) 2018 IEEE. Personal use is permitted, but republication/redistribution requires IEEE permission. See http://www.ieee.org/publications_standards/publications/rights/index.html for more information.

This article has been accepted for publication in a future issue of this journal, but has not been fully edited. Content may change prior to final publication. Citation information: DOI 10.1109/JESTPE.2018.2823904, IEEE Journal of Emerging and Selected Topics in Power Electronics

Generation System," *IEEE Trans. on Ind. Elect.,* vol. 62, pp. 5458-5467, 2015.
[9] B. Anvari, M. Shirinabadi, and E. Afjei, "Design and Simulation of Z-Source Inverter for Brushless DC Motor Drive," *International Research Journal of Applied and Basic Sciences,* vol. 7, pp. 417-421, 2013.
[10] D. Cao, S. Jiang, X. Yu, and F. Z. Peng, "Low-cost semi-Z-source inverter for single-phase photovoltaic systems," *IEEE Transactions on Power Electronics,* vol. 26, pp. 3514-3523, 2011.
[11] A. Ayad, P. Karamanakos, and R. Kennel, "Direct Model Predictive Current Control Strategy of Quasi-Z-Source Inverters," *IEEE Trans. on Pow. Elect.,* vol. PP, pp. 1-1, 2016.
[12] D. Hamza, M. Qiu, and P. K. Jain, "Application and Stability Analysis of a Novel Digital Active EMI Filter Used in a Grid-Tied PV Microinverter Module," *IEEE Trans. on Pow. Elect.,* vol. 28, pp. 2867-2874, 2013.
[13] A. Abdelhakim, P. Davari, F. Blaabjerg, and P. Mattavelli, "Switching Loss Reduction in the Three-Phase Quasi-Z-Source Inverters Utilizing Modified Space Vector Modulation Strategies," *IEEE Transactions on Power Electronics,* 2017.
[14] V. Erginer and M. H. Sarul, "A novel reduced leakage current modulation technique for Z-source inverter used in photovoltaic systems," *IET Power Electronics,* vol. 7, pp. 496-502, 2013.
[15] N. Noroozi and M. R. Zolghadri, "Three-Phase Quasi-Z-Source Inverter with Constant Common-Mode Voltage for Photovoltaic Application," *IEEE Transactions on Industrial Electronics,* 2017.
[16] Y. Zhou, L. Liu, and H. Li, "A high-performance photovoltaic module-integrated converter (MIC) based on cascaded quasi-Z-source inverters (qZSI) using eGaN FETs," *IEEE Transactions on Power Electronics,* vol. 28, pp. 2727-2738, 2013.
[17] J. Anderson and F. Z. Peng, "Four quasi-Z-Source inverters," in *2008 IEEE Power Electronics Specialists Conference*, 2008, pp. 2743-2749.
[18] A. Anurag, Y. Yang, and F. Blaabjerg, "Thermal performance and reliability analysis of single-phase PV inverters with reactive power injection outside feed-in operating hours," *IEEE Journal of emerging and selected topics in power electronics,* vol. 3, pp. 870-880, 2015.
[19] A. Hoke, M. Shirazi, S. Chakraborty, E. Muljadi, and D. Maksimovic, "Rapid Active Power Control of Photovoltaic Systems for Grid Frequency Support," *IEEE Journal of Emerging and Selected Topics in Power Electronics,* 2017.
[20] Y. Yang, H. Wang, and F. Blaabjerg, "Reactive Power Injection Strategies for Single-Phase Photovoltaic Systems Considering Grid Requirements," *IEEE Transactions on Industry Applications,* vol. 50, pp. 4065-4076, 2014.
[21] F. Cleveland, "Recommendations for Advanced Functions for Distributed Energy Resources (DER) Systems," March 12, 2015 ed. California: Public Utilities Commision, 2015, pp. 1-12.
[22] P. Cortes, M. P. Kazmierkowski, R. M. Kennel, D. E. Quevedo, and J. Rodriguez, "Predictive Control in Power Electronics and Drives," *IEEE Trans. on Ind. Elect.,* vol. 55, pp. 4312-4324, 2008.
[23] N. Panten, N. Hoffmann, and F. W. Fuchs, "Finite control set model predictive current control for grid-connected voltage-source converters with LCL filters: A study based on different state feedbacks," *IEEE Transactions on Power Electronics,* vol. 31, pp. 5189-5200, 2016.
[24] M. B. Shadmand, M. Mosa, R. S. Balog, and H. Abu-Rub, "Model Predictive Control of a Capacitorless Matrix Converter-Based STATCOM," *IEEE Journal of Emerging and Selected Topics in Power Electronics,* vol. 5, pp. 796-808, 2017.
[25] S. Vazquez, J. Rodriguez, M. Rivera, L. G. Franquelo, and M. Norambuena, "Model Predictive Control for Power Converters and Drives: Advances and Trends," *IEEE Trans. on Ind. Elect.,* vol. 64, pp. 935-947, 2017.
[26] L. Tarisciotti, A. Formentini, A. Gaeta, M. Degano, P. Zanchetta, R. Rabbeni, *et al.*, "Model Predictive Control for Shunt Active Filters With Fixed Switching Frequency," *IEEE Trans. on Ind. App.,* vol. 53, pp. 296-304, 2017.
[27] V. Yaramasu, B. Wu, M. Rivera, and J. Rodriguez, "A new power conversion system for megawatt PMSG wind turbines using four-level converters and a simple control scheme based on two-step model predictive strategy—Part II: Simulation and experimental analysis," *IEEE Journal of Emerging and Selected Topics in Power Electronics,* vol. 2, pp. 14-25, 2014.
[28] H. A. Hussain, B. Anvari, and H. A. Toliyat, "A control method for linear permanent magnet electric submersible pumps in a modified integrated drive-motor system," in *IEEE International Electric Machines and Drives Conference (IEMDC)*, 2017, pp. 1-7.
[29] D. M. Vilathgamuwa, C. J. Gajanayake, and P. C. Loh, "Modulation and control of three-phase paralleled Z-source inverters for distributed generation applications," *IEEE Transactions on energy conversion,* vol. 24, pp. 173-183, 2009.
[30] Y. Liu, B. Ge, H. Abu-Rub, H. Sun, F. Z. Peng, and Y. Xue, "Model Predictive Direct Power Control for Active Power Decoupled Single-Phase Quasi-Z-Source Inverter," *IEEE Trans. on Ind. Inform.,* vol. 12, pp. 1550-1559, 2016.
[31] W. Wu, Y. He, T. Tang, and F. Blaabjerg, "A New Design Method for the Passive Damped LCL and LLCL Filter-Based Single-Phase Grid-Tied Inverter," *IEEE Transactions on Industrial Electronics,* vol. 60, pp. 4339-4350, 2013.
[32] J. Xu, S. Xie, and T. Tang, "Active Damping-Based Control for Grid-Connected LCL-Filtered Inverter With Injected Grid Current Feedback Only," *IEEE Trans. on Ind. Elect.,* vol. 61, pp. 4746-4758, 2014.
[33] S. Jayalath and M. Hanif, "Generalized LCL-Filter Design Algorithm for Grid-Connected Voltage-Source Inverter," *IEEE Trans. on Ind. Elect.,* vol. 64, pp. 1905-1915, 2017.
[34] D. Pan, X. Ruan, C. Bao, W. Li, and X. Wang, "Optimized Controller Design for LCL-Type Grid-Connected Inverter to Achieve High Robustness Against Grid-Impedance Variation," *IEEE Trans. on Ind. Elect.,* vol. 62, pp. 1537-1547, 2015.
[35] J. Khajesalehi, K. Sheshyekani, M. Hamzeh, and E. Afjei, "High-performance hybrid photovoltaic -battery system based on quasi-Z-source inverter: application in microgrids," *IET Generation, Transmission & Distribution,* vol. 9, pp. 895-902, 2015.
[36] Y. Zhang, S. Huang, and S. Hu, "Ride-through strategy of quasi-Z-source wind power generation system under the asymmetrical grid voltage fault," *IET Electric Power Applications,* vol. 11, pp. 504-511, 2017.
[37] M. Mosa, R. Balog, and H. Abu-Rub, "High Performance Predictive Control of Quasi Impedance Source Inverter," *IEEE Trans. on Power Elect.,* vol. PP, pp. 1-1, 2017.
[38] K. S. Tey and S. Mekhilef, "Modified Incremental Conductance Algorithm for Photovoltaic System Under Partial Shading Conditions and Load Variation," *IEEE Trans. on Ind. Elect.,* vol. 61, pp. 5384-5392, 2014.
[39] S. Bayhan, M. Trabelsi, H. Abu-Rub, and M. Malinowski, "Finite Control Set Model Predictive Control for a Quasi-Z-Source Four-Leg Inverter Under Unbalanced Load Condition," *IEEE Trans. on Ind. Elect.,* vol. PP, pp. 1-1, 2016.
[40] M. Mirhosseini, J. Pou, and V. G. Agelidis, "Single- and Two-Stage Inverter-Based Grid-Connected Photovoltaic Power Plants With Ride-Through Capability Under Grid Faults," *IEEE Trans. on Sust. Energy,* vol. 6, pp. 1150-1159, 2015.
[41] S. Bayhan, H. Abu-Rub, and R. S. Balog, "Model Predictive Control of Quasi-Z-Source Four-Leg Inverter," *IEEE Trans. on Ind. Elect.,* vol. 63, pp. 4506-4516, 2016.
[42] S. Bayhan, M. Trabelsi, and H. Abu-Rub, "Model Predictive Control of Z-Source four-leg inverter for standalone Photovoltaic system with unbalanced load," in *2016 IEEE (APEC)*, 2016, pp. 3663-3668.
[43] I. W. Group, "IEEE recommended practices and requirements for harmonic control in electrical power systems," *IEEE STD,* pp. 519-1992, 1992.

Sarthak Jain (S'13) received the B.Tech. degree in electrical engineering from GGSIPU, Delhi, India, in 2014. He is currently working towards his master's degree in electrical engineering from Texas A&M University, College Station, TX, USA.

He was research associate in Renewable Energy and Advanced Power Electronics Laboratory from 2016-2017. Before joining Texas A&M University, he was research associate at Delhi Technological University, Delhi, INDIA from 2014-2016. There, he worked on a project titled 'Reliability and Efficient System for Community Energy Solutions (RESCUES)' under Imperial College London and DST INDIA. His research interest includes power electronics circuit design, DC/AC PV grid tied inverters, DC/DC resonant converters, etc.

2168-6777 (c) 2018 IEEE. Personal use is permitted, but republication/redistribution requires IEEE permission. See http://www.ieee.org/publications_standards/publications/rights/index.html for more information.

This article has been accepted for publication in a future issue of this journal, but has not been fully edited. Content may change prior to final publication. Citation information: DOI 10.1109/JESTPE.2018.2823904, IEEE Journal of Emerging and Selected Topics in Power Electronics

Mohammad B. Shadmand (S'09, M'15) received the B.S. degree in electrical engineering from Qatar University, Doha, Qatar, in 2010. He received the M.S. and PhD degrees in electrical engineering from Texas A&M University, College Station, TX, USA in 2012 and 2015.

He was a research associate in renewable energy and advanced power electronics research laboratory, TX, USA from 2010-2015. He was a visiting researcher with Smart Grid Center, Texas A&M University at Qatar, 2014. He was an instructor in Department of Electrical and Computer Engineering, Texas A&M University, College Station, TX, USA from 2015-2016. He was a TEES research engineer in renewable energy and advanced power electronics research laboratory, TX, USA from 2016-2017. He is currently an Assistant Professor in the Department of Electrical and Computer Engineering and Director of the Renewable Energy and Power Quality Research Laboratory at Kansas State University, Manhattan, KS, USA since 2017. He has published more than 50 journal and conference papers. His current research interests include advanced model predictive control, grid-tied power electronics interfaces with advance functionalities, matrix converter, and control of smart microgrid systems.

Dr. Shadmand was awarded second place in the IEEE Industrial Application Society Graduate Thesis Contest for his M.S. thesis in 2013. He received the IEEE Standard Education award for the project "fixed-step model predictive control of grid-tied photovoltaic inverter" in 2014. He was awarded Michelle Munson_serban Simu Keystone Research Scholar, Kansas State University in 2017.

Robert S. Balog (S'92–M'96–SM'07) received the B.S. degree in electrical engineering from Rutgers – The State University of New Jersey, New Brunswick, NJ in 1996 and the M.S. and Ph.D. degrees in electrical engineering from the University of Illinois at Urbana-Champaign, Urbana, IL in 2003 and 2006 respectively.

He was an Engineer with Lutron Electronics, Coopersburg, PA from 1996 to 1999, a Researcher with the U.S. Army Corp of Engineers, Engineering Research and Development Center (ERDEC), Construction Engineering Research Lab (CERL), Champaign, IL from 2005-2006, a Senior Engineer at SolarBridge Technologies (now SunPower Inc.), Champaign, IL from 2006 to 2009, then joined Texas A&M University, College Station, Tx, where he is currently an Associate Professor in the Department of Electrical and Computer Engineering and Director of the Renewable Energy & Advanced Power Electronics Research Laboratory. He holds a joint faculty appointment with the Department of Electrical Engineering at Texas A&M University in Qatar.

He holds 18 issued U.S. patent with additional patents pending. His current research interests include power converters for solar energy, particularly microinverters for ac photovoltaic (ACPV) modules and highly reliable electrical power and energy systems including dc microgrids. Dr. Balog is a Registered Professional Engineer in Illinois. He received the IEEE Joseph J. Suozzi INTELEC Fellowship in Power Electronics in 2001. He is a member of Eta Kappa Nu, Sigma Xi, the National Society of Professional Engineers, the American Solar Energy Society and the Solar Electric Power Association. He is the 2011 recipient of the Rutgers School of Engineering Distinguished Engineer award.

2168-6777 (c) 2018 IEEE. Personal use is permitted, but republication/redistribution requires IEEE permission. See http://www.ieee.org/publications_standards/publications/rights/index.html for more information.

ResearchGate

See discussions, stats, and author profiles for this publication at: https://www.researchgate.net/publication/324195499

Design and Optimization of Composite Horizontal Axis Wind Turbine (Hawt) Blade

Article · April 2018

DOI: 10.4271/2018-01-1034

CITATIONS
0

READS
30

3 authors, including:

Naveen Kumar
Delhi Technological University
115 PUBLICATIONS **877** CITATIONS

SEE PROFILE

Some of the authors of this publication are also working on these related projects:

Flow Simulation and Aerodynamic analysis View project

Alternative fuel View project

All content following this page was uploaded by Naveen Kumar on 08 April 2018.

The user has requested enhancement of the downloaded file.

Downloaded from SAE International by Naveen Kumar, Sunday, April 08, 2018

2018-01-1034 Published 03 Apr 2018

Design and Optimization of Composite Horizontal Axis Wind Turbine (Hawt) Blade

Rohan Brella, Mayank Sehgal, and Naveen Kumar Delhi Technological University

Citation: Brella, R., Sehgal, M., and Kumar, N., "Design and Optimization of Composite Horizontal Axis Wind Turbine (Hawt) Blade," SAE Technical Paper 2018-01-1034, 2018, doi:10.4271/2018-01-1034.

Abstract

Wind energy is clean and renewable source of energy that is an attractive alternative to non-conventional sources of energy. Due to rapid increase in global energy requirements, this form of energy is gaining its share of importance. Unlike nuclear power or tar sand oils, wind energy does not leave a long-term toxic legacy. Using MATLAB algorithms, multi-optimization of wind turbine design can be achieved. Therefore, an aerodynamic mathematical model is developed to obtain the optimal chord length and twist angle distribution along the blade span. Further, a promising generic blade design is used to initialize a detailed structure optimization wherein leading edge panel (LEP), Spar cap, Shear web, Trailing edge panel (TEP) reinforcement are sized using composite laminates so that the blade is according to the intended design standard. Initially blade airfoils are analyzed on 2D platform and then the results are used to construct 3D model of Horizontal Axis Wind Turbine (HAWT) blade. The 3D designing of composite HAWT blade is done by CAD software Solidworks v16.0 through different airfoil for root, primary and tip and optimization of material thickness and overall mass reduction by the use of composite material through optimization of skin thickness of wind turbine is achieved. This paper is focused on the importance of structural design for optimization of HAWT blade. On further analysis, an increase in aerodynamic power generation as well as marked improvements in overall blade deformation and tip deflection characteristics is observed.

Introduction

Over hundreds of years, historic designs have been used to generate power. Different types of designs include windmills which were constructed from wood, cloth and stone that was used for pumping water or grinding corn. Historic designs were typically large, heavy and inefficient; hence, in the 19th century, they were replaced by fossil fuel engines through implementation of a nationally distributed power network. A greater understanding of aerodynamics and advances in materials, particularly polymers, has led to the return of wind energy in the latter half of the 20th century. Wind power devices are now used to produce electricity, and are commonly termed as wind turbines. The parameters that should be kept in mind while designing the blades are:

- Shape of the airfoil
- Tip speed ratio
- Angle of attack
- Rated wind speed

These parameters are decided on the basis of blade element momentum (BEM) theory [1]. The space shape of the blade is complex; in addition, today's high performance wind turbine blades are made of glass fibre or carbon fibre composite layer structure, to model the blade precisely in order to describe the layer structure becomes a difficult problem, which is also important in mechanical analysis [2].

The design and modelling of the wind turbine blade was done using MATLAB [13], to solve three-dimensional coordinates of each blade section, and then it was extracted through Solidworks to build the solid model [3, 4]. Finally, the finite element method was used for static strength analysis of the blade through the shell element discretization over the skin and three-dimensional sandwich element to simulate the spar web [5]. Composite materials are able to satisfy complex design constraints such as lower weight and proper stiffness, at the same time they provide good resistance to the static and aerodynamic loading. The investigations and design evaluations of the materials and manufacturing issues of large wind turbine blades and rotors resulted in the and preliminary design specifications for candidate blades with length [6] ranging from 30 to 70 m and rotors with diameter [7] in the range of 80 to 120 m.

Taking the above issues into consideration, this paper aims at developing a computer program that would enable optimization of the blade induction factors and build a blade model to precisely describe the blade's actual shape and layer structure for analysis of dynamic and mechanical properties. Also, we minimized the blade mass of the wind turbine while satisfying structural, physical and design requirements.

© 2018 SAE International. All Rights Reserved.

Downloaded from SAE International by Naveen Kumar, Sunday, April 08, 2018

Aerodynamic Analysis

BEM Theory Blade Element Momentum theory equates two methods of examining how a wind turbine operates. The first method is to use a momentum balance on a rotating annular steam tube passing through a turbine. The second is to examine the forces generated by the aerofoil lift and drag coefficients at various section along the blade.

The equations for BEM theory are derived from momentum theory and the blade forces.

Equations (1) and (2) are derived from the momentum theory and express the axial thrust and the torque in terms of flow parameters.

$$dT = 4a\rho U_\infty^2 (1-a)\pi r dr \tag{1}$$

$$dQ = 4a'(1-a)\rho U \pi r^3 \Omega dr \tag{2}$$

Equations (3) and (4) are derived from the consideration of blade forces and express the axial force and torque in terms of the lift and drag coefficients of the airfoil.

$$dF_N = \frac{\sigma' \pi \rho U^2 (1-a)^2 [C_l \cos\varnothing + C_d \sin\varnothing] r dr}{(\sin\varnothing)^2} \tag{3}$$

$$dQ = \frac{\sigma' \pi \rho U^2 (1-a)^2 [C_l \sin\varnothing - C_d \cos\varnothing] e^2 dr}{(\sin\varnothing)^2} \tag{4}$$

To calculate rotor performance, equations from the momentum balance are used with equations from force calculation. Equations (5) and (6) are obtained by equating the equations from the momentum theory and the force equations.

$$\frac{a'}{1-a} = \frac{\sigma' C_l}{4\lambda_r \sin\varnothing} \tag{5}$$

$$\frac{a}{1-a} = \frac{\sigma' C_l \cos\varnothing}{4(\sin\varnothing)^2} \tag{6}$$

The proposed code first divides the blade into number of elements and then assigns an airfoil to each element depending on the pre-specified distribution. Table 1 represents the distribution of airfoils along the wind turbine blade length.

The solution for a given blade cannot be found directly from the equations. An iterative approach is required to obtain the solution. The value of 'a' and 'a' 'is taken as a guess value and then iteration is carried out. Figure 1 shows the procedure for carrying out induction factor and design parameter.

Design Parameter For maximizing the performance of wind turbine, optimum airfoil is chosen. Wind turbine blade designed using single airfoils are inefficient so, a multi airfoil blade should be designed to harvest the maximum energy from the wind. So, a blade using 3 airfoils is developed in this project.

TABLE 1 Distribution of Airfoil along blade length

Airfoil	Region	Blade Span Position
S818	Root	Root to 15%
S830	Primary	15% to 75%
S831	Tip	75% to Tip

© SAE International

FIGURE 1 A Flow Chart of the analysis process

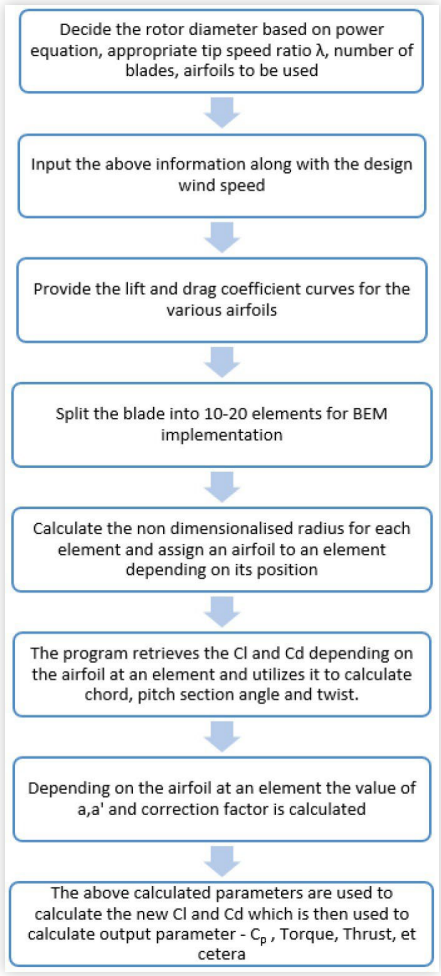

© SAE International

In case of small wind turbine blades, structural analysis can be overlooked as gravity does not play a major role but for large wind turbine rotors (70-120 m) gravitational force became significant and cannot be neglected. Both aerodynamic and structural aspects should meet the optimal blade design. Hence, according to requirements, different airfoils are applied at different section of blade.

In the current paper, a 41.25 m blade is designed which produces 2 MW of energy. It is divided into 3 sections namely:

(1) Root
(2) Primary
(3) Tip

For root section, structural aspects are more important than the aerodynamic aspects as the root section has to bear all the aerodynamic, gravitational, centrifugal, gyroscopic, operational loads acting on the blade, therefore the root section of blade is generally thick in cross-section.

For the primary and tip sections, thin airfoils are used in order to reduce the drag. Here aerodynamic aspects are important over the structural aspects. In this section lift force rotates the blades which in turn run the generator to produce electricity. Ideally, the downstream velocity should be zero to completely

© 2018 SAE International. All Rights Reserved.

Downloaded from SAE International by Naveen Kumar, Sunday, April 08, 2018

TABLE 2 Design Variables

S.No.	Parameter	Specification
1	Wind speed	12 m/s
2	Design Tip Speed Ratio	9
3	Root Chord Upper Limit	2.5 m
4	Tip Chord Lower Limit	1 m
5	Number of Blade	3
6	Radius	41.25 m
7	Density of Air	1.205 kg/m^3
8	Design Rotational Speed	2.58 rad/s
9	Power	2 MW

© SAE International

TABLE 3 Airfoils Design Conditions

Airfoil	Region	C_l	C_l/C_d	Angle of Attack(α)
S818	Root	1.61	105.9	9.25
S830	Primary	1.57	117.8	6.25
S831	Tip	1.48	152.7	6.50

© SAE International

harvest the wind energy. But in reality, the downstream velocity is not zero and has some value, so airfoil in this section is chosen so that maximum energy can be extracted from it. Hence, twist angle and chord length (performance parameters) of airfoil is chosen so that the ratio of lift force to the drag force is maximized [14]. Table 2 represents the operating conditions that were decided for the purpose of blade designing.

Before the designing of blades, Reynolds number should be calculated at each blade section. Lift and drag should also be determined at each section. As wind turbine blade is rotating, the velocity of flow at each airfoil does not correspond to the velocity of wind, rather it corresponds to the effective flow velocity which is a combined consequence of tangential velocity of blade and wind velocity.

After calculating the Reynolds number, optimum airfoil is selected for each blade section. From a number of airfoils that were analyzed we narrowed down to a list of three airfoils. These airfoils were selected for their good aerodynamic performance within the Reynolds number range.

XFLR5 (which is an open source software) [15] code is used for obtaining performance curves of Cl with Cd and another between Cl and. The analysis on airfoil has been performed in the range of Reynolds number from 4000000 to 10000000.

It is observed from the performance curve that C_l varies linearly at small angles till stall and then drops abruptly. A curve of C_l/C_d with is studied and the value of is determined for maximum C_l/C_d. Table 3 below shows the different conditions of airfoil design of airfoils S818, S830 and S831.

Structural Analysis

Blade Design In this section, the initial composite layout of 2 MW wind turbine blade is designed. The mathematical model is developed to optimize the thickness of various panels of wind turbine blade using software called CoBlade [16] used for structural Analysis of composite blade for wind turbine and hydrokinetic turbine based on MATLAB. CoBlade is used to compute span variants (laminate material thickness) structural properties of composite blade and is the pre-processor for aeroelastic simulation codes that require the structural properties as input to model the majority of flexible components of wind turbine such as the blade and towers [9].

To further aid in the preliminary design of composite blades, CoBlade offers an optimization mode that can also optimize the layup of composite materials within the blade using optimization algorithms (pattern search). For a given external blade shape and design load, CoBlade gives a fitness function which minimizes the blade mass while simultaneously satisfying constraints on maximum stress, buckling, deflection, and placement of blade natural frequencies.

Layout This part is focused on the structural design of the 3-bladed, 82.5 m diameter, 2 MW, variable-speed, variable-pitch turbine. Two shear webs are utilized in each airfoil. It is shown in Figure 3 that the webs divide the blade section into three parts. From the left to the right, the section can be named as the Leading Edge Panels (LEP), the spar cap and Trailing Edge Panels (TEP). Spar webs glued in between the two spar caps are often called a sandwich construction because such a construction is made up of different layers. It is seen that the spar cap and the webs form a box-like structure. The box-like structure acts like a main beam that can improve the flap-wise stiffness, in which a thick root section transitions into a main spar with two shear webs that run through the length of the blade, as illustrated in Figure 3. The LEP and TEP are sandwiched composite laminates which form the aerodynamic shape of the blade. Figures 3 and 4 illustrates that the blade consists of 9 unique laminate schedules with a total of 8 possible materials (where each material can have its own unique properties defined).

The thickness of each material along the length of the blade is defined by the linear variation between control points Figure 5 shows how the material thicknesses in the LEP, TEP, spar cap, and shear webs vary along the length of the blade. The example in Figure 6 shows 2 control points per material (only 2 control points for the shear webs); however, control points more or less than 2 can be used for greater degree-of-freedom or greater computational efficiency.

The theory implemented within the CoBlade software is based upon the combination of the classical lamination theory (CLT) with the Euler Bernoulli theory and shear flow theory applied to composite beams. At first, the blade is represented as a cantilever beam under the influence of flap wise and edgewise bending, axial deflection, and elastic twist. Additional coupling between bending, extension, and torsion, due to the offsets between the beam shear centre, tension centre, and centre of mass from the blade pitch axis are accounted for. The beam cross section is assumed as a thin-walled, closed, and single or multi-cellular and the periphery of each beam cross section is discretized as a connection to the flat composite laminates [1].

During both, the structural analysis and the optimization mode, the nine unique laminate schedules are formed with a total of eight possible materials (where each material can have its own unique defined properties). In our study, these properties are derived from Sandia 100 m blade SNL-100 [6] and the glass fabrics and epoxy resin materials are chosen. The three basic types of

© 2018 SAE International. All Rights Reserved.

Downloaded from SAE International by Naveen Kumar, Sunday, April 08, 2018

TABLE 4 Reynolds Number flow over Blade

% Blade span(r/R)	Element Radius [m]	Wind Speed[m/s]	Tangential velocity[m/s]	Effective velocity [m/s]	Estimated Chord Length	Reynolds number (x10^6)
0.075	3.093	12	7.981	14.411	3.521	2.90
0.125	5.156	12	13.303	17.915	3.325	4.02
0.175	7.218	12	18.624	22.155	3.274	5.42
0.225	9.281	12	23.945	26.783	3.195	6.85
0.275	11.345	12	29.272	31.636	3.111	7.83
0.325	13.406	12	34.588	36.610	2.965	8.65
0.375	15.468	12	39.909	41.674	2.818	9.36
0.425	17.531	12	45.230	46.794	2.672	9.96
0.475	19.593	12	50.551	51.955	2.527	10.46
0.525	21.656	12	55.873	57.147	2.380	10.84
0.575	23.718	12	61.194	62.359	2.233	11.10
0.625	25.781	12	66.515	67.588	2.088	11.24
0.675	27.843	12	71.836	72.831	1.941	11.27
0.725	29.906	12	77.158	78.085	1.798	11.19
0.775	31.968	12	82.479	83.347	1.659	11.02
0.825	34.031	12	87.800	88.616	1.527	10.79
0.875	36.093	12	93.121	93.891	1.396	10.44
0.925	38.156	12	98.443	99.171	1.264	9.99
0.975	40.218	12	103.764	104.455	1.133	9.43
1	41.25	12	106.425	107.099	1	8.53

© SAE International

FIGURE 2 A plot between C_l/C_d with α

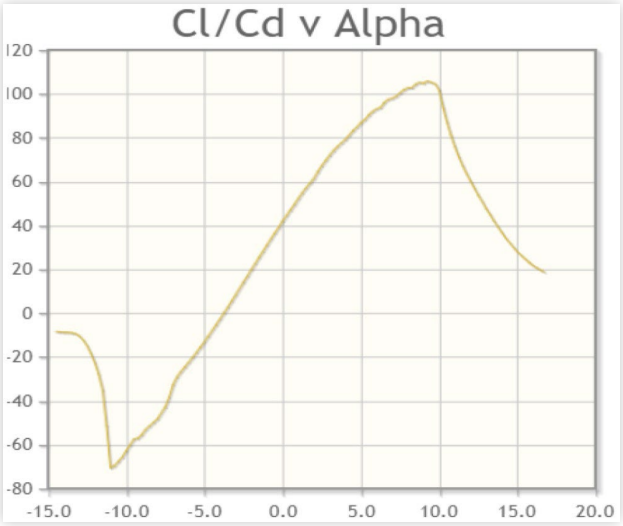

© SAE International

FIGURE 3 Composite blade in cross section

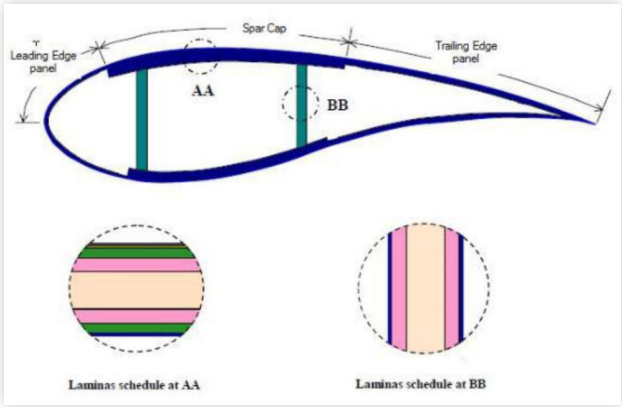

© SAE International

FIGURE 4 The composite blade model, indicating different laminate stacking orders

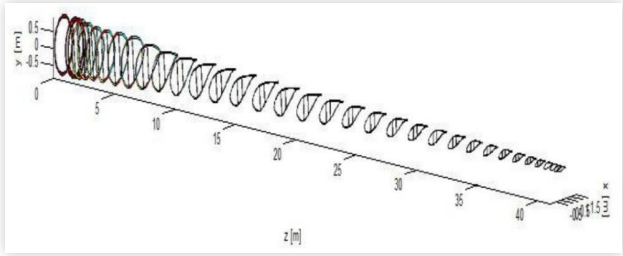

© SAE International

glass/epoxy composites are: unidirectional laminate, bi-axial (Saertex [±45]4) and tri-axial laminate. Table 5 lists the mechanical properties utilized in the structural design of the blade.

Optimization

Objective Function Optimization of the twist angle and the chord length along the span and the overall thickness of laminates of various panels of wind turbine blade will be performed separately.

Optimization design for span-wise shape of wind turbine blade is done to obtain the maximum wind energy utilization coefficient using some methods. An advanced method-Wilson

© 2018 SAE International. All Rights Reserved.

Downloaded from SAE International by Naveen Kumar, Sunday, April 08, 2018

FIGURE 5 Plan form view of the turbine blade configuration used in the optimization study, showing the laminate material schedules in the root build-up, leading edge panel (LEP), spar cap, trailing edge panel (TEP), shear webs, and blade tip.

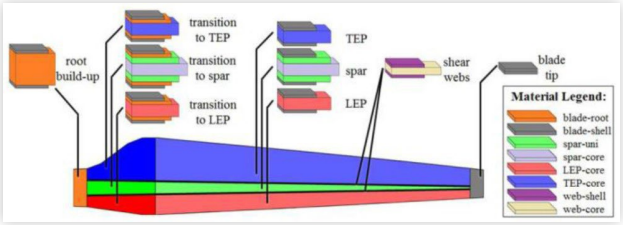

© SAE International

FIGURE 6 The material thicknesses are defined along the blade length by linear variations between the control points.

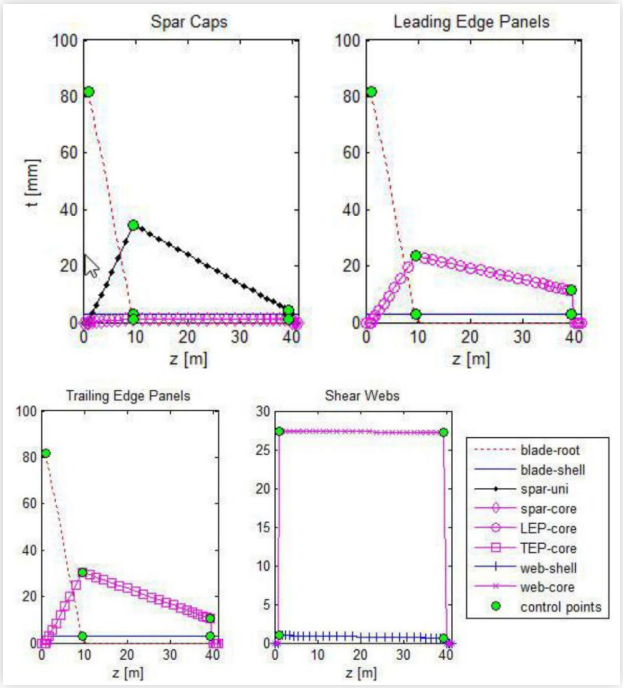

© SAE International

method was adopted in this paper, which is based on Blade Element - Momentum Theory. The blade is divided into a number of blade elements along the span. The chord length and twist angle of each blade element should be calculated so as to make the wind energy utilization factor of each blade element dCP $d\lambda$ maximum. The optimization model [11] is given as follows:

$$minimize \qquad \frac{-dC_p}{d\lambda} = \frac{8}{\lambda^2} b(a-1) F \lambda^3 \tag{7}$$

$$s.t. \qquad a(1-aF) = b(1-a)\lambda^2 \tag{8}$$

$$F = \frac{2}{\pi} \arccos\left(e^{-f}\right) \tag{9}$$

$$f = \frac{B}{2} \frac{R-r}{R \sin\varphi} \tag{10}$$

$$\tan\varphi = \frac{1-a}{1+b} \frac{1}{\lambda} \tag{11}$$

$$\theta = \varphi - \alpha \tag{12}$$

$$\frac{BCC_l}{r} = \frac{8\pi b F \cos\varphi}{1+b} \tag{13}$$

The structural objective function in Eqn. (14) is formulated as an additive penalty function in which the constraints are accounted for, by penalty factors pi. This function is set to minimize the blade mass while satisfying constraints on maximum stress, buckling, tip deflection, and separation of the blade natural frequencies from the blade rotation frequency. The structural objective function f(x) is minimized when the blade mass is minimum and all of the penalty factors,p1-p8 are less than unity [12]. Mathematically, this optimization problem is formulated in the user guide as follows [9]:

$$\text{Minimize } f(\bar{x}) = Blade\ mass * \prod_{n=1}^{B} \max\{1, p_n\}^2 \tag{14}$$

$$p_1 = \frac{\sigma_{11,\max}}{\sigma_{11,fT}} \tag{15}$$

$$p_2 = \frac{\sigma_{11,\min}}{\sigma_{11,fC}} \tag{16}$$

$$p_3 = \frac{\sigma_{22,\max}}{\sigma_{22,yT}} \tag{17}$$

$$p_4 = \frac{\sigma_{22,\min}}{\sigma_{22,yC}} \tag{18}$$

$$p_5 = \frac{|\tau_{12}|,\max}{\tau_{12,y}} \tag{19}$$

$$p_6 = \left(\frac{\sigma}{\sigma_{buckle}}\right)^{\alpha} + \left(\frac{\tau}{\tau_{buckle}}\right)^{\beta} \tag{20}$$

$$p_7 = \frac{tip\ Deflection}{\max Tip\ Deflection} \tag{21}$$

$$p_8 = \max\left\{\frac{MIN_{FREQ_{SEP}}}{|\omega_m - \omega_{rotor}|}\right\}, m = 1, M_{modes} \tag{22}$$

$$s.t. \qquad \overline{x_{LB}} \le \bar{x} \le \overline{x_{UB}} \tag{23}$$

$$A\bar{x} \le \bar{b} \tag{24}$$

Constraints Conditions In the process of optimizing the design for the blade, the objective is not only to meet the structural strength requirements, but also to prevent the collision between the blade tip and the tower. Since the blade is made of composite materials which exhibit anisotropy, the strength constraint of the maximum stress is not appropriate [10]. The Tasi - Wu failure criterion is selected for this study to perform

© 2018 SAE International. All Rights Reserved.

Downloaded from SAE International by Naveen Kumar, Sunday, April 08, 2018

TABLE 5 Material Properties for Composite Blade

E11(Pa)	E22(Pa)	G12(Pa)	υ	ρ (kg/m³)	Material Name	Material Application
2.56e + 08	2.60e + 08	2.20e + 07	0.3	200	Foam Core	LEP Core
2.56e + 08	2.60e + 08	2.20e + 07	0.3	200	Foam Core	TEP Core
2.56e + 08	2.60e + 08	2.20e + 07	0.3	200	Foam Core	Spar Core
2.56e + 08	2.60e + 08	2.00e + 07	0.3	200	Foam Core	Web Core
2.77e + 10	1.36e + 10	7.20e + 09	0.4	1850	SNL Triax	Blade Shell
1.36e + 10	1.33e + 10	1.20e + 10	0.5	1780	Saertex [±45]	Web Shell
4.18e + 10	1.40e + 10	3.00e + 09	0.28	1920	E-LT-5500	Spar Uni
2.77e + 10	1.36e10	7.20e + 09	0.4	1850	SNL Triax	Blade Root

© SAE International

failure verification. The distance between the blade tip and tower is considered to prevent the collision between the blade tip and the tower and is therefore taken about 4.1 m and the displacement of the tip deflection is not allowed to exceed this value.

Tsai-Wu failure criterion:

$$F_1\sigma_1 + F_2\sigma_2 + F_{11}\sigma_1^2 + F_{22}\sigma_2^2 + F_{66}\sigma_6^2 + 2F_{12}\sigma_1\sigma_2 \le 1 \quad (25)$$

Where σ_1, σ_2 and σ_3 are the three in-plane stress components in the local orthotropic ply axis, and $F_1, F_2, F_{11}, F_{22}, F_{66}$ are the strength parameters of the composite material.

Calculations and Results

For Twist Angle and Chord Length Along the Span On providing input files to the code the chord length, twist angle, axial induction factor, tangential induction factor and other parameters are determined.

A plot of the chord length variation with the non-dimensional radius is shown in Figure 7. From the graph it is observed that chord length first increases from a value to the maximum value and then decreases along the span through primary up to the tip. The increase in chord length takes place due to the factor r*(1-cos θ) (term in determining the chord). The rate of increase with respect to non-dimensional radius is greater for increase in chord length than decrease in chord length. The change in chord length is almost linear. The least chord length occurs at the section 1 and the maximum occur at section 0.225. Table 6 shows the variation of chord length along the span of the blade.

The local tip speed ratio, which is defined as the relationship between the rotor blade velocity and relative wind velocity at the specified section, increases from blade root towards the tip of the blade. As each section of blade experiences a different effective velocity flows so the blade is twisted along the span. Airfoil at roots are twisted at higher angles due to low values of local tip speed ratio and it decreases linearly along the blade length and becomes zero at the tip of the blade. The twist angle changes from 41.62 deg at the root to 0 deg at the tip. Figure 8 shows the variation of twist angle along the span.

TABLE 6 Structural Optimization Result Output

	Initial Value Thickness(mm)		Pattern Search Thickness(mm)	
Variable	CP1	CP2	CP1	CP2
LEP Core	32	12	8	3
TEP Core	45	15	16	6
Spar Core	5	5	2	2
Web Core	30	30	28	28
Blade Shell	5	5	2.2	2.2
Web Shell	5	5	1.9	1.9
Spar Uni	40	5	31.5	4.1

© SAE International

Various Panels' Thickness and Mass For the structural optimization of wind turbine blade, deterministic pattern search optimization method is used. Initially blade mass was started from 8210 Kg and reduced to 7538 Kg by the use of pattern search algorithm. Pattern search algorithm is a global optimization algorithm and is less sensitive to initial points and the numerous constraints on design variable. The

FIGURE 7 Distribution of Chord Length along Blade Span

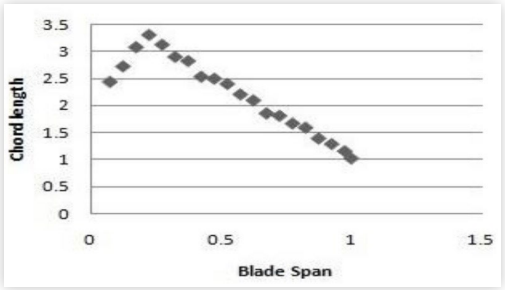

© SAE International

FIGURE 8 Distribution of Twist Angle along Blade Span

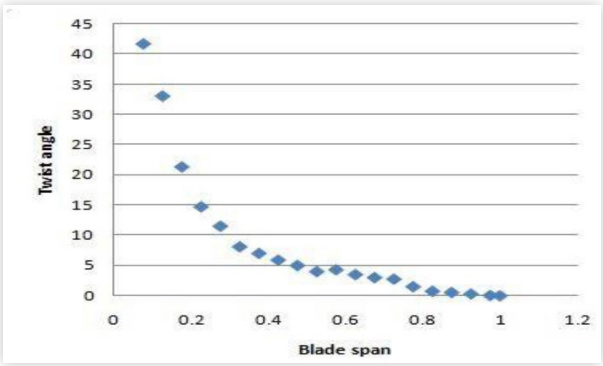

© SAE International

© 2018 SAE International. All Rights Reserved.

Downloaded from SAE International by Naveen Kumar, Sunday, April 08, 2018

converged blade design obtained by pattern search satisfies all of the design criteria i.e. all the constraints of maximum allowable stresses, Blade tip deflection, buckling stresses and placement of blades natural frequency are satisfied. Table 6 below shows the initial thickness of various sections of blade and the optimum thickness obtained from pattern search algorithm.

Conclusions and Discussions

A wind turbine blade of a wind turbine consisting of 3 blades is designed which can be operated with a wind velocity of 12 m/s in optimum conditions. The tip speed ratio of 9 was taken. In MATLAB code, 3 airfoil optimum blades was developed using S818, S830, S831 airfoils for the root, the primary, and the tip respectively. The airfoil is analyzed in XFLR5 at different Reynolds number ranging from 4000000 to 12000000 and the BEM theory was used to generate the blade profile.

As the use of multi airfoils decreases the twist of sections along the length of blade, hence by using the proposed code, a wind turbine blade composed of multi airfoils can be designed for other operating conditions also. For the structural optimization, a preliminary structural and optimization tool, capable of evaluating and designing composite layups and study their effect is used. As our code was inspired from CoBlade, it provides a more realistic approach to write the objective function in terms of the blade mass only along with an additional nonlinear constraint that characterize the static failure. The use of pattern search algorithm results in more realistic mass of the turbine blade. As the designing is a trade-off between structural and aerodynamic aspects so, In future a complimentary coupling between the two can be provided in which one will act as a optimization function and other will acts as a constraint to it so that the performance of wind turbine blade can be increased further.

References

1. Manwell, J., McGowan, J., and Rogers, A., "*Wind Energy Explained*," (Chichester, Wiley, 2002).
2. Lin, H., "The Finite Element Analysis of Wind Turbine Blade," *Journal of Mianyang Normal University* 26(8), 2007.
3. Tian, H., Zeng, Q., and Huang, C., "The Design and Modelling of Wind Turbine Blade," *Machinery* 47(3):6-8, 2009.
4. Guoning Li, Fuzeng Yang, Baishi Du et al. Design and Modelling of Wind Wheel of Wind Mill Based on MATLAB and Pro/E,
5. Kong, C. and Bang, J., "Structural Investigation of Composite Wind Turbine Blade Considering Various Load Cages and Fatigue Life," *Energy*.
6. Griffith, D. T. and Ashwill, T. D., "The Sandia 100-Meter All-Glass Baseline Wind Turbine Blade: SNL100-00," 2011.
7. Griffin, D. A. and Ashwill, T. D., "Alternative Composite Materials for Megawatt-Scale Wind Turbine Blades: Design Considerations and Recommended Testing," *ASME 2003 Wind Energy Symposium*, 2003, 125, 4, 515.
9. Sale, D. C., "Software for Structural Analysis of Composite Blades," 2012.
10. Chehouri, A., Lebanese, R.Y., Ilinca, A., and Perron, J., "Optimal Design for a Composite Wind Turbine Blade with Fatigue and Failure Constraints," *Trans. Can. Soc. Mech. Eng.*, 2015.
11. Wang, X., "Design and Three-Dimension Modelling of Wind Turbine Blade," Guangxi University, 2006.
12. D. Sale, A. Aliseda, M. Motley, and Y. Li, "Structural Optimization of Composite Blades for Wind and Hydrokinetic Turbines," *1st Marine Energy Technology Symposium*, Oct 2013.
13. MATLAB: "MATLAB R2017a, the Math Works, Natick, 2017."
14. Chaudhary, M. and Roy, A., "Design and Optimization of a Small Wind Turbine Blade for Operation at Low Wind Speed," *World Journal of Engineering* 12(1):83-94, 2015.
15. Katz, J. and Plotkin, A., "*Low Speed Aerodynamics, From Wing Theory to Panel Methods*", Cambridge University Press, 2nd Ed. 2001 Website for download: http://www.xflr5.com.
16. Sale, D., User's Guide to Co-Blade: Software for Structural Analysis of Composite Blades, Northwest National Marine Renewable Energy Center, 2012.

Contact Information

Name: **Rohan Brella**
rohanbrella@gmail.com
Mobile: +91 9717378137

Definitions/Abbreviations

a - Axial Induction Factor
a′ - Axial Induction Factor
ρ - Air Density
U_o - Wind Speed
dT - Thrust
dQ - Torque
R - Blade Radius
r - Blade Element Radius
Ω - Rotational Velocity
dFn - Axial Force
σ′ - Local Solidity
Cl - Lift coefficient
Cd - Drag Coefficient
Φ - Oncoming Flow Angle
λ - Tip Speed Ratio
λr - Local Tip Speed Ratio
α - Angle of Attack

© 2018 SAE International. All Rights Reserved.

Downloaded from SAE International by Naveen Kumar, Sunday, April 08, 2018

Cp - Power Coefficient
C - Airfoil Chord Length
B - Number of Blade
θ - Twist Angle
LEP - Leading Edge Panel
TEP - Trailing Edge Panel
HAWT - Horizontal Axis Wind Turbine
BEM - Blade Element Momentum Theory

All rights reserved. No part of this publication may be reproduced, stored in a retrieval system, or transmitted, in any form or by any means, electronic, mechanical, photocopying, recording, or otherwise, without the prior written permission of the copyright holder.

Positions and opinions advanced in this paper are those of the author(s) and not necessarily those of SAE International. The author is solely responsible for the content of the paper.

ISSN 0148-7191

View publication stats

2017 Conference on Information and Communication Technology (CICT'17)

Design, Analysis, and Comparison of LNA topologies for IEEE 802.15.4 Zigbee Standard

Aditi, Malti Bansal
Department of Electronics & Communication Engineering, Delhi Technological University (DTU),
Delhi-110042, India
(maltibansal@gmail.com)

***Abstract*— We have designed common source cascode low noise amplifier with feedforward distortion cancellation, common source inductive degeneration low noise amplifier, common source inductive degeneration low noise amplifier with feedforward distortion cancellation, common source shunt resistive feedback low noise amplifier, common gate low noise amplifier in this paper using 0.13um CMOS technology. The low noise amplifiers have been optimized for working in the 2.4 GHz band. All the above low noise amplifiers are having pi-matching at input for improving gain. Advanced Design System (ADS) software is used for simulation. The designed low noise amplifiers use 1.2V supply voltage. The performance target is to achieve high gain and low noise figure without degrading the overall linearity.**

Keywords*— Advanced Design Simulation (ADS) software, Low Noise Amplifier (LNA), Cascode, Common Gate (CG), Feedforward Cancellation (FDC), Common Source (CS), Inductively Degenerated Cascode, Shunt Resistive Feedback, Third Order Intercept Point (IIP3), Noise Figure (NF.

I. INTRODUCTION

Nowadays, RF transceivers which utilize low-power and have good noise performance are in great demand for operating in ISM band; and significant developments in this domain have been possible due to advancements in wireless sensor networks (WSN) [1]. It is now possible to integrate all elements of RF transceiver on a single chip, because of the rapid advancement and acceleration in scaling of CMOS and in the designing techniques of RF CMOS circuits in the past few years. Moreover, to implement all the necessary RF functions for existing and emerging ISM band applications, inexpensive CMOS technologies can be successfully used [2]. However, the transmitter and receiver comprising communication systems will not only experience attenuation but will also experience the interference at the receiver end. Hence, the operation of the demodulator circuit, is hindered, making it necessary to increase the signal strength before it is fed into the demodulator circuit, but the desired signal along with the noise is also amplified by the amplifier. Therefore, it is important to use amplifier which adds as minimum noise as possible and such type of amplifier is called low noise amplifier (LNA). The low noise amplifier is therefore, the first active and also, an essential block in the receiver chain of communication system [3],[4],[5]. It is used at the front end of the receiver, is connected directly to the antenna and the noise performance of low noise amplifier directly impacts the overall noise performance of the receiver. Crucial design specification, i.e., noise figure (NF) has trade-offs with other design specifications such as gain, power consumption and third order intercept point (IIP3). So, LNA design consists of trade-offs between gain, noise figure, linearity, input and output matching, and power consumption. However, to achieve good overall system performance, several desired parameters are required such as low power consumption, high gain, high third order intercept point, low noise figure and good input and output impedance matching.

Combination of three stages forms low noise amplifier [6],[7].

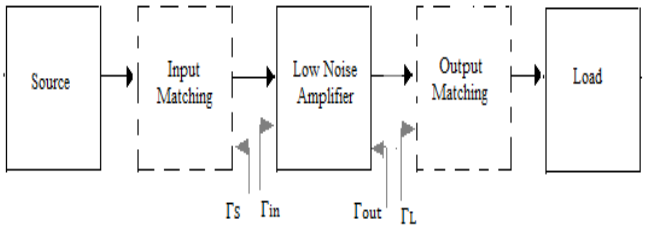

Fig. 1 Basic Components of Low Noise Amplifier with input/output of amplifier (two-port network)

where,
Γs is reflection coefficient of source of two-port network, Γ_L is reflection coefficient of load of two-port network, Γin is reflection coefficient at input of the amplifier and Γout is reflection coefficient at output of amplifier

A. Input matching network.

The input matching network is present so that the input return loss or input reflection coefficient (S_{11}) is minimum, without additional noise introduction. The ideal value of the input impedance is infinite if the low noise amplifier is considered as voltage amplifier. So, to obtain minimum noise figure, a transformation network is required before low noise amplifier, if viewed from noise point of view while conjugate matching between antenna and low noise amplifier is required if viewed from signal point of view. Each of the above choices has its own advantages and disadvantages; however, the latter is commonly used in today's systems. Therefore, LNA is designed such that it has input impedance equal to 50Ω resistance.

The LNA is designed to make gain and linearity as high as possible and make noise figure as low as possible. However,

978-1-5386-1866-0/17/$31.00 ©2017 IEEE

gain and linearity are the two parameters which are poles apart and it is difficult to balance them i.e., gain will be affected while trying to improve the linearity and vice versa [8], [9]. Gain is enhanced in Pi-matching when compared to T-matching. So, in order to obtain reasonable linearity at low power, pi-matching is used and hence, is adopted in this paper.

B. Main Amplifier Section

Amplifier section ensures maximum gain and linearity and also, minimum noise figure and power consumption. It also provides input impedance matching at the same time.

1) Power Gain

In Fig.1, the input/output power gain of low noise amplifier i.e. a two port network is shown. Power gain is defined as the ratio of the power dissipated in the load i.e., output power to the power supplied to the amplifier i.e., input power. The power gain mathematically, can be expressed as:

$$G = \frac{P_{out}}{P_{in}} \quad (1)$$

2) Noise Figure

Noise Figure is the ratio of the signal to noise ratio of the input port to that of output port and is larger than 1 dB and is given by:

$$NF = \frac{SNR_{out}}{SNR_{in}} \quad (2)$$

For the single-stage amplifier, its noise figure is seen as follows:

$$F = F_{min} + \frac{4r_n|\Gamma_s - \Gamma_{opt}|}{(1-|\Gamma_s|^2)|1+\Gamma_{opt}|^2} \quad (3)$$

In the formula, F_{min} is the minimum noise figure. Γ_{opt}, r_n and Γ_s are the best source reflection coefficient, the equivalent noise resistance of the transistor and the input reflection coefficient of the transistor when F_{min} is obtained.

For multi-stage amplifier, the noise figure is decided by the Friis formula:

$$NF = F_1 + \frac{F_2-1}{G_{A1}} + \frac{F_3-1}{G_{A2}} + \dots \quad (4)$$

where,

F_n is the noise figure of the first n-amplifier and G_n is the gain of the first n-amplifier.

C. *Output Matching Network*

The output matching network is present to guarantee that the output impedance is 50Ω.

In this paper, LNA having common source cascode with feed forward distortion calculation, common source inductive degeneration, common source inductive degeneration with feed forward distortion cancellation, common source with shunt resistive feedforward and common gate, working at 2.4GHz frequency have been designed at 0.13um technology.

II. Circuit Designs for Different LNA Topologies

A. Common Source Cascode Low Noise Amplifier with Feed Forward Distortion cancellation (FDC) technique

The M_1 transistor is used in CS stage, forming cascode structure with M_2. Gate of M_3 and drain of M_1 are connected and M_3 transistor's output is given to base of M_2; for boosting the gain. M_3 and R_1 form another CS amplifier. M_4 transistor is used in common gate (CG) mode as an auxiliary transistor. C_6 and L_2 are used as load and C_7, C_8, and L_1 are forming pi – matching at input.

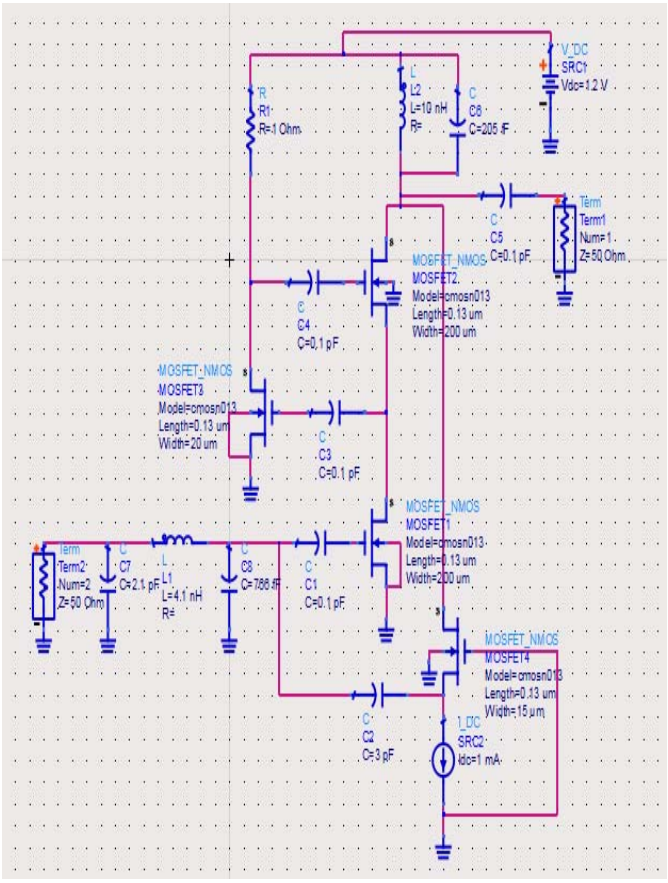

Fig. 2 Schematic of CS Cascode LNA with FDC

B. Common Source Inductive Degeneration Low Noise Amplifier

M_1 and M_2 are in CS stage forming cascode structure and degenerative inductor L_4 is present at the source of M_1. M_3 and R_1 form current mirror circuit. The signal path is isolated from the biasing circuit by M_1. M_3 is the biasing transistor in the circuit which forms current mirror with M_1. To avoid heavy current consumption, the W/L ratio of M_3 should not be large.

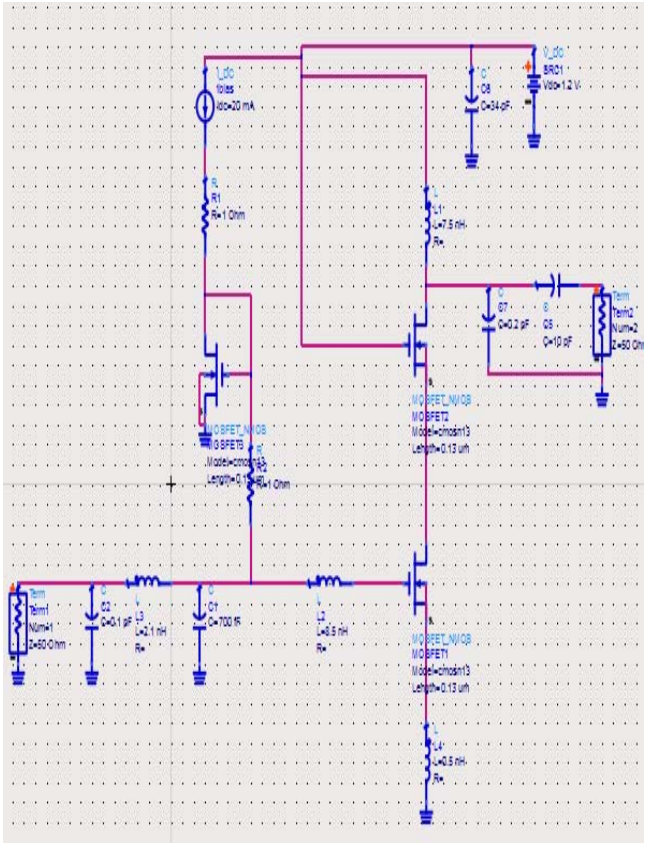

Fig. 3 Schematic of CS Inductive Degeneration LNA

C. Common Source Inductive Degeneration Low Noise Amplifier with Feed Forward Distortion cancellation (FDC) technique

M_2 and M_3 forms the basic cascode structure. A common gate transistor (M_2) is used as a current buffer at the output of M_3 to overcome the Miller effect. R_4 and L_4 serve as cascode stage (M_2-M_3) load. The feed-forward distortion cancellation is provided by transistor M_4 and capacitor C_4. C_4 is a blocking capacitor. L_1, C_1 and C_2 form pi-matching network. The M_5 transistor is in common source stage and R_5-L_5 serve as the load M_5.

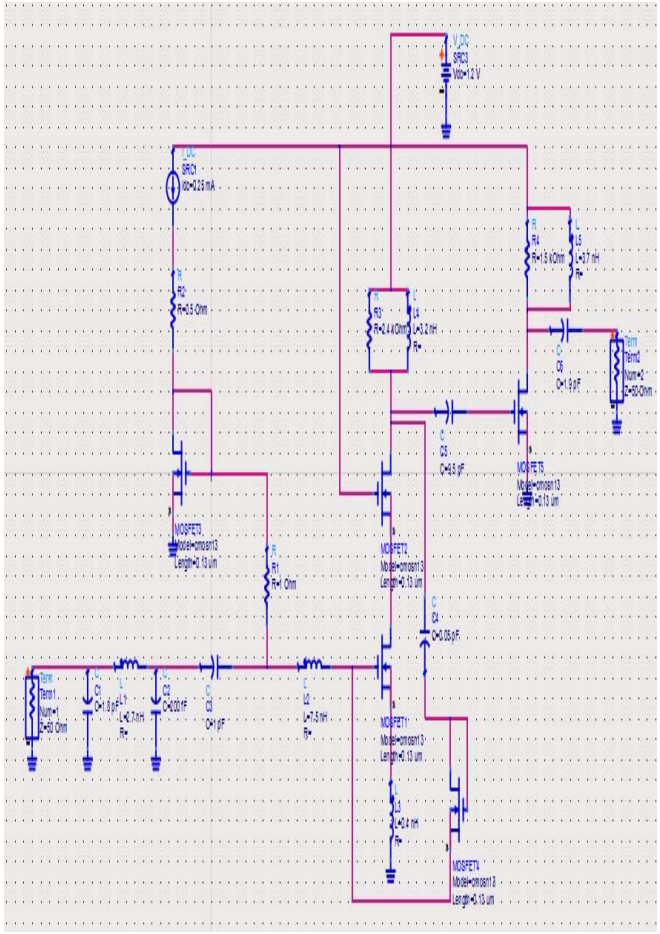

Fig.4 Schematic of CS Inductive Degeneration LNA with FDC

D. Common Source Shunt Resistive Feedback Low Noise Amplifier

A CS and CG transistor is present in the first stage, and these are connected in cascode configuration. R_1 is used as the feedback resistor and is in shunt configuration to achieve broadband matching of input and also to get negative feedback. C_3 is the blocking capacitor. L_4 in parallel configuration with C_4 serves as cascode stage loading element. The second stage is a source follower stage and M_3 transistor is present in this stage. L_1, C_1 and C_2 form pi – matching network.

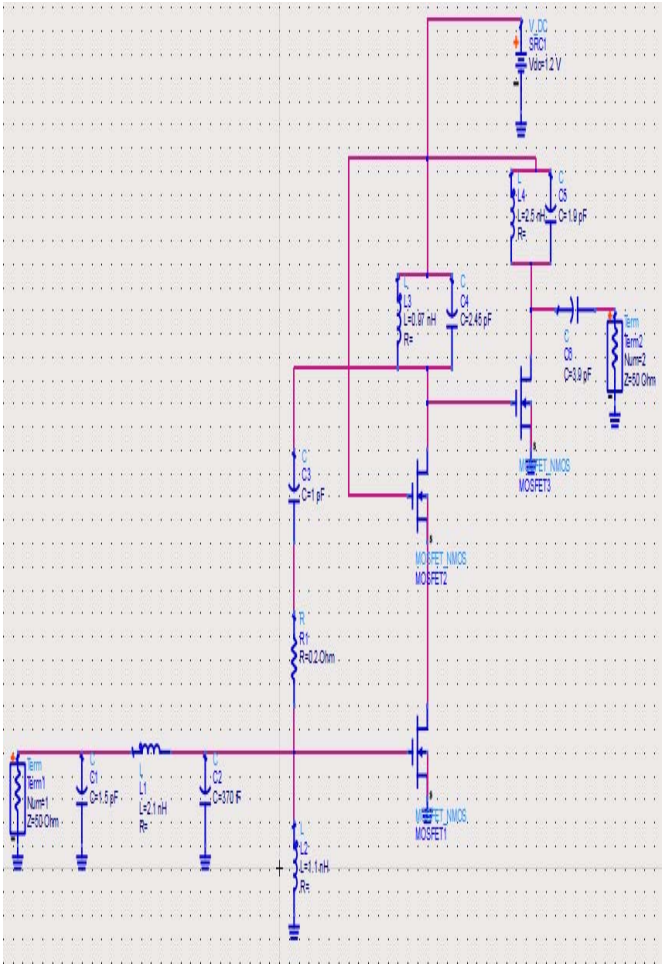

Fig. 5 Schematic of CS Shunt Resistive Feedback LNA

E. Common Gate Low Noise Amplifier

A common source amplifier is used in second stage of this circuit to compensate for the power gain, as the power gain of common gate amplifier is lower than common source amplifier. To ensure that the circuit is optimized, the LC tank circuit is matched for center frequency and to block RF leakage to ground, the inductor L_2 is present. Compared to common source amplifier, the value of L_2 for common gate amplifier is higher. C_1, L_1 and C_2 form pi-matching network at input and C_5 is the DC blocking capacitor.

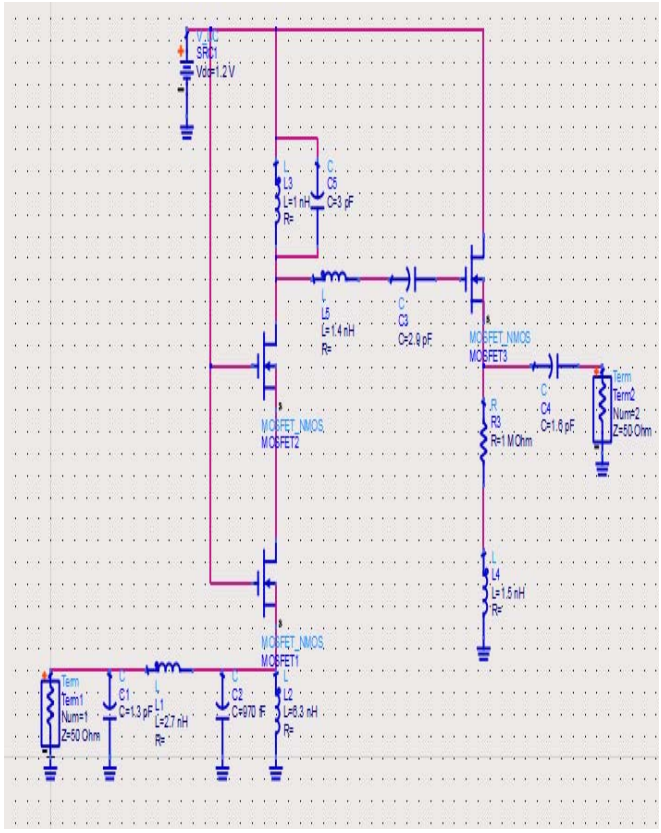

Fig. 6 Schematic of CG LNA

III. SIMULATION RESULTS AND COMPARISON

Simulations of the LNA for 0.13 um CMOS process were performed using ADS. The circuit operation requires 1.2 V power supply. The simulated results of the above circuits are shown below:

F. S-Parameters and Noise Figure

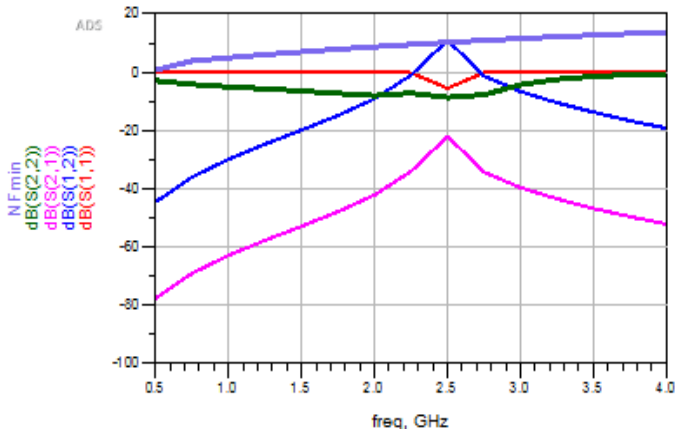

Fig. 7 CS Cascode LNA with FDC

From the Fig. 7, we can observe that S_{11} is -5.562 dB, S_{12} is -22.06 dB, S_{21} is 10.976 dB, S_{22} is -8.707 dB and NF is 10.26 dB for common source cascode LNA configuration with FDC.

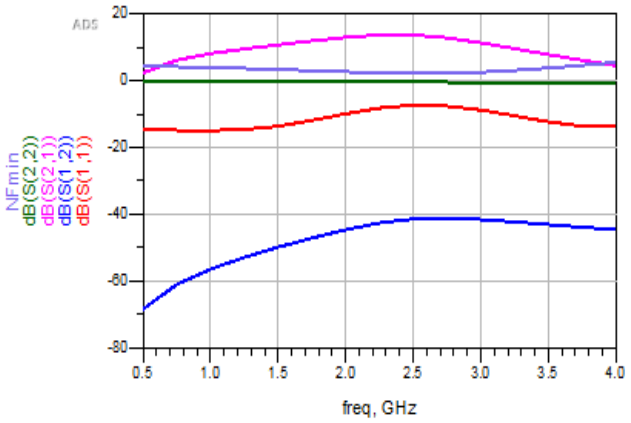

Fig. 8 CS Inductive Degeneration LNA

From the Fig. 8, we can observe that S_{11} is -7.375 dB, S_{12} is -41.47 dB, S_{21} is 24.227 dB, S_{22} is -0.28 dB and NF is 2.109 dB for common source inductive degeneration LNA configuration.

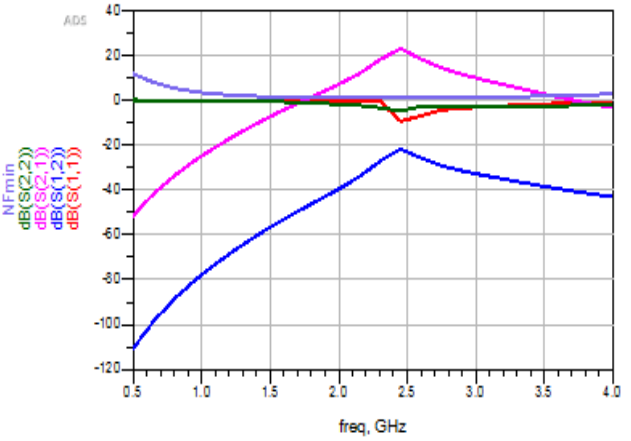

Fig. 9 CS Inductive Degeneration LNA with FDC

From the Fig. 9, we can observe that S_{11} is -9.408 dB, S_{12} is -21.732 dB, S_{21} is 23.032 dB, S_{22} is -4.730 dB and NF is 0.988 dB for common source inductive degeneration LNA configuration with FDC.

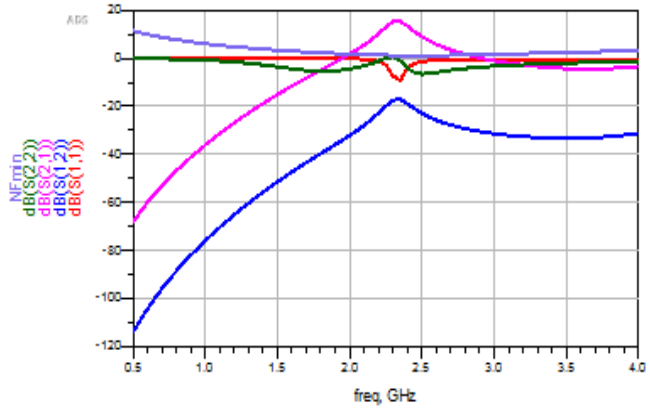

Fig. 10 CS Shunt Resistive Feedback LNA

From the Fig. 10, we can observe that S_{11} is -9.170 dB, S_{12} is -18.909 dB, S_{21} is 15.417 dB, S_{22} is -6.204 dB and NF is 1.182 dB for common source shunt resistive feedback LNA configuration.

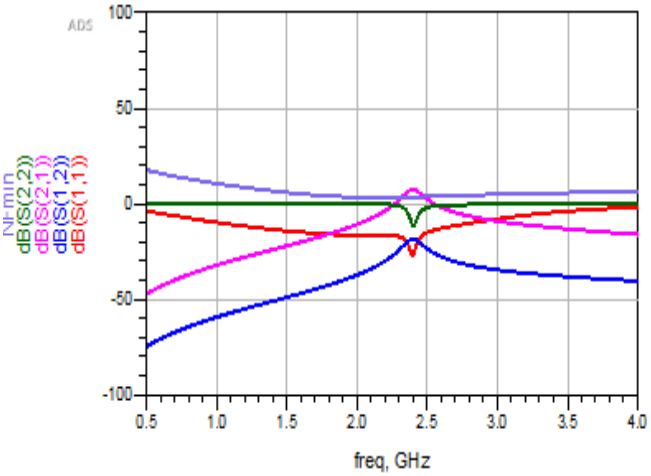

Fig. 11 CG LNA

From the Fig. 11, we can observe that S_{11} is -26.894 dB, S_{12} is -18.604 dB, S_{21} is 7.526 dB, S_{22} is -12.264 dB and NF is 3.513 dB for common gate LNA configuration.

G. Third-Order Intercept Point (IIP3)

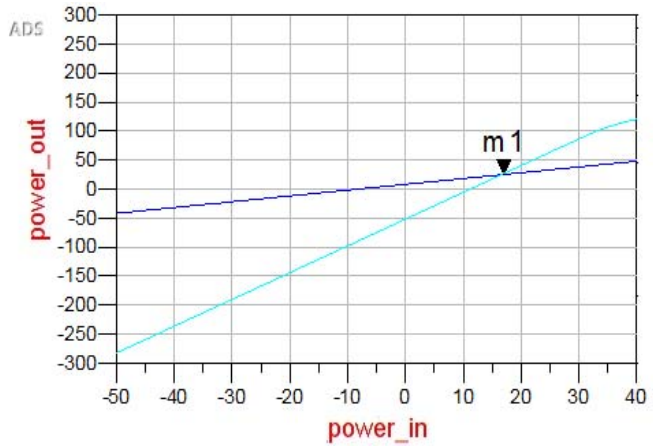

Fig. 12 CS Cascode LNA with FDC

From the Fig. 12, we observe that IIP3 point is 17 dBm for common source cascode LNA configuration with FDC.

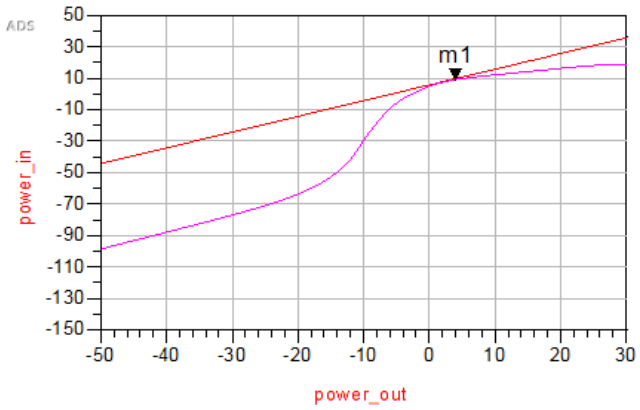

Fig. 13 CS Inductive Degeneration LNA

From the Fig. 13, we observe that IIP3 point is 4 dBm for common source inductive degeneration LNA configuration.

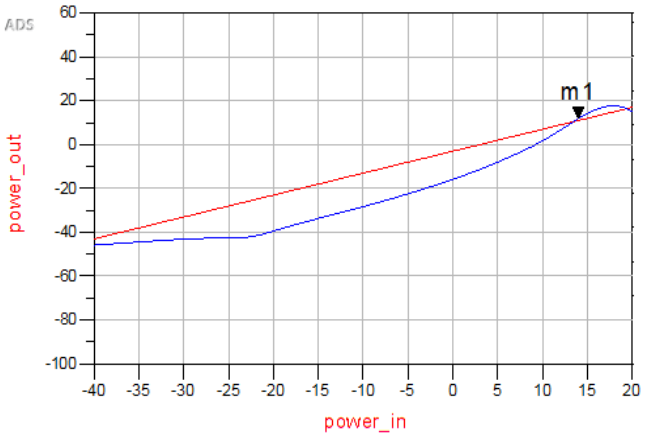

Fig. 14 CS Inductive Degeneration LNA with FDC

From the Fig. 14, we observe that IIP3 point is 14 dBm for common source inductive degeneration LNA configuration with FDC.

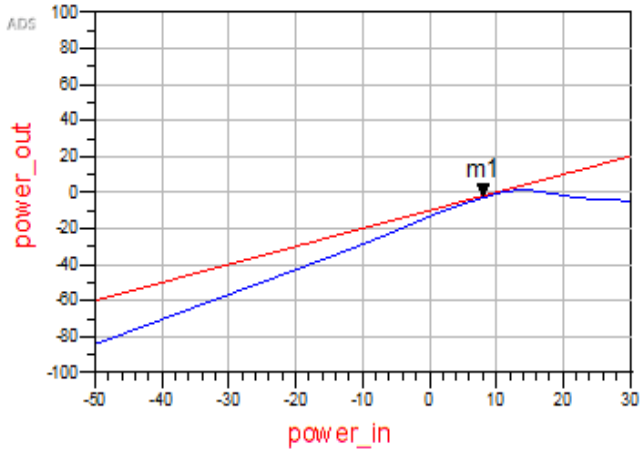

Fig. 15 CS Shunt Resistive Feedback LNA

From the Fig. 15, we observe that IIP3 point is 8 dBm for common source shunt resistive feedback LNA configuration.

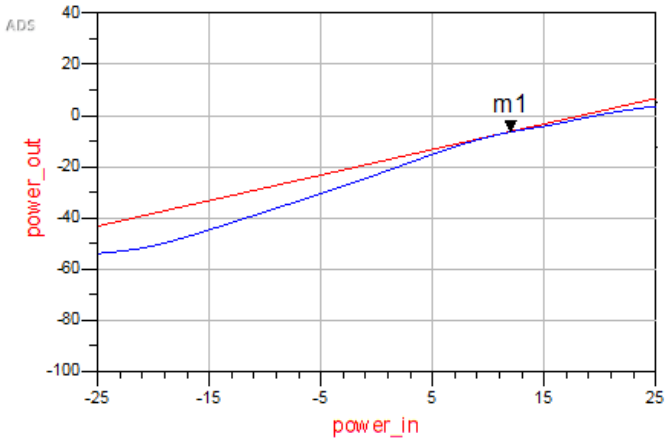

Fig. 16 CG LNA

From the Fig. 16, we observe that IIP3 point is 12 dBm for common gate LNA configuration.

TABLE I. COMPARISON OF LNA TOPOLOGIES

Para-meter	CS Cascode with FDC	CS Inductive Degenera-tion LNA [11]	CS Inductive Degenera-tion LNA with FDC	CS Shunt Resistive Feedback LNA	CG LNA
S_{11} (dB)	-5.562	-7.375	-9.408	-9.170	-26.894
S_{12} (dB)	-22.06	-41.47	-21.732	-18.909	-18.604
S_{21} / Gain (dB)	10.976	24.227	23.032	15.417	7.526

S_{22} (dB)	-8.707	-0.28	-4.730	-6.204	-12.264
Noise Figure (dB)	10.26	2.109	0.988	1.182	3.513
IIP3 (dBm)	17.0	4.0	14.0	8.0	12.0

From Table I, it can be concluded that highest gain is obtained from common source inductive degenerated LNA while common source inductively degenerated LNA with FDC provides the lowest noise figure. Highest linearity is achieved by common source cascode LNA with FDC; and for highest input impedance matching, common gate LNA should be preferred.

IV. CONCLUSION

In this paper, a 2.4GHz CMOS LNA for IEEE 802.15.4 ZigBee standard has been designed and analyzed, using various LNA topologies. The common source inductively degenerated LNA with FDC has a high gain of 23.032 dB, high linearity of 14 dBm, low noise figure of 0.988 dB and good input impedance matching ≈ 10 dB. So, inductively degenerated LNA with FDC is the best LNA topology as compared to others, for IEEE 802.15.4 Zigbee standard.

ACKNOWLEDGMENT

One of the authors (Aditi) acknowledges the fellowship support she is receiving from Delhi Technological University (DTU), for carrying out this work, as a part of her Master of Technology Thesis work in the domain of Microwave and Optical Communication. She also acknowledges the guidance support from her thesis mentor, Dr. Malti Bansal, Assistant Professor, Department of Electronics and Communication Engineering, DTU, for carrying out this research work.

REFERENCES

[1] A. Azizan, S. A. Z. Murad, R. C. Ismail and M. N. M. Yasin, "A review of LNA topologies for wireless applications," *2014 2nd International Conference on Electronic Design (ICED)*, Penang, 2014, pp. 320-324.

[2] C. H. Doan, S. Emami, D. A. Sobel, A. M. Niknejad and R. W. Brodersen, "Design considerations for 60 GHz CMOS radios," in *IEEE Communications Magazine*, vol. 42, no. 12, pp. 132-140, Dec. 2004.

[3] Bosco Leung, "VLSI for wireless communication," *Springer Science & Business Media*, 2011.

[4] Chung-Yu Wu and Chung-Yun Chou, "A 5-GHz CMOS double-quadrature receiver front-end with single-stage quadrature generator," in *IEEE Journal of Solid-State Circuits*, vol. 39, no. 3, pp. 519-521, March 2004.

[5] Koon Hung Lee and M. N. El-Gamal, "A very low-voltage (0.8 V) CMOS receiver frontend for 5 GHz RF applications," *2002 IEEE International Symposium on Circuits and Systems. Proceedings* (Cat. No.02CH37353), 2002, pp. I-125-I-128 vol.1.

[6] P. K. Dakua, A. S. N. Varma, P. Kabisatpathy and S. Mishra, "Study on Design and Performance Analysis of Low Noise High Speed Amplifier," in *International Conference of Signal Processing, Communication, Power and Embedded System (SCOPES)*, Odhisa, 2016, pp.1-6

[7] J. Sureja, S. Oza and J. Thathagar, "A 0.1–3 GHz low power cascode CS LNA using 0.18µm CMOS technology," *2012 1st International Conference on Emerging Technology Trends in Electronics, Communication & Networking*, Gujarat, 2012, pp. 1-6.

[8] G. B. Rao, "A high gain and high linear LNA for low power receiver front-end applications," *2016 International Conference on Communication and Signal Processing (ICCSP), Melmaruvathur*, 2016, pp. 1964-1967.

[9] T. T. N. Tran, C. C. Boon, M. A. Do and K. S. Yeo, "A 2.4 GHz ultra low-power high gain LNA utilizing π-match and capacitive feedback input network," *2011 IEEE 54th International Midwest Symposium on Circuits and Systems (MWSCAS)*, Seoul, 2011, pp. 1-4.

[10] B. Razavi, *RF Microelectronics*, Prentice-Hall, 1997.

[11] Aditi, M. Bansal, "A High Gain and Moderate Linearity Inductively Degenerated Cascode CMOS LNA for 2.4GHz ISM Band," *2017 Proceedings of International Conference on Innovations in Information, Embedded and Communication Systems (ICIIECS),* Coimbatore, 2017, vol. 5, no. 71, pp. 382-385.

Accepted Manuscript

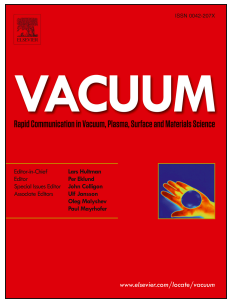

Design, development and characterization of MEMS silicon diaphragm force sensor

Rajesh Kumar, Shanay Rab, B.D. Pant, S. Maji

PII: S0042-207X(17)31817-1

DOI: 10.1016/j.vacuum.2018.04.029

Reference: VAC 7934

To appear in: *Vacuum*

Received Date: 12 December 2017

Revised Date: 7 April 2018

Accepted Date: 13 April 2018

Please cite this article as: Kumar R, Rab S, Pant BD, Maji S, Design, development and characterization of MEMS silicon diaphragm force sensor, *Vacuum* (2018), doi: 10.1016/j.vacuum.2018.04.029.

This is a PDF file of an unedited manuscript that has been accepted for publication. As a service to our customers we are providing this early version of the manuscript. The manuscript will undergo copyediting, typesetting, and review of the resulting proof before it is published in its final form. Please note that during the production process errors may be discovered which could affect the content, and all legal disclaimers that apply to the journal pertain.

ACCEPTED MANUSCRIPT

Design, development and characterization of MEMS Silicon diaphragm Force sensor

Rajesh Kumar[1*], Shanay Rab[2], B. D. Pant[3] and S Maji[4]

[1] *CSIR-National Physical Laboratory (CSIR-NPL), New Delhi, India- 110012*
[2] *Indian Institute of Technology (Indian School of Mines), Dhanbad,* India- *826004*
[3]*CSIR- Central Electronics Engineering Research Institute, Pilani, Rajasthan, India*
[4]*Delhi Technological University, Delhi, India*

Abstract

The aim of the paper is to describe the design, development and experimental characterization of a MEMS silicon diaphragm based force sensor. In the presented design, a unique combination of a thin single crystal silicon diaphragm has been used as a mechanical sensing element. The force sensor is based on the principle of conversion of applied force to an electrical quantity (e.g. voltage) consists of four piezoresistors in a Wheatstone-bridge configuration. The sensor has been modeled with the help of modern CAD tools and, after several iterations, the diaphragm size and thickness have been optimized to obtain a high sensitivity against an applied load in the designed range. The finite element analysis (FEA) has been carried out for computational investigations to have an approximate evaluation in regard of mechanical design and features. The important parameters like stress, strain and deflection are found to be within permissible limits. The fabricated sensor has been characterized by its metrological capabilities. The relative error due to repeatability is found to be < 1 % in the working range of the sensor. The sensitivity has been found to be in order of 0.35 –0.40 mV/V/N for 10 N to 50 N force range.

Keywords: CAD; Characterization; FEM; Force sensor; MEMS

1. Introduction

For many decades various type of force sensors have been used for force measurement in different industrial applications such as steel, cement, defense, space, railways, aviation, shipping, heavy industries and serve as force standards for disseminating the unbroken chain of measurement traceability from the National Metrology Institute (NMI) to the various manufacturing of industrial products (production hub).Various different force transducer analogous force proving rings or elliptical shaped bow dynamometer, standardizing box, tuning fork type, Hall effect and strain gauge type have been used over the years based on different principles and have different grades of uncertainty. In the Indian scenario about 60-70% analogous ring shaped force transducers are more commonly used despite their many inherited demerits such as non linearity, required temperature correction, limited use for specific points only, inability to interpolate, or, cannot be used for automation purposes. All these demerits are overcome by a strain gauge force transducer which employs strain gauges arranged in the form of Wheatstone bridge and their output is recorded through suitable digital indicators. Some Commercially available force transducers of make GTM-Germany, Interface Inc.-USA, HBM-Germany among others, are available in the market. Machining of these complex elements along with their strain gauging are a very difficult task, which is a critical barrier to the development of such force transducers at laboratory level [1-4]. There is practical constraint found with the analogous and the strain gauged force transducers in the Newton and sub-Newton lower force range.

A new class of force sensors based on Micro-electro mechanical systems (MEMS) has also come up during last one and half decades as new generation devices which have high sensitivity, are small in size and cost effective. With the evolution of this kind of technology; one can combine several techniques in the fabrication of a force sensing chip which is able to measure a wide range of forces. These force sensors utilize the mechanical properties of single crystal silicon as the load or force sensing element and the piezoresistive properties of mono-crystalline or that of polycrystalline Si for the transduction of the stress generated during the sensing of the force. The biggest advantage of this kind of force sensors is that the

*Corresponding author. Tel.: +91-11-45608516
E-mail address: rajeshkumarh33@gmail.com

Gauge Factor of the Si piezoresistors is as high as 200, leading to high sensitivity [5-10].

The present paper discusses the design, development and characterization of a circular shaped MEMS diaphragm load sensor. The force sensor has been developed for a capacity of 50 N and analytical as well as simulation studies have been done for measurement of stress, strain and deflection. The deflection values are computed by theoretical and computational methods at different loading conditions and there is a good agreement between the two approaches. The computational stress and stress values are found to be within permissible limits. The sensitivity and repeatability of the force sensor are measured according to the standard guidelines. The procedures and results are discussed.

2. Computational Investigations (Simulation)

The force sensor has been modeled in 3D with the help of software tool SolidWorks™. A detailed 3D model has been generated (Figure 1) in order to have a rigorous evaluation of force sensor for its structural behavior under action of the force applied. The applied loads are in the range of 10 to 50 N and the load acted at the centre of the sensor diaphragm with compressive nature. Suitable boundary conditions were applied and 3D finite element analysis has been carried out using the software tool Ansys Multiphysics™. Deflection, stress, strain and deformation have been evaluated for a realistic evaluation of the sensing element (Figures 2, 3 and 4). Stress is found to be within permissible limits. For FEM, yield strength and modulus of elasticity have been taken for Si as 7000 MPa and 190 GPa respectively. Poisson ratio is considered to be 0.23.

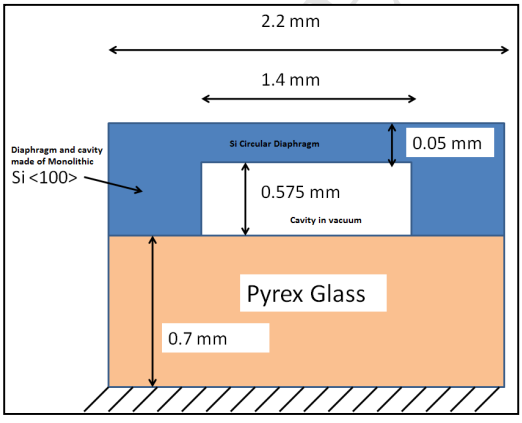

Fig. 1: Schematic cross-section of the force sensing element

2.1 Deflection theory

In the design process we consider various assumptions like small deflection, uniform diaphragm thickness and perfectly elastic behavior of the material used. According to the small deflection theory, deflection w(r) is the function of radial distance ***r*** in a circular plate [11-12]. The deflection at point of circular plate would be written as

$$w(r) = \frac{Fa^4}{64AD}\left\{1 - \left(\frac{r}{a}\right)^2\right\}^2 \quad (1)$$

Where "r" and "a" is the radial coordinate and diaphragm radius respectively. F is the applied load and A is the area of the plate over which the load is applied. Due to applied load, maximum deflection w_0 in the plate is observed at the centre of the plate, and hence the deflection equation becomes

$$w_0 = \frac{Fa^4}{64AD} \quad (2)$$

D is the flexural rigidity, which is a measurement of stiffness and is defined by

$$D = \frac{Eh^3}{12(1-\mu^2)} \quad (3)$$

Where E, h and μ are the modulus of elasticity, thickness of plate and Poisson's ratio, respectively. The deflection is the most important parameter in diaphragm based sensor design [13]. At different loading conditions, simulated deflections obtained are shown in figure 2. The maximum deflection is at the centre of the diaphragm, but it tends to decrease along the radius and is almost negligible at periphery of the sensor. Due to the similar deflection trend we have only considered the one side deflection from the centre of the diaphragm.

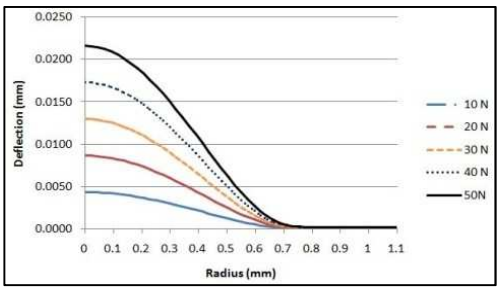

Fig. 2: Diaphragm deflection at different loads

2.2 Simulation Studies on a Force Sensor

The most appropriate geometry of the sensor was worked out by modeling software SolidWorks™. After several iterations on diaphragm thickness; the most optimized dimension was selected (Figure1). Silicon is used as the mechanical sensing element because of its higher yield strength which is more than three times that of stainless steel, additionally, Silicon in the form of circular wafers is extremely flat for coatings and additional thin film layers for either being integral structural parts, or performing precise electromechanical functions. Silicon shows virtually no mechanical hysteresis. It is, thus, an ideal candidate for use as sensors and actuators. The model was simulated with different loading condition from 10 N to 50 N. The obtained results by Ansys are found satisfactory. In the first stage figure 3 (a) with the help CAD modeling software, sensor model was created. Then in next stage fig. 3(b) meshing was carried out on the model.

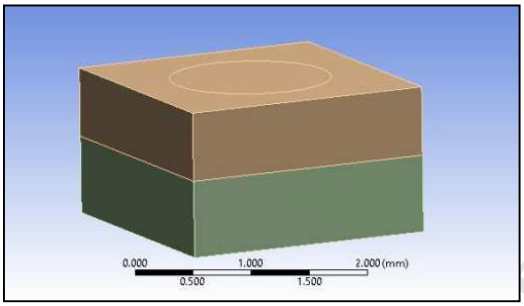

(a)

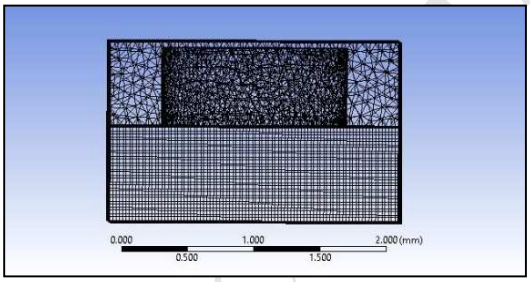

(b)

Fig.3: (a) CAD model of the sensor (b) Meshing

Then the necessary boundary conditions were applied in Ansys. Thus the results obtained by the simulation program found within permissible limits are depicted in figure 4. The computational studies have been found to be very useful for finding the most appropriate location of the piezoresistors. The exact location of piezoresistors plays the vital role in the sensitivity of the MEMS sensor [14-16].

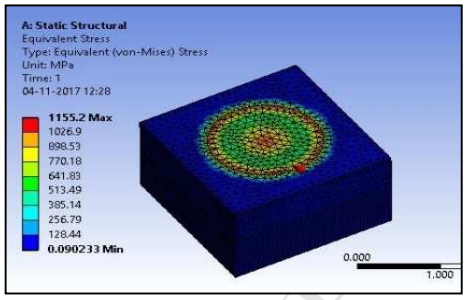

(a)

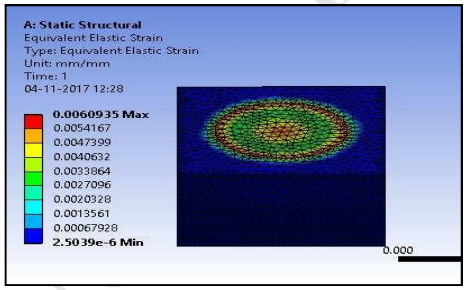

(b)

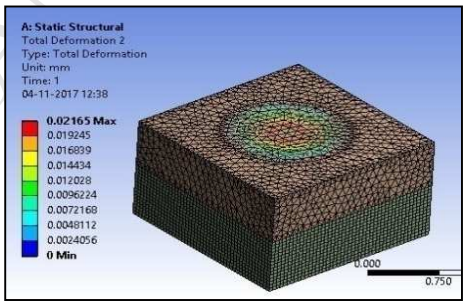

(c)

Fig.4: (a) Stress (b) Strain and (c) Deflection in force sensor at 50N

3. Development and Fabrication of Force Sensor

After fixing the dimensions of the diaphragm, the cavity, the outer size of the chip as well as the location of the piezoresistors on the top surface, through designing, modeling and simulation, the mask layouts were generated for each material layer using Tanner Tools software Ledit™. The whole fabrication process consists of five levels of masks. Each layout was thoroughly and precisely verified for etching layer dimensions, alignment and registration marks. The masks were then fabricated at CSIR-CEERI using the Heidelberg pattern generator. The Si load cell fabrication was carried out using a batch of 150 mm double side polished (DSP) single crystal p-Si <100> wafers (Table-1).

ACCEPTED MANUSCRIPT

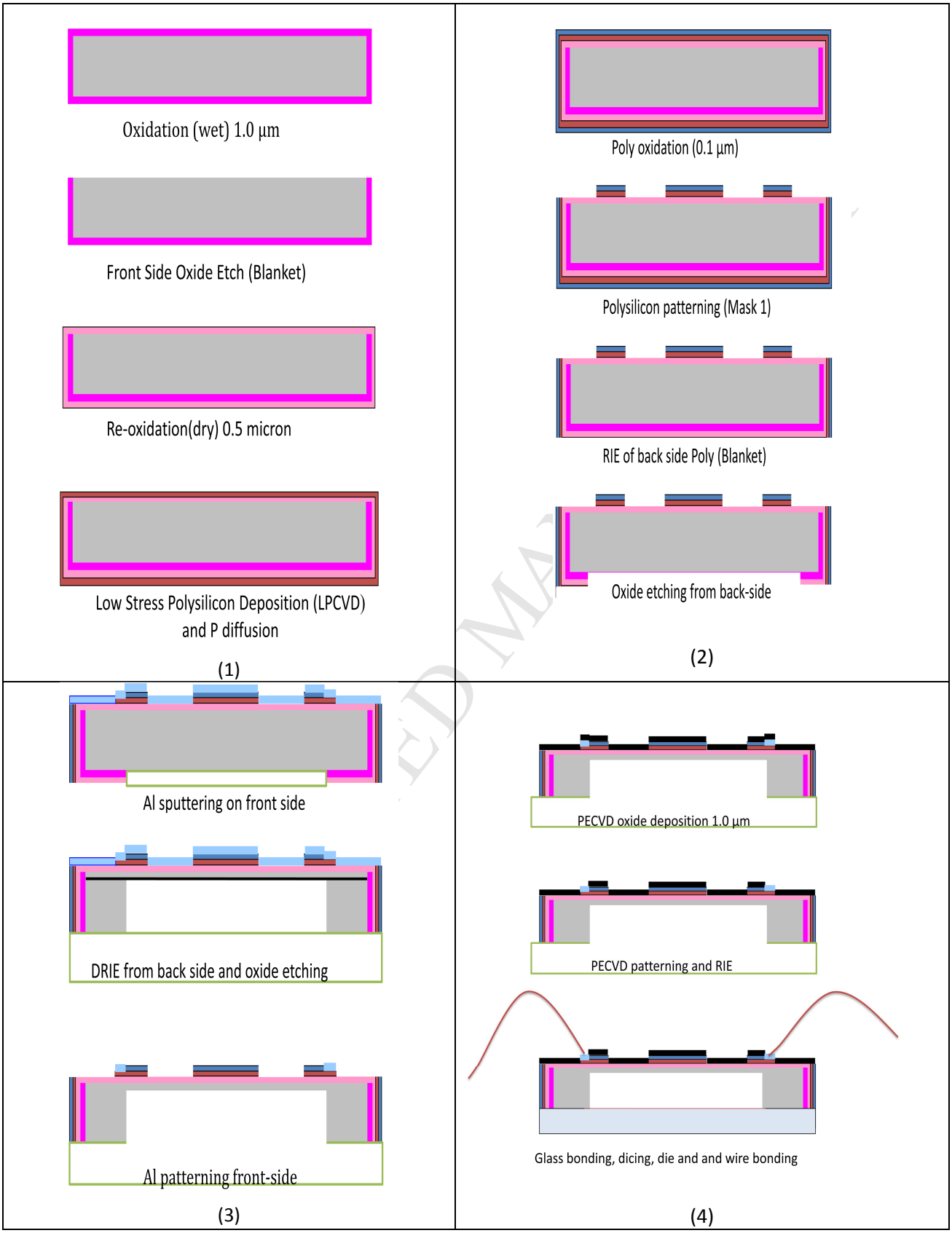

Fig.5: Process Flow Chart

In the present work, we have designed and developed Si diaphragm force sensor array entirely on a silicon substrate of 150 mm diameter and a thickness of 625 micron. The fabrication steps have been summarized in Table 1, whereas the complete fabrication process is illustrated in figure 5. The value of the four piezoresistors was designed to be in three variations: 5, 8 and 12 KΩ. These piezoresistors were fabricated using LPCVD (Low Pressure Chemical Vapor Deposition) process and their resistance was controlled through Phosphorous-diffusion in a diffusion furnace. Metal lines were fabricated using Al sputtering and subsequent patterning followed by wet process [17-21]. Figure 6(a) shows the Si diaphragm just device was carried out after the DRIE process step. After This step each wafer was bonded with a 0.7 mm thick Pyrex glass using an Anodic Bonding process [22-24]. After the DRIE process wafer level testing of each etching was done. The diaphragm was realized through dry bulk micromachining (DRIE-Deep Reactive Ion Etching). The wafers were then diced using a double spindle Disco Dicing Machine.

Table-1: Fabrication Process Steps including PLG-Mask Stages

Wafer cleaning and wet Oxidation (1µm)	**Photolithography (PLG) – Mask 1** (Resistor definition)	**PLG-Mask 3** (opening of contact holes)	Deposition of PECVD Oxide (Front side) 1.0 µm
Front side Oxide etch	RIE of PolySi and PolySi backside etch	Oxide etching from contact holes	**PLG-Mask 5** Contact pad opening
Dry Oxidation (0.5 µm)	**PLG-Mask 2 (Back Side Alignment)** (diaphragm definition)	Al Sputtering	Anodic Bonding (Silicon-Glass)
Low Stress Polysilicon deposition (LPCVD)	Oxide etching from diaphragm (Backside)	**PLG- Mask 4** Al etch: Contact lines	Dicing and Die bonding
Polysilicon Phosphorous di diffusion and Annealing	DRIE of Si for diaphragm	PRCleaning (Blanket UV) and Al-Sintering	Packaging and wire bonding

The chips of the size 2.2 × 2.2 mm^2 were separated and cleaned in acetone (figure 6(b)). After cleaning, individual chips were mounted on a specially designed PCB (Printed circuit board) and wire-bonded using a wire bonding machine. The bonding wires and the chip were covered with an epoxy carefully in such a way that the diaphragm remains open for the application of load over it, figure 6(c). Figure 6 shows the fabricated Si load cell and packaged device. After packaging the device was tested and characterized.

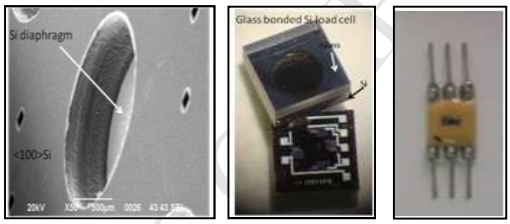

(a) (b) (c)

Fig. 6: Developed Si diaphragm load cell (Laboratory model)

4. Experimental Setup

An experimental setup is designed and fabricated to test the small Si diaphragm type force transducers from 10 N to 50 N force ranges at an equal interval of 10 N force steps. 3 sets of observations are taken for the given force series (10 N to 50 N) for each of the Si force sensors developed and their repeatability has been evaluated. Figure 7 (a) shows the various computational views of the experimental setup. The experimental setup is customized to meet the requirements of developed force sensors. Figure 7 (b) and (c) shows the real setup with loading arrangement. A high resolution digital indicator (6 1/2 digital multimeters, make of Fluke) has been used for recording the observations over the excitation voltage 1 V.

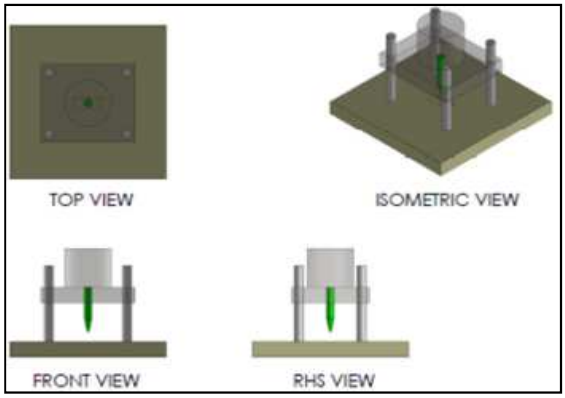

Fig.7: (a) Experimental setup design views

(b)

(c)

Fig.7: (b and c**)** Experimental setup

4.1 Experimental Procedure

Metrological characterization of the MEMS force sensors has been done by adopting the following procedure:

a. Environmental conditions (temperature and relative humidity) are maintained 23 ± 2^{o}C and 50 ± 10 % respectively.

b. The digital indicator is switched ON for at least 30 minutes.

c. The force sensor is preloaded with its nominal capacity 3 times.

d. The force sensor is loaded for 3 series in ascending order from 10 N to 50 N with incremental force of 10 N each. Observations were recorded.

e. Relative repeatability of the force sensor was evaluated

5. Results and Discussion

With reference to procedure discussed in section 4.1, the results are summarized as follows (Figure 8). With reference to literature discussed, we would like to bring to the attention of the readers that generally the repeatability of piezoresistive force sensors falls into the range of 5% or below, which is widely accepted for the applications concerned [25, 26]. In contrast to such commercial force sensors, the present study depicts the force sensors with repeatability of up to 1 % or lower in the working range. The experimental observation clearly shows that the repeatability is less than 1 % in the 20 to 50 N force range. Only at one initial point (10 N) the value of repeatability is in the 2 % or lower range.

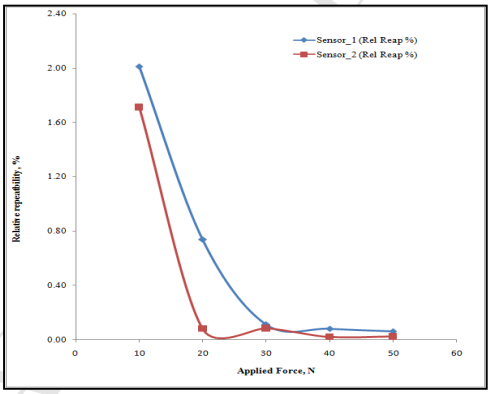

Fig. 8: Summary of experimental observations

The developed force sensor is tested up to 50 N. The computational deflection data plotted in figure 2 with different loading conditions shows the maximum deflection occurs at the centre of the diaphragm. The maximum theoretical value of deflection is found to be 18 micron at 50 N loads. The theoretical deflection (analytical) data obtained by using mathematical equation and simulated deflection obtained by Ansys, shown in figure 9, follows a similar trend and values are very close to each other.

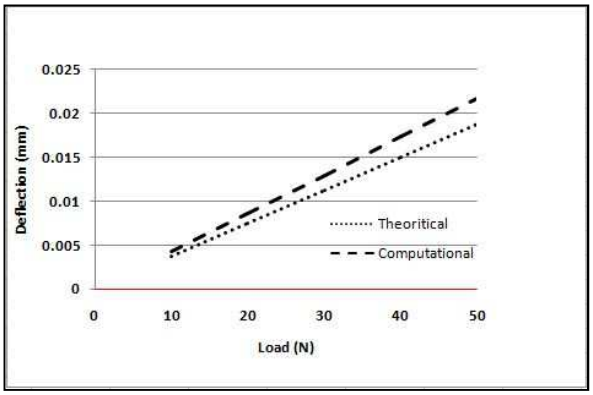

Fig.9: comparison between computational and theoretical results

Figure 10 depicts the stress distribution in the load sensor with different loading conditions. Maximum stress is found at the centre of the sensor diaphragm where the load is applied. Maximum stress is found to be 1155.2 MPa which is lower than the yield stress of the material used (7000 MPa). The second maximum stress is found to be 919.09 MPa, which is 0.61875 mm away from the centre of the sensor. Maximum highest stresses at the centre of the diaphragm have been rejected due to practical constraints and design factors, so the second maximum stress location is the most appropriate location of resistors. Similarly the strain distributions follow the same pattern as stress distribution. The maximum and second maximum strain is 5.38 x 10^{-3} and 4.91 x 10^{-3} mm , respectively.

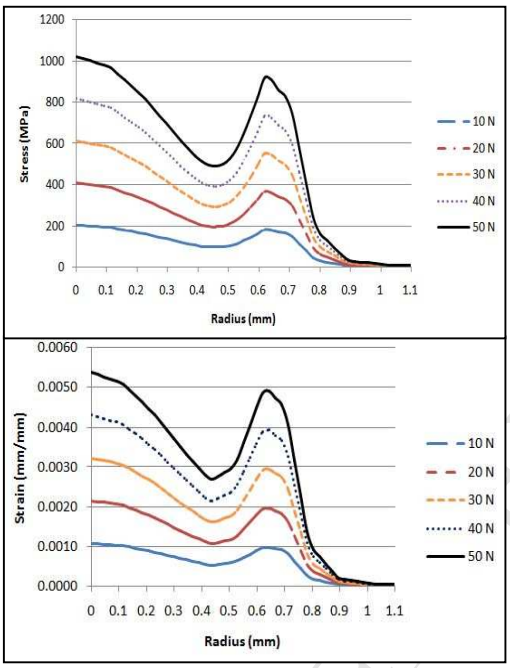

Fig.10: Stress and strain distribution curve

6. Conclusions

The design parameters along with dimensions and selection of the material have been validated with finite element analysis. The simulation results obtained by Ansys for maximum deflection from 10 to 50 N loads are in close agreement with analytical results. The value obtained for maximum stress and strain are within permissible limits. The location of four resistors is 0.61875 mm from the centre, perfectly obtained by the second maximum stress and strain location curves. The repeatability is found to be less than 1% in the working range of the force sensor. The experimentally obtained sensitivity was of order 0.35-.0.40 mV/V/N for 10 to 50 N ranges. An indigenous silicon diaphragm based load sensor has thus been successfully designed, developed and tested for its metrological performance.

Future Work

Further we can minimize repeatability and other metrological factors by suitable change in the experimental setup. The small size and low weight with high sensitivity would ensure its portability, thereby opening up new applications in the field of biomedical, aviation industry, and research laboratory application. We can commercialize these sensors because there is limited availability of commercial force sensors in this sensitivity with limited practical viability up to best of knowledge of authors.

Acknowledgment

Authors are thankful to Director, CSIR-NPL and CSIR-CEERI for their constant encouragement and support. Authors are also thankful to the Head, Physico-Mechanical Division and Head, Force & Hardness Standards for their support and motivation at CSIR-NPL.

References

[1] M. Rehman and S. Rehman, A computer program for designing circular proving rings of uniform strength, J. Inst. Eng. (India) Mech. Eng. Div., 88 (2007), 3–7.

[2] R. Kumar, B. D. Pant, S. Maji, Development and Characterization of a Diaphragm-Shaped Force Transducer for Static Force Measurement, MAPAN-Journal of Metrology Society of India, DOI 10.1007/s12647-017-0207-7

[3] H. Kumar, C. Sharma and A. Kumar, The development and characterization of a square ring shaped force transducer, Meas. Sci. Technol., 24 (9) (2013) 095007.

[4] R. Kumar, H. Kumar and A. Vikram, Long term uncertainty investigations of 1 MN force calibration machine at NPL, India (NPLI), Meas. Sci. Rev., 12 (2012) 147–150.

[5] S. Santosh Kumar, B. D. Pant Design principles and considerations for the ‘ideal’ silicon piezore sistive pressure sensor: a focused review, Microsyst Technol.

ACCEPTED MANUSCRIPT

[6] Ivo W. Rangelow, Dry etching-based silicon micro-machining for MEMS, Vacuum 62 (2001); 279-291.

[7] H. Toshiyuki, K. Yoshihisa, U. Kazunaga, et al., Evaluation of tuning fork type force transducer as a transfer standard, Measurement 41 (2008) 941–949.

[8] ISO, – Metallic materials – Calibration of force proving instruments used for the verification of uniaxial testing machines,ISO 376, 2011.

[9] K. D. Wise, Integrated sensors, MEMS, and microsystems: reflections on a fantastic voyage, Sensor. Actuat. A - Phys. (2007), Vol. 136, pp. 39-50.

[10] Eaton WP, Smith JH, Micromachined pressure sensors: review and recent developments. Smart Mater Struct 6(5) (1997) 530–539.

[11] Elgamel HE, Closed-form expressions for the relationships between stress, diaphragm deflection, and resistance change with pressure in silicon piezoresistive pressure sensors. Sens Actuators A (1995) 50:17–22.

[12] Yadollah Hezarjaribi, Mohd Hamidon1,Roslina Sidek, Keshmiri Hossein, Raja Abdulla and Alireza Bahadorimehr, "Evaluation for Diaphragm's Deflection for Touch Mode MEMS Pressure Sensors, The International Arab Journal of Information Technology, Vol. 8, No. 2 (2011).

[13] Libo Zhao, Xudong Fang, Yulong Zhao, Zhuangde Jiang, and Yong Li, A High Pressure Sensor with Circular Diaphragm Based on MEMS Technology, Key Engineering Materials Vol 483 (2011) 206-211.

[14] Bray A. Role of stress analysis in the design of force standard transducers. Exp Mech (1981) 21:1–20.

[15] Shaby SM, Juliet AV, Design and analysis of MEMS pressure sensor by using ANSYS. In: Proceedings of the 2nd international conference on mechanical, automotive and materials engineering (MAME'12), Bali (Indonesia), (2012) 132–135.

[16] R. Kumme, O. Mack, B. Bill, H.R. Haab, C. Gossweiler, Dynamic Properties and Investigations of Piezoelectric Force Measuring Devices, VDI-Bericht 1685, VDI Verlag GmbH, Du¨ sseldorf (2002), ISBN 3-18-091685-0,161–172.

[17] Mäuselein, S., Mack, O., Schwartz, R., Investigations into the use of single-crystalline silicon as mechanical spring in force sensors, XVIII IMEKO World Congress, Brazil, September 2006.

[18] M. Olfatniaa, T. Xua, J.M. Miaoa, L.S. Onga, X.M. Jing a, L. Norfordb, Piezoelectric circular micro diaphragm based pressure sensors, Sensors and Actuators A 163 (2010) 32–36.

[19] Kumar SS, Pant BD (2012) Design of piezoresistive MEMS absolute pressure sensor. In: Proceedings of the SPIE 854.

[20] J. C. Andle and J. F, Vetelino, Acoustic wave biosensors, Sens. Actuators A, Vol. 44, (1994) 167-176.

[21] Marco Dienel, Michael Naumann, Alexander Sorger, Dirk Tenholte, Sebastian Voigt, Jan Mehner, On the influence of vacuum on the design and characterization of MEMS, Vacuum 86 (2012) 536-546.

[22] Thomas M. et.al. Detailed characterization of anodic bonding process between glass and thin-film coated silicon substrates, Sensors and Actuators A: Physical, Volume 86, Issues 1–2, (2000) 103-107.

[23] R. Stengl et. al. A Model for the Silicon Wafer Bonding Process, Japanese Journal of Applied Physics, Volume 28, Part 1, Number 10.

[24] H Moriceau et. al. Overview of recent direct wafer bonding advances and applications, Advanced inNanoScience and Nanotechnology Nat. Sci.: Nanosci. Nanotechnol. 1 (2010) 043004.

[25] https://www.tekscan.com/resources/ebook/load Cellvs-force-sensor (accessed on 18 January 2018).

[26] http://www.rfwirelessworld.com/Terminology/ Advantages-and-Disadvantages-of-force Sensor.html (sensor (accessed on 18 January 2018).

ACCEPTED MANUSCRIPT

- The design parameters along with dimensions and materials have been validating with finite element analysis. An indigenous silicon diaphragm based load sensor is designed, developed and tested for its metrological performance.
- The simulation results obtained by Ansys for maximum deflection with different loading from 10 N to 50 N are in very good agreement with theoretical calculated results. The value obtain for maximum stress and strain are in permissible limit.
- Location of the four resistors is 0.61875 mm from centre, perfectly obtained by second maximum stress and strain location graph.
- The obtained sensitivity in the order of 0.35 – 0.40 mV/V/N for 10 N to 50 N force range. The repeatability is found to be less than < 1 %, in the working range of the force sensor.

ACCEPTED MANUSCRIPT

J. Inst. Eng. India Ser. B
https://doi.org/10.1007/s40031-018-0322-z

ORIGINAL CONTRIBUTION

Economic Load Dispatch Using Adaptive Social Acceleration Constant Based Particle Swarm Optimization

N. K. Jain[1] · Uma Nangia[1] · Jyoti Jain[1]

Received: 21 July 2017 / Accepted: 2 March 2018
© The Institution of Engineers (India) 2018

Abstract In this paper, an Adaptive Social Acceleration Constant based Particle Swarm Optimization (ASACPSO) has been developed which uses the best value of social acceleration constant (Csg). Three formulations of Csg have been used to search for the best value of Csg. These three formulations led to the development of three algorithms–ALDPSO, AELDPSO-I and AELDPSO-II which were implemented for Economic Load Dispatch of IEEE 5 bus, 14 bus and 30 bus systems. The best value of Csg was selected based on the minimum number of Kounts i.e. number of function evaluations required to minimize the function. This value of Csg was directly used in basic PSO algorithm which led to the development of ASACPSO algorithm. ASACPSO was found to converge faster and give more accurate results compared to BPSO for IEEE 5, 14 and 30 bus systems.

Keywords Convergence · Economic load dispatch · Iteration · Kounts · PSO

List of Symbols

F	Objective function to be optimized
F_C	Cost of the generation
P_L	System transmission losses
a_i, b_i, c_i	Cost coefficient of i^{th} generator
P_{gi}	Active power generation of the i^{th} generator
P_{gimax}	Maximum power generation limits of i^{th} generator
P_{gimin}	Minimum power generation limits of i^{th} generator
P_D	Total system demand
P_g	Total power generated
K	Penalty factor
N_g	Total number of generators in the system
B_{ij}, B_{oi}, B_{oo}	Loss co-efficients
p	Number of particles in the swarm
v_{ij}^k	Velocity of j^{th} particle of i^{th} generator at k^{th} iteration
W	Inertia weight factor
c_p, c_g	Acceleration coefficients
r_p, r_g	Random number between 0 and 1
x_{ij}^k	Current position of j^{th} particle of i^{th} generator at k^{th} iteration
$x_{pbestij}^k$	Personal best position of j^{th} particle of i^{th} generator at k^{th} iteration
x_{gbesti}^k	Global best position of swarm for i^{th} generator at k^{th} iteration
IT	Maximum number of iterations
k	Current iteration
C_{gmax}	Maximum value of social acceleration constant
C_{gmin}	Minimum value of social acceleration constant
C_{sg}	Adaptive social acceleration constant
C_{sg1}	Social acceleration constant based on linearly decreasing function
C_{sg2}	Social acceleration constant based on exponential of linearly decreasing function

✉ N. K. Jain
uma.nangia62@gmail.com

[1] Electrical Engineering Department, Delhi Technological University, Delhi 110042, India

Published online: 25 April 2018

C_{sg3}	Social acceleration constant based on exponentially decreasing function consisting of exponential of constant multiplied by linearly decreasing function

Introduction

Thermal power plants (coal, natural gas, oil and nuclear) are responsible for roughly 80% of global electricity production. Commercial power stations are usually constructed on a large scale and designed for continuous operation. The direct cost of electric energy produced by a thermal power station is the result of cost of fuel, capital cost for the plant, operator labor, maintenance, and such factors as ash handling and disposal. The sizes of the electric power system are increasing rapidly to meet the energy requirement. So the number of power plants are connected in parallel to supply the system load by an interconnection of the power system. In the grid system, it becomes necessary to operate the plant units more economically. Economic Load Dispatch (ELD) problem allocates loads to plants at a minimum cost while satisfying the equality and inequality constraints [1]. Now a days ELD Problems are solved by intelligent techniques like Differential Evolution [2], Grey wolf algorithm [3], Firefly algorithm [4], Genetic algorithm [5], Particle swarm optimization [6, 7] etc. Dhillon et al. [8] proposed economic emission load dispatch problem to minimize the fuel cost and environmental emission. Non inferior sets are developed using weighted minimax technique and fuzzy set theory is used for decision making process of optimal solution. Baskar et al. [9] proposed a new Particle Swarm Optimization (PSO) using constriction factor and implemented it on security constraint ELD problem. The author showed that new PSO overcame the problem of premature convergence. Niu et al. [10] proposed a Simple Cultural Algorithm based (SCAPSO) to solve the ELD with valve point loading effect to increase the convergence speed in large search area. SCAPSO was compared to EP, EP-SQP, PSO, PSO-SQP, MPSO, NPSO-LRS, GA, DE, IGA-MU and GA-PS-SQP. The authors found the minimum cost achieved by SCAPSO is lower than many other methods except for DE and GA-PS-SQP.

Rani et al. [11] suggested the solution for minimum fuel cost and emission cost using new PSO technique, in new PSO technique authors updated the worst position and its group's previous worst position instead of personal best and global best position for velocity. They implemented this idea to solve Emission Constrained Economic Dispatch (ECED) problem for 6-generator, 30-bus test system. Labbi et al. [12] presented a hybrid technique using PSO and Pattern search to solve ELD problem consisting of 15 thermal units. The authors compared this technique with SA,GA,TSA,PSO, MTS and PS and found computational time of PS algorithm to be the lowest. Dubey et al. [13] presented a hybrid TVPSOGSA to solve the environmental\economic dispatch problem for 3, 6 and 40 generators. In this paper the authors converted the multi-objective problem into single objective using the price penalty method and determined the best compromise solution using Fuzzy technique. Abbas et al. [14] presented a survey paper on ELD using PSO, and found that PSO offer best results compared to GA, EP, DE, SA and PS.

Kumar et al. [15]. presented a research article on PSO. The authors updated Inertia weight using sinusoidal modulation, to increase the coarse search during early half and by assigning lower values to particle velocities during the later half. They implemented the proposed PSO to solve ELD problem considering variety of constrants. They found the proposed PSO to be superior than existing PSO and other stochastic methods. Singh et al. [16] designed a software package tool using Matlab GUI for solving ELD problem with real time coal quantity as an additional inequality constraints. This is used to design a graphical layout for calculating the cost of generation for thermal power plant. Singh et al. [17] solved the ELD problem with valve point loading effect for 3 and 10 generators with and without considering the transmission losses. The authors demonstrated that the results were significantly improved by properly tuning of PSO parameters. Jain et al. [18] developed initial selection based particle swarm optimization to solve ELD problem for IEEE 5,14 and 30 Bus Systems. Using this technique computational time decreases. Zhao et al. [19] presented solution for multiobjective problem for three objectives: cost, loss and emission. Set of pareto optimal solutions was obtained by MPPSO and compromised solution was obtained by fuzzy based mechanism. L.V. Narasimha [20] solved the Economic Load Dispatch Problem of an n-unit Plant using lambda iteration method and Particle Swarm Optimization. From the results the authors concluded that, the convergence of lambda iteration method depends on initial value of lambda, whereas the convergence of PSO method does not depend on initial value of lambda.

In this paper, an attempt has been made to develop an Adaptive Social Acceleration Constant based PSO (ASACPSO). The Adaptive Social Acceleration Constant has been searched using three formulations which led to the development of three algorithms-ALDPSO, AELDPSO-I and AELDPSO-II. All three were implemented on IEEE 5 bus system. The best value of Csg was selected based on the minimum number of function evaluations or kount

required to minimize the function. This value of Csg has been used directly in basic PSO algorithm which led to the development of ASACPSO. This algorithm was found to converge faster and give more accurate results for IEEE 5, 14 and 30 bus systems.

Mathematical Formulation of ELD Problem

Mathematically, ELD problem is defined as: Minimize

$$F_C = \sum_{i=1}^{NG} F\left[C_i\left(P_{gi}\right)\right] \tag{1}$$

where cost function is defined as:

$$C_i\left(P_{gi}\right) = \sum_{i=1}^{NG}\left(a_i P_{gi}^2 + b_i Pg_i + c_i\right) \tag{2}$$

The objective function used to find the system transmission losses is given by

$$P_L = \sum_{i=1}^{NG}\sum_{j=1}^{NG} P_{gi} B_{ij} P_{gj} + \sum_{j=1}^{NG} B_{oj} P_{gj} + B_{oo} \tag{3}$$

Subject to the constraintsEquality constraint

$$\sum_{j=1}^{NG} P_{gi} = P_D + P_L \tag{4}$$

Inequality constraint

$$P_{gimin} \le P_{gi} \le P_{gimax} \quad i = 1, 2\ldots NG \tag{5}$$

To consider the equality constraint of the problem, the function has been modified by inclusion of a parameter K. The objective function becomes as follows:

$$F = F_C + K\left(P_D + P_L - P_{gi}\right) \tag{6}$$

where parameter K is fixed at 1000 for all three IEEE 5, 14, and 30 bus systems. Different values of K were considered and it was observed that ELD problem converged when it was fixed to 1000 for IEEE 5,14 and 30 bus systems.

For optimum solution the change in the value of function value during successive iterations must be less than the limit specified which is $T = 10^{-6}$. To meet the constraint the absolute value of difference between generation, demand and losses is less than $T = 10^{-6}$.

Basic Particle Swarm Optimization (BPSO)

PSO is a swarm intelligence technique developed by Eberhart and Kennedy [7] in 1995, inspired by the social behavior of birds. It is applicable for optimization of economic load dispatch and multiobjective ELD nonlinear problems. In the multidimensional space where the optimal solution is sought, each particle in the swarm is moved towards the optimal point by adding a velocity to its position. The velocity of a particle is influenced by three components: namely inertial, cognitive, and social. The inertial component simulates the inertial behaviour of the bird to fly in the previous direction. The cognitive component models the memory of the bird about its previous best position, and the social component models the memory of the bird about the best position among the particles (interaction inside the swarm). At each iteration the particle move towards optimum solution, through its present velocity, personal best solution obtained by themselves and global best solution obtained by all the particles until they find the optimal solution.

In an n-dimensional search space, position and velocity of particle j are represented by vectors $X_{ij} = (X_{i1}, X_{i2}\ldots - X_{ip})$ and $V_{ij} = (V_{i1}, V_{i2}\ldots.V_{ip})$ respectively. Let Xpbest vector and Xgbest be the personal and global best positions of the particles for ith variable. In case of ELD problem, the generations are the independent variables of the problem. The modified velocity and position of each particle can be calculated using current velocity and distance from Xpbest and Xgbest as follows:

$$v_{ij}^{k+1} = w^* v_{ij}^k + c_p r_p\left(x_{pbestij}^k - x_{ij}^k\right) + c_g r_g\left(x_{gbesti}^k - x_{ij}^k\right) \quad i = 1, 2, \ldots NG; \quad j = 1, 2\ldots p; \tag{7}$$

Position update equation is given by

$$x_{ij}^{k+1} = x_{ij}^k + v_{ij}^{k+1} \quad i = 1, 2\ldots NG; \quad j = 1, 2\ldots p \tag{8}$$

Adaptive Social Acceleration Constant Based PSO (ASACPSO)

Social Acceleration coefficient, C_g regulates the maximum step size in the direction of the global best particle. In basic PSO, both the acceleration coefficient C_p and C_g are fixed to 1.0, whereas in ASACPSO, Cg is searched adaptively and is called as adaptive social acceleration constant C_{sg}. The adaptive social acceleration based constant C_{sg} has been searched using following three formulations.

I Linearly decreasing function

$$C_{sg1} = C_{gmax} - \left(k * \left(C_{gmax} - C_{gmin}\right)/IT\right) \tag{9}$$

II Exponential of linearly decreasing function

$$C_{sg2} = \exp(-1) * \left(C_{gmax} - \left(k * \left(C_{gmax} - C_{gmin}\right)/IT\right)\right) \tag{10}$$

III Exponential decreasing function consisting of exponential of constant multiplied by linearly decreasing function.

$$C_{sg3} = \exp(-0.34) * \left(C_{gmax} - \left(k * \left(C_{gmax} - C_{gmin}\right)/IT\right)\right) \quad (11)$$

PSOs based on C_{sg1}, C_{sg2}, C_{sg3} have been named as Adaptive Linearly Decreasing PSO (ALDPSO), Adaptive Exponential Linearly Decreasing PSO (AELDPSO-I) and Adaptive Exponential Linearly Decreasing PSO-II (AELDPSO-II) respectively. All the three algorithms have been implemented to solve Economic load dispatch problem of IEEE 5, 14, and 30 bus systems. The best value of Adaptive–Social Acceleration Constant C_{sg} for each algorithm is searched by applying Eq. (9), (10) and (11) after second, third, fourth and up to seventh iteration. The convergence was not achieved when Csg was implemented after 7^{th} iteration. The results of ALDPSO, AELDPSO-I and AELDPSO-II for IEEE 5 bus system are shown in Tables 1, 2 and 3 respectively. The best value of C_{sg} is selected based on minimum number of kounts required to optimize the function. Adaptive Social Acceleration Constant based PSO (ASACPSO) is then developed using the best value of C_{sg}. Kount is number of function evaluations which indicates the number of times the function has been evaluated during optimization of ELD problem. This is taken as the measure of computational time. The measure of computational time in seconds or minutes will depend on the technology. So time has been measured in terms of function evaluations.

The sequence for the solution of Economic Load Dispatch problem using ASACPSO algorithm is explained as follows:

1. Initialize the population between the limits of power.
2. Initialize the velocity of particles between the limits $\left(\pm P_{gmax/2}\right)$.
3. Fix the no. of maximum iterations IT, tolerance value T and penalty parameter K. For optimum solution the change in the function value during successive iterations must be less than the limit specified which is $T = 10^{-6}$.

Table 1 Results of ELD using ALDPSO for IEEE 5 bus system

Condition for Implementation of C_{sg1} (1)	C_{sg1} (2)	F_C ($/h) (3)	P_L (MW) (4)	Kount (5)	No of iteration (6)	P1 (MW) (7)	P2 (MW) (8)
iter > 2	1.37	761.63	5.08	9080	113	90.08	74.99
iter > 3	1.37	762.29	5.06	8920	111	87.19	77.87
iter > 4	1. 384	761.14	5.09	8440	105	91.18	73.91
iter > 6	1.363	761.27	5.1	9960	124	92.34	72.76

Table 2 Results of ELD using AELDPSO-I for IEEE 5 bus system

Condition for implementation of C_{sg2} (1)	C_{sg2} (2)	F_C ($/h) (3)	P_L (MW) (4)	Kount (5)	No of iteration (6)	P_1 (MW) (7)	P_2 (MW) (8)
iter > 2	x						
iter > 3	x						
iter > 4	0.6703	762.57	5.06	8480	105	86.20	78.85
iter > 5	x						
iter > 6	x						
iter > 7	x						

Table 3 Results of ELD using AELDPSO-II for IEEE 5 bus system

Condition for implementation of C_{sg3} (1)	C_{sg3} (2)	F_C ($/h) (3)	P_L (MW) (4)	Kount (5)	No of iteration (6)	P_1 (MW) (7)	P_2 (MW) (8)
iter > 2	0.617	762.96	5.52	6040	75	109.65	55.87
iter > 3	0.616	761.03	5.06	5800	72	99.59	65.38
iter > 5	0.615	762.16	5.06	5480	68	87.70	77.36
iter > 6	0.616	761.50	5.08	5560	69	90.83	74.25

4. To meet the constraint the absolute value of difference between generation, demand and losses must be less than T = 10^{-6}.
5. Set iteration count k = 0 & Kount = 0.
6. Fix the Cost Coefficients, Loss coefficients, load demand and calculate the Cost using (2) and Loss using (3) for each particle. Evaluate function value for each particle using (6).
7. At 0th iteration the personal and global best positions are same as the initial random position.
8. Increase the iteration value 'k' and kount by 1.
9. Calculate the velocity of each particle by replacing C_g by C_{sg} in (7).
10. Check if velocity is within the limits. If not fix the velocity to the limit violated.
11. Calculate the new positions of the particles using (8).
12. Calculate ELD function value using (6) for the new position of particles.
13. Update x_{pbest} and x_{gbest}, values.
14. Check if both the stopping criteria are satisfied, If not then go to step 8, else stop.
15. Display the optimize values for cost of generation, and for optimized value of power generation calculate transmission losses.
16. Display iterations and numbers of Kounts required to optimize the function.

Computational Results

The basic PSO (BPSO) and proposed PSO algorithms – ALDPSO, AELDPSO-I, AELDPSO-II, ASACPSO have been implemented for Economic Load Dispatch of IEEE 5-bus,14-bus and 30-bus systems. For all the algorithms the parameters were fixed as:

$$P = 40, \quad rp = rg = cp = 1; \quad C_g max = 1.5, \quad C_g min = 0.4, \quad IT = 1000$$

The Results of ELD using ALDPSO, AELDPSO-I and AELDPSO-II for IEEE 5 bus system are shown in Tables 1, 2 and 3 respectively.

Column (1) of Table 1 represents condition for implementation of C_{sg1}. Column (2) shows the searched value of C_{sg1}. Column (3) and (4) shows the Cost of generation and system transmission losses of IEEE 5 Bus Systems. Column (5) and (6) represents the number of function evaluation (Kount) and number of iterations required to optimize the function. Column (7) and (8) shows the output of generator (1) and (2) respectively. C_{sg1} is implemented after 2^{nd} to 6^{th} iteration. When C_{sg1} is implemented after 5^{th} iteration then function is not optimized. Minimum cost is obtained in minimum number of kounts when C_{sg1} is implemented after 4^{th} iteration. This row has been highlightd in Table 1.

Results of AELDPSO-I, searched by C_{sg2} is shown in Table 2. C_{sg2} is implemented after 2^{nd} to 7^{th} iteration. It is observed that for this algorithm the results are obtained only for the case when C_{sg2} is implemented after 4^{th} iteration. Therefore, this algorithm has not been implemented on IEEE 14 and 30 Bus systems.

Table 3 shows the results of AELDPSO-II. The minimum cost is obtained when C_{sg3} is implemented after third iteration. The best value of C_{sg3} is found to be 0.616. Keeping this value of C_{sg3} results in the development of ASACPSO. This algorithm is implemented on IEEE 5 bus system and the results are shown in last row of Table 4. This table also shows the results of BPSO and AELDPSO-II for IEEE 5 bus system.

It is observed that ASACPSO converges faster than BPSO and AELDPSO-II and results in saving of 34.44% of kounts as compared BPSO.

Figure 1 shows the comparison in terms of Kounts and cost of generation respectively as obtained by BPSO, AELDPSO-II and ASACPSO for IEEE 5- bus system.

It is clearly seen from Fig. 1 that both the PSO algorithms –AELDPSO-II and ASACPSO require less number of Kounts than BPSO. Figure 2 shows that cost of generation is also less for both the algorithms compared to BPSO.

Economic Load Dispatch has also been done on IEEE 14 bus and IEEE 30 bus system using BPSO, AELDPSO-II and ASACPSO. Results of IEEE 14 and IEEE 30 Bus systems are shown in Tables 5 and 6 respectively.

Figures 3 and 4 Show the comparison in terms of Kounts and cost of generation respectively for BPSO, AELDPSO-II and ASACPSO for IEEE 14 bus system.

Figures 5 and 6 show the comparison in terms of kounts and cost of generation respectively as obtained by BPSO, AELDPSO-II and ASACPSO for IEEE 30 bus system.

Table 7 shows the percentage saving in Kounts obtained by AELDPSO-II and ASACPSO for IEEE 5,14 and 30 bus systems.

It has been observed that saving in kounts obtained by AELDPSO-II for IEEE 5, 14, and 30 bus systems are 30.62, 35.83 and 41.98% respectively and 34.4, 26.66 and 41.98% for ASACPSO respectively.

The results of all the PSO algorithms have been compared with lambda iteration method are shown in Table 8 for IEEE 5, 14 and 30 Bus systems.

Table 4 Results of ELD for IEEE 5 bus system

S. no.	Algorithms	F_C ($/h)	P_L (MW)	P_1 (MW)	P_2 (MW)	Kount	% Saving in kount
1	BPSO	761.43	5.093	91.25	73.84	8360	
2	AELDPSO-II	761.03	5.06	99.59	65.38	5800	30.62
3	ASACPSO	761.37	5.09	91.65	73.44	5480	34.44

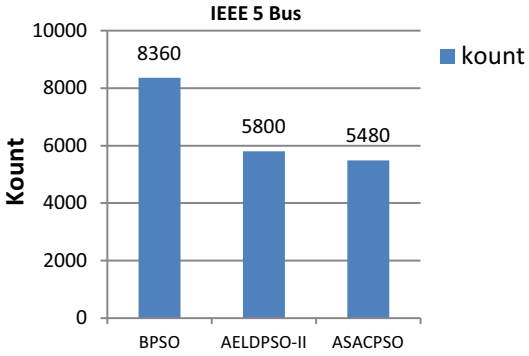

Fig. 1 Comparison in terms of kount

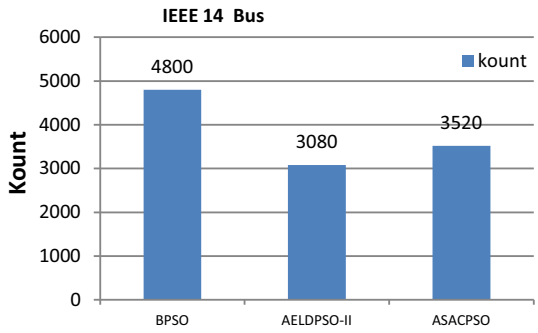

Fig. 3 Comparison in terms of kount

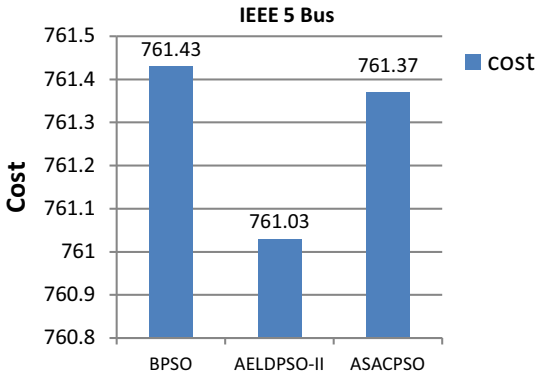

Fig. 2 Comparison in terms of (F_C) cost

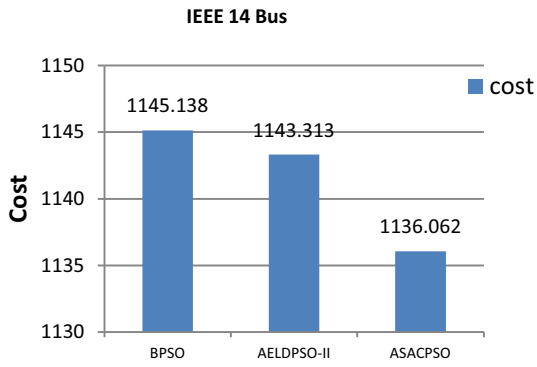

Fig. 4 Comparison in terms of (F_C) cost

Table 5 Results of ELD using BPSO, AELDPSO-II and ASACPSO for IEEE 14 bus system

Algorithms	F_C ($/h)	P_L (MW)	P_1 (MW)	P_2 (MW)	P_3 (MW)	Kount	% Saving
BPSO	1145.138	7.938	126.89	78.99	60.86	4800	
AELDPSO-II	1143.313	7.834	131.03	74.75	61.04	3080	35.83
ASACPSO	1136.062	8.6115	151.58	70.35	45.67	3520	26.66

Table 6 Results of ELD using BPSO, AELDPSO-II and ASACPSO for IEEE 30 bus system

Algorithms	F_C ($/h)	P_L (MW)	P_1 (MW)	P_2 (MW)	P_3 (MW)	Kount	% Saving in Kount
BPSO	1266.97	11.05	154.3	49.26	90.85	5240	
AELDPSO-II	1258.99	10.94	140.92	83.36	70.06	3040	41.98
ASACPSO	1258.66	10.93	140.91	83.36	70.06	3040	41.98

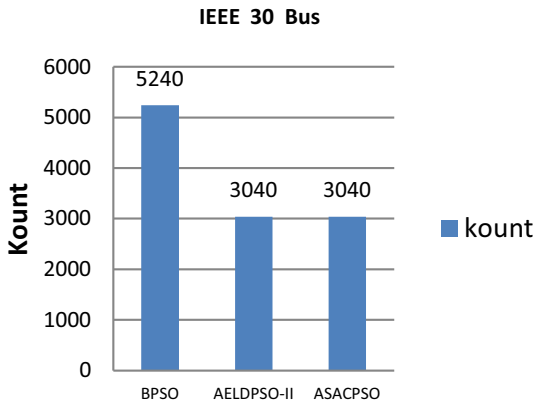

Fig. 5 Comparison in terms of kount

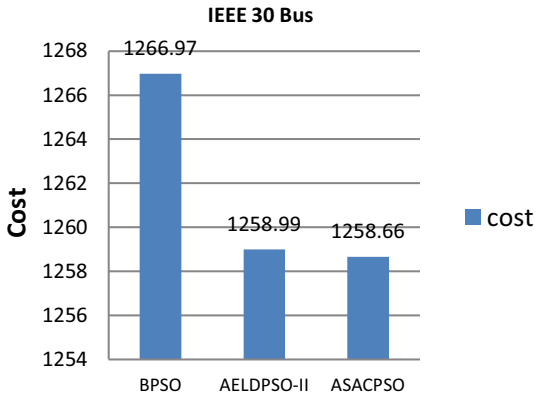

Fig. 6 Comparison in terms of (F_C) cost

Discussion

In this paper, three algorithms of PSO based on social acceleration constant–ALDPSO, AELDPSO-I, AELDPSO-II have been developed and implemented for Economic Load Dispatch of IEEE 5,14 and 30 bus systems. These algorithms have been compared with BPSO in terms of number of function evaluations (kount) taken to optimize the functions. The % saving in kount has been shown in Table 7 for IEEE 5,14 and 30 bus systems. It is observed that ASACPSO is the fastest and saving of 34.44, 26.66 and 41.98% in Kounts has been obtained for IEEE 5,14 and 30 bus systems respectively. It is further observed that AELDPSO-II gives the same % saving in kounts (41.98%) as ASACPSO for 30 bus system whereas higher % saving in Kounts for IEEE 14 bus system. For IEEE 14 bus system 35.83% saving in kount is obtained by AELDPSO-II algorithm. For IEEE 5 bus system, this algorithm gives only 30.62% saving in kount compared to BPSO.

The results of all PSO algorithms developed in this paper have also been compared with lambda iteration method which are shown in row 1 of Table 8. Row 2, 3, and 4 show the results of BPSO, AELDPSO-II and ASACPSO respectively for IEEE 5,14 and 30 bus system. It is observed that ASACPSO algorithm gives encouraging results for IEEE 14 bus system as both cost of generation and system transmission losses are less than that determined by lambda iteration method. In case of IEEE 5 bus

Table 7 Saving in Kounts for IEEE 5, 14 and 30 bus systems

Algorithms	5 BUS		14 BUS		30 BUS	
	Kounts	% Saving in Kount	Kounts	% Saving in kount	Kounts	% Saving in Kount
BPSO	8360		4800		5240	
AELDPSO-II	5800	30.62	3080	35.83	3040	41.98
ASACPSO	5480	34.44	3520	26.66	3040	41.98

The saving has been calculated by following formula

Saving in kount % = 100* (Kounts for BPSO–kounts for AELDPSO-II)/kounts for BPSO

Table 8 Comparison of results of ELD by lambda iteration method and PSO algorithms

S. no.	Method/Algorithms	IEEE 5 bus		IEEE 14 bus		IEEE 30 bus	
		Cost $/h	Loss (MW)	Cost $/h	Loss (MW)	Cost $/h	Loss (MW)
1	Lambda iteration	761.16	5.181	1139	9.185	1256.2	12.28
2	PSO	761.43	5.093	1145.138	7.938	1266.97	11.05
3	AELDPSO-II	761.03	5.06	1143.313	7.834	1258.99	10.94
4	ASACPSO	761.37	5.09	1136.062	8.6115	1258.66	10.93

system, AELDPSO-II algorithm gives encouraging results as both cost of generation and system transmission losses are found to be less than that determined by lambda iteration method. ASACPSO algorithm gives higher cost of generation but lower transmission losses in case of IEEE 5 and 30 bus systems. These results should not be compared only in terms of cost of generation achieved by lambda iteration and ASACPSO algorithm. It is observed that in case of IEEE 5 bus system, cost of generation increases by 0.21$/h (0.02%) whereas system transmission losses decreases by 0.091 MW(1.7%). Similarly, in case of IEEE 30 bus system, system transmission loss decreases by 1.35 MW (10.99%) whereas cost of generation increases by only 2.46$/h (0.19%). It is clearly observed that the proposed algorithm (ASACPSO) gives larger decrease in transmission losses with marginal increase in cost of generation.

These algorithms should be tested for dynamic ELD problem and for multiobjctive optimization considering various objectives of power systems. An effort should also be made to enhance the computational efficiency of these algorithms.

Conclusions

Following are the definite contributions of this paper:

1. PSO Algorithms-AELDPSO, AELDPSO-I, AELDPSO-II and ASACPSO have been developed by searching the best Adaptive Social Acceleration Constant Csg.
2. The above algorithms were implemented for Economic load dispatch of IEEE 5 bus system. These were compared in terms of number of function evaluations (Kounts) required to optimize the functions. AELDPSO-II and ASACPSO algorithms were found to converge faster than BPSO, AELDPSO and AELDPSO-I.
3. BPSO, AELDPSO-II and ASACPSO were implemented on IEEE 5,14 and 30 bus systems and were compared in terms of number of kounts. ASACPSO was found to converge faster than BPSO and AELDPSO-II.
4. With AELDPSO-II algorithm saving in kount achieved for IEEE 5,14and 30 bus system is 30.62, 35.83 and 41.98% respectively.
5. ASACPSO gave higher saving in Kount (34.44%) for IEEE 5 bus system and same saving as AELDPSO-II (41.98%) for IEEE 30 bus system. However, with this algorithm lower saving in Kount was achieved for IEEE 14 bus system.
6. The results of ASACPSO have also been compared with lambda – iteration method. It is observed that cost of generation increases slightly for IEEE 5 bus system (0.02%) and IEEE 30 bus system (0.19%).But there is 1.7% decrease in system transmission losses for IEEE 5 bus system and 10.99% decrease in system transmission losses for IEEE 30 bus system.
7. The proposed algorithm may be tested for Economic Load dispatch of higher systems considering different constraints–prohibited operating zones, ramp rates and multi-fuel options. The proposed PSO algorithms should also be tested for other power system problems–dynamic economic dispatch, reactive power dispatch and multiobjective optimization considering various important objectives of power systems.

References

1. C.L. Wadhwa, Economic Load Dispatch, in Electrical power system, 6th ed New age international, pp. 628, 2010
2. N. Nomana, I. Hitoshi, Differential evolution for economic load dispatch problems. Electr. Power Syst. Res. **78**(8), 1322–1331 (2008)
3. M. Provas, P.K. Roy, T. Pal, Grey Wolf optimization applied to economic load dispatch problems. Int. J. Electr. Power Energy Syst. **83**, 325–334 (2016)
4. N. Saxena, G. Souvik, Solar and wind power estimation and economic load dispatch using firefly algorithm, in *Procedia Computer Science, 4th International Conference on Eco-friendly Computing and Communication Systems (ICECCS)*, Vol. 70, 2015, pp. 688–700
5. N.K. Jain, U. Nangia, J Jain, GA based multiobjective economic load dispatch by maximization of minimum relative attainments, in *IEEE 5th India International Conference 2012, IICPE* 2012, pp. 1–6
6. N.K. Jain, U. Nangia, A. Jain, PSO for multiobjective economic load dispatch (MELD) for minimizing generation cost and transmission losses. J. Inst. Eng. (India): Series B **97**(2), 185–191 (2016)
7. J. Kennedy, R. Eberhart, Particle swarm optimization, in *Proceedings IEEE International Conference on Neural Networks (Perth, Australia), 1995, IEEE Service Center* (Piscataway, NJ, 1995), pp. 1942–1948
8. J.S. Dhillon, S.C. Parti, Stochastic Economic Emission Load Dispatch. Electr. Power Syst. Res. **26**(3), 179–186 (1993)
9. G. Baskar, M.R. Mohan, Security constrained economic load dispatch using improved particle swarm optimization suitable for utility system. Electr. Power Energy Syst. **30**, 609–613 (2008)
10. Q. Niu, X. Wang, Z. Zhoua, An efficient cultural particle swarm optimization for economic load dispatch with valve-point effect. Elsevier, Procedia Eng. **23**, 828–834 (2011)
11. C. Rani, A. Yazdani, Emission constrained economic dispatch using various PSO algorithm. Int. J. Power Syst. Oper. Energy Manag. (IJPSOEM) **1**(1), 57–63 (2011)
12. Y. Labbi, D.B. Attous, A hybrid particle swarm optimization and pattern search method to solve the economic load dispatch problem. Int. J. Syst. Assur Manag. **5**(3), 435–443 (2014)

13. H.M. Dubey, M. Pandit, B.K. Panigrahi, M. Udgir, A fuzzified improved hybrid pso-gsa for environmental/economic power dispatch. Int. J. Eng. Sci. Technol. **6**(4), 11–23 (2014)
14. G. Abbas, G.U. Jason, U. Farooq, M.U. Asad, M.E.L. Hawary, Solution of economic problem through particle swarm optimization: a detailed survey–Part-I, in *IEEE Access*, 5, 2017
15. V.K. Jadoun, N. Gupta, K.R. Niazi, A. Swarnkar, Nonconvex economic dispatch using particle swarm optimization with time varying operators. Adv. Electr. Eng. 2014, Article ID 301615, p. 13
16. M. Singh, Deepika, M. kumar, Economic load dispatch calculator, 978-1-4799-6042-2/14/$31.00 © 2014 IEEE
17. P.S. Bhullar, J.K. Dhami, Particle swarm optimization based economic load dispatch with valve point loading. Int. J. Eng. Res. Technol. (IJERT), ISSN: 2278-0181,IJERTV4IS050998
18. N.K. Jain, U. Nangia, J. Jain, An improved PSO based on initial selection of particles (ISBPSO) for economic load dispatch, in *First International Conference on Power Electronics, Intelligent Control and Energy Systems(ICPEICES 2016)*, 4–6 July, 2016
19. Z. Bo, Y. Cao, Multiple objective particle swarm optimization technique for economic load dispatch. J. Zhejiang Univ. Sci. ISSN 1009-3095, August 7, 2004
20. L.V. Narasimha Rao, PSO technique for solving the economic dispatch problem considering the generator constraints. Int. J. Adv. Res. Electr. Electron. Inst. Eng. (An ISO 3297: 2007 Certified Organization) **3**(7), July 2014

International Journal on Interactive Design and Manufacturing (IJIDeM)
https://doi.org/10.1007/s12008-018-0474-8

ORIGINAL PAPER

Effect of hybrid wire EDM conditions on generation of residual stresses in machining of HCHCr D2 tool steel under ultrasonic vibration

Sanjay Kumar[1] · Sandeep Grover[1] · R. S. Walia[2]

Received: 15 January 2018 / Accepted: 14 March 2018
© Springer-Verlag France SAS, part of Springer Nature 2018

Abstract
This experimental examination exhibit a novel Hybrid Wire electrical discharge machining (H-WEDM) process of ultrasonic vibration combined with traditional Wire-EDM. The metal cutting for form tool and extrusion die with WEDM is liked to give better surface morphology. The effect of residual stresses has been dissected for H-WEDMed machined surface alongside the surface roughness and erosion rate to enhance surface integrity and longer service life of High Carbon High Chromium D2 tool steel. The process parameters chose for this investigation are type of vibration continuous/discontinues, amplitude of vibration, workpiece dimension, duty cycle, peek current and wire feed rate with objective to optimize the residual stresses and erosion rate. Portable X-ray Residual Stress Analyzer, a non-destructive X-ray analyzer is used to measure the residual stress efficiently by detecting the full Debye ring data from a single incident X-ray angle and Non goniometer stage influence on the measurements. An endeavor was made to compare the residual stresses for continuous/discontinues vibration and without vibration. The impacts of amplitude of vibration, peak current, duty cycle and wire feed rate variations on erosion rate was study using Taguchi method. From experimental study, it was observed that discontinuous vibration enhances the erosion rate and diminishes the resultant stresses. High Peak current and duty cycle altogether deteriorate the surface texture, which creates high tensile residual stresses because of debris and micro cracks. The optimum value of residual stresses 86.53 MPa and material erosion rate 6.45 mm/min was achieved using H-WEDM.

Keywords Ultrasonic vibration · Wire EDM · Residual stress · Debey ring · Duty cycle · Peak current · X-ray

1 Introduction and literature review

Wire electrical discharge machining (WEDM) is well recognized technique utilized as a part of metal current industry for high-exactness machining of a wide range of conductive materials. The WEDM process is supposed to give better surface morphology, particularly for materials used in aircraft, automobile, cutting tools, die and mold making modern industries. The cutting costs and the residual stresses associated with these materials during normal WEDM process are the major impedances that the industrial peoples facing today. In metal forming process, the friction forces between the tool, die and the workpiece somewhat destroys the working and cutting surfaces of tools, thereby constraining their perseverance and service life. These frictional forces were related to surface nature of a forming tool and expulsion die material. In typical shaping practice, frictional forces more often than not included alluding to working hardness, and additionally particular surface morphology of forming tool/die material [6]. The surface morphology of forming tools surface was influenced by the residual stresses created because of pervious material or machining processing [20]. These residual stresses conveyed if areas of a material are non-homogeneous plastically deformed in such an enduring metal evacuating process, to the point that strain opposite qualities happen. Forming tools surfaces that were produced with conventional Die-sink EDM/Wire-EDM persevere through sharp temperature gradients and metallurgical changes. The high-

✉ Sanjay Kumar
sanjaykpec@yahoo.co.in

Sandeep Grover
groversandeep@hotmail.com

R. S. Walia
waliaravinder@yahoo.com

[1] Department of Mechanical Engineering, YMCA University of Science and Technology, Faridabad, Haryana 121006, India

[2] Department of Mechanical, Production and Industrial and Automation, Delhi Technological University, Delhi 110042, India

Published online: 31 March 2018

est layer of surface with potential temperature variety and metallurgical change on work piece surface was determined as heat influenced layer. This layer fundamentally comprises of plastically deformed material that re-sets back. Amid re-solidification residual stresses alongside micro-hole, micro cracks and small droplet developed in this layer [4]. A normal EDM process can achieve temperature 40,000 K at the work surface of the work piece amid machining. This caused non homogeneous heat streams and metallurgical changes and deteriorated the surface integrity [16]. The residual stresses so created go about as a pre-stress state and changes the yield strength of machined surface. The intensity of these stresses was found much more than the yield point of the material [13]. The fundamental detriment of the traditional EDM process was the low-metal evacuation rate and the antagonistic impacts of the high temperature gradient on surface integrity in the topmost surface layers [30]. The development of a generalized experimental and interactive numerical model for these residual stresses was the major concern for the majority of the researchers [11]. These residual stresses on the machined surface might be good or troublesome relying upon the specific user of machined segments. Be that as it might, it was required to have low tensile residual stresses parts surface for benefit life of the EDMed machined surface [20]. Antar et al. [1] discovered the residual stress magnitude of intensity 600 MPa in tradition WEDM amid machining of Udimet 720 and there unfavorable impact on Fatigue response. Although, some interactive approaches has been attempted by investigators in the previous couple of decades to limit the determinant impact of these residual stresses in normal WEDMed process. Klinka et al. [14] evaluated surface integrity for powder metallurgical tool steel with WEDM. They observed that the high tensile residual stresses were delivered with close profile examples of WEDMed surface and sizes for both in oil and water dielectrics. The patterns of these residual stresses were relatively indistinguishable in both the directions parallel and perpendicular to the wire feed. A finite element model was proposed by Liu and Guo [17] to anticipate the stochastic idea of residual stresses in EDMed process by consolidating gigantic arbitrary discharges. The intensity of these stresses was high in sub-surface rather than top surface and discharge energy directly influences these. An FEA model was proposed by Singh et al. [26] to demonstrate the pumping action of ultrasonic vibrating workpiece in die-sink EDM. Sidhom et al. [25] inferred that the quick cooling and phase changes in the top white layer initiate cracking of AISI316L SS in chloride dielectric medium because of residual stresses, the EDMed machining surface had to anneal to enhance corrosion resistance. The vast majority of fatigue failures in the wire EDMed surface were caused by crack initiation site probably due local stresses [28]. The tensile residual stresses had a negative effect over several functional aspects of machined components such as fatigue life [6], corrosion and wear resistance [3], as these stresses advanced crack development and engendering by fatigue or corrosion cracking [25].

Ultrasonic vibration in wire EDM was a hybrid processes developed to address unwavering quality and sturdiness. The usage of Ultrasonic vibration (UV) in EDM has the potential to enhance the surface morphology and thereby service life of the machined components with high accuracy and repeatability [27]. Guo et al. [8] implemented ultrasonic vibration in wire EDM, and found that a cozy relationship exists between surface integrity and the residual stresses. Their results indicated that the surface roughness straightforwardly relative to the discharge energy. UV in wire EDM diminished the average value of discharge energy by initiating multi-point discharge and thereby decreased the extent of tensile residual stresses of machined surfaces [7]. Kremer et al. [15]. actualized UV in Die-sink EDM and observed same estimation of residual stresses with or without vibration. Shabgard and Alenabi [24] explained phenomena of ultrasonic tool vibration EDM enhanced the MRR in rough mode of machining. They concluded that the ultrasonic frequency of tool was not sufficient for evacuation of molten metal that result in high length and thickness of breaks in recast layer in rough mode. The resultant was extensive residual stresses in rough machining. But in roughing mode the amount of the molten material and the residual stress levels were high and the workpiece yields and cracks. The pressure gradient in discharge gap enhanced efficient discharge and hence reduced the residual stresses significantly [29]. It was observed by the authors that only a few authors *endeavor* to develop a structured method useful for engineers to quantify these residual tensile residual stresses in UV assisted WEDM. Khosrozadeh and Shabgard [13] experimentally investigated the effect of ultrasonic vibration of tool on surface integrity and residual stresses for die-sink EDM. They utilized nano-indentation method to measure the magnitude of residual development of ultrasonic vibration assisted EDM. The comparative results of their study confirm that residual stresses were partial lower than the conventional EDM process. The evaluation of residual stresses using interactive designing and manufacturing approach for the continuous/ discontinuous vibration assisted WEDM process was the novelty of this study. Authors have proposed a structured method for evaluating the residual stresses that would be useful for WEDM engineers. Interactive designing hear did not simple mean the use of software to investigate the various attribute under consideration. In this approach basic concentration was on developing the process/product rather than focusing the technicality of attributes involved in that [5]. This research work deal with application and comparison of continuous/discontinuous UV in WEDM. However the previous approaches focused mainly on the effects of single or a small range of vibration amplitude with continuous vibrations. This study summarizes the

Table 1 Constant parameters for experiment

Parameters	Constant values
Cutting tool wire	Brass wire of diameter 0.25 mm
Servo feed	1150 unit
Spark voltage	20 volts
Conductivity of dielectric	2 units (110 volt DC)
Work material	High carbon/high chromium D2 tool steel
Wire tension	8 Unit

current state-of-the-art in modeling of residual stresses in UV assisted WEDM process and facilitate the WEDM user to achieve better surface morphology.

2 Experimentation

2.1 Experimentation set-up design details

The experiments were performed on CNC wire-cut EDM (ELEKTRA SPRINTCUT 734) of Electronica Machine Tools Ltd. Aside from the chose parameters in Table 5; alternate parameters were kept consistent amid entire tests and are specified in Table 1. High performance ultrasonic transducer with 21.5 kHz settled frequency and 120 W Ultrasonic PCB was utilized by the authors to develop an ultrasonic mechanical vibration generator. A suitable frame and housing were designed, which were important to oblige the framework and appropriate working of the setup to stay away from the resonance. The resonance with the ultrasonic vibration device was the basic issue; it turned out to be more urgent when bestowed to workpiece in the traditional EDM system [16]. These resonances developed clamors and oppose the fruitful execution of ultrasonic vibration in ultrasonic vibration assisted EDM system. A special consideration has been given by the authors for designing of horn. The continuous vibrations were achieved in the default case, as and when discontinuous vibration was required the selected through a relay. The frequency of discontinuity was achieved with customizable by an electronic circuit after trials. However the frequency of the ultrasonic transducer must be kept up at 21.5 KHz, remained same in both of the modes.

The transfer of work piece ultrasonic vibration was executed through a steel plate. A schematic US-WEDM line diagram for experimental set up used is shown in Fig. 1. The programming for machining was done with the reference to the world coordinate system of CNC Wire-EDM machine tool. Also, dielectric fluid was flushed to the machining gap through nozzle jet from top and bottom. Each set of experiments were performed at room temperature in a narrow temperature range ($32 \pm 2\,^{\circ}\mathrm{C}$). Figure 2 shows the developed set up design, one end of steel strip was fixed to machine table and the other end was provided with a holding fixture for the workpiece. The steel strip was treated as a cantilever beam for experiment. The UV action was transferred to the strip through ultrasonic horn at a distance 31.11 mm from the fixed end. The variable amplitude of vibration was obtained through varying the position of holding the work piece as shown in Fig. 3.

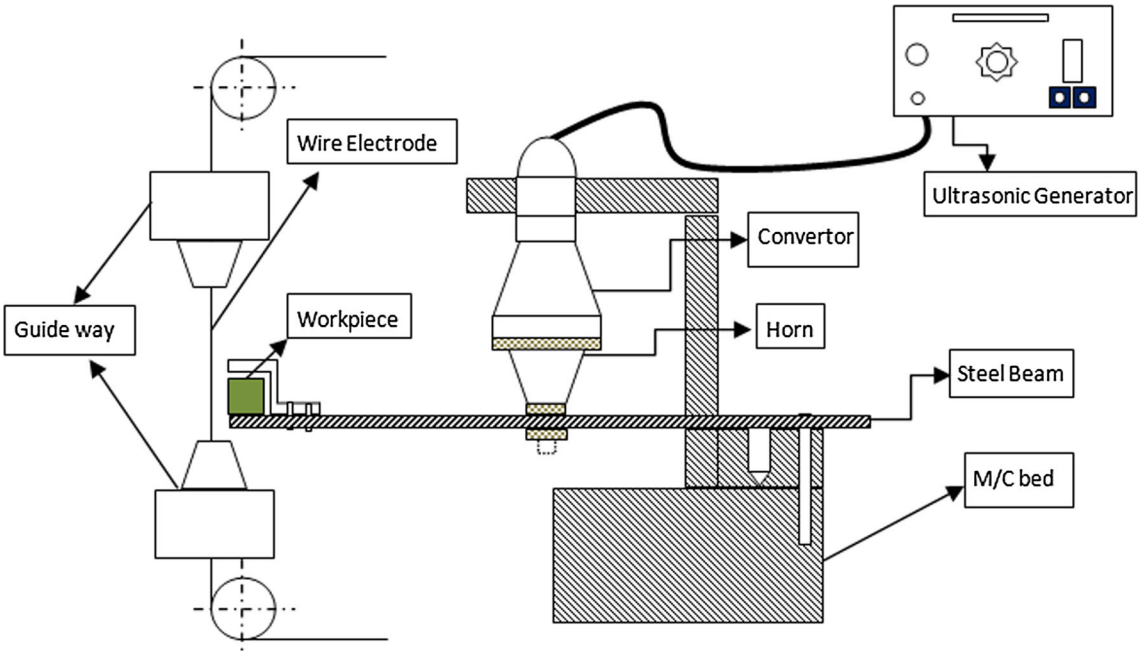

Fig. 1 Schematic diagram of experimental setup for ultrasonic vibration of work piece in wire-EDM

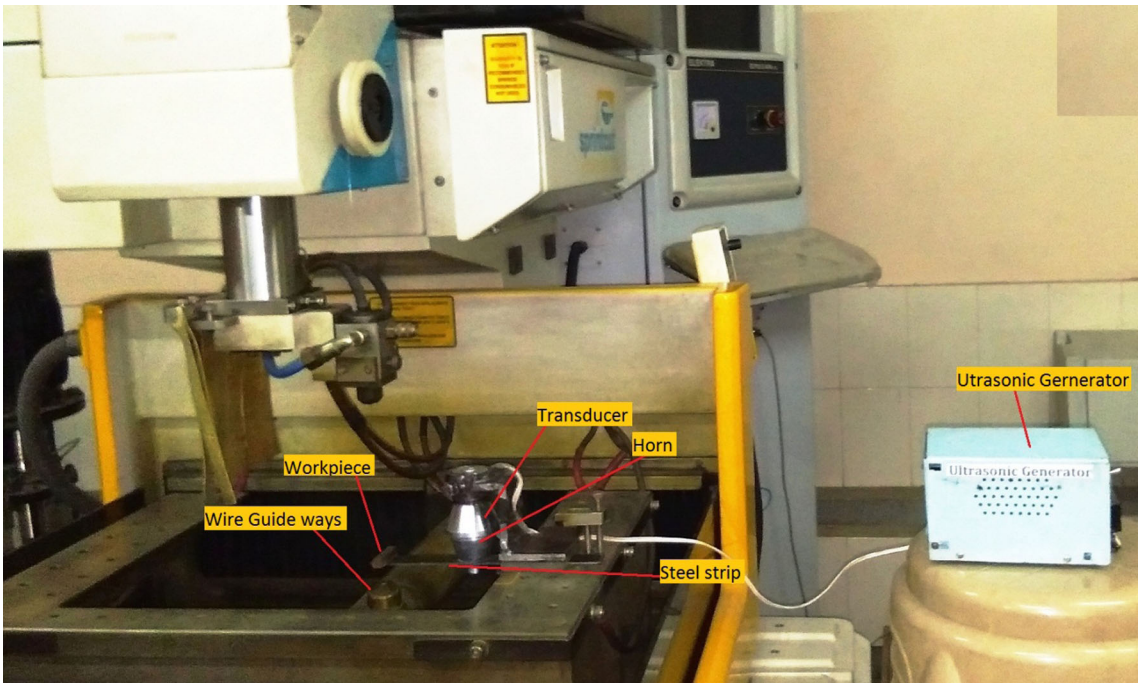

Fig. 2 The developed set up design for ultrasonic vibration assisted wire-EDM

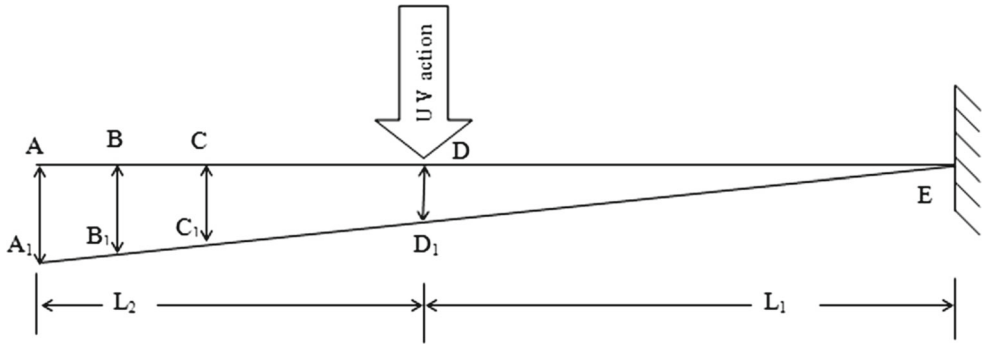

Fig. 3 Cutting edge ultrasonic vibration as a cantilever beam

The steel strip was designed for ultrasonic vibration at a distance of 70 mm point 'D_1' from the fixed end. The amplitude of vibration varied corresponding at the points A, B and C at the actual cutting tip. The output variable amplitude of Ultrasonic vibration of the work piece was obtained by changing the position of holding positions of workpiece. Three different level of amplitude of vibration obtained for this study were 10, 14 and 18 µm as shown in Fig. 3. Using triangular rule the amplitude of vibration can be controlled at EA distance from the fixed end.

From Fig. 3, similarity of the triangle $\Delta EDD_1 \cong \Delta EAA_1$

$$\frac{AA_1}{DD_1} = \frac{EA}{ED} = \frac{L_1 + L_2}{L_1}$$

$$AA_1 = \frac{EA}{ED} DD_1$$

DD_1 = Amplitude of vibration of transducer with Horn assembly.

ED = 70 mm (fixed point for transfer of ultrasonic vibration to the steel strip).

EA = Distance of cutting actual cutting tip from the end point.

AA_1 = Amplitude of vibration obtained.

In this work the portable X-ray Residual Stress Analyzer µ-X360,a non-destructive X-ray analyzer of Pulstec Industrial Corporation Limited was used for measuring the residual stress in Wire-EDMed machined surfaces. This analyzer could measure the stress efficiently by detecting the full Debye ring data from a single incident X-ray angle and Non goniometer stage influence on the measurement result. Measurement conditions for residual stresses in present experiment were demonstrated in the Table 2.

Table 2 Measurement condition for X-ray residual measurement equipment

Measurement	Units
Measurement area	All (3.000–30.000)
Pitch	50 [um]
X-ray irradiation time (setup)	30 [s]
X-ray irradiation time (meas.)	30 [s]
X-ray irradiation time (max)	120 [s]
X-ray tube current	1.00 [mA]
X-ray tube voltage	30.00 [kV]
Sample distance (monitor)	39.000 [mm]
Sample distance (analysis)	39.263 [mm]
Offset of alpha angle	0 [deg]
X-ray wavelength (K-Alpha)	2.29093 [A]
X-ray wavelength (K-Beta)	2.08480 [A]
X-ray tube total use time	106.83 [h] (384601
Detection sensitivity	20.3 [%] (174204)
Level of ambient light	0.2 [%]
Correction coefficient	0.00xx + 1.00x + 0.00
Valid range of alpha angle	18.00 <−−−> 90.
Peak analysis method	Fitting Lorentz

The inter-planer spacing (d) of certain crystal is utilizes as the gauge length for measuring strain. When particular wavelength X-ray incident on crystalline grain that satisfies Bragg's law gets diffracted and form as a cone around the axis of incident ray. This is because of the varying orientation of crystalline grain. According to the Bragg's law, a numerical relationship between incident X-ray and the inter-planer spacing of a crystal could be expressed as Eq. (1);

$$n\lambda = 2dsin\theta \tag{1}$$

where 'n' = An integer represents "order" of reflection,

λ = The X-rays wavelength,
d = The inter-planar spacing of the crystal,
θ = The incidence angle/diffraction angle

When a crystalline structure is under the stress, X-ray incident angle ψ_i is smaller and therefore the magnitude of Strain (ε_i) developed can be expressed as;

$$\text{Strain } (\varepsilon_i) = \frac{d_f - d_i}{d_i} \tag{2}$$

where d_i = Initial inter = planar spacing of the crystal, and d_f = Final inter-planar spacing of the crystal after machining. The magnitude of strain developed is calculated using formula in Eqs. (3 and 4) by acquiring the full Debye–Sherrer ring with a position detector sensor [2]. The strain increases as a result of increase in (d_f) and there by decrease (θ) in Eq. (2). The residual stresses are calculated from the change of diffraction normal angle (ψ) as shown in Fig. 4.

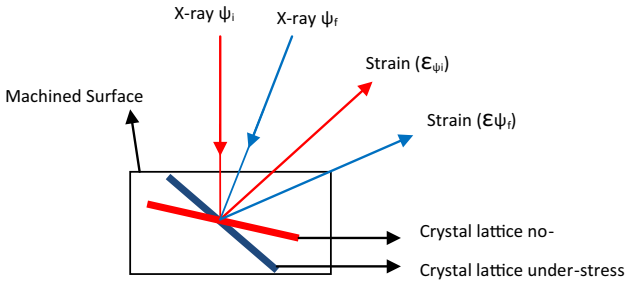

Fig. 4 Change in strain with 'crystal lattices orientation calculated for X-ray diffraction normal angle ψ

$$\varepsilon_{\alpha 1} = \frac{1}{2}\{(\varepsilon_{\alpha} - \varepsilon_{\pi+\alpha}) + (\varepsilon_{-\alpha} - \varepsilon_{\pi-\alpha})\} \tag{3}$$

$$\varepsilon_{\alpha 2} = \frac{1}{2}\{(\varepsilon_{\alpha} - \varepsilon_{\pi+\alpha}) + (\varepsilon_{-\alpha} - \varepsilon_{\pi-\alpha})\} \tag{4}$$

$$\varepsilon_{\alpha 1} = \frac{1+\nu}{E}\sigma_x . \sin 2\eta . \sin 2\psi_i . \cos\alpha \tag{5}$$

$$\varepsilon_{\alpha 2} = \frac{1+\nu}{E}\tau_{xy} . \sin 2\eta . \sin \psi_i . \sin\alpha \tag{6}$$

where; = Strain measured in the direction of $\boldsymbol{\alpha}$,

$\boldsymbol{\varepsilon_{\pi+\alpha}}$ = Strain measured in the direction of $\boldsymbol{\pi + \alpha}$,
$\boldsymbol{\varepsilon_{\alpha 1}}$ = Strain measured in the vertical direction,
$\boldsymbol{\varepsilon_{\alpha 2}}$ = Strain measured in the horizontal direction,
$\boldsymbol{\sigma}_x$ = Residual axial stress, τ_{xy} = Residual shear stress,
V = Poisson's ratio,
E = Young's Modulus of Elasticity,
Ψ_i = Diffraction normal angle,
$\boldsymbol{\alpha}$ = Azimuth angle of Debye–Sherrer ring,
$\boldsymbol{\eta}$ = Angle between Debye–Sherrer ring axis and the sample diffraction detector of X-ray,

This diffracted cone shape around the axis is the Debye–Scherrer ring. The full Debye–Scherrer ring is procured by a single short duration X-Ray presentation. The residual stresses are determined by precisely estimating the position of the Debye–Scherrer rings; their positions are an immediate measure of strains $\varepsilon_{\alpha 1}$ and $\varepsilon_{\alpha 2}$. The residual stresses can be calculated with the formula expressed in Eqs. (5 and 6) [18].

In this study erosion rate was measured in mm/min directly on machine control unit panel. Diameter of wire remained constant and the kerf width variation was assumed negligible compare to cutting speed and material thickness [19].

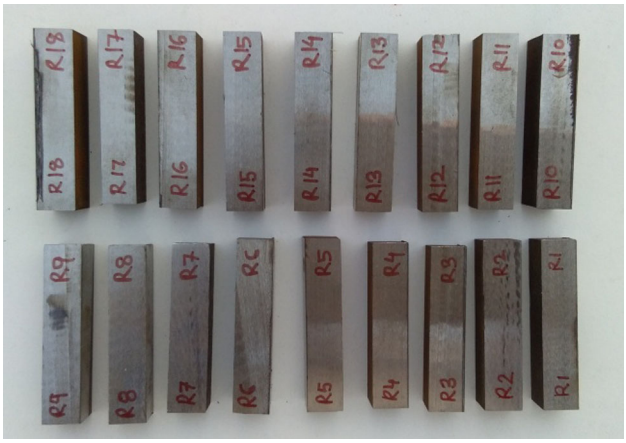

Fig. 5 Workpiece material sample cut for experimentation

Table 3 Chemical composition of workpiece material (HCHCr D2 tool steel)

% Weight composition of components									
C	Si	Mn	Mo	P	S	V	W	Cr	Ni
1.55	0.30	0.35	0.75	0.03	0.03	0.90	–	10.41	0.30

Table 4 Properties at room temperature for HCHCr D2 tool steel

Young's modulus, E (GPa)	190–210
Ultimate tensile strength (N/mm^2)	2010
Yield strength (N/mm^2)	2150
Poisson's ratio	0.27–0.30
Rockwell hardness	62
Density (Kg/m^3)	7700
Thermal expansion (10^6/°C)	12

2.2 Workpiece material

The workpiece material was chosen high carbon-high chromium Cold Work Tool Steel, as utilized widely in dies and mold metal forming industry. The 18 experiments with three repetitions shown in Fig. 5 were cut to cuboids shape with 4 × 10 × 20, 7 × 10 × 20, 10 × 10 × 20 mm^3 eighteen each on Wire-EDM, and after that confronted and ground with diamond grinding wheel.

Chemical composition of workpiece material and principle mechanical properties has been recorded in Tables 3 and 4, separately.

Among the more vital utilizations of tool steel were the deep drawing and forming dies on, cold drawing punches, hobbing, blanking, lamination and stamping dies, shear blades, burnishing rolls, master tools and gauges, slitting cutters, thread rolling and wire dies, extrusion dies and so on. These major applications of the workpiece material helped the authors to select the same for this research work.

2.3 Taguchi methodology and machining parameters selection

An off-line quality amelioration strategy for a product/process was proposed by Taguchi. According to him, the quality should be built into the process rather than inspecting it into the product produced form that process [20]. This could be accomplished through interactive design and manufacturing approach through process parameters and the tolerance design for a particular process under consideration. But a full factorial design of experimentation for US-WEDM process critical parameters was difficult to implement because of the unavailability of generalized acceptable guidelines. Therefore a fractional-factorial design of experiment was used as recommended by the Taguchi's parameter design approach. In this experimental investigation, six process parameters viz. Type of vibration, amplitude of vibration, thickness of workpiece, wire feed rate, peak current, duty factor were selected. The pilot experiments were conducted to investigate the range of selected parameters. The effect of ultrasonic vibration (Type and Amplitude of vibration), workpiece (thickness), electrical (peak current and duty Cycle) and non electrical (wire feed rate) parameters was worthy of notice. The process parameters along the symbols, level and coded values used in this study are shown in Table 5.

The experiments were conducted according to the test conditions specified by the Taylor's L_{18} orthogonal array. Taguchi recommends the use of S/N ratio to measure the quality characteristics deviating from the desired values. The S/N ratio is concurrent interactive quality measure associated with the loss function, which can be maximized and minimized by controlling the response attributes. It was taken as the S/N ratio for the "higher-the-better" and "lower-the-better" of response could be computed as Eqs. (7) and (8): [21,22]. The US-WEDM process performance characteristic was taken "higher the better" for Erosion rate and "lower-the better" for residual stresses.

$$(S/N)_{HB} = -10\log\left[\frac{1}{R}\sum_{j=1}^{R}(Y_j^{-2})\right] \tag{7}$$

$$(S/N)_{LB} = -10\log\left[\frac{1}{R}\sum_{j=1}^{R}(Y_j^{2})\right] \tag{8}$$

where $Y_j (j = 1, 2, 3\ldots n)$ is the response value under the trail condition repeated R times.

The analysis of Variance (ANOVA) was performed to distinguish the procedure parameters that were factually huge. With the S/N and ANOVA examinations, the ideal mix of the process parameters was anticipated. The S/N proportion esteems were figured utilizing Eqs. (7 and 8), where 'Y' was the individual measured response value and 'n'

Table 5 The controlled parameters and their levels of experimental design

Factors	Parameters	Levels		
		Level 1	Level 2	Level 3
A	Type of vibration	Continuous	Discontinues	–
B	Amplitude of work piece vibration (μm)	10	14	18
C	Peak current (Ampere)	100	140	180
D	Duty cycle (%)	66%	72%	78%
E	Workpiece thickness (mm)	10	7	4
F	Wire feed rate (mm/min)	5	8	11

Table 6 Experimental plan and results of performance characteristics

Column no.	Type of vibration	Amplitude of vibration	Peak current	Duty cycle	Workpiece thickness	Wire feed rate	Response for erosion rate (mm/min)				Response for residual stress (MPa)			
Ex no.	A	B	C	D	E	F	R1	R2	R3	S/N ratio	R1	R2	R3	S/N ratio
1	C	10	100	66	10	5	0.43	0.45	0.46	− 7.01	198	185	198	− 45.75
2	C	10	140	72	7	8	2.9	2.82	2.98	9.24	252	260	266	− 48.28
3	C	10	180	78	4	11	5.22	5.32	5.26	14.43	292	295	287	− 49.29
4	C	14	100	66	7	8	2.39	2.41	2.45	7.66	134	136	142	− 42.76
5	C	14	140	72	4	11	4.63	4.65	4.54	13.27	225	256	265	− 47.93
6	C	14	180	78	10	5	3.52	3.51	3.47	10.88	302	310	305	− 49.71
7	C	18	100	72	10	11	1.45	1.47	1.43	3.23	235	234	220	− 47.23
8	C	18	140	78	7	5	2.76	2.78	2.66	8.73	226	227	216	− 46.97
9	C	18	180	66	4	8	4.16	4.18	4.08	12.34	284	298	286	− 49.23
10	D	10	100	78	4	8	3.51	3.58	3.45	10.91	291	287	268	− 49.01
11	D	10	140	66	10	11	1.92	1.88	1.92	5.60	193	218	265	− 47.13
12	D	10	180	72	7	5	3.75	3.83	3.77	11.56	268	243	243	− 48.01
13	D	14	100	72	4	5	3.63	3.75	3.65	11.31	175	183	234	− 45.98
14	D	14	140	78	10	8	4.45	4.57	4.73	13.22	221	226	231	− 47.08
15	D	14	180	66	7	11	3.53	3.75	3.79	11.33	126	134	136	− 42.42
16	D	18	100	78	7	11	2.76	2.88	2.78	8.96	170	167	174	− 44.63
17	D	18	140	66	4	5	3.37	3.49	3.36	10.64	231	154	167	− 45.44
18	D	18	180	72	10	8	4.23	4.35	4.24	12.61	267	265	284	− 48.70

Table 7 Analysis of variance of raw data for erosion rate

Source	SS	DOF	V	P	F-ratio	Rank
Type of vibration	2.91	1.00	2.91	3.95	6.93	6
Amplitude of vibration	6.02	2.00	3.01	8.16	7.16	3
Peak current	26.89	2.00	13.45	36.49	6.93	1
Duty cycle	10.96	2.00	5.48	14.88	13.04	2
Workpiece thickness	4.67	2.00	2.34	6.34	5.56	4
Wire feed rate	4.58	2.00	2.29	6.21	5.45	5
ERROR	17.65	42.00	0.42	23.96		
T	73.69	53.00		100		

Significant at 95% confidence level
SS Sum of Squares, *DOF* Degree of Freedom, *V* Variance
F-Fisher test factor tabulated for Type of vibration: 4.07, F-Fisher test factor tabulated for other parameters: 3.22

Table 8 Analysis of variance of S/N ratio for erosion rate

Source	SS	DOF	V	P	F-ratio	Rank
Type of vibration	30.35	1.00	30.35	7.27	8.75	6
Amplitude of vibration	43.82	2.00	21.91	10.50	6.31	4
Peak current	125.75	2.00	62.88	30.13	18.12	1
Duty cycle	64.81	2.00	32.41	15.53	9.34	3
Workpiece thickness	98.77	2.00	49.38	23.67	14.23	2
Wire feed rate	32.99	2.00	16.50	7.91	4.75	5
ERROR	20.82	6.00	3.47	4.99		
Total	417.31	17.00	*	100		

Significant at 95% confidence level
SS Sum of Squares, *DOF* Degree of Freedom, *V* Variance
F-Fisher test factor tabulated for Type of vibration: 5.99
F-Fisher test factor tabulated for other parameters: 5.14

Table 9 Analysis of variance of raw data for residual stresses

Source	SS	DOF	V	P	F-ratio	Rank
Type of vibration	9414.24	1.00	9414.24	6.40	9.27	5
Amplitude of vibration	16398.81	2.00	8199.41	11.15	8.07	3
Peak current	27476.59	2.00	13738.30	18.68	13.52	2
Duty cycle	33825.93	2.00	16912.96	23.00	16.65	1
Workpiece thickness	9933.87	2.00	4966.94	6.75	4.89	4
Wire feed rate	7349.15	2.00	3674.57	5.00	3.62	6
ERROR	42674.17	42.00	1016.05	29.01		
T	147072.80	53.00		100		

Significant at 95% confidence level
SS Sum of Squares, *DOF* Degree of Freedom, *V* Variance
F-Fisher test factor tabulated for Type of vibration: 4.07
F-Fisher test factor tabulated for other parameters: 3.22

Table 10 Analysis of variance of S/N ratio for residual stresses

Source	SS	DOF	V	P	F-ratio	Rank
Type of vibration	4.24	1.00	4.24	5.45	4.03	5
Amplitude of vibration	11.23	2.00	5.62	14.45	5.34	4
Peak current	12.25	2.00	6.13	15.76243	5.82	2
Duty cycle	20.83	2.00	10.42	26.80	9.90	1
Workpiece thickness	19.41	2.00	9.71	24.98	9.23	3
Wire feed rate	3.45	2.00	1.73	4.44	1.64	6
ERROR	6.31	6.00	1.05	8.12		
Total	77.73	17.00	*	100		

Significant at 95% confidence level
SS Sum of Squares, *DOF* Degree of Freedom, *V* Variance
F-Fisher test factor tabulated for Type of vibration: 5.99
F-Fisher test factor tabulated for other parameters: 5.14

was the number of measurements. Independent of the kind of characteristic, the biggest estimation of S/N proportion demonstrated the ideal state of the parameter for the given reaction.

2.4 ANOVA and S/N ratio experimental details

Each trial was rehashed three times in each of the trail conditions. In each run conditions and for each replication, the Erosion rate and Residual stresses were measured. The exploratory plan for every trail is shown in Table 6 along with the response of erosion rate and residual stresses. The S/N ratio and ANOVA investigation for erosion rate and resid-

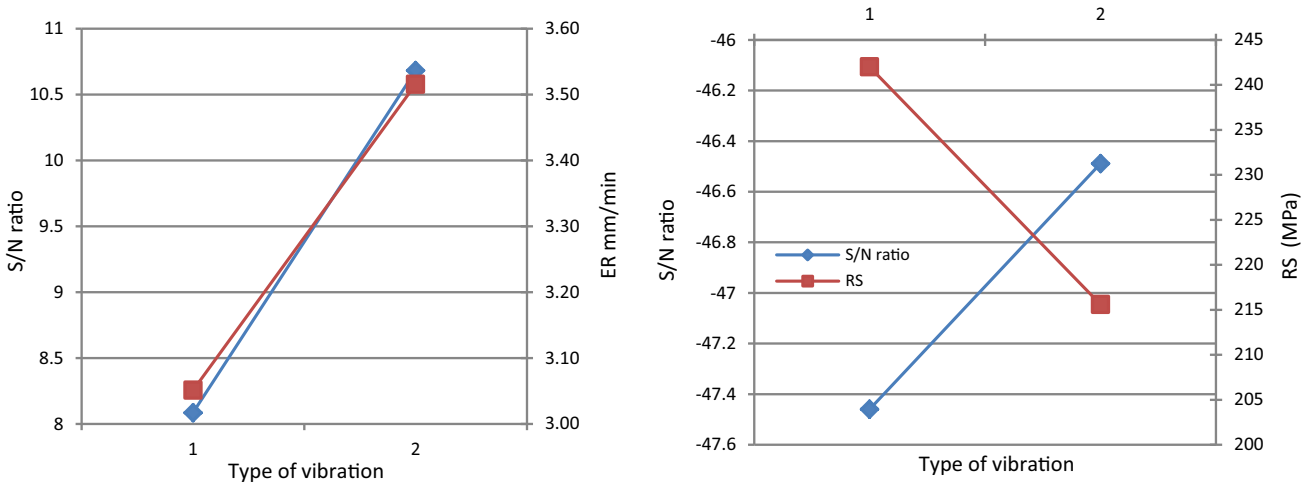

Fig. 6 Main effect and S/N ratio of type of vibration on erosion rate and residual stress

ual stress were obtained by utilizing excel sheet in Microsoft office and the values acquired are given in respective tables.

Tables 8 and 9 represent the analysis of variance for raw date and the S/N ration for the erosion rate respectively. The results reveal the factors significantly affected the erosion rate for USWEDM process for both the raw date and S/N ratio. The column "P" represents the % contribution of the particular factor to the response characteristic. The results of main effects for erosion rate form Figs. 6, 8, 10, 11, 12 and 13 reveal that the optimum levels of erosion rate (ER) for the USWEDM were obtained: Discontinuous type of vibration (level 2), 14 µm amplitude (level 2), 180 A peak current (level 3), 78% duty cycle (level 3), 4mm workpiece thickness (level 3), and 8 mm/min wire feed rate (level 2), which provide maximum ER for proposed USWEDM process.

Tables 7 and 8 indicate that the duty cycle (15.53%), peak current (30.13%), amplitude of vibration (10.50%), and workpiece thickness (23.67%), are the highest contributors. Whereas wire feed rate and type of vibration are contributors for raw data but not significant for S/N ratio. The interdependency of process quantitative controllable parameters in USWEDM is complex due to other qualitative parameter such as cavitation, abnormal discharge and flushing of contaminated dielectric medium. This interactive manufacturing method helped in ranking and selecting the corresponding optimum level the process parameters under study.

Tables 9 and 10 represent the analysis of variance for raw date and the S/N ration for the residual stress respectively. The results of Main effects of residual stresses from Figs. 6, 8, and 10, 11, 12 and 13 reveal that the optimum levels of residual stresses for the USWEDM are: Discontinuous vibration (level 2), 14 µm amplitude (level 2), 60 A peak current (level 1), 66% duty cycle (level 1), 7 mm workpiece thickness (level 2), and 11 mm/min wire feed rate (level 3), which provide minimum residual stresses.

It could be further noticed that in case of all the parameters, the higher values of average response characteristics correspond to higher values of S/N ratio. It is clear that parameter peak current, duty cycle, workpiece thickness and amplitude of vibration significantly affect both ER and residual stresses. The qualitative factors mentioned above influenced every other parameters and results high error values for USWEDM process. In any case, the small improvement in traditional WEDM is appreciable in USWEDM. The percentage contribution of duty cycle was highest (35.20%), and for type of vibration (8.20%), workpiece thickness (21.90%), peak current (19.05%), the amplitude of vibration (11.56%) and wire feed rate (2.01%).

The principle controllable factors were amplitude of vibration, workpiece thickness, peak current and duty cycle that affected the USWEDM response characteristics. It was being demonstrated greatest S/N ratio for each factor in Tables 8 and 10.

3 Results and discussion

3.1 Effect of type of vibration

The impact of continuous vibration on erosion rate in wire EDM has been perceived for quite a while. It was presumed that ultrasonic vibration prompt increment in erosion rates. The ultrasonic vibration helped in enhancing 30% MRR for wire EDM when it was contrasted and traditional unaided EDM [7].

This was affirmed in the pilot trails in present experimental study. Further additional experiments were conducted with discontinuous vibration in wire EDM with Taguchi experimental design. Figure 6 demonstrated the graphical variation of erosion rate and residual stresses, which upgraded with

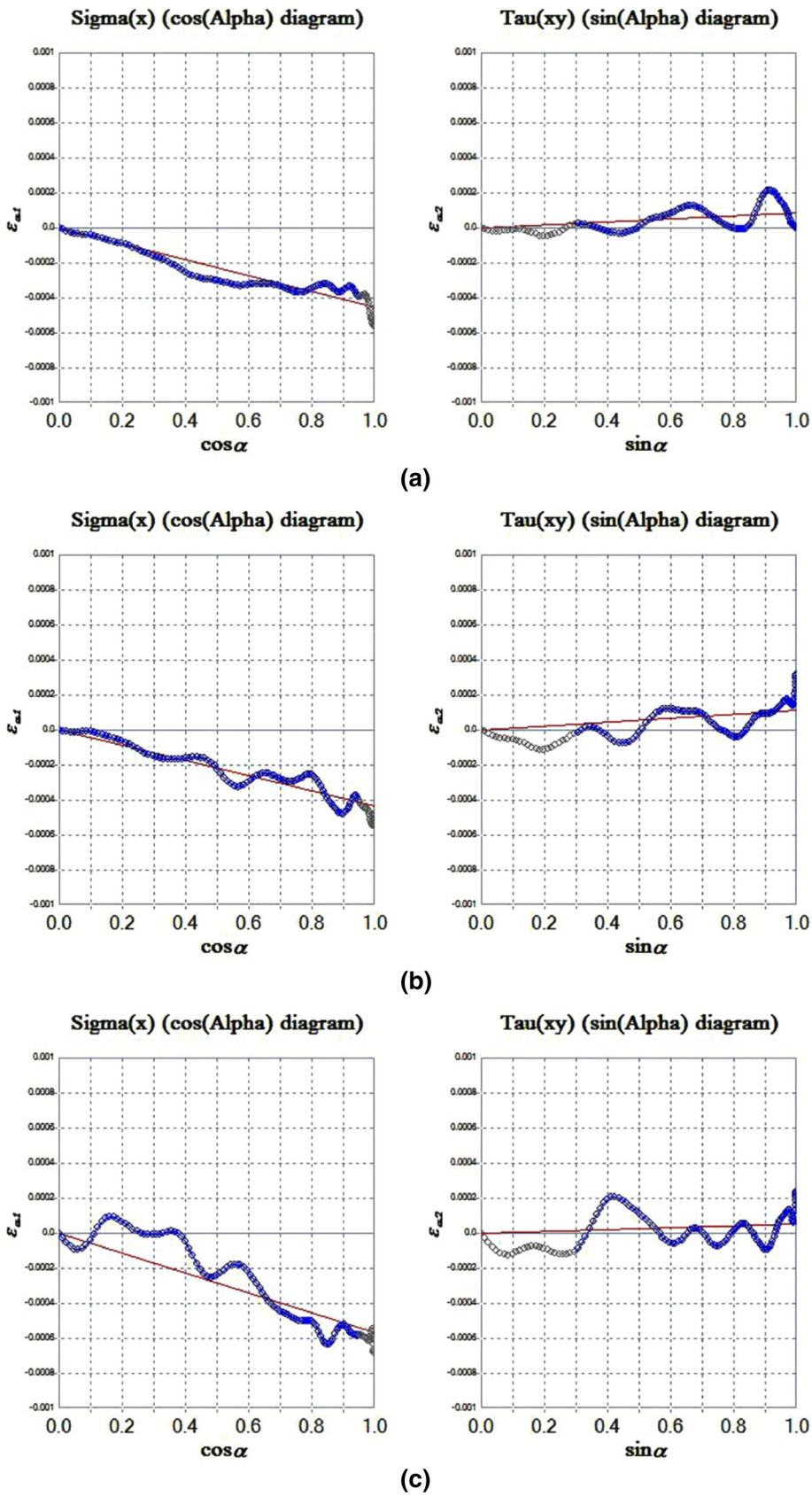

Fig. 7 **a** Residual stress graph for continuous vibration, **b** residual stress graph for discontinuous vibration, **c** residual stress graph for no-vibration

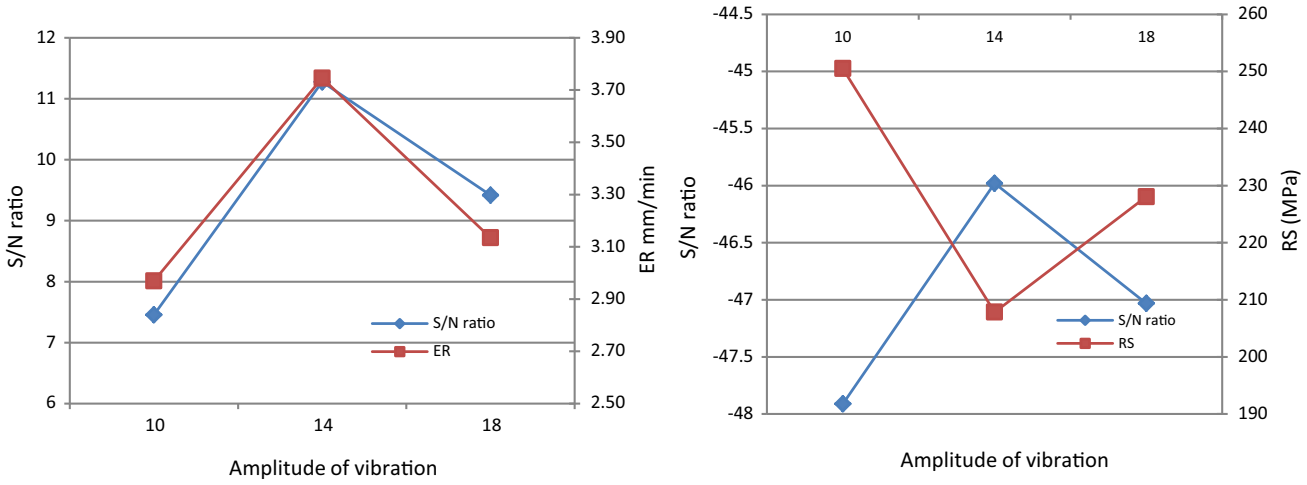

Fig. 8 Main effect and S/N ratio of amplitude of vibration on erosion rate and residual stress

discontinuous vibration. The principle impact of vertical discontinuous vibration was multiple discharge point with enough time ranges to empty the debris and gas bubble. In the meantime the extra inertial forces setup in the work piece helped the clearing of debris. The upside of giving vibration to the workpiece is the opportunity from the wire resonance as if there should arise an occurrence of ultrasonic vibration bestowed to the wire. With discontinuous vibration, it was clearly observed that residual stresses diminish as vibration on the workpiece provided more change than continuous vibration of workpiece. At the point when vibration was connected to the workpiece, last recorded residual stress was around 20% than without vibration. What's more, when discontinuous vibration was connected to the workpiece the change was roughly 27%. This was because the peak discharge density was much smaller in periodic vibration than created by the continuous workpiece vibration. The dielectric circulation and the flushing of debris were more uniformed in this case. The material under investigation was a α Fe(211) with Lattice constant (a) 2.8664 A. The X-Ray wave with Wavelength K-Alpha Diffraction angle (2θ) 156.396 deg, Diffraction lattice angle (2Eta) 23.604 deg was used for measurement. The workpiece specification obtained during measurements were Inter-planar spacing (d) 1.170, Diffraction plane (h,k,l) 2, 1, 1 and B.C.C Crystal structure, Young's modulus (E) 224.000 GPa, Poisson's ratio (v) 0.280. The values of the constants were Sigma (x) stresses constant (K) − 465.097 GPa, τ_{xy} stress constant (K) 380.985 GPa and σ_y stress constant (K) − 2091.661 GPa.

As appeared in Fig. 7a–c horizontal axis cos α is the COS of Azimuth angle of Debye–Sherrer ring and the vertical axis is a strain ($\varepsilon_{\alpha 1}$). This incline of the bend so acquired was the measure of residual stresses. In Fig. 7a for continuous vibration the incline is higher as contrast with the slope in Fig. 7b for discontinuous vibration. Though, in case of no-vibration the slope was comparatively very high as shown in Fig. 7c.

3.2 Effect amplitude of vibration

The high amplitude of vibration caused a vast pressure difference between the wire anode and the work piece. This pressure gradient prompted a pumping and mixing impact in discharge gap. This improved the flushing of debris and gas bubbles prompted high machining effectiveness. As appeared in Fig. 8 the erosion rate increments from 10 to 14 µm amplitudes of vibration, however past that it diminishes. This was on account of the higher amplitude of vibration disturbance to the essential discharge condition for the wire EDM process. The secondary discharge occurred between the debris and wire electrode and develop an abnormal discharge condition and short circuit. However, at this higher amplitude of vibration could be clarified as; the pace of debris evacuation lingers behind the debris aggregation. It was watched that there exist a cozy connection between erosion rate and surface integrity. Disintegration rate was an element of discharge energy, increment with the amplitude of vibration up to 14 µm than additionally diminish at 18 µm.The tractable residual stresses were the warm generation of the temperature gradient of re-solidified metal on the machined surface.

These residual stresses were produced in the EDMed surface because of metallurgical changes and non-homogeneity of the heat stream. The strong flushing impact ascribed to higher amplitude of vibration to lessen the heat concentration and re-solidification. Scientist demonstrated that the stresses decrease with the amplitude. However, when amplitude limit crossed a certain limit, the impact was invert [13]. Figure 9a–c shows comparative full width at half maximum (FWHM) distribution of entire Debye—Scherrer ring at different amplitude of vibration. At 10 µm

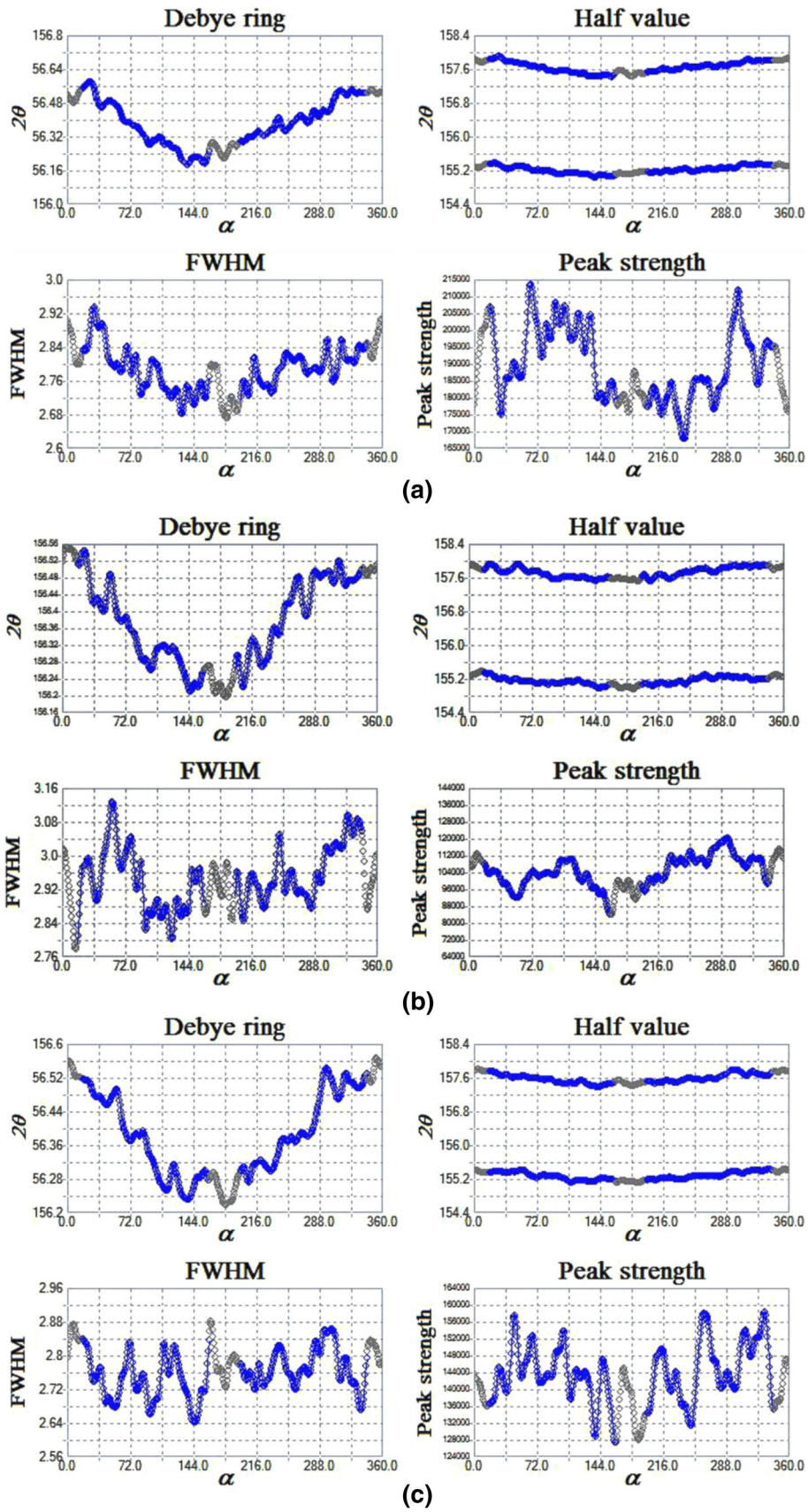

Fig. 9 **a** FWHM graph at 10 μm amplitude of vibration. **b** FWHM graph at 14 μm amplitude of vibration. **c** FWHM graph at 18 μm amplitude of vibration

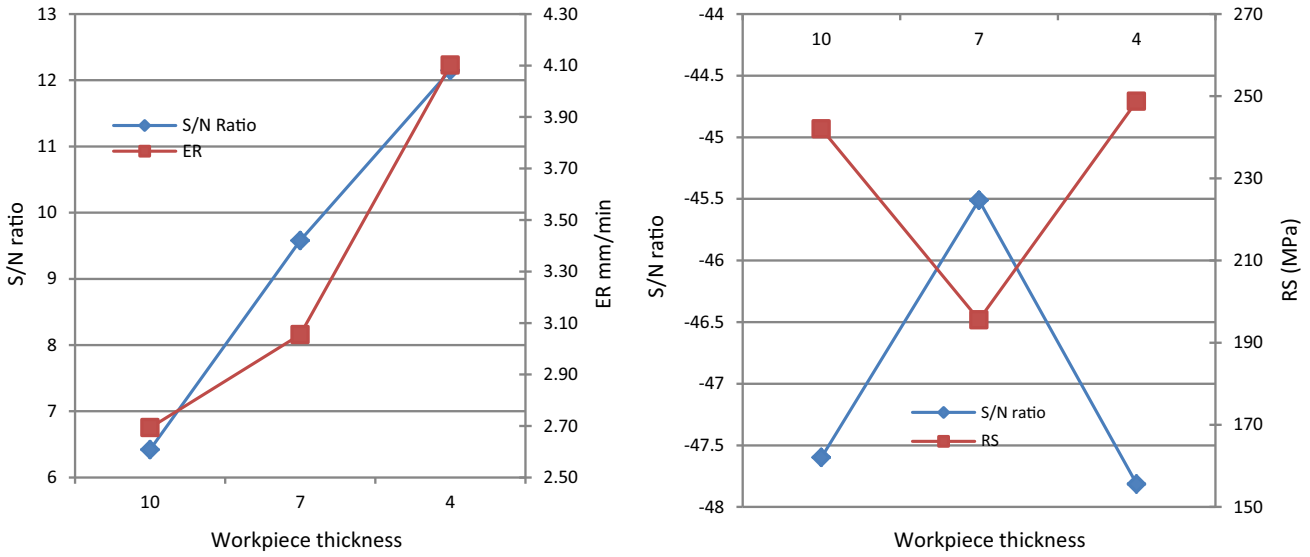

Fig. 10 Main effect and S/N ratio of workpiece thickness on erosion rate and residual stress

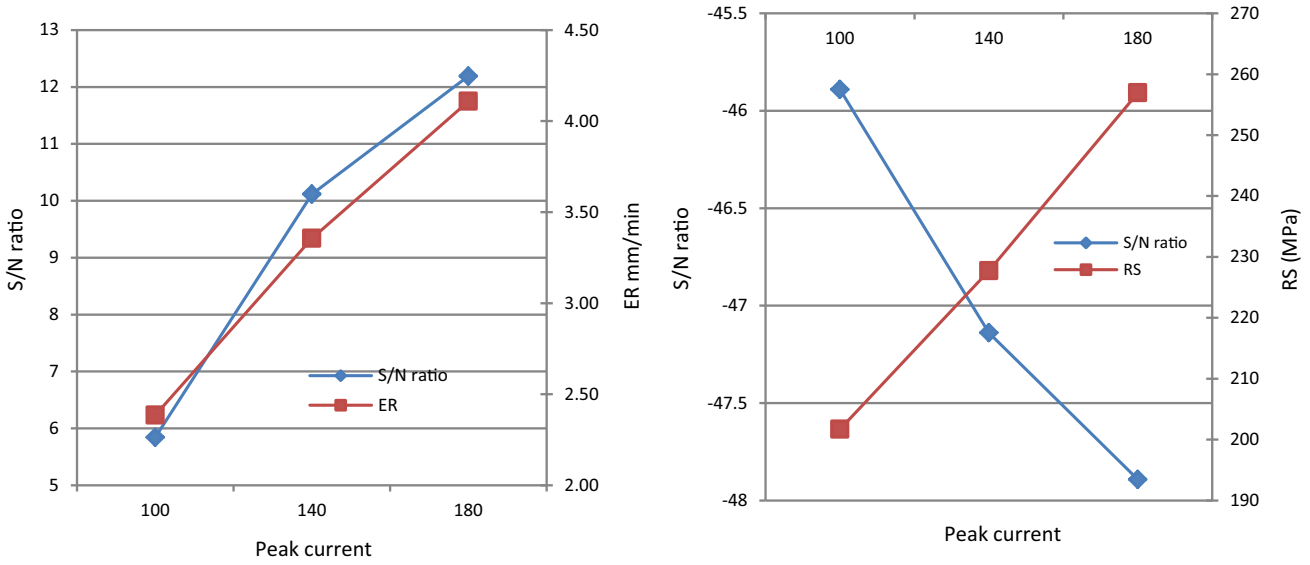

Fig. 11 Main effect and S/N peak current of vibration on erosion rate and residual stress

the FWHM 2.79° the variation lies between (2.68–2.93 deg) and α_{Max} 30.96° and α_{Min} 131.04°.with Peak strength (Ave) 189k. Considering other parameters constant the value of FWHM 2.95° lie between (2.80–3.13°) α_{Max} 57.60° to α_{Min} 125.28° at a 14μm amplitude of vibration with Peak strength (Ave) 104 k. At 18μm the FWHM 2.75 deg the variation lie between (2.64–2.86°) α_{Max} 301.68° α_{Min} 144.72° Peak strength (Ave) 143 k. The Peak strength is maximum at 10 μm and minimum at 14 μm that indicated the intensity of residual stresses. Peak broadening could be used to quantify the average crater size; micro strain might also create peak broadening [23]. But by analyzing the peak widths over a long range of 2θ one could differentiate micro strain and crater size.

Disordering of full width at half maximum (FWHM) distribution of entire Debye–Scherrer ring at 18 μm in minimum and at 14 μm was maximum, which represents the poor surface integrity at that amplitude. Surface texture appeared decreased from 10 to 14 μm, but after that it appears improving.

3.3 Effect of material thickness parameters

Although the erosion rate increased and residual stresses decreased with discontinuous vibration, when comparing with the continuous vibration, but the effect was more prominent for the thinner workpiece. However, it was further noticed that residual stresses decreases with the decrease of

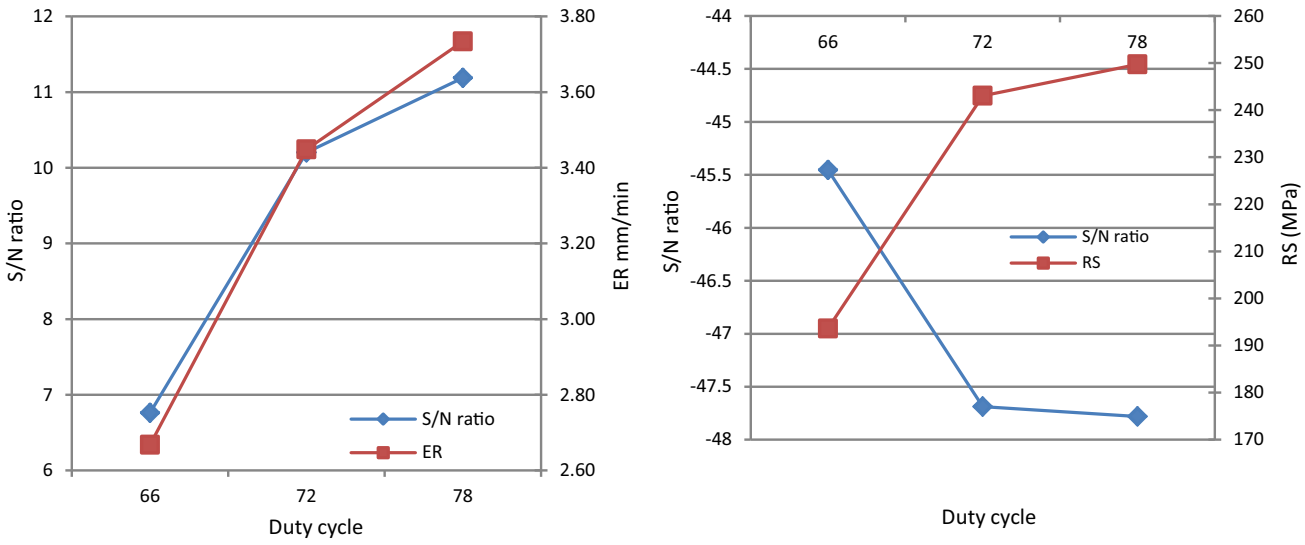

Fig. 12 Main and S/N ratio for duty cycle

workpiece sizes up to 7 mm, after that it further increases. This was because of the high string effect obtained at 7 mm thickness. The vibration of workpiece was less effective at higher thickness of workpiece. Although high flushing effect could be attained at high amplitude of vibration, but also the resonance of workpiece vibration restricts improvement of debris. The workpiece thickness significant play a role in residual stresses improvement. The erosion rate decreases with thickness.

3.4 Effect of electrical parameters

The peak current range was selected from 100–180 ampere in the increment of 40 ampere and duty cycle from 66–78% in the increment of 8, after carrying out the pilot experiments run for the selected performance characteristics.

The duty cycle selected for experiments was the percentage pulse-on-time with respect to the total of the pulse on and off time setting for a particular cutting condition. The duty cycle basically represents the utilization of discharge energy in a given pulse-on-time interval. It was observed that combination of high peak current and high duty cycle increase the wire breakage frequency. So, the values of parameters SV = 20 volt; WT = 8 unit; SF = 1150 unit were kept low. For continuous/discontinuous vibration at higher value of peak current, discharge became unstable with an improper combination of spark voltage and duty cycle settings. That developed high discharge energy of wire, so machining performance was affected negatively [10]. In this experiment, it was observed that the erosion rate and residual stresses were vitally affected by peak current and duty cycle. These were the sure factor; peak current and duty showed linear effect to the residual stress and erosion rate as shown in Figs. 11 and 12.

Table 11 provides the corresponding residual stresses results of map of 3D debey ring profile with peak current varies from 100–180 Amp, other parameters kept constant under three different modes No, Continuous and Discontinuous vibration. As shown, the 3D Debye–Scherrer rings at 100 Amp peak current were uniform and clear with small residual stresses compare to 140 and 180 amp peak current. With an increase in peak current the shape of 3D Debye–Scherrer ring became more distorted. Surface residual stresses were the resultant of molten melt the layer of workpiece surface, expelled away by the fresher dielectric medium, while the workpiece underneath remains solid. That temperature difference also createds poor surface texture [9]. At higher values of peak current the discharge energies were high that resulted higher residual stress, micro-pin holes and micro-cracks. The Distorted 3D Debye–Scherrer ring was an indication of damaged workpiece surface and high residual stresses. With discontinues vibration, the uniformity of 3D Debye ring comparatively was high. The proposed model can further being up-date by utilizing interactive simulation with the application the finite element model. A user interactive simulation for the residual stresses would help to predict the life of the machined surface at different levels of design parameters such as fatigue, heat affected zone and crater size. This would facilitate in further development of USWEDM process performance.

Table 12 represents the residual stress profile by controlling XY stage with duty cycle varies from 66 to 78%. The duty cycle is percentage utilization of length of pulse on time. Peak strength increases with the duty cycle, whereas peak width decreases from continuous vibration to discontinuous

Table 11 Experimental results of Map of 3D debey ring and its residual stresses profile with peak current varies from 100 to 180 Amp (1) no vibration; (2) continuous vibrations; (3) discontinuous vibration; other parameters constant

Peak current (Amp)	No vibration	Continuous vibration	Discontinuous vibration
100	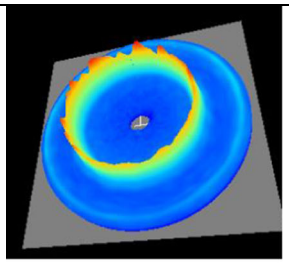 σ_x =195	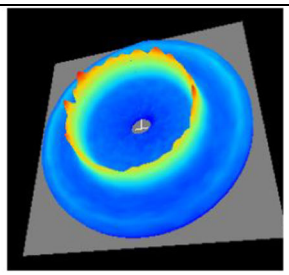 σ_x =186	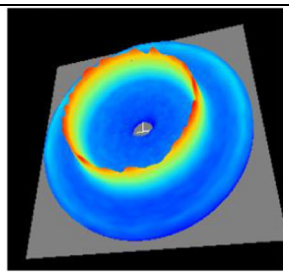 σ_x =159
140	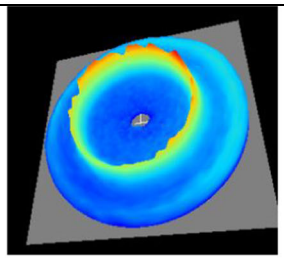 σ_x =276	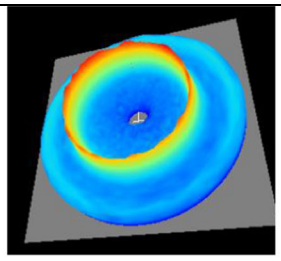 σ_x =253	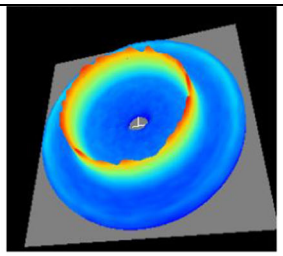 σ_x =203
180	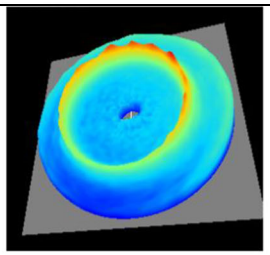 σ_x =317	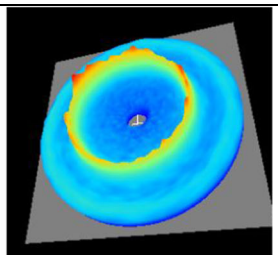 σ_x =287	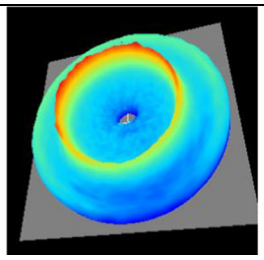 σ_x =257

vibration. The increase in duty cycle results in increase in residual stresses. The results confirmed with those of Guo et al. [7]. The reason for high erosion rate was more electrical discharge energy was conducted into the machining gap within single pulse internal and more work-piece material erosion. That spark discharge energy was a function of peak current and the length of the pulse on-time [12].

3.5 Effect of wire feed rate (non electrical parameter)

The wire is passed at a particular speed through a wire guided path for continuous sparking in the discharge gap. It was preferred to set the wire feed rate to its maximum to reduce wire breakage. Figure 13 show the graph of wire feed rate versus response characteristics.

It was observed that the effect of wire feed rate is wavy in nature. There was insignificant affect observed for erosion rate and remained almost constant between 5–11 mm/min and with slight increase at 8 mm/min. Although, the residual stress curve was also wavy in nature as it first increased with increase in the wire feed rate and then decreased. So it is always preferred to have a high wire feed rate. The higher wire feed rate reduced the wire breakage frequency.

4 Estimation of optimum residual stress response

The optimum value of Residual stresses (RS) (MPa) was predicted at the selected levels of significant parameters $A_2B_2C_1D_1E_2F_3$. The estimated mean (μ_{RS}) of the response characteristic RS was determined as in Eq. (9) [21] and [22];

$$\mu_{RS} = \overline{A}_2 + \overline{B}_2 + \overline{C}1 + \overline{D}1 + \overline{E}2 + \overline{F}3 - 5\overline{\times T} \quad (9)$$

where T: overall mean of RS = 228.80, A_2: average RS at the second level of type of vibration = 215.59, B_2: average RS at the second level of amplitude of vibration

Table 12 Experimental results of residual stress profile by controlling XY axis stage with duty cycle varies from 66 to 78% using; (1) no vibration; (2) continuous vibrations; (3) discontinuous vibration; other parameters constant

Duty cycle	No vibration	Continuous vibration	Discontinuous vibration
66	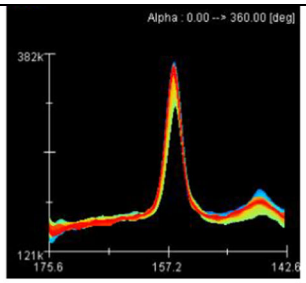 σ_x =220	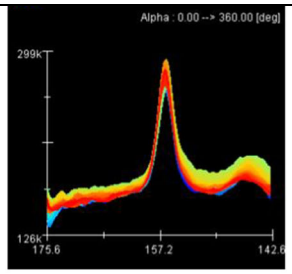 σ_x =203	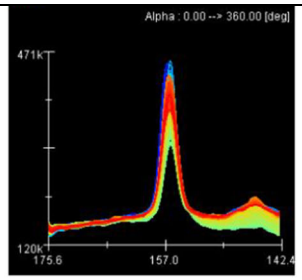 σ_x =186
72	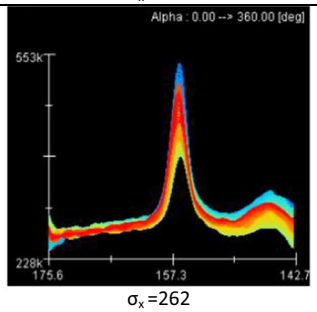 σ_x =262	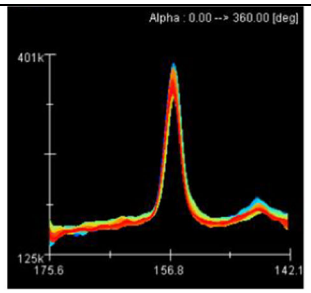 σ_x =246	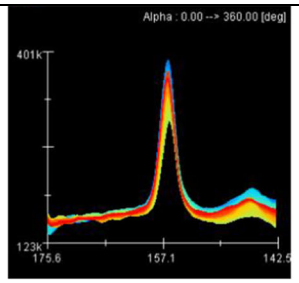 σ_x =233
78	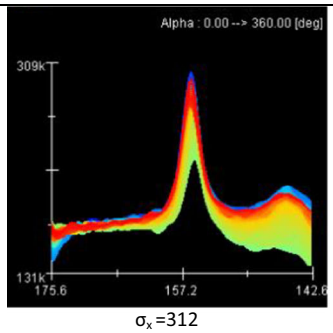 σ_x =312	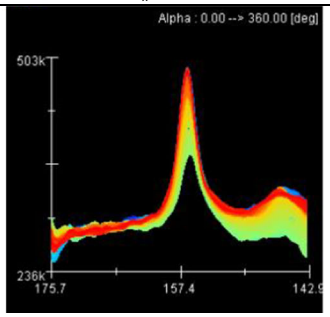 σ_x =276	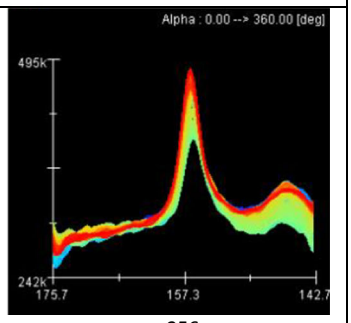 σ_x =256

= 207.8333, C_1: average RS at the first level of peak current = 201.72, D_1: average RS at the first level of duty cycle = 193.61, E_2: average RS at the second level of workpiece thickness = 195.56, F_3: average RS at the third level of wire feed rate = 216.22, reference from Figs. 6, 8, 10, 11, 12 and 13. Substitute the values of various terms in the Eq. (9)

$$\mu_{RS} = 215.59 + 207.8333 + 201.72 + 193.61 + 195.56 + 216.22 - 5 \times 228.80 = 86.53$$

The 95% confidence interval of confirmation experiments (CI_{CE}) and of population (CI_{pop}) was calculated by using the following Eqs. (10) and (11):

$$CI_{CE} = \sqrt{F_\alpha(1, f_e) V_e \left[\frac{1}{n_{eff}} + \frac{1}{R}\right]} \tag{10}$$

$$CI_{POP} = \sqrt{\frac{F_\alpha(1, f_e) V_e}{n_{eff}}} \tag{11}$$

where $F_\alpha(1, f_e)$: the F ratio at the confidence level of $(1-\alpha)$ against DOF 53 and error DOF $f_e = 42$, N: total number of results = 54 (Treatment = 18, Repetition = 3), R : sample size for confirmation experiments = 3 V_e: error variance = 657.24 (Ref. Table 11), f_e error DOF = 42. The value of n_{eff} is calculated with the Eq. (12).

$$n_{eff} = \frac{N}{1+[\text{ DOF associated in the estimate of mean response }]} = 4.5 \tag{12}$$

$F_{0.05}(1, 42) = 4.076$ (tabulated F value), So $CI_{CE} = \pm 48.16$, $CI_{POP} = \pm 24.40$.

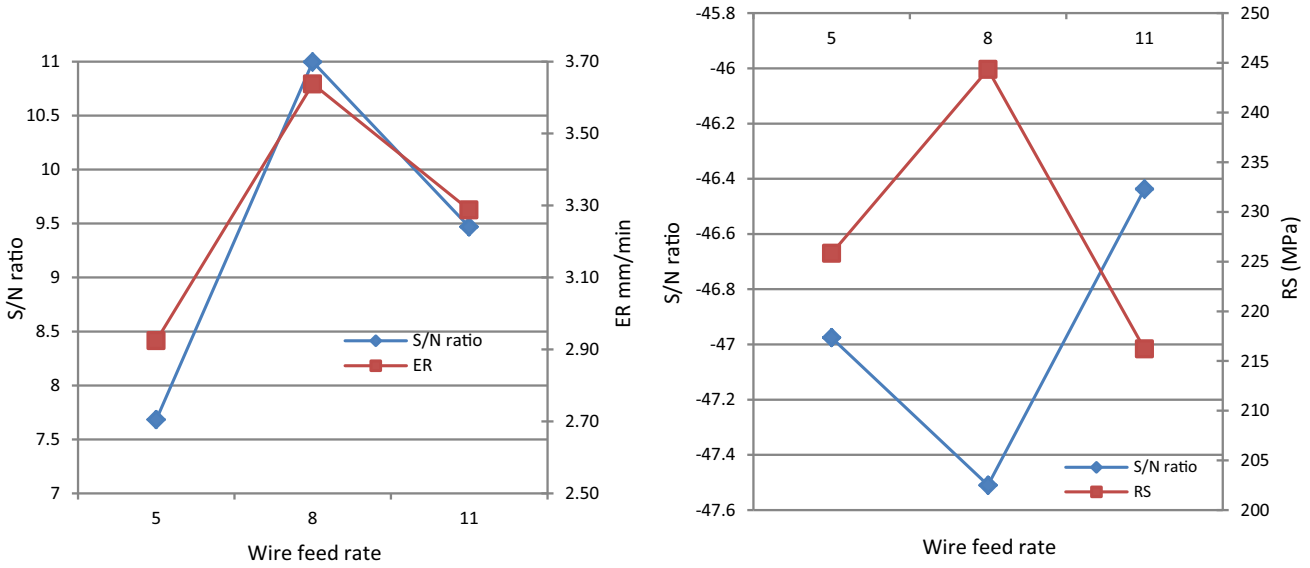

Fig. 13 Main effect and S/N wire feed rate on erosion rate and residual stress

The predicted optimal range (for a confirmation runs of three experiments) was:

$$\mu_{RS} - CI_{CE} < \mu_{RS} < \mu_{RS} + CI_{CE;} 38.37 < \mu_{RS} < 134.69$$

The 95% conformation interval of the predicted mean was as follows:

$$\mu_{RS} - CI_{POP} < \mu_{RS} < \mu_{RS} + CI_{POP}; 62.13 < \mu_{RS} < 110.93$$

5 Estimation of optimum erosion rate response

The optimum value of erosion rate (ER) (mm/min) was predicted at the selected levels of significant parameters $A_2B_2C_3D_3E_3$. The estimated mean (μ_{ER}) of the response characteristic ER was determined as in Eq. (9). Where T: overall mean of ER = 3.28, A_2: average RS at the second level of type of vibration = 3.52, B_2: average ER at the second level of amplitude of vibration = 3.75, C_3: average ER at the third level of peak current = 4.11, D_3: average ER at the third level of duty cycle = 3.73, E_3: average ER at the third level of workpiece thickness = 4.10; F_2: average ER at the second level of workpiece thickness = 3.64; reference from Figs. 6, 8, 10, 11, 12 and 13 . Substituting the values of various terms in the Eq. (9)

$$\mu_{ER} = 3.52 + 3.75 + 4.11 + 3.73 + 4.10 + 3.64 - 5 \times 3.28 = 6.45$$

The 95% confidence interval of confirmation experiments (CI_{CE}) and of population (CI_{pop}) was calculated by using the following Eqs. (10) and (11). Where $F_\alpha(1, f_e)$: the F ratio at the confidence level of $(1-\alpha)$ against DOF 53 and error DOF $f_e = 42$, N: total number of results = 54 (Treatment = 18, Repetition = 3), R : sample size for confirmation experiments = 3 V_e: Error variance = 3.47 (Ref. Table 8), f_e error DOF = 42. The value of n_{eff} is calculated with the eqaution (12).

$$F_{0.05}(1, 42) = 4.076 \text{(tabulated F value)}, \text{So } CI_{CE} = \pm 2.81, CI_{POP} = \pm 1.77$$

The predicted optimal range (for a confirmation runs of three experiments) is:

$$\mu_{ER} - CI_{CE} < \mu_{ER} < \mu_{ER} + CI_{CE;} 3.64 < \mu_{ER} < 9.26$$

The 95% conformation interval of the predicted mean is as follows:

$$\mu_{ER} - CI_{POP} < \mu_{ER} < \mu_{ER} + CI_{POP}; 4.68 < \mu_{ER} < 8.22$$

6 Conclusions

The erosion rate and residual stresses estimations were made on high carbon, high chromium D2 tool steel and all the residual stresses were observed tensile in nature. The higher erosion rate attained by the workpiece ultrasonic vibration is attributed to enchantment in dielectric dissemination. On the bases of scope of test conditions utilized in the thorough test examinations, explanatory work, the accompanying significant conclusions can be drawn:

1. The residual stresses are down in discontinuous vibration as a contrast with continuous vibration. Discontinuous vibration gives adequate time traverse to normal steady state discharge condition, and furthermore enables additional inertial forces to evacuate the debris and gas bubbles from the wire electrode and the work piece discharge gap.
2. As contrasted with constant ultrasonic vibrations, the discontinuous ultrasonic vibrations enhance the erosion rate by increase the time period to flushing of debris evacuation from the gap and better release condition. This reduces the abnormal discharge per pulse.
3. Although, higher amplitude is desired to create a strong string effect in the discharge gap by producing large pressure gradient to enhance flushing. When amplitude of vibration increased beyond 14 μm has negative effects on response. This is caused by the insufficient time interval to clear the gap from contaminated. A noteworthy contrast is seen in the surface integrity while machining with continuous and discontinuous ultrasonic vibration helped wire EDM.
4. The optimal value of process parameters for the predicted range of optimal Residual stresswere as follows: type of vibration (A, 2nd level), amplitude of vibration (B, 2nd level) = 14μm, peak current (E, 1st level) = 100 Amp., duty cycle (F, 1st level) = 66%, workpiece thickness (C, 2nd level) = 7 mm and wire feed rate (D, 3rd level) = 11 mm/min.
5. The optimal value of process parameters for the predicted range of optimal material erosion ratewere as follows: Type of Vibration (A, 2nd level) = discountinous, Amplitude of Vibration (B, 2nd level) = 14 μm, Peak Current (E, 3rd level) = 180 Amp., Duty cycle (F, 3rd level) = 78%, Workpiece Thickness (E, 3rd level) = 4 mm and Wire feed rate (D, 2nd level) = 8 mm/min.

From ANOVA it was observed that the peak current and duty cycle were the fundamental controlling parameters. Increased residual stresses were seen with an increase in erosion rate. In any case, the interdependency of different process quantitative controllable parameters in USWEDM is complex. This entomb reliance is because of other qualitative uncontrollable parameter, for example, cavitation, irregular release and flushing of tainted dielectric medium.

Acknowledgements The authors acknowledge Department Mechanical Engineering, YMCA UST Faridabad, India, for providing the necessary wire electric discharge machine tool with additional set-up for experimentation. The authors are also thankful to Department of Mechanical and Production, DTU Delhi, India, for providing stress analyzer facility.

References

1. Antar, M.T., Soo, S.L., Aspinwall, D.K., Sage, C., Cuttell, M., Perez, R., et al.: Fatigue response of Udimet 720 following minimum damage wire electrical discharge machining. Mater. Des. **42**, 295–300 (2012)
2. Ashyralyev, A.: Nonlocal boundary-value problems for elliptic equations: well-posedness in bochner spaces. AIP Conf. Proc. **1309**, 66–84 (2010)
3. Capello, E.: Residual stresses in turning: part I: influence of process parameters. J. Mater. Process. Technol. **160**(2), 221–228 (2004)
4. Ekmekci, B., Elkoca, O., Tekkaya, A.E., Erden, A.: Residual stress state and hardness depth in electrical discharge machining: deionizaed water as dielectric liquid. Mach. Sci. Technol. **9**, 39–61 (2007)
5. Fischer, X., Coutellier, D.: Research in Interactive Design. Springer, Paris (2007)
6. Ghanem, F., Fredj, N.B., Sidhom, H., Braham, C.: Effects of finishing processes on the fatigue life improvements of electro machined surfaces of tool steel. Int. J. Adv. Manuf. Technol. **52**, 583–595 (2011)
7. Guo, Z.N., Lee, T.C., Yue, T.M., Lau, W.S.: A study of ultrasonic-aided wire electrical discharge machining. J. Mater. Process. Technol. **63**, 823–828 (1997)
8. Guo, Z.N., Lee, T.C., Yue, T.M., Lau, W.S.: Study on the machining mechanism of WEDM with ultrasonic vibration of the wire. J. Mater. Process. Technol. **69**, 212–221 (1997)
9. Guu, Y.H., Chou, Y.C., Chiou, S.-T.: Study of the effect of machining parameters on the machining characteristics in electrical discharge machining of Fe–Mn–Al alloy. Mater. Manuf. Process. **20**(6), 905–916 (2004)
10. Han, G., Soo, S.L., Aspinwall, D.K., Bhaduri, D.: Research on the ultrasonic assisted WEDM of Ti–6Al–4V. Adv. Mater. Res. **797**, 315–319 (2013)
11. Ho, K.H., Newman, S.T.: State of the art electrical discharge machining (EDM). Int. J. Mach. Tools Manf. **43**, 1287–1300 (2003)
12. Kansal, H.K., Singh, S., Kumar, P.: Parametric optimization of powder mixed electrical ischarge machining by response surface methodology. J. Mater. Process. Technol. **169**(3), 427–436 (2005)
13. Khosrozadeh, B., Shabgard, M.: Effects of hybrid electrical discharge machining processes on surface integrity and residual stresses of Ti–6Al–4V titanium alloy. Int. J. Adv. Manuf. Technol. **93**, 1999–2011 (2017)
14. Klinka, A., Guo, Y.B., Klockea, F.: Surface integrity evolution of powder metallurgical tool steel by main cut and finishing trim cuts in wire-EDM. Procedia Eng. **19**, 178–183 (2011)
15. Kremer, D., Lebrun, J.L., Hosari, B., Moisan, A.: Effects of ultrasonic vibrations on the performances in EDM. Ann. ClRP **38**(1), 199–202 (1989)
16. Kumar, s, Grover, S., Walia, R.S.: Optimisation strategies in ultrasonic vibration assistedelectrical discharge machining: a review. Int. J. Precis. Technol. **7**(1), 51–84 (2017)
17. Liu, J.F., Guo, Y.B.: Residual stress modeling in electric discharge machining (EDM) by incorporating massive random discharges. Procedia CIRP **45**, 299–302 (2016)
18. Peterson, N., Kobayashi, Y., Traeger, B., Sanders, P.: Assessment and validation of Cos? Method for residual stress measurement. In: 13th International Conference on Shot Peening, pp. 80–86 (2017)
19. Ramakrishnana, R., Karunamoorthy, L.: Modeling and multi-response optimization of Inconel 718 on machining of CNC WEDM process. J. Mater. Process. Technol. **207**, 343–349 (2008)
20. Rao, P.S., Ramji, K., Satyanarayana, B.: Effect of wire EDM conditions on generation of residual stresses in machining of aluminum 2014 T6 alloy. Alex. Eng. J. **55**, 1077–1085 (2016)

21. Ross, P.J.: Taguchi Techniques for Quality Engineering. McGraw-Hills Book Company, New York (1988)
22. Roy, R.K.: A Primer on Taguchi Method. Van Nostrand Reinhold, New York (1990)
23. Sasaki, T., Miyazaki, T., Ito, H., Furukawa, T., Mihara, T.: X-ray residual stress analysis of nickel base alloys. Adv. Mater. Res. **922**, 274–279 (2014)
24. Shabgard, M.R., Alenabi, H.: Ultrasonic assisted electrical discharge machining of Ti–6Al–4V alloy. Mater. Manuf. Process. **30**, 991–1000 (2015)
25. Sidhom, H., Ghanem, F., Amadou, T., Gonzalez, G., Braham, C.: Effect of electro discharge machining (EDM) on the AISI316L SS white layer micro structureand corrosion resistance. Int. J. Adv. Manuf. Technol. **65**, 141–153 (2013)
26. Singh, J., Walia, R.S., Satsangi, P.S., Singh, V.P.: FEM modeling of ultrasonic vibration assisted workpiece in EDM process. Int. J. Mech. Syst. Eng. **1**(1), 8–16 (2012)
27. Singh, J., Walia, R.S., Satsangi, P.S., Singh, V.P.: Hybrid electric discharge machining process with continuous and discontinuous ultrasonic vibrations on workpiece. Int. J. Mech. Syst. Eng. **2**(1), 22–33 (2012)
28. Soo, S.L., Antar, M.T., Aspinwall, D.K., Sage, C., Cuttell, M., Perez, R., et al.: The effect of wire electrical discharge machining on the fatigue life of Ti–6Al–2Sn–4Zr–6Mo aerospace alloy. Procedia CIRP **6**, 215–219 (2013)
29. Srivastava, V., Pandey, P.M.: Effect of process parameters on the performance of EDM process with ultrasonic assisted cryogenically cooled electrode. J. Manuf. Process. **14**, 393–402 (2012)
30. Walia, R.S., Shan, H.S., Kumar, P.: Improving EDM process efficiency by ultrasonic vibrations. J. Pure Appl. Ultrason. **26**(2/3), 84–89 (2004)

Journal of Solid State Electrochemistry
https://doi.org/10.1007/s10008-018-3963-6

ORIGINAL PAPER

Electrochemical studies of novel olivine-layered ($LiFePO_4$-Li_2MnO_3) dual composite as an alternative cathode material for lithium-ion batteries

Rakesh Saroha[1] · Amrish K. Panwar[1] · Anurag Gaur[2] · Yogesh Sharma[3] · Vinay Kumar[1] · Pawan K. Tyagi[1]

Received: 27 November 2017 / Revised: 15 March 2018 / Accepted: 7 April 2018
© Springer-Verlag GmbH Germany, part of Springer Nature 2018

Abstract
In the present work, olivine-layered composites, i.e., $LiFePO_4$-Li_2MnO_3, are successfully synthesized in the form of a single monolithic electrode and *layer arrangement*. X-ray diffraction (XRD) patterns revealed that the prepared compositions exhibit the peaks correspond to the layered *m*-Li_2MnO_3 (*C2/m* space group) and orthorhombic $LiFePO_4$ with *Pnma* space group. Microstructural investigations indicate that all the samples possess nearly same morphology with a combination of smaller as well as bigger grains. CV results demonstrate that all the prepared samples possess anodic peak around 3.6 and 4.7 V along with a broad cathodic peak around 3.2 V which is due to intercalation of Li-ion at *16c* octahedral sites of the spinel structure formed by MnO_2. Among all the compositions, *layer arrangement* of $LiFePO_4$ and Li_2MnO_3, i.e. LFP/LMO layered arrangement, shows the best cycling and rate performances. LFP/LMO exhibits a discharge capacity of 178 ± 5 mA h/g at a current density 10 mA/g and holds 98% of the capacity up to 100 charge/discharge cycles measured at 20 mA/g.

Keywords Olivine-layered composite · Electrochemical performance

Introduction

Cathode materials with a formula $Li[Li_xMn_yM_z]O_2$ [M represents transition metal] become a popular choice in the recent time because of their higher experimental specific discharge capacity (> 200 mA h/g) as compared to the commercially available $LiCoO_2$ [1, 2]. All the cathode materials fall into the category of $Li[Li_xMn_yM_z]O_2$ that shows a charging plateau at 4.5 V versus Li^+/Li which is quite similar to the behavior exhibit by layered Li_2MnO_3. However, $Li[Li_{1/3}Mn_{2/3}]O_2$ cathode material known as Li_2MnO_3 possesses much higher theoretical specific discharge capacity (458 mA h/g) as compared to $Li[Li_xMn_yM_z]O_2$ [1, 3–6]. Despite high theoretical discharge capacity, its commercialization is still unfeasible because of various drawbacks which include electrochemical inactiveness in the 2.2–4.4 V (vs. Li^+/Li) voltage range, the higher cut-off voltage for activation (~4.8 V), and non-oxidizing nature of Mn^{4+} ions in the octahedrally coordinated system [7–10]. However, several efforts have been made worldwide by research fraternity to overshadow these shortcomings which include extracting lithium and oxygen simultaneously in the form of Li_2O to activate Li_2MnO_3 [11, 12], substitution at Li/Mn site partially with another metal ion [13–15], and even with different morphologies [16].

On the other hand, olivine-type $LiFePO_4$ has drawn the vast attention of the scientific community over the past two decades. Its high theoretical capacity of 170 mA h/g, low cost, excellent capacity retention, structural stability, and environmental benignity due to its non-toxicity make it an attractive candidate for cathode material in rechargeable lithium-ion batteries [17–26]. In the present work, blending of olivine and layered cathode materials into the same electrode structure as a novel composite has been discussed. Composite functional structures of $LiFePO_4$ and Li_2MnO_3 were made using two different configurations: (i) fully intermixed in a single monolithic electrode using ball milling, (ii) the *layer arrangement* with the high-rate $LiFePO_4$ layer is kept in contact with the aluminum current collector while Li_2MnO_3 coated over $LiFePO_4$. There are several parameters which can be

✉ Amrish K. Panwar
panwaramar@gmail.com

[1] Department of Applied Physics, Delhi Technological University, Delhi 110042, India

[2] Department of Physics, National Institute of Technology Kurukshetra, Kurukshetra, Haryana 136119, India

[3] Department of Physics, Indian Institute of Technology Roorkee, Roorkee, Uttarakhand 247667, India

Published online: 21 April 2018

manipulated in creating such blended active materials such as the mass ratio of the active materials, compositions, and morphology of the active cathodes [27]. However, in the present study, the effect of the different mass ratios of the active materials has been only taken into consideration. All the synthesized compositions in the present work were examined for phase analysis using X-ray diffraction (XRD) and microstructural investigation using scanning electron microscopy (SEM). Electrochemical characterizations were performed for the synthesized compositions to study the electrochemical performance and kinetics for lithium ion.

Experimental

Synthesis of olivine-layered ($LiFePO_4$-Li_2MnO_3) composites

Layered Li_2MnO_3 and olivine-$LiFePO_4$ powders were prepared using the sol-gel and solid-state method, respectively [3, 28]. The dual composite powders were prepared by mixing the two active materials into a single monolithic electrode with different mass ratios using a ball mill and abbreviated as 1LFP/3LMO, 1LFP/1LMO, and 3LFP/1LMO corresponding to the mass ratio of 1:3, 1:1, and 3:1, respectively, of olivine to the layered cathode. Another layered configuration was also made with the high-rate $LiFePO_4$ layer is in contact with the aluminum current collector and layered Li_2MnO_3 coated over $LiFePO_4$ *(LFP:LMO = 1:1)* and arrangement was abbreviated as LFP/LMO.

Material characterization of synthesized samples

Phase composition and quantitative analysis of the crystal structure for synthesized powders was conducted using RIGAKU make X-ray diffractometer attached with $CuK_{\alpha 1}$ radiation ($\lambda = 1.540$ Å). The 2θ range for XRD data collection was kept at 10°–70° with a step size of 0.02°. The morphological characterization of the synthesized compositions was studied using HITACHI make S-3700N scanning electron microscope working at 15 kV.

Preparation of electrode and characterization

Electrochemical tests were performed using CR2032 coin-type half cells. The positive working electrode was made by dispersing active material, super P as a conductive carbon and polyvinylidene difluoride (PVDF) as a binder in N-methyl-2-pyrrolidinone (NM2P) as a solvent in a wt.% ratio of 70:15:15, respectively. The precise description of electrode preparation method has been described elsewhere [29]. *However, for the layer arrangement, slurry of olivine-$LiFePO_4$ was coated first on the aluminum foil and allowed to dry for 2 h in air. After that slurry of layered Li_2MnO_3 was coated over $LiFePO_4$ coating in order to have layer arrangement, the final coating was dried overnight at 80 °C in a vacuum oven.* Electrochemical behavior was investigated by cyclic voltammetry (CV) tests in 2.0–4.8 V potential window (vs. Li/Li^+ metal) and further supported by charging/discharging (GCD) performance test. Cycling stability/rate performance for various C-rates and electrochemical impedance spectroscopy (EIS) in 10 mHz–10 kHz frequency range were also performed at room temperature (298 K).

Results and discussion

Phase and morphological analysis

Figure 1 displays the as-obtained XRD patterns of the prepared compositions. The diffraction pattern shows peaks corresponding to both *m*-Li_2MnO_3 and $LiFePO_4$ with *C2/*m and *Pnma* space groups, respectively. It shows that the prepared compositions possess both the phases depending upon the extent of intermixing. Weak diffraction peaks situated around 20°–30° can be assigned to the lattice superstructure ordering caused due to the arrangement of Mn ion into Li-Mn layers of LMO structure. Such type of peaks are characteristics of Li-rich materials. The XRD patterns of dual composites, i.e., 1LFP/3LMO, 1LFP/1LMO, and 3LFP/1LMO, comprise peaks of olivine and layered structures. *As the amount of LFP/LMO increases/decreases, respectively, the XRD pattern shows the prominent olivine phase*. The crystalline nature of all the prepared compositions is confirmed by the presence of intense and sharp peaks in the XRD pattern.

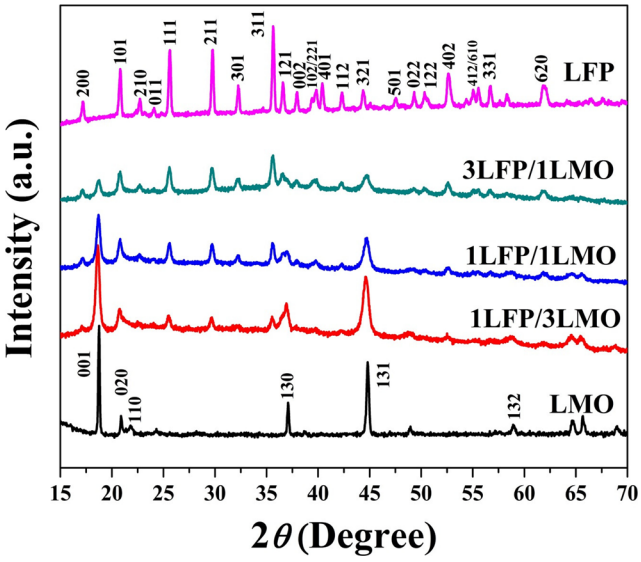

Fig. 1 XRD patterns of olivine-layered compositions in different mass ratios

The effect of variation in mass ratio value on the morphologies of $LiFePO_4$-Li_2MnO_3 dual composites is shown in Fig. 2a–c. All synthesized compositions show more or less identical morphological characteristics with a combination of smaller as well as bigger grains. No calcination/sintering was performed after the ball mill. Hence, the grains are simply a mixture of $LiFePO_4$ and Li_2MnO_3 particles. SEM micrographs also reveal that the prepared compositions have agglomerated grains with smaller sized grains get accumulated over the surface of bigger sized grains. The average grain size was observed using ImageJ software and lies in the range of 500 nm–2 μm with the scattered morphology.

Electrochemical performance of olivine-layered ($LiFePO_4$-Li_2MnO_3) composites

Cyclic voltammetry (CV) results of the prepared compositions in the voltage range of 2.0–4.8 V are shown in Fig. 3a. CV measurements were performed at 0.05 mV/s scan rate. It is evident from Fig. 3a that the weak anodic peak around 4.7 V is due to the presence of LMO in all the compositions. However, no symmetric cathodic peak is found. This is due to the removal of lattice oxygen in the form of Li_2O from the monoclinic crystal structure [3]. Therefore, LMO activation will take place at 4.7 V and will be irreversible. Anodic peak around 3.6 V is due to the transition reaction between Fe^{3+} ($FePO_4$) and Fe^{2+} ($LiFePO_4$) [28]. However, instead of a symmetric cathodic peak around 3.6 V, broad peaks around 3.2 V were observed which are due to Li-ion intercalation at *16c* octahedral centers in spinel arrangement originated due to the presence of MnO_2 [3]. Therefore, the co-occurrence of olivine, as well as layered structure, has been confirmed by CV results as indicated by XRD analysis.

Figure 3b reveals the initial charging-discharging capacity graphs of prepared compositions with different mass ratios of Li_2MnO_3 and $LiFePO_4$ in the voltage range 2.0–4.8 V measured at 10 mA/g current density. The initial discharge capacities of samples 1LFP/3LMO, 1LFP/1LMO, 3LFP/1LMO, and LFP/LMO were observed to 40 ± 5, 118 ± 5, 169 ± 5, and 180 ± 5 mA h/g, respectively. It can be analyzed from charge/discharge curves that with decrease in LMO mass ratio capacity increases and attains maximum value for 3LFP/1LMO sample. The *layer arrangement* of LFP and LMO (LFP/LMO) was found to exhibit the highest discharge capacity as compared to other synthesized compositions. *The possible reasons for capacity enhancement are not known but it could be the electrode arrangement as more conducting $LiFePO_4$ is in direct contact with the aluminum current collector which facilitates the lithium-ion diffusion as compared to other mixed configuration.* The charging-discharging profile of the compositions shows voltage plateaus around 3.6/3.2 V which are consistent with CV results. The length of discharge voltage plateau at 3.2 V increases with a decrease in the mass ratio of LMO reaching maximum for the layered

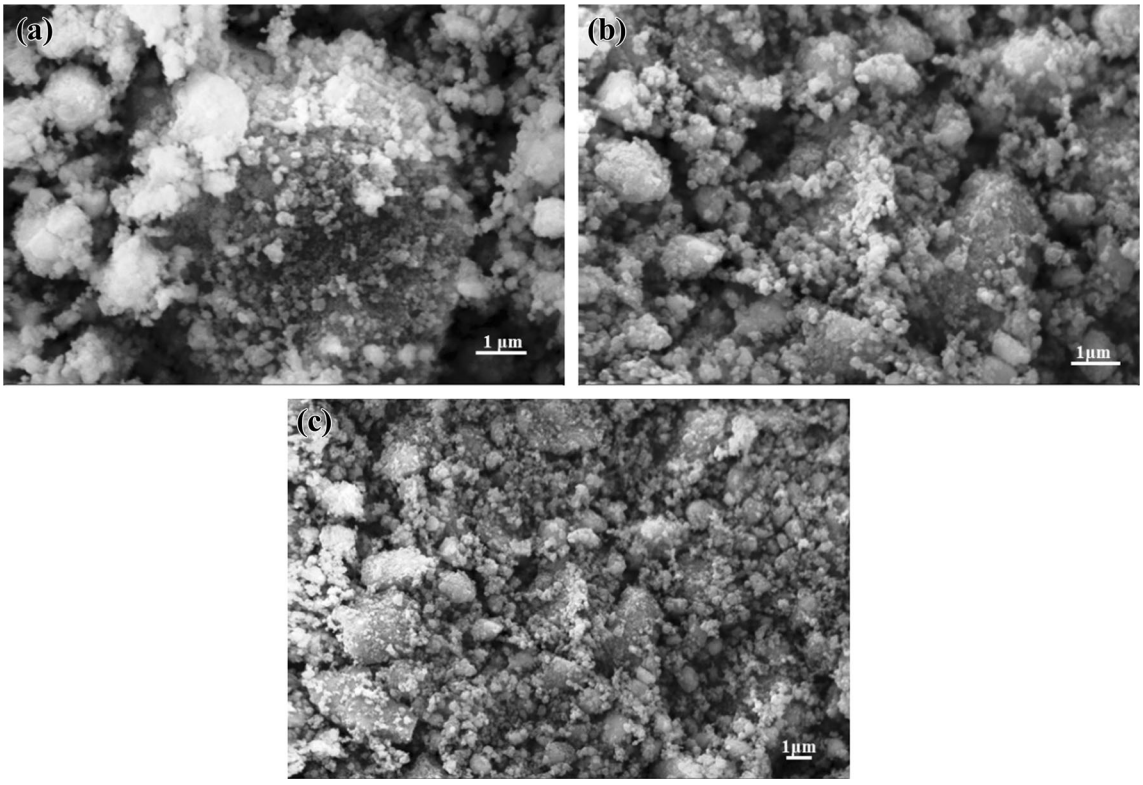

Fig. 2 SEM micrographs of synthesized compositions **a** 1LFP/3LMO, **b** 1LFP/1 LMO, and **c** 3LFP/1LMO

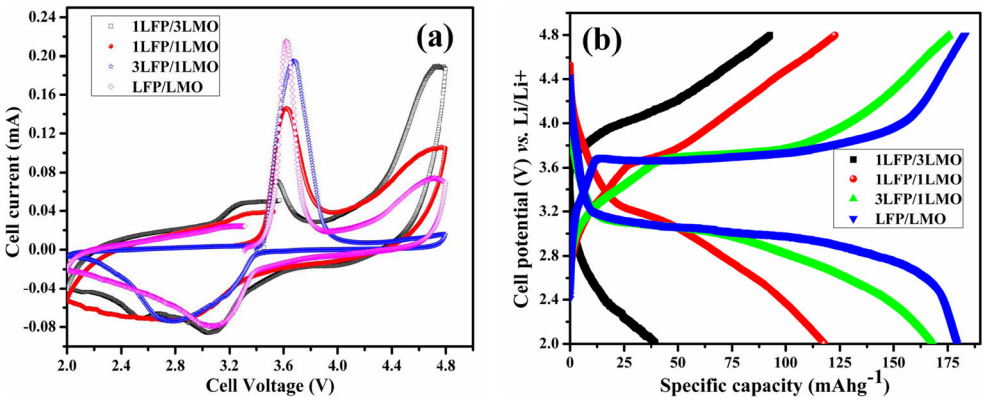

Fig. 3 **a** Cyclic voltammograms at 0.05 mV/s scan rate and **b** initial charge-discharge curves measured at 10 mA/g ($i_{charge} = i_{discharge}$) of the olivine-layered compositions at room temperature

arrangement of LFP/LMO. The low capacity of intermixed composites with a high mass ratio of LMO can be correlated to the high polarization effects arising due to the difference in electronic conductivity of layered LMO and olivine LFP. As only *layer arrangement* LFP/LMO and fully intermixed 3LFP/1LMO samples exhibit higher discharge capacities, therefore, these two samples have been selected for further electrochemical characterization.

Figure 4a, b displays the charging/discharging graphs of 3LFP/1LMO and LFP/LMO, respectively for 1st, 2nd, and 10th cycles at 20 mA/g. From Fig. 4a, it is evident that 3LFP/1LMO composition shows slightly lower capacity at the 10th cycle. However, LFP/LMO compositions (Fig. 4b) display nearly same capacities for 1st, 2nd, and 10th cycles. Therefore, the obtained results suggest that the structural stability of LFP/LMO is much better for repeated charge/discharge cycling. Figure 4c, d reveals the charging/discharging graphs for the 1st cycle of the prepared compositions for various current *densities* from 10 to 500 mA/g. It has been observed that LFP/LMO composition (Fig. 4d) exhibits the highest capacity for all values of current *density* while 3LFP/1LMO composition (Fig. 4c) delivers an initial discharge capacity of 169 (± 5) mA h/g at 10 mA/g with ~ 44% capacity retention at 0.5 A/g. These results indicate that among the best samples, layered arrangement of LFP and LMO, i.e., LFP/LMO, proves to be better electrode material.

Figure 5a displays rate capability of 3LFP/1LMO and LFP/LMO compositions for various current *densities* that lie between 10 and 500 mA/g. The composition LFP/

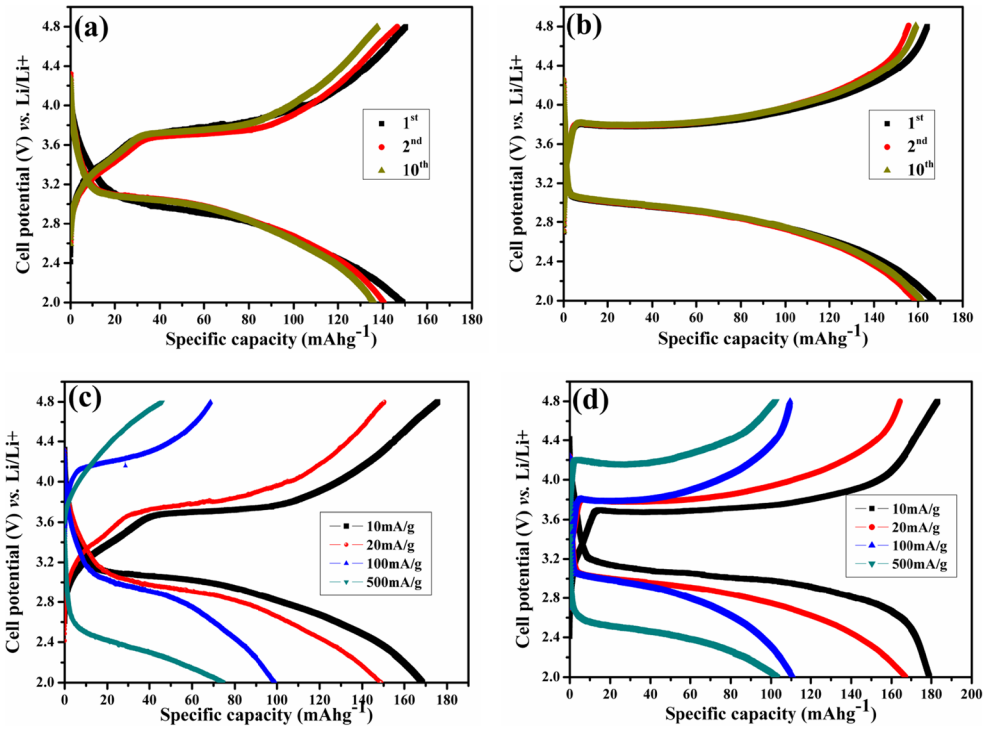

Fig. 4 Charge/discharge curves of **a** 3LFP/1LMO and **b** LFP/LMO for 1st, 2nd, and 10th cycles at 20 mA/g and 1st charging/discharging curves measured at different current *densities* for **c** 3LFP/1LMO and **d** LFP/LMO

LMO has been found to exhibit the highest capacity measured at 10–500 mA/g. The 1st discharge capacity value for 3LFP/1LMO and LFP/LMO was observed around 169 ± 5 and 178 ± 5 mA h/g, respectively at 10 mA/g. All discharge capacities values at various current *densities* w.r.t to 10 mA/g are listed in Table 1. *Layer arrangement*, i.e., LFP/LMO, shows the highest value of specific discharge capacity with ~ 57% capacity retention at 0.5 A/g current density. The discharge capacity loss at high values of current *density* is due to high polarization effects which slow down the diffusion of lithium ions in the prepared composition. Figure 5b shows the cycling capability of the prepared compositions at 20 mA/g current density for 100 charging-discharging cycles. It can be observed from Fig. 5b and Table 1 that LFP/LMO exhibits a discharge capacity 167 (± 5) mA h/g with ~ 98% capacity retention up to 100 charging/discharging cycles at 20 mA/g. Figure 5c shows discharge voltage plateau (as delivered by the synthesized dual composite) as a function of charge/discharge current density. As observed from Fig. 5c, the discharge potential value remains same at lower current density for 3LFP/1LMO and LFP/LMO configurations. However, at higher current *density*, layered arrangement shows slightly better discharge voltage value as compared to the 3LFP/1LMO arrangement. These results can be correlated to the enormous polarization effects of the composites which hindered diffusion of lithium ion. Figure 5d shows the Ragone plot of pristine 3LFP/1LMO and LFP/LMO. Figure 5d indicates that LFP/LMO cathode material retains its energy storage capacity. Even at 16-min charge/discharge rate, 3LFP/1LMO cathode gives the high energy density (~ 253 W h/kg) and power density (~ 947 W/kg).

Table 1 Electrochemical performance of synthesized compositions at different current densities and cycling capability at 20 mA/g

Samples	R^a (%)				20 mA/g (± 5) (mA h/g)		
	10 mA/g (± 5) (mA h/g)	20 mA/g	0.1 A/g	0.5 A/g	1st	100th	R^b (%)
3LFP/1LMO	169	88.3	58.8	44.2	149	145	97.3
LFP/LMO	178	93.2	62.1	57.4	167	164	98.2

[a] Capacity holding percentage of compositions at different current densities w.r.t to 10 mA/g

[b] Capacity holding percentage of compositions as compared to the 1st cycle at 20 mA/g

EIS and electrochemical performances at high and low temperatures

Electrochemical impedance spectroscopy was performed *for all the fresh cells* at room temperature for all the

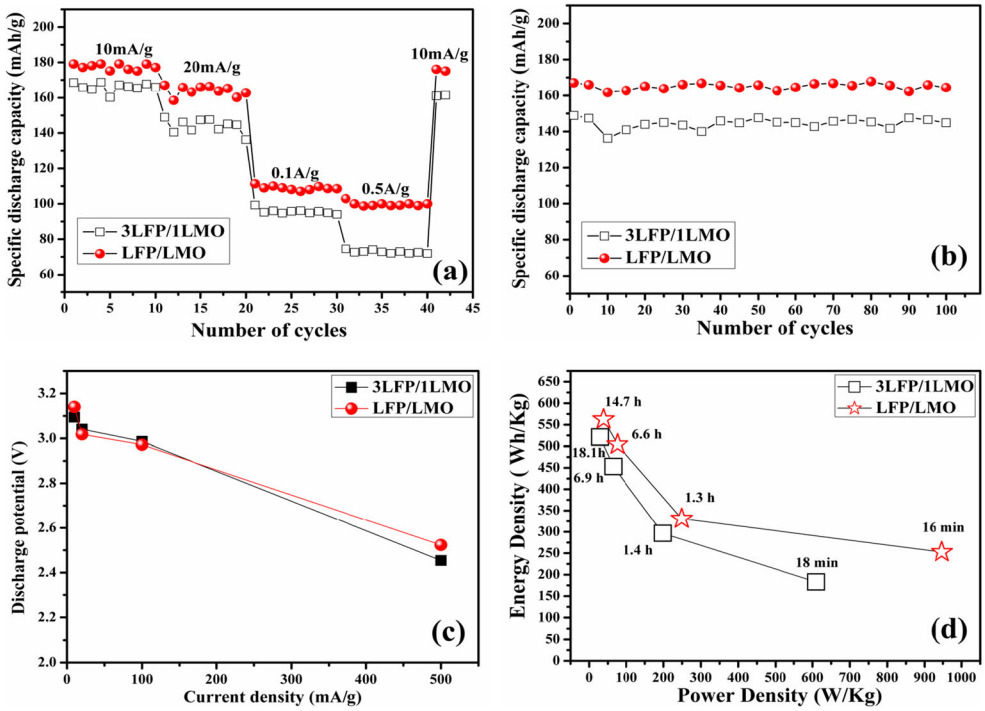

Fig. 5 Performance of 3LFP/1LMO and LFP/LMO compositions: **a** Discharge rate capability for various current *densities* ($i_{charge} = i_{discharge}$), **b** cycling stability for 100 charging/discharging cycles measured at 20 mA/g. **c** Discharge plateau as a function of discharge rate and **d** Ragone plot of energy density versus power density

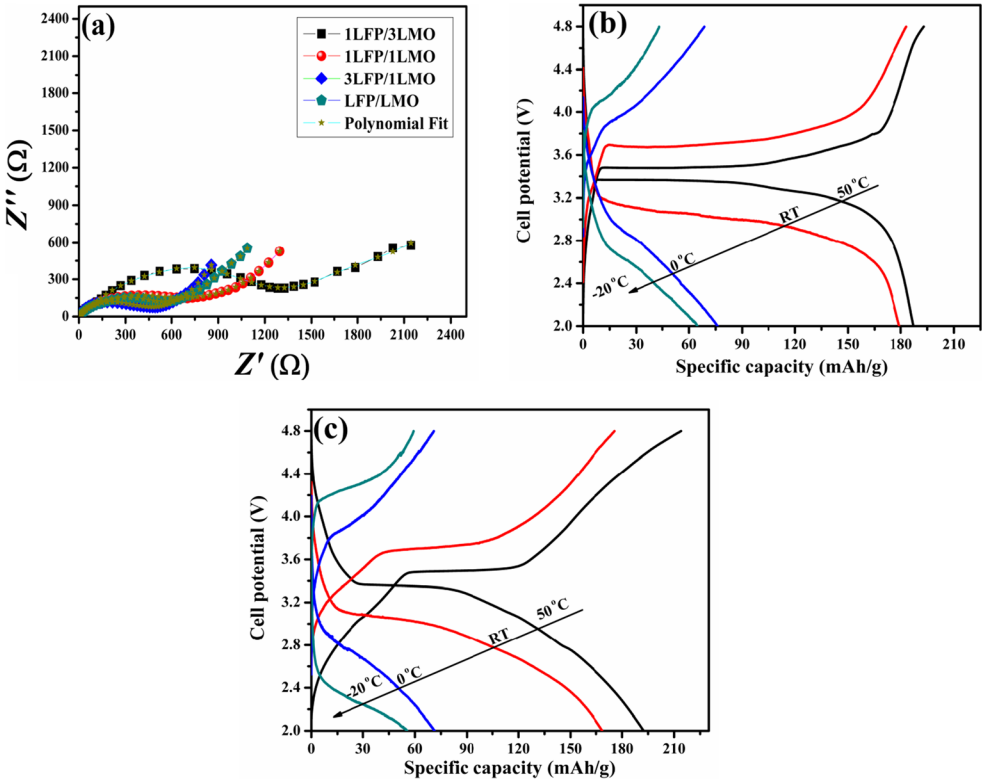

Fig. 6 Electrochemical impedance curves of prepared compositions observed for AC pulse of 5 mV amplitude **a** and comparison of charge/discharge performances of LFP/LMO (**b**) and 3LFP/1LMO (**c**) for different temperatures measured at 10 mA/g

synthesized compositions to analyze the changes in electrode impedance. Figure 6a demonstrates the EIS curves of all the configuration in 10 mHz–10 kHz frequency range using an AC pulse with 5 mV amplitude. It can be observed from Fig. 6a that among all the configurations, 1LFP/3LMO possesses the highest R_{ct} because of the presence of a high ratio of LMO. 1LFP/1LMO sample shows slightly higher charge transfer as compared to 3LFP/1LMO and LFP/LMO configurations which deliver nearly same R_{ct}. This difference in charge transfer resistance can also be understood by the difference in electronic conductivity of $LiFePO_4$ and Li_2MnO_3.

High- and low-temperature galvanostatic charge/discharge performances were studied to examine the effect of temperature on the electrochemical properties of prepared samples. Figure 6b, c shows the charge/discharge performances of the LFP/LMO and 3LFP/LMO samples at various temperatures, respectively. It can be observed that 3LFP/LMO sample delivers discharge capacities 191 (± 5), 168 (± 5), 71 (± 5), and 55 (± 5) mA h/g at a current density of 100 mA/g. On the other hand, LFP/LMO powders deliver discharge capacities 187 (± 5), 178 (± 5), 76 (± 5), and 64 (± 5) mA h/g at 50 °C, RT, 0 °C, and − 20 °C, respectively, at the same rate. Therefore, LFP/LMO composition exhibit better electrochemical performance at high as well low temperature which proves its feasibility for commercialization.

Conclusions

A series of olivine-layered composites, i.e., $LiFePO_4$-Li_2MnO_3, were successfully synthesized in the form of a single monolithic electrode and *layer arrangement*. XRD results show the existence of olivine as well as layered structure. Microstructural investigations reveal that all the samples possess nearly same morphology with a combination of smaller as well as bigger grains. Among all the arrangements, LFP/LMO layered arrangement shows the best cycling stability and rate capability *which can be attributed to low charge transfer resistance of the layered arrangement originated because of the electrode structure. The direct contact of relatively more conducting $LiFePO_4$ with the current collector allows better lithium-ion kinetics as compared to mixed arrangements.* LFP/LMO exhibits a discharge capacity around 178 ± 5 mA h/g measured at 10 mA/g current density. LFP/LMO sample also indicates better performance at both the low and high *temperatures*.

References

1. Denis YW, Yanagida K, Kato Y, Nakamura HI (2009) Electrochemical activities in Li2MnO3. J Electrochem Soc 156(6):A417–A424

2. Lin J, Mu D, Jin Y, Wu B, Ma Y, Wu F (2013) Li-rich layered composite Li[Li0.2Ni0.2Mn0.6]O2 synthesized by a novel approach as cathode material for lithium ion battery. J Power Sources 230:76–80
3. Saroha R, Gupta A, Panwar AK (2017) Electrochemical performances of Li-rich layered-layered Li_2MnO_3-$LiMnO_2$ solid solutions as cathode material for lithium-ion batteries. J Alloys Compd 696:580–589
4. Dong X, Xu Y, Xiong L, Sun X, Zhang Z (2013) Sodium substitution for partial lithium to significantly enhance the cycling stability of Li_2MnO_3 cathode material. J Power Sources 243:78–87
5. Zhang Q, Hu X, Zhan D, Peng T (2013) Pyrolysis of in situ formed lithium stearate: an effective strategy to activate Li_2MnO_3. Electrochim Acta 113:424–432
6. Yang G, Wang L, Wang J, Yan W (2017) Fabrication and formation mechanism of Li2MnO3 ultrathin porous nanobelts by electrospinning. Ceram Int 43(1, Part A):71–76
7. Torres-Castro L, Shojan J, Julien CM, Huq A, Dhital C, Paranthaman MP, Katiyar RS, Manivannan A (2015) Synthesis, characterization and electrochemical performance of Al-substituted Li_2MnO_3. Mater Sci Eng B 201:13–22
8. Kim D, Gim J, Lim J, Park S, Kim J (2010) Synthesis of xLi$_2$MnO$_3$·(1−x)LiMO$_2$ (M= Cr, Mn, Co, Ni) nanocomposites and their electrochemical properties. Mater Res Bull 45(3):252–255
9. Park C, Kim S, Mangani IR, Lee J, Boo S, Kim J (2007) Synthesis and materials characterization of Li_2MnO_3–$LiCrO_2$ system nanocomposite electrode materials. Mater Res Bull 42(7):1374–1383
10. Kim S, Kim C, Noh JK, Yu S, Kim SJ, Chang W, Choi WC, Chung KY, Cho BW (2012) Synthesis of layered–layered xLi2MnO3·(1−x)LiMO2 (M= Mn, Ni, Co) nanocomposite electrodes materials by mechanochemical process. J Power Sources 220:422–429
11. Sun Y, Shiosaki Y, Xia Y, Noguchi H (2006) The preparation and electrochemical performance of solid solutions $LiCoO_2$–Li_2MnO_3 as cathode materials for lithium ion batteries. J Power Sources 159(2):1353–1359
12. Rossouw MH, Thackeray MM (1991) Lithium manganese oxides from Li2MnO3 for rechargeable lithium battery applications. Mater Res Bull 26(6):463–473
13. Zhao W, Xiong L, Xu Y, Xiao X, Wang J, Ren Z (2016) Magnesium substitution to improve the electrochemical performance of layered Li_2MnO_3 positive-electrode material. J Power Sources 330:37–44
14. Tabuchi M, Nabeshima Y, Takeuchi T, Tatsumi K, Imaizumi J, Nitta Y (2010) Fe content effects on electrochemical properties of Fe-substituted Li_2MnO_3 positive electrode material. J Power Sources 195(3):834–844
15. Mori D, Sakaebe H, Shikano M, Kojitani H, Tatsumi K, Inaguma Y (2011) Synthesis, phase relation and electrical and electrochemical properties of ruthenium-substituted Li_2MnO_3 as a novel cathode material. J Power Sources 196(16):6934–6938
16. Cheng M, Zhu K, Yang L, Zhu L, Li Y, Tang W (2016) Electrochemical properties of Li_2MnO_3 nanowires with polycrystalline and monocrystalline states. J Alloys Compd 686:496–502
17. Padhi AK, Nanjundaswamy K, Goodenough J (1997) Phospho-olivines as positive-electrode materials for rechargeable lithium batteries. J Electrochem Soc 144(4):1188–1194
18. Lin X, Wu K, Shao L, Shui M, Wang D, Long N, Ren Y, Shu J (2014) In situ growth of coiled carbon nanotubes on $LiFePO_4$ as high performance lithium storage material. J Electroanal Chem 726:71–76
19. Lv YJ, Su J, Long YF, Cui XR, Lv XY, Wen YX (2014) Effects of ball-to-powder weight ratio on the performance of $LiFePO_4$/C prepared by wet-milling assisted carbothermal reduction. Powder Technol 253:467–473
20. Qin G, Ma Q, Wang C (2014) A porous C/LiFePO 4/multiwalled carbon nanotubes cathode material for lithium ion batteries. Electrochim Acta 115:407–415
21. Huang K-P, Fey GT-K, Lin Y-C, Wu P-J, Chang J-K, Kao H-M (2017) Magnetic impurity effects on self-discharge capacity, cycle performance, and rate capability of $LiFePO_4$/C composites. J Solid State Electrochem 21(6):1767–1775
22. Swiderska-Mocek A, Lewandowski A (2017) Kinetics of Li-ion transfer reaction at $LiMn_2O_4$, $LiCoO_2$, and $LiFePO_4$ cathodes. J Solid State Electrochem 21(5):1365–1372
23. Cai G, Fung KY, Ng KM, Chu KL, Hui K, Xue L (2016) Critical assessment of particle quality of commercial $LiFePO_4$ cathode material using coin cells—a causal table for lithium-ion battery performance. J Solid State Electrochem 20(2):379–387
24. Chiu Huang CK, Huang H-YS (2015) Critical lithiation for C-rate dependent mechanical stresses in LiFePO4. J Solid State Electrochem 19(8):2245–2253
25. Mathew V, Gim J, Kim E, Alfaruqi MH, Song J, Ahn D, Im WB, Paik Y, Kim J (2014) A rapid polyol combustion strategy towards scalable synthesis of nanostructured $LiFePO_4$/C cathodes for Li-ion batteries. J Solid State Electrochem 18(6):1557–1567
26. Buzlukov A, Gerbaud G, Bourbon C, Hediger S, De Paëpe G, Patoux S, Bardet M (2013) Application of 7 Li NMR to characterize the evolution of intercalated and non-intercalated lithium in LiFePO 4-based materials for Li-ion batteries. J Solid State Electrochem 17(5):1421–1427
27. Whitacre J, Zaghib K, West W, Ratnakumar B (2008) Dual active material composite cathode structures for Li-ion batteries. J Power Sources 177(2):528–536
28. Saroha R, Panwar AK, Sharma Y (2017) Physicochemical and electrochemical performance of LiFe1−xNixPO4 ($0 \leq x \leq 1.0$) solid solution as potential cathode material for rechargeable lithium-ion battery. Ceram Int 43(7):5734–5742
29. Saroha R, Panwar AK, Sharma Y, Tyagi PK, Ghosh S (2017) Development of surface functionalized ZnO-doped $LiFePO_4$/C composites as alternative cathode material for lithium ion batteries. Appl Surf Sci 394:25–36

Accepted Manuscript

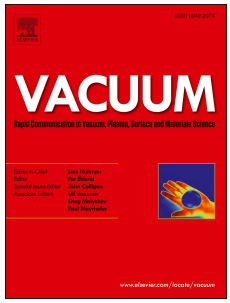

Electrophoretically deposited nanostructured PdO thin film for room temperature amperometric H_2 sensing

Kamal Arora, Nitin K. Puri

PII: S0042-207X(17)31860-2

DOI: 10.1016/j.vacuum.2018.04.023

Reference: VAC 7928

To appear in: *Vacuum*

Received Date: 15 December 2017

Revised Date: 8 April 2018

Accepted Date: 12 April 2018

Please cite this article as: Arora K, Puri NK, Electrophoretically deposited nanostructured PdO thin film for room temperature amperometric H_2 sensing, *Vacuum* (2018), doi: 10.1016/j.vacuum.2018.04.023.

This is a PDF file of an unedited manuscript that has been accepted for publication. As a service to our customers we are providing this early version of the manuscript. The manuscript will undergo copyediting, typesetting, and review of the resulting proof before it is published in its final form. Please note that during the production process errors may be discovered which could affect the content, and all legal disclaimers that apply to the journal pertain.

ACCEPTED MANUSCRIPT

Electrophoretically deposited nanostructured PdO thin film for room temperature amperometric H_2 sensing

Kamal Arora[1] and Nitin K. Puri[1*]

[1] Advanced Sensor Laboratory, Department of Applied Physics, Delhi Technological University, Bawana road, Delhi 110042, India

Abstract

In the present work, economical and facile hydrothermal sol-gel method is employed for the synthesis of palladium oxide (PdO) nanoparticles. Uniform thin film of PdO nanoparticles are fabricated using Electrophoretic deposition (EPD) set-up. The crystal structure, surface framework, shape and size of PdO nanoparticles are determined using X-ray diffraction spectroscopy (XRD), Transmission electron microscopy (TEM) and scanning electron microscopy (SEM) respectively. An optical band-gap of 1.9 eV is observed using UV-Visible (UV-Vis) spectroscopy. Amperometric sensing of hydrogen gas is studied using PdO thin film as working electrode and characteristics properties have been obtained for different hydrogen (H_2)/Argon (Ar) gas concentrations using potentiostat/galvanostat Autolab instrument at room temperature. The PdO nanoparticles based amperometric hydrogen gas sensor shows high sensitivity of 0.222 μA/%H_2 with fast response and recovery time.

Keywords: Electrochemical sensor, Hydrogen sensor, Amperometry, Palladium oxide nanoparticles, Metal oxides

*corresponding author.

Email address: nitinkumarpuri@dtu.ac.in, nitinpuri2002@yahoo.co.in, nitin.phy@dce.edu

1. Introduction

H_2 is a clean and renewable energy carrier which is used extensively in several petrochemical, medical and aerospace industries. It is highly flammable in nature and could be devastating for the surrounding if its concentration exceeds 4% in air. Thus, it is necessary to fabricate a highly stable, selective and sensitive sensor which can trace H_2 even in small concentrations at room temperature [1].

Out of different types of sensors available in the market today, two sensors have attracted a widespread attention of the researchers and industries due to their peculiar merits over others i.e. conductometric and electrochemical sensors. Conductometric sensors works on the principle of change in conductivity on adsorption of gases on its surface with time, but low relative humidity (RH) and high temperature are required for its efficient working which is in contrast with electrochemical sensors which can detect with high sensitivity and selectivity at room temperature [2-3]. Amperometric and potentimetric are the two classifications of electrochemical sensors which differ in their working and sensing response. Potentiometric sensors show logarithmic response that lacks accuracy, whereas, amperometric sensor demonstrates precise and calibrated linear sensing response [4].

Many wide band-gap metal oxides such as Tin oxide (SnO_2), Indium oxide (In_2O_3) and Zinc oxide (ZnO) have been extensively researched in application for Hydrogen (H_2) gas sensing along with other transition metal oxide elements, as they have distinctive as well as favorable electronic and physical properties [5-8].

Nevertheless, these pristine metal oxides sensor works optimally only at high temperatures and low relative humidity. Also, standalone metal oxides sensor have low sensitivity for hydrogen, but the adsorption rate of H_2 on their surface can be

enhanced by doping them with highly electroactive elements such as palladium (Pd) and platinum (Pt) due to the process of hydrogen spillover [9-11]. Pure Pd metal is irreversibly poisoned by gases present in the atmosphere and also it gets damaged by hydrogen embrittlement process on exposure to H_2. On the other hand, palladium oxide (PdO) is protected by the cover of oxide layer and it does not get contaminated due to its high working temperature [12-13]. Hence, PdO nanoparticles are more favorable candidates for H_2 sensing as compared to pure Pd. PdO is a hole majority carrier (p-type) semiconductor and its band-gap lies in range of visible light. Okamoto et. al. found that the optical band-gap of PdO lies in the range of 1 to 2 eV with a hole mobility of about 17 cm V^{-1} s^{-1} [14].

The electrophoretic deposition (EPD) is a versatile and economical technique for the fabrication of uniform coatings or films of metal oxides, graphene along with their composites on conductive substrates as compared to other conventional methods because it consists of simple, low cost apparatus and allows the usage of desired shape of the substrate [15]. EPD gives control over thickness of the film by varying the deposition time and applied potential. Yet, deposition of films depends on two factors i.e. characteristics of the liquid suspension and EPD processing parameters. The thickness and uniformity depends not only on deposition time and applied potential but also on the dielectric constant, viscosity, conductivity and stability of colloidal suspension [16-17]. Thus, these parameters need to be adjusted to achieve desired thickness of the film.

Nanostructured PdO and its composite with other metal oxides have been used as a sensing element for methane, toluene, ethanol and carbon monoxide conductometric gas sensing. They showed high sensitivity on comparison with pristine metal oxides, but the working temperature of the sensors exceeds 200^{o}C [18-24].

Few research works have been reported using nanostructured PdO and its thin films for sensing H_2 though conductometric sensor. They demonstrated high selectivity and sensitivity for H_2, but the working temperature of these sensors are high [25-26]. Sipra Choudhury et. al. showed room temperature H_2 sensing using Langmuir-Blodgett precursor synthesized PdO nanoparticles layered thin film by employing sophisticated and costly KSV 5000 instument [27]. However, room temperature amperometric H_2 sensing by PdO nanoparticles synthesized by cost effective sol-gel hydrothermal method has not been reported yet.

In the present work, PdO nanoparticles have been synthesized using economical and facile hydrothermal sol-gel method. Thin film of PdO nanoparticles have been fabricated on ITO glass substrates by electrophoretic deposition process. PdO/ITO thin film is employed as working electrode (WE) in indigenously fabricated electrochemical cell which is used for amperometric H_2 gas sensing at 25 ^{o}C.

2. Experimental work

2.1 Materials used

Palladium chloride ($PdCl_2$), ethanol (C_2H_5OH) and hydrochloric acid (HCl) are purchased from Sigma Aldrich, Merck and Fisher Scientific respectively. These chemicals are used in the synthesis of PdO nanoparticles and they belong to AR grade purity (~99.9 %).

2.2 Synthesis of PdO nanoparticles

$PdCl_2$ is dissolved in C_2H_5OH to form 0.1 Molar solution, 1 v/v % HCl is added to solution drop wise to enhance the solubility of $PdCl_2$ in the solution and a transparent brown colored solution is obtained after stirring for 30 minutes. The resultant solution is allowed to age for 24 hours. The solution is transferred to

Teflon hydrothermal vessel and allowed to be heated at 200 ^{o}C. Thereafter, brown colored powder is obtained which is consequently washed with D.I. water and annealed at 600 ^{o}C to remove organic as well chloride ions impurities that yielded a black colored fine powder. X-ray diffraction (XRD), transmission electron microscopy (TEM), and ultraviolet-Visible (UV-Vis) absorption spectroscopy is used to detect crystal structure, shape, size and optical band-gap of synthesized black powder. Data obtained from these analytical studies of as synthesized black powder confirmed the creation of PdO nanoparticles.

2.3 Fabrication of PdO thin film

Thin films of PdO nanoparticles are deposited on (5 mm x 10 mm) ITO coated glass substrates using electrophoretic deposition (EPD) process at various constant electrophoretic deposition potential (10, 15, 20, 25, 30 and 35 Volts) respectively with deposition time of 2 minutes. ITO substrate and platinum (Pt) rod serves the role of anode and cathode respectively, these electrodes are placed in a 20 mL glass beaker at separation of 1 cm. 0.1 g of PdO powder is dispersed in 10 mL of ethanol to obtain electrolyte solution. Consequently, 100 µL of magnesium nitrate [$Mg(NO_3)_2$. $6H_2O$] is added to the solution as a dispersant to improve the conductivity and mobility of the ions present in the electrolyte. These processing parameters are experimentally calibrated to obtain uniform coating of 1µm thick film on the surface of the substrate. Also, uniformity of the film gets distorted on modifying the deposition time and applied potential for the given concentrations of colloidal suspension.

2.3 Amperometric sensing setup

The Amperometric sensing setup contains an indigenously fabricated three electrodes electrochemical cell which is connected to Potentiostat Autolab instrument (Fig 1).

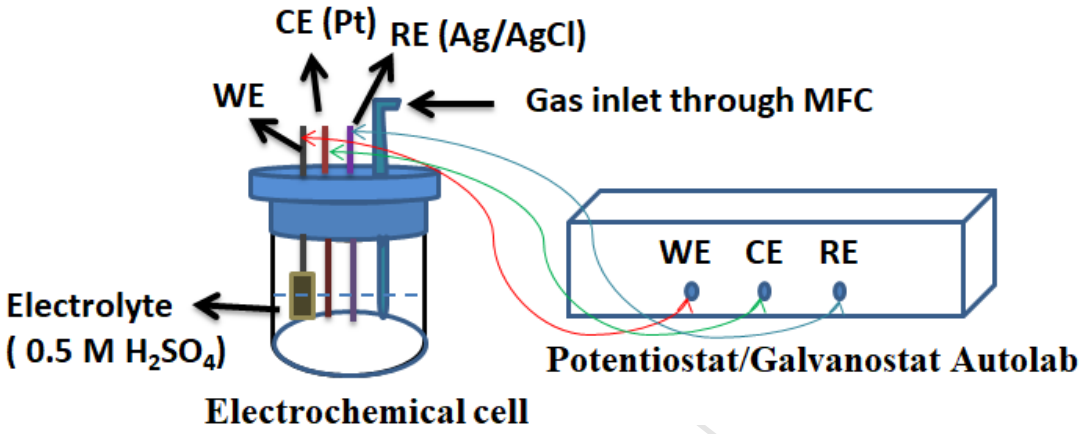

Fig. 1. Electrochemical gas sensing setup

PdO thin film/ITO substrate is used as working electrode (WE), whereas platinum rod act as a counter electrode (CE) and Nafion coated Silver/Silver chloride (Ag/AgCl) rod is employed as reference electrode (RE). These three electrodes are dipped into 0.5 M Sulphuric acid (H_2SO_4) electrolyte and placed inside a 30 mL glass beaker. The electrochemical cell is sealed with Teflon cylindrical disk which consist of circular inlets for introduction of electrodes and gas. The cell is attached to the ALICAT gas mix mass flow controller (MFC) through Teflon pipes.

3. Results

3.1 X-ray Diffraction study

XRD spectroscopy is performed using PANalytical (Germany), X-ray diffractometer. It can be inferred after comparing with published JCPDS data (CAS number: 750584) that the most intense peak at 33.8^o corresponds to (101) plane, whereas other moderately intense peaks at 42^o, 54.7^o, 60.12^o, 61^o and 71.3^o

represent (110), (112), (103), (200) and (202) of tetragonal PdO (t-PdO) respectively (Fig.2). The average crystallite size of t-PdO can be calculated using Scherrer's formula [Eq. 1] [15] and it is found to be equal to 14 nm.

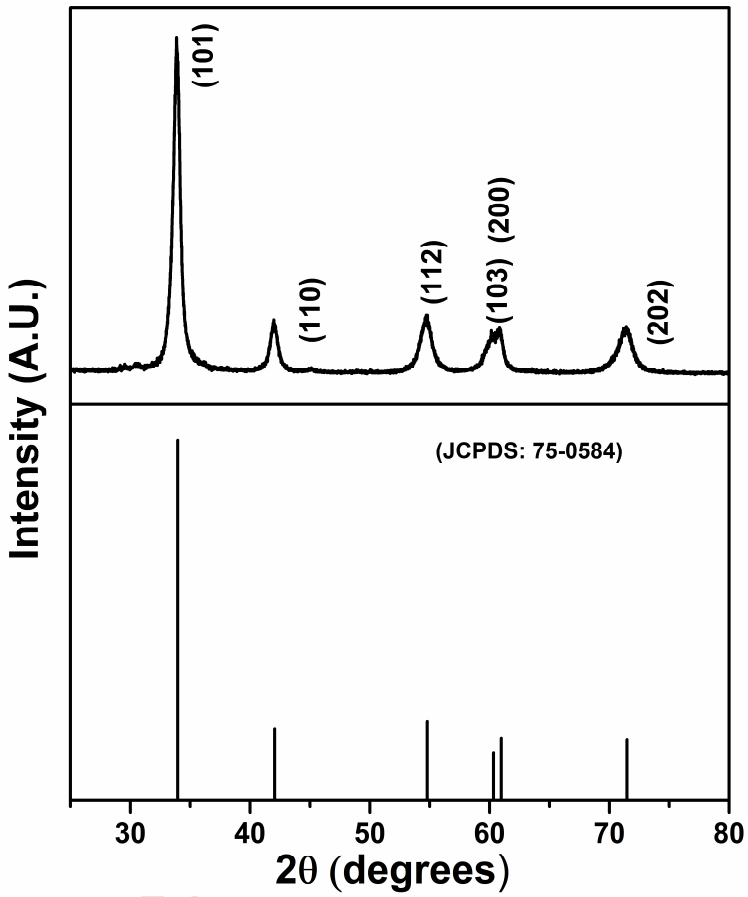

Fig. 2. XRD graph of PdO nanoparticles

$$t = \frac{0.9\lambda}{\beta \cos\theta} \qquad \text{(Eq. 1)}$$

Where, β is the FWHM (Full width half maxima), t is average crystallite size, λ is wavelength and θ is the angle having maximum intensity.

Thus, the XRD analysis confirms the formation of t-PdO crystal structure with average crystallite size of 14 nm.

3.2 Transmission electron microscopy

The size and shape of the particles has been observed by TEM images using JEOL (USA) 2100F, Transmission electron microscope (Fig. 3). The particles size ranges from 20 to 80 nm are visible in TEM image (Fig 3(a)), with high density of nanoparticles with size 20-40 nm comparatively (Fig 3(d)). HRTEM image shows the presence of parallel crystallographic planes with interplanar spacing of 0.264 nm which represents the (101) planes of t-PdO (Fig 3(b)), whereas presence of concentric rings formed by dots correspond to (101), (112), (200) and (202) planes

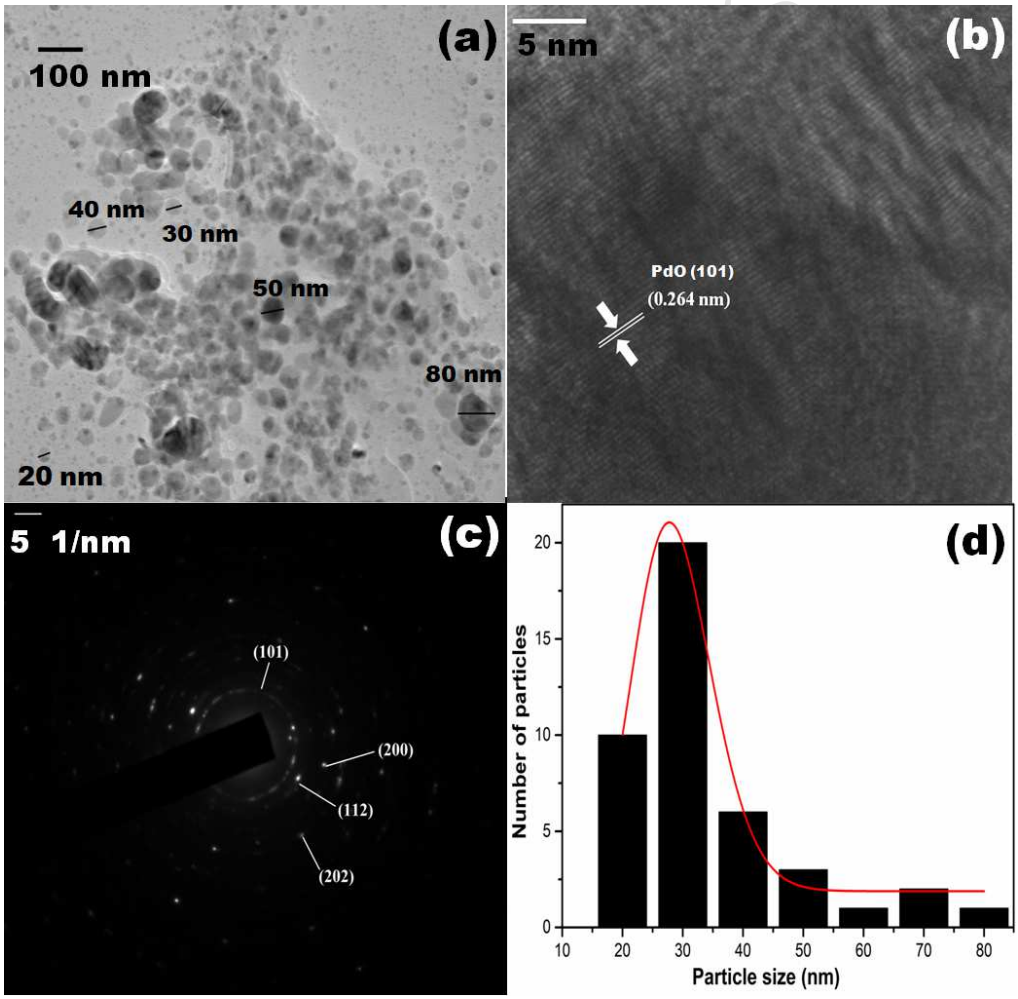

Fig. 3. (a) TEM image (b) HRTEM image (c) SAED image (d) Particle size distribution

of polycrystalline t-PdO (CAS number: 750584). Thus, TEM validates the presence of t-PdO in as-synthesized black powder and coincides with the XRD study.

3.3 UV-Vis spectroscopy

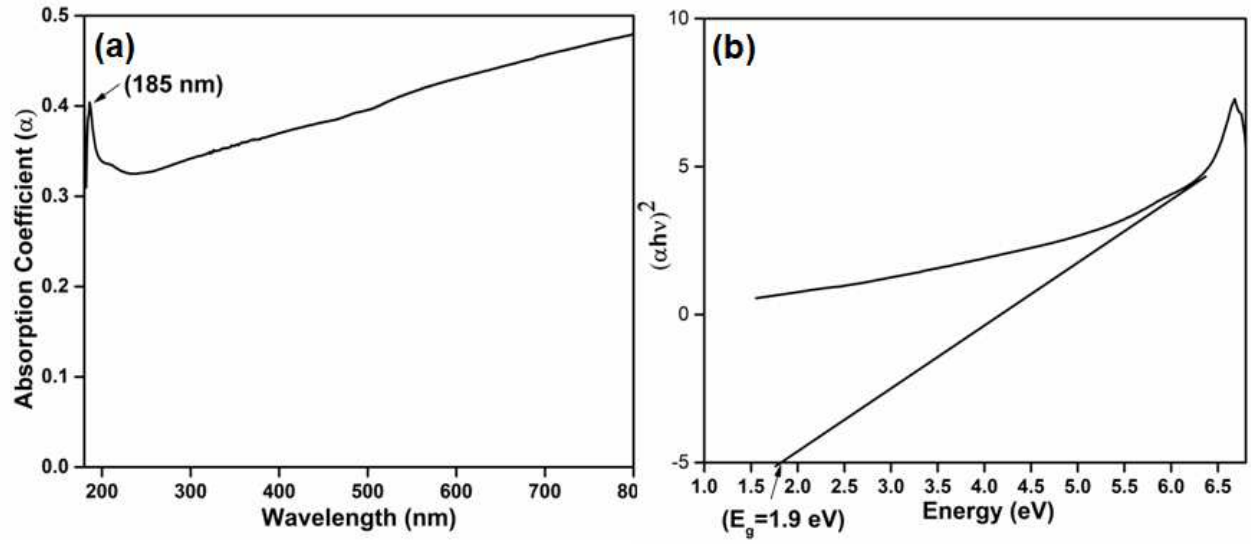

Fig. 4. (a) UV-Vis absorption spectra (b) Tauc plot

In UV-Vis absorption spectra obtained using LAMBDA 950 UV/Vis Spectrophotometer, PerkinElmer (USA), an absorption peak can be observed at 185 nm, which corresponds to absorption of ultraviolet wavelength absorbed by PdO nanoparticles (Fig. 4(a)) [13].

The optical band-gap of PdO nanoparticles is found to be 1.9 eV by plotting $(\alpha h\nu)^2$ versus $h\nu$ (energy) (Fig. 4(b)), i.e. Tauc plot, where α is absorption coefficient, h is Planck's constant and ν is frequency of radiation.

3.4 Scanning electron microscopy

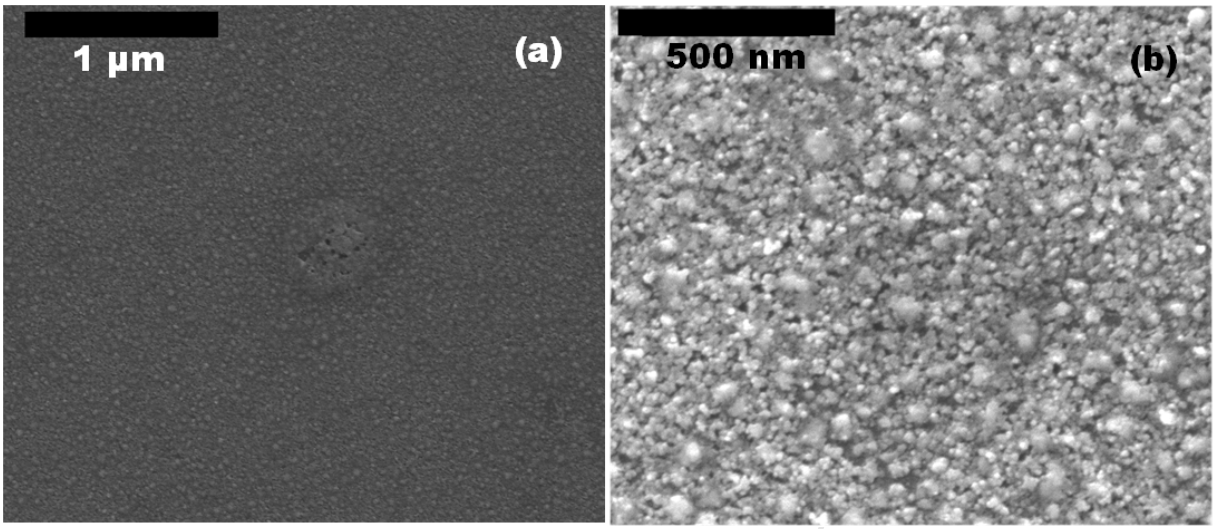

Fig. 5. SEM images with resolutions (a) 1µm (b) 500 nm

Fig. 5 shows SEM images of PdO nanoparticles thin film deposited on the surface of the ITO glass substrate at deposition voltage of 30 V, captured using MIRA II LMH from TESCAN (Czech Republic). The surface morphology is uniform and continuous with no visible cracks on the surface of the thin film. However, small voids can be seen on the surface within the particles which aid in adsorption of gas molecules. Particles are visible in 500 nm resolution images, but due to agglomeration, particles shape and size cannot be defined distinctly using SEM (Fig. 5(b)). Nevertheless, TEM images confirm the formation of spherical PdO nanoparticles with particle size ranging from 20 to 80 nm.

Figure 6 (a), (b), (c) and (d) represents the high resolution SEM images of PdO thin film deposited on ITO glass substrates at 10 V, 20 V, 25 V, 30 V and 35 V deposition voltages respectively with deposition time of 2 minutes. The particle density on surface of thin film deposited at 10 V is sparse, separated and randomly distributed. However, density increases comprehensively and surface gets more uniformly distributed with less separation as the deposition potential rises to 35 V (Fig. 6.). As the deposition potential rises, the concentration of nanoparticles

increases which results in linking of nanoparticles, identical to the process of nanojoining [28]. The aggregation of particles takes place at deposition potential of 30 V and number of gaps present on surface decreases with higher surface uniformity.

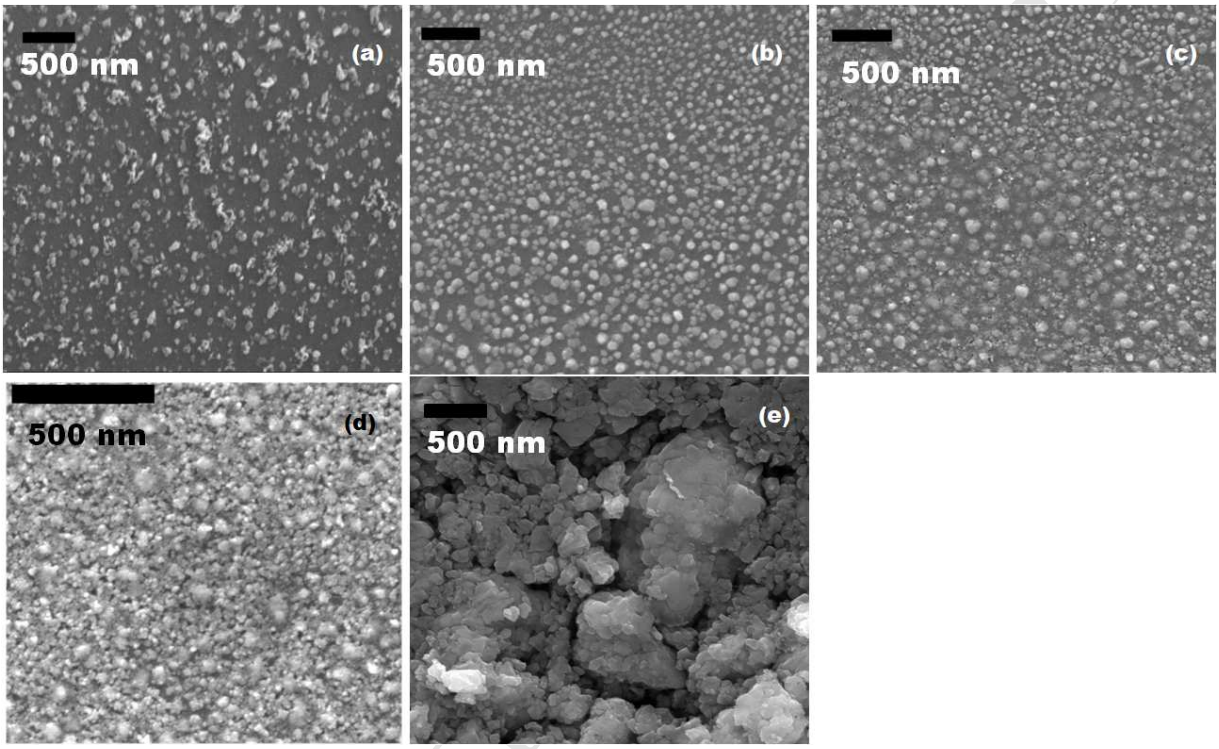

Fig. 6. SEM images of working electrodes deposited at Electrophoresis deposition potential of (a) 10 V, (b) 20 V, (c) 25 V, (d) 30 V and (e) 35 V

However, there is large amount of agglomeration present on surface of working electrode deposited at 35 V, which has resulted in the formation of large nanoclusters leading to less homogeneity and uniformity of surface morphology.

Additionally, the particles size changes on modifying the deposition potential; the particles are smaller in size at 10 V deposited electrode, whereas the particles gets bigger in nature as deposition potential reaches 30 V. This variation in the size of

the nanoparticles may be explained by the process of recrystallization of Pd^{2+} ions in the electrolyte solution. Also, there is a possibility that electrochemical reaction occurs simultaneously with electrophoretic process which leads to reduction of Pd^{2+} ions into Pd atoms which are then attached to nanoparticles present on the surface of working electrode [29].

3.4 Amperometric sensing study

H_2/Argon gas with different percentage concentrations is allowed to flow at rate of 80 mL/min into the Teflon sealed electrochemical gas sensing setup (Fig. 1) by passing it through mass flow controller (MFC) at 25 ^{o}C. The inlet for the gas is covered with fluorinated ethylene propylene (FEP) H_2 gas permeable membrane.

The amperometric sensing is performed by passing H_2 gas into the cell for 200 seconds and then stopped to allow it to recover. A constant potential of 1 V is applied across the electrodes through Metrohm (Netherland) Potentiostat Autolab instrument. The sensing response for 10 to 70 % H_2 gas is recorded and plotted using response curve (Fig. 6). There is fast rise in the magnitude of current during the duration of the flow of gas, which decays exponentially on gas cut off. Also, the magnitude of current increases as the percentage concentration of H_2 gas increases. This can be attributed to the redox reactions occurring at WE and CE as gas starts diffusing into the electrolyte (Eq. 2, 3 and 4) [27].

$$PdO(s) \rightarrow Pd(s) + \frac{1}{2}O_2^{2-} \qquad \text{(Eq. 2) (Reduction of PdO at WE)}$$

$$H_{2ads} - Pd(s) \rightarrow 2H^+ + 2e^- \qquad \text{(Eq. 3) (Oxidation of hydrogen at WE)}$$

$$\frac{1}{2}O_2^{2-} + 2H^+ + 2e^- \rightarrow H_2O(l) \qquad \text{(Eq. 4) (Reduction of oxygen at CE)}$$

Where ‘s’ is solid phase, ‘l’ is liquid phase and ‘ads’ is adsorbed species respectively.

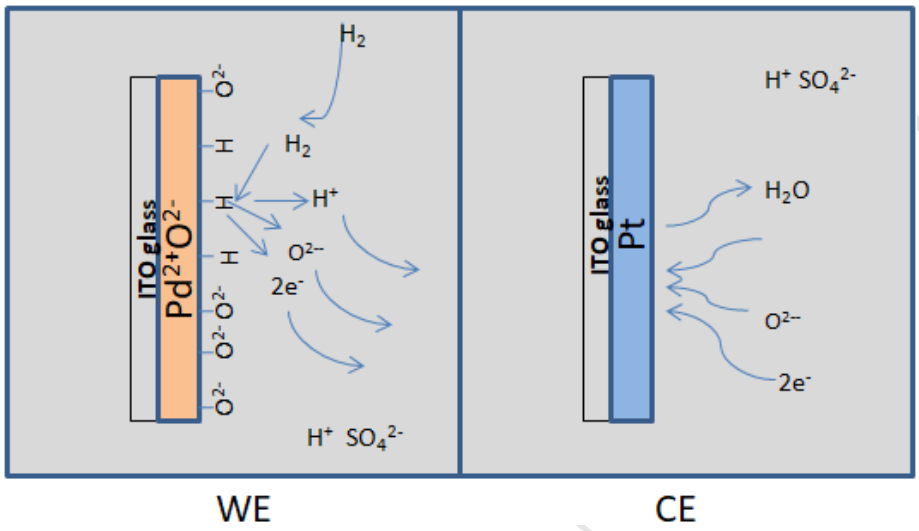

Scheme 1. Schematic representation of Amperometric H_2 sensing by PdO thin film

In the vicinity of H_2, PdO gets reduced to Pd which binds itself with H atom which results in release of peroxide ions and free electrons at the WE. The hydrogen ion (H^+) present in the electrolyte travels toward the CE and reacts with the peroxide ions on consuming free electrons resulting in water molecules. The exchange of free electrons from WE to CE completes the circuit and gives rise to increase in current at different concentration of hydrogen gas (Scheme 1). Electrochemical sensing response of PdO nanoparticles thin film deposited electrophoretically at deposition potential of 30 V is linearly calibrated and shows high sensitivity (S) of (0.222±0.008) μA/%H_2 with variance of 0.98602 (Fig. 7).

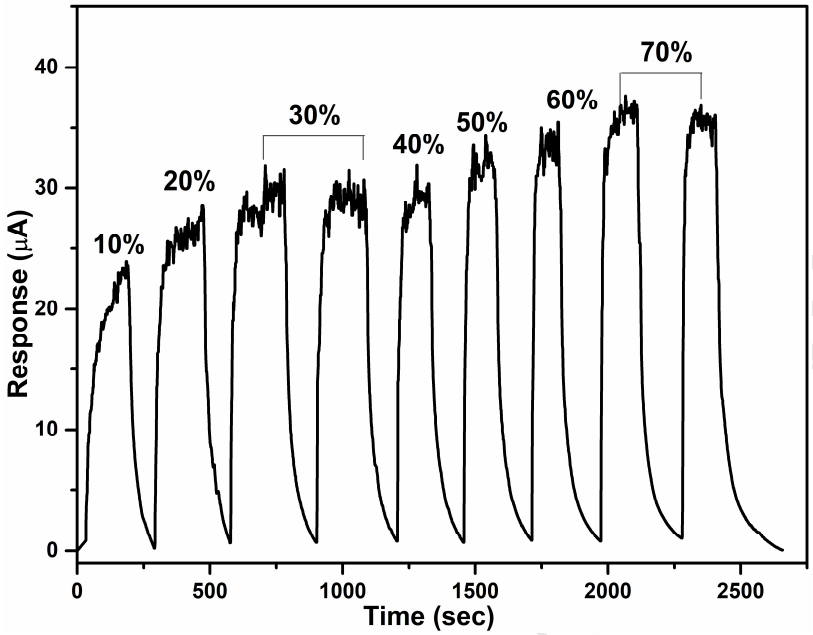

Fig. 7. Response curve

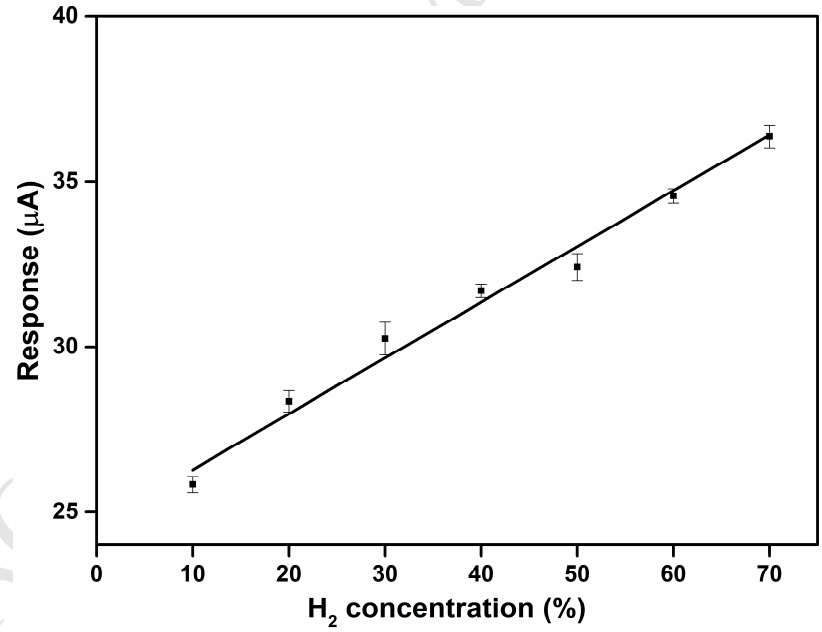

Fig. 8. Calibration plot of response curve

Limit of detection (LOD) of the fabricated sensor is defined as equal to (3S/N), where S is net sensitivity of the sensor and N is the noise and it is estimated to be

equal to 0.1% H_2 for this sensor. The fitting is done using linear regression equation y=24.59 + 0.222x, where x is H_2 gas concentration percentage and y is response current (μA) respectively.The response is fast and stable with quick recovery time. The steady state current time (t_{90}) ranges from 15 to 60 seconds for various percentage of H_2 gas.

3.5 Effect of deposition voltage on sensing response

The sensing response of working electrodes (WE) deposited electrophoretically at 10, 15, 20, 25, 30 and 35 Volts deposition potential respectively has been obtained for 10, 20 and 30 % H_2 gas concentration correspondingly (Fig. 9.). It can be observed that the sensing current rises linearly as the deposition potential is increased from 10 V to 30 V, thereafter it decreases as deposition voltage reaches 35 V. This increase in sensitivity may be attributed to increase in nanoparticles density and uniformity of thin film as deposition potential rises from 10 V to 30 V.

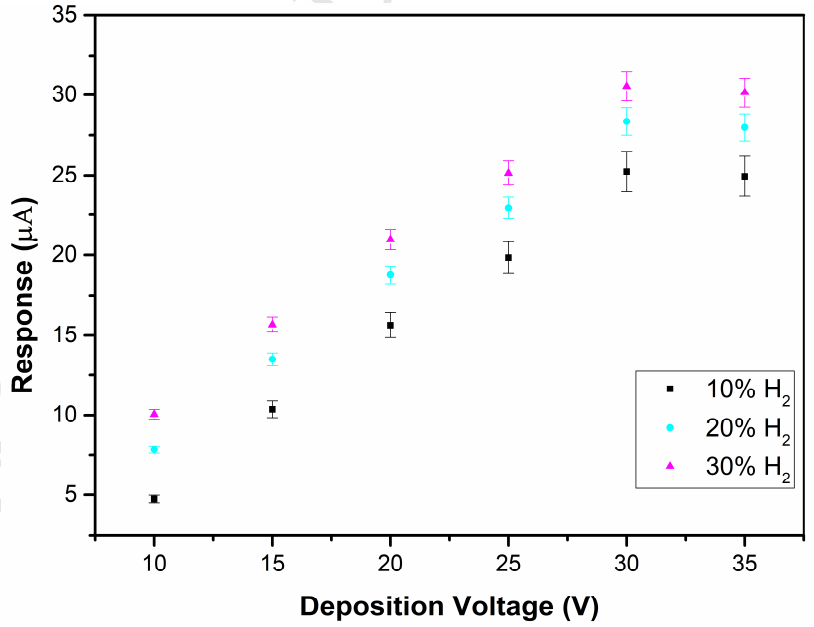

Fig. 9. Relationship between Sensing response and deposition potential

As the deposition potential reaches to 30 V, the aggregation within the particles enhances (Fig. 6.), which yields in formation of interstitial gaps and voids on the surface that favors as adsorption sites for H_2, thus leads to rise in the sensing response of WE.

When the deposition potential is increased to 35 V, the rate of deposition becomes too rapid which hinders the order and homogeneity of the film due to formation of large size nanoparticles that result in decrease in the sensitivity of the working electrode [30-31]. Additionally, at higher deposition voltage, there is reduction in porosity due to high packing density of deposited particles which drops the amount of voids present on the surface which may result in low sensing response [31].

The sensing characteristic of the proposed room temperature hydrogen gas sensor has been compared with the similar work reported in literature (table 1).

Gas	**Sensing Electrode**	**Electrolyte**	**LOD (%H_2)**	**References**
H_2	Pt/Carbon	5M H_2SO_4	-	[32]
H_2	Gold	9M H_2SO_4	-	[33]
H_2	Pt-Ag/AgCl	1M H_2SO_4	<1%	[34]
H_2-Air	Pt-Ag/AgCl	H_2SO_4	<0.2%	[35]
H_2-Nitrogen	Pt-Ag/AgCl	H_2SO_4	<0.4%	[35]
H_2-Ar	**PdO**	**0.5M H_2SO_4**	**<0.2%**	**Present work**

Table 1. Amperometric H_2 sensors based on liquid electrolytes

4. Conclusion

Room temperature amperometric hydrogen gas sensing by PdO nanoparticles have been demonstrated in this paper. PdO nanoparticles are synthesized using economical and facile hydrothermal sol-gel process. XRD spectra show formation

of tetragonal crystal structure of PdO which also agrees with the results reflected by SAED and HRTEM images. The size of nanoparticles ranges from 20 to 80 nm as observed from TEM images. Electrophoretic deposition technique is used to fabricate thin film of PdO nanoparticles on ITO glass substrate. PdO/ITO electrode deposited electrophoretically at deposition potential of 30 V shows high sensitivity of 0.222 μA/%H_2 at 25 ^oC with 0.1% H_2 limit of detection (LOD), sensing response ranging from 15 to 60 seconds and fast recovery time for 10 to 70 percent concentration of H_2. These studies show application of this sensor for low as well as high concentration H_2 sensing at room temperature. Pristine PdO nanoparticles can be doped or composited with hydrogen philic materials and various nanostructures of PdO can be employed to enhance the sensitivity and selectivity of the sensor.

Acknowledgements

We would thank Prof. Yogesh Singh, Vice chancellor, Delhi Technological University, Delhi, India for arranging the research facilities. We are grateful to Jawahar Lal University (JNU), New Delhi for assisting in characterization of materials. The financial support received from Department of Atomic Energy - Board of Research in Nuclear Sciences (DAE-BRNS), India, SERB, DST, India (EMR/2016/007479), IUAC sponsored project (Grant No. IUAC/XIII.7/UFR-56324), and DST, India (Grant No. IFA14-MS-34) are gratefully acknowledged.

References

[1] G. Korotcenkov, S.D. Han, J.R. Stetter, Review of electrochemical hydrogen sensors, Chemical reviews 109(3) (2009) 1402-1433.
[2] J.R. Stetter, J. Li, Amperometric gas sensors a review, Chemical reviews 108(2) (2008) 352-366.
[3] W.J. Buttner, M.B. Post, R. Burgess, C. Rivkin, An overview of hydrogen safety sensors and requirements, International Journal of Hydrogen Energy 36(3) (2011) 2462-2470.

[4] X. Lu, S. Wu, L. Wang, Z. Su, Solid-state amperometric hydrogen sensor based on polymer electrolyte membrane fuel cell, Sensors and Actuators B: Chemical 107(2) (2005) 812-817.
[5] N. Shirahata, W. Shin, N. Murayama, A. Hozumi, Y. Yokogawa, T. Kameyama, Y. Masuda, K. Koumoto, Reliable Monolayer-Template Patterning of SnO2 Thin Films from Aqueous Solution and Their Hydrogen-Sensing Properties, Advanced Functional Materials 14(6) (2004) 580-588.
[6] A. Qurashi, T. Yamazaki, E. El-Maghraby, T. Kikuta, Fabrication and gas sensing properties of In 2 O 3 nanopushpins, Applied Physics Letters 95(15) (2009) 153109.
[7] L.-J. Bie, X.-N. Yan, J. Yin, Y.-Q. Duan, Z.-H. Yuan, Nanopillar ZnO gas sensor for hydrogen and ethanol, Sensors and Actuators B: Chemical 126(2) (2007) 604-608.
[8] T. Hübert, L. Boon-Brett, G. Black, U. Banach, Hydrogen sensors–a review, Sensors and Actuators B: Chemical 157(2) (2011) 329-352.
[9] H.-T. Wang, B. Kang, F. Ren, L. Tien, P. Sadik, D. Norton, S. Pearton, J. Lin, Hydrogen-selective sensing at room temperature with ZnO nanorods, Applied Physics Letters 86(24) (2005) 243503.
[10] T. Samerjai, N. Tamaekong, C. Liewhiran, A. Wisitsoraat, A. Tuantranont, S. Phanichphant, Selectivity towards H 2 gas by flame-made Pt-loaded WO 3 sensing films, Sensors and Actuators B: Chemical 157(1) (2011) 290-297.
[11] V.V.e. Rozanov, O.V. Krylov, Hydrogen spillover in heterogeneous catalysis, Russian chemical reviews 66(2) (1997) 107-119.
[12] M. Khanuja, B. Mehta, S. Shivaprasad, Two approaches for enhancing the hydrogenation properties of palladium: Metal nanoparticle and thin film over layers, Journal of Chemical Sciences 120(6) (2008) 573-578.
[13] K. Arora, D. Sandil, G. Sharma, S. Srivastava, N.K. Puri, Effect of low pressure hydrogen environment on crystallographic properties of PdO nanoparticles, International Journal of Hydrogen Energy 41(47) (2016) 22155-22161.
[14] P. Nilsson, Optical properties of PdO in the range of 0.5-5.4 eV, Journal of Physics C: Solid State Physics 12(7) (1979) 1423.
[15] S. Srivastava, V. Kumar, M.A. Ali, P.R. Solanki, A. Srivastava, G. Sumana, P.S. Saxena, A.G. Joshi, B. Malhotra, Electrophoretically deposited reduced graphene oxide platform for food toxin detection, Nanoscale 5(7) (2013) 3043-3051.
[16] L. Besra, M. Liu, A review on fundamentals and applications of electrophoretic deposition (EPD), Progress in materials science 52(1) (2007) 1-61.
[17] P. Sarkar, P.S. Nicholson, Electrophoretic deposition (EPD): mechanisms, kinetics, and application to ceramics, Journal of the American Ceramic Society 79(8) (1996) 1987-2002.
[18] G. Xie, P. Sun, X. Yan, X. Du, Y. Jiang, Fabrication of methane gas sensor by layer-by-layer self-assembly of polyaniline/PdO ultra thin films on quartz crystal microbalance, Sensors and Actuators B: Chemical 145(1) (2010) 373-377.
[19] M. Yuasa, T. Masaki, T. Kida, K. Shimanoe, N. Yamazoe, Nano-sized PdO loaded SnO 2 nanoparticles by reverse micelle method for highly sensitive CO gas sensor, Sensors and Actuators B: Chemical 136(1) (2009) 99-104.
[20] M. Tong, G. Dai, D. Gao, Gas-sensing properties of PdO-modified SnO 2–Fe 2 O 3 double-layer thin-film sensor prepared by PECVD technique, Vacuum 59(4) (2000) 877-884.
[21] I.J. Kim, S. Do Han, I. Singh, H.D. Lee, J.S. Wang, Sensitivity enhancement for CO gas detection using a SnO 2–CeO 2–PdO x system, Sensors and Actuators B: Chemical 107(2) (2005) 825-830.
[22] Z. Lou, J. Deng, L. Wang, L. Wang, T. Fei, T. Zhang, Toluene and ethanol sensing performances of pristine and PdO-decorated flower-like ZnO structures, Sensors and Actuators B: Chemical 176 (2013) 323-329.
[23] Y.-J. Chiang, F.-M. Pan, PdO nanoflake thin films for CO gas sensing at low temperatures, The Journal of Physical Chemistry C 117(30) (2013) 15593-15601.

ACCEPTED MANUSCRIPT

[24] L. Wang, Z. Lou, R. Wang, T. Fei, T. Zhang, Ring-like PdO–NiO with lamellar structure for gas sensor application, Journal of Materials Chemistry 22(25) (2012) 12453-12456.
[25] Y.-J. Chiang, K.-C. Li, Y.-C. Lin, F.-M. Pan, A mechanistic study of hydrogen gas sensing by PdO nanoflake thin films at temperatures below 250° C, Physical Chemistry Chemical Physics 17(5) (2015) 3039-3049.
[26] Y.T. Lee, J.M. Lee, Y.J. Kim, J.H. Joe, W. Lee, Hydrogen gas sensing properties of PdO thin films with nano-sized cracks, Nanotechnology 21(16) (2010) 165503.
[27] S. Choudhury, C. Betty, K. Bhattacharyya, V. Saxena, D. Bhattacharya, Nanostructured PdO thin film from Langmuir–Blodgett precursor for room-temperature H2 gas sensing, ACS applied materials & interfaces 8(26) (2016) 16997-17003.
[28] X.-Y. Zhang, F. Shan, H.-L. Zhou, D. Su, X.-M. Xue, J.-Y. Wu, Y.-Z. Chen, N. Zhao, T. Zhang, Silver nanoplate aggregation based multifunctional black metal absorbers for localization, photothermic harnessing enhancement and omnidirectional light antireflection, Journal of Materials Chemistry C (2018).
[29] S.-Q. Zhu, T. Zhang, X.-L. Guo, Q.-L. Wang, X. Liu, X.-Y. Zhang, Gold nanoparticle thin films fabricated by electrophoretic deposition method for highly sensitive SERS application, Nanoscale research letters 7(1) (2012) 613.
[30] S.K. Dondapati, P. Lozano-Sanchez, I. Katakis, Controlled electrophoretic deposition of multifunctional nanomodules for bioelectrochemical applications, Biosensors and Bioelectronics 24(1) (2008) 55-59.
[31] R. Zhang, Y. Zhu, J. Huang, S. Xu, J. Luo, X. Liu, Electrochemical Sensor Coating Based on Electrophoretic Deposition of Au-Doped Self-Assembled Nanoparticles, ACS applied materials & interfaces 10(6) (2018) 5926-5932.
[32] V. Nikolova, I. Nikolov, P. Andreev, V. Najdenov, T. Vitanov, Tungsten carbide-based electrochemical sensors for hydrogen determination in gas mixtures, Journal of applied electrochemistry 30(6) (2000) 705-710.
[33] K. Okamura, T. Ishiji, M. Iwaki, Y. Suzuki, K. Takahashi, Electrochemical gas sensor using a novel gas permeable electrode modified by ion implantation, Surface and Coatings Technology 201(19) (2007) 8116-8119.
[34] Y.C. Liu, B.J. Hwang, Y.L. Chen, Nafion Based Hydrogen Sensors: Pt/Nafion Electrodes Prepared by Takenata-Torikai Method and Modified with Polypyrrole, Electroanalysis 14(7-8) (2002) 556-558.
[35] Y. Chao, S. Yao, W.J. Buttner, J.R. Stetter, Amperometric sensor for selective and stable hydrogen measurement, Sensors and Actuators B: Chemical 106(2) (2005) 784-790.

Highlights

- Palladium oxide (PdO) nanoparticles have been synthesized using hydrothermal sol-gel method.
- PdO nanoparticles thin film has been used as working electrode (WE) for amperometric hydrogen gas sensing at room temperature.
- Electrochemical sensor shows good sensitivity (0.222 μA/%H_2) and linearly calibrated stable response.
- The time taken by the sensor to reach the 90% steady state (t_{90}) ranges from 15 to 60 seconds with fast recovery time.

ACCEPTED MANUSCRIPT

Accepted Manuscript

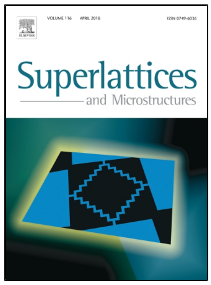

Ellipsoidal all-dielectric Fano resonant core-shell metamaterials

Reena Reena, Yogita Kalra, Ajeet Kumar

PII:	S0749-6036(17)32875-6
DOI:	10.1016/j.spmi.2018.03.067
Reference:	YSPMI 5597
To appear in:	*Superlattices and Microstructures*
Received Date:	06 December 2017
Revised Date:	26 March 2018
Accepted Date:	27 March 2018

Please cite this article as: Reena Reena, Yogita Kalra, Ajeet Kumar, Ellipsoidal all-dielectric Fano resonant core-shell metamaterials, *Superlattices and Microstructures* (2018), doi: 10.1016/j.spmi.2018.03.067

This is a PDF file of an unedited manuscript that has been accepted for publication. As a service to our customers we are providing this early version of the manuscript. The manuscript will undergo copyediting, typesetting, and review of the resulting proof before it is published in its final form. Please note that during the production process errors may be discovered which could affect the content, and all legal disclaimers that apply to the journal pertain.

ACCEPTED MANUSCRIPT

Ellipsoidal all-dielectric Fano resonant core-shell metamaterials

Reena Reena,[a] Yogita Kalra,[a] and Ajeet Kumar[a]

[a]*TIFAC-Center of Relevance and Excellence in Fiber Optics and Optical Communication, Department of applied Physics, Delhi Technological University (Formerly Delhi College of Engineering, University of Delhi) Bawana Road, Delhi-110042, India*

Abstract

In this paper, ellipsoidal core (Si) and shell (SiO_2) metamaterial has been proposed for highly directional properties. At the wavelength of magnetic resonance, Fano dip occurs in the backward scattering cross section and forward scattering enhancement takes place at the same wavelength so that there is an increment in the directivity. Effect on the directivity by changing the length of ellipsoidal nanoparticle along semi-axes has been analyzed. Two Fano resonances have been observed by decreasing the length of the nanoparticle along the semi-axis having electric polarization, where first and second Fano resonances are attributed to the dipole and quadrupole moments, respectively. These Fano resonant wavelengths in ellipsoidal nanoparticle exhibit higher directivity than the Kerker's type scattering or forward scattering shown by symmetrical structures like sphere. So, this core-shell metamaterial can act as an efficient directional nanoantenna.

Keywords: Directional nanoantennas; Magnetic response; Fano resonance; metamaterials.

1. Introduction

Recent advances in the field of metamaterials have revolutionized the emerging field of nanophotonics by manipulating light at the subwavelength scales. This astonishing property of metamaterials is underpinning a lot of applications in nanoantennas [1], [2], photovoltaics [3], [4], super lens [5], [6], cloaking [7]-[9] and biomedicine [10]. However, metallic nanoparticles do a great job of confining light to deep-subwavelength structures. But conductive losses of metallic nanoparticles make them less attractive and in the visible region, losses of metals become more prominent. So they are prohibited to many important applications like nanoantennas, sensing and quantum light sources. Moreover, it is very cumbersome to fabricate such a complicated geometry of split ring resonators (SRRs) which are used to obtain magnetic response in metallic nanoparticles.

In order to overcome these inevitable problems of metallic nanostructures, recently all-dielectric metamaterials have been proposed [11]-[22]. All-dielectric resonators support electric as well as strong magnetic resonance even in the visible region. In the dielectric nanoparticles, magnetic resonance takes place by circular displacement current and in the metallic SRRs, resonance occurs due to conduction current. However, in both the structures, electric field revolves around the resonator and magnetic field oscillates up and down in the middle of the resonator at the magnetic resonance. First experimental demonstration of magnetic resonance in the dielectric resonators has been shown in the GHz region, where it has been proved that dielectric resonators have three times higher quality factor than that of metallic SRRs [12]. Now, magnetic resonance has also been achieved in the visible region in all-dielectric nanoparticles [17], [18]. Dielectric nanostructures deliver another striking phenomenon of directional scattering which is well explained using Kerker's type scattering [24]-[26]. Further, to improve directional scattering, Fano resonance has been achieved in the dielectric nanoparticles [27]-[29]. Fano

ACCEPTED MANUSCRIPT

resonance has asymmetric line profile in contrast to usual resonance profile or Lorentzian resonance profile [30], [31]. It is the constructive and destructive interference of discrete and continuum states of a system. In dielectric nanoparticles, broad electric dipole and narrow magnetic dipole resonances interfere to yield a Fano dip in the backward scattering.

In this paper, ellipsoidal core/shell (Si/SiO_2) meta-atom has been considered in order to enhance the directivity as compared to the spherical nanoparticles. Meta-atom is the unit cell of the metamaterial which are artificially structured materials. Magnetic resonance is induced in the all-dielectric ellipsoidal nanoparticle at a particular wavelength owing to its shape and dimensions which otherwise is not exhibited by natural non-magnetic materials. Hence, the optimized ellipsoidal nanoparticle exhibiting magnetic resonance has been referred to as the meta-atom. In the design, core is made up of Silicon (Si) and shell is made up of Silica (SiO_2). As the length of the semi-axis of the ellipsoidal nanoparticle along the electric field is decreased, it has been observed that two Fano resonances are formed, which is not possible in spherical nanoparticles. First Fano resonance appears due to the interaction of dipolar moments and another Fano resonance is attributed to the interaction of quadrupolar moments created at the lower wavelengths. Fabrication of these ellipsoidal nanoparticles can be done using femtosecond laser ablation [32] and then silica layer can be formed by thermally oxidized the nanoparticles in dry air [27].

2. Design and analysis

The ellipsoidal nanoparticle having core of Si and shell made up of SiO_2 has been considered. The refractive index of SiO_2 has been taken to be 1.45 and dispersion curve of refractive index with wavelength has been used for Si from Palik [33]. The core of the ellipsoidal nanoparticle has dimensions, a = 35 nm, b = 70 nm and c = 150 nm, where, a, b and c are the semi-axes of the ellipsoidal nanoparticle. The thickness of the SiO_2 shell of the proposed ellipsoidal nanoparticle has been taken to be a_1 = 45 nm, b_1 = 80 nm, c_1 = 160 nm i.e. 10 nm more than the length of the respective semi-axis of the Si core as shown in figure 1.

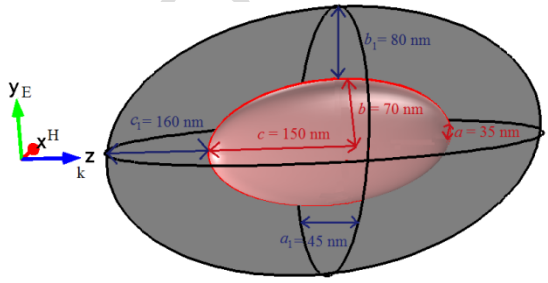

Fig. 1. Labeled diagram of the ellipsoidal core-shell meta-atom.

Magnetic dipoles can be induced in the high dielectric nanoparticles when they interact with the light of wavelength comparable to their size. Simultaneously, the electric dipole and other higher order modes are formed at the lower wavelengths. The induced multipoles in the nanoparticle i.e. electric dipole **p**, magnetic dipole **m**, electric quadrupole $Q_{\alpha\beta}$ and magnetic quadrupole $M_{\alpha\beta}$ are given by [25]

$$\mathbf{p} = \varepsilon_0(1-\varepsilon_{eff})\int_V \mathbf{E}(\mathbf{r})dV \qquad 1(a)$$

ACCEPTED MANUSCRIPT

$$\mathbf{m} = \frac{i\omega\,\varepsilon_0(1-\varepsilon_{eff})}{2c}\int_V [\mathbf{r}\times\mathbf{E}(\mathbf{r})]dV \qquad 1(b)$$

$$Q_{\alpha\beta} = \frac{\varepsilon_0(1-\varepsilon_{eff})}{2}\int_V \left[r_\alpha E_\beta + r_\beta E_\alpha - \frac{2}{3}(\mathbf{r}.\mathbf{E}(\mathbf{r}))\delta_{\alpha\beta}\right]dV \qquad 1(c)$$

$$M_{\alpha\beta} = \frac{i\omega\,\varepsilon_0(1-\varepsilon_{eff})}{3c}\int_V \left[(\mathbf{r}\times\mathbf{E}(\mathbf{r}))_\alpha r_\beta + (\mathbf{r}\times\mathbf{E}(\mathbf{r}))_\beta r_\alpha\right]dV \qquad 1(d)$$

where, c, ε_0 and ε_{eff} are the speed of light in vacuum, vacuum permittivity and effective permittivity of the core-shell meta atom, respectively, ω is the angular frequency, **E**(**r**) is the electric field confined in the nanoparticle of volume V and α and β are the corresponding cartesian components. Effective permittivity ε_{eff} has been calculated by the Maxwell Garnett formula as follows [34]

$$\varepsilon_{eff} = \varepsilon_s + \frac{\frac{1}{3}f_c(\varepsilon_c-\varepsilon_s)\sum_{k=1}^{3}\frac{\varepsilon_s}{\varepsilon_s+N_k(\varepsilon_c-\varepsilon_s)}}{1-\frac{1}{3}f_c(\varepsilon_c-\varepsilon_s)\sum_{k=1}^{3}\frac{N_k}{\varepsilon_s+N_k(\varepsilon_c-\varepsilon_s)}} \qquad (2)$$

where, ε_s is the relative permittivity of shell, ε_c is the relative permittivity of core, fc is the volume fraction occupied by the core, N_k is the depolarization factor of the ellipsoidal nanoparticle whose definition and formula can be found in [35] and the index k =1, 2, 3 represents x, y and z cartesian coordinates.
Total scattered power is the sum of the power scattered by each multipole given by [25]

$$P_{scat} = \frac{c^2k_0^4z_0}{12\pi}|\mathbf{p}|^2 + \frac{c^2k_0^4z_0}{12\pi}|\mathbf{m}|^2 + \frac{c^2k_0^6z_0}{40\pi}\Sigma|Q_{\alpha\beta}|^2 + \frac{c^2k_0^6z_0}{160\pi}\Sigma|M_{\alpha\beta}|^2 \qquad (3)$$

where, $k_0 = \omega/c$ and $z_0 = 1/\varepsilon_0 c$ are the free space wave number and impedance, respectively. Then total scattering cross section of each multipole has been calculated from scattered power in equation (1) using the equation

$$\sigma_{scat} = \frac{P^p_{scat} + P^m_{scat} + P^Q_{scat} + P^m_{scat}}{I_0} \qquad (4)$$

where, P^p_{scat} , P^m_{scat} , P^Q_{scat} and P^M_{scat} are the scattered powers by electric dipole, magnetic dipole, electric quadrupole and magnetic quadrupole, respectively. I_0 denotes the incident power density.

Electric field inside the nanoparticle **E**(**r**) has been calculated using Comsol Multiphysics FEM based software. Electric dipole **p**, magnetic dipole **m**, electric quadrupole $Q_{\alpha\beta}$ and magnetic quadrupole $M_{\alpha\beta}$ has been calculated using Matlab using the equations 1(a)-(d). Total scattered power has been calculated using equation (3). Then scattering spectra can be obtained using equation (4).

Directivity of the radiation pattern is the ratio of the radiation intensity in a given direction (in our case, it is forward direction) to the radiation intensity averaged over all directions. It is represented by D and it is dimensionless quantity which can be written in the mathematical form as [36]

ACCEPTED MANUSCRIPT

$$D = \frac{4\pi U}{P_{rad}} \tag{5}$$

where, U is the radiation intensity in the particular direction and P_{rad} is total radiated power radiated in all directions.

3. Results and discussion

First of all, scattering spectra of the considered core-shell nanoparticle has been analyzed. It has been observed that magnetic dipole resonance is obtained at the wavelength of 640 nm and electric dipole moment has a broad spectrum having very small peak at 550 nm as shown in figure 2(a). In order to understand Fano resonance in the core-shell nanoparticle, scattering spectra has been analyzed distinctly for electric dipole and induced magnetic dipole. Due to the interference between narrow magnetic dipole resonance and broad electric dipole spectrum, Fano dip has been observed in the backward scattering at the wavelength of magnetic dipole i.e. 640 nm as shown in figure 2(b). At the same wavelength, forward scattering gets enhanced. At this wavelength, Kerker's first condition is not satisfied, according to which forward scattering takes place at the wavelength of interference of electric dipole and magnetic dipole [24], still there is suppression of backward scattering with enhancement of forward scattering. Hence, this can be completely attributed to the directional Fano resonance exhibited by the ellipsoidal nanoparticle. Fano resonance occurs in the vicinity of the wavelength of narrow spectra [37]. In our case, magnetic dipole and magnetic quadrupole have narrow spectrum as compared to the spectrum of electric dipole and electric quadrupole. So, Fano resonance occurs at the wavelengths of dipolar and quadrupolar magnetic resonances as shown in figures 3(a) and 3(b). Further, at the wavelength of Fano resonance, on-resonant (at the wavelength of magnetic resonance) scattering takes place whereas the wavelength at which the Kerker's condition is satisfied, off-resonant scattering takes place. Thereby leading to the higher directivity at the wavelength of Fano resonance as compared to the directivity observed at the wavelength at which the Kerker's condition is satisfied [27].

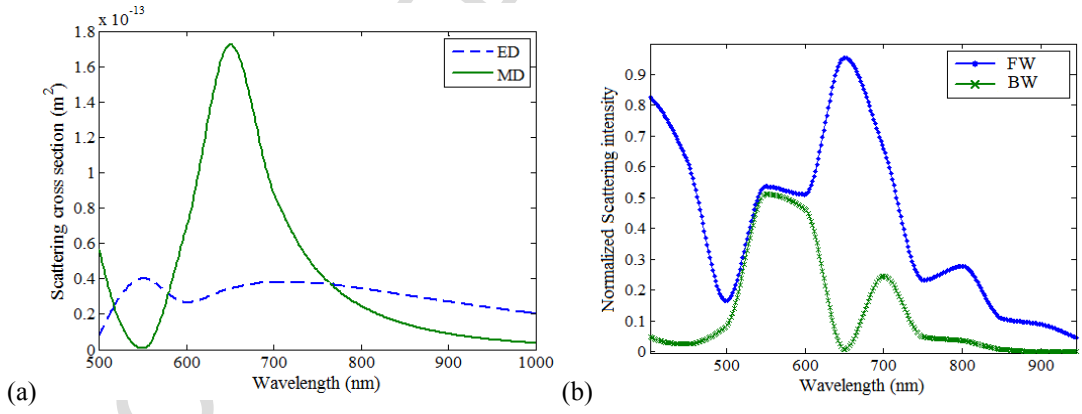

Fig. 2. (a) Scattering cross section of the nanoparticle representing broad electric dipole (ED) spectra and narrow magnetic dipole (MD) resonance. (b) Normalized forward (FW) and backward (BW) scattering intensity showing Fano dip of backward scattering at λ = 640 nm and enhancement of forward scattering at the same wavelength.

To study the variation in the Fano resonance, length of the ellipsoidal nanoparticle along its semi-axis *b* has been varied which is in the direction of the electric field. It has been observed that as the length of the ellipsoidal

ACCEPTED MANUSCRIPT

core nanoparticle along semi-axis *b* is decreased, two Fano resonances are exhibited. One of the Fano resonances is due to interaction of narrow magnetic dipole resonance with comparatively broad electric dipole resonance as shown figure 3(a). The Fano resonance dip in the backward scattering occurs at the wavelength of 490 nm followed by a peak in the forward scattering at the same wavelength as shown in the figure 3(b).

Another Fano resonance obtained at the wavelength of 440 nm as shown in figure 3(b) occurs due to the interference of broad electric quadrupole moment and narrow magnetic quadrupole moment, as shown in figure 3(a).

However to obtain the two Fano dips in the backward scattering in the visible region requires the larger size of the spherical nanoparticles. In case of ellipsoidal nanoparticle, magnetic quadrupole is formed near the electric dipole. Magnetic dipole mode and magnetic quadrupole mode with rotating electric field has been shown in figures 3(c) and 3(d) respectively. Far-field scattering patterns at these wavelengths of Fano resonance i.e. 490 nm and 440 nm have been shown in the figures 3(e) and 3(f) respectively which exhibit forward scattering at these wavelengths. Further, directivities (D) at the wavelengths 490 nm and 440 nm have been obtained to be 3.1 and 3.4, respectively, calculated from equation (5).

The enhanced directivity at the wavelengths of Fano resonance can be attributed to the sudden π phase shift from constructive to destructive stage or vice-versa [37]. The wavelengths at which constructive and destructive interference takes place are very near to each other leading to an asymmetric profile called Fano resonance. The forward scattering gets enhanced and the backward scattering is suppressed resulting in the enhanced directivity.

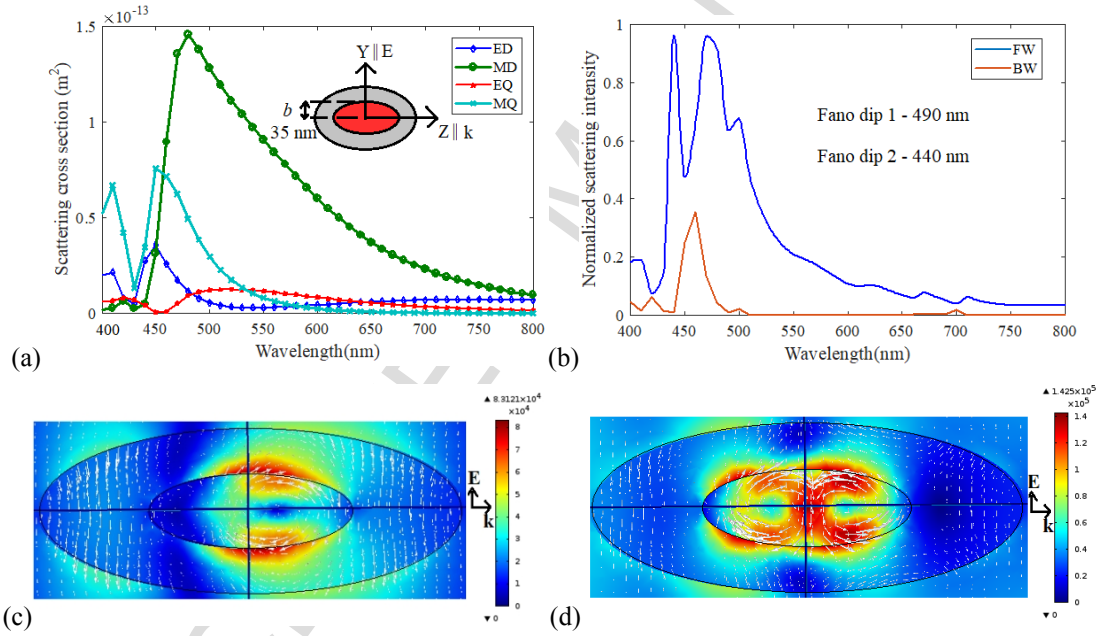

ACCEPTED MANUSCRIPT

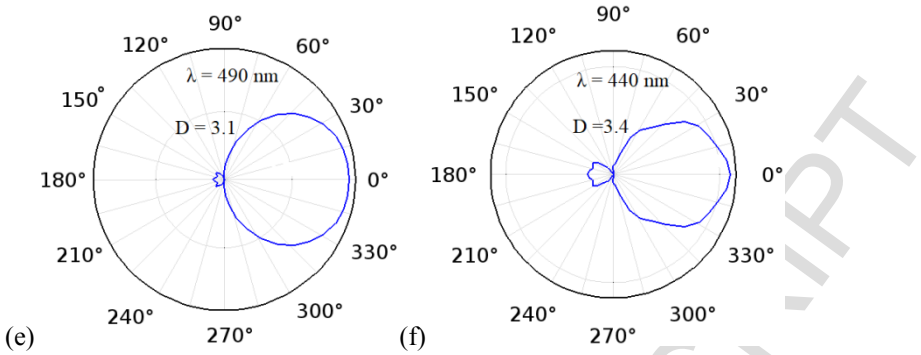

Fig. 3 (a) Scattering spectra of ellipsoidal nanoparticle depicting distinct curves of dipoles and quadrupoles for core radius b = 35 nm. (b) Forward and backward normalized scattering intensity showing Fano dips in the backward scattering at the wavelengths 490 nm and 440 nm due to dipole and quadrupole moments respectively. (c) Magnetic dipole mode at 490 nm (d) magnetic quadrupole mode at 440 nm, white arrows indicate the electric lines of force. Far-field scattering patterns (e) at the Fano dip wavelength λ = 490 nm showing directivity D = 3.1 and (f) at the wavelength λ = 440 nm showing directivity D = 3.4.

Further, the length of the core nanoparticle along semi-axis b has been increased to 55 nm leading to the red shift of the dipole moment as well as the quadrupole moment and hence the Fano resonance wavelengths as shown in figure 4(a). First Fano dip is obtained at the wavelength of 600 nm due to the interaction of electric and magnetic dipole moments whereas the second Fano dip is obtained at the wavelength of 540 nm due to the interaction of electric and magnetic quadrupole moments as shown in figure 4(b). Far field scattering patterns at the wavelengths of 600 nm with directivity 2.55 and 540 nm having directivity 2.64 have been shown in the figures 4(c) and 4(d), respectively.

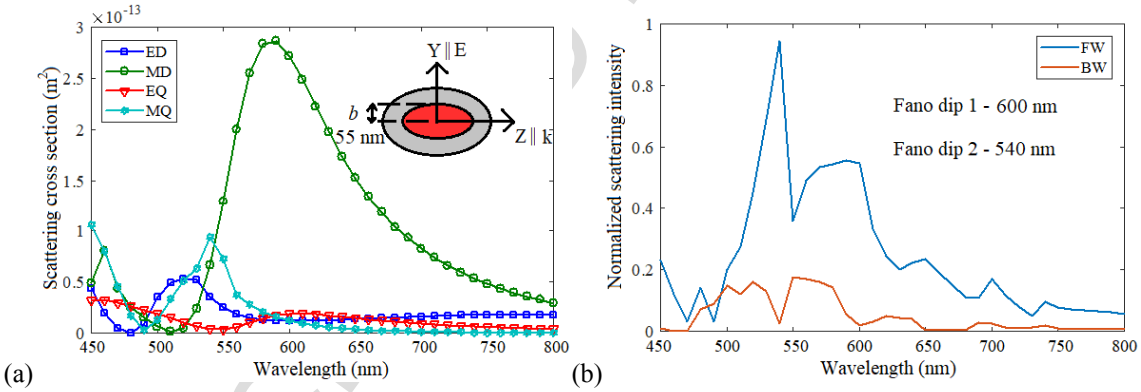

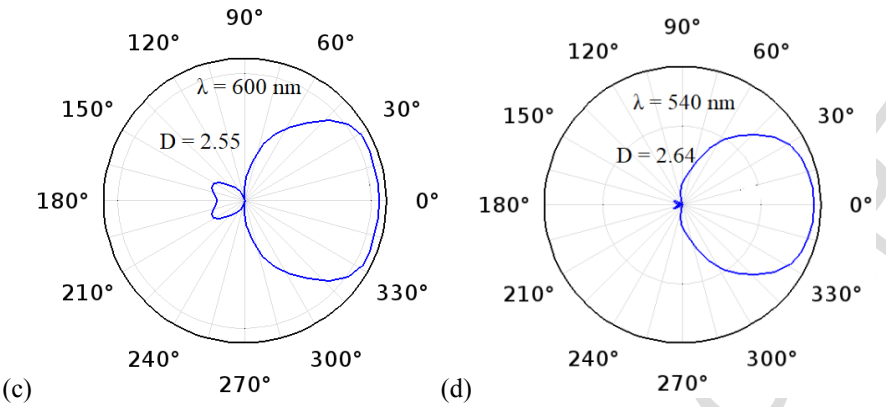

Fig. 5 (a) Scattering spectra of the ellipsoidal nanoparticle at b = 55 nm. (b) Forward and backward normalized scattering intensity showing Fano dips in the backward scattering at the wavelengths 600 nm and 540 nm. (c) – (d) Far-field scattering patterns at the Fano dip wavelengths showing directivities D = 2.55 at wavelength λ = 600 nm and D = 2.64 at the wavelength λ = 540 nm.

Further, the length of the core nanoparticle along semi-axis b has been increased to 75 nm. In this case, only one Fano resonance is observed at the wavelength of 650 nm. This Fano resonance is due to the interaction of the electric and magnetic dipole moments. The scattering cross-section profile due to magnetic quadrupole becomes broader as we increase the size of the ellipsoidal nanoparticle along b-axis, as shown in figure 5(a). Thus, no Fano resonance occurs due to the interaction of quadrupolar moments as shown in figure 5(b). Figure 5(c) shows that the wavelength of Fano dip 1 (FD_1) and Fano dip 2 (FD_2) increase with the length of b-axis. But, as the length of the b-axis increases after 68 nm, the FD_2 vanishes. The far-field scattering pattern at the wavelength of Fano dip i.e. 650 nm has been shown in figure 5(d). From the far-field pattern, it has been observed that back-scattering is completely suppressed; however, there is small decrease in directivity due to enlarged beam- width of the lobe by increasing the length of nanoparticle along semi-axis b.

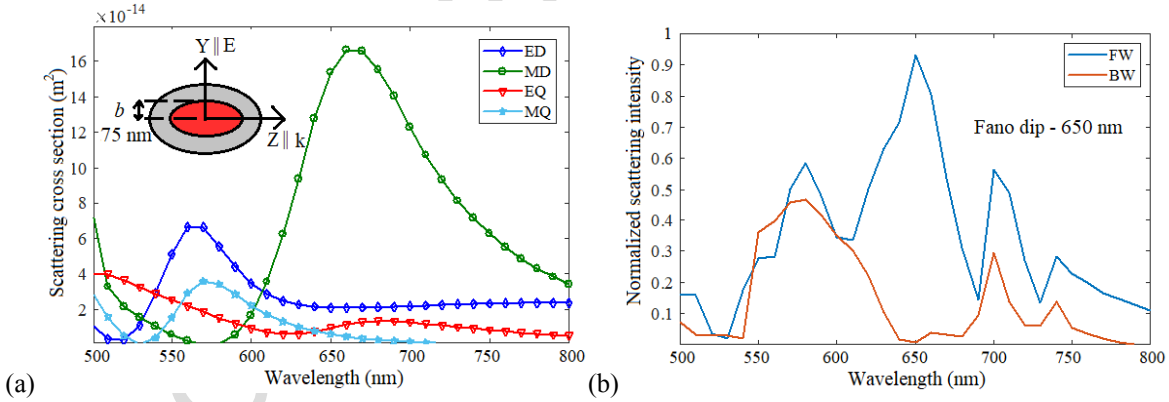

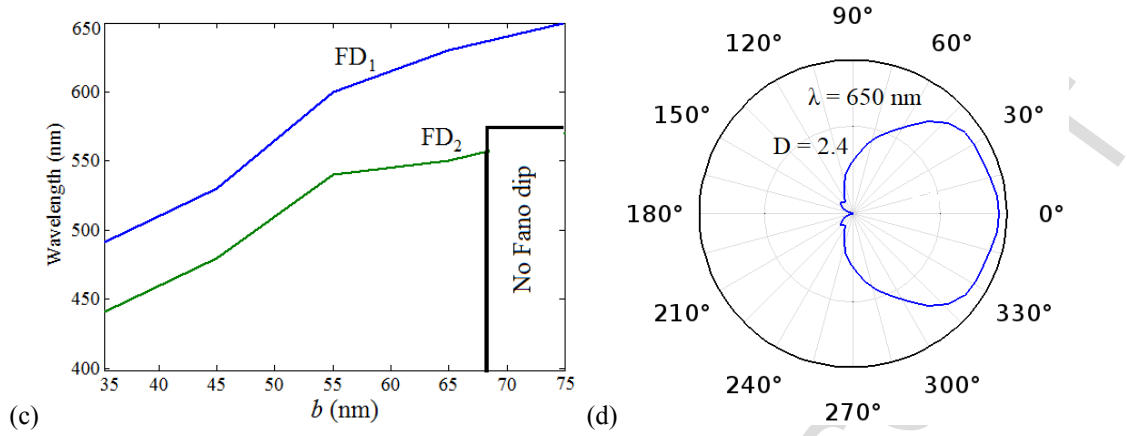

Fig. 6 (a) Scattering spectra of the ellipsoidal nanoparticle at b = 75 nm. (b) Forward and backward normalized scattering intensity showing Fano dip in the backward scattering at the wavelength 650 nm due to dipole moments only. (c) Variation of wavelength of Fano dips, FD_1 and FD_2 with length of semi-axis of ellipsoidal nanoparticle along electric field. (d) Far field scattering pattern at 650 nm showing directivity D = 2.4 at the wavelength λ = 650 nm.

However, the length of the ellipsoidal nanoparticle along semi-axis a and c are kept constant i.e. a = 35 nm and c = 150 nm, because by increasing the length along semi-axis a or by decreasing the length along semi-axis b, ellipsoid approaches to sphere which results in diminishing of quadrupoles. In order to compare the results of ellipsoid and sphere, scattering cross section has been plotted in figure 6(a) for sphere having core radius 70 nm and shell thickness 80 nm. It has been observed that there is only one Fano dip at 630 nm due to narrow magnetic dipole and broad electric dipole as shown in the figure 6(b). But no Fano dip is observed due to the interaction of quadrupoles because magnetic quadrupole moment is very small in case of spherical nanoparticle as compared to ellipsoidal nanoparticle. Also, low directivity is obtained in case of spherical nanoparticle as compared to the directivity obtained in ellipsoidal nanoparticle as shown in figure 6(c).

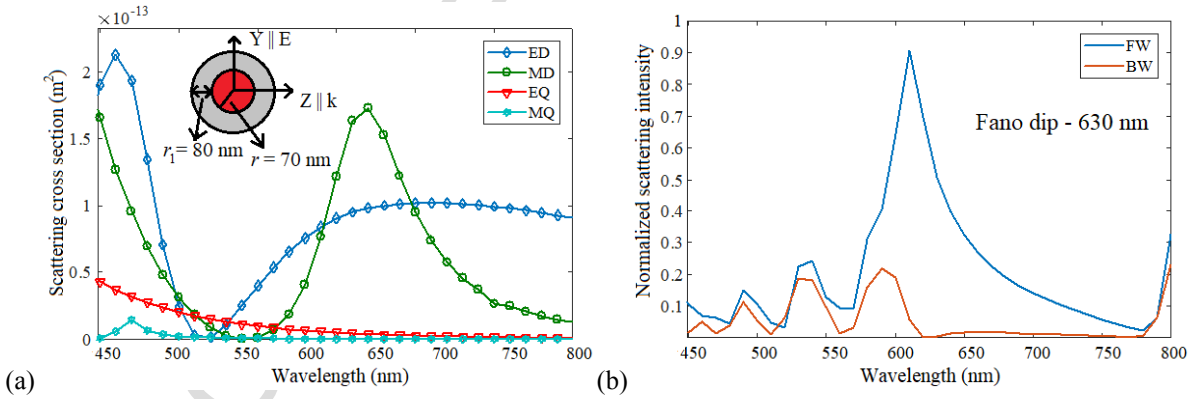

ACCEPTED MANUSCRIPT

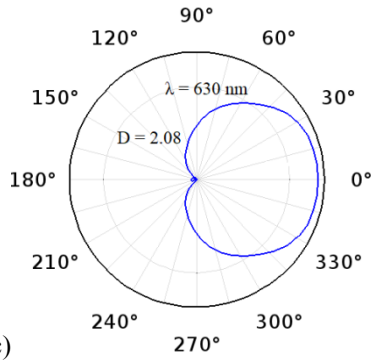

(c)

Fig. 6(a) Scattering spectra of the spherical nanoparticle of core radius 70 nm and shell thickness 80 nm. (b) Forward and backward normalized scattering intensity showing Fano dip in the backward scattering at the wavelength 630 nm due to dipole moments only. (c) Far field scattering pattern at λ = 630 nm showing directivity D = 2.08.

4. Conclusion

In this paper, ellipsoidal core-shell nanoparticle has been considered in which magnetic dipole has been optically induced. Electric dipole and higher order multipoles are created at lower wavelength side. Fano resonance has been observed at the wavelength of magnetic dipole due to the interaction of broad electric dipole and narrow magnetic dipole. When length of the semi-axis has been decreased which is along the electric field, double Fano resonance has been observed, one is due to the interaction of broad electric dipole moment and narrow magnetic dipole moment, whereas the other is attributed to the interaction of broad electric quadrupole and narrow magnetic quadrupole. At these wavelengths of Fano resonance, directivity enhancement takes place which makes these ellipsoidal core-shell metamaterials promising candidate for nanoantenna applications.

Acknowledgments

Authors gratefully (i) acknowledge the initiatives and support from TIFAC-Center of Relevance and Excellence in Fiber Optics and Optical Communication at Delhi College of Engineering, now DTU, and Delhi under Mission REACH Program of Technology vision-2020, Government of India and (ii) Support through DST-RMES (Indo-Russian) joint research project on “All Dielectric, Plasmonic and Hybrid Photonic Nanostructures” and (iii) DST-RFBR (Indo-Russian) joint research project on “From Plasmonics to Dielectric and Hybrid nanoantennas: Novel approaches to control electromagnetic waves and light.”

References

[1] K. Lindfors, D. Dregely, M. Lippitz, N. Engheta, M. Totzeck, and H. Giessen, Imaging and steering unidirectional emission from nanoantenna array metasurfaces. ACS Photonics, 3 (2) (2016) 286-292.

ACCEPTED MANUSCRIPT

[2] J. Yan, M. Churong, L. Pu, W. Chengxin, and Y. Guowei, Electrically controlled scattering in a hybrid dielectric-plasmonic nanoantenna. Nano Letters 17 (8) (2017) 4793-4800.
[3] Y. Pang, J. Wang, Q. Cheng, S. Xia, X. Y. Zhou, Z. Xu, T. J. Cui and S. Qu, Thermally tunable water-substrate broadband metamaterial absorbers. App. Phy. Lett. 110(10) (2017) 104103.
[4] D. Lee, H. Jeong and S. Lim, Electronically Switchable Broadband Metamaterial Absorber Sci. Rep. 7(1) (2017) 4891.
[5] G. Lipworth, J. Ensworth, K. Seetharam, D. Huang, J. S. Lee, P. Schmalenberg, T. Nomura, M.S. Reynolds, D.R. Smith and V. Urzhumov, Magnetic metamaterial superlens for increased range wireless power transfer. Sci. repo. 4 (2014) 3642.
[6] A. O. Bak, E. O. Yoxall, P. Sarriugarte, V. Giannini, S. A. Maier, R. Hillenbrand, J. B. Pendry and C. C. Phillips, Harnessing a Quantum Design Approach for Making Low-Loss Superlenses. Nano letters, 16(3), (2016) 1609-1613.
[7] Z. J. Wong, W. Yuan, O'Brien Kevin, R. Junsuk, Y. Xiaobo, Z. Shuang, F. Nicholas, Y. Ta-Jen, and Z. Xiang, Optical and acoustic metamaterials: superlens, negative refractive index and invisibility cloak. J. Opt. 19 (8) (2017) 084007.
[8] D. Shin, Y. Urzhumov, Y. Jung, G. Kang, S. Baek, M. Choi, H. Park, K. Kim, and D. R. Smith, Broadband electromagnetic cloaking with smart metamaterials. Nat. commun. 3 (2012) 1213.
[9] W. Cai, U. K. Chettiar, A. V. Kildishev, and V. M. Shalaev, Optical cloaking with metamaterials. Nat. phot.1 (4) (2007) 224-227.
[10] Y. Jin, Engineering plasmonic gold nanostructures and metamaterials for biosensing and nanomedicine. Adv. Mater., 24 (38) (2012) 5153-5165.
[11] S. Jahani, and Z. Jacob. All-dielectric metamaterials. Nat. Nanotechnol., 11 (1) (2016) 23-36.
[12] B. I. Popa, and S. A. Cummer. Compact dielectric particles as a building block for low-loss magnetic metamaterials. Phys. Rev. Lett. 100 (20) (2008) 207401.
[13] Q. Zhao, J. Zhou, F. Zhang, and D. Lippens, Mie resonance-based dielectric metamaterials. Mat. Today, 12 (12) (2009) 60-69.
[14] Y. Yang, A. E. Miroshnichenko, S. V. Kostinski, M. Odit, P. Kapitanova, M. Qiu, and Y. S. Kivshar, Multimode directionality in all-dielectric metasurfaces. Phys. Rev. B 95 (16) (2017) 165426.
[15] A. Ahmadi, and H. Mosallaei, Physical configuration and performance modeling of all-dielectric metamaterials. Phys. Rev. B 77 (4) (2008) 045104.
[16] D. A. Powell, Interference between the Modes of an All-Dielectric Meta-atom. Phys. Rev. Appl. 7 (3), (2017) 034006.
[17] A. I. Kuznetsov, A. E. Miroshnichenko, Y. H. Fu, J. B. Zhang, and B. Luk'yanchuk, Magnetic light. Scientific Reports 2 (2012) 492.
[18] A. B. Evlyukhin, S. M. Novikov, U. Zywietz, R. L. Eriksen, C. Reinhardt, S. I. Bozhevolnyi, and B. N. Chichkov, Demonstration of magnetic dipole resonances of dielectric nanospheres in the visible region. Nano lett. 12 (7) (2012) 3749-3755.
[19] N. A. Butakov, and J. A. Schuller. Designing Multipolar Resonances in Dielectric Metamaterials. Sci. Rep. 6 (2016) 38487.
[20] N. Shankhwar, R. K. Sinha, Y. Kalra, S. Makarov, A. Krasnok, and P. Belov, High-quality laser cavity based on all-dielectric metasurfaces. Photonics and Nanostructures-Fundamentals and Applications 24 (2017) 18-23.
[21] P. Moitra, B. A. Slovick, W. Li, I. I. Kravchencko, D. P. Briggs, S. Krishnamurthy, and J. Valentine, Large-scale all-dielectric metamaterial perfect reflectors. ACS Photonics 2 (6) (2015) 692-698.
[22] F. Zhang, L. Kang, Q. Zhao, J. Zhou, and D. Lippens, Magnetic and electric coupling effects of dielectric metamaterial. New J. Phys. 14 (3), (2012) 033031.
[23] R. Gomez-Medina, B. Garcia-Camara, I. Suarez-Lacalle, F. Gonzalez, F. Moreno, M. Nieto-Vesperinas, and J. J. Saenz, Electric and magnetic dipolar response of germanium nanospheres: Interference effects, scattering anisotropy, and optical forces, J. Nanophoton. 5 (1), (2011) 053512.
[24] Reena, Y. Kalra, A. Kumar, and R. K. Sinha, Tunable unidirectional scattering of ellipsoidal single nanoparticle. J. Appl. Phys. 119 (24), (2016) 243102.
[25] D. Sikdar, W. Cheng, and M. Premaratne, Optically resonant magneto-electric cubic nanoantennas for ultra-directional light scattering. J. Appl. Phys. 117 (8) (2015) 083101.
[26] I. Devi, R. Dalal, Y. Kalra, and R. K. Sinha, Modeling and design of all-dielectric cylindrical nanoantennas. J. Nanophoton. 10 (4) (2016) 046011.
[27] Y. Tsuchimoto, T. Yano, T. Hayashi, and M. Hara, Fano resonant all-dielectric core/shell nanoparticles with ultrahigh scattering directionality in the visible region. Opt. exp. 24 (13) (2016) 14451-14462.
[28] A. E. Miroshnichenko and Y. S. Kivshar, Fano resonances in all-dielectric oligomers, Nano Lett. 12 (12) (2012) 6459–6463.
[29] J. Yan, P. Liu, Z. Lin, H. Wang, H. Chen, C. Wang, and G. Yang, Directional Fano resonance in a silicon nanosphere dimer, ACS Nano 9 (3) (2015) 2968–2980.
[30] A. E. Miroshnichenko, S. Flach, and Y. S. Kivshar, Fano resonances in nanoscale structures. Rev. Mod. Phys. 82 (3) (2010) 2257.
[31] B. Luk'yanchuk, N. I. Zheludev, S. A. Maier, N. J. Halas, P. Nordlander, H. Giessen, and C. T. Chong. The Fano resonance in plasmonic nanostructures and metamaterials. Nat. Mat. 9 (9) (2010) 707-715.
[32] P. A. Dmitriev, S. V. Makarov, V. A. Milichko, I. S. Mukhin, A. S. Gudovskikh, A. A. Sitnikova, A. K. Samusev, A. E. Krasnok, and P. A. Belov. Laser fabrication of crystalline silicon nanoresonators from an amorphous film for low-loss all-dielectric nanophotonics. Nanoscale 8 (9) (2016) 5043-5048.
[33] E. D. Palik, Handbook of Optical Constants of Solids, E. D. Palik, ed., Academic Press, Orlando, Florida, U.S. 1985.

ACCEPTED MANUSCRIPT

[34] M. Y. Koledintseva, R. E. DuBroff, and R. W. Schwartz. A Maxwell Garnett model for dielectric mixtures containing conducting particles at optical frequencies. Prog. In Electromagn. Research, 63 (2006) 223-242.
[35] C. F. Bohren, and D. R. Huffman. Absorption and scattering of light by small particles, John Wiley & Sons, 2008.
[36] C. A. Balanis, Antenna theory: analysis and design 3rd ed., John Wiley & Sons, Hoboken, New Jersey, U.S. 2005.
[37] B. S. Luk'yanchuk, A. E. Miroshnichenko, and Y. S. Kivshar, "Fano resonances and topological optics: an interplay of far- and near-field interference phenomena," J. Opt. 15 (7) (2013) 073001.

ACCEPTED MANUSCRIPT

ACCEPTED MANUSCRIPT

Highlights

- Ellipsoidal core (Si) and shell (SiO_2) metamaterial has been proposed for highly directional properties.
- Fano resonances takes place at the wavelengths of dipolar and quadrupolar magnetic resonance which results in suppression of backward scattering and enhancement of forward scattering.
- It has been shown that ellipsoidal nanoparticles have more directional properties than the symmetrical nanoparticles like sphere.

ACCEPTED MANUSCRIPT

arXiv:1804.05693v1 [gr-qc] 13 Apr 2018

Evolution and thermodynamics of new holographic dark energy with bulk viscosity in modified $f(R,T)$ gravity

C. P. Singh[1] **and Milan Srivastava**[2]

[1,2] Department of Applied Mathematics,
Delhi Technological University,
Bawana Road, Delhi-110 042, India.
[1]cpsphd@rediffmail.com
[2]milandtu@gmail.com

Abstract. In this paper, bulk viscosity is introduced in new holographic dark energy (HDE) to describe the effects of cosmic non-perfect fluid on the evolution of the universe in modified $f(R,T)$ gravity. Assuming $f(R,T) = R+\lambda T$, where R is the Ricci scalar, T, the trace of energy-momentum tensor and λ is a constant, we derive a general function of Hubble parameter with bulk viscous form to provide a procedure for the viscous new HDE model building. Especially, we assume the total bulk viscosity coefficient proportional to the velocity of the expansion of the universe in such a way that $\zeta = \zeta_0 + \zeta_1 H$. We obtain the solutions of the scale factor and deceleration parameter and classify all the possible scenarios (deceleration, acceleration and their transition) with different parameter regions chosen properly for positive and negative ranges of λ, and ζ_0 and ζ_1 to analyze the evolution of the universe. It is observed that there is a transition from decelerated phase to accelerated phase at early or late time depending on the values of viscous terms. For large values of viscous terms it always accelerates through out the evolution. Furthermore, we also investigate the statefinder pair $\{r,s\}$ and Om diagnostics for the viscous new HDE model to discriminate with other existing DE models. The model evolution behaviors are shown in the planes of $r-s$, $r-q$ and $Om-z$. It is found that behavior of trajectories in different planes depend on the bulk viscous coefficient. A small combination of ζ_0 and ζ_1 gives the quintessence like behavior whereas large combination of these two terms give Chaplygin gas like model. However, both the model approaches to ΛCDM model in late time of evolution of the universe. Our viscous model is also different from other existing dark energy models. The evolution of effective equation of state parameter is -0.9745 which is very close to the observation. The entropy and generalized second law of thermodynamics are valid for this model under some constraints of bulk viscous coefficient. The analysis shows that the dark energy phenomena may be explained as the effect of bulk viscosity in the cosmic medium.

Keywords: Cosmology; Bulk viscosity; Dark energy; Modified $f(R,T)$ gravity.

[1]Corresponding author

Contents

1 Introduction **2**

2 Review of Modified $f(R,T)$ gravity **5**

3 Field equations of bulk viscous new HDE model **5**
3.1 Evolution of the scale factor 7
3.2 Behavior of the deceleration parameter 10
3.3 Statefinder diagnostic 13
3.4 *Om* diagnostic 16
3.5 Effective Equation of state parameter 17
3.6 Entropy and second law of thermodynamics 18

4 Conclusion **22**

1 Introduction

The observational studies including type Ia supernovae (SNeIa) [1,2], cosmic microwave background radiation (CMB) [3] and large scale structure (LSS) [4], among others have confirmed that the present observable universe is in the phase of accelerated expansion. All these observations indicate the existence of a dark energy (DE) having negative pressure. The most important theoretical candidate for dark energy is the cosmological constant Λ [5–7], which fits the observations well, but it suffers from severe theoretical difficulties like fine -tuning and cosmic coincidence problems. Thus, dynamical dark energy models become popular, because they may alleviate the theoretical challenges faced by the ΛCDM model. In cosmology, there are many phenomenological models of DE, *e.g.*, quintessence [8–13], k-essence [14], phantom energy [15–17], quintom [18, 19], exotic Chaplygin gas [20], modified gravity theories [21,22], holographic dark energy [23], New agegraphic dark energy models [24]. Thus, dark energy has become one of the most important research areas in cosmology. However, our understanding about the nature of this energy is very modest, despite substantial progress both in theoretical and observational fields.

In recent times, the holographic dark energy (HDE) is considered as a dynamics vacuum energy. It is stimulated by the holographic principle [25, 26], which says that the number of degrees of freedom of a physical system should scale with its bounding area rather than with its volume. It was suggested by Cohen *et al.* [27] that in quantum field theory a short distance cutoff is related to a long distance cutoff due to the limit set by the formation of a black hole. They also suggested that the total energy in a region of size L should not exceed the mass of a black hole of the same size. Under this assumption, Li [23] proposed the HDE density as $\rho_\Lambda = 3c^2 M_p^2 L^{-2}$, where c^2 is a dimensionless constant, $M_p^{-2} = 8\pi G$ is the reduced Planck mass.

Now, the problem is how to choose an appropriate infrared cutoff for the theory. Li [23] has assumed Hubble length as the infrared cutoff ($\rho_d \propto H^2$) which resolves the fine-tuning problem but yields a wrong equation of state of DE, $\omega_d = 0$ [28,29], which can not drive the cosmic acceleration. Later on, particle horizon as a different infrared cutoff was proposed which also gives $\omega_d > -1/3$. A suitable choice of infrared cutoff as a future event horizon was suggested by Li *et al.* [30], which

explains the accelerated expansion of the universe. Gao *et al.* [31] has proposed infrared cutoff by replacing the future event horizon area with the inverse of the Ricci scalar curvature. They call this model the Ricci dark energy (RDE) model. Granda and Oliveros [32] have proposed a new cutoff based on purely dimensional grounds, by adding a term involving the first derivative of the Hubble parameter. According to this new infrared cutoff, the energy density of HDE is given by

$$\rho_d = 3M_p^2(\alpha H^2 + \beta \dot{H}) \tag{1}$$

where H is the Hubble parameter and α and β are constants which must satisfy the restrictions imposed by the current observational data. This is known as the new holographic dark energy (HDE). There are some works on the new version of the holographic dark energy model [33–36]. Therefore, it will be interesting to work with this new HDE model.

It is observed that early inflation and recent expansion of the universe can be investigated through dissipative fluid. The role of the dissipative processes has been conscientiously studied [37–40] in the evolution of the universe. Viscosity is basically a measurement of a fluid's resistance to flow and is classified into two types, namely, bulk and shear viscosity. The general theory of dissipation in relativistic imperfect fluid was put on a firm foundation by Eckart [41], and, in a somewhat different formulation by Landau and Lifshitz [42]. This is only the first order deviation from equilibrium and may has a causality problem, the full causal theory was developed by Israel and Stewart [43], and has also been studied in the evolution of the early universe. However, because of the simple form of Eckart theory, it has been widely used by several authors to characterize the bulk viscous fluid. The Eckart approach has been used in models explaining the recent acceleration of the universe with bulk viscous fluid. The idea of viscous DE models has been presented in different ways to understand the evolution of the universe. Many authors [44–55] have studied the DE phenomenon as an effect of the bulk viscosity in the cosmic medium. All these cited works are pioneer papers on bulk viscosity which show that for an appropriate viscosity coefficient, an accelerating cosmology can be achieved without the need of a cosmological constant [56]. At the late times, since we do not know the nature of the universe content very clearly, concern about the bulk viscosity is reasonable and practical. To our knowledge, such a possibility has been investigated only in the context of the primordial universe, concerning also the search of non-singular models. But many investigations show that the viscous pressure can play the role of an agent that drives the present acceleration of the universe. The motivation of the present work is to drive the present acceleration using the bulk viscous pressure in new HDE model.

The modification in the geometrical part of Einstein-Hilbert action is very attractive way to resolve many problems in cosmology. The most famous modification of general relativity is the $f(R)$ gravity in which the Ricci scalar R is replaced by a general function $f(R)$. This theory is consistent with the observations [57,58]. Harko *et al.* [59] proposed a new modified theory known as $f(R,T)$ gravity theory, where R is the Ricci Scalar and T stands for the trace of energy-momentum tensor. This modified theory presents a maximal coupling between geometry and matter. Many authors [60–64] have studied modified $f(R,T)$ theory in different context to explain early and late time evolution of the universe. The new HDE model has not been yet discussed in detail in framework of $f(R,T)$ theory. Therefore, our aim is to study new HDE model with bulk viscosity in $f(R,T)$ gravity theory to explain the accelerated expansion of the universe.

HDE is a great arena for modified gravity for a few reasons. The DE models (like ΛCDM) are alone able to explain the acceleration of the universe in the framework of the general relativity but

it suffers some problems, like cosmological constant (the fine-tunning problem) and cosmic coincidence problems. To resolve these problems, either the left hand side of Einstein field equations, *i.e.*, geometrical part or right hand side, energy-momentum tensor has been modified.

As a non-renormalizable theory, and currently the only known non-renormalizable theory, gravity is ultraviolet sensitive. In HDE the ultraviolet cutoff of the theory depends on the infrared cutoff. The infrared cutoff is set at the cosmological scale for the concern of dark energy. As a result, the ultraviolet cutoff is much affected. As we do not have a firm general relativity equation for quantum gravity, the best we can do is to take a modified gravity theory with the presence of HDE as a candidate of the infrared gravity theory. For this reason, actually, even if a modified theory is ruled out on earth, solar system or galactic scale experiments, the modified theory may still be considered together with HDE because cosmological scale is a completely different scale.

For many modified models to work as dark energy, they still have to solve the old cosmological constant problem and coincidence problem. HDE solves the problem for this modified theories. Thus, the modified theory in HDE can focus on the naturalness from first principle, dynamics of dark energy, agreement with observations, *etc.* Observationally, HDE has two parameters, which is relatively few compared with most dark energy models (although the cosmological constant has one parameter only). Thus, modified on top of HDE has stronger predictability compared to those on top of dark energy scenarios with more parameters (or even free functions). Modified gravity theories have rich dynamics. It is thus interesting to study reconstructing those modified gravity theories using the dynamics of HDE. Different modified theories has different degree of freedoms and dynamics.

The present paper is devoted to explore the effect of bulk viscosity in new HDE model within the context of modified $f(R,T)$ gravity. We consider the viscous new HDE model with pressureless matter. The time-dependent bulk viscous coefficient $\zeta = \zeta_0 + \zeta_1 H$, where ζ_0 and ζ_1 are constants, has been assumed to discuss the evolution. We briefly discuss how the presence of viscous fluid could produce the late time acceleration. The viscous new HDE model gives time-dependent deceleration parameter which shows phase transition. We discuss the behavior of deceleration parameter by constraining on ζ_0 and ζ_1 and gravity parameter λ which are summarize in tables. We also find the two independent geometrical diagnostics, namely statefinder pair and Om to discriminate the new HDE model with other existing DE models. The effective equation of state parameter, entropy and generalized second law of thermodynamics are also discussed.

This paper is organized in the following manner. In Section 2 the background and gravitational field equations of modified $f(R,T)$ gravity are written down. Section 3 deals with field equations for the viscous new HDE model in $f(R,T)$ gravity theory. Further, Section 3 is divided into subsections 3.1 – 3.6 in which we find the solutions of the scale factor and the relevant physical and geometrical quantities like deceleration parameter, statefinder parameters, Om diagnostic, effective equation of state parameter, and entropy and generalized second law of thermodynamics, respectively, and discuss their evolutions in detail. We discuss and summarize our results in Section 4.

In the present paper, we assume $8\pi G = 1$ and $c = 1$.

2 Review of Modified $f(R,T)$ gravity

The action of modified $f(R,T)$ gravity [59] is defined as

$$S=\frac{1}{2}\int d^4x\sqrt{-g}[f(R,T)+2\mathcal{L}_m], \tag{2}$$

where $f(R,T)$ is an arbitrary function of the Ricci scalar R and trace T of the stress energy tensor $T_{\mu\nu}$ of the matter, g is the determinant of the metric tensor $g_{\mu\nu}$ and $\mathcal{L}_m$ represents the matter Lagrangian density. The stress energy tensor is defined as

$$T_{\mu\nu}=-\frac{2}{\sqrt{-g}}\frac{\delta(\sqrt{-g}\mathcal{L}_m)}{\delta g^{\mu\nu}}. \tag{3}$$

Assuming that the Lagrangian density $\mathcal{L}_m$ of matter depends only on the metric tensor $g_{\mu\nu}$ which leads to

$$T_{\mu\nu}=g_{\mu\nu}\mathcal{L}_m-2\frac{\delta\mathcal{L}_m}{\delta g_{\mu\nu}}. \tag{4}$$

Variation of the action (2) with respect to the metric tensor $g_{\mu\nu}$ gives the field equations

$$f_R(R,T)R_{\mu\nu}-\frac{1}{2}f(R,T)g_{\mu\nu}+(g_{\mu\nu}\Box-\nabla_\mu\nabla_\nu)f_R(R,T)=T_{\mu\nu}-f_T(R,T)(T_{\mu\nu}+\ominus_{\mu\nu}), \tag{5}$$

where the tensor $\ominus_{\mu\nu}$ is given by

$$\ominus_{\mu\nu}=-2T_{\mu\nu}+g_{\mu\nu}\mathcal{L}_m-2g^{\alpha\beta}\frac{\partial^2\mathcal{L}_m}{\partial g^{\mu\nu}\partial g^{\alpha\beta}}. \tag{6}$$

Here, $f_R=\partial f/\partial R$, $f_T=\partial f/\partial T$, $\Box\equiv\nabla^\mu\nabla_\mu$, ∇_μ is the covariant derivative.

Harko *et al.* [59] introduced the form of $f(R,T)=R+f(T)$, where $f(T)=\lambda T$, λ is an arbitrary constant. Using this form of $f(R,T)$, the field equations (5) are

$$R_{\mu\nu}-\frac{1}{2}R\,g_{\mu\nu}=T_{\mu\nu}-\lambda\,(T_{\mu\nu}+\ominus_{\mu\nu})+\frac{1}{2}\lambda\,g_{\mu\nu}\,T, \tag{7}$$

According to Harko *et al.* [59] the matter Lagrangian $\mathcal{L}_m$ may be chosen as $\mathcal{L}_m=-p$, where p is the thermodynamical pressure of matter content of the universe. Then, Eq.(6) becomes as $\ominus_{\mu\nu}=-2T_{\mu\nu}-p\,g_{\mu\nu}$. Substituting this value into Eq.(7), we get

$$R_{\mu\nu}-\frac{1}{2}R\,g_{\mu\nu}=T_{\mu\nu}+\lambda\,(T_{\mu\nu}+p\,g_{\mu\nu})+\frac{1}{2}\lambda T\,g_{\mu\nu}. \tag{8}$$

3 Field equations of bulk viscous new HDE model

We assume that the universe is filled with bulk viscous HDE fluid and dust dark matter(excluding the baryonic matter), and its geometry is given by a spatially flat Friedmann-Robertson-Walker (FRW) metric

$$ds^2=dt^2-a^2(t)\left[dr^2+r^2(d\theta^2+sin^2\theta d\phi^2)\right], \tag{9}$$

where $a(t)$ is the scale factor, t is the cosmic time and (r, θ, ϕ) are the comoving coordinates.

The stress-energy-momentum tensor in the presence of bulk viscous term is given by

$$T_{\mu\nu} = (\rho_m + \rho_d)u_\mu u_\nu + (g_{\mu\nu} + u_\mu u_\nu)\tilde{p_d}, \tag{10}$$

where ρ_m and ρ_d are respectively the energy density of DM and new HDE, and $\tilde{p_d}$ is an effective pressure composed by the pressure p_d of new HDE plus the bulk viscous pressure.

Because of the assumed isotropic and homogeneity of the model, the shear viscosity plays no role, and only the bulk viscosity ζ has to be considered. In general, the presence of ζ does not have any influence upon the (00)-component of the equations of motion. The only change in the formalism because of viscosity is that the thermodynamical pressure becomes replaced with the effective pressure $\tilde{p_d}$ defined as

$$\tilde{p_d} = p_d - \zeta \nabla_\nu u^\nu, \tag{11}$$

where ζ is a coefficient of bulk viscosity that arises in a fluid when it it out of local thermodynamic equilibrium and that induces a viscous pressure equals to $-\zeta \nabla_\nu u^\nu$. The form of the above equation was originally proposed by Eckart [41] in the context of relativistic dissipative process occurring in thermodynamic systems went out of local thermal equilibrium. Many authors [65–68] have used Eckart approach to explain the recent acceleration of the universe with bulk viscous fluid. In particular, it has been used to model bulk viscous dark fluids as responsible of the observed acceleration of the universe. It is assumed that the approximation of vanishing relaxation time is valid for this purpose for instance [69–71]. In a paper [69], it is mentioned that Hiscock and Salmonson [72] showed that a flat FRW model with a bulk viscous Boltzmann gas expands faster when the Eckart framework is used. These motivate us to use Eckart formalism, especially when one tries to look at the phenomenon of recent acceleration of the universe.

In $f(R,T)$ theory when it is considered the effective pressure, the matter Lagrangian is $\mathcal{L}_m = -\tilde{p_d}$. Therefore, Eq.(6) gives $\ominus_{\mu\nu} = -2T_{\mu\nu} - \tilde{p_d}\ g_{\mu\nu}$, where the trace, $T = g^{\mu\nu}T_{\mu\nu}$, has now the form of $T = \rho_m + \rho_d - 3(p_d - \zeta \nabla_\nu u^\nu)$.

Using above values of $\tilde{p_d}$, $\ominus_{\mu\nu}$ and T, the field equations (8) for the line element (9) and energy stress tensor (10) yield

$$3H^2 = \rho_m + \rho_d + \lambda\ (\rho_m + \rho_d + p_d - 3\zeta H) + \frac{1}{2}\lambda\ T, \tag{12}$$

$$2\dot{H} + 3H^2 = -p_d + 3\zeta H + \frac{1}{2}\lambda\ T. \tag{13}$$

where $H = \dot{a}/a$ is the Hubble parameter and the bulk viscous pressure $-\zeta \nabla_\nu u^\nu$ can be written as $-3\zeta H$. An over dot denotes time derivative. We assume that a relation between p_d and ρ_d is connected by an equation of state (EoS), $p_d = \omega_d\ \rho_d$, where ω_d is the EoS parameter of new HDE. Therefore, from dynamical equations (12) and (13), a single evolution equation for H can be obtained as

$$2\dot{H} + (1+\lambda)[\rho_m + (1+\omega_d)\rho_d] - 3(1+\lambda)\zeta H = 0. \tag{14}$$

Following the Granda and Oliveros [32], the energy density of new HDE can be written as

$$\rho_d = 3(\alpha H^2 + \beta \dot{H}), \tag{15}$$

where α and β are the dimensionless parameters, which must satisfy the restrictions imposed by the current observational data.

Using (15) into (12), the energy density ρ_m of DM can be obtained as

$$\rho_m = \frac{3}{(2+3\lambda)}\left[(2-2\alpha-3\lambda\alpha+\lambda\alpha\omega_d)H^2-\lambda\zeta H-\beta(2+3\lambda-\lambda\omega_d)\dot{H}\right]. \tag{16}$$

Substituting (15) and (16) into (14), we get finally the first order differential equation for the Hubble parameter as

$$\dot{H}+(1+2\lambda\alpha\omega_d+\alpha\omega_d)AH^2-(1+2\lambda)\zeta AH=0. \tag{17}$$

where $A=\frac{3(1+\lambda)}{2+3\lambda+3\beta(1+\lambda)(1+2\lambda)\omega_d}$.

On the thermodynamical grounds, ζ is conventionally chosen to be a positive quantity and generically depends on the cosmic time t, or redshift z, or the scale factor a, or the energy density ρ_d, or a more complicated combination form. Maartens [73] assumed the bulk viscous coefficient as $\zeta \propto \rho^n$, where n is a constant. Li and Barrow [74] have studied a unified model for the dark sectors with a single component universe consisting of bulk viscous dark matter. They have assumed the bulk viscous coefficient as a function of energy density alone. They have observed that the model shows an early deceleration and late time acceleration. In the Refs. [49, 50, 75], the most general form of bulk viscosity has been considered with generalized equation of state. Many authors have considered various forms of bulk viscous coefficient to discuss the cosmological models. Here, we analyze the properties of viscous new HDE by considering bulk viscous coefficient as [49, 50, 69, 75]

$$\zeta=\zeta_0+\zeta_1 H, \tag{18}$$

where ζ_0 and ζ_1 are positive constants. The motivation for choosing this bulk viscosity is that the viscosity phenomenon is associated with velocity and acceleration. We discuss the cosmological issues through a parameterized bulk viscosity that is a linear combination of two terms. The second term $\zeta_1 H$ describes bulk viscosity proportional to the Hubble parameter H, i.e., expansion ratio of the universe. The model with first term is discussed by many authors. Thus, a linear combination of these two terms may provide better results.
Using the ansatz (18) into (17), we get the evolution equation as

$$\dot{H}+\{1+(1+2\lambda)(\alpha\omega_d-\zeta_1)\}AH^2-(1+2\lambda)\zeta_0 AH=0. \tag{19}$$

In what follows we solve (19) to find the cosmological parameters, Hubble parameter, scale factor, deceleration parameter in terms of cosmic time t and a and discuss the behavior in detail.

3.1 Evolution of the scale factor

On solving (19), we get

$$H=\frac{e^{(1+2\lambda)A\zeta_0 t}}{c_1+\frac{\{1+(1+2\lambda)(\alpha\omega_d-\zeta_1)\}}{(1+2\lambda)\zeta_0}\,e^{(1+2\lambda)A\zeta_0 t}}, \tag{20}$$

where c_1 is the constant of integration. Now, using $H = \dot{a}/a$, we can obtained the scale factor as

$$a = c_2 \left[c_1 + \frac{\{1 + (1+2\lambda)(\alpha\omega_d - \zeta_1)\}}{(1+2\lambda)\zeta_0} e^{(1+2\lambda)A\zeta_0 t} \right]^{\frac{1}{A\{1+(1+2\lambda)(\alpha\omega_d-\zeta_1)\}}}, \tag{21}$$

where c_2 is another integration constant. Assuming $H = H_0$ at $t = t_0$, where t_0 is the present time when viscous new HDE starts to dominate, Eq.(20) can be written as

$$H(t) = H_0 e^{(1+2\lambda)A\zeta_0(t-t_0)} \left[1 + \frac{\{1 + (1+2\lambda)(\alpha\omega_d - \zeta_1)\}H_0}{(1+2\lambda)\zeta_0} \left(e^{(1+2\lambda)A\zeta_0(t-t_0)} - 1 \right) \right]^{-1}. \tag{22}$$

If we consider $a = a_0 = 1$ at $t = t_0$, then the scale factor (21) can be written as

$$a(t) = \left[1 + \frac{\{1 + (1+2\lambda)(\alpha\omega_d - \zeta_1)\}H_0}{(1+2\lambda)\zeta_0} \left(e^{(1+2\lambda)A\zeta_0(t-t_0)} - 1 \right) \right]^{\frac{1}{A\{1+(1+2\lambda)(\alpha\omega_d-\zeta_1)\}}}, \tag{23}$$

where $\lambda \neq -1/2$ and $\zeta_0 \neq 0$. It is observed that the scale factor is of exponential form which can explain the phase transition. We can analyzed the behavior of the scale factor for all possible combinations of (ζ_0, ζ_1) and model parameter λ. Taking $a(t) = 0$, we obtain the cosmic time when the Big-Bang happens

$$t(\text{at Big-Bang}) = t_0 + \frac{1}{(1+2\lambda)A\zeta_0} \, ln \left[1 - \frac{(1+2\lambda)\zeta_0}{\{1 + (1+2\lambda)(\alpha\omega_d - \zeta_1)\}H_0} \right]. \tag{24}$$

In early time of evolution, the scale factor (23) can be approximated by

$$a \sim \left[1 + \frac{3H_0(1+\lambda)\{1 + (1+2\lambda)(\alpha\omega_d - \zeta_1)\}}{2 + 3\lambda + 3\beta(1+\lambda)(1+2\lambda)} (t - t_0) \right]^{\frac{1}{A\{1+(1+2\lambda)(\alpha\omega_d-\zeta_1)\}}}, \tag{25}$$

which shows the decelerated expansion in early time. In late time of evolution, the scale factor behaves as

$$a(t) \sim exp\left[(1+2\lambda)\zeta_0 A(t - t_0)\right], \tag{26}$$

which shows the de Sitter universe, *i.e.*, the universe expands with accelerated rate in the late-time of the evolution. This shows that the scale factor at the respective limits has an earlier decelerated phase followed by an accelerated phase in the later stage of the evolution.

Let us compute the second order derivatives of (23), which is given by

$$\begin{aligned} \frac{d^2a}{dt^2} &= H_0^2 \left(e^{2(1+2\lambda)\zeta_0 A(t-t_0)} \right) \left[1 + \frac{[(1+2\lambda)\zeta_0 - \{1 + (1+2\lambda)(\alpha\omega_d - \zeta_1)\}H_0]A}{H_0} e^{-(1+2\lambda)\zeta_0 A(t-t_0)} \right] \\ &\times \left[1 + \frac{\{1 + (1+2\lambda)(\alpha\omega_d - \zeta_1)\}H_0}{(1+2\lambda)\zeta_0} \left(e^{(1+2\lambda)\zeta_0 A(t-t_0)} - 1 \right) \right]^{\frac{1}{A\{1+(1+2\lambda)(\alpha\omega_d-\zeta_1)\}}-2}. \end{aligned} \tag{27}$$

Equating (27) to zero to get the transition time, $t_{\,trans}$ between the decelerated to the accelerated expansion epochs, which is given by

$$t_{\,trans} = t_0 + \frac{1}{A(1+2\lambda)\zeta_0} \, ln \left\{ \frac{A[\{1 + (1+2\lambda)(\alpha\omega_d - \zeta_1)\}H_0 - (1+2\lambda)\zeta_0]}{H_0} \right\}. \tag{28}$$

Using (23) into (22), the Hubble parameter in terms of the scale factor can be written as

$$H(a)=\frac{(1+2\lambda)H_0}{[1+(1+2\lambda)(\alpha\omega_d-\zeta_1)]}\left[\frac{\zeta_0}{H_0}+\left\{\frac{[1+(1+2\lambda)(\alpha\omega_d-\zeta_1)]}{(1+2\lambda)}-\frac{\zeta_0}{H_0}\right\}a^{-A\{1+(1+2\lambda)(\alpha\omega_d-\zeta_1)\}}\right]. \tag{29}$$

Differentiating (29) with respect to a, we obtain

$$\begin{aligned}\frac{d\dot{a}}{da} &= \frac{(1+2\lambda)H_0}{[1+(1+2\lambda)(\alpha\omega_d-\zeta_1)]}\left[\frac{\zeta_0}{H_0}-\left(\frac{[1+(1+2\lambda)(\alpha\omega_d-\zeta_1)]}{(1+2\lambda)}-\frac{\zeta_0}{H_0}\right)\right.\\ &\left.\times\left(\frac{1+3(1+\lambda)(1+2\lambda)\{(\alpha-\beta)\omega_d-\zeta_1\}}{2+3\lambda+3\beta(1+\lambda)(1+2\lambda)\omega_d}\right)a^{-A\{1+(1+2\lambda)(\alpha\omega_d-\zeta_1)\}}\right].\end{aligned} \tag{30}$$

Equating (30) to zero, the transition between the decelerated to the accelerated phase in terms of the scale factor can be written as

$$\begin{aligned}a_T &= \left[\left\{\frac{1+3(1+\lambda)(1+2\lambda)[(\alpha-\beta)\omega_d-\zeta_1]}{(1+2\lambda)\{2+3\lambda+3\beta(1+\lambda)(1+2\lambda)\omega_d\}\zeta_0}\right\}\right.\\ &\left.\times\left\{[1+(1+2\lambda)(\alpha\omega_d-\zeta_1)]H_0-(1+2\lambda)\zeta_0\right\}\right]^{\frac{1}{A[1+(1+2\lambda)(\alpha\omega_d-\zeta_1)]}},\end{aligned} \tag{31}$$

and the corresponding transition redshift $z=a^{-1}-1$ is

$$\begin{aligned}z_T = &= \left[\left\{\frac{1+3(1+\lambda)(1+2\lambda)[(\alpha-\beta)\omega_d-\zeta_1]}{(1+2\lambda)\{2+3\lambda+3\beta(1+\lambda)(1+2\lambda)\omega_d\}\zeta_0}\right\}\right.\\ &\left.\times\left\{[1+(1+2\lambda)(\alpha\omega_d-\zeta_1)]H_0-(1+2\lambda)\zeta_0\right\}\right]^{-\frac{1}{A[1+(1+2\lambda)(\alpha\omega_d-\zeta_1)]}}-1.\end{aligned} \tag{32}$$

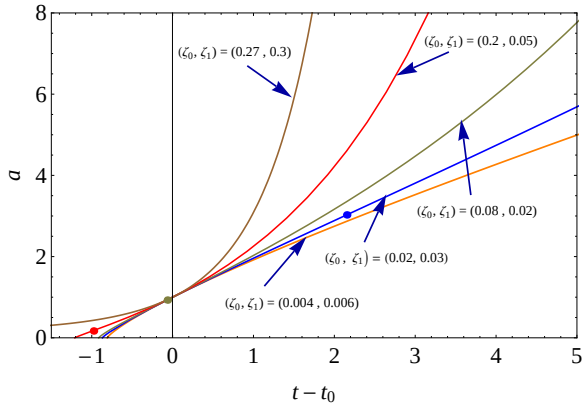

Fig.1 The evolution of scale factor with respect to $(t-t_0)$ for different combination of ζ_0 and ζ_1 with $\omega_d=-0.5$, $\lambda=0.06$ $H_0=1$, $\alpha=0.8502$ and $\beta=0.4817$.

Here, T stands for transition. From (31) and (32), we observe that the transition from decelerated to accelerated epoch takes place at present time, *i.e.*, at $a_T = 1$ or $z_T = 0$ for $(\zeta_0 + H_0\zeta_1) = \frac{\{1+3(1+\lambda)(1+2\lambda)(\alpha-\beta)\omega_d\}H_0}{3(1+\lambda)(1+2\lambda)}$ depending on positive or negative value of λ. Especially, substituting the observational values of model parameters $\alpha = 0.8502$ and $\beta = 0.4817$ [76] along with $\omega_d = -0.5$, $H_0 = 1$, we get $\zeta_0 + \zeta_1 = 0.096$ for positive value of $\lambda = 0.06$ and $\zeta_0 + \zeta_1 = 0.218$ for negative value of $\lambda = -0.06$, respectively. Thus, for the present time transition from deceleration to acceleration takes place at $\zeta_0 + \zeta_1 = 0.096$ for positive values of $\lambda = 0.06$ and for negative value of $\lambda = -0.06$, we get $\zeta_0 + \zeta_1 = 0.218$. A plot of the evolution of the scale factor is given in Fig. 1. for different values of a combination of ζ_0 and ζ_1 and positive value of λ. For $0 < (\zeta_0 + \zeta_1) < 0.096$, the scale factor has a deceleration phase followed by an accelerated phase in late time. For $(\zeta_0 + \zeta_1) = 0.096$, the transition takes place at present time and for $(\zeta_0 + \zeta_1) > 0.096$, the transition from decelerated phase to accelerated phase occurs at early time. For higher combination of (ζ_0, ζ_1), acceleration takes place in infinite past. Similar behavior can be observed for the negative value of λ. Fig.1 plots the graph of the scale factor versus time for different combinations of (ζ_0, ζ_1). A dot on each trajectory denotes the present time transition from decelerated phase to accelerated phase.

3.2 Behavior of the deceleration parameter

Now, the evolutionary behavior of the universe can also be discussed by the deceleration parameter, which is defined by $q = -\frac{a\ddot{a}}{\dot{a}^2}$. Using (23), the deceleration parameter can be obtained as

$$q(t) = \left\{\frac{[\{1 + (1+2\lambda)(\alpha\omega_d - \zeta_1)\}H_0 - (1+2\lambda)\zeta_0]A}{H_0}\right\}e^{-(1+2\lambda)\zeta_0 A(t-t_0)} - 1. \tag{33}$$

Equation (33) shows that the deceleration parameter is time-dependent which may describe the phase transition. It can be observed that deceleration parameter must change its sign at $t = t_0$. The sign of q is positive for $t < t_0$ and it is negative for $t > t_0$.

The deceleration parameter in terms of a can be obtained as

$$\begin{aligned} q(a) = {} & A[\{1 + (1+2\lambda)(\alpha\omega_d - \zeta_1)\}H_0 - (1+2\lambda)\zeta_0] \\ & \times \left[\frac{[1 + (1+2\lambda)(\alpha\omega_d - \zeta_1)]}{(1+2\lambda)\zeta_0\left\{a^{A[1+(1+2\lambda)(\alpha\omega_d-\zeta_1)]} - 1\right\} + [1 + (1+2\lambda)(\alpha\omega_d - \zeta_1)]H_0}\right] - 1. \end{aligned} \tag{34}$$

In the terms of redshift, the deceleration parameter is given by

$$\begin{aligned} q(z) = {} & A[\{1 + (1+2\lambda)(\alpha\omega_d - \zeta_1)\}H_0 - (1+2\lambda)\zeta_0] \\ & \times \left[\frac{[1 + (1+2\lambda)(\alpha\omega_d - \zeta_1)]}{(1+2\lambda)\zeta_0\left\{(1+z)^{-A[1+(1+2\lambda)(\alpha\omega_d-\zeta_1)]} - 1\right\} + [1 + (1+2\lambda)(\alpha\omega_d - \zeta_1)]H_0}\right] - 1. \end{aligned} \tag{35}$$

The present value of q corresponds to $z = 0$ or $a = 1$ is,

$$q_0 = \frac{[\{1 + (1+2\lambda)(\alpha\omega_d - \zeta_1)\}H_0 - (1+2\lambda)\zeta_0]A}{H_0} - 1. \tag{36}$$

Table 1: Variation of q for $\omega_d = -0.5$, $\alpha = 0.8502$, $\beta = 0.4817$

λ	Constraints on ζ_0 and ζ_1	q	Evolution of the Universe
$\lambda \geq 1.272$	For all $\zeta_0 > 0$ and $\zeta_1 > 0$	Positive	Decelerated expansion
$0.24 \leq \lambda < 1.272$	For all $\zeta_0 > 0$ and $\zeta_1 > 0$	Negative	Accelerated expansion
$-0.5 < \lambda < 0.24$	$0 < (\zeta_0 + H_0\zeta_1) < \frac{\{1-0.55275(1+\lambda)(1+2\lambda)\}H_0}{3(1+\lambda)(1+2\lambda)}$	+ve to −ve	Transition from dec. to acc.
	$(\zeta_0 + H_0\zeta_1) \geq \frac{\{1-0.55275(1+\lambda)(1+2\lambda)\}H_0}{3(1+\lambda)(1+2\lambda)}$	Negative	Accelerated expansion
$-0.69 \leq \lambda \leq -0.5$	For all $\zeta_0 > 0$ and $\zeta_1 > 0$	Positive	Decelerated expansion
$-1 \leq \lambda < -0.69$	For all $\zeta_0 > 0$ and $\zeta_1 > 0$	Negative	Accelerated expansion
$-1.73 \leq \lambda < -1$	$0 < (\zeta_0 + H_0\zeta_1) < \frac{\{1-0.55275(1+\lambda)(1+2\lambda)\}H_0}{3(1+\lambda)(1+2\lambda)}$	−ve to +ve	Transition from acc. to dec.
	$(\zeta_0 + H_0\zeta_1) \geq \frac{\{1-0.55275(1+\lambda)(1+2\lambda)\}H_0}{3(1+\lambda)(1+2\lambda)}$	Positive	Decelerated expansion
$\lambda < -1.73$	For all $\zeta_0 > 0$ and $\zeta_1 > 0$	Positive	Decelerated expansion

Table 2: Variation of q for $\omega_d = -1$, $\alpha = 0.8502$, $\beta = 0.4817$

λ	Constraints on ζ_0 and ζ_1	q	Evolution of the Universe
$\lambda \geq 0.265$	For all $\zeta_0 > 0$ and $\zeta_1 > 0$	Positive	Decelerated expansion
$-0.032 \leq \lambda < 0.265$	For all $\zeta_0 > 0$ and $\zeta_1 > 0$	Negative	Accelerated expansion
$-0.5 < \lambda < -0.032$	$0 < (\zeta_0 + H_0\zeta_1) < \frac{\{1-1.1055(1+\lambda)(1+2\lambda)\}H_0}{3(1+\lambda)(1+2\lambda)}$	+ve to −ve	Transition from dec. to acc.
	$(\zeta_0 + H_0\zeta_1) \geq \frac{\{1-1.1055(1+\lambda)(1+2\lambda)\}H_0}{3(1+\lambda)(1+2\lambda)}$	Negative	Accelerated expansion
$-0.727 < \lambda \leq -0.5$	For all $\zeta_0 > 0$ and $\zeta_1 > 0$	Positive	Decelerated expansion
$-1 \leq \lambda \leq -0.727$	For all $\zeta_0 > 0$ and $\zeta_1 > 0$	Negative	Accelerated expansion
$-1.46 \leq \lambda < -1$	$0 < (\zeta_0 + H_0\zeta_1) < \frac{\{1-1.1055(1+\lambda)(1+2\lambda)\}H_0}{3(1+\lambda)(1+2\lambda)}$	−ve to +ve	Transition from acc. to dec.
	$(\zeta_0 + H_0\zeta_1) \geq \frac{\{1-1.1055(1+\lambda)(1+2\lambda)\}H_0}{3(1+\lambda)(1+2\lambda)}$	Positive	Decelerated expansion
$\lambda < -1.46$	For all $\zeta_0 > 0$ and $\zeta_1 > 0$	Positive	Decelerated expansion

This equation shows that if $(\zeta_0 + H_0\zeta_1) = \frac{\{1+3(1+\lambda)(1+2\lambda)(\alpha-\beta)\omega_d\}H_0}{3(1+\lambda)(1+2\lambda)}$, the value of $q_0 = 0$. Thus, the transition into accelerating phase would occur at present time for this combination of (ζ_0, ζ_1). Especially, taking $\alpha = 0.8502$, $\beta = 0.4817$, $\omega_d = -0.5$, $H_0 = 1$ and $\lambda = 0.06$ in above expression, we get $\zeta_0 + \zeta_1 = 0.096$, which gives $q_0 = 0$.

Tables 1-3 discuss the behavior of deceleration parameter and corresponding evolution for different ranges of λ under constraints on $(\zeta_0 + H_0\zeta_1)$. We consider three different values of ω_d of three different phases, *e.g.*, $\omega_d = -0.5$, -1 and -1.1414, respectively. We assume the observational values of the model parameters are $\alpha = 0.8502$ and $\beta = 0.4817$ [76].

In table 1, we observe that for any positive value of ζ_0 and ζ_1, the model corresponds to the decelerated expansion throughout the evolution for $\lambda \geq 1.272$, $-0.69 \leq \lambda \leq -0.5$ and $\lambda <$

Table 3: Variation of q for $\omega_d = -1.1414$, $\alpha = 0.8502$, $\beta = 0.4817$

λ	Constraints on ζ_0 and ζ_1	q	Evolution of the Universe
$\lambda \geq 0.145$	For all $\zeta_0 > 0$ and $\zeta_1 > 0$	Positive	Decelerated expansion
$-0.072 \leq \lambda < 0.145$	For all $\zeta_0 > 0$ and $\zeta_1 > 0$	Negative	Accelerated expansion
$-0.5 < \lambda < -0.072$	$0 < (\zeta_0 + H_0\zeta_1) < \frac{\{1-1.26182(1+\lambda)(1+2\lambda)\}H_0}{3(1+\lambda)(1+2\lambda)}$	+ve to −ve	Transition from dec. to acc.
	$(\zeta_0 + H_0\zeta_1) \geq \frac{\{1-1.26182(1+\lambda)(1+2\lambda)\}H_0}{3(1+\lambda)(1+2\lambda)}$	Negative	Accelerated expansion
$-0.735 \leq \lambda \leq -0.5$	For all $\zeta_0 > 0$ and $\zeta_1 > 0$	Positive	Decelerated expansion
$-1 \leq \lambda < -0.735$	For all $\zeta_0 > 0$ and $\zeta_1 > 0$	Negative	Accelerated expansion
$-1.42 \leq \lambda < -1$	$0 < (\zeta_0 + H_0\zeta_1) < \frac{\{1-1.26182(1+\lambda)(1+2\lambda)\}H_0}{3(1+\lambda)(1+2\lambda)}$	−ve to +ve	Transition from acc. to dec.
	$(\zeta_0 + H_0\zeta_1) \geq \frac{\{1-1.26182(1+\lambda)(1+2\lambda)\}H_0}{3(1+\lambda)(1+2\lambda)}$	Positive	Decelerated expansion
$\lambda < -1.42$	For all $\zeta_0 > 0$ and $\zeta_1 > 0$	Positive	Decelerated expansion

-1.73, and the model corresponds to the accelerated expansion throughout the evolution for $0.24 \leq \lambda < 1.272$ and $-1 \leq \lambda < -0.69$. For smaller values of ζ_0 and ζ_1, *i.e.*, $0 < (\zeta_0 + H_0\zeta_1) < \frac{\{1-0.55275(1+\lambda)(1+2\lambda)\}H_0}{3(1+\lambda)(1+2\lambda)}$, the universe shows the phase transition from positive to negative for $-0.5 < \lambda < 0.24$ and shows the phase transition from negative to positive for $-1.73 \leq \lambda < -1$. The larger values of ζ_0 and ζ_1, *i.e.*, $(\zeta_0 + H_0\zeta_1) \geq \frac{\{1-0.55275(1+\lambda)(1+2\lambda)\}H_0}{3(1+\lambda)(1+2\lambda)}$, shows that the universe represents the accelerated expansion throughout the evolution for $-0.5 < \lambda < 0.24$ and represents the decelerated expansion throughout the evolution for $-1.73 \leq \lambda < -1$.

Table 2 represents the analysis of the evolution of the universe for $\omega_d = -1$ along with the observational values of model parameters. We observe that for any positive value of ζ_0 and ζ_1, the model corresponds to the decelerated expansion throughout the evolution for $\lambda \geq 0.265$, $-0.727 < \lambda \leq -0.5$ and $\lambda < -1.46$ ranges of λ, and the model corresponds to the accelerated expansion throughout the evolution for $-0.032 \leq \lambda < 0.265$ and $-1 \leq \lambda \leq -0.727$. For smaller values of ζ_0 and ζ_1, *i.e.*, $0 < (\zeta_0 + H_0\zeta_1) < \frac{\{1-1.1055(1+\lambda)(1+2\lambda)\}H_0}{3(1+\lambda)(1+2\lambda)}$, the universe shows the phase transition from deceleration to acceleration for $-0.5 < \lambda < -0.032$ and shows the phase transition from acceleration to deceleration for $-1.46 \leq \lambda < -1$. The larger values of ζ_0 and ζ_1, *i.e.*, $(\zeta_0 + H_0\zeta_1) \geq \frac{\{1-1.1055(1+\lambda)(1+2\lambda)\}H_0}{3(1+\lambda)(1+2\lambda)}$, shows that the universe accelerates throughout the evolution for $-0.5 < \lambda < -0.032$ and decelerates throughout the evolution for $-1.46 \leq \lambda < -1$.

In Table 3, we consider the value of $\omega_d < -1$, *e.g.*, $\omega_d = -1.1414$ with the same observational values of model parameters. We observe that for any positive value of ζ_0 and ζ_1, the model shows the decelerated expansion throughout the evolution for $\lambda \geq 0.145$, $-0.735 \leq \lambda \leq -0.5$ and $\lambda < -1.42$, and the model corresponds to the accelerated expansion throughout the evolution for $-0.072 \leq \lambda < 0.145$ and $-1 \leq \lambda < -0.735$. The smaller values of ζ_0 and ζ_1 , *i.e.*, $0 < (\zeta_0 + H_0\zeta_1) < \frac{\{1-1.26182(1+\lambda)(1+2\lambda)\}H_0}{3(1+\lambda)(1+2\lambda)}$, shows the phase transition from deceleration to acceleration for $-0.5 < \lambda < -0.072$ and the phase transition from acceleration to deceleration occur for $-1.42 \leq \lambda < -1$. For the larger values of ζ_0 and ζ_1, *i.e.*, $(\zeta_0 + H_0\zeta_1) \geq \frac{\{1-1.26182(1+\lambda)(1+2\lambda)\}H_0}{3(1+\lambda)(1+2\lambda)}$, the universe represents the accelerated expansion throughout the evolution for $-0.5 < \lambda < -0.072$ and shows the decelerated expansion throughout the evolution for $-1.42 \leq \lambda < -1$.

3.3 Statefinder diagnostic

Sahni *et al.* [77] and Alam *et al.* [78] proposed a new geometrical diagnostic pair $\{r, s\}$ called statefinder. The statefinder is a geometrical diagnostic in the sense that it is constructed from a space-time metric directly, and allows us to characterise the properties of DE in a model independent manner. It is dimensionless and is constructed from the scale factor $a(t)$ and its derivatives up to the third order. The statefinder pair is defined as

$$r = \frac{\dddot{a}}{aH^3} \quad \text{and} \quad s = \frac{r-1}{3(q-1/2)}. \tag{37}$$

This pair has a fixed point values $\{r, s\} = \{1, 0\}$ and $\{r, s\} = \{1, 1\}$ for ΛCDM and $SCDM$ models, respectively. The statefinder method has been extensively used in the literature to distinguish among various models of dark energy and modified theories of gravity.

On substituting the required values in above, we get

$$\begin{aligned} r &= 1 + \left[\frac{3A\left\{1 - \frac{A[(1+(1+2\lambda)(\alpha\omega_d - \zeta_1)]}{3}\right\}\left\{(1+2\lambda)\zeta_0 - [(1+(1+2\lambda)(\alpha\omega_d - \zeta_1)]H_0\right\}}{H_0\, e^{(1+2\lambda)\zeta_0 A(t-t_0)}}\right] \\ &+ \left[\frac{A^2\left\{(1+2\lambda)\zeta_0 - [(1+(1+2\lambda)(\alpha\omega_d - \zeta_1)]H_0\right\}^2}{H_0^2\, e^{2(1+2\lambda)\zeta_0 A(t-t_0)}}\right], \end{aligned} \tag{38}$$

and

$$s = \frac{\frac{2A\left\{1 - \frac{A[(1+(1+2\lambda)(\alpha\omega_d - \zeta_1)]}{3}\right\}\left\{(1+2\lambda)\zeta_0 - [(1+(1+2\lambda)(\alpha\omega_d - \zeta_1)]H_0\right\}}{3H_0 e^{(1+2\lambda)\zeta_0 A(t-t_0)}} + \frac{2A^2\left\{(1+2\lambda)\zeta_0 - [(1+(1+2\lambda)(\alpha\omega_d - \zeta_1)]H_0\right\}^2}{9H_0^2 e^{2(1+2\lambda)\zeta_0 A(t-t_0)}}}{\frac{2A\left\{[(1+(1+2\lambda)(\alpha\omega_d - \zeta_1)]H_0 - (1+2\lambda)\zeta_0\right\}}{3H_0 e^{(1+2\lambda)\zeta_0 A(t-t_0)}} - 1}, \tag{39}$$

which are time dependent due to the presence of bulk viscosity coefficient. Equations (38) and (39) show that in the limit $(t - t_0) \to \infty$, the statefinder parameters $\{r, s\} \to \{1, 0\}$, a value corresponding to the ΛCDM model. Hence, the viscous new HDE model resembles the ΛCDM model in future. Now, we can plot the $r - s$ trajectory in $r - s$ plane and $r - q$ trajectory in $r - q$ plane to analyse viscous new HDE model in the framework of $f(R, T)$ theory. It can be observed that the values of $\{r, s\}$ depend on the choice of coupling parameter λ and the viscosity coefficients (ζ_0, ζ_1). We consider the observational values of model parameters $\alpha = 0.8502$, $\beta = 0.4817$ and $H_0 = 1$, $t_0 = 1$, $\omega_d = -0.5$ to plot these trajectories for positive and negative value of λ along with the different combinations of (ζ_0, ζ_1). The $r - s$ and $r - q$ trajectories for different combinations of (ζ_0, ζ_1) and positive value of λ (*e.g.*, $\lambda = 0.06$) are shown in Figs. 2a and 2b, respectively. Figs. 3a and 3b show the respective $r - s$ and $r - q$ trajectories for different combinations of (ζ_0, ζ_1) and

negative value of λ (*e.g.*, $\lambda = -0.06$). The present value of the statefinder pair are

$$r_0 = 1 + \left[\frac{3A\left\{1 - \frac{A[(1+(1+2\lambda)(\alpha\omega_d-\zeta_1)]}{3}\right\}\left\{(1+2\lambda)\zeta_0 - [(1+(1+2\lambda)(\alpha\omega_d-\zeta_1)]H_0\right\}}{H_0}\right] + \left[\frac{A^2\left\{(1+2\lambda)\zeta_0 - [(1+(1+2\lambda)(\alpha\omega_d-\zeta_1)]H_0\right\}^2}{H_0^2}\right], \tag{40}$$

and

$$s_0 = \frac{\frac{2A\left\{1-\frac{A[(1+(1+2\lambda)(\alpha\omega_d-\zeta_1)]}{3}\right\}\left\{(1+2\lambda)\zeta_0-[(1+(1+2\lambda)(\alpha\omega_d-\zeta_1)]H_0\right\}}{3H_0} + \frac{2A^2\left\{(1+2\lambda)\zeta_0-[(1+(1+2\lambda)(\alpha\omega_d-\zeta_1)]H_0\right\}^2}{9H_0^2}}{\frac{2A\left\{[(1+(1+2\lambda)(\alpha\omega_d-\zeta_1)]H_0-(1+2\lambda)\zeta_0\right\}}{3H_0} - 1}. \tag{41}$$

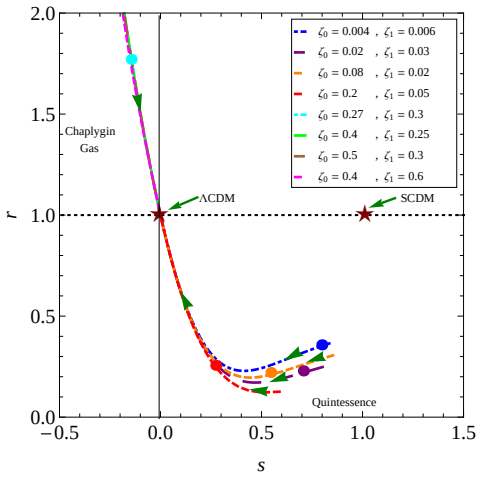

Fig.2(a) The $r-s$ trajectories are plotted in $r-s$ plane for different combinations of (ζ_0, ζ_1) with $\omega_d = -0.5$, $\alpha = 0.8502$, $\beta = 0.4817$ and $\lambda = 0.06$. The arrows represent the directions of the evolutions of statefinder diagnostic pair with time.

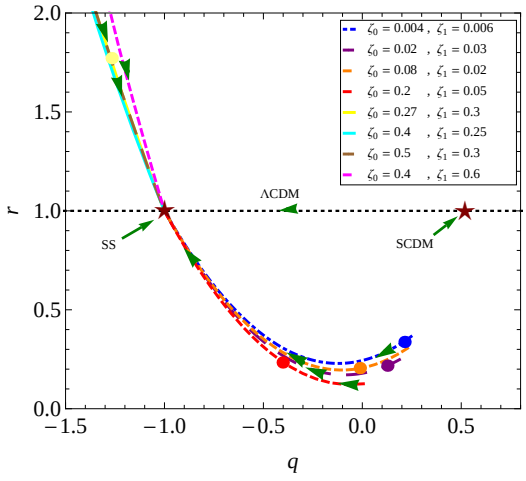

Fig.2(b) The $r-q$ trajectories are plotted in $r-q$ plane for different combinations of (ζ_0, ζ_1) with $\omega_d = -0.5$, $\alpha = 0.8502$, $\beta = 0.4817$ and $\lambda = 0.06$. The arrows represent the directions of the evolutions of statefinder diagnostic pair with time.

In Figs. 2a and 3a, stars represent the fixed point values of ΛCDM and $SCDM$ models, dots represent the present time values of $\{r, s\} = \{r_0, s_0\}$ and $\{r, q\} = \{r_0, q_0\}$, and the arrows represent the direction of the trajectories. The $r-s$ planes in Fig. 2a and 3a are divided into two regions $r < 1$, $s > 0$ and $r > 1$, $s < 0$ by a vertical line passing through the point (1,0). The trajectories in the $\{r, s\}$ planes lying in the region $r < 1$, $s > 0$, a feature similar to the quintessence model(Q-model) of DE [79]. The trajectories in the $\{r, s\}$ planes lying in the region $r > 1$, $s < 0$, a feature

similar to the generalized Chaplygin gas (CG) model of DE [77, 78]. Here, we obtain a parabolic trajectory for both cases on λ. From Fig. 2a, for $\lambda = 0.06$ we notice that the model behaves like Q-model for $0 < (\zeta_0+\zeta_1) \leq 0.46$, whereas for $(\zeta_0+\zeta_1) > 0.46$ the model mimic like CG model. The trajectories in both the regions converge to ΛCDM model in late time of evolution. In the case $\lambda = -0.06$, we observe from Fig. 3a that all the $r-s$ trajectories lie in the region $(r < 1, s > 0)$ for $0 < (\zeta_0 + \zeta_1) \leq 0.71$ which imply that the viscous new HDE model corresponds to Q model while the trajectories lie in $(r > 1, s < 0)$ region for $(\zeta_0 + \zeta_1) > 0.71$, *i.e.*, the model behaves like CG model. In late time the viscous new HDE model approaches to ΛCDM. For some combinations like $(\zeta_0, \zeta_1) = (0.08, 0.02)$, the trajectory starts in the vicinity of the $SCDM$ model and approaches to ΛCDM. Thus, we can conclude that for any value of λ (either positive or negative), our viscous new HDE model in the framework of $f(R,T)$ theory mimic like Q and CG models for specific range of viscosity coefficients and in late time of evolution it always converges to ΛCDM model.

The $r-q$ trajectories in $r-q$ plane for positive and negative values of λ and for different combinations of (ζ_0, ζ_1) are shown in Figs 2b and 3b, respectively. Here, in both the figures stars represent the fixed point values $\{r, q\} = \{1, 0.5\}$ for $SCDM$ model and $\{r, q\} = \{1, -1\}$ for Steady State (SS) model. The arrows represent the direction of the trajectories and the horizontal line at $r = 1$ represents the time evolution of the ΛCDM model. It can be observed that q changes its sign from positive to negative with respect to time for $0 < (\zeta_0 + \zeta_1) \leq 0.46$ in case of $\lambda = 0.06$ and for $0 < (\zeta_0 + \zeta_1) \leq 0.71$ in case $\lambda = -0.06$, which show the phase transition from decelerated phase to accelerated phase. For $(\zeta_0 + \zeta_1) > 0.46$ when $\lambda = 0.06$ and $(\zeta_0 + \zeta_1) > 0.71$ when $\lambda = -0.06$, q is always negative showing behavior of phantom. In the beginning this model behaves different from ΛCDM model but in late time it behaves the same as ΛCDM which converges to SS model in late time evolution. In Fig.3b, we observe that for some small values of (ζ_0, ζ_1), like $(\zeta_0, \zeta_1) = (0.08, 0.02)$, the $r-q$ trajectory starts in the neighbourhood of the $SCDM$ model. The present position of $\{r, s\} = \{r_0, s_0\}$ is indicated by dot in the plot. This means that the present viscous new HDE model is distinguishably different from the ΛCDM model but in late time it converges to SS model.

The present viscous new HDE model can also be discriminated from the holographic dark energy model with event horizon as the infrared cutoff, in which the $r-s$ evolution starts from a region $r \sim 1$, $s \sim 2/3$ and ends on the ΛCDM point [80]. It can also be discriminated from Ricci dark energy model in which (r, s) trajectory is a vertical segment, *i.e.*, s is a constant during the evolution of the universe [81].

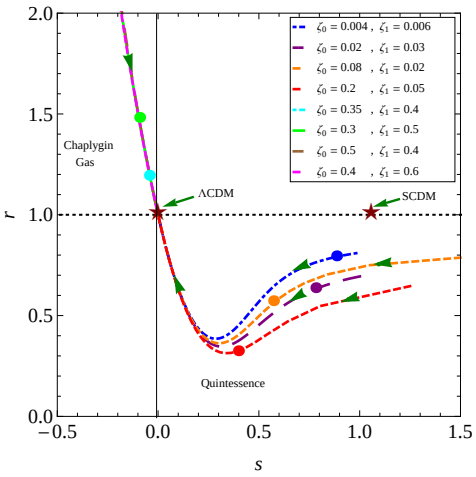

Fig.3(a) The $r-s$ trajectories are plotted in $r-s$ plane for different combinations of (ζ_0, ζ_1) with $\omega_d = -0.5$, $\alpha = 0.8502$, $\beta = 0.4817$ and $\lambda = -0.06$. The arrows represent the directions of the evolutions of statefinder diagnostic pair with time.

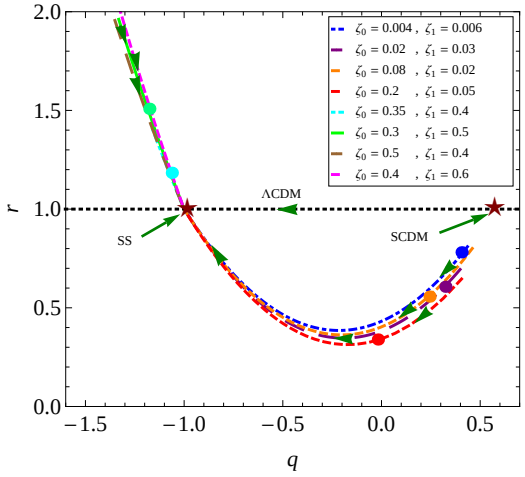

Fig.3(b) The $r-q$ trajectories are plotted in $r-q$ plane for different combinations of (ζ_0, ζ_1) with $\omega_d = -0.5$, $\alpha = 0.8502$, $\beta = 0.4817$ and $\lambda = -0.06$. The arrows represent the directions of the evolutions of statefinder diagnostic pair with time.

3.4 *Om* diagnostic

Sahni *et al.* [82] introduced a new geometrical diagnostic known as *Om*, which is a combination of the Hubble parameter and the cosmological redshift. Like the statefinder, *Om* depends only upon the expansion history of the universe. But, it's dependency only on the first derivative of the scale factor imply that it is easier to construct the *Om* as compare to statefinder parameters. It can discriminate dynamical dark energy models from ΛCDM, in a robust way, even if the value of the matter density is not precisely known. Secondly, it can provide a null test of ΛCDM hypothesis, *i.e.*, *Om(z)* - $\Omega_{0m} = 0$, if dark energy is a cosmological constant. *Om* has zero, negative and positive curvatures for ΛCDM, quintessence and phantom models, respectively. Many authors [83–85] have studied the DE models based on *Om(z)* diagnostic. Following Sahni *et al.* [82], *Om(z)* for spatially flat universe is defined as

$$Om(z) = \frac{\frac{H^2(z)}{H_0^2} - 1}{(1+z)^3 - 1}, \tag{42}$$

where H_0 is the present value of the Hubble parameter. On substituting the required value of $H(z)$ from (29) into (42), we get the value of *Om(z)* as

$$Om(z) = \frac{\frac{(1+2\lambda)^2}{[1+(1+2\lambda)(\alpha\omega_d-\zeta_1)]^2}\left[\frac{\zeta_0}{H_0} + \left\{\frac{[1+(1+2\lambda)(\alpha\omega_d-\zeta_1)]}{(1+2\lambda)} - \frac{\zeta_0}{H_0}\right\}(1+z)^{A[1+(1+2\lambda)(\alpha\omega_d-\zeta_1)]}\right]^2 - 1}{[(1+z)^3-1]}. \tag{43}$$

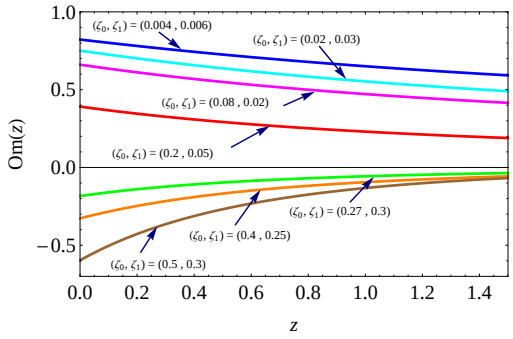

Fig.4(a) The $Om-z$ trajectories are plotted in $Om-z$ plane for different values of ζ_0 and ζ_1 with $\omega_d = -0.5$ and $\lambda = 0.06$ along with the observational value of $\alpha = 0.8502$ and $\beta = 0.4817$.

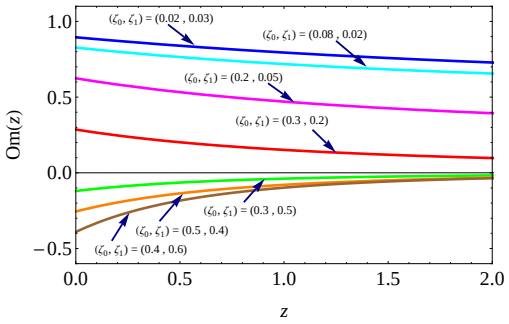

Fig.4(b) The $Om-z$ trajectories are plotted in $Om-z$ plane for different values of ζ_0 and ζ_1 with $\omega_d = -0.5$ and $\lambda = -0.06$ along with the observational value of $\alpha = 0.8502$ and $\beta = 0.4817$.

In Fig. 4a, we plot the evolution of *Om(z)* against redshift z corresponding to different values of a combination of (ζ_0, ζ_1), $\alpha = 0.8502$, $\beta = 0.4817$, $\omega_d = -0.5$ $H_0 = 1$ and $\lambda = 0.06$. Similarly, in Fig. 4b, we plot the evolution of *Om(z)* against redshift z corresponding to different values of a combination of (ζ_0, ζ_1), $\alpha = 0.8502$, $\beta = 0.4817$, $\omega_d = -0.5$ $H_0 = 1$ and $\lambda = -0.06$. The trajectory in Fig.4a is divided horizontally into two regions. In lower region, it may be seen that *Om(z)* decreases as z decreases for $(\zeta_0 + \zeta_1) > 0.46$, so positive slope of *Om(z)* suggests phantom $(\omega_d < -1)$ like behavior in the presence of viscosity with positive values of $\lambda = 0.06$. However, in upper region, *Om(z)* increases as z decreases for $0 < (\zeta_0 + \zeta_1) \leq 0.46$, so negative slope of *Om(z)* indicating quintessence like behavior in the presence of viscosity.

Similarly, the trajectory in Fig.4b is divided horizontally into two regions. In lower region, it may be seen that *Om(z)* decreases as z decreases for $(\zeta_0 + \zeta_1) > 0.71$, so positive slope of *Om(z)* suggests phantom $(\omega_d < -1)$ like behavior in the presence of viscosity with positive values of $\lambda = -0.06$. However, in upper region, *Om(z)* increases as z decreases for $0 < (\zeta_0 + \zeta_1) \leq 0.71$, so negative slope of *Om(z)* indicating quintessence like behavior in the presence of viscosity. In the late time of evolution when $z = -1$, we get $Om(z) = 1 - \frac{(1+2\lambda)^2\zeta_0^2}{[1+(1+2\lambda)(\alpha\omega_d-\zeta_1)]^2H_0^2}$, which is the constant value of *Om(z)*, *i.e.*, zero curvature. Thus, in late time the viscous new HDE corresponds to ΛCDM.

3.5 Effective Equation of state parameter

Let us discuss the bulk viscous effect on effective equation of state parameter, ω_{eff} which is given by

$$\omega_{eff} = \frac{p_d - 3\zeta H}{\rho_m + \rho_d}, \tag{44}$$

where $p_m = 0$. On substituting the values of p_d, ζ, H, ρ_m and ρ_d in Eq. (44), we get

$$\omega_{eff} = \frac{(2+3\lambda)\left[\frac{\{(1+2\lambda)A\beta\omega_d-1\}[(1+2\lambda)\zeta_0-\{1+(1+2\lambda)(\alpha\omega_d-\zeta_1)\}H_0]}{e^{(1+2\lambda)A\zeta_0(t-t_0)}} - H_0\right]}{\left[\frac{\{(1+2\lambda)A\beta\omega_d-1\}[(1+2\lambda)\zeta_0-\{1+(1+2\lambda)(\alpha\omega_d-\zeta_1)\}H_0]\lambda}{e^{(1+2\lambda)A\zeta_0(t-t_0)}} + (2+3\lambda+\alpha\lambda+2\alpha\lambda^2)H_0\right]}. \tag{45}$$

The evolutions of ω_{eff} *versus* t are shown in Figs. 5a and 5b for different pairs of (ζ_0, ζ_1) in respect of $\lambda = 0.06$ and $\lambda = -0.06$, respectively. Figure 5a shows that the trajectories of ω_{eff} start from $\omega_{eff} > -1$ (it may also start from matter-dominated era) for small values and $\omega_{eff} < -1$ for large values of (ζ_0, ζ_1) in respect of $\lambda = 0.06$. As $t \to \infty$, ω_{eff} approaches to a constant for all values of (ζ_0, ζ_1), *i.e.*, $\omega_{eff} \to -0.9745$. There is no $\omega_{eff} = -1$ crossing for small values of (ζ_0, ζ_1) but for large values of (ζ_0, ζ_1) it will cross the $\omega_{eff} = -1$. In Fig. 5b where we have $\lambda = -0.06$, we can observe the similar evolution of ω_{eff}. However, $\omega_{eff} \to -1.0252$ in late times, *i.e.*, it crosses $\omega_{eff} = -1$ for small values of (ζ_0, ζ_1) but it will not cross for large values of (ζ_0, ζ_1). Thus, the effective equation of state parameter for both models shows consistency with the observational data given in Ref. [86]. We can say that the dark energy phenomena may be obtained in the presence of viscous fluid.

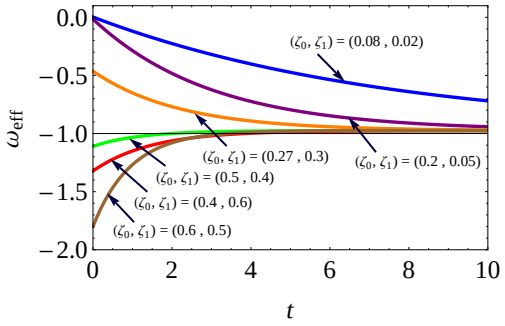

Fig.5(a) The evolution of ω_{eff} for different values of (ζ_0, ζ_1) in respect of $\lambda = 0.06$. We take $H_0 = 1$, $\omega_d = -0.5$, $\alpha = 0.8502$ and $\beta = 0.4817$.

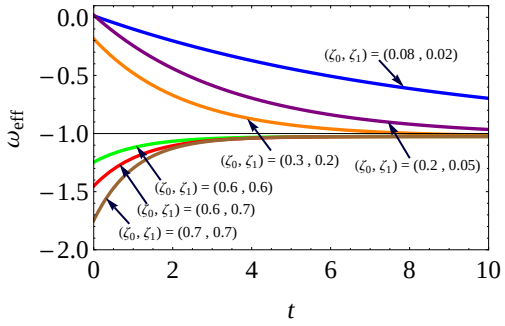

Fig.5(b) The evolution of ω_{eff} for different values of (ζ_0, ζ_1) in respect of $\lambda = -0.06$. We take $H_0 = 1$, $\omega_d = -0.5$, $\alpha = 0.8502$ and $\beta = 0.4817$.

3.6 Entropy and second law of thermodynamics

The local entropy production for a fluid on a flat FRW spacetime is expressed as [87]

$$T\nabla_\nu s^\nu = \zeta(\nabla_\nu u^\nu)^2 = 9H^2\zeta \tag{46}$$

where T is the temperature, $\nabla_\nu s^\nu$ is the rate at which entropy is being generated in unit volume, and ζ is the total bulk viscosity.

The second law of thermodynamics can be stated as

$$T\nabla_\nu s^\nu \geq 0 \tag{47}$$

Since the Hubble parameter H is positive in an expanding universe, then ζ has to be positive in order to preserve the validity of the second law of thermodynamics. Thus, equation (46) implies that

$$\zeta \geq 0. \tag{48}$$

Thus, for the present model the inequality (48) can be written as

$$\zeta = \zeta_0 + \zeta_1 H \geq 0. \tag{49}$$

Using (29), we find the expression for the total bulk viscosity $\zeta(a)$ as

$$\zeta(a) = \zeta_0 + \zeta_1\left[\frac{(1+2\lambda)H_0}{[1+(1+2\lambda)(\alpha\omega_d-\zeta_1)]}\left(\frac{\zeta_0}{H_0}+\left\{\frac{[1+(1+2\lambda)(\alpha\omega_d-\zeta_1)]}{(1+2\lambda)}-\frac{\zeta_0}{H_0}\right\}\right.\right.$$
$$\left.\left. + \; a^{-A\{1+(1+2\lambda)(\alpha\omega_d-\zeta_1)\}}\right)\right]. \tag{50}$$

The value of the scale factor, at which the transition of the total bulk viscosity between negative to positive values happen, is

$$a_{np} = \left[\frac{\{1+(1+2\lambda)\alpha\omega_d\}\zeta_0}{\{(1+2\lambda)(\zeta_0+\zeta_1H_0-\alpha\omega_d)-1\}\zeta_1}\right]^{-\frac{1}{A[1+(1+2\lambda)(\alpha\omega_d-\zeta_1)]}}, \tag{51}$$

where, the subscript "np" stands for "negative to positive" values. In late time of evolution, *i.e.*, at $a \to \infty$ the total bulk viscosity is $\zeta(a) = \frac{\{1+(1+2\lambda)\alpha\omega_d\}\zeta_0}{\{1+(1+2\lambda)(\alpha\omega_d-\zeta_1)\}}$.

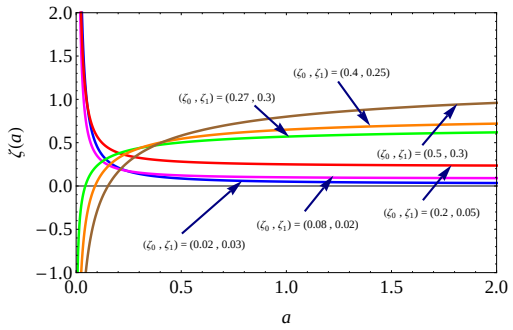

Fig.6(a) The evolution of $\zeta(a)$ for different combination of ζ_0 and ζ_1 with $\omega_d = -0.5$, $\lambda = 0.06$, $\alpha = 0.8502$ and $\beta = 0.4817$.

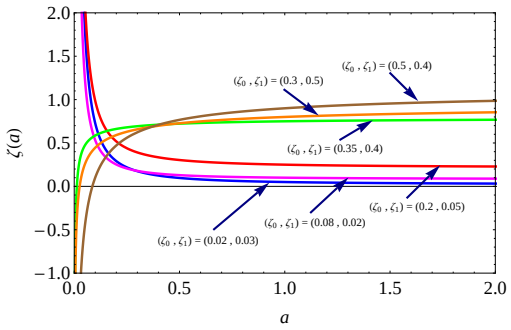

Fig.6(b) The evolution of $\zeta(a)$ for different combination of ζ_0 and ζ_1 with $\omega_d = -0.5$, $\lambda = -0.06$, $\alpha = 0.8502$ and $\beta = 0.4817$.

Figures 6a and 6b represent the evolution of the total bulk viscous coefficient ζ with respect to the scale factor for the different combinations of the (ζ_0, ζ_1) with positive ($\lambda = 0.06$) and negative ($\lambda = -0.06$) values of the coupling parameter, respectively. The figures 6a and 6b show that the total bulk viscosity is positive throughout the evolution of the universe for $0 < (\zeta_0 + \zeta_1) \leq 0.46$ with $\lambda = 0.06$, and $0 < (\zeta_0 + \zeta_1) \leq 0.71$ with $\lambda = -0.06$, respectively. These curves have been shown above the line (0,0). Therefore, the model does not violate the entropy law for these ranges. The figures also show that the total bulk viscous coefficient is evolving from negative to positive value for $(\zeta_0 + \zeta_1) \geq 0.46$ and $(\zeta_0 + \zeta_1) \geq 0.71$, respectively. Thus, the rate of entropy production is negative for large values of $(\zeta_0 + \zeta_1)$ in early epoch and positive in the later epoch. Hence the entropy law violates in the early epoch and obeys in the later epoch for these values of $(\zeta_0 + \zeta_1)$.

In an absolute way the status of the second law of thermodynamics should be considered along with the accounting of the entropy generation from the horizon. In those circumstances, the second law becomes the generalised second law (GSL) of thermodynamics, according to which the total sum of the entropies of the fluid components of the universe plus that of the horizon entropy should never decrease [88, 89]. In the present model this means the rate of change of complete entropy

along with horizon must be greater than or equal to 0. Mathew *et al.* [89] have discussed the status of GSL for flat FRW universe with matter and cosmological vacuum. Karami *et al.* [90] have discussed the status of GSL in a flat universe with viscous dark energy and have shown that the GSL is valid in FRW universe with apparent horizon as the boundary. Many authors [91, 92] have verified the status of GSL with apparent horizon as the boundary. The status of GSL in the modified gravity theories have also been discussed by many authors [93–96] with the apparent horizon as the boundary.

Let us verify the GSL of thermodynamics for this model. As stated above we consider the apparent horizon as the boundary of the universe. Then, the GSL can be stated as

$$\frac{d}{dt}(S_{tot}) = \frac{d}{dt}(S_m + S_d + S_p + \tilde{S_h}) \geq 0, \tag{52}$$

where S_m, S_d, S_p and $\tilde{S_h}$ are the entropies of the dark matter, dark energy, the entropy production and the entropy of the apparent horizon, respectively.

From the first law of thermodynamics the change of entropy of the viscous matter inside the apparent horizon can be obtained using Gibbs equation

$$T_i dS_i = d(\rho_i V) + p_i dV, \tag{53}$$

where T_i is the temperature and $S_i = S_m + S_d$, is the sum of the entropies of the dark matter and dark energy, ρ_i represents the sum of the densities of the dark matter and dark energy, $V = \frac{4\pi \tilde{r_h}}{3}$ is the volume of the apparent horizon with $\tilde{r_h}$ as a radius of the apparent horizon and $p_i = \tilde{p_d} = p_d - 3\zeta H$ as the effective pressure.

In the present viscous model the above Gibbs equation modifies to [94–96]

$$T_i dS_i = d(\rho_i V) + p_i dV - T_i dS_p. \tag{54}$$

The radius $\tilde{r_h}$ of the apparent horizon for a flat FRW universe, is defined as [96]

$$\tilde{r_h} = \frac{1}{H}. \tag{55}$$

In the $f(R,T)$ theories the entropy associated with the apparent horizon is defined as

$$\tilde{S_h} = \frac{\tilde{A_h}}{4} \frac{f_R(R,T)}{\left(\frac{1}{8\pi} + \frac{f_T(R,T)}{8\pi}\right)} = \frac{2\pi \tilde{A_h}}{(1+\lambda)} = \frac{8\pi^2 \tilde{r_h}^2}{(1+\lambda)}, \tag{56}$$

where $\tilde{A_h} = 4\pi \tilde{r_h}^2$ is the area of the apparent horizon. In this paper, we have taken $8\pi G = 1$. Taking the derivative of Eq. (56) with respect to time t, we get

$$\dot{\tilde{S}_h} = \frac{16\pi^2 \tilde{r_h} \dot{\tilde{r_h}}}{(1+\lambda)} = \frac{16\pi^2}{(1+\lambda)H} \left(-\frac{\dot{H}}{H^2}\right). \tag{57}$$

Now, from (54) we have

$$T_i(\dot{S}_m + \dot{S}_d + \dot{S}_p) = 4\pi \tilde{r_h}^2 (\dot{\tilde{r_h}} - 1)\{\rho_m + (1+\omega_d)\rho_d - 3\zeta_0 H - 3\zeta_1 H^2\}. \tag{58}$$

Under the thermal equilibrium conditions between the fluids and the horizon, we have $T_i = \tilde{T}_h$. We take the temperature $\tilde{T}_h = \frac{H}{2\pi}$, which is equal to the Hawking temperature of the horizon with the assumption that the fluid within the horizon is in equilibrium with the horizon, so there is no effective flow of the fluid toward the horizon [97]. Now, Eq. (58) become as

$$\dot{S}_m + \dot{S}_d + \dot{S}_p = \frac{8\pi^2}{H^3}\left(-\frac{\dot{H}}{H^2} - 1\right)\{\rho_m + (1+\omega_d)\rho_d - 3\zeta_0 H - 3\zeta_1 H^2\}. \tag{59}$$

Now, using the definition of deceleration parameter $q = \left(-\frac{\dot{H}}{H^2} - 1\right)$ and Eqs. (57) and (59) into (52), we get the change of the sum of all the entropies as

$$\begin{aligned}\dot{S}_{tot} &= \dot{S}_m + \dot{S}_d + \dot{S}_p + \dot{\tilde{S}}_h \\ &= \frac{8\pi^2 q}{H^3}\{\rho_m + (1+\omega_d)\rho_d - 3\zeta_0 H - 3\zeta_1 H^2\} + \frac{16\pi^2(q+1)}{(1+\lambda)H}.\end{aligned} \tag{60}$$

On substituting the required values in above equation and simplifying, we get the change in total entropy as

$$\begin{aligned}\dot{S}_{tot} &= \left[\frac{16\pi^2[\{1+(1+2\lambda)(\alpha\omega_d-\zeta_1)\}H_0-(1+2\lambda)\zeta_0]\left\{1+\frac{\{1+(1+2\lambda)(\alpha\omega_d-\zeta_1)\}H_0\left(e^{(1+2\lambda)A\zeta_0(t-t_0)}-1\right)}{(1+2\lambda)\zeta_0}\right\}}{H_0^2 e^{2(1+2\lambda)A\zeta_0(t-t_0)}}\right] \\ &\quad\times\left[\frac{A}{(1+\lambda)} + \frac{3\{1-(1+2\lambda)A\beta\omega_d\}}{(2+3\lambda)H_0}\left\{\frac{[\{1+(1+2\lambda)(\alpha\omega_d-\zeta_1)\}H_0-(1+2\lambda)\zeta_0]A}{e^{(1+2\lambda)A\zeta_0(t-t_0)}} - H_0\right\}\right].\end{aligned} \tag{61}$$

From Eq. (61), it is noticed that the rate of change of entropy can not clearly state either the change in entropy is greater than and equal to zero. We plot the evolution of $\dot{S}$ in Figs. 7a and 7b, respectively for positive and negative values of the λ (*e.g.*, $\lambda = 0.06$, $\lambda = -0.06$) taking $\alpha = 0.8502$, $\beta = 0.4817$, $\omega_d = -0.5$, $H_0 = 1$ and $t_0 = 1$ for different values of viscosity coefficients (ζ_0, ζ_1). Figure 7a shows that the GSL is always valid for $\zeta_0 > 0$ and $0 < \zeta_1 \leq 0.85$ whereas it holds for $\zeta_0 > 0$ and $0 < \zeta_1 \leq 1$ in Fig. 7b. We also notice that in both the cases, the total entropy corresponds to zero in late time of the evolution.

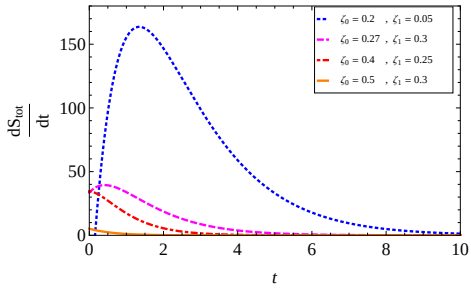

Fig.7(a) The change in total entropy with respect to t for different combination of ζ_0 and ζ_1 with $\omega_d = -0.5$, $\lambda = 0.06$, $\alpha = 0.8502$ and $\beta = 0.4817$.

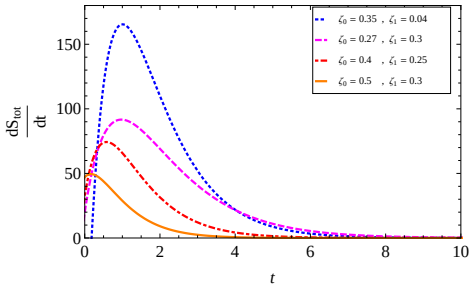

Fig.7(b) The change in total entropy with respect to t for different combination of ζ_0 and ζ_1 with $\omega_d = -0.5$, $\lambda = -0.06$, $\alpha = 0.8502$ and $\beta = 0.4817$.

4 Conclusion

In this paper, we have explored the bulk viscous new HDE model in modified $f(R,T)$ gravity with bulk viscosity of the form $\zeta = \zeta_0 + \zeta_1 H$. We have considered that the universe is filled with the pressureless dark matter and the new HDE proposed by Granda and Oliveros [32]. We have analyzed the different possible phases of the universe according to the dimensionless bulk viscous parameters ζ_0 and ζ_1. We have calculated the scale factor, deceleration parameter, statefinder and Om diagnostics, effective equation of state parameter, entropy and generalized second law of thermodynamics to observe the evolution of the universe. In what follows we summarize the result.

The field equations of viscous new HDE model in modified $f(R,T)$ gravity have been solved for a most general bulk viscous coefficient. The scale factor has been obtained in the form of exponential which describes the phase transition of the universe. We have analyzed the behavior of the scale factor for all possible combination of (ζ_0, ζ_1) and model parameter λ. We have obtained the cosmic time when the Big Bang happens. In early time the scale factor is approximated by power-law expansion which shows that the model expands with decelerated rate in early time. In late time the scale factor behaves as a de Sitter like expansion, *i.e*, expands with accelerated rate. This shows that the scale factor at the respective limits has an earlier decelerated phase followed by an accelerated phase in the later stage of the evolution. We have calculated the transition time between decelerated to accelerated epoch. We have expressed Hubble parameter in terms of scale factor to get the transition between decelerated to accelerated epoch in terms of scale factor a_T and redshift z_T. Thus, for the present time transition from deceleration to acceleration takes place at $\zeta_0 + \zeta_1 = 0.096$ for positive values of $\lambda = 0.06$ and for negative value of $\lambda = -0.06$, we get $\zeta_0 + \zeta_1 = 0.218$. A plot of the evolution of the scale factor is given in Fig. 1. for difference values of a combination of ζ_0 and ζ_1 and positive value of λ. For $0 < (\zeta_0 + \zeta_1) < 0.096$, the scale factor has an earlier deceleration phase followed by an acceleration phase in late time. For $(\zeta_0 + \zeta_1) > 0.096$, the transition takes place in past of the universe. Similar behavior can be observed for the negative value of λ.

We have also studied the evolution of the deceleration parameter q. We have obtained time-dependent deceleration parameter. As $(t - t_0) \to \infty$, we get $q \to -1$, which shows that the model accelerates in late time. We have observed that for $\zeta_0 + \zeta_1 = 0.096$, we have $q_0 = 0$. Therefore, the transition into acceleration phase would occur at present time. We have discussed the behavior of q and corresponding evolution for different ranges of coupling parameter λ and constraints on $(\zeta_0 + H_0\zeta_1)$. The results are summarized in tables 1-3 for $\omega_d = -0.5$, $\omega_d = -1$ and $\omega_d = -1.1414$, and model parameters $\alpha = 0.8502$, $\beta = 0.4817$. The tables show that the deceleration or acceleration or their transition depend on the values of ζ_0, ζ_1 and λ. The behavior of q has already been discussed in detail in subsection 3.2 .

We have discussed two geometrical diagnostics, namely statefinder and Om to observe the discrimination with the other existing DE models. Let us first discuss about the statefinder diagnostic for viscous new HDE model. In the late time as $(t - t_0) \to \infty$, the statefinder pair $\{r, s\}$ for the viscous new HDE model tends to $\{1, 0\}$, a value corresponding to ΛCDM model. We have plotted the trajectory of statefinder pair $\{r, s\}$ in $r - s$ plane for different combinations of (ζ_0, ζ_1) as shown in Fig.2a and Fig. 3a for positive and negative values of coupling parameter λ, respectively. It has been observed that for any value of λ (either positive or negative), our viscous new HDE model in the framework of $f(R,T)$ theory mimics like Q and CG models for specific range of viscosity

coefficients and in late time of evolution it always converges to ΛCDM model.

We have also plotted the trajectory of $\{r, q\}$ for different combinations of (ζ_0, ζ_1) and positive and negative values of λ as shown in Fig. 2b and Fig. 3b. It can be observed that q changes its sign from positive to negative with respect to time for $0 < (\zeta_0 + \zeta_1) \leq 0.46$ in case of $\lambda = 0.06$ and for $0 < (\zeta_0 + \zeta_1) \leq 0.71$ in case $\lambda = -0.06$, which show the phase transition from decelerated phase to accelerated phase. For $(\zeta_0 + \zeta_1) > 0.46$ when $\lambda = 0.06$ and $(\zeta_0 + \zeta_1) > 0.71$ when $\lambda = -0.06$, q is always negative showing behavior of phantom. Thus, in the beginning this model behaves different from ΛCDM model but in late time it behaves the same as ΛCDM which converges to SS model in late time evolution. The present viscous new HDE model can also be discriminated from the holographic dark energy model with event horizon as the infrared cutoff, in which the $r - s$ evolution starts from a region $r \sim 1$, $s \sim 2/3$ and ends on the ΛCDM point [80]. It can also be discriminated from Ricci dark energy model in which $r - s$ trajectory is a vertical segment, i.e., s is a constant during the evolution of the universe [81].

The second geometrical diagnostic, namely Om has been carried out in section 3.4 . We have plotted the $Om(z)$ versus redshift z trajectories for different combinations of (ζ_0, ζ_1) in respect of positive and negative values of λ as shown in Fig.4a and Fig. 4b, respectively. We have observed two types of trajectory, one has the positive curvature which suggests the phantom like behavior and second has the negative curvature which suggests the quintessence like behavior.

We have calculated the effective EoS parameter for this model and analyzed the evolution of it graphically for different suitable values of viscosity coefficients. We have observed that $\omega_{eff} \rightarrow$ -0.9745 and -1.0252, respectively as $t \rightarrow \infty$ in case positive and negative values of λ which is very close to -0.93 predicted in the Ref. [98].

At the end, we have discussed the entropy and second law of thermodynamics for viscous new HDE model. Figures 6a and 6b plot the evolution of the total bulk viscous coefficient. It has been observed that the total bulk viscosity is positive throughout the evolution of the universe for $0 < (\zeta_0 + \zeta_1) \leq 0.46$ with $\lambda = 0.06$, and $0 < (\zeta_0 + \zeta_1) \leq 0.71$ with $\lambda = -0.06$, respectively. Therefore, the model does not violate the entropy law for these ranges. The figures also show that $\zeta(a)$ is evolving from negative to positive value for $(\zeta_0 + \zeta_1) > 0.46$ and $(\zeta_0 + \zeta_1) > 0.71$, respectively. Thus, the rate of entropy production is negative for large values of $(\zeta_0 + \zeta_1)$ in early epoch and positive in the later epoch. Hence the entropy law violates in the early epoch and obeys in the later epoch for these values of $(\zeta_0 + \zeta_1)$. We have also studied the generalized second law of thermodynamics. It has been observed that it is always valid for $\zeta_0 > 0$ and $0 < \zeta_1 \leq 0.85$ when λ is positive whereas it holds for $\zeta_0 > 0$ and $0 < \zeta_1 \leq 1$ when λ is negative which are shown in Figs. 7a and 7b, respectively. We have also noticed that in both the cases, the total entropy corresponds to zero in late time of the evolution.

Let us Summarize the results with the outcome of this work. In cosmology, the idea of viscous dark energy models has been presented in different ways to understand the evolution of the universe. The notion of bulk viscosity has also been extensively studied in modified theories. This paper has explored the behavior of viscosity by considering dust matter and new HDE in the background of modified $f(R, T)$ gravity. The above investigations show that this model predicts an early deceleration followed by late time acceleration. We can conclude that the dark energy era may be obtained in the presence of bulk viscous fluid.

Acknowledgements
One of the author MS would like to thank to University Grant Commission, India for providing Senior Research Fellowship (SRF) under UGC-NET scholarship.

References

[1] A.G. Riess *et al.*, *Observational evidence from supernovae for an accelerating universe and a cosmological constant*, *Astron. J.* **116** (1998) 1009.

[2] S. Perlmutter *et al.*, *Measurements of Omega and Lambda from 42 high redshift supernovae*, *Astrophys. J.* **517** (1999) 565.

[3] D.N. Spergel *et al.*, *Three-Year Wilkinson Microwave Anisotropy Probe (WMAP) Observations: Implications for cosmology*, *Astrophys. J. Suppl.* **170** (2007) 377.

[4] M. Tegmark *et al.*, *Cosmological parameters from SDSS and WMAP*, *Phys. Rev. D* **69** (2004) 103501.

[5] T. Padmanabham, *Cosmological constantthe weight of the vacuum*, *Phys. Rep.* **380** (2003) 235.

[6] V. Sahni and A. Starobinsky, *The case for a positive cosmological Λ-term*, *Int. J. Mod. Phys. D* **9** (2000) 373.

[7] P.J.E. Peebles and B. Ratra, *The cosmological constant and dark energy*, *Rev. Mod. Phys.* **75** (2003) 559.

[8] S. Capozziello, V.F. Cardone, E. Piedipalumbo and C. Rubano, *Dark energy exponential potential models as curvature quintessence*, *Class. Quantum Grav.* **23** (2006) 1205.

[9] Yu. Zhang and Y.X. Gui, *Quasinormal modes of gravitational perturbation around a Schwarzschild black hole surrounded by quintessence*, *Class. Quantum Grav.* **23** (2006) 6141.

[10] T. Chiba, T. Okabe, and M. Yamaguchi, *Kinetically driven quintessence*, *Phys. Rev. D* **62** (2000) 023511.

[11] R.R. Caldwell, *A phantom menace? Cosmological consequences of a dark energy component with super-negative equation of state*, *Phys. Lett. B* **545** (2002) 23.

[12] B. Feng, X.L. Wang, X.M. Zhang, *Dark energy constraints from the cosmic age and supernova*, *Phys. Lett. B* **607** (2005) 35.

[13] Z.K. Guo, Y.S. Piao, X.M. Zhang and Y.Z. Zhang, *Cosmological evolution of a quintom model of dark energy*, *Phys. Lett. B* **608** (2005) 177.

[14] R.J. Scherrer, *Purely kinetic k Essence as unified dark matter*, *Phy. Rev. Lett.* **93** (2004) 011301.

[15] R.R. Caldwell, M. Kamionkowski and N.N. Weinberg, *Phantom energy: dark energy with $w < -1$ causes a cosmic doomsday*, *Phys. Rev. Lett.* **91** (2003) 071301.

[16] L.P. Chimento and R. Lazkoz, *Constructing Phantom Cosmologies from Standard Scalar Field Universes*, *Phy. Rev. Lett.* **91** (2003) 211301.

[17] A. Vikman, *Can dark energy evolve to the phantom?*, *Phys. Rev. D* **71** (2005) 023515.

[18] H. Wei, R.-G. Cai and D.-F. Zeng, *Hessence: a new view of quintom dark energy*, *Class. Quantum Grav.* **22** (2005) 3189.

[19] G.B. Zhao, J.-Q. Xia, M. Li, B. Feng and X. Zhang, *Perturbations of the quintom models of dark energy and the effects on observations*, *Phys. Rev. D* **72** (2005) 123515.

[20] M.R. Setare, *Interacting holographic generalized Chaplygin gas model*, *Phys. Lett. B*, **654** (2007) 1.

[21] S. Nojiri and S.D. Odintsov, *Introduction to modified gravity and gravitational alternative for dark energy*, *Int. J. Geom. Methods Mod. Phys.* **4** (2007) 115.

[22] T.P. Sotiriou and S. Liberati, *Metric-affine $f(R)$ theories of gravity*, *Ann. Phys.* **322** (2007) 935.

[23] M. Li, *A model of holographic dark energy*, *Phys. Lett. B* **603** (2004) 1.

[24] H. Wei and R.G. Cai, *A new model of agegraphic dark energy*, *Phys. Lett. B* **660** (2008) 113.

[25] G. t'Hooft, *Dimensional reduction in quantum gravity Conf.Proc.C* **930308** (1993) 284 [gr-qc/9310026].

[26] R. Bousso, *The holographic principle*, *Rev. Mod. Phys.* **74** (2002) 825.

[27] A.G. Cohen, D.B. Kaplan and A.E. Nelson, *Effective field theory, black holes, and the cosmological constant*, *Phys. Rev. Lett.* **82** (1999) 4971.

[28] S.D.H. Hsu, *Entropy bounds and dark energy*, *Phys. Lett. B* **594** (2004) 13.

[29] L. Xu, W. Li and J. Lu, *Holographic dark energy in Brans-Dicke theory*, *Eur. Phys. J. C* **60** (2009) 135.

[30] M. Li, X.D. Li, S. Wang and X. Zhang, *Holographic dark energy models: a comparison from the latest observational data*, *JCAP* **06** (2009) 036.

[31] C. Gao, F. Wu and X. Chen, *Holographic dark energy model from Ricci scalar curvature*, *Phys. Rev. D* **79** (2009) 043511.

[32] L.N. Granda and A. Oliveros, *Infrared cut-off proposal for the holographic density*, *Phys. Lett. B* **669** (2008) 275.

[33] M. Malekjani, A. Khodam-Mohammadi and N. Nazari-pooya, *Cosmological evolution and statefinder diagnostic for new holographic dark energy model in non flat universe*, *Astrophys. Space Sci.* **332** (2011) 515.

[34] L.N. Granda and A. Oliveros, *New infrared cut-off for the holographic scalar fields models of dark energy*, *Phys. Lett. B* **671** (2009) 199.

[35] K. Karami and J. Fehri, *Holographic dark energy in a non-flat universe with Granda-Oliveros cut-off*, *Int. J. Theor. Phys.* **49** (2010) 1118.

[36] F. Yu, J. Zhang, J. Lu, W. Wang and Y. Gui, *A more general interacting model of holographic dark energy*, *Phys. Lett. B* **688** (2010) 263.

[37] J.D. Barrow, *The deflationary universe: An instability of the de Sitter universe*, *Phys. Lett. B* **180** (1986) 335.

[38] I. Brevik and O. Gorbunova, *Dark energy and viscous cosmology*, *Gen. Relativ. Gravit.* **37** (2005) 2039.

[39] I. Brevik and S.D. Odintsov, *Cardy-Verlinde entropy formula in viscous cosmology*, *Phys. Rev. D* **65** (2002) 067302.

[40] D.J. Liu and X.Z. Li, *Dynamics of quintessence with thermal interactions*, *Phys. Lett. B* **611** (2005) 8.

[41] C. Eckart, *The Thermodynamics of Irreversible Processes*, *Phys. Rev.* **58** (1940) 919.

[42] L.D. Landau and E.M. Lifshitz, *Fluid Mechanics*. Butterworth Heinemann, Stoneham (1987).

[43] W. Israel and J.M. Stewart, *Thermodynamics of nonstationary and transient effects in a relativistic gas*, *Phys. Lett. A* **58** (1976) 213.

[44] Y.D. Xu, Z.G. Huang and X.H. Zhai, *Generalized Chaplygin gas model with or without viscosity in the $w - w'$ plane*, *Astrophys. Space Sci.* **337** (2012) 493.

[45] C.J. Feng and X.Z. Li, *Viscous Ricci dark energy*, *Phys. Lett. B* **680** (2009) 355.

[46] S. Nojiri and S.D. Odintsov, *Inhomogeneous equation of state of the universe: Phantom era, future singularity, and crossing the phantom barrier*, *Phys. Rev. D* **72** (2005) 023003.

[47] S. Capozziello, V.F. Cardone, E. Elizalde, S. Nojiri and S.D. Odintsov, *Observational constraints on dark energy with generalized equations of state*, *Phys. Rev. D* **73** (2006) 043512.

[48] N. Cruz, S. Lepe and F. Peña, *Dissipative generalized Chaplygin gas as phantom dark energy*, *Phys. Lett. B* **646** (2007) 177.

[49] X.H. Meng, J. Ren and M.G. Hu, *Friedmann cosmology with a generalized equation of state and bulk viscosity*, *Commun. Theor. Phys.* **47** (2007) 379.

[50] J. Ren and X.H. Meng, *Cosmological model with viscosity media (dark fluid) described by an effective equation of state*, *Phys. Lett. B* **633** (2006) 1.

[51] M.G. Hu and X.H. Meng, *Bulk viscous cosmology: Statefinder and entropy*, *Phys. Lett. B* **635** (2006) 186.

[52] P. Kumar and C.P. Singh, *Viscous cosmology with matter creation in modified $f(R,T)$ gravity*, *Astrophys. Space Sci.* **357** (2015) 120.

[53] C.P. Singh, *Bulk viscous cosmology in early universe*, *Pramana J. Phys.* **71** (2008) 33.

[54] C.P. Singh, S. Kumar and A. Pradhan, *Early viscous universe with variable gravitational and cosmological 'constants'*, *Class. Quantum Gravit.* **24** (2007) 455.

[55] C.P. Singh and P. Kumar, *Friedmann model with viscous cosmology in modified $f(R,T)$ gravity theory*, *Eur. Phys. J.C* **74** (2014) 3070.

[56] J.S. Gagnon and J. Lesgourgues, *Dark goo: bulk viscosity as an alternative to dark energy*, *J. Cosmol. Astropart. Phys.* **09** (2011) 026.

[57] S. Nojiri and S.D. Odintsov, *Unified cosmic history in modified gravity: From $F(R)$ theory to Lorentz non-invariant models*, *Phys. Rep.* **505** (2011) 59.

[58] K. Bamba, S. Capozziello, S. Nojiri and S.D. Odintsov, *Dark energy cosmology: the equivalent description via different theoretical models and cosmography tests*, *Astrophys. Space Sci.* **342** (2012) 155.

[59] T. Harko, F.S.N. Lobo, S. Nojiri and S.D. Odintsov, *$f(R,T)$ gravity*, *Phys. Rev. D* **84** (2011) 024020.

[60] M. Sharif, M. Zubair, *Thermodynamics in $f(R,T)$ theory of gravity*, *J. Cosmol. Astropart. Phys.* **03** (2012) 028.

[61] S. Chakraborty, *An alternative $f(R,T)$ gravity theory and the dark energy problem*, *Gen. Relativ. Gravit.* **45** (2013) 2039.

[62] T. Harko, *Thermodynamic interpretation of the generalized gravity models with geometry-matter coupling*, *Phys. Rev. D* **90** (2014) 044067.

[63] C.P. Singh and V. Singh, *Reconstruction of modified $f(R,T)$ gravity with perfect fluid cosmological models*, *Gen. Relativ. Gravit.* **46** (2014) 1696.

[64] E.H. Baffou *et al.*, *Cosmological viable $f(R,T)$ dark energy model: dynamics and stability*, *Astrophys. Space Sci.* **356** (2015) 173.

[65] G.M. Kremer and F.P. Devecchi, *Viscous cosmological models and accelerated universes*, *Phys. Rev. D* **67** (2003) 047301.

[66] M. Cataldo, N. Cruz and S. Lepe, *Viscous dark energy and phantom evolution*, *Phys. Lett. B* **619** (2005) 5.

[67] J.C. Fabris, S.V.B. Goncalves and R. de S Ribeiro, *Bulk viscosity driving the acceleration of the Universe*, *Gen. Rel. Grav.* **38** (2006) 495.

[68] M.-G. Hu and X.-H. Meng, *Bulk viscous cosmology: Statefinder and entropy*, *Phys. Lett. B* **635** (2006) 186.

[69] A. Avelino and U. Nucamendi, *Can a matter-dominated model with constant bulk viscosity drive the accelerated expansion of the universe?*, *J. Cos. Astropart. Phys.* **04** (2009) 006.

[70] A. Avelino and U. Nucamendi, *Constraining a bulk viscous matter-dominated cosmological model using SNe Ia, CMB and LSS*, in proceeding of XI Mexican Workshop on Particles and Fields, Tuxtla Gutierrez Mexico November 7-12 2007, *API Conf. Proc.* **1026** (2008) 300.

[71] A. Avelino and U. Nucamendi, *Exploring a matter-dominated model with bulk viscosity to drive the accelerated expansion of the universe*, *J. Cosmol. Astropart. Phys.* **08** (2010) 009.

[72] W.A. Hiscock and J. Salmonson, *Dissipative Boltzmann-Robertson-Walker cosmiologies*, *Phys. Rev. D* **55** (1991) 3249.

[73] R. Maartens, *Dissipative cosmology*, *Class. Quantum Gravity* **12** (1995) 1455.

[74] B. Li and J.D. Barrow, *Does Bulk Viscosity Create a Viable Unified Dark Matter Model? Phys. Rev D* **79** (2009) 103521.

[75] X.H. Meng and X. Dou, *Friedmann cosmology with bulk viscosity: A concrete model for dark energy*, *Commun. Theor. Phys.* **52** (2009) 377.

[76] Y. Wang and L. Xu, *Current observational constraints to the holographic dark energy model with a new infrared cutoff via the Markov chain Monte Carlo method*, *Phys. Rev. D* **81** (2010) 083523.

[77] V. Sahni, T.D. Saini, A.A. Starobinsky and U. Alam, *Statefinder-A new geometrical diagnostic of dark energy*, *JETP Lett.* **77** (2003) 201.

[78] U. Alam, V. Sahni, T.D. Saini and A.A. Starobinsky, *Exploring the expanding universe and dark energy using the statefinder diagnostic*, *Mon. Not. R. Astron. Soc.* **344** (2003) 1057.

[79] Y.B. Wu , S. Li, M.H. Fu and J. He, *A modified Chaplygin gas model with interaction*, *Gen. Relativ. Gravity* **39** (2007) 653.

[80] D.J. Liu and W.Z. Liu, *Statefinder diagnostic for cosmology with the abnormally weighting energy hypothesis*, *Phys. Rev.D* **77** (2008) 027301.

[81] C.J. Feng, *Statefinder diagnosis for Ricci dark energy*, *Phys. Lett. B* **670** (2008) 231.

[82] V. Sahni, A. Shafieloo and A.A. Starobinsky, *Two new diagnostics of dark energy*, *Phys. Rev. D* **78** (2008) 103502.

[83] M.L. Tong and Y. Zhang, *Cosmic age, statefinder, and Om diagnostics in the decaying vacuum cosmology*, *Phys. Rev. D* **80** (2009) 023503.

[84] J.B. Lu and L.X. Xu, *Geometrical diagnostic for the generalised chaplygin gas model*, *Int. J. Mod. Phys. D* **18** (2009) 1741.

[85] Z.G. Huang, H.Q. Lu and K. Zhang, *Om diagnostic for dilaton dark energy*, *Astrophys. Space Sci.* **331** (2011) 331.

[86] P.A.R. Ade, N. Aghanim and M. Arnaud, *et al.*, *Planck 2015 results-XIII.cosmological parameters*, *Astron. Astrophys.*, **594**, (2016) A13.

[87] S. Weinberg, *Gravitation and Cosmology: principles and applications of the general relativity*, *Wiley, New York* (1972).

[88] G.W. Gibbons and S.W. Hawking, *Cosmological event horizon, thermodynamics, and particle creation* , *Phy. Rev. D* **15** (1977) 2738.

[89] T.K. Mathew, R. Aiswarya and K.S. Vidya, *Cosmological horizon entropy and generalized second law for flat Friedmann universe*, *Eur. Phys. J. C* **73** (2013) 2619.

[90] K. Karami, A. Sheykhi, N. Sahraei and S. Ghaffari, *Generalized second law of thermodynamics in modified FRW cosmology with corrective entropy- area relation*, *Europhys. Lett.* **93** (2011) 29002.

[91] A. Sasidharan and T.K. Mathew, *Bulk viscous matter and recent acceleration of the universe*, *Eur. Phys. J. C* **75** (2015) 348.

[92] M.R. Setare and A. Sheykhi, *Viscous dark energy and generalised second law of thermodynamics*, *Int. J. Mod. Phys. D* **19** (2010) 1205.

[93] S.-F. Wu, B. Wang, G.-H. Yang and P.-M. Zhang, *The generalised second law of thermodynamics in generalized gravity theories*, *Class. Quantum Grav.* **25** (2008) 235018.

[94] M. Sharif and M. Zubair, *Thermodynamic in $f(R,T)$ theory of gravity*, *J. Cos. Astro. Phys.* **03** (2012) 028.

[95] M. Sharif and M. Zubair, *Thermodynamic behavior of particular $f(R,T)$ gravity model*, *J. Exper. Theor. Phys.* **117** (2013) 248.

[96] D. Momeni, P.H.R.S. Moraes and R. Myrzakulov, *Generalized second law of thermodynamics in $f(R,T)$ theory of gravity*, *Atro. Space Sci.* **361** (2016) 228.

[97] T.K. Mathew, M.B. Aswathy and M. Manoj, *Cosmology and thermodynamics of FLRW universe with bulk viscous stiff fluid*, *Eur. Phy. J. C* **74** (2014) 3188.

[98] E. Komatsu *et al.*, *WMAP* Collaboration, *Seven-year Wilkinson Microwave Anisotropy Probe (WMAP) observations: Cosmological interpretation*, Astrophys. J. Suppl. **192** (2011) 18.

Volume 6 Issue 1 (2018) 58-60 ISSN 2347 - 3258
International Journal of Advance Research and Innovation

Factors affecting the remanucaturing of a product

Saurabh Agrawal
Mechanical, Production & Industrial Engineering Department, Delhi Technological University, Delhi, India

Article Info
Article history:
Received 25 January 2018
Received in revised form
20 February 2018
Accepted 28 February 2018
Available online 15 March 2018

Keywords
Remanufacturing, materials, pricing, recycle

Abstract
Remanufacturing activities in India are still in nascent stages. However, the substantial growth of Indian economy, coupled with serious issues of population and environmental burden demands a radical shift in market strategies and legislations. The scattered and inefficient product recovery methods prevalent in India are unable to cope with increasing environmental and economic burden on the society remanufacturing seems to be a promising strategy to explore for these. Growing concerns about environmental problems such as climate change and biodiversity loss, and social problems related to poverty, health, safety and inequity, have fostered new approaches to resource-effective, sustainable product innovation. The present article is aimed at understanding the strategies for pricing, quality emphasis and warranty strategy and identifying their components.

1. Introduction

Remanufacturing is an activity having proven to have economical, environmental and social advantages. As per Remanufacturing Industry Council (RIC), "Remanufacturing is a comprehensive industrial process by which a previously sold, worn, or non-functional product or module is returned to a "like-new" or "better than new" condition and warranted in performance level and quality" (RIC, 2013). Fig. 1 illustrates how remanufacturing offers multiple life cycles to a product. The remanufacturing process consists of five phases:
(1) Disassembly,
(2) Inspection,
(3) Cleaning and Refurbishing
(4) Assembly, and
(5) Final testing
After its 'End of Life' (EOL) or 'End of Use' (EOU) the product is collected by the Original Equipment Manufacturer (OEM) or remanufacturing agency. This product is then disassembled, inspected and sorted. After disassembling, all the parts are cleaned and examined. The objective of the examination is to identify the worn-out parts which are to be either refurbished or replaced with cannibalized or new parts. According to Thierry et al. (1995) "product recovery management encompasses the management of all used and discarded products. The objective of PRM is to recover as much of the economic and ecological value as reasonably possible, thereby reducing the ultimate quantity of waste". They also discussed the five product recovery techniques such as repair, refurbish, remanufacture, cannibalization and recycling. Remanufacturing has an escalating significance in product recovery or EOL/EOU strategies since it retains much of the embodied values of the product. Three interesting issues areas in remanufacturing are
(1) Pricing
(2) Quality And
(3) Warranty (Pagell et al., 2007)
All these issues further have attributes on which they depend. The remanufactured product is derived from an end-of-use product. Therefore, its availability highly depends on the lifecycle of the product. A new product with a short lifecycle will lead to limited availability of used products. The price of the remanufactured product can be higher because of the supply shortage. Therefore, lifecycle becomes an important factor for considering pricing problems, especially short lifecycle products. Consumer high technology products, such as smartphones, digital cameras and laptops are cases in point. Remanufacturers' momentum and motivation could be enhanced if quality is pursued. However, deemphasizing quality may leave consumers unsatisfied. Therefore, exploring an optimal remanufacturing quality strategy that satisfies various consumer preferences is essential to guiding remanufacturers' decisions. Gehin et al. (2008) stated that remanufacturing is a process to improve the quality of remanufactured products to a new level. This process must ensure that remanufactured products reach the quality standard and function accurately to avoid potential risks and barriers that impede customers' willingness to pay (Hamzaoui et al., 2010; Hatcher et al., 2011). Warranties, given their role in perceived value, can be employed as valuable tools in marketing. Warranties are capable of communicating value through their application as persuasive marketing tenets, whether promotional or protectionist. When deployed as a promotional tool, warranties may be used to promote the reliability and quality of the product. As a protectionist instrument, warranties provide the consumer assurance against defective products that are incapable of performing satisfactorily over the duration of the warranty period. Through the effective marketing of a warranty, the degree of risk that is associated with the purchase of a given product on behalf of the consumer is reduced, thereby increasing its value and the likelihood of purchase. Warranties are noted for their capacity to reduce the perceived performance risk of a product through the provision of protection against product defects that lead to failures, within the scope of the warranty period. The financial risk to the consumer is also reduced through the warranty, as repair costs that fall under the scope of the warranty are realized by the remanufacturer and not the consumer. (Alqahtani and Gupta, 2017).

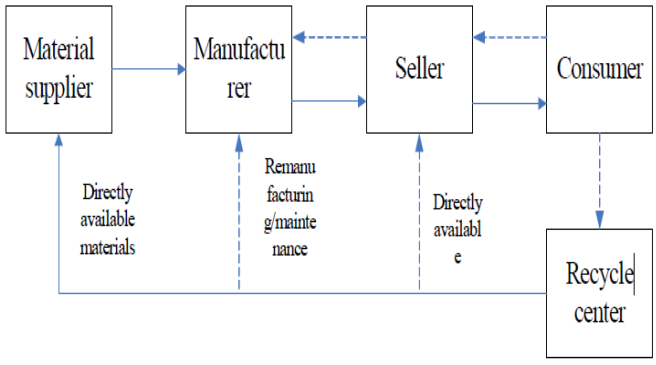

Fig. 1 Basic flow of material

2. Identification of factors

Pricing of remanufactured goods is dependent on various factors. These, factors are further dependent on sub attributes. For pricing, main considerations are manufacturers' considerations, consumers

***Corresponding Author,**
E-mail-address: agrawals.iit@gmail.com
All rights reserved: http://www.ijari.org

considerations and retailer's/collector's considerations. These considerations further have sub factors on which they are dependent which are facility limitations, competitors in the market and economic litigation for the manufacturer's consideration. Consumer's considerations include Retention index, Perceived price and Purchase intention, and retailers/collectors considerations (Jofre and Morioka, 2005).

2.1 Facility

One of the downsides of starting a manufacturing company is the overhead costs associated with doing so. A company that creates products can bank on paying for marketing, materials and labor, while -- unless the product is wholly new -- competing with other companies offering similar goods. This generally leads to a low profit margin, making manufacturing a risky venture unless the business model is well thought (Wolf et al., 2013).

2.2 Competitors

When two products have similar core features, but are produced by different companies, competition results. Competition-based pricing strategy involves setting prices based on competitors' prices rather than one's own cost and profit objectives. Price environment, Product comparison, target market are key factors in this.

2.3 Litigation

Pricing decisions are affected by federal and state regulations. Regulations are designed to protect consumers, promote competition, and encourage ethical and fair behavior by businesses.

2.4 Retention index

The benefits that consumers perceive in deciding to return the used products come from the retailer or manufacturer. Discount, exchange, warranty, incentive and SF are emerged as positive factors in the RI.

2.5 Perceived Price

Individuals act and recent on the basis of their perceptions, not on the basis of objective reality. in reality is a totally personal phenomenon, based on that persons need, want s, values, and personal experiences.

2.6 Purchase intention

The willingness of a customer to buy a certain product or a certain service is known as purchase intention.

2.7 Retailer's/Collector's considerations

At their end of life, the products need to be returned to the original manufacturer, through various channels. These forethoughts fall into this category.

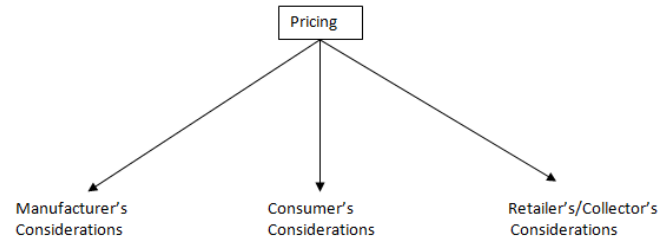

Fig 2: Components of pricing

Remanufacturers' momentum and motivation could be enhanced if quality is pursued. However, deemphasizing quality may leave consumers unsatisfied. Therefore, exploring an optimal remanufacturing quality strategy that satisfies various consumer preferences is essential to guiding remanufacturers' decisions. Gehin et al. (2008) stated that remanufacturing is a process to improve the quality of remanufactured products to a new level. This process must ensure that remanufactured products reach the quality standard and function accurately to avoid potential risks and barriers that impede customers' willingness to pay (Hamzaoui et al., 2010; Hatcher et al., 2011). Degree of remanufacture, Performance and serviceability and brand equity are some of the factors affecting quality of remanufactured products.

A warranty is a contractual obligation realized by the manufacturer when a product is sold. The warranty establishes liability on behalf of the manufacturer should the item sold prematurely fail or prove incapable of performing the intended function. Warranties define the product performance to be expected by the consumer, and should the performance definition not be met, the buyer is then afforded compensation as outlined in the warranty (Blischke, 1993). Warranties serve a variety of purposes, with Heal (1977) noting that insurance and protection are central, as it enables the buyer to transfer product risk failure to the vendor. Product warranties may also signify dependability to the consumer (Gal-Or, 1989; Soberman, 2003; Spence, 1977). Lutz and Padmanabhan (1995) note that vendors may realize additional profitability through the provision of warranties. Warranty dependence on replacement policy, retailer's knowledge of usage of products and repair cost has been considered.

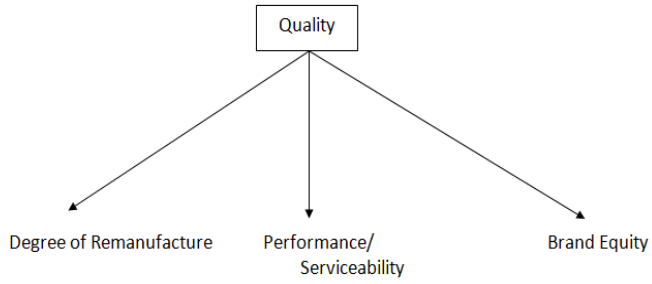

Fig. 3 Components of quality

2.8 Degree of remanufacture

Suggests the amount of rework done on the particular product to obtain a high degree of quality product.

2.9 Performance and serviceability

Performance is indicative of the accomplishment of a given task and governs the product quality.

2.10 Brand Equity

The commercial value that derives from consumer perception of the brand name of a particular product or service, rather than from the product or service itself.

2.11 Replacement policy

Replacement policy is an insurance policy between an insurance company and a consumer which promises to pay the insured the replacement value of the subject of the policy if a loss occurs. This is particularly important For remanufactured goods.

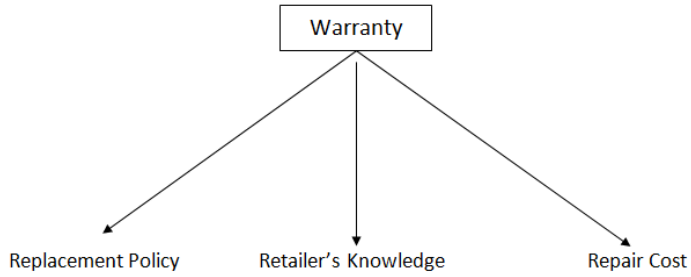

Fig. 4 components of Warranty

3. Conclusions

Quality, pricing, and warranty plays an important role in remanufacturing of a product. A comprehensive literature review

was carried out and factors related quality, pricing, and warranty were identified. These factors will help the academicians and researchers for further analysis of impact of these factors on remanufacturing of products.

References

[1]. M Pagell, Z Wu, NN Murthy. The supply chain implications of recycling. Business Horizons, 50(2), 2007, 133-143.
[2]. A Gehin, P Zwolinski, D Brissaud. A tool to implement sustainable end-of-life strategies in the product development phase. Journal of Cleaner Production, 16(5), 2008, 566-576.
[3]. LHamzaoui Essoussi, JD Linton. New or recycled products: how much are consumers willing to pay?. Journal of Consumer Marketing, 27(5), 2010, 458-468.
[4]. GD Hatcher, WL Ijomah, JFC Windmill. Design for remanufacture: a literature review and future research needs. Journal of Cleaner Production, 19(17-18), 2004-2014.
[5]. AY Alqahtani, SM Gupta. Warranty cost analysis within sustainable supply chain. Ethics and Sustainability in Global Supply Chain Management, 2017, 1-25.
[6]. S Jofre, T Morioka. Waste management of electric and electronic equipment: comparative analysis of end-of-life strategies. Journal of Material Cycles and Waste Management, 7(1), 2005, 24-32.
[7]. DM Wolf, LC Rhoads, MH Puranik, S Newhouse, M Miller, J Boggess, CL Kimes. U.S. Patent Application No. 13/188,693, 2013.
[8]. W Blischke. Warranty cost analysis. CRC Press, 1993.
[9]. G Heal. Guarantees and risk-sharing. The Review of Economic Studies, 1977, 549-560.
[10]. E Gal-Or. Warranties as a Signal of Quality. Canadian Journal of Economics, 1989, 50-61.
[11]. DA Soberman. Simultaneous signaling and screening with warranties. Journal of Marketing Research, 40(2), 2003, 176-192.
[12]. AM Spence, Entry, capacity, investment and oligopolistic pricing. The Bell Journal of Economics, 1977, 534-544.
[13]. NA Lutz, V Padmanabhan. Why do we observe minimal warranties?. Marketing Science, 14(4), 1995, 417-441.

Gate Metal Engineered Heterojunction DG-TFETs for Superior Analog Performance and Enhanced Device Reliability

Jaya Madan[1] Skanda Shekhar[2] and Rishu Chaujar*[3]
Microelectronics Research Lab, Department of Engineering Physics,
Delhi Technological University, Bawana Road, Delhi-110042, India
jayamadan.2012@gmail.com[1] skanda.shekhar15@gmail.com[2] and rishu.phy@dce.edu*[3]

***Abstract*— This work aims at demonstrating the superiority of a Germanium (Ge) source Double Gate Tunnel Field Effect Transistor (DG-TFET) as compared to a conventional Silicon (Si) source DG-TFET in terms of improved analog characteristics. In particular, the influence of Interface Trap Charges (ITC) present at the dielectric semiconductor interface on the reliability of the device is investigated. In addition, a Gate Material Engineered (GME) Ge source DG-TFET is proposed to improve the device reliability through a modification of the flatband voltage of the device near the source channel junction. A comparative analysis of the influence of ITC on a Ge source DG-TFET and a Ge source DG-TFET with Gate Material Engineering (GME) reveals superior device reliability with the amalgamation of GME onto Ge source DG-TFET.**

***Keywords—Band to Band Tunneling, Heterojunction, Interface Trap Charges, Gate Metal Engineering, Tunnel FET*.**

I. INTRODUCTION

For over half a century now, the MOSFET has been a ubiquitous component of Integrated Circuits and computer chips. However, attempts to scale down MOSFETs so as to keep pace with projections of Moore's law give rise to certain limitations, which manifest themselves primarily as short channel effects. Additionally, the carrier injection mechanism in MOSFETs limits the Subthreshold Swing (SS) of the device to 60mV/decade. These restrictions have prompted researchers to look at novel transistor designs called super-steep slope transistors with SS less than 60 mV/decade [1, 2]. One such device is the TFET, which is a gated p-i-n transistor operated in reverse bias. Quantum Mechanical Band to Band Tunneling (BTBT) is the primary carrier injection mechanism in TFETs as opposed to thermal carrier injection in MOSFETs [3-5]. This shields TFETs from hot carrier degradation effects that commonly plague MOSFETs with short channel lengths. Although TFETs are currently in their nascent stages, they have proved to be promising alternatives to MOSFETs due to steeper SS, lower I_{OFF} and their compatibility with CMOS architecture. In TFETs, BTBT takes place at the source channel interface due to the bending of energy bands owing to the applied voltages [6, 7]. The properties of the source material of a TFET significantly affect this bending of bands at the tunneling junction and hence influence the device characteristics [8-10]. Earlier, Hanna *et al.* [9] have shown that the use of a material with lower energy bandgap as the source in comparison to material of the channel leads to significant enhancement in the working of the TFET. Therefore, in this work, a Ge source DG-TFET is the primary device under consideration as Ge (0.67 eV) has energy bandgap lower than Si (1.12 eV) in accordance with the aforementioned conclusion. The structure thus formed is a semiconductor heterojunction, the properties of which are determined by Anderson's rule. In 1960, R. L. Anderson specified how energy band diagrams of semiconductor heterojunctions are formed. This rule is analogous to the often cited Schottky-Mott rule which relates the Schottky barrier height of a metal-semiconductor interface to the difference between the work function of the metal and the vacuum ionization energy (electron affinity) of the semiconductor. Similarly, Anderson's rule requires the vacuum levels of the semiconductors on either side of a semiconductor heterojunction to be aligned. Following this vacuum level alignment, one may calculate the conduction and valence band offsets using the known electron affinity (defined as the difference between the vacuum energy and the bottom of the conduction band of a semiconductor) and energy bandgap values of the semiconductors. Finally, Poisson's equation can be used in concurrence with the estimated values of the conduction and valence band offsets to determine the band structure at the heterojunction. Some compound semiconductors like InAs and InSb have energy band gaps of 0.36 eV and 0.17 eV respectively, which are lower than the band gap of Ge (0.67 eV). However, the heterojunction formed between them and Si has limited band bending due to the formation of a kink (similar to a Schottky barrier, as discussed earlier) in the energy band diagram of the device. Therefore, the aforementioned conclusion is not a standalone one, but can only be used as a rule-of-thumb. It is limited by other factors such as the vacuum ionization energies of the semiconductor. Since no such kink is formed in the case of a Ge-Si heterojunction, a Ge source is studied in this work. The primary attempt here has been to minimize the width of the tunneling barrier, which is a condition satisfied by the Ge source.

Since, electronic devices, unlike mechanical systems, do not undergo mechanical wear out, different definitions and methods of analyzing electronic device reliability are required. While electronic device reliability is mainly considered to be based on phenomena like electromigration and environmental factors like temperature, pressure and other transient stresses over the lifetime of the device, there is one crucial factor that plays a role during fabrication of device itself i.e. introduction of Interface Trap Charges (ITC) at dielectric-semiconductor interface. Work done earlier in this domain seldom takes into account the device's reliability, which must be considered for any realistic transistor under consideration [11-14]. This is due

978-1-5386-1866-0/17/$31.00 ©2017 IEEE

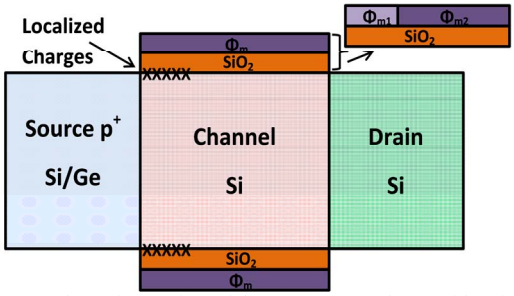

Fig. 1: Schematic 2D view of the DG-TFET under consideration.

to the general assumption of silicon dioxide (SiO_2) being a perfect insulator. By implication, there are no traps in SiO_2 or along the SiO_2-Si interface. However, in reality, a large number of positive or negative charges can be found along the SiO_2-Si interface. Additionally, ionic charges may be found within the SiO_2 layer as well. In general, there are four types of charges that can be found at the SiO_2-Si interface and inside the SiO_2 layer – oxide charges (fixed and mobile), oxide trapped charges and interface charges. These charges inevitably appear during the fabrication of the transistor. Although the number of such charges has been reduced significantly with continuous improvements in fabrication technology, they cause a strong degradation in the operation of the device due to the high packing density of transistors in microchips today. The reliability of the device is strongly affected by the presence of ITC. Therefore, in this work we probe the effect of ITC on the operation and reliability of the device.

In addition, a Gate Metal Engineered (GME) Ge source DG-TFET has been proposed to alleviate this degradation leading to immunity against ITC i.e. improved reliability of device in comparison to a Ge source DG-TFET. The GME scheme involves the use of two metals in gate of the TFET. The two metals differ in their work functions and the gate is fabricated in such a way that the metal with lower work function is near the source-channel interface (tunneling junction) [15]. The use of such a scheme leads to a clear improvement in the reliability of the device, which can be attributed to changes in the flatband voltage caused by the lower metal work function of the gate metal used near the source side.

II. Device Structure and its Description

Fig. 1 illustrates the architecture of the device under consideration (DUC). It consists of a p+ (n+) source (drain) with uniform doping of 10^{20} ($5x10^{18}$) /cm^3. Two source materials with differing bandgap i.e. Si and Ge have been taken into consideration to investigate the effect of source material on the device performance. The lightly p-doped channel has a length, width and doping density of 50 nm, 10 nm and 10^{15}/cm^3 respectively. The metal gate of the DUC has an optimum workfunction (Φ_m) of 4.3 eV. To investigate the efficacy of the GME scheme, the gate of the proposed device has been engineered to incorporate two metals with Φ_{m1} = 4.1eV and Φ_{m2} = 4.3 eV, with the metal with lower Φ_{m1} placed at the tunneling interface. To account for the device reliability, a uniform distribution of ITC of ±1E12 /cm^2 is considered up to a length of 10 nm over the tunneling junction [13]. In TFETs, the tunneling junction is also the junction where the electric field attains its peak value. This forms the logical foundation of the aforementioned consideration as maximum degradation due to ITC must take place at the region in the device where the electric field attains its maximum value [12]. The influence of both acceptor and donor traps has been simulated to analyze the device characteristics along with the ideal case wherein there are no ITC.

All numerical simulations have been performed using Technology Computer Aided Design (TCAD) Silvaco ATLAS [16] at an absolute temperature of 300 K. The simulator uses the Fermi-Dirac statistical model to account for majority charge carrier distribution along with the Shockley-Read-Hall (SRH) recombination model to simulate recombination of majority and minority charge carriers. The mobility model is incorporated in the simulation environment, which allows the simulator to solve carrier drift and diffusion equations. The Bandgap Narrowing (BGN) model accounts for the shrinkage of the bandgap as a result of overlapping impurity states in semiconductors with large impurity atom concentrations. Finally, the Non-local Band-to-Band Tunneling (BTBT) model has been used to simulate BTBT. The Non-local BTBT model models the electric field that an electron moving from the source to the channel tunnels through after accounting for the dynamic variation of electric field at the tunneling interface. Earlier literature on TFETs widely used the Kane model to simulate BTBT. This model approximates the tunneling barrier as a rectangular potential barrier. This approximation leads to significant deviation from the operation of actual physical devices. Hence, the Non-local BTBT model has been used here to perform accurate simulations that can be calibrated with experimentally obtained results easily [17].

III. Results and Discussion

The variation of the peak electric field at the tunneling interface of the Si source DG-TFET, Ge source DG-TFET and GME Ge source DG-TFET in ON-state @ V_{ds} = 1.0 V and V_{gs} = 1.2 V for acceptors ITC and donors ITC is indicated in Fig. 2(a). The formation of a hetrojunction has a significant impact on the peak electric field at the junction. The peak electric field at the tunneling juction is a result of the properties of the heterojunction and the the applied gate and drain voltages. Analysis of the plot reveals that the peak value of the electric field at the tunneling junction increases (decreases) for donor (acceptor) ITC as compared to the ideal case. This variation in the peak electric field can be attributed to the instrinsic electric field generated by the ITC as a conseqeunce of them being charged ions themselves. Therefore, positively (negatively) charged ITC have generative (absorptive) effect on the electric field at the tunneling junction leading to an increase (decrease) in the net eletcric field at the tunneling junction as compared to the ideal case. A decrease (increase) in the flatband voltage (V_{fb}) due to positive (negative) ITC leads to an increase (decrease) in the effective voltage V_{eff} (=V_{gs}-V_{fb}) at the

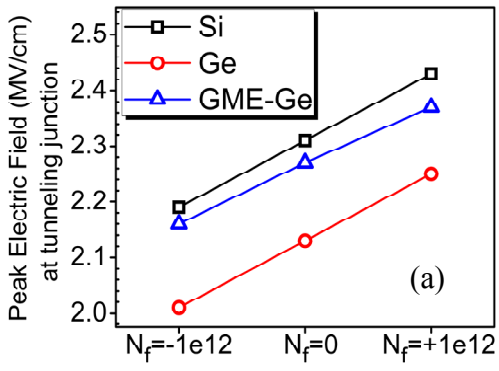

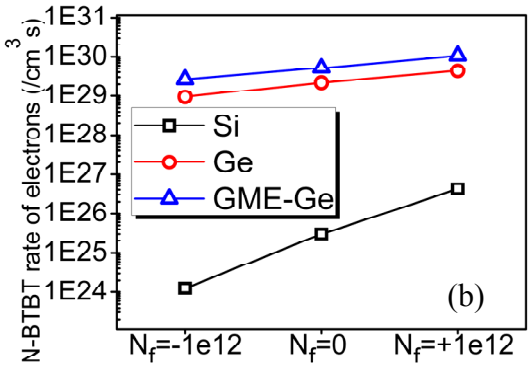

Fig. 2: (a) Peak electric field at tunneling junction (b) Peak rate of Non-local BTBT through tunneling junction for the Si source DG-TFET, Ge source DG-TFET and GME-Ge source DG-TFET in the ON-state for negative, positive and no ITC respectively.

junction, thereby causing a net increase (decrease) in the electric field at the junction. Additionally, the peak value of the electric field for GME Ge source DG-TFET is higher than that of the Ge source DG-TFET owing to a change in V_{fb} due to the lower workfunction of gate metal (Φ_{m1}) present at the tunneling interface. Fig. 2(b) shows the variation of the rate of Non-local BTBT of electrons for the aforementioned devices in ON-state for negative and positive ITC. All three device experience an increase (decrease) in the Non-local BTBT rate of electrons through the tunneling junction for positive (negative) ITC. The Non-local BTBT rate of electrons depends on the tunneling probability through the junction which, in turn, depends on both, the electric field at the junction and the width of the tunnel barrier (L_{BW}). The interplay of these two factors leads to the trend observed in the plot. Therefore, the GME Ge source DG-TFET has the highest rate of Non-local BTBT followed by the Ge and Si source DG-TFETs respectively.

The plot of the drive current (I_{ds}) with the gate voltage (V_{gs}) at constant V_{ds} = 1.0 V for the DUC is shown in Fig. 3. The observed variation in the plot are a direct consequence of the variation in the rate of Non-local BTBT shown in Fig. 2(b). The plot indicates the enhancement in I_{ds} when the source material is changed from Si to Ge. This is attributed to the significantly lower bandgap of Ge as compared to Si. There is a clear improvement in the transfer characteristics of the device due to the formation of a heterostructure resulting in significant improvement in band bending at the tenneling junction. This leads to a substancial reduction in L_{BW} that explains the observed improvements in I_{ds}.

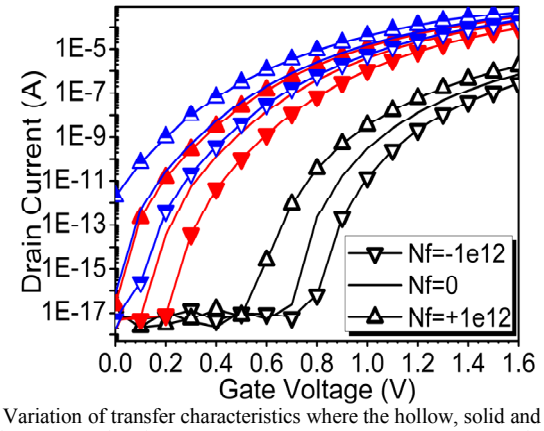

Fig. 3: Variation of transfer characteristics where the hollow, solid and solid up symbols represent the Si source DG-TFET, Ge source DG-TFET and GME-Ge source DG-TFET for negative, positive and no ITC respectively.

The application of the GME scheme significantly improves the transfer characteristics of the Ge source DG-TFET in the ideal case with no ITC and with acceptor ITC. There is a small degradation in the I_{OFF} of GME Ge source DG-TFET in the presence of donor ITC which is attributed to high rate of BTBT in the OFF-state due to narrow barrier width (L_{BW}). The presence of trap charges significantly affects all three devices. I_{ds} is higher (lower) for a given V_{gs} for donor (acceptor) ITC for all three devices which can be atrributed to the aforementioned increase (decrease) in the rate of electron tunneling through the junction. It is evident from the plot that the immunity of the Ge source DG-TFET to the presence of ITC is enhanced by the use of GME scheme due to the small change in the flatband voltage caused by the reduction in Φ_m near the source. This enhanced immunity of the GME Ge source DG-TFET to ITC translates into enhanced reliability of the device. Hence, the application of GME scheme makes the device more immune to localized charges, which is the primary intention behind the proposal of this scheme in this work.

The current switiching ratio (I_{ON}/I_{OFF}) is an important parameter of the device and indicates how distinctly the ON- and OFF-state currents of the device differ from each other. I_{ON}/I_{OFF} plays an important role in determining the ability of a transistor to function as a switch. The variation of I_{ON}/I_{OFF} is shown in Fig. 4(a) for the three aforementioned devices for negative and positive ITC along with the ideal case. A threefold increase in I_{ON}/I_{OFF} is observed when GME scheme is applied to the Ge source DG-TFET for acceptor ITC. The increase in I_{OFF} of the GME Ge source DG-TFET for donor ITC results in a strong degradation in I_{ON}/I_{OFF} of the GME Ge source DG-TFET. Since there is a large improvement in I_{ON}/I_{OFF} for both Ge source DG-TFET and GME Ge source DG-TFET for all types of ITC, the GME Ge source DG-TFET gives the most favourable results inspite of the slight degradation in I_{OFF} for donor ITC. Fig. 4(b) shows the variation of V_{th} for the three devices. V_{th} is another important device parameter that incicated how quickly the device is turned ON. It must be accounted for in low power applications

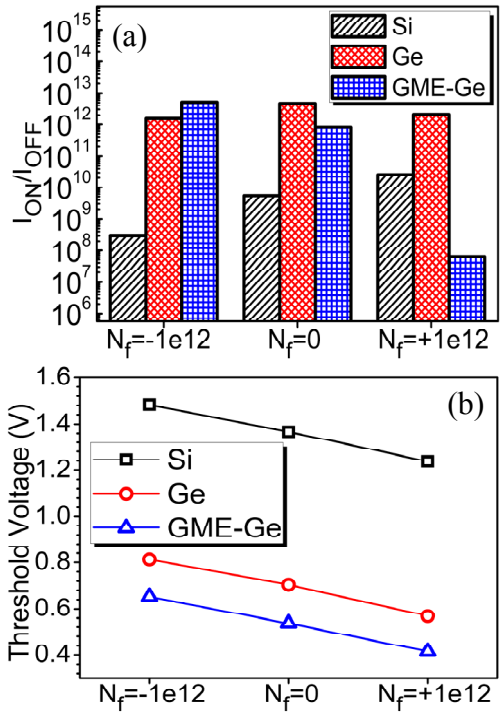

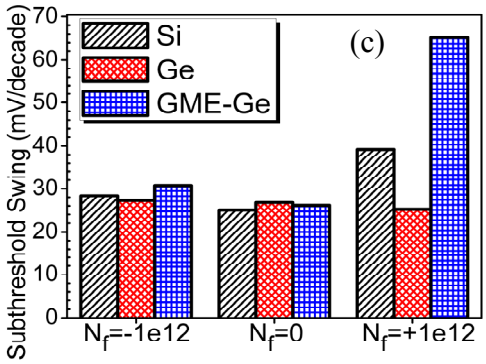

Fig. 4: Plot of (a) I_{ON}/I_{OFF}, (b) V_{th} and (c) SS of DUC for donor and acceptor ITC for the Si source DG-TFET, Ge source DG-TFET and GME-Ge source DG-TFET respectively for negative, positive and no ITC respectively.

as a lower V_{th} indicates that the device can be turned ON more quickly at a lower gate voltage. Here again, the GME Ge source DG-TFET shows the best V_{th}. Quantitatively, a 19.65%, 23.80% and 27.11% decrease in V_{th} of GME-GE source DG-TFET is observed for acceptors ITC, no ITC and donors ITC respectively as compared to the Ge source DG-TFET. Any realistically implementable alternative to the MOSFET must show SS less than 60 mV/decade for fast switching characteristics. The variation of SS of the three devices for positive ITC and negative ITC is shown in Fig. 4(c). The GME Ge source DG-TFET shows best SS when the device is undamaged i.e. there are no ITC which is about 3% lower than that of the Ge source TFET. When acceptor ITC are present, the GME Ge source DG-TFET has a SS that is 19.65% higher than that of the Ge source DG-TFET. This degradation in SS can be attributed to the increase in I_{OFF} in the presence of positive trap charges. Even though this degradation appears significant, the SS of the GME Ge souce DG-TFET is only about 60 mV/decade. Since this situation indiates the worst case performance of the device at a high donor ITC concentration of 1E12 /cm^2, it is evident that the device outperforms the MOSFET in terms of SS. Therefore, the GME Ge source DG-TFET offers favorable I_{ON}/I_{OFF}, V_{th} and SS, while significantly ehancing the imunity of the device to the presence of ITC.

IV. CONCLUSION

The primary study of this investigation is to evaluate the effect of interface trap charges on the analog performance of DG-TFETs with regard to the source material and the concomitant effect on device reliability. There is a clear enhancement in the performance of the DG-TFET when Ge is used as the source material in place of Si. Additionally, a GME Ge source DG-TFET is proposed which showed improved device characteristics as compared to the Ge source DG-TFET as well. The study of the reliabilities of the three devices indicates the improved reliability of the GME Ge source DG-TFET due to its improved immunity to the presence of ITC as compared to Ge and Si source TFETs. Therefore, such a GME Ge source DG-TFET can be considered as a potential alternative to conventional transistors both, in terms of low power operation and fast switching capabilities. Further investigations into GME DG-TFETs with suitable gate material engineering are bound to have promising outcomes.

ACKNOWLEDGEMENTS

The authors would like to express their sincere gratitude to the Microelectronics Research Lab, Department of Engineering Physics, Delhi Technological University (formerly DCE). In addition, one of the authors (Jaya Madan) thanks the University Grant Commission (UGC) for providing the financial assistance required to carry out this research.

REFERENCES

[1] K. Boucart and A. M. Ionescu, "Double-gate tunnel FET with high-gate dielectric," 2007.
[2] K. Boucart and A. M. Ionescu, "Length scaling of the double gate tunnel FET with a high-k gate dielectric," *Solid-State Electronics,* vol. 51, pp. 1500-1507, 2007.
[3] A. M. Ionescu and H. Riel, "Tunnel field-effect transistors as energy-efficient electronic switches," *Nature,* vol. 479, pp. 329-337, 2011.
[4] Y. Khatami and K. Banerjee, "Steep subthreshold slope n-and p-type tunnel-FET devices for low-power and energy-efficient digital circuits," *IEEE Transactions on Electron Devices,* vol. 56, pp. 2752-2761, 2009.
[5] V. Nagavarapu, R. Jhaveri, and J. C. Woo, "The tunnel source (PNPN) n-MOSFET: A novel high performance transistor," *IEEE Transactions on Electron Devices,* vol. 55, pp. 1013-1019, 2008.
[6] J. Madan and R. Chaujar, "Gate drain-overlapped-asymmetric gate dielectric-GAA-TFET: a solution for suppressed ambipolarity and enhanced ON state behavior," *Applied Physics A,* vol. 122, p. 973, 2016.
[7] J. Madan and R. Chaujar, "Gate Drain Underlapped-PNIN-GAA-TFET for Comprehensively Upgraded Analog/RF Performance," *Superlattices and Microstructures,* vol. 102, pp. 17-26, 2// 2017.
[8] A. Hanna and M. M. Hussain, "Si/Ge hetero-structure nanotube tunnel field effect transistor," *Journal of Applied Physics,* vol. 117, p. 014310, 2015.
[9] A. N. Hanna, H. M. Fahad, and M. M. Hussain, "InAs/Si hetero-junction nanotube tunnel transistors," *Scientific reports,* vol. 5, p. 9843, 2015.
[10] C.-H. Shih and N. D. Chien, "Sub-10-nm tunnel field-effect transistor with graded Si/Ge heterojunction," *IEEE Electron Device Letters,* vol. 32, pp. 1498-1500, 2011.
[11] W. Cao, C. Yao, G. Jiao, D. Huang, H. Yu, and M.-F. Li, "Improvement in reliability of tunneling field-effect transistor with pnin structure," *IEEE Transactions on Electron Devices,* vol. 58, pp. 2122-2126, 2011.
[12] J. Madan and R. Chaujar, "Interfacial Charge Analysis of Heterogeneous Gate Dielectric-Gate All Around-Tunnel FET for Improved Device Reliability," *IEEE Transactions on Device and Materials Reliability,* vol. 16, pp. 227-234, 2016.
[13] J. Madan and R. Chaujar, "Numerical Simulation of N+ Source Pocket PIN-GAA-Tunnel FET: Impact of Interface Trap Charges and Temperature," *IEEE Transactions on Electron Devices,* vol. 64, pp. 1482-1488, 2017.
[14] K. E. Moselund, D. Cutaia, H. Schmid, M. Borg, S. Sant, A. Schenk, *et al.*, "Lateral InAs/Si p-Type Tunnel FETs Integrated on Si—Part 1: Experimental Devices," *IEEE Transactions on Electron Devices,* vol. 63, pp. 4233-4239, 2016.
[15] N. Cui, R. Liang, and J. Xu, "Heteromaterial gate tunnel field effect transistor with lateral energy band profile modulation," *Applied Physics Letters,* vol. 98, p. 142105, 2011.
[16] A. U. s. Manual, "Silvaco," *Santa Clara, CA,* 2010.
[17] A. Biswas, S. S. Dan, C. Le Royer, W. Grabinski, and A. M. Ionescu, "TCAD simulation of SOI TFETs and calibration of non-local band-to-band tunneling model," *Microelectronic Engineering,* vol. 98, pp. 334-337, 2012.

PAPER • **OPEN ACCESS**

Generation of high power sub millimeter radiation using free electron laser

To cite this article: J Panwar *et al* 2018 *IOP Conf. Ser.: Mater. Sci. Eng.* **331** 012014

View the article online for updates and enhancements.

Related content

- Terahertz radiation generation by using modulated electron beam with plasma wave wiggler
  J Panwar, S C Sharma and R Sharma
- Terahertz pulses in a periodic plasma channel via modulated electron beam
  Pratibha Malik, Suresh C Sharma and Rinku Sharma
- Experimental study of the compact FEL with the electrostatic accelerator and the micro wiggler in the short millimeter wave region
  S. Fujii, H. Takeda, T. Fujita et al.

This content was downloaded from IP address 14.139.251.107 on 03/04/2018 at 11:53

IOP Conf. Series: Materials Science and Engineering **331** (2018) 012014 doi:10.1088/1757-899X/331/1/012014

Generation of high power sub millimeter radiation using free electron laser

J Panwar, **S C Sharma, P Malik, M Yadav and R Sharma**

[1]Department of Applied Physics, Delhi Technological University (DTU), Bawana Road, Delhi- 110042, India
E-mail: panwar.jyots2010@gmail.com

Abstract. We have developed an analytical formalism to study the emission of high power radiation lying in the sub millimetre range. A relativistic electron beam (REB) is velocity modulated by the pondermotive force exerted by the laser beams. After passing through the drift space, the beam gets density modulated which further interacts with the strong field wiggler and acquires a transverse velocity that couples with the modulated density of the beam in the presence of ion channel which contribute to the non-linear current density which further leads to the emission of the radiation. The output radiation can be modified by changing the wiggler parameters and the energy of the electron beam. The power of the output radiation is found to increase with the modulation. The obtained radiation can be employed for various applications.

1. Introduction

The emission of high power terahertz (sub millimetre) radiation has attained a great interest in the field of research due to its potential applications including spectroscopy, remote sensing, biomedical, communication and security imaging [1-4]. THz waves are preferred over microwaves for broadband mobile communications and local area network due to their high frequency and more bandwidth [5]. A modulated electron beam is an efficient source for the generation of radiation using free electron laser as a high frequency device [6-7]. Xiang *et al* [8] have studied experimentally the generation of terahertz radiation using electron beam, modulated by the down conversion of the frequency of optical lasers and observed that the radiation can be altered by the by varying the lasers frequency and the electron beam energy. Bhasin and Sharma [9] have employed an energy modulated electron beam in a dielectric loaded waveguide in the presence of external magnetic field. They observed that the gain and efficiency of the radiation increases with the modulation and the growth rate decreases monotonically with the radiation frequency. Ion channel acts as guiding medium for the electron beam. The emission of terahertz radiation using helical wiggler in the presence of ion channel has been studied by Hasanbeigi *et al* [10]. They concluded that the power of the output radiation increases with the ion density, energy and radius of the electron beam.

In this paper, we have analysed the power of the output terahertz radiation, emitted by the interaction of a density modulated relativistic electron beam with an electromagnetic wave wiggler in the presence of an ion channel.

Content from this work may be used under the terms of the Creative Commons Attribution 3.0 licence. Any further distribution of this work must maintain attribution to the author(s) and the title of the work, journal citation and DOI.
Published under licence by IOP Publishing Ltd

2. Physical Model

We consider two laser beams which employ a pondermotive force on interacting with the REB which leads to velocity modulation of the beam. When this beam further travels through the drift space, the current modulation converts into density modulation. This mechanism of premodulation is similar to that of klystron [11]. The modulated beam density (n_{mb}) [12] is obtained as

$$n_{mb} = -2n_0 J_1\left(\frac{\omega_b \rho \xi}{v_b}\right)\cos\left(\omega_b \tau_3 - \phi\right), \tag{1}$$

where n_0 is the initial beam density, v_b is the initial velocity of the beam, ω_b is the frequency difference of two lasers in terahertz range, ρ is the length of drift space, $\xi = \frac{k_b \rho}{2\gamma_0^4}\frac{c^2}{v_b^2}\frac{eA_I}{m\omega_I c}\frac{eA_{II}^*}{m\omega_{II} c}\frac{\sin(\varphi)}{\varphi}$, where $\varphi = \frac{(\omega_b - k_b v_b)\rho}{2v_b}$ is the phase angle of the modulation, k_b is the beam wave vector, A_I, A_{II} and ω_I, ω_{II} are the amplitudes of electric field and frequencies of two laser beams, respectively.

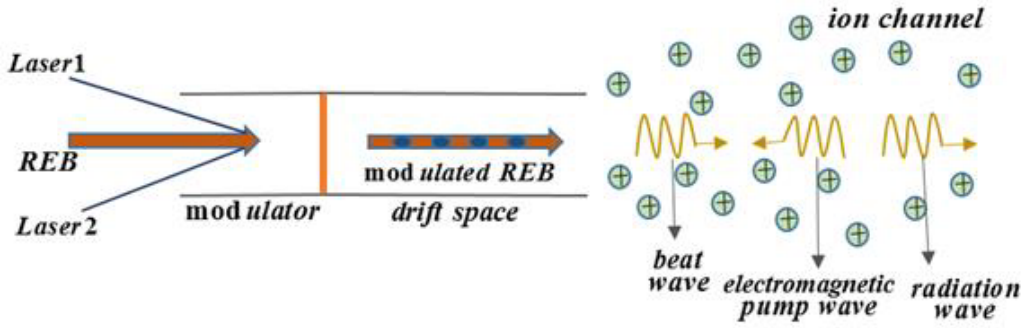

Figure 1: Interaction of laser modulated REB with the electromagnetic pump wave in the presence of ion channel.

Further we consider the propagation of modulated REB in the field of the electromagnetic wave and the uniform density ion channel. The modulated REB acquires normalized oscillatory velocity $\left(\overrightarrow{\beta_{bw}}\right)$ due to the pump wave and the ion channel field.

$$\overrightarrow{\beta_{bw}} = \frac{\Omega_0(\beta_b + \beta_0)^2}{\omega_+^2 - (\beta_b + \beta_0)^2}\cos(k_0 z + \omega_0 t), \tag{2}$$

where $\Omega_0 = \frac{eB_0}{\gamma_0 mc^2 k_0}$ is the normalized frequency of wiggler, B_0 is the wiggler magnetic field, $\left(\omega_0, k_0\right)$ is the frequency and wave vector of the wiggler wave respectively, β_b is the normalized beam velocity $\omega_+ = \left(\frac{2\pi e^2 n_+}{\gamma_0 m_+ k_0^2 c^2}\right)^{1/2}$ is the normalized frequency of ion channel, n_+ is the ion density, m_+ is the mass of ions.

This oscillatory velocity couples with the modulated beam density to give non-linear current density. The magnetic field of the terahertz wave calculated using vector potential helps in evaluating the average power $(4\pi r^2 S_{av},\ S_{av} = \hat{r}\frac{c}{2\mu_0}\left|\vec{B}\right|^2$ is the average poynting vector) of the radiation.

$$\text{Average power} = \frac{\pi c \mu_0 \omega_1^2 n_b^2 e^2 \Omega_0^2 l_b^2 r_0^2 (\beta_b + \beta_0)^4}{2[\omega_+^2 - (\beta_b + \beta_0)^2]^2} J_1^2\left(\frac{\omega_b \rho \xi}{v_b}\right), \quad (3)$$

where l_b is the electron bunch length, r_0 is the size of electron beam, ω_1 is radiation frequency.

3. Results and Discussion

Typical parameters used for calculation are: $v_b = 0.95c$, $\gamma_0 = 3.2$, $n_b = 4\times10^{14} cm^{-3}$, $\rho = 500\mu m$, $l_b = 0.3cm$, $\frac{eA_I}{m\omega_I c} = 0.05$, $\frac{eA_{II}}{m\omega_{II} c} = 0.05$.

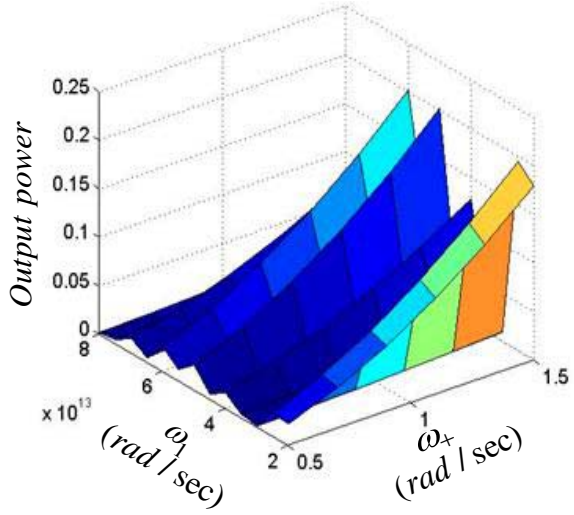

Figure 2: The figure shows the variation of output average power ($4\pi r^2 \vec{S}_{av}$) with radiation frequency (ω_1) and ion channel frequency (ω_+).

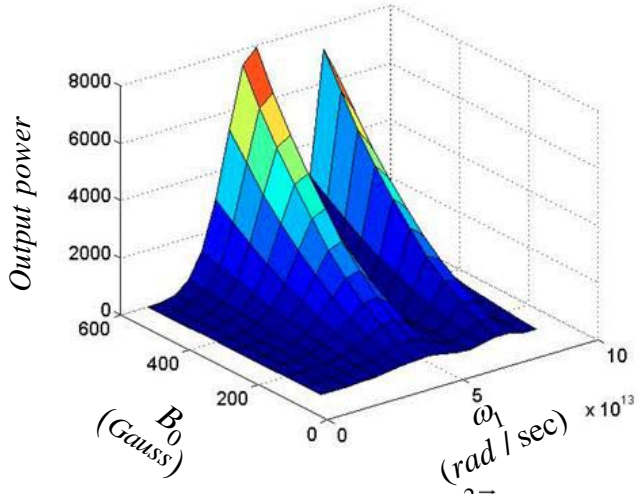

Figure 3: The figure shows the variation of output power ($4\pi r^2 \vec{S}av$) with radiation frequency (ω_1) and pump field amplitude (B_0).

From figure 2, it can be seen that the average output power of the radiation for a fixed value of ion density, increases with the radiation frequency upto a certain maximum value and then decreases and further repeats the pattern. This pattern is followed by the Bessel's function which appears due to the modulation of the electron beam density. The power also increases with the frequency of the ion channel. From figure 3, it is observed that the output power increases with the amplitude of magnetic field of the pump wave. It also increases with the radiation frequency and shows Bessel's function character.

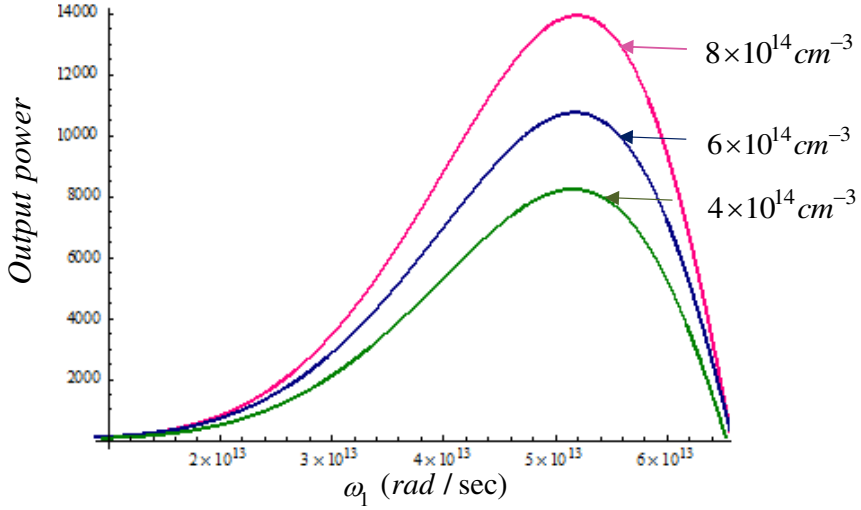

Figure 4: The figure illustrates the variation of output average power with the radiation frequency for different beam densities.

It can be inferred from figure 4 that the output average power of the radiation wave increases with the increase of density of the electron beam as more the number of electrons will be available to transfer their energy to the radiation wave. Further, it increases initially with the output frequency, attains a maximum value at a point where resonance occurs and then starts decreasing.

4. Conclusion

The terahertz radiation emitted using a density modulated beam with the effects of ion channel can be modified by varying the parameters of electron beam, amplitude of the pump field and frequency of the ion channel. Increase in ion channel density helps in enhancement of the output power. The modulation of the beam is affected by the parameters of the laser beams and the electron beam. The power scales as square of the electron beam density and the amplitude of the pump wiggler field. The tuned radiation thus obtained can be used for future practical applications.

References

[1] Malik A K, Malik H K and Kawata S 2010 Investigations on terahertz radiation generated by two superposed femtosecond laser pulses *J. Appl. Phys.* **107** 113105
[2] Chen Z Y, Li X Y and Yu W 2013 Intense terahertz emission from relativistic circularly polarized laser pulses interaction with overdense plasmas *Phys. Plasmas* **20** 103115
[3] Pickwell E and Wallace V P 2006 Biomedical applications of terahertz technology *J. Phys. D: Appl. Phys.* **39** 301
[4] Fitch M J and Osiander R 2004 Terahertz waves for communication and sensing *Johns Hopkins Apl TechnicaL Digest* **25** 348
[5] Zhu B, Chen Y, Deng K, Hu W, and Yao Z S Terahertz Science and Technology and Applications 2009 *PIERS Proceedings* 1166

[6] Freund H P, O'Shea P G and J. Neumann 2003 Simulation of prebunching in free-electron lasers *J Nucl. Instrum. Methods Phys. Res. A* **507** 400
[7] Sharma S C, Panwar J and Sharma R 2017 Modeling of terahertz radiation emission from a free-electron laser *Contrib. Plasma Phys.* **57** 167
[8] Xiang D and Stupakov G 2009 Enhanced tunable narrow band THz emission from laser modulated electron beams *Phys. Rev. ST Accel. Beams* **12** 080701
[9] Bhasin A and Sharma S C 2009 Effect of beam premodulation and guide magnetic fields on slow wave free electron laser: Nonlocal theory *IEEE J. Quantum Electronics* **45** 1129
[10] Hasanbeigi A, Mehdian H and Gomar P 2015 Enhancement of terahertz radiation power from a prebunched electron beam using helical wiggler and ion-channel guiding *Phys. Plasmas* **22** 123116
[11] Liao S Y 1990 Microwave Devices and Circuits (Prentice Hall, New Jersey)
[12] Kumar M and Tripathi V K 2012 Terahertz radiation from a laser bunched relativistic electron beam in a magnetic wiggler *Phys. Plasmas* **19** 073109

International Journal of Research in Engineering and Innovation (IJREI)
journal home page: http://www.ijrei.com
ISSN (Online): 2456-6934

Irreversibility analysis of three stage vapour compression refrigeration systems with flash-intercooler using eco-friendly new refrigerants (R134a, R1234yf, R1234ze, R227ea and R245fa)

R.S. Mishra

Department of Mechanical Engineering, Delhi Technological University, Delhi, India

Abstract

In this paper, comparison between three vapour compression refrigeration systems (i.e.System-1: Three stage compression with multiple expansion valves and water coolers and System-2: Three stage compression with multiple expansion valves and flash inter cooling chambers in parallel and System-3: Three stage compression with multiple expansion valves and flash inter cooling chambers in series)using environmental friendly refrigerants on the basis of energetic and exergetic approach have been made. It has been observed that for all selected new eco-friendly refrigerants, energy and exergetic efficiency of system-2 is lower than system-1 and sytem-3.The best performance using R134a was observed in system-3. For all Vapour compression refrigeration systems R227ea showed lowest thermal performance in terms of COP, second law efficiency whereas performances of R134a is better in comparison of other selected refrigerants 2.Thermodynamic second law performance of R134ze is less than R1234yf . Since R134a is easily available and also gives better thermodynamic performances, therefore R134a may also be used for practical applications without taking of any safety precautions. .
© 2018 ijrei.com. All rights reserved
Key words: Irreversibility Computation, VCRS, Energy-Exergy Analysis**,** Thermodynamics of Refrigeration systems

1. Introduction

Nowadays most of the energy utilize in cooling and air conditioning in industrial as well as for domestic applications, in addition to energy consumption, using of refrigerants in cooling and air conditioning having high GWP and ODP which are responsible for increasing global warming and ozone depletion. The primary requirements of ideal refrigerants are having good physical and chemical properties. Due to good physical and chemical properties such as non-corrosiveness, non-toxicity, non- flammability, low boiling point, Chlorofluorocarbons (CFCs) have been used over the last many decades, but hydro chlorofluorocarbons (HCFCs) and Chlorofluorocarbons (CFCs) having large amount of chlorine content as well as high global warming potential and ozone depletion potential, so after 90s refrigerants under these categories these kinds of refrigerants are almost prohibited [1]. Most of the study has been carried out for the performance evaluation of vapour compression refrigeration system using energetic analysis, but with the help of first law analysis irreversibility destruction or losses in components of system unable to determined [2], so that second law thermodynamic analysis is the advanced approach for thermodynamic analysis which gives an additional practical view of the processes [3-5]. The utility of second law analysis on vapour compression refrigeration systems is well defined because it gives the idea for improvements in efficiency due to modifications in existing design in terms of reducing exergy destructions in the components. The second law exergetic analysis also provides new thought for development in the existing system [6].Xuan and Chen [7] presented explained about the replacement of R502 by mixture of HFC-161 and found that mixture of HFC-161 gives same and higher performance than R404a at lower and higher evaporative temperature respectively on the vapour compression refrigeration system designed for R404a.Cabello et al. [8] considered the effect of condensing pressure, evaporating pressure and degree of superheating experimentally on the single stage vapour compression refrigeration system using R22, R134a and R407c.It was observed that mass flow rate is greatly affected by change in

Corresponding author: R.S. Mishra
Email Id: hod.mechanical.rsm@dtu.ac.in

suction conditions of compressor in results on refrigeration capacity because refrigeration capacity depended on mass flow rate through evaporator. It was also found that for higher compression ratio R22 gives lower COP than R407C. Similarly Spatz and Motta [9] also focused on the replacement of R12 with R410a and conducted experimental investigation of medium temperature vapour compression refrigeration cycles and carried out thermodynamic analysis. The comparison was made of heat transfer and pressure drop characteristics and found that the R410a gives best thermodynamic performances among R404a. Han et al. [10] carried out experimental investigation under different working conditions and their results revealed that there could be replacement of R407c in vapour compression refrigeration system having rotor compressor with mixture of R32/R125/R161 showing higher first law performance in terms of COP and less pressure ratio along with slightly high discharge compressor temperature without any modification in the existing design. Cabello et al [11] had studied about the effect of operating parameters on COP, work input and cooling capacity of single-stage vapour compression refrigeration system. There is great influence on energetic parameters due change in suction pressure, condensing and evaporating temperatures. With exergetic efficiency chlorine content as well as high global warming potential and ozone depletion potential, so after 90s refrigerants under these categories these kinds of refrigerants are almost prohibited [1].Most of the study has been carried out for the performance evaluation of vapour compression refrigeration system using energetic analysis, but with the help of first law analysis irreversibility destruction or losses in components of system unable to determined [2], so exergetic analysis is the advanced approach for thermodynamic analysis which gives an additional practical view of the processes [3-5]. The utility of second law analysis on vapour compression refrigeration systems is well defined because it gives the idea for improvements in efficiency due to modifications in existing design in terms of reducing exergy destructions in the components. In addition to this second law analysis also provides new thought for development in the existing system [6].Xuan and Chen [7] presented in this manuscript about the replacement of R502 by mixture of HFC-161.Through experimental study it was found that mixture of HFC-161 gives same and higher performance than R404A at lower and higher evaporative temperature respectively on the vapour compression refrigeration system designed for R404A.Cabello et al.[8] effect of condensing pressure, evaporating pressure and degree of superheating was experimentally investigated on single stage vapour compression refrigeration system using R22, R134a and R407C.It was observed that mass flow rate is greatly affected by change in suction conditions of compressor in results on refrigeration capacity because refrigeration capacity depended on mass flow rate through evaporator. It was also found that for higher compression ratio R22 gives lower COP than R407C.Spatz and Motta [9] focused on replacement of R12 with R410a through experimental investigation of medium temperature vapour compression refrigeration cycles. In terms of thermodynamic analysis, comparison of heat transfer and pressure drop characteristics, R410a gives best performance among R12, R404a and R290a.Han et al.[10]under different working conditions experimental results revealed that there could be replacement of R407C in vapour compression refrigeration system having rotor compressor with mixture of R32/R125/R161 showing higher COP, less pressure ratio and slightly high discharge compressor temperature without any modification in the same system. Cabello et al [11] had studied about the effect of operating parameters on COP, work input and cooling capacity of single-stage vapour Getu and Bansal [12] had optimized the design and operating parameters of like condensing temperature, sub cooling temperature, evaporating temperature, superheating temperature and temperature difference in cascade heat exchanger R744-R717 cascade refrigeration system. A regression analysis was also done to obtain optimum thermodynamic parameters of same system. Mohanraj et al [13] through experimental investigation of domestic refrigerator they arrived on conclusions that under different environmental temperatures COP of system using mixture of R290 and R600a in the ratio of 45.2: 54.8 by weight showing up to 3.6% greater than same system using R134a, also discharge temperature of compressor with mixture of R290 and R600a is lower in the range of 8.5-13.4K than same compressor with R134a.Padilla et al [14]exergy analysis of domestic vapour compression refrigeration system with R12 and R413a was done. They concluded that performance in terms of power consumption, irreversibility and exergy efficiency of R413A is better than R12.The impact on second law efficiency (exergetic efficiency) with change in temperature of low, intermediate and high temperature evaporator of three systems. As variation in second law efficiency is reciprocal to coefficient of performance. It is also observed that second law efficiency decrease with increase in evaporator temperature. R134a and R227ea have maximum and minimum second law efficiency for both systems similar to performance evaluation in terms of energetic efficiency. It was also found that temperature variation in low and intermediate evaporator put great impact on second law efficiency in comparison with temperature evaporator, for all three systems [1].Most of the study has been carried out for the performance evaluation of vapour compression refrigeration system using energetic analysis, but with the help of first law analysis irreversibility destruction or losses in components of system unable to determined [2], so exergetic analysis is the advanced approach for thermodynamic analysis which gives an additional practical view of the processes [3-5]. The utility of second law analysis on vapour compression refrigeration systems is well defined because it gives the idea for improvements in efficiency due to modifications in existing design in terms of reducing exergy destructions in the components. In addition to this second law analysis also provides new thought for development in the existing system [6].Xuan and Chen [7] presented in this manuscript about the replacement of R502 by mixture of HFC-161.Through

experimental study it was found that mixture of HFC-161 gives same and higher performance than R404A at lower and higher evaporative temperature respectively on the vapour compression refrigeration system designed for R404A.Cabello et al.[8] effect of condensing pressure, evaporating pressure and degree of superheating was experimentally investigated on single stage vapour compression refrigeration system using R22, R134a and R407C.It was observed that mass flow rate is greatly affected by change in suction conditions of compressor in results on refrigeration capacity because refrigeration capacity depended on mass flow rate through evaporator. It was also found that for higher compression ratio R22 gives lower COP In this paper great emphasis put on saving of energy and using of ecofriendly refrigerants due to increase of energy crises, global warming anddepletion of ozone layer. The work input required running the vapour compression refrigeration system reduced by using compound compression and further decreased by flash intercooling between compressors. COP of system can also be enhanced by compressing the refrigerant very close to the saturation line this can be achieved by compressing the refrigerants in more stages with intermediate intercoolers. The refrigeration effect can be increase by maintaining the condition of refrigerants in more liquid stage at the entrance of evaporator which can be achieved by expanding the refrigerant very close to the liquid line. The expansion can be brought close to the liquid line by sub cooling the refrigerant and removing the flashed vapours by incorporating the flash chamber in the working cycle. The evaporator size can be reduced because unwanted vapours formed are removed before the liquid refrigerant enters in the evaporator. Multi-stage vapour compression with flash intercooler and individual throttle valves (system-1), three compressors arranged in compound compression, individual throttle valves, condenser and evaporator (system-2)and Multiple evaporators at different temperatures with compound compression, flash intercooler and multiple throttle valves and system-3 consists of three compressors arranged in compound compression, multiple throttle valves, condenser and evaporator than R407C.Spatz and Motta [9]focused on replacement of R12 with R410a through experimental investigation of medium temperature vapour compression refrigeration cycles. In terms of thermodynamic analysis, comparison of heat transfer and pressure drop characteristics, R410a gives best performance among R12, R404a and R290a.Han et al. [10]under different working conditions experimental results revealed that there could be replacement of R407C in vapour compression refrigeration system having rotor compressor with mixture of R32/R125/R161 showing higher COP, less pressure ratio and slightly high discharge compressor temperature without any modification in the same system. Cabello et al [11] had studied about the effect of operating parameters on COP, work input and cooling capacity of single-stage vapour compression refrigeration system.

2. Energy and exergy analysis

For carrying out energetic and exergetic analysis, computational models of system-1 and system-2 has been developed and impact of chosen refrigerants on these systems has been analyzed using EES [15].In this investigation following assumptions are made:

1. Load on the low, intermediate and high temperature evaporator is 10TR,
2. Dead state temperature (T0): 25^0C
3. Difference between evaporator and space temperature (Tr-Te):5^0C.
4. Adiabatic efficiency of compressor: 76%.
5. Dead state enthalpy (Φ0) and entropy (s0) of the refrigerants have been calculated corresponding to the dead state temperature (T0) of 25^0 C.
6. Variation in kinetic and potential energy is negligible.
7. Expansion process is adiabatic
8. Temperature of low, intermediate and high temperature evaporators are -10^0C, 0^0C and 10^0C respectively.
9. Condenser temperature : 50^0C
10. Degree of sub cooling : 10^0

2.1 Thermodynamic Analysis

First law of thermodynamic gives the idea of energy balance of system.

$$\dot{m}_{c1} = \dot{m}_{e1} = \frac{\dot{Q}_{e1}}{(\Phi_1 - \Phi_{10})} \quad (1)$$

$$\dot{m}_{e2} = \frac{\dot{Q}_{e2}}{(\Phi_3 - \Phi_9)} \quad (2)$$

$$\dot{m}_{f1} = \frac{\dot{m}_{c1}(\Phi_2 - \Phi_3)}{(\Phi_3 - \Phi_9)} \quad (3)$$

$$\dot{m}_{c2} = \dot{m}_{c1} + \dot{m}_{e2} + \dot{m}_{f1} \quad (4)$$

$$\dot{m}_{e3} = \frac{\dot{Q}_{e3}}{(\Phi_5 - \Phi_8)} \quad (5)$$

$$\dot{m}_{f2} = \frac{\dot{m}_{c2}(\Phi_4 - \Phi_5)}{(\Phi_5 - \Phi_8)} \quad (6)$$

$$\dot{m}_{c3} = \dot{m}_{c2} + \dot{m}_{e3} + \dot{m}_{f2} \quad (7)$$

Energy consumption for sytem-1

$$P_{c1} = \frac{\dot{m}_{c1}(\Phi_2 - \Phi_1)}{60} \quad (8)$$

$$P_{c2} = \frac{\dot{m}_{c2}(\Phi_4 - \Phi_3)}{60} \quad (9)$$

$$P_{c3} = \frac{\dot{m}_{c3}(\Phi_6 - \Phi_5)}{60} \quad (10)$$

Energetic efficiency of system-1

$$\mathrm{COP} = \frac{\dot{Q}_e}{P_c * 60} \quad (11)$$

2.2 Rate of exergy loss due to irreversibility($T_o\dot{S}_{gen}$) in various components of system-1

The concept of exergy was given by second law of thermodynamics, which always decreases due to

thermodynamic irreversibility. Exergy is defined as the measure of usefulness, quality or potential of a stream to cause change and an effective measure of the potential of a substance to impact the environment [12].

Exergy at any state is given as

$$X = (\Phi - \Phi_0) - T_0(s - s_0) \quad (12)$$

Compressors

$$(T_o\dot{S}_{gen})_{c1} = \dot{W}_{c1} + \dot{m}_{c1}(X_2 - X_1) \quad (13)$$
$$(T_o\dot{S}_{gen})_{c2} = \dot{W}_{c2} + \dot{m}_{c2}(X_4 - X_3) \quad (14)$$
$$(T_o\dot{S}_{gen})_{c3} = \dot{W}_{c3} + \dot{m}_{c3}(X_6 - X_5) \quad (15)$$
$$\dot{\Psi}_c = (T_o\dot{S}_{gen})_{c1} + (T_o\dot{S}_{gen})_{c2} + (T_o\dot{S}_{gen})_{c3} \quad (16)$$

Evaporators

$$(T_o\dot{S}_{gen})_{e1} = \dot{m}_{e1}(X_1 - X_{10}) - \dot{Q}_{e1}\left(1 - \frac{T_0}{T_{r1}}\right) \quad (17)$$
$$(T_o\dot{S}_{gen})_{e2} = \dot{m}_{e2}(X_3 - X_9) - \dot{Q}_{e2}\left(1 - \frac{T_0}{T_{r2}}\right) \quad (18)$$
$$(T_o\dot{S}_{gen})_{e3} = \dot{m}_{e3}(X_5 - X_8) - \dot{Q}_{e3}\left(1 - \frac{T_0}{T_{r3}}\right) \quad (19)$$
$$\dot{\Psi}_e = (T_o\dot{S}_{gen})_{e1} + (T_o\dot{S}_{gen})_{e2} + (T_o\dot{S}_{gen})_{e3} \quad (20)$$

Condenser

$$\dot{\Psi}_{cond} = (T_o\dot{S}_{gen})_{cond} = \dot{m}_{c3}(X_6 - X_7) - \dot{Q}_e\left(1 - \frac{T_0}{T_r}\right) \quad (21)$$
$$(T_o\dot{S}_{gen})_{tv1} = \dot{m}_{e1}(X_{77} - X_{10}) \quad (22)$$
$$(T_o\dot{S}_{gen})_{tv2} = (\dot{m}_{e2} + \dot{m}_{f1})(X_{77} - X_9) \quad (23)$$
$$(T_o\dot{S}_{gen})_{tv3} = (\dot{m}_{e3} + \dot{m}_{f2})(X_{77} - X_8) \quad (24)$$
$$\dot{\Psi}_{tv} = (T_o\dot{S}_{gen})_{tv1} + (T_o\dot{S}_{gen})_{tv2} + (T_o\dot{S}_{gen})_{tv3} \quad (25)$$

Liquid subcooler

$$\dot{\Psi}_{lsc} = (T_o\dot{S}_{gen})_{sc} = \dot{m}_{c3}(X_7 - X_{77}) \quad (26)$$

Flash intercoolers

$$(T_o\dot{S}_{gen})_{f1} = \dot{m}_{f1}(X_9 - X_3) + \dot{m}_{c1}(X_2 - X_3) \quad (27)$$
$$(T_o\dot{S}_{gen})_{f2} = \dot{m}_{f2}(X_8 - X_5) + \dot{m}_{c1}(X_4 - X_5) \quad (28)$$
$$\dot{\Psi}_f = (T_o\dot{S}_{gen})_{f1} + (T_o\dot{S}_{gen})_{f2} \quad (29)$$
$$\sum\dot{\Psi}_k = \dot{\Psi}_e + \dot{\Psi}_c + \dot{\Psi}_{cond} + \dot{\Psi}_{tv} + \dot{\Psi}_{lsc} + \dot{\Psi}_f \quad (30)$$
$$\dot{m}_{c1'} = \dot{m}_{e1'} = \frac{\dot{Q}_{e1'}}{(\Phi_{1'} - \Phi_{12'})} \quad (31)$$
$$\dot{m}_{e2'} = \frac{\dot{Q}_{e2'}}{(\Phi_{3'} - \Phi_{10'})} + \dot{m}_{c1'}\left(\frac{x_{10'}}{1 - x_{10'}}\right) \quad (32)$$
$$\dot{m}_{f1'} = \frac{\dot{m}_{c1'}(\Phi_{2'} - \Phi_{3'})}{(\Phi_{3'} - \Phi_{10'})} \quad (33)$$
$$\dot{m}_{c2'} = \dot{m}_{c1'} + \dot{m}_{e2'} + \dot{m}_{f1'} \quad (34)$$
$$\dot{m}_{e3'} = \frac{\dot{Q}_{e3'}}{(\Phi_{5'} - \Phi_{8'})} + \dot{m}_{c2'}\left(\frac{x_{8'}}{1 - x_{8'}}\right) \quad (35)$$
$$\dot{m}_{f2'} = \frac{\dot{m}_{c2'}(\Phi_{4'} - \Phi_{5'})}{(\Phi_{5'} - \Phi_{8'})} \quad (36)$$

Power required for running the compressors

$$P_{c1'} = \frac{\dot{m}_{c1'}(\Phi_{2'} - \Phi_{1'})}{60} \quad (37)$$
$$P_{c2'} = \frac{\dot{m}_{c2'}(\Phi_{4'} - \Phi_{3'})}{60} \quad (38)$$
$$P_{c3'} = \frac{\dot{m}_{c3'}(\Phi_{6'} - \Phi_{5'})}{60} \quad (39)$$
$$\text{Energetic efficiency} = \frac{\dot{Q}_{e'}}{P_{c'} * 60} \quad (40)$$

2.3 Rate of exergy loss due to irreversibility ($T_o\dot{S}_{gen}$) in various components of system-2

$$(T_o\dot{S}_{gen})_{c1'} = \dot{W}_{c1'} + \dot{m}_{c1'}(X_{2'} - X_{1'}) \quad (41)$$
$$(T_o\dot{S}_{gen})_{c2'} = \dot{W}_{c2'} + \dot{m}_{c2'}(X_{4'} - X_{3'}) \quad (42)$$
$$(T_o\dot{S}_{gen})_{c3'} = \dot{W}_{c3'} + \dot{m}_{c3'}(X_{6'} - X_{5'}) \quad (43)$$
$$\dot{\Psi}_{c'} = (T_o\dot{S}_{gen})_{c1'} + (T_o\dot{S}_{gen})_{c2'} + (T_o\dot{S}_{gen})_{c3'} \quad (44)$$

Evaporators

$$(T_o\dot{S}_{gen})_{e1'} = \dot{m}_{e1'}(X_{1'} - X_{12'} - \dot{Q}_{e1'}\left(1 - \frac{T_0}{T_{r1'}}\right) \quad (45)$$
$$(T_o\dot{S}_{gen})_{e2'} = \dot{m}_{e2'}(X_{3'} - X_{10'}) - \dot{Q}_{e2'}\left(1 - \frac{T_0}{T_{r2'}}\right) \quad (46)$$
$$(T_o\dot{S}_{gen})_{e3'} = \dot{m}_{e3'}(X_{5'} - X_{8'}) - \dot{Q}_{e3'}\left(1 - \frac{T_0}{T_{r3'}}\right) \quad (47)$$
$$\dot{\Psi}_{e'} = (T_o\dot{S}_{gen})_{e1'} + (T_o\dot{S}_{gen})_{e2'} + (T_o\dot{S}_{gen})_{e3'} \quad (48)$$

Condenser

$$\dot{\Psi}_{cond'} = (T_o\dot{S}_{gen})_{cond'} = \dot{m}_{c3'}(X_{6'} - X_{7'}) - \dot{Q}_{e'}\left(1 - \frac{T_0}{T_{r'}}\right) \quad (49)$$

Throttle Valves

$$(T_o\dot{S}_{gen})_{tv1'} = \dot{m}_{e1'}(X_{11'} - X_{12'}) \quad (50)$$
$$(T_o\dot{S}_{gen})_{tv2'} = \dot{m}_{c2'}(X_{9'} - X_{10'}) \quad (51)$$
$$(T_o\dot{S}_{gen})_{tv3'} = \dot{m}_{c3'}(X_{77'} - X_{8'}) \quad (52)$$
$$\dot{\Psi}_{tv'} = (T_o\dot{S}_{gen})_{tv1'} + (T_o\dot{S}_{gen})_{tv2'} + (T_o\dot{S}_{gen})_{tv3'} \quad (53)$$

Liquid subcooler

$$\dot{\Psi}_{lsc'} = (T_o\dot{S}_{gen})_{lsc'} = \dot{m}_{c3'}(X_{7'} - X_{77'}) \quad (54)$$

Flash intercoolers

$$(T_o\dot{S}_{gen})_{f1'} = \dot{m}_{f1'}(X_{10'} - X_{3'}) + \dot{m}_{c1'}(X_{2'} - X_{3'}) \quad (55)$$

$$(\mathrm{T_o}\dot{\mathrm{S}}_{\mathrm{gen}})_{\mathrm{f2}'} = \dot{\mathrm{m}}_{\mathrm{f2}'}(\mathrm{X}_{8'} - \mathrm{X}_{5'}) + \dot{\mathrm{m}}_{\mathrm{c2}'}(\mathrm{X}_{4'} - \mathrm{X}_{5'}) \quad (56)$$

$$\dot{\Psi}_{\mathrm{f}'} = (\mathrm{T_o}\dot{\mathrm{S}}_{\mathrm{gen}})_{\mathrm{f1}'} + (\mathrm{T_o}\dot{\mathrm{S}}_{\mathrm{gen}})_{\mathrm{f2}'} \quad (57)$$

Total irreversibility destruction in system-1

$$\sum \dot{\Psi}_{\mathrm{k}'} = \dot{\Psi}_{\mathrm{e}'} + \dot{\Psi}_{\mathrm{c}'} + \dot{\Psi}_{\mathrm{cond}'} + \dot{\Psi}_{\mathrm{tv}'} + \dot{\Psi}_{\mathrm{lsc}'} + \dot{\Psi}_{\mathrm{f}'} \quad (58)$$

2.4 Exergetic efficiency

$$\text{Exergetic efficiency} = \frac{\text{Exergy of cooling load of evaporators}}{\text{Compressors work}} = \frac{\dot{\mathrm{E}}\mathrm{P}}{\dot{\mathrm{W}}} \quad (59)$$

$$\text{Exergetic efficiency of system} - 1 = \frac{(\dot{\mathrm{Q}}_{\mathrm{e1}}+\dot{\mathrm{Q}}_{\mathrm{e2}}+\dot{\mathrm{Q}}_{\mathrm{e3}}) - \mathrm{T_o}\left(\frac{\dot{\mathrm{Q}}_{\mathrm{e1}}}{\mathrm{T_{r1}}}+\frac{\dot{\mathrm{Q}}_{\mathrm{e2}}}{\mathrm{T_{r2}}}+\frac{\dot{\mathrm{Q}}_{\mathrm{e3}}}{\mathrm{T_{r3}}}\right)}{P_c * 60} \quad (60)$$

$$\text{Rational efficiency of system} - 2 = \frac{\left(\dot{\mathrm{Q}}_{\mathrm{e1}'}+\dot{\mathrm{Q}}_{\mathrm{e2}'}+\dot{\mathrm{Q}}_{\mathrm{e3}'}\right) - \mathrm{T_o}\left(\frac{\dot{\mathrm{Q}}_{\mathrm{e1}'}}{\mathrm{T_{r1}}'}+\frac{\dot{\mathrm{Q}}_{\mathrm{e2}'}}{\mathrm{T_{r2}}'}+\frac{\dot{\mathrm{Q}}_{\mathrm{e3}'}}{\mathrm{T_{r3}}'}\right)}{\mathrm{P_{c'}} * 60} \quad (61)$$

3. Result and Discussion

The effect of various ecofriendly refrigerants with coefficient of performance for considered refrigerants of system-1 and system-2 is shown by Table-1 to Table-5 respectively.

Table-1: First Law efficiency in terms of COP of various Refrigeration Systems of 35 kW cooling capacity

Refrigerant	System-1 Three stage Compression with multiple expansion Valves and water coolers	System-2 Three stage Compression with multiple expansion Valves and flash inter cooling Chambers in parallel	System-3 Three stage Compression with multiple expansion Valves and flash inter cooling Chambers in series
R134a	2.754	2.65	3.275
R1234yf	2.293	2.256	3.005
R1234ze	2.412	2.373	3.116
R227ea	1.882	1.951	2.956
R245fa	2.355	2.367	3.228

Table-2: Second Law efficiency in terms of Exergetic Efficiency of various Refrigeration Systems of 35 kW cooling capacity

Refrigerant	System-1 Three stage Compression with multiple expansion Valves and water coolers	System-2 Three stage Compression with multiple expansion Valves and flash inter cooling Chambers in parallel	System-3 Three stage Compression with multiple expansion Valves and flash inter cooling Chambers in series
R134a	0.3658	0.3520	0.4351
R1234yf	0.3313	0.3259	0.4342
R1234ze	0.2425	0.2387	0.3134
R227ea	0.1657	0.1717	0.2603
R245fa	0.2025	0.1987	0.2734

Table-3: Exergy Destruction Ratio based on exergy input of various Refrigeration Systems of 35 kW cooling capacity

Refrigerant	System-1 Three stage Compression with multiple expansion Valves and water coolers	System-2 Three stage Compression with multiple expansion Valves and flash inter cooling Chambers in parallel	System-3 Three stage Compression with multiple expansion Valves and flash inter cooling Chambers in series
R134a	0.6342	0.6480	0.5649
R1234yf	0.6687	0.6741	0.5658
R1234ze	0.7575	0.7613	0.6866
R227ea	0.8343	0.8383	0.7397
R245fa	0.7925	0.8013	0.7266

Table-4: Exergy Destruction Ratio based on exergy input of various Refrigeration Systems of 35 kW cooling capacity

Refrigerant	System-1 Three stage Compression with multiple expansion Valves and water coolers	System-2 Three stage Compression with multiple expansion Valves and flash inter cooling Chambers in parallel	System-3
R134a	1.734	1.832	1.222
R1234yf	2.018	2.068	1.229
R1234ze	3.123	3.189	2.081
R227ea	5.036	4.823	2.692
R245fa	3.93	4.0	2.29

Table-5: Exergy input of various Refrigeration Systems

Refrigerant	System-1 Three stage Compression with multiple expansion Valves and water coolers	System-2 Three stage Compression with multiple expansion Valves and flash inter cooling Chambers in parallel	System-3 Three stage Compression with multiple expansion Valves and flash inter cooling Chambers in series
R134a	12.71	13.21	10.69
R1234yf	15.26	15.52	11.65
R1234ze	14.51	14.75	11.23
R227ea	18.6	17.94	11.84
R245fa	14.51	14.78	10.84

Both systems (system-1& system-2) were analytically analyzed and it was observed that COP (energetic efficiency) of system-3 is higher than system-2The COP of all systems increases with increase in evaporator temperature for chosen refrigerants. It was also observed that R134a shows better thermodynamic performances in terms of COP and exergetic efficiency and R-227ea gives low first law performance in term of COP and second law efficiency in terms of exergetic efficiency for all systems. The irreversibility analysis of systems, the exergy destruction Ratio based on exergy of fuel in terms of total power and also exergy destruction Ratio based on exergy of products are shown in Table-3 to Table-4 respectively. However the exergy of fuel in terms of total power required to run the system are shown in Table-5 respectively. It was observed that the exergy destruction ratio of system-3 is lower than system-1. Tabl-6 to Table-8 are showing the power required to run all compressors in all system using five ecofriendly refrigerants.

Table-6: Power required (kW) to run the compressor-1for all vapour compression refrigeration systems of 35 kW cooling capacity

Refrigerant	System-1 Three stage Compression with multiple expansion Valves and water coolers	System-2 Three stage Compression with multiple expansion Valves and flash inter cooling Chambers in parallel	System-3 Three stage Compression with multiple expansion Valves and flash inter cooling Chambers in series
R134a	4.892	4.892	3.433
R1234yf	5.906	5.906	3.686
R1234ze	5.602	5.602	3.565
R227ea	7.246	7.246	3.687
R245fa	5.75	5.75	3.44

Table-7: *Power required (kW) to run the compressor-2for all vapour compression refrigeration systems of 35 kW cooling capacity*

Refrigerant	System-1 Three stage Compression with multiple expansion Valves and water coolers	System-2 Three stage Compression with multiple expansion Valves and flash inter cooling Chambers in parallel	System-3 Three stage Compression with multiple expansion Valves and flash inter cooling Chambers in series
R134a	4.957	5.195	4.307
R1234yf	5.943	6.081	4.711
R1234ze	5.655	5.777	4.542
R227ea	7.208	6.938	4.813
R245fa	5.778	5.762	4.388

Table-8: Power required (kW) to run the compressor-III for all vapour compression refrigeration systems of 35 kW cooling capacity

Refrigerant	System-1 Three stage Compression with multiple expansion Valves and water coolers	System-2 Three stage Compression with multiple expansion Valves and flash inter cooling Chambers in parallel	System-3 Three stage Compression with multiple expansion Valves and flash inter cooling Chambers in series
R134a	2.86	3.121	2.946
R1234yf	3.415	3.529	3.251
R1234ze	3.257	3.369	3.124
R227ea	4.146	3.759	3.34
R245fa	3.336	3.273	3.014

4. Conclusions and Recommendations

Thermodynamic energy-exergy analysis of multi-stage vapour compression refrigerator and flash intercooler with individual or multiple throttle valves have been done in terms of COP, second law efficiency and irreversibility destruction ratio based on exergy of fuel and Exergy destruction based on exergy of product and following conclusions have been made

1. First law performance in terms of COP and second law exergetic performance of system-3 is higher than system-2for selected new ecofriendly refrigerants.
2. For all vapour compressor refrigeration systems R227ea shows minimum thermal performance in terms of COP, second law efficiency.
3. System 1 also gives higher thermodynamic performance than system-2 and lower than system-3.

References

[1] Camelia Stanciu,Adina Gheorghian,Dorin Stanciu, Alexandru Dobrovicescu(2011)-Exergy analysis and refrigerant effect on the operation and performance limits of a one stage vapour compression refrigeration system,Termotehnia, 36-42.

[2] V. Siva Reddy,N. L. Panwar ,S. C. Kaushik(2011)-Exergetic analysis of a vapour compression refrigeration system with R134a, R143a, R152a, R404A, R407C, R410A, R502 and R507A,Clean Techn Environ Policy,14:47–53.

[3] J.U. Ahamed , R. Saidur, H.H. Masjuki(2011)-A review on exergy analysis of vapor compression refrigeration system, Renewable and Sustainable Energy Reviews,15: 1593–1600.

[4] Szargut D, Petela R, Egzergia(1965),WNT.

[5] Szargut J, Morris D, Steward F(1998)-Exergy analysis of thermal, chemical and metallurgical processes.,New York: Hemisphere Publishing Corporation.

[6] Saidur R, Masjuki HH, Jamaluddin MY(2007)-An application of energy and exergy analysis in residential sector in Malaysia. Energy Policy, 35: 1050–63.

[7] Yongmei Xuan, Guangming Chen. Experimental study on HFC-161 mixture as an alternative refrigerant to R502. Int J Refrigeration. Article in Press.

[8] R.Cabello a, E.Torrella b, J.Navarro-Esbr. Experimental evaluation of a vapour compression plant performance using R134a, R407C and R22 as working fluids. Int J Applied Thermal Engineering.2004; 24:1905-1917.

[9] Mark W. Spatz, Samuel F. Yana Motta. An evaluation of options for replacing HCFC-22 in medium temperature refrigeration systems. Int J Refrigeration.2004; 27:475-483.

[10] X.H. Han, Q. Wang, Z.W. Zhu, G.M. Chen. Cycle performance study on R32/R125/R161 as an alternative refrigerant to R407C. Int J Applied Thermal Engineering.2007; 27:2559-2565.

[11] R. Cabello, J. Navarro-Esbrı, R. Llopis, E. Torrella. Analysis of the variation mechanism in the main energetic parameters in a single-stage vapour compression plant. Int J Applied Thermal Engineering.2007; 27:167-176.

[12] H.M Getu, P.K Bansal. Thermodynamic analysis of an R744-R717 cascade refrigeration system. Int J Refrigeration.2008; 31:45-54.

[13] M. Mohanraj, S. Jayaraj, C. Muraleedharan, P. Chandrasekar.Experimental investigation of R290/R600a mixture as an alternative to R134a in a domestic refrigerator. Int J Thermal Sciences.2009; 48:1036-1042.

[14] M. Padilla, R. Revellin, J. Bonjour. Exergy analysis of R413A as replacement of R12 in a domestic refrigeration system. Int J Energy Conversion and Management.2010; 51:2195-2201.

[15] Klein, S.A., Alvarado, F., 2005. Engineering Equation Solver, Version 7.441. F Chart Software, Middleton, WI.

.

International Journal of Research in Engineering and Innovation (IJREI)
journal home page: http://www.ijrei.com
ISSN (Online): 2456-6934

Irreversibility analysis of Two and three stage vapour compression refrigeration systems with multi evaporators and flash-intercooler using new ecofriendly refrigerants (R227ea, R236fa, R245fa, R1234yf, R1234ze) for replacing R134a

R.S. Mishra

Department of Mechanical Engineering, Delhi Technological University, Delhi, India

Abstract

The performance parameters for HFO-1234yf are around ten% lesser than that of HFC-134a, so it can a good alternative to HFC-134a because of its environmental friendly properties. Similarly HFO-1234ze can replace the conventional HFC-134a after having slight modification in the design as the performance parameters are 4% to 5% less than using R134a. However by using liquid vapor heat exchanger, the first law performances improved slightly. The numerical computation have been carried out for ecofriendly refrigerants and hydrocarbons and it is concluded that mixture of hydrocarbon with slightly modification in system design can also replace R134a.
© 2018 ijrei.com. All rights reserved
Key words: Thermodynamic Analysis, Vapour compression Refrigeration system, Irreversibility Analysis

1. Introduction

The most commonly used refrigerants in recent past were R11, R12, and R22 which because of their high ODP have been either phased out or under consideration for the same. After the revelation of the harmful effects of CFC and HCFC refrigerants on the ozone layer, search to find alternative working fluids gained more interest in the recent few years. The HFC134a was found to be a suitable candidate for replacing R12 and is being successfully used to date in small equipment like domestic refrigerators and water coolers and in mobile air-conditioning. HFC134a has very high GWP which is a matter of environmental concern [1]. HFO stands for hydro-fluoro-olefin (HFO-1234yf) is a low global warming potential (GWP) refrigerant for use in automotive air-conditioning systems. HFC-134a is a hydro-fluoro-carbon refrigerant, while (HFO-1234yf) is a hydro-fluoro-olefin refrigerant. Hydro-fluoro-olefin, or in short HFO, is a definition that is familiar to many of us. R1234yf, R1234ze are few examples of HFOs. They are used in a number of applications today, but have been barely studied just a decade agoHFO-1234yf was developed to meet the European directive 2006/40/EC in 2011 requiring use of HFO refrigerant in AC system with a GWP below 150. HFO-1234yf, which has a 100-year GWP lower than 1. These refrigerants are used as a "near drop-in replacement" for R-134a, the current product used in automobile AC systems, which has a 100-year GWP of 1430. HFO-1234yf has the lowest cost among the currently proposed alternatives (i.e.R134a). Thermophysical properties of Refrigerants are shown in table-1

Table 1: Thermophysical properties of HFO Refrigerants.

Properties	HFO-1234yf	HFO-1234ze	HFC-134a
Boiling Point, Tb	-29°C	-19°C	-26°C
Critical Point, Tc	94.7°C	109.4°C	101°C
Pvap, MPa at 25°C	0.682	0.500	0.665
Pvap, MPa at 80°C	2.519	2.007	2.635
Liquid Density, kg/m3 at 25°C	1092	1162	1207
Vapour Density, kg/m3 at 25°C	37.94	26.76	32.34

The initial cost of refrigeration and air conditioning system using R1234yf is much higher than that of R-134a and handled in repair shops in the same way as R-134a. Although it would require different, specialized equipment to perform the service due to the mild flammability of HFO-1234yf and another issue affecting the compatibility between HFO-1234yf and R-134a-

Corresponding author: R.S. Mishra
Email Id: hod.mechanical.rsm@dtu.ac.in

based systems due to choice of lubricating oil. The current lubricating oil is showing signs of damage to plastic and aluminium, and issues with health, including mouth dryness, rashes, and sore throat, among other effects.

2. Literature Review

HFO-1234yf would be adopted as a replacement of R-134a automotive air-conditioning refrigerant. Mishra [2] concluded that the first law efficiency in terms of coefficient of performance COP and second law efficiency in terms of exergetic efficiency of HFC-134a and HFO- 1234ze is almost same having a difference of 5.6%, which decreases with the increase in evaporator temperature, whereas it is 14.5-5% higher than HFO-1234yf. Hence HFO-1234yf can be a good drop-in' replacement of HFC-134a at higher value of evaporator temperature and HFO-1234ze can be a good replacement after certain modification [3]. From the irreversibility or exergy destruction viewpoint, worst component is condenser followed by compressor, throttle valve, evaporator and liquid vapour heat exchanger, the most efficient component. Total efficiency defect is more for HFO-1234yf followed by HFO-1234ze and HFC-134a, but the difference is small. Increase in ambient state temperature has a increasing (positive) effect on second law efficiency in terms of exergetic efficiency and exergy destruction ratio which was computed based on exergy of fuel or based on exergy of product (EDR). When exergy destruction ratio (EDR) reduced, then exergetic efficiency increases. Therefore HFO-1234yf gives lesser values of exergetic efficiency whereas HFO-1234ze gives approximately similar values.4. HFC-134a gives higher COP and exergetic efficiency than HFO-1234yf but lesser value than HFO- 1234ze. However reverse trend is seen when effectiveness of heat exchanger is increased from 0 to 1. Hence, it can be concluded that even though the values of performance parameters for HFO-1234yf are smaller than that of HFC-134a, but the difference is small, so it can a good alternative to HFC-134a because of its environmental friendly properties. HFO-1234ze can replace the conventional HFC-134a after having slight modification in the design as the performance parameters are almost similar.

3. Energy Exergy Analysis of Vapor Compression Refrigeration Systems

The second law analysis (i.e. exergy Computation) is widely accepted as a useful tool for obtaining overall performances of any system for finding various exergy losses occurred in its components Exergy analysis also helps in taking account the important engineering decisions regarding design parameters of a system by finding maximum exergy destruction using entropy generation principle Many researchers have carried out exergy studies of different thermal energy conversion systems describing various approach for exergy analysis and its usefulness for improving existing designs by reducing exergy destruction in a more simple and effective manner [2-3] Padilla et al. [4] computed the exergy performance of a domestic vapor compression refrigeration system (VCRS) by using zeotropic mixture (R413A) for direct replacement of R12 and found that the overall energy and exergy performances of this system working with R413A is far better than R12. Arora and Kaushik [5] presented a detailed exergy analysis of an actual vapour compression refrigeration (VCR) cycle and developed computational model for computing coefficient of performance (COP), exergy destruction, exergetic efficiency and efficiency defects for R502, R404A and R507A and found that the R507A is a better substitute to R502 than R404A. The efficiency defect in condenser is highest, and lowest in liquid vapour heat exchanger for R502, R404A and R507A refrigerants in the range of −50 °C to 0 °C evaporator temperature and in the range and 40 °C to 55 °C condenser temperature respectively. Anand S and Tyagi S. K. [6] presented a detailed experimental analysis of 2 ton of refrigeration capacity vapor compression refrigeration cycle using R22 as working fluid for different percentage of refrigerant charge using exergy analysis and evaluated thermal performances (i.e. coefficient of performance, exergy destruction, and exergetic efficiency) under variable quantity of refrigerant and found that the losses in the compressor are more pronounced, while the losses in the condenser are less pronounced as compared to other components. A computational model based on the exergy analysis is presented by Yumrutas et. al [7] for the investigation of the effects of the evaporating and condensing temperatures on the pressure losses, exergy losses, second law of efficiency, and the COP of a vapour compression cycle. Dincer [8] asserts that conventional energy analysis, based on the first law of thermodynamics, evaluates energy mainly on its quantity but analysis that are based on second law considers not only the quality of energy, but also quantity of energy. Kumar et al. [9] also carried out to carry out the exergetic analysis of a VCR system using R11 and R12 as refrigerants. Nikolaidis and Probert [10] used exergy method for computing thermodynamic performances of R22 in a two-stage compound compression cycle, with flash intercooling. Bejan [11] developed, thermodynamic model by considering heat transfer irreversibility and showed that the exergetic efficiency decreases as evaporator temperature decreases.

Getu and Bansal [12] had optimized the design and operating parameters of like condensing temperature, sub cooling temperature, evaporating temperature, superheating temperature and temperature difference in cascade heat exchanger R744-R717 cascade refrigeration system. A regression analysis was also done to obtain optimum thermodynamic parameters of same system.

From the irreversibility or exergy destruction viewpoint, worst component is condenser followed by compressor, throttle valve, evaporator and liquid vapour heat exchanger, the most efficient component. Total efficiency defect is more for HFO-1234yf followed by HFO-1234ze and HFC-134a, but the

difference is small. Increase in ambient state temperature has a increasing (positive) effect on second law efficiency in terms of exergetic efficiency and exergy destruction ratio which was computed based on exergy of fuel or based on exergy of product (EDR). When exergy destruction ratio (EDR) reduced, then the exergetic efficiency increases. Therefore HFO-1234yf gives lesser values of exergetic efficiency whereas HFO-1234ze gives approximately 4% less values. HFC-134a gives higher COP and exergetic efficiency than HFO-1234yf but lesser value than HFO- 1234ze [13].

In this investigation the work input required running the vapour compression refrigeration system reduced by using compound compression and further decreased by flash intercooling between compressors. COP of system can also be enhanced by compressing the refrigerant very close to the saturation line this can be achieved by compressing the refrigerants in more stages with intermediate intercoolers. The refrigeration effect can be increase by maintaining the condition of refrigerants in more liquid stage at the entrance of evaporator which can be achieved by expanding the refrigerant very close to the liquid line. The expansion can be brought close to the liquid line by subcooling the refrigerant and removing the flashed vapours by incorporating the flash chamber in the working cycle. The evaporator size can be reduced because unwanted vapours formed are removed before the liquid refrigerant enters in the evaporator. Multi-stage vapour compression with flash intercooler and individual throttle valves (system-1) consists of three compressors arranged in compound compression, individual throttle valves, condenser and evaporators as shown in Fig.1. Multiple evaporators at different temperatures with compound compression, flash intercooler and multiple throttle valves (system-2) consists of three compressors arranged in compound compression, multiple throttle valves, condenser and evaporators as shown in Fig.2.

4. Energy and exergy analysis

For carrying out energetic and exergetic analysis, computational models of system-1 and system-2 has been developed and impact of chosen refrigerants on these systems has been analyzed using Engineering Equation Solver software[16].In this investigation following assumptions are made:

1. Load on the low, intermediate and high temperature evaporators are 10TR, 20 TR and 30 TR respectively.
2. Dead state temperature (T0): 25^0C
3. Difference between evaporator and space temperature (Tr-Te):5^0C.
4. Adiabatic efficiency of compressor: 76%.
5. Dead state enthalpy (Φ0) and entropy (s0) of the refrigerants have been calculated corresponding to the dead state temperature (T0) of 25^0C.
6. Variation in kinetic and potential energy is negligible.
7. Expansion process is adiabatic
8. Temperature of low, intermediate and high temperature evaporators are -10^0C,0^0 C and 10^0C respectively.
9. Condenser temperature : 40^0C
10. Degree of sub cooling : 10^0C

4.1 Thermodynamic Analysis

First law of thermodynamic gives the idea of energy balance of system.

$$\dot{m}_{c1} = \dot{m}_{e1} = \frac{\dot{Q}_{e1}}{(\Phi_1 - \Phi_{10})} \quad (1)$$

$$\dot{m}_{e2} = \frac{\dot{Q}_{e2}}{(\Phi_3 - \Phi_9)} \quad (2)$$

$$\dot{m}_{f1} = \frac{\dot{m}_{c1}(\Phi_2 - \Phi_3)}{(\Phi_3 - \Phi_9)} \quad (3)$$

$$\dot{m}_{c2} = \dot{m}_{c1} + \dot{m}_{e2} + \dot{m}_{f1} \quad (4)$$

$$\dot{m}_{e3} = \frac{\dot{Q}_{e3}}{(\Phi_5 - \Phi_8)} \quad (5)$$

$$\dot{m}_{f2} = \frac{\dot{m}_{c2}(\Phi_4 - \Phi_5)}{(\Phi_5 - \Phi_8)} \quad (6)$$

$$\dot{m}_{c3} = \dot{m}_{c2} + \dot{m}_{e3} + \dot{m}_{f2} \quad (7)$$

Energy consumption for sytem-1

$$P_{c1} = \frac{\dot{m}_{c1}(\Phi_2 - \Phi_1)}{60} \quad (8)$$

$$P_{c2} = \frac{\dot{m}_{c2}(\Phi_4 - \Phi_3)}{60} \quad (9)$$

$$P_{c3} = \frac{\dot{m}_{c3}(\Phi_6 - \Phi_5)}{60} \quad (10)$$

Energetic efficiency of system-1

$$\mathrm{COP} = \frac{\dot{Q}_e}{P_c * 60} \quad (11)$$

4.2 Rate of exergy loss due to irreversibility($T_o\dot{S}_{gen}$) in various components of system-1

The concept of exergy was given by second law of thermodynamics, which always decreases due to thermodynamic irreversibility. Exergy is defined as the measure of usefulness, quality or potential of a stream to cause change and an effective measure of the potential of a substance to impact the environment [12].

Exergy at any state is given as

$$\mathrm{X} = (\Phi - \Phi_0) - \mathrm{T}_0(\mathrm{s} - \mathrm{s}_0) \quad (12)$$

Compressors

$$\left(T_o\dot{S}_{gen}\right)_{c1} = \dot{W}_{c1} + \dot{m}_{c1}(X_2 - X_1) \quad (13)$$

$$(T_o\dot{S}_{gen})_{c2} = \dot{W}_{c2} + \dot{m}_{c2}(X_4 - X_3) \quad (14)$$

$$(T_o\dot{S}_{gen})_{c3} = \dot{W}_{c3} + \dot{m}_{c3}(X_6 - X_5) \quad (15)$$

$$\dot{\Psi}_c = (T_o\dot{S}_{gen})_{c1} + (T_o\dot{S}_{gen})_{c2} + (T_o\dot{S}_{gen})_{c3} \quad (16)$$

Evaporators

$$(\mathrm{T_o\dot{S}_{gen}})_{e1} = \dot{m}_{e1}(X_1 - X_{10}) - \dot{Q}_{e1}\left(1 - \frac{T_0}{T_{r1}}\right) \quad (17)$$

$$\left(\mathrm{T_o\dot{S}_{gen}}\right)_{e2} = \dot{m}_{e2}(X_3 - X_9) - \dot{Q}_{e2}\left(1 - \frac{T_0}{T_{r2}}\right) \quad (18)$$

$$(\mathrm{T_o\dot{S}_{gen}})_{e3} = \dot{m}_{e3}(X_5 - X_8) - \dot{Q}_{e3}\left(1 - \frac{T_0}{T_{r3}}\right) \quad (19)$$

$$\dot{\Psi}_e = (\mathrm{T_o\dot{S}_{gen}})_{e1} + (\mathrm{T_o\dot{S}_{gen}})_{e2} + (\mathrm{T_o\dot{S}_{gen}})_{e3} \quad (20)$$

Condenser

$$\dot{\Psi}_{cond} = \left(\mathrm{T_o\dot{S}_{gen}}\right)_{cond} = \dot{m}_{c3}(X_6 - X_7) - \dot{Q}_e\left(1 - \frac{T_0}{T_r}\right) \quad (21)$$

$$(\mathrm{T_o\dot{S}_{gen}})_{tv1} = \dot{m}_{e1}(X_{77} - X_{10}) \quad (22)$$

$$\left(\mathrm{T_o\dot{S}_{gen}}\right)_{tv2} = (\dot{m}_{e2} + \dot{m}_{f1})(X_{77} - X_9) \quad (23)$$

$$(\mathrm{T_o\dot{S}_{gen}})_{tv3} = (\dot{m}_{e3} + \dot{m}_{f2})(X_{77} - X_8) \quad (24)$$

$$\dot{\Psi}_{tv} = (\mathrm{T_o\dot{S}_{gen}})_{tv1} + (\mathrm{T_o\dot{S}_{gen}})_{tv2} + (\mathrm{T_o\dot{S}_{gen}})_{tv3} \quad (25)$$

Liquid subcooler

$$\dot{\Psi}_{lsc} = (\mathrm{T_o\dot{S}_{gen}})_{sc} = \dot{m}_{c3}(X_7 - X_{77}) \quad (26)$$

Flash intercoolers

$$(\mathrm{T_o\dot{S}_{gen}})_{f1} = \dot{m}_{f1}(X_9 - X_3) + \dot{m}_{c1}(X_2 - X_3) \quad (27)$$

$$(\mathrm{T_o\dot{S}_{gen}})_{f2} = \dot{m}_{f2}(X_8 - X_5) + \dot{m}_{c1}(X_4 - X_5) \quad (28)$$

$$\dot{\Psi}_f = (\mathrm{T_o\dot{S}_{gen}})_{f1} + (\mathrm{T_o\dot{S}_{gen}})_{f2} \quad (29)$$

$$\sum \dot{\Psi}_k = \dot{\Psi}_e + \dot{\Psi}_c + \dot{\Psi}_{cond} + \dot{\Psi}_{tv} + \dot{\Psi}_{lsc} + \dot{\Psi}_f \quad (30)$$

$$\dot{m}_{c1'} = \dot{m}_{e1'} = \frac{\dot{Q}_{e1'}}{(\Phi_{1'} - \Phi_{12'})} \quad (31)$$

$$\dot{m}_{e2'} = \frac{\dot{Q}_{e2'}}{(\Phi_{3'} - \Phi_{10'})} + \dot{m}_{c1'}\left(\frac{x_{10'}}{1 - x_{10'}}\right) \quad (32)$$

$$\dot{m}_{f1'} = \frac{\dot{m}_{c1'}(\Phi_{2'} - \Phi_{3'})}{(\Phi_{3'} - \Phi_{10'})} \quad (33)$$

$$\dot{m}_{c2'} = \dot{m}_{c1'} + \dot{m}_{e2'} + \dot{m}_{f1'} \quad (34)$$

$$\dot{m}_{e3'} = \frac{\dot{Q}_{e3'}}{(\Phi_{5'} - \Phi_{8'})} + \dot{m}_{c2'}\left(\frac{x_{8'}}{1 - x_{8'}}\right) \quad (35)$$

$$\dot{m}_{f2'} = \frac{\dot{m}_{c2'}(\Phi_{4'} - \Phi_{5'})}{(\Phi_{5'} - \Phi_{8'})} \quad (36)$$

Power required for running the compressors

$$P_{c1'} = \frac{\dot{m}_{c1'}(\Phi_{2'} - \Phi_{1'})}{60} \quad (37)$$

$$P_{c2'} = \frac{\dot{m}_{c2'}(\Phi_{4'} - \Phi_{3'})}{60} \quad (38)$$

$$P_{c3'} = \frac{\dot{m}_{c3'}(\Phi_{6'} - \Phi_{5'})}{60} \quad (39)$$

$$\text{Energetic efficiency} = \frac{\dot{Q}_{e'}}{P_{c'} * 60} \quad (40)$$

4.3 Rate of exergy loss due to irreversibility ($T_o\dot{S}_{gen}$) in various components of system-2

$$(\mathrm{T_o\dot{S}_{gen}})_{c1'} = \dot{W}_{c1'} + \dot{m}_{c1'}(X_{2'} - X_{1'}) \quad (41)$$

$$(\mathrm{T_o\dot{S}_{gen}})_{c2'} = \dot{W}_{c2'} + \dot{m}_{c2'}(X_{4'} - X_{3'}) \quad (42)$$

$$(\mathrm{T_o\dot{S}_{gen}})_{c3'} = \dot{W}_{c3'} + \dot{m}_{c3'}(X_{6'} - X_{5'}) \quad (43)$$

$$\dot{\Psi}_{c'} = (\mathrm{T_o\dot{S}_{gen}})_{c1'} + (\mathrm{T_o\dot{S}_{gen}})_{c2'} + (\mathrm{T_o\dot{S}_{gen}})_{c3'} \quad (44)$$

Evaporators

$$\left(\mathrm{T_o\dot{S}_{gen}}\right)_{e1'} = \dot{m}_{e1'}(X_{1'} - X_{12'} - \dot{Q}_{e1'}\left(1 - \frac{T_0}{T_{r1'}}\right) \quad (45)$$

$$\left(\mathrm{T_o\dot{S}_{gen}}\right)_{e2'} = \dot{m}_{e2'}(X_{3'} - X_{10'}) - \dot{Q}_{e2'}\left(1 - \frac{T_0}{T_{r2'}}\right) \quad (46)$$

$$\left(\mathrm{T_o\dot{S}_{gen}}\right)_{e3'} = \dot{m}_{e3'}(X_{5'} - X_{8'}) - \dot{Q}_{e3'}\left(1 - \frac{T_0}{T_{r3'}}\right) \quad (47)$$

$$\dot{\Psi}_{e'} = (\mathrm{T_o\dot{S}_{gen}})_{e1'} + (\mathrm{T_o\dot{S}_{gen}})_{e2'} + (\mathrm{T_o\dot{S}_{gen}})_{e3'} \quad (48)$$

Condenser

$$\dot{\Psi}_{cond'} = \left(\mathrm{T_o\dot{S}_{gen}}\right)_{cond'} = \dot{m}_{c3'}(X_{6'} - X_{7'}) - \dot{Q}_{e'}\left(1 - \frac{T_0}{T_{r'}}\right) \quad (49)$$

Throttle Valves

$$(\mathrm{T_o\dot{S}_{gen}})_{tv1'} = \dot{m}_{e1'}(X_{11'} - X_{12'}) \quad (50)$$

$$\left(\mathrm{T_o\dot{S}_{gen}}\right)_{tv2'} = \dot{m}_{c2'}(X_{9'} - X_{10'}) \quad (51)$$

$$(\mathrm{T_o\dot{S}_{gen}})_{tv3'} = \dot{m}_{c3'}(X_{77'} - X_{8'}) \quad (52)$$

$$\dot{\Psi}_{tv'} = (\mathrm{T_o\dot{S}_{gen}})_{tv1'} + (\mathrm{T_o\dot{S}_{gen}})_{tv2'} + (\mathrm{T_o\dot{S}_{gen}})_{tv3'} \quad (53)$$

Liquid subcooler

$$\dot{\Psi}_{lsc'} = (\mathrm{T_o\dot{S}_{gen}})_{lsc'} = \dot{m}_{c3'}(X_{7'} - X_{77'}) \quad (54)$$

Flash intercoolers

$$(\mathrm{T_o\dot{S}_{gen}})_{f1'} = \dot{m}_{f1'}(X_{10'} - X_{3'}) + \dot{m}_{c1'}(X_{2'} - X_{3'}) \quad (55)$$

$$(\mathrm{T_o\dot{S}_{gen}})_{f2'} = \dot{m}_{f2'}(X_{8'} - X_{5'}) + \dot{m}_{c2'}(X_{4'} - X_{5'}) \quad (56)$$

$$\dot{\Psi}_{f'} = (\mathrm{T_o\dot{S}_{gen}})_{f1'} + (\mathrm{T_o\dot{S}_{gen}})_{f2'} \quad (57)$$

Total irreversibility destruction in system-1

$$\sum \dot{\Psi}_{k'} = \dot{\Psi}_{e'} + \dot{\Psi}_{c'} + \dot{\Psi}_{cond'} + \dot{\Psi}_{tv'} + \dot{\Psi}_{lsc'} + \dot{\Psi}_{f'} \quad (58)$$

4. Result and Discussion

Following Data have been assumed in present investigation Evaporator pressure= 2 bar=200 KPa, Condenser Pressure 12 bar, P2= P3= 8 bar and Qeva= 10 TR=35kW, First compressor efficiency=second compressor efficiency =Third compressor

efficiency =0.8

Table-2 and table-3 show the effect of eco-friendly refrigerants on following three type of systems, it was observed that R134a gives better thermodynamic first law performance in terms of coefficient of performance (COP) and second law thermal performance in terms of exergetic efficiency (Rational Efficiency) as compared to other new eco-friendly refrigerants. System-3 with multiple expansion valves and flash intercoolers gives best exergetic second law and first law performances than other two systems. Although R245fa also gives similar thermodynamic first law performance (COP) in all systems but and second law exergetic performances using R236fa and R245fa is badly affecting for second system as shown in table-3. Due to higher GWP of R134a R1234ze can be used for replacing R134a for higher temperature applications. R1234yf give better second law exergetic performance than R1234ze for domestic applications. Similarly, Table-4 shows exergy destruction ratio of all three systems using eco-friendly refrigerants. For computations of irreversibility, the exergy destruction ratio was defined by several investigators, in terms of total exergy losses occurred in the system or thermodynamic cycle to the exergy of product while other investigators also defined EDR based on the exergy input in terms of exergy of fuel (i.e. total power required to run the whole system as total power used in the compressors). It was observed that R236fa gives maximum exergy destruction ratio lowering the exergetic efficiency as compared to R134a. As comparing to all systems, system-3 gives lowest EDR using R-134a.

Table-2: Thermodynamic first law thermal performances (COP_{Over_all}) of two stage vapour compression refrigeration system using eco-friendly refrigerants

Eco Friendly Refrigerant	System-1 with water intercoolers	System-2 with flash intercoolers	System-3 with multiple expansion valves and Flash intercoolers
R-134a	2.886	3.08	3.086
R1234ze	3.038	3.157	3.159
R1234yf	2.551	2.796	2.782
R227ea	3.098	3.134	3.137
R236fa	7.503	6.377	7.916
R245fa	9.03	6.954	9.38

Table-3: Thermodynamic second law thermal performances (exergetic efficiency)of two stage vapour compression refrigeration system using eco-friendly refrigerants

Eco Friendly Refrigerant	System-1 with water intercoolers	System-2 with flash intercoolers	System-3 with multiple expansion valves and Flash intercoolers
R-134a	0.3833	0.4091	0.4099
R1234ze	0.3095	0.3175	0.3177
R1234yf	0.3686	0.4040	0.4020
R227ea	0.2727	0.2760	0.2762
R236fa	0.2270	0.1921	0.2395
R245fa	0.2533	-19.51	-0.2632

Table-4: Thermodynamic second law thermal losses oftwo stage vapour compression refrigeration system using eco-friendly refrigerants

Eco Friendly Refrigerant	System-1 with water intercoolers	System-2 with flash intercoolers	System-3 with multiple expansion valves and Flash intercoolers
R-134a	1.609	1.373	1.35
R1234ze	2.231	2.133	2.128
R1234yf	1.713	1.391	1.379
R227ea	2.666	2.618	2.615
R236fa	3.406	4.445	3.065
R245fa	-4.947	-7.672	-4.375

Table-5: *Total Power required to runtwo stage vapour compression refrigeration system using eco-friendly refrigerants*

Eco Friendly Refrigerant	System-1 with water intercoolers (kW)	System-2 with flash intercoolers	System-3 with multiple expansion valves and Flash intercoolers
R-134a	12.13	10.73	17.01
R1234ze	11.37	11.09	16.62
R1234yf	13.72	12.52	18.87
R227ea	11.30	11.7	16.73
R236fa	4.665	5.488	6.632
R245fa	3.876	5.033	5.597

Table-6: Power required to run First Compressor of two stage vapour compression refrigeration system using eco-friendly refrigerants

Eco Friendly Refrigerant	System-1 with water intercoolers (kW)	System-2 with flash intercoolers	System-3 with multiple expansion valves and Flash intercoolers
R-134a	5.455	4.348	7.224
R1234ze	5.288	5.043	7.565
R1234yf	6.177	5.218	7.828
R227ea	5.409	5.297	7.946
R236fa	4.375	5.11	7.665
R245fa	3.72	4.885	7.327

Table-7: Power required to run second Compressor of two stage vapour compression refrigeration system using eco-friendly refrigerants

Eco Friendly Refrigerant	System-1 with water intercoolers	System-2 with flash intercoolers	System-3 with multiple expansion valves and Flash intercoolers
R-134a	6.674	6.386	9.791
R1234ze	6.084	6.044	9.056
R1234yf	7.546	7.302	11.05
R227ea	5.89	5.869	8.789
R236fa	0.2899	0.3782	-1.033
R245fa	0.1561	-0.01481	-1.731

Table-8: Thermodynamic first law performances /Overall coefficient of performance ($COP_{_Over_All}$)of two stage vapour compression refrigeration system with water intercoolers using eco-friendly refrigerants

Eco Friendly Refrigerant	System-1 with water intercoolers	System-2 with flash intercoolers	System-3 with multiple expansion valves and Flash intercoolers
R-134a	2.886	3.08	3.086
R152a	3.016	3.134	3.152
R404a	1.943	2.407	2.354
R410a	2.136	2.566	2.582
R407c	2.408	2.782	2.784
R717	3.097	3.26	3.363
R123	9.185	6.468	9.587
R125	1.751	2.296	2.206
R290	2.191	2.492	2.477
R600	7.213	6.164	7.511
R-600a	6.263	5.778	6.624

Table-9: Thermodynamic second law performances (exergetic efficiency) of two stage vapour compression refrigeration system with water intercoolers using eco-friendly refrigerants

Eco Friendly Refrigerant	System-1 with water intercoolers	System-2 with flash intercoolers	System-3 with multiple expansion valves and Flash intercoolers
R-134a	0.3833	0.4091	0.4099
R152a	0.3676	0.382	0.3842
R404a	0.4436	0.5496	0.5375
R410a	0.5607	0.6734	0.6776
R407c	0.4456	0.5148	0.5150
R717	0.5322	0.5603	0.5779
R123	0.6623	0.4664	-0.6913
R125	0.4231	0.5549	0.5330
R290	0.4449	0.5059	0.5030
R600	0.1497	0.1279	0.1559
R-600a	0.4011	0.3701	0.4242

Table-10: Irreversibility Ratio in terms of exergy destruction ratio based on exergy of product of two stage vapour compression refrigeration system with water intercoolers using eco-friendly refrigerants

Eco Friendly Refrigerant	System-1 with water intercoolers	System-2 with flash intercoolers	System-3 with multiple expansion valves and Flash intercoolers
R-134a	1.609	1.373	1.35
R152a	1.72	1.58	1.557
R404a	1.254	0.4411	0.3647

R410a	0.7836	0.1386	0.0295
R407c	1.244	0.8263	0.7737
R717	0.8791	0.7110	0.6394
R123	2.51	-4.561	-2.156
R125	1.364	0.2811	0.1882
R290	1.248	0.7853	0.7409
R600	5.68	7.566	5.173
R-600a	1.493	1.726	1.342

Table-11: Power required to run two stage vapour compression refrigeration system with water intercoolers using eco-friendly refrigerants

Eco Friendly Refrigerant	System-1 with water intercoolers	System-2 with flash intercoolers	System-3 with multiple expansion valves and Flash intercoolers
R-134a	12.13	10.73	17.01
R152a	11.6	11.17	16.66
R404a	18.01	14.54	22.3
R410a	16.39	13.64	20.34
R407c	14.53	12.58	18.86
R717	11.3	10.3	15.61
R123	3.81	5.411	5.476
R125	19.99	15.24	23.80
R290	15.97	14.05	21.19
R600	4.852	5.678	6.99
R-600a	5.588	6.057	7.926

Table-12: Power required to run first compressor of two stage vapour compression refrigeration system with water intercoolers using eco-friendly refrigerants

Eco Friendly Refrigerant	System-1 with water intercoolers	System-2 with flash intercoolers	System-3 with multiple expansion valves and Flash intercoolers
R-134a	5.455	4.348	7.224
R152a	5.251	4.87	7.305
R404a	7.598	5.053	7.58
R410a	6.708	4.668	7.04
R407c	6.288	4.727	7.091
R717	4.831	4.348	6.522
R123	3.66	5.273	7.909
R125	8.35	5.007	7.511
R290	6.874	5.377	8.065
R600	4.649	5.48	8.219
R-600a	5.267	5.678	8.517

Table-13: Power required to run second compressor of two stage vapour compression refrigeration system with water intercoolers using eco-friendly refrigerants

Eco Friendly Refrigerant	System-1 with water intercoolers	System-2 with flash intercoolers	System-3 with multiple expansion valves and Flash intercoolers
R-134a	6.674	6.386	9.791
R152a	6.354	6.299	9.351
R404a	10.41	9.485	14.72
R410a	9.677	8.975	13.3
R407c	8.245	7.852	11.27
R717	6.471	6.386	9.08
R125	11.64	10.24	16.29
R290	8.101	8.669	13.13

Table-5 shows the exergy of fuel in terms of total power required to run all three compressors in the three stage vapour compression refrigeration systems, it was observed that system-3 required less power consumptions to system-1 and system-2. The By using R134a, the minimum exergy input in terms of exergy of fuel (kW) needed as compared to R1234yf

and R1234ze in system-3 as compared to system -1. Similarly, by using R227ea and R236fa eco-friendly refrigerants, the power consumption is higher in the three stage systems by running all compressors as compared to R-134a while R245fa gives lower power consumption as compared to R227ea and R236fa.The power required to run various compressors in the three stage vapour compression refrigeration system using eco-friendly refrigerants are shown in Table-6 to Table-8 respectively. It was observed that R227ea gives maximum power consumptions in all compressors while less power consumptions required to run first compressor using R -134a. It was shown that first compressor used in system-3 gives lowest power consumption as compared to system-1 and system-2. By using new refrigerants, the power consumption is first compressor is more. Similarly, maximum power consumption using R227ea was observed as compared to R-236fa and R245fa. The lowest power consumption was observed using R134a in system -3 as compared to system-1 and system-2. Similarly, R1234yf and R1234ze gives slightly higher power consumption as compared to R1234yf and R1234ze. The power required to run compressor -3 in three stage vapour compression refrigeration system, the same trend was observed because system -3 is always gives better thermodynamic performance and lower power consumption.

5. Conclusion

Following conclusions were drawn from present investigations.

(i) System-3 gives better thermodynamic performance and less power consumption than other two systems.
(ii) The percentage first law improvement in ystem-1 is varying from 14.5% to 16% while power consumption is 13% less as compared to simple saturation cycle working between the pressure limit to 2 bar and 12 bar.
(iii) System-3 gives lowest power consumption (less than 20%) as compared to system -1 (13%) and first law improvement around 20% in system-3 as compared to 15.2%.
(iv) The System-2 required 10% less power required as compared to simple saturation cycle along with 0% of improvement in the first law performance.

References

[1] R. S. Mishra, Appropriate Vapour Compression Refrigeration Technologies for Sustainable Development International Journal of Advance Research & Innovations, 2014, 551-556.

[2] K. Chopra, V. Sahni, R. S. Mishra, Thermodynamic Analysis of Multiple evaporators vapour compression Refrigeration Systems with R-410a, R290, R1234yf, R502, R404a, R152a and R134a, International Journal of Air conditioning and Refrigeration, 22(1), 2014, 14

[3] K. Chopra, V. Sahni, R. S. Mishra, Methods for improving first and second law efficiencies of vapour compression refrigeration systems using flash intercooler with ecofriendly refrigerants, 1, 2014, 50- 64

[4] Padilla M, Revellin R, Bonjour J. Exergy analysis of R413Aas replacement of R12 in a domestic refrigeration system. Energy Convers Manag. 2010;51:2,195–201

[5] Arora A, Kaushik SC. Theoretical analysis of vapor compression refrigeration system with R502, R404A and R507A. Int J Refrig. 2008;31:998–1005

[6] Anand S and Tyagi S. K Exergy analysis and experimental study of a vapor compression refrigeration cycle

[7] Yumrutas et. al Exergy analysis of vapour compression refrigeration systems, Exergy, an Int J, 2 (2002) 266-272

[8] Dincer I. Refrigeration systems and applications. London: Wiley; 2003. pp. 26–27

[9] Kumar S, Prevost M, Bugarel R. Exergy analysis of a compression refrigeration system. Heat Recovery Syst CHP. 1989;9(2):151–7

[10] Nikolaidis C, Probert D. Exergy-method analysis of a two stage vapor compression refrigeration plants performance. Appl Energy. 1998;60:241–56

[11] Bejan A, Theory of heat transfer irreversible refrigeration plants, Int J Heat mass transfer, 32(9), (1989), 1631-39.

[12] H.M Getu, P.K Bansal. Thermodynamic analysis of an R744-R717 cascade refrigeration system. Int J Refrigeration.2008; 31:45-54.

[13] R. S. Mishra, Irriversibility Analysis of MultiEvaporators Vapour Compression Refrigeration Systems Using New and Refrigerants: R134a, R290, R600, R600a, R1234yf,R502, R404a and R152a and R12, R502" International Journal Advance Research & Innovations International Journal of Advance Research & Innovations, 1, 2013, 180-193

[14] R.S. Mishra, Irreversibility analysis of three stage vapour compression refrigeration systems with flash-intercooler using eco-friendly new refrigerants (R134a, R1234yf, R1234ze, R227ea and R245fa), International Journal of Research in Engineering and Innovation, vol-2, issue-2, 136-142, 2018.

[15] R.S. Mishra, Thermodynamic model analysis of vapour compression refrigeration systems by using ecofriendly refrigerant (R1234yf) in primary circuit and R718 in the secondary circuit by mixing Nano particles (Al2O3) for improving thermal efficiencies, International Journal of Research in Engineering and Innovation, vol-2, issue-1, 51-59, 2018.

[16] R.S. Mishra, Thermodynamic performance analysis of two stage vapour compression refrigeration systems with flash-intercooler using eco-friendly new refrigerants (R134a, R1234yf, R1234ze, R227ea and R152a), International Journal of Research in Engineering and Innovation, vol-2, issue-1, 156-161, 2018.

RESEARCHERID
THOMSON REUTERS

[Rani*, 7(4): April, 2018]
IC™ Value: 3.00

ISSN: 2277-9655
Impact Factor: 5.164
CODEN: IJESS7

IJESRT

INTERNATIONAL JOURNAL OF ENGINEERING SCIENCES & RESEARCH TECHNOLOGY

MODAL ANALYSIS OF CANTILEVER BEAM TO DETECT FAILURE ZONE

Dr. Sushila Rani*

* Assistant Professor, Mechanical Engineering Department, Delhi Technological University, New Delhi, India

DOI: 10.5281/zenodo.1215420

ABSTRACT

Modal analysis is performed to determine the vibration characteristics i.e. natural frequencies and mode shapes of structures. The natural frequencies and mode shapes are important parameters in the design for dynamic loading conditions. The knowledge of modal parameters is necessary to understand structural dynamics of structures. Modal parameters are global properties of a structure and any changes in these parameters can be used to detect and locate structural faults. The structural fault affects mass, damping and stiffness properties of structures. Modal parameters of structures could be obtained either by experimental modal analysis or from finite element analysis. In this research work, modal analysis of a mild steel cantilever beam has been carried out using finite element based software *ANSYS®* and the results of computational analysis are validated analytical. The calculated percentage difference of natural frequencies between computational analysis results and analytical results lies within the range of 1.5%. The stress concentration regions found on cantilever beam corroborated well with the failed zone.

KEYWORDS: *Mode shapes, Resonant frequency, Cantilever beam, ANSYS® Software.*

I. INTRODUCTION

The design of structures vibration applications demands an understanding of modal parameters. There are two ways to get modal parameters of structures. The modal parameters could be obtained either by finite element analysis or from experimental modal analysis. Today computational power is much larger, more reliable, and relatively cheap and as most technological related setups have access to computers, the popularity of using numerical methods is an ever increasing phenomenon. Especially finite element methods are being used at large extent for structural analysis. It is considered to be one of the best methods for solving a wide variety of practical problems efficiently. Finite element method has now become a very important tool of engineering analysis. Its versatility is reflected in its popularity among engineers and designers belonging to nearly all the engineering disciplines. The finite element method has become popular due to its relative simplicity of approach and accuracy of results. In the modern technological environment the conventional methodology of design cannot compete with the modern trends of Computer Aided Engineering (CAE) techniques (*Khawaja, 2007 [1]*). Various researchers have analyzed vibration and stress analyses problems using finite elements methods (*Ramamurti et al., 1998 [2]; Khan et al., 2006[3]; Krishnakanth et al., 2013 [4]*).

Finite element analysis (FEA) is a computerized method for predicting how a product reacts to real-world forces, vibration, heat, fluid flow and other physical effects. The methods has been extensively used in the field of structural mechanics; it has also been successfully applied to solve several other types of engineering problem, such as heat conduction, fluid dynamics, seepage flow, and electric and magnetic fields. Various software such as *Catia, Ansys, Pro-E, Solidworks* etc. are used for performing finite element modeling and analysis of structures. Finite element analysis (FEA) is used to perform static, dynamic/modal, harmonic and fatigue analysis of structures. *ANSYS®* has verified finite element methods by solving several problems and provided number of verification manuals related to static, modal, harmonic and fatigue analyses (*Zienwick et al., 1994 [5]). Yinming et al., 2004[6]* created and analyzed a CAD model of a cantilever. They have compared controlled and uncontrolled impulse responses at the free end of the beam in time domain and frequency domain. They have found that this proposed procedure can be used for solving complex structures problems.

ISSN: 2277-9655
Impact Factor: 5.164
CODEN: IJESS7

Khan et al., 2013 [7] analyzed a double cracked cantilever beam through finite element analysis. In this work, the modal parameters of a mild steel cantilever been has been obtained through dynamic analysis of beam using ANSYS® software. The computational result has been verified analytically.

II. COMPUTATIONAL ANALYSIS OF A MILD STEEL CANTILEVER BEAM

Computational analysis of structures has performed to evaluate structural and vibration characteristics of structures. A three dimensional CAD model of cantilever beam is created as shown in Fig. 1 through safe life design approach. Square surface mesh is made using auto meshing feature. The generated mesh modal of cantilever beam has 683 nodes and 80 elements as shown in Fig. 2. The boundary conditions are provided by making one end of cantilever beam fully built-in. The material properties and dimensions of mild steel cantilever beam are listed in Table 1and Table 2 respectively.

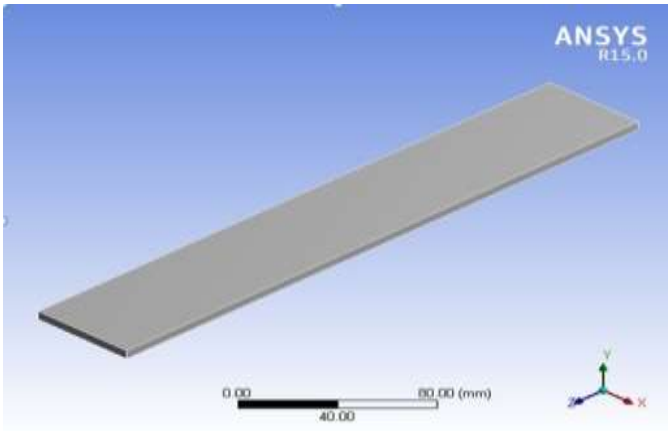

Fig. 1: CAD model of cantilever beam

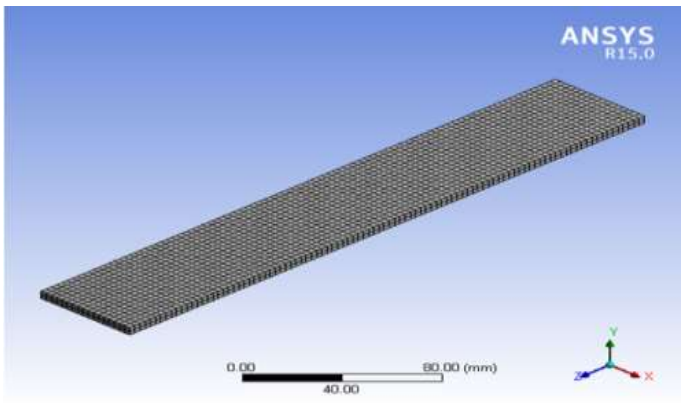

Fig. 2: Mesh model of cantilever beam

Table 1. Material properties of cantilever beam.

Material Properties	Cantilever beam
Young's Modulus, (N/m2)	$2x10^{11}$
Poisson's Ratio	0.3
Density (Kg/m^3)	7850
Bulk Modulus, (N/m^2)	$1.1667x10^{11}$
Shear Modulus, (N/m^2)	$7.6923x10^{10}$
Tensile Yield Strength, (N/m^2)	$2.5x10^8$
Tensile Ultimate Strength, (N/m^2)	$4.6x10^8$

ISSN: 2277-9655
Impact Factor: 5.164
CODEN: IJESS7

Table 2. Dimensions of cantilever beam.

Material Properties	Cantilever beam
Length, L,(m)	0.29
Breadth, b,(m)	0.05
Depth, h,(m)	0.005

MODAL ANALYSIS OF CANTILEVER BEAM

Modal analysis is performed to determine the vibration characteristics i.e. natural frequencies and mode shapes of cantilever beam. The natural frequencies and mode shapes are important parameters in the design for dynamic loading conditions (*Shaikh et al., 2014 [8]; Lafta et al., 2014 [9]).* The first three resonant frequencies of beam are found at *49.20 Hz, 307.79 Hz,* and *861.46Hz* and their respective mode shapes are shown in Fig. 3(a),(b) and (c).

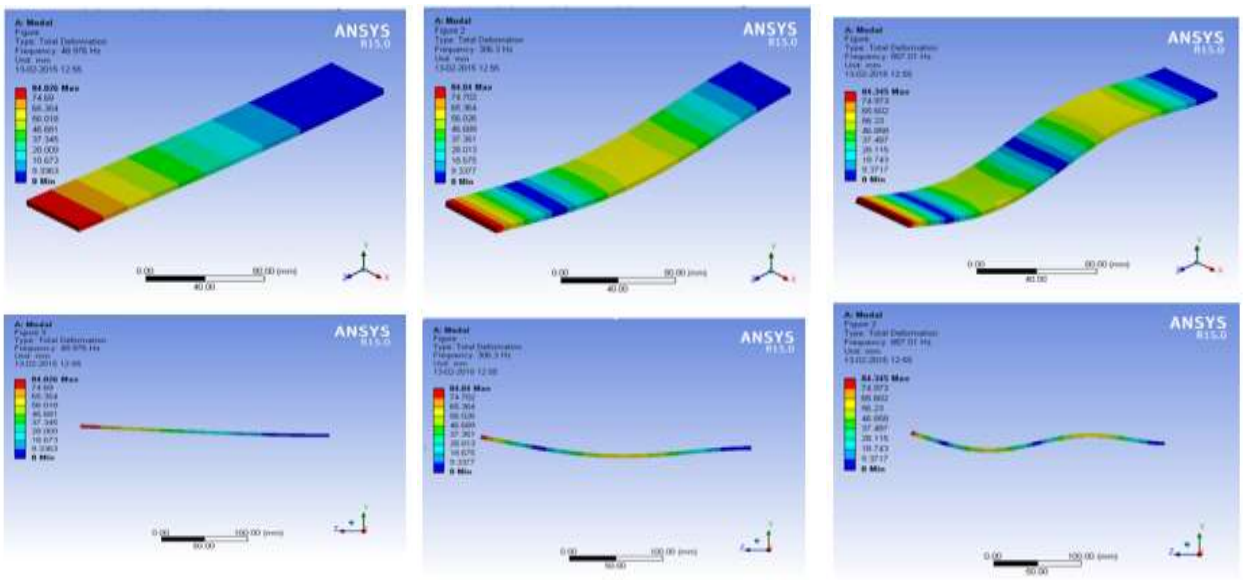

Fig. 3 (a): Mode 1 of cantilever beam (b) Mode 2 of cantilever beam (c) Mode 3 of cantilever beam

III. MODAL ANALYSIS OF CANTILEVER BEAM (ANALYTICAL)

For a cantilever beam Fig. (12), which is subjected to free vibration Fig. (13) and the system is considered as continuous system in which the beam mass is considered as distributed along with the stiffness of the shaft, the equation of motion can be written as

$$\frac{d^2}{dx^2}\left[EI(x)\frac{d^2y(x)}{dx^2}\right]=\omega^2 m(x) \tag{1}$$

Where, *E* is the modulus of rigidity of cantilever beam material, *I* is the moment of inertia of the beam cross-section, *Y*(*x*) is displacement in *y* direction at distance *x* from fixed end, *ω* is the natural frequency, *m* is the mass per unit length, $m = \rho A(x)$, ρ is the material density, x is the distance measured from the fixed end.

Boundary conditions for cantilever beam are

$$\text{At } x=0,\ y(x)=0,\ \frac{dy(x)}{dx}=0 \text{ and } \text{At } x=l,\ \frac{d^2y(x)}{dx^2}=0,\ \frac{d^3y(x)}{dx^3}=0 \tag{2}$$

From equation of motion, we get

$$\frac{d^4y(x)}{dx^4}-\beta^4 y(x)=0,\quad \text{where } \beta^4=\frac{\omega^2 m}{EI} \tag{3}$$

The mode shapes of a cantilever beam is given as

$$f_n(x)=A_n\{(\sin\beta_n L-\sinh\beta_n L)(\sin\beta_n x-\sinh\beta_n x)+(\cos\beta_n L-\cosh\beta_n L)(\cos\beta_n x-\cosh\beta_n x)\} \tag{4}$$

ISSN: 2277-9655
Impact Factor: 5.164
CODEN: IJESS7

Where n=0, 1, 2, 3 ...∞ and $\beta_n L = n\pi$

Natural frequency of cantilever beam using equations (15) and (16) can be written as

$$\omega_n = \alpha_n^2 \sqrt{\frac{EI}{mL^4}} \qquad \text{Where } \alpha_n = 1.875, 4.694, 7.85 \qquad (5)$$

The first three resonant frequencies of cantilever beam having same length (L) 0.29m, breadth (b) 0.05m and depth (h) 0.005m are calculated using Eq. (5) are 49.69Hz, 311.40Hz, 872.01Hz. The analytical results are tabulated in Table 3.

Table 3: Analytical results for modal frequencies of cantilever beam

Natural frequency	Formula	Natural frequency (rad/sec)	Natural frequency (Hz)
1.	$\omega_1 = (1.875)^2 \times \sqrt{\frac{EI}{\rho AL^4}}$	$\omega_1 = (1.875)^2 \times \sqrt{\frac{2\times10^{11}\times0.005^2}{12\times7850\times0.29^4}}$ =312.053 rad/sec	ω_1 =49.69Hz
2.	$\omega_2 = (4.694)^2 \times \sqrt{\frac{EI}{\rho AL^4}}$	$\omega_2 = (4.694)^2 \times \sqrt{\frac{2\times10^{11}\times0.005^2}{12\times7850\times0.29^4}}$ = 1955.592 rad/sec	ω_2 = 311.40 Hz
3.	$\omega_3 = (7.855)^2 \times \sqrt{\frac{EI}{\rho AL^4}}$	$\omega_3 = (7.855)^2 \times \sqrt{\frac{2\times10^{11}\times0.005^2}{12\times7850\times0.29^4}}$ = 5476.222 rad/sec	ω_3 = 872.01 Hz.

IV. RESULTS AND DISCUSSION

The comparison of natural frequencies between computational modal analysis results and analytical results is given in Table 4. The computational modal analysis results of beam are corroborated well with the analytical results. The calculated percentage difference of natural frequencies between the analytical results and computational modal analysis results lies within the range of 1.5 %. The graphical representation of comparison is shown in Fig. 4.

Table 4. Comparison between computational and analytical modal analysis results.

Mode	Analytical Results Frequency [Hz]	Computational Results Frequency [Hz]	Difference [%] b/w Computational &Analytical Results
Mode 1	49.69	49.20	0.98
Mode 2	311.40	307.79	1.15
Mode 3	872.01	861.46	1.20

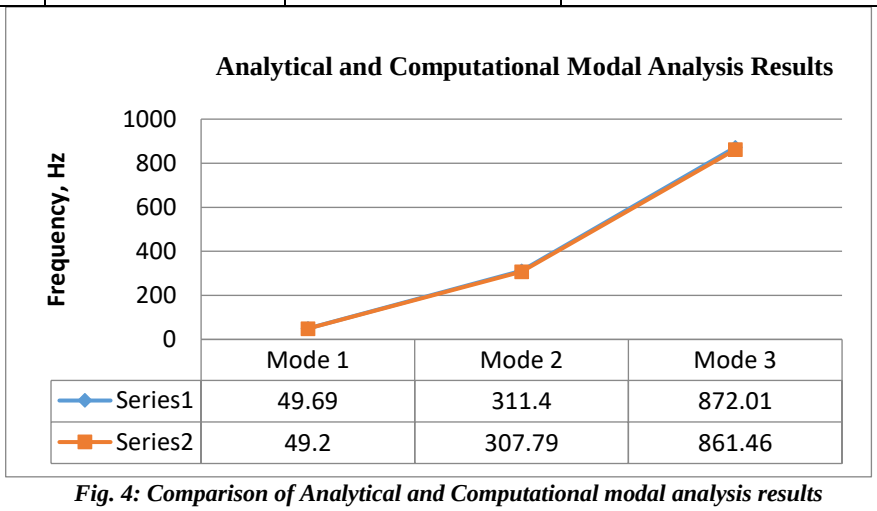

Fig. 4: Comparison of Analytical and Computational modal analysis results

The comparisons of mode shapes of computational and analytical modal analysis results are tabulated in Table 5.

ISSN: 2277-9655
Impact Factor: 5.164
CODEN: IJESS7

Table 5. Comparison of mode shapes of computational and analytical results

1.	Computational	$\omega_1 = 49.20$Hz	
	Analytical	$\omega_1 = 49.69$Hz	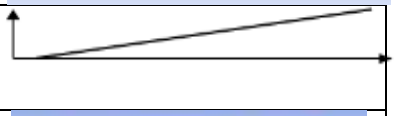
2.	Computational	$\omega_2 = 307.79$Hz	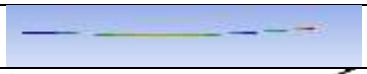
	Analytical	$\omega_2 = 311.40$Hz	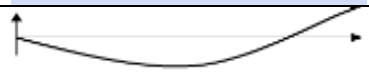
3.	Computational	$\omega_4 = 861.46$Hz	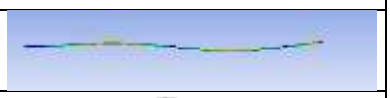
	Analytical	$\omega_4 = 872.01$Hz	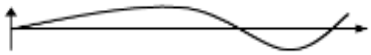

V. CONCLUSIONS

In this work, modal analysis of cantilever beam has been carried out both computationally and analytically. The following conclusions have been drawn:

1. Modal analysis is performed to determine the vibration characteristics i.e. natural frequencies and mode shapes of a mild steel cantilever beam using finite element based software *ANSYS*® and analytically.
2. The computational modal analysis results of beam are corroborated well with the analytical results.
3. The calculated percentage difference of natural frequencies between the analytical results and computational modal analysis results lies within the range of 1.5 %.
4. The knowledge of modal parameters is necessary to understand structural dynamics of structures.
5. The stress concentration regions found on cantilever beam corroborated well with the failed zone.

IV. REFERENCES

[1] Khawaja H.A., Khan A.M., "Modal and harmonic analysis of L.P. turbine of a small turbofan engine using finite element method", FAILURE OF ENGINEERING MATERIALS & STRUCTURES, pp. 22-27, 2007.
[2] Ramamurti V., Subramani D. A., Sridhara K., "Free vibration of a turbocharger centrifugal compressor impeller", MECHANISM AND MACHINE THEORY, Vol. 30, No. 4, pp. 619-628, 1995.
[3] Khan A.M., Ahmed M.N., Mustaq S., "Stress analysis of a major load bearing frame of medium weight aircraft using finite element method", JOURNAL OF ENGINEERING & APPLIED SCIENCE, Vol. 25, No. 1, pp. 47-55, 2006.
[4] Krishnakanth P.V., Raju G.N., Prasad RDV., Saisrinu R., "Structural & thermal analysis of gas turbine blade by using F.E.M." INTERNATIONAL JOURNAL OF SCIENTIFIC RESEARCH ENGINEERING & TECHNOLOGY, Vol. 2, No. 2, pp. 060-065, 2013.
[5] Zienwick O.C., Taylor R.L., "The finite element method", fourth edition (1994); McGraw Hill.
[6] Yinming S., Hongxing H., and Hugo S., "The finite element analysis and experimental study of beams with active constrained layer damping treatments", JOURNAL OF SOUND AND VIBRATIONS, Vol. 278, No. 1, pp. 343-363, 2004.
[7] Khan I.A., Parhi D.R.,"Finite Element Analysis of double cracked beam and its experimental validation", PROCEDIA ENGINEERING, Vol. 53, pp. 703-708, 2013.
[8] Shaikh N., Rathod W.S., Ansari K., "Modal and harmonic analysis of turbocharger turbine using finite element method", INTERNATIONAL JOURNAL OF APPLICATION OR INNOVATION IN ENGINEERING AND MANAGEMENT, Vol. 2, No. 7, pp. 6-9, 2013.
[9] Lafta H.S., Gupta A.V.S.S.K.S., "Finite element analysis of a gas turbine rotor blade", INTERNATIONAL JOURNAL OF SCIENTIFIC ENGINEERING AND TECHNOLOGY RESEARCH Vo. 3, No. 20, pp. 4173-4180, 2014.

ISSN: 2277-9655
Impact Factor: 5.164
CODEN: IJESS7

[10] Cook R.D., "Finite element method for stress analysis", John Wiley and Sons (1995).

Received: 6 October 2017 | Revised: 1 January 2018 | Accepted: 15 February 2018

DOI: 10.1002/ctpp.201700138

ORIGINAL ARTICLE

Contributions to Plasma Physics

Modelling the effects of nitrogen doping on the carbon nanofiber growth via catalytic plasma-enhanced chemical vapour deposition process

Ravi Gupta | **Suresh C. Sharma***

Department of Applied Physics, Delhi Technological University (DTU), Delhi, India

***Correspondence**
Suresh C. Sharma, Department of Applied Physics, Delhi Technological University (DTU), Shahbad Daulatpur, Bawana Road, Delhi 110042, India.
Email: suresh321sharma@gmail.com

An analytical model is developed to describe the effects of nitrogen doping on the growth of the carbon nanofibers (CNFs) and to elucidate the growth mechanism of nitrogen-contained carbon nanofibers (N-CNFs) on the catalyst substrate surface through the plasma-enhanced chemical vapour deposition (PECVD) process. The analytical model accounts for the charging of CNFs, kinetics of all plasma species (electrons, ions, and neutrals) in the reactive plasma, generation of carbon species on the catalyst nanoparticle surface due to dissociation of hydrocarbons, CNF growth due to diffusion and precipitation of carbon species, and various other processes. First-order differential equations have been solved for glow discharge plasma parameters for undoped CNFs (CNF growth in C_2H_2/H_2 plasma) and nitrogen-doped CNFs (N-CNF growth in C_2H_2/NH_3 plasma). Our investigation found that nitrogen-doped CNFs exhibit lower tip diameters and smaller heights compared to the undoped CNFs. In addition, we have estimated that nitrogen-doped CNFs have more enhanced field emission characteristics than the undoped CNFs. Moreover, we have also observed that N-CNFs' growth rate increases and tip diameter decreases as the C_2H_2/NH_3 gas ratio decreases. The theoretical results of the present investigation are consistent with the existing experimental observations.

KEYWORDS

nitrogen-contained carbon nanofibers (N-CNFs), nitrogen doping, PECVD

1 | INTRODUCTION

The growth of carbon nanofibers (CNFs) is an unexpectedly developing field of nanotechnology. Within the purview of a catalyst, diverse techniques can be utilized to synthesize CNFs, such as electric arc discharge, laser ablation, pyrolysis of organic precursor, and plasma-enhanced chemical vapour deposition (PECVD). The PECVD technique gathers continually growing interest because of its capability to grow vertically aligned CNFs at low temperatures. This is possible because the electric field existing within the plasma sheath aids the CNFs' growth in the vertical direction[1] and by substituting high thermal energy required in the growth process by dissociation of hydrocarbon precursors induced in plasma.[2]

The growth and synthesis of nitrogen-doped CNFs/nitrogen-contained carbon nanofibers (N-CNFs) receives constantly developing interest as the incorporation of nitrogen into the CNF grid leads to extraordinary physical and chemical properties.[3,4] Along with doping, catalysed growth is essential to control the characteristics of the resulting CNF by properly selecting the reaction conditions[5]. Merkulov et al.[6] synthesized the isolated N-CNFs and observed that nitrogen concentration in the plasma environment strictly affects the growth rate, tip diameter, and nitrogen content in the resulting CNF. It is also observed that, by the proper selection of the gas ratio, that is, hydrocarbon to ammonia, the morphology of the N-CNFs can be controlled.[7] Saidin

 © 2018 WILEY-VCH Verlag GmbH & Co. KGaA, Weinheim

TABLE 1 Plasma species considered in the present model

Type	Ions	Neutrals
a	$C_2H_2^+$, C_2H^+	C_2H_2, C_2H
b	H_2^+, H^+	H_2, H
c	NH_3^+, NH_4^+, NH_2^+, HCN^+, N^+	NH_3, NH_4, NH_2, HCN, N

et al.[8] observed a decrease in CNF diameter and increase in CNF growth rate when the ammonia gas flow rate is increased in reactive plasma. Moreover, Teo et al.[9] observed the change in CNF shape on increasing the gas ratio.

One of the most promising utilizations of CNFs is in the field emission devices.[10] The superior field emission obtained from CNFs/CNTs (carbon nanotubes) comes from their geometry rather than their crystalline structure.[2] Therefore, decent field emitters must have a high aspect ratio structure. CNFs hosting small diameters and comparatively excessive lengths can generate a high electric field (field enhancement) at the tip surface of the emitters to reap superior field emission; therefore, the greater the field enhancement factor of the emitter, the larger would be the field emission of electrons. Doping of CNFs with heteroatoms is essential for their practical applications.[11] Nitrogen atoms substitute carbon atoms in the graphene layers (graphene matrix of CNFs) and thus enhance the n-type electrical conductivity.[12] Kimura et al.[10] synthesized N-CNFs using the microwave plasma chemical vapour deposition (MPCVD) technique and observed the reduction in turn on field and increment in the field-enhancement factor when N-CNFs are utilized as field emitters.

Our previous studies suggest that the plasma-assisted catalysed growth of CNFs is affected by the plasma parameters[13] (i.e., the number density of plasma species) and by the different types of etchants present in the bulk plasma.[14] Motivated by the above-mentioned studies[3–12] on controlling the growth and field emission properties of the CNFs by nitrogen doping, we try to explain the effects of nitrogen doping on the growth of CNFs and their field emission properties through the plasma kinetics-based model. The model used in previous work relies on selected absorbed species; however, one of the main advantages of plasma-based growth is the ability to generate the highly reactive plasma species, which significantly affect CNF growth. Therefore, in the present paper, numerous additional species of the reactive plasma have been accounted. Moreover, the basic growth mechanisms of CNFs in the presence of reactive plasma remains the same, but to point out the consequent effects of nitrogen doping, many additional terms and equations have been incorporated in the present paper, which are given in Section 2. The theoretical results of the present work are discussed in Section 3, and the conclusion is given in Section 4.

2 | MODEL

The present analytical model elucidates the effects of nitrogen doping on the growth and field emission properties of CNFs, that is, the growth mechanism of N-CNFs in the reactive plasma composed of acetylene (C_2H_2) and ammonia (NH_3). In reality, the C_2H_2/NH_3 plasma mixture contains a large number of species[15,16] (ions and neutrals). However, following the experimental studies of Bell et al.[17] and Merkulov et al.[18], the plasma species accounted in the present model are listed in Table 1. Figure 1 shows the schematic of deposition of these plasma species and N-CNF growth mechanism considered in the present model. The nickel catalyst nanoparticle placed over the silicon substrate is considered to be the nucleation site for N-CNFs' nucleation. When a negatively biased substrate surface with a catalyst nanoparticle is subjected to the reactive plasma, an electric field $\vec{E}$ is induced between the bulk plasma and the substrate surface as a result of a charge separation region known as the plasma sheath. This induced electric field is assumed to be in a vertically downward direction, that is, from bulk plasma to substrate surface. The motion of ions is governed by this induced electric field, whereas neutrals have a random motion. At very low temperatures, it has been observed that no CNF grows when a small negative potential is applied to the substrate or a positive potential is applied to the substrate.[14] To investigate the sheath structure, fluxes, and energies of these plasma species, the following sheath equations are considered.[13]

$$\frac{d}{dx}n_k u_{kx} = \nu_i n_e, \tag{1}$$

$$M_k n_k u_{kx}\frac{du_{kx}}{dx} = e n_k \frac{d\phi}{dx} - M_k n_k \nu_{kn} u_{kx}, \tag{2}$$

$$\frac{d^2\phi}{dx^2} = -4\pi e \sum \Omega_k n_k, \tag{3}$$

where Equations 1–3 denote the continuity equation, ion–momentum balance equation, and Poisson's equation, respectively; k refers to either electrons or ions that are considered in the present model, and n_k, M_k, and u_{kz} are their number density, mass in

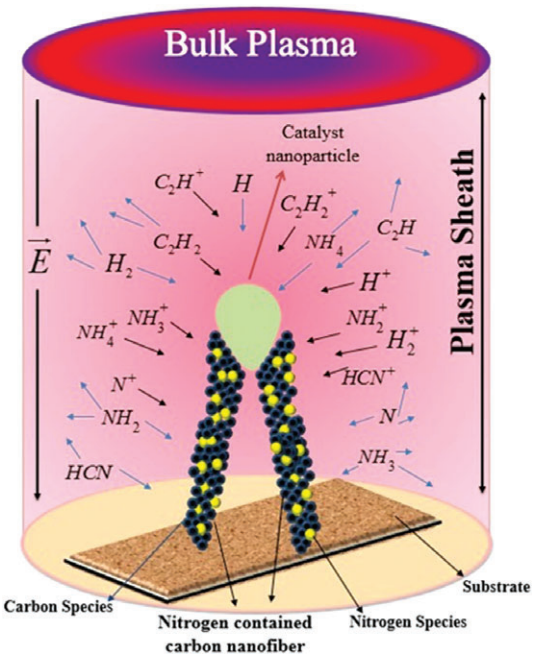

FIGURE 1 Schematic of the plasma species (ions and neutrals) deposition during nitrogen-contained carbon nanofibers (N-CNFs) growth

plasma, and fluid velocity, respectively; ν_i is the ionization frequency; E is the electric field; ν_{kn} is the collision frequency; Ω_k is the k^{th} ion to electron number density ratio; φ is the electrostatic potential; $\Sigma\Omega_k = 1$; and $0 < \Omega_k < 1$.

The presumptions of the present model are as follows: (a) negatively biased substrate is considered; (b) temperature of substrate and catalyst nanoparticle is considered to be the same; (c) the Maxwellian distribution of electrons, as well as ions, is considered; and (d) in the plasma sheath region, the electron number density is considered to be less than the ion number density $[n_i(x) > n_e(x)]$.

The elementary processes considered to study the effects of nitrogen insertion/doping on the growth of CNFs in the reactive plasma are:

1. Generation of carbon species on the catalyst nanoparticle surface (which is exposed to plasma) due to the dissociation of hydrocarbons on the catalyst nanoparticle surface.[19]
2. Surface and bulk diffusion of carbon species through the catalyst nanoparticle and formation of graphene layers around the catalyst nanoparticle.[20]
3. Transformation and deformation of catalyst nanoparticle shape due to stress exerted by these graphene layers.[21]
4. Etching of nanofiber side walls and tip by the etchants present in the plasma.[13]
5. Vertical growth due to alignment force provided by the electric field induced by plasma sheath.[22]

2.1 | Charging of the N-CNFs surface

The following equation describes the charge developed on the N-CNF surface due to the accumulation of electrons and positively charged ions on the surface, considering plasmas to be the thermodynamically open system.[23,24]

$$q = \sum_{a=1}^{2}[(I_{ia})_{\text{tip}} + (I_{ia})_{\text{cur}}] + \sum_{b=1}^{2}[(I_{ib})_{\text{tip}} + (I_{ib})_{\text{cur}}] + \sum_{c=1}^{5}[(I_{ic})_{\text{tip}} + (I_{ic})_{\text{cur}}] - \gamma_e[(I_e)_{\text{tip}} + (I_e)_{\text{cur}}], \tag{4}$$

where q is the charge over the entire CNF (i.e., tip and curved surface), and $(I_{ij})_{\text{tip}}$ and $(I_{ij})_{\text{cur}}$ are the ion collection currents at the CNF tip and the curved surface, respectively (where j refers to the ions of type a, b, and c). $(I_e)_{\text{tip}}$ and $(I_e)_{\text{cur}}$ are the electron collection currents at the CNF tip and the curved surface,[13,23–25] respectively.

2.2 | Number density equalization of electrons

$$n_e = \sum_{a=1}^{2}\beta_a n_a + \sum_{b=1}^{2}\beta_b n_b + \sum_{c=1}^{4}\beta_c n_c - \sum_{a=1}^{2}\alpha_a n_e n_{ia} - \sum_{b=1}^{2}\alpha_b n_e n_{ib} - \sum_{c=1}^{5}\alpha_c n_e n_{ic} - \gamma_e n_{\text{ncnf}}[(I_e)_{\text{tip}} + (I_e)_{\text{cur}}], \tag{5}$$

TABLE 2 Ion-neutral reactions between various plasma species in the bulk plasma considered in the present model

Reactions in bulk plasma		
Reaction	**Reaction rate (cm^3/s)**	**Reference**
$NH_3^+ + H_2 \rightarrow NH_4^+ + H$	4.00×10^{-13}	[16]
$NH_3^+ + H_2 \rightarrow NH_3 + H_2^+$	9.63×10^{-13}	[16]
$NH_3^+ + H_2 \rightarrow NH_3 + H^+ + H$	8.46×10^{-10}	[16]
$NH_3^+ + H_2 \rightarrow H_2^+ + NH_2 + H$	2.18×10^{-09}	[16]
$NH_3^+ + H_2 \rightarrow H^+ + NH_2 + H_2$	6.8×10^{-9}	[27]
$NH_3^+ + H_2 \rightarrow H^+ + H + NH_3$	8.46×10^{-10}	[27]
$NH_2^+ + H_2 \rightarrow NH_2 + H_2^+$	1.0×10^{-9}	[16]
$H_2^+ + NH_2 \rightarrow NH_2^+ + H_2$	5.00×10^{-10}	[16]
$H_2^+ + NH_2 \rightarrow NH_3^+ + H$	5.00×10^{-11}	[16]
$H_2^+ + NH_3 \rightarrow NH_3^+ + H_2$	5.70×10^{-9}	[16]
$H_2^+ + NH_3 \rightarrow NH_4^+ + H$	5.00×10^{-11}	[16]
$H^+ + NH_3 \rightarrow NH_3^+ + H$	5.00×10^{-11}	[16]
$H^+ + NH_2 \rightarrow NH_2^+ + H$	5.00×10^{-11}	[16]
$H_2^+ + C_2H_2 \rightarrow C_2H_2^+ + H_2$	5.30×10^{-9}	[16]
$H^+ + C_2H_2 \rightarrow C_2H^+ + H_2$	4.30×10^{-9}	[16]
$H^+ + C_2H \rightarrow C_2H^+ + H$	1.50×10^{-9}	[28]
$H_2^+ + C_2H \rightarrow C_2H^+ + H_2$	1.00×10^{-9}	[28]
$H_2^+ + C_2H \rightarrow C_2H_2^+ + H$	1.00×10^{-9}	[28]

where β_j is the coefficient of ionization of neutral atoms,[26] α_j is the coefficient of recombination of electrons and positively charged ions,[13] and γ_e is the sticking coefficient of electrons.

Equation 5 indicates the time evolution of electron number density in the plasma. The first three terms of Equation 5 correspond to increase in electron number density per unit time due to ionization of neutral species of type a, b, and c, respectively. The next three terms represent the decrease in electron number density per unit time due to recombination of electrons with ions of type a, b, and c, respectively. The last term represents the decrease in electron density in the plasma due to the electron collection current at the CNF surface.

2.3 | Number density equalization of positively charged ions

$$n_{ia} = \beta_a n_a - \alpha_a n_e n_{ia} - n_{ncnf}[(I_{ia})_{tip} + (I_{ia})_{cur}] - J_{aia} + J_{despa} + \sum_{lab} k_l n_a n_{ib}, \tag{6}$$

$$n_{ib} = \beta_b n_a - \alpha_b n_e n_{ib} - n_{ncnf}[(I_{ib})_{tip} + (I_{ib})_{cur}] - J_{aib} + J_{despb} + \sum_{mbc} k_m n_b n_{ic}, - \sum_{lab} k_l n_a n_{ib} + J_{thd}, \tag{7}$$

$$n_{ic} = \beta_c n_c - \alpha_c n_e n_{ic} - n_{ncnf}[(I_{ic})_{tip} + (I_{ic})_{cur}] - J_{aic} + J_{despc} + \sum_{pbc} k_p n_b n_{ic}, \tag{8}$$

where J_{aij} and J_{desp} are the ion adsorption flux and ion desorption flux onto/from the catalyst substrate surface, respectively (j refers to the ions of type a, b, and c). k_l, k_m, and k_p are the reaction rate coefficients of ion-neutral reactions, and J_{thd} is the hydrogen flux due to thermal dehydrogenation.

In Equations 6–8, various processes are taken into account to equalize the number density of ions in the reactive plasma, such as gain in ion density per unit time on account of ionization of neutral atoms (first term), decrease in positively charged ion number density due to electron–ion recombination (second term), and ion collection current at the surface of the CNF (third term), adsorption (fourth term) and desorption of ions (fifth term) to/from the catalyst–substrate surface, and increase and decrease in ion number density due to ion-neutral reactions between different plasma species (sixth and seventh term). The main ion-neutral reactions considered in the present model are listed in Table 2. The last term of Equation 7 indicates the increase in hydrogen ion number density due to thermal dehydrogenation.

2.4 | Number density equalization of neutral atoms

$$n_a = \alpha_a n_e n_{ia} - \beta_a n_a + n_{ncnf}(1-\gamma_{ia})[(I_{ia})_{tip} + (I_{ia})_{cur}] - n_{ncnf}\gamma_a[(I_a)_{tip} + (I_a)_{cur}] - \sum_{lab} k_l n_a n_{ib} + IF_a - OF_a, \quad (9)$$

$$n_b = \alpha_b n_e n_{ib} - \beta_b n_b + n_{ncnf}(1-\gamma_{ib})[(I_{ib})_{tip} + (I_{ib})_{cur}] - n_{ncnf}\gamma_b[(I_b)_{tip} + (I_b)_{cur}] + \sum_{lab} k_l n_a n_{ib} - \sum_{mbc} k_m n_b n_{ic} + IF_b - OF_b, \quad (10)$$

$$n_c = \alpha_c n_e n_{ic} - \beta_c n_c + n_{ncnf}(1-\gamma_{ic})[(I_{ic})_{tip} + (I_{ic})_{cur}] - n_{ncnf}\gamma_c[(I_c)_{tip} + (I_c)_{cur}] + \sum_{pbc} k_p n_b n_{ic} + IF_c - OF_c, \quad (11)$$

where $(I_j)_{tip}$ and $(I_j)_{cur}$ are neutral atom collection currents at the tip and the curved surface of CNF, respectively[13] (j refers to the neutrals atoms of type a, b, and c). In Equations 9–11, the processes taken into account to equalize the neutral atom number density are: increase in neutral atom number density due to electron–ion recombination (first term) and neutralization of ions collected at the N-CNFs surface (third term), the decay rate of neutral atom density due to ionization of neutrals (second term) and accumulation of neutrals on the N-CNF surface (fourth term), and increase and decrease in neutral atom number density due to the ion-neutral reactions between different plasma species (fifth and sixth term) that are listed in Table 2. Moreover, the last two terms represent the j^{th} species inflow rate [$IF_j = 4.4 \times 10^{17} \times f/V$] into the plasma chamber and j^{th} species outflow rate [$OF_j = R_p \times n_a/V$] from the plasma chamber, where f is the inlet flow of corresponding gas, V is the volume of the chamber ($\approx 2 \times 10^4$ cm^3), and R_p is the pumping rate.[29]

2.5 | Growth rate of carbon species on the catalyst surface

At the initial stage, applied plasma power dissociates the input gases and creates highly energetic ions and electrons [cf. ref. 13], which further breaks the catalyst's thin film into many catalyst nanoparticles [cf. ref. 13], and these catalyst nanoparticles act as the fundamental sites for the nucleation and growth of CNFs.[30] At this nucleation stage, numerous carbon species (N_c) are generated on the catalyst nanoparticle front surface (plasma-exposed surface) via various surface processes that are discussed in Equation 9. In the present model, the catalyst nanoparticle size (D) is assumed to be 100 nm.

$$N_C = \sum_{a=1}^{2} J_a(1-\theta_t) + 2\sum_{a=1}^{2} n_{sa}\upsilon \exp\left(\frac{-\delta E_{td}}{k_B T_S}\right) + 2\sum_{a=1}^{2}\frac{n_{sa}y_d}{\upsilon_0}\sum_{a=1}^{2} J_{ia} + \sum_{a=1}^{2} J_{ia} + J_C - \sum_{a=1}^{2}\frac{J_a\sigma_{ads}J_b}{\upsilon} - \frac{N_c\sigma_{ads}J_b}{\upsilon} - N_c\upsilon\exp\left(\frac{-E_{ev}}{k_B T_S}\right) - n_{sa}\upsilon\exp\left(\frac{-E_{dhc}}{k_B T_S}\right), \quad (12)$$

where $n_{sj}(=\theta_j \upsilon_0)$ is the surface concentration of neutral atoms,[31,32] θ_j is the surface coverage by the respective species, υ_0 is the adsorption sites per unit area, $J_j(=n_j v_{th}/4)$ is the flux of neutral impinging species on the catalyst nanoparticle surface from the plasma, $J_{ij}\left(=n_{ij}\sqrt{k_B T_{ij}/m_{ij}}\right)$ is the ions flux on the catalyst nanoparticle surface from the plasma,[32] υ is the thermal vibration frequency, $\sigma_{ads}(=6.8\times10^{-16}$ cm$^2)$ is the cross section for the interaction among the various species,[32] $\delta E_{td}(=$ 2.1 eV) is the hydrocarbons dissociation energy, $\delta E_{ev}(=$ 1.8 eV) is the carbon evaporation energy, and $\delta E_{dhc}(=$1.8 eV) is the hydrocarbon desorption energy.[33] The explanation of various terms as well as their corresponding surface reactions involved in the Equation 12 are listed in Table 3.

TABLE 3 Various surface processes and their corresponding reactions on the catalyst nanoparticle surface (refs 31–36) considered in the Equation 12 where "ads" and "des" corresponds to the adsorption and desorption of plasma species to/from the catalyst surface, respectively

Functional term	Explanation and reactions involved
$J_a(1-\theta_t)$	Adsorption of hydrocarbons on the catalyst nanoparticle surface $C_2H_{2(plasma)} \rightarrow C_2H_{2(ads)}$, $C_2H_{(plasma)} \rightarrow C_2H_{(ads)}$
$n_{sa}\nu \exp\left(\frac{-\delta E_{td}}{k_B T_S}\right)$	thermal dissociation of hydrocarbons $C_2H_{2(ads)} \rightarrow 2C_{(ads)} + 2H_{(ads)}$, $C_2H_{(ads)} \rightarrow 2C_{(ads)} + H_{(ads)}$
$\frac{n_a y_d}{\upsilon_0} J_{ia}$	Ion induced dissociation of hydrocarbons $C_2H_2{}^+ + C_2H_{2(ads)} \rightarrow 2C_{(ads)} + H_{2(plasma)} + C_2H_2{}^+$, $C_2H^+ + C_2H_{(ads)} \rightarrow 2C_{(ads)} + H_{(ads)} + C_2H^+$, $C_2H_2{}^+ + C_2H_{(ads)} \rightarrow 2C_{(ads)} + H_{(ads)} + C_2H_2{}^+$, $C_2H^+ + C_2H_{2(ads)} \rightarrow 2C_{(ads)} + H_{2(plasma)} + C_2H^+$
J_{ia}	Ion decomposition $C_2H_2{}^+ \rightarrow 2C_{(ads)} + H_{2(plasma)}$, $C_2H^+ \rightarrow 2C_{(ads)} + H_{(ads)}$
J_C	Direct carbon flux towards catalyst surface
$\frac{J_a \sigma_{ads}}{\nu} J_b$	Loss of adsorbed hydrocarbons at interaction with atomic hydrogen from plasma $C_2H_{2(ads)} + H_{(plasma)} \rightarrow C_2H_{3(plasma)}$, $C_2H_{(ads)} + H_{(plasma)} \rightarrow C_2H_{2(plasma)}$
$\frac{N_c \sigma_{ads}}{\nu} J_b$	Loss of generated carbon species at interaction with atomic hydrogen $C_{(ads)}H_{(plasma)} \rightarrow CH_{(plasma)}$
$N_c \nu \exp\left(\frac{-E_{ev}}{k_B T_S}\right)$	Evaporation of carbon $C_{(ads)} \rightarrow C_{(evaporation)}$
$n_{sa}\nu \exp\left(\frac{-E_{dhc}}{k_B T_S}\right)$	Desorption of hydrocarbons $C_2H_{2(ads)} \rightarrow C_2H_{2(des)}$, $C_2H_{(ads)} \rightarrow C_2H_{(des)}$

2.6 | Growth of N-CNFs

$$\begin{aligned}\frac{d}{dt}[\pi(D^2-d^2)h] = &\left[\frac{D_s N_C}{\upsilon}\pi D + \frac{D_b N_C}{\upsilon}\pi D + 4kN_C\pi D^2\right] \times (1-\Omega_c) \times \left(\frac{P}{\rho_{ncnf} I_{ia}}\right) \\ &+ \frac{D_m m_{cat}}{\rho_{cat} \times \pi D^2} + \left[\sum_{b=1}^{2} J_b(1-\theta_t) + \sum_{b=1}^{2} J_b \exp\left(\frac{-E_{th}}{k_B T_S}\right) + \sum_{a=1}^{2} \frac{n_{sa} y_d}{\upsilon_0} \sum_{b=1}^{2} J_{ia}\right. \\ &+ \sum_{b=1}^{2} J_{ib} + \sum_{a=1}^{2} n_{sa}\upsilon \exp\left(\frac{-\delta E_{td}}{k_B T_S}\right) + \sum_{c=1}^{3} \theta_c \left(J_{ic} y_d + \upsilon_0 \upsilon \exp\left(\frac{-\delta E_{td}}{k_B T_S}\right)\right) \\ &\left. - \sum_{b=1}^{2} n_{sb} \exp\left(\frac{-E_{dH}}{k_B T_S}\right)\right] \frac{\pi D^2}{4\sum_{b}^{2} n_{ib}} + \left\{\sum_{a=1}^{2} \gamma_a I_a + \sum_{c=1}^{5} \gamma_c I_c,\right\} \frac{\pi D^2 h}{4}, \end{aligned} \tag{13}$$

where D is the catalyst nanoparticle diameter, d is the CNF tip diameter, h is the CNF height, $D_s[= D_{s0} \times \exp(-\varepsilon_s/k_B T_s)]$ is the surface diffusion coefficient, $D_{s0} = a_0^2 \nu$, $a_0(=0.34\,\text{nm})$ is the carbon atoms' interatomic distance, $\varepsilon_s(=0.3\,\text{eV})$ is the energy barrier for carbon species diffusion through the catalyst nanoparticle surface,[31] $D_b[=D_{b0}\exp(-\varepsilon_s/k_B T_s)]$ is the bulk diffusion coefficient, $D_{b0} = D\nu/2\pi$, $\varepsilon_b(=1.6\,\text{eV})$ is the energy barrier for carbon species bulk diffusion through catalyst nanoparticle,[31] $P(\approx 20\,\text{GPa})$ is the pressure exerted by graphene layers on catalyst nanoparticle, $k = A_k \exp(-\delta\varepsilon_{inc}/k_B T_S)$ is the carbon species incorporation speed in the graphene layers,[13] $A_k = a_0\nu$, $\delta_{inc} = (0.4\,\text{eV})$ is the carbon species energy barrier to diffuse along the nanofiber–catalyst interface, ρ_{cnf} is the nanofiber density, m_{cat} is the mass of the metal catalyst particle, and ρ_{cat} is the density of metal catalyst nanoparticle. $D_m[=D_{m0}\exp(-\varepsilon_{SD}/k_B T_s)]$ is the metal atoms' diffusion coefficient,[31] and $\delta E_{th}(=1.87\,\text{eV})$ is the energy for thermal dehydrogenation of hydrocarbons.[33]

All complex processes involved in Equation 13 to describe the growth mechanism of N-CNFs on the catalyst nanoparticle are listed in Table 4. The surface and bulk diffusion of carbon species significantly affect the growth of nanostructures, and their relative contribution depends on the catalyst nanoparticle temperature. At high temperatures, bulk diffusion dominates, and at low temperatures, surface diffusion dominates, whereas at intermediate temperatures, both are significant for growth.[31,34,37–39] Therefore, in the present paper, we have taken both the diffusion processes into account because the temperature of the catalyst nanoparticle is assumed to be constant through the growth process. The dissociation of hydrocarbons and the diffusion of carbon species is a key step for nanostructure growth. The growth of nanostructures terminates when the dissociation rate

TABLE 4 Various surface processes and their corresponding reactions on the catalyst nanoparticle surface (refs 31–36) considered in the Equation 13 where "ads" and "des" corresponds to the adsorption and desorption of plasma species to/from the catalyst surface, respectively

Functional term	Explanation and reactions involved
$\frac{D_s N_C}{\nu}\pi D$	Surface diffusion of carbon species through catalyst nanoparticle
$\frac{D_b N_C}{\nu}\pi D$	Bulk diffusion of carbon species through catalyst nanoparticle
$4kN_C\pi D^2$	Incorporation of the carbon species in the form of graphene layers.
$\frac{D_m m_{cat}}{\rho_{cat}\times\pi D^2}$	Metal atoms self-diffusion
$J_b \exp(1-\theta_t)$	Hydrogen adsorption on the catalyst nanoparticle surface $H_{(plasma)} \rightarrow H_{(ads)}$ $H_{2(plasma)} \rightarrow H_{2(ads)}$
$J_b \exp\left(\frac{-E_{ih}}{k_B T_S}\right)$	Hydrogen ion incoming flux due to hydrocarbon ions thermal dehydrogenation
$\frac{n_{sa} y_d}{\nu_0} J_{ib}$	Generation of hydrogen due to ion induced decomposition of hydrocarbons $C_2H^+ + C_2H_{(ads)} \rightarrow 2C_{(ads)} + H_{(ads)} + C_2H^+$, $C_2H_2{}^+ + C_2H_{(ads)} \rightarrow 2C_{(ads)} + H_{(ads)} + C_2H_2{}^+$,
J_{ib}	Direct hydrogen ion flux
$n_{sa}\nu \exp\left(\frac{-\delta E_{td}}{k_B T_S}\right)$	The flux of H atom due to thermal dissociation of hydrocarbons $C_2H_{2(ads)} \rightarrow 2C_{(ads)} + 2H_{(ads)}$, $C_2H_{(ads)} \rightarrow 2C_{(ads)} + H_{(ads)}$
$\theta_c J_{ic} y_d$	Generation of hydrogen due to ion induced dissociation of ammonia $NH_3^+ + NH_{(ads)} \rightarrow 2N_{(ads)} + 3H_{(ads)} + N_3^+$, $NH_4^+ + NH_{4(ads)} \rightarrow 2N_{(ads)} + 4H_{(ads)} + N_4^+$, $NH_2^+ + NH_{2(ads)} \rightarrow 2N_{(ads)} + 2H_{(ads)} + N_2^+$,
$\theta_c \nu_0 \nu \exp\left(\frac{-\delta E_{td}}{k_B T_S}\right)$	Generation of hydrogen due to thermal decomposition of ammonia $NH_{3(ads)} \rightarrow C_{(ads)} + 3H_{(ads)}$, $NH_{4(ads)} \rightarrow C_{(ads)} + 4H_{(ads)}$, $NH_{2(ads)} \rightarrow C_{(ads)} + 2H_{(ads)}$,
$n_{sb} \exp\left(\frac{-E_{dH}}{k_B T_S}\right)$	Hydrogen desorption from the catalyst nanoparticle surface $H_{(ads)} \rightarrow H_{(des)}$
$\gamma_a I_a$	Sticking of hydrocarbon neutrals on the CNF surface
$\gamma_c I_c$	Sticking of ammonia neutrals on the CNF surface

of hydrocarbons on the catalyst nanoparticle surface decreases because of the formation of the continuous carbon layer on the catalyst nanoparticle surface, which consequently prevents the diffusion of carbon species. Thus, term $(1-\Omega_c)$, related to amorphous carbon deposition, is taken into account, where $\Omega_c = n_c \times \pi D^2$.

Moreover, the realization of these carbon species in the form of a graphene layer is taken into account. Now, the continuously formed graphene layers around the catalyst nanoparticle due to continuous diffusion of carbon species exerts significant pressure on the catalyst nanoparticle and results in the catalyst nanoparticle shape deformation; therefore, the pressure term (outside the first bracket) is taken into account in Equation 10. The catalyst nanoparticle shape deformation is an important process behind the inclination of graphene layers around catalyst nanoparticles during nanofiber growth. Therefore, the change in catalyst nanoparticle shape due to the metal atoms' self-diffusion is also taken into account. Due to continuous carbon supply, both vertical as well as in-plane growth of carbon precipitation continuous, but in-plane growth stops as a result of etching of terminal carbons by the active hydrogen radicals and ions. Moreover, due to the presence of nitrogen in the reactive plasma, nitrogen incorporation is also taken into account in this equation. Nitrogen insertion/doping in the CNF lattice significantly affects the physical structure and growth of CNFs.

3 | RESULTS AND DISCUSSION

In the present paper, an analytical model has been used to describe the N-CNF growth (i.e., the effects of nitrogen doping on the CNF growth) and its field emission properties through the catalyst-assisted PECVD process. The analytical model incorporates the charging of N-CNFs; kinetics of plasma species (electron, ions, and neutrals); surface as well as bulk diffusion, accretion, and adsorption of carbon species on the catalyst nanoparticle surface; sticking of nitrogen atoms on the catalyst nanoparticle surface; incorporation of carbon species in the form of graphene layers around the catalyst nanoparticle; and vertical growth due to the plasma sheath effect.

The numerical solutions of the first-order, simultaneous differential Equations 1–13 given in Section 2 have been obtained using MATHEMATICA software for experimentally determined boundary conditions and the glow discharge plasma parameters. The detailed overview of different sources of plasma excitation and process-related parameters, such as plasma power, gas pressure, substrate temperature, and plasma composition, used for the PECVD growth of CNFs/CNTs based on experimental

TABLE 5 The different sources of plasma excitation and process-related parameters used for the plasma-enhanced chemical vapour deposition (PECVD) growths of carbon nanofibers (CNFs)/CNTs based on experimental works

Source of plasma excitation	Gas mixture	Gas ratio (flow rate) (sccm)	Pressure	Substrate temperature (°C)	Plasma power (W)	Reference
Direct-current (dc)	C_2H_2/NH_3	40/80	3 Torr	700	123	[6]
dc	C_2H_2/NH_3	(0–76)/200	1.875 Torr	650	—	[17]
dc	C_2H_2/NH_3	(0–150)/200	3.5 Torr	750	—	[40]
dc	C_2H_2/NH_3	50/200	1.125 Torr	120–500	—	[41]
dc	C_2H_2/NH_3	50/200	—	250	20	[42]
dc	C_2H_2/NH_3	30/200	1.5 mbarr	200	—	[43]
dc	C_2H_2/NH_3	50/200	0.7 mbarr	500	20	[44]
Micro-wave (MW)	C_2H_2/NH_3	200	20 Torr	825	—	[45]
MW	CH_4/NH_3	(150–240)/(60–150)	21 Torr	650–1000	—	[46]
Inductive coupled plasma (ICP)	CH_4/H_2	20/80	0.5–20 Torr	800–1000	120	[47]
ICP	C_2H_4/H_2	(5–20)/(80–95)	3 Torr	600–1000	50–200	[48]
ICP	CH_4/H_2	50/50	1 Torr	500–650	—	[49]
ICP	C_2H_2/H_2	(37.5–88)/(12–62.5)	50 mTorr	700	27	[50]
ICP	C_2H_2/H_2	15/85	20 mTorr	500	400	[51]
Radio frequency (RF)	CH_4/H_2	0.4/20	5 Pa	400	350	[52]
RF	C_2H_2/NH_3	5/20	—	450	180	[53]

TABLE 6 Parameters used in the present model

Parameter	Value
Pressure	3 Torr
Plasma power	123 W
Substrate temperature	700 °C
C_2H_2 gas flow rate	40 sccm
H_2 gas flow rate	80 sccm
NH_3 gas flow rate	80 sccm
Electron temperature	2.2 eV
Ion temperature	2200 K
Neutral temperature	2000 K
Substrate potential	–300 V

works have been summarized in Table 5. Following Merkulov et al.[6] and Mao and Bogaerts,[16] the process parameters and boundary conditions used in the present study are listed in Tables 6 and 7. Moreover, other parameters used in the present model are: $m_{ia} = m_a = 26$ and 25 amu for C_2H_2 and C_2H, respectively; $m_{ib} = m_b = 2$ and 1 amu for H_2 and H, respectively; $m_{ic} = m_c = 17$ amu, 18 amu, 16 amu, 14 amu, and 27 amu for NH_3, NH_4, NH_2, N, and HCN, respectively; atomic mass of nickel (m_{cat}) = 58.69 amu; density of catalyst nickel (ρ_{ct}) = 8.96 g/cm3); coefficient of recombination of electrons and ions ($\alpha_{a0} \approx \alpha_{b0} \approx \alpha_{c0}$) = 1.12×10^7 cm^3/s; $\kappa = -1.2$; sticking coefficient of electrons (γ_e) = 1; sticking coefficient of ions ($\gamma_{ia} = \gamma_{ib} = \gamma_{ic}$) = 1; and sticking coefficient of neutral atoms ($\gamma_a = \gamma_b = \gamma_c$) = 1.

Figure 2 shows the time variation of tip diameter for undoped (growth of CNF in C_2H_2/H_2 gas plasma) and nitrogen-doped CNF (growth of CNF in C_2H_2/NH_3 plasma). The tip diameter of both undoped and nitrogen-doped CNFs decreases with growth time. This can be easily explained by the fact that the diameter of catalyst nanoparticles at the tips of vertically aligned CNFs decreases during growth due to the stress exerted by growing graphene layers on the catalyst particles and self-diffusion of metal atoms of the catalyst.[13,36] Moreover, from Figure 2, it can also be seen that the tip diameter d of the CNF decreases rapidly in the case of nitrogen-doped CNFs compared to the undoped CNFs. This reduction in tip diameter on account of nitrogen doping can be clarified with various facts. One such clarification is that, on ammonia insertion in the plasma, the amount of atomic hydrogen species (H and H^+) in the plasma increases (cf. Figure 3), and consequently, the etching of CNFs increases. Moreover, on ammonia addition, many additional etchant species, that is, atomic nitrogen and cyanide species (N, N^+, HCN^+), form in the plasma. Thus, the relative etching of CNFs on account of nitrogen increases compared to undoped CNFs.

As nitrogen doping has been taken into account, the height of CNFs decreases, as can be seen from Figure 4. On ammonia addition, ammonium ions are formed in the plasma, which contains pentavalent nitrogen. Therefore, the incorporation of

TABLE 7 Boundary conditions for the various plasma species considered in the present model

Parameter	Value	
	Undoped carbon nanofiber (CNF) (C_2H_2/H_2 gas mixture)	**Nitrogen doped CNF (C_2H_2/NH_3 gas mixture)**
Electron number density (n_{e0})	10^{10} cm^{-3}	10^{10} cm^{-3}
Hydrocarbon ion number density (n_{ia0})		
$C_2H_2^+$	0.645 n_{e0}	0.55 n_{e0}
C_2H_2+	0.05 n_{e0}	0.04 n_{e0}
Hydrogen ion number density (n_{ib0})		
H_2^+	0.34 n_{e0}	0.05 n_{e0}
H^+	0.01 n_{e0}	0.05 n_{e0}
Hydrocarbon neutral atom number density (n_{a0})		
C_2H_2	0.5×10^{14} cm^{-3}	0.5×10^{14} cm^{-3}
C_2H	0.2×10^{11} cm^{-3}	0.2×10^{11} cm^{-3}
Hydrogen neutral atom number density (n_{b0})		
H_2	10^{15} cm^{-3}	10^{15} cm^{-3}
H	0.2×10^{14} cm^{-3}	0.1×10^{14} cm^{-3}
Dopant ion number density (n_{ic0})		
NH_3^+		0.09 n_{e0}
$NH4^+$		0.1 n_{e0}
$NH2^+$		0.1 n_{e0}
HCN^+		0.01 n_{e0}
N^+		0.01 n_{e0}
Dopant neutral atom number density (n_{c0})		
NH_3		0.5×10^{15} cm^{-3}
NH_4		0.5×10^{13} cm^{-3}
NH_2		0.5×10^{13} cm^{-3}
HCN		0.2×10^{12} cm^{-3}
N		0.9×10^{11} cm^{-3}

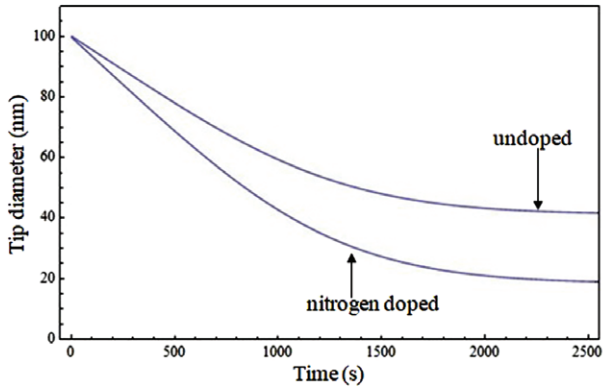

FIGURE 2 The time variation of tip diameter for undoped CNF (growth of CNF in C_2H_2/H_2 gas plasma) and nitrogen-doped CNF (growth of CNF in C_2H_2/NH_3 plasma) at C_2H_2 flow rate = 40 sccm, H_2 flow rate = 80 sccm, and NH_3 flow rate = 80 sccm. Other parameters are given in the text

nitrogen in the CNF lattice generates more electrons, and consequently, the ionization of neutral hydrocarbon increases. This suppresses the concentration of hydrocarbon neutrals available for growth (cf. Figure 5). Moreover, hydrocarbon ions in the plasma form cyanide species on reacting with ammonia. Thus, these cyanide species also decrease the concentration of carbon species available for growth. A similar effect of nitrogen doping on the diameter and height was observed by Sumpter et al.[54] in their nitrogen-mediated growth of bamboo-shaped carbon nanotubes (CNFs).

The superior field emission from carbon nanostructures (CNTs and CNFs) comes from their geometry rather than their crystalline structure,[11] and therefore, field emission is primarily characterized by the field enhancement factor $\beta(=h/r)$, where h is the height of the CNF and r is the CNF tip radius, which signifies the electric field amplification at the tip of the emitter. Thus, from the results obtained, we have estimated the variation in the field enhancement factor for undoped CNFs and N-CNFs.

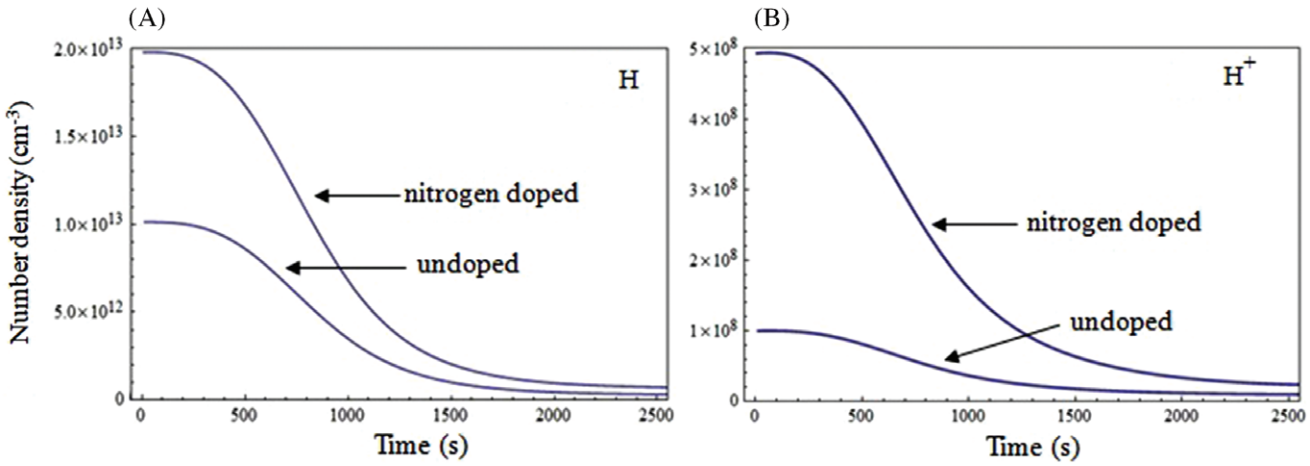

FIGURE 3 The time variation of number density for (a) H and (b) H^+ in the plasma for undoped (growth of CNF in C_2H_2/H_2 gas plasma) and nitrogen-doped CNF (growth of CNF in C_2H_2/NH_3 plasma) at C_2H_2 flow rate = 40 sccm, H_2 flow rate = 80 sccm, and NH_3 flow rate = 80 sccm. Other parameters are given in the text

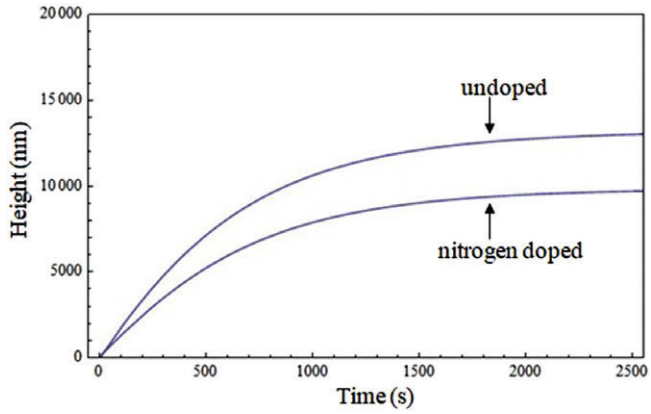

FIGURE 4 The time variation of height for undoped (growth of CNF in C_2H_2/H_2 gas plasma) and nitrogen-doped CNF (growth of CNF in C_2H_2/NH_3 plasma) at C_2H_2 flow rate = 40 sccm, H_2 flow rate = 80 sccm, and NH_3 flow rate = 80 sccm. Other parameters are given in the text

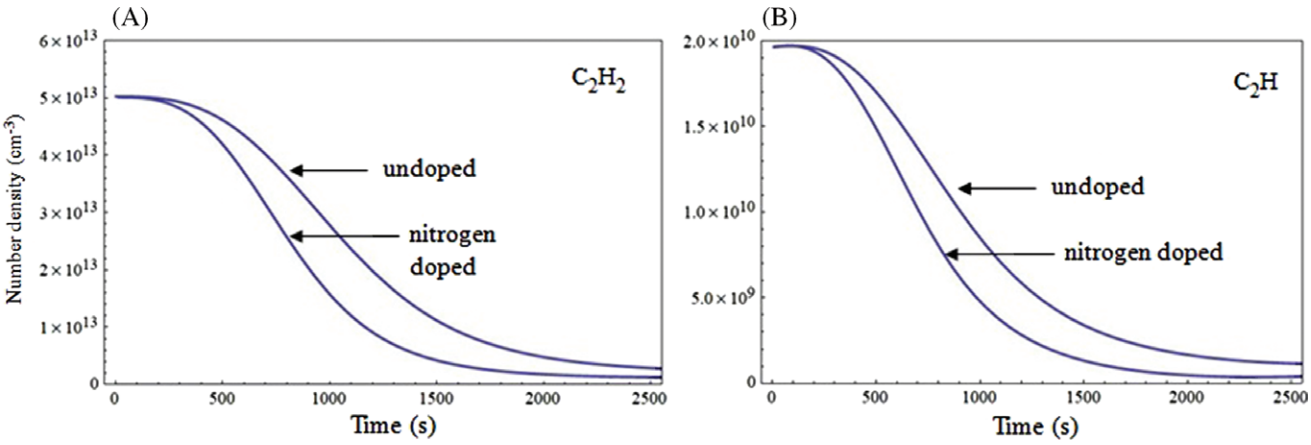

FIGURE 5 Time variation of nitrogen density for (a) C_2H_2 and (b) C_2H for undoped (growth of CNF in C_2H_2/H_2 gas plasma) and nitrogen-doped CNF (growth of CNF in C_2H_2/NH_3 plasma) at C_2H_2 flow rate = 40 sccm, H_2 flow rate = 80 sccm, and NH_3 flow rate = 80 sccm. Other parameters are given in the text

From Table 8, it can be seen that the field enhancement factor is much larger for nitrogen-doped CNFs as compared to undoped CNFs. Kimura et al.[10] experimentally observed improved field emission from nitrogen-treated CNFs.

Moreover, we have also observed that the relative concentration of hydrocarbon and nitrogen (ammonia) in the plasma significantly affects the N-CNFs growth and structure. Figure 6a shows the time variation of N-CNF height at different hydrocarbon (i.e., C_2H_2) gas flow rates, and Figure 6b shows the N-CNFs growth rate (height of N-CNFs per unit deposition time) as a function of hydrocarbon (i.e., C_2H_2) to nitrogen feedstock gas (ammonia) ratio in C_2H_2/NH_3 plasma. The results demonstrated in Figure 6 are obtained for a fixed ammonia gas flow rate and variable acetylene gas flow rate. As can be seen, N-CNF height

TABLE 8 Estimation of field enhancement factor for undoped and nitrogen-doped carbon nanofibers (CNFs) from the result obtained in Figures 2 and 4

CNFs	Height (nm)	Tip diameter (nm)	Field enhancement factor
Undoped	13,105	43.8	299.2
Nitrogen doped	10,031	21.1	475.4

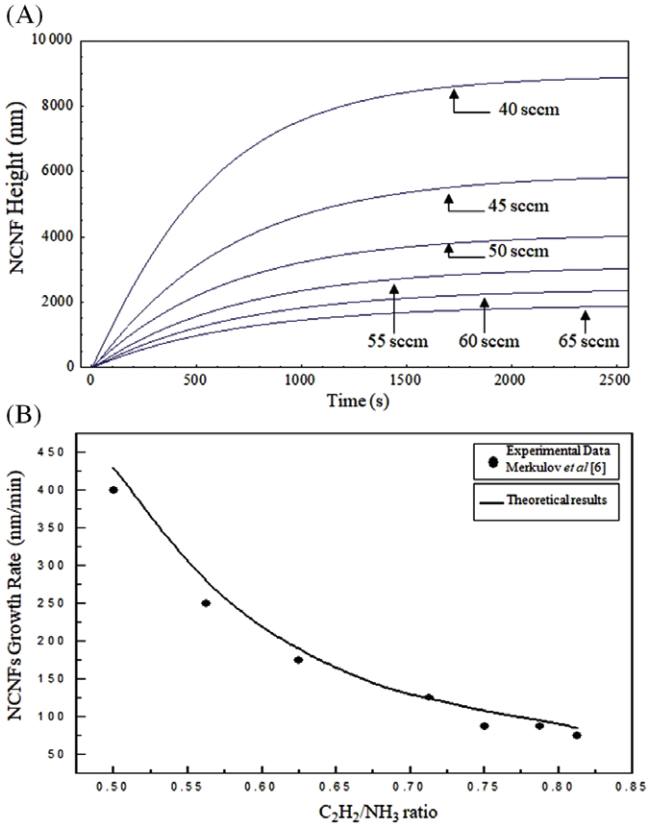

FIGURE 6 (a) The time variation of N-CNF height for different C_2H_2 gas flow rates in C_2H_2/NH_3 plasma, keeping NH_3 gas flow rate constant at 80 sccm. (b) N-CNFs growth rate as a function of C_2H_2/NH_3 ratio for variable C_2H_2 gas flow rate and constant NH_3 gas flow rate. Other parameters are given in the text

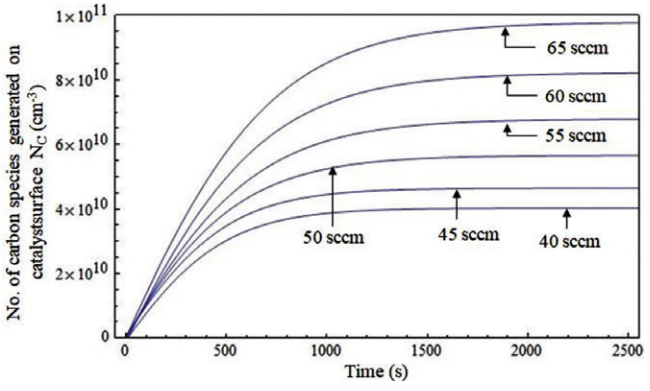

FIGURE 7 Time variation of the number of carbon species per unit area generated on the catalyst nanoparticle surface for different C_2H_2 gas flow rates in C_2H_2/NH_3 plasma, keeping NH_3 gas flow rate constant at 80 sccm. Other parameters are given in the text

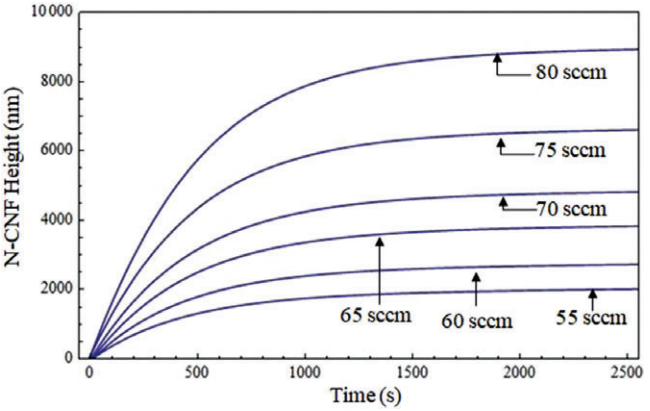

FIGURE 8 Time variation of N-CNF height for different NH_3 gas flow rates in C_2H_2/NH_3 plasma, keeping C_2H_2 gas flow rate constant at 40 sccm. Other parameters are given in the text

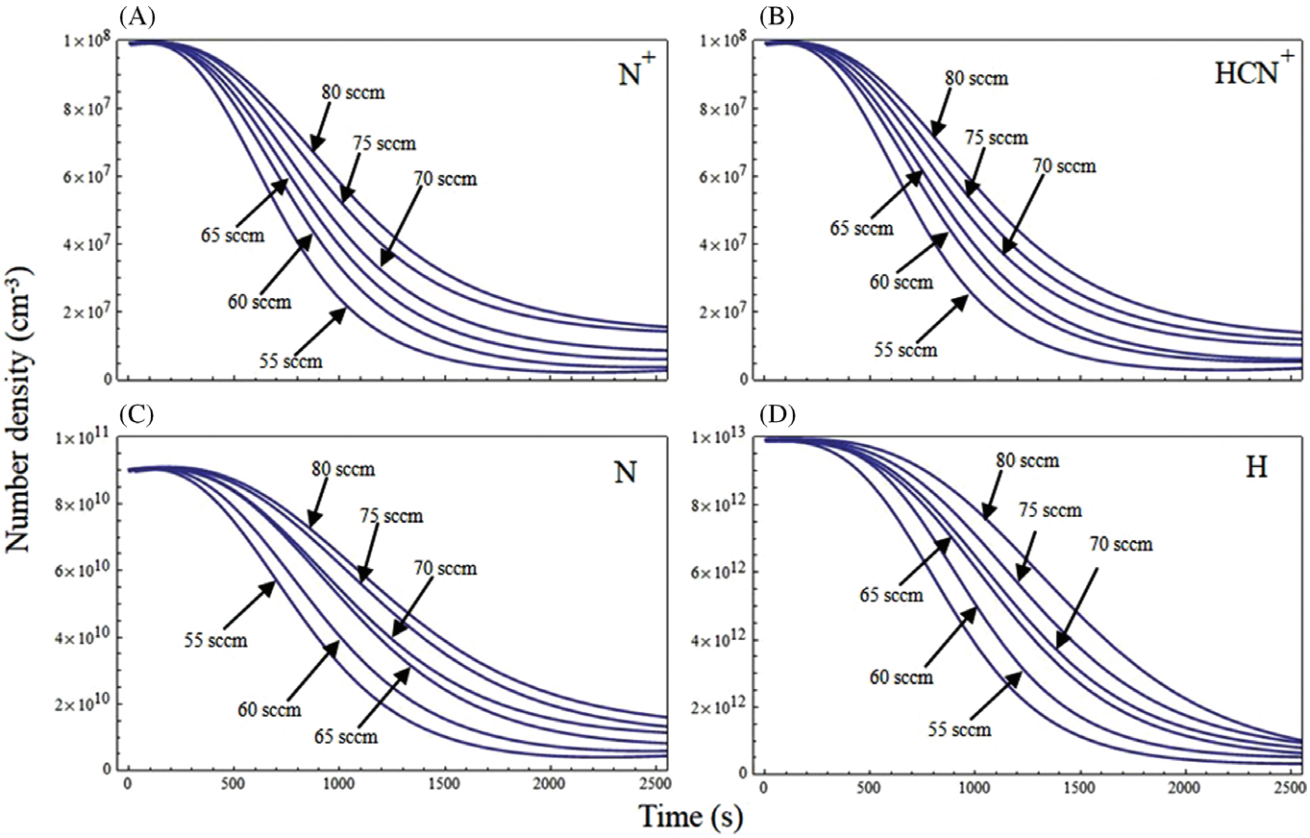

FIGURE 9 Time variation of nitrogen density for (a) N^+, (b) HCN^+, (c) N, and (d) H for different NH_3 gas flow rates in C_2H_2/NH_3 plasma, keeping C_2H_2 gas flow rate constant at 40 sccm. Other parameters are given in the text

decreases when C_2H_2 gas flow rate increases, that is, N-CNFs growth rate decreases with increase in C_2H_2/NH_3 ratio. This result is somewhat surprising because one would think that higher carbon supply content would lead to a higher growth rate. However, the reverse trend is followed in reality. This astonishing growth of N-CNFs can be explained in many ways. One possible explanation is the poisoning of the catalyst particle. As C_2H_2 gas flow rate increases, carbon species generated on the catalyst nanoparticle surface increase (cf. Figure 7), which leads to the formation of a thin amorphous carbon layer on the catalyst nanoparticle surface, which blocks the diffusion of carbon species through catalyst nanoparticles. Thus, N-CNFs grow at a lower rate due to loss of catalytic activity of nanoparticles. The curve obtained in Figure 6b is compared with the experimental data of Merkulov et al.[6]. One can see from this figure that the N-CNFs growth rate curve fits best with the experimental data of Merkulov et al.[6] in the broad range of C_2H_2/NH_3 ratios. However, one might wonder whether the same trend is to be followed if the NH_3 flow rate is varied, keeping the C_2H_2 flow rate constant. Figure 8 shows the time variation of N-CNFs height for different ammonia gas flow rates. From Figure 8, it can be seen that N-CNF height increases with increase in ammonia gas flow rate, and therefore, N-CNF growth rate increases with the decrease in C_2H_2/NH_3 ratio. This is imputable to the fact that number density of etchant species (i.e., N, N^+, HCN^+) increases in the reactive plasma as NH_3 gas flow rate increases [cf. Figure 9a–c]. Moreover, reactions between hydrocarbons, hydrogen, and ammonia in the reactive plasma produce a large amount of active hydrogen (cf. Table 2). Thus, the number density of active hydrogen increases in the plasma, with an increase in NH_3 flow rate [cf. Figure 9d]. Therefore, these species etch the amorphous carbon layer formed on the catalyst surface and contributes to the higher growth rate.

In Figure 10, the dependence of N-CNF tip diameter as a function of C_2H_2/NH_3 ratio is shown for the PECVD case. From Figure 10, it can be seen that the N-CNFs tip diameter decreases with decrease in C_2H_2/NH_3 ratio; that is, reduction in N-CNFs tip diameter is observed when either C_2H_2 content is decreased or NH_3 content is increased in reactive plasma. If the C_2H_2 gas flow rate increases, carbon deposition on the catalyst nanoparticle surface (which is at the tip of the N-CNFs) increases, and consequently, N-CNFs tip diameter increases. However, when the NH_3 inflow rate increases, that is, C_2H_2/NH_3 ratio decreases, the number of etchant species, as explained above, increases in the reactive plasma, and therefore, the relative etching of catalyst nanoparticles increases, and N-CNFs tip diameter decreases. From Figure 10, one can also see that the dependence of N-CNFs tip diameter on C_2H_2/NH_3 ratio fits better with the experimental data of Merkulov et al.[6] A similar effect of the C_2H_2/NH_3 ratio on the tip diameter was observed by Saidin et al.[8]

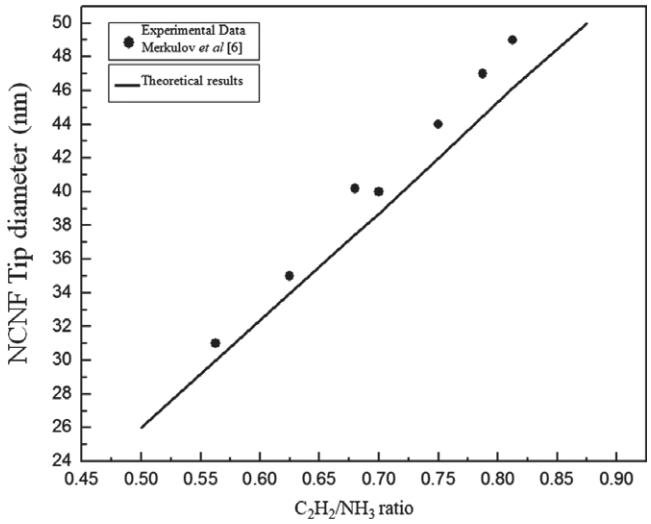

FIGURE 10 N-CNF tip diameter as function of C_2H_2/NH_3 ratio for variable C_2H_2 gas flow rate and constant NH_3 gas flow rate. Other parameters are given in the text

4 | CONCLUSION

An analytical model to study the effects of nitrogen doping on the growth of CNFs and hence the growth mechanism of N-CNFs through PECVD process is developed, and its field emission properties have been estimated. From the results obtained, it can be seen that, on nitrogen doping, the height and the tip diameter of the CNFs decreases. The field enhancement factor β calculated from these results reveals that nitrogen-doped CNFs have enhanced field emission characteristics than undoped CNFs. Moreover, it has also been observed that the C_2H_2/NH_3 gas ratio is the crucial parameter for the N-CNFs growth. The N-CNF growth rate increases and the tip diameter decreases with a decrease in the C_2H_2/NH_3 gas ratio. These results have been explained based on variation in the number density of etchant species in the reactive plasma. The present work is envisioned practically to fabricate the highly efficient CNF-based field emission devices.

ACKNOWLEDGMENT

One of the authors (R.G.) is thankful to the University Grant Comission (UGC) of India for partial support.

REFERENCES

[1] V. I. Merkulov, A. V. Melechko, M. A. Guillorn, D. H. Lowndes, M. L. Simpson, *Appl. Phys. Lett.* **2001**, *79*, 2970.
[2] T. M. Minea, S. Point, A. Granier, M. Touzeau, *Appl. Phys. Lett.* **2004**, *85*, 1244.
[3] P. Serp, M. Corrias, P. Kalch, *Appl. Catal. A* **2003**, *253*, 337.
[4] K. P. De Jong, J. W. Geus, *Catal. Rev. Sci. Eng.* **2009**, *42*, 48.
[5] O. Y. Podyacheva, Z. R. Ismagilov, A. E. Shalagina, V. A. Ushakov, A. N. Shmakov, S. V. Tsybulya, V. V. Kriventsov, A. V. Ischenko, *Carbon* **2010**, *48*, 2792.
[6] V. I. Merkulov, D. K. Hensley, A. V. Melechko, M. A. Guillorn, D. H. Lowndes, M. L. Simpson, *J. Phys. Chem B* **2002**, *106*, 10570.
[7] V. I. Merkulov, A. V. Melechko, M. A. Guillorn, D. H. Lowndes, M. L. Simpson, *Appl. Phys. Lett.* **2002**, *80*, 476.
[8] M. A. R. Saidin, A. F. Ismail, S. M. Sanip, P. S. Goh, M. Aziz, M. Tanemura, *Thin Solid Films* **2012**, *520*, 2575.
[9] K. B. K. Teo, S. B. Lee, M. Chhowalla, V. Semet, V. T. Binh, O. Groening, M. Castignolles, A. Loiseau, G. Pirio, P. Legagneux, D. Pribat, D. G. Hasko, H. Ahmed, G. A. J. Amaratunga, W. I. Milne, *Nanotechnology* **2003**, *14*, 204.
[10] C. Kimura, Y. Yamamuro, H. Aoki, T. Sugino, *Diamond Relat. Mater.* **2007**, *16*, 1383.
[11] J. W. G. Wildoer, L. C. Venema, A. G. Rinzler, R. E. Smalley, C. Dekker, *Nature* **1998**, *391*, 59.
[12] Z. R. Ismagilov, A. E. Shalagina, O. Y. Podyacheva, A. V. Ischenko, L. S. Kibis, A. I. Boronin, Y. Chesalov, D. I. Kochubey, A. I. Romanenko, O. B. Anikeeva, T. I. Buryakov, E. N. Tkachev, *Carbon* **2009**, *47*, 1992.
[13] R. Gupta, S. C. Sharma, R. Sharma, *Plasma Sources Sci. Technol.* **2017**, *26*, 024006.
[14] R. Gupta, S. C. Sharma, *Phys. Plasmas* **2017**, *24*, 073504.
[15] M. Mao, J. Benedikt, A. Consoli, A. Bogaerts, *J. Phys. D Appl. Phys.* **2008**, *41*, 225201.
[16] M. Mao, A. Bogaerts, *J. Phys. D Appl. Phys.* **2010**, *43*(205), 201.
[17] M. S. Bell, R. G. Lacerda, K. B. K. Teo, N. L. Rupesinghe, G. A. J. Amaratunga, W. I. Milne, M. Chhowalla, *Appl. Phhys. Lett.* **2004**, *85*, 1137.
[18] V. I. Merkulov, M. A. Guillon, D. H. Lowndes, M. L. Simpson, E. Voelkl, *Appl. Phys. Lett.* **2001**, *79*, 1178.
[19] C. S. Cojocaru, A. Senger, F. L. Normand, *J. Nanosci. Nanotech.* **2006**, *6*, 1.
[20] N. M. Rodriguez, *J. Mater. Res.* **1993**, *8*, 3233.
[21] G. B. Zheng, K. Kouda, H. Sano, Y. Uchiyama, Y. F. Shi, H. J. Quan, *Carbon* **2004**, *42*, 635.
[22] H. W. Wei, K. C. Leou, M. T. Wei, Y. Y. Lin, C. H. Tsai, *J. Appl. Phys.* **2005**, *98*, 044313.
[23] K. N. Ostrikov, S. V. Viladimirov, M. V. Yu, G. E. Morfill, *Phys. Plasmas* **2000**, *7*, 461.
[24] S. V. Viladimirov, K. N. Ostrikov, M. V. Yu, *Phys. Rev. E* **1998**, *58*, 8046.
[25] A. V. Keudell, W. Moller, *J. Appl. Phys.* **1994**, *75*, 7718.
[26] M. S. Sodha, S. Misra, S. K. Mishra, *Phys. Plasmas* **2010**, *17*, 113705.
[27] D. B. Hash, M. S. Bell, K. B. K. Teo, B. A. Cruden, W. I. Milne, M. Meyyappan, *Nanotechnology* **2005**, *16*, 925.

[28] UMIST. http://www.udfa.net/
[29] I. B. Denysenko, S. Xu, J. D. Long, P. P. Rutkevych, N. A. Azarenkov, K. Ostrikov, *J. Appl. Phys.* **2004**, *95*, 2713.
[30] H. Cui, X. Yang, M. L. Simpson, D. H. Lowndes, M. Varela, *Appl. Phys. Lett.* **2004**, *84*, 20.
[31] I. Denysenko, N. A. Azarenkov, J. Phys, *D: Appl. Phys.* **2011**, *44*(174), 031.
[32] I. Denysenko, K. Ostrikov, *J. Phys. D Appl. Phys.* **2009**, *42*, 015208.
[33] Z. Marvi, S. Xu, G. Foroutan, K. Ostrikov, *Phys. Plasmas* **2015**, *22*, 013504.
[34] I. Denysenko, K. Ostrikov, *Appl. Phys. Lett.* **2007**, *90*(251), 501.
[35] H. Mehdipour, K. Ostrikov, A. E. Rider, *Nanotechnology* **2010**, *21*(455), 605.
[36] I. Denysenko, K. Ostrikov, M. Y. Yu, N. A. Azarenkov, *J. Appl. Phys.* **2007**, *102*, 074308.
[37] M. Yudasaka, R. Kikuchi, T. Matsui, Y. Ohki, S. Yoshimura, E. Ota, *Appl. Phys. Lett.* **1995**, *67*, 2477.
[38] O. A. Louchev, T. Laude, Y. Sato, H. Kanda, *J. Chem. Phys.* **2003**, *118*, 7622.
[39] S. Hofmann, G. Csanyi, A. C. Ferrari, M. C. Payne, J. Robertson, *Phys. Rev. Lett.* **2005**, *95*, 036101.
[40] M. Chhowalla, K. B. K. Teo, C. Ducati, N. L. Rupesinghe, G. A. J. Amaratunga, A. C. Ferrari, D. Roy, J. Robertson, W. I. Milne, *J. Appl. Phys.* **2001**, *90*, 5308.
[41] S. Hofmann, C. Ducati, J. Robertson, B. Kleinsorge, *Appl. Phys. Lett.* **2003**, *83*, 135.
[42] M. Cantoro, V. B. Golovkob, S. Hofmanna, D. R. Williamsa, C. Ducatic, J. Gengb, B. O. Boskovicc, B. Kleinsorgea, D. A. Jeffersonb, A. C. Ferraria, B. F. G. Johnsonb, J. Robertsona, *Diamond Relat. Mater.* **2005**, *14*, 733.
[43] S. Hoffmann, C. Ducati, B. Kleinsorge, J. Robertson, *Appl. Phys. Lett.* **2003**, *83*, 4661.
[44] S. Hofmann, M. Cantoro, M. Kaempgen, D. J. Kang, V. B. Golovko, H. W. Li, Z. Yang, J. Geng, W. T. S. Huck, B. F. G. Johnson, S. Roth, J. Robertson, *Appl. Phys. A* **2005**, *81*, 1559.
[45] C. Bower, W. Zhu, S. Jin, O. Zhou, *Appl. Phys. Lett.* **2000**, *77*, 830.
[46] H. Cui, O. Zhou, B. R. Stoner, *J. Appl. Phys.* **2000**, *88*, 6072.
[47] L. Delzeit, I. McAninch, B. A. Cruden, D. Hash, B. Chen, J. Han, M. Meyyappan, *J. Appl. Phys.* **2002**, *91*, 6027.
[48] K. Matthews, B. A. Cruden, B. Chen, M. Meyyappan, L. Delzeit, *J. Nanosci. Nanotechnol.* **2002**, *2*, 475.
[49] C. H. Weng, C. S. Yang, H. Lin, C. H. Tsai, K. C. Leou, *J. Nanosci. Nanotechnol.* **2008**, *8*, 2526.
[50] J. B. O. Caughman, L. R. Baylor, M. A. Guillorn, V. I. Merkulov, D. H. Lowndes, L. F. Allard, *Appl. Phys. Lett.* **2003**, *83*, 1207.
[51] Y. Y. Lin, H. W. Wei, K. C. Leou, H. Lin, C. H. Tung, M. T. Wei, C. Lin, C. H. Tsai, *J. Vac. Sci. Technol. B* **2006**, *24*, 97.
[52] Y. Shiratori, H. Hiraoka, Y. Takeuchi, S. Itoh, M. Yamamoto, *Appl. Phys. Lett.* **2003**, *82*, 2485.
[53] H. S. Kang, H. J. Yoon, C. O. Kim, J. P. Hong, I. T. Han, S. N. Cha, B. K. Song, J. E. Jung, N. S. Lee, J. M. Kim Chem, *Phys. Lett.* **2001**, *349*, 196.
[54] B. G. Sumpter, V. Meunier, J. M. Romo-Herrera, E. Cruz-Silva, D. A. Cullen, H. Terrones, D. J. Smith, M. Terrones, *ACS Nano* **2007**, *1*, 369.

How to cite this article: Gupta R, Sharma SC. Modelling the effects of nitrogen doping on the carbon nanofiber growth via catalytic plasma-enhanced chemical vapour deposition process. *Contributions to Plasma Physics* 2018;1–14. https://doi.org/10.1002/ctpp.201700138

International Journal of Engineering Technology Science and Research
IJETSR
www.ijetsr.com
ISSN 2394 – 3386
Volume 5, Issue 4
April 2018

Multi-Metal Citrate Complex

Anil Kumar*
Department of Applied Chemistry, Delhi Technological University,
Bawana Road, Delhi , India

Abstract: Hydrothermal synthesis of multi-metal citrate metal-organic framework complexes was carried out using diffrent route of synthesis and characterized by different technioques of spectroscopy.

Keywords: Citric acid; metal-organic framework; powder X- ray diffraction; luminescence; stability.

INTRODUCTION

Metal-organic frameworks comes under the category of coordination polymers with porous crystalline nature. These framework can be easily upgraded by several metals haiving different properties. These complexes shows properties like exceptionally large surface area, tunable structure, high porosity, variable pore dimensions . [1-5] The mixed metal oxides such as hollow ZnO-NiO hybrid microsphere fabricated by the annealing of Zinc-Nickel-Citrate in air constitute the most promising candidates as anode material due to their excellent electrochemical properties, replacing the traditional graphite anodes in lithium ion batteries used in devices such as electric vehicles.

EXPERIMENTAL

Materials and Physical measurements

All the chemicals used were commercially available analytical grade and used as obtained without further purification.

Synthesis of complex **1**: Complex **1** was synthesized by dissolving 10mmol each of $NiSO_4.6H_2O$ and $ZnSO_4.7H_2O$ in 20 mL of double distilled water. Lime juice was squeezed from fresh fruit and strained. 20 mL of fresh lime juice was added to the solution of $NiSO_4.6H_2O$ and $ZnSO_4.7H_2O$. The resultant mixture was heated to 30-40 ºC under stirring for 30 minutes and stirring continued for another four hours. The pH of the reaction mixture was between 3 and 4. The mixture was left undisturbed at room temperature. The bluish green crystals of the complex **1** separated out in 58% yield after 48 hours and subsequently re-crystallized from distilled water.

Synthesis of complex **2**: Complex **2** was synthesized by dissolving 10mmol each of $CuSO_4.5H_2O$ and $FeSO_4.7H_2O$ in 20 mL of double distilled water. The same procedure was followed as reported for complex **1.** Yellow green crystals in 42% yield were obtained after the solution being kept undisturbed for ten days.

Synthesis of complex **3**: Complex **3** was synthesized by dissolving 10mmol each of $CuSO_4.5H_2O$, $FeSO_4.7H_2O$ and $NiSO_4.6H_2O$ in 20 mL of double distilled water. The same procedure was followed as reported for complex **1.** Dark green crystals in 60% yield were obtained after the solution being kept undisturbed for four days.

Synthesis of complex **4**: Complex **4** was synthesized by the same procedure as adopted for complexes 1, 2 and 3 by mixing a solution of 10mmol each of $CuSO_4.5H_2O$, $FeSO_4.7H_2O$, $NiSO_4.6H_2O$ and $ZnSO_4.7H_2O$ in 20 mL of double distilled water with 20 mL of fresh squeezed and strained lime juice. Bluish green crystals were obtained in 54% yield after four days.

International Journal of Engineering Technology Science and Research
IJETSR
www.ijetsr.com
ISSN 2394 – 3386
Volume 5, Issue 4
April 2018

RESULTS AND DISCUSSION

All four complexes have been characterized by Fourier Transform Infrared Spectroscopy, Scanning Electron Microscopy, Energy Dispersive Spectroscopy, Fluorescence spectroscopy and Powder X - ray diffraction techniques. The crystal structure of these complexes could not be established by single crystal X-ray diffraction technique probably due to overlapping of reflections caused by their large unit cells.[6]The stability of these complexes has been established by their Thermogravimetric analysis.

Fourier Transform Infrared spectroscopy of the multi-metal citrate complexes

The Fourier Transform Infrared spectroscopy of the multi-metal citrate complexes synthesized by hydrothermal technique, in KBr indicates the presence of vibrationally active carboxylate group. The FTIR spectra of the complexes exhibit both symmetric and anti-symmetric stretching vibrations of the carboxylate groups present in the coordinated citrate ligand. A strong band between 1630 cm^{-1} and 1620.5 cm^{-1} is assigned to anti-symmetric stretching vibrations while the one between 1401.2 cm^{-1} and 1384.0 cm^{-1} is due to symmetric stretching vibrations of the carboxylate groups of citrate ligand in the complexes.[7] The difference between the anti-symmetric and symmetric stretching vibrations being greater than 200 cm^{-1} suggests that the carboxylate groups of citrate ligand in these complexes are coordinated to metal ions in a mono dentate fashion.[8] A peak at 1726.5cm^{-1} in complex **1** reveals that a fraction of the hydrogen atoms of carboxylate groups of citric acid remain bound while others are replaced by metal atoms forming multi-metal citrate complexes.[9] A similar peak at 1726.7 cm^{-1} and 1724.2cm^{-1} was also observed in complexes when synthesized using commercially available citric acid.[30] A peak around 1100 cm^{-1} in all complexes can be assigned to C-O being coordinated to metal cations.[31] A weak band between 575.5cm^{-1} and 573.0 cm^{-1} in these complexes can be attributed to the in plane vibration of O─C═O group. A vibrational band around 980 cm^{-1} appears due to C-C skeletal bond of citric acid moiety. The characteristic vibrational bands of alcoholic hydroxyl group of citric acid at 3450, 1290, 1265, 1165, 1125, 1060, 925, 890 and 820 cm^{-1} are absent in the FTIR spectra of the prepared complexes. In-plane and out-of-plane O-H bending vibrational bands of carboxylic acid at 1430 cm^{-1} and 930 cm^{-1} also disappear in these complexes. The hydroxyl group of citrate ligand is thus coordinated as shown by Hedwig *et al.* through potentiometric and spectroscopic study for the synthesis of Ni^{2+} complex with citric acid in aqueous solution in the pH range of 3-6. The removal of proton from the hydroxyl group of citric acid depends upon the nature of metal ion bound to citric acid, with Cu bound to citric acid tetraionised Cit^{4-} is formed at pH 4. A broad band between 3732.2 cm^{-1} and 3200 cm^{-1} in these complexes is assigned to hydrogen bonded hydroxyl group of coordinated water, lying between the tetrahedral and octahedral sheets in the complexes. Further two vibrational bands between 765.2 cm^{-1}- 750.7 cm^{-1} and 635.9 cm^{-1}- 615.0 cm^{-1} due to rocking $\rho r(H_2O)$ and wagging $\rho w(H_2O)$ vibrations of water confirm the presence of coordinated water molecules in these complexes. Absorption band at 3154.8cm^{-1} in complex **1** is assigned to symmetric -OH stretching mode associated to tetrahedral coordinated water molecules. Based on their Fourier transform infrared spectroscopy, a layered structure similar to the one reported in the literature for metal carboxylates is thus proposed for the multi-metal citrate complexes synthesized from lime juice in the present research. The infra-red spectra of complexes **1**-**4**.

Absorption and fluorescence spectroscopy

The electronic spectra and fluorescence spectra of the multi-metal citrate complexes **1**-**4** were recorded in water at room temperature. The excitation spectra were recorded from 350 to 600 nm to monitor the transition between the metal 3d orbitals. Each complex shows one absorption line at 392 nm. The crystal-field splitting of the 3d orbital was not observed in the complexes because of the large coordination number. Emission spectra were recorded for **l**-**4** upon excitation at 310 nm and emission was observed in between 400-422 nm, which corresponds to excitation into the lowest energy d-level of metal.

International Journal of Engineering Technology Science and Research
IJETSR
www.ijetsr.com
ISSN 2394 – 3386
Volume 5, Issue 4
April 2018

CONCLUSIONS

The multi-metal citrate complexes synthesized through green synthetic pathways using lime juice squeezed from a fresh fruit as the source of citric acid, are well defined crystalline solids with cubic geometry. These complexes exhibit an extraordinary high thermal stability and possess a highly stable rigid supramolecular structure due to extensive hydrogen bonding between the layers. The devised method has the merits of being a simple one pot synthesis and being environmentally benign as the use of harmful organic solvent such as DEF and DMF has completely been avoided. The extraction of citric acid from citrus fruit or its artificial synthesis, which itself is a time consuming process has been eliminated in the present synthesis. The adopted method is thus appreciably economical in terms of time and energy. The complexes thus prepared may reveal the potential applications in hydrogen storage for mobile applications as a green automobile fuel due to vacant metal sites associated with a combination of metal ions in their structure, as an optical material and in bio-medical field due to their photo luminescent properties.

REFERENCES

1. J. L. C. Rowsell, E. C Spencer, J. Eckert, J. A. K. Howard, O. M. Yaghi, *Science* **309** (2005) 1350.
2. D. Sun, S. Ma, Y. Ke, D. J Collins, H. C. Zhou, *J. Am. Chem. Soc.* **128** (2006) 3896.
3. S. Keskin, *J. Phys. Chem. C* **114** (2010) 13047.
4. I. Erucar, S. Keskin, *Chem. Eng. Sci*. **130** (2015) 120.
5. E. Barea, C. Montoro, J. A. R Navarro, *Chem. Soc. Rev*. **43** (2014) 5419.
6. L. Hu, Q. Chen, *Nanoscale* **6** (2014) 1236.
7. Q. Xie, Y. Ma, D. Zeng, L. Wang, G. Yue, D. L. Peng, *Sci. Rep.* **5** (2015) 8351.
8. O. M. Yaghi, H. Li, *J. Am. Chem. Soc.* **117** (1995) 10401.
9. J. L. Crane, K. E. Anderson, S. G. Conway, *J. Chem. Educ.* **92** (2015) 373.

IOP Conference Series: Materials Science and Engineering

PAPER • OPEN ACCESS

Numerical analysis of THz radiation wave using upper hybrid wave wiggler

To cite this article: Pratibha Malik *et al* 2018 *IOP Conf. Ser.: Mater. Sci. Eng.* **331** 012021

View the article online for updates and enhancements.

Related content

- Terahertz pulses in a periodic plasma channel via modulated electron beam
  Pratibha Malik, Suresh C Sharma and Rinku Sharma
- Terahertz radiation generation by using modulated electron beam with plasma wave wiggler
  J Panwar, S C Sharma and R Sharma
- Lasers drive coherent terahertz radiation

This content was downloaded from IP address 14.139.251.107 on 03/04/2018 at 11:53

IOP Conf. Series: Materials Science and Engineering **331** (2018) 012021 doi:10.1088/1757-899X/331/1/012021

Numerical analysis of THz radiation wave using upper hybrid wave wiggler

Pratibha Malik*[1], Suresh C. Sharma[1], Jyotsna Panwar[1] and Rinku Sharma[1]

[1]Department of Applied Physics, Delhi Technological University, Shahbad Daulatpur, Bawana Road, Delhi-110042, India
*pratibhamalik27@gmail.com

Abstract. A theory for upper hybrid wave induced by relativistic electron beam in magnetized plasma emits tuneable and coherent terahertz radiation. The nonlinear interaction with REB is used to generate terahertz radiation. The enhancement in the amplitude of THz wave is also observed when pre-bunched REB is used. The ponderomotive force applied on beam electrons due to radiation wave and upper wave wiggler modifies the dispersion relation. By solving the dispersion relation, we have derived the growth rate of the radiation wave. Numerical studies indicate that by increasing the beam energy the growth rate of the radiation wave decreases, while it increases with wiggler frequency. Besides this, the growth rate of the radiation wave increases with beam density and decreases with radiation frequency and static magnetic field.

1. Introduction

For past few decades the production of terahertz (0.3- 10 THz) radiation has been witnessed by the researchers in the broad range of spectroscopy, military security, sensing and communications [1-3]. Since several approaches have been demonstrated to generate the terahertz radiation such as laser based sources, electron beam based sources. In electron beam based sources: surface plasmons [4] and free electron lasers (consist of an electron beam and electromagnetic wiggler i.e., provides magnetic field) [5-6], which are the perfect sources for the generation of tuneable high frequency radiation. On account of high cost and larger size the implication of such kind of wigglers are replaced by the plasma wigglers [7]. In this scheme, the upper hybrid wave is employed as an electrostatic wiggler to generate the THz radiation.

2. Enhancement of THz radiation

We consider an upper hybrid wave of potential $\phi = \phi \exp(-i(\omega t - \vec{k}.\vec{r}))$ propagates in x-z plane is being dipped in magnetized plasma (B_1). The interaction of relativistic electron beam ($v_{bo}\hat{z}$) with upper hybrid wave ($\vec{E}_{\omega}$) produces the nonlinear current density and responsible to obtain the nonlinear dispersion relation. The ponderomotive force and nonlinear REB induced upper hybrid wave wiggler is the main mechanism for the enhanced THz radiation emission. We have derived the results using fluid equation model and the equations as mentioned as below.

Content from this work may be used under the terms of the Creative Commons Attribution 3.0 licence. Any further distribution of this work must maintain attribution to the author(s) and the title of the work, journal citation and DOI.
Published under licence by IOP Publishing Ltd

The interaction of REB with upper hybrid wave produces the electron oscillatory velocity $\vec{v}_0$ and taking into account the equation of motion as

1. $$\frac{\partial}{\partial t}(\gamma_1\vec{v})+(\vec{v}.\nabla)(\gamma_1\vec{v})=-\frac{e}{m}\vec{E}_{\omega}-v_0\times(\omega_c\vec{z}) \quad (1)$$

2. Equation of continuity

$$\frac{\partial n}{\partial t}+\nabla.(n\vec{v})=0 \quad (2)$$

3. The magnetic field of the radiation wave

$$\vec{B}=\frac{c}{\omega_1}(\vec{k}_1 x\vec{E}) \quad (3)$$

Here the terms n , $\vec{v}$ and m are defined as density of electrons, velocity and mass of the electron respectively, relativistic gamma factor $\gamma_1=\gamma_{b0}(\approx(1-v_{bo}^2/c^2)^{-1/2})+\gamma_{10}$ and beam velocity $\vec{v}=v_{bo}\hat{z}+\vec{v}_0$. However, the cyclotron frequency is represented as $\omega_c(=eB_1/mc)$.
The electromagnetic wave with electric field $\vec{E}=\hat{x}E\exp(-i(\omega_1 t-\vec{k}_1.\vec{z}))$ is assumed the perturbation field for the equilibrium. In addition, the potential offered by negatively charged beam wave is $\phi_b=\phi_b\exp(-i(\omega_b t-\vec{k}_b.\vec{z}))$.

The frequency of THz radiation wave is calculated as $\omega_1=2\gamma_{b0}^2(k_z v_{b1}+\omega)-2\gamma_{b0}^{1/2}\omega_{pb}$, where $\omega_{pb}=\left(4\pi n_{b1}e^2/m\right)^{1/2}$ is the beam plasma frequency. We obtain the relations as $\omega_1=k_1 c$ and $\omega_b=k_{bz}v_{bo}-\omega_{pb}/\gamma_{b0}^{3/2}$.

However, the beam wave is characterized as $n=n_{b1}+n_{b2}\exp[-i\omega_m(t-z/v_{b0})]+n_{b3}\exp[-i(\omega_1 t-\vec{k}_1.\vec{x})]$ and $n_{b2}=\Delta n_{b1}$, where n_{b1} is the beam velocity at equilibrium. However, n_{b3} is the perturbed density due radiation wave and Δ is the modulation index.

Therefore, the ponderomotive force [8] produced by radiation wave $(\omega_1,\vec{k}_1)$ and wave wiggler $(\omega,\vec{k})$ on beam electrons at $(\omega_b,\vec{k}_b)$ is obtained as

$$\vec{F}_p=-\frac{m}{2}[\vec{v}.\nabla(\gamma_1\vec{v})]-\frac{e}{2c}(v_o\times B) \quad (4)$$

and $$\vec{F}_p=-e\nabla\phi_p$$

After using Eqs. (1), (2) and Eq.(4) and solving them , the nonlinear current density due to ponderomotive force and non-linearity, becomes

$$\vec{J}^{nl}_{(\omega_1,\vec{k}_1)}=-\frac{1}{2}n_{b3}e\vec{v}_0 \quad (5)$$

Now, solving Maxwell's wave equation and simplifying the terms after putting the value of current density and approximate value of static magnetic field, we get instability of the radiation wave and derived the dispersion relation. Thus, the amplification of the radiation wave is perceived as long as the beam velocity is larger than the phase velocity of the radiation wave. In this case, we get the small frequency mismatch i.e., the imaginary part of the radiation frequency $\omega_1=k_1 c+\delta$. This leads to the enhancement in the radiation wave.
The growth rate of the radiation wave i.e., the imaginary part of δ

$$\alpha=\text{Img }\delta=\frac{\sqrt{3}}{2}\left[\frac{\omega^2 v_{os}^2\omega_{pb}[(1+\Delta k_{bz})+\Delta k_{bzo}]|k_z|}{32\omega_1\omega_c\gamma_{b0}^{1/2}}\right]^{\frac{1}{3}}. \quad (6)$$

where $v_{os}(=e\phi k_x/m\omega\gamma_{bo})$ is the measurement of beam oscillatory velocity due to wiggler wave along x-direction. The Equation (6), represents the relation for the growth rate $\alpha(\text{in sec}^{-1})$ of the unstable mode of THz radiation wave.

3. Results and Discussions

The typical parameters are used to analyse the behaviour of terahertz radiation wave in the magnetized plasma: electronic mass m = 9.1x10^{-28} g, electronic charge e = 4.8 x10^{-10} Statcoulomb, electron plasma density $n_p = 4.1x10^{18}\,cm^{-3}$, wiggler wave frequency $\omega = 1.6x10^{14}$ rad/sec, electron cyclotron frequency $\omega_c = 0.2\omega$, 0.15ω, and 0.09ω etc, static magnetic field $B_1 = 100$kG, 105 kG and 111 kG etc. The modulation index Δ ranges from 0 to 1 in the steps of 0.1.

Using Equation (6), we have plotted Figure1, which illustrates the variation of growth rate $\alpha(\text{in sec}^{-1})$ of the radiation wave with beam energy γ_{b0} and radiation frequency $\omega_1(\text{in rad/sec})$. This figure reveals that the growth rate decreases with beam energy and radiation frequency. The physical mechanism may be: As long as the beam velocity is larger than the phase velocity of the radiation wave, the amplification in the growth rate of unstable radiation mode keeps on rising.

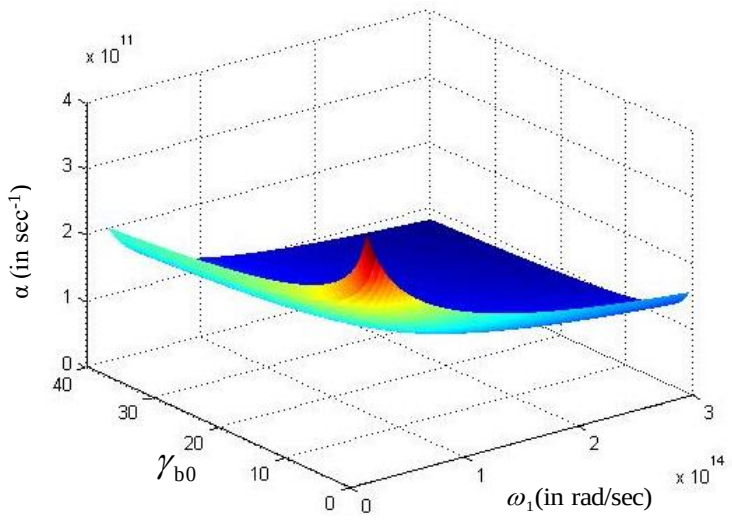

Figure 1: Variation of growth rate $\alpha(\text{in sec}^{-1})$ of radiation wave with radiation frequency $\omega_1(\text{in rad/sec})$ and beam energy γ_{b0} at modulation index $\Delta = 0.8$.

However, Figure 2 depicts the variation of growth rate $\alpha(\text{in sec}^{-1})$ of the unstable radiation mode with static magnetic field $\omega_c(\text{in rad/sec})$ and beam density $n_{b1}(\text{in cm}^{-3})$ of electrons. In this sketch, we see that the growth rate of radiation unstable mode increases with beam density but decreases as static magnetic field increases [9]. The reason may be understood as: for the increased values of magnetic field, the amplitude of the radiation wave is suppressed.

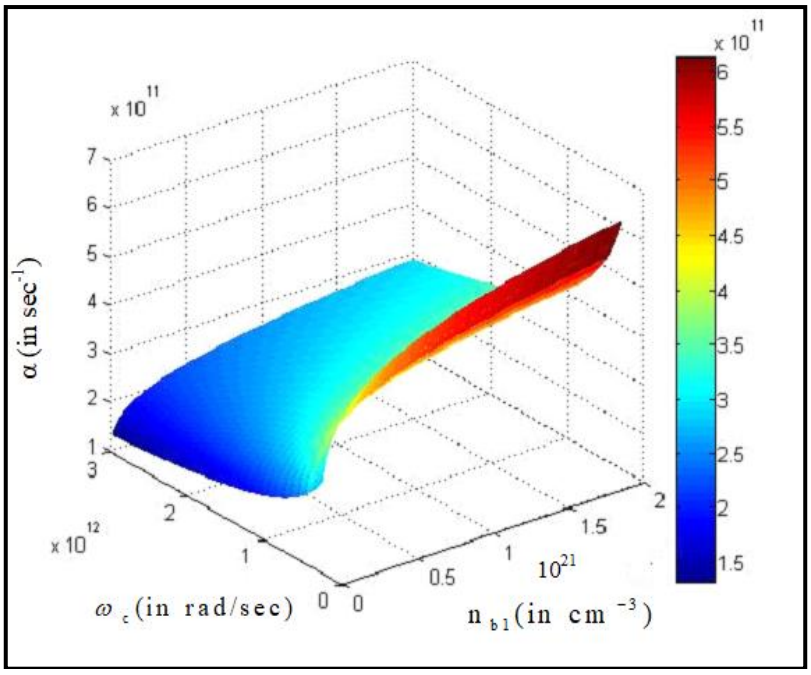

Figure 2: Variation of growth rate $\alpha(\text{in sec}^{-1})$ of radiation wave with cyclotron frequency $\omega_c(\text{in rad/sec})$ or magnetic field B_1 and beam density $n_{b1}(\text{in cm}^{-3})$ at modulation index $\Delta = 0.6$.

4. Conclusion

The present work shows the possibility of upper hybrid wave as a wiggler for producing the coherent terahertz radiation. The interaction of relativistic electron beam with such wiggler is analogous to free electron laser, which shows the coherence and tuneability of the radiation in THz frequency range, if phase matching conditions are satisfied. The nonlinear current is involved to obtain the nonlinear dispersion relation and that leads to the instability of growth rate of the radiation wave.

References

[1] Mittleman D M, Jacobsen R H, and Nuss M C 1996 *IEEE J. Sel. Top. Quantum Electron* **2** 679
[2] Ferguson B and Zhang X C 2002 *Nat. Mater.***1** 26
[3] Pickwell E and Wallace V P 2006 *J. Phys. D* **39,** 301
[4] Sharma S C and Malik P 2015 *Phys. Plasmas* **22** 043301
[5] Dattoli G , Ottaviani P L and Renieri A 2005 *Laser Part. Beams* **23** 303
[6] Geddes C G R, Toth C, Van Tilborg J, Esarey E, Schroeder C B, Bruhwiler D, Nieter C, Cary J and Leemans W P 2004 *Nature* **431** 538
[7] Joshi C, Katsouleas T, Dawson J M, Yan Y T and Slater Jack M 1987 *IEEE J. Quant. Electron* **23,** 1571
[8] Liu C S and Tripathi V K, 1994 *Interaction of Electromagnetic Waves with Electron Beams and Plasmas* (World Scientific publishing Co. Pvt. Ltd., Singapore)
[9] Namiot V A and Shchurova L Y 2011 *Phys. Lett.* A **375** 2759

This article has been accepted for inclusion in a future issue of this journal. Content is final as presented, with the exception of pagination.

Pentavariate $V_{\min}$ Analysis of a Subthreshold 10T SRAM Bit Cell With Variation Tolerant Write and Divided Bit-Line Read

Shourya Gupta, *Student Member, IEEE*, Kirti Gupta, *Member, IEEE*, and Neeta Pandey, *Senior Member, IEEE*

***Abstract*— Subthreshold and near-threshold operations are viable approaches towards reducing both static and dynamic power in Static Random Access Memory (SRAM). However, supply scaling in SRAM cells is severely limited by process variations. Additionally, cell performance is greatly affected by local mismatch in subthreshold region, thereby prohibiting low voltage operation. In order to mitigate these issues, we present a ten-transistor (10T) SRAM cell with capability of performing a variation tolerant write operation in deep subthreshold region without the implementation of additional peripheral circuitry or assist technique. The unique topology of the proposed cell also aids in reducing the bit line offset voltage, thereby improving read access performance. In addition to read and write performance, the hold stability has also been improved, resulting in significant V_{min} gains. The V_{min} of all cells has been evaluated at the 6σ failure point ($P_{Fail} = 10^{-9}$) using a comprehensive pentavariate probability anaylsis, considering both static and dynamic measures. At respective V_{min}, the proposed 10T cell consumes up to 39× and 6.6× lower hold power than the conventional 6T and 8T cells, making it a viable candidate for portable electronics or low power sensors.**

***Index Terms*— 10T SRAM, data retention voltage, leakage current, low power, subthreshold, V_{min}, write margin.**

I. Introduction

STATIC Random Access Memory, which forms a significant portion of system-on-a-chip (SoC) has become an area of significant interest due to the emergence of battery powered portable devices and very low power sensor applications. Scaling of supply voltage for quadratic reduction in active power and linear reduction in standby power has been a popular choice but is severely limited by process-voltage-temperature (PVT) variations in deep sub-micrometer region [1]. With nominal supply voltages, the active power dominates over standby power. But as power supply is scaled down, switching power is reduced greatly due to its quadratic relation with current, thereby making standby power the dominant component [2]. However, this also leads to significant loss in performance due to diminished V_{DD}–V_{TH}, which leads to several orders of magnitude of reduction in frequency. Although there is an overall reduction in power consumption, the exponential increase in delay at low V_{DD} increases the total leakage power consumption per instruction [3]. This contention among the different trends of scaling results in a point where energy per cycle reaches minimum value. This point is usually near the subthreshold region, making subthreshold and near-threshold operation a viable approach for low power applications. But achieving subthreshold operation is a challenge in itself. It is greatly affected by V_{TH} mismatch due to random dopant fluctuations (RDF) and line edge roughness (LER), thereby limiting memory yields [4]. The device mismatch in deep sub-micrometer technologies is greatest in minimum sized devices, which is often the case with SRAMs [5]. Subthreshold operation in SRAMs is also greatly limited by cells at the *Slow nMOS-Fast pMOS* (SF) corner. At SF corner, the pMOS becomes stronger than an equivalently sized nMOS. This effect is exacerbated at lower temperatures due to the relative increase in pMOS's subthreshold slope [4]. Since pMOS current becomes greater than nMOS current, the required strength ratio for a write operation is severely degraded.

To enable low voltage operations, many bit cell designs have been proposed [6]–[13], [15]–[19]. Some of these designs attempt to internally weaken feedback of inverters [6] or weaken the supply path [7], [8]. While these designs improve upon the conventional cells, they still suffer from ultra-low voltage write incapability or hold stability problems. Some cells have asymmetric sizing to improve margins [9], [10]. However, increased sizing not only decreases memory density but may also increase leakage currents and bit line/word line capacitances, thus increasing delay and power. Some cells incorporate a multi-V_{TH} design [11]–[13]. But the implementation of multiple threshold devices in close vicinity is both expensive and difficult to fabricate [14]. The design in [15] exploits the reverse short channel effect to reduce V_{TH} but the improved performance comes at the expense of significant area overhead and increased leakage power. The SRAM cell in [16] improves read performance by decoupling the read port from write port while still maintaining a differential scheme. However, its write performance deteriorates at lower voltages due to its use of two pass transistors in series. Some designs such as the supply feedback SRAM [17] and the Schmitt Trigger based SRAMs [18], [19] have been quite successful at performing low voltage write operations,

Manuscript received October 6, 2017; revised December 21, 2017 and January 31, 2018; accepted February 27, 2018. This paper was recommended by Associate Editor I. Kale. *(Corresponding author: Shourya Gupta.)*

S. Gupta and K. Gupta are with the Bharati Vidyapeeth's College of Engineering, New Delhi 110063, India (e-mail: shourya.gupta94@gmail.com).

N. Pandey is with the ECE Department, Delhi Technological University, Delhi 110042, India.

Color versions of one or more of the figures in this paper are available online at http://ieeexplore.ieee.org.

Digital Object Identifier 10.1109/TCSI.2018.2813326

1549-8328 © 2018 IEEE. Personal use is permitted, but republication/redistribution requires IEEE permission.
See http://www.ieee.org/publications_standards/publications/rights/index.html for more information.

This article has been accepted for inclusion in a future issue of this journal. Content is final as presented, with the exception of pagination.

but these still suffer from reduced read access performance and sense amplifier input offset problems.

The main limitation of novel bit cell design is that they often improve only one of the read, write and hold operations. It is imperative that the read, write and hold operations be improved simultaneously for continuous supply voltage scaling. This is because continuous scaling can be done to the V_{min} point, which is the minimum supply level at which the cell can perform all the three operations. Often, an assist technique is implemented in order to improve restricted cell performance. In general, assist techniques work in a targeted manner in order to improve performance limited by process variations. These include the problematic worst-case SF corner for write ability, *Fast nMOS-Slow pMOS* (FS) corner for read and hold stability, SF corner for read-access, FS corner for bit line voltage offset etc. However, the implementation of a dedicated assist to resolve limitations imposed by a specific corner can be inefficient in terms of area and energy due to meagre gains in performance at other corners. Also, the V_{min} improvement in a particular operation gained by implementing an assist may not help in overall V_{min} reduction. Still, assists remain a valuable tool in cases where performance bottleneck is due to a specific issue. Some of the assist techniques include diminished bit cell supply voltage and world-line underdrive [20], negative bit line [21], [22], boosted word-line [23], boosted cell ground [24] and negative cell ground [25]. However, supply collapse and ground and bit line boost techniques degrade the hold stability of half selected cells. The word line underdrive degrades the write ability of cells. And the application of a negative rail is challenging. Transient voltage collapse (TVC) technique has also been used to enable a low voltage write operation by momentarily collapsing the cell supply path. However, conventional TVC circuits which implement simpler biasing circuits to lower SRAM supply voltage have significant energy overheads. A recent work [26] gets around this problem by implementing a capacitive charge shared TVC circuit with a self-timed pulse for controlling the magnitude of voltage collapse.

However, the implementation of an assist poses challenges of its own. It may require one or more additional rails or layers and the routing and placement of which may increase cost. The designer has to be meticulous about the assist's peripheral control logic and its proper timing and delivery analysis. Assist implementation not only increases energy per access but also increases area, which is a significant trade-off, given the rising demand for larger and denser memories.

In this work, we propose a ten-transistor cell with write operation capability in deep subthreshold region for low power applications without the need of a dedicated write assist circuit. The issue of reduced read access performance in larger SRAM macros has also been addressed in the proposed 10T bit cell. In addition to the improvement in read access and write performance, the proposed cell also exhibits improved hold stability, resulting in significant V_{min} gains. The proposed cell has been compared with the well-known 6T and 8T SRAM cells (Fig. 1) in this work. Additionally, two 10T SRAM cells, shown in Fig. 1 have also been included in the performance evaluation and comparison.

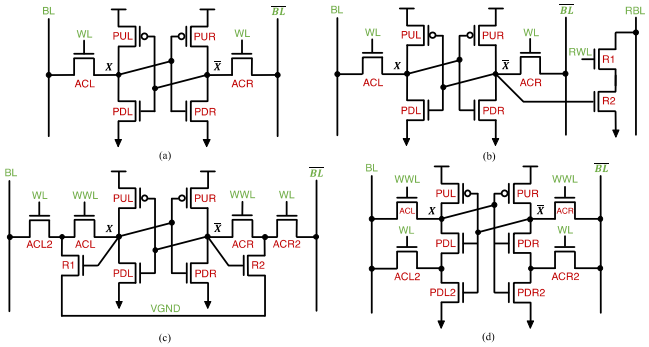

Fig. 1. Schematic of different SRAM cells (a) 6T cell (b) 8T cell (c) 10T diff. cell [16] (d) 10T ST cell [19].

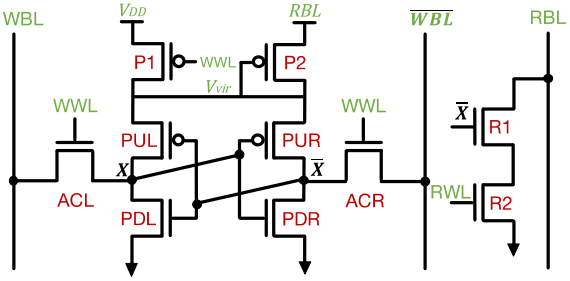

Fig. 2. Schematic of the proposed 10T cell.

The paper has been constructed as follows. Section II describes the proposed cell architecture and its working, Section III includes the SRAM pentavariate V_{min} evaluation of various bit cells, Section IV describes the improved read access of the proposed bit cell and Section V discusses its layout and area. Section VI summarizes and concludes the paper.

II. Proposed 10T SRAM Bit Cell

A. Topology of Proposed Bit Cell

The topology of the proposed 10T SRAM cell is shown in Fig. 2. It comprises of cross coupled inverters (PUL-PDL and PUR-PDR) which store one-bit information. Access transistors (ACL and ACR) are used to write into the cell. Two nMOS (R1 and R2) are used to perform a single ended read operation. Two pMOS (P1 and P2) help to enable low voltage write operations. This implementation has been explained in the next section.

B. Proposed Bit Cell Working Mechanism

A write operation in subthreshold region can be made possible by weakening the supply path in some way or another. In order to weaken the supply path during a write operation, a floating metal line has previously been used [27], [28]. Yamaoka *et al.* [27] separate the V_{DD} line of each column and connect it to a power switch which is enabled by a separate signal. During a write operation, the V_{DD} line of each column is floated by disabling the power switch. However, such an implementation leads to the instability of unselected cells.

This article has been accepted for inclusion in a future issue of this journal. Content is final as presented, with the exception of pagination.

Also, the combined leakage from all cells on a single column may lower the floating supply metal line even further, often causing data retention problems for both selected and unselected cells. Moreover, the separate signals and power lines may require additional metal layer for routing, which may further increase cost. It also requires special write drivers to implement the logic, which may increase design time and layout area. Calhoun *et al.* [28] float the supply line row wise. The rows, comprising of 10T cells are "folded," which means that the supply line is shared amongst cells of two rows at a time. Although, the implementation in [28] allows subthreshold write operation, it still has its problems. Since the supply line is shared amongst two rows at a time, all unselected cells are prone to stability problems. The combined leakage and write operation current from all the cells on two rows may also inadvertently pull down the virtual supply line during a write operation. This in turn puts a limitation on the number of cells implemented per row. Even if a separate supply line is made available for each row, the area overhead penalty can be very large. Since the basic structure of the cell in [28] still remains the same as the 6T cell, the overall cell leakage largely remains unchanged. Our work presented here presents a better solution to all the issues mentioned above while simultaneously achieving subthreshold write operation.

During a write operation, the supply line is disconnected from the cell using the P1 pMOS. The cell supply is instead connected to the read bit line through P2 pMOS. Due to the flow of write current during the write operation, a fall in the gate voltage of the P2 pMOS occurs. This leads to a gradual increase in its current drive. However, this in turn increases the gate voltage again and leads to its weakening. Thus, the P2 pMOS remains in contention and acts like a weak source which is similar in nature to a floating metal line. Due to the large capacitance of the read bit line, the continuous action of the keeper pMOS and the fact that only one active bit cell is connected to the read bit line during a write operation, it remains at supply level. After the write operation ends, P1 pMOS is turned back on and the cell supply is reconnected to the power rail. Since each cell of the selected row is connected to its own supply line, the limitation on number of cells per row is also resolved. Also, no additional peripheral circuit or supply lines are needed for such an implementation. The proposed write mechanism helps to perform variation tolerant writes even in deep subthreshold region. To simply illustrate the variation tolerant write ability of the proposed cell, a comparison of the write margin of the proposed 10T cell against a conventional 6T cell is shown in Fig. 3. The comparison is evaluated on the 32nm technology node using a 1 000-point Monte Carlo simulation under global and 1σ independent local process variations. As shown in Fig. 3, the proposed cell exhibits a much larger write margin and much lower variation than the conventional cell. A detailed write ability analysis is presented in the next section.

The read operation of the proposed cell is same as that of the conventional 8T cell, using two nMOS (R1−R2) to perform a single ended read operation. During the hold mode, the P1 pMOS is always on, resulting in stable storage of a single bit data by the cross coupled inverter pair. Fig. 4 shows

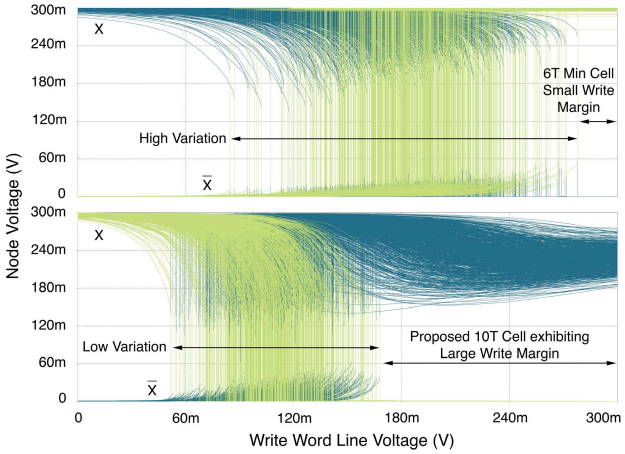

Fig. 3. Comparison of the proposed 10T cell and 6T mincell in terms of variation and write ability (1000-point Monte Carlo simulation under global and local process variations).

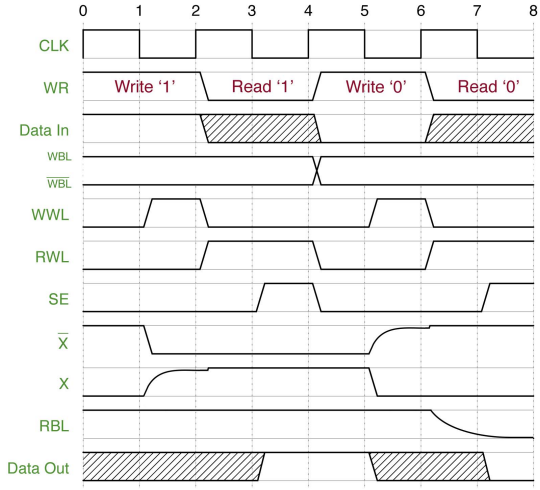

Fig. 4. Timing diagram for subsequent write and read operations in the proposed cell.

the subsequent read and write operations for the proposed cell. When a write operation begins, the data is loaded on to the bit lines (WBL and $\overline{WBL}$) and the write word line (WWL) is enabled. The new data is written into the cell, as represented by the change in X and $\overline{X}$. The toggle of WWL back to low level marks the end of the write operation. During a read operation, the read word line (RWL) is enabled and a drop in the read bit line is allowed to develop conditionally. Both the RWL and WWL control signals are enabled at the negative edge of the clock (CLK). The sense-enable (SE) is toggled during the second half of the read operation, to allow a sense mechanism to produce logical output.

III. SRAM Bit-Cell $V_{\min}$ Analysis

The design of large SRAMs, which can range in size up to several MBs, require millions of Monte Carlo runs to ensure desired failure probability and yield. However, the large

This article has been accepted for inclusion in a future issue of this journal. Content is final as presented, with the exception of pagination.

TABLE I
CELL DIMENSIONS

S. No.	Bit Cell Topology	ACL/ACR	PUL/ PUR	PDL/PDR	R1/R2	ACL2/ACR2	PDL2/PDR2	P1/P2
1	6T Mincell	72	72	144	-	-	-	-
2	6T Iso-Area Cell	216	216	432	-	-	-	-
3	8T Mincell	72	72	72	72	-	-	-
4	8T Iso-Area Cell	504	72	72	72	-	-	-
5	10T Diff. Cell	72	72	72	72	72	-	-
6	Schmitt Trigger Cell	72	72	72	-	72	72	-
7	**Proposed 10T Cell**	72	108	54	72	-	-	72

number of simulations required in this approach can be computationally expensive. Therefore, in this work, we opt for an analytical modelling based approach in order to reduce the number of required sample runs to just a few. This approach is based on establishing that performance parameters following a Gaussian distribution can be easily modelled as a linear function of random parameter variations in various transistors of the SRAM cell. Consequently, the failure probability and yield can be easily predicted. This has been explained and verified in the following subsection.

When calculating the V_{min} of different SRAM cells, it is important to take into consideration the area occupied by each cell. This is because an increase in device sizing lowers variations and V_{min}, thereby increasing yield. The proposed 10T cell consumes approximately twice the area of the conventional 6T mincell, therefore it is only fair to compare the 6T cell with the proposed cell under iso-area conditions. Since any resizing along the vertical direction will cause large increase in bit line capacitance and power, the cell has been resized laterally for iso-area analysis. The 8T cell has a decoupled read and write operation and thus for its iso-area analysis, all sizing increase has been made in the width of its access transistors. Table I shows the device sizing for all the cells considered in this work. All simulations have been performed on the 32nm technology node.

A. Write Failure Probability

The write failure probability is calculated by measuring the write margin of the cell. According to [29], the write margin of a cell signifies its write ability. A higher write margin translates to ease of writing, while a lower write margin translates to a harder write operation. A well-balanced write margin is necessary to ensure required write ability while simultaneously safeguarding the cell against unwanted writes. Reference [30] proves that the definition of write margin presented in [29] is the most appropriate and closest assessment of actual cell write ability. Therefore, the same metric has been used to evaluate the write ability of all cells in this work.

The variation in threshold voltage due to Random Dopant Fluctuations ($\sigma_{VT,RDF}$), transistor length variations ($\sigma_{VT,L}$), Random Telegraphic Noise ($\sigma_{VT,RTN}$), and other sources of variability ($\sigma_{VT,Other}$), which affect stability and performance of the cell can be modelled as

$$\sigma_{VT} = \sqrt{\sigma^2_{VT,RDF} + \sigma^2_{VT,L} + \sigma^2_{VT,RTN} + \sigma^2_{VT,Other}} \quad (1)$$

For a given technology with given minimum transistor sizing (W_{min} and L_{min}), the deviation in threshold voltage ($\sigma V_{th,i}$) for any transistor can be calculated as

$$\sigma V_{th,i} = \sigma_{VT} \times \sqrt{\frac{L_{min} W_{min}}{(LW)}} \quad (2)$$

To calculate the write failure probability, the dependence of differential coefficients on deviation in V_{TH} must be determined first.

If $x_1, x_2, \ldots x_n$ are independent Gaussian random variables with mean η_i and variance σ_i, then the function $y = f(x_1, x_2, \ldots x_n)$ can be expressed using the multivariable Taylor series expansion as

$$f(x_1, \ldots x_n) = f(\eta_1, \ldots \eta_n) + \sum_{i=1}^{n} \left.\frac{\partial f}{\partial x_i}\right|_{\eta_1, \ldots \eta_n} (x_i - \eta_i) + r(x_1, \ldots x_n) \quad (3)$$

where $r(x_1, x_2, \ldots x_n)$ is the higher order term. If $r(x_1, x_2, \ldots x_n)$ is small, $f(x_1, x_2, \ldots x_n)$ can be approximated to a linear combination of x_i's. Then, the mean and the variance of y, i.e., μ_y and σ_y, respectively, can be expressed as follows

$$\mu_y = f(\eta_1, \eta_2, \ldots \eta_n) \quad (4)$$

$$\sigma_y^2 = \sum_{i=1}^{n} \left(\left.\frac{\partial f(x_1, x_2, \ldots x_n)}{\partial x_i}\right|_{\eta_1, \ldots \eta_n} \right)^2 \sigma_i^2 \quad (5)$$

Therefore, applying these expressions to an SRAM cell, the variance of write margin, can be related to the V_{TH} of transistors as

$$\sigma^2_{WM} = \sum_{i=1}^{n} \left(\frac{\partial WM}{\partial Vth_i} \right)^2 \sigma^2_{Vthi} \quad (6)$$

The sum is taken over all the transistors in a given cell. In this work, the differential coefficients have been evaluated for $3/\mu = 30\%$ independent variation in threshold voltage of each transistor. The differential coefficients for the 6T mincell have been evaluated and shown in Fig. 5. As shown in Fig. 5, the differential coefficients are constant over a wide range of variation in threshold voltage and thus, the write margin is expected to follow a Gaussian distribution. Similarly, the linear behavior of differential coefficients can be demonstrated for other cells. If the evaluated differential coefficient with respect to change in threshold voltage variation in a particular

This article has been accepted for inclusion in a future issue of this journal. Content is final as presented, with the exception of pagination.

TABLE II
V_{min} COMPARISON OF VARIOUS BIT CELL TOPOLOGIES

S. No.	Bit Cell Topology	Write V_{min} (mV)	Read V_{min} (mV)	Hold V_{min} (mV)	Write Access V_{min} (mV)	Read Access V_{min} (mV)	Normalized Area	Trivariate V_{min} (mV)	Pentavariate V_{min} (mV)
1	6T Mincell	748	985	500	795	722	1	985	985
2	6T Iso-Area Cell	686	602	330	688	572	2	686	688
3	8T Mincell	730	465	465	785	Fail*	1.15	730	-
4	8T Iso-Area Cell	375	465	465	583	Fail*	2	465	-
5	10T Diff. Cell	842	465	465	855	860	2.3	842	860
6	10T ST Cell	587	464	386	758	894	2	587	894
7	**This Work**	338	420	420	707	737	2	420	737

*Failed to reach desired probability under given set of constraints

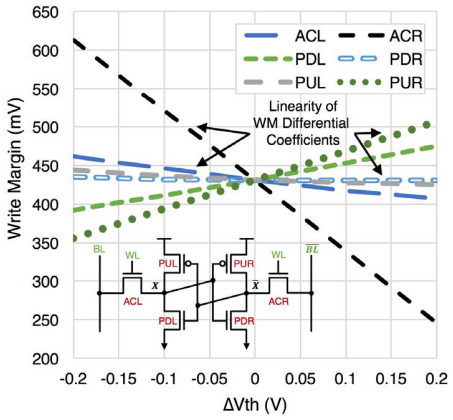

Fig. 5. Write Margin with varying independent V_{TH} deviation in all transistors of 6T mincell.

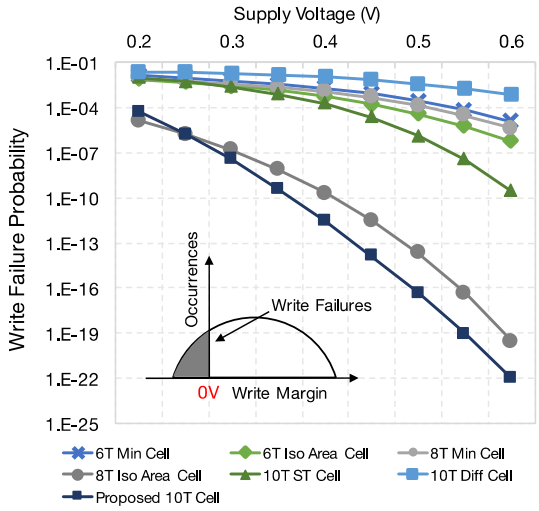

Fig. 6. Write failure probability for various cells.

transistor is zero or negligible, then it maybe concluded that the transistor does not have an impact on the write margin. The write failure probability is then evaluated as

$$P_{fail} = \int_{-\infty}^{-\frac{\mu_{WM}}{\sigma_{WM}}} \frac{1}{\sqrt{2\pi}} exp\left(\frac{-x^2}{2}\right) dx \tag{7}$$

And the write yield loss Y_W as

$$Y_W = N \times P_{fail} \tag{8}$$

where N is the number of cells [30]. The write failure probability with varying supply voltage for different cells has been calculated and shown in Fig. 6. The write V_{min} is determined at the 6σ failure probability (i.e., $P_{WM-Fail} = 10^{-9}$). As seen in Fig. 6, the 10T diff. cell exhibits degraded write ability due to the use of two series connected nMOS. The write V_{min} for the 10T diff. cell was found to be 842mV. To combat the write issue, the authors in [16] boosted both the write word line and word line by 100mV. However, this resulted in an area overhead. As seen in Fig. 6, the 8T iso-area cell exhibits enhanced write ability. This is due to the fact that the access transistors are $7\times$ wider than the pull up pMOS. The proposed 10T cell shows enhanced write ability in subthreshold region, achieving a write V_{min} of 338mV. The 6σ write V_{min} comparison for all cells is shown in Table II.

B. Read Failure Probability

The read failure probability is calculated by measuring the read static noise margin. This noise margin metric was defined first in [31] as the side length of the largest square that can be embedded in the butterfly curve. If the read static noise margin falls below the thermal voltage ($kT = 26$mV at 300K), the bit cell data may be corrupted due to thermal noise. The read failure probability is estimated in a similar manner as the write failure probability. It is determined at the 6σ failure probability (i.e., $P_{RSNM-Fail} = 10^{-9}$). The read failure probability for different cells is shown in Fig. 7. As seen in Fig. 7, the failure probability for the 6T cell is very high, limiting low voltage operation. The iso-area 6T cell shows lower failure probability due to increased sizing. The 10T ST cell shows lower read failure probability due to its inherent process tolerance. The proposed 10T cell has a decoupled read operation and the cell nodes are not disturbed during a write operation. As such, its read failure probability is equivalent to its hold failure probability. Similarly, for all other cells with a decoupled read operation, the read failure probability is equivalent to its hold failure probability. The hold failure probability has been evaluated in the next section.

C. Hold Failure Probability

The hold failure probability is calculated by measuring the hold static noise margin. This noise margin metric was defined

This article has been accepted for inclusion in a future issue of this journal. Content is final as presented, with the exception of pagination.

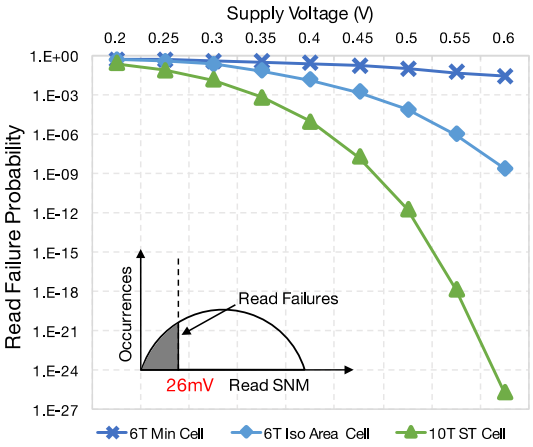

Fig. 7. Read failure probability for various cells.

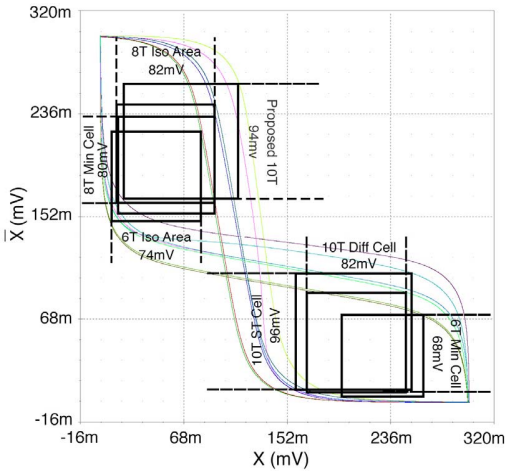

Fig. 8. Nominal HNM comparison for various cells at $V_{DD} = 0.3V$.

first in [31] as the side length of the largest square that can be embedded in the butterfly curve. For a nominal comparison between the hold noise margin (HNM) of all cells considered in this work, the butterfly curves have been plotted in Fig. 8. The curves were plotted on the typical corner at $V_{DD} = 0.3V$ and 27°C. As seen in Fig. 8, the proposed 10T cell has the second highest hold noise margin amongst all the cells considered. While the proposed cell has a higher nominal hold noise margin, its hold failure probability is higher than the 6T iso-area cell and the Schmitt Trigger based cell. This has been explained next.

The hold failure probability is estimated in a similar manner as the read failure probability. The hold failure probability is determined at the 6σ failure probability (i.e., $P_{RSNM-Fail} = 10^{-9}$). The hold failure probability for different cells is shown in Fig. 9. As seen in Fig. 9, the failure probability for the 6T and 8T cells is high. Since the sizing of the cross coupled inverters of each of the 8T mincell, 8T iso-area cell and 10T diff. cell is same, their hold failure probability is also the same. The iso-area 6T cell has the lowest failure probability due to increased sizing. The Schmitt Trigger SRAM cell has low hold failure probability due to the feedback nature it possesses. The proposed 10T cell has

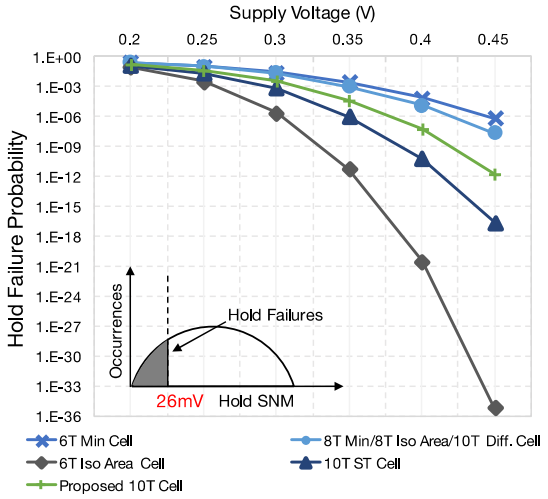

Fig. 9. Hold failure probability for various cells.

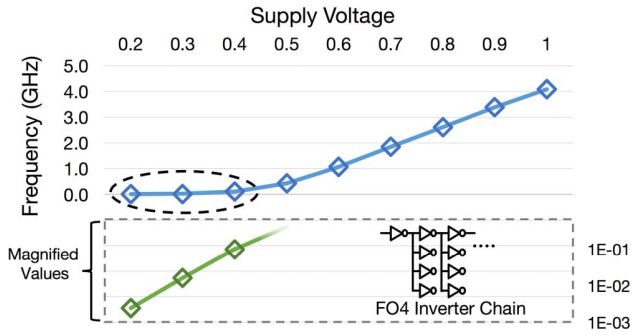

Fig. 10. Clock frequency variation with respect to change in supply voltage.

lower hold failure probability than the conventional 6T and 8T mincells. This is because the pull-up pMOS of the inverters have been widened to twice the minimum width, thereby improving its hold noise margin. The proposed 10T cell has highly enhanced write ability, and thus its pull-up pMOS can be widened without affecting much of its write capability. This approach of increasing the width of pull-up pMOS to ensure a higher hold margin is not possible in conventional cells which depend upon a higher access to pull-up transistor strength ratio for a successful write operation.

D. Write Access Failure Probability

The probability failure analyses given above assume static conditions and do not account for the dynamic ability of an SRAM cell. For example, a write operation may be successful when the allowed time to write is large but might fail for shorter duration of pulses. Therefore, all operations pertaining to an SRAM cell are subject to timing constraints and consequently, in addition to static margins, their dynamic performance must also be evaluated. In order to evaluate dynamic ability, the clock period must be evaluated first. The clock frequency varies with respect to supply voltage and thus has been calculated by assuming one clock period as the delay of 20 minimum sized fan-out of four inverters. The frequency variation with respect to supply voltage scaling is shown in Fig. 10.

This article has been accepted for inclusion in a future issue of this journal. Content is final as presented, with the exception of pagination.

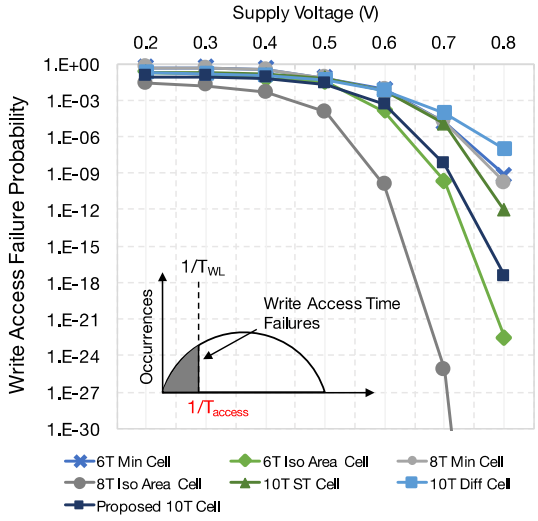

Fig. 11. Write access failure probability for various cells.

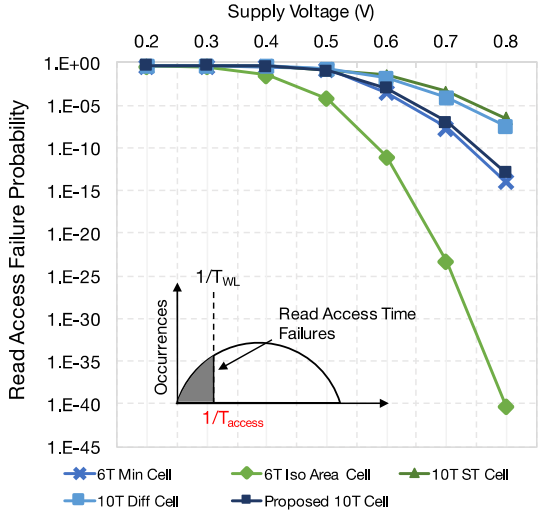

Fig. 12. Read access failure probability for various cells.

Write failure is caused when an SRAM cell is unable to reach desired value in the time duration of the clock pulse width. For a successful write operation, the node storing 'one,' must be pulled down before the end of the word line pulse. Therefore, in this case, the write failure probability can be expressed as

$$P_W = Prob\left(T_W < T_{WL}^W\right) \tag{9}$$

where T_W is the time required to pull down the node storing 'one' and T_{WL}^W is the write word line pulse width. T_W cannot be easily approximated because its distribution has a tail. Evaluation of the tail is necessary because it determines the write access failure probability. However, it has been shown in [32], that the inverse of T_W follows a normal distribution which can be easily approximated. Therefore, the write access failure probability can be calculated by evaluating the sensitivities of $(1/T_W)$ with respect to threshold voltage variation.

$$P_W = Prob\left(\frac{1}{T_W} < \frac{1}{T_{WL}^W}\right) = \Phi\left(\frac{\frac{1}{T_{WL}^W} - \left(\frac{1}{T_W}\right)_{nom}}{\sigma_W}\right) \tag{10}$$

where σ_W is the standard deviation of $(1/T_W)$. The write access failure probability is determined at the 6σ failure probability (i.e., $P_W = 10^{-9}$). The write access failure probability for all cells considered in this work is shown in Fig. 11. As seen in the Fig. 11, the 10T diff. cell has the worst write access failure probability. The 6T and 8T mincells have similar failure probability. However, the 8T mincell has a slightly lower failure probability due to its narrower pull down nMOS which decrease contention with its access transistors. The 10T Schmitt Trigger cell enables two control signals during a write operation which improves its write access. The 6T and 8T iso-area cells have a much lower write access failure probability due to decrease in threshold variations because of up scaled devices. The proposed 10T cell exhibits superior write access ability than all other non-scaled cells due to weakening of supply path, thereby achieving a low write access V_{min} of 707mV.

E. Read Access Failure Probability

A read access failure occurs when the sense amplifier fails to produce desired logical output because the precharged bit lines are unable to develop a sufficient voltage differential within the duration of the pulse width. Just like write access time, the inverse of read access time follows a normal distribution and thus can be approximated in the same way. In this work, the read access time has been evaluated for one hundred twenty-eight bit cells per column and when the differential between the bit lines reaches 50mV. The read operation and sense-amplifier-enable form two halves of one clock cycle, with the former occurring before the latter. If the differential voltage does not reach 50mV before the sense amplifier is triggered, the read operation will fail. Therefore, the read access failure probability is defined as

$$P_A = Prob\left(T_A < T_{WL}^A\right) \tag{11}$$

where T_A is the read access time and T_{WL}^A is the word line pulse width. The read access failure probability can be evaluated as

$$P_A = Prob\left(\frac{1}{T_A} < \frac{1}{T_{WL}^A}\right) = \Phi\left(\frac{\frac{1}{T_{WL}^A} - \left(\frac{1}{T_A}\right)_{nom}}{\sigma_A}\right) \tag{12}$$

where σ_A is the standard deviation of $(1/T_A)$. The read access failure probability is determined at the 6σ failure probability (i.e., $P_A = 10^{-9}$). The read access failure probability has been evaluated with the worst-case bit line offset for all cells considered in this work and is shown in Fig. 12. Since the 10T ST cell suffers from increased pass gate leakage and relatively lower read currents, its read access performance is degraded. The 10T diff. cell has better read performance than the 10T

This article has been accepted for inclusion in a future issue of this journal. Content is final as presented, with the exception of pagination.

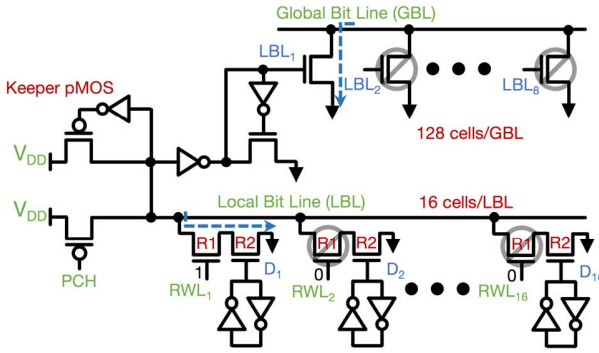

Fig. 13. Hierarchical bit line sensing for the single ended 8T cell.

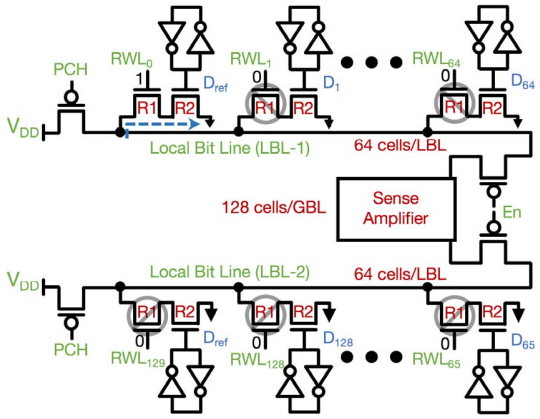

Fig. 14. Divided bit line sensing for the proposed 10T cell.

ST cell but still suffers due to higher bit line capacitance. The 6T mincell has the lowest bit line capacitance and wider pull down nMOS, leading to improved read access performance. The 6T iso-area cell shows the best read access performance due to up scaled transistors. Even though it shows the lowest read access V_{min}, it becomes increasing difficult to create larger SRAM arrays with it. This is because its large combined pass gate leakage limits arrays to just a few cells per column, especially at higher temperatures.

Cells with an isolated single ended read port like the 7T [12], 8T and 9T [17] suffer from reduced read performance. The conventionally used hierarchical sensing architecture for such cells is shown in Fig. 13. This architecture implements bit cells on multiple local bit lines and does not employ a sense amplifier. The read access time for such a topology is evaluated as the total time from read word line enable to global bit line data evaluation. This non-differential mode of sensing increases the nominal read access time, thereby increasing failure probability. For the time constraint assumed in this work, the 8T cell fails to successfully evaluate the global bit line before the end of the read access operation. As such, its read access V_{min} has been marked as 'fail' in Table II. In order to achieve desired failure probability for the 8T cell, the frequency must be lowered. In general, all the read and write access failure probabilities can be improved a lot by modifying frequency and array design parameters as per requirement. In practice, many small portable devices and sensors work on substantially lower frequencies, thereby decreasing their access failure rate. The access failure rate is thus case specific and discretionary in nature. Still, it is obvious that the single ended read operation is inferior to a differential one, irrespective of operating frequency. Therefore, to avoid the conventionally used sensing architecture for single ended cells, the read mechanism of the proposed 10T cell has been modified in order to achieve differential sensing. Each column in the array is divided into two equal subsections. The single read bit line from both subsections is then used as inputs to a sense amplifier. The topology of the divided line sensing is shown in Fig. 14. By implementing this topology, the bit line capacitance is reduced to half of the original, thereby leading to large gains in read access performance. The divided bit line read mechanism for the proposed cell allows it to reach a read access V_{min} of 737mV, which is much lower than both the 10T ST and 10T diff. cell, despite its larger vertical sizing. The divided bit line architecture can also be applied to other single-ended-read cells such as the 8T cell for improved read access performance. However, simulations showed that even if the single ended 8T mincell is implemented with the divided bit line architecture, it fails to outperform the proposed cell due to its limiting write-access performance. The 8T iso-area cell, implemented with the divided bit line architecture also cannot outperform the proposed cell in terms of the static trivariate V_{min}. It can only outperform the proposed cell in terms of the pentavariate V_{min}. However, an array implemented with 8T iso-area cells is limited to very few cells per column due to its wide access transistors. The cell is prone to large bit line offset and inadvertent pull down of bit line due to large combined pass gate leakage. Since each sub-block will be very small in capacity, the peripheral circuitry area penalty will also be extremely large.

F. Iso-Area V_{min} Comparison

The V_{min} comparison of all SRAM cells included in this work has been presented in Table II. The V_{min} considering only the three static margins can be calculated as

$$V_{min} = \text{Max.}\,[Write-V_{min}, Read-V_{min}, Hold-V_{min}] \tag{13}$$

The pentavariate V_{min} including the static and dynamic failure criterion, can be calculated as

$$V_{min} = \text{Max.}\,[Write-V_{min}, Read-V_{min}, Hold-V_{min}, WriteAccess-V_{min}, ReadAccess-V_{min}] \tag{14}$$

Both V_{min} have been evaluated and summarized for all cells in Table II. The trivariate V_{min} point for all cells is mostly due to their inherent structure and is therefore fixed. However, the pentavariate V_{min} point can be improved greatly by changing the operating frequency or implementing small changes in the array architecture. As seen in Table II, the conventional 6T mincell is greatly limited by its read stability. The 8T mincell which decouples its read operation shows improved V_{min} but is

This article has been accepted for inclusion in a future issue of this journal. Content is final as presented, with the exception of pagination.

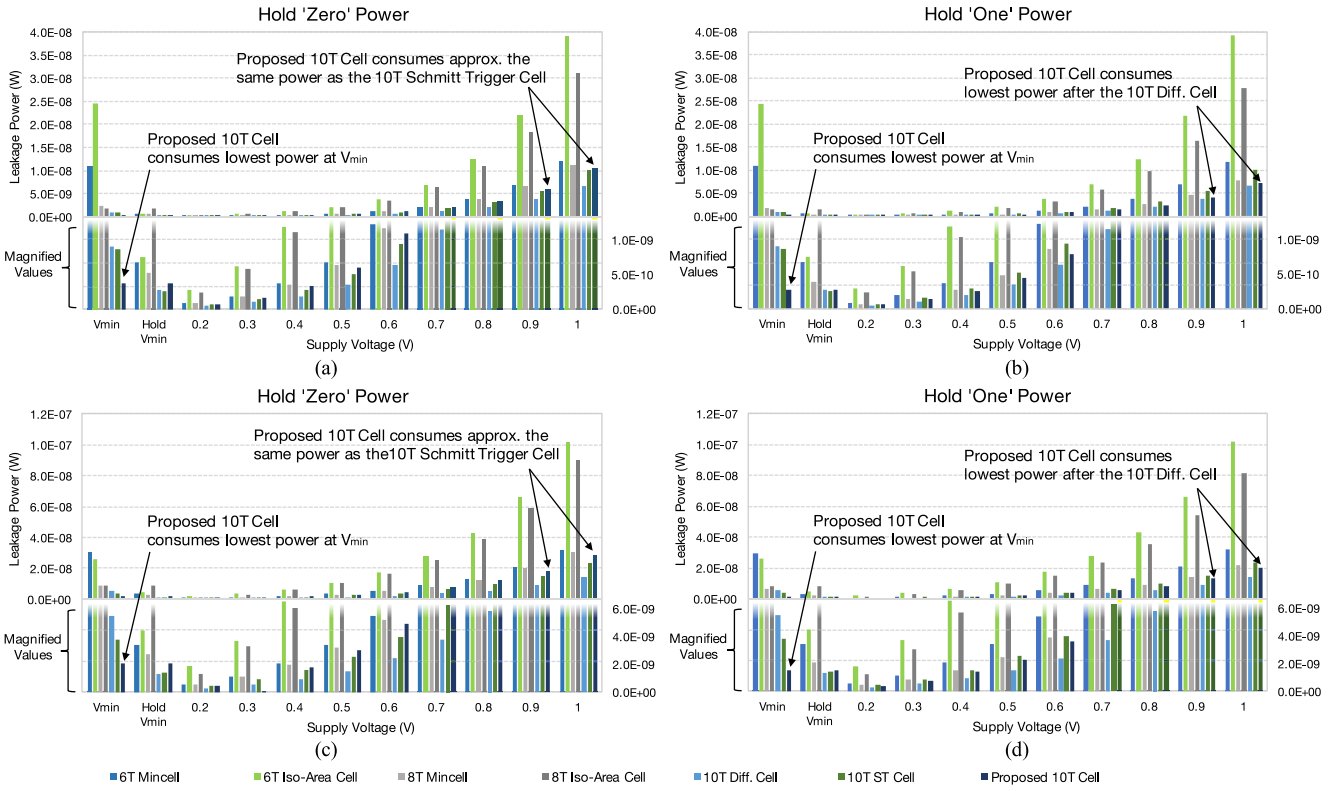

Fig. 15. Comparison of hold (a) 'zero' power at 27°C (b) 'one' power at 27°C (c) 'zero' power at 110°C (d) 'one' power at 110°C with varying supply voltage for different cells.

still limited by its write ability. The 6T iso-area cell improves its failure probability due to increased sizing, but is still not able to reach a low V_{min} as other 10T cells. The 8T iso-area cell improves upon its write ability, but it still suffers from hold stability and increased leakage currents. The 10T diff. cell is also limited by its write ability, but it consists of a differential read scheme which is highly preferred. The 10T Schmitt Trigger cell has a highly robust hold state due to the feedback nature it possesses but is limited by its write ability. Although the proposed 10T cell does not possess the hold prowess of the 10T ST cell, it significantly improves its write operation which results in the lowest static V_{min} of 420mV.

G. Leakage Power

Since the activity factor of SRAM memory is low, the hold leakage power consumption becomes a significant portion of the total power consumption. The leakage power consumption for all cells considered in this work has been plotted at 27°C and 110°C for varying supply voltages in Fig. 15. The leakage power has also been plotted at the respective hold and overall V_{min} point of each cell. Since the read and write access V_{min} are subject to operation frequency and design parameters, only the trivariate static V_{min} has been considered in this section for power evaluation. As seen in the Fig. 15, the iso-area cells have the highest leakage power consumption. The 10T diff. cell has the lowest power consumption due to two series connected access nMOS. The proposed 10T cell consumes approximately the same power as the 10T Schmitt Trigger cell when it stores 'zero'. When the proposed cell stores 'one,' the read port leakage is reduced and its overall hold power consumption falls and becomes comparable to that of the 10T diff. cell. Due to the improved V_{min} point of the proposed cell, large leakage power savings can be observed. At V_{min}, the proposed 10T cell consumes up to 2.4× and 3.1× less power than the next lowest power consuming cell (10T ST cell) when it stores 'zero' and 'one' respectively. At V_{min}, the proposed 10T cell also observes up to 29.3× and 6.6× reduction in leakage power in hold 'zero' state over the 6T and 8T mincell respectively. In hold 'one' state, the proposed cell observes up to 39× and 6.3× reduction in leakage power over the 6T and 8T mincell respectively.

IV. Improved Read Access Performance

The pass-gate leakage in SRAM cells presents a challenge when building larger memories. The combined leakage lowers the bit line voltage, which in turn reduces the effective read current. The worst case is when the entire column stores the opposite of the value which is stored in accessed bit cell. This creates an offset voltage amongst the differential bit lines which degrades the read access. The pass-gate leakage also puts a limit on the number of bit cells per column. The combined leakage current may inadvertently pull down the read bit line leading to a false read operation. The bit line leakage scenario for all cells considered in this work is

This article has been accepted for inclusion in a future issue of this journal. Content is final as presented, with the exception of pagination.

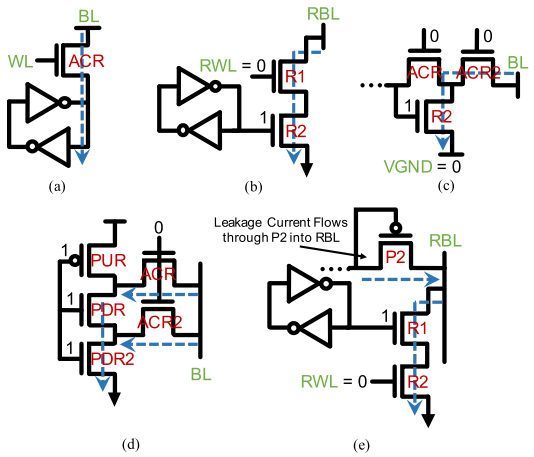

Fig. 16. Bit line leakage in (a) 6T (b) 8T (c) 10T diff. (d) ST (e) Proposed 10T cell.

shown in Fig. 16. The bit line offset in the 6T cell is due to the flow of leakage current from bit line to the low value node through the access transistor. The bit line leakage in the 8T cell is data dependent and is worst when the cell holds 'zero'. The 10T diff. bit cell lifts the ground to supply level during hold mode, but brings it back to low level during a read operation. The worst case bit line offset then occurs as shown in Fig 16. (c). As seen in Fig. 16 (d), the 10T Schmitt Trigger cell has two pass transistors, which increases the overall bit line leakage current. In Fig. 16 (e), the proposed 10T cell is able to negate some of the read port leakage. The P2 pMOS allows flow of leakage current through it into the reduced read bit line voltage, thereby improving the read access. As with the 8T cell, the worst case offset occurs in the proposed 10T cell when it stores 'zero'. The worst case bit line voltage offset for all cells with varying supply voltage and bit cells per column is shown in Fig. 17. The offset was evaluated at typical corner and 110°C. The pre-charge device sizing was made same for all cells and a keeper pMOS was not implemented. The offset for the proposed cell was measured without the implementation of divided read bit line topology. As seen in Fig. 17, the 10T Schmitt Trigger cell has the worst bit line offset voltage. The 6T and 8T mincells approximately have the same offset voltage. However, the proposed 10T cell exhibits the lowest bit line offset voltage of all the cells compared. This helps to create SRAM columns with greater number of cells, which can help reduce the amount of peripheral circuitry needed, thereby offsetting some of the area overhead of the larger proposed bit cell.

V. Cell Layout and Area

The thin-layout [33] for various SRAM cells is shown in Fig. 18. The cells have been drawn on the 32nm technology node ($\lambda = 0.018\ \mu$m). The layout for the 10T diff. cell shown in [16] has a 61% area penalty over the 8T cell [16]. This is because it is not in thin form and has significant unused space per bit cell. Therefore, for a fair comparison, a thin and compact form for the 10T diff. cell has been presented in this work. The layout for the proposed 10T cell is shown in Fig. 19.

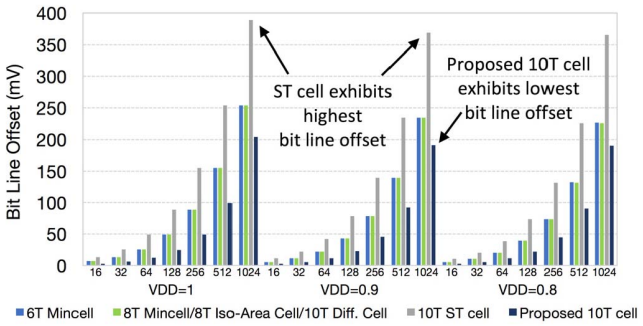

Fig. 17. Bit line offset voltage with varying supply voltage and bit cells per column.

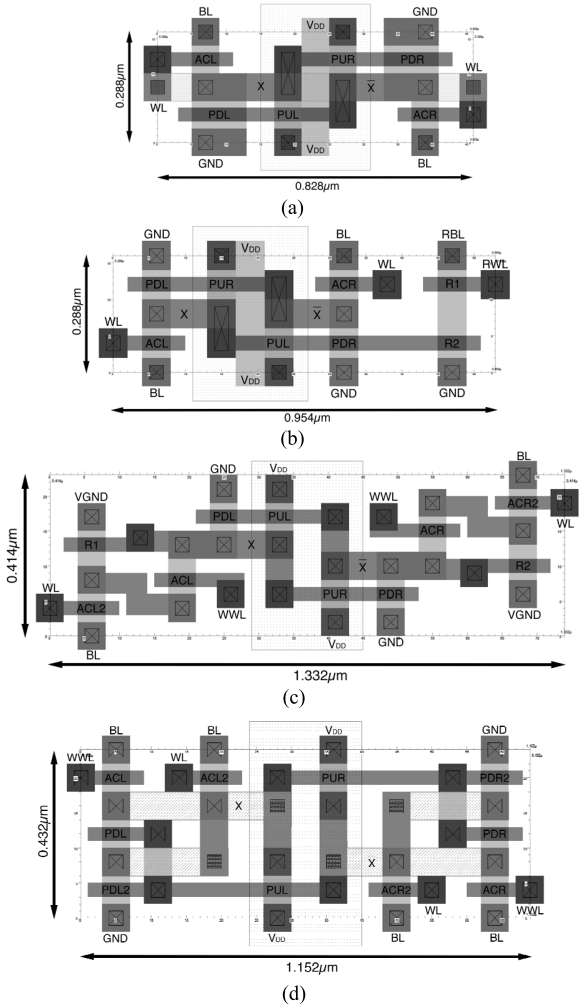

Fig. 18. Layout of (a) 6T min (b) 8T min (c) 10T diff. (d) Schmitt Trigger SRAM cells.

The proposed 10T cell was drawn primarily on the metal one layer with the constraint of unidirectional poly, which resulted in increased vertical sizing [Fig. 19 (a)]. Nonetheless, another possible layout for the proposed cell was drawn with smaller vertical sizing for reduced bit line capacitances, lower power consumption, improved read access performance and lower bit cell area, albeit with multi-layer internal routing which has the

This article has been accepted for inclusion in a future issue of this journal. Content is final as presented, with the exception of pagination.

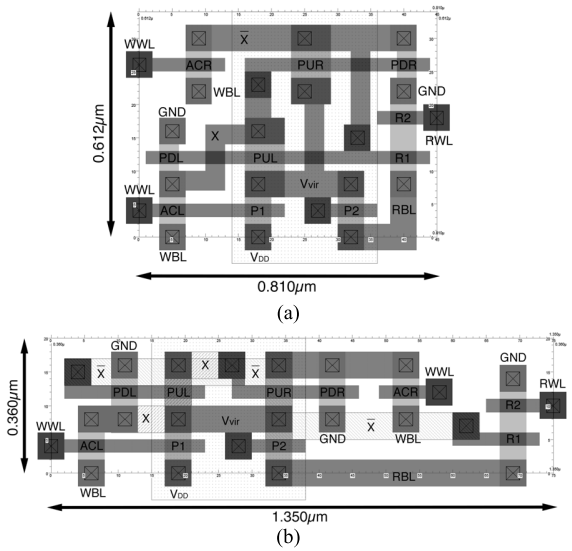

Fig. 19. Layout of the (a) proposed 10T cell (b) proposed 10T cell in thin form.

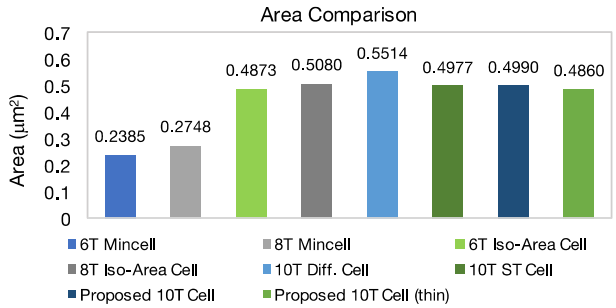

Fig. 20. Layout area comparison of different SRAM cells on the 32nm technology node.

possibility of increased cost. It should also be noted that all analyses presented in this work have been performed according to the layout in Fig. 19 (a). The layout area comparison of all bit cells considered in this work is shown in Fig. 20.

VI. Conclusion

In this work, we presented a ten-transistor SRAM cell with write operation capability in deep subthreshold region for low power applications without the need of a dedicated write assist circuit. The issue of reduced read access performance due to bit line offset in larger SRAM macros was also addressed in the proposed 10T bit cell. Up to 50% reduction in bit line offset over other cells was observed. A divided bit line scheme was implemented to enable differential sensing, thereby greatly improving read access performance. In addition to the improvement in read access and write performance, the proposed cell also exhibited improved hold stability, resulting in significant V_{min} gains. A comprehensive pentavariate V_{min} analysis was presented in order to evaluate V_{min} for all cells. The static V_{min} for the proposed 10T cell was evaluated to be 420mV, which is 565mV lower than the V_{min} of the 6T mincell, 266mV lower than the V_{min} of the 8T mincell and 167mV lower than the V_{min} of the Schmitt Trigger cell. The proposed cell also exhibited better read and write access performance than most other cells. The lower V_{min} of the proposed 10T cell resulted in about 39× and 6.6× lower hold power consumption than the conventional 6T and 8T cells, making it a viable candidate for portable electronics or low power sensors. The proposed cell occupied an area of $0.499\mu m^2$ on the 32nm technology node. Additionally, a thinner form of the bit cell was presented, which occupied an area of $0.486\mu m^2$.

References

[1] S. O. Toh, Z. Guo, T.-J. K. Liu, and B. Nikolic, "Characterization of dynamic SRAM stability in 45 nm CMOS," *IEEE J. Solid-State Circuits*, vol. 46, no. 11, pp. 2702–2712, Nov. 2011.

[2] E. Morifuji, T. Yoshida, M. Kanda, S. Matsuda, S. Yamada, and F. Matsuoka, "Supply and threshold-voltage trends for scaled logic and SRAM MOSFETs," *IEEE Trans. Electron Devices*, vol. 53, no. 6, pp. 1427–1432, Jun. 2006.

[3] G. Chen *et al.*, "Yield-driven near-threshold SRAM design," *IEEE Trans. Very Large Scale Integr. (VLSI) Syst.*, vol. 18, no. 11, pp. 1590–1598, Nov. 2010.

[4] B. H. Calhoun and A. P. Chandrakasan, "Static noise margin variation for sub-threshold SRAM in 65-nm CMOS," *IEEE J. Solid-State Circuits*, vol. 41, no. 7, pp. 1673–1679, Jul. 2006.

[5] A. Sheikholeslami, "Process variation and Pelgrom's law," *IEEE Solid-State Circuits Mag.*, vol. 7, no. 1, pp. 8–9, Feb. 2015.

[6] R. E. Aly, M. I. Faisal, and M. A. Bayoumi, "Novel 7T SRAM cell for low power cache design," in *Proc. IEEE Int. SOC Conf.*, Sep. 2005, pp. 171–174.

[7] L. Wen, Z. Li, and Y. Li, "Single-ended, robust 8T SRAM cell for low-voltage operation," *Microelectron. J.*, vol. 44, no. 8, pp. 718–728, 2013.

[8] M. F. Chang *et al.*, "A differential data-aware power-supplied (D^2AP) 8T SRAM cell with expanded write/read stabilities for lower VDDmin applications," *IEEE J. Solid-State Circuits*, vol. 45, no. 6, pp. 1234–1245, Jun. 2010.

[9] S. Nalam and B. H. Calhoun, "5T SRAM with asymmetric sizing for improved read stability," *IEEE J. Solid-State Circuits*, vol. 46, no. 10, pp. 2431–2442, Oct. 2011.

[10] H. Farkhani, A. Peiravi, and F. Moradi, "A new asymmetric 6T SRAM cell with a write assist technique in 65 nm CMOS technology," *Microelectron. J.*, vol. 45, no. 11, pp. 1556–1565, Nov. 2014.

[11] H. Jiao, Y. Qiu, and V. Kursun, "Variability-aware 7T SRAM circuit with low leakage high data stability SLEEP mode," *Integr., VLSI J.*, vol. 53, pp. 68–79, Mar. 2016.

[12] S. A. Tawfik and V. Kursun, "Low power and robust 7T dual-V_t SRAM circuit," in *Proc. IEEE Int. Symp. Circuits Syst. (ISCAS)*, May 2008, pp. 1452–1455.
G. Chen et al., "Yield-Driven Near-Threshold SRAM Design," IEEE Transactions on Very Large Scale Integration (VLSI) Systems, vol. 18, no. 11, pp. 1590–1598, Nov. 2010.

[13] M. H. Chang, Y.-T. Chiu, and W. Hwang, "Design and iso-area V_{min} analysis of 9T subthreshold SRAM with bit-interleaving scheme in 65-nm CMOS," *IEEE Trans. Circuits Syst. II, Exp. Briefs*, vol. 59, no. 7, pp. 429–433, Jul. 2012.

[14] S. Borkar, "Design challenges for 22 nm CMOS and beyond," in *IEDM Tech. Dig.*, Dec. 2009, p. 1.

[15] T. H. Kim *et al.*, "A voltage scalable 0.26 V, 64 kb 8T SRAM with V_{min} lowering techniques and deep sleep mode," *IEEE J. Solid-State Circuits*, vol. 44, no. 6, pp. 1785–1795, Jun. 2009.

[16] I. J. Chang, J.-J. Kim, S. P. Park, and K. Roy, "A 32 kb 10T sub-threshold SRAM array with bit-interleaving and differential read scheme in 90 nm CMOS," *IEEE J. Solid-State Circuits*, vol. 44, no. 2, pp. 650–658, Feb. 2009.

[17] A. Teman, L. Pergament, O. Cohen, and A. Fish, "A 250 mV 8 kb 40 nm ultra-low power 9T supply feedback SRAM (SF-SRAM)," *IEEE J. Solid-State Circuits*, vol. 46, no. 11, pp. 2713–2726, Nov. 2011.

[18] J. P. Kulkarni, K. Kim, and K. Roy, "A 160 mV robust Schmitt trigger based subthreshold SRAM," *IEEE J. Solid-State Circuits*, vol. 42, no. 10, pp. 2303–2313, Oct. 2007.

[19] J. P. Kulkarni and K. Roy, "Ultralow-voltage process-variation-tolerant Schmitt-trigger-based SRAM design," *IEEE Trans. Very Large Scale Integr. (VLSI) Syst.*, vol. 20, no. 2, pp. 319–332, Feb. 2012.

This article has been accepted for inclusion in a future issue of this journal. Content is final as presented, with the exception of pagination.

[20] V. P.-H. Hu, M.-L. Fan, P. Su, and C.-T. Chuang, "Analysis of GeOI FinFET 6T SRAM cells with variation-tolerant WLUD read-assist and TVC write-assist," *IEEE Trans. Electron Devices*, vol. 62, no. 6, pp. 1710–1715, Jun. 2015.
[21] S. Mukhopadhyay, R. M. Rao, J.-J. Kim, and C.-T. Chuang, "SRAM write-ability improvement with transient negative bit-line voltage," *IEEE Trans. Very Large Scale Integr. (VLSI) Syst.*, vol. 19, no. 1, pp. 24–32, Jan. 2011.
[22] Y.-H. Chen *et al.*, "A 16 nm 128 Mb SRAM in high-κ metal-gate FinFET technology with write-assist circuitry for low-$V_{\min}$ applications," in *IEEE ISSCC Dig. Tech. Papers*, Feb. 2014, pp. 238–239.
[23] M. Yabuuchi *et al.*, "16 nm FinFET high-κ/metal-gate 256-kbit 6 T SRAM macros with wordline overdriven assist," in *IEDM Tech. Dig.*, Dec. 2014, pp. 3.3.1–3.3.3.
[24] A. Bhavnagarwala *et al.*, "A sub-600 mV, fluctuation tolerant 65 nm CMOS SRAM array with dynamic cell biasing," in *IEEE Symp. VLSI Circuits Dig.*, Jun. 2007, pp. 78–79.
[25] M. Yabuuchi, K. Nii, Y. Tsukamoto, S. Ohbayashi, Y. Nakase, and H. Shinohara, "A 45 nm 0.6 V cross-point 8 T SRAM with negative biased read/write assist," in *Proc. IEEE Symp. VLSI Circuits*, Jun. 2009, pp. 158–159.
[26] E. Karl *et al.*, "A 0.6 V, 1.5 GHz 84 Mb SRAM in 14 nm FinFET CMOS technology with capacitive charge-sharing write assist circuitry," *IEEE J. Solid-State Circuits*, vol. 51, no. 1, pp. 222–229, Jan. 2016.
[27] M. Yamaoka *et al.*, "90-nm process-variation adaptive embedded SRAM modules with power-line-floating write technique," *IEEE J. Solid-State Circuits*, vol. 41, no. 3, pp. 705–711, Mar. 2006.
[28] B. H. Calhoun and A. P. Chandrakasan, "A 256-kb 65-nm sub-threshold SRAM design for ultra-low-voltage operation," *IEEE J. Solid-State Circuits*, vol. 42, no. 3, pp. 680–688, Mar. 2007.
[29] N. Gierczynski, B. Borot, N. Planes, and H. Brut, "A new combined methodology for write-margin extraction of advanced SRAM," in *Proc. IEEE Int. Conf. Microelectron. Test Struct. (ICMTS)*, Mar. 2007, pp. 97–100.
[30] H. Makino *et al.*, "Reexamination of SRAM cell write margin definitions in view of predicting the distribution," *IEEE Trans. Circuits Syst. II, Exp. Briefs*, vol. 58, no. 4, pp. 230–234, Apr. 2011.
[31] E. Seevinck, F. J. List, and J. Lohstroh, "Static-noise margin analysis of MOS SRAM cells," *IEEE J. Solid-State Circuits*, vol. SSC-22, no. 5, pp. 748–754, Oct. 1987.
[32] K. Agarwal and S. Nassif, "Statistical analysis of SRAM cell stability," in *Proc. Design Autom. Conf.*, 2006, pp. 57–62.
[33] K. Osada *et al.*, "Universal-V_{dd} 0.65-2.0 V 32 kB cache using voltage-adapted timing-generation scheme and a lithographical-symmetric cell," *IEEE J. Solid-State Circuits*, vol. 36, no. 11, pp. 1738–1744, Nov. 2001.

Shourya Gupta (S'17) was born in New Delhi, India, in 1994. He received the B.Tech. degree in electronics and communication engineering from Guru Gobind Singh Indraprastha University, New Delhi, in 2017.

His current research interests include the design of low power logic and memory circuits in emerging and exploratory technologies.

Kirti Gupta (M'15) received the B.Tech. degree in electronics and communication engineering from the Indira Gandhi Institute of Technology, New Delhi, India, in 2002, the M.Tech. degree in information technology from the School of Information Technology, New Delhi, in 2006, and the Ph.D. degree in electronics and communication engineering from Delhi Technological University, New Delhi, India, in 2016.

She was with the Bharati Vidyapeeth's College of Engineering, New Delhi, as an Assistant Professor from 2002 to 2007 and an Associate Professor from 2008 to 2016, where she is currently a Professor. She has authored over 60 technical papers in various international conferences and journals. Her current research interests include digital integrated circuit design.

Dr. Gupta is a Life Member of the ISTE.

Neeta Pandey (M'04–SM'14) received the M.E. degree in microelectronics from the Birla Institute of Technology and Sciences, Pilani, India, and the Ph.D. degree from Guru Gobind Singh Indraprastha University, New Delhi, India.

She has served with the Central Electronics Engineering Research Institute, Pilani, the Indian Institute of Technology, New Delhi, the Priyadarshini College of Computer Science, Noida, and the Bharati Vidyapeeth's College of Engineering, New Delhi, in various capacities. She is currently a Professor with the Electronics and Communication Engineering Department, Delhi Technological University, New Delhi. She has authored over 170 technical papers in reputed national and international conferences and journals. Her current research interests include analog and digital VLSI design.

Dr. Pandey is a member of the WIE Affinity Group and a Life Member of the ISTE.

International Journal for Research in Applied Science & Engineering Technology (IJRASET)
ISSN: 2321-9653; IC Value: 45.98; SJ Impact Factor : 6.887
Volume 6 Issue II, February 2018- Available at www.ijraset.com

Performance Analysis of 4 Stroke Compression Ignition Engine by Using Diesel and Biodiesel Blend of Hingot Oil

Mr. Akash Singh Raikwar[1], Mr. Amit Agarwal[2], Dr. Amit Pal[3]
[1]*Department of Mechanical Engineering, SRCEM Bamore, Morena)*
[2]*Department of Mechanical Engineering, SRCEM Bamore, Morena)*
3Department of Mechanical Engineering, Delhi Technical University, Delhi India

Abstract : Looking to present scenario of rapidly increases the pollution in our country and worldwide too the need of some clean and non toxic fuels which helps the environment from the pollution, also the rise of petroleum is hike day by day and we all know petroleum is limited we can't have petroleum after next 50 year if the same rate of consumption is continue so for a future we needs some alternatives of petroleum, there are lot of alternative fuels is discovered in present days out of which biodiesel is most convenient fuel from our society. Biodiesel is clean, non toxic, biodegradable and environment friendly alternative fuels Since biodiesel is produce from the vegetable oil or animal fats hence its generally renewable fuels.

In this paper I have tested the performance of compressed ignition engine in varying load conditionby using biodiesel which is produced in a laboratory of Delhi Technological University, Delhi from a seed of Hingot (Balanitesaegyptiaca Del.) by Mechanical stirring method, testing is done with the diesel blend which have different properties at B0, B10, B20 and B30. Among the all blends, the the specific fuel consumption, brake specific fuel consumption and brake thermal efficiency is calculate and compare with the all samples of blends.

Keyword: Biodiesel, Performance test, Brake power, Blend, Brake thermal efficiency

I. TRODUCTION

Compressed Ignition Engine is a type of IC Engine which is generally used for a run heavy engine and generator and uses Diesel a fuel in this if we use the blend of biodiesel in place of pure biodiesel without any modification in engine then it run smoothly up to a certain percentage of biodiesel in diesel called blend. There aremany of past experiments says that CI engine run smoothly with biodiesel blends. Gopal el al.[1] performed experiments on a constant speed single cylinder, 4 stroke ,air cooled diesel engine for agriculture purpose used to test the fuel. Raw material used for biodiesel production was waste cooking oil which was collected from difference sources, specific energy consumption changes with increase in blends due to the lower value of biodiesel. Shahidet al.[2]observed B100 is also used an engine but B20 are increases the fuel consumption and 10% decreases the brake thermal efficiency. Zakira el al.[3] also used Waste cooking oil for producing biodiesel and perform the test at B20, B40, B60, B80 and B100 and observed the lowest BHP. Higher BHP obtained when engine was fueled by blends with low biodiesel contained also it was found that average brake specific fuel consumption of B100 is 9.45% higher than diesel fuel. Sharmaet al [4] uses WCO for produce biodiesel, B20 and B40 blend result the brake thermal efficiency is higher with respect to diesel at higher load, this is due to better combustion of biodiesel blends due to present of extra amount of oxygen, in case of brake specific fuel values are higher at the beginning due to higher viscosity. Srinivas et al. [5] observed at B20 blend brake thermal efficiency is 37.855% and it is 0.275% less than of standard diesel operation. Rao et al.[5] used cooking methyl ester UCME which has low calorif value than that of biodiesel hence specific fuel consumption is slightly higher than that of biodiesel for UCME and its blends. Brake thermal efficiency of UCME and its blend is lower than pure diesel. Algasim et al.[6] used turbocharged diesel engine for testing, standard diesel produced the higher brake torque and power at the engine for all engine speeds. This is due to lower calorific value of the biodiesel compare to standard value, at full load operation, the lowest specific fuel consumption was for the standard diesel compare to biodiesel.

II. PERFORMANCE TESTING

A. Engine test setup

The setup of engine is consist of single cylinder, four stroke, kirloskar diesel engine connected to an eddy current dynamometer for loading. The setup has stand-alone panel box consisting of air box, two fuel tanks for duel fuel testing, fuel measuring unit,

©IJRASET (UGC Approved Journal): All Rights are Reserved

manometer, transmitters for air and fuel flow measurements, process indicator and engine indicator. Rotameters are provided for cooling water and calorimeter water flow measurement. The setup enables study of engine of engine performance various parameters like brake power, indicated power, frictional power, break mean effective pressure (BMEP), indicated mean effective pressure (IMEP), indicating thermal efficiency, mechanical efficiency, volumetric efficiency, specific fuel consumption, air/fuel ratio and heat balance. The aim of these experiments is to study the effects of various parameters on performance of kirloskar engine for different blends of diesel and biodiesel.

B. Engine Specifications

Table:1Constructional Specifications of engine test setup.

S.No.	Component	Specifications
1.	Product	Kirloskar engine test setup 1 cylinder, 4stroke diesel engine.
2.	Product code	234
3.	Engine	Make kirloskar, type 1 cylinder, 4 stroke diesel, water cooled, power 3.5kW at 1500rpm, stroke 110mm, bore 87.5mm. 661cc CR17.5
4.	Dynamometer	Type eddy current, water cooled with loading unit
5.	Propeller shaft	With universal joint
6.	Air box	M S fabricated with orifice meter and manometer
7.	Fuel tank	Capacity 15L with glass fuel metering column
8.	Calorimeter	Type pipe in pipe
9.	piezo powering unit	Make cuadra, Model AX-409
10.	Digital milivoltmeter	Range 0-500mV, panel mounted
11.	Load indicator	Digital, range 0-50Kg, Supply 230V AC
12.	Load sensor	Load cell, type strain gauge, range 0-50Kg
13.	Rotameter	Engine cooling 40-400LPH: calorimeter 25-250LPH

Table: 2 Technical Specifications of engine test setup.

S.No.	Component	Specifications
1.	Number of cylinder	1
2.	Number of stroke	4
3.	Fuel	HS diesel
4.	Rated power	3.5KW @ 1500rpm
5.	Cylinder diameter	87.5mm
6.	Stroke length	110mm
7.	Connecting rod length	234mm
8.	Compression ratio varies	12 to 18:1
9.	Orifice diameter	20mm
10.	Dynamometer arm length	185mm

C. Preparation of Blends

Three different blends of biodiesel were prepared as explained below:

1) B10 (10% biodiesel + 90% diesel): To make a sample 500ml of B10, 450ml pure diesel was mixed in 50ml of biodiesel prepared from vegetable oil in a beaker.

2) B20 (20% biodiesel + 80% diesel): To make a sample 500ml of B20, 400ml pure diesel was mixed in 100ml of biodiesel prepared from vegetable oil in a beaker.

3) B30 (30% biodiesel + 70% diesel): To make a sample 500ml of B30, 350ml pure diesel was mixed in 150ml of biodiesel prepared from vegetable oil in a beaker.

©IJRASET (UGC Approved Journal): All Rights are Reserved

Density of pure diesel=811Kg/m^3
Density of biodiesel=859.7Kg/m^3

Table: 3 Description of diesel, biodiesel and different blends of biodiesel

Type of blend	Amount of biodiesel (ml)	Amount of pure diesel (ml)	Resultant density (Kg/m^3)
Diesel	0	500	811
Biodiesel	500	0	859.7
B10	50	450	816.7
B20	100	400	820.3
B30	150	350	826.9

Table:4Properties of diesel, biodiesel and different blends of biodiesel

Type of blend	Viscosity of biodiesel (mPa.s)	Kinematics viscosity of pure diesel (mm^2/s)	Resultant density (Kg/m^3)
Diesel B0	2.4811	3.0593	811
Biodiesel B100	4.6340	5.3905	859.7
B10	2.5500	3.1222	816.7
B20	2.6487	3.2288	820.3
B30	2.7689	3.3066	826.9

D. Performance Evaluations

All the experiments were performed on a single cylinder, 4 stroke kirloskar diesel engine. There were two separate fuel inlet arrangement is available in a setup, one for the diesel and another for biodiesel blend. Fuel was supplied to the engine from an outside tank. A 5-10min warm up period is provided from first run data collection. Initial engine is started with the diesel and then after 5-10min. period blend is use. The gap of 4-5min. was provided between the two consecutive runs for accurate data obtaining. Engine speed, specific fuel consumptions, brake power, heat balance etc. were measure during each run. During load test take rpm constant (1500rpm) and load on engine varied from 0 to 12kg by adjusting the load knob provided on the control panel of the test ring. The tests were performed with pure diesel (B0)and biodiesel blends (B10, B20, B30)

E. Pure diesel: B0, Biodiesel Blend: B10, Biodiesel Blend: B20 and Biodiesel Blend: B30

Engine performance parameters obtained from performance testing in single cylinder four stroke CI Engine against different loads for pure diesel ie B0 and Biodiesel Blend B10, B20 and B30

III. RESULTS AND DISCUSSION

A. Brake thermal efficiency vs Brake Power for Diesel and Biodiesel Blends

From the fig. it is observed that Brake thermal efficiency BTHE for both pure diesel and biodiesel blends increases with increase in brake power. Also the efficiency of biodiesel blends is more than pure diesel i.e. B0 and maximum is observed in the blend of B10. The reason is that is presence of more oxygen in biodiesel blends compare to pure diesel. With further increases the percentage of biodiesel in the blend a slight decreases in BTHE is seen in a fig. The reason for the decreases in BTHE in high % blend B20, B30 may be due to less volatility of biodiesel as compare to pure diesel B0.The maximum brake thermal efficiency is achieved 33.67 at a brake power of 2.79kW for B10. The value of BTHE for pure diesel B0 at a same load is obtained 32.46%. A condition of minimum load of BTHE is minimum 11.73% for B0 and 13.01% for B10. The variation of BTHE vs BP for different blends of diesel and pure diesel is shown in fig.1

©IJRASET (UGC Approved Journal): All Rights are Reserved

International Journal for Research in Applied Science & Engineering Technology (IJRASET)
ISSN: 2321-9653; IC Value: 45.98; SJ Impact Factor : 6.887
Volume 6 Issue II, February 2018- Available at www.ijraset.com

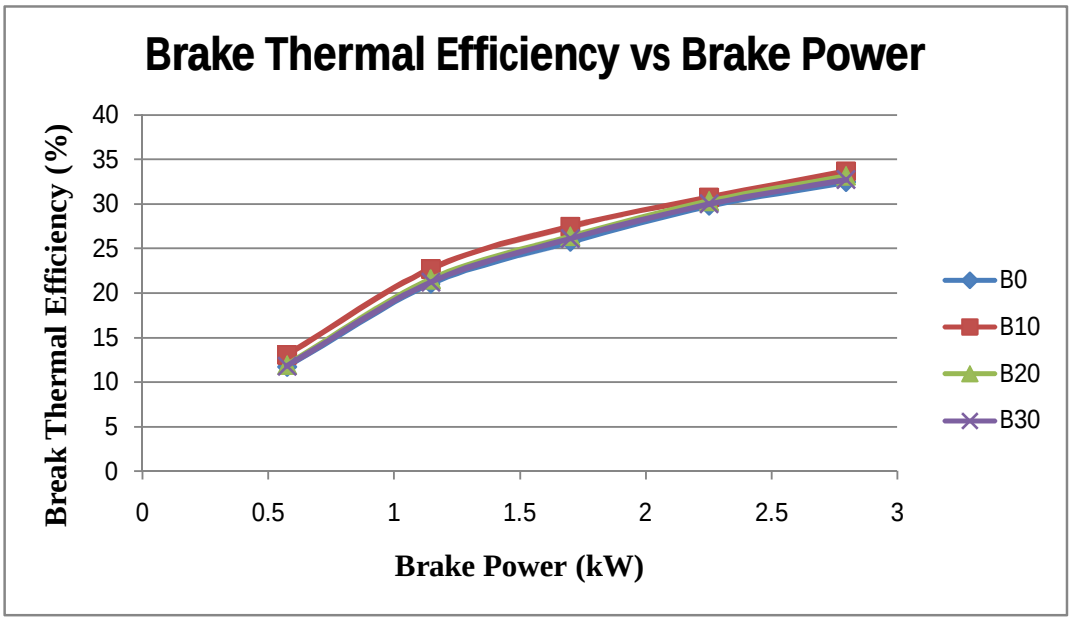

Fig.1 Brake thermal efficiency vs Brake Power for diesel and biodiesel blends

B. Brake Specific Fuel Consumption Vs Brake Power For Diesel And Biodiesel Blends

From the fig. it is observed that Brake specific fuel consumption BSFC for both pure diesel and biodiesel blends decreases with increase in brake power. As we know the total fuel consumption increases with increases the percentage of biodiesel increases in blends of biodiesel the reason is that biodiesel has low calorific value as compare to pure diesel so more fuel is induced in blends of biodiesel. Thus BSFC increases with increases in biodiesel percentage in blend.

It is Also observed from the fig that Brake specific fuel consumption BSFC for blends B10, B20, B30 at the maximum brake power of 2.79kW is 0.257, 0.261, 0.264 (in kg/kW-h) respectively. And for the minimum load (brake power 0.574kW) BSFC is observed for B10, B20, B30 is 0.661, 0.722, 0.731 (in kg/kW-h) respectively. The variation of BSFC vs BP for different blends of diesel and pure diesel is shown in fig.2

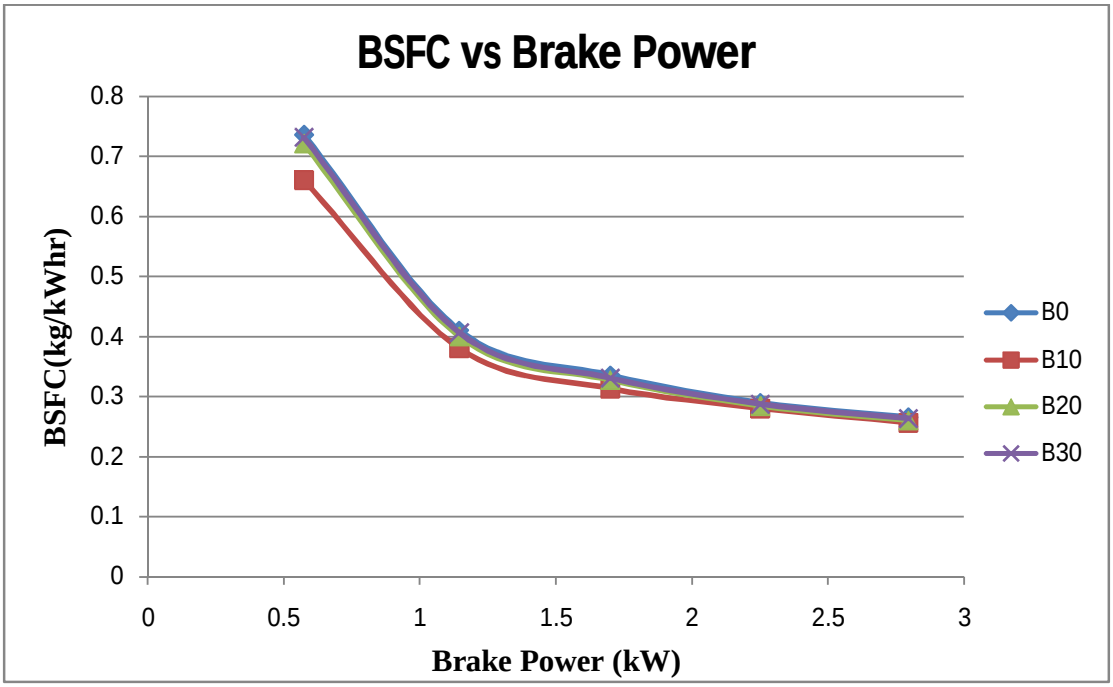

Fig.2 Brake specific fuel consumption vs Brake Power for diesel and biodiesel blends

©IJRASET (UGC Approved Journal): All Rights are Reserved

C. Brake Specific Energy Consumption Vs Brake Power For Diesel And Biodiesel Blends

The concept of brake specific energy consumption BSEC is same as brake specific fuel consumption BSFC because in mathematical expression of BSEC is the product of BSFC and calorific value of fuel. So the variation of BSFC and BSEC is same. BSEC is also increases with increases of percentage of biodiesel in blend.It is Also observed from the fig that Brake specific energy consumption BSEC for blends B10, B20, B30 at the maximum brake power of 2.79kW is 10.687, 10.855, 10.991 (in MJ/kW-h) respectively. And for the minimum load (brake power 0.574kW) BSFC is observed for B10, B20, B30 is 27.519, 30.078, 30.508 (in MJ/kW-h) respectively. The variation of BSFC vs BP for different blends of diesel and pure diesel is shown in fig.18

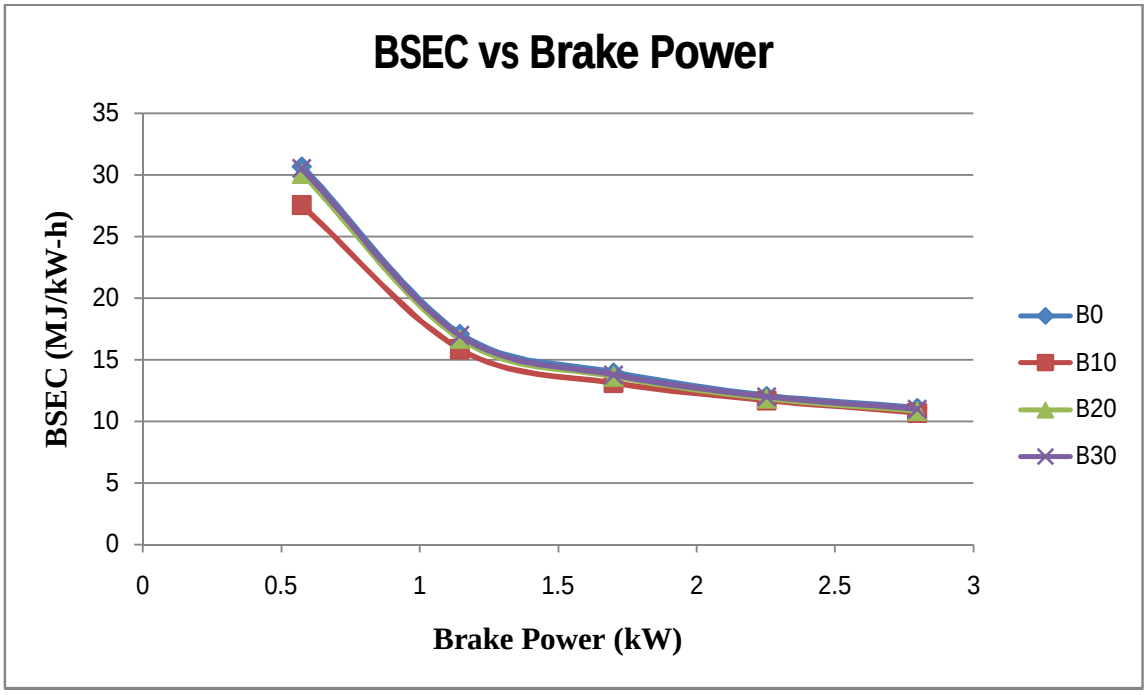

Fig.3 Brake specific energy consumption vs Brake Power for diesel and biodiesel blends

IV. CONCLUSION

A. Following Conclusion Has Been Made From The Experiments

1) For the engine performance testing it can be concluded that the performance parameter for blend of Hingot Biodiesel have gave better results than that of pure diesel without modification in engine setup.

2) The BTHE increases with increases brake power from low to high. This variation is shows because of better combustion biodiesel blends compare to pure diesel.

3) The BSFC decreases with increases in brake power. The BSFC is increases with increases in percentage of biodiesel in blend.

4) The BSEC also decreases with increases in brake power. The BSEC is increases with increases in percentage of biodiesel in blend just like BSFC.

5) It is also observed that BSEC and BSFC curves obtained by B20, B30 are very similar to pure diesel performed on the same engine at same load. Finally it can be concluded that the Hingot is also a one of the seed identified from which a biodiesel is also produced. Blend of Hingot Biodiesel is an industrial viable substitute for diesel engine.

REFRENCES

[1] K. NanthaGopal, Arindam Pal, Sumit Sharma, CharanSamanchi, K. sarthyananarayanan, T.Elango "Investigation of emissions and combustion characterstics of a CI Engine fueled with waste cooking oil methyl ester and diesel blends" , Alexanderia Engineering journal(2014) 53,pp281-287

[2] E.M Shahid, Y.Jamal, A.N. Shah, N. Rumzan, M. munsha. "Effect of used cooking oil methyl ester on Combustion Ignition Engine", Journal of Quantity and Technology Management, Volume VIII, Issue II, December 2012, pp.91-104

[3] Sheila M.Zakiya, Susun A. Roces, Nathaniel P.Dugos, Michael Angelo B. promentilla and Masahiro Shioj. "Emissions and Performance of Diesel Engine Fueled with Waste Cooking oil Methyl Ester Diesel Blends" , Iranica journal of Energy & Environment 5(1), (2014) pp.73-77

[4] R.B. Sharma, Dr. Amit Pal and JuhiSharaf. "Experimental Investigation of Bio-diesel Obtained from waste cooking oil and its Blends with diesel on Single Cylinder Engine", International Journal of Engineering Research and applications, ISSN: 2248-9622, Vol.4, Issue 1(Version 1), January 2014, pp.193-200.

©IJRASET (UGC Approved Journal): All Rights are Reserved

[5] K. Srinivas, N.Ramakrishna, B.Balunaik and K.Kalyaniradha. "Performance and emission analysis of waste vegetable oil and its blends with diesel and additives", Journal of Engineering Research and Application, ISSN: 2248-9622, vol.3, Issue 6, Nov-Dec 2013,pp.473-478

[6] Narayan Rao, G Lakshmi, S Sampath and K Rajagopal. " Experimental Studies on the combustipon and emission characterstics of a diesel engine fuelled with using cooking oil methyl ester and its diesel blends" World Academy of Science, Engineering and Technology Vol:2 2008, pp.01-25

[7] Hamad. M. Algasim and John Field house. "Performance and emissions of Compression Ignition Engines Using Waste Cooked Oil as fuel" Computing and Engineering Researcher's Conference, University of Huddersfield, Dec 2010, pp.65-70

[8] Amit Pal, Shashank Mohan and DhananjayTrivedi. " Production and Performance Testing of Waste Frying oil Biodiesel", International Journal of current Engineering and Technology, E-ISSN 2277-4104, Vol.4 No.3 (June-2014) pp. 347-516.

[9] R.B. Sharma, Dr. Amit Pal and JuhiSharaf. "Experiment Investigation of Bio-Diesel Obtained From Waste Cooking Oil and Its Blends with diesel on Single Cylinder Engine", International Journal of Engineering Research and Application, ISSN: 2248-9622, Vol.4, Issue 1(Version 1), January 2014, pp.193-200.

[10] NeeleshSoni, Om PrakashChaurasia "Experimental Investigation of 4 Stroke Compression Ignition Engine by using diesel and processed waste cooking blend" International Journal of Current Engineering and Scientific Research, ISSN: 2394-0697, Volume-3 Issue-1, 2016

©IJRASET (UGC Approved Journal): All Rights are Reserved

Engineering Science and Technology, an International Journal xxx (2018) xxx–xxx

HOSTED BY

Contents lists available at ScienceDirect

Engineering Science and Technology, an International Journal

journal homepage: www.elsevier.com/locate/jestch

Full Length Article

Performance analysis of solar parabolic trough collectors driven combined supercritical CO_2 and organic Rankine cycle

Harwinder Singh *, R.S. Mishra

Department of Mechanical, Production & Industrial, Automobile Engineering, Delhi Technological University, Shahbad Daulatpur, Bawana Road, New Delhi 110042, India

ARTICLE INFO

Article history:
Received 15 November 2017
Revised 10 March 2018
Accepted 26 March 2018
Available online xxxx

Keywords:
Supercritical CO_2cycle
Organic Rankine cycle
Exergetic performance
SPTCs
Organic fluids

ABSTRACT

In this paper, attempts have been made on the detailed energy and exergy analysis of solar parabolic trough collectors (SPTCs) driven combined power plant. The combination of supercritical CO_2 (SCO_2) cycle and organic Rankine cycle (ORC) integrated with SPTCs has been used to produce power, in which SCO_2 cycle and ORC are arranged as a topping and bottoming cycle. Five organic working fluids like R134a, R1234yf, R407c, R1234ze, and R245fa were selected for a low temperature bottoming ORC. Five key exergetic parameters such as exergetic efficiency, exergy destruction rate, fuel depletion ratio, irreversibility ratio, and improvement potential were also examined. It was revealed that exergetic and thermal efficiency of all the combined cycles enhances as the direct normal irradiance increases from 0.5 kW/m^2 to 0.95 kW/m^2. As can be seen, R407c combined cycle has the maximum exergetic as well as thermal efficiency which is around 78.07% at 0.95 kW/m^2 and 43.49% at 0.95 kW/m^2, respectively. Alternatively, the R134a and R245fa combined cycle yields less promising results with the marginal difference in their performance. As inferred from the study that SCO_2 turbine and evaporator has a certain amount of exergy destruction which is around 9.72% and 8.54% of the inlet exergy, and almost 38.10% of the total exergy estruction in case of R407c combined cycle. Moreover, the maximum mount of exergy destructed by the solar collector field which is more than 25% of the solar inlet exergy and around 54% of the total destructed exergy. Finally, this study concludes that R407c combined cycle has a minimum fuel depletion ratio of 0.2583 for a solar collector and possess the highest power output of 3740 kW.
© 2018 Karabuk University. Publishing services by Elsevier B.V. This is an open access article under the CC BY-NC-ND license (http://creativecommons.org/licenses/by-nc-nd/4.0/).

1. Introduction

Supercritical CO_2 cycle can effectively use different heat sources including coal power, solar thermal power, waste heat from the high temperature fuel cell, geothermal energy and natural gas [1]. The utilization of solar energy has become pivotal and it should be enhanced significantly in the near future. So it becomes imperative to upgrade the performance of solar thermal power plants. Moreover, among all the other options, solar parabolic trough collector (SPTC) technology considered as the most instituted solar thermal power technology for electricity production. Hence, for the purpose of exergy analysis, SPTC system considered as the efficient heat source. Nowadays, SCO_2 cycle and organic Rankine cycle integrated with various renewable heat sources are considered for the purpose of power generation, e.g. [2–8]. Cheng Zhou [2] compared the performance of hybrid solar and geothermal energy in a supercritical ORC with the different subcritical hybrid plants, standalone solar as well as geothermal plant. Finally, he concluded that the performance of hybrid plant using a supercritical ORC exceeds by producing 4–17% more electricity than the hybrid plant using a subcritical ORC by utilizing the same energy resources. Jing Li et al. [3] assessed the performance by using 17 dry and isentropic working fluids in a novel solar ORC system with the direct vapor generation (DVG). They found that with the rise in critical temperature of fluid, the collector efficiency reduces continuously and efficiency of a combined ORC and DVG system enhances. They further examined that R123 exhibits the highest overall performance among all other working fluids. Al-Sulaiman [4] conducted an exergy analysis of combined steam and ORC power system integrated by SPTC and he found that R134a shows the highest exergy efficiency of 26% which has the maximum amongst other refrigerants followed by R152a. Niu et al. [5] carried out a optimal arrangement of the solar collectors with a supercritical CO_2 based solar Rankine cycle system along with three different modes of collector arrangement, i.e. five units only in series, parallel and cascade with each five units in series. Lastly, their results found that the solar collectors in a cascade arrangement produce large amount of electric power. Cardemil et al. [6] carried out a thermodynamic study

* Corresponding author.
E-mail address: harrymehrok14@gmail.com (H. Singh).
Peer review under responsibility of Karabuk University.

https://doi.org/10.1016/j.jestch.2018.03.015
2215-0986/© 2018 Karabuk University. Publishing services by Elsevier B.V.
This is an open access article under the CC BY-NC-ND license (http://creativecommons.org/licenses/by-nc-nd/4.0/).

Please cite this article in press as: H. Singh, R.S. Mishra, Performance analysis of solar parabolic trough collectors driven combined supercritical CO_2 and organic Rankine cycle, Eng. Sci. Tech., Int. J. (2018), https://doi.org/10.1016/j.jestch.2018.03.015

Nomenclature

A_A	aperture area, m^2
A_a	area of the absorber tube, m^2
A_{co}	area of the absorber cover, m^2
Cp	specific heat, [kJ/kg-K]
Col_s	total no. of solar collector per single row in series
Col_p	total no. of solar collector in parallel rows
$D_{co,o}$	outside diameter of cover, m
D	diameter, m
Ex	exergy, kW
Ex_{inl}	inlet exergy, kW
$\dot{E}x_d$	rate of exergy destruction, kW
F	collector efficiency factor
F_R	collector heat removal factor
G_b	direct normal irradiance, W/m^2
h	specific enthalpy, kJ/kg
$h_{coa,i}$	heat loss coefficient between absorber and glass cover, [kW/m^2 K]
$h_{c,amco}$	convection heat loss coefficient between ambient and cover, [kW/m^2 K]
$h_{r,amco}$	radiation heat loss coefficient between ambient and cover, [kW/m^2 K]
$h_{r,coa}$	radiation heat loss coefficient between absorber and glass cover, [kW/m^2 K]
HX	heat exchanger
IMP	improvement potential
K_{air}	thermal conductivity of air, [W/m-K]
K_m	incident angle modifier
L	collector length, m
$\dot{m}_a$	mass flow rate through the absorber tube, kg/s
Nu	Nusselt number
ORC	organic Rankine cycle
$\dot{Q}$	heat rate, kW
Q_{inl}	total inlet heat, kJ
$\dot{Q}_u$	useful heat gain per unit time, kW
s	specific entropy, [kJ/kg-K]
S	absorbed heat flux by absorber tube, W/m^2
SCO_2	supercritical CO_2
tCO_2	transcritical CO_2
T	temperature, K
T_{su}	temperature of sun, K
U_L	overall heat loss coefficient of solar collector between ambient and absorber, [kW/m^2 K]
U_o	overall heat loss coefficient, [kW/m^2K]
$\dot{V}$	volume flow rate, m^3/s
W	width of collector, m
w	specific work output, kJ/kg
Y_{DEP}	fuel depletion ratio
Y^*	irreversibility ratio

Greek letters

ρ_r	mirror's reflectance
α	absorbance of absorber tube
γ	intercept factor
τ	glass cover's transmittance
η	efficiency
ε_{co}	emittance of the cover
ε_a	emittance of the absorber
σ	Stefan–Boltzmann constant, [kW/m^2 K^4]
φ	expansion ratio

Subscripts

a	absorber
a_o	absorber outlet
a_i	absorber inlet
am	ambient
avg	average
f	organic working fluid
co	cover
e	exit
ex	exergy per unit mass flow rate, kJ/kg
elec	electrical
i	inlet
ins	instantaneous
o	outside
0	environmental conditions
Q	property value at state Q
u	useful

of CO_2 based power cycles (i.e. Rankine or Brayton) with four different working fluids such as ethane, toluene, D4siloxane and water for the purpose of relative performance assessment. Ultimately, this study reveals that the first law efficiency of power cycle based on CO_2 could be lower than other fluids, while the exergetic efficiency of CO_2 could be crucially higher than competing fluids. Garga et al. [7] conducted a comparative study between trans-critical condensing CO_2 cycle (i.e. high temperature and pressure) and trans-critical steam cycle. They found that temperature variations did not affect the performance of trans-critical CO_2 cycle and it requires only single heat transfer fluid (HTF) loop as compared to trans-critical steam cycle coupled with two HTF loops in series. Osorio et al. [8] carried out a study to analyze the dynamic behavior of SCO_2 power cycle integrated with a concentrated solar power system (i.e. central receiver), hot and cold energy storage, heat exchange device, recuperator and multi-stage compression-expansion subsystem along with the intercooler and reheater as an integral component employed between the compressor and turbine. Their results showed that the process efficiency and maximum power output is 21% and 1.6 MW respectively. At last, they concluded that the SCO_2 cycle's operating time after optimization was increased from 220 to 480 min because of thermal storage application.

Further, few researchers considered the integrated SPTC with ORC for various applications like waste heat recovery and cogeneration process. Nafey and Sharaf [9] conducted a analysis related to exergy energy and cost evaluation of the ORC using parabolic trough collector as a heat source for generating mechanical power to drive desalination system by using reverse osmosis (RO). Delgado-Torres and García-Rodríguez [10,11,12] performed a detailed thermal analysis of ORC coupled with the parabolic trough collectors and a seawater RO unit to examine the ORC system for the production of water by RO process [10], and in another study, they carried out the various investigations related to preliminary designs of the low-temperature solar thermal collector driven RO desalination for sea water and brackish water. It was found that by using R245fa in a solar thermal driven RO system, the productivity of solar desalination system can be increased up to a maximum value (i.e. below 2%) [11], further they also performed a research to examine the effect of different working fluids such as butane, isobutene, R245ca, and R245fa on the aperture area of the SPTC system for water desalination and power production [12]. Al-Sulaiman et al. [13] carried out a study to assess the performance of a novel system integrated with SPTC and ORC for combined cooling, heating and power (CCHP). They used the part of waste heat from ORC for cooling as well as heating cogeneration,

Please cite this article in press as: H. Singh, R.S. Mishra, Performance analysis of solar parabolic trough collectors driven combined supercritical CO_2 and organic Rankine cycle, Eng. Sci. Tech., Int. J. (2018), https://doi.org/10.1016/j.jestch.2018.03.015

and examined the different output parameters. Finally, his study reveals that the electrical efficiency significantly enhances from 15% to 94% for a solar mode (i.e. without energy storage). Gao et al. [14] conducted a performance study of solar powered ORC and found that the efficiency increases as the inlet temperature and pressure of turbine increases when the system is located above the critical temperature limit. Wang and Dai [15] performed a exergoeconomic and comparative analysis of SCO_2/tCO_2 and SCO_2/ORC configuration and found that at a lower compression pressure ratio, the SCO_2/tCO_2 cycle performs better than SCO_2/ORC. Moreover, it was found that as compared to SCO_2/tCO_2 cycle, the SCO_2/ORC cycle has slightly lower value of total product unit cost. Singh and Mishra [16] carried out a performance analysis of the SPTC integrated supercritical ORC and found that R600a possess the maximum value of exergy efficiency which is around 96.09% at direct solar irradiation of 0.95 kW/m^2. Lastly, their study reveals that the improvement potential, fuel depletion ratio and irreversibility ratio in case of SPTC system was found to be 11859 kW, 0.579 and 0.9296, respectively. Ferrara at al. [17] conducted a thermodynamic analysis of concentrated solar power system integrated with ORC and found from their optimization results that acetone is the best choice for ORC system as compared to R134a and R245fa. Calise et al. [18] analysed the performance of the system based on evacuated flat-plate collector and ORC under the different climate conditions. It was observed that the efficiency of ORC always remains close to 10% during the entire year as compared to solar collector whose efficiency was high (>50%) in summer and low (down to 20%) in winter. Rayegan and Tao [19] developed a procedure to compare the capability of various fluids such as refrigerant and non-refrigerant used for a solar Rankine cycle. They found that the refrigerants (R-245fa and R-245ca), high performance non-refrigerants (Acetone and Benzene) and medium performance non-refrigerants (Butane, Isopentane, Trans-butene, and Cis-butene) can be effectively utilized in a solar ORC at medium temperature level. At last, their results showed that as the collector efficiency increases from 70% to 100%, the enhancement in the limit of irreversibility reduction and exergy efficiency was reported around 35% and 5%, respectively.

Hettiarachchi et al. [20] performed a optimization study of low temperature geothermal plant integrated with ORC and found that ammonia utilized the maximum amount of geothermal water. It was also observed that ammonia is a best choice according to the ratio of efficiency to objective function as compared to HCFC 123, n-Pentane, and PF5050. Gimelli et al. [21] performed a multi-objective optimization of the ORC system to optimize the efficiency as well as overall heat exchanger area, and obtained a set of optimal solution with the help of genetic algorithm. Finally, they characterized the solution of pareto optimal front with the range of electrical efficiency (i.e. 14.1% to 18.9%) and heat transfer area (i.e. 446–1079 m^2).

Apart from ORC, SCO_2 power cycle can be utilized for the exhaust/waste heat recovery process. Firms such as Echogen - power systems LLC (Ohio, USA) and General Electric (New York, USA) have already patents related to this application [22,23].

It is clearly understood from the literature review that there is no energy and exergy analysis of combined SCO_2 and ORC cycle integrated with SPTC. In the literature, exergy analysis of the combined steam Rankine cycle and ORC was performed [4]. This paper focuses its attention on the combination of SCO_2 and ORC, because SCO_2 cycle is able to replace the steam Rankine cycle due to some reasons for instance at the same temperature SCO_2 found to be less corrosive than steam which can effectively increase the inlet temperature of the turbine [1]. Also, smaller cycle pressure ratio and high outlet temperature of the turbine has been noticed in case of SCO_2 cycle as compared to steam Rankine cycle which results in increases the thermal efficiency [1]. Therefore, the concept of combined configuration in the current study is original and its aim is to find an energetic and exergetic performance of the combined SCO_2 and ORC power system integrated with SPTCs plant. Based on this, exergetic performance parameters like the rate of exergy destruction, improvement potential, fuel depletion ratio and irreversibility ratio were also examined in this research work.

2. System description

The present study considers a combined system integrated with solar parabolic trough collector as shown in Fig. 1. In this configuration, the SCO_2 cycle is a topping cycle while the ORC is a bottoming cycle and it is directly equipped with SCO_2 cycle for the purpose of utilization of waste heat. Temperature entropy diagram of the combined cycle is shown in Fig. 2. CO_2 as a working fluid used in the topping cycle at the critical conditions (i.e. 30.98 °C and 7.38 MPa) and it becomes incompressible near the critical point [1]. In the literature, the SCO_2 density has been compared with the water density by Wright et al. [49] and it was found that the density of CO_2 is 60% of the water density at the inlet of compressor, which can effectively reduced the need of compression power [50]. Fig. 3 shows the variations in density of CO_2 at different pressure and temperature conditions and a very high density can be noticed around the critical point, Thus compression work considerably reduced as compared to other fluids [50]. Apart from density, it was found that the thermal conductivity of CO_2 also possess the highest value at the critical conditions which is around 148.95 $\frac{mW}{m\text{-}K}$ at 305 K [50]. Also, specific heat of CO_2 varies radically with the pressure and temperature variations as shown in Fig. 4. As can be seen, the difference in temperature of fluids fluctuates broadly with in recuperator, which directly affect the design of recuperator with respect to the pitch point location [50]. Moreover, combined cycle also has an advantage over simple configuration because it can reduce the system design complexity due to condensation at atmospheric pressure not upon vacuum pressure as in simple configuration [4]. Multiple solar thermal collectors (i.e. SPTC field) are considered as a heat source for the combined cycle. SPTC field consists of 50 modules that are arranged in series per collector row and each having length of 12.27 m [4,13,24] and efficient single axis tracking system can be employed to track the sun movement so as to maximize the efficiency. Moreover, solar loop can be equipped with thermal storage facility to avoid the situation of sun set or blocked by clouds but this facility also includes some type of costs such as operating, storage medium, pipings, containers and insulating materials which results in increases the operational cost of overall plant. Table 1 lists the data related to geometrical parameters selected for a solar collector and Table 2 lists the thermal properties of working fluid flowing through the collector. Some refrigerants were selected for investigating the low-temperature ORC based on literature review. For specific heat source conditions, five refrigerants are selected: R134a, R407C, R1234yf, R1234ze and R245fa as listed in Table 3. These refrigerants are well suited for the low-temperature ORC coupled in combined cycle as a bottoming cycle and the fluid selection process is depends upon the thermodynamic and heat transfer properties, safety data, environmental as well as economy aspects [55]. Syltherm 800 is selected as the heat transfer fluid (HTF) for solar collector due to its maximum working temperature range of 420 °C [25] and it is best suited in this application amongst the other types of working fluids. In addition, it has a mass flow rate of 0.575 kg/s and 100 bar operating pressure in the SPTC field. The modified LS-3 (Luz third generation trough collector) is a latest SPTC design which has been chosen from the solar electric generating system (SEGS) with the collector row exit temperature of

Please cite this article in press as: H. Singh, R.S. Mishra, Performance analysis of solar parabolic trough collectors driven combined supercritical CO_2 and organic Rankine cycle, Eng. Sci. Tech., Int. J. (2018), https://doi.org/10.1016/j.jestch.2018.03.015

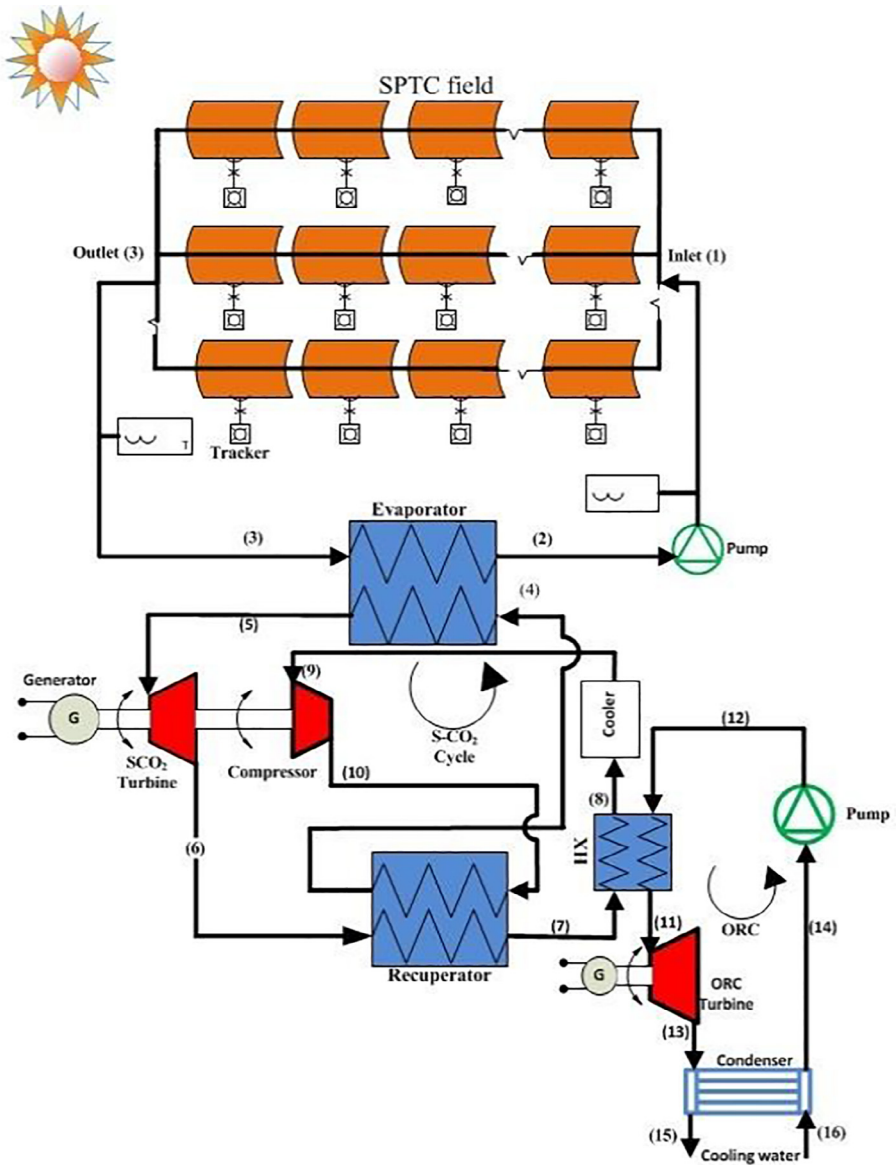

Fig. 1. Schematic of the solar parabolic trough collectors integrated with SCO_2 cycle and ORC.

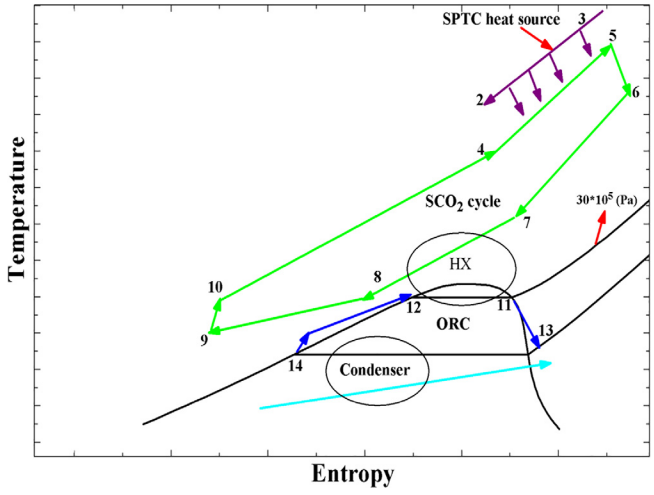

Fig. 2. Temperature entropy (T-S) diagram of combined cycle (SCO_2-ORC).

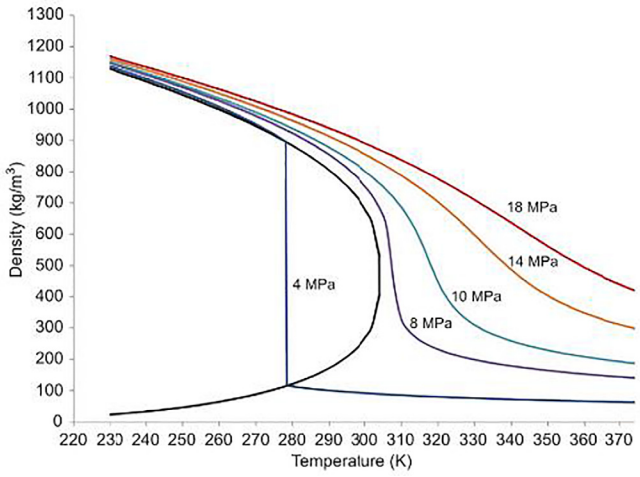

Fig. 3. Variations in density of CO_2 at different pressure and temperature [27,50].

Please cite this article in press as: H. Singh, R.S. Mishra, Performance analysis of solar parabolic trough collectors driven combined supercritical CO_2 and organic Rankine cycle, Eng. Sci. Tech., Int. J. (2018), https://doi.org/10.1016/j.jestch.2018.03.015

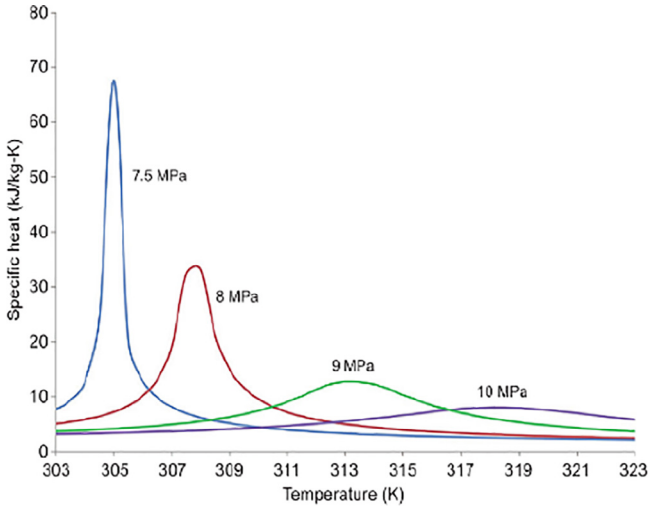

Fig. 4. Variations in specific heat of CO_2 at different pressure and temperature [27,50].

Table 1
Input data adapted for the system.

Solar parabolic collectors [4,26]	
Collector row length	500 m
Collector type	Modified LS-3
Collector width	5.76 m
Collector length (single)	12.27 m
Inner diameter of absorber tube	0.05 m
Outer diameter of absorber tube	0.07 m
Inner diameter of cover	0.115 m
Outer diameter of cover	0.121 m
Emittance of the cover	0.86
Emittance of the absorber tube	0.15
Reflectance of mirror	0.94
Intercept factor	0.93
Transmittance of glass cover	0.96
Absorbance of absorber tube	0.96
Shading loss	0.97
Structural loss	0.95
Concentration ratio	82:1
Intensity of direct irradiation	0.5–0.9 kW/m^2
Incidence angle modifier	1
No of collector in series (col_s)	50 [13]
No. of parallel collector rows (Col_p)	7 [13]
Row orientation	North-South
Mirror optical efficiency	73.27%
Maximum outlet pressure	100 bar
Maximum outlet temperature	673 K
Ambient conditions	
Ambient temperature	298.15 K
Ambient pressure	101.3 kPa
Combined cycle configuration	
SCO_2 turbine efficiency	90% [27,52]
Compressor efficiency	89% [27,48]
Organic pump efficiency	85% [27,52]
Organic turbine efficiency	87% [27,52]
Mass flow rate of SCO_2	10 kg/s
Pinch point temperature	5 °C [27,52]
SCO_2 cycle high pressure	25 MPa [27,48,52]
Baseline ORC turbine inlet pressure	3 MPa
Mass flow rate of ORC	2 kg/s
Recuperator effectiveness	95% [27,52]
Heat exchanger effectiveness	92%

400 °C (i.e. 673 K) [26]. The reason to choose LS-3 collector is that it has a larger aperture than LS-2 which results in 15% more receivers are required in case of LS-2 field. Also, LS-3 has a lower mirror cost on a per square meter as compared to LS-2 collector [54].

Table 2
Thermal properties of syltherm 800 at 650 K [28].

Thermal properties	Value
Specific heat capacity (c_p)	2218.26 [J/kg K]
Density (ρ)	577.70 kg/m^3
Thermal conductivity (λ)	0.067833 [W/m K]
Viscosity (μ)	0.000284 Pa-s

In the combined cycle, SCO_2 at high pressure and temperature expands in the turbine (process 5 to 6) up to a low temperature and pressure and then it goes to recuperator (process 6 to 7), where it extracts thermal energy from the hot stream and utilize this part of the energy to preheat the cold stream. After recuperation, the stream goes to heat exchanger (process 7 to 8), where stream gives the sufficient energy input to the ORC. Also, stream - cooled in the cooler unit (process 8 to 9) and then it goes to compressor unit which is driven by turbine (process 9 to 10), where stream pressure and temperature increases again. Then stream after passed through the recuperator reaches the evaporator unit (process 4 to 5), where SCO_2 steam extracts heat from the syltherm 800 fluid flowing through the SPTC system. Finally, it enters the turbine again and complete the cycle. Also, Power is generated by the combined cycle can be possible through the help of a generator as its rotor is directly connected to the turbine shaft as shown in Fig. 1.

3. Mathematical modeling

The modeling of combined cogeneration system is discussed in this section. The mathematical modeling of large-scale solar parabolic trough collector (SPTC) has been performed which is followed by the modeling of combined SCO_2 and ORC system. Exergy analysis of the SPTC system has been conducted by using the equations derived from previous research [4,29,30] and solved by computational numerical technique, i.e. Engineering Equation solver (EES) Software. Results from these equations were validated with the experiment work of Dudley et al. [31] and theoretical study of Al-Sulaiman [4]. Apart from this, assumptions made that the pressure drop in the system is neglected except in case of pump and turbine; the system is at steady state which mean that system should be in unchanged condition even after transformation; pump and turbine efficiency are always constant as mentioned in Table 1 for all the organic fluids.

3.1. Exergy model for SPTC based combined cycle

In this section, modeling of the SPTC based combined cycle is discussed. In the literature, Al-Sulaiman [4] conducted the modeling of the parabolic trough collector with receiver tube along with the evaluation of exergy destruction rate, exergy efficiency, exergetic fuel depletion ratio, irreversibility ratio, and improvement potential for combined cycle.

Useful energy collected by the solar collector per unit time is defined as:

$$\dot{Q}_u = \dot{m}_a \cdot Cp_a \cdot (T_{a_o} - T_{a_i}) \quad (1)$$

where Cp is the specific heat and $\dot{m}_a$ is the mass flow rate of liquid flowing in the absorber tube. The subscripts a_o and a_i refers to the absorber outlet and absorber inlet. Further, the useful heat gain can also be evaluated from the another formula which is given by:

$$\dot{Q}_u = A_A \cdot F_R \cdot \left(S - \frac{A_a}{A_A} U_L (T_{ai} - T_0) \right) \quad (2)$$

Please cite this article in press as: H. Singh, R.S. Mishra, Performance analysis of solar parabolic trough collectors driven combined supercritical CO_2 and organic Rankine cycle, Eng. Sci. Tech., Int. J. (2018), https://doi.org/10.1016/j.jestch.2018.03.015

Table 3
Physical, environmental properties and security data of the selected working fluids for ORC adapted from [38,39,40,44].

Working substance	Physical properties data					Security group	Environmental properties		
	Type[a]	Weight (kg/kmol)	T_b[b] (°C)	T_c[c] (°C)	P_c[d] (MPa)		Lifetime (years)	ODP[e]	GWP[f]
R134a	I	102.03	−26.1	101	4.059	A1	14	0	1430
R407C	W	86.20	−43.6	86.79	4.597	A1	n.a.	0	1800
R1234yf	I	114.04	−29.5	94.7	3.38	A2L	0.029	0	<1
R1234ze(E)	I	114.04	−19.0	109.4	3.64	A2L	0.045	0	<1
R245fa	D	134.05	15.1	154.1	3.65	B1	7.7	0	1050

[a] W = Wet; D = Dry; I = Isentropic.
[b] T_b = normal boiling temperature.
[c] T_c = critical temperature.
[d] P_c = critical pressure.
[e] ODP = potential of ozone depletion relative to R11.
[f] GWP = potential of global warming relative to CO_2.

where F_R is a collector heat removal factor, A_A is the area of aperture, S is the heat flux absorbed by absorber tube, T_0 is the atmospheric temperature, and U_L is the overall heat loss coefficient of the solar collector. Absorbed heat flux and aperture area can be defined as:

$$S = \eta_a \cdot G_b \tag{3}$$

$$\eta_a = \rho_r \cdot \alpha \cdot \gamma \cdot \tau \cdot K_m \tag{4}$$

$$A_A = (W - D_{co,o}) \cdot L \tag{5}$$

where W is the width of collector, η_a is the efficiency of absorber or receiver, $D_{co,o}$ is the outside diameter of cover, L is the collector length, ρ_r is mirror's reflectance, α is absorbance of absorber tube, γ is intercept factor, τ is glass cover's transmittance, K_m is incident angle modifier which is determined by dividing the instantaneous thermal efficiency (η_i) at a given value of angle of incidence to the peak efficiency of SPTC [32], and G_b is direct solar irradiance. Apart from these parameters, the ratio of S to G_b gives the efficiency of the absorber tube η_a. All the necessary data related to these parameters has been listed in Table 1. Further, heat removal factor is defined as below:

$$F_R = \frac{\dot{m}_a \cdot C_{Pa}}{A_a \cdot U_L}\left(1 - \exp\left(-\frac{F \cdot A_a \cdot U_L}{\dot{m}_a \cdot C_{Pa}}\right)\right) \tag{6}$$

where $A_a = \pi D_{a,O} L$ and F is collector efficiency factor which is defined as below:

$$F = \frac{U_o}{U_L} \tag{7}$$

where U_o is the overall heat loss coefficient between surrounding and fluid flowing through the absorber tube, and U_L is the heat loss coefficient of solar collector between ambient and absorber tube which is defined as:

$$U_o = \left[\frac{1}{U_L} + \frac{D_{a,o}}{h_{coa,i} D_{a,i}} + \left(\frac{D_{a,o}}{2K_a}\ln\left(\frac{D_{a,o}}{D_{a,i}}\right)\right)\right]^{-1} \tag{8}$$

where $h_{coa,i}$ is the heat loss coefficient between absorber and glass cover as shown below:

$$h_{coa,i} = \frac{Nu_a \cdot k_a}{D_{a,i}} \tag{9}$$

Now heat loss coefficient of solar collector is defined as below:

$$U_L = \left[\frac{A_a}{(h_{c,amco} + h_{r,amco})A_{co}} + \frac{1}{h_{r,coa}}\right]^{-1} \tag{10}$$

where subscripts a & co refers to the absorber and cover, $h_{c,amco}$ is the convection heat loss coefficient between ambient and cover, $h_{r,amco}$ is the radiation heat loss coefficient, and $h_{r,coa}$ is the radiation heat loss coefficient between absorber and glass cover which is defined as below:

$$h_{c,amco} = \frac{Nu \cdot K_{air}}{D_{co,o}} \tag{11}$$

$$h_{r,amco} = \varepsilon_{co} \cdot \sigma \cdot (T_{co}^2 + T_{am}^2)(T_{co} + T_{am}) \tag{12}$$

and

$$h_{r,coa} = \frac{\sigma \cdot (T_{co} + T_{a,avg})(T_{co}^2 + T_{a,avg}^2)}{\frac{1}{\varepsilon_a} + \frac{A_a}{A_{co}}\left(\frac{1}{\varepsilon_{co}} - 1\right)} \tag{13}$$

Here the subscript am refers to ambient and avg refers to average, K_{air} is thermal conductivity of air, Nu is Nusselt number, σ is Stefan–Boltzmann constant, ε_{co} is emittance of the cover, ε_a is emittance of the absorber. Further, temperature of cover is defined as:

$$T_{co} = \frac{h_{r,coa}T_{a,am} + \frac{A_{co}}{A_a}(h_{c,amco} + h_{r,amco})T_{am}}{h_{r,coa} + \frac{A_{co}}{A_a}(h_{c,amco} + h_{r,amco})} \tag{14}$$

The total amount of solar flux directed (i.e. beam radiation) upon the SPTC which is assumed as total heat available for the combined system.

$$\dot{Q}_s = A_A \cdot F_R \cdot S \cdot Col_s \cdot Col_p \tag{15}$$

where Col_s&Col_p is the total no. of collectors per single row in series and the total no. of collectors in parallel rows arrangement.Energy efficiency ($\eta_{en,SPTC}$) of SPTC can be expressed as [56]:

$$\eta_{en,SPTC} = \eta_o - c_1\frac{(T_m - T_a)}{G_b} - c_2\frac{(T_m - T_a)^2}{G_b} \tag{16}$$

where η_o is the optical efficiency the SPTC, c_1 is the first order coefficient [W/m^2 °C] and c_2 is the second order coefficient [W/m^{2+}°C^2], T_m is the mean temperature of heat transfer oil which is defined as:

$$T_m = \frac{(T_1 + T_3)}{2} \tag{17}$$

Further, the term exergy is defined as the theoretical maximum work obtained from system as it interacts with the surrounding in an equilibrium condition. Therefore, steady state exergy balance of the control volume for each component based on physical boundary approach in a combined cycle is defined as:

$$\sum_Q\left(1 - \frac{T_o}{T_Q}\right)\dot{Q}_Q - \dot{w}_{c.v.} - \sum_i(\dot{m}_i Ex_i) - \sum_j(\dot{m}_e Ex_e) - \dot{Ex}_d = 0 \tag{18}$$

where $\dot{Ex}_d$ is the rate of exergy destruction, subscripts O and Q refers to the value of physical property at surrounding or dead state

Please cite this article in press as: H. Singh, R.S. Mishra, Performance analysis of solar parabolic trough collectors driven combined supercritical CO_2 and organic Rankine cycle, Eng. Sci. Tech., Int. J. (2018), https://doi.org/10.1016/j.jestch.2018.03.015

(i.e. T_0 = 298.15 K and P_0 = 101.3 kPa) and for a particular state, subscripts e and i refers to the exit and inlet state. Further, the Ex is the exergy per unit mass flow rate and chemical exergy value assumed to be negligible in the system.

Now physical exergy per unit mass flow rate after neglecting the change in both velocity and elevation can be defined as under [4,33]:

$$Ex^{ph} = (h - h_0) - T_0(s - s_0) \tag{19}$$

where h and s are specific enthalpy and specific entropy. Further, exergy at the inlet point of system ($\dot{E}x_{inl}$) is known as the maximum useful work available from solar radiation which is calculated by the Petela's formula as defined below [4,34,35,36]:

$$Ex_{inl} = A_A \cdot G_b \cdot \left[1 + \frac{1}{3}\left(\frac{T_o}{T_{su}}\right)^4 - \frac{4}{3}\left(\frac{T_o}{T_{su}}\right)\right] \tag{20}$$

where, T_{su} is the temperature of superficial surface of the sun (black body) i.e. 5800 K [4].

Exergy ($\dot{E}x_u$) gain by working fluid from the SPTC can be expressed as [56]:

$$\dot{E}x_u = \frac{\dot{Q}_u}{T_3 - T_1}\left[(T_3 - T_1) - \left(T_o \ln\frac{T_3}{T_1}\right)\right] \tag{21}$$

The exergy efficiency of SPTC can be defined as:

$$\eta_{ex,SPTC} = \frac{\dot{E}x_u}{Ex_{inl}} \tag{22}$$

Further, the input parameters required for the exergy and energy analysis of combined cycle has been listed in Table 1. Also, modelling of the combined cycle is based on the thermodynamic as well as exergetic equations which are derived from the literature [37,51,52].

The overall electrical exergy efficiency can be defined as the ratio of net electrical output to the exergy at input, '$\eta_{elec,ex}$' for combined cycle is given by:

$$\eta_{elec,ex} = 1 - \frac{Ex_{DES_{Total}}}{Ex_{inl}} \tag{23}$$

where $Ex_{DES_{Total}}$ is the total exergy destruction in combined cycle and it is defined as:

$$\begin{aligned} Ex_{DES_{Total}} = {} & Ex_{DES_{SCO2,Turbine}} + Ex_{DES_{Recuperator}} + Ex_{DES_{Evaporator}} \\ & + Ex_{DES_{Heatexhanger}} + Ex_{DES_{compressor}} + Ex_{DES_{ORC,Turbine}} \\ & + Ex_{DES_{Condensor}} + Ex_{DES_{Pump}} \end{aligned} \tag{24}$$

Now the fraction of total exergy destruction of a component can be defined as the difference of input and output exergy, which is calculated as:

$$Ex_{DES_{SCO2,Turbine}} = \frac{((Ex_5 - Ex_6) - W_{SCO2,Turbine})}{Ex_{inl}} \tag{25}$$

$$Ex_{DES_{Recuperator}} = \frac{((Ex_7 - Ex_6) - (Ex_4 - Ex_{10}))}{Ex_{inl}} \tag{26}$$

$$Ex_{DES_{Evaporator}} = \frac{(Ex_{inl} - (Ex_5 - Ex_4))}{Ex_{inl}} \tag{27}$$

$$Ex_{DES_{Heatexhanger}} = \frac{((Ex_7 - Ex_8) - (Ex_{11} - Ex_{12}))}{Ex_{inl}} \tag{28}$$

$$Ex_{DES_{compressor}} = \frac{(W_{Compressor} - (Ex_{10} - Ex_9))}{Ex_{inl}} \tag{29}$$

$$Ex_{DES_{ORC,Turbine}} = \frac{((Ex_{11} - Ex_{13}) - W_{ORC,Turbine})}{Ex_{inl}} \tag{30}$$

$$Ex_{DES_{Condensor}} = \frac{((Ex_{13} - Ex_{14}) - (Ex_{15} - Ex_{16}))}{Ex_{inl}} \tag{31}$$

$$Ex_{DES_{Pump}} = \frac{(W_{Pump} - (Ex_{12} - Ex_{14}))}{Ex_{inl}} \tag{32}$$

Total heat input provided by solar collector to the combined cycle in evaporator unit can be defined as:

$$Q_{inl} = \dot{m}_{SCO_2} \cdot (h_5 - h_4) \tag{33}$$

where $\dot{m}_{SCO_2}$ is the mass flow rate of SCO_2 in the topping cycle.

Thermodynamic process (5 to 6) in SCO_2 turbine can be described as:

$$W_{SCO_{2,Turbine}} = \dot{m}_{SCO_2} \cdot (h_5 - h_{6s}) \cdot \eta_{SCO_{2,Turbine}} \tag{34}$$

where h_{6s} is the isentropic enthalpy at the outlet of SCO_2 turbine.

Thermodynamic balance in the recuperator (process 6 to 7) can be expressed as:

$$Q_{Recuperator} = \dot{m}_{SCO_2} \cdot (h_6 - h_7) = \dot{m}_{SCO_2} \cdot (h_4 - h_{10}) \tag{35}$$

The effectiveness factor and recuperative ratio is given as:

$$\varepsilon = \frac{h_6 - -h_7}{h_6 - -h_7(T_{10}, P_7)} \tag{36}$$

where $h_7(T_{10}, P_7)$ is the enthalpy at the state 7 which is based on the assumption that the temperature of SCO_2 stream leaving the recuperator at state 7 reaches the temperature of incoming SCO_2 stream from the compressor at state 10.

Now waste heat provided by SCO_2 cycle to ORC through the HX unit (process 7 to 8) can be defined as:

$$Q_{inl,ORC} = \dot{m}_{SCO_2} \cdot (h_7 - h_8) \tag{37}$$

Thermodynamic relation for HX unit (process 6 to 7) is given by:

$$Q_{HX} = \dot{m}_{SCO_2} \cdot (h_7 - h_8) = \dot{m}_f \cdot (h_{11} - h_{12}) \tag{38}$$

where $\dot{m}_f$ is the mass flow rate of working fluid in bottoming ORC unit.

Process (8 to 9) for cooler unit can be written as:

$$Q_{Cooler} = \dot{m}_{SCO_2} \cdot (h_8 - h_9) \tag{39}$$

Process (9 to 10) for SCO_2 compressor is given by:

$$W_{SCO_{2,Compressor}} = \frac{\dot{m}_{SCO_2} \cdot (h_{10s} - h_9)}{\eta_{SCO_{2,Compressor}}} \tag{40}$$

Now thermal process (11 to 13) for ORC turbine is defined by:

$$W_{ORC,Turbine} = \dot{m}_f \cdot (h_{11} - h_{13s}) \cdot \eta_{ORC,Turbine} \tag{41}$$

where h_{13s} is the isentropic enthalpy at the outlet of ORC turbine.

Process (13 to 14) for condenser unit can be written as:

$$Q_{Condenser} = \dot{m}_f \cdot (h_{13} - h_{14}) \tag{42}$$

Process (14 to 12) for pump is given as:

$$W_{ORC,Pump} = \frac{\dot{m}_f \cdot (h_{12s} - -h_{14})}{\eta_{ORC,Pump}} \tag{43}$$

where h_{12s} is the isentropic enthalpy at the outlet pump.

Further the thermal efficiency of the combined cycle can be expressed as:

$$\eta_{combined} = \frac{W_{net,SCO_2} + W_{net,ORC}}{Q_{inl}} \tag{44}$$

Please cite this article in press as: H. Singh, R.S. Mishra, Performance analysis of solar parabolic trough collectors driven combined supercritical CO_2 and organic Rankine cycle, Eng. Sci. Tech., Int. J. (2018), https://doi.org/10.1016/j.jestch.2018.03.015

Net power output from SCO_2 cycle and ORC can be calculated as:

$$W_{net,SCO_2} = W_{SCO2,Turbine} - W_{SCO_{2,Compressor}} \quad (45)$$

$$W_{net,ORC} = W_{ORC,Turbine} - W_{ORC,Pump} \quad (46)$$

Now outlet temperature of SPTC can be assumed as constant. Therefore, total exergy input to the cycle is given by:

$$Ex_{inl} = Q_{inl} \cdot \left[1 - \frac{T_O}{T_3}\right] \quad (47)$$

Apart from these, few important terms like exergetic fuel depletion ratio (Y_{DEP}), irreversibility ratio (Y^*), improvement potential (IMP) for a particular state Q, and the expansion ratio (φ) are defined as under:

Fuel depletion ratio is also an important exergetic parameter for the improvement in system performance. It is defined as the ratio of rate of exergy destruction to the inlet exergy.

$$Y_{DEP(state\ Q)} = \frac{Ex_{DES_{(State\ Q)}}}{Ex_{Total,inl}} \quad (48)$$

Irreversibility ratio is a another crucial parameter and it is defined as the ratio of exergy destructed to the total exergy destruction rate in a system.

$$Y^*_{(State\ Q)} = \frac{Ex_{DES_{(State\ Q)}}}{Ex_{DES_{Total}}} \quad (49)$$

Improvement potential (IMP) is an important exergetic parameter used to identify that how much improvement can be possible in the combined system.

$$IMP_{(State\ Q)} = (1 - \frac{\eta_{elec,ex}}{100}) Ex_{DES_{(State\ Q)}} \quad (50)$$

Lastly, expansion ratio of the ORC cycle can be calculated as:

$$\varphi = \left[\frac{\dot{V}_{13}}{\dot{V}_{11}}\right] \quad (51)$$

where $\dot{V}$ is the volume flow rate.

3.2. Validation of SPTC model

Validation of the working solar collector has been possible through the comparison of current model results with the experimental study performed by Dudley et al. [31] and theoretical study of Al-Sulaiman [4] as shown in Table 4. The variation in heat loss was calculated corresponding to the change in average temperature above the ambient temperature of fluid flowing inside the receiver. The results of current model show good agreement with the existing experimental work. It has been found that very modest variations exist in the results as compared to experimental results [31] attributed to the approximation used for the evaluation of heat loss coefficients. In this study, baseline simulation of the combined system shows that the average fluid temperature in absorber is 288.8 °C above the ambient temperature, while in the previous study related to exergy modeling of trigeneration system the average absorber fluid temperature is less than 200 °C above the ambient temperature [41]. Lastly, all physical and environmental properties along with security data for all the selected fluids are listed in Table 3.

Table 4
Change in heat losses with average temperature of the fluid above the ambient of the absorber.

Temp. difference (°C)	Heat loss (W/m^2) (Current model)	Heat loss (W/m^2) (Dudley et al. [31])	Heat loss (W/m^2) (Al-Sulaiman [4])
100.6	10.78	10.6	8.7
149.1	17.24	19.3	19.3
196.7	32.15	30.6	34.2
245.8	54.48	45.4	53
293.3	67.69	62.9	75.5

For the purpose of validation of considered system, numerous researches [51,52,53] are selected from the available literature. The simulation results of current study as well as results of previous researches are shown in Table 5 and the comparison indicates that the simulation results of present model properly agree with that of literature work at the same baseline conditions, thus it can be used to analyse the performance of combined cycle.

4. Results and discussion

In this study, a comprehensive exergetic analysis for individual component of the considered system is presented first. Then the exergetic performance of SPTC driven combined cycle has been examined against the variations of solar irradiation intensity and inlet pressure of SCO_2 turbine by using EES software. Currently, SPTC system is designed on the basis of the average value of direct normal irradiance, i.e. 850 W/m^2 according to Indian climate conditions in which combined (SCO_2-ORC) cycle is assumed to be operated. Furthermore, the effect of solar irradiation on the combined cycle performance was examined during the daytime between the full range of direct normal irradiance, i.e. 500 W/m^2 to 950 W/m^2.

4.1. Results of detailed exergetic analysis of the system components

To assess the performance of components associated with the combined cycle, an exergetic and energetic analysis has been conducted in this study. The benefit and motivation behind this exergy and energy method that it is helpful in find out the quality of heat transfer in a particular process [46] and to check the sustainability level of system [47]. The numerical computational method by EES software is used to solve the equations related to the exergetic paramters. The thermodynamic properties at different stations for the R134a based SPTC integrated combined cycle under the baseline conditions has been listed in Table 6. Key exergetic parameters like fuel depletion ratio, improvement potential, rate of exergy destruction, and irreversibility ratio also has been examined. A major part of total exergy loss was found in the solar collector, solar heat exchanger (i.e. evaporator) and SCO_2 turbine as shown in Table 7. The reason behind the highest rate of exergy destruction is the large temperature difference between incoming and outgoing fluid stream. Results of the study conclude that R407c combined cycle showed the least exergy destruction rate for the net electrical power of 3740 kW. Furthermore, exergetic parametric values are given in Table 7 and these values have been evaluated under the fixed baseline conditions such as inlet pressure of 25 MPa for SCO_2 turbine, direct normal irradiance of 850 W/m^2, inlet or high temperature of 653 K, and 10 kg/s mass flow rate of SCO_2. Also, R245fa has the highest rate of exergy destruction, i.e. around 6092 kW in the solar collector, 2108 kW in the SCO_2 turbine, and 1895 kW in the evaporator, which is depend upon the different mass flow rate of working fluids flowing in the solar collector, SCO_2 cycle, and ORC.

As can be seen, solar collector has the highest value of exergy destruction rate in the overall plant. Therefore, it requires careful design process to improve the exergetic performance. Improvement potential (IMP) for the solar collector in R407c combined cycle was found to be 5282 kW and for other

Please cite this article in press as: H. Singh, R.S. Mishra, Performance analysis of solar parabolic trough collectors driven combined supercritical CO_2 and organic Rankine cycle, Eng. Sci. Tech., Int. J. (2018), https://doi.org/10.1016/j.jestch.2018.03.015

Table 5
Validation results of combined cycle model.

Working fluid	Reference	Thermal efficiency in reference	Thermal efficiency predicted	Error estimation
SCO_2	Besarati et al. [52]	0.4507	0.4333	−3.8%
SCO_2	Song et al. [51]	0.491	0.482	−1.8%
Working fluid	Reference	Thermal efficiency in reference	Thermal efficiency predicted	Error estimation
R245fa	Clemente et al. [53]	0.11	0.119	8.1%
R245fa	Song et al. [51]	0.114		4.3%
Working fluid	Reference	Thermal efficiency in reference	Thermal efficiency predicted	Error estimation
R245fa	Besarati et al. [52]	0.5140	0.5203	1.2%

Table 6
Thermodynamic properties at selected stations for R134a based SPTC integrated combined cycle [42,43].

SPTC integrated combined cycle (SPTC-SCO_2-ORC)	Selected stations	Fluid type	$\dot{m}$ (kg/s)	P (bar)	T (K)	h (kJ/kg)	s (kJ/kg K)
	SPTC inlet (1)	Syltherm 800	0.575	100	544.6	718.8	1.712
	SPTC outlet (3)	Syltherm 800	0.575	100	673	832.3	2.379
	SCO_2 Turbine inlet (5)	SCO_2	10	250	653	819.58	2.4044
R134a	SCO_2 Turbine outlet (6)	SCO_2	10	155.8	562.3	723.18	2.4533
	Recuperator outlet (7)	SCO_2	10	155.8	388.3	487.23	1.8254
	Compressor inlet (9)	SCO_2	10	155.8	327.5	324.63	1.3658
	Compressor outlet (10)	SCO_2	10	250	362.8	381.35	1.3987
	Evaporator inlet (4)	SCO_2	10	250	524.6	654.72	2.1230
	ORC Turbine inlet (11)	R134a	2	30	368.9	446.24	1.7268
	ORC Turbine outlet (13)	R134a	2	6.386	310.6	405.46	1.7622
	Condenser Outlet (14)	R134a	2	6.386	298.5	382.39	1.6226
	HX inlet (12)	R134a	2	30	318.8	392.26	1.6705

Table 7
Detailed exergetic parameters of combined cycle for all the selected working fluids [43].

Exergetic parameter	System components	Combined cycle				
		R134a	R245fa	R1234ze	R407c	R1234yf
Exergy Destruction(kW)	SPTC field	5810	6092	5563	5310	5679
	Evaporator	1880	1895	1773	1756	1825
	Solar pump	2.576	2.368	2.478	5.515	2.404
	SCO_2 turbine	2099	2108	1987	1999	2045
	ORC turbine	565.2	505.1	529.8	516.2	517.3
	ORC pump	4.705	3.916	2.08	5.403	7.494
	Recuperator	46.56	41.4	44.6	60.37	45.21
	HX	89.4	87.19	75.34	23.47	76.23
	Condenser	0.0355	0.0382	0.0374	0.0436	0.0377
	Compressor	407.6	404.3	388.1	308	404
IMP (kW)	SPTC field	5783	6064	5535	5282	5651
	Evaporator	1866	1881	1760	1743	1812
	Solar pump	2.564	2.357	2.465	5.487	2.392
	SCO_2 turbine	2083	2093	1973	1984	2030
	ORC turbine	561.1	501.4	525.9	511.6	513.5
	ORC pump	4.671	3.887	2.065	5.362	7.439
	Recuperator	46.23	41.1	44.27	59.92	44.88
	HX	88.75	86.56	74.78	23.29	75.67
	Condenser	0.0352	0.0379	0.0371	0.0433	0.0375
	Compressor	404.6	401.4	385.2	305.7	401
Y_{DEP}	SPTC field	0.2826	0.2963	0.2705	0.2583	0.2762
	Evaporator	0.1006	0.1015	0.09437	0.0934	0.09743
	Solar pump	$1.253 * 10^{-4}$	$1.152 * 10^{-4}$	$1.205 * 10^{-4}$	$2.683 * 10^{-4}$	$1.169 * 10^{-4}$
	SCO_2 turbine	0.1124	0.113	0.1058	0.1063	0.1092
	ORC turbine	$3.026 * 10^{-2}$	$2.706 * 10^{-2}$	$2.82 * 10^{-2}$	$2.764 * 10^{-2}$	$2.761 * 10^{-2}$
	ORC pump	$2.519 * 10^{-4}$	$2.098 * 10^{-4}$	$1.107 * 10^{-4}$	$2.873 * 10^{-3}$	$4.0 * 10^{-4}$
	Recuperator	$2.493 * 10^{-3}$	$2.218 * 10^{-3}$	$2.374 * 10^{-3}$	$3.211 * 10^{-3}$	$2.413 * 10^{-3}$
	HX	$4.786 * 10^{-3}$	$4.671 * 10^{-3}$	$4.01 * 10^{-3}$	$1.248 * 10^{-3}$	$4.069 * 10^{-3}$
	Condenser	$1.901 * 10^{-6}$	$2.047 * 10^{-6}$	$1.994 * 10^{-6}$	$2.32 * 10^{-6}$	$2.017 * 10^{-6}$
	Compressor	$2.182 * 10^{-2}$	$2.166 * 10^{-2}$	$2.066 * 10^{-2}$	$1.638 * 10^{-2}$	$2.156 * 10^{-2}$
Y^*	SPTC field	0.5387	0.553	0.5426	0.5388	0.5416
	Evaporator	0.1743	0.172	0.1729	0.1782	0.1741
	Solar pump	$2.388 * 10^{-4}$	$2.15 * 10^{-4}$	$2.417 * 10^{-4}$	$5.596 * 10^{-4}$	$2.293 * 10^{-4}$
	SCO_2 turbine	0.4121	0.4179	0.414	0.4295	0.4156
	ORC turbine	0.111	0.1001	0.1104	0.1053	0.1051
	ORC pump	$9.239 * 10^{-4}$	$7.761 * 10^{-4}$	$4.334 * 10^{-4}$	$1.161 * 10^{-3}$	$1.523 * 10^{-3}$
	Recuperator	$9.144 * 10^{-3}$	$8.205 * 10^{-3}$	$9.292 * 10^{-3}$	$1.297 * 10^{-2}$	$9.187 * 10^{-3}$
	HX	$1.756 * 10^{-2}$	$1.728 * 10^{-2}$	$1.57 * 10^{-2}$	$5.042 * 10^{-3}$	$1.549 * 10^{-2}$
	Condenser	$6.973 * 10^{-6}$	$7.573 * 10^{-6}$	$7.804 * 10^{-6}$	$9.373 * 10^{-6}$	$7.677 * 10^{-6}$
	Compressor	$8.004 * 10^{-2}$	$8.013 * 10^{-2}$	$8.084 * 10^{-2}$	$6.617 * 10^{-2}$	$8.209 * 10^{-2}$

Please cite this article in press as: H. Singh, R.S. Mishra, Performance analysis of solar parabolic trough collectors driven combined supercritical CO_2 and organic Rankine cycle, Eng. Sci. Tech., Int. J. (2018), https://doi.org/10.1016/j.jestch.2018.03.015

combined cycles is listed in Table 7. IMP represents that the major exergy loss can be avoided through the design improvement of the whole solar collector plant by maximizing the collector's optical efficiency as well as minimizing the overall heat losses of collector area. Other part of the combined cycle requires also a excellent design to improve the system performance, for instance evaporator, recuperator, and heat exchanger have a significant amount of exergy destructions. Therefore, these components need a larger area for heat transfer with respect to betterment of the system design. In case of R245fa, the maximum exergy destruction rate of solar collector field was found to be 29.6% of the inlet exergy (i.e. 20,562 kJ), and almost 19.4% of the inlet exergy has been destructed in the SCO_2 turbine and evaporator. From the Table 7, it is clear that R407c combined cycle has comparatively minimum value of fuel depletion ratio among all the other systems which is around 0.2583, 0.1063, and 0.0934 for the solar collector, SCO_2 turbine, and evaporator, respectively.

Moreover, solar collector and SCO_2 turbine have the highest value of irreversibility ratio in the complete cycle (SPTC-SCO_2-ORC). Evaporator also has an accountable value ofi rreversibility ratio as shown in Table 7 for all working fluids. In addition, variation in the results of thermal efficiency and expansion ratio for the various organic fluids are presented in Fig. 5. It has been observed from the study that with the increase in evaporating temperature of ORC, expansion ratio also increases. Therefore, the maximum expansion ratio value of 1.143 has been noticed in case of R134a, while R407c possess the maximum thermal efficiency value of 41.92%. Lastly, Fig. 6 illustrates the variation in power generation of selected combined cycles at the fixed baseline conditions as mentioned above. The study also reveals that R407c combined cycle showed the maximum power generation value of 3740 kW among all other organic fluids.

4.2. Effect on system performance with variation in intensity of solar irradiation

The exergetic performance of considered system is clearly affected by the changes in solar irradiation intensity as illustrated in Fig. 7. From the Fig. 7, it has been observed that the exergy efficiency of combined cycle (SCO_2-ORC) increases with the increase in solar irradiation intensity which has been analyzed under the simulation conditions of high pressure and mass flow rate of SCO_2 (i.e. 25 MPa and 10 kg/s). As can be seen, the increasing solar irradiation intensity upon the collector field gives the better and efficient utilization of specific range of the solar collector rows available in the overall solar field, which results in exergetic performance enhances. Among all the selected refrigerants for the combined cycle, R407c showed the maximum exergetic efficiency followed by R1234ze, R1234yf, R245fa, and R134a.

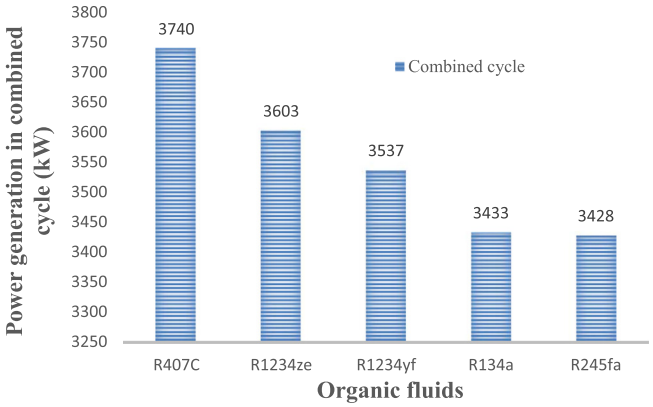

Fig. 6. Variations in power generation of combined cycle (SCO_2-ORC).

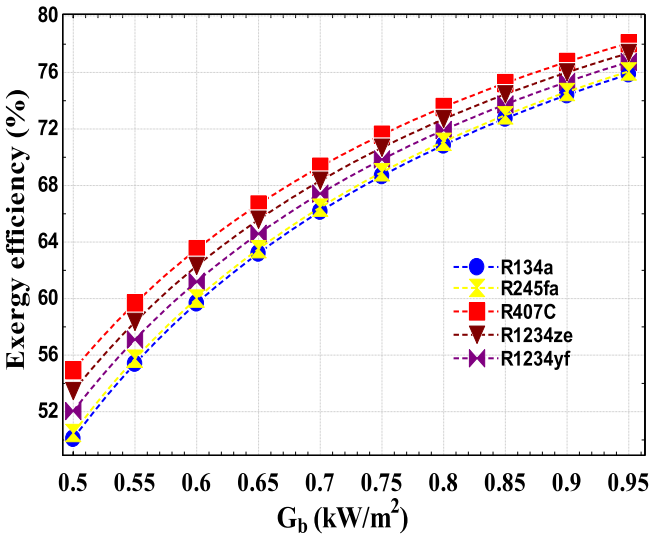

Fig. 7. Exergy efficiency of combined cycle (SCO_2-ORC) versus solar irradiation intensity.

Fig. 7 indicates that the exergy efficiency of R407c based combined cycle increases continuously from 54.93% at 500 W/m^2 to

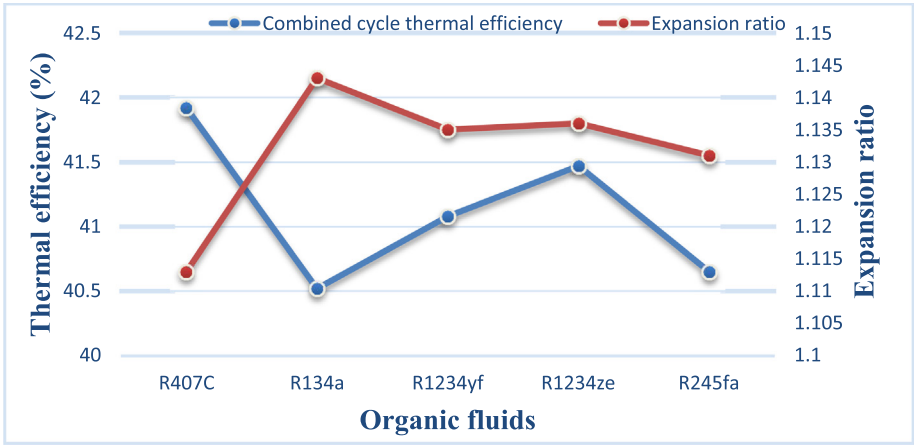

Fig. 5. Variations in expansion ratio and thermal efficiency of combined cycle.

Please cite this article in press as: H. Singh, R.S. Mishra, Performance analysis of solar parabolic trough collectors driven combined supercritical CO_2 and organic Rankine cycle, Eng. Sci. Tech., Int. J. (2018), https://doi.org/10.1016/j.jestch.2018.03.015

78.07% at 950 W/m^2. While the study revealed that R134a and R245fa cycles have the subsidiary differences between their exergetic efficiency values, i.e. 75.87% and 76.07% at 950 W/m^2, respectively. Fig. 8 illustrates that R407c has the highest thermal efficiency value among the other considered combined cycles, which is increases from 30.6% at 500 W/m^2 to 43.49% at 950 W/m^2. Alternatively, R134a has the lowest value of thermal efficiency which is around 27.91% at 500 W/m^2 increases to 42.26 at 950 W/m^2. The thermal efficiency of other cycles is between these two cycle's values.

Also, Fig. 9 shows that rate of total exergy destruction for combined cycle (SCO_2-ORC) decreases with the increase in solar irradiation intensity which has been analyzed under the same simulated conditions as described above. The rate of exergy destruction has the opposite behavior from exergetic efficiency and it was found that R407c based combined cycle has the minimum rate of exergy destruction, i.e. decreases from 8412 kW at 500 W/m^2 to 4093 kW at 950 W/m^2. On the other side, R134a combined cycle has the highest rate of exergy destruction which is declining from 9321 kW to 4508 kW as the direct normal irradiance increases from 500 W/m^2 to 950 W/m^2.

At last, in the case of complete plant, i.e. SPTC integrated combined cycle (SPTC-SCO_2-ORC), the exergy destruction rate in solar collector area (i.e. SPTC field) found to be comparatively higher than SCO_2 cycle and ORC which is generally due to the fact that large amount of exergy input to the solar collector but low rate of exergy conversion to working fluid at the same time [45]. It is evident from Fig. 10 that the exergy destruction rate in SPTC-SCO_2-ORC decreases gradually as the solar irradiation intensity increases which can be due to effective utilization of the solar collector field. It is obvious that if large amount of solar irradiation intensity falling upon the fewer solar collector rows consist with the multiple SPTCs which are arranged in series and parallel combination in the whole SEGS plant can effectively reduce the exergy destruction rate. From the Fig. 10, it has been observed that R245fa has the highest amount of exergy destruction rate in SPTC-SCO_2-ORC, and its value decreases from 18743 kW at 500 W/m^2 to 9855 kW at 950 W/m^2. On the other hand, R407c has the lowest rate of the total exergy destruction rate among the other working fluids which is decreases from 16,767 kW at 500 W/m^2 to 8816 kW at 950 W/m^2. While the exergy destruction rate of other cycles is between these values of two cycles as mentioned above.

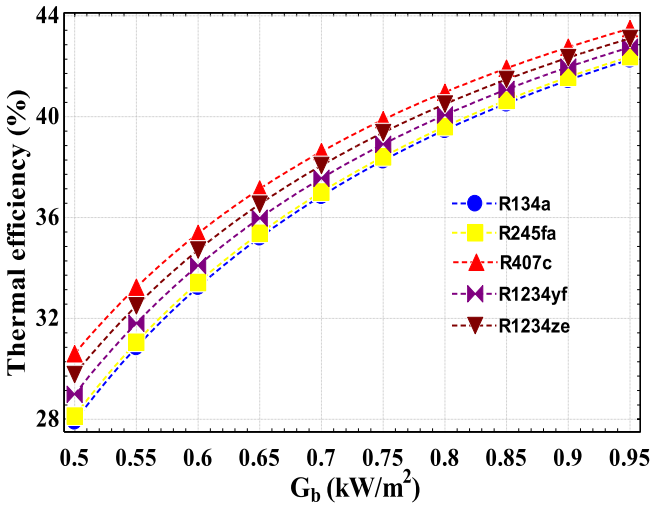

Fig. 8. Thermal efficiency of combined cycle (SCO_2-ORC) versus solar irradiation intensity.

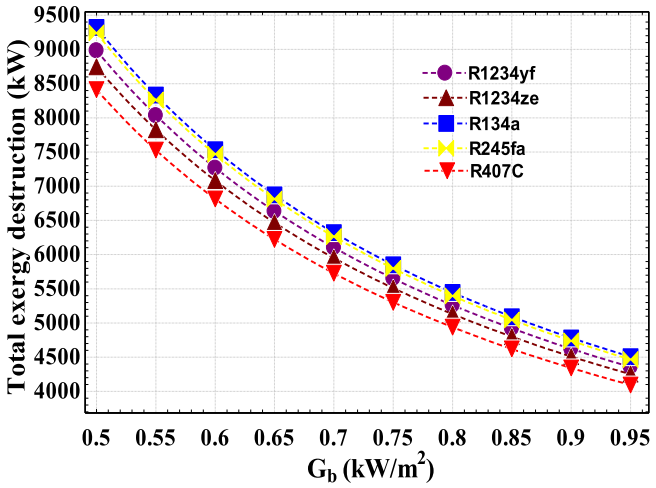

Fig. 9. Total exergy destruction of combined cycle (SCO_2-ORC) versus solar irradiation intensity.

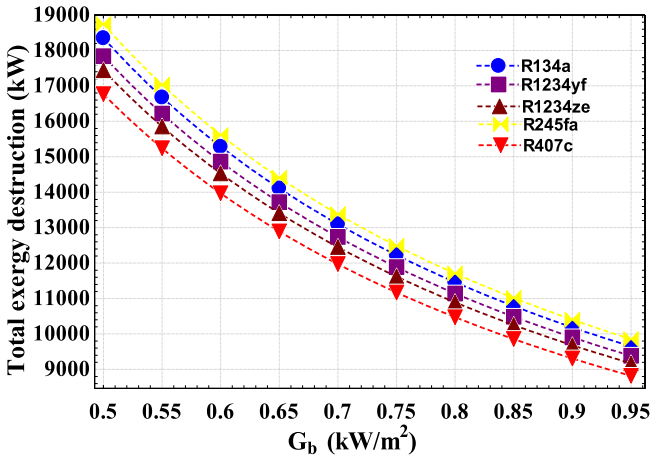

Fig. 10. Total exergy destruction of complete plant (SPTC-SCO_2-ORC) versus solar irradiation intensity.

4.3. Effect on the system performance with variation in inlet pressure of SCO_2 turbine

The inlet pressure of SCO_2 turbine is the important key parameter that has been used to analyze the performance as well as improve the design of combined cycle. The effect of variation in the inlet pressure of SCO_2 turbine on the exergy efficiency of combined (SCO_2-ORC) cycle has been observed under the fixed simulated conditions like the value of direct normal irradiance of 850 W/m^2, maximum temperature of 653 K, and mass flow rate of 10 kg/s in SCO_2 cycle. Fig. 11 demonstrates that the exergetic efficiency is slightly increases as the inlet pressure of SCO_2 turbine increases. It is revealed that R407c has the maximum exergetic efficiency, i.e. increases from around 75.03% at 14 MPa to 75.21% at 23 MPa. In addition, both R245fa and R134a has the minimum value of exergetic efficiency with the marginal differences in their performance values. Also, R1234yf and R1234ze based combined cycles also showed an incremental behavior along with the comparable value of exergy efficiency which is around 73.75% and 74.44%, respectively. Fig. 12 illustrates that R407c has the highest value of thermal efficiency which is enhances slightly from 41.8% at 14 MPa to 41.9% at 23 MPa. Alternatively, R245fa has the minimum value of thermal efficiency which is around 40.4% at 14 MPa and increases to 40.62% at 23 MPa. As can be seen, R134a and

Please cite this article in press as: H. Singh, R.S. Mishra, Performance analysis of solar parabolic trough collectors driven combined supercritical CO_2 and organic Rankine cycle, Eng. Sci. Tech., Int. J. (2018), https://doi.org/10.1016/j.jestch.2018.03.015

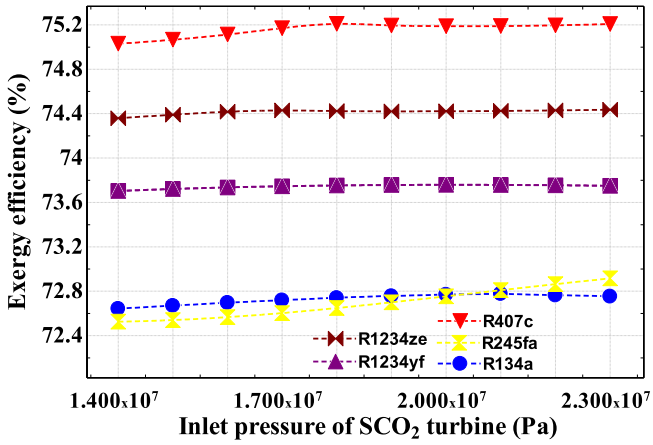

Fig. 11. Exergy efficiency of combined cycle (SCO_2-ORC) versus inlet pressure of SCO_2 Turbine.

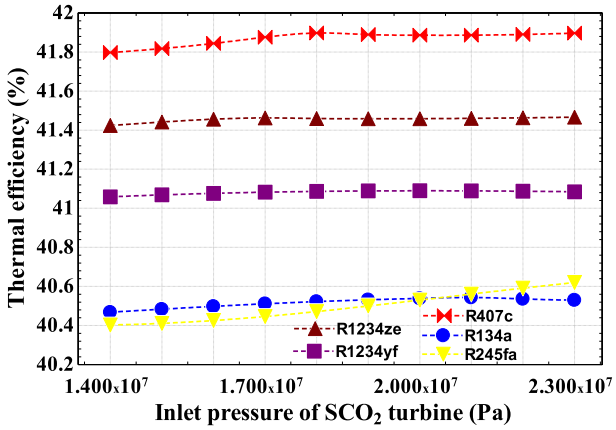

Fig. 12. Thermal efficiency of combined cycle (SCO_2-ORC) versus inlet pressure of SCO_2 Turbine.

R245fa both have comparable values of thermal and exergy efficiency.

Moreover, it has been observed that as the inlet pressure increases, the rate of total exergy destruction in combined cycle (SCO_2-ORC) decreases as shown in Fig. 13, and R407c combined cycle has the minimum rate of total exergy destruction, which is

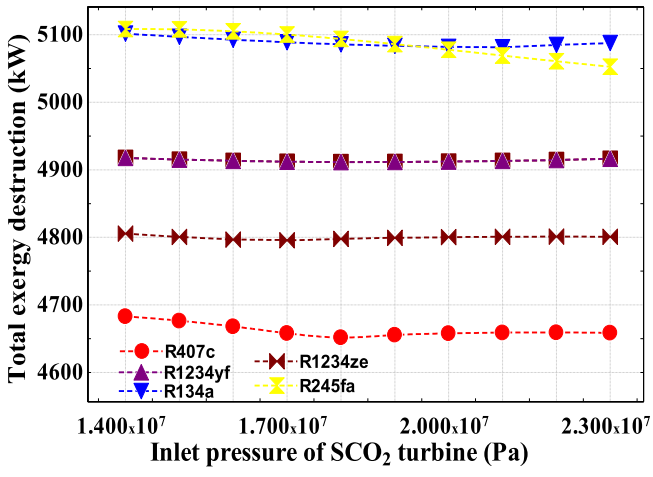

Fig. 13. Total exergy destruction in combined cycle (SCO_2-ORC) versus inlet pressure of SCO_2 Turbine.

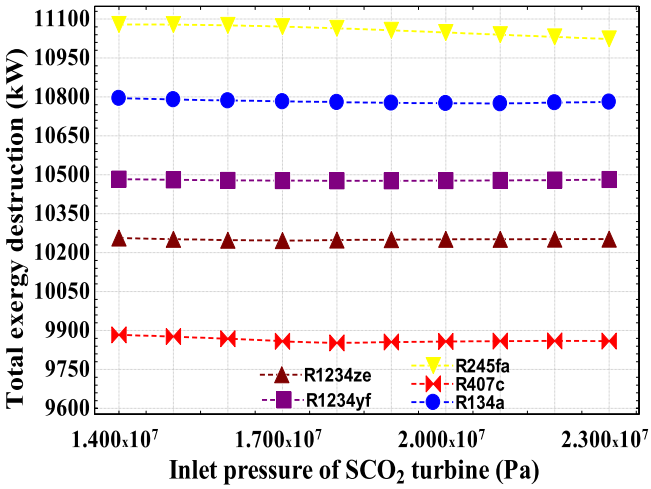

Fig. 14. Total exergy destruction in complete plant (SPTC-SCO_2-ORC) versus inlet pressure of SCO_2 Turbine.

around 4683 kW at 14 MPa and decreases to 4659 kW at 23 MPa. On the other hand, R245fa and R134a combined cycles have comparatively highest rate of total exergy destruction which is around 5053 kW and 5088 kW at 23 MPa, respectively.

It is also revealed that in the complete plant (SPTC-SCO_2-ORC), the highest amount of exergy loss which is around 50% to 60% occurs in the solar collector field only as illustrated in Fig. 14, and this loss is partly caused by the temperature and material limits of SPTCs. Therefore, it is necessary to investigate the amount of exergy loss due to solar collector for the further improvement in design of overall plant with respect to better exergetic and energetic performance. Fig. 14 also demonstrates that R407c has the lowest exergy destruction rate in the SPTC-SCO_2-ORC which is decreases from 9884 kW at 14 MPa to 9859 kW at 23 MPa. Alternatively, R245fa has the highest exergy destruction rate which is declining from 11079 kW at 14 MPa to 11023 kW at 23 MPa. While the exergy destruction rate of other considered cycles is between these two cycles as mentioned above. Finally, it has been concluded that the major value of exergy destruction rate is due to solar collector only which is around 6092 kW in case of R245fa, and this value is precisely equal to 55.3% of the total exergy destruction rate in complete cycle.

5. Conclusion

In this study, complete exergetic and energetic analysis of the SPTC integrated combined cycle has been conducted. This research has considered five various refrigerants for the ORC (i.e. bottoming cycle): R134a, R245fa, R1234yf, R1234ze and R407c. The following results have been concluded as given below:

1. Exergetic efficiency of the combined cycle (SCO_2-ORC) increases as the solar irradiation intensity increases. Results of the study concludes that R407c combined cycle has the highest value of exergy efficiency which is around 78.07% at 950 W/m^2 followed by the R1234ze, R1234yf, and R245fa. Alternatively, R134a combined cycle has the lowest exergy efficiency value, i.e. 75.87% at 950 W/m^2 which can be due to the maximum amount exergy loss present in this cycle. On the other hand, rate of exergy destruction continuously shows an decreasing trend with the increase in solar irradiation intensity. Thus, R407c has the lowest exergy destruction rate of 4093 kW at 950 W/m^2 and R134a has the highest exergy destruction rate of 4508 kW at 950 W/m^2.

Please cite this article in press as: H. Singh, R.S. Mishra, Performance analysis of solar parabolic trough collectors driven combined supercritical CO_2 and organic Rankine cycle, Eng. Sci. Tech., Int. J. (2018), https://doi.org/10.1016/j.jestch.2018.03.015

2. In addition, thermal efficiency of the combined cycle increases as the solar irradiation intensity increases. The study reveals that R407c has the highest thermal efficiency of 43.49% at 950 W/m^2, while the R134a has the lowest thermal efficiency value of 42.26% at 950 W/m^2.
3. It has also been observed that exergetic as well as thermal performance increases slightly as the inlet pressure of the turbine increases. Therefore, R407c combined cycle gives the best exergetic and thermal efficiency which is around 75.21% and 41.9% at 23 MPa, respectively. Alternatively, R407c possess the lowest rate of total exergy destruction rate as compared to other selected fluids, i.e. 4659 kW at 23 MPa.
4. It has been found that SPTC is the primary source of exergy destruction in which more than 25% of the solar inlet exergy has been destructed in the solar collector field only, which is a crucial amount and this value accounts for 54% of the total exergy destruction rate. Therefore, it requires a necessary care during the designing of SPTC plant to decrease down the exergy destruction rate in the solar driven combined cycle.
5. Moreover, SCO_2 turbine and evaporator are another major source of exergy destruction, in which 9.72% and 8.54% of the solar inlet exergy has been destructed. Also, the exergy destructed in these components have almost 38.10% of the total exergy destruction rate which has been noticed in case of R407c based complete plant.
6. In case of R407c combined cycle, the improvement potential, fuel depletion ratio, and irreversibility ratio for the SPTC field was found to be 5282 kW, 0.2583, and 0.5388, respectively.
7. The study also reveals that R134a and R245fa based combined cycles (SCO_2-ORC) have the marginal differences between their exergy and energy performance. Lastly, R134a has the highest value of expansion ratio which is around 1.143, and R407c combined cycle has the highest thermal efficiency value and power generation, i.e. almost 41.92% and 3740 kW, respectively.

Acknowledgement

The author (Harwinder Singh) acknowledges the support of Department of Mechanical, Industrial & Production, Automobile Engineering of the Delhi Technological University, New Delhi, India.

References

[1] Y. Ahn, S.J. Bae, M. Kim, S.K. Cho, S. Baik, J.I. Lee, J.E. Cha, Review of supercritical CO_2 power cycle technology and current status of research and development, Nucl. Eng. Technol. 47 (2015) 647–661.
[2] C. Zuo, Hybridisation of solar and geothermal energy in both subcritical and supercritical Organic Rankine Cycles, Energy Convers. Manage. 81 (2014) 72–82.
[3] J. Li, J.Z. Alvi, G. Pei, J. Ji, P. Li, H. Fu, Effect of working fluids on the performance of a novel direct vapor generation solar organic Rankine cycle system, Appl. Therm. Eng. 98 (2016) 786–797.
[4] F.A. Al-Sulaiman, Exergy analysis of parabolic trough solar collectors integrated with combined steam and organic Rankine cycles, Energy Convers. Manage. 77 (2014) 441–449.
[5] X.-D. Niu, H. Yamaguchi, Y. Iwamoto, X.-R. Zhang, Optimal arrangement of the solar collectors of a supercritical CO_2-based solar Rankine cycle system, Appl. Therm. Eng. 50 (2013) 505–510.
[6] J.M. Cardemil, A.K. da Silva, Parametrized overview of CO_2 power cycles for different operation conditions and configurations – an absolute and relative performance analysis, Appl. Therm. Eng. 100 (2016) 146–154.
[7] P. Garga, K. Srinivasan, P. Duttac, P. Kumard, Comparison of CO_2 and steam in transcritical Rankine cycles for concentrated solar power, Energy Proc. 49 (2014) 1138–1146.
[8] J.D. Osorio, R. Hovsapian, J.C. Ordonez, Dynamic analysis of concentrated solar supercritical CO2-based power generation closed-loop cycle, Appl. Therm. Eng. 93 (2016) 920–934.
[9] A.S. Nafey, M.A. Sharaf, Combined solar organic Rankine cycle with reverse osmosis desalination process: energy, exergy, and cost evaluations, Renewable Energy 35 (2010) 2571–2580.
[10] A.M. Delgado-Torres, L. García-Rodríguez, V.J. Romero-Ternero, Preliminary design of a solar thermal-powered seawater reverse osmosis system, Desalination 216 (2007) 292–305.
[11] A.M. Delgado-Torres, L. García-Rodríguez, Preliminary design of seawater and brackish water reverse osmosis desalination systems driven by low-temperature solar organic Rankine cycles (ORC), Energy Convers. Manage. 51 (2010) 2913–2920.
[12] A.M. Delgado-Torres, L. García-Rodríguez, Analysis and optimization of the low-temperature solar organic Rankine cycle (ORC), Energy Convers. Manage. 51 (2010) 2846–2856.
[13] F.A. Al-Sulaiman, F. Hamdullahpur, I. Dincer, Performance assessment of a novel system using parabolic trough solar collectors for combined cooling, heating, and power production, Renewable Energy 48 (2012) 161–172.
[14] W. Gao, H. Li, G. Xu, Y. Quan, Working fluid selection and preliminary design of a solar organic rankine cycle system, Environ. Prog. Sustainable Energy 34 (2014) 619–626.
[15] X. Wang, Y. Dai, Exergoeconomic analysis of utilizing the transcritical CO2 cycle and the ORC for a recompression supercritical CO2 cycle waste heat recovery: a comparative study, Appl. Energy 170 (2016) 193–207.
[16] H. Singh, R.S. Mishra, Performance evaluation of the supercritical organic rankine cycle (SORC) integrated with large scale solar parabolic trough collector (SPTC) system: An exergy energy analysis, Environ. Prog. Sustainable Energy (2017), https://doi.org/10.1002/ep.12735.
[17] F. Ferrara, A. Gimelli, A. Luongo, Small-scale concentrated solar power (CSP) plant: ORCs comparison for different organic fluids, Energy Proc. 45 (2014) 217–226.
[18] F. Calise, M.D. d'Accadia, M. Vicidomini, M. Scarpellino, Design and simulation of a prototype of a small-scale solar CHP system based on evacuated flat-plate solar collectors and Organic Rankine Cycle, Energy Convers. Manage. 90 (2015) 347–363.
[19] R. Rayegan, Y.X. Tao, A procedure to select working fluids for Solar Organic Rankine Cycles (ORCs), Renewable Energy 36 (2011) 659–670.
[20] H.D.M. Hettiarachchi, M. Golubovic, W.M. Worek, Y. Ikegamib, Optimum design criteria for an Organic Rankine cycle using low-temperature geothermal heat sources, Energy 32 (2007) 1698–1706.
[21] A. Gimelli, A. Luongo, M. Muccillo, Efficiency and cost optimization of a regenerative Organic Rankine Cycle power plant through the multi-objective approach, Appl. Therm. Eng. 114 (2017) 601–610.
[22] M.A. Lehar, V. Michelassi, System and Method for Recovery of Waste Heat from Dual Heat Sources, US 20130247570.A1, 2013.
[23] T.J. Held, S. Hostler, J.D. Miller, Heat Engine and Heat to Electricity Systems and Methods with Working Fluid Mass Management Control, US 8096128.B2, 2012.
[24] E. Zarza, M.E. Rojas, L. González, J.M. Caballero, F. Rueda, INDITEP: the first pre-commercial DSG solar power plant, Sol. Energy 80 (2006) 1270–1276.
[25] Plataforma Solar de Almería (PSA). Annual report 2002. http://www.psa.es/en/techrep/2002/atr2002_ing.pdf (accessed on 24.03.2017)
[26] L. Valenzuela, E. Zarza, M. Berenguel, E.F. Camacho, Control concepts for direct steam generation in parabolic troughs, Sol. Energy 78 (2005) 301–311.
[27] Y. Goswami, Thermodynamic Cycles for CSP http://www.iitj.ac.in/CSP/material/19dec/thermodynamic.pdf (accessed on 28.12.2017)
[28] A. Mwesigye, T. Bello-Ochende, J.P. Meyer, Minimum entropy generation due to heat transfer and fluid friction in a parabolic trough receiver with non-uniform heat flux at different rim angles and concentration ratios, Energy 73 (2014) 606–617.
[29] S. Kalogirou, Solar Energy Engineering: Processes and Systems, st ed., Academic Press/Elsevier, California, USA, 2008.
[30] J. Duffie, W. Beckman, Solar Engineering of Thermal Processes, 4th ed., John Wiley & Sons Inc, Hoboken, New Jersey, USA, 2013.
[31] V.E. Dudley, G.J. Koib, A.R. Mahoney, T.R. Mancini, C.W. Matthews, M. Sloan, D. Keamey, SEGS LS-2 solar collector test results. Report of Sandia National Laboratories. SANDIA94-1884, 1994.
[32] M. Chafie Ben, M.F. Aissa, S. Bouadila, M. Balghouthi, A. Farhat, A. Guizani, Experimental investigation of parabolic trough collector system under Tunisian climate: design, manufacturing and performance assessment, Appl. Therm. Eng. 101 (2016) 273–283.
[33] LUZ International Limited, Solar electric generating system IX technical description, LUZ International Limited, 1990.
[34] R. Petela, Exergy analysis of the solar cylindrical-parabolic cooker, Sol. Energy 79 (2005) 221–233.
[35] R. Boehm, Maximum performance of solar heat engines, Appl. Energy 23 (1986) 281–296.
[36] R. Petela, Exergy of undiluted thermal radiation, Sol. Energy 74 (2003) 469–488.
[37] J. Sarkar, Second law analysis of supercritical CO2 recompression Brayton cycle, Energy 34 (2009) 1172–1178.
[38] S. Aghahosseini, I. Dincer, Exergoenvironmental analysis of renewable/waste heat based organic rankine cycle (ORC) using different working fluids, Proceeding of global conference on global warming, Lisbon, Portugal, 2011.
[39] B. Saleh, Parametric and working fluid analysis of a combined organic Rankine-vapor compression refrigeration system activated by low-grade thermal energy, J. Adv. Res. 7 (2016) 651–660.

Please cite this article in press as: H. Singh, R.S. Mishra, Performance analysis of solar parabolic trough collectors driven combined supercritical CO_2 and organic Rankine cycle, Eng. Sci. Tech., Int. J. (2018), https://doi.org/10.1016/j.jestch.2018.03.015

[40] B.F. Tchanche, G. Papadakis, G. Lambrinos, A. Frangoudakis, Fluid selection for a low-temperature solar organic Rankine cycle, Appl. Therm. Eng. 29 (2009) 2468–2476.
[41] F.A. Al-Sulaiman, I. Dincer, F. Hamdullahpur, Exergy modeling of a new solar driven trigeneration system, Sol. Energy 85 (2011) 2228–2243.
[42] E.W. Lemmon, M.O. McLinden, M.L. Huber, NIST Reference Fluid Thermodynamic and Transport Properties—REFPROP, National Institute of Standards and Technology, Gaithersburg, MD, NIST Standard Reference Database 23.
[43] S.A. Klein, Engineering Equation Solver (EES), Academic Commercial V7.714. F-Chart Software, www.fChart.com, 2006.
[44] J. Vivian, G. Manente, A. Lazzaretto, A general framework to select working fluid and configuration of ORCs for low-to-medium temperature heat sources, Appl. Energy 156 (2015) 727–746.
[45] I. Dincer, A. Midilli, H. Kucuk, Progress in Exergy, Energy, and the Environment, Springer international publishing Switzerland, 2014.
[46] I. Dincer, Y.A. Cengel, Energy, entropy and exergy concepts and their roles in thermal engineering, Entropy 3 (2001) 116–149.
[47] T.H. Karakoc, M.B. Ozerdem, M.Z. Sogut, C.O. Colpan, O. Altuntas, E. Açıkkalp, Sustainable Aviation: Energy and Environmental Issues, Springer international publishing Switzerland, 2016.
[48] R.V. Padilla, Y.C.S. Too, R. Benito, W. Stein, Exergetic analysis of supercritical CO_2 Brayton cycles integrated with solar central receivers, Appl. Energy 148 (2015) 348–365.
[49] S.A. Wright, R.F. Radel, T.M. Conboy, G.E. Rochau, Modeling and Experimental Results for Condensing Supercritical CO2 Power Cycles, Sandia Report, SAND2010-8840, Sandia National Laboratories, Livermore (CA), January 2011.
[50] M. Blanco, L.R. Santigosa, Advances in Concentrating Solar Thermal Research and Technology, Woodhead publishing series in energy (Elsevier), 2017, ISBN: 978-0-08-100516-3.
[51] J. Song, X.-s. Li, X.-d. Ren, C.-w. Gu, Performance analysis and parametric optimization of supercritical carbon dioxide (S-CO 2) cycle with bottoming Organic Rankine Cycle (ORC), Energy 143 (2018) 406–416.
[52] S.-M. Besarati, D.Y. Goswami, Analysis of advanced supercritical carbon dioxide power cycles with a bottoming cycle for concentrating solar power applications, J. Solar Energy Eng. 136 (2014) 010904-1-7.
[53] S. Clemente, D. Micheli, M. Reini, R. Taccani, Bottoming organic Rankine cycle for a small scale gas turbine: a comparison of different solutions, Appl. Energy 106 (2013) 355–364.
[54] H. Price, D. Kearney, Reducing the cost of energy from parabolic trough solar power plants, in: International Solar Energy Conference 2003, Hawaii, USA, 2003, pp. 591–599.
[55] J. Nouman, Comparative studies and analyses of working fluids for Organic Rankine Cycles – ORC. KTH School of Industrial Engineering and Management, Master of Science Thesis 2012, Stockholm.
[56] U. Sahoo, R. Kumar, P.C. Pant, R. Chaudhary, Resource assessment for hybrid solar-biomass power plant and its thermodynamic evaluation in India, Sol. Energy 139 (2016) 47–57.

Please cite this article in press as: H. Singh, R.S. Mishra, Performance analysis of solar parabolic trough collectors driven combined supercritical CO_2 and organic Rankine cycle, Eng. Sci. Tech., Int. J. (2018), https://doi.org/10.1016/j.jestch.2018.03.015

Photonic Network Communications
https://doi.org/10.1007/s11107-018-0766-8

ORIGINAL PAPER

PL approximation of DBPSK in DF-based cooperative FSO network with pointing error

Deepti Agarwal[1] · **Ankur Bansal**[2] · **Ashwni Kumar**[1]

Received: 9 November 2017 / Accepted: 28 March 2018
© Springer Science+Business Media, LLC, part of Springer Nature 2018

Abstract
In this paper, we utilize piecewise linear (PL) approximation to analyze the performance of cooperative free space optical (FSO) network employing differentially modulated binary phase shift keying (DBPSK) data with multiple decode-and-forward (DF) relays. The maximum-likelihood (ML) decoding rule at the destination is approximated by PL approximation which considers the possibility of erroneous relaying and performs very similar to the ML decoder with reduced decoding complexity. The atmospheric fading optical links are modeled by Gamma–Gamma distribution subject to both types of detection techniques, i.e., heterodyne detection and intensity modulation/direct detection (IM/DD) with pointing error. We analytically formulate the probability of error for the multiple-DF relay-based FSO network. However, the novel unified expression of average bit error rate (BER) of PL decoder with single relay and single source to destination pair is derived. Further, we also derive the asymptotic approximate BER of DF-FSO network with multiple relays at high signal-to-noise ratio (SNR) of source to relay links considering heterodyne detection with negligible pointing error. In addition, the unified closed-form expressions of outage probability with single and multiple DF relays are derived in terms of Meijer G function. The expression of outage probability is examined at high SNR in order to obtain analytical diversity order. The impact of different power distribution techniques on outage probability is determined by utilizing power distribution parameters. The derived analytical results are validated through simulation.

Keywords Differential modulation · Gamma–Gamma (GG) fading · Free space optics (FSO) · Decode and forward (DF) relaying · Pointing error · Piecewise linear (PL) approximation

1 Introduction

Free-space optical communication (FSO) has gained significant interest among researchers due to its various advantages such as license-free spectrum, large bandwidth, high data rate, robustness to electromagnetic interference, and high security, making it beneficial for the applications like disaster recovery, last-mile access, backhaul for cellular systems, and high-quality video transmission [1–3]. However, the main impairments in FSO are imposed due to atmospheric turbulence and pointing errors. Atmospheric turbulence is caused by refractive index fluctuations along the transmission path, whereas pointing error occurs due to the misalignment between transmitting and receiving aperture caused by earthquakes, wind loads, and building sway [3]. Several schemes have been proposed in the literature to mitigate the effect of atmospheric turbulence and pointing errors. Cooperative diversity or relay-assisted network is one of the popular techniques that not only enhances the performance of FSO network but also helps to broaden the signal coverage area. It has emerged as an alternative solution for realizing spatial diversity advantages [4–6]. It has recently gained significant interest due to enhanced performance of the destination receiver, improved capacity, and reduced effect of turbulence-induced fading [7,8]. To omit the requirement of channel coefficients and phase tracking, differential modulation in cooperative networks has been considered in the

✉ Ankur Bansal
bansal.ankur143@gmail.com

Deepti Agarwal
deepti.agarwal1983@gmail.com

Ashwni Kumar
drashwnikumar@gmail.com

[1] Department of ECE, IGDTUW, Kashmiri Gate, New Delhi, India

[2] Division of ECE, Netaji Subhas Institute of Technology, Dwarka, New Delhi, India

Published online: 16 April 2018

literature, which simplifies the receiver structure and also enhances the spectral efficiency of the system [9,10].

Various cooperative strategies like amplify and forward (AF) [11] and decode and forward (DF) [12,13] have been used for relay-assisted FSO. In AF, relay only scales the received signal from the source by some constant value. In DF, the source sends the coded data to the relay and relay attempts to decode it perfectly. However, the relay cannot always decode the code word correctly. So there is the possibility of erroneous relaying in DF protocol. It is shown in [14–16] that the performance of DF-based cooperative RF network can be enhanced by utilizing optimal maximum-likelihood (ML) decoder in the destination receiver. The ML decoder considers the probability of erroneous decoding at relay and maximizes the probability density function (pdf) of received data at destination. Therefore, it improves the diversity order of DF-FSO network. Moreover, a suboptimal piecewise linear (PL) decoder provides less complex receiver structure as compared to ML decoder but its performance is very similar to optimum one [15]. As seen from the previous studies, the main detection technique in FSO network is intensity modulation/direct detection (IM/DD) but heterodyne detection performs better in the presence of thermal noise [17].

The performance of cooperative FSO network over Gamma-Gamma (GG) turbulence has been analyzed in [9] for differentially modulated BPSK (DBPSK) data considering selective relaying. In selective relaying approach, the relay transmits the data to destination only if it has decoded it correctly, otherwise it remains idle. The impact of incorrect decoding at relay has been considered in [18] while evaluating the performance of DF-FSO system. The analysis in above works [9,18] does not consider the impact of pointing error which is important issue in urban areas where FSO equipments are placed on high-rise buildings [19]. Most of the earlier works on cooperative FSO network [9,13,18] with or without erroneous relay and pointing error consider IM/DD scheme at receiver. However, as per authors' best knowledge, unified performance analysis of PL decoder over GG turbulence with pointing error and DBPSK data is not available in the literature so far. Moreover, the diversity analysis for multiple-DF relay-based cooperative FSO network over GG channel with heterodyne scheme has not been done in the literature. Motivated by the above-mentioned facts, we investigate and present most of the useful results as given in this paper. In this work, our main contributions are: (1) We analytically formulate the probability of error for the multiple-relay-based DF-FSO network. The unified novel expression of average BER of PL decoder is derived with single relay and single source destination pair. (2) Further, the asymptotic average BER for the multiple-DF relay-based network is obtained considering high signal to noise ratio (SNR) of source to relay links. (3) The unified closed-form expression of outage probability is also derived for the considered system with single and multiple parallel DF relays. (4) We examine the impact of different power distribution techniques by utilizing the derived outage probability expression. (5) Moreover, we also analyze analytical outage probability expression at high SNR in order to obtain the diversity order.

The cooperative network with DBPSK data transmission is referred to as differential cooperative network in the remaining paper. The paper has been organized as follows: Sect. 2 describes system and channel model. The PL decoder for differential data in DF-based cooperative FSO system is derived in Sect. 3 while conditional and average BER analysis for differential cooperative FSO system with single and multiple relays is performed in Sect. 4. The outage analysis of the considered network is presented in Sect. 5. Section 6 discusses the analytical and simulation results, and the paper is concluded in Sect. 7.

2 System model

We consider DF-FSO network for transmitting the DBPSK data between a source (S) and destination (D) which is assisted by multiple DF relays, $R_i, i \in \{1, 2 \ldots M\}$, as shown in Fig. 1. The transmission is done in two orthogonal phases. In first phase, S transmits the data to R_i relays and D. In the second phase, R_i relays decode the data utilizing ML decoder, re-encode it, and forward it to D.

2.1 Transmission protocol

Let $z[n] \in \{-1, 1\}$ is the BPSK symbol to be transmitted by S in the n-th time interval. The differentially encoded data at the transmitter are

$$w[n] = w[n-1]z[n], \quad n = 0, 1, 2, 3.... \tag{1}$$

where DBPSK signal $w[n] \in \{-1, 1\}$ and $|w[n]|^2 = 1$. $w[0] = 1$ is the symbol for initialization. In the first phase, the received signals $y_{s,r_i}[n]$ and $y_{s,d}[n]$ at the i-th relay and destination, respectively, are given as

$$\begin{aligned} y_{s,r_i}[n] &= \eta_{s,r_i} I_{s,r_i} w[n] + e_{s,r_i}[n], \\ y_{s,d}[n] &= \eta_{s,d} I_{s,d} w[n] + e_{s,d}[n], \end{aligned} \tag{2}$$

where $\eta_{a,b}$, $a, b \in \{s, r_i, d\}, i = \{1, 2, \ldots, M\}$, $a \neq b$, is the optical to electrical conversion coefficients for the $a-b$-th link; $I_{a,b}$ denotes the real-valued irradiance of $a-b$-th link with $\mathbb{E}[I_{a,b}^2] = 1$; and $e_{a,b}[n] \sim \mathscr{CN}(0, \sigma_{a,b}^2)$ is the complex-valued additive white Gaussian noise (AWGN). $\mathbb{E}[\cdot]$ denotes expectation operator, and the term $\mathscr{CN}(\cdot, \cdot)$ is the complex Gaussian distribution. Here, it is assumed that

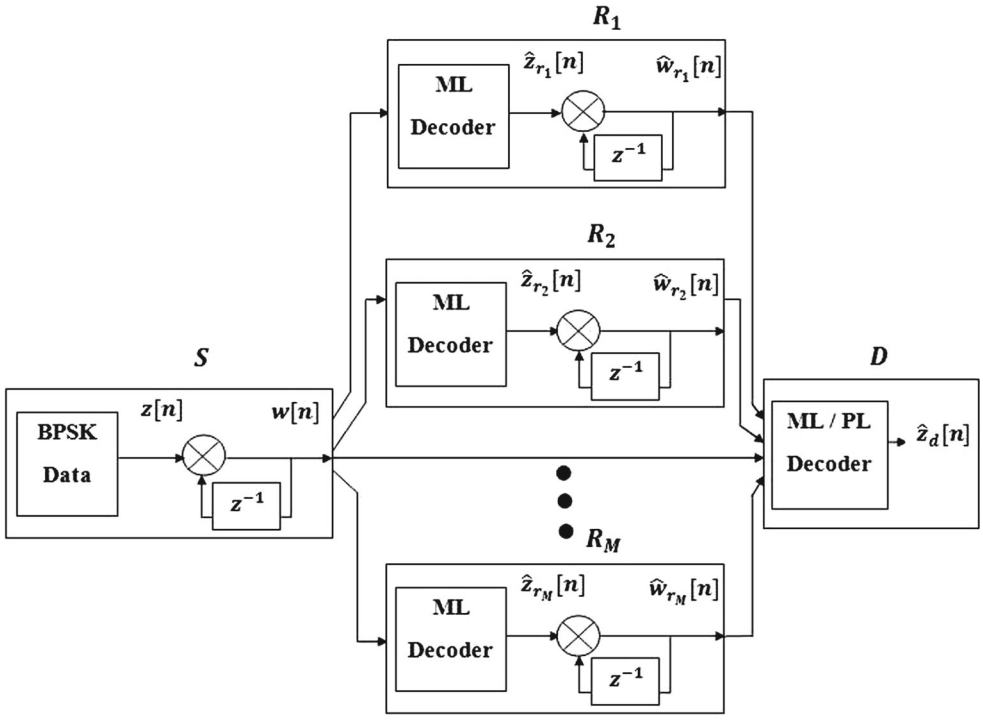

Fig. 1 System model of differential DF-FSO network with M relays. The term z^{-1} represents the delay element

noise and irradiance fluctuations of all the links are independent of each other. The data received at D in the second phase from R_i are

$$y_{r_i,d}[n] = \eta_{r_i,d} I_{r_i,d} \hat{w}_{r_i}[n] + e_{r_i,d}[n], \tag{3}$$

where $\hat{w}_{r_i}[n] \in \{-1, 1\}$ is the re-encoded symbol by the relay; $\hat{w}_{r_i}[n] = \hat{w}_{r_i}[n-1]\hat{z}_{r_i}[n]$. The ML-decoded data by the relay is denoted by $\hat{z}_{r_i}[n]$. From (1) and (2), we obtain

$$\begin{aligned} y_{s,r_i}[n] &= y_{s,r_i}[n-1]z[n] + \check{e}_{s,r_i}[n], \\ y_{s,d}[n] &= y_{s,d}[n-1]z[n] + \check{e}_{s,d}[n], \end{aligned} \tag{4}$$

where $\check{e}_{s,r_i}[n] = e_{s,r_i}[n] - e_{s,r_i}[n-1]z[n]$, $\check{e}_{s,r_i}[n] \sim \mathscr{CN}(0, 2\sigma^2_{s,r_i})$ and $y_{s,r_i}[n]|_{y_{s,r_i}[n-1],z[n]} \sim \mathscr{CN}(y_{s,r_i}[n-1]z[n], 2\sigma^2_{s,r_i})$. Similarly, we obtain $\check{e}_{s,d}[n] = e_{s,d}[n] - e_{s,d}[n-1]z[n]$, $\check{e}_{s,d}[n] \sim \mathscr{CN}(0, 2\sigma^2_{s,d})$ and $y_{s,d}[n]|_{y_{s,d}[n-1],z[n]} \sim \mathscr{CN}(y_{s,d}[n-1]z[n], 2\sigma^2_{s,d})$; $v|_{b_1,b_2}$ represents the random variable v conditioned on b_1 and b_2. From (1) and (3), we can write $y_{r_i,d}[n] = y_{r_i,d}[n-1]\hat{z}_{r_i}[n] + \check{e}_{r_i,d}[n]$.

2.2 Channel statistics

We consider that the all the links in cooperation are independent of each other and the irradiance of $a-b$-th FSO link $I_{a,b}$, $a, b \in \{s, r_i, d\}$, $a \neq b$ is GG distributed with pointing error. The probability density function (PDF) of $I_{a,b}$ with pointing error can be given as

$$\begin{aligned} &f_{I_{a,b}}(I_{a,b}; \alpha_{a,b}, \beta_{a,b}, \xi_{a,b}) \\ &= \frac{\xi^2_{a,b}}{I_{a,b}\Gamma(\alpha_{a,b})\Gamma(\beta_{a,b})} G^{3,0}_{1,3}\left(\alpha_{a,b}\beta_{a,b}\frac{I_{a,b}}{A_0}\,\middle|\, \begin{matrix}\xi^2_{a,b}+1 \\ \mathscr{Z}_{a,b}\end{matrix}\right), \end{aligned} \tag{5}$$

where $\mathscr{Z}_{a,b} = \{\xi^2_{a,b}, \alpha_{a,b}, \beta_{a,b}\}$, $\Gamma(\cdot)$ is Gamma function defined in [20, Eq. (8.310)] and $G^{m,n}_{p,q}\left(\cdot\,\middle|\, \begin{matrix}\cdot \\ \cdot\end{matrix}\right)$ is Meijer-G function defined in [21, Section 2.24)]. The ratio between equivalent beam radius at the receiver and the pointing error displacement jitter (standard deviation) at the receiver is denoted by ξ [17,22], where $\xi = w_{z_{eq}}/2\sigma_s$. The relations $v = \sqrt{\pi}r/\sqrt{2}w_z$, $w^2_{z_{eq}} = w^2_z\sqrt{\pi}\text{erf}(v)/2v\exp(-v^2)$, and $A_0 = [\text{erf}(v)]^2$ are used to find the parameter $w_{z_{eq}}$. The beam waist at distance z is represented by w_z, and erf$(\cdot)$ is the error function.

The unified PDF of instantaneously received SNR ($\gamma_{a,b}$) for $a-b$-th FSO link with both types of detection techniques, i.e., heterodyne and IM/DD, can be written using [23] as

$$\begin{aligned} &f_{\gamma_{a,b}}(\gamma_{a,b}; \alpha_{a,b}, \beta_{a,b}, \xi_{a,b}, \bar{\gamma}_{a,b}) \\ &= \frac{\gamma^{-1}_{a,b} q^{-1} \xi^2_{a,b}}{\Gamma(\alpha_{a,b})\Gamma(\beta_{a,b})} G^{3,0}_{1,3}\left(d_{a,b}\alpha_{a,b}\beta_{a,b}\left(\frac{\gamma_{a,b}}{K_{q,a,b}}\right)^{\frac{1}{q}}\,\middle|\, \begin{matrix}\xi^2_{a,b}+1 \\ \mathscr{Z}_{a,b}\end{matrix}\right), \end{aligned} \tag{6}$$

where $q = 1, 2$ denotes the heterodyne and IM/DD detection, respectively; $d_{a,b} = \frac{\xi^2_{a,b}}{(\xi^2_{a,b}+1)}$ and $K_{q,a,b}$ denotes the

average electrical SNR of $a-b$-th FSO link. When $q=1$, $K_{1,a,b}=K_{\text{heterodyne},a,b}=\mathbb{E}[\gamma_{a,b}]=\bar{\gamma}_{a,b}$, where $\bar{\gamma}_{a,b}$ is average SNR of $a-b$-th FSO link, and when $q=2$, $K_{2,a,b}=K_{\text{IM/DD},a,b}=\bar{\gamma}_{a,b}\frac{\mathbb{E}^2[I_{a,b}]}{\mathbb{E}[I_{a,b}^2]}=\frac{\alpha_{a,b}\beta_{a,b}\bar{\gamma}_{a,b}\xi_{a,b}^2(\xi_{a,b}^2+2)}{(\alpha_{a,b}+1)(\beta_{a,b}+1)(\xi_{a,b}^2+1)^2}$ [23].

3 PL approximation of differential data in DF-FSO network

In this section, we provide the optimal ML decoding rule in the destination of the differential cooperative DF-FSO network. Further, we approximate the ML decoding rule by utilizing PL approximation. The ML decoding of DBPSK symbol formulates binary hypothesis testing problem [24], whose unique solution is provided by the likelihood ratio test in which the conditional PDF of received data is maximized at R_i to get the decision variable. Therefore, relays require to evaluate the following log likelihood ratio for ML decoding of source data [24].

$$\zeta^{R_i}=\ln\left[\frac{f_{y_{s,r_i}[n]}(y_{s,r_i}[n]|_{y_{s,r_i}[n-1],z[n]=1})}{f_{y_{s,r_i}[n]}(y_{s,r_i}[n]|_{y_{s,r_i}[n-1],z[n]=-1})}\right], \tag{7}$$

where $f_{y_{s,r_i}[n]}(y_{s,r_i}[n]|_{y_{s,r_i}[n-1],z[n]=1})$ denotes the conditional PDF of $y_{s,r_i}[n]$, given as

$$f_{y_{s,r_i}[n]}(y_{s,r_i}[n]|_{y_{s,r_i}[n-1],z[n]=1})=\frac{1}{2\pi\sigma_{s,r_i}^2}e^{-|y_{s,r_i}[n]-y_{s,r_i}[n-1]|^2/2\sigma_{s,r_i}^2}. \tag{8}$$

Similarly, we can write

$$f_{y_{s,r_i}[n]}(y_{s,r_i}[n]|_{y_{s,r_i}[n-1],z[n]=-1})=\frac{1}{2\pi\sigma_{s,r_i}^2}e^{-|y_{s,r_i}[n]+y_{s,r_i}[n-1]|^2/2\sigma_{s,r_i}^2}. \tag{9}$$

By substituting (8) and (9) in (7), we get

$$\zeta^{R_i}=\ln\left[e^{-\left(|y_{s,r_i}[n]-y_{s,r_i}[n-1]|\right)^2/2\sigma_{s,r_i}^2+\left(|y_{s,r_i}[n]+y_{s,r_i}[n-1]|\right)^2/2\sigma_{s,r_i}^2}\right]. \tag{10}$$

With the help of (10), and utilizing the relation $|b_1+b_2|^2=|b_1|^2+|b_2|^2+2\text{Re}\{b_1^*b_2\}$ for the complex numbers b_1 and b_2, we get decision variable at relay as $\zeta^{R_i}=\frac{2}{\sigma_{s,r_i}^2}\text{Re}\{y_{s,r_i}^*[n]y_{s,r_i}[n-1]\}$. This log likelihood ratio-based ML decoder at relay decides as $\zeta^{R_i}\underset{-1}{\overset{1}{\gtrless}}0$. The estimation of data in R_i does not require the channel statistics of $S-R_i$ links because of differential modulation.

By utilizing the PDFs of $y_{s,d}[n]$ and $y_{r_i,d}[n]$ as given in [14, Subsection III-A], we can write the log likelihood ratio-based ML decoder in the destination as

$$\zeta_i^D=\mathscr{U}+\sum_{i=1}^{M}\underbrace{\ln\left(\frac{\varepsilon_i+(1-\varepsilon_i)e^{\mathscr{V}_i}}{\varepsilon_i e^{\mathscr{V}_i}+(1-\varepsilon_i)}\right)}_{\triangleq\mathscr{H}(\mathscr{V}_i,\varepsilon_i)}, \tag{11}$$

where ε_i is the average probability of error for $S-R_i$ links, $\mathscr{U}=\frac{2}{\sigma_{s,d}^2}\text{Re}\{y_{s,d}^*[n]y_{s,d}[n-1]\}$, $\mathscr{V}_i=\frac{2}{\sigma_{r_i,d}^2}\text{Re}\{y_{r_i,d}^*[n]y_{r_i,d}[n-1]\}$.

Remark 1 It follows from (11) that the logarithmic function $\mathscr{H}(\mathscr{V}_i,\varepsilon_i)$ approaches to the $\pm\mathscr{V}_{0i}=\pm\ln\left(\frac{(1-\varepsilon_i)}{\varepsilon_i}\right)$ for very high and very low values of $\mathscr{V}_i$ while for $-\mathscr{V}_{0i}\le\mathscr{V}_i\le\mathscr{V}_{0i}$, $\mathscr{H}(\mathscr{V}_i,\varepsilon_i)$ follows straight line i.e., $\mathscr{H}(\mathscr{V}_i,\varepsilon_i)\approx\mathscr{V}_i$.

Therefore, we can approximate the function $\mathscr{H}(\mathscr{V}_i,\varepsilon_i)$ by the PL function as

$$\mathscr{H}(\mathscr{V}_i,\varepsilon_i)\approx\mathscr{H}_{PL}(\mathscr{V}_i,\varepsilon_i)\triangleq\begin{cases}-\mathscr{V}_{0i}, & \text{if } \mathscr{V}_i<-\mathscr{V}_{0i},\\ \mathscr{V}_i, & \text{if } -\mathscr{V}_{0i}\le\mathscr{V}_i\le\mathscr{V}_{0i},\\ \mathscr{V}_{0i} & \text{if } \mathscr{V}_i>\mathscr{V}_{0i},\end{cases} \tag{12}$$

The suboptimal PL decoder at the receiver can be obtained by utilizing approximation of (12) in (11) as

$$\zeta_i^D=\mathscr{U}+\sum_{i=1}^{M}\mathscr{H}_{PL}(\mathscr{V}_i,\varepsilon_i). \tag{13}$$

This PL decoder in (13) is applicable for differential binary data in FSO cooperative networks with multiple DF relays.

4 Error analysis of PL decoder in differential cooperative FSO network

In this section, we provide the analytical framework for the calculation of probability of error for PL decoder with multiple DF relays and single $S-D$ pair. Further, we derive the unified expression of average BER of PL decoder with single relay. We also obtain the asymptotic approximate BER of differential DF-FSO network with multiple parallel DF relays at high SNR of source to relay links considering heterodyne detection and negligible pointing error.

4.1 Conditional BER analysis with multiple DF relays

Let us assume that the average probability of error for source to i-th relay is same $\forall i$, i.e., $\varepsilon_i=\varepsilon$ and therefore, we can

write $\mathscr{V}_{0i} = \mathscr{V}_0$. The PL decoder in (13) utilizes a PL function (defined in (12)) which clips the variable $\mathscr{V}_i$ to $\pm\mathscr{V}_{0i}$ and remains linear in between for all $R_i - D$ links. Therefore, we define three sets of relays depending upon the value of $\mathscr{V}_i$ for i-th R-D link. Let Ξ_1 be a set containing the relays for which $\mathscr{V}_i < -\mathscr{V}_0$. Similarly, sets Ξ_2 and Ξ_3 contain the relays for which $\mathscr{V}_i > \mathscr{V}_0$ and $-\mathscr{V}_0 < \mathscr{V}_i < \mathscr{V}_0$, respectively. Moreover, the cardinality of set $\Xi_k = \delta_k, k = 1, 2, 3$ with $\sum_{k=1}^{3} \delta_k = M$. If the variable $\mathscr{V}_i$ for the relays under set Ξ_k is denoted by $\mathscr{V}_{ik}$, then we can define a set $\mathscr{A}_k$ containing all $\mathscr{V}_{ik}$'s corresponding to relays under set Ξ_k such that $|\mathscr{A}_k| = \delta_k$ and $\bigcap_{k=1}^{3} \mathscr{A}_k = \phi$ where ϕ denotes the empty set. We consider that $z[n] = 1$ is transmitted by S, then the conditional BER for the PL decoder of (13) using DBPSK data can be written as

$$
\begin{aligned}
&P_e\left(\gamma_{s,d}, \{\gamma_{r_i,d}\}_{i=1}^{M}\right) \\
&= \sum_{\delta_1=0}^{M} \binom{M}{M-\delta_1} \sum_{\delta_2=0}^{M-\delta_1} \binom{M-\delta_1}{M-\delta_1-\delta_2} \\
&\quad \times \Pr\Bigg\{ \mathscr{U} - \delta_1\mathscr{V}_0 + \delta_2\mathscr{V}_0 \\
&+ \sum_{\substack{\delta_3 \text{ terms} \\ \text{of} \mathscr{A}_3}} \mathscr{V}_{i3} < 0 \;\Bigg|\; \bigcap_{\substack{\delta_1 \text{ terms} \\ \text{of} \mathscr{A}_1}} \{\mathscr{V}_{i1} < -\mathscr{V}_0\}, \bigcap_{\substack{\delta_2 \text{ terms} \\ \text{of} \mathscr{A}_2}} \{\mathscr{V}_{i2} > \mathscr{V}_0\}, \\
&\quad \bigcap_{\substack{\delta_3 \text{ terms} \\ \text{of} \mathscr{A}_3}} \{-\mathscr{V}_0 \le \mathscr{V}_{i3} \le \mathscr{V}_0\}\Bigg\} \\
&\times \Pr\left\{ \bigcap_{\substack{\delta_1 \text{ terms} \\ \text{of} \mathscr{A}_1}} \{\mathscr{V}_{i1} < -\mathscr{V}_0\} \right\} \Pr\left\{ \bigcap_{\substack{\delta_2 \text{ terms} \\ \text{of} \mathscr{A}_2}} \{\mathscr{V}_{i2} > \mathscr{V}_0\} \right\} \\
&\quad \times \Pr\left\{ \bigcap_{\substack{\delta_3 \text{ terms} \\ \text{of} \mathscr{A}_3}} \{-\mathscr{V}_0 \le \mathscr{V}_{i3} \le \mathscr{V}_0\} \right\} \qquad (14)
\end{aligned}
$$

Considering example of $M = 2$, the conditional BER in (14) can be expressed as

$$
\begin{aligned}
&P_e(\gamma_{s,d}, \gamma_{r_1,d}, \gamma_{r_2,d}) \\
&= \Pr\{\mathscr{U} - 2\mathscr{V}_0 < 0 | \mathscr{V}_1 < -\mathscr{V}_0, \mathscr{V}_2 < -\mathscr{V}_0, z[n] = 1\} \\
&\times \Pr\{\mathscr{V}_1 < -\mathscr{V}_0 | z[n] = 1\} \Pr\{\mathscr{V}_2 < -\mathscr{V}_0 | z[n] = 1\} \\
&+ \Pr\{\mathscr{U} < 0 | \mathscr{V}_1 > \mathscr{V}_0, \mathscr{V}_2 < -\mathscr{V}_0, z[n] = 1\} \\
&\times \Pr\{\mathscr{V}_1 > \mathscr{V}_0, |z[n] = 1\} \Pr\{\mathscr{V}_2 < -\mathscr{V}_0 | z[n] = 1\} \\
&+ \Pr\{\mathscr{U} + \mathscr{V}_1 - \mathscr{V}_0 < 0, -\mathscr{V}_0 \le \mathscr{V}_1 \le \mathscr{V}_0 | \mathscr{V}_2 \\
&< -\mathscr{V}_0, z[n] = 1\} \\
&\times \Pr\{\mathscr{V}_2 < -\mathscr{V}_0\} \\
&+ \Pr\{\mathscr{U} < 0 | \mathscr{V}_1 < -\mathscr{V}_0, \mathscr{V}_2 > \mathscr{V}_0, z[n] = 1\} \\
&\times \Pr\{\mathscr{V}_1 < -\mathscr{V}_0 | z[n] = 1\} \Pr\{\mathscr{V}_2 > \mathscr{V}_0 | z[n] = 1\} \\
&+ \Pr\{\mathscr{U} + 2\mathscr{V}_0 < 0 | \mathscr{V}_1 > \mathscr{V}_0, \mathscr{V}_2 > \mathscr{V}_0, z[n] = 1\} \\
&\times \Pr\{\mathscr{V}_1 > \mathscr{V}_0, |z[n] = 1\} \Pr\{\mathscr{V}_2 > \mathscr{V}_0 | z[n] = 1\} \\
&+ \Pr\{\mathscr{U} + \mathscr{V}_1 + \mathscr{V}_0 < 0, -\mathscr{V}_0 \le \mathscr{V}_1 \le \mathscr{V}_0 | \mathscr{V}_2 \\
&> \mathscr{V}_0, z[n] = 1\} \\
&\times \Pr\{\mathscr{V}_2 > \mathscr{V}_0\} \\
&+ \Pr\{\mathscr{U} - \mathscr{V}_0 + \mathscr{V}_2 < 0 | \mathscr{V}_1 < -\mathscr{V}_0, \\
&- \mathscr{V}_0 \le \mathscr{V}_2 \le \mathscr{V}_0, z[n] = 1\} \\
&\times \Pr\{\mathscr{V}_1 < -\mathscr{V}_0 | z[n] = 1\} \Pr\{-\mathscr{V}_0 \le \mathscr{V}_2 \le \mathscr{V}_0 | z[n] = 1\} \\
&+ \Pr\{\mathscr{U} + \mathscr{V}_0 + \mathscr{V}_2 < 0 | \mathscr{V}_1 > \mathscr{V}_0, \\
&- \mathscr{V}_0 \le \mathscr{V}_2 \le \mathscr{V}_0, z[n] = 1\} \\
&\times \Pr\{\mathscr{V}_1 > \mathscr{V}_0, |z[n] = 1\} \Pr\{-\mathscr{V}_0 \le \mathscr{V}_2 \le \mathscr{V}_0 | z[n] = 1\} \\
&+ \Pr\{\mathscr{U} + \mathscr{V}_1 + \mathscr{V}_2 < 0, -\mathscr{V}_0 \le \mathscr{V}_1 \le \mathscr{V}_0 | \\
&- \mathscr{V}_0 \le \mathscr{V}_2 \le \mathscr{V}_0, z[n] = 1\} \\
&\times \Pr\{-\mathscr{V}_0 \le \mathscr{V}_2 \le \mathscr{V}_0\}. \qquad (15)
\end{aligned}
$$

It can be noticed from (15) that the conditional BER of PL decoder has a complex structure even for two DF relays. Moreover, increasing number of relays further increases the complexity due to increased number of Hermitian quadratic variables $\mathscr{V}_i, i \in \{1, 2 \ldots, M\}$. Therefore, we derive the unified expression of probability of error for the single-DF relay-based FSO network employing DBPSK constellation.

4.1.1 Conditional BER with single DF relay

For single relay, i.e., $M = 1$, based differential cooperative FSO network, the expression of conditional BER in (14) can be written as [18]

$$
\begin{aligned}
P_e(\gamma_{s,d}, \gamma_{r_1,d}) = &\Pr\{\mathscr{U} - \mathscr{V}_0 < 0 | \mathscr{V}_1 < -\mathscr{V}_0, z[n] = 1\} \\
&\times \Pr\{\mathscr{V}_1 < -\mathscr{V}_0 | z[n] = 1\} \\
&+ \Pr\{\mathscr{U} + \mathscr{V}_0 < 0 | \mathscr{V}_1 > \mathscr{V}_0, z[n] = 1\} \\
&\times \Pr\{\mathscr{V}_1 > \mathscr{V}_0 | z[n] = 1\} \\
&+ \Pr\{\mathscr{U} + \mathscr{V}_1 < 0, \\
&- \mathscr{V}_0 \le \mathscr{V}_1 \le \mathscr{V}_0 | z[n] = 1\}, \\
&\triangleq \mathscr{D}_1(\gamma_{s,d}, \gamma_{r_1,d}) + \mathscr{D}_2(\gamma_{s,d}, \gamma_{r_1,d}) \\
&+ \mathscr{D}_3(\gamma_{s,d}, \gamma_{r_1,d}). \qquad (16)
\end{aligned}
$$

Since there is the possibility of correct / erroneous decoding at R_1, we can write

$$
\begin{aligned}
&\Pr\{\mathscr{V}_1 < -\mathscr{V}_0 | z[n] = 1\} \\
&= \Pr\{\mathscr{V}_1 < -\mathscr{V}_0 | z[n] = 1, \hat{z}_{r_1}[n] = 1\} \\
&\quad \times (1 - \varepsilon) + \varepsilon \Pr\{\mathscr{V}_1 < -\mathscr{V}_0 | z[n] = 1, \hat{z}_{r_1}[n] = -1\}, \\
&\Pr\{\mathscr{V}_1 > \mathscr{V}_0 | z[n] = 1\}
\end{aligned}
$$

$$= \Pr\{\mathscr{V}_1 > \mathscr{V}_0 | z[n] = 1, \hat{z}_{r_1}[n] = 1\} \times (1-\varepsilon) + \varepsilon \Pr\{\mathscr{V}_1 > \mathscr{V}_0 | z[n] = 1, \hat{z}_{r_1}[n] = -1\}. \quad (17)$$

We can rewrite different terms in conditional BER expression given by (16) as

$$\begin{aligned}
\mathscr{D}_1(\gamma_{s,d}, \gamma_{r_1,d}) &= F_{\mathscr{U}}(\mathscr{V}_0)[(1-\varepsilon)F_{\mathscr{V}_1}(-\mathscr{V}_0) + \varepsilon F_{\tilde{\mathscr{V}}_1}(-\mathscr{V}_0)] \\
&= P_{e_1}(\gamma_{s,d})[P_{e_2}(\gamma_{r_1,d}) + P_{e_3}(\gamma_{r_1,d})], \\
\mathscr{D}_2(\gamma_{s,d}, \gamma_{r_1,d}) &= F_{\mathscr{U}}(-\mathscr{V}_0)[1-(1-\varepsilon)F_{\mathscr{V}_1}(\mathscr{V}_0) - \varepsilon F_{\tilde{\mathscr{V}}_1}(\mathscr{V}_0)] \\
&= P_{e_4}(\gamma_{s,d})[1 - P_{e_5}(\gamma_{r_1,d}) - P_{e_6}(\gamma_{r_1,d})], \\
\mathscr{D}_3(\gamma_{s,d}, \gamma_{r_1,d}) &= (1-\varepsilon)\int_{-\mathscr{V}_0}^{0} F_{\mathscr{U}}(-n) f_{\mathscr{V}_1}(n) dn \\
&\quad + (1-\varepsilon)\int_{0}^{\mathscr{V}_0} F_{\mathscr{U}}(-n) f_{\mathscr{V}_1}(n) dn \\
&\quad + \varepsilon \int_{-\mathscr{V}_0}^{0} F_{\mathscr{U}}(-n) f_{\tilde{\mathscr{V}}_1}(n) dn \\
&\quad + \varepsilon \int_{0}^{\mathscr{V}_0} F_{\mathscr{U}}(-n) f_{\tilde{\mathscr{V}}_1}(n) dn \\
&= P_{e_7}(\gamma_{s,d}, \gamma_{r_1,d}) + P_{e_8}(\gamma_{s,d}, \gamma_{r_1,d}) \\
&\quad + P_{e_9}(\gamma_{s,d}, \gamma_{r_1,d}) + P_{e_{10}}(\gamma_{s,d}, \gamma_{r_1,d}),
\end{aligned} \quad (18)$$

where $F_X(\cdot)$ denotes the cumulative distribution function (CDF) of a random variable (RV) X. From the definition of the decision variables $\mathscr{U}$ and $\mathscr{V}$ given after (11), it can be deduced that $\mathscr{U}$ and $\mathscr{V}$ follow Hermitian quadratic distribution in complex Gaussian variates [25]. Therefore, by utilizing the PDF and CDF of a Hermitian quadratic RV from [25, Section IV], we can evaluate the various conditional BER terms as

$$\begin{aligned}
P_{e_1}(\gamma_{s,d}) &= 1 - \frac{e^{-2\gamma_{s,d}}}{2}\sum_{k=0}^{\infty}\frac{(2\gamma_{s,d})^k}{k!}\sum_{n=0}^{k}\frac{\Gamma(k-n+1,\mathscr{V}_0)}{(k-n)!2^n}, \\
P_{e_2}(\gamma_{r_1,d}) &= (1-\varepsilon)\frac{e^{-\gamma_{r_1,d}}}{2}e^{-\mathscr{V}_0}, \\
P_{e_3}(\gamma_{r_1,d}) &= \varepsilon\frac{e^{-2\gamma_{r_1,d}}}{2}\sum_{k=0}^{\infty}\frac{(2\gamma_{r_1,d})^k}{k!}\sum_{n=0}^{k}\frac{\Gamma(k-n+1,\mathscr{V}_0)}{(k-n)!2^n}, \\
P_{e_4}(\gamma_{s,d}) &= \frac{e^{-\gamma_{s,d}}}{2}e^{-\mathscr{V}_0}, \\
P_{e_5}(\gamma_{r_1,d}) &= (1-\varepsilon)\left[1 - \frac{e^{-2\gamma_{r_1,d}}}{2}\sum_{k=0}^{\infty}\frac{(2\gamma_{r_1,d})^k}{k!} \times \sum_{n=0}^{k}\frac{\Gamma(k-n+1,\mathscr{V}_0)}{(k-n)!2^n}\right], \\
P_{e_6}(\gamma_{r_1,d}) &= \varepsilon\left[1 - \frac{e^{-2\gamma_{r_1,d}}}{2}e^{-\mathscr{V}_0}\right],
\end{aligned} \quad (19)$$

where $\Gamma(a,x) = \int_x^{\infty} e^{-t}t^{a-1}dt$ is the upper incomplete Gamma function [26, Eq. (6.5.3)]. The other terms given in (18) can also be evaluated as

$$\begin{aligned}
&P_{e_7}(\gamma_{s,d}, \gamma_{r_1,d}) \\
&= \left(\frac{1-\varepsilon}{2}\right)(1-e^{-\mathscr{V}_0})e^{-\gamma_{r_1,d}} - \left(\frac{1-\varepsilon}{4}\right) \\
&\times e^{-2\gamma_{s,d}-\gamma_{r_1,d}}\sum_{k=0}^{\infty}\sum_{n=0}^{k}\sum_{l=0}^{k-n}\frac{(2\gamma_{s,d})^k 2^{-(l+1)}}{k!l!2^n}\gamma(l+1,2\mathscr{V}_0), \\
&P_{e_8}(\gamma_{s,d}, \gamma_{r_1,d}) = \left(\frac{1-\varepsilon}{4}\right)e^{-\gamma_{s,d}-2\gamma_{r_1,d}} \\
&\times \sum_{k=0}^{\infty}\sum_{n=0}^{k}\frac{(2\gamma_{r_1,d})^k 2^{-(k-n+1)}\gamma(k-n+1,2\mathscr{V}_0)}{k!(k-n)!2^n}, \\
&P_{e_9}(\gamma_{s,d}, \gamma_{r_1,d}) = \frac{\varepsilon}{2}e^{-2\gamma_{r_1,d}}\sum_{k=0}^{\infty}\sum_{n=0}^{k}\frac{(2\gamma_{r_1,d})^k\gamma(k-n+1,\mathscr{V}_0)}{k!(k-n)!2^n} \\
&- \frac{\varepsilon}{4}e^{-2\gamma_{s,d}-2\gamma_{r_1,d}}\sum_{k=0}^{\infty}\sum_{n=0}^{k}\sum_{i=0}^{\infty}\sum_{j=0}^{i}\sum_{l=0}^{i-j}\frac{(2\gamma_{s,d})^k(2\gamma_{r_1,d})^i}{k!(k-n)!2^{n+j}\,i!\,l!} \\
&\times 2^{-(k-n+l+1)}\gamma(k-n+l+1,2\mathscr{V}_0), \\
&P_{e_{10}}(\gamma_{s,d}, \gamma_{r_1,d}) \\
&= \varepsilon\frac{(1-e^{-2\mathscr{V}_0})}{8}e^{-\gamma_{s,d}-\gamma_{r_1,d}},
\end{aligned} \quad (20)$$

where $\gamma(a,x) = \int_0^x e^{-t}t^{a-1}dt$ is the lower incomplete Gamma function defined in [26, Eq. (6.5.2)].

4.2 Average BER analysis

The conditional probabilities terms $P_{e_k}(\gamma_{s,d})$ given in (19) can now be averaged as $P_{e_k} = \mathbb{E}_{\gamma_{s,d}}[P_{e_k}(\gamma_{s,d})] = \int_0^{\infty} P_{e_k}(\gamma_{s,d}) f_{\gamma_{s,d}}(\gamma_{s,d})d\gamma_{s,d}; k = 1, 4$, and the remaining conditional BER terms $P_{e_k}(\gamma_{r_1,d})$ of (19) can be averaged as $P_{e_k} = \mathbb{E}_{\gamma_{r_1,d}}[P_{e_k}(\gamma_{r_1,d})] = \int_0^{\infty} P_{e_k}(\gamma_{r_1,d}) f_{\gamma_{r_1,d}}(\gamma_{r_1,d})d\gamma_{r_1,d}; k = 2, 3, 5, 6$. Using (6), [27, Eq. (07.34.03.0228.01)] and [27, Eq. (07.34.21.0013.01)], we obtain

$$\begin{aligned}
P_{e_1} &= 1 - \mathscr{J}_1'\sum_{k=0}^{\infty}\sum_{n=0}^{k}\frac{\Gamma(k-n+1,\mathscr{V}_0)}{(k-n)!2^n k!}\mathscr{J}_1, \\
P_{e_2} &= (1-\varepsilon)e^{-\mathscr{V}_0}\mathscr{J}_4'\mathscr{J}_4, \\
P_{e_3} &= \varepsilon\mathscr{J}_2'\sum_{k=0}^{\infty}\sum_{n=0}^{k}\frac{\Gamma(k-n+1,\mathscr{V}_0)}{(k-n)!2^n k!}\mathscr{J}_2, \\
P_{e_4} &= e^{-\mathscr{V}_0}\mathscr{J}_3'\mathscr{J}_3, \\
P_{e_5} &= (1-\varepsilon)\left[1 - \mathscr{J}_2'\sum_{k=0}^{\infty}\sum_{n=0}^{k}\frac{\Gamma(k-n+1,\mathscr{V}_0)}{(k-n)!2^n k!}\mathscr{J}_2\right], \\
P_{e_6} &= \varepsilon\left[1 - \left(e^{-\mathscr{V}_0}\mathscr{J}_4'\mathscr{J}_4\right)\right],
\end{aligned} \quad (21)$$

where

$$\mathscr{J}_1^{'} = \frac{\xi_{s,d}^2 q^{\alpha_{s,d}+\beta_{s,d}-2}}{2(2\pi)^{q-1}\Gamma(\alpha_{s,d})\Gamma(\beta_{s,d})},$$
$$\mathscr{J}_2^{'} = \frac{\xi_{r_1,d}^2 q^{\alpha_{r_1,d}+\beta_{r_1,d}-2}}{2(2\pi)^{q-1}\Gamma(\alpha_{r_1,d})\Gamma(\beta_{r_1,d})},$$
$$\mathscr{J}_3^{'} = \frac{\xi_{s,d}^2 q^{\alpha_{s,d}+\beta_{s,d}-2}}{(2\pi)^{q-1}\Gamma(\alpha_{s,d})\Gamma(\beta_{s,d})},$$
$$\mathscr{J}_4^{'} = \frac{\xi_{r_1,d}^2 q^{\alpha_{r_1,d}+\beta_{r_1,d}-2}}{(2\pi)^{q-1}\Gamma(\alpha_{r_1,d})\Gamma(\beta_{r_1,d})},$$
$$\mathscr{J}_1 = G_{q+1,3q}^{3q,1}\left(\frac{(d_{s,d}\alpha_{s,d}\beta_{s,d})^q}{2k_{q,s,d}q^{2q}}\middle|\begin{matrix}1-k, \Delta(q,\xi_{s,d}^2+1)\\ \Delta(q,\mathscr{Z}_{s,d})\end{matrix}\right),$$
$$\mathscr{J}_2 = G_{q+1,3q}^{3q,1}\left(\frac{(d_{r_1,d}\alpha_{r_1,d}\beta_{r_1,d})^q}{2k_{q,r_1,d}q^{2q}}\middle|\begin{matrix}1-k, \Delta(q,\xi_{r_1,d}^2+1)\\ \Delta(q,\mathscr{Z}_{r_1,d})\end{matrix}\right),$$
$$\mathscr{J}_3 = G_{q+1,3q}^{3q,1}\left(\frac{(d_{s,d}\alpha_{s,d}\beta_{s,d})^q}{k_{q,s,d}q^{2q}}\middle|\begin{matrix}1, \Delta(q,\xi_{s,d}^2+1)\\ \Delta(q,\mathscr{Z}_{s,d})\end{matrix}\right),$$
$$\mathscr{J}_4 = G_{q+1,3q}^{3q,1}\left(\frac{(d_{r_1,d}\alpha_{r_1,d}\beta_{r_1,d})^q}{k_{q,r_1,d}q^{2q}}\middle|\begin{matrix}1, \Delta(q,\xi_{r_1,d}^2+1)\\ \Delta(q,\mathscr{Z}_{r_1,d})\end{matrix}\right), \tag{22}$$

where $\Delta(a,b) = b/a,\ldots,(b+a-1)/a$.

Further, conditional probabilities terms given in (20) can be averaged as $P_{e_k} = \mathbb{E}_{\gamma_{s,d},\gamma_{r_1,d}}[P_{e_k}(\gamma_{s,d},\gamma_{r_1,d})] = \int_0^\infty\int_0^\infty P_{e_k}(\gamma_{s,d},\gamma_{r_1,d})f_{\gamma_{s,d}}(\gamma_{s,d})f_{\gamma_{r_1,d}}(\gamma_{r_1,d})d\gamma_{s,d}d\gamma_{r_1,d}$; $k = 6,7\ldots10$. By utilizing (6), [27, Eq.(07.34.03.0228.01)] and [27, Eq.(07.34.21.0013.01)], we obtain

$$\begin{aligned}
P_{e_7} &= (1-\varepsilon)(1-e^{-\mathscr{V}_0})(\mathscr{J}_4^{'}\mathscr{J}_4) - (1-\varepsilon)(\mathscr{J}_4^{'}\mathscr{J}_4)\\
&\quad\times\mathscr{J}_1^{'}\sum_{k=0}^{\infty}\sum_{n=0}^{k}\sum_{l=0}^{k-n}\frac{2^{-l-1}\gamma(l+1,2\mathscr{V}_0)}{l!2^n k!}\mathscr{J}_1,\\
P_{e_8} &= (1-\varepsilon)\left(\mathscr{J}_3^{'}\mathscr{J}_3\right)\\
&\quad\times\mathscr{J}_2^{'}\sum_{k=0}^{\infty}\sum_{n=0}^{k}\frac{2^{-(k-n+1)}\gamma(k-n+1,2\mathscr{V}_0)}{k!(k-n)!2^n}\mathscr{J}_2,\\
P_{e_9} &= \varepsilon\mathscr{J}_2^{'}\sum_{k=0}^{\infty}\sum_{n=0}^{k}\frac{\gamma(k-n+1,\mathscr{V}_0)}{k!(k-n)!2^n}\mathscr{J}_2 - \varepsilon(\mathscr{J}_1^{'}\mathscr{J}_2^{'})\\
&\quad\times\sum_{k=0}^{\infty}\sum_{n=0}^{k}\sum_{i=0}^{\infty}\sum_{j=0}^{i}\sum_{l=0}^{i-j}\frac{2^{-(k-n+l+1)}\mathscr{J}_1\mathscr{J}_2}{k!(k-n)!2^{n+j}i!l!}\\
&\quad\times\gamma(k-n+l+1,2\mathscr{V}_0),\\
P_{e_{10}} &= \varepsilon\frac{(1-e^{-\mathscr{V}_0})}{2}\left(\mathscr{J}_3^{'}\mathscr{J}_3\right)\left(\mathscr{J}_4^{'}\mathscr{J}_4\right).
\end{aligned} \tag{23}$$

We can obtain the closed-form expression of average BER by applying (21)–(23) in $P_e = P_{e_1}(P_{e_2}+P_{e_3}) + P_{e_4}(1-P_{e_5}-P_{e_6}) + P_{e_7} + P_{e_8} + P_{e_9} + P_{e_{10}}$.

4.3 Asymptotic BER analysis with multiple DF relays

In this subsection, we provide the asymptotic BER of PL decoder in the DF-FSO network with multiple relays considering heterodyne detection and negligible pointing error case. For this, we assume that $\bar{\gamma}_{s,d} = \bar{\gamma} = \bar{\gamma}_{r_i,d}, \forall i$. we also assume that all the relays are error free, i.e., $\varepsilon_i \to 0$ or $\bar{\gamma}_{s,r_i} \to \infty$, for all i. Since for $\varepsilon_i \to 0$, $\mathscr{V}_{0i} \to \infty$, the PL function in (12) reduces to the linear function as $\underset{\varepsilon_i\to0}{\mathscr{H}}(\mathscr{V}_i,\varepsilon_i) = \mathscr{V}_i, -\infty \le \mathscr{V}_i \le \infty$, the low-complex PL decoder at the destination given in (13) can be rewritten as

$$\zeta_i^D = \mathscr{U} + \sum_{i=1}^{M}\mathscr{V}_i, \tag{24}$$

The conditional asymptotic BER of PL decoder with DBPSK data can be obtained as

$$\tilde{P}_e\left(\gamma_{s,d},\{\gamma_{r_i,d}\}_{i=1}^M\right) = F_{\zeta_i^D}(0) = \Pr\left\{\mathscr{U} + \sum_{i=1}^{M}\mathscr{V}_i < 0,\right\}. \tag{25}$$

By utilizing the CDF of a Hermitian quadratic RV from [25, Section IV)] and using [20, Eq. (8.970.1)], we evaluate the conditional BER as

$$\tilde{P}_e\left(\gamma_{s,d},\{\gamma_{r_i,d}\}_{i=1}^M\right) = \sum_{n=0}^{M}\sum_{u=0}^{n}(-1)^u\binom{n+M}{n-u}\frac{e^{-\gamma_e}\gamma_e^u}{2^{n+M+1}u!}, \tag{26}$$

where $\gamma_e = \gamma_{s,d} + \sum_{i=1}^{M}\gamma_{r_i,d}$. The PDF of instantaneous SNR over GG-distributed atmospheric turbulence with heterodyne detection scheme in the absence of pointing error can be given as

$$f_\gamma(\gamma;\alpha,\beta,\bar{\gamma}) = \frac{\alpha\beta}{\bar{\gamma}\Gamma(\alpha)\Gamma(\beta)}G_{0,2}^{2,0}\left(\frac{\alpha\beta\gamma}{\bar{\gamma}}\middle|\begin{matrix}-\\ \alpha-1,\beta-1\end{matrix}\right). \tag{27}$$

The approximate PDF expression of equivalent SNR γ_e can be obtained by following (27) and [28] as

$$\begin{aligned}
f_{\gamma_e}(\gamma_e;\alpha^{'},\beta^{'},\bar{\gamma}_e) &= \frac{\alpha^{'}\beta^{'}}{\bar{\gamma}_e\Gamma(\alpha^{'})\Gamma(\beta^{'})}\\
&\quad\times G_{0,2}^{2,0}\left(\frac{\alpha^{'}\beta^{'}\gamma_e}{\bar{\gamma}_e}\middle|\begin{matrix}-\\ \alpha^{'}-1,\beta^{'}-1\end{matrix}\right),
\end{aligned} \tag{28}$$

where $\alpha^{'} = (M+1)\alpha + \Delta$, $\beta^{'} = (M+1)\beta$, and Δ is an adjustment parameter which can be added to either α or β for the better accuracy of results and is defined as [28]

$$\Delta = M \times \frac{-0.127 - 0.95\alpha - 0.005\beta}{1 + 0.00124\alpha + 0.98\beta}. \tag{29}$$

The expression in (28) is valid for $\alpha > \beta$, and the adjustment parameter Δ must be added to β for $\alpha < \beta$.

The average asymptotic BER of the considered PL decoder with DBPSK constellation can be derived by averaging (26) over γ_e. By using (26), (28), and [27, Eq. (07.34.21.0088.01)], we obtain the average BER as

$$\tilde{P}_e = \sum_{n=0}^{M}\sum_{u=0}^{n}(-1)^{2u}\binom{n+M}{n-u} \times \frac{\alpha'\beta'}{2^{n+M+1}u!\bar{\gamma}_e\Gamma(\alpha')\Gamma(\beta')}G_{1,2}^{2,1}\left(\frac{\alpha'\beta'}{\bar{\gamma}_e}\middle|\begin{matrix}-u\\ \alpha'-1,\ \beta'-1\end{matrix}\right). \tag{30}$$

In order to obtain the diversity order, we analyze the performance of considered system at asymptotically high equivalent SNR, i.e., $\bar{\gamma}_e \to \infty$. Now, by utilizing [27, Eq. (07.34.06.0006.01)], the average BER of (30) can be written as

$$\tilde{P}_e = \sum_{n=0}^{M}\sum_{u=0}^{n}(-1)^{2u}\binom{n+M}{n-u}\frac{\alpha'\beta'}{2^{n+M+1}u!\bar{\gamma}_e\Gamma(\alpha')\Gamma(\beta')} \times \sum_{g=1}^{2}\prod_{j=1,j\neq g}^{2}\frac{\Gamma(h_j - h_g)}{\Gamma(1+h_g)} \times \Gamma(1+u+h_g)\left(\frac{\alpha'\beta'}{\bar{\gamma}_e}\right)^{h_g}, \tag{31}$$

where $h_g = \{\alpha' - 1, \beta' - 1\}$ for $g = \{1, 2\}$. It can be observed from (31) that

$$\tilde{P}_e \propto \frac{1}{\bar{\gamma}_e^{h_g+1}} \tag{32}$$

At high SNR, the BER can be approximated as $\tilde{P}_e \approx (G_c\bar{\gamma})^{-G_d}$, where G_c and G_d are coding gain and diversity order, respectively [29]. From (30) and (32), we obtain the diversity order of DF-based differential cooperative FSO network with M error-free relays as

$$G_d = \min\{\alpha', \beta'\}. \tag{33}$$

5 Outage analysis of differential cooperative FSO network

In this section, the outage probability of the differential DF-FSO network is derived with single and multiple relays considering GG-distributed atmospheric turbulence with pointing error. We have also analyzed the asymptotic outage behavior in order to investigate the effect of fading parameters on system performance.

5.1 Outage probability with single DF relay

The outage probability of direct FSO link can be written as

$$\mathscr{P}_{O,S-D} = F_{\gamma_{s,d}}(\gamma_{th}), \tag{34}$$

where $F_{\gamma_{a,b}}(\gamma_{th}) = \int_0^{\gamma_{th}} f_{\gamma_{a,b}}(\gamma)d\gamma$, $a, b \in \{s, r_i, d\}$, $i = \{1, 2\ldots, M\}$, $a \neq b$. For DF based relay link, the end to end instantaneous SNR can be written using [30] as

$$\gamma = \min(\gamma_{s,r_1}, \gamma_{r_1,d}), \tag{35}$$

The outage probability of relayed link can be written as [30]

$$\mathscr{P}_{O,S-R_1-D} = F_{\gamma_{s,r_1}}(\gamma_{th}) + F_{\gamma_{r_1,d}}(\gamma_{th}) - F_{\gamma_{s,r_1}}(\gamma_{th})F_{\gamma_{r_1,d}}(\gamma_{th}), \tag{36}$$

where γ_{s,r_1}, $\gamma_{s,d}$, and $\gamma_{r_1,d}$ denote the instantaneous SNR from S to R_1 link, $S-D$ link and R_1 to D link, respectively. The end-to-end outage probability of the considered system can be written as

$$\mathscr{P}_O = \mathscr{P}_{O,S-D}\mathscr{P}_{O,S-R_1-D}. \tag{37}$$

The CDF of $\gamma_{a,b}$ evaluated at threshold SNR under the effect of atmospheric turbulence and pointing error can be derived using (6) and [21, Eq. (2.24.2.2)] as

$$F_{\gamma_{a,b}}(\gamma_{th}; \alpha_{a,b}, \beta_{a,b}, \xi_{a,b}, \bar{\gamma}_{a,b}) = \frac{\xi_{a,b}^2 q^{\alpha_{a,b}+\beta_{a,b}-2}}{(2\pi)^{q-1}\Gamma(\alpha_{a,b})\Gamma(\beta_{a,b})} \times G_{q+1,3q+1}^{3q,1}\left(\frac{(d_{a,b}\alpha_{a,b}\beta_{a,b})^q\gamma_{th}}{k_{q,a,b}q^{2q}}\middle|\begin{matrix}1, \Delta(q, \xi_{a,b}^2+1)\\ \Delta(q, \mathscr{Z}_{a,b}), 0\end{matrix}\right), \tag{38}$$

Using (34)–(38), we can obtain the unified closed-form expression of end-to-end outage probability for the considered system with different turbulence conditions and pointing error values.

5.2 Outage probability with multiple parallel DF relays

The outage probability of the differential cooperative FSO network with single DF relay is given by (37). The generalized equation for multiple-DF relay-based FSO network can be written as

$$\mathscr{P}_O = \mathscr{P}_{O,S-D}\prod_{i=1}^{M}\mathscr{P}_{O,S-R_i-D}, \tag{39}$$

where $\mathscr{P}_{O,S-R_i-D}$ denotes the outage probability of the i-th relay link. If we assume that all the $S-R_i$ links have same average SNR $\bar{\gamma}_{s,r_1}$, and all the R_i-D links also have equal average SNR $\bar{\gamma}_{r_1,d}$, then the end-to-end outage probability of multiple-relay-based FSO system can be written as

$$\mathscr{P}_O = F_{\gamma_{s,d}}(\gamma_{th})[F_{\gamma_{s,r_1}}(\gamma_{th}) + F_{\gamma_{r_1,d}}(\gamma_{th}) - F_{\gamma_{s,r_1}}(\gamma_{th})F_{\gamma_{r_1,d}}(\gamma_{th})]^M. \quad (40)$$

The closed-form expression of overall outage probability in (40) can be obtained by utilizing the CDFs from (38) for different values of atmospheric turbulence and pointing error.

5.3 Asymptotic outage analysis

Next, we investigate the diversity order of the considered differential cooperative system with single DF relay, using outage probability expression under the combined effect of pointing error and atmospheric turbulence. Let us assume again that all the links are identical, hence we can write $F_{\gamma_{a,b}}(\gamma_{th};\alpha_{a,b},\beta_{a,b},\xi_{a,b},\bar{\gamma}_{a,b}) = \mathscr{F}(\gamma_{th})$, $a,b \in \{s,r_1,d\}$. The outage probability can be written using (34)–(37) as

$$\mathscr{P}_0 = 2\mathscr{F}^2(\gamma_{th}) - \mathscr{F}^3(\gamma_{th}), \quad (41)$$

where $\mathscr{F}(\gamma_{th})$ can be approximated using [27, Eq. (07.34.06.0005.01)] as

$$\mathscr{F}(\gamma_{th}) = \frac{\xi_{a,b}^2 q^{\alpha_{a,b}+\beta_{a,b}-2}}{(2\pi)^{q-1}\Gamma(\alpha_{a,b})\Gamma(\beta_{a,b})} \times \sum_{m=1}^{3q} \frac{\prod_{j=1,j\neq m}^{3q}\Gamma(h_j-h_m)\gamma_{th}^{h_m}}{\prod_{j=2}^{q+1}\Gamma(c_j-h_m)} \left[\frac{(d_{a,b}\alpha_{a,b}\beta_{a,b})^q}{K_{q,a,b}q^{2q}}\right]^{h_m}, \quad (42)$$

where $\{c_j\} = \left\{1, \Delta(q,\xi_{a,b}^2+1)\right\}$, $j = 1,...,(q+1)$, and $\{h_m\} = \left\{\Delta(q,\mathscr{Z}_{a,b}),0\right\}$, $m = 1,...,3q+1$. The expressions in (42) contain $3q+1$ terms in the summation, and all are decaying at different rates with $\bar{\gamma}$. At high SNR, the term with minimum power of $\bar{\gamma}^{-1}$ will dominate. Therefore, we can write the following from (42) for high SNR conditions:

$$\mathscr{F}(\gamma_{th}) \propto \frac{1}{\bar{\gamma}^{g_d}}, \quad (43)$$

where $g_d = \min\left\{\xi^2/q, \alpha/q, \beta/q\right\}$. At high SNR, the outage probability can be approximated as $\tilde{\mathscr{P}}_O \approx (G_c\bar{\gamma})^{-G_d}$, where G_c and G_d are coding gain and diversity order, respectively [29]. From (41) and (43), we obtain the diversity order of differential cooperative FSO network as

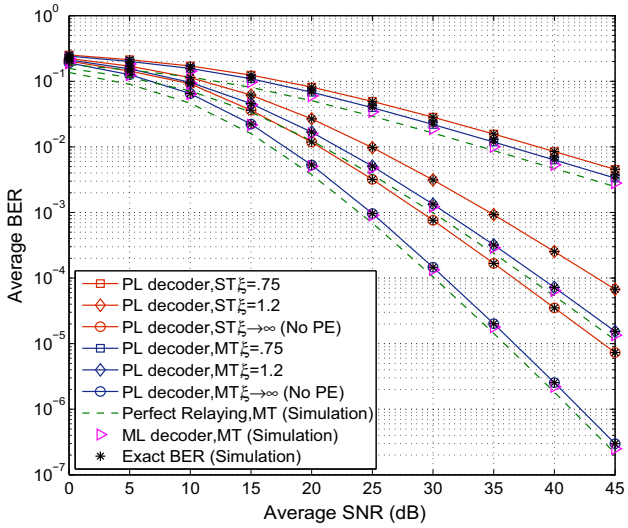

Fig. 2 Average BER performance of differential DF-FSO network for IM/DD detection with different turbulence conditions and pointing error (PE) values

$$G_d = 2g_d = \min\{2\xi^2/q, 2\alpha/q, 2\beta/q\}. \quad (44)$$

Remark 2 It can be deduced from asymptotic analysis given in Subsection V-III that the diversity order of differential DF-FSO network with heterodyne detection is twice than that of IM/DD detection. Therefore, heterodyne technique shows better system performance as compared with IM/DD technique for all the considered channel conditions.

6 Analytical and simulation results

For the analytical and simulation results, we assume (1) equal average SNRs of all the cooperative links, i.e., $\bar{\gamma}_{s,d} = \bar{\gamma}_{s,r_i} = \bar{\gamma}_{r_i,d} = \bar{\gamma}$, (2) identical channel parameters, i.e., $\alpha_{s,d} = \alpha_{s,r_i} = \alpha_{r_i,d} = \alpha$, $\beta_{s,d} = \beta_{s,r_i} = \beta_{r_i,d} = \beta$, $\xi_{s,d} = \xi_{s,r_i} = \xi_{r_i,d} = \xi$ and optical to electrical conversion coefficient $\eta_{s,d} = \eta_{s,r_i} = \eta_{r_i,d} = 1$, and (3) the noise variance of each link to be unity. We have considered two different turbulence conditions for GG-distributed FSO links as strong turbulence (ST) : $\alpha = 4.2$, $\beta = 1.4$ and moderate turbulence (MT) : $\alpha = 4.0$, $\beta = 1.9$. For pointing error, various values of ξ are considered as $\xi = 0.75$ for strong pointing error, $\xi = 1.2$ for moderate pointing error, and $\xi \to \infty$ for negligible or no pointing error.

6.1 Error performance of differential DF-FSO network

Figure 2 depicts the BER performance of the ML and PL decoders for differential DF-FSO network experiencing GG-distributed atmospheric turbulence with pointing error. It can

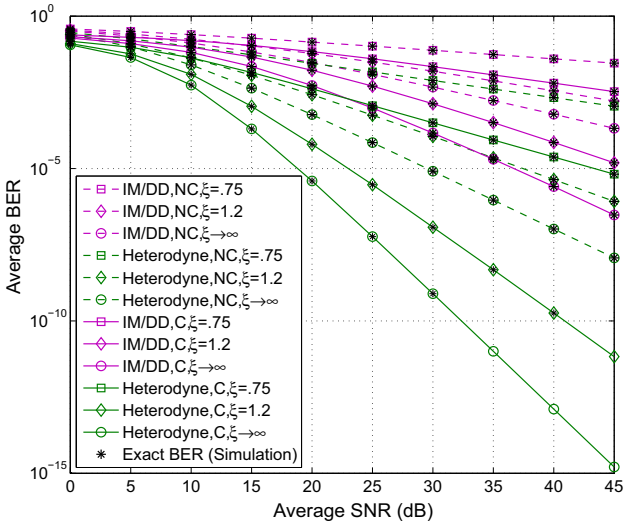

Fig. 3 Average BER versus average SNR performance of differential cooperative (C) and noncooperative (NC) FSO network under MT

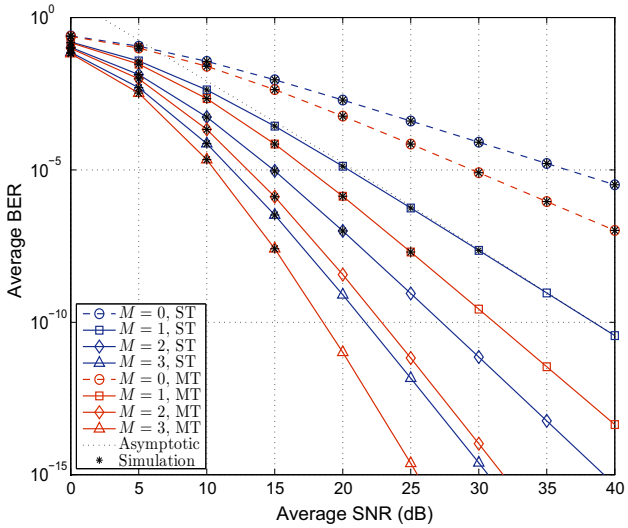

Fig. 4 Average BER of differential cooperative FSO network under heterodyne detection with varying turbulence conditions, $\bar{\gamma}_{s,r_i} \rightarrow \infty$, $\bar{\gamma}_{s,d} = \bar{\gamma}_{r_i,d} = \bar{\gamma}$ and $M = 0, 1, 2, 3$

be observed from Fig. 2 that the derived analytical results closely follow the exact simulation results for all the considered turbulence conditions and pointing error values. It can be noticed that the slope of BER curve of PL decoder is nearly same as that of perfect relaying case and performance of PL decoder is slightly worse than that of ML decoder. The effect of pointing error can also be noticed from Fig. 2 as the value of ξ increases (i.e., pointing error reduces), the BER performance improves for a given atmospheric condition. Moreover, for a constant ξ, the BER performance degrades as atmospheric turbulence conditions get severe.

In Fig. 3, we have investigated the average BER with respect to (w.r.t) average SNR for both heterodyne ($q = 1$) and IM/DD ($q = 2$) detection. It can also be observed from Fig. 3 that differential FSO network with single DF relay outperforms that of the noncooperative differential FSO network. Further, it can be noticed that the performance of heterodyne detection is superior than that of IM/DD detection. In Fig. 4, we have plotted the asymptotic approximate BER of (30) considering heterodyne detection and negligible pointing error with $M = 0, 1, 2, 3$ relays, $\bar{\gamma}_{s,r_i} \rightarrow \infty$, and $\bar{\gamma}_{s,d} = \bar{\gamma}_{r_i,d} = \bar{\gamma}$. It can be seen from Fig. 4 that putting more number of parallel DF relays enhances the error performance of considered system. Moreover, one can notice from Fig. 4 that for considered channel conditions with $M = 1$, ST, $\alpha' = 6.665$, $\beta' = 2.8$, we get BER of $= 9.136 \times 10^{-10}$ and $= 3.645 \times 10^{-11}$ at SNRs $= 35$ dB and $= 40$ dB, respectively. This ensures a diversity of 2.79 (numerically), which is very close its theoretical value 2.8, calculated as $G_d = \min\{\alpha', \beta'\}$.

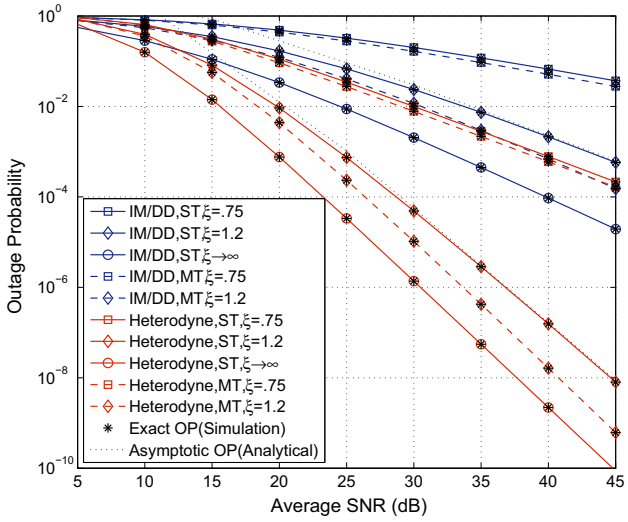

Fig. 5 Outage performance for both IM/DD and heterodyne detection with varying turbulence conditions and pointing error values

6.2 Average and asymptotic outage performance

Figure 5 demonstrates the outage performance of differential DF-FSO system using different turbulence conditions and ξ values for single relay. We can notice from Fig. 5 that heterodyne detection outperforms the IM/DD detection for all the considered channel conditions. Next, we have also shown the asymptotic outage performance of the considered system in Fig. 5. It can be observed from Fig. 5 that the rate of decay of asymptotic curves matches with the rate of decay of analytical curves for high SNR values. Therefore, it can be deduced from Fig. 5 that the derived analytical results provide maximum achievable diversity.

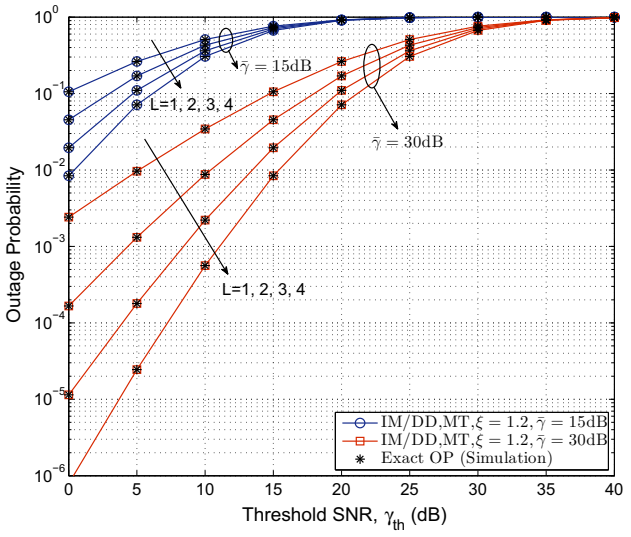

Fig. 6 Outage probability versus average SNR performance for varying number of parallel DF relays with $\bar{\gamma} = 15, 30$ dB

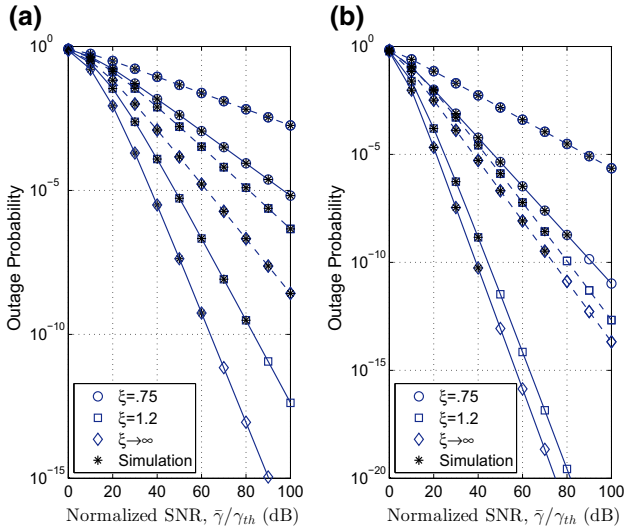

Fig. 7 Outage probability as a function of normalized SNR for differential cooperative (C) and noncooperative (NC) FSO system with varying turbulence conditions and pointing error values; —- and −− lines are representing C and NC networks, respectively. **a** MT, IMDD, **b** ST, heterodyne

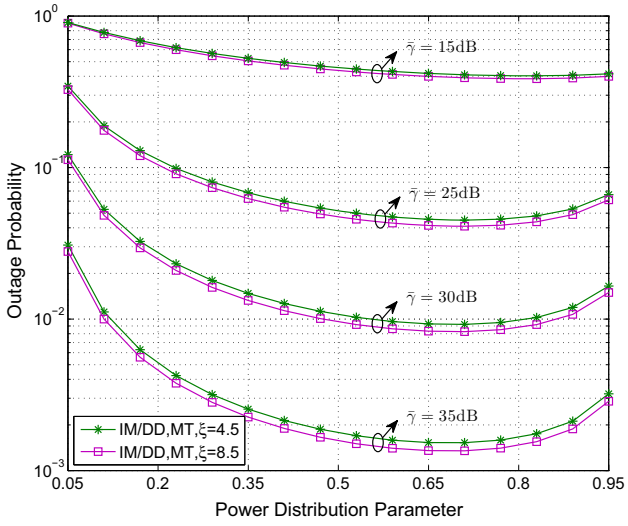

Fig. 8 Outage probability as a function of power distribution parameter for IM/DD with different values of average SNR and pointing error

Now, we have plotted the outage probability w.r.t threshold SNR for multiple parallel relays between S and D with IM/DD detection in Fig. 6. The curves have been plotted for MT and moderate pointing error values. We have shown that the outage performance improves as the value of $\bar{\gamma}$ increases from $\bar{\gamma} = 15$ dB to $\bar{\gamma} = 30$ dB. We can observe from Fig. 6 that the probability of going into outage increases with increasing values of threshold SNR (γ_{th}). It can also be seen that the increasing number of relays provides improvement in the system performance.

In Fig. 7, we have plotted the outage probability as a function of normalized SNR ($\bar{\gamma}/\gamma_{th}$) for both IM/DD and heterodyne detection with varying turbulence conditions and pointing error values. It can be deduced from Fig. 7 that the outage performance of differential FSO network with single DF relay is superior than that of the noncooperative differential FSO network. Moreover, the probability of going into outage decreases as we move from lower to higher normalized threshold value for all the considered channel conditions.

6.3 Power distribution in differential DF-FSO network

Figure 8 illustrates the impact of different power distribution techniques for DF relay. We consider equal distances between S, R_1, and D such that equal power is allocated to S and R_1. Further, we utilize a power distribution parameter Λ that controls the power allocation as : $\bar{\gamma}_{s,r_1} = \bar{\gamma}_{s,d} = \Lambda\bar{\gamma}$ and $\bar{\gamma}_{r_1,d} = (1-\Lambda)\bar{\gamma}$. The value of Λ ranges from 0 to 1. If $\Lambda < 0.5$, less power is allocated to S than R_1 and vice versa. In Fig. 8, outage probability is plotted w.r.t Λ for a threshold SNR (γ_{th}) = 10 dB and different values of average SNRs. It can be observed from Fig. 8 that lowest BER is obtained when Λ is approximately 0.75, i.e., power allocated to S is nearly thrice than that of R_1.

7 Conclusion

In this paper, we evaluate the performance of PL decoder for differential data in FSO network with multiple DF relays. It has been shown that the PL decoder which incorporates the possibility of erroneous relaying performs similar to that of ML decoder but with reduced complexity. We have pre-

sented the novel unified expressions of average BER and outage probability for differential cooperative FSO network with single DF relay. Further, the approximate BER analysis with multiple relays has also been carried out at asymptotically high SNR of source to relay links in order to obtain the diversity order analytically. It has been shown by analysis and simulations that the presence of severe atmospheric turbulence and pointing error strongly impedes the BER and outage performance of the PL decoder. We can conclude from the results that heterodyne detection outperforms the IM/DD detection for all the considered channel conditions. We have also demonstrated that as the number of error-free relays increases, the network performance improves. Moreover, the asymptotic outage analysis has also been performed in order to have better insight of system performance at high SNR.

References

[1] Andrews, L., Phillips, R., Hopen, C.: Laser Beam Scintillation With Applications. SPIE, New York (2001)

[2] Kedar, D., Arnon, S.: Urban optical wireless communication networks: the main challenges and possible solutions. IEEE Commun. Mag. **42**(5), s2–s7 (2004)

[3] Kaushal, H., Kaddoum, G.: Optical communication in space: challenges and mitigation techniques. IEEE Commun. Surv. Tutor. **19**(1), 57–96 (2017)

[4] Nosratinia, A., Hunter, T.E., Hedayat, A.: Cooperative communication in wireless networks. IEEE Commun. Mag. **42**(10), 74–80 (2004)

[5] Laneman, J.N., Tse, D.N.C., Wornell, G.W.: Cooperative diversity in wireless networks: efficient protocols and outage behavior. IEEE Trans. Inf. Theory **50**(12), 3062–3080 (2004)

[6] Sendonaris, A., Erkip, E., Aazhang, B.: User cooperation diversity—Part I: system description. IEEE Trans. Commun. **51**(11), 1927–1938 (2003)

[7] Safari, M., Uysal, M.: Relay-assisted free-space optical communication. IEEE Trans. Wirel. Commun. **7**(12), 5441–5449 (2008)

[8] Abou-Rjeily, C., Haddad, S.: Cooperative diversity for free-space optical communications: transceiver design and performance analysis. IEEE Trans. Commun. **59**(3), 658–663 (2011)

[9] Bhatnagar, M.R.: Average BER analysis of differential modulation in DF cooperative communication system over Gamma–Gamma fading FSO links. IEEE Commun. Lett. **16**(8), 1228–1231 (2012)

[10] Zhao, Q., Li, H.: Differential modulation for cooperative wireless system. IEEE Trans. Signal Process. **55**(5), 2273–2283 (2007)

[11] Trinh, H.V., Thang, T.C., Pham, A.T.: Two-way all-optical AF relaying FSO systems over Malaga ($\mathscr{M}$) channels with pointing errors. In: Proceedings of IEEE International Conference on Communications (ICC). Kuala Lumpur, Malaysia, pp. 1–7, May 2016

[12] Ju, M., Kim, I.-M.: ML performance analysis of the decode-and-forward protocol in cooperative diversity networks. IEEE Trans. Wirel. Commun. **8**(7), 3855–3867 (2009)

[13] Sharma, P.K., Bansal, A., Garg, P., Tsiftsis, T., Barrios, R.: Relayed FSO communication with aperture averaging receivers and misalignment errors. IET Commun. **11**(1), 45–52 (2017)

[14] Bhatnagar, M.R.: Decode-and-Forward based differential modulation for cooperative communication system with unitary and non-unitary constellations. IEEE Trans. Veh. Technol. **61**(1), 152–165 (2012)

[15] Bansal, A., Bhatnagar, M.R., Hjrungnes, A., Han, Z.: Low-complexity decoding in DF MIMO relaying system. IEEE Trans. Veh. Technol. **62**(3), 1123–1137 (2013)

[16] Bansal, A., Bhatnagar, Manav R., Hjrungnes, Are: Decoding and performance bound of demodulate-and-forward based distributed alamouti STBC. IEEE Trans. Wirel. Commun. **12**(2), 702–713 (2013)

[17] Sandalidis, H.G., Tsiftsis, T.A., Karagiannidis, G.K.: Optical wireless communications with heterodyne detection over turbulence channels with pointing errors. IEEE/OSA J. Lightw. Technol. **27**(20), 4440–4445 (2009)

[18] Bansal, A., Sharma, P.K., Bhatnagar, M.R.: DF cooperation over Gamma–Gamma fading FSO links with an erroneous relay. In: Proceedings of IEEE International Conference on Commnications (ICC), London, UK, pp. 1–6, June 2015

[19] Ansari, I.S., Yilmaz, F., Alouini, M.S.: Performance analysis of free-space optical links over M*á*laga ($\mathscr{M}$) turbulence channels with pointing errors. IEEE Trans. Wirel. Commun. **15**(1), 91–102 (2016)

[20] Gradshteyn, I.S., Ryzhik, I.M.: Table of Integrals, Series and Products, 6th edn. Academic Press, San Diego (2000)

[21] Brychkov, Yu A., Marichev, O.I.: Integrals and Series: More Special Functions, vol. 3. Gordon and Breach Science Publishers, London (1990)

[22] Gappmair, W.: Further results on the capacity of free-space optical channels in turbulent atmosphere. IET Commun. **5**(9), 1262–1267 (2011)

[23] Ansari, I.S., Yilmaz, F., Alouini, M.S.: Performance analysis of FSO links over unified Gamma–Gamma turbulence channels. In: Vehicular Technology Conference (VTC Spring' 2015), Glasgow, Scotland, pp. 1–5, May 2015

[24] Trees, H.L.V.: Detection, Estimation, and Modulation Theory: Part I. Detection, Estimation, and Linear Modulation Theory. Wiley, New York (2001)

[25] Biyari, K.H., Lindsey, W.C.: Statistical distributions of hermitian quadratic forms in complex Gaussian variables. IEEE Trans. Inf. Theory **39**(3), 1076–1082 (1993)

[26] Abramowitz, M., Stegun, I.A.: Handbook of Mathematical Functions. Dover Publications, New York (1972)

[27] Wolfram Research, I.: Mathematica Edition: Version 8.0. Wolfram Research, Inc. (2010)

[28] Chatzidiamantis, N.D., Karagiannidis, G.K.: On the distribution of the sum of Gamma–Gamma variates and applications in RF and optical wireless communications. IEEE Trans. Commun. **59**(5), 1298–1308 (2011)

[29] Proakis, J.G., Salehi, M.: Digital Communications, 5th edn. McGraw-Hill, New York (2008)

[30] Papoulis, A., Pillai, S.U.: Probability, Random Variables and Stochastic Processes, 4th edn. McGraw Hill, New York (1991)

Deepti Agarwal received her B.Tech. degree in Electronics & Communications Engineering from Uttar Pradesh Technical University (UPTU), Lucknow, in 2005 and M.Tech. in Energy & Environmental Management from Indian Institute of Technology Delhi (IITD), New Delhi, in 2009. She is currently pursuing Ph.D. degree from Indira Gandhi Delhi Technical University for women (IGDTUW) Delhi, India. Her research interest includes free-space optics, cooperative communications, non-coherent communication systems. She has worked as an Assistant Professor in Mahatma Gandhi Mission's College of Engineering & Technology, Noida, India, from 2005 to 2014.

Ankur Bansal has received his Ph.D. degree from Indian Institute of Technology Delhi, India, in 2013. He received his B.Tech. and M.Tech. degrees in Electronics and Communication Engineering and Signal Processing from the Uttar Pradesh Technical University, Lucknow, and Netaji Subhas Institute of Technology, Delhi, respectively. Currently, he is working as an Assistant Professor in the Division of Electronics and Communication Engineering at Netaji Subhas Institute of Technology, Delhi. His main research interests include various wireless communication technologies such as multiple-input multiple-output (MIMO), multi-user based communications, free-space optical communications, and distributed antenna-based cooperative communication technology. Dr. Bansal has published several research papers in reputed international journals like IEEE Transactions on Wireless Communications, IEEE Transactions on Vehicular Technology, and IEEE/OSA Journal of Lightwave Technologies, etc. He has served as a reviewer of several IEEE and IET journals.

Ashwni Kumar received the M.E. degree from Delhi College of Engineering, Delhi University, in 1993 in Electronics & Communications and Ph.D. degree from Delhi College of Engineering, Delhi University, in 2000 in Digital Signal Processing. He also received MBA degree from Faculty of Management Sciences, Delhi University, in 1998 in Technology Management. He has 16 years of research and development experience in C-DOT, Research and Development Center of Ministry of Communication, Gov of India. He is currently a Professor with the Department of Electronics and Communication Engineering, Indira Gandhi Delhi Technical University for Women (IGDTUW), Delhi, India. His area of interest includes optical communication, digital signal processing, and strategic management.

Int. J. Electron. Commun. (AEÜ) 90 (2018) 163–170

Contents lists available at ScienceDirect

Int. J. Electron. Commun. (AEÜ)

journal homepage: www.elsevier.com/locate/aeue

Regular paper

Programmable gain amplifier using operational floating current conveyors

Prateek Pahalwan, Prateek Tripathi, Prashant Gola, Neeta Pandey*, Deva Nand

Department of Electronics and Communication Engineering, Delhi Technological University, Bawana Road, Delhi, India

ARTICLE INFO

Keywords:
Programmable gain amplifiers
Operational floating current conveyor

ABSTRACT

This paper presents new operational floating current conveyor (OFCC) based Programmable Gain Amplifier (PGA). It operates in trans-impedance mode i.e. it receives current signal as input and provides voltage as output. It uses four blocks – a current amplifier, digitally controlled trans-impedance amplifier, digitally controlled R-2R ladder network and a voltage buffer. First block amplifies input signal. Second and third blocks of proposed PGA provide control over coarse and fine gain through bits (B_5–B_0) and a total of 60 different gain values are possible through the arrangement. The last block provides output at low impedance thereby avoiding need of impedance matching circuit. The operation of the proposal has been verified through SPICE simulations using 0.5 μm technology model parameters from MOSIS (AGILENT). The simulated variable gain range is found to be 56.76 dB Ω to 95.84 dBΩ. The total power dissipation is 3.13 mW under maximum gain settings. The equivalent input referred noise is found to be 6.9 pA/√Hz. Experimental verification of proposed PGA is also done by bread boarding the entire circuit. The measured results are found to be in close agreement with the theoretical and simulated values.

1. Introduction

Amplifiers, in particular programmable gain amplifiers, find applications in instrumentation, photodiode circuits, ultrasound pre-amplifiers, sonar, wide dynamic range sensors, driving ADCs (some ADCs have on-chip PGAs), automatic gain control (AGC) loops [1,2]. Fig. 1 [2] depicts a typical use of PGA in data acquisition system wherein it is placed between a sensor and analog to digital converter (ADC). Additional signal processing circuitry, as per demand of application, may be placed before or after the PGA. Former location is, however, preferred as it allows to condition a larger signal. Typically, operational amplifiers are employed in designing PGAs. However, the advantage of current mode signal processing [3,4] has motivated researchers to explore the PGA designs based on current mode building blocks. The features of available PGAs [5–27] are summarized in Table 1 on the basis of type of input being processed and output made available, active block used, input/output impedance and gain controlling mechanism.

Following observations are made:

- The PGA designs [5–27] provide voltage output and process data from voltage sensor. A current to voltage converter is needed if data is sensed from current sensor.
- The PGA design [5] processes data sensed from current sensor and provides current output. A current to voltage converter is required in case there is a need of interfacing it with circuit having input as voltage.
- Different active blocks such as second generation current conveyor (CCII) [7,19] and its variants such as Digitally Programmable CCII (DPCCII) [5], Digitally Controlled Fully Differential CCII (DCFDCCII) [6] and Fully Differential CCII (FDCCII) [20]; Current Feedback Amplifier topologies (CFAs) [8] and its variant such as Fully Differential Current Feedback Op Amp (FDCFOA) [9]; operational floating current conveyor (OFCC) is used in [10]; the topologies [12,16,17,21,24] employ differential amplifier; CMOS based simple, single ended and fully differential gate driven variable gain amplifier (VGA) with programmable gain is also reported in [22,23]; few topologies with Operational transconductance amplifier (OTA) is reported in [25,26]; whereas [27] employs op-amp for PGA design.
- The input and output impedances are proper in [8,10,11,13,14,17,22–24,27] while additional active block is needed in [5–7,9,12,15,16,18–21,25,26] to satisfy impedance condition.
- Gain tuning is achieved through current division networks (CDN) [6,7,18], weighted transistor arrays [5,17], potentiometer [8,9,16,20] or switches [10,11–13,15]; digitally controlled exponential function [14] or current mirrors [19]; 4-bit Digitally controlled look up table and pre-calibration method [21]; DAC gain control (dB linear/digital) [22]; 4-bit and 5-bit digitally programmable VGA [23]; source degenerated capacitor array [24]; two

* Corresponding author.
E-mail address: n66pandey@rediffmail.com (N. Pandey).

https://doi.org/10.1016/j.aeue.2018.04.022
Received 5 October 2017; Accepted 20 April 2018
1434-8411/ © 2018 Elsevier GmbH. All rights reserved.

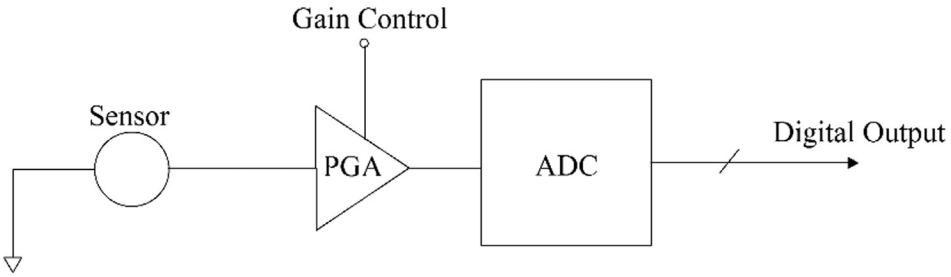

Fig. 1. PGAs in data acquisition systems [2].

Table 1
Literature Survey on previously reported PGAs.

Ref. no.	Input/output	Active block used	Input/output impedance	Gain control mechanism
[5]	I/I; V/V	DPCCII	Low/High; High/High	Code word controlled transistor arrays by effectively changing the transconductance
[6]	V/V	DCFDCCII	High/High	Code word controlled Current division network (CDN)
[7]	V/V	CCII, Op Amp	Low/Low	Fine Gain- Tuning of external resistors, Coarse Gain- CDN
[8]	V/V	CFA	High/Low	Tuning of feedback resistor
[9]	V/V	FDCFOA	High/High	Resistor tuning
[10]	V/V	OFCC	High/Low	Switched Resistor array
[11]	V/V	Op Amp	High/Low	Switched resistor array
[12]	V/V	Diff. Amp with CMFB	High/High	Source resistor tuning from switch array
[13]	V/V	Diff. Amp with Current Feedback	High/Low	Resistor array
[14]	V/V	Hybrid Exponential Approximation using Diode connected load	High/Low	Bit controlled exponential function
[15]	V/V	MOSFET based differential amplifier array	High/High	Binary weighted switched resistor array
[16]	V/V	FGA with loop amplifier and CMFB	Low/Low	Resistor tuning
[17]	V/V	Diff. Amp with CMFB and DC offset cancellation circuitry	High/Low	Weighted transistor array (trans-conductance control circuitry)
[18]	V/V	CDN and Generic Amplifier	Low/Low	CDN
[19]	V/V	CCII, OTA and Current Mirrors	High/High	Digitally controlled current mirrors
[20]	V/V	FDCCII	High/High	Tuning of resistors
[21]	V/V	Differential Amplifier	High/High	4-bit Digitally controlled look up table and pre-calibration method.
[22]	V/V	CMOS based VGA, 10 bit DAC	High/Low	DAC gain control (dB linear/digital)
[23]	V/V	Single ended gate driven VGA	High/Low	4 bit digitally programmable gain
[23]	V/V	Fully differential gate driven VGA	High/Low	5 bit digitally programmable gain
[24]	V/V	Differential FVF amplifier	High/Low	Source degenerated capacitor array
[25]	V/V	OTA, input negative transconductor	High/High	Two stacked transistors and PMOS bulk driven forward bias
[26]	V/V	OTA, switched capacitor based DAC	High/High	Switched capacitor array (9 bit gain and offset DAC)
[27]	V/V	Op-amp	High/Low	Resistor array with MOS switches
Proposed work	I/V	OFCC	Low/Low	Bit Controlled R-2R ladder network and resistor array

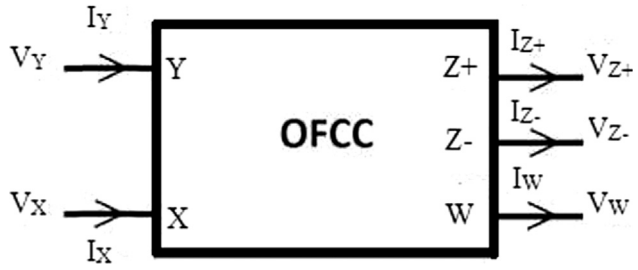

Fig. 2. Circuit block of OFCC. [10].

stacked transistors [25]; switched capacitor array [26]; and resistor array with MOS switches [27].

- Explicit mechanism for fine and coarse gain tuning is applied in [7,10] and [27].

It is clear from above discussion that no PGA design is available that works in trans-impedance mode i.e. processes data that is available from current sensor and provides voltage output. To bridge this gap, a new OFCC based PGA topology, operating in trans-impedance mode, is put forward in this paper. The proposal has gain control via both coarse and fine gain bits. The operation of the circuit is verified through SPICE simulations and substantiated through experimentation. The contents of present work are arranged in four sections including the introductory

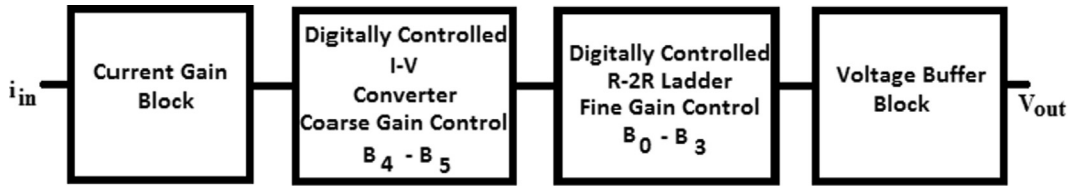

Fig. 3. Block diagram of proposed Programmable Gain Amplifier.

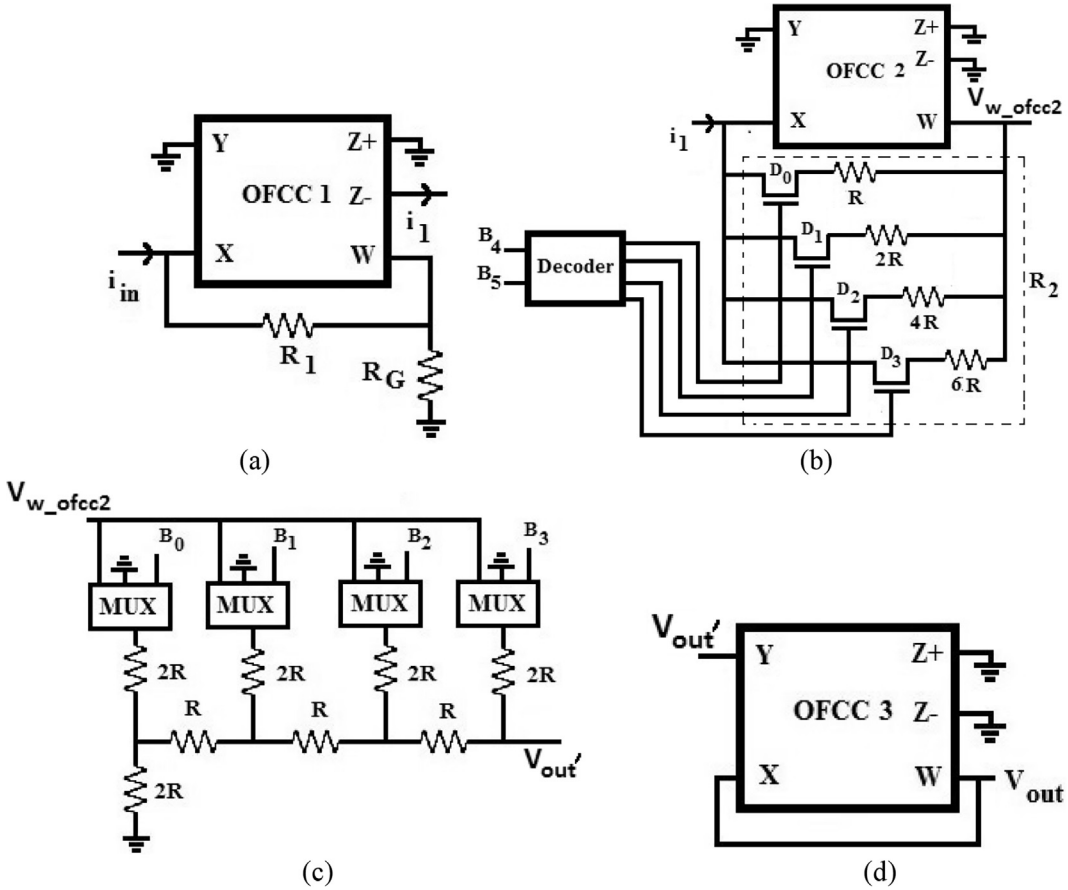

Fig. 4. (a) Current Gain Block (b) Digitally controlled I-V converter (c) R-2R Ladder Network (d) Voltage Buffer.

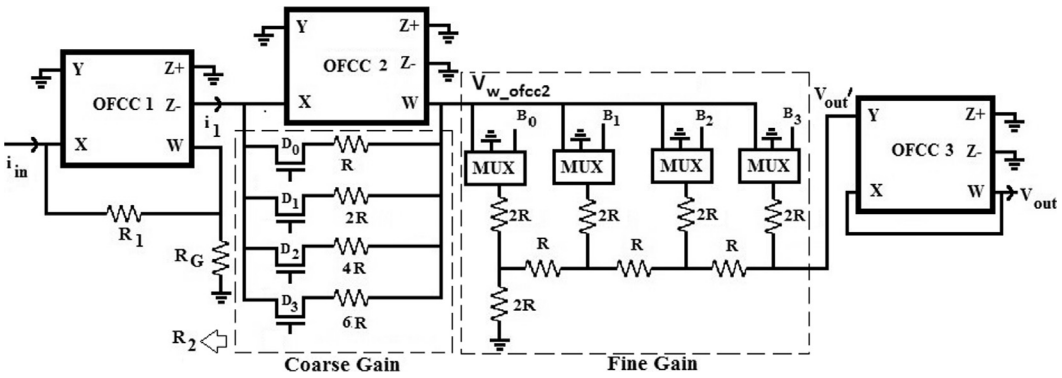

Fig. 5. Circuit Level Realization Proposed Programmable Gain Amplifier.

one. The functioning of OFCC is briefly reviewed in Section 2 along with detailed discussion of the proposed PGA. The functional verification of the proposal encompassing simulation and experimentation is placed in Section 3. Conclusions are drawn in Section 4.

2. OFCC and proposed circuit

The block diagram of OFCC [10] is depicted in Fig. 2. It consists of two input ports Y, X and three output terminals W, Z+ and Z−. The input impedance of port Y (X) is high (low), therefore it is suitable for voltage (current) sensing. The output impedance of port W (Z+ and Z−) is low (high), thereby making it appropriate for voltage (current) output. The port relationship of OFCC is given by (1).

$$\begin{bmatrix} I_Y \\ V_X \\ V_W \\ I_{Z+} \\ I_{Z-} \end{bmatrix} = \begin{bmatrix} 0 & 0 & 0 & 0 & 0 \\ 1 & 0 & 0 & 0 & 0 \\ 0 & Z_t & 0 & 0 & 0 \\ 0 & 0 & 1 & 0 & 0 \\ 0 & 0 & -1 & 0 & 0 \end{bmatrix} \begin{bmatrix} V_Y \\ I_X \\ I_W \\ V_{Z+} \\ V_{Z-} \end{bmatrix} \quad (1)$$

It may be observed that the voltage at port X is equal to the voltage at port Y and the input current at port X is multiplied by large transimpedance gain (Z_t) to produce voltage at port W. The output current flowing into port W is replicated to port Z+ in phase and to port Z- out of phase.

The block diagram of proposed OFCC based PGA is depicted in Fig. 3. The realization of constituent blocks of Fig. 3 are shown in Fig. 4(a)–(d). The first block (Fig. 4(a)) of proposed PGA is a current gain block. It uses OFCC based current amplifier and its gain is given by (2) including the effect of single pole model transimpedance gain ($Z_t(s)$):

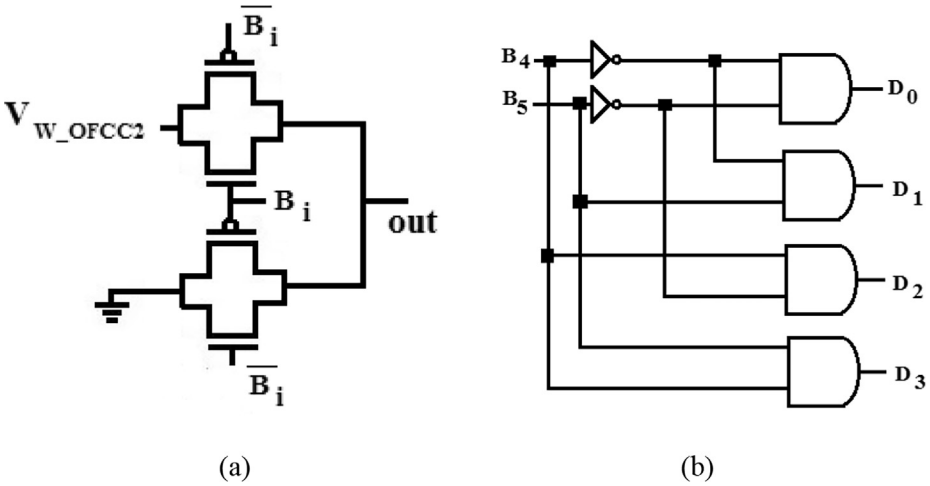

Fig. 6. Schematic of (a) 2 × 1 Multiplexer using Transmission Gates (b) 2 × 4 Decoder.

Table 2
Truth Table for 2 × 1 Multiplexer in Fig. 6(a).

B_i	Out
0	0
1	V_{W_OFCC2}

Table 3
Truth table for 2 to 4 decoder of Fig. 6(b).

B_5	B_4	D_0	D_1	D_2	D_3	Equivalent resistance at the block, R_2 (kΩ)
0	0	1	0	0	0	1
0	1	0	1	0	0	2
1	0	0	0	1	0	4
1	1	0	0	0	1	6

$$i_1 = -i_{in}\left[1 + \frac{R_1}{R_G}\right]\frac{1}{1 + \frac{R_1}{Z_t(s)}} \tag{2}$$

The second and third blocks of proposed PGA provide control over coarse and fine gain using bits (B_5–B_4) and (B_3–B_0) respectively. The output of first block is applied to second block (Fig. 4(b)) along with coarse gain control bits (B_5–B_4). A 2 to 4 decoder is used to convert bits (B_5–B_4) to bits (D_3–D_0) which enable one out of the four switches connected between X and W port of OFCC2 of second block, thus

Table 4
Aspect ratios of MOS transistors [10].

Transistor	$W(\mu m)/L(\mu m)$
M1,M2	50/1
M3,M4,M11,M12,M14	50/2.5
M5,M7,M10,M15	20/2.5
M6,M8	40/2.5
M9,M13	100/2.5

resulting in coarse gain variation of proposed PGA. The current input (i_1) is converted into voltage ($V_{W.OFCC2}$) and its value is computed as

$$V_{W.OFCC2} = -i_1 \cdot R_2 \frac{1}{1 + \frac{R_2}{Z_t(s)}} = i_{in} \cdot R_2 \left[1 + \frac{R_1}{R_G}\right]\frac{1}{1 + \frac{R_1}{Z_t(s)}} \cdot \frac{1}{1 + \frac{R_2}{Z_t(s)}} \tag{3}$$

where the value of R_2 is given by (4)

$$R_2 = [D_0 \times R + D_1 \times 2R + D_2 \times 4R + D_3 \times 6R] \tag{4}$$

Eq. (3) may be rewritten as

$$V_{W.OFCC2} = i_{in} \cdot R_2 \left[1 + \frac{R_1}{R_G}\right]\frac{1}{1 + \frac{R_1 R_2}{Z_t^2(s)} + \frac{R_1}{Z_t(s)} + \frac{R_2}{Z_t(s)}} \tag{5}$$

The second order term ($R_1R_2/Z_t^2(s)$) in denominator of (5) may be neglected as Z_t (s) is very high. Therefore (5) modifies to

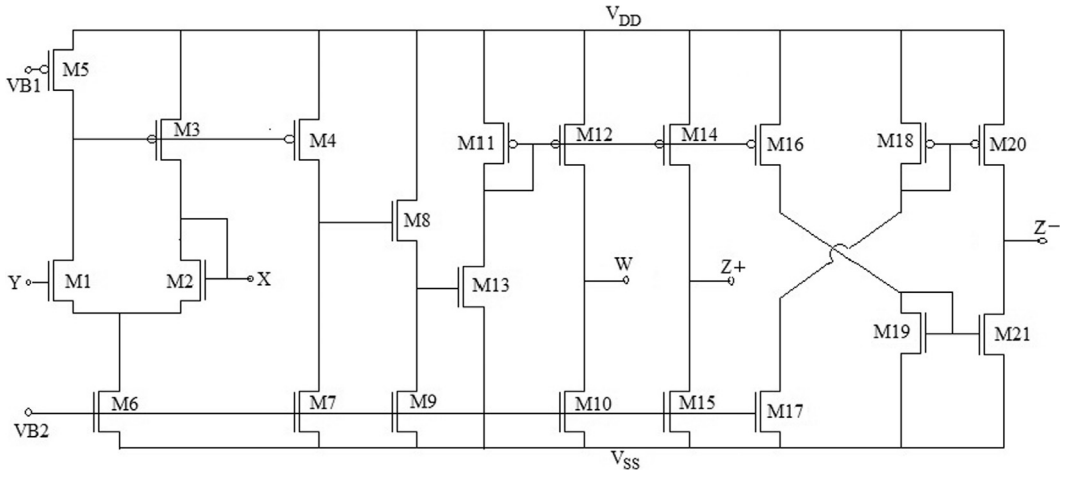

Fig. 7. CMOS Schematic of OFCC [10].

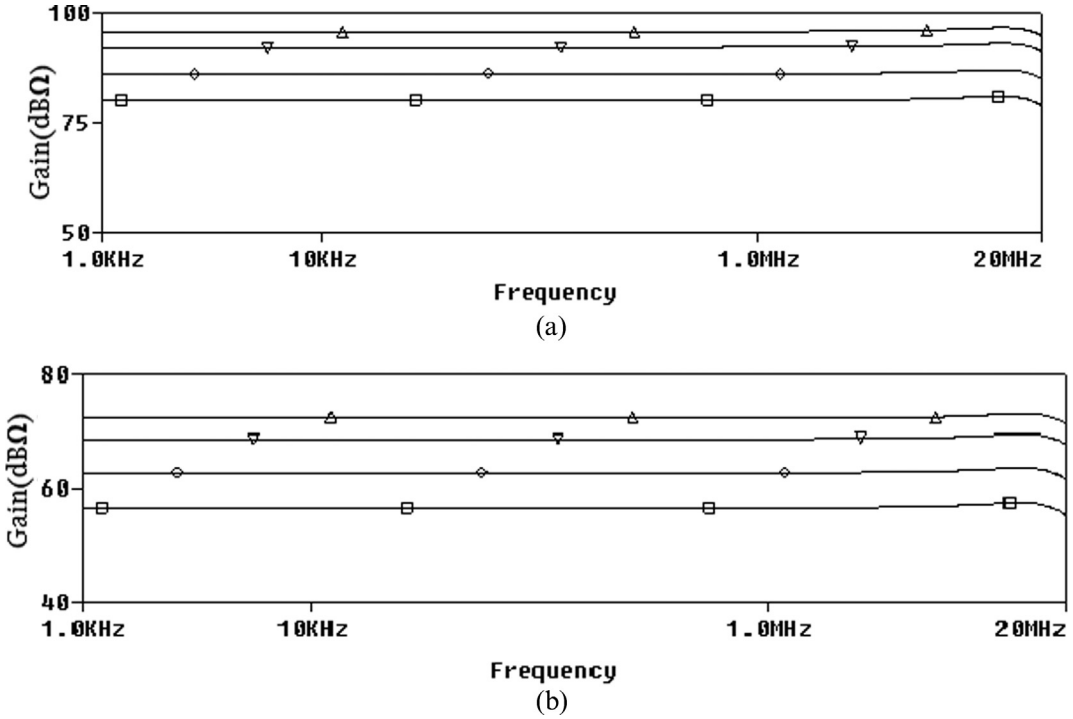

Fig. 8. Coarse gain setting for (a) maximum gain values (b) minimum gain values.

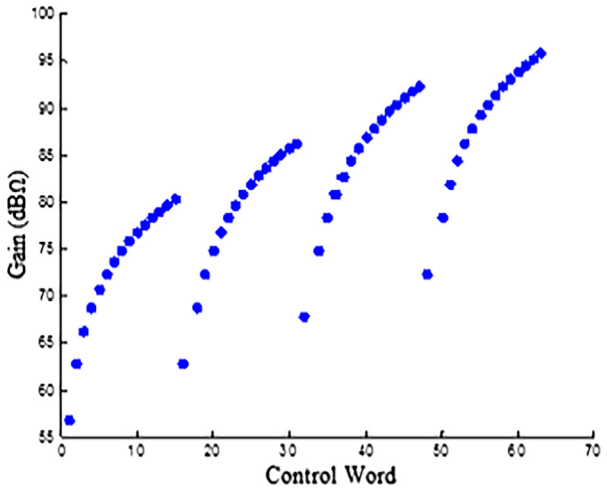

Fig. 9. Variation in Gain with respect to Control Word of the proposed PGA.

$$V_{W.OFCC2} \approx i_{in} \cdot R_2 \left[1 + \frac{R_1}{R_G}\right] \frac{1}{1 + \frac{R_1}{Z_t(s)} + \frac{R_2}{Z_t(s)}} \tag{6}$$

Taking single pole model and high frequency approximation for $Z_t(s) = 1/(sC_p)$, (6) modifies to

$$V_{W.OFCC2} \approx i_{in} \cdot R_2 \left[1 + \frac{R_1}{R_G}\right] \left[\frac{1}{1 + (R_1 + R_2)sC_p}\right] \tag{7}$$

Eq. (7) indicates that there is a pole at $s = 1/(R_1 + R_2)sC_p$ which may affect the processing of high frequency signals.

The third block (Fig. 4(c)) is digitally controlled R-2R ladder network. It adds fine gain control through multiplexers whose operation is controlled by bits (B_3-B_0). The bits (B_3-B_0) can vary from 0001 to 1111 therefore fifteen possible gain combinations exist. Taking the coarse and fine gain variations into account, the proposed PGA can be tuned to 60 possible gain values.

The output of the third block is computed as

$$V_{out} = V_{W.OFCC2}\left[\frac{B_0}{16} + \frac{B_1}{8} + \frac{B_2}{4} + \frac{B_3}{2}\right] \tag{8}$$

As the output of the third block is not available at low output impedance terminal, an OFCC based buffer is used as the fourth block (Fig. 4(d)). Thus, the final output can be used for further processing without any impedance matching problem. The overall proposal at the circuit level is presented in Fig. 5.

The multiplexer and decoder in Fig. 4(b) and (c) are realized using transmission gate and static CMOS schematic as shown in Fig. 6(a) and Fig. 6(b) respectively. Their corresponding functionality is listed in Table 2 and Table 3 respectively.

3. Functional verification

This section describes functional verification of the proposed PGA through simulations and experimentations. The performance parameters of the proposed PGA are compared with those available in literature.

3.1. Simulation results

SPICE simulations are carried out for functional verification using 0.5 µm technology model parameters from MOSIS (AGILENT), wherein OFCC is realized using CMOS based schematic [10] of Fig. 7. Supply voltages (V_{DD} and V_{SS}) are taken as ± 1.5 V and bias voltages (V_{B1} and V_{B2}) of ± 0.8 V are applied. The aspect ratios of MOS transistors are placed in Table 4. The resistance R_1 and R_G in current gain block (Fig. 4(a)) are taken as 15 kΩ and 1 kΩ respectively. The value of R in second and third block of proposed PGA (Fig. 4(b) and 4(c)) is 1 kΩ.

The frequency response of the proposed PGA under maximum coarse gain setting i.e. B_3–B_0 = 1111 for all the combinations of B_4 and B_5 are found out to be 95.84 dBΩ, 92.32 dBΩ, 86.3 dBΩ and 80.28 dBΩ and are presented in Fig. 8 (a). Similarly, the gain variation under minimum coarse gain setting i.e. B_3–B_0 = 0001 are found as 72.31 dBΩ, 67.79 dBΩ, 62.78 dBΩ, 56.76 dBΩ for all combinations of B_4 and B_5 are presented in Fig. 8(b) with a gain range of 39 dBΩ with a 3-dB bandwidth of approximately 20 MHz.

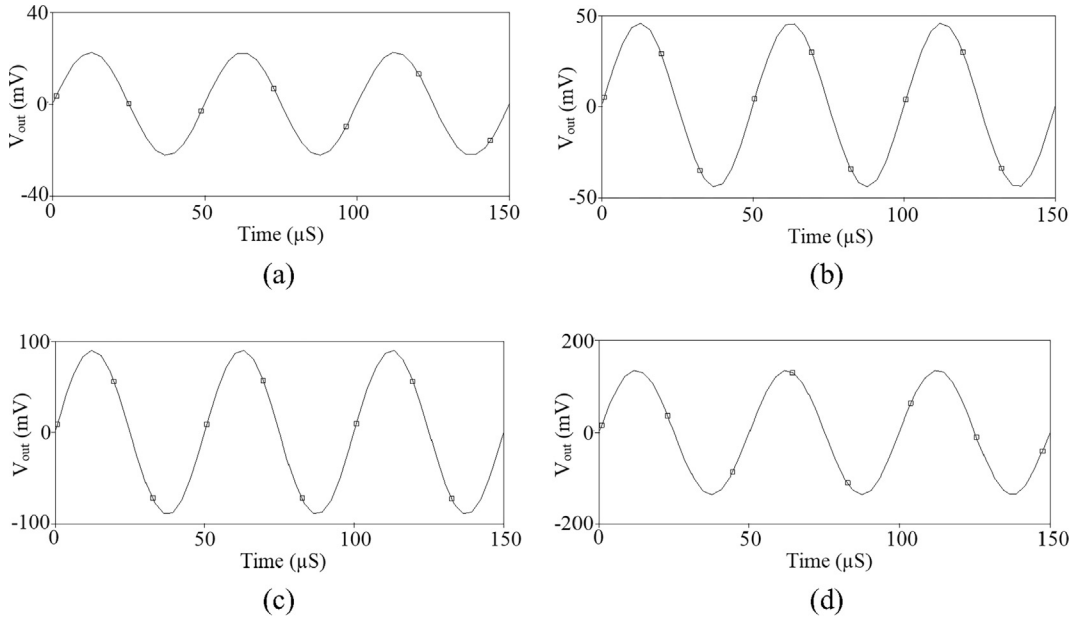

Fig. 10. Transient responses of proposed PGA for sinusoidal current input of I_{in} = 1.5μA, 20 KHz with coarse gain setting B_3-B_0 = 1111 and fine gain settings as (a) B_4B_5 = 00 (b) B_4B_5 = 01 (c) B_4B_5 = 10 (d) B_4B_5 = 11.

Table 5
Performance analysis of previously reported PGAs.

Ref. No.	Bandwidth	Dynamic range (dB)	(Min. gain - max gain) (dB)	Input referred noise	Supply (V)	Power consumption
[5]	35 MHz	33.8	−16.9 to 16.9	N/A	± 0.75	2.71 mW
[6]	N/A	24	0 to 24	N/A	± 1.5	N/A
[7]	0.05 MHz to 0.8 MHz	41	−5 to 36	N/A	1.5	N/A
[8]	9.48 MHz(at max. gain)	54	6 to 60	N/A	3.3	2.4 mW
[9]	10 MHz	16	0 to 16	N/A	± 1.5	1.14 mW
[10]	42 MHz	42	5 to 47	N/A	± 1.5	3.12 mW
[11]	125 MHz	19	0 to 19	8.63 /√Hz	3.3	21 mW
[12]	50 MHz	24	−10 to 14	2.5 nV/√Hz	1.8	11.18 mW
[13]	10 MHz	22.5	13.8 to 36.3	7.41 /√Hz	3	12.6 mW
[14]	39 MHz	34.4	4.6 to 39	3.54 nV/√Hz	1.8	6.16 mW
[15]	60 MHz	42	−21 to 21	N/A	1.5	3.12 mW
[16]	30 MHz	30	−10 to 20	11.2 nV/√Hz	1.8	2.43 mW
[17]	60 MHz	48	−16 to 32	N/A	1	1.2 mW
[18]	4.1 MHz	25	0 to 25	21 nV/√Hz	3	N/A
[19]	1 MHz	17	0 to 17	N/A	± 10	N/A
[20]	26 MHz	16	0 to 16	65 nV/√Hz	± 1.5	N/A
[21]	80 MHz	47	−24 to 23	N/A	1.8	1.42 mW
[22]	3.5 GHz	57	−33 to 24	N/A	1.2	96 mW
[23]	2 KHz	20	0 to 20	N/A	± 0.18	0.15 μW
[23]	8 KHz	27	0 to 27	N/A	± 0.08	0.07 μW
[24]	6 GHz	20	10 to 30	N/A	1.2	11.78 mW
[25]	0.98 MHz	18.2	0.2 to 18.4	N/A	0.36	15.4 μW
[26]	> 500 MHz	9.53	−1.93 to 7.60	N/A	1.8	18.18 mW
[27]	35 MHz	23	−6 to 17	22 nV/√Hz	1.8	3.96 mW
Proposed work	20 MHz	39	56.8 to 95.8	6.9 pA/√Hz	± 1.5	3.13 mW

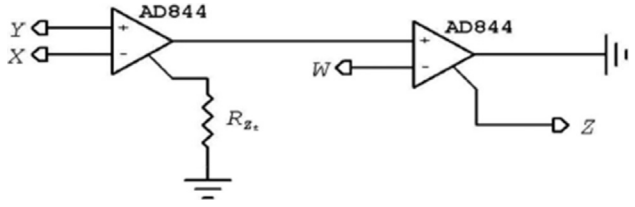

Fig. 11. Realization of OFCC using AD-844.

The variation in gain setting (dBΩ) with respect to the control word inputs (B_5–B_0) of the proposed PGA are shown in Fig. 9. It may be noted that wide variety of gains can be achieved with the amplifier using appropriate control bits tuning thus verifying overall programmability of the proposed PGA while preserving the dB-linear characteristic of the amplifier.

Simulations are also carried out to examine the noise performance of the proposed PGA. The simulated total input referred noise current was found to be 6.9 pA/√Hz. The power dissipation of the overall circuit under maximum gain setting was found to be 3.13mW.

Time domain simulations are also carried out to investigate transient behavior of the proposed PGA. A current sinusoid of 1.5 μA, 20 KHz is applied to proposed PGA with maximum coarse gain setting i.e. B_3–B_0 = 1111 and B_4B_5 are taken as 00, 01, 10 and 11. The corresponding outputs are placed at Fig. 10(a)–(d) and respective simulated output values are found as 22.5 mV, 45 mV, 90 mV and 135 mV. The performance comparison of proposed PGA with those available in literature, is done in Table 5 on the basis of parameters such as

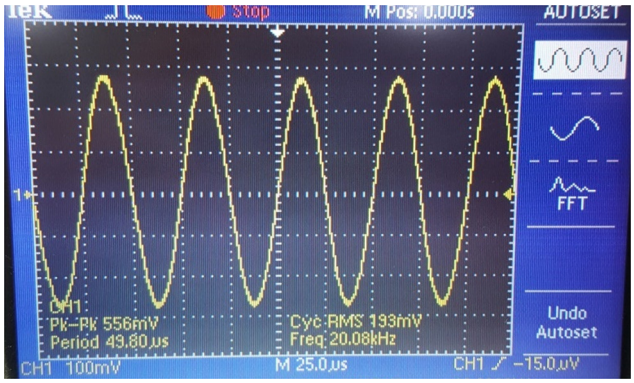

Fig. 12. Output at Bit combination (101111) of Control word input.

Table 6
Experimental measurement results and error calculation.

Control word input ($B_5B_4B_3B_2B_1B_0$)	Measured output (mV)	Theoretical output (mV)	Error (%)
001,111	137	147.9	7.4
000,001	10.8	9.86	9.5
001,000	73.2	78.9	7.2
000,111	63.2	69	8.4
011,111	270	295.8	8.7
010,001	19.8	19.72	0.4
011,000	145	157.8	8.1
010,111	126	138	8.71
101,111	556	591.6	6
100,001	37.2	39.44	5.7
101,000	295.3	315.6	6.4
100,111	262	276	5.1
111,111	816	887.4	8
110,001	56	59.16	5.3
111,000	441	473.4	6.8
110,111	395	414	4.6

bandwidth, dynamic range, maximum and minimum gain, input referred noise, power supply used and power consumption. Following are the observations from Table 5:

- The proposed PGA demonstrates a superior dynamic range than the presented works in [5,6,9,11–14,16,18–20,21,23–27]. While many works claim substantial theoretical dynamic range, it might be misleading as certain works in [5,7,12,15–17,21,22,26,27] have overall gain values less than 0 dB which have no practical advantage as incoming data is already severely attenuated after passing through skin layers and incurring other losses due to mismatches. Thereby decreasing their effective dynamic range further.
- The proposed work possesses better bandwidth than [7–9,13,18,19,23,25], lower input referred noise than [11–14,16,18,20,27] along with a lower power consumption than [11–14,22,24,26,27] which further demonstrates the competitive performance of our design.
- The proposed PGA provides maximum gain of 95.8 dBΩ which is highest among available ones. The input referred noise is also very small. Therefore, proposed design is capable of processing weaker signals and getting them to an acceptable range.

3.2. Experimental results

Experimental verification of proposed PGA circuit done using commercially available IC AD844 (Fig. 11) with supply voltages of ± 5 V and sinusoidal current input of 10 µA, 20 KHz is applied. The resistance values are kept same as those used in simulations. Experimental results for bit combination (101111) of control word input are shown in Fig. 12 for authentication.

Measurements for other bit combinations are also performed and the observations are enlisted in Table 6 along with the calculated errors. The variation in experimental gain values from theoretical gain values is attributed to tolerances of resistances used in prototyping and non-idealities of OFCC. It may be noted that proposed PGA behaves well with a mean error of 6.64% in observation window which demonstrates the fidelity of the circuit. The error in output is attributed to component tolerances and device tracking errors. The precision can be further improved by usage of high impedance current source, precision resistors, higher quality probes and proper insulation of the circuit which cannot be achieved using a breadboard.

4. Conclusion

A novel programmable gain amplifier design working in trans-impedance mode has been proposed in this paper. The design employs variable gain stage using OFCC followed by R-2R ladder network to achieve coarse and fine gain tuning of the amplifier. Due to the nuanced mixed signal processing used in this design, a wide range of gains 56.76–95.84 dBΩ can be achieved using the control words with a high degree of precision along with its low input noise current of 6.9 pA/√Hz and low power properties like 3.13mW. The fidelity of the simulated and experimental results with respect to the corresponding theoretical values further demonstrate and exhibit the competitive performance of the proposed design.

References

[1] Mehr I, Paterson D, Abaskharoun N, Lloyd J, L'Bahy H, DeSimone A. An integrated mixed-signal front-end for broadband modems. IEEE Symp. VLSI Circuits Dig. Tech. Papers, 2002;38–41.
[2] Jung WG. Op Amp applications handbook. Newnes; 2005.
[3] Yuan F. CMOS current-mode circuits for data communications. Springer; 2007.
[4] Mohan PA. Current-mode VLSI analog filters: design and applications. Springer Science & Business Media; 2012.
[5] Mahmoud SA. Low voltage current-mode digitally controlled VGA based on digitally programmable current conveyors. In: 51st IEEE Midwest Symposium on Circuits and Systems 2008;814–817.
[6] Mahmoud SA. Low voltage high current gain CMOS digitally controlled fully differential CCII. IEEE Int Sympos Circuits Syst 2005:1000–3.
[7] Farag FA, Khalaf YA. Digitally Controlled variable gain amplifier based on current conveyor with opamp and inverters only. In: 22nd international conference on microelectronics 2010;224–227.
[8] Chao HL, Ma D. CMOS variable-gain wide-bandwidth CMFB-free differential current feedback amplifier for ultrasound diagnostic applications. IEEE Int Sympos Circuits Syst 2006:649–52.
[9] Mahmoud SA, Awad IA. Fully differential CMOS current feedback operational amplifier. J Analog Integrated Circuits Signal Process 2005;43(1):61–9.
[10] Hassan HM, Soliman AM. Novel CMOS realizations of the operational floating current conveyor and applications. J Circuits Syst Comput 2005;14(6):1113–43.
[11] Hsu CC, Wu JT. A highly linear 125 MHz CMOS switched-resistor programmable-gain amplifier. IEEE J Solid-State Circuits 2003;38(10):1663–70.
[12] Rahmatian B, Mirabbasi S. A low-power 75-dB digitally programmable variable-gain amplifier in 0.18 µm CMOS. Can J Electr Comput Eng 2007;32(4):181–6.
[13] Wang Y, Koen M, Ma D. Low-noise TGC Amplifier with adaptive gain control for ultrasound imaging receivers. IEEE Trans Circuits Syst II: Express Briefs 2011;58(1):26–30.
[14] Tsai PK, Ku PC, Lu CC, Shih CM, Lu LH. A precise decibel-linear programmable gain amplifier for ultrasound imaging receivers. Int. Symp. on VLSI Design, Automation and Test 2016;1–4.
[15] Nguyen HH, Nguyen HN, Lee JS, Lee SG. A binary-weighted switching and reconfiguration-based programmable gain amplifier. IEEE Trans Circuits Syst. II, Express Briefs 2009;56(9):699–703.
[16] Tsou SC, Li CF, Huang PC. A low-power CMOS, linear-in-decibel variable gain amplifier with programmable bandwidth and stable group delay. IEEE Trans Circuits Syst II, Express Briefs 2006;53(12):1436–40.
[17] Kang SY, Ryu ST, Park CS. A precise decibel-linear programmable gain amplifier using a constant current-density function. IEEE Trans Microwave Theory and Tech 2012;60(9):2843–50.
[18] Elwan H, El Adawi A, Ismail M, Olsson HK, Soliman A. Digitally controlled dB-linear CMOS variable gain amplifier. Electronics Lett. 1999;35(20):1725–7.
[19] Angkeaw K, Prommee P. Two digitally programmable gain amplifiers based on current conveyors. Analog Int Cir Sig Proc 2011;67(2):253–60.
[20] Mahmoud SA. New fully differential CMOS second generation current conveyor. ETRI J 2006;28(4):495–501.
[21] Chen C-C, Lu NK, Zeng YZ. Low gain error, linear-in-dB variable gain amplifier with programmable gain range and gain steps. Int J Electron Commun (AEU)

2010;64:1203–6.
[22] Cheng X, Zhang L, Deng X. High-dynamic-range programmable gain amplifier with linear-in-dB and DAC gain control. Analog Integrated Circuits Signal Process 2018;94(1):83–96.
[23] Pourashraf S, Ramirez-Angulo J, Lopez-Martin AJ, Carvajal RG, Díaz-Sánchez A. ± 0.18-V supply voltage gate-driven PGA with 0.7-Hz to 2-kHz constant bandwidth and 0.15-μW power dissipation. Int J Circuit Theory Appl 2018;46(2):272–9.
[24] Li YT, Liu ZR, Wu YH, Chi BY. A wideband and high linearity Programmable Gain Amplifier for 60GHz receiver in 65nm CMOS. In: 13th IEEE international conference on solid-state and integrated circuit technology (ICSICT) IEEE, 2016 Oct 25; 1549–1551.
[25] Severo L, Van Noije W. 0.36 V PGA combining single-stage OTA and input negative transconductor for low energy RF receivers. Electronics Lett 2018;54(5):319–20.
[26] Zhang H, Li X, Chen Y, Cheng J. A switched-capacitor programmable-gain amplifier for high-definition video analog front-ends. In: 11th International conference on solid-state and integrated circuit technology (ICSICT) IEEE; 2012 Oct 29; 1–3.
[27] Shen X, Yan T, Lu Y, Zhou J. A 0.25 dB gain step high linear programmable gain amplifier. In: 9th international conference on ASIC (ASICON) IEEE; 2011 Oct 25. p. 1062–5.

International Journal of Engineering Technology Science and Research
IJETSR
www.ijetsr.com
ISSN 2394 – 3386
Volume 5, Issue 3
March 2018

Recent Developments in Corrole Synthesis

Anil Kumar
Department of Applied Chemistry,
Delhi Technological University

ABSTRACT

New synthetic methods for the synthesis of corroles have been discussed in details. Corrole are very robust molecule and are extensively used in metallocatalyst.

Keywords: Corrole, Synthesis, Recent

1. INTRODUCTION

Corrole is considered as a member of corrinoid family. Corrinoids are a group of compounds containing four reduced pyrrole rings joined into a macrocyclic ring by links betweena position, three of these links are formed by a one carbon unit and the other by a direct Cα-Cα bond.They include various vitamins B_{12} factors and related derivatives bases upon the skeleton of corrin $C_{19}H_{24}N_4$. The atoms are numbered and the rings are lettered as shown in figure 1.4. The numbering is the same that of porphyrin nucleus. Number 20 is omitted in corrole and corrin ring to retain comparability with the inner core nitrogen atoms numbered from 21 to 24. In the corrole structure, the imino nitrogen atom is located at position 24.The major structural differences of corrole to porphyrin are that the corrole have a somewhat more condensed N_4 coordination core (i.e. inner cavity size smaller), act as trianionic rather than dianionic ligands, and are of lower symmetry (C_{2v}). The synthesis of corrole is very tedious process and results in low yield. Since after the discovery of new methodologies developed by Gross et. al. in 1999, there is tremendous increase in the literature of corroles and their applications. Herein, we are giving brief outline of synthetic approaches adopted [1].

2. SYNTHETIC APPROACHES OF CORROLE

The interesting structure of corrole remained as a synthetic challenge. The synthesis of β-substituted corroles dates back to the historic efforts to prepare vitamin B_{12}. Such synthesis involved inconvenient stepwise procedures. Unlike the case with porphyrin, synthesis of meso-submitted corroles from readily available starting materials did not exist prior to the late 1990's. Until 1999, corrole synthesis was quite difficult. [2-5]. The following methods were used prior to 1999.

2.1: SYNTHESIS FROM BIPYRROLIC UNITS.

The condensation of dipyrromethene and a bipyrrole unit provides a route for the formation of corrole macrocycle through "2+2" approach. This method was reported by Johnson and coworkers. [6]. In this method, condensation occurs in presence of acid followed by reaction with cobalt(II) acetate and triphenylphosphine give rise to the corresponding corrole complex. It was found that cobalt is necessary for the tetramerization of ring as no corrole formation occur in the absence of cobalt ion which was studied by Vogel and coworkers. [7]

2.2 SYNTHESIS FROM A, C-BILADIENES

The most general method to synthesize corroles was cyclization of a, c-biladienes. This tetrapyrrolic precursor is generally obtained as a crystalline dihydrobromide salt by condensation of a dipyrromethene dicarboxylic acid with two equivalents of 2-formylpyrrole in the presence of hydrogen bromide. [8]. During the first synthesis of corrole, cyclization of a, c-biladienes occur photochemically in basic medium. Later, it was

investigated that basic conditions were always necessary to allow the cyclization of a, c-biladienes even in the absence of irradiation. [9]

2.3 SYNTHESIS FROM 2-SUBSTITUTED PYRROLE

In this method, substituted pyrrole i.e. 2-(a-hydroxy-benzyl)pyrrole was first reacted in acidic ethanol which was followed by the reaction with cobalt(II) acetate in the presence of triphenylphosphine to produce penta-coordinated cobalt complex. Only Cobalt ion has shown such template effect. Such hypothesis was given that the formation of corrole occurred by the ring contraction of porphyrinogen(intermediate) that was catalyzed by the cobalt ion. This reaction is analogous with the biochemical synthesis of the corrin of Vitamin $B_{12}$from uroporphyrinogen III. [10]

2.4 SYNTHESIS BY MACROCYCLIC RING CONTRACTION

This method involved the formation of corrole by an electrocyclic reaction involving loss of sulfur from a nonaromatic intermediate, the meso-thiaphlorin. This meso-thiaphlorin macrocycle was synthesized from "2+2" acidic condensation of a dipyrrylsulfide dialdehyde with dipyrromethene [11]. This ring contraction method has not been further developed because of the difficulty in the synthesis of sulfur containing starting materials. Before 1999, the synthesis of corrole remained quite a difficult task. But, in year 1999, paolesse [4-5] and Gross [1] who each reported one-pot, facile synthetic methodologies for the synthesis of corroles bearing three identical substituents at meso position from the reaction pyrrole with an aldehyde. These facile methods are:

2.5 SOLVENT FREE CONDENSATION

Gross [1] reported a new approach in which solvent free condensation occurs between pyrrole and aldehydes. The reaction condition consists of heating of mixer of pyrrole and aldehyde in equimolar ratio on a solid support like silica or alumina for few hours, followed by its oxidation by DDQ.

REFERENCES:

1. Gross, Z.; Galili, N.; Saltsman, I. *Angew. Chem. Intl. Ed*. **1999**, 38, 1427.
2. Woodward, R.; Hoffman, R. *Angew. Chem. Intl. Ed*. **1969**, 8, 71.
3. Rose, E.; Kossyani, A. *J. Am. Chem. Soc*. **1996**, 118, 1567.
4. Paolesse, R.; Boschi, T.; *Inog. Chim. Acta***1993**, 203, 107.
5. Licoccia, S.; Paolesse, R. *J. Org. Chem*. **1998**, 63, 3190.
6. Conlon, M.; Johnson, A. W. *J. Chem. Soc. Perkin Trans*. **1973**, 2281.
7. Vogel, E.; Broring, M.; *Angew. Chem. Intl. Ed*. **1995**, 34, 2511.
8. Johnson,A. W.; Kay, I. T. *J. Chem. Soc*, **1965**, 1620.
9. Dolphin, D. *J. Chem. Soc. B*, **1966**, 880-885.
10. Rasetti, V.; Pfaltz, A.; *PNAS, USA*, **1981**, 78, 16.
11. Johnson, A. W.; Kay, I. T. *Chem. Comm*., **1970**, 807.
12. Narayana, S. J.; Chandrashekhar, T. K.; *Org. Lett*. **1999**, 1, 587.
13. Cho, W. S.; Lee, C. H. *Tett. Lett*. **2000**, 41, 497.
14. Simkhovich, L.; Gross, Z. *Inorg. Chem*. **2002**, 41, 5433.

SentiMozart: Music Generation based on Emotions

Rishi Madhok[1,*], Shivali Goel[2,*] and Shweta Garg[1,*]
[1]*Department of Computer Science and Engineering, Delhi Technological University, New Delhi, India*
[2]*Department of Information Technology , Delhi Technological University, New Delhi, India*

Keywords: LSTM, Deep Learning, Music Generation, Emotion, Sentiment.

Abstract: Facial expressions are one of the best and the most intuitive way to determine a persons emotions. They most naturally express how a person is feeling currently. The aim of the proposed framework is to generate music corresponding to the emotion of the person predicted by our model. The proposed framework is divided into two models, the Image Classification Model and the Music Generation Model. The music would be generated by the latter model which is essentially a Doubly Stacked LSTM architecture. This is to be done after classification and identification of the facial expression into one of the seven major sentiment categories: Angry, Disgust, Fear, Happy, Sad, Surprise and Neutral, which would be done by using Convolutional Neural Networks (CNN). Finally, we evaluate the performance of our proposed framework using the emotional Mean Opinion Score (MOS) which is a popular evaluation metric for audio-visual data.

1 INTRODUCTION

It was only a few decades ago that Machine Learning was introduced. Since then the phenomenal progress in this field has opened up exciting opportunities for us to build intelligent computer programs that could discover, learn, predict and even improve itself given the data without the need of explicit programming. The advancements in this field have allowed us to train computer not only to mimic human behavior but also perform tasks that would have otherwise required considerable human effort.

In our paper we present two such problems. First, we try and capture the emotions of people from their images and categorize the sentiments into 7 major categories: Angry, Disgust, Fear, Happy, Sad, Surprise and Neutral using Convolutional Neural Network (CNN).

Second, we try to generate music based on these emotions.Music composition, given its level of complexity, abstractness and ingenuity is a challenging task and we aim to generate music that not necessarily approximates to the exact way people play music but one which is pleasant to hear and is appropriate according to the mood of the situation in which it is being played.

A challenge accompanied with music generation is that music is a flowing melody in which one note can be followed by several different notes, however, when humans compose music they often impose a set of restrictions on notes and can choose exactly one precise note that must follow a given sequence of notes. One music pattern cant repeat itself forever, apart from adding a local perspective to our music generation algorithm, global view must also be considered. This shall ensure correct departure from a pattern at the correct instant of time. Magentas RL Tuner (Jaques et al., 2016) is an advancement in this direction however more concentrated effort is required for overcoming such difficulties while developing a near-to-ideal music generation algorithm based on rule discovery. Music experts and machine learning enthusiasts must work hand in gloves with each other so as to create complete orchestral compositions, orchestrating one instrument at a time. Another challenge is the development of flexible programs. Extensive training with large number of iterations and epochs tend to produce more accurate results but there is a need of periodically updating and adding additional information to our program so as to get a better understanding of music composition and artificial intelligence.

So far, fusion of analyzing sentiments from images and generation of music on the basis of that hasn't been explored much. Previous work done in

*These authors contributed equally to this work.

Madhok, R., Goel, S. and Garg, S.
SentiMozart: Music Generation based on Emotions.
DOI: 10.5220/0006597705010506
In *Proceedings of the 10th International Conference on Agents and Artificial Intelligence (ICAART 2018) - Volume 2*, pages 501-506
ISBN: 978-989-758-275-2
Copyright © 2018 by SCITEPRESS – Science and Technology Publications, Lda. All rights reserved

this field includes (Sergio et al., 2015) in which the author analyses the image using the HSV color space model. The author converts the RGB format image to HSV format and then scans the image to find the dominant colors in certain patches of the image. This results in the generation of a color map which is then directly mapped to musical notes which were calculated using the harmonics of a piano. This notes map is then used to generate music. The problem with this approach is that it does not work for a dataset in which every image is a face of a person. The most dominant color every time, would be similar in all the images namely the skin color hence the same set of notes would be generated.

Our model can be incorporated as a feature in various social networking applications such as Snapchat, Instagram etc. where when a person is uploading his/her Snapchat story, depending on the image obtained from the front camera of the electronic device, a sentiment analysis of the image can be done which can then be used to generate music for the user which the user can add to his/her Snapchat story. For example, we would generate a party type peppy melody for a happy expression and a soft romantic melody for a sad expression.

In this paper, we discuss the previous work done in the field of music generation in the next section Section II. Section III describes the proposed model and the details of the training of the model, which is then followed by the analysing of the results obtained in Section IV. We use the Mean Opinion Score (MOS) approach to showcase our results. We finally conclude our paper in Section V.

2 RELATED WORK

2.1 Music Generation

Since last many years a lot of work has been done in generating music. (Graves, 2013) uses the Recurrent Neural Network (RNN) architecture, Long Short Term Memory (LSTM) for generating sequences such as handwriting for a given text. (Chung et al., 2014) extend this concept to compare another type of RNN which is Gated Recurrent Unit (GRU) with LSTM for music and speech signal modeling. Inspired by this approach our model uses LSTM architecture to generate music. (Boulanger-Lewandowski et al., 2012) introduce a probabilistic approach, a RNN-RBM (Recurrent Neural Network Restricted Boltzmann Machine) model which is used to discover temporal dependencies in high space model. The authors introduce the RBM model so that representation of the complicated distribution for each time step in the sequence is easily possible where parameters at a current time step depends on the previous parameters. Currently, the Google Brain Team is working on its project Magenta which would generate compelling music in the style of a particular artist. While magenta also generates music, our model does it based on emotions (facial sentiments). Magentas code has been released as open source as they wish to build a community of musicians, coders and machine learning enthusiasts. (Jaques et al., 2016).

2.2 Music Playlist Generation

Our work shares the high-level goal of playing music based on emotions with (Zaware et al., 2014) however while we aim to generate music, they present a playlist of songs to a user based on the users current mood. They converted images into a binary format and then fed into a Haar classifier for facial detection. Important features were then extracted such as eyes, lips etc. to classify the emotion of the person. (Hirve et al., 2016) use the same thought for generating music as done by (Zaware et al., 2014), they use a Viola-Jones algorithm for face detection and Support Vector Machine (SVM) for emotion detection. While the work by these authors provide music based on a persons emotion, they present a list of songs as a playlist which is a recommender system rather than generating new music.

2.3 Mapping Colors to Music

Similar work also includes the research project by Gregory Granito (Gregory, 2014) that links colors used in the image with music. The author uses a method to calculate the average color value of the image, searches for areas of high concentration of a color and of major changes in hue, this is then used to associate certain colors to motions such as the Yellow color invokes a cheerful emotion in a person. (Sergio et al., 2015) analyses image using the HSV color space model. The author scans the image and generates a color map for the image which is then used to obtain the notes map and music is subsequently generated. While this direct mapping approach is very popular, it has a shortcoming we cannot use this for music generation based on peoples facial expressions because each image in the dataset focuses only on the face of a person and hence would generate the same dominant color for every image.

2.4 Speech Analysis and Hand Gestures to Generate Music

Apart from using images, music has previously been generated by many other ways such as after doing the sentiment analysis of speech of a person or by making use of hand motions. (Rubin and Agrawala, 2014) is one such example in which emotion labels on the users speech are gathered using methods such as hand-labeling, crowd sourcing etc. which is then used to generate emotionally relevant music. A novel application for generation of music was introduced by (Ip et al., 2005) in their work in which they make use of motion-sensing gloves to allow people even non-musicians to generate melodies using hand gestures and motions.

3 PROPOSED FRAMEWORK

3.1 Research Methodology

The proposed framework consists of two models, the first is the Image Classification model and the second is the Music Generation model. The former model classifies the image of the person into one of the seven sentiment class i.e. Angry, Disgust, Fear, Happy, Sad, Surprise and Neutral and the latter model then generates music corresponding to the identified sentiment class.

In the Image Classification model, a Convolutional Neural Network (CNN) is used. The input to the CNN is a 48X48 grayscale image which is then passed onto the first Convolutional layer consisting of 64 filters of size 3X3 each. The output of this layer is then passed onto the second convolutional layer consisting of 128 filters of size 3X3 each. After these two layers, the feature maps are down sampled using a Max Pooling Layer having a window size of 2X2. These set of layers are repeated again with the same specification of layers and filter sizes as shown in Figure 1. Following the second Max Pooling layer, the output is now passed onto the Fully Connected Layer or the Dense Layer having 7 nodes, one for each sentiment class. The output of this Dense layers goes through a Softmax layer at the end, which then finally predicts the sentiment of the image. More details about this model are explained in the section below.

In the Music Generation Model, a Doubly Stacked LSTM Architecture is used as shown in Figure 1. A doubly stacked LSTM architecture is essentially an architecture in which one LSTM layer is stacked over the other LSTM layer and outputs from the first layer is passed onto the second layer. After the Image Classification task, a vector of length 7 is obtained in one hot encoded form, whose each value corresponding to respective sentiment class. This vector is then converted to a new vector of length 3 for Happy, Sad and Neutral classes respectively to choose the dataset for the Music Generation Model as shown above in the Figure 1 Certain classes are merged for the Music Generation Task such as Fear, Disgust and Angry were merged into the Sad Sentiment Class. Also, the Surprise sentiment class was merged into the Happy sentiment class. The dataset contains 200 MIDI files for each sentiment class i.e. Happy, Sad and Neutral. As there was no such dataset of MIDI files available for emotions, these MIDI files were labeled by a group of 15 people. This is explained diagrammatically in Figure 1 and more details about this model are explained in the section below.

3.2 Image Classification Model

The Convolutional Neural Network (CNN) model was implemented for the classification of images into its respective sentiment class. The dataset was split into 80% of the images used for training, and remaining 20% used for cross validation. The model used batch training with a batch size of 256, in which the images were processed in batches of the given size. Consequently, all the training samples were processed similarly through the learning algorithm which comprised one forward pass. After finishing one forward pass, a loss function, here categorical cross entropy loss function, was computed which was minimized by back propagating through all the images and updating the weight matrices using the Adaptive Gradient Descent Optimizer(Adagrad), this comprised one backward pass. One forward pass and one backward pass comprise a single epoch. There were a total of 100 epochs with 1 epoch taking an average of 13 minutes to run on a standard 2.5 GHz i5 processor. The CNN Model had 6 hidden layers, with 4 convolutional layers and 2 max-pool layers which were alternated and 1 fully connected layer with 7 neurons each for the respective sentiment class. Two dropout layers were also added which helped to prevent overfitting.

3.3 Music Generation Model

A doubly stacked LSTM model is trained for the Music Generation Model. The input given to the LSTM is the one Hot Representation of the MIDI files from a particular dataset belonging to a sentiment class. The one hot representation of a MIDI file has

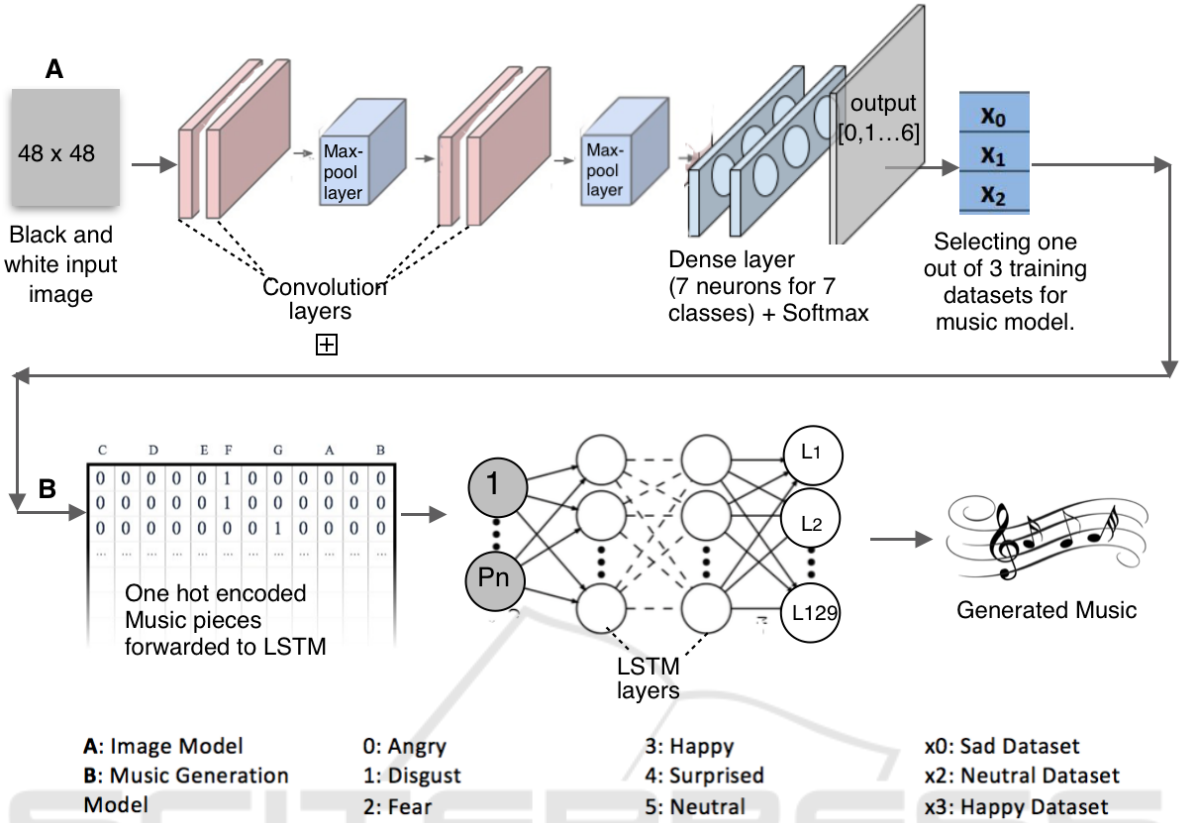

Figure 1: SentiMozart Model.

a shape as (sequence_length, Notes_in_MIDI) where sequence_length is the number of notes in the MIDI file and Notes_in_MIDI is 129 (128 for each MIDI Note number + 1 for EOS). Thus, the overall shape of the dataset which is given as input to the LSTM is (Num_files, Max_Sequence_Length,Notes_in_MIDI) where Num_files is 200 MIDI files in the dataset, Max_Sequence_Length is the maximum sequence length of one of the files in the dataset and Notes_in_MIDI is 129 as explained earlier.

The input is then passed through the first LSTM Layer which outputs sequences, which are then passed to the second LSTM Layer. The Second LSTM layer then outputs a vector which is passed finally through the Fully Connected Layer having 129 nodes. After each layer except for the last layer,there is a Dropout Layer which prevents overfitting of the model. Categorical cross entropy is used as the Loss function of the model and Adaptive Moment Estimation (Adam), a variant of Gradient Descent is used as the Optimizer of the model. The model is run for 2000 epochs following which a MIDI file is generated for the particular sentiment.

3.4 Why MIDI?

The proposed model uses MIDI (Musical Instrument Digital Interface) files to generate music. MIDI format is one of the best options present today to generate new music as the file contains only synthesizer instructions hence the file size is hundreds of times smaller than the WAV format (Waveform Audio Format) which contains digitized sound and hence has a very large size (hundreds of megabytes).

One advantage of WAV format over MIDI is that the WAV format has a better quality of sound because sound depends on the sampling rate and hence will be same for different computers. This is not the case for MIDI files, and hence the quality of sound is different for different computers. Hence we have a trade-off.

4 RESULTS

4.1 Dataset Used

Dataset used for image sentiment classification was the collection of 35,887 grayscale images of 48X48 pixel dimensions prepared by Pierre-Luc Carrier and

Aaron Courville for their project (Goodfellow et al., 2013).

MIDI files corresponding to all 7 categories of facial expressions could not be found. Hence, the following sentiment classes - sad, fear, angry and disgust were merged into the sad sentiment class, happy and surprise were merged into the happy sentiment class and left neutral class as it is. Exploring better evaluation metrics for judging emotion of generated music remains a challenge. Self-prepared dataset of 200 midi files for each sentiment class - Happy, Sad and Neutral was used for the training of music generation model. The music files were mostly Piano music MIDI files and annotated manually by a group of 15 people. The MIDI files dataset is available by request from the authors.

4.2 Result of Image Classification Model

The accuracy obtained in the proposed model was 75.01%. Figure 2 shows the gradual decrease in the loss number obtained for each epoch in the Image Sentiment Classification model till it finally tends to converge after 100 epochs.

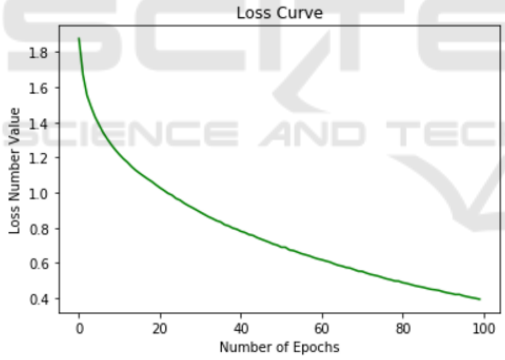

Figure 2: Loss Curve for CNN Model.

4.3 Evaluation Model

To evaluate the quality of our model we use emotional Mean Opinion Score (MOS) which is a common measure for quality evaluation of audio-visual data. Since we classify the songs based on three emotional categories, we choose a rating scale of 0 to 10, where 0 represents sad emotion, 5 represents neutral and 10 represents happy emotion. The rating scale is shown in Figure 3.

30 people gave scores based on the rating scale for 30 randomly chosen images (10 of each class) and their corresponding music generated. The average of the scores was taken and plotted on the graph shown in Figure 4. The images and music was presented before the participant in no particular order so as to avoid any bias between the type of image shown and the likeliness of music belonging to the same category.

Correlation between the two curves was calculated to be 0.93. It is calculated according to the formula given below. As expected this must be high as the facial expression and the music generated must express the same sentiment. During the experiment we observed extreme scoring for facial data but conservative scoring for scoring generated music. Other important observation was for both neutral images and songs most participants tend to assign a perfectly balanced score 5, while deviated the scores conservatively for sad and happy emotion.

Where x is the Image MOS, y is the Music MOS and r determines the correlation. The value of r is always between 1 and 1. $\bar{x}$ and $\bar{y}$ are the means of the x and y values respectively.

When we used upbeat and peppy songs in our training set for the happy emotion, an output file with a similar pattern of notes was generated. Also, when slow and soothing melodies were used in the training set for a sad emotion, consequently, a melody having similar patterns was generated. The model generates the type of songs it is supposed to, that is, depending upon the emotion detected, for instance sad ones for a sad expression and happy ones for a happy expression.

Figure 3: MOS Scale.

5 CONCLUSION

In this paper, the SentiMozart framework is presented which generates relevant music based upon the facial sentiments of a person in the image. It is able to do so by first classifying the facial expression of the person in the image into one of the seven sentiment classes by using the Image Classification Model and then it generates relevant music based upon the sentiment of the person using the Music Generation Model. Finally, we evaluated the performance of our proposed framework using the emotional Mean Opinion Score (MOS) which is a popular evaluation metric for audio-visual data. The high correlation value and the user analysis on the generated music files shows

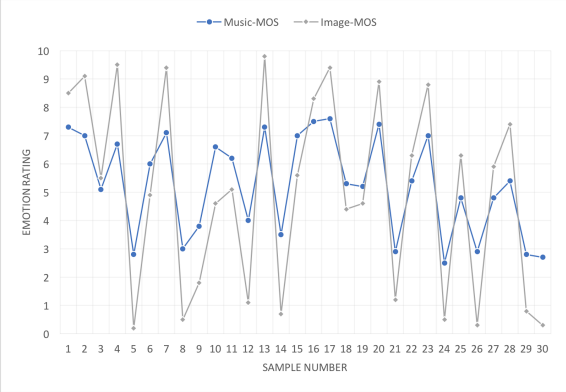

Figure 4: MOS Graph.

the self-sufficiency of the number of training samples in the Music Generation Model.

Music is not just art and creativity but is also based on a strong mathematical background. So, often computer creativity is doubted in its ability to produce fresh and creative works. New notions of computer creativity can evolve by amalgamation of different techniques, use of high performing systems and bio inspiration.

Also, computer scientists and music composers must work in synergy together. Making music composers able enough to use the program by having a basic understanding of the program and learning various commands would enable them to give constructive feedback and radically change the process of music composition, and consequently the way market for music operates. Market opportunities would include incorporating such features in instant multimedia messaging applications such as Snapchat, Instagram and any other application which deals with images.

ACKNOWLEDGEMENTS

We whole heartedly thank our mentor Dr. Rajni Jindal, Head of Department, Computer Science Department at Delhi Technological University for guiding us through this project.

REFERENCES

Boulanger-Lewandowski, N., Bengio, Y., and Vincent, P. (2012). Modeling Temporal Dependencies in High-Dimensional Sequences: Application to Polyphonic Music Generation and Transcription. *ArXiv e-prints*.

Chung, J., Gulcehre, C., Cho, K., and Bengio, Y. (2014). Empirical Evaluation of Gated Recurrent Neural Networks on Sequence Modeling. *ArXiv e-prints*.

Goodfellow, I. J., Erhan, D., Carrier, P. L., Courville, A., Mirza, M., Hamner, B., Cukierski, W., Tang, Y., Thaler, D., Lee, D.-H., Zhou, Y., Ramaiah, C., Feng, F., Li, R., Wang, X., Athanasakis, D., Shawe-Taylor, J., Milakov, M., Park, J., Ionescu, R., Popescu, M., Grozea, C., Bergstra, J., Xie, J., Romaszko, L., Xu, B., Chuang, Z., and Bengio, Y. (2013). Challenges in Representation Learning: A report on three machine learning contests. *ArXiv e-prints*.

Graves, A. (2013). Generating Sequences With Recurrent Neural Networks. *ArXiv e-prints*.

Gregory, G. (2014). Generating music through image analysis.

Hirve, R., Jagdale, S., Banthia, R., Kalal, H., and Pathak, K. (2016). Emoplayer: An emotion based music player. *Imperial Journal of Interdisciplinary Research*, 2(5).

Ip, H. H. S., Law, K. C. K., and Kwong, B. (2005). Cyber composer: Hand gesture-driven intelligent music composition and generation. In *11th International Multimedia Modelling Conference*, pages 46–52.

Jaques, N., Gu, S., Bahdanau, D., Hernández-Lobato, J. M., Turner, R. E., and Eck, D. (2016). Sequence Tutor: Conservative Fine-Tuning of Sequence Generation Models with KL-control. *ArXiv e-prints*.

Rubin, S. and Agrawala, M. (2014). Generating emotionally relevant musical scores for audio stories. In *Proceedings of the 27th Annual ACM Symposium on User Interface Software and Technology*, UIST '14, pages 439–448, New York, NY, USA. ACM.

Sergio, G. C., Mallipeddi, R., Kang, J.-S., and Lee, M. (2015). Generating music from an image. In *Proceedings of the 3rd International Conference on Human-Agent Interaction*, HAI '15, pages 213–216, New York, NY, USA. ACM.

Zaware, N., Rajgure, T., Bhadang, A., and Sapkal, D. (2014). Emotion based music player. *International Journal of Innovative Research and Development*, 0(0).

Accepted Manuscript

Title: Spectroscopic studies of Dy^{3+} doped Borate Glasses for Cool White Light Generation

Authors: Sumandeep Kaur, Amit K. Vishwakarma, Nisha Deopa, Aman Prasad, M. Jayasimhadri, A.S. Rao

PII: S0025-5408(18)30291-5
DOI: https://doi.org/10.1016/j.materresbull.2018.04.002
Reference: MRB 9940

To appear in: *MRB*

Received date: 27-1-2018
Revised date: 18-3-2018
Accepted date: 1-4-2018

Please cite this article as: Kaur S, Vishwakarma AK, Deopa N, Prasad A, Jayasimhadri M, Rao AS, Spectroscopic studies of Dy^{3+} doped Borate Glasses for Cool White Light Generation, *Materials Research Bulletin* (2010), https://doi.org/10.1016/j.materresbull.2018.04.002

This is a PDF file of an unedited manuscript that has been accepted for publication. As a service to our customers we are providing this early version of the manuscript. The manuscript will undergo copyediting, typesetting, and review of the resulting proof before it is published in its final form. Please note that during the production process errors may be discovered which could affect the content, and all legal disclaimers that apply to the journal pertain.

ACCEPTED MANUSCRIPT

Spectroscopic studies of Dy^{3+} doped Borate Glasses for Cool White Light Generation

Sumandeep Kaur, Amit K.Vishwakarma, Nisha Deopa, Aman Prasad, M. Jayasimhadri, A.S. Rao*

Department of Applied Physics, Delhi Technological University, Bawana Road,
New Delhi-110 042, India.

*_Corresponding author:_ Email: drsrallam@gmail.com, Tel: +91 8586039007, Fax: +91 01127871023.

Graphical abstract

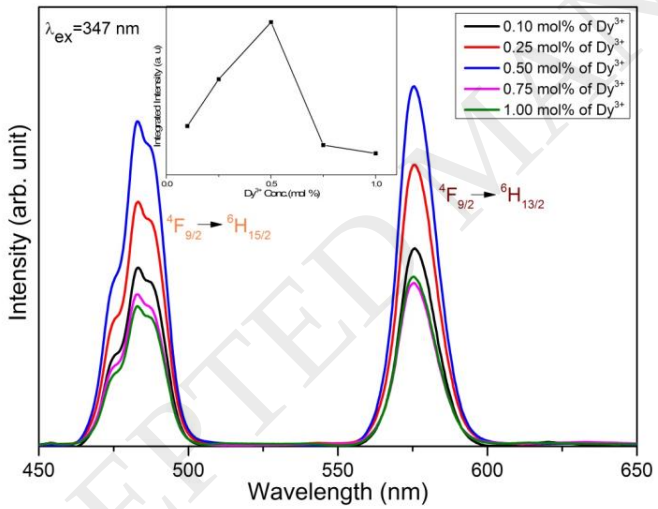

Emission spectra of Dy^{3+} ions doped BAZN glasses

ACCEPTED MANUSCRIPT

Highlights

- BAZN glasses with Dy^{3+} ions were prepared using melt quench technique.
- Under n-UV excitation the BAZN glasses show white light emission.
- Energy transfer through cross-relaxation leads to concentration quenching.
- Calculated CIE coordinates are close to the commercial w-LED.
- 0.5 mol% of Dy^{3+} in these glasses are apt for cool white light generation.
- Y/B intensity ratio for all the BAZN glasses are close to one.

Abstract

The Dy^{3+} ions doped Na_2O-ZnO-Al_2O_3-B_2O_3 (BAZN) glasses with variable doping concentrations were synthesized by melt-quenching technique. The XRD pattern reveals amorphous nature of the as-synthesized glass. The FT-IR spectrum reveals various stretching and bending vibration of aluminates, borate and some other groups. The emission spectra exhibit two intense bands at around 482 nm (blue) and 575 nm (yellow) corresponds to the $^4F_{9/2} \rightarrow {}^6H_{15/2}$ and $F_{9/2} \rightarrow {}^6H_{13/2}$ transitions respectively. The CIE chromaticity coordinates of the as-synthesized glasses are lying in white region and in proximity to the coordinates for white light specified by National Television Standard Committee and commercial phosphor converted white light emitting devices. The decay profile of BAZN glasses showed bi-exponential behavior due to the energy transfer mechanism from excited donor ion to unexcited acceptor ion. The above-mentioned studies show potential of the as-synthesized Dy^{3+} doped BAZN glasses in solid state lighting.

1. Introduction

In quite recent years, awareness about climate change, environmental problems and harmful impact of using fossil fuels as a source of energy on environmental issues has been increased to an extent where people are now seeking some alternatives for fossil fuels, which are

ACCEPTED MANUSCRIPT

less hazardous to environment. Lighting consumes major fraction of energy; therefore, research is highly targeting on reducing consumption of energy for lighting purposes. Quite recently, white Light Emitting Diodes (w-LEDs) have replaced the conventional incandescent and fluorescent lamps to reduce the usage of fossil fuels and also to meet global power requirements by producing more efficient light. The phosphor based w-LEDs have attracted great attention due to its extraordinary luminescent efficiency, low power consumption, small volume, long persistence and environment friendliness [1-4]. These phosphor-based w-LEDs exhibit high color rendering index, but these w-LEDs have disadvantage that phosphor material used to produce it requires a coating of organic resin having poor heat resistance which reduces the luminous efficacy [4-7]. Therefore, it is needed to develop a phosphor free w-LED that can emit white light with improved luminous efficacy and color rendering index with stable color temperature and cost effective in comparison to the conventional w-LEDs. Now-a-days, glasses are found to be a suitable alternative for resin based phosphors. The rare earth (RE) doped glasses have several advantages over RE doped phosphors such as high brightness, low power consumption, possibility of wavelength tuning, high doping proficiency, shape and size control, no aging effects and free of organic resin [8-10]. More over glasses doped with RE ions are receiving great attention for its wide range of applications such as solid-state lighting, photovoltaic cells, FED applications, X-ray sensors, optical temperature sensors, optical amplifiers, UV-visible converters, plasma display devices, bio imaging and bio sensing, w-LEDs [11-20].

The optical and fluorescence properties of RE ions depend upon the local environment and phonon energies of the host glass system [21]. Borate glasses are well studied due to its ease of preparation, good strength, high transparency, and excellent isotropic nature. Borate glasses are generally known for their high thermal stability, low melting point, different coordination

ACCEPTED MANUSCRIPT

numbers and good solubility of RE ions, but their phonon energy is quite high (1300cm^{-1}) which makes them unsuitable for lighting purposes [22-24]. In general, heavy metal oxides having low phonon energy are mixed with borates to reduce the redundant phonon energy of borate glasses and make it more suitable to be used in the development of optoelectronic devices, solar energy converters, gas sensors and UV lasers [25-27]. Based on the concentration of heavy metal oxides in the glass, it can act as a glass former as well as glass modifier. ZnO have attracted many researchers because of its optical, electrical and magnetic properties along with its non-toxic and non-hygroscopic nature and having wide direct band gap, large exciting binding energy and intrinsic emitting property [28]. It also improves chemical durability, stability and RE ion solubility in the glass. By adding Al_2O_3 in oxide glasses, devitrification of glass is foreclosed, the transition temperature of glass decreases, and the coefficient of thermal expansion increases [29]. Being a network intermediate, reshuffling of glass network occurs, Al-O bond formation of AlO_4 tetrahedral unit takes place, and B-O-Al structure builds which increases the rigidity with the addition of Na_2O (responsible for stability during melting) in glasses [30].

Dy^{3+} is one of the best RE ions suitable for preparation of luminescent materials, because it can be easily excited by n-UV/UV excitation source as it exhibits several 4f-4f electronic transitions. The Dy^{3+} ions have two characteristic intense bands in visible region that correspond to yellow and blue emission. To obtain white light from Dy^{3+} doped glasses with a suitable yellow to blue (Y/B) intensity ratio, optimization of the local environment is required, and that can be obtained by varying the composition of the glass or by changing the dopant (Dy^{3+}) ion concentration in the host matrix [228, 31-32].

In the present work, BAZN (B_2O_3-Al_2O_3-ZnO-Na_2O) glasses with varying concentration of Dy^{3+}ions were prepared by melt quenching technique to study the luminescent properties for the suitability of these glasses for UV/n- UV based w-LEDs.

ACCEPTED MANUSCRIPT

2. Experimental procedure and characterizations

Dy^{3+} doped NaZnAlB glasses were prepared by using melt quenching technique with a molar composition of $30Na_2O$-$10ZnO$-$(10-x)Al_2O_3$-$50B_2O_3$-xDy_2O_3 (where x = 0.1, 0.25, 0.50, 0.75, and 1.0 mol%). For convenience, these glasses are designated as D010, D025, D050, D075, and D100 based on the Dy^{3+} content from 0.1 to 1.0 mol% respectively. The required amounts of AR grade chemicals were taken and mixed homogeneously in an agate mortar for an hour. The thoroughly mixed and grounded powdered chemicals were taken into a silica crucible and heated at 1100°C in an electric furnace for one hour. The melt was then poured onto a thick preheated brass plate and then pressed quickly by a similar plate to obtain transparent glasses. The colorless glass samples were subsequently annealed at 375 °C to alleviate internal stresses and obtain thermal and structural stability of the glass samples.

The XRD measurement for an un doped glass sample was recorded using high resolution X-ray Bruker D8 Advance Diffractometer having nickel filtered Cu-Kα radiation (=1.5406Å) in the 2θ angle range $10° \leq \theta \leq 80°$. The FT-IR spectral measurements were recorded for un-doped glass sample by using Perkin Elmer's Frontier Spectrometer. The PL spectral recordings were recorded by using a SHIMADZU RF-5301 PC-Spectrofluorophotometer with a Xenon arc lamp as the source of UV radiation. PL decay spectral measurements have been performed using an Edinburgh FLSP 900 spectrofluorophotometer with spectral resolution of 0.1 nm using Xenon flash lamp as an excitation source. All characterizations have been conducted at room temperature.

3. Results and discussion

3.1. Structural Analysis

ACCEPTED MANUSCRIPT

The XRD spectrum recorded for an un-doped glass in the spectral range $10° \leq \theta \leq 80°$ is depicted in Fig.1. It shows a broad hump with a wide band at the lower angle of diffraction (20°-38°) which reveals the characteristic long-range disorder structure and confirms amorphous nature of the glass.

3.2. FT-IR Spectroscopy

The FT-IR spectrum for an optimized glass sample (0.5mol% of Dy^{3+} ions) has been recorded in the range 400-3600 cm^{-1} and is shown in the Fig. 2. As shown in Fig. 2, the FT-IR spectrum has shoulders located nearby 464.0, 664.0, 717.0, 989.3, 1384.1, 2348.4, and 3448.3 cm^{-1}. The shoulder around 464.0 cm^{-1} may be attributed to the bending vibration of Al_2O_3 [33] and may also be attributed to the Zn-O stretching vibration of ZnO_4 unit [34]. The shoulder around 664.0 cm^{-1} may be assigned to the combined bending vibration of bridging oxygen atoms between boron atoms and AlO_6 groups [35]. The shoulder around 717.0 cm^{-1} may be designated to the bending of B-O-B linkage and vibration of bridging oxygen atoms [36]. The shoulder around 989.3 cm^{-1} may represent the vibration of diborate group and asymmetric stretching vibration of tetrahedral BO_4 unit [35]. The shoulder around 1384.1 cm^{-1} may correspond to asymmetric stretching vibration of B-O and $B\text{-}O^-$ bond in trigonal BO_3 units. The shoulder around 2348.4 cm^{-1} may represent – O-H group. The shoulder at 3448.3 cm^{-1} may be attributed to the stretching peak of hydroxyl group [37]. This IR band has low intensity which indicates the low OH content in the glass sample. The low OH content signifies lesser non- radiative losses and better quantum efficiency for the RE doped luminescent materials. To estimate the OH content we have used the equation $\alpha_{OH} = \ln(T_0/T_D)/l$ where T_0 is the highest transmission, T_D is the transmission at 3000 cm^{-1} and l is the thickness of the glass sample. The OH content for the optimized glass is found to be 58.46 ppm which is lesser than LHG-8L (128.00 ppm) [38],

ACCEPTED MANUSCRIPT

LBTAF (123.00 ppm) [39], and ZnAlBIB (65.48 ppm) glasses [40], making it more suitable for efficient lasers with reduced non-radiative losses.

3.3. Photoluminescence properties

To record the emission spectra of Dy^{3+} ions doped BAZN glasses, we need to know about the excitation wavelength. The excitation spectrum of the Dy^{3+} doped BAZN glass recorded by monitoring the emission wavelength at 575 nm is shown in Fig. 3. The spectrum consists of six bands located at around 293, 322, 335, 347, 362, and 385 nm representing the transitions from ground states to multiple excited states i.e., $^6H_{15/2}\rightarrow {}^4H_{11/2}$, $^4K_{13/2}$, $^4L_{13/2}$, $^6H_{15/2}\rightarrow {}^4M_{17/2}$, $^6P_{3/2}$, $^6H_{15/2}\rightarrow {}^4I_{9/2}$, $^6H_{15/2}\rightarrow {}^4M_{15/2}$, $^6P_{7/2}$, $^6H_{15/2}\rightarrow {}^4I_{11/2}$, $^6P_{5/2}$, and $^6H_{15/2}\rightarrow {}^4I_{13/2}$, $^4F_{7/2}$ respectively, which suggests UV or n-UV excitation source can be effectively used to excite the Dy^{3+} ions doped BAZN glasses [41-42]. From Fig. 3, it could be visualized that the peak corresponding to 347 nm is highly intense and therefore, it has been used as an excitation wavelength to record the emission spectra. Fig. 4 represents the emission spectra recorded at the room temperature under 347 nm excitation. The emission spectra consist of two bands located at around 482 nm and 575 nm which are assigned to the transitions $^4F_{9/2}\rightarrow {}^6H_{15/2}$ and $^4F_{9/2}\rightarrow {}^6H_{13/2}$ respectively [43]. The position of the bands and their shape do not show considerable variations for varying Dy^{3+} concentration because of the shielded nature of 4f electrons by the 5s and 5p outer electrons. The two spectral transitions $^4F_{9/2}\rightarrow {}^6H_{15/2}$ (blue) and $^4F_{9/2}\rightarrow {}^4H_{13/2}$ (yellow) corresponds to magnetic dipole (MD) transition and forced electric dipole (ED) transition respectively. The $^4F_{9/2}\rightarrow {}^6H_{15/2}$ transition is not much sensitive to crystal field strength of host matrix whereas the $^4F_{9/2}\rightarrow {}^4H_{13/2}$ transition is hypersensitive to the surroundings obeying the selection rule $\Delta L=2$, $\Delta S=0$, $\Delta J=2$. The emission intensity of hypersensitive transition is highly influenced by the host matrix [45]. Relatively higher spectral intensity of $^4F_{9/2}\rightarrow {}^4H_{13/2}$ transition when compared to the $^4F_{9/2}\rightarrow {}^6H_{15/2}$ transition is due to the location of Dy^{3+} ions at low symmetry sites without inversion centers as

ACCEPTED MANUSCRIPT

depicted in Fig. 4. Higher the intensity of hypersensitive transition, higher is the asymmetry which implies greater interaction between RE ion and host matrix. The broadening of the bands is due to large number of stark levels for $^4F_{9/2,}$ $^6H_{15/2}$ and $^4H_{13/2}$ levels [46].

The spectral intensities of the bands corresponding to $^4F_{9/2}\rightarrow{}^6H_{15/2}$ and $^4F_{9/2}\rightarrow{}^4H_{13/2}$ transition is enhanced by increasing the dopant concentration up to 0.5 mol% and then reduces with further increase in the dopant ion concentration. The intensity variation with concentration of dopant is shown in the inset of Fig. 4. The decrease in the spectral intensity of the bands beyond 0.5mol% of Dy^{3+} ion concentration is due to the well-known phenomenon of concentration quenching; which arises due to the energy migration among Dy^{3+}-Dy^{3+} ions. This energy migration takes place due to the resonant energy transfer between $^4F_{9/2}\rightarrow{}^6H_{15/2}$ energy levels or via cross relaxation and dispel energy through phonons [43]. The energy transfer mechanism responsible for the phenomenon of concentration quenching can be studied by employing Dexter theory [44]. The variation of emission intensity with doping concentration can be expressed as:

$$log\frac{I}{x} = logf - \frac{slog(x)}{d}; \quad where\ (K' = logk - log\beta)$$

where I is the emission intensity, x is the doping concentration, d (= 3) is the dimension of compound, f is constant and independent of doping concentration. The value of s define the type of interaction among the nearest neighbor ions, s = 6, 8, and 10 for dipole-dipole, dipole-quadrupole, and quadrupole-quadrupole interaction respectively. A plot of log(I/x) vs log(x) has been plotted with a straight-line slope (s/d) as shown in Fig. 5. the calculated value of 's' from the slope of the graph is 4.83 close to 6. Hence, it can be concluded that dipole-dipole interaction among Dy^{3+} ions is responsible for concentration quenching mechanism in Dy^{3+} doped BAZN glasses. The calculated yellow to blue (Y/B) luminescence intensity ratio for varying concentration of Dy^{3+} ion is calculated and tabulated in Table. 1. The Y/B intensity ratio lies in

ACCEPTED MANUSCRIPT

close propinquity to 1, the higher value of Y/B ratio confirms the high covalent nature between Dy^{3+} and O^{2-} ions. Insignificant variation in Y/B intensity ratio signifies its independency on Dy^{3+} ion concentration instead strong dependency on the host matrix [45]. The energy level diagram of Dy^{3+} doped BAZN glass is represented in Fig. 6. The excitation energies are greater than the energy of $^4F_{9/2}$ level and therefore the excess energy lost through non-radiative channels, thereby enhancing the population of $^4F_{9/2}$ level from where the radiative emission takes place. Various radiative and non-radiative transitions have been shown in Fig. 6.

3.4. Colorimetric properties

The CIE coordinates are used to characterize the color and location of all the color coordinates produces the perimeter of CIE chromaticity diagram. The CIE coordinates of BAZN glasses for different concentration of Dy^{3+} ion are calculated from emission spectra and tabulated in Table. 1. The CIE coordinates for varying concentrations of Dy^{3+} at an excitation of 347 nm have been calculated and found to be in close approximation for all the glasses as depicted in Fig. 7. The CIE coordinates at optimized concentration of Dy^{3+} i.e., for D050 glass are (0.34, 0.38); which lies near standard equal energy white light points (0.33, 0.33), National Television Standard Committee (NTSC) white light points (0.31, 0.31), and also to the coordinates of commercial phosphor converted w-LED (0.32, 0.32) [47].

The color correlated temperature is used to describe non-black body source. The color correlated temperature (CCT) is defined as the temperature of the blackbody radiator which closely resembles the color from a source of equal brightness. The CCT is measured by McCamy approximate formula using CIE coordinates as follows:

$$CCT = -449n^3 + 3525n^2 – 6823.3n + 5520.33$$

ACCEPTED MANUSCRIPT

where $n = (x - x_e)/(y - y_e)$ is inverse slope line and $x_e = 0.332$, $y_e = 0.186$ is epicenter [48]. The CCT for all the investigated BAZN glasses with different concentration of Dy^{3+} ion has been calculated and found to be 4913K, 4891K, 5029K, 4892K, and 4796K for D010, D025, D050, D075, and D100, respectively as presented in Table. 1. The range of CCT for the as-prepared glasses is found to be in cool white light region which makes it suitable for solid state lighting applications.

3.5. Decay analysis

The lifetime decay for $^4F_{9/2}$ excitation level of Dy^{3+} ion doped glasses under the excitation of 347 nm have been estimated by scrutinizing the decay profile of $^4F_{9/2} \rightarrow {}^4H_{13/2}$ transition as shown in Fig. 8. The decay profile is found to be bi-exponential. The bi-exponential nature may be because of the reason that the energy transfer from excited donor ion to unexcited acceptor ion transpires. The intensity of luminescence can be articulated as follows:

$$I = I_0 + A_{1*}\exp(-t/\tau_1) + A_{2*}\exp(-t/\tau_2)$$

where, I_0 is the intensity at t=0, and I is intensity at time t, A_1 and A_2 are the amplitudes of decay constants and τ_1 and τ_2 are the luminescence lifetimes for fast and slow channels of decay respectively. The average values of decay time are calculated by using the formula given as:

$$\tau_{avg} = (A_1 *\tau_1^2 + A_{2*} \tau_2^2)/(A_{1*} \tau_1 + A_{2*} \tau_2)$$

The average lifetime values for 0.1, 0.25, 0.50, and 0.75 mol% of Dy^{3+} ion doped glasses are found to be 507, 342, 226, and 138 μs respectively and is shown in the inset of Fig. 8. It can be seen from the inset table that the average lifetime decreases with increase in Dy^{3+} ion concentration signifying the energy transfer between Dy^{3+} -Dy^{3+} ions [49-50].

4. Conclusion

ACCEPTED MANUSCRIPT

The structural and optical properties of Dy^{3+} doped BAZN glasses with varying dopant concentration prepared via melt-quenching technique have been investigated. The glass samples emit blue and yellow light and quenching concentration has been found to be 0.5 mol%. The emission spectra exhibit intense yellow and blue emission under n-UV excitation. The optimized concentration is found to be 0.5 mol%. The Y/B ratio lies close to 1 and the CIE coordinates calculated lies in close proximity to standard equal energy white light points (0.33, 0.33), National Television Standard Committee (NTSC) white light (0.31, 0.31), and also to the coordinates of commercial phosphor converted w-LED (0.32, 0.32) implies its suitability to emit white light. The CCT range for glass samples lies in cool white light region indicates its feasibility in solid state lighting applications. The decay analysis shows bi-exponential fitting with decay time in the range of microseconds. All these results indicate potential candidature of Dy^{3+} doped BAZN glasses in w-LEDs.

Acknowledgements

One of the authors, Ms. Sumandeep Kaur is grateful to University Grants Commission (UGC) (Ref.No:22/06/2014 (i)EU-V) for providing financial support in the form of Senior Research Fellowship (SRF) to her. The author, Dr. M. Jayasimhadri is grateful to DST-SERB, Govt. of India, New Delhi for the sanction of a research project (No. SB/FTP/PS-082/2014, Dt. 02/03/2015). The author, Prof. A.S. Rao is thankful to DST-SERB, Govt. of India, New Delhi for awarding him with a Major Research Project (EMR/2016/007766).

ACCEPTED MANUSCRIPT

ACCEPTED MANUSCRIPT

References

[1] H. Masai, Y. Yamada, Y. Suzuki, K. Teramura, Y. Kanemitsu,T. Yoko, Sci. Rep. 3 (2013) 3541-3547.

[2] H. Li, R. Zhao, Y. Jia, W. Sun, J. Fu, L. Jiang, S. Zhang, R. Pang, C. Li, ACS Appl. Mater. Interfaces, 6 (2014) 3163-3169.

[3] W. Wang, Y. Kaihatsu, F. Iskandar, K. Okuyama, Chem. Mater. 21 (2009) 4685–4691.

[4] B.V. Ratnam, M. Jayasimhadri, G. Bhaskar Kumar, K. Jang, S.S. Kim, Y.I. Lee, J.M. Lim,D.S. Shin, T.K. Song, , J. Alloys Compd. 564 (2013) 100 – 104.

[5] A. K. Vishwakarma, K. Jha, M. Jayasimhadri, A.S. Rao, K. Jang, B. Sivaiah, D. Haranath, J. Alloys Compd. 622 (2015) 97–101.

[6] H. Ma, R. Ye, Y. Gao, Y. Hua, D. Deng, Q. Yang, S. Xu, J. Non-Cryst. Solids 402 (2014) 231–235.

[7] P. Du, J. S. Yu, Sci Rep., 7 (2017) 11953-11962.

[8] R. J. Amjad, M.R. Sahar, S. K. Ghoshal, M. R. Dousti, R. Arifin, Opt Mater 35 (2013) 1103-1108.

[9] A.S. Rao, Y.N. Ahammed, R.R. Reddy, T.V.R. Rao, Opt. Mater., 10 (1998) 245-252.

[10] K. Swapna, Sk. Mahamuda, A.S. Rao, M. Jayasimhadri, S. Shakya, G. Vijaya Prakash, J. Lumin., 156 (2014) 180-187.

[11] P. Du, J.S. Yu, Mater. Res. Bull., 84 (2016) 303-313.

[12] P. Du, K. Bharat, X-Y. Guan, J. S. Yu, J. Appl. Phys., 117 (2015) 083112-083117.

[13] B. R. Anderson, R. Gunawidjaja, H. Eilers, J. Lumin., 188 (2017) 238-245.

[14] T. Monzon-Heirro, J. Sanchiz, S. Gonzalez-Perez, B. Gonzalez-Diaz, S. Holenski, D. Borchert, C. Hernandez-Rodriguez, R. Guerrero-Lemus, Sol. Energy Mater. Sol. Cells, 136 (2015) 187-192.

ACCEPTED MANUSCRIPT

[15] R.L. Leonard, S.K. Gray, S.D. Albritton, L.N. Brothers, R.M. Cross, A.N. Eastes, H.Y. Hah, H.S. James, J.E. King, S.R. Mishra, J.A. Johnson, J. Non-Cryst. Solids, 366 (2013) 1-5.

[16] V. Kumar, A.K. Bedyal, S. S. Pitale, O. M. Ntwaeaborwa, H. C. Swart, J. Alloys. Compd., 554 (2013) 214-220.

[17] P. Molina, V. Vasyliev, E. G. Villora, K. Shimamura, J. Appl. Phys. 110 (2011) 123527-123533.

[18] A. Boccolini, J. Marques-Hueso, D. Chen, Y. Wang, B. S. Richards, Sol. Energy Mater. Sol. Cells 122 (2014) 8-14.

[19] B. Shanmugavelu, V. V. R. Kanth Kumar, J. Lumin. 146 (2014) 358-363.

[20] H. Schneckenburger, Curr. Opin. Biotechnol. 16 (2005) 13-18.

[21] Y.G. Choi., J. Heo, J. Non-Cryst. Solids 217 (1997) 199-207.

[22] N. Deopa, A.S. Rao, A. Choudhary, S. Saini, A. Navhal, M. Jayasimhadri, D. Haranath, G. Vijaya Prakash, Mater. Res. Bull., 100 (2018) 206-212.

[23] N. Soga, K. Hirao, M. Yoshimoto, H. Yamamoto, J.Appl. Phys. 63(1988) 4451-4454.

[24] S.M. Kaczmarek, Opt. Mater. 19 (2002) 189-194.

[25] A. D. Sontakke, k. Annapurna, J. Lumin. 138 (2013) 229-234.

[26] L. Zur, J. Pisarska, W. A. Pisarski, Opt. Acta. 42 (2012) 345-352.

[27] F. EL-Diasty, M. A. Moustafa, F. A. Abdel-Wahab, M. Abdel-Baki, A. M. Fayab, J. Alloys Compd. 605 (2014) 157-163.

[28] Sk. Mahamuda, K. Swapna, P. Packiyaraj, A. SrinivasaRao, G. VijayaPrakash, J. Lumin. 153 (2014) 382-392.

[29] L. N.Chakraborty, D. E. Day, J. Am. Ceram. Soc. 68 (1985) 641-645.

[30] M. Ding, C. Lu, Q. Cui, Y. Ni, Z. Xu, Ceram. Int. 40 (2013) 233-239.

ACCEPTED MANUSCRIPT

[31] K. Swapna, Sk. Mahamuda, A. SrinivasaRao, M. Jayasimhadri, T. Sasikala, L. R. Moorthy, J. Lumin. 139 (2013) 119-124.

[32] B. V. Ratnam, M. Jayasimhadri, K. Jang, H. S. Lee, J. Am. Ceram. Soc. 93[11] (2010) 3857-3861.

[33] C. Yusufali, R.J. Kshirsagar, Jagannath, R.K. Mishra, R.S. Dutta, G.K. Dey, J. Non-Cryst. 366 (2013) 54–58

[34] A. Tarafder, A. R. Molla, S. Mukhopadhyay, B. Karmakar, Opt Mater. 36 (2014) 1463-1470.

[35] G. P. Singh, S. Kaur, P. Kaur, D.P. Singh, Physica B 407 (2012) 1250-1255.

[36] L. Balachandera, G. Ramadevudub, Md. Shareefuddin, R. Sayanna, Y.C. Venudhar, ScienceAsia 39 (2013) 278-283.

[37] P.F. Wang, Zh.H. Li, J. Li, Y.M. Zhu, Solid State Sci. 11 (2009) 1427–1432.

[38] T. I. Suratwala, R. A. Steele, G. D. Wilke, J. H. Campbell, K. Takeuchi, J. Non-Cryst Solids 263-264 (2000) 213-227.

[39] T. Suhasini, B. C. Jamalaiah, T. Chengaiah, J. Suresh Kumar, L. Rama Moorthy, Physica B 407 (2012) 523- 527.

[40] Sk. Mahamuda, K. Swapna, P. Packiyaraj, A. S. Rao, G. V. Prakash, Opt. Mater. 36 (2013) 362-371.

[41] X. Y. Sun, S. M. Huang, X. S. Gong, Z. P. Ye, C. Y. Cao, J. Non-Cryst. Solids 356 (2010) 98-101.

[42] W. T. Carnall, P. R. Fields, K. Rajnak, J. Chem. Phys. 49 (1968) 4424-4442.

[43] J. S. Kumar, K. Pavani, A. M. Babu, N. K. Giri, S. B. Rai, L. R. Moorthy, J. Lumin. 130 (2010) 1916-1923.

[44] P. Du, X. Huang, J. S. Yu, Chem. Eng. J., 337(2018) 91-100.

ACCEPTED MANUSCRIPT

[45] L. Zur, J. Janek, M. Soltys, J. Pisarska, W. A. Pisarski, Phys. Scr. T157 (2013) 014035-014038.

[46] J. B. Gruber, B. Zandi, U. V. Valiev, S. A. Rakhimov, J. App. Phys. 94 (2003) 1030-1034.

[47] A.K. Vishwakrma, K.Jha, M. Jayasimhadri, B. Sivaiah, B. Gahtori, D. Haranath, Dalt. Trans., 44 (2015) 17166-17174.

[48] C S McCamy, Color Res Appl. 17 (1992) 142-144.

[49] M. V. S. Kumar, D. Rajesh, A. Balakrishna, Y. C. Ratnakaram, J. Mol. Struct. 1041 (2013) 100-105.

[50] J. D. Furman, G. Gundiah, K. Page, N. Pizarro, A. K. Cheetham, Chem. Phys. Lett. 465 (2008) 67-72.

ACCEPTED MANUSCRIPT

ACCEPTED MANUSCRIPT

Figure Captions:

Fig. 1: XRD spectrum of an un doped BAZN glass.

Fig. 2: FT-IR Spectrum of D050 glass.

Fig. 3: Excitation spectrum of BAZN glass under emission wavelength of 575 nm.

Fig. 4: Emission spectra of various concentration of Dy^{3+} doped BAZN glasses under the excitation wavelength of 347 nm.

Fig. 5: Plot of log(I/x) versus log(x).

Fig. 6: Energy level diagram of Dy^{3+} ion in BAZN glass depicting radiative and non-radiative transitions.

Fig. 7: CIE chromaticity diagram for various concentration of Dy^{3+} doped BAZN glasses.

Fig. 8: Decay profile of $^4F_{9/2}$ emission level of Dy^{3+} doped BAZN glasses.

ACCEPTED MANUSCRIPT

ACCEPTED MANUSCRIPT

Fig. 1:

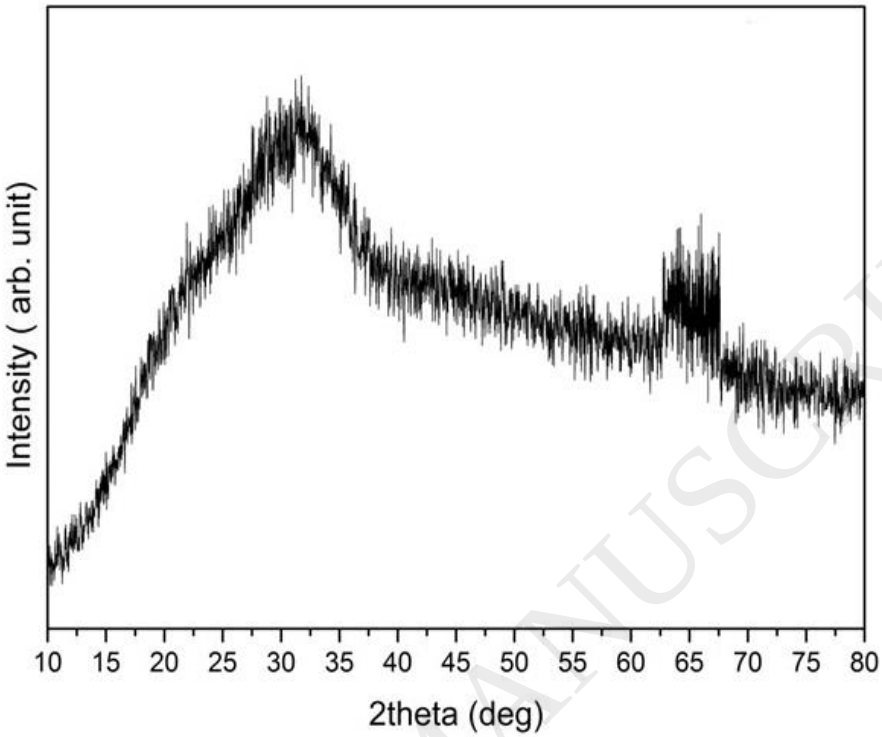

ACCEPTED MANUSCRIPT

ACCEPTED MANUSCRIPT

Fig. 2:

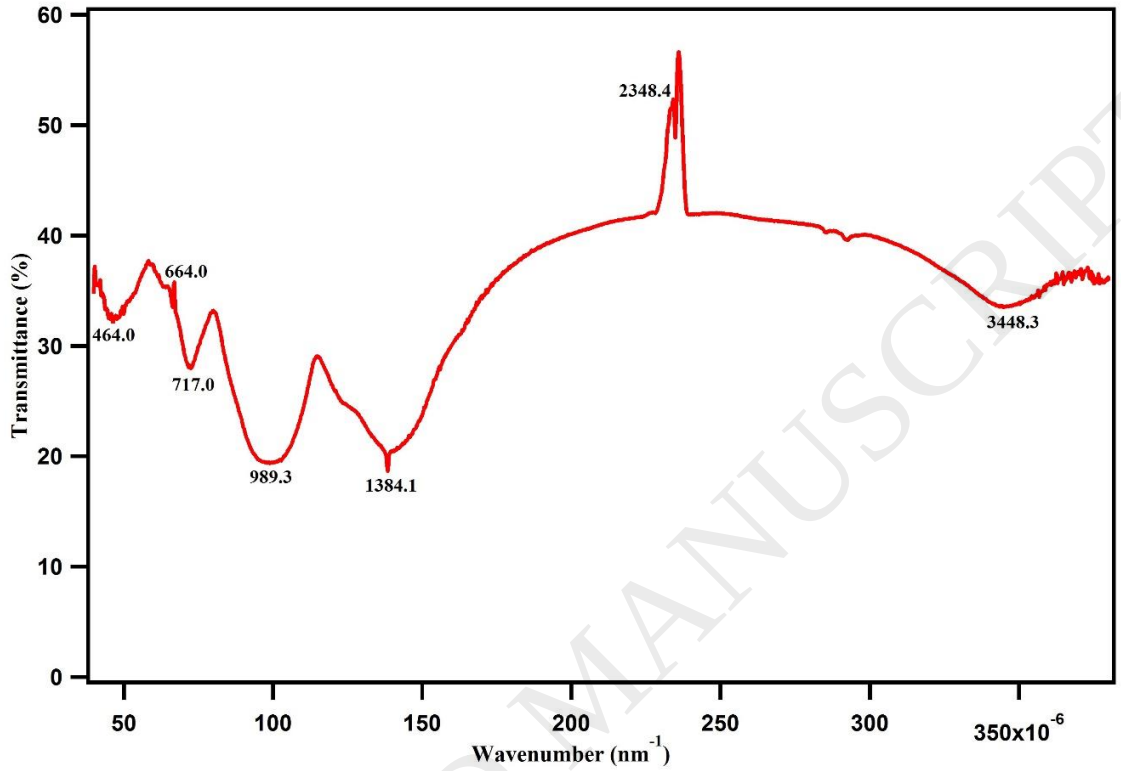

ACCEPTED MANUSCRIPT

ACCEPTED MANUSCRIPT

Fig. 3:

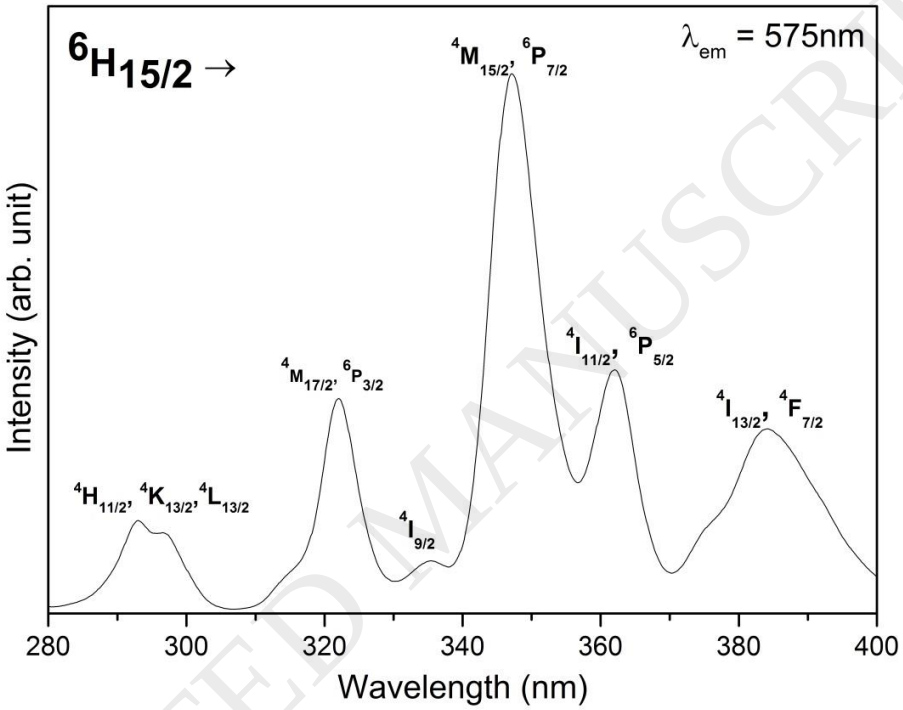

ACCEPTED MANUSCRIPT

ACCEPTED MANUSCRIPT

Fig. 4:

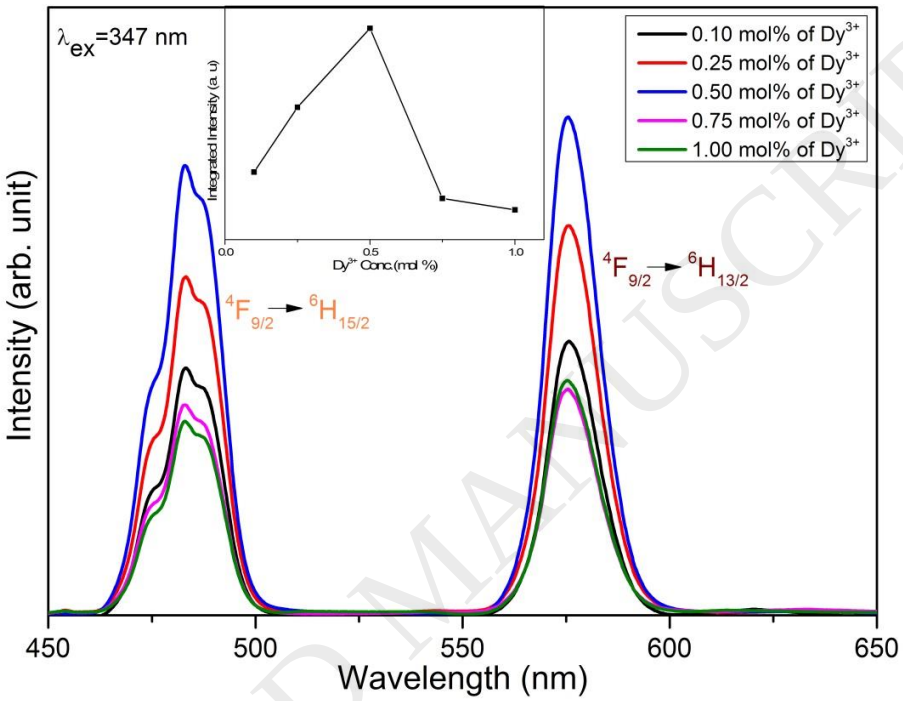

ACCEPTED MANUSCRIPT

ACCEPTED MANUSCRIPT

Fig. 5:

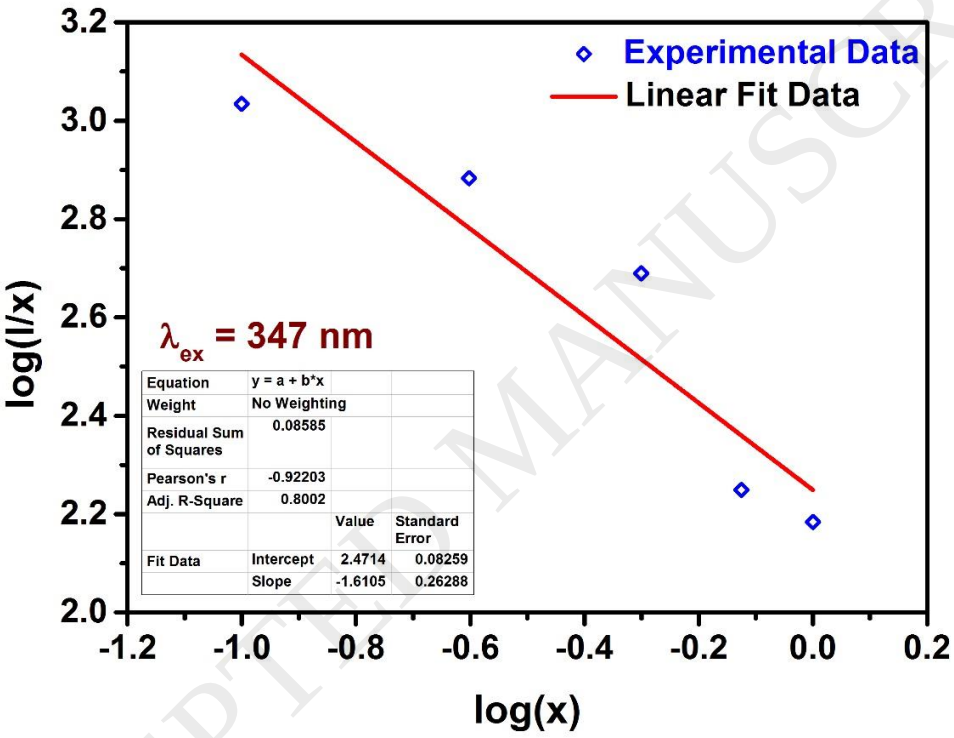

ACCEPTED MANUSCRIPT

ACCEPTED MANUSCRIPT

Fig. 6:

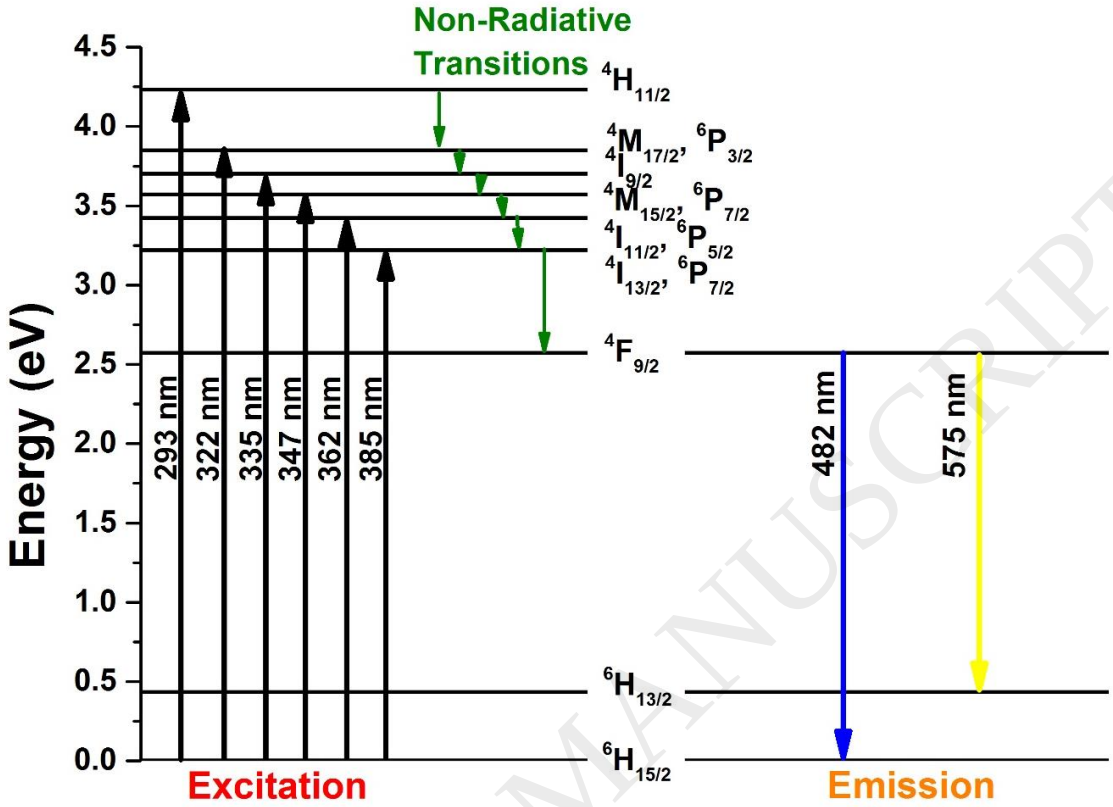

ACCEPTED MANUSCRIPT

ACCEPTED MANUSCRIPT

Fig. 7:

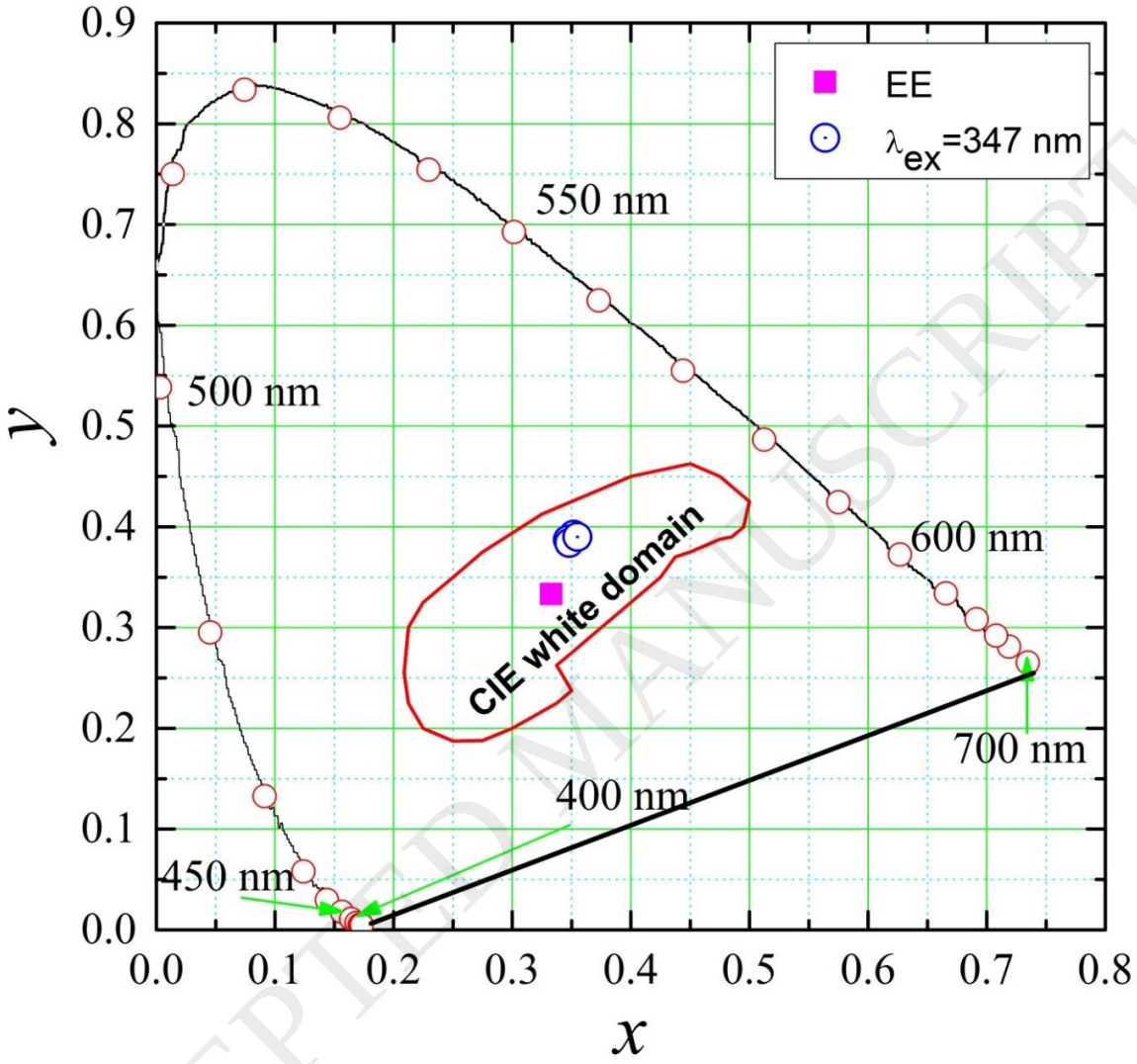

ACCEPTED MANUSCRIPT

ACCEPTED MANUSCRIPT

Fig. 8:

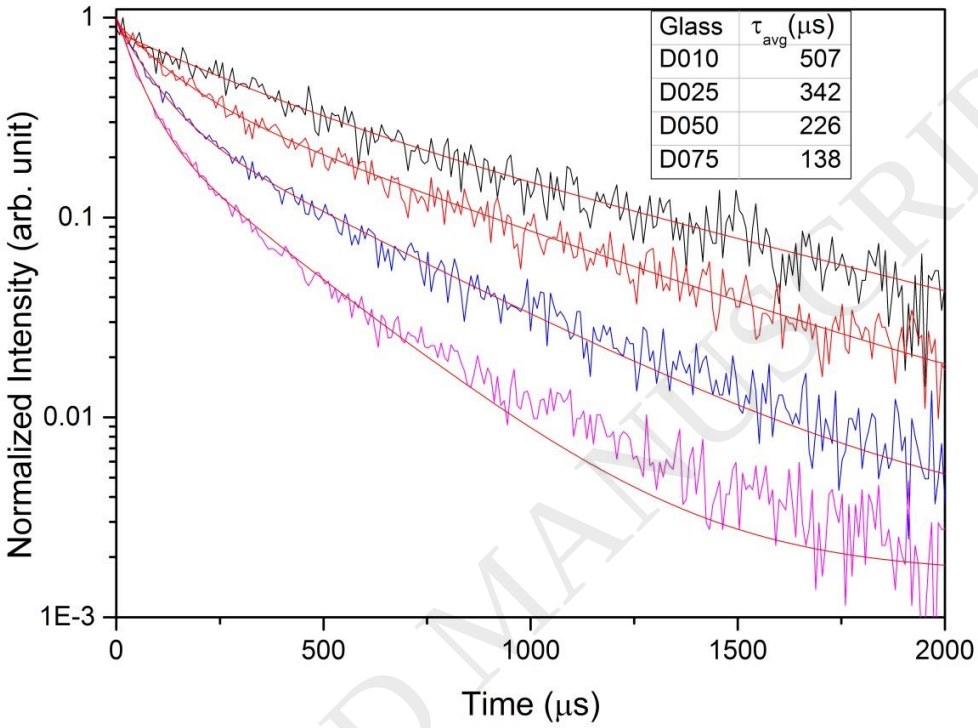

ACCEPTED MANUSCRIPT

ACCEPTED MANUSCRIPT

Table.1: Y/B ratio, CCT and CIE coordinates of BAZN glasses.

Glass Samples	**Y/B ratio**	**CCT (K)**	**CIE co-ordinate (x, y)**
D010	1.10	4913	(0.35, 0.38)
D025	1.15	4891	(0.35, 0.39)
D050	1.10	5029	(0.34, 0.38)
D075	1.07	4972	(0.34, 0.38)
D100	1.20	4796	(0.35, 0.39)

ACCEPTED MANUSCRIPT

Preprints (www.preprints.org) | NOT PEER-REVIEWED | Posted: 25 April 2018 doi:10.20944/preprints201804.0320.v1

Type of the Paper (Article)

Stabilization and Protection of Biomaterial through Biomineralization via Surface Interaction: An Astrobiological Approach

Preeti Bhatt[1]*, Chandra Kala Pant[1]*, Pramod Pandey[1]†, Yogesh Pandey[1], Satish Chandra Sati[1], Mohan Singh Mehata[2]

[1] *Chemical Laboratory, Department of Chemistry, DSB Campus, Kumaun University, Nainital 263002, Uttarakhand, India.*

[2] *Department of Applied Physics, Delhi Technological University, Bawana Road, New Delhi 110042, India.*

† *State Key Laboratory for Molecular Reaction Dynamics, Dalian Institute of Chemical Physics, Chinese Academy of Sciences, 457 Zhongshan Road, Dalian 116023, Liaoning, China (Current address).*

* Correspondence: preetibhatt00@gmail.com, preeti_bhatt@kunainital.ac.in; Tel.: +91-945-631-9780, +91-9634249370; ckp_ku@yahoo.co.in, ckp.astrochem@gmail.com; +91-976-135-4035, +91-863-035-8334

Abstract: A Cytosine (CYN), core constituent of both RNA and DNA, is a well-known functional biomaterial of living system. Adsorption of such molecule on primigenial mineral surfaces transacts a very specific and selective role in biocompatibility and biomineralization. The adsorption behaviour of CYN, with change in pH, concentration, time and temperature on siliceous Montmorillonite (MMT) surface, a prominent nanoclay of smectite group with specific surface area, was studied systematically and methodically using different spectral techniques (viz. UV, FTIR, SEM and XRD). Biogenic metal dication [M^{2+}= Mg^{2+}, Ca^{2+}, Fe^{2+} and Cu^{2+}] entrapped nanocomposites of MMT were prepared separately by cation-exchange approach. The results reveal significant role of MMT and biogenic metal ions on the quantity of CYN adsorbed. The adsorption isotherm elegantly evinces monolayer formation of the biomaterial on the surface of MMT and MMT-M^{2+}. The Langmuir adsorption parameters (K_L & X_m) delineated appreciable interaction of CYN on MMT-Fe^{2+} surface as compared to MMT alone and other metal confined MMTs. The present work throws light on affinity of MMT nanoclay (having multifarious applications in biological systems) involving biogenic metal ions on stabilization and protection of biomaterials through biomineralization during prebiotic chemical evolution of biomolecules. The results embarks better adsorption capability of transition metal ion incorporated MMT than the clay without metal ion and with alkaline Earth dications due to better coordination properties of transition metal ions involving their d-orbitals for stable complex formation with negative sites of cytosine molecules as ligands. Since metal ions are key components of various enzymes which can catalyse a number of biochemical reactions in the living systems, the present study give better understanding regarding the pathways of aggregation of biomonomers on solid surfaces which themselves might have catalysed the formation of complex biomolecules via polymerization and condensation in enzyme free environment of early Earth and also influences implant biocompatibility.

Keywords: Adsorption; Cytosine; Montmorillonite; Biogenic metal ions; Langmuir adsorption parameters; Prebiotic chemical evolution.

1. Introduction

Life can be seen as the result of chemical activity of biocompatible and water soluble bionanoassemblies such as proteins, nucleic acid bases, sugars and phosphate molecules. In early periods of the Earth, Life is supposed to be originated from lifeless environment through chemical evolutionary processes. Proteins and nucleic acids constitute the main matrix of living systems. How

© 2018 by the author(s). Distributed under a Creative Commons CC BY license.

Preprints (www.preprints.org) | NOT PEER-REVIEWED | Posted: 25 April 2018 doi:10.20944/preprints201804.0320.v1

did these complex biomolecules, capable of self-replication and self-organisation, appear abiotically on primitive Earth from their monomeric building blocks is a question of paramount importance [1-8]. The fundamental pathways from non-living matter to life forming molecules, starting with the build-up of nucleobases, over the synthesis of nucleotides and finally to the formation of RNA and DNA, are still shrouded in mystery.

Bernal in 1951 independently speculated and stressed the potential importance of clays as solid mineral surfaces for concentration of biomolecules via adsorption [9]. Clay minerals have the capacity to concentrate, protect and catalyse the polymerisation of enormous organic molecules due to their fine particle size, specific surface area and charge characteristics [10-14]. Recently, layered clay minerals are reported to be advantageous for adsorption [15-18] and phyllosilicates containing Fe-Mg strongly bind the nucleotides by exchanging their ligands and thereby preserving the genetic information inside the inorganic templets. In succession the polymer formation needs excessive assemblence of nucleotides under favoured conditions of thermodynamics [19, 20].

Montmorillonite a prominent nanoclay with confined metal dications especially known to have particular affinities for organic molecules by adsorbing them on and in between their silicate layers [21-24]. Metal entrapped smectite clays provide good adsorbent sites for the frequent concentration of biologically active molecules [25-28] and also can act as catalyst for their polymerization as it might have happened on contemporaneous primeval Earth [29-35]. In silico surface interaction studies of nucleobases, nucleotides and their polymers with MMT and boron nitride nanotubes were also reported [36-39] along with electronic properties of metal semiconductor structures with cytosine biopolymer [40,41].

An extensive contemplation of the affinities of clay minerals towards surface interaction of biomolecules has fascinated the minds of great thinkers in past few decades [42-49, 50 (and references therein)]. Currently, several inquisitive researchers are engaged in exploring various aspects of MMT nanoclay as a drug carrier system with multitudinous applications and its biocompatibility outcomes [51-54]. Among all four nucleic acid bases, cytosine (CYN), a potent biomolecule and a viable functional biogenic material [55], seems to be significant from surface interaction point of view during the course of formation of genetic macromolecules (DNA and RNA) and their monomers [56-58]. Therefore, CYN is taken as model for adsorption studies on the prominent nanoclay MMT, with and without entrapped metal diions [Mg^{2+}, Ca^{2+}, Fe^{2+} and Cu^{2+}], which may relevant to stabilization and protection of biomolecule through biomineralization in prebiotic scenario of Earth.

Metal ions have been associated with biological systems for billions of years, through the interplay of biogeochemical weathering and metabolic pathways involving the products of that weathering. A number of metal ions play a vital role in a vast number of widely differing biological processes essential for the activity of enzymes [59]. All life forms have an absolute requirement for metals, as metals play critical roles in fundamental processes, including osmotic regulation, catalysis, metabolism, biomineralization, and signalling [60]. It is increasingly recognized that metals are involved in cellular and subcellular functions and also used as inorganic drugs for many diseases [61].

The present study throws light upon adsorption of CYN on prebiotically available MMT and its biogenic metal dications modified nanocomposites showing the inevitability of adsorption phenomenon in primitive era of the Earth as well as its biological implications.

2. Materials and Methods

2.1. Procurement of chemicals

Analytical grade reagents were used during all experimentation. Montmorillonite (MMT K10) was procured from Sigma Aldrich, Germany; Cytosine (CYN) from Loba Chemie, India; $CaCl_2$ from CDH, India and H_2O_2, $MgCl_2$, $FeCl_2$, $CuCl_2$ from Qualigens, India. All solutions were prepared in triple distilled deionised water ($_{td}H_2O$ = pH 6.8±0.2) and borosilicate glasswares were used throughout the work.

Preprints (www.preprints.org) | NOT PEER-REVIEWED | Posted: 25 April 2018 doi:10.20944/preprints201804.0320.v1

96
97 ***2.2. Preparation and purification of sensitizers/adsorbents***
98 Preparation and purification of MMT and MMT-M^{2+} i.e., metal [Mg^{2+}, Ca^{2+}, Fe^{2+} and Cu^{2+}]
99 entrapped MMT nanocomposites were carried out as described in earlier reports [25, 28, 62]. After
100 drying in vacuum desiccators the adsorbents were grounded, sieved to mesh sized for further
101 experimentation (Scheme I).

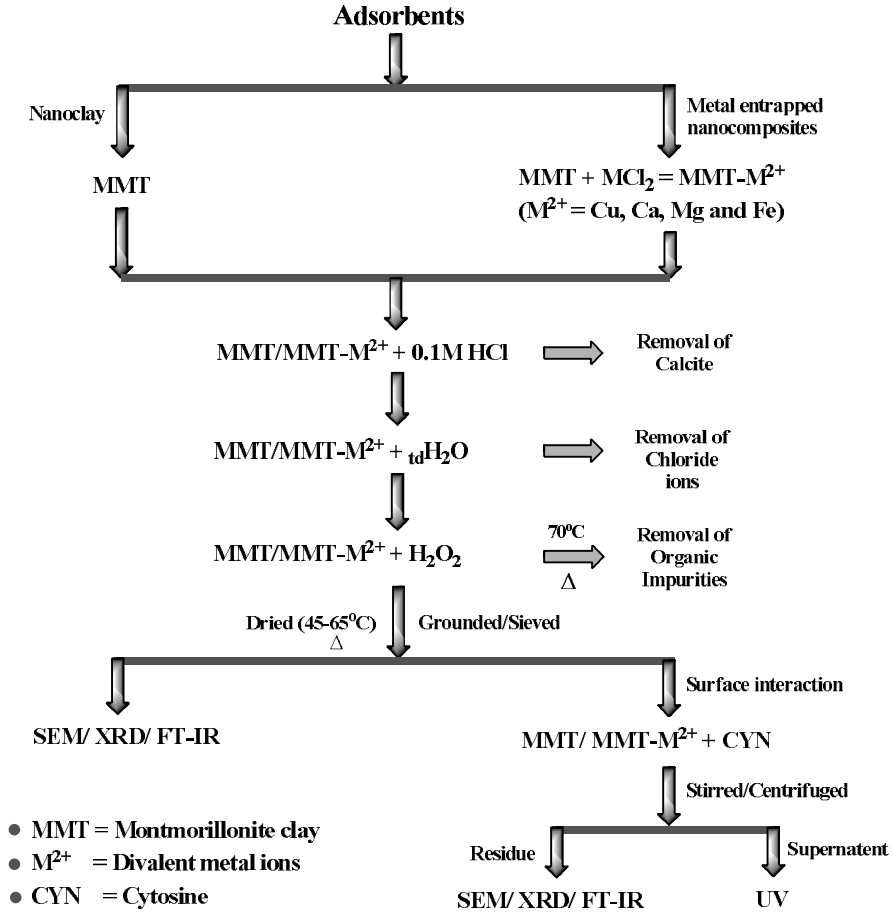

102
103 Scheme I. Schematic presentation of various steps involved in the preparation as well as purification
104 of adsorbents and their characterization before and after adsorption.
105
106
107 ***2.3 Experimental procedure***
108 The adsorption studies of CYN (Figure 1) separately on MMT and MMT confined with biogenic
109 metal ions [Mg^{2+}, Ca^{2+}, Fe^{2+} and Cu^{2+}] were carried out in aqueous environment as a function of pH
110 (4.0-9.3) and concentrations (1.0×10^{-5}M – 9.0×10^{-5}M) of adsorbate at room temperature in order to
111 obtain saturation point by adding relevant buffer i.e., acetic acid-acetate (pH 4.0-6.0) or boric
112 acid-borax (6.6-9.3), to the adsorbate solution (3ml each) containing different adsorbents
113 MMT/MMT-M^{2+} [M^{2+}= Mg^{2+}, Ca^{2+}, Fe^{2+}, Cu^{2+}] (30mg each), kept in separate conical flasks (10 ml) ,
114 stirred mechanically for 15min and allowed to stand at room temperature to find out the adsorption
115 capability of the given adsorbents.
116

Preprints (www.preprints.org) | NOT PEER-REVIEWED | Posted: 25 April 2018 doi:10.20944/preprints201804.0320.v1

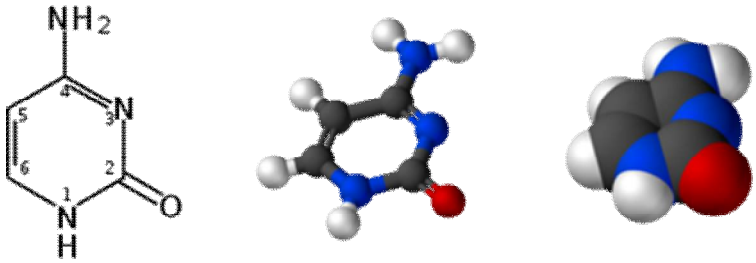

Figure 1. Chemical structure (2D & 3D) of cytosine.

In each experiment the adsorption of CYN was measured after a period of 18hrs. The suspensions were then centrifuged at 3500rpm for 30min and the supernatant solutions were decanted for subsequent quantitative estimation, leaving the adsorption adduct as residue and the pH of the solution was again noted which was found to be almost unaffected. Adducts were separated, washed and then dried under vacuum at ambient temperature and used for further analytical investigations. The complete procedure was triplicated and the formation of degradation product after adsorption (if any) was checked by chromatographic techniques (PC and HPLC) [28].

2.4. Analysis and characterization

2.4.1. Properties of adsorbent

The colour of MMT K10 used as adsorbent was found 10R8/1 (White) on Munsell Notations with water holding capacity (W.H.C.) 95%, pH 3.6 and cation exchange capacity (CEC) 200.17meq/100g.

2.4.2. Absorbance measurements

The different concentrations of CYN in supernatant were determined by recording their absorbances at λ_{max} = 263 nm by using Systronics double beam UV/Vis spectrophotometer 2203^{smart} and quartz cuvette with 1cm path length. pH was recorded on Hanna pH meter (model pHep) with an accuracy of ±0.1pH unit.

The amount of CYN adsorbed under optimized conditions was calculated from the difference between initial concentration and concentration after adsorption in each case. The equilibrium concentration of CYN and the amount adsorbed were used to obtain adsorption isotherms [28] (Figure 2).

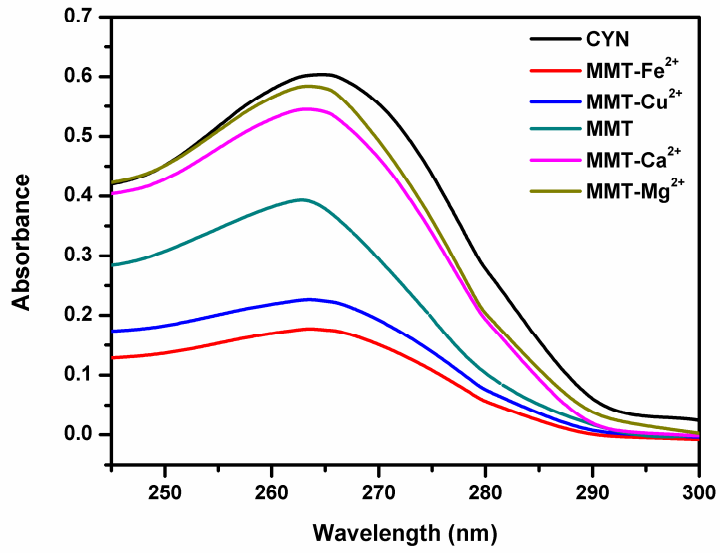

Figure 2. Optical absorbance of cytosine solution before and after adsorption.

Preprints (www.preprints.org) | NOT PEER-REVIEWED | Posted: 25 April 2018 doi:10.20944/preprints201804.0320.v1

2.4.3. Morphological observation

Scanning electron microscopy (SEM) was used to observe the surface morphology of adsorbate, adsorbents with or without divalent metal ions and their respective adducts using a Hitachi S-3700N instrument with an acceleration voltage 15.0kV, take-off angle 44.1° and ZEISS EHT 20kV.

2.4.4. Relative intensity and inter-planar spacing identification

X-ray diffraction (XRD) studies were performed to check the crystalline nature as well as to confirm purity and to know the relative intensity and inter-planar spacing. A Thermal X-TRA ARL diffractometer equipped with a 'Peltier' detector, using Cu Kα radiation (wavelength=1.5406Å) operated at 30mA and 40kV with graphite monochrmator detection between the range 10-80° 2θ angle was used for powder diffraction analysis of adsorbents and adsorption adducts.

2.4.5. Vibrational studies

A PerkinElmer DX-II FT-IR spectrophotometer equipped with DTGS detector was used to determine the IR adsorption frequencies. The data were collected at 4cm^{-1} resolution and 100 scan with frequency range 400-4000cm^{-1}.

3. Results and Discussion

This Surface interaction studies of CYN on MMT and on MMT-M^{2+} [M^{2+}= Mg^{2+}, Ca^{2+}, Fe^{2+}, Cu^{2+}] has been carried out under varied conditions of pH (4.0-9.3) and concentration (10µM-90µM) at room temperature (298K) to figure out the possible affinity of the clay and its biologically active metal entrapped nanocomposites in abiotic formation of complex biomolecules and their stabilization and protection through biomineralization (Figure 3) in relevance to origin of life.

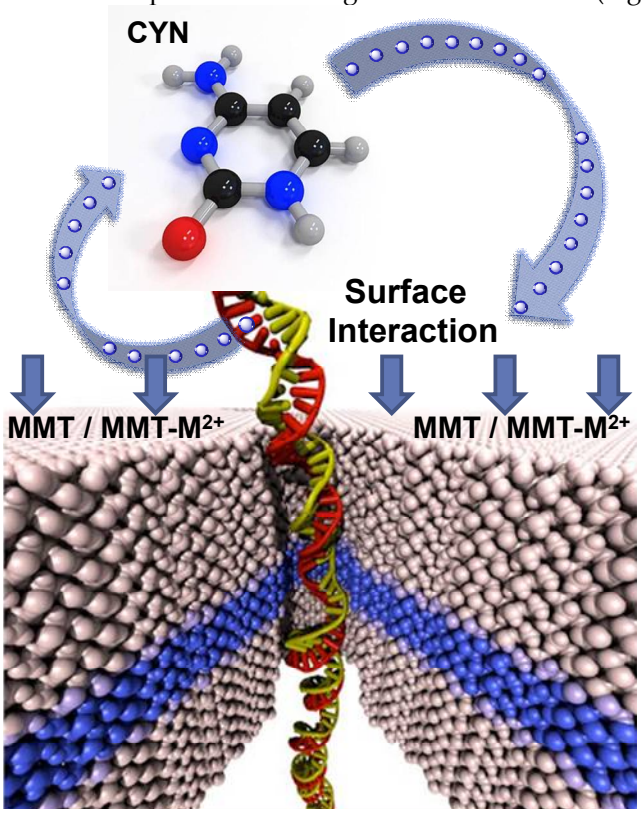

Figure 3. Surface interaction of biomaterial CYN on the nanoclay MMT and biogenic metal entrapped MMT (i.e., MMT-M^{2+}) at optimized conditions of pH and temperature.

CYN can exist in two tautomeric forms (Figure 4), in which the amino form facilitate normal biological traits in living systems, while the imino form causes mutation (i.e., the precursors to many molecular-based diseases, including cancer) via forming a stable hydrogen bond, pairing with adenine instead of guanine. Therefore, amino being stable and less energetic state predominates in solution phase [63].

Preprints (www.preprints.org) | NOT PEER-REVIEWED | Posted: 25 April 2018 doi:10.20944/preprints201804.0320.v1

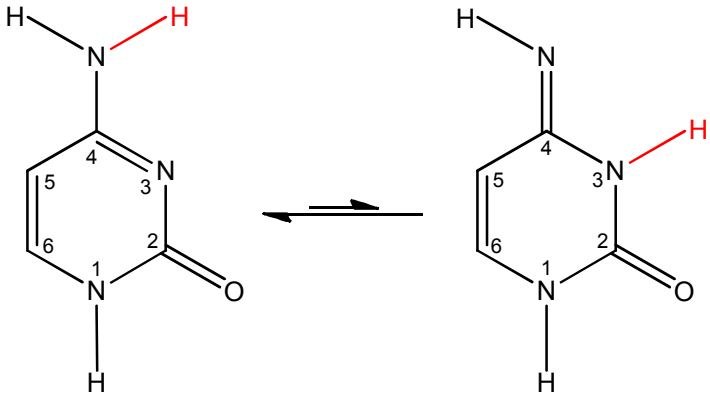

Figure 4. Amino and imino Tautomers of CYN.

Protonation is known to increase the number of possible pairing modes leading to structural diversity [64]. In CYN molecule protonation takes place at N3 position because of the maximum electron density, while the amino group is electron deficient. The amino group of CYN is hydrogen donor, and the ring nitrogen atom N3 is hydrogen acceptor. CYN also has a hydrogen acceptor group at C2 position, thus can form three hydrogen bonds with guanine. The hydrogen-bonding patterns of bases have important consequences for the three-dimensional structure of nucleic acids. Further, deamination of CYN can lead to the formation of uracil, which pairs with A and implement RNA replication or 5-methyl cytosine can be converted directly to T. The functional role of the exocyclic amino group of CYN is aminating pyruvate (an ∝-keto acid) to the corresponding amino acid alanine, in a hydrophobic, reducing microenvironment, without the need for extreme pH [65].

3.1. Adsorption (steady state observations)

The standard concentration curve plotted between optical absorbance versus molar concentration of various CYN solutions monitored at their absorption maxima (λ_{max}=263nm) showed the amount of CYN adsorbed during adsorption (Figure S1). Linear relationship between absorbance and concentration of CYN has been observed showing r^2 = 0.99. Preliminary studies showed that the amount of nucleic acid base adsorbed is dependent on pH of the solution and was found maximum at pH 6.6 (Figure 5). Subsequent studies were therefore carried out at pH 6.6 and at room temperature.

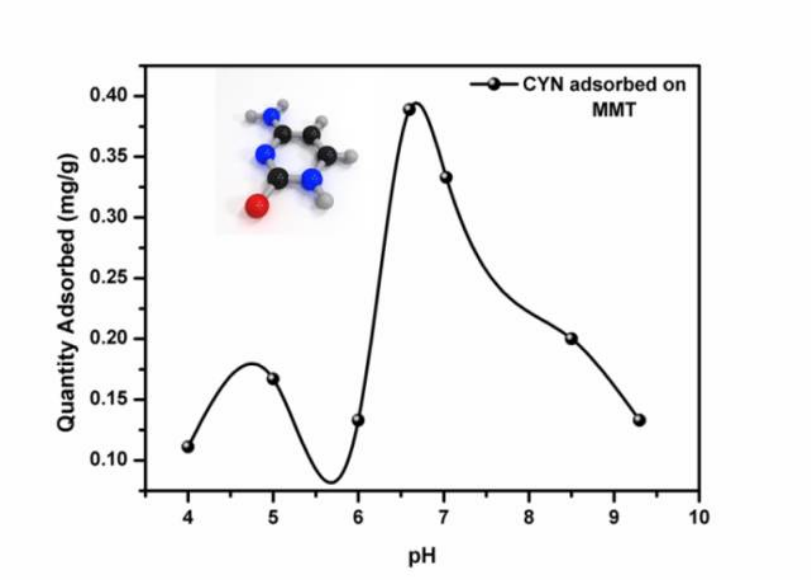

Figure 5. Quantity (mg g^{-1}) of CYN adsorbed on MMT at different pH.

Preprints (www.preprints.org) | NOT PEER-REVIEWED | Posted: 25 April 2018 doi:10.20944/preprints201804.0320.v1

The maximum surface interaction of CYN at this pH may be attributed to the ionic interaction, as at this pH, CYN is in cationic form, while the surface of adsorbents (MMT/MMT-M^{2+}) is negatively charged, so that, the specificity of CYN towards adsorption may be traced out. For adsorption study, 3 ml solution of adsorbate has been treated with 30 mg of adsorbent using 100 µl buffer solution. The influence of buffer solution on the optical density (OD) of different CYN solution has been investigated and no effect of buffer on the OD has been observed. Results are recorded in Tables (Table 1 and 2) and illustrated in Figures (Fig. 2, 3, 5-8).

3.2. *Adsorption isotherm*

The adsorption isotherm indicate the amount of CYN adsorbed on MMT/MMT-M^{2+} increases as their equilibrium concentration increases in solution upto saturation point, above which the adsorption become independent of adsorbate concentration (Figure 6). Initially, plots show linear relationship where the coefficient of correlation, i.e., r^2 and the value 1.0 was taken as limit of significance.

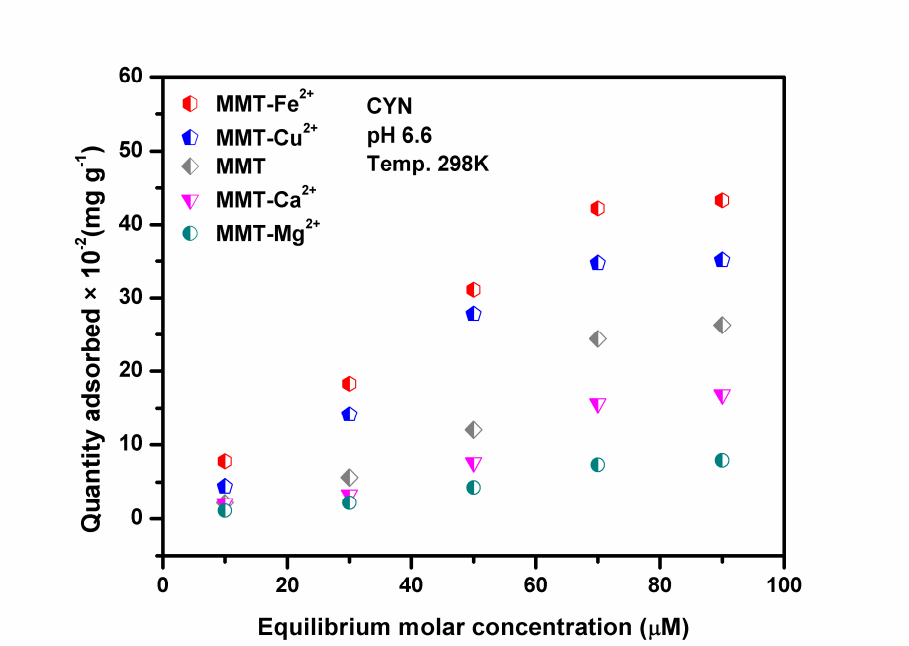

Figure 6. Graph showing adsorption behaviour of CYN as a function of quantity adsorbed versus equilibrium molar concentration.

The asymptotic nature of curve (Figure 6) suggests Langmuir type of adsorption or monolayer formation as calculated by the Equation (1) [66, 67];

$$\left|\frac{C_{eq}}{X_e}\right| = \left|\frac{1}{K_L \cdot X_m}\right| + \left|\frac{C_{eq}}{X_m}\right|, \quad (1)$$

Where, C_{eq} is equilibrium concentration of the nucleic acid base, K_L is a constant related to enthalpy (ΔH) of adsorption ($K_L \propto e^{-\Delta H/RT}$), X_e the amount (mg) of solute adsorbed per gram weight of adsorbent and X_m the amount (mg) of solute required per gram weight of adsorbent for complete monolayer formation.

As shown in Figure 7 the Langmuir adsorption parameters X_m and K_L were calculated from the slope and the intercept obtained from the graph between C_{eq}/X_e vs C_{eq}. X_e can be obtained asymptotically from Figure 6 on extrapolating the adsorption curve towards Y-axis when saturation phenomenon occurs. It was observed that the adsorption trend (% binding and Langmuir constants) of adsorbate adsorbed on MMT with or without entrapped dications largely depends on the nature of adsorbate as well as adsorbent.

Preprints (www.preprints.org) | NOT PEER-REVIEWED | Posted: 25 April 2018 doi:10.20944/preprints201804.0320.v1

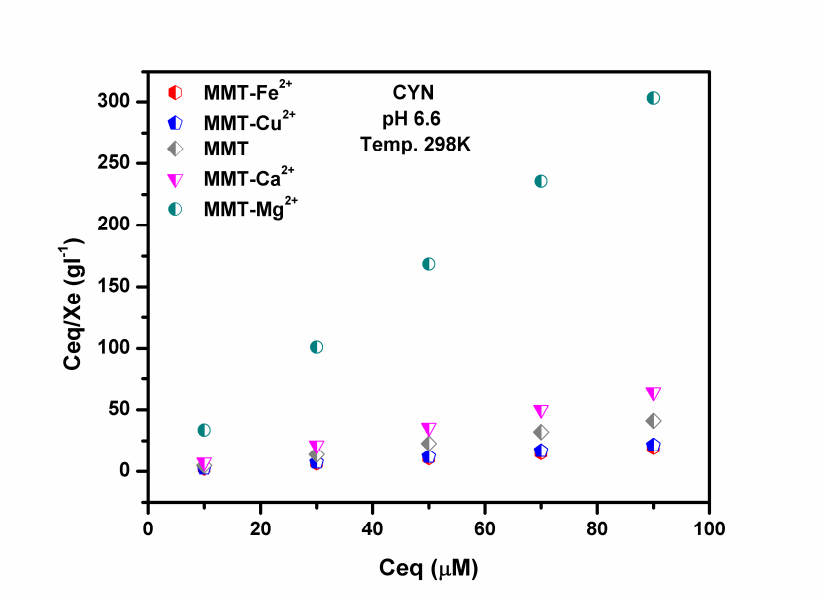

Figure 7. Graph showing Langmuir adsorption isotherm of CYN for different adsorbents.

The percent binding was calculated by the following equation (Equation 2);

$$\% \text{ binding} = \left|\frac{C_{be} - C_{af}}{C_{be}}\right| \times 100. \quad (2)$$

Where, C_{be} and C_{af} are concentration before and after adsorption respectively. Table 1 shows the Langmuir constants and % binding for adsorption of CYN on MMT and different MMT nanocomposites at pH 6.6 and temperature 298K.

Table 1. Langmuir adsorption parameters and (%) binding of CYN on the surface of various adsorbents.

Adsorbents	**pH**	**% Binding**	**Langmuir Isotherm Parameters**		
			X_m (mgg^{-1})	K_L (Lmg^{-1})	r^2
MMT-Fe^{2+}	6.6±0.1	67	0.47×10^{-3}	-21.27×10^{-5}	1
MMT-Cu^{2+}	6.6±0.1	60	0.42×10^{-3}	-47.61×10^{-5}	1
MMT	6.6±0.1	31	0.22×10^{-3}	-15.15×10^{-5}	1
MMT-Ca^{2+}	6.6±0.1	20	0.14×10^{-3}	-17.85×10^{-5}	1
MMT-Mg^{2+}	6.6±0.1	04	0.29×10^{-6}	-61.80×10^{-6}	1

In terms of % binding and X_m data, the effectiveness of various adsorbents in adsorption of CYN on MMT/MMT-M^{2+} was found in order (Figure 8);

MMT-Fe^{2+} > MMT-Cu^{2+} > MMT > MMT-Ca^{2+} > MMT-Mg^{2+}

The above results embarks better adsorption capability of transition metal ion incorporated MMT than the clay without metal ion and with alkaline Earth dications. It may be due to better coordination properties of transition metal ions involving their d-orbitals for stable complex formation with negative sites of cytosine molecules as ligands. With montmorillonite, adsorption is also influenced by the nature of the exchangeable cations [14]. The interactive forces, alone, cannot

Preprints (www.preprints.org) | NOT PEER-REVIEWED | Posted: 25 April 2018 doi:10.20944/preprints201804.0320.v1

solely be responsible for this adsorption, as size of the metal ions should also be considered. MMT-Mg^{2+} has shown the least affinity with CYN due to smaller size of the Mg^{2+} ions, intercalated into the aluminosilicates. The adsorbate which are not intercalate between the clay layers, have the higher rate of desorption when treated with the water [42] and the same observation has also been found for MMT-Mg^{2+} adsorption adduct of CYN.

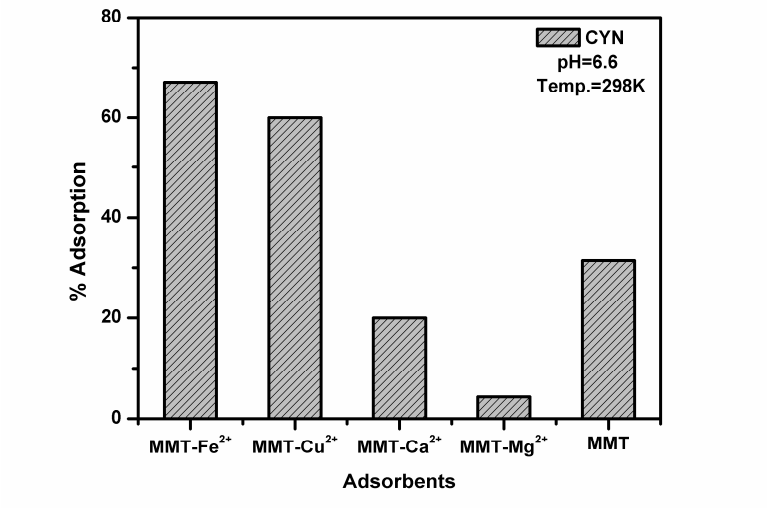

Figure 8. Affinity of CYN towards different adsorbents.

Since metal ions are key components of various enzymes which can catalyse a number of biochemical reactions in the living systems [29-31, 33, 41, 59], the present study give better understanding regarding the pathways of aggregation of biomonomers on solid surfaces through surface interaction which themselves might have catalysed the formation of complex biomolecules via polymerization and condensation in enzyme free environment of early Earth which may influences implant biocompatibility [54].

Minerals may have a pivotal role in the prebiotic evolution of complex chemical systems including metals, which are known to be involved in many enzymatic reactions, where metal-binding proteins carry out at least one step in almost all biological pathways [68], so that, metal ions are deemed essential because without them biological function is impaired. Due to the abundance of iron on Earth and its role in biological systems, the transition and mineralogical stages of iron have played a key role in Earth surface systems and in marine geochemistry [69, 70].

Moreover, the characterization of the spectroscopic features of biomolecule-mineral complexes also provides a support in remote sensing spectroscopy for detecting organic compounds on planetary surfaces or cometary grains and asteroid surfaces [71, 72]. It is believed that nucleobases might have played a critical role at the dawn of life due to their photoprotective properties which indeed suggest that their structure could have been naturally selected for the ability to dissipate electronic energy through ultrafast photophysical decay [73, 74].

3.3. *Physico-chemical characterization of adduct*

3.3.1. SEM observations

The surface morphology of adsorbate (Figure 9a), adsorbents (Figure 9b&c) and adsorption adduct (Figure 9d) was characterized by scanning electron microscopy (SEM). The morphology depict that surface of adduct was finely covered after adsorption.

Preprints (www.preprints.org) | NOT PEER-REVIEWED | Posted: 25 April 2018 doi:10.20944/preprints201804.0320.v1

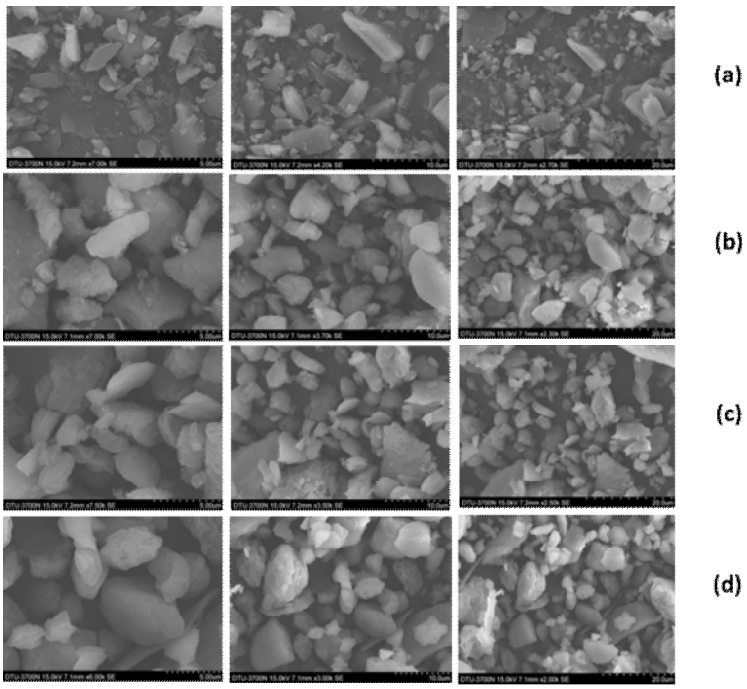

Figure 9.Different SEM images of (a) CYN, (b) MMT, (c) MMT-Fe^{2+}, and (d) adsorption adduct of MMT-Fe^{2+} + CYN after adsorption.

3.3.2. XRD pattern

The crystalline nature of clay was confirmed by X-ray diffraction analysis. The size of the intercalated metal ions (viz. K^{+}, Na^{+}, Mg^{2+}, Ca^{2+}, Fe^{2+}, Cu^{2+}) in the aluminosilicates influence the basal spacing of the structure. Further, water molecules are also allocated in the interlayer sheets and coordinated by these exchangeable cations, which in turn, also increases the basal spacing to a greater extent [75]. Percentage adsorption data have also shown that adsorption affinity increases in direct proportion with the increase of the size of the exchangeable metal ion (Table 1 and Fig. 8).

Apart from the size of the divalent metal ions, water coordination affinity of metal ions is also significant for this enhanced surface interaction of MMT with CYN [76]. Following, XRD data of the adsorbate, adsorbent and adsorption adduct also suggest the increase in the basal spacing of the adsorbents (Table 2 and Fig. 10).

Table 2. XRD data showing 2θ and basal spacing (Å) for adsorbent and adsorption adduct.

S/N	Probe	2θ	d (Å)
1.	CYN	20.22	4.4577
2.	MMT	20.2	4.4629
3.	MMT-Fe^{2+}	20.08	4.4876
4.	MMT-Fe^{2+}-CYN	20.06	4.4915

CYN interact with different sites of the clay surface, i.e., the interlayer region and the faces of the lamella showing expansion of the interlayer was greater due to the inclusion of CYN. Results demonstrate the higher affinity of MMT-Fe^{2+} interlayer for CYN.

Preprints (www.preprints.org) | NOT PEER-REVIEWED | Posted: 25 April 2018 doi:10.20944/preprints201804.0320.v1

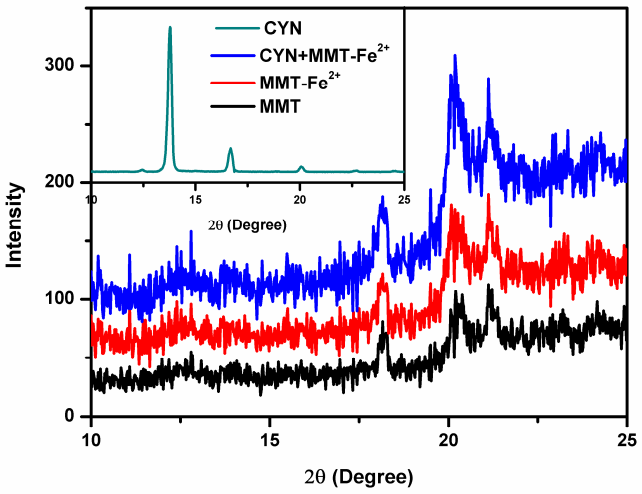

Figure 10. XRD graph of CYN, MMT, MMT-Fe^{2+} and CYN+MMT-Fe^{2+} adduct after adsorption.

Another reason for the maximum affinity of CYN with MMT-M^{2+} is the affinity of M^{2+} to form complexes (CYN-M^{2+}) with the inorganic divalent metal ions. Zaia et al. have shown that the interaction of NBs, cannot be regarded as simple physio-adsorption as NBs penetrate into the interlayer of the clays and oxidise Fe^{2+} to Fe^{3+} [77].

3.3.3. FTIR spectra

The above results were complemented by vibrational data where the possible interactive sites of CYN on MMT-Fe^{2+} were investigated by FTIR spectra (Fig. 11). The absorption frequencies lying in between 1600-1800cm^{-1} are important for sensitivity of molecular interactions between clays and nucleobases, as pyrimidines absorb strongly in this region [76]. The spectra of CYN set forth a large number of vibrational frequencies (Fig. 11a), where the IR bands at 3377.4cm^{-1} and 1651.9cm^{-1} corresponds to N-H stretching and C=O stretching respectively [45, 78], while band at 1537.4cm^{-1} points out N-H bending. Bands at 792.2cm^{-1} and 532.6cm^{-1} could be attributed to C-H and OCN deformation.

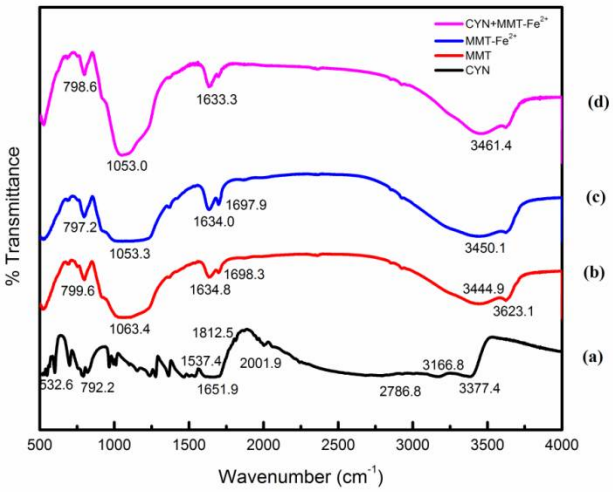

Figure 11. FT-IR spectra of (a) CYN, (b) MMT, (c) MMT-Fe^{2+} and (d) adsorption adduct, CYN + MMT-Fe^{2+} after adsorption.

Preprints (www.preprints.org) | NOT PEER-REVIEWED | Posted: 25 April 2018 doi:10.20944/preprints201804.0320.v1

In the IR spectrum of MMT the band at 3623.1cm^{-1} coincides –OH stretching and bands at 3444.9cm^{-1} and 1634.8cm^{-1} could be due to stretching and bending vibrations of water adsorbed in MMT, whereas the band at 1063.4cm^{-1} adapts Si-O-Si stretching vibration [28] (Fig. 11b). After encapsulation of Fe^{2+} ions in MMT a shift displayed in frequencies from 3444.9cm^{-1} to 3450.1cm^{-1} and 1063.4cm^{-1} to 1053.3cm^{-1} respectively, while the band at 3623.1cm^{-1} disappeared, revealing interaction of Fe^{2+} with MMT (Fig. 11c). This interaction may be due to the attractive forces between opposite charges of Fe^{2+} and the lone pair of electrons on oxygen or negative charges on silica layers binding alumina layer in between.

The IR spectrum manifests a complete sweep out of number of vibrational frequencies in the finger print region of CYN and a remarkable shift in various absorption frequencies from 3377.4cm^{-1} to 3461.4cm^{-1}, 1651.9cm^{-1} to 1633.6cm^{-1}, 792.2cm^{-1} to 798.6cm^{-1}, 532.6cm^{-1} to 526.9cm^{-1} and 440.9cm^{-1} to 466.6cm^{-1} after adsorption of CYN on MMT-Fe^{2+} (Fig. 11d) explicitly indicate the interaction of CYN to MMT-Fe^{2+} particularly via N-H and C=O bonds. These consequences are in perfect accordance with the findings reported earlier [76, 79].

4. Conclusions

The present contribution credibly evinces the illation of adsorption of CYN onto the siliceous material MMT along with its biogenic metal dications [M^{2+} = Mg^{2+}, Ca^{2+}, Fe^{2+}, Cu^{2+}] entrapped nanocomposites (MMT-M^{2+}), which was potentially found optimum at pH 6.6 and temperature 298K. Adsorption parameters and percent binding data endorse that CYN was adsorbed appreciably on MMT-Fe^{2+} followed by MMT-Cu^{2+} as compared to MMT alone and with Ca^{2+} and Mg^{2+}. As metal ions in the form of metalloenzymes are very good reflectors of biogenic activities in living systems, the results substantiate the efficacy of biogenic divalent metal ions particularly transition metal ions in prebiological adsorption processes through which concentration and condensation of biomonomers might have facilitated the formation of complex biopolymers. Moreover, during the formation of planet Earth iron was the most abundant element which might have contributed a lot in chemical evolution and origin of life [69, 70]. Our present results are also in good agreement with this scenario.

Iron is also the most abundant multivalent element in planetary reservoirs like Mars, which may record signatures of processes, occurred during the formation and subsequent differentiation of the terrestrial planets [80-83], focuses on extinct or extant life on Mars [84, 85]. Biological informational polymers such as nucleic acids have the potential to provide unambiguous evidence of life beyond Earth [86]. To summarize the most recent achievements in the field of astrobiology [87] reviews on experimental studies of space [88, 89] and on the Earth [90], as a tool for astrobiology, have also been compiled. One of the key goals of astrobiology is to explore planetary bodies of our solar system in order to determine their potential for habitability and extra-terrestrial life.

FTIR spectra emphasize that CYN interacted with Fe^{2+} encapsulated MMT through electrostatic forces via N-H and C=O bonds. XRD data insinuated that CYN interact with different sites of the clay surface, i.e., the interlayer region and the faces of the lamella showing expansion of the interlayer was greater due to the inclusion of CYN. Results demonstrate the higher affinity of MMT-Fe^{2+} interlayer for CYN. SEM observations showed the alignment of biomolecule on nanocrystalline solid and surface morphology accordingly. Henceforth, upon adsorption on mineral matrices CYN could be stabilized and protected from hazardous electromagnetic radiations directly coming from Sun in ozone free primitive environment and thus become available for successive molecular evolution.

In a wider perspective the interplay between minerals and organic molecules not only could have provided support necessary for prebiological chemical evolution, but also could modify structural and physico-chemical properties of the matrix itself, thus changing the micro environment where evolution occurs. Mineral matrices could in turn provide a new level of support in the evolutionary dynamics of prebiological systems [76]. The physico-chemical parameters of the study also deliberate several aspects of MMT nanoclay as drug carrier system with multifarious applications in biological assay.

Preprints (www.preprints.org) | NOT PEER-REVIEWED | Posted: 25 April 2018 doi:10.20944/preprints201804.0320.v1

The work provides insight into the prebiotic biogeochemical as well as biological processes such as biomineralization, biomedical implants, primigenial chemical evolution implicated to origin of first life [91, 76, 50]. The interstellar bodies also evidently endue protobiomolecules viz. amino acids, nucleic acid bases, peptides, nucleotides, lipids and extracellular polymeric substances, firmly allied with inorganic templets [92-94]. Therefore, surface interaction studies of such precious molecules on clay minerals are interesting and motivating to explore the extraterrestrial genesis and plausibility of life beyond Earth.

Supplementary Materials: The following are available online at www.mdpi.com/link, Figure S1: Standard concentration curve (optical absorbance v/s molar concentration) of cytosine.

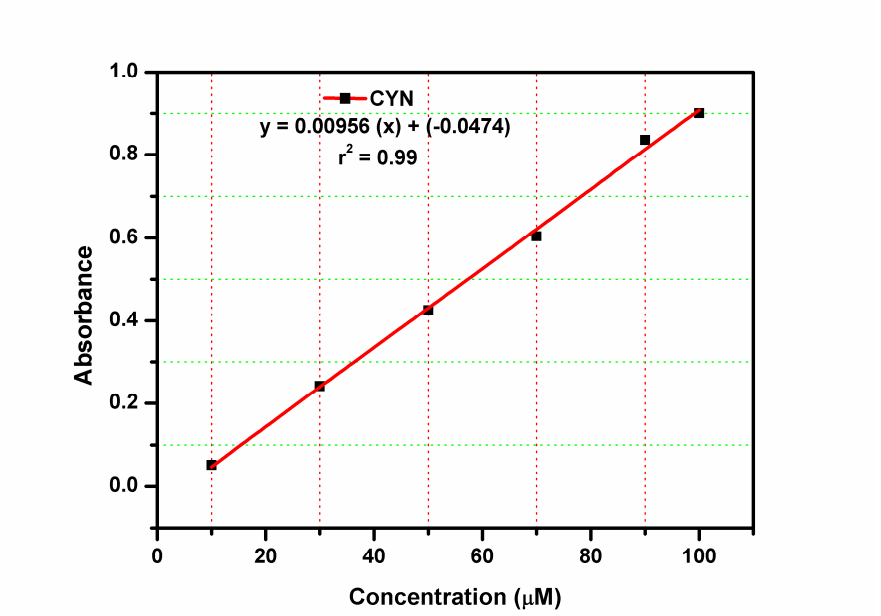

Figure S1. Standard concentration curve (optical absorbance v/s molar concentration) of cytosine.

Acknowledgments: Authors are grateful to the Head of Chemistry Department, DSB Campus, Kumaun University, Nainital 263002, Uttarakhand, India, to endow requisite research facilities and also thankful to the Department of Applied Physics, Delhi Technological University, New Delhi 110042, India, for required analysis of samples. Author P. B. is extremely thankful to EMR-I, CSIR-HRDG group (Sanction No/F.No. 09/428(0075)2K17 and ACK No. 121412/2K15/1 dated 31-3-2017), CSIR Complex, Library avenue, Pusa, New Delhi 110012, India for providing financial assistance through CSIR-SRF (Council of Scientific & Industrial Research-Senior Research Fellow) award.

Author Contributions: The manuscript was written through contributions of all authors. P.B. coordinated the experiments and wrote the manuscript. C.K.P. contributed to data interpretation and commented on the paper. C.K.P., P.P. and M.S.M. contributed equally. They reviewed and commented on the paper. All authors have reviewed and given approval to the final version of the manuscript.

Conflicts of Interest: The authors declare no conflict of interest.

References

1. N. Kitadai and S. Maruyama, Origins of building blocks of life: A review. Geoscience Frontiers, xxx (2017), 1-37.
2. T. Ebisuzaki and S. Maruyama, Nuclear geyser model of the origin of life: Driving force to promote the synthesis of building blocks of life. Geoscience Frontiers, 8 (2017), 275-298.
3. T. Hassenkam, M. P. Andersson, K. N. Dalby, D. M. A. Mackenzie and M. T. Rosing, Elements of Eoarchean life trapped in mineral inclusions. Nature, 548:7665 (2017), 78–81.

Preprints (www.preprints.org) | NOT PEER-REVIEWED | Posted: 25 April 2018 doi:10.20944/preprints201804.0320.v1

4. M. S. Dodd, D. Papineau, T. Grenne, J. F. Slack, M. Rittner, F. Pirajno, J. O'Neil and C. T. S. Little, Evidence for early life in Earth's oldest hydrothermal vent precipitates. Nature, 543:7643 (2017), 60–64.
5. K. Michaelian, Microscopic dissipative structuring and proliferation at the origin of life. Heliyon, 3:10 (2017), e00424.
6. M. C. Maurel and F. Leclerc, From foundation stones to life: Concepts and results (In tribute to J. P. Ferris). Elements, 12:6 (2016), 1811-5209.
7. N. T. Arndt and E. G. Nisbet, Processes on the young Earth and the habitats of early life. Annu. Rev. Earth Planet. Sci., 40 (2012), 521–549.
8. M. Franchi and E. Gallori, Origin, Persistence and Biological Activity of Genetic Material in Prebiotic Habitats. Orig. life evol. Biosph., 34 (2004), 133–141.
9. J. D. Bernal, The Physical Basis of Life. Routledge and Kegan Paul: London, UK, (1951), p. 364.
10. W. H. Yu, N. Li, D. S. Tong, C. H. Zhou, C. Xiang (Cynthia) Lin and C. Y. Xu, Adsorption of proteins and nucleic acids on clay minerals and their interactions: A review. Applied Clay Science, 80–81 (2013), 443-452.
11. L. Sciascia, M. L. T. Liveri and M. Merli, Kinetic and equilibrium studies for the adsorption of acid nucleic bases onto K10 montmorillonite. Applied Clay Science, 53:4 (2011), 657-668.
12. J. P. Ferris, Mineral catalysis and prebiotic synthesis: Montmorillonite-catalyzed formation of RNA. Elements, 1.3 (2005), 145–149.
13. C. De La Rocha and D. J. Conley, The origin of life was brought to you in part by silicate rocks (Ch. 2), Silica Stories, XI, 201 (2017), p. 39.
14. H. Hashizume, Adsorption of Nucleic Acid Bases, Ribose, and Phosphate by Some Clay Minerals. Life, 5 (2015), 637-650.
15. B. K. G. Theng, The Chemistry of Clay-Organic Reactions. Adam Hilger: London, UK, (1974), p. 343.
16. J. I. Dawson and R. O. C. Oreffo, Clay: New Opportunities for Tissue Regeneration and Biomaterial Design. Adv. Mater., 25 (2013), 4069–4086.
17. C. Aguzzi, P. Cerezo, C. Viseras and C. Caramella, Use of clays as drug delivery systems: Possibilities and limitations. Applied Clay Science, 36 (2007), 22-36.
18. B. Gre´goire, V. Erastova, D. L. Geatches, S. J. Clark, H. C. Greenwell and D. G. Fraser, Insights into the behaviour of biomolecules on the early Earth: The concentration of aspartate by layered double hydroxide minerals. Geochimica et Cosmochimica Acta, 176 (2016), 239–258.
19. U. Pedreira-Segade, C. Feuillie, M. Pelletier, L. J. Michot and I. Daniel, Adsorption of nucleotides onto ferromagnesian phyllosilicates: Significance for the origin of life. Geochimica et Cosmochimica Acta, 176 (2016), 81–95.
20. J. R. Michalski, J. Cuadros, J. L. Bishop, M. D. Dyar, V. Dekov and S. Fiore, Constraints on the crystal-chemistry of Fe/Mg-rich smectitic clays on Mars and links to global alteration trends. Earth and Planetary Science Letters, 427 (2015) 215–225.
21. G. Ertem and J. P. Ferris, Sequence- and regio-selectivity in the montmorillonite-catalyzed systems of RNA. Orig. Life Evol. Biosph., 30 (2000), 411–422.
22. G. Ertem and J. P. Ferris, Synthesis of RNA oligomers on heterogenous templates. Nature, 379 (1996), 238–240.
23. P. C. Joshi, M. F. Aldersley, J. W. Delano and J. P. Ferris, Mechanism of montmroillonite catalysis in the formation of RNA oligomers. J. Am. Chem. Soc., 131 (2009), 13369–13374.
24. E. M. Pecini and M. J. Avena, Measureing the isoelectric point of the edges of clay mineral particles: The case of montmorillonite. Langmuir, 29 (2013), 14926–14934.
25. S. Kalra, C. K. Pant, H. D. Pathak and M. S. Mehata, Studies on the adsorption of peptides of glycine/alanine on montmorillonite clay with or without co-ordinated divalent cations. Colloids and Surfaces A: Physicochem. Eng. Aspects, 212 (2003), 43–50.
26. C. K. Pant, H. Lata, H. D. Pathak and M. S. Mehata, Heat-initiated prebiotic formation of peptides from glycine/aspartic acid and glycine/valine in aqueous environment and clay suspension. Int. J. Astrobiol., 8:2 (2009), 107–115.
27. K. Gururani, C. K. Pant, N. Pandey and P. Pandey, Heat induced formation of peptides from reaction mixture of glycine-glutamic acid and glycine-leucine in presence and absence of montmorillonite clay with or without metal ions under wetting drying cycles of primitive Earth. Int. J. Scie. Techno. Res., 1:8 (2012), 159–163.

Preprints (www.preprints.org) | NOT PEER-REVIEWED | Posted: 25 April 2018 doi:10.20944/preprints201804.0320.v1

28. P. Pandey, C. K. Pant, K. Gururani, P. Arora, N. Pandey, P. Bhatt, Y. Sharma, J. S. Negi and M. S. Mehata, Affinity of smectite and divalent metal ions (Mg2+, Ca2+, Cu2+) with L-leucine: An experimental and theoretical approach relevant to astrobiology. Orig. Life Evol. Biosph., 45 (2015), 411–426.
29. R. J. P. Williams, Systems biology of evolution: the involvement of metal ions. BioMetals, 20:2 (2007), 107–112.
30. C. Andreini, I. Bertini, G. Cavallaro, G. L. Holliday and J. M. Thornton, Metal ions in biological catalysis: From enzyme databases to general principles. Journal of Biological Inorganic Chemistry, 13:8 (2008), 1205–1218.
31. M. Kleczkowski and M. Garncarz, The role of metal ions in biological oxidation- the past and the present. Polish Journal of Veterinary Sciences, 15:1 (2012),165–173.
32. M. Franchi, J. P. Ferris, and E. Gallori, Cations as mediators of the adsorption of nucleic acids on clay surfaces in prebiotic environments, Orig. Life Evol. Biosph., 33 (2003), 1–16.
33. W. Maret, The Metals in the biological periodic system of the elements: Concepts and conjectures. Int. J. Mol. Sci., 17 (2016), 66.
34. L. Belmonte and S. S. Mansy, Metal catalysts and the origin of life. Elements, 12.6 (2016), 413–418.
35. M. Paecht-Horowitz, The influence of various cations on the catalytic properties of clays. Journal of Molecular Evolution, 11.2 (1978), 101–107.
36. P. Mignon, P. Ugleingo and M. Sodupe, Theoretical study of the adsorption of RNA/DNA bases on the external surfaces of Na+-montmorillonite. J. Phys. Chem. C, 113 (2009), 13741–13749.
37. D. C. Mathew and Z. Luthey-Schulten, Influence of montmorillonite on nucleotide oligomerization reactions: A molecular dynamics study. Orig. Life Evol. Biosph., 40 (2010), 303–317.
38. J. B. Swadling, P. V. Coveney, and H. C. Greenwell, Clay minerals mediate folding and regioselective interactions of RNA: A large-scale atmistic simulation study. J. Am. Chem. Soc., 132 (2010), 13750–13764.
39. S. Mukhopadhyay, S. Gowtham, R. H. Scheicher, R. Pandey and S. P. Karna, Theoretical study of physisorption of nucleobases on boron nitride nanotubes: A new class of hybrid nano-biomaterials. Nanotechnology, 21 (2010), 165703, 6pp.
40. Ö. Güllü and A. Türüt, Electronic properties of Cu/n-InP metal semiconductor structures with cytosine biopolymer. Acta Physica Polonica A, 128 (2015), 383-388.
41. R. N. Gonzalez and C. Ponnamperuma, Role of trace metal ions in chemical evolution: The case of free radical reactions. Advances in Space Research, 15:3 (1995), 357–364.
42. J. F. Lambert, Adsorption and polymerization of amino acids on mineral surfaces: A review. Orig. Life Evol. Biosph., 38 (2008), 211–242.
43. G. E. Lailach, T. D. Thompson and G. W. Brindley, Adsorption of pyrimidines, purines, and nucleosides by Li-, Na-, Mg-, and Ca-montmorillonite (Clay-Organic Studies XII) clays. Clay Miner., 16 (1968a), 285–293.
44. G. E. Lailach, T. D. Thompson and G. W. Brindley, Adsorption of pyrimidines, purines, and nucleosides by Co-, Ni-, Cu-, and Fe(III)- montmorillonite (Clay-Organic Studies XIII) clays. Clay Miner., 16 (1968b), 295–301.
45. L. O. B. Benetoli, H. de Santana, C. T. B. V. Zaia and D. A. M. Zaia, Adsorption of nucleic acid bases on clays: An investigation using Langmuir and Freundlich isotherms and FT-IR spectroscopy. Monatsh. Chem., 139 (2008), 753–761.
46. L. Perezgasga, A. Serrato-Díaz, A. Negron-Mendóza, L. D. Galán and F. G. Mosqeira, Sites of adsorption of adenine, uracil and their corresponding derivatives on sodium montmorillonite. Orig. Life Evol. Biosph., 35 (2005), 91–110.
47. D. Winter and G. Zubay, Binding of adenine and adenosine-related compounds to the clay montmorillonite and the mineral hydroxyapatite. Orig. Life Evol. Biosph., 25 (1995), 61–81.
48. H. Hashizume, S. van der Gaast and B. K. G. Theng, Adsorption of adenine, cytosine, uracil, ribose, and phosphate by Mg-exchanged montmorillonite. Clay Miner., 45 (2010), 469–475.
49. P. Bhatt, C. K. Pant, Hemlata, S. C. Sati, Adsorption of bionanomolecule on clay minerals in relevance to chemistry-biology interfacial phenomenon. J. Chem. Eng. Chem. Res., 3:11 (2016), 1075-1078.
50. H. J. Cleaves II, A. M. Scott, F. C. Hill, J. Leszczynski, N. Sahai, R. Hazen, Mineral–organic interfacial processes: Potential roles in the origins of life. Chem. Soc. Rev. 41 (2012), 5502–5525.
51. S. Jayrajsinh, G. Shankar, Y. K. Agrawal and L. Bakre, Montmorillonite nanoclay as a multifaceted drug delivery carrier: A review. Journal of Drug Delivery Science and Technology, 39 (2017), 200-209.

Preprints (www.preprints.org) | NOT PEER-REVIEWED | Posted: 25 April 2018 doi:10.20944/preprints201804.0320.v1

52. I. Calabrese, G. Gelardi, M. Merli, M. L. T. Liveri and L. Sciascia, Clay-biosurfactant materials as functional drug delivery systems: Slowing down effect in the in vitro release of cinnamic acid. Applied Clay Science, 135 (2017), 567-574.
53. M. A. Alavijeh, M. N. Sarvi and Z. R. Afarani, Properties of adsorption of vitamin B12 on nanoclay as a versatile carrier. Food Chemistry, 219 (2017), 207-214.
54. P. Thevenot, W. J. Hu and L. P. Tang, Surface chemistry influences implant biocompatibility. Current Topics in Medicinal Chemistry, 8 (2008), 270–280.
55. M. A. Meyers, Po-Yu Chen, A. Yu-Min Lin and Y. Seki, Biological materials: Structure and mechanical properties. Progress in Materials Science, 53 (2008), 1–206.
56. B. Basile, A. Lazcano and J. Oró, Prebiotic syntheses of purines and pyrimidines, Advances in Space Research, 4:12 (1984), 125–131.
57. M. P. Robertson and S. L. Miller, An efficient prebiotic synthesis of cytosine and uracil, Nature, 375:6534 (1995), 772–774.
58. C. Menor-Salván, M. Ruiz-Bermejo, M. I. Guzmán, S. Osuna-Esteban and S. Vintemillas-Verdaguer, Synthesis of pyrimidines and triazines in ice: Implications for the prebiotic chemistry of nucleobases. Chemistry: A European Journal Weinheim, Germany, 15:17 (2009), 4411–4418.
59. P. Chellan and P. J. Sadler, The elements of life and medicines, Philos. Trans. R. Soc., A373 (2015), 21040182.
60. K. P. Carter, A. M. Young, and A. E. Palmer, Fluorescent Sensors for Measuring Metal Ions in Living Systems. Chem. Rev., 114 (2014), 4564−4601.
61. J. Anastassopoulou and T. Theophanides, The role of metal ions in biological systems and medicine, Bioinorganic Chemistry, Kluwer Academic Publishers (ASIC, volume 459) D.P. Kessissoglou (ed.), (1995), 209-218.
62. A. Parbhakar, J. Cuadros,M. A. Sephton, W. Dubbin, B. J. Coles and D. Weiss, Adsorption of L-lysine on montmorillonite. Colloids and Surfaces A: Physicochem. Eng. Aspects, 307 (2007), 142-149.
63. V. Singh, B. I. Fedeles and J. M. Essigmann, Role of tautomerism in RNA biochemistry: A review. RNA, 21 (2014), 1–13.
64. R. Krishnamurthy, Role of pKa of nucleobases in the origins of chemical evolution. Accounts of Chemical Research , 45: 12 (2012), 2035–2044.
65. Y. Gounaris, C. Litinas and E. Evgenidou, A possible prebiotic function of cytosine as amino acid synthesizer. Hypothesis, 12:1 (2014), e5, doi:10.5779/hypothesis.v12i1.369.
66. I. Langmuir, The adsorption of gases on plane surfaces of glass, mica and platinum. J. Am. Chem. Soc., 40 (1918), 1361-1403.
67. A. H. Herz, R. P. Danner and G. A. Janussonis, Adsorption from aqueous solution [Adv. Chem. Ser., No. 79] Am. Chem. Soc., Washington DC, (1968) p.173.
68. T. Fornaro, J. R. Brucato, A. Pucci and S. Branciamore, Planetary and Space Science, 86 (2013), 75.
69. K. G. Taylor and K. O. Konhauser, Iron in Earth surface systems: A major player in chemical and biological processes. Elements, 7:2 (2011), 83–88.
70. N. R. Posth, D. E. Canfield and A. Kappler, Biogenic Fe(III) minerals: From formation to diagenesis and preservation in the rock record. Earth-Science Reviews, 135 (2014), 103–121.
71. T. Fornaro, J. R. Brucato, S. Branciamore and A. Pucci, International Journal of Astrobiology, 12 (2013), 78.
72. T. Fornaro, I. Carnimeo and M. Biczysko, J. Phys. Chem. A, 119:21 (2015), 5313.
73. T. Gustavsson, Á. Bányász, E. Lazzarotto, D. Markovitsi, G. Scalmani, M. J. Frisch, V. Barone and R. Improta, J. Am. Chem. Soc., 128 (2006), 607.
74. T. Fornaro, D. Burini, M. Biczysko and V. Barone, J. Phys. Chem. A, 119:18 (2015), 4224.
75. I. Calabrese, G. Cavallaro, C. Scialabba, M. Licciardi, M. Merli, M. Liria and T. Liveri, International Journal of Pharmaceutics, 45 (2013), 224–236.
76. A. Pucci, S. Branciamore, M. Casarosa, L. P. D'Acqui and E. Gallori, Implications for an RNA-clay world: Interaction of cytosine with clay minerals. Journal of Cosmology, 10 (2010), 3398-3407.
77. C. E. A. Carneiro, G. Berndt, I. G. de S. Souza, C. M. D. de Souza, A. Jr. Paesano, A. C. S. da Costa, E. di Mauro, H. de Santana, C.T.B.V. Zaia and D. A. M. Zaia, Orig. Life Evol. Biosph., 41 (2011), 453-468.
78. T. Yamada, K. Shirasaka, A. Takano and M. Kawai, Adsorption of cytosine, thymine, guanine and adenine on Cu (10) studied by infrared reflection absorption spectroscopy. Surf. Sci., 561 (2004), 233.

Preprints (www.preprints.org) | NOT PEER-REVIEWED | Posted: 25 April 2018 doi:10.20944/preprints201804.0320.v1

79. J. P. Ferris, G. Ertem and V. Agarwal, Mineral catalysis of the formation of dimers of 5′-AMP in aqueous solution: The possible role of montmorillonite clays in the prebiotic synthesis of RNA. Orig. Life Evol. Biosph., 19:2 (1989), 165-178.
80. P. A. Sossi, O. Nebel, M. Anand and F. Poitrasson. On the iron isotope composition of Mars and volatile depletion in the terrestrial planets, Earth and Planetary Science Letters, 449 (2016), 360–371.
81. P. Craig, V. Chevrier, M. R. G. Sayyed and R. Islam, Spectral analysis of Deccan intrabasaltic bole beds: Implications for the formation and alteration of phyllosilicates on Mars. Planetary and Space Science, 135 (2017), 55–63.
82. M. Anand, S. S. Russell, R. L. Blackhurst, M. M. Grady, Searching for signatures of life on Mars: An Fe-isotope perspective. Phil. Trans. R. Soc. B, 361 (2006), 1715–1720.
83. P. Pandey, C. K. Pant, K. G., P. Arora, S. Kumar, Y. Sharma, H. D. Pathak and M. S. Mehata, Surface interaction of L-alanine on Hematite: An astrobiological implication. Orig. Life Evol. Biosph., 43 (2013), 331–339.
84. F. Westall, F. Foucher, N. Bost, M. Bertrand, D. Loizeau, J. L. Vago, G. Kminek, F. Gaboyer, K. A. Campbell, J.-B. Bréhéret, P. Gautret and C. S. Cockell, Biosignatures on Mars: what, where and how? Implications for the search for Martian life. Astrobiology, 15 (2015), 998–1029.
85. J. F. Banfield, J. W. Moreau, C. S. Chan, S. A. Welch and B. Little, Mineralogical biosignatures and the search for life on Mars. Astrobiology, 1:4 (2001), 447–465.
86. A. Mojarro, G. Ruvkun, M. T. Zuber and C. E. Carr, Nucleic acid extraction from synthetic Mars analog soils for in situ life detection. Astrobiology, 17:8 (2017), 747–760.
87. H. Cottin, J. M. Kotler, K. Bartik, H. J. Cleaves, C. S. Cockell, J-P. P. de Vera, P. Ehrenfreund, S. Leuko, I. L. ten Kate, Z. Martins, R. Pascal, R. Quinn, P. Rettberg and F. Westall, Astrobiology and the Possibility of Life on Earth and Elsewhere. Space Sci. Rev. (2015). doi:10.1007/s11214-015-0196-1
88. G. Horneck et al., AstRoMap European Astrobiology Roadmap. Astrobiology, 16 (2016), 201–243.
89. H. Cottin, J. M. Kotler, C. S. Cockell, R. Demets, P. Ehrenfreund, A. Elsaesser, L. d'Hendecourt, J. van Loon, Z. Martins, S. Onofri, R. Quinn, E. Rabbow, P. Rettberg, A. J. Ricco, K. Slenzka, R. de la Torre, J.-P. de Vera, F. Westall, N. Carrasco, A. Fresneau, Y. Kawaguchi, Y. Kebukawa, D. Nguyen, O. Poch, K. Saiagh, F. Stalport, A. Yamagishi, H. Yano and B. A. Klamm, Space as a tool for astrobiology: Review and recommendations for experimentations in Earth orbit and beyond. Space Sci. Rev. (2017). doi:10.1007/s11214-017-0365-5
90. Z. Martins, H. Cottin, J. M. Kotler, N. Carrasco, C. S. Cockell, R. de la T. Noetzel, R. Demets, J.-P. de Vera, L. d'Hendecourt, P. Ehrenfreund, A. Elsaesser, B. Foing, S. Onofri, R. Quinn, E. Rabbow, P. Rettberg, A. J. Ricco, K. Slenzka, F. Stalport, I. L. ten Kate, J. J. W. A. van Loon and F. Westall, Earth as a tool for astrobiology—A european perspective. Space Sci. Rev., 209 (2017), 43–81.
91. E. Greiner, K. Kumar, M. Sumit, A. Giuffre, W. Zhao, J. Pedersen and N. Sahai, Adsorption of L-glutamic acid and L-aspartic acid to γ-Al2O3. Geochimica et Cosmochimica Acta, 133 (2014), 142–155.
92. V. K. Pearson, M. A. Sephton, A. T. Kearsley, P. A. Bland, I. A. Franchi and I. Gilmour, Clay mineral–organic matter relationships in the early solar system. Meteorit. Planet. Sci., 37 (2002), 1829-1833.
93. Z. Martins, O. Botta and M. L. Fogel, et al. Extraterrestrial nucleobases in the Murchison meteorite. Earth and Planetary Science Letters. Amsterdam, the Netherlands: Elsevier, 270:1–2 (2008), 130–136.
94. Y. Kebukawa, Q. H. S. Chan, S. Tachibana, K. Kobayashi and M. E. Zolensky, One-pot synthesis of amino acid precursors with insoluble organic matter in planetesimals with aqueous activity. Sci. Adv., 3 (2017), e1602093.

International Journal of Technical Innovation in Modern Engineering & Science (IJTIMES)
Impact Factor: 3.45 (SJIF-2015), e-ISSN: 2455-2585
Volume 4, Issue 03, March-2018

STATISTICAL ANALYSIS OF RESERVOIR INDUCED SEISMICITY AT A RESERVOIR SITE

Munendra Kumar[1*], T. Vijaya Kumar[2], Saurabh Sah[3]

[1'2] *Associate Professor Department of civil engineering, Delhi Technological University, Delhi, India*
[3] *Research Scholar Department of civil engineering, Delhi Technological University, Delhi, India*

ABSTRACT: This paper presents a statistical probability method to find the probability of a particular intensity of earthquake at a reservoir site which can be used to assign degree of risk associated with the site. Reservoir impoundment at certain sites leads to increase seismicity at the site which makes the structures in the vicinity of the reservoir vulnerable to earthquake forces which might not have been considered according to conventional seismic design, thus it becomes important to include the effect of Reservoir Induced Seismicity (RIS) in the design of structure which are in proximity to the reservoir site. So we are presenting a modified earthquake design for a site which is suspected to be in the category of RIS by using additional parameters along with conventional parameters of earthquake design. The nature of our design where seismicity have been induced due to reservoir impoundment is a slightly different from tectonic earthquake design considering the fact that this particular design is well supplemented with a rational statistical analysis hence requiring us to design the structures for increased design forces to fulfil the basic earthquake design criteria.

Keywords: - Bayes conditional probability, Proximity factor, RIS factor, Statistical probability, Reservoir Induced Seismicity.

INTRODUCTION

Purpose

The purpose of this paper is to provide guidance for designing structures at a reservoir site both normal occupancy structures and important structures (hydraulic, building, hospitals etc.). Since finding suitable sites for dams is very difficult task in itself hence it might not be possible to reject a site just on the basis of RIS. Hence it will be more practical to follow a modified earthquake design to ensure the safety of a structure that is going to be constructed near a reservoir site.

Scope

A rational statistical work has been proposed to analyze the nature, causes and intensity of Reservoir induced seismicity.

(a) To present a statistical probability method giving probability of a particular intensity of earthquake at a reservoir site using data of reservoir sites experiment this phenomena in the past.
(b) To formulate Risk factor associated with a reservoir site using probability and energy of a particular magnitude of earthquake.
(c) To formulate RIS factor and proximity factor to be included in the seismic design.

LITERATURE REVIEW

The first incidence of reservoir induced seismicity was observed as early as 1931 in Marathon reservoir of Greece. As of today, over 90 sites have been globally identified where earthquakes have been triggered by filling of water reservoirs. The phenomenon of earthquakes induced due to impoundment of reservoirs has been addressed and reviewed in a number of paper and books. The most significant contribution in this field is by a leading Harsh Kumar

Gupta [1] who defines the occurrence as: "earthquake occurring in the vicinity of artificial water reservoir as a consequence of impoundment." (Gupta, H.K, 2002)

The study conducted by H K Gupta [2] highlights the following points:

1. Depth of water in the reservoir and the volume of water play an important role in triggering an earthquake.
2. One characteristic of RIS is that the magnitude of the foreshock is higher than the magnitude of the aftershock and both values are generally higher than in cases of natural earthquakes.
3. The effect of RIS can be rapid (following the initial impoundment of reservoir) or delayed (Occurring later in the life of reservoir).

Another study was done by Jauhari V.P to find out the mechanism of RIS. He wrote the following about RIS in a paper prepared for the world commission on Dams. "The most widely accepted explanation of how dams cause earthquakes is related to the extra Water pressure created in the micro-cracks and fissures [5] in the ground under and near a reservoir. When the pressure of water in the rocks increases it acts to lubricate faults which are already under tectonic strain but are prevented from slipping by the friction of the rock surfaces."

METHODOLOGY ADOPTED

1. Use of statistical probability and bays conditional probability theory to find the probability of a particular intensity of earthquake at a reservoir site.
2. Development of risk factor using probability and energy of earthquake.
3. Classification of a reservoir site with reference to low, moderate and high risk.
4. To propose the seismic design changes for normal occupancy structures and important structures at a reservoir site.

FACTORS AFFECTING RESERVOIR INDUCED SEISMICITY

Using study conducted in the past it can be deduced that not all reservoirs are capable of triggering seismicity in an area instead there are certain geological, tectonic, and reservoir characteristics [3] whose mutual interaction results in enhanced seismic response of the reservoir site. There are seven factors considered in this study:

1. Depth of reservoir water
2. Geological condition in the reservoir area.
3. Tectonic stress environment
4. Fault activity
5. Karst development degree
6. Communication relationship with reservoir water.
7. Earthquake activity background.

Table 1: Influencing factors for reservoir induced seismicity

Influencing factors	**1**	**2**	**3**
Depth of reservoir water(D)	Less than 100m	100-150m	Greater than 150m
Geological condition in the reservoir area.(G)	Blocked rock mass	Stratified rock mass	Carbonate rock mass
Tectonic stress environment(S)	Reverse fault environment	Normal fault environment	Strike -Slip fault environment
Fault activity(F)	Activity	Inactivity	…….
Karst development degree(K)	Strong	Weak	No karst
Communication relationship with reservoir water	Contact directly	Contact indirectly but with communication	No communication
Earthquake activity background	Strong	medium	Weak

STATISTICAL ANALYSIS OF RESERVOIR DATA

This part includes the reservoir characteristics of ninety reservoirs from all over the world which have experienced the phenomena of reservoir induced seismicity in the past.

Table 1: Factors affecting reservoir induced seismicity

Reservoir/ Dam	Height	Magnitude	Site Coordinate	Reservoir/ Dam	Height	Magnitude	Site Coordinate
Hsinfengkiang	105	6.10	$D_2G_1S_3F_1K_3C_1E_2$	Dhamni	59	3.80	$D_3G_2S_2F_1K_3C_2E_3$
Kariba	128	6.20	$D_2G_1S_3F_1K_3C_1E_1$	Donjiang	157	3.20	$D_1G_1S_3F_1K_3C_3E_3$
Koyna	103	6.30	$D_2G_1S_3F_1K_3C_1E_2$	Emborcacao	158	3.01	$D_1G_1S_3F_1K_3C_2E_2$
Kremasta	160	6.20	$D_2G_3S_2F_2K_1C_2E_1$	Emmosson	180	3.00	$D_1G_3S_3F_1K_1C_2E_3$
Aswan	111	5.60	$D_2G_3S_3F_1K_1C_1E_1$	Fierza	167	3.00	$D_1G_2S_3F_1K_2C_1E_2$
Benmore	110	5.00	$D_2G_2S_3F_1K_2C_3E_2$	Gandipe	36	3.50	$D_3G_3S_3F_2K_1C_1E_3$
Charvak	148	5.30	$D_2G_3S_1F_2K_1C_2E_2$	Grancarevo	123	3.00	$D_2G_2S_3F_1K_2C_1E_2$
Eucumbene	116	5.00	$D_2G_2S_2F_1K_1C_1E_2$	HendrikVerwo	66	3.00	$D_3G_3S_3F_2K_1C_2E_3$
Geheyan	151	4.00	$D_1G_3S_1F_1K_2C_1E_3$	Huangshi	40	3.00	$D_3G_1S_1F_2K_3C_3E_1$
Hoover	221	5.00	$D_1G_1S_3F_1K_3C_1E_2$	Hunanzhen	129	3.00	$D_2G_1S_3F_1K_3C_1E_3$
Marathon	67	5.70	$D_3G_1S_1F_2K_2C_3E_3$	Idukki	169	3.50	$D_1G_1S_2F_1K_3C_3E_2$
Oroville	236	5.70	$D_1G_2S_2F_1K_2C_1E_1$	Itezhitezhi	65	3.80	$D_3G_1S_3F_2K_3C_3E_3$
Srinagarind	140	5.90	$D_2G_3S_3F_1K_1C_1E_2$	Jocasse	107	3.20	$D_2G_1S_3F_1K_3C_2E_3$
Warna	80	5.00	$D_3G_1S_3F_1K_1C_1E_1$	Kamafusa	47	3.00	$D_3G_2S_3F_1K_2C_2E_2$
Aksombo Main	136	5.00	$D_2G_1S_3F_2K_3C_3E_3$	Katse	185	3.10	$D_1G_3S_1F_2K_1C_1E_1$
BajinaBasta	90	4.5-5	$D_3G_2S_3F_1K_2C_2E_2$	Keban	212	3.50	$D_1G_2S_2F_1K_2C_2E_2$
Bhatsa	88	4.90	$D_3G_1S_2F_1K_1C_1E_3$	Kouris	124	3.00	$D_2G_2S_3F_1K_2C_3E_2$
Brastk	100	4.20	$D_2G_1S_2F_1K_3C_2E_1$	Kurupsai	100	3.00	$D_2G_1S_3F_1K_3C_2E_2$
Camarillas	49	4.10	$D_3G_3S_1F_2K_1C_3E_3$	Lake Gordon	140	3.00	$D_2G_1S_3F_1K_3C_2E_3$
Canelles	150	4.70	$D_1G_2S_2F_2K_2C_1E_3$	LG 3	80	3.70	$D_3G_3S_3F_2K_1C_1E_2$
CapivariCachore	58	6.00	$D_3G_2S_3F_1K_2C_2E_2$	Lubuge	103	3.40	$D_2G_1S_1F_3K_2C_2E_2$
Clark Hill	60	4.30	$D_3G_2S_1F_1K_1C_1E_2$	Makio	105	3.00	$D_2G_1S_1F_1K_3C_3E_1$
Dahua	74.5	4.50	$D_3G_2S_3F_2K_3C_3E_3$	Monticello	129	3.00	$D_2G_1S_1F_1K_3C_3E_1$
Danjiangkou	97	4.70	$D_3G_3S_3F_2K_2C_1E_3$	Mula	56	3.00	$D_3G_3S_2F_2K_1C_1E_3$
Foziling	74	4.50	$D_3G_3S_3F_2K_1C_2E_3$	Nagawado	155	3.00	$D_2G_1S_3F_1K_3C_1E_3$
Grandval	88	5.00	$D_1G_2S_1F_2K_3C_3E_3$	Nanchong	45	3.00	$D_3G_2S_1F_1K_2C_2E_2$
HoaBinh	125	4.90	$D_2G_3S_3F_1K_1C_2E_2$	Nanshui	81	3.00	$D_3G_1S_2F_2K_3C_3E_2$
Kastraki	96	4.60	$D_3G_2S_2F_1K_2C_1E_1$	Novo Ponte	48	3.70	$D_3G_1S_3F_2K_3C_3E_3$
Kerr	60	4.90	$D_1G_1S_3F_1K_2C_2E_2$	OuedFodda	101	3.00	$D_2G_2S_3F_1K_2C_2E_3$
Komani	130	4.20	$D_2G_1S_3F_2K_3C_1E_2$	Paraibuna	94/105	3.00	$D_2G_1S_3F_1K_3C_1E_3$

Kurobe	186	4.90	$D_1G_3S_3F_1K_1C_1E_2$	Qianjin	50	3.00	$D_3G_1S_3F_2K_3C_2E_3$
Lake Baikal	160	4.0-4.8	$D_1G_2S_2F_1K_2C_1E_2$	Ridracoli	103	3.50	$D_2G_1S_3F_1K_3C_1E_2$
Lake Pukaki	106	4.60	$D_2G_1S_2F_1K_3C_1E_3$	Salanfe	165	2.50	$D_1G_3S_2F_1K_1C_1E_2$
Manicouagan 3	108	4.10	$D_2G_2S_1F_1K_2C_2E_3$	Schlegeis	117	2.00	$D_2G_1S_3F_1K_3C_3E_2$
Marimbondo	94	4.00	$D_3G_3S_1F_2K_3C_1E_2$	Shasta	183	3.00	$D_1G_3S_3F_2K_1C_1E_2$
Monteynard	155	4.90	$D_1G_3S_2F_1K_1C_1E_1$	Shengjiaxia	35	3.60	$D_3G_1S_3F_1K_3C_3E_2$
Nurek	317	4.60	$D_1G_3S_3F_1K_1C_1E_2$	Shuikou	101	3.20	$D_2G_3S_2F_1K_1C_2E_2$
P. Colombia	40/56	4.20	$D_3G_2S_2F_1K_3C_2E_3$	Sobradinho	43	3.00	$D_3G_1S_3F_1K_3C_2E_1$
Piastra	93	4.40	$D_3G_2S_1F_2K_1C_1E_2$	Sriramsagar	43	3.20	$D_3G_2S_3F_2K_2C_3E_2$
Pieve de Cadore	116	5.00	$D_2G_2S_2F_1K_2C_1E_3$	Talbingo	162	3.50	$D_1G_1S_1F_2K_3C_1E_3$
Shenwo	50	4.80	$D_3G_3S_3F_2K_2C_1E_2$	Thomson	153	3.00	$D_1G_2S_2F_1K_3C_2E_3$
Vouglans	130	4.40	$D_2G_2S_2F_1K_2C_2E_3$	Toktogul	215	3.00	$D_1G_3S_3F_1K_3C_2E_3$
Acu	31	3.00	$D_3G_1S_3F_1K_1C_2E_2$	Tongjiezi	74	3.00	$D_3G_2S_2F_2K_1C_1E_3$
Blowering	112	3.50	$D_2G_1S_3F_1K_3C_2E_2$	Tucurui	100	3.40	$D_2G_1S_1F_2K_3C_1E_2$
Capivara	59	3.70	$D_3G_1S_3F_2K_3C_1E_2$	Vajont	262	3.00	$D_1G_1S_3F_1K_3C_1E_2$
Carmo doCajuru	22	3.70	$D_3G_3S_2F_2K_1C_1E_3$	Zhelin	62	3.20	$D_3G_2S_3F_1K_2C_1E_3$
Contra	220	3.00	$D_1G_1S_1F_2K_1C_1E_2$	Wujiangdu	165	3.00	$D_1G_3S_3F_1K_1C_1E_2$
				Yantan	110	3.50	$D_2G_3S_3F_1K_1C_2E_2$

Table 2: Probability of a particular intensity of earthquake

Earthquake category	Probability of occurrence
Strong (M_6)	0.04
Moderate strong (M_5)	0.11
Moderate (M_4)	0.29
Small (M_3)	0.55

Table 3: Conditional probability for M>6

Site condition	1	2	3
Depth of reservoir water(D)	0.25	0.75	0.0
Geological condition in the reservoir area (G)	0.75	0.0	0.25
Tectonic stress environment(S)	0.0	0.25	0.75
Fault activity (F)	0.75	0.25	0.0
Karst development degree(K)	0.25	0.0	0.75

Communication relationship with reservoir water	0.75	0.25	0.0
Earthquake activity background	0.5	0.5	0.0
Depth of reservoir water(D)	0.3	0.5	0.2
Geological condition in the reservoir area.(G)	0.3	0.3	0.4
Tectonic stress environment(S)	0.2	0..2	0.6
Fault activity(F)	0.8	0.2	0.0
Karst development degree(K)	0.4	0.4	0.2
Communication relationship with reservoir water	0.7	0.1	0.2
Earthquake activity background	0.3	0.5	0.2

Table 4: Conditional probability for 4<M<5

Site condition	1	2	3
Depth of reservoir water(D)	0.32	0.28	0.39
Geological condition in the reservoir area.(G)	0.21	0.46	0.32
Tectonic stress environment(S)	0.18	0.36	0.46
Fault activity(F)	0.71	0.28	0.0
Karst development degree(K)	0.28	0.43	0.28

Table 5: Conditional probability for 3<M<4

Site condition	**1**	**2**	**3**
Depth of reservoir water(D)	0.35	0.29	0.36
Geological condition in the reservoir area.(G)	0.52	0.19	0.29
Tectonic stress environment(S)	0.63	0.19	0.17
Fault activity(F)	0.57	0.42	
Karst development degree(K)	0.31	0.23	0.46
Communication relationship with reservoir water	0.36	0.41	0.21
Earthquake activity Background	0.06	0.52	0.42

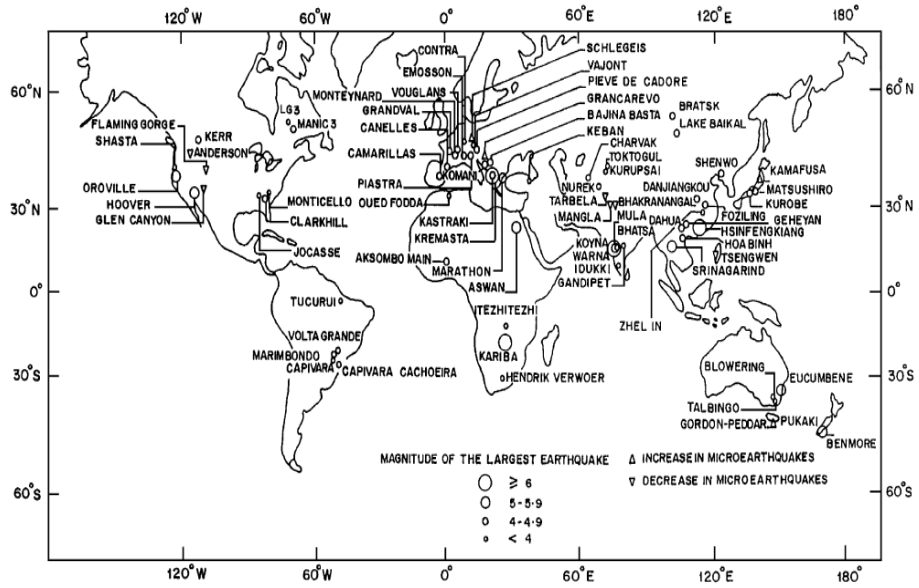

Fig. 1. Worldwide distribution of reservoir-triggered changes in the seismicity. The figure is updated from Gupta (1992) to include all sites where triggered earthquakes of $M>4$ occurred. Sites where RTS events of $M<4$ occurred are too numerous and not updated. For details, please see Table 1.

Figure 1: seismicity induced sites in the world

APPLICATION OF THE ANALYSIS TO A RESERVOIR WITH ASSUMED GEOLOGICAL, TECTONIC, AND RESERVOIR CHARACTERISTICS

According to bayes conditional probability theory [4] the statistical model for predicting reservoir seismicity is:

$$P(Mi/Di,Gi,Si,Fi,Ki,Ci,Ei)=[P(Mi)P(Di,Gi,Si,Fi,Ki,Ci,Ei/Mi)]\div[\sum P(Mi)P(Di,Gi,Si,Fi,Ki,Ci,Ei/Mi)] \quad (1.1)$$

Where,

$P(Di,Gi,Si,Fi,Ki,Ci,Ei/Mi)=P(Di/Mi)P(Gi/Mi)P(Si/Mi)P(Fi/Mi)P(Ki/Mi)P(Ci/Mi)P(Ei/Mi)P(Mi/Di,Gi,Si,Fi,Ki,Ci,Ei)$is the probability of an earthquake of magnitude of intensity Mi under given condition of depth of reservoir ,geological condition in the reservoir area ,tectonic stress environment,faultactivity,Karst development degree, communication relationship with reservoir waterand activity background.

- P (Mi) is the probability of earthquake of magnitude Mi.
- P (Di,Gi,Si,Fi,Ki,Ci,Ei/Mi) is the probability of given conditions of depth of reservoir, geological condition in the reservoir area ,tectonic stress environment, fault activity,Karst development degree, communication relationship with reservoir water and activity background such that they have triggereda earthquake of magnitude M in the past.
- P(Di/Mi) is the probability that the depth of reservoir is Di such that it triggered an earthquake of magnitude Mi
- P(Gi/Mi) is the probability that the geological condition at the reservoir site is Gisuch that it triggered an earthquake of magnitude Mi
- P(Si/Mi) is the probability that the tectonic stress environment is Si such that it triggered an earthquake of magnitude Mi
- P(Fi/Mi) is the probability that the fault activity is Fi such that it triggered an earthquake of magnitude Mi
- P(Ki/Mi) is the probability that the Karst development degree is Ki such that it triggered an earthquake of magnitude Mi
- P(Ci/Mi) is the probability that the communication relationship with reservoir Cisuch that it triggered an earthquake of magnitude Mi
- P (Ei/Mi) is the probability that the earthquake activity background is E is such that it triggered an earthquake of magnitude Mi.

Table 6: Site condition

Depth of reservoir water(D)	250m
Geological condition in the reservoir area.(G)	Stratified rock mass
Tectonic stress environment(S)	Reverse fault
Fault activity(F)	Active
Karst development degree(K)	weak
Communication relationship with reservoir water	Contact indirectly but with communication.
Earthquake activity background	Strong

Now the conditional probability of occurrence of reservoir induced earthquakes of different categories are as follows-
Strong- 0
Moderate strong- 0.0798
Moderate – 0.633
Small - 0.287

FORMULATION OF RISK FACTOR AND RIS CLASSIFICATION
Risk factor is the classification factor which is determined by combining the probability of earthquake at the reservoir site and the energy of a particular magnitude of earthquake.

Risk factor = $P_1E_1+P_2E_2+P_3E_3+P_4E_4$ 1.3

The range of risk factor comes out to be 2-180

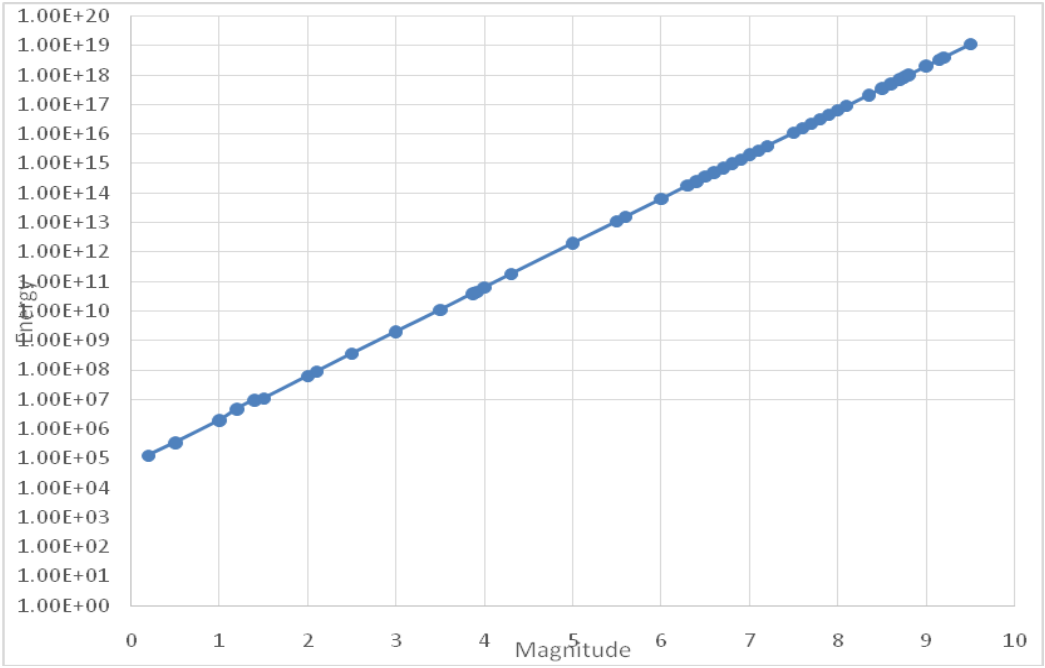

Figure 3: Energy Vs. Magnitude

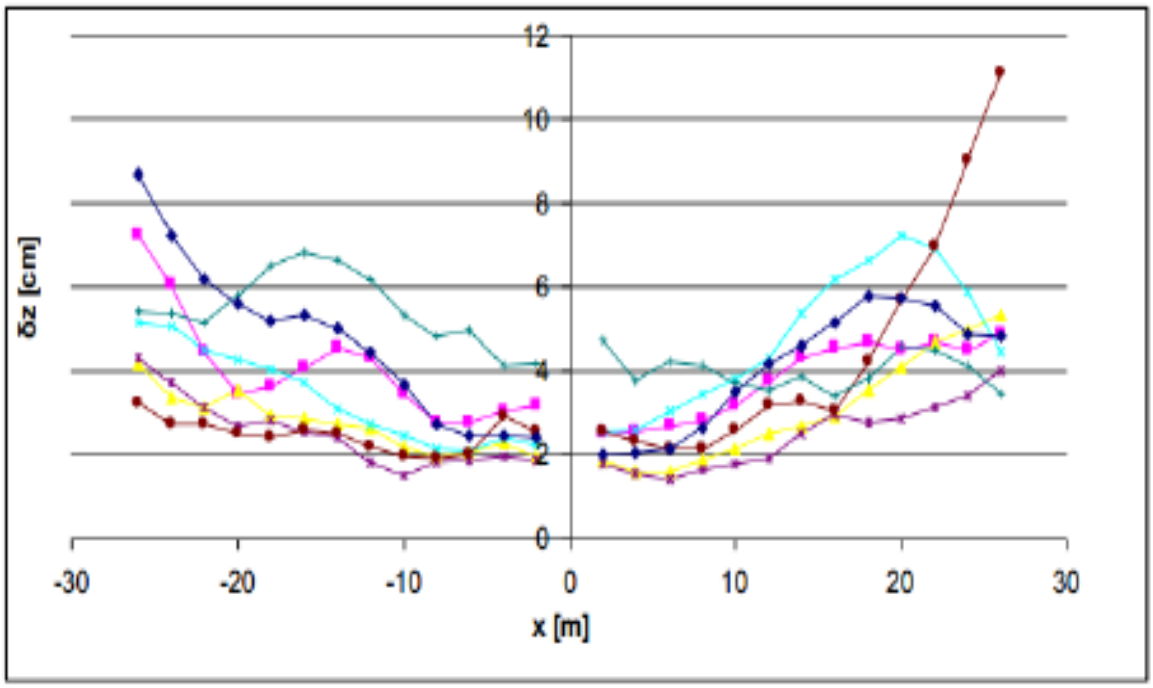

Figure 2: Standard deviation root-mean squared with mean difference from DTM as a function of cross track distance, mean depth equal to 8.5m.

Table 7: Classification of a site depending upon the value of risk factor

Reservoir site classification	Risk factor
Low	<2
Moderate	2-63
High	63-180

MODIFIED SEISMIC DESIGN AT THE RESERVOIR SITE

In order to find out the design seismic forces at a reservoir site the horizontal acceleration coefficient A_h is required to be modified and to fulfil this purpose three additional parameters along with conventional parameters are required to be incorporated in the design.

1. Z+1 Factor

This factor is included in the design of every structure where it is located in the region of high, medium and low reservoir. Thus it is the minimum safety factor we are providing in a building subjected to seismic loading for the earthquake induced by reservoir impoundment.

2. RIS Factor (F_R)

This factor has been introduced in the design to quantify the extent of reservoir induced seismicity risk as it is the only factor which will take into account the low, moderate , high reservoir induced seismicity risk categories. RIS Factor has been given a value 1-2 in case of normal occupancy structure and value of 1.5-3 in case of important structures. These value are not based on any rational analysis but on earthquake design philosophies where we are reducing the risk by different magnitudes so as to increase the factor of safety.

3. Proximity Factor (F_P)

The factor used in the design is a reduction factor because of the fault that the effect of RIS is in contradistinction to a tectonic earthquake. So we can't design each and every structure located in particular earthquake zone by this prior analysis .Thus this factor is introduced to limit the boundary within which this particular design is to be followed. Since the extent of this boundary will vary from place to place depending upon tectonic and reservoir conditions. Hence for every site this detailed analysis is to be done and using this particular boundary is to be defined:

Development of proximity factor:

Within RIS boundary : 1
Without RIS boundary : $0.5F_R$

CONCLUSIONS

The analysis based upon rational data and engineering judgement provides a method to ensure the safety of hydraulic structure as well as building in its vicinity by giving simple approach to be followed whenever a dam site is chosen. When it comes to design of dam or structure in the vicinity of dam. RIS never got the importance. It should have been given considering the fact; it is already too difficult to find a suitable site for dam. Since it is quite imperative that nobody is going to change the site because of this phenomenon. But we hope that we will prove beneficial not only in finding the severity of reservoir site for inducing earthquake activities but also in providing a solution by modifying design keeping in view that in any case the collapse of the structure is to be prevented. Even though this particular work might not be significant during present time where not much attention is given to its effects. But this ignorance can't be justified in coming years where huge numbers of dams are being built with outmost fervour risking life of so many numbers of people. This work will see the light of day when there is considerable awareness among the engineering community about the devastating effects of RIS.

REFERENCES

1. Gupta H.K.(1985) The present status of reservoir induced seismicity investigation with special emphasis on koyna earthquake.Tectnophysics 118:3/4
2. Gupta H.K.(1992) Reservoir induced earthquakes. New York: Elsevier.
3. Sun Junxiu.(1996) A study of prediction method for reservoir induced earthquakes. Seismology and geology.
4. G. B. Breacher (1982) Statistical examination of reservoir induced seismicity.
5. Simpson, D.W., Narasimhan, T.N., 1990. Inhomogeneities in rock properties and their influence on reservoir induced seismicity.
6. CWPRS Specification report for Indira Sagar Dam Instrumentation Project, NHDC, 2002.
7. Dam safety Guidelines. Part 4: Investigations, monitoring & surveillance of dams"., Auckland Regional Council.
8. Annandale, G. W., Morris, G. L., and Karki, P. (2016). Extending the Life of Reservoirs:
9. Sustainable Sediment Management for Dams and Run-of-River Hydropower. The World Bank, The World Bank 1818 H Street NW, Washington, DC 20433.
10. Banerji, S., V. B. L. (1972). "Silting of reservoirs: Indian data and the needed direction of efforts." symposium on Water in Man's Life, INSA, New Delhi., New Delhi, 5–7.
11. Central Water Commission. (2015). Compendium on silting of reservoirs in India. New Delhi.
12. Duan, J. G. (2013). "A Simple Total Sediment Load Formula." World Environmental and
13. Water Resources Congress 2013, American Society of Civil Engineers, Reston, VA, 1942–1950.
14. Fan, J., and Morris, G. L. (1992). "Reservoir Sedimentation. I: Delta and Density Current Deposits." Journal of Hydraulic Engineering, 118(3), 354–369.

Structural physical approximation for the realization of the optimal singlet fraction with two measurements

Satyabrata Adhikari*
Delhi Technological University, Shahbad Daulatpur, Main Bawana Road, Delhi-110042, India

(Received 28 February 2018; published 27 April 2018)

Structural physical approximation (SPA) has been exploited to approximate nonphysical operation such as partial transpose. It has already been studied in the context of detection of entanglement and found that if the minimum eigenvalue of SPA to partial transpose is less than $\frac{2}{9}$ then the two-qubit state is entangled. We find application of SPA to partial transpose in the estimation of the optimal singlet fraction. We show that the optimal singlet fraction can be expressed in terms of the minimum eigenvalue of SPA to partial transpose. We also show that the optimal singlet fraction can be realized using Hong-Ou-Mandel interferometry with only two detectors. Further we have shown that the generated hybrid entangled state between a qubit and a binary coherent state can be used as a resource state in quantum teleportation.

DOI: 10.1103/PhysRevA.97.042344

I. INTRODUCTION

Entanglement is a nonclassical correlation [1] and is a necessary ingredient to build a quantum computer that can outperform the classical computer. It has also been used as a quantum resource in various quantum communication tasks such as teleportation [2], superdense coding [3], secret sharing [4], and quantum-key distribution [5]. To perform the quantum communication task, we need to generate entanglement but the issue in the generation of entanglement is that it is never free from imperfections and noise. Therefore, the generated state may or may not be entangled. Thus it is important to develop an efficient way to detect entanglement.

Positive maps are stronger detectors of entanglement but they are not physical and hence cannot be realized in the laboratory. On the other hand, completely positive maps play an important role in quantum information processing as they are capable of describing an arbitrary quantum transmission channel [6]. In addition, they have also approximated nonphysicaql operations such as quantum cloners and universal-NOT gates [7]. A physical way by which positive maps can be approximated by completely positive maps is called structural physical approximation (SPA) [8]. SPA thus transforms nonphysical operations to physical operations.

Here, we restrict our discussion to the two-qubit system. Let P denote the positive map in four-dimensional Hilbert space and let CP denote the completely positive map that transforms all quantum states ρ onto maximally mixed state $\frac{I}{4}$, i.e., $CP(\rho) = \frac{I}{4}$ [9,10]. Since the positive map P is not a physically realizable map we approximate it with the CP map in such a way that it would be a physical map. Therefore, SPA to the map P is given by

$$\widetilde{P} = (1 - p^*)P + \frac{p^*}{4} I_4 \tag{1}$$

where p^* is the minimum value of p for which the approximated map $\widetilde{P}$ is a completely positive map [11].

Partial transposition (PT) is another strong entanglement detection criterion given by Peres [12]. Later, Horodecki *et al.* [13] proved that the PT criterion is necessary and sufficient for 2×2 and 2×3 systems. Although the partial transposition criterion works well in qubit-qubit and qubit-qutrit systems it cannot be implemented in a laboratory for the detection of entanglement as it is a nonphysical operation. Therefore, to make the partial transposition map a physical operation we can approximate it in such a way that it would be a completely positive map. Let us consider that the partial transposition operation acts on the second subsystem and is given by $\mathrm{id} \otimes T$, where T denotes the positive transposition map and id represents the identity operator. In general, partial transposition operation $\mathrm{id} \otimes T$ can be approximated as [8]

$$\widetilde{\mathrm{id} \otimes T} = (1 - q^*)(\mathrm{id} \otimes T) + \frac{q^*}{4} I_A \otimes I_B \tag{2}$$

where $q^* = \frac{16\nu}{1+16\nu}$ and $\nu = -\min_{Q>0} \mathrm{Tr}[Q(\mathrm{id} \otimes T)|\psi^+\rangle\langle\psi^+|]$, $|\psi^+\rangle = \frac{1}{\sqrt{2}}(|00\rangle + |11\rangle)$. The map $\mathrm{id} \otimes T$ is a nonphysical map but its approximate map $\widetilde{\mathrm{id} \otimes T}$ is a completely positive map and corresponds to a quantum channel that can be experimentally implementable [8,11].

Let σ_{12} be a two-qubit state and the task is to determine whether it is an entangled state or a separable state. Since it is a two-qubit system we can apply the partial transposition detection criterion. The PT criterion states that if $\sigma_{12}^{T_B}$ (T_B denotes partial transposition with respect to the second subsystem B) has a negative eigenvalue then the state σ_{12} is an entangled state. But partial transposition is not a physical operation so apply

*satyabrata@dtu.ac.in

 ©2018 American Physical Society

SPA-PT operation (2) on σ_{12}, and at the output we have $\widetilde{\sigma_{12}}$. Since the SPA-PT operation is completely positive the output $\widetilde{\sigma_{12}}$ also represents a state. Therefore, the practical problem of finding the eigenvalue of $\sigma_{12}^{T_B}$ (T_B denotes partial transposition with respect to the second subsystem B) reduces to determine the eigenvalue of $\widetilde{\sigma_{12}}$. Hence the PT criterion is modified as the SPA-PT criterion, which states that if the minimum eigenvalue of $\widetilde{\sigma_{12}}$ is less than $\frac{2}{9}$ then the state σ_{12} is entangled and vice versa [8]. The minimum eigenvalue can be estimated by the procedure given in [14,15].

Recently, Lim *et al.* [16] have demonstrated the experimental realization of SPA-PT for two-qubit photonic systems using single-photon polarization qubits and linear optical devices. They provided the decomposition of SPA-PT for a two-qubit state σ_{12} as

$$\widetilde{\sigma_{12}} = \widetilde{I \otimes T}(\sigma_{12}) = \left[\tfrac{1}{3}(I \otimes \tilde{T}) + \tfrac{2}{3}(\tilde{\Theta} \otimes D)\right]\sigma_{12} \tag{3}$$

where $\tilde{T}$ denotes SPA for transpose operation, Θ denotes the inversion map and works as $\Theta(\sigma) = -\sigma$, $\tilde{\Theta}$ denotes its SPA and can be constructed by the prescription given in (1), and $D(\sigma) = \frac{I_2}{2}$ denotes the polarization. Since $I \otimes \tilde{T}$ and $\tilde{\Theta} \otimes D$ are local operations and are completely positive operators $\widetilde{I \otimes T}$ is a physically realizable operator.

The motivation of this paper is twofold. First, the method of finding the eigenvalues in [14,15] requires more than one copy of the given state and the method described in [14] for estimating the eigenvalues works well asymptotically. Therefore, to circumvent these problems we take the approach of the witness operator to determine the minimum eigenvalue, which requires a single copy of SPA-PT of the given state. Also, we show that the minimum eigenvalue determined by our method requires a setup that needs only two measurements. Second, Verstraete and Verschelde [17] have established a relationship between the optimal singlet fraction and partial transpose of a given state, and using the derived relation they have shown that the two-qubit state is useful as a resource state for teleportation if and only if the optimal singlet fraction is greater than $\frac{1}{2}$. But the partial transposition is a nonphysical operation and cannot be implemented in a laboratory so it would not be easy to realize the optimal singlet fraction. Also the filtering operation used in [17] to achieve the optimal singlet fraction depends on the quantum state under investigation. Thus information about the state under investigation is needed. To overcome these problems, we apply SPA-PT method and show that the optimal singlet fraction does not depend on the state under investigation and also can be realized in experiment.

This paper is organized as follows: In Sec. II, we construct the witness operator to determine the minimum eigenvalue of SPA-PT of a given state ρ_{12}. In Sec. III, we show that the number of measurements needed to determine the minimum eigenvalue is 2. In Sec. IV, we show that the teleportation fidelity can be determined experimentally using Hong-Ou-Mandel interferometry with only two detectors. In Sec. V, we study the hybrid entangled state between a qubit and a binary coherent state (BCS) and show that the mixed hybrid entangled state can be used as a resource state for teleportation. We conclude in Sec. VI.

II. WITNESS OPERATOR THAT DETERMINES THE MINIMUM EIGENVALUE OF SPA-PT OF THE TWO-QUBIT STATE

Any arbitrary two-qubit density operator in the computational basis is given by

$$\rho_{12} = \begin{pmatrix} t_{11} & t_{12} & t_{13} & t_{14} \\ t_{12}^* & t_{22} & t_{23} & t_{24} \\ t_{13}^* & t_{23}^* & t_{33} & t_{34} \\ t_{14}^* & t_{24}^* & t_{34}^* & t_{44} \end{pmatrix}, \quad \sum_{i=1}^{4} t_{ii} = 1 \tag{4}$$

where $(*)$ denotes the complex conjugate.

SPA-PT of ρ_{12} is given by

$$\widetilde{\rho_{12}} = \left[\tfrac{1}{3}(I \otimes \tilde{T}) + \tfrac{2}{3}(\tilde{\Theta} \otimes \tilde{D})\right]\rho_{12} = \begin{pmatrix} E_{11} & E_{12} & E_{13} & E_{14} \\ E_{12}^* & E_{22} & E_{23} & E_{24} \\ E_{13}^* & E_{23}^* & E_{33} & E_{34} \\ E_{14}^* & E_{24}^* & E_{34}^* & E_{44} \end{pmatrix} \tag{5}$$

where

$$\begin{aligned} &E_{11} = \tfrac{1}{9}(2 + t_{11}), E_{12} = \tfrac{1}{9}(-it_{12} + t_{12}^*), \\ &E_{13} = \tfrac{1}{9}[t_{13} - i(t_{13}^* + t_{24}^*)], E_{14} = \tfrac{1}{9}(-it_{14} + t_{23}), \\ &E_{22} = \tfrac{1}{9}(2 + t_{22}), E_{23} = \tfrac{1}{9}(t_{14} + it_{23}), \\ &E_{24} = \tfrac{-i}{9}(t_{13}^* + t_{24}^*), E_{33} = \tfrac{1}{9}(2 + t_{33}), \\ &E_{34} = \tfrac{1}{9}(-it_{34} + t_{34}^*), E_{44} = \tfrac{1}{9}(2 + t_{44}). \end{aligned} \tag{6}$$

We note that the matrix $\widetilde{\rho_{12}}$ is not only a Hermitian matrix but also has non-negative eigenvalues. The trace of the matrix is equal to unity. So, it possesses all the properties of a state and thus the matrix can be regarded as a density matrix $\widetilde{\rho_{12}}$. The minimum eigenvalue of $\widetilde{\rho_{12}}$ detects whether the state ρ_{12} is entangled or not. Therefore, our task is to construct the witness operator that detects whether the minimum eigenvalue of $\widetilde{\rho_{12}}$ is less than $\frac{2}{9}$.

To start, we consider the operator $O = \widetilde{\rho_{12}} - \frac{1}{9}\rho_{12}^{T_2}$, where T_2 denotes the partial transpose with respect to the second subsystem. The expectation value of the operator O in the state $|\phi\rangle = \alpha|00\rangle + \beta|11\rangle (\alpha^2 + \beta^2 = 1)$ is given by

$$\begin{aligned} &\langle\phi|O|\phi\rangle = \mathrm{Tr}\left[\left(\widetilde{\rho_{12}} - \tfrac{1}{9}\rho_{12}^{T_2}\right)|\phi\rangle\langle\phi|\right] = \tfrac{2}{9} \\ &\Rightarrow \mathrm{Tr}[|\phi\rangle\langle\phi|\widetilde{\rho_{12}}] - \tfrac{1}{9}\mathrm{Tr}[|\phi\rangle\langle\phi|^{T_2}\rho_{12}] = \tfrac{2}{9} \\ &\Rightarrow \mathrm{Tr}[W^{\mathrm{opt}}\rho_{12}] = \mathrm{Tr}[\widetilde{\rho_{12}}|\phi\rangle\langle\phi|] - \tfrac{2}{9} \end{aligned} \tag{7}$$

where $W^{\mathrm{opt}} = \frac{1}{9}|\phi\rangle\langle\phi|^{T_2}$ is the optimal witness operator that detects whether the state ρ_{12} is entangled or not.

Let $\lambda_{\min}$ be the minimum eigenvalue of $\widetilde{\rho_{12}}$ and let $|\phi\rangle$ be the eigenvector corresponding to the minimum eigenvalue; then the eigenvalue equation is given by

$$\widetilde{\rho_{12}}|\phi\rangle = \lambda_{\min}|\phi\rangle. \tag{8}$$

Using (8) in (7), we have

$$\mathrm{Tr}(W^{\mathrm{opt}}\rho_{12}) = \lambda_{\min} - \tfrac{2}{9}. \tag{9}$$

For any separable state ρ_{12}^s, we have [8]

$$\mathrm{Tr}\big(W^{\mathrm{opt}}\rho_{12}^s\big) \geqslant 0 \Rightarrow \lambda_{\min} \geqslant \tfrac{2}{9}. \tag{10}$$

If ρ_{12} is an entangled state and W^{opt} detects that entangled state then

$$\mathrm{Tr}(W^{\mathrm{opt}}\rho_{12}) < 0 \Rightarrow \lambda_{\min} < \tfrac{2}{9}. \tag{11}$$

The inequality (11) gives us the condition when ρ_{12} is an entangled state.

Since the above condition is a purely mathematical condition, naturally one can ask the question of whether we can achieve this inequality experimentally. To investigate this, let us again recall (7) and write it in a different form as

$$\mathrm{Tr}(W^{\mathrm{opt}}\rho_{12}) = \mathrm{Tr}\big[\big(|\phi\rangle\langle\phi| - \tfrac{2}{9}I\big)\widetilde{\rho_{12}}\big]. \tag{12}$$

When W^{opt} detects an entangled state ρ_{12}, $\mathrm{Tr}(W^{\mathrm{opt}}\rho_{12}) < 0$ and hence we arrive at a condition given by

$$\mathrm{Tr}\big[\big(|\phi\rangle\langle\phi| - \tfrac{2}{9}I\big)\widetilde{\rho_{12}}\big] < 0. \tag{13}$$

The above condition (13) is the equivalent form of the condition (11) and hence the inequality implies that the eigenvalue of $\widetilde{\rho_{12}}$ is less than $\frac{2}{9}$.

Let $\mathbf{V} \equiv |\phi\rangle\langle\phi| - \frac{2}{9}I$. Then the inequality (13) can be reexpressed as

$$\mathrm{Tr}(\mathbf{V}\widetilde{\rho_{12}}) < 0. \tag{14}$$

Next we investigate a few properties of the operator $\mathbf{V}$.

(1) The expectation value of $\mathbf{V}$ for any separable state $\widetilde{\rho_{12}}^{\mathrm{sep}}$ is non-negative, i.e., $\mathrm{Tr}(\mathbf{V}\widetilde{\rho_{12}}^{\mathrm{sep}}) \geqslant 0$.

Proof. The separable state $\widetilde{\rho_{12}}^{\mathrm{sep}}$ is given by

$$\widetilde{\rho_{12}}^{\mathrm{sep}} = \begin{pmatrix} E_{11}^s & E_{12}^s & E_{13}^s & E_{14}^s \\ (E_{12}^s)^* & E_{22}^s & E_{23} & E_{24} \\ (E_{13}^s)^* & (E_{23}^s)^* & E_{33}^s & E_{34}^s \\ (E_{14}^s)^* & (E_{24}^s)^* & (E_{34}^s)^* & E_{44}^s \end{pmatrix} \tag{15}$$

where $E_{11}^s = \frac{1}{9}(2 + t_{11}^s), E_{12}^s = \frac{1}{9}[-it_{12}^s + (t_{12}^s)^*], E_{13}^s = \frac{1}{9}\{t_{13}^s - i[(t_{13}^s)^* + (t_{24}^s)^*]\}, E_{14} = \frac{1}{9}(-it_{14}^s + t_{23}^s), E_{22}^s = \frac{1}{9}(2 + t_{22}^s), E_{23}^s = \frac{1}{9}(t_{14}^s + it_{23}^s), E_{24}^s = \frac{-i}{9}[(t_{13}^s)^* + (t_{24}^s)^*], E_{33}^s = \frac{1}{9}(2 + t_{33}^s), E_{34}^s = \frac{1}{9}[-it_{34}^s + (t_{34}^s)^*]$, and $E_{44}^s = \frac{1}{9}(2 + t_{44}^s)$. Here, t_{ij}^s denote the elements of a separable state ρ_{12}^s.

Equation (12) can be reexpressed for any separable state ρ_{12}^s as

$$\mathrm{Tr}(W^{\mathrm{opt}}\widetilde{\rho_{12}}^{\mathrm{sep}}) = \mathrm{Tr}\big(\mathbf{V}\widetilde{\rho_{12}}^{\mathrm{sep}}\big). \tag{16}$$

Since W^{opt} is a witness operator the expectation value of W^{opt} over any separable state $\widetilde{\rho_{12}}^{\mathrm{sep}}$ is non-negative. Thus,

$$\mathrm{Tr}\big(W^{\mathrm{opt}}\widetilde{\rho_{12}}^{\mathrm{sep}}\big) \geqslant 0. \tag{17}$$

Using (16) and (17), we have

$$\mathrm{Tr}\big(\mathbf{V}\widetilde{\rho_{12}}^{\mathrm{sep}}\big) \geqslant 0. \tag{18}$$

(2) It can be easily shown that $\mathbf{V}$ has at least one negative eigenvalue.

Thus, the operator $\mathbf{V}$ possesses all the properties of a witness operator and hence it detects whether or not the eigenvalue of $\widetilde{\rho_{12}}$ is less than $\frac{2}{9}$. If $\mathbf{V}$ detects that the eigenvalue of $\widetilde{\rho_{12}}$ is less than $\frac{2}{9}$ then we can say that the state described by the density operator ρ_{12} is entangled.

Since $\mathbf{V}$ is a Hermitian operator it is an observable and can be implemented experimentally. Therefore the inequality (13) is useful to detect the entangled state experimentally.

III. NUMBER OF MEASUREMENTS NEEDED TO DETERMINE THE VALUE OF $\mathrm{Tr}(\mathbf{V}\widetilde{\rho_{12}})$

The operator $\mathbf{V}$ can be expressed in terms of local Pauli matrices as

$$\mathbf{V} = \tfrac{9}{28}\big[\tfrac{7}{9}I \otimes I + (\alpha^2 - \beta^2)(I \otimes \sigma_z + \sigma_z \otimes I) + 2\alpha\beta(\sigma_x \otimes \sigma_x + \sigma_y \otimes \sigma_y) + \sigma_z \otimes \sigma_z\big]. \tag{19}$$

We find that the decomposition of the operator $\mathbf{V}$ in terms of local Pauli observables needs more than two measurements to realize it. So in this section our task is to show that it is possible to realize the operator $\mathbf{V}$ with just two measurements.

To achieve our goal, we approximate the entanglement witness operator $\mathbf{V}$ in a way that we approximate the positive but not completely positive operator. Therefore, approximate entanglement witness operator $\widetilde{\mathbf{V}}$ can be expressed as

$$\widetilde{\mathbf{V}} = p\mathbf{V} + (1 - p)I, \quad 0 \leqslant p \leqslant 1. \tag{20}$$

Choose the minimum value of p in such a way that the operator $\widetilde{\mathbf{V}}$ will become a positive semidefinite operator. The Hermitian operator $\widetilde{\mathbf{V}}$ is positive semidefinite if $p_{\min} = \frac{8}{15}$. Therefore, $\widetilde{\mathbf{V}}$ can be reexpressed as

$$\widetilde{\mathbf{V}} = \tfrac{8}{15}\mathbf{V} + \tfrac{7}{15}I. \tag{21}$$

We can observe that the operator $\widetilde{\mathbf{V}}$ is not a normalized operator so it can be expressed after normalization as

$$\widetilde{\mathbf{V}} = \tfrac{2}{9}\mathbf{V} + \tfrac{7}{36}I. \tag{22}$$

Since $\widetilde{\mathbf{V}}$ is positive semidefinite and $\mathrm{Tr}(\widetilde{\mathbf{V}}) = 1$ the operator $\widetilde{\mathbf{V}}$ can be treated as a quantum state.

Again, $\mathrm{Tr}(\mathbf{V}\widetilde{\rho_{12}})$ can be written in terms of $\mathrm{Tr}(\widetilde{\mathbf{V}}\widetilde{\rho_{12}})$ as

$$\mathrm{Tr}(\mathbf{V}\widetilde{\rho_{12}}) = \tfrac{15}{8}\mathrm{Tr}(\widetilde{\mathbf{V}}\widetilde{\rho_{12}}) - \tfrac{7}{8}. \tag{23}$$

It can be shown that $\mathrm{Tr}(\widetilde{\mathbf{V}}\widetilde{\rho_{12}})$ is equal to the average fidelity for two mixed quantum states $\widetilde{\mathbf{V}}$ and $\widetilde{\rho_{12}}$ [18]:

$$\mathrm{Tr}(\widetilde{\mathbf{V}}\widetilde{\rho_{12}}) = F_{\mathrm{avg}}(\widetilde{\mathbf{V}}, \widetilde{\rho_{12}}). \tag{24}$$

Using (23) and (24), we have

$$\mathrm{Tr}(\mathbf{V}\widetilde{\rho_{12}}) = \tfrac{15}{8}F_{\mathrm{avg}}(\widetilde{\mathbf{V}}, \widetilde{\rho_{12}}) - \tfrac{7}{8}. \tag{25}$$

Kwong *et al.* [18] have shown that the average fidelity between two mixed quantum states can be estimated experimentally by Hong-Ou-Mandel interferometry with only two detectors. Thus the quantity $\mathrm{Tr}(\mathbf{V}\widetilde{\rho_{12}})$ needs only two measurements to estimate it in experiment.

Again, the minimum eigenvalue can be expressed in terms of $F_{\mathrm{avg}}(\widetilde{\mathbf{V}}, \widetilde{\rho_{12}})$ as

$$\lambda_{\min} = \tfrac{15}{8}F_{\mathrm{avg}}(\widetilde{\mathbf{V}}, \widetilde{\rho_{12}}) - \tfrac{47}{72}. \tag{26}$$

Since the minimum eigenvalue of the quantum state $\widetilde{\rho_{12}}$ can be determined using two measurements and the minimum eigenvalue is responsible for the detection of entanglement

we can say that the presence of entanglement in ρ_{12} can be detected using two measurements only.

IV. REALIZATION OF THE OPTIMAL SINGLET FRACTION WITH ONLY TWO MEASUREMENTS

The singlet fraction is defined as

$$F(\rho_{12}) = \max[\langle\phi^+|\rho_{12}|\phi^+\rangle\,\langle\phi^-|\rho_{12}|\phi^-\rangle \tag{27}$$

$$\langle\psi^+|\rho_{12}|\psi^+\rangle\,\langle\psi^-|\rho_{12}|\psi^-\rangle] \tag{28}$$

where $\{|\phi^+\rangle,|\phi^-\rangle,|\psi^+\rangle,|\psi^-\rangle\}$ are the maximally entangled Bell states.

Verstraete and Verschelde [17] suggested the optimal trace preserving protocol for maximizing the singlet fraction of a given state. The optimal singlet fraction is given by

$$F^{\text{opt}}(\rho_{12}) = \tfrac{1}{2} - \text{Tr}\big(X_{\text{opt}}\rho_{12}^{T_B}\big). \tag{29}$$

X_{opt} is given by

$$X_{\text{opt}} = (A \otimes I_2)|\psi^+\rangle\langle\psi^+|(A^\dagger \otimes I_2), \tag{30}$$

where I_2 represents an identity matrix of order 2, $|\psi^+\rangle = \frac{1}{\sqrt{2}}(|00\rangle + |11\rangle)$, and $A = \left(\begin{smallmatrix} a & 0 \\ 0 & 1 \end{smallmatrix}\right)$, where $-1 \leqslant a \leqslant 1$.

We note that if the state ρ_{12} is entangled then $\rho_{12}^{T_B}$ has at least one negative eigenvalue and hence $F^{\text{opt}}(\rho_{12})$ is greater than $\frac{1}{2}$. Thus every entangled two-qubit state is useful for teleportation. But there are two problems in estimating the quantity $F^{\text{opt}}(\rho_{12})$ given in (29): (i) $\rho_{12}^{T_B}$ cannot be realized in the laboratory and (ii) the parameter in X_{opt} is state dependent and hence to construct X_{opt} we need to know the state under investigation.

In this section, we obtain the optimal singlet fraction in terms of minimum eigenvalue λ_{min} of SPA-PT of the state ρ_{12} using local filtering operation but in this scenario the parameter of the local filtering operation does not depend on the state under investigation. Since we found in the previous section that λ_{min} can be estimated for any arbitrary state with two measurements we can say that the optimal singlet fraction of any arbitrary states can be calculated using two measurements.

A. Optimal singlet fraction in terms of λ_{min}

To start, let us consider the operator $X_{\text{opt}}(\widetilde{\rho_{12}} - \frac{1}{9}\rho_{12}^{T_2})$, where X_{opt} is given in (30). Calculate the trace of it, and after some simple algebra (29) reduces to

$$F^{\text{opt}}(\rho_{12}) = \tfrac{1}{2} - [9\text{Tr}(X_{\text{opt}}\widetilde{\rho_{12}}) - (a^2+1)]. \tag{31}$$

It can be easily seen from (31) that $F^{\text{opt}}(\rho_{12}) > \frac{1}{2}$ if and only if $9\text{Tr}(X_{\text{opt}}\widetilde{\rho_{12}}) - (a^2+1) < 0$. This condition leads to

$$\text{Tr}(X_{\text{opt}}\widetilde{\rho_{12}}) < \frac{a^2+1}{9}, \quad -1 \leqslant a \leqslant 1. \tag{32}$$

In $\{|00\rangle,|11\rangle\}$ subspace, the operator $\frac{1}{a^2+1}X$ can be expressed as

$$\frac{2}{a^2+1}X_{\text{opt}} = |\chi\rangle\langle\chi| \tag{33}$$

where $|\chi\rangle = \frac{1}{\sqrt{a^2+1}}(a|00\rangle + |11\rangle)$.

We note that the vector $|\chi\rangle$ and the eigenvector $|\phi\rangle$ of the operator $\widetilde{\rho_{12}}$ are parallel vectors and thus there exists a real scalar k such that

$$|\chi\rangle = k|\phi\rangle. \tag{34}$$

Using (34), it can be easily shown that the vector $|\chi\rangle$ is also an eigenvector corresponding to the minimum eigenvalue λ_{min}. Hence, the resource state ρ_{12} is useful for teleportation iff

$$\lambda_{\text{min}} < \tfrac{2}{9}. \tag{35}$$

The singlet fraction $F^{\text{opt}}(\rho_{12})$ given by (31) can be reexpressed in terms of the minimum eigenvalue λ_{min} as

$$F^{\text{opt}}_{(a,\lambda_{\text{min}})}(\rho_{12}) = \frac{1}{2} - \frac{9(a^2+1)}{2}\left[\lambda_{\text{min}} - \frac{2}{9}\right], \quad -1 \leqslant a \leqslant 1. \tag{36}$$

Further, we find that if the minimum eigenvalue λ_{min} is restricted to lie in the interval $[\frac{1}{6},\frac{2}{9})$ then the singlet fraction $F^{\text{opt}}_{(a,\lambda_{\text{min}})}(\rho_{12})$ lies in the interval

$$\frac{1}{2} < F^{\text{opt}}_{(a,\lambda_{\text{min}})}(\rho_{12}) < \frac{1}{2} + \frac{a^2+1}{4}, \quad -1 \leqslant a \leqslant 1. \tag{37}$$

The optimal singlet fraction can be achieved by putting $a = \pm 1$ in (36) and it is given by

$$F^{\text{opt}}_{(\pm1,\lambda_{\text{min}})}(\rho_{12}) = \tfrac{1}{2} - 9\big[\lambda_{\text{min}} - \tfrac{2}{9}\big], \quad \tfrac{1}{6} \leqslant \lambda_{\text{min}} < \tfrac{2}{9}. \tag{38}$$

Without any loss of generality, we can take $a = 1$ and thus we have $X^{\text{opt}} = |\psi^+\rangle\langle\psi^+|$. Afterward, we denote $F^{\text{opt}}_{(\pm1,\lambda_{\text{min}})}(\rho_{12})$ as simply $F^{\text{opt}}_{\lambda_{\text{min}}}(\rho_{12})$. Therefore,

$$F^{\text{opt}}_{\lambda_{\text{min}}}(\rho_{12}) = \tfrac{1}{2} - 9\big[\lambda_{\text{min}} - \tfrac{2}{9}\big], \quad \tfrac{1}{6} \leqslant \lambda_{\text{min}} < \tfrac{2}{9}. \tag{39}$$

We note here that the problem of finding the optimal singlet fraction reduces to finding the minimum eigenvalue of SPA-PT of any arbitrary state ρ_{12}.

B. Optimal singlet fraction in terms of average fidelity $F_{\text{avg}}(\widetilde{\mathbf{V}},\widetilde{\rho_{12}})$

Now, we are in a position to give the expression for the optimal singlet fraction in terms of average fidelity $F_{\text{avg}}(\widetilde{\mathbf{V}},\widetilde{\rho_{12}})$.

The optimal singlet fraction in terms of λ_{min} can be rewritten as

$$F^{\text{opt}}_{\lambda_{\text{min}}}(\rho_{12}) = \tfrac{1}{2} - 9\big[\lambda_{\text{min}} - \tfrac{2}{9}\big], \quad \tfrac{1}{6} \leqslant \lambda_{\text{min}} < \tfrac{2}{9}. \tag{40}$$

Using (26) in (40), we get

$$F^{\text{opt}}_{\lambda_{\text{min}}}(\rho_{12}) = \tfrac{1}{2} - \tfrac{135}{8}\big[F_{\text{avg}}(\widetilde{\mathbf{V}},\widetilde{\rho_{12}}) - \tfrac{7}{15}\big], \quad \tfrac{59}{135} \leqslant F_{\text{avg}}(\widetilde{\mathbf{V}},\widetilde{\rho_{12}}) < \tfrac{7}{15}. \tag{41}$$

Since $F_{\text{avg}}(\widetilde{\mathbf{V}},\widetilde{\rho_{12}})$ can be determined experimentally [18] $F^{\text{opt}}_{\lambda_{\text{min}}}(\rho_{12})$ can be realized using Hong-Ou-Mandel interferometry with only two detectors.

C. Optimal teleportation fidelity for the two-qubit system

For the two-qubit system, optimal teleportation fidelity $f_{\text{opt}}(\rho_{12})$ and optimal singlet fraction $F^{\text{opt}}_{\lambda_{\text{min}}}(\rho_{12})$ are related

by [19]

$$f_{\rm opt}(\rho_{12}) = \frac{2F^{\rm opt}_{\lambda_{\rm min}}(\rho_{12})+1}{3} = \frac{2}{3} - \frac{135}{12}\left[F_{\rm avg}(\widetilde{\mathbf{V}},\widetilde{\rho_{12}}) - \frac{7}{15}\right], \quad \frac{59}{135} \leqslant F_{\rm avg}(\widetilde{\mathbf{V}},\widetilde{\rho_{12}}) < \frac{7}{15}. \tag{42}$$

We can say a teleportation scheme is quantum if teleportation fidelity is greater than $\frac{2}{3}$. We can find that the teleportation fidelity given in (42) is always greater than $\frac{2}{3}$. Since $f_{\rm opt}(\rho_{12})$ depends only on $F_{\rm avg}(\widetilde{\mathbf{V}},\widetilde{\rho_{12}})$, again the optimal teleportation fidelity can be realized by Hong-Ou-Mandel interferometry with only two detectors.

V. APPLICATION

In this section, we will study a particular type of hybrid entangled system prepared with a qubit and a BCS in the context of quantum teleportation, although the coherent state is described by infinite-dimensional Hilbert space but the binary coherent state can be described by two-dimensional Hilbert space [20]. The states $|+\alpha\rangle$ and $|-\alpha\rangle$ are called BCSs and the set $\{|+\alpha\rangle,|-\alpha\rangle\}$ forms a nonorthogonal BCS basis. The state $|\alpha\rangle$ is given by

$$|\alpha\rangle = \exp\left(\frac{-|\alpha|^2}{2}\right)\sum_n \frac{\alpha^n}{n!}|n\rangle. \tag{43}$$

The BCS basis can be expressed in terms of the computational basis as [20]

$$|+\alpha\rangle = \cos(\theta)|0\rangle + \sin(\theta)|1\rangle, \quad |-\alpha\rangle = \sin(\theta)|0\rangle + \cos(\theta)|1\rangle, \quad 0 < \theta \leqslant \frac{\pi}{4}. \tag{44}$$

The parameter θ can be determined by the overlapping between the nonorthogonal states $|+\alpha\rangle$ and $|-\alpha\rangle$ and it is given by

$$\langle+\alpha|-\alpha\rangle = \sin(2\theta). \tag{45}$$

A. Generation of the hybrid entangled state between a qubit and a BCS

We now describe the method suggested in [21] for the generation of the hybrid entangled state between a qubit and a BCS. We should note that strong Kerr nonlinear media can be used to generate hybrid entanglement but these nonlinear effects in existing media are extremely weak. Thus it would be better to use weak Kerr nonlinearity to generate entanglement. The weak Kerr nonlinearity interaction Hamiltonian is given by $H_k = \hbar\chi a_1^\dagger a_1 a_2^\dagger a_2$. The interaction between a single-photon qubit $|\psi\rangle_1 = c|0\rangle_1 + d|1\rangle_1, |c|^2 + |d|^2 = 1$, and a coherent state $|\alpha\rangle_2$ under interaction Hamiltonian H_k is described as

$$|\Psi^{(\vartheta)}\rangle_{12} = \exp\left(\frac{iH_k t}{\hbar}\right)|\psi\rangle_1|\alpha\rangle_2 = c|0\rangle_1|\alpha\rangle_2 + d|1\rangle_1|\alpha\exp(i\vartheta)\rangle_2. \tag{46}$$

Taking $\vartheta = \pi$ in (46), the state $|\Psi^{(\vartheta)}\rangle_{12}$ reduces to

$$|\Psi^{\vartheta=\pi}\rangle_{12} = c|0\rangle_1|\alpha\rangle_2 + d|1\rangle_1|-\alpha\rangle_2. \tag{47}$$

Equation (47) represents a hybrid entangled system between a qubit and a BCS.

We may note here that an optical fiber of about 3000 km is required for $\vartheta = \pi$ for an optical frequency of $\omega = 5\times10^{14}$ rad/s using currently available Kerr nonlinearity [22].

B. Qubit-BCS hybrid entangled state as a nonmaximally two-qubit entangled state

We will now show that the hybrid entangled state (47) can be used as a resource state for quantum teleportation. To accomplish our task, we first express the BCS in the computational basis as in (44) and then treat the hybrid entangled state as an entangled state in four-dimensional Hilbert space. Therefore, qubit-BCS hybrid entangled state (47) can be expressed in the computational basis as

$$|\Psi_{12}\rangle = c\cos(\theta)|00\rangle_{12} + c\sin(\theta)|01\rangle_{12} + d\sin(\theta)|10\rangle_{12} + d\cos(\theta)|11\rangle_{12}. \tag{48}$$

Let us assume that Alice has generated the hybrid entangled state (48). She attaches an ancilla prepared in $|0\rangle_a$ to the state $|\Psi_{12}\rangle$. Therefore, the resulting three-qubit state $|\Psi_{12a}\rangle$ is given by

$$|\Psi_{12a}\rangle = [c\cos(\theta)|00\rangle_{12} + c\sin(\theta)|01\rangle_{12} + d\sin(\theta)|10\rangle_{12} + d\cos(\theta)|11\rangle_{12}]\otimes|0\rangle_a. \tag{49}$$

Alice then applies a two-qubit controlled-NOT gate on qubit "2" and qubit "a." The state $|\Psi_{12a}\rangle$ reduces to

$$|\Phi_{12a}\rangle = c|0\rangle_1\otimes[\cos(\theta)|00\rangle_{2a} + \sin(\theta)|11\rangle_{2a}] + d|1\rangle_1\otimes[\sin(\theta)|00\rangle_{2a} + \cos(\theta)|11\rangle_{2a}]. \tag{50}$$

She performs a single-qubit measurement in $\{|0\rangle_1,|1\rangle_1\}$ basis. If the measurement result is $|0\rangle_1$ then with probability $|c|^2$ she prepares the state

$$\left|\Phi^{(1)}_{2a}\right\rangle = \cos(\theta)|00\rangle_{2a} + \sin(\theta)|11\rangle_{2a}. \tag{51}$$

Again, if the measurement result is $|1\rangle_1$ then with probability $|d|^2$ she prepares the state

$$\left|\Phi^{(2)}_{2a}\right\rangle = \sin(\theta)|00\rangle_{2a} + \cos(\theta)|11\rangle_{2a}. \tag{52}$$

C. Mixed qubit-BCS entangled system shared between two distant parties as a resource state for quantum teleportation

Case 1. Let us assume that Alice has succeeded in generating the nonmaximally entangled state $|\Phi^{(1)}_{2a}\rangle$ given by (51). She now wants to share a subsystem with her distant partner Bob so that they can use the shared entangled state in sending the quantum information. To achieve this, Alice sends subsystem "2" to Bob through the memoryless amplitude damping channel. The transformation under the memoryless amplitude damping channel with parameter p $(0 \leqslant p \leqslant 1)$ that governs the evolution of the system and the environment is given by

$$|0\rangle_2\otimes|0\rangle_E \to |0\rangle_2\otimes|0\rangle_E, \quad |1\rangle_2\otimes|0\rangle_E \to \sqrt{1-p}|1\rangle_2\otimes|0\rangle_E + \sqrt{p}|0\rangle_2\otimes|1\rangle_E. \tag{53}$$

When the qubit in mode "2" of the hybrid system $|\Phi^{1)}_{2a}\rangle$ passes through the memoryless amplitude damping channel then the

system evolves as a mixed state and it is given by

$$\rho_{2a} = \sum_{i=0}^{1} (K_i \otimes I)\left|\Phi_{2a}^{(1)}\right\rangle\left\langle\Phi_{2a}^{(1)}\right|(K_i^\dagger \otimes I)$$
$$= \begin{pmatrix} \cos^2(\theta) & 0 & 0 & \frac{\sqrt{1-p}}{2}\sin(2\theta) \\ 0 & p\sin^2(\theta) & 0 & 0 \\ 0 & 0 & 0 & 0 \\ \frac{\sqrt{1-p}}{2}\sin(2\theta) & 0 & 0 & (1-p)\sin^2(\theta) \end{pmatrix} \tag{54}$$

where the Kraus operators K_0 and K_1 are given by

$$K_0 = \begin{pmatrix} 1 & 0 \\ 0 & \sqrt{1-p} \end{pmatrix}, \quad K_1 = \begin{pmatrix} 1 & \sqrt{p} \\ 0 & 0 \end{pmatrix}. \tag{55}$$

Now our task is to investigate whether the mixed state ρ_{2a} shared between Alice and Bob is still entangled and, if it is entangled, under what condition. If we find that the state ρ_{2a} is entangled under certain conditions then the state ρ_{2a} can be used as a resource state for quantum teleportation. To probe the above question, we calculate the optimal singlet fraction given in (39). The optimal singlet fraction for the state ρ_{2a} is given by

$$F^{\text{opt}}_{(p,\theta)}(\rho_{2a}) = \frac{1}{2} + \frac{1}{2}[\sqrt{(1-p)\sin^2(2\theta) + p^2\sin^4(\theta)} - p\sin^2(\theta)], \quad 0 < \theta \leqslant \frac{\pi}{4}. \tag{56}$$

For $0 < p < 1$ and $0 < \theta \leqslant \frac{\pi}{4}$, we have

$$F^{\text{opt}}_{(p,\theta)}(\rho_{2a}) > \tfrac{1}{2}. \tag{57}$$

Hence, the hybrid system described by the density matrix ρ_{2a} is useful as a resource state for the teleportation of a single qubit. Further we observe the following points.

(i) For any value of the nonorthogonal parameter $\theta (0 < \theta < 1)$, the value of the quantity $F^{\text{opt}}_{(p,\theta)}(\rho_{2a})$ decreases as the noise parameter p increases from zero to unity.

(ii) For any value of the noise parameter p $(0 < p < 1)$, the value of the quantity $F^{\text{opt}}_{(p,\theta)}(\rho_{2a})$ increases as the nonorthogonal parameter θ increases from zero to $\frac{\pi}{4}$.

Case 2. If Alice has succeeded in generating the nonmaximally entangled state $|\Phi_{2a}^{(2)}\rangle$ given by (52) then also the result remains the same as in case 1.

VI. CONCLUSION

To summarize, we have constructed the witness operator by approximating the partial transposition operation, that can detect the entangled state in a bipartite system. The constructed witness operator can be decomposed into Pauli matrices and therefore we find that it needs more than two measurements to realize the witness operator. To minimize the number of measurements, we approximate the entanglement witness, which is a positive semidefinite operator. Then we express the minimum eigenvalue of SPA-PT of the state under investigation in terms of average fidelity between the approximated entanglement witness and SPA-PT of the state. The latter can be realized by Hong-Ou-Mandel interferometry with only two detectors. So we infer that the minimum eigenvalue of SPA-PT of the state can be realized by Hong-Ou-Mandel interferometry with only two detectors. Further, we have obtained the minimum eigenvalue $\frac{1}{6}$ for a large class of states and claimed that it holds for any two-qubit states. We derived a relation between the optimal singlet fraction and the minimum eigenvalue of SPA-PT of the state under investigation. Therefore, the optimal singlet fraction can also be realized by Hong-Ou-Mandel interferometry with only two detectors. Lastly, we have shown that the hybrid entangled state between a qubit and a binary coherent state can be used as a resource state in quantum teleportation.

[1] M. Piani, S. Gharibian, G. Adesso, J. Calsamiglia, P. Horodecki, and A. Winter, Phys. Rev. Lett. **106**, 220403 (2011); R. Horodecki, P. Horodecki, M. Horodecki, and K. Horodecki, Rev. Mod. Phys. **81**, 865 (2009).

[2] C. H. Bennett, G. Brassard, C. Crepeau, R. Jozsa, A. Peres, and W. K. Wootters, Phys. Rev. Lett. **70**, 1895 (1993).

[3] C. H. Bennett and S. J. Wiesner, Phys. Rev. Lett. **69**, 2881 (1992).

[4] M. Hillery, V. Buzek, and A. Berthiaume, Phys. Rev. A **59**, 1829 (1999); S. Adhikari, I. Chakrabarty, and P. Agrawal, Quantum Inf. Comput. **12**, 0253 (2012).

[5] C. H. Bennett and G. Brassard, in *Proceedings of the IEEE International Conference on Computers, Systems and Signal Processing, Bangalore, India* (IEEE, New York, 1984), p. 175; A. K. Ekert, Phys. Rev. Lett. **67**, 661 (1991); N. Gisin, G. Ribordy, W. Tittel, and H. Zbinden, Rev. Mod. Phys. **74**, 145 (2002).

[6] B. Schumacher, Phys. Rev. A **54**, 2614 (1996).

[7] J. Fiurasek, Phys. Rev. A **64**, 062310 (2001).

[8] P. Horodecki and A. Ekert, Phys. Rev. Lett. **89**, 127902 (2002).

[9] J. Fiurasek, Phys. Rev. A **66**, 052315 (2002).

[10] J. K. Korbicz, M. L. Almeida, J. Bae, M. Lewenstein, and A. Acín, Phys. Rev. A **78**, 062105 (2008).

[11] J. Bae, Rep. Prog. Phys. **80**, 104001 (2017).

[12] A. Peres, Phys. Rev. Lett. **77**, 1413 (1996).

[13] M. Horodecki, P. Horodecki, and R. Horodecki, Phys. Lett. A **223**, 1 (1996).

[14] M. Keyl and R. F. Werner, Phys. Rev. A **64**, 052311 (2001).

[15] T. Tanaka, Y. Ota, M. Kanazawa, G. Kimura, H. Nakazato, and F. Nori, Phys. Rev. A **89**, 012117 (2014).

[16] H.-T. Lim, Y.-S. Kim, Y.-S. Ra, J. Bae, and Y.-H. Kim, Phys. Rev. Lett. **107**, 160401 (2011).

[17] F. Verstraete and H. Verschelde, Phys. Rev. Lett. **90**, 097901 (2003).

[18] C. J. Kwong, S. Felicetti, L. C. Kwek, and J. Bae, arXiv:1606.00427.

[19] M. Horodecki, P. Horodecki, and R. Horodecki, Phys. Rev. A **60**, 1888 (1999).

[20] C. R. Muller, G. Leuchs, C. Marquardt, and U. L. Andersen, Phys. Rev. A **96**, 042311 (2017).

[21] B. Yurke and D. Stoler, Phys. Rev. Lett. **57**, 13 (1986).

[22] B. C. Sanders and G. J. Milburn, Phys. Rev. A **45**, 1919 (1992).

STUDY OF REDUCING WASTAGE OF WATER IN HOUSEHOLD USING FOOT TAP

Munendra Kumar[1]*, Dharmender Tiwari[2]

1. Associate professor, Department of Civil Engineering, Delhi technological University,
1. Delhi-110042, India

2M.tech student, Department of Civil Engineering, Delhi technological University,
2. Delhi,-110042, India

ABSTRACT

To develop regulating strategies for reduction in consumption of domestic water, more proactive approach is to determine behavior of domestic consumers of water. During analysis, we found that water usage in domestic households consists of water closet, kitchen, bathing, wash-basins and many other minor or major occasional usages. From experimental study we found that water is wasted during cleaning of utensils in sink, washing of hands, trimming of beard, brushing in wash-basin because of continuous running of tap water during all these actions. This wastage happens due to the fact that we perform all these actions by our hands and also operate the tap with our hands. So, if we operate these taps without using our hands we can create breaks in continuous flow of water and water can be used efficiently. By keeping all these requirements in mind, we made an apparatus to operate tap by feet instead of hand and the amount of water save is computed. Results shows that for urban households of Delhi, water can be saved up to 34.78% and sometimes even more than this.

Keywords: ***Foot Tap, Household, New Technology, Water Conservation;***

INTRODUCTION

Rapid population growth, urbanization, water pollution and climate change increases water scarcity not only in India but also in whole world.From statistical data, it is observed that one fifth of world population lives in areas with water scarcity which means that water is not sufficient to meet the basic demands and one third of world population doesn't have clean drinking water. So, it is our key requirement to make policies, different strategies and activities to sustain-ably use natural resources of water, to fulfil the current and future demands. In this paper, we conducted an activity by using an experimental setup (Tap operated by using feet). Firstly, we determined the activities where water is wasted within the domestic households. The result obtained showedthat water is wasted during cleaning of utensils in sink, washing of hands, trimming of beard, brushing in wash-basin because of continuous running of tap water during all these actions. So, Alternative approach is thought and analyzed by conducting experiments. This is done by making set up which controls all taps by using foot instead of hand. This allows doing the work with hand while operating the tap by foot. So, if we operate these taps without using our hands we can create breaks in continuous flow of water and water can be used efficiently.

LITERATURE REVIEW

Arjun Wagh in his paper titled "Modern Methods of Water Conservation in India", suggested methods for conserving water in India. He has givenmany processes for water conservation including: protection of water from pollution, redistribution of water (using canal), rational use of groundwater (proper management of crops within the regions), population control, renovation of traditional water sources, use of modern irrigation techniques, increasing density of cover, crop rotation techniques, management of flood (out of total 32.8 crore hectare 4 crore hectare land is flood effected), limited use of water within the industries, reuse of urban waste water.

C.R.Ramakrishnaiah in his paper titled "Urban water management", showed that better policies, reallocation, automatic and semiautomatic valves, reuse of rinsing water, and low grade water, can save water efficiently. For this purpose he did case study of countries including Indonesia, Melbourne (Australia), and Israel.

Gary A. Gagnon (1984) in his article"The role of water audits in water conservation", shows that water can be conserved by controlling leakage form water distribution system by executing proper water audits. Water audits can be accomplished in three phases including meter testing, leakage detection, and quantification, and system inventory. This results in saving of water to a factor of approximately 12% to 70%.

Yixing Shan et al..(2015), in their article "Household water consumption: insight from a survey in Greece and Poland", surveyed major elements to know the behavior of domestic water consumers. These elements include: end user behaviors, socio-demographic and property characteristics, psychosocial conditions i.e., attitudes and beliefs.

Bill Randolph and Patrick Troy (2008) in their paper "Attitude to conservation and water consumption", conducted a survey to know the attitude of households in various types of housing using telephonic interview and making focus groups form the same areas. In this paper, shaping in demand of water was analyzed in relation to socio-demographic composition in different households in different dwelling conditions, cultural, behavioral and institutional aspects.

By reading all listed papers, we concluded that along with these traditional water conservation techniques we should develop something that can be really helpful same as automatic and semiautomatic valves as mentioned by "C.R. Ramakrishnaiah" in his paper. So, we made a temporary apparatus for experimental purpose to know how much water can be saved by using foot tap in place of traditional tap in households.

METHODOLOGY AND APPARATUS USED

Four inches broad wooden plank, gate valve, Nails of different varieties according to requirement, Modded iron strip (modded similar to gear of bike and used in place of valve operating handle), ½ inches elbow 90^0,2 inches and 6 inches nipples, male adaptor brass threaded, 2 feet PVC pipe, brass elbow, tap, spring, two clamps, three feet plastic pipe, one adhesive tube.

- **EXPERIMENTAL SET UP**

1) Cut 4 inches broad plank in 12 inches, 7 inches and 8 inches long pieces.
2) Attach 12 inches and 7 inches planks perpendicularly with 8 inches plank with the help of 4 small nails: two on each plank (Figure 1). This serves as foundation for our apparatus.
3) With the help of iron strip make assembly analogous to gear of bike which serves the purpose of handle of gate valve operated with the help of feet(Figure 2).

Figure 1.

Figure 2.

4) Remaining assembly is divided in two parts, bottom part (below gate valve) and top part (above gate valve).
5) Top part: - This part is formed by assembling "male adaptor brass threaded" followed by 2 feet PVC pipe which is further followed by brass elbow and then tap is installed.
6) Bottom part: - This part consists of two inches nipple attached to elbow followed by six inches nipple and then plastic pipe is attached to it(Figure 3).
7) Both the parts are assembled at top and bottom of gate valve. Then, whole product is attached with wooden planks with the help of clamps and nails. Spring is attached by using nail and hole in the modded iron strip handle (Figure 4).
8) Now this assembly is used in kitchen sink, washbasins to know the water used by this apparatus.

Figure 3.

Figure 4.

RESULTS

- **PROCEDURE AND OBSERVATIONS**

The wash-basins, kitchen sink are mainly found in urban part of Delhi. So, we used data only for urban part of Delhi for experimental purpose.

Estimated number of households in Delhi = 36.26 Lakh
Urban household =34.6 Lakh
Average household sizes in Urban = 4.51

Table.1 Data for conventional tap system

Activities	Average time taken(sec)	Number of Times per day	Water used (L) per day
Rinsing mouth and cleaningtongue(while Brushing)	60	2	4.4
Washing Hands	30	2	2.4
Shaving	80	2/7	0.915
Washing Utensils in sink	80	2	6.4

- **Water used for conventional tap system**

1) Rinsing mouth and cleaning tongue(while Brushing)- $34.6x10^5x4.51x4.4 = 68.66$ ML
2) Washing Hands - $34.6x10^5x4.51x2.4 = 37.4$ ML
3) Shaving (considering one member per family) - $34.6x10^5 x(6.4/7)= 3.16$ ML
4) Washing Utensils in sink - $34.6x 10^5 x6.4 = 22.12$ ML

Total usage of water in Delhi households per day = 131.34 ML

Table.2 Data for Foot tap system

Activities	Average time taken(sec)	Number of Times per day	Water used (L) per day
Rinsing mouth and cleaningtongue(while Brushing)	40	2	3
Washing Hands	18	2	1.5
Shaving	40	2/7	0.428
Washing Utensils in sink	50	2	4

- **Water used for Foot tap system**

1) Rinsing mouth and cleaning tongue(while Brushing)- 34.6x 10^5 x4.51x3 = 46.81 ML
2) Washing Hands - 34.6x10^5 x4.51x1.5 = 23.37 ML
3) Shaving (considering one member per family) - 34.6x10^5 x(3/7)= 1.48 ML
4) Washing Utensils in sink - 34.6x10^5 x4 = 13.825 ML

Total usage of water in Delhi household per day = 85.485 ML

Total amount of water save using foot tap instead of conventional tap =(131.34-85.485)ML
= 45.855ML

Percentage of water saved = 34.78%

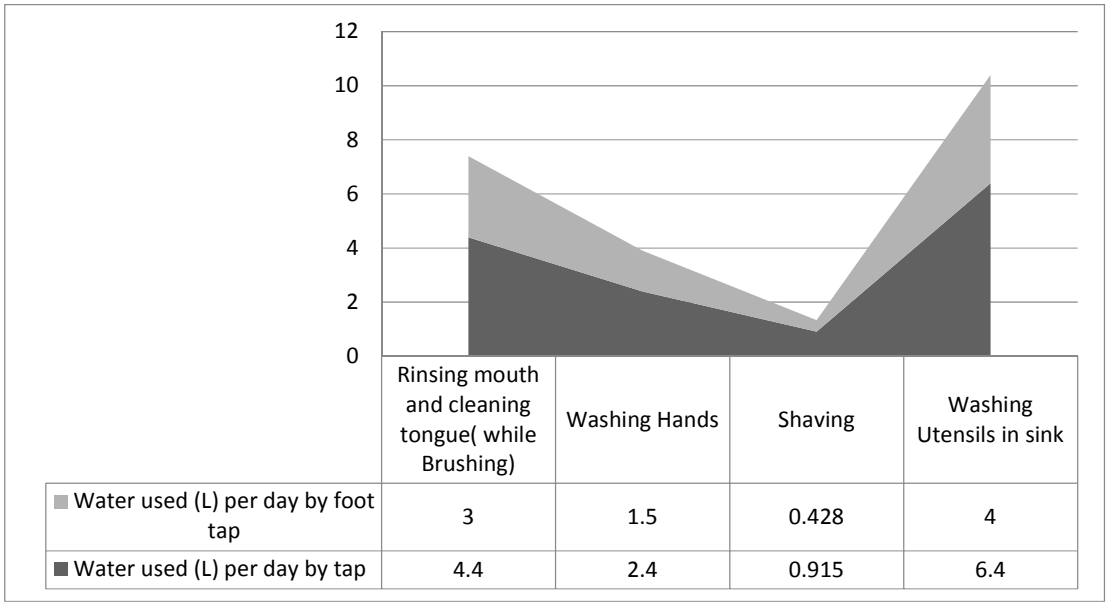

Figure 5.

Total amount of water saved using foot tap instead of conventional tap= (131.3-85.485)ML
= 45.855ML

Percentage of water saved = 34.78%

CONCLUSION

Scarcity of water is spread all over the world as we cannot create water we can only save it by using it efficiently. So, it is our sole responsibility to invent something that will cut down the usage of water by meeting all the demands.To fulfill these requirements we developed an experimental setup for operating tap by using foot instead of hands. Based on the results of this experiment we recommend that this apparatus should be used in every household, so that the water usage can be reduced to 34.78 percentage or even more.

REFERENCES

1. Bill Randolph and Patrick Troy (2008) " Attitudes to conservation and water consumption" . ELSEVIER
2. C.R. Ramakrishnaiah (2014) " Urban water management: best practice cases". Scientific research publishing Inc.
3. ArjunWagh and Rani Shinde (2017) " Modern methods of water conservation in India". Research front.
4. F. Abu- Taleb and Maher M. Murad (1999) "Use of focus groups and surveys to evaluate water conservation campaign" . Journal of water resources planning and management.
5. Gary A. Gagnon (1984) " The role of water audits in water conservation" . Journal of water resources planning and management.
6. Yixing Shan, Lili Yang, Kim Perren, Tannin Zhang (2015) " Household water consumption: insight from a survey in Greece and Poland". Science direct ELSEVIER.
7. Yushiou Tsai, Sara Cohen, and Richard M.Vogel (2011)"The impacts of water conservation strategies on water use" . Journal of American water resources association.

ResearchGate

See discussions, stats, and author profiles for this publication at: https://www.researchgate.net/publication/324362468

Study of Starting Friction during the Running of Plain Journal Bearing under Hydrodynamic Lubrication Regime

Article · January 2018

CITATIONS
0

READS
28

3 authors, including:

R. C. Singh
Delhi Technological University
41 PUBLICATIONS **47** CITATIONS
SEE PROFILE

Rajiv Chaudhary
Delhi Technological University
47 PUBLICATIONS **72** CITATIONS
SEE PROFILE

Some of the authors of this publication are also working on these related projects:

Working in the area of Tribology (Engine tribology, bearing design, tribology by nano particles and tubes.
View project

Dates Extended for Full manuscript Submission at ICAPIE 2016, Delhi, India View project

All content following this page was uploaded by R. C. Singh on 10 April 2018.

The user has requested enhancement of the downloaded file.

Downloaded from SAE International by Vipin Sharma, Thursday, March 29, 2018

2018-01-0838 Published 03 Apr 2018

Study of Starting Friction during the Running of Plain Journal Bearing under Hydrodynamic Lubrication Regime

Vipin Kumar Sharma Maharaja Agrasen Institute of Technology

Ramesh Chandra Singh and Rajiv Chaudhary Delhi Technological University

Citation: Sharma, V.K., Singh, R.C., and Chaudhary, R., "Study of Starting Friction during the Running of Plain Journal Bearing under Hydrodynamic Lubrication Regime," SAE Technical Paper 2018-01-0838, 2018, doi:10.4271/2018-01-0838.

Abstract

Study of starting friction during the running of the engineering application has an important role in designing them, especially working at low speed and high load conditions. A significant portion of research and development today is concentrated on saving the energy by reducing the friction. The present paper addresses the measurement technique and analysis of the starting friction during the running of the journal bearing. The experiments were performed during the hydrodynamic lubrication regime using SAE 15W-30 lubricating oil. A journal bearing having journal diameter as 22 mm, length/diameter ratio 1 and 0.027 mm radial clearance has been designed and fabricated to test the starting friction. Analysis of starting friction and average friction torque during the running of journal bearing was done at 900, 1150, 1400, 1650, 1900, 2150 and 2400 revolution per minute (rpm) speed of the journal at load values of 250, 400 and 500 N. The variation of starting friction with increasing speed of the journal is described by graphs and limiting speed is obtained at which the starting friction begin to decrease. The findings of the present work could be used by bearing user and designers to design the bearings.

Introduction

Friction and wear are the two most critical factors due to which a particular machine component fails. During the designing of the elements, these two are kept in mind by the designers. The material of the journal (shaft) and bearing, surface roughness values, operating conditions are some of the factors on which the wear and friction coefficient value in a journal bearing depend. Bouyer and Fillon experimentally found out the effect of different shaft materials, roughness, and rotational speed on the friction coefficient in a lubricated journal bearing [1]. The starting friction characteristics for an un-lubricated bearing were numerically evaluated by Sun and Jing [2]. The analysis of friction coefficient during the dry starting condition was also done by McCarthy and Glavatskih [3], the friction coefficient and wear values were evaluated during the transition between stationary state and moving state at the startup. A block ring test apparatus was used by authors for the investigation. Some authors also developed software models to predict the behavior of the system during start-up. Krithivasan and Khonsari modeled a finite element model for the journal bearing system and predict the seizure of the journal during startup conditions [4]. Ettles et al. [5] generates some design models for the thrust bearings and suggested the technique of jacking oil lift during the shutdown and start-up of the thrust bearing to prevent its seizure. The starting friction also causes the rise in temperature of the oil film. Wang et al. [6] compare the fast and slow start-up conditions for the measurement of oil film temperature. The amount of temperature rise of the oil film in case of a fast start-up was low as compared to slow start-up conditions. On similar terms, Harnoy [7] suggested having increasing acceleration in the starting to reduce the amount of wear.

Pistner conducted an experimental study of the start-up friction of the shoe bearing of a hydraulic pump. The temperature of the thrust pad increases very fast during the initial stage of the running i.e. start-up, which in results, induces the rupture of the lubricant film. This problem of sudden temperature rise could be minimized by preheating the thrust pad before using for the actual working [8] or supplying the lubricating oil at a bit higher temperature. Similarly, the use of mineral and synthetic oils can also minimize the friction and wear of the elements [9]. There is a number of different methods which are used by researchers to reduce the friction force and wear from the journal bearing tribopair. To reduce the friction in a journal bearing assembly Lu and Khonsari [10] used grease in place of lubricating oil. Besides grease, surface texturing is the other method which is adopted by researchers to reduce the friction and wear of the journal bearings. A polymer liner was incorporated by Linjamaa et al. [11] in a hybrid journal bearing and various elastic and thermal deformations of the surface of bearing were evaluated to enhance the performance of the bearing. Finite element modeling technique was used by authors to evaluate the parameters. To improve the load carrying capacity and coefficient of friction improvement

© 2018 SAE International. All Rights Reserved.

Downloaded from SAE International by Vipin Sharma, Thursday, March 29, 2018

Bompos et al. [12] proposed a multistep journal bearing. Overall there was an improvement of 38 % in coefficient of friction and 9.8 % in load carrying capacity of the multistep bearing as compared to the plain journal bearing. Khatri and Sharma [13] used FEM for solving the Reynolds equation. Power law was used for shear stress-strain relation. Textured and untextured bearing surfaces were studied and textured resulted in better stability. Sinanoglu et al. [14] developed a neural network and analyze the pressure development of journal bearing in different surface textures (trapezoidal and saw profile) of the shaft and also with various rotational speeds (1000-2000 rpm). The effects of compound and simple dimple surface textures on the performance of journal bearing were studied by Meng [15], two-layer pores were used by authors to generate the dimples on the bearing surface. Fluid-solid interaction (FSI) method along with Navier Strokes equation was solved for the analysis of the dimple effects.

The change in the viscosity of the lubricating oil also influences the starting friction torque greatly. Kim and Jeon [16] experimentally found out the effects of engine oil viscosity change on the engine oil seat frictional torque. It is reported by authors that, engine oil seat frictional torque decreases with low viscosity engine oil.

In the past, researchers have used different methods to reduce the friction torque between the journal and bearing surface. Most of the work is related with the average friction torque for the complete running of the journal bearing setup. A very limited work is reported on the analysis of the starting friction torque. Starting friction torque represents the friction torque during the initially running of the journal. It is as important as the average friction torque, as it represents the loss of energy during the initial starting of the setup. By reducing it, energy could be saved.

So, in the present paper, the starting friction torque during the running of journal bearing setup is studied. Experiments were performed using a bronze bearing and steel shaft with varying the speed of journal and applied load.

Experimental Test Rig

A journal bearing has a cylindrical component around a rotating shaft. It is used to support the radial load or used to guide for the smooth and efficient transfer of torque. The space between the bearing and shafts is filled with lubricating oil. In hydrodynamic lubrication technique, as the shaft starts to rotate, it tries to climbs the bearing surface and as rotational speed of the shaft is further increased, the lubricating oil forces itself into a wedge-shaped region. This wedging action of the lubricating oil helps in generating the pressure within the system. In the present work, in order to find out the pressure and frictional torque, a journal bearing rig TR-660 was used. Figure 1(a) represents the basic parts of the test rig and Figure 1(b) shows the location of pressure sensors. Journal bearing test rig is a sturdy versatile apparatus, easy to operate with provision to measure pressure at a different angular position on the bottom half of journal bearing. The journal is mounted horizontally on a shaft supported on self-aligned bearings, the shaft is rotated by a motor with timer belt. A loaded bronze flawless

FIGURE 1 (a) Journal bearing test rig (b) Location of pressure sensors

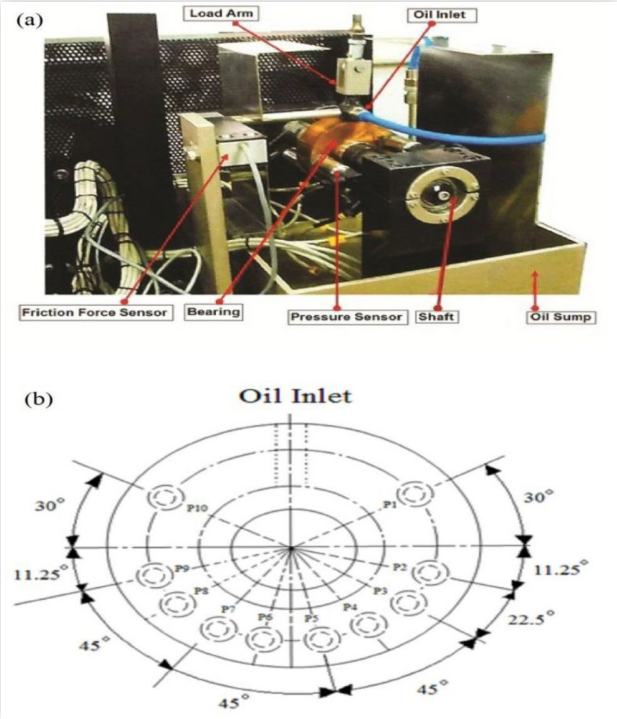

© SAE International

bearing freely slides over the journal and as it rotates bearing is formed, radial load is applied on bearing by pulling it upwards against journal by a loading lever. Ten numbers of sensors were fixed on the circumference of bearing with their terminal ends ending in the junction box. The permissible error in the measurement of pressure was ± 1 % MPa. A friction sensor was used to measure the frictional torque with a permissible error of ± 1% Nm. The journal is driven by belt & two-step pulley arrangement and speed required is set on software. Radial load & journal speed were varied to suit the test conditions.

The test rig is capable of measuring the friction torque and pressure generation for a maximum shaft speed of 8000 rpm and a load of 10000 N (maximum). A hydraulic system is used to supply the lubricating oil at a constant flow. The maximum lubricant oil pressure provided by system is 0.25 MPa. SAE 15W-30 lubricating oil was used for the experimentation and each experiment was performed three times with measurement of frictional torque for accurate analysis of it.

Table 1 provides the details of the journal bearing setup and input parameters of the experimentation. SAE 15W-30 lubricating oil was used for the experimentation. The oil inlet temperature and oil inlet supply were maintained at 40°C and 0.08 MPa.

Measurement of Starting Frictional Torque

Figure 2 represents the journal bearing with all the sensors. Friction torque, pressure, and temperature sensor were calibrated before using for the experimental work. Frictional torque measurement unit consists of an arm which is in contact with the journal bearing assembly. The data

© 2018 SAE International. All Rights Reserved.

Downloaded from SAE International by Vipin Sharma, Thursday, March 29, 2018

TABLE 1 Experimental details of the journal bearing test rig

Parameter (Unit)	Value
Bearing diameter (mm)	22.035
Shaft diameter (mm)	22 ± 0.005
Bearing material	Leaded Bronze
Shaft material	Stainless Steel
Lubricant oil	SAE 15W-30
Lubricant viscosity at 40°C (cst)	104.6
Lubricant supply Pressure (MPa)	0.08
Lubricant supply temperature (°C)	40
l/d ratio	1
Load (N)	250, 400, 500
Speed of Journal (rpm)	900, 1150, 1400, 1650, 1900, 2150, 2400

© SAE International

FIGURE 2 Location of sensors for measuring different performance parameters of journal bearing performance

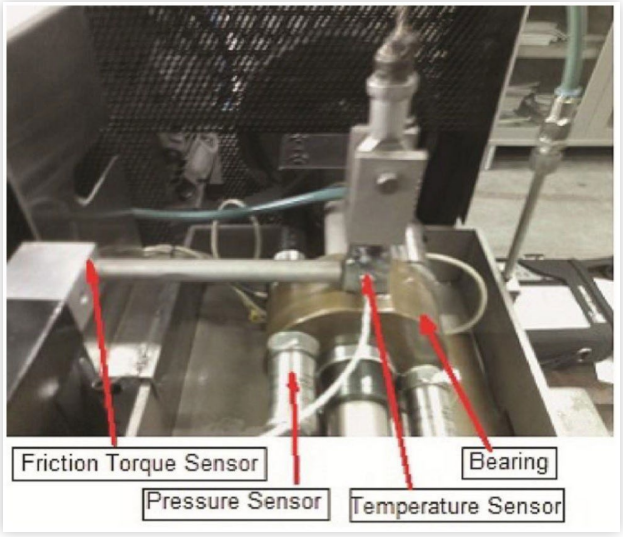

© SAE International

acquisition system which connects the sensor measures the startup torque. For the measurements of friction toque, all other pressure probes were removed in order to get the minimum disturbances from the other components.

The surface roughness of the bearing also plays an important role in the measurement of starting torque. The starting friction torque increases with the increase in roughness value [1]. So, for the accuracy the initial roughness values of the journal and bearing for all the experiments were 0.2 µm (Ra) value. The running duration of the journal consists of 10 seconds of the start-up and 100 seconds at a nominal speed. The starting torque was measured at a load of 250, 400 and 500 N and 900, 1150, 1400, 1650, 1900, 2150, 2400 rpm. All the experiments were repeated thrice for the accuracy.

Results and Discussion

In the first phase of the experimental work, the frictional torque was measured during the initial starting of the journal to the time when it reaches to its maximum value as per the experimental plan. In the second phase, the journal speed was maintained its full speed and average frictional torque and maximum pressure generated was measured.

Figure 3, represents the variation of friction torque with increasing speeds. It is quite interesting to note that the average friction torque decreases with the increase in rotational speed till 1900 rpm for all the load value of 250, 400 and 500N. However, at 500 N loads, it started to increases as the rotational speed is further increased to 2150 rpm and more. The rupture of the lubricating film at high speed (more than 1900 rpm) is the possible reason for this increase in the friction torque. This increase in friction torque is also made confirm by drawing the graph between rotational speed and maximum pressure generation in the oil film.

Figure 4 represents the variation of maximum pressure generation in the lubricating oil film. The pressure values used in plotting the graph are detected by a pressure sensor number 7 located at 213.75° from the lubricant oil entry point (see Figure 1(b)) on the bearing surface. It is seen that as the rotation speed is increasing, the oil film pressure also increases and reaches a maximum value of 1.15 MPa at 1600 rpm, and it falls to a minimum value (0.8 MPa) as the rotational speed is further increases to 1900 rpm. So, at 1900 rpm and 500 N load values, the oil film gets rupture and maximum pressure generated falls to 0.8 MPa. Also during the lower speeds, the sliding and rolling between the asperities of the journal and bearing will be very less, which would result in less friction torque. As the speed of the journal increases, the sliding and rolling with the journal, bearing and lubricant oil will be more. After attaining a maximum value of 0.048 Nm at 1650 rpm, the friction torque tends to decreases.

Figure 5, 6 and 7 represents the starting fiction torque for the initial 6 s time duration at different load values of 250, 400 and 500 N. Figure 5 shows that for all the speed values, the friction torque first reaches a maximum value and then it falls down. The circles position on the graph represents the maximum frictional torque value. The graphical region has been divided

FIGURE 3 Average Friction torque with different journal speed.

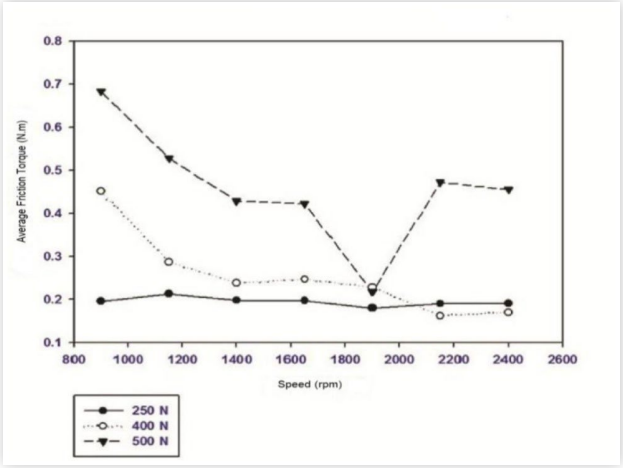

© SAE International

© 2018 SAE International. All Rights Reserved.

Downloaded from SAE International by Vipin Sharma, Thursday, March 29, 2018

FIGURE 4 Maximum pressure variation at different journal speed

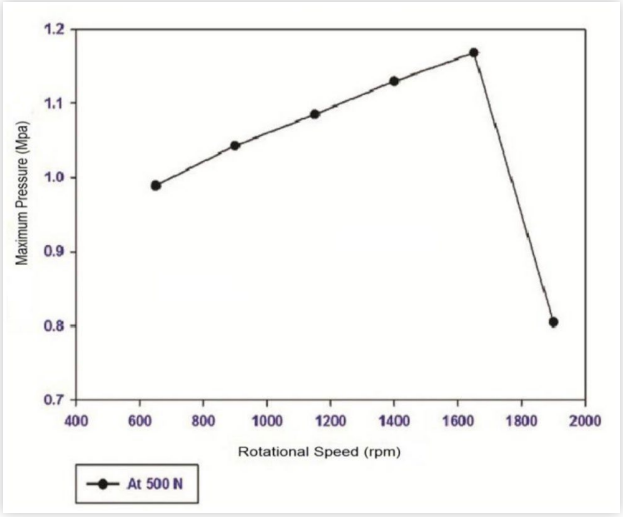

© SAE International

FIGURE 5 Variation of Friction torque at 250 N load.

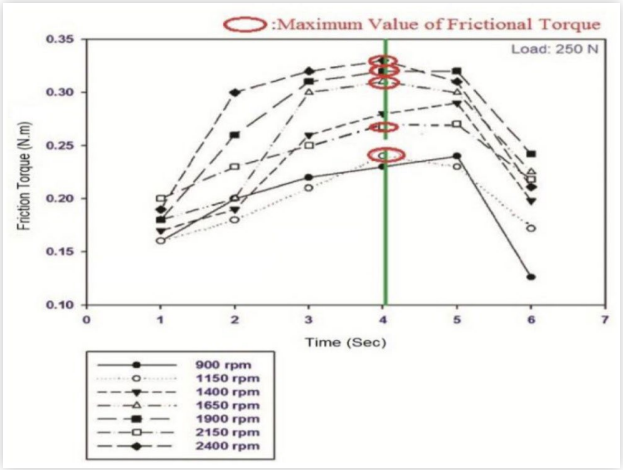

© SAE International

into two parts. Left part describes the initial starting friction and its maximum limit, and right part represents the change in friction torque value after it reaches the maximum value.

Similarly, Figure 6 represents the variation of starting frictional torque of at 400 N load and increasing speeds. The lower rotational speed results in maximum starting friction and it tends to decreases with increase in speed. The frictional torque attends a maximum value at nearly 5 s of time and after that, it tends to decrease with time.

Figure 7 shows the starting frictional torque values at 500 N. It seen that with increase in load from 400 N to 500 N, the frictional torque also increases. At higher load values the temperature of the lubricant will also get increase which in result changes the viscosity. This change in viscosity also affects the frictional torque and increases it. It is also observed that at higher load, the time utilized in attaining the maximum frictional torque also increases. Maximum value of friction torque for 500 N is attained in 6 s of time.

FIGURE 6 Variation of Friction torque at 400 N load.

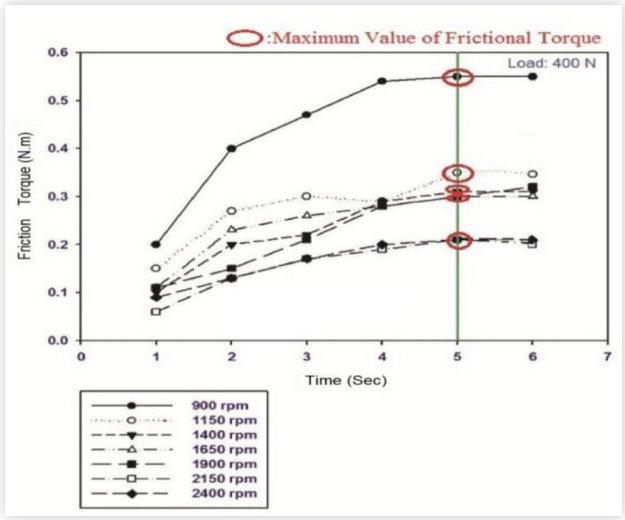

© SAE International

FIGURE 7 Variation of Friction torque at 500 N load.

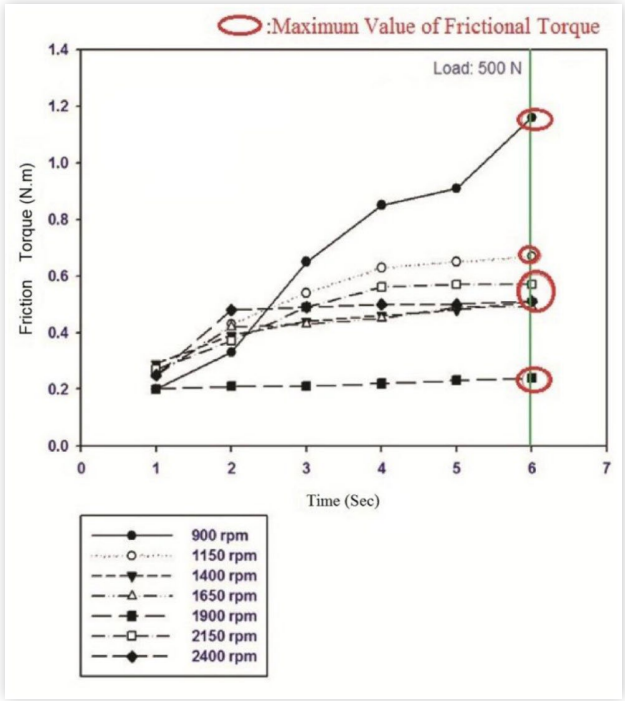

© SAE International

Summary/Conclusions

In the present work, starting friction torque between a bronze bearing and stainless steel journal is measured at varying journal speed and applied load. The average friction torque and a maximum pressure of the lubricant film were also recorded using friction torque sensor and pressure sensors. The analysis of starting friction torque of the present study could be utilized by bearing users in planning the experimental design for the investigation of performance of journal bearings. Following are the main conclusions of this experimental study:

© 2018 SAE International. All Rights Reserved.

Downloaded from SAE International by Vipin Sharma, Thursday, March 29, 2018

1. Starting friction first reaches a maximum value and then falls down to a lower value as the journal attains the nominal speed. At 250 N of load, the maximum frictional torque is attained in 4 seconds of time for almost all rotational speeds of the journal. Similarly, at 400 N, the attainment time is 5 seconds and 6 seconds at 500 N of load. It could be concluded that, as the applied load is increased, the time to attain the maximum frictional torque also increases.
2. For 250 N and 400 N load, with an increase in the load on bearing the friction torque increases for all the values of the rotational speed of the journal. For 500 N of load the frictional torque increases till 1900 rpm, and thereafter it starts decreasing.
3. For 500 N, the friction torque decreases with the increase in rotational speed of the journal till 1900 rpm, after that it starts increasing with rotational speed value at 2150 and 2400 rpm. So, the optimum speed to maintain the minimum friction torque is 1900 rpm for 500 N of the load.
4. The maximum pressure also increases with increase in rotational speed till 1900 rpm, after that it starts decreasing because of the rupture of the lubricating oil film.

References

1. Bouyer, J. and Fillon, M., "Experimental Measurement of the Friction Torque on Hydrodynamic Plain Journal Bearings during Start-Up," *Tribology International* 44:772-781, 2011, doi:10.1016/j.triboint.2011.01.008.
2. Sun, D.C. and Xu, J., "A Study of the Starting Characteristics of an Unlubricated Journal Bearing," *Journal of Tribology* 117:216-223, 1995, doi:10.1115/1.2831230.
3. Mccarthy, D.M.C. and Glavatskih, S.B., "Assessment of Polymer Composites for Hydrodynamic Journal-Bearing Applications," *Lubrication Science* 21:331-341, 2009, doi:10.1002/ls.92.
4. Krithivasan, R. and Khonsari, M.M., "Thermally Induced Seizure in Journal Bearings During Startup and Transient Flow Disturbance," *Journal of Tribology* 125:833-841, 2003, doi:10.1115/1.1538619.
5. Ettles, C.M., Seyler, J., and Bottenschein, M., "Some Effects of Start-Up and Shut-Down on Thrust Bearing Assemblies in Hydro-Generators Measurements of Transient Effects in Thrust Bearings," *Journal of Tribology* 125:824-832, 2003, doi:10.1115/1.1576428.
6. Wang, H., Liu, Z., Zou, L., and Yang, J., "Influence of Both Friction and Wear on the Vibration of Marine Water Lubricated Rubber Bearing," *Wear* 376-377:920-930, 2017, doi:10.1016/j.wear.2017.02.006.
7. Harnoy, A., "Model-Based Investigation of Friction During Start-Up of Hydrodynamic Journal Bearings," *Transactions of the ASME, Journal of Tribology* 117:667-673, 1995, doi:10.1115/1.2831533.
8. Pistner, C.A., "Some Effects of Start-up Transient Loads on Shoe Bearings for Large Hydraulic Pump/turbines," *Tribology Transactions* 39:93-98, 1996, doi:10.1080/10402009608983507.
9. Din, M.D. and Kassfeldt, E., "Wear Characteristics with Mixed Lubrication Conditions in a Full Scale Journal Bearing," *Wear* 232:192-198, 1999, doi:10.1016/S0043-1648(99)00145-3.
10. Lu, X. and Khonsari, M.M., "On the Lift-off Speed in Journal Bearings," *Tribology Letters* 20:299-305, 2005, doi:10.1007/s11249-005-9124-y.
11. Linjamaa, A., Lehtovaara, A., Larsson, R., Kallio, M., and Sochting, S., "Modelling and Analysis of Elastic and Thermal Deformations of a Hybrid Journal Bearing," *Tribology International* 118:451-457, 2016, doi:10.1016/j.triboint.2017.02.029.
12. Bompos, D.A. and Nikolakopoulos, P.G., "Tribological Design of a Multistep Journal Bearing," *Simulation Modelling Practice and Theory* 68:18-32, 2016, doi:10.1016/j.simpat.2016.07.002.
13. Khatri, C.B. and Sharma, S.C., "Influence of Textured Surface on the Performance of Non-Recessed Hybrid Journal Bearing Operating with Non-Newtonian Lubricant," *Tribology International* 95:221-235, 2016, doi:10.1016/j.triboint.2015.11.017.
14. Sinanoğlu, C., Nair, F., and Karamiş, M.B., "Effects of Shaft Surface Texture on Journal Bearing Pressure Distribution," *Journal of Materials Processing Technology* 168:344-353, 2005, doi:10.1016/j.jmatprotec.2005.02.252.
15. Meng, F.M., Zhang, L., Liu, Y., and Li, T.T., "Effect of Compound Dimple on Tribological Performances of Journal Bearing," *Tribology International* 91:99-110, 2015, doi:10.1016/j.triboint.2015.06.030.
16. Kim, H.G. and Jeon, S.I., "Effect on Friction of Engine Oil Seal with Engine Oil Viscosity," *International Journal of Automotive Technology* 9:601-606, 2008, doi:10.1007/s12239-008-0071-0.

Contact Information

Corresponding Author: **Vipin Kumar Sharma**
Mailing address: Maharaja Agrasen Institute of Technology
Rohini Sec-22, Delhi 110086
vipin.dtu@gmail.com
Phone no: +91-9582868647.

All rights reserved. No part of this publication may be reproduced, stored in a retrieval system, or transmitted, in any form or by any means, electronic, mechanical, photocopying, recording, or otherwise, without the prior written permission of the copyright holder.

Positions and opinions advanced in this paper are those of the author(s) and not necessarily those of SAE International. The author is solely responsible for the content of the paper.

ISSN 0148-7191

View publication stats

STUDY OF THE IMPACT OF INCLINATION ON SCOURING AROUND THE BRIDGE PIER

Munendra Kumar[1*]
[1]Associate Professor Department of Civil Engineering,
Delhi Technological University, Delhi, India
Email: mkumar66@gmail.com

ABSTRACT

The scouring has the tendency to affect the structural capacity of the piers, which results in the failure of the bridge due to the undermining action of the water around the foundation of bridge piers. This failure results in the loss of human lives, loss of economical values and loss of money and time. So the safeties of structures, like bridges are a matter of utmost importance. For reducing the scouring, the various researchers have developed various methods. In the present study we have adopted inclination for the reduction of scouring. After collision and overloading, the third main cause for bridge failure is scouring around bridge pier. It is estimated that nearly two-third of bridge failure occurs due to scouring and other flow related causes. Scouring around a bridge pier is a phenomenon that can never be totally ended to zero but can surely be reduced upto a great extent. So the objective of this work is to study the effects of inclination of a bridge pier on local scouring around a bridge pier. In the present research study experimental work was done for the same dimensions with different shapes i.e., circular, octagonal and square. Each pier was founded in a test section inside the hydraulic flume and inclined to desired angle by using a pier inclining model. The experimental work was done for three different discharge values in hydraulic flume. The experimental study reveals that the average scouring got reduced by 15 % for the circular shaped pier, 22% for the octagonal shaped pier and 21% for the circular pier by inclining the piers towards downstream direction. Thus we can conclude that the maximum reduction in scour depth occurs in octagonal shaped pier.

Keywords: *Bridge Piers, Inclined Bridge piers, Open Channel, Scouring, Scour depth Reduction.*

1. INTRODUCTION

The erosion of the bed material around any substance or obstruction is known as scouring. The vertical extent of the soil bed around the structure is called scour depth. When the bed particles get washed away from the bed near the obstruction resulting in the formation of depression is called scour hole. The phenomenon of removal of bed particles from just adjacent to the pier is called local scouring. It occurs due to the obstruction caused by the pier to the direction of flow. This interference of the obstruction to the flow results in the acceleration of the flow. This acceleration of flow results in the formation of the vortex flow around the supporting structure that washes away the bed particles from the pier surrounding area. If flow forms the vortices around the substructure then it results in scouring. If the bed material has cohesive material like clay it requires large force to remove the individual particle. If the flow which is coming towards the pier or abutment, carries any soil particle from the past then it is called live bed scour, and if it does not contain any soil particle from the past then it is called clear water scour. When the flow comes with a certain velocity then there is stagnation of the flow at front face of the pier, when the flow comes in contact with the soil bed, it results in the formation of depression at the front of the pier. Due to this, vortices are created in the

area near the piers. The vortex goes downstream the pier and then passes along the sides of pier. This type of vortex flow is called the horseshoe vortex because it resembles with horseshoe. Due to this, the hole which was formed earlier will go on increasing depth wise, till the shear on the bed particles becomes less than the critical shear stress. As we know bridge failures results in the loss of human lives, loss of economical values and loss of money and time. So there safety is our responsibility, for their safety there are generally two ways for checking against scouring, one way is to strengthen the soil around the pier and the other way is to regulate the flow of water around the pier. For strengthening the soil, we can do application of riprap, grout filled bags etc. and for regulating the flow we can control the flow alignment to breath the vortex flow which reduces the velocity of water in the adjoining area of the pier, this can be achieved by the use of sacrificial piles, collars, submerged in the vanes, slot, threading, inclining the pier towards d/s side etc.

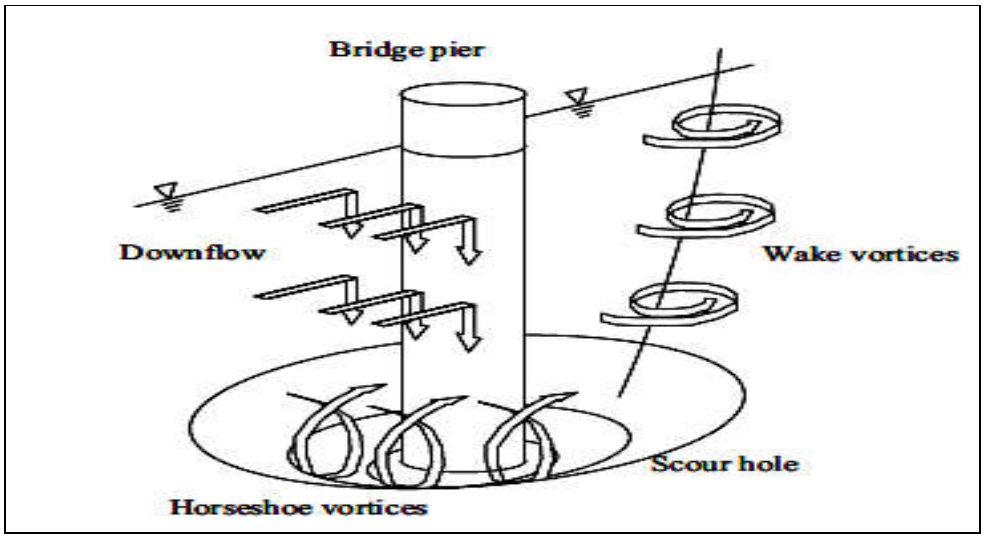

Fig. 1. Schematic view of scour process

TYPES OF SEDIMENTS AND THEIR BEHAVIOUR

Generally the material present in the bed is more important for knowing the scouring process.

1. Non- cohesive Material: These materials are composed of the granular structure, with the possibility of individual particles getting washed away when its stabilizing force is overcome by the force of approach flow. The capability of the individual to get washed away depends upon its shape, density and its packing on the bed.
2. Cohesive Material: These particles generally consist of clay. These materials require large velocity of flowing water to overcome the stabilizing force of individual particle but when it is achieved, it can be easily transported by flowing water.
3. Armoring: The process of preserving a large particle and let the washing away of the small particle in well graded channel is called Armoring. This controls the scouring up to some extent. This includes the laying of elongated shape materials on the bed.

FACTORS AFFECTING THE SCOUR

1. Type of flow: Type of flow is responsible for the scouring. If the flow forms vortices then there will be more scouring around the pier and if the flow is turbulent it also leads to scouring as the velocity of the flow is high. High flood flows also causes scouring.
2. Type of Fluid: Type of the fluid is also another factor on which the scouring depends. The fluid may be considered as erosive fluid or non –erosive fluid. In the erosive fluid, velocity is more if it contains any debris or any other material on the other hand, the non-erosive fluid does not erode the particles and hence scouring does not take place.
3. Shape of Substructure: This is also an important factor on which the scouring depends. Shape of substructure may be circular, square, etc. and extent of scouring is different for different shapes.
4. River bed Material: Extent of scouring also depends on the material which is present in the river bed. The river bed may contain non-cohesive or cohesive material. If the river bed contains non- cohesive material then there is a possibility of individual particle getting washed away if the stabilizing force of the particle is overcome by the force of approaching water. On the other hand, if the river bed contains cohesive material like clay then the possibility of individual particle getting washed away is less because of the large force requirement or high velocity water to overcome the stabilizing force of the individual particle.

LITERATURE REVIEW

SCOURING MEASUREMENT IMPORTANCE

Scour is a topical issue in the marine environment due to the recent development of offshore wind farms in coastal waters. This is an active area of research because it is currently difficult to accurately predict the scour depth that will occur at a structure's foundations in the field. Simplified scale modeling in laboratory flumes can help to advance understanding of the mechanisms for scour and the interactions between the fluid, structure, and sediment. A suitable measurement technique needs to be implemented to monitor the scour depth detesting. In practice this is difficult because of the need for the method to be non-intrusive but still operate at the required time and spatial resolutions at the small scale. Consequently, a wide range of measurement systems have been presented in the scour [1]. Earlier the equation and models that were used to predict the pier scour provided a single maximum value of scour depth rather than scour depth as a function of time. Therefore the number of years in which the scour depth will be reached cannot be estimated. So in this research, a time dependent model and subsequent risk of failure analysis has been used and this has enabled the design engineering to base a bridge pier design on an estimated probability of failure rather than on the basis of experience, thus providing it to be a method of safer design of bridges [2].

METHODS FOR THE PROTECTION OF BRIDGE PIERS

Some research work on the protection of bridge pier is briefly described below:

1. Use of combination of riprap and collar they used an application of riprap alone and a combination of riprap and a collar to control the scour around rectangular bridge piers. A collar three times wider than the pier's width was installed around the pier at the streamed level. The results of the experiments showed that with increase in both the skew angle and the aspect ratio of the piers, the stable riprap size and extent also got increased [3]. Researchers used independent and continuous pier collar in combination with riprap for reducing local scour around bridge pier group. The effectiveness of collar was evaluated experimentally. The results showed that in the case of two piers in line, combination of continuous collar sand riprap results in the most significant scour reduction of about 50 and 60 for the front and rear piers respectively [4].

2. Replacement of solid pier by Group of piers in their research, they have replaced the solid pier by a group of three smaller piers. The extent of pier scouring in the pier group in its best orientation is compared with that due to a solid pier of diameter of the pier group. The results showed that scour reduction is about 40% in the pier group [5].
3. Use of slot and combination of slot and collar a researcher used a slot alone and a combination of slot and collar as devices for controlling the depth of scour. The results showed that scour got reduced by as much as 20% on using a slot alone. The combination of slot and collar further reduced the scour hole [6]. Another researcher used a slot alone and a combination of bedsill as a countermeasure against local scouring at a smooth circular bridge pier. The effectiveness of the slot was evaluated by changing its sinking depth into a sand bed. The results showed that maximum scour depth reduction was about 30% in the best configurations. And the scour reduction when using the combination system of slot and bedsill was about 45% on average [7].
4. Use of Bed sill as scour reduction device in a research work researchers used a bedsill located at downstream side of the circular piers as a scour reduction device. The effectiveness with the distance between the pier and sill was evaluated. The results showed that a bedsill placed at a small distance downstream of the pier reduces the scour depth upto a great extent [8].
5. By inclining the bridge piers researcher used the effects of inclination of a bridge pier on local scour depths around bridge pier experimentally. Single circular pier inclined towards the downstream direction was founded in a uniform bed material. The results showed that the scour depth decreased as they increased the inclination angle of the pier [9]. In this research work scour around circular shaped bridge piers with two different diameters and different inclination angles towards downstream side has been investigated experimentally under clear water condition and different discharges. The results showed that an increase in the inclination angle leads to a significant decrease in the scour depth [10].

METHODOLOGY

EXPERIMENTAL SETUP

The experimental setup consists of:-

- Tilting hydraulic flume
- Pier inclining model
- Circular pier
- Octagonal pier
- Square pier
- Trowel

For performing the experimental runs we take three different shapes of the pier i.e., circular, octagonal and square. The experimental runs are first performed for circular shaped pier of diameter 4 cm and length 50 cm. The flume is first cleaned off dust by allowing free discharge through it. After this a test section of 1.1 m length and 14 cm height is set inside the flume. The circular pier is then placed in the test section and inclined at an angle of 0˚ with respect to vertical axis with the help of pier inclining model. Sand is then laid in the test section and flattened perfectly with the help of trowel. Water is allowed to flow in the flume for 4 hours. After 4 hours water is allowed to drain out of the flume and readings are taken for the scour hole so formed. The same procedure is then again repeated for circular pier after changing the inclination angle to 5˚, 10˚, 15˚, 20˚. Similarly same procedure is then repeated for the other shapes of pier.

RESULTS AND CONCLUSIONS

In this research work, we have taken 45 different experimental runs to observe the trend of scouring. Three different shapes of the pier were used. Five different inclination angles were set for each of the pier i.e., 0˚, 5˚,10˚,15˚, 20˚ and the experimental runs were taken on three different discharge values i.e., Froude no. 0.281, 0.300 and 0.311. Results obtained from these three Froude no's are represented in graphical manner below.

CONCLUSIONS

In our experimental study, we found that the effect inclination of a bridge pier on local scouring around bridge pier. The results revealed as follows:

- As we increased the angle of inclination of a bridge pier towards the downstream direction from 0˚ to 20˚ w.r.t the vertical axis, the local scouring around a bridge pier got reduced accordingly.
- The scouring depends on the shape of a bridge pier i.e., scouring is minimum for a circular pier, intermediate for an octagonal pier and maximum for a square pier of same dimensions.
- Dimension of a pier is also a function of scouring greater the obstruction to the flow, greater is the scouring around it.
- The scouring also depends on the Froude number i.e., as we increased the Froude number, the scouring also got increased.

REFERENCES

[1] Bateni, S. M., Borghei, S. M., and Jeng, D.-S. (2007). "Neural network and neuro-fuzzy assessments for scour depth around bridge piers." Eng. Appl. Artif. Intell., 20(3), 401–414.

[2] Breusers, H. N. C., Nicollet, G., and Shen, H. W. (1977). "Local scour around cylindrical piers." J. Hydraul. Res., 15(3), 211–252.

[3] Coleman, N. L. (1971). "Analyzing laboratory measurements of scour at cylindrical piers in sand beds." Proc., 14th Congress I.A.H.R.,

[4] Firat, M., and Gungor, M. (2009). "Generalized regression neural networks and feed forward neural networks for prediction of scour depth around bridge piers." Adv. Eng. Softw., 40(8), 731–737.

[5] Froehlich, D. C. (1988). "Analysis of onsite measurements of scour at piers." ASCE Nat. Hydraul. Eng. Conf., ASCE, Colorado Springs, CO, 534–539.

[6] Gao, D., Posada, G. L., and Nordin, C. F. (1993). "Pier scour equations used in the People's Republic of China." FHWA-SA-93-076, Federal Highway Administration, Washington, DC.

[7] Grimaldi,C., gaudio, r., Calomino, F., Cardoso, A. " countermeasures against local scouring at bridge piers: slot and combined system of slot and bedsill". Journal of Hydraulic Engineering, 2009, 135(5): 425-431.

[8] Grimaldi,C., gaudio, r., Calomino, F., Cardoso, A. " Control of scour at bridge piers by a downstream bedsill". Journal of Hydraulic engineering, 2009, 135(1): 13-21.

[9] International Association of Hydraulic Research. Dey, S., Bose, S., and Sastry, G. (1995). "Clear water scour at circular piers: A model." J. Hydraul. Eng., 10.1061/(ASCE)0733-9429(1995)121:12 (869), 869–876.

[10] Kate Porter, Richard Simons and John Harris"Comparison of three techniques for scour depth measurement photogrammetry, ecosounder profiling and a calibrated pile", Costal Engineering 2014 pp-1-12.

[11] Mashahir, M.B., Zarrati, A.R., Mokallat, E. "Application of Riprap and Collar to prevent Scouring around Rectangular bridge piers". Journal of Hydraulic Engineering,2010, 136(3): 183-187.

[12] P. Johnson."Advanced Bridge Pier Scouring engineering".J.prof.Issues Eng. Edu. Pract., 117(1):48-55

[13] Vittal, N., Kothyari, U.C., Haghighat, M. " Clear- water scour around bridge pier group". Journal of Hydraulic Engineering, 1994, 120(11): 1309-1318.

[14] Vaghefi, M., ghodsian, M., Salimi, S. " the effect of circular bridge piers with different inclination angles towards downstream on scour". Indian academy of sciences, 2016, 41(1): 75-86.

[15] Y.M. Chiew. " scour protection at Bridge piers". Journal of Hydraulic Engineering, 1992, 118(9): 1260-1269.

[16] Zafer, B., yildiz, O. " effects of inclination of bridge piers on scouring depth". Journal of Hydraulic Engineering, 2004, 130(8): 827-832.

[17] Zarrati, A. R., nazariha, M., mashahir, M.B. " reduction of local scour in the vicinity of bridge pier groups using collar and riprap". Journal of Hydraulic Engineering, 2006, 132(2): 154-162.

ResearchGate

See discussions, stats, and author profiles for this publication at: https://www.researchgate.net/publication/324223006

Sustainable development of groundwater: A case study of Begamganj block in Bina River Basin of Madhya Pradesh, India

Conference Paper · March 2018

CITATIONS
0

READS
6

4 authors:

Sushant Kumar
Delhi Technological University
3 PUBLICATIONS **0** CITATIONS
SEE PROFILE

Munendra Kumar
Delhi Technological University
9 PUBLICATIONS **1** CITATION
SEE PROFILE

Tejram Nayak
National Institute of Hydrology
16 PUBLICATIONS **63** CITATIONS
SEE PROFILE

Anil Kumar sahu Sahu
Delhi Technological University,Delhi-110042
13 PUBLICATIONS **72** CITATIONS
SEE PROFILE

Some of the authors of this publication are also working on these related projects:

Post Graduate Program View project

Integrated Assessment of Drought Vulnerability for Water Resources Management in Bina Basin in Madhya Pradesh View project

All content following this page was uploaded by Sushant Kumar on 05 April 2018.

The user has requested enhancement of the downloaded file.

Sushant Kumar et al. International Journal of Recent Research Aspects ISSN: 2349-7688, Vol. 5, Issue 1, March 2018, pp. 197-200

Sustainable development of groundwater: A case study of Begamganj block in Bina River Basin of Madhya Pradesh, India.

Sushant Kumar[1], A.K.Sahu[2], Munendra Kumar[3], M.K. Choudhary[4], T.R.Nayak[5]

[1]Ph.D Research Scholar, Department of Civil Engineering, Delhi Technological University, India
Corresponding author Email Id- Sushantkumar2792@gmail.com
[2]Professor, Department of Civil Engineering, Delhi Technological University, India.
[3]Associate Professor, Department of Civil Engineering, Delhi Technological University, India.
[4]Associate Professor, Department of Civil Engineering, Maulana Azad National Institute of Technology, India.
[5]Scientist E and Head, National Institute of Hydrology, Bhopal, India.

Abstract: **The present study is focused on steady-state groundwater modelling in Begamganj block of Bina river basin in the state of Madhya Pradesh, India. Bina river is a main source of water for the domestical and irrigation supply for the local people. Results provided by the modelling after proper calibration and validation are helpful to identify the water scarce zone which can be further helpful in applying management strategies for meeting groundwater demand for the future need. In this steady state modelling, the top aquifer has been taken into account for the simplification of the model process. Aquifers below the top aquifer were not found suitable in meeting the water quality parameter for domestic usage, as per the norms of Government of India. Management strategies can be applied for the sustainable development of groundwater aquifer in the study area. ILWIS an open source GIS software was used to prepare the required files for the input of Visual MODFLOW. Aquifer data was collected from the data provided by Central Ground Water Board (CGWB) Bhopal, Madhya Pradesh, India and Water Resources Department (WRD) Bhopal, Madhya Pradesh, India. The validation of the model was carried out by matching the field value collected by CGWB and WRD. After identification of water scare zone management tools can be applied for rejuvenation in the aquifer.**

Keywords: **Aquifer, FDM, ILWIS, MODFLOW, Sustainable development, Water resources development**

I. INTRODUCTION

Groundwater is very important due to its good quality and availability. Earlier groundwater was considered safe for domestic use, but recently it is getting depleted in many countries. It is now becoming our need to understand the processes by which groundwater is made available to us. Using mathematical equations, groundwater models can simulate the performance of groundwater system and estimate changes in the water balance caused by pumping, climate, etc. and its affect on groundwater storage, lake levels, stream flow etc. Human activities and natural processes affects the groundwater systems thus require management strategies to keep good condition of groundwater resources. Groundwater management strategies and policy-making should be take account of past and present behaviour of groundwater system, likely response to future changes. Numerical groundwater models have proven to be best predictive tools for managing an aquifers system. These models are used to enhance ground water-resources management. Safe groundwater abstraction and implementing groundwater management is vital key for the sustainability use of it. Begamganj is semi-arid areas and hence facing water scarcity mostly during the dry season. Due to the increase in population and urbanization in the area, over-pumping at inc. Groundwater models have an important role in development and management and in groundwater prediction. With rapid increases in computational ability and ease of access of computers and modelling software, groundwater modelling has become a standard tool for effective groundwater management. In this study, MODFLOW is used to develop a steady state groundwater flow model in Begamganj block of Bina River basin.

II. LITERATURE REVIEW

- **Sushant K et al. (2017)** simulated a groundwater model using MODFLOW for Bina River Basin, Bina, Madhya Pradesh, India. Groundwater Monitoring was the primary concern in this study to identify the water deficit area in the catchment. In this paper, modelling was done with ten-year data of observation well for the year 2009.
- **Graafi et al. (2015)** simulated a model in a natural dynamic steady state that estimated specific yield by modelling only one unconfined layer and it help to access fluctuations in the groundwater level. But the capillary rise of water table has not been implemented which can affect soil moisture, evaporation or even precipitation.
- **Maxwell et al. (2015)** analysed and simulated an integrated model for surface and groundwater interaction under steady-state conditions. They also discussed about imperfection of the model and the difficulties that occurs in a modelling while inputting correct data and its calibration. Their model

© 2018 IJRAA All Rights Reserved

represents advancement in understanding of hydrologic scaling in continental river basins.

- **Singhal and Goyal (2011)** developed a conceptual 3-D groundwater flow model Using GMS (Groundwater modeling system) in which spatially distributed recharge values had been utilized as lump sum average of recharge that is normally obtained by method of water budgeting. They used GIS for pre-processing of, geological, hydrogeological and hydrological data. It provided better tools for developing a conceptual model for handling groundwater modelling problems.
- **Zare and Koch (2014)** simulated a groundwater model using MODFLOW of an irrigation/drainage network from 2007 to 2009 by studying groundwater fluctuation. They found that after 10 years of irrigation operation in that land water table will continue to rise and it will result 50% of the plain area to be water logged.
- **Wels (2012)** reviewed benefits of groundwater modelling and its application mainly in Transport modelling, Impact assessment of natural resource. He also described the difficulties involved while modelling groundwater. Results of the calibration process were presented for both steady-state and transient in the form of observed vs. calculated head residuals.

III. DESCRIPTION OF THE AREA UNDER STUDY

The area selected for present study is Begamganj block in Bina River basin of Madhya Pradesh, India. It is located on a river Bina which is a tributary of Betwa River in Bundelkhand region of Madhya Pradesh. Begamganj is a city in Raisen with elevation of 498 metresand having population of 34,031 according to 2011 senses. It is one of the five divisions of Raisen district. Begamganj is located at 23.6°N 78.33°E. Begamganj area in Bina river basin is nearly 91200 ha. The upper part of the study area is highly undulating and covered by forests, barren lands. Later is mostly gently sloping to plain topography largely covered with agricultural fields. The streams are dry after the monsoon months despite enough rainfall. Average annual rainfall recorded for the year 2011 over the basin is 925.3 mm. It has semi-arid to sub-tropical climate. The long-term average (normal) of maximum temperature varies from about 25˚ C in January to 41˚C in May. The wind speed ranges from 170 Km/day in December to 288 Km/day in June. The humidity in these months varies from 91 to 93% in the morning. The average evapotranspiration value of AET was 703 mm/year.

The area around Bina river basin is mostly fertile black cotton soil and some area under red soil. As per the demographic information collected for villages in catchment area, around 40% of area in Rabi season is under wheat cultivation. Gram is grown in around 38% of area cultivated in Rabi. Less than 20% area in Rabi season is under lintel cultivation. The Kharif crops are mostly rain fed and there is no canal irrigation facility. The farmers make their own arrangements to irrigate the crops by pumping groundwater or surface water bodies, in order to save the crops during the dry spell period in Kharif season. The main crops grown in Rabi season are wheat, red gram and main crops grown in Kharif season are soyabeen, urad and paddy Other staple crops like linseed, chickpeas, sorghum, oilseeds are also grown in the study area. Mostly wheat crops grown in the Rabi season are irrigated through the groundwater pumping, as there are limited surface water storage structures, like check dams, tanks, ponds, weirs etc. Therefore, groundwater is exploited for domestic and agricultural uses during Rabi season causing depletion of the water table in most of the area.

IV. METHODOLOGY

A simplified model of the groundwater of Begamganj block of Bina River basin was developed. UTM Projection coordinate system was adopted to generate a general coordinate system for the study area (WGS 84). In this projection system the coordinates can be assigned in metric and geographic units both. ILWIS 3.8.5 software has been used to process all the GIS based data like catchment, Calculation of Area of Blocks of Bina, Digitization of River, Location of well, DEM of Bina. Groundwater recharge occurs naturally due to precipitation from Bina River. Estimating groundwater recharge rate is a elementary prerequisite of proficient aquifer management. The annual average rainfall was taken 925.3 mm in Begamganj block of Bina River basin, Rainfall Data has been taken from State Data Centre, WRD, Bhopal (Madhya Pradesh). The rainfall is a major aspect for the estimating recharge in the area. The pumping well is assigned to each block as per the amount of draft in the area due to data unavailability of pumping wells. Water is abstracted throughout the year from the wells and the abstraction rate of the well was considered to be approximately 800 m^3/day based on the records provided by CGWB and WRD, Bhopal (Madhya Pradesh, India). Ten years of groundwater head level monitoring data were collected from the CGWB and WRD. The groundwater level data from observation wells, recorded by CGWB Bhopal, Madhya Pradesh, India was used to serve model input for the year 2011. Rainfall, ET and soil type are the major factors that affects groundwater recharge. The recharge in the area occurs from rainfall. The recharge in the study area is estimated to be around 30%-40% of rain events.

The hydraulic property plays an important role in subsurface studies and for this study it is derived from aquifer pumping tests carried out by CGWB.. The hydraulic conductivity is not uniform over the catchment. First Aquifer has average hydraulic conductivity K_x and K_y = $2.71X10^{-05}$ m/s K_z=$2.71x10^{-06}$ m/s. The variability in the hydraulic properties are mainly due to heterogeneity. Total porosity is 0.30 for and effective porosity is nearly 0.15. Specific yield (S_y) of aquifer is found out to be 0.11 according to CGWB, Bhopal. Specific storage is calculated by dividing Storage coefficient by the thickness of aquifer layer and average value of S_s in all the wells and it is found out to be $6.46x10^{-05}$ (1/m). For this study area, the static water level records of the wells are obtained from CGWB and WRD, the initial hydraulic heads for the Begamganj blocks of Bina River basin approximately ranges from 8 to 30 meters below ground level. In this Study area Wall Boundary separate groundwater flow from the adjacent watershed in the upper parts of the catchment. The Thickness of wall boundary is interpreted to be 2 m. Finite difference grid of 80 x 80 numbers of Rows and columns are taken into

© 2018 IJRAA All Rights Reserved

consideration. The Finite Difference grid size was selected from many by trial runs for maintaining a balance between accuracy of the model and its computational time.

V. MODEL CALIBRATION AND VALIDATION

Model calibration was carried out by hit and trial method and model is validated for the year 2009.

VI. MODELLING RESULTS

The calculated groundwater levels at Begamganj block of Bina was shown to have the satisfactory result as compared to measured levels and the flow patterns obtained indicated that few area was poorly represented by the model.

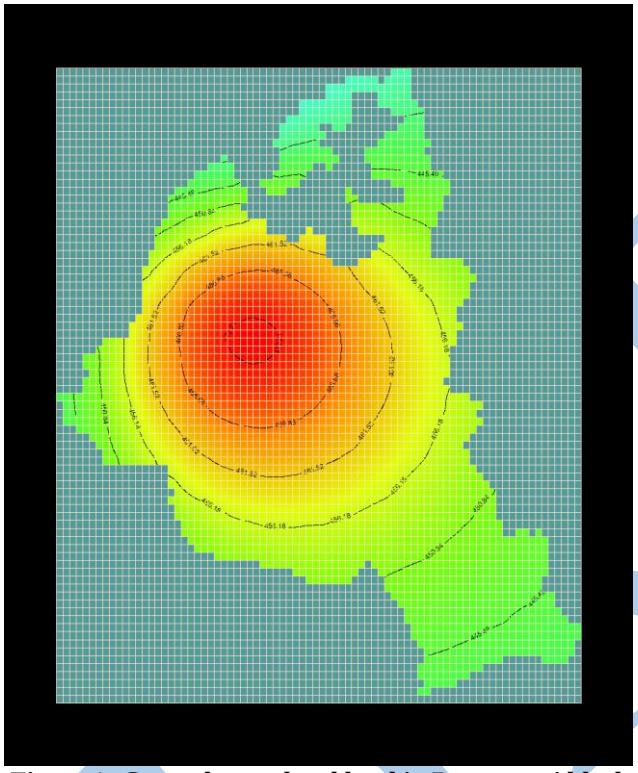

Figure 1: Groundwater head level in Begamganj block of Bina River Basin (in m)

The flow pattern at Bina River watershed can be judged to be reliable since spatial distribution of the soil types at Bina river basin was assumed to be fairly accurate. Along the pathway of the flow through some observation well drainages and pond located were not included in the model and might have influenced the flow pattern.

VII. CONCLUSIONS

Groundwater modelling has become more vital because of its promptly falling groundwater levels because of overexploitation. Groundwater models are important tools which are often used in studying the nature of groundwater flow systems. A groundwater model is an easy representation of the groundwater system of complex nature. It has proven to be very useful tools over the decades for addressing a wide range of groundwater problems and hence supporting the decision-making process. In the present study, a monitoring model is developed to estimate water level of Begamganj block of Bina River basin with the known boundary conditions and the known field observations. GIS was used for pre-processing of hydrogeological, hydrological and geological data. The methodology presented here delivers better tools for a conceptual model development to deal with groundwater modelling problems. The result shows a huge water depletion in the area marked with red colour in Figure 1 as groundwater depletion rates is high in Bina River basin due rising Agricultural and domestic demand due to which a local cone of depression is formed. The groundwater in the basin is exploited for irrigation to the largest because there is no major reservoir and canal water supply in the area. The surface water in the study area is generally available for the beginning of the Rabi season only till the end of December and farmers are dependent on the groundwater pumping from the private dug wells or tube wells. Few number of minor irrigation tanks are available is this basin to supply irrigation water in the Rabi season. During the summer months, almost all villages depend on the groundwater for their drinking and domestic purposes; however pond water is used for live stocks. More water conservation measures are required to maintain the sustainable groundwater in the sub-basin. The development of groundwater resources for sustainable use is greatly dependent on the groundwater model predictions. Hence this study can help in management studies for sustainable groundwater management in the area. The government of India has been extending technical and financial support to the state government for implementing Artificial recharge studies by CGWB the Central Ground Water Board, under the Central Sector Scheme in rural and urban areas of the district but yet at present no such project have been taken. Artificial Recharge is needed the area for efficient groundwater management in the study area.

VIII. FUTURE SCOPE

To obtain a better understanding of general hydraulic properties of the aquifer, additional pumping tests could be taken into consideration. One aspect to understand the groundwater transmission better in the anisotropy porous media. However, note should be taken that when determining the anisotropy, due to lack of data the hydraulic conductivity in the vertical direction was not that accurate. There is a need for improvement in anisotropy. Only the Horizontal conductivity was obtained from the pumping tests. Neither was any grain size analysis conducted for these types of material because no samples were available. It is thus recommended that if future borehole investigations are conducted, a sampling of these materials should be carried out as well. The modelling could perhaps have been better made if Drainage, River boundary conditions could be included. Detail data of River parameters like River Leakance, Thickness, Stage, bottom etc. are required. Drain data was not sufficient enough to apply drainage boundary condition. Nevertheless, a global model has to be relatively correct for a local model to apply and there are still major uncertainties. It is impossible to understand the sub-surface accurately, and the groundwater flow processes. We can construct bores for observation and pumping to monitor water level and other physical features of the system.

IX. ACKNOWLEDGEMENT

© 2018 IJRAA All Rights Reserved

We would like to acknowledge the profound sense of gratitude to Dr. Bijendra Kumar Baghel (Scientific officer State Water Resource Data Centre, Govt. of M.P., Bhopal), Dr. Subhash Singh (Scientist D, Central Ground Water Board, Bhopal) and Dr. Surjeet Singh, Scientist D (Groundwater Hydrology Division, National institute of Hydrology, Roorkee) for providing me their valuable time and knowledge.

X. REFERENCES

[1]. Fetter C.W. (2001) "applied hydrogeology" text book 4th Ed. Macmillan College, New York.

[2]. Gebregziabher B (2003) "Integrated geophysical methods to investigate the geological structures and hydrostratigraphic unit of the Aynalem area, Southeast Mekelle" MSc thesis, Addis Ababa University, Ethiopia.

[3]. Graafi I et al. (2015) "A high-resolution global-scale groundwater model" *J. Hydrol. Earth Syst. Sci.*, Vol .19, pp.823–837.

[4]. https://en.wikipedia.org/wiki/Begamganj

[5]. Maxwell R et al. (2015) "A high-resolution simulation of groundwater and surface water over most of the continental US with the integrated hydrologic model ParFlow v3" *J. Geosci. Model Dev*. Vol. 8, pp. 923-937.

[6]. Nayak TR et al. (2015) "GIS Based Mapping of groundwater fluctuations in Bina Basin" J. International conference on water resources, coastal and ocean engineering (ICWRCOE 2015)

[7]. Singhal V and Goyal R (2011) "Development of conceptual groundwater flow model for Pali Area, India" *J. African Journal of Environmental Science and Technology* Vol. 5(12), pp. 1085-1092.

[8]. Sushant Kumar et al. (2017) "Groundwater Modelling in Bina River Basin, India using Visual MODFLOW" Journal IJSRD -International Journal for Scientific Research & Development, Vol. 5, Issue 05,2017, pp. 1398-1402.

[9]. Wels C (2012) "Guidelines for Groundwater Modelling to Assess Impacts of Proposed Natural Resource Development Activities" British Columbia Ministry of Environment, pp.2-289.

[10]. Zare M and Koch M. (2014) "3D- groundwater flow modelling of the effects of the construction of an irrigation/drainage network on possible water logging in the Miandarband plain, Iran". *J. Basic Research Journal of Soil and Environmental Science ISSN 2345-4090* Vol. 2(2) pp.29-39.

IJRAA

© 2018 IJRAA All Rights Reserved

View publication stats

Tb^{3+} and Eu^{3+} doped zinc phosphate glasses for solid state lighting applications

Kaushal Jha, Amit K. Vishwakarma, M. Jayasimhadri, D. Haranath, and Kiwan Jang

Citation: AIP Conference Proceedings **1942**, 070036 (2018); doi: 10.1063/1.5028834
View online: https://doi.org/10.1063/1.5028834
View Table of Contents: http://aip.scitation.org/toc/apc/1942/1
Published by the American Institute of Physics

Tb^{3+} and Eu^{3+} Doped Zinc Phosphate Glasses for Solid State Lighting Applications

Kaushal Jha[1,3], Amit K Vishwakarma[1], M. Jayasimhadri[1,a)], D. Haranath[2] and Kiwan Jang[3,a)]

[1]*Luminescent Materials Research Lab, Department of Applied Physics, Delhi Technological University, Delhi 110 042, India.*
[2]*CSIR-National Physical Laboratory, Dr. K.S. Krishnan Road, New Delhi 110 012, India.*
[3]Department of Physics, Changwon National University, Changwon 641-773, Republic of Korea.
[a)]Corresponding authors: jayaphysics@yahoo.com, kwjang@changwon.ac.kr

Abstract: Tb^{3+} and Eu^{3+} doped zinc phosphate (ZP) glasses were prepared by conventional melt-quenching technique and their photoluminescence properties were investigated in detail. For, Tb^{3+} doped glasses the intense emission was at 545 nm corresponding to $^5D_4 \rightarrow {}^7F_5$ transition under 377 nm n-UV excitation. The optimized concentration for Tb^{3+} doped zinc phosphate glass was 3 mol% and above this concentration quenching takes place. The Eu^{3+} doped zinc phosphate glass revealed intense emission at 613 nm attributed to the $^5D_0 \rightarrow {}^7F_2$ transition under intense 392 nm n-UV excitation. The concentration quenching phenomenon was not observed in the Eu^{3+} doped ZP glasses. The CIE chromaticity coordinates for 3 mol% Tb^{3+} and 5 mol% Eu^{3+} doped ZP glasses were found to (0.283, 0.615) and (0.652, 0.331) lying in the green and red regions, respectively. The above mentioned results indicate that the prepared glass are suitable for application in the field of lighting and display devices.

INTRODUCTION

In the recent era, white-light emitting diodes (W-LEDs) in solid-state-lighting (SSL) technology are receiving great importance, as it offers higher efficiency, longer lifetime and environment-friendly characteristics in comparison to incandescent and fluorescent lamps. Currently, W-LEDs are fabricated using a phosphor (wavelength converter) in combination with the LED chips. The phosphor can single or multitude in nature which is being excited by UV/n-UV/blue LED chips [1,2]. However, the phosphor is suspended in the form of powder inside an epoxy-resin which is made up of polymer/organic material. This epoxy-resin gets damaged by high power/excitation LED chips, which leads to the yellowing and carbonization of epoxy. Further, this high temperature leads to the reduction in phosphor emission. As a result, there is a decrement in the luminous efficiencies and chromaticity shift takes place, which hampers the optical performance drastically [3,4]. To overcome these shortcomings, a futuristic material with excellent optical properties, simpler manufacturing technique, and high thermal and chemical resistance is required. A luminescent glass is the best alternative as they possess all the characteristics mentioned above, in addition to that they serve both the purpose of wavelength converter and encapsulant. Therefore, luminescent glasses can be considered as the potential alternative candidate for fabrication of w-LEDs. Among different glass formers, phosphates have the low melting temperature, very high transparency in the broad spectral region and offer excellent solubility for the transition and rare earth metals. Phosphates glasses have a broad range of applications in lasers, optical amplifiers, waveguides and solid state lighting. However, the phosphate glasses are hygroscopic in nature and to eliminate Zinc oxide (ZnO) are incorporated in the phosphate glass batch to eliminate the hygroscopic nature. ZnO offers chemical and thermal stability to the phosphate structure. Barium oxide (BaO) incorporation in the phosphate glasses can enhance the mechanical strength. Further, the addition of titanium oxide (TiO_2) to the glass batch can provide stabilization and improves chemical durability [5–8]. Among various rare-earth

DAE Solid State Physics Symposium 2017
AIP Conf. Proc. 1942, 070036-1–070036-4; https://doi.org/10.1063/1.5028834
Published by AIP Publishing. 978-0-7354-1634-5/$30.00

ions, Eu3+ with 4f6 electronic configuration has gained enormous attention due to its emission in the red region. It also finds application as a structural probe for site occupancy and local symmetry determination in the host lattice. Tb3+ with 4f8 configuration has emission originating from 5D4→7FJ transition and find application in lasers and lighting [9–11]. In the present work, zinc phosphate (ZP) glasses were doped with Eu3+ and Tb3+ to determine its applicability in the solid state lighting applications under n-UV excitation.

EXPERIMENTAL DETAILS

The glasses were prepared in the molar composition (40-x)ZnO-35P_2O_5-20BaO-5TiO_2-xTb_2O_3 (x = 0.1, 0.5, 1.5, 3.0 and 4.0 mol%). Another set of glasses were prepared in the molar composition as (40-x)ZnO-35P_2O_5-20BaO-5TiO_2-xEu_2O_3 (x = 0.5, 1.0, 3.0, and 5.0 mol%). The starting materials were analytical reagent (AR) grade $NH_4H_2PO_4$, ZnO, TiO_2, $BaCO_3$ and high purity Tb_2O_3 and Eu_2O_3. The chemicals were weighed as per stoichiometry and were ground using agate mortar pestle for an hour using ethanol as the wetting medium. The chemical mixture was then placed inside the programmable muffle furnace at 1150 °C for an hour to obtain a transparent and bubble free melt. The melt was then quickly taken out and poured on the preheated brass plate and was subsequently annealed at 400 °C for 3 hours for removal stresses. The photoluminescence excitation (PLE) and emission properties were measured using Shimadzu RF-5301PC spectrofluorophotometer fitted with xenon flash lamp.

RESULTS AND DISCUSSION

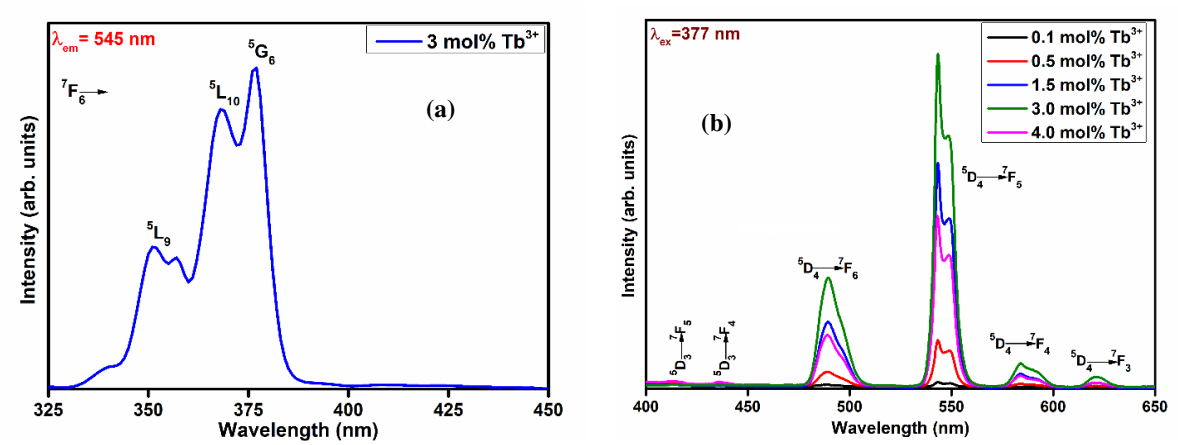

FIGURE 1 (a) Excitation spectrum for 3 mol% Tb^{3+} doped ZP glass by monitoring emission at 545 nm and (b) emission spectra for Tb^{3+} doped ZP glasses under 377 nm excitation

Figure 1 (a) represents the excitation spectrum of 3 mol% Tb3+ doped ZP glass by monitoring emission at 545 nm. The excitation spectrum reveals peaks at 351, 368 and 377 nm corresponding to the transitions arising from the ground 7F6 level to excited 5L9, 5L10, and 5G6 levels, respectively. The excitation peak at 377 nm has the highest intensity among all peaks. Therefore, the emission spectra for varying concentration of Tb3+ were recorded under 377 nm excitation as represented in Fig. 1 (b). The emission spectra reveal peaks originating from 5D3 and 5D4 levels. The emissions from 5D3 are very weak, which indicate pronounced energy transfer to lower 5D4 level via non-radiative relaxation. The emission spectra give four emission bands centered at 488, 545, 586, and 625 nm attributed to transition 5D4→7F6, 5D4→7F5, 5D4→7F4, and 5D4→7F3 transitions, respectively. The intense emission at 545 nm corresponding to the 5D4→7F5 is magnetic dipole in nature, while the transition at 488 nm corresponding to the 5D4→7F4 is of forced electric dipole nature. The emission at 545 nm splits into two peaks due to the crystal field splitting [12,13]. The emission intensity increases up to 3 mol% Tb3+ and decreases after that. The concentration quenching of 5D4 level is observed due to the energy migration, cross-relaxation phenomenon or cooperative energy transfer to higher lying states [14,15]. Figure 2 (a) represents the excitation spectrum of 5 mol% Eu3+ doped ZP glasses by monitoring emission at 613 nm. The excitation spectrum revealed five peaks at 360, 381, 392, 412, and 462 nm attributed to 7F0→5D4, 7F0→5L7, 7F0→5L6, 7F0→5D3, and 7F0→5D2 transitions,

respectively. The most intense peak was observed at 392 nm in the n-UV region corresponding to the 7F0→5L6 transition, which well with the excitation of n-UV LEDs. The emission spectra are shown in the Fig. 2 (b) under the excitation of 392 nm. The emission spectra revealed peaks at 577, 591, 613, 655, and 700 nm originating from excited state 5D0 to different ground states 7F0, 7F1, 7F2, 7F3, and 7F4. The emission intensity of the peaks increase with the increase in the Eu3+ concentration and the concentration quenching phenomenon is not observed in the present work up to 5 mol%. The most intense emission at 613 nm is forced electric dipole in nature, while the peak at 591 nm is magnetic dipole in nature [16–18]. The emission intensity ratio of (5D0→7F2/5D0→7F1) is known as the asymmetric ratio and is a measure of the site symmetry. For 5 mol %, the value of the asymmetric ratio is 2.18, which indicates that the red emission is stronger than the orange emission [11,19,20]. The value of the asymmetric ratio also suggests that the Eu3+ ions are located at sites without an inversion symmetry.

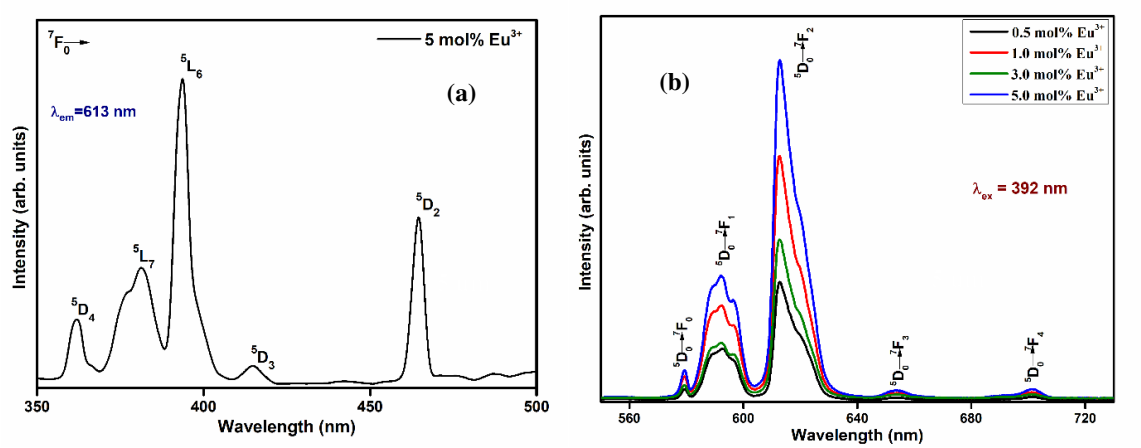

FIGURE 2 (a) Excitation spectrum for 5 mol% Eu^{3+} doped ZP glass by monitoring emission at 613 nm and (b) emission spectra for Eu^{3+} doped ZP glasses under 392 nm excitation

Based on the emission spectra, the CIE chromaticity coordinates were calculated for the 3 mol% Tb3+ doped and Eu3+ doped ZP glasses as represented in Fig. 3. The chromaticity values for the 3 mol% Tb3+ doped glass were found to be (0.283, 0.615) which lie in the green region on the CIE 1931 plot. For 5 mol% Eu3+ doped ZP glass the chromaticity coordinates were (0.652, 0.331) lying in the red region. The results based on the emission spectra and the chromaticity coordinates indicate that Tb3+ and Eu3+ ZP glasses are a potential candidate for green and red photoluminescent component for lighting and display applications.

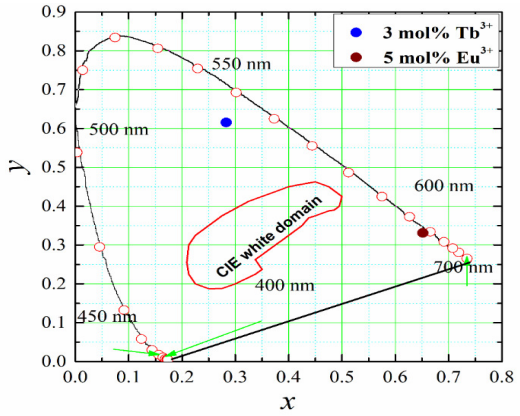

FIGURE 3. CIE chromaticity coordinates for 3 mol% Tb^{3+} and 5 mol% Eu^{3+} doped ZP glasses.

CONCLUSIONS

Barium zinc phosphate glasses doped with Tb^{3+} and Eu^{3+} were prepared by conventional melt-quenching technique. The Tb^{3+} and Eu^{3+} doped ZP glasses reveal emission in the green and red spectral region with the intense peak centered at 545 and 613 nm under n-UV excitations of 377 and 392 nm, respectively. The CIE chromaticity were (0.283, 0.615) and (0.652, 0.331) for Tb^{3+} and Eu^{3+} ZP glasses, respectively. The obtained results indicate that these luminescent glasses are a potential candidate for display and lighting applications under n-UV excitation.

ACKNOWLEDGEMENTS

Kaushal Jha is grateful to University Grant Commission (UGC), New Delhi, for providing financial support in the form of Senior Research Fellowship and DST, India and NRF, South Korea for Indo-Korean research fellowship. The author (M. Jayasimhadri) is grateful to DST-SERB, Govt. of India for the sanction of a research project (No. SB/FTP/PS-082/2014, dt. 02/03/2015). This work is also supported by the National Research Foundation of Korea funded by the Ministry of Education, Science and Technology (NRF–2015–056886).

REFERENCES

1. R.-J. Xie, N. Hirosaki, M. Mitomo, K. Takahashi, and K. Sakuma, Appl. Phys. Lett. **88**, 101104 (2006).
2. J.S. Kim, P.E. Jeon, J.C. Choi, H.L. Park, S.I. Mho, and G.C. Kim, Appl. Phys. Lett. **84**, 2931 (2004).
3. X. Zhang, L. Huang, F. Pan, M. Wu, J. Wang, Y. Chen, and Q. Su, ACS Appl. Mater. Interfaces **6**, 2709 (2014).
4. K. Jha, A.K. Vishwakarma, M. Jayasimhadri, and D. Haranath, J. Alloys Compd. **719**, 116 (2017).
5. C. Ming, F. Song, L. An, and X. Ren, Appl. Phys. Lett. **102**, 141903 (2013).
6. S. Jiang, T. Luo, B.C. Hwang, F. Smekatala, K. Seneschal, J. Lucas, and N. Peyghambarian, J. Non. Cryst. Solids **263**, 364 (2000).
7. J.H. Campbell and T.I. Suratwala, J. Non. Cryst. Solids **264**, 318 (2000).
8. D.V.R. Murthy, A.M. Babu, B.C. Jamalaiah, L.R. Moorthy, M. Jayasimhadri, K. Jang, H.S. Lee, S.S. Yi, and J.H. Jeong, J. Alloys Compd. **491**, 349 (2010).
9. Maheshwary, B.P. Singh, J. Singh, and R. a. Singh, RSC Adv. **4**, 32605 (2014).
10. S.K. Gupta, P.S. Ghosh, M. Sahu, K. Bhattacharyya, R. Tewari, and V. Natarajan, RSC Adv. **5**, 58832 (2015).
11. D. Uma Maheswari, J. Suresh Kumar, L.R. Moorthy, K. Jang, and M. Jayasimhadri, Phys. B Condens. Matter **403**, 1690 (2008).
12. M. Reza Dousti and R.J. Amjad, J. Non. Cryst. Solids **420**, 21 (2015).
13. M. Jayasimhadri, K. Jha, B.V. Ratnam, H.-J. Woo, K. Jang, A.S. Rao, and D. Haranath, J. Alloys Compd. **711**, 395 (2017).
14. A.D. Sontakke, K. Biswas, and K. Annapurna, J. Lumin. **129**, 1347 (2009).
15. Y.Y. Choi, K.-S. Sohn, H.D. Park, and S.Y. Choi, J. Mater. Res. **16**, 881 (2001).
16. [A.K. Vishwakarma, K. Jha, M. Jayasimhadri, A.S. Rao, K. Jang, B. Sivaiah, and D. Haranath, J. Alloys Compd. **622**, 97 (2015).
17. K. Jha and M. Jayasimhadri, J. Am. Ceram. Soc. **100**, 1402 (2017).
18. B. V. Ratnam, M.K. Sahu, A.K. Vishwakarma, K. Jha, H.J. Woo, K. Jang, and M. Jayasimhadri, J. Lumin. **185**, 99 (2017).
19. P.A. Azeem, M. Kalidasan, K. Rama Gopal, and R.R. Reddy, J. Alloys Compd. **474**, 536 (2009).
20. Q. Wang, S. Ouyang, W. Zhang, B. Yang, Y. Zhang, and H. Xia, J. Rare Earths **33**, 13 (2015).

International Journal of Research in Engineering and Innovation (IJREI)
journal home page: http://www.ijrei.com
ISSN (Online): 2456-6934

Thermal performance of combined cycle power plant with solar reheating and regeneration using ecofriendly organic fluids

Radhey Shyam Mishra

Department of Mechanical Engineering, Delhi Technological University, Delhi, India

Abstract

The use of solar energy in natural gas combined cycle has been demonstrated in various countries since several years. There are many parameters which governed the cost on combined solar integrated cycles that are initially the reintegration of available running power plants. The main objective of the solar integrated power plant is to mitigate the emission and risk associated with the already running power plants .The other important purpose of integration of solar energy system into already running power cycles is to minimize the running cost in the existing equipment.

In this paper, thermodynamic (exergy and energy) analysis of Gas turbine-Organic Rankine combined cycle with the solar reheating of organic fluid is done and the results are compared with combined cycle with the solar reheating, with the simple combined cycle and combined cycle with regeneration of organic fluids. The thermal performance of system is compared with different organic fluids like R134a, R227ea, R245fa, R1234ze and R1234yf at different organic Rankine cycle maximum temperature and maximum pressure. It was observed that R1234yf shows maximum increase in second law efficiency by regeneration around 49.2%. 42.94% using ORC and 48.2%, using ORC with Regeneration and solar Reheat system while R134a shows maximum organic Rankine cycle efficiency of 48.3%. exergetic efficiency of combined cycle with regeneration and reheating using R1234ze organic fluid. However maximum first law efficiency comes out by using R134a fluid. For practical applications and various problems associated with ecofriendly organic fluids (such as flammability and explosion risk should be considered), R134a can be used as better option in regeneration combined cycle plant with solar reheating.
© 2018 ijrei.com. All rights reserved
Key words: Organic Rankine Cycles, Regeneration, Solar heating combined cycle power plants, Energy-Exergy Analysis

1. Introduction

Several solar integrated combined cycles (ISCCs) are being used in all the world and there are many projects are processing. The integrated solar combined cycles (ISCCs) have several advantages as compared to solar thermal power plants, because these give higher conversion solar efficiency, and it have very low investment cost. Many entrepreneurs and owners are ready to invest the many due to it low risk associated with the smaller plants as compared to the solar thermal power plants.

The procedure for changing over the vitality in a fuel into electric power incorporates the formation of mechanical work, which is then changed over into electric power by a generator. Contingent upon fuel sort and thermodynamic process, the in general productivity of this change can be as low as 33 %. This implies 67% of the inert vitality of the fuel goes up squandered. For instance, steam electric power plants which utilizes boilers to combust a petroleum derivative normal 33% efficiency. Basic cycle gas turbine (GTs) plants normal just shy of 30 percent productivity on gaseous petrol, and around 25 % on fuel oil. Quite a bit of this squandered vitality misfortunes as warm vitality in the hot fumes gasses from the ignition procedure. To build the general proficiency of electric power plants, various procedures can be consolidated to recoup and use the leftover warmth vitality in hot fumes gasses. In joined cycle mode, control plants can accomplish electrical efficiencies up to 60 %. The expression "joined cycle" alludes to the consolidating of numerous thermodynamic cycles to create control. Joined cycle operation utilizes a heat recovery boiler (HRB) that assimilates warm from high temperature deplete gasses to deliver natural vapor, which is then provided to a natural turbine to produce additional electric power. The procedure for making vapor to create work utilizing a natural

Corresponding author: R.S. Mishra
Email Id: hod.mechanical.rsm@dtu.ac.in

turbine depends on the Rankine cycle. The most widely recognized sort of combined cycle control plant uses gas turbines and is known as a combined cycle gas turbine (CCGT) plant. Since gas turbines have low effectiveness in straightforward cycle operation, the yield delivered by the steam turbine represents about portion of the CCGT plant yield. There are various designs for CCGT control plants, yet normally each GT has its own related HRB, and different HRBs supply vapor to at least one organic turbines. Energy-exergy analysis gives a uniform base for correlation of different thermodynamic procedures. This analysis demonstrates the data with respect to losses that incorporate their area subjectively and quantitatively. This data can be utilized for further change in the outline and operation of the framework. By finding the exergy destruction in the each component and exergy destruction ratio of whole system, the system thermodynamic performance can be enhanced by enhancing the exegetic performance of the component and the whole system. The scope and purpose of this paper is to develop effective methodology to achieve energy-exegetic optimizations of CCGT power plants to improve thermodynamic performance of the power plant by integration of ORC and energy-exergy optimization method. With the help of this method, it would be possible to (a) provide information about the exergy destruction and exergy losses along with their location. b) Predict the highest exergy destruction components of the system. c) Suggest ways of improving the exergetic efficiency. d) Find the optimal values of operating parameters, which gives the maximum possible power output and thermal efficiency so that it would be possible to calculate minimum possible exergy destructions in the component by modifications in existing design.

2. Literature Review

In order to have an idea of the present methodology development in the area of performance and optimization of combined cycle gas turbine power plant, a brief survey of available literature was made. However, this chapter is concerned with a review of literature on optimization performed on various thermal systems. In general, some authors focus on the gas turbine operating parameters (topping cycle), others optimize the steam plant (bottoming cycle) based on a given gas turbine, whereas others propose appropriate optimization methods for the whole combined cycle power plant without integration of ORC. Furthermore, the optimization can be analyzed from a thermodynamic point of view, according to the first and/or second law analysis, or using a thermo economic or environmental-economic strategy Jaafar et al [1], Dincer et.al.[2],Boyano et al [3] , Cabrera M., et al [4] etc. From the point of view of optimization methodology, there are many types of analyses. In this work, the review will highlight most common methodology: the exergy destruction method, and the efficiency improvement method.

2.1 Thermodynamic Analysis and Optimization

The gas turbine operating parameters which influence the combined cycle gas turbine performance are; ambient conditions, compressor pressure ratio, and turbine inlet temperature. One of the factors that affect gas turbine performance is the ambient conditions, mainly ambient temperature, atmospheric pressure, and the relative humidity of air. These parameters affect the generated electric power and the heat-rate during operation. The location of power plant plays a major role on its performance. The atmospheric air, which enters the compressor, becomes hotter after compression and it is directed to a combustion chamber. Several authors reported the effect of ambient temperature: Ibrahim et al [5], Ameri and Hejazi [6],Boonnasa et al [7] and Hosseini et al [8]. The properties of air entering combustion chamber depend upon the compressor pressure ratio studied. Ibrahim and Rahman [9], and Khaliq and Kaushik et al [10] performed a parametric thermodynamic analysis of a combined cycle gas turbine. They investigated the effect of operating parameters, compression ratio, gas-turbine peak temperature ratio, isentropic compressor and efficiency and air fuel ratio on the overall plant performance. Their results show that the compression ratios, air to fuel ratio as well as the isentropic efficiencies are strongly influenced by the overall thermal efficiency of the combined cycle gas turbine power plant. The overall thermal efficiency increases with compression ratio as well as isentropic compressor and turbine efficiency. However, the variation of overall thermal efficiency is minor at the lower compression ratio while it is very significant at the higher compression ratio for both isentropic compressor and turbine efficiency. The overall efficiencies for combined cycle gas turbine are much higher than the efficiencies of gas turbine plants power output decreases linearly with the increase temperature. The efficiency of steam power plants can be improved by increasing the live steam and reheat-steam parameters, and by introducing high-efficiency, low-loss turbine blade geometries. The first goal, to increase the steam parameters, is primarily achieved by choosing appropriate materials for the components operating under live-steam and reheat-steam conditions while retaining the proven designs. Collaborative European programs have led to the development and qualification of steels with much improved creep properties at temperatures of up to 600 °C, appropriate for the manufacture of key components. At the same time, optimization of the blade profiles and geometries allowed further major improvements in operating efficiency. The achievable improvements in efficiency is about 0.5% per 10 °C live steam and reheat (RH) temperature increase, and 0.2 % per 10 bar pressure increase. Second important part of the bottoming cycle is the heat recovery steam turbine (HRSG), its design and optimization affects to a large extent influence the efficiency and the cost of the whole plant.

Mohagheghi M [11] carried out thermodynamic optimization of design variables and properties of air entering combustion chamber depend upon the compressor pressure ratio heat exchangers layout in a heat recovery steam generator HRSG

for combined cycle gas turbine CCGT using a genetic algorithm. Their method was introduced for modelling the steam cycle in advanced combined cycles by organizing the non-linear equations and their simultaneous used solutions with numerical methods. 8 In addition to the optimization of design variables of the recovery boiler, they performed the distribution of heat exchangers among different sections and optimized their layouts in HRSGs. A standard gas turbine was assumed, and then outlet gas stream conditions (mass flow rate, temperature, and chemical composition of gas stream) were considered as the inlet parameters for the recovery boiler model. From the optimization process maximum output power from a steam cycle for different HRSGs was then analyzed. Bracco S [12] studied the combined cycle power plant with a single level heat recovery steam generator HRSG. They developed a mathematical model to determine the optimal steam pressure values in the HRSG according to different objective functions (in the HRSG for a given gas turbine). Their work reports numerical results for the combined cycle power plant considering four different gas turbines. The optimization approach was focused on the study of the heat transfer between the steam and the exhaust gas in the HRSG, based on an exergetic analysis and comparison among different objective functions that refer to the HRSG specifically or to the whole bottoming cycle. In their mathematical model, they considered the presence of specific constraints for the operating parameters of the power plant, the most important constraints that were considered refer to the steam quality at the turbine outlet, the HRSG outlet exhaust gas temperature and the steam turbine blade height. In their work, a parametric analysis was also performed to evaluate the influence of the gas temperature at the HRSG inlet and the pinch point temperature difference on the considered objective functions. Woudstra et al [15**]** performed the thermodynamic evaluation of combined cycle plants with the same gas turbine and different steam bottoming cycles. The evaluation showed that the increasing the number of pressure levels of steam generation will reduce the losses due to heat transfer in the HRSG, but also the exergy loss due to the exhaust of flue gas to the stack. Among the investigated configurations for bottoming cycle, triple pressure reheat was the best option from exergy point of view. Mansouri et al [16] investigated the effect of pressure levels of steam generation at heat recovery steam generator HRSG on the energetic and exergetic efficiency of HRSG, bottoming cycle and combined cycle power plants, as well as the effect of Xiang and Chen [17]considered a combined cycle with three-pressure HRSG, equipped with the GE PG9351FA gas turbine. They maximized the combined cycle efficiency through the optimization of the HRSG operating parameters by minimizing exergy losses. Moreover, they highlighted the influence of the HRSG inlet gas temperature on the bottoming cycle efficiency. They studied the influence of HRSG inlet gas temperature on the steam bottoming cycle efficiency. Their result shows that increasing the HRSG inlet temperature has less improvement to steam cycle efficiency when it is over 590ºC. Kelly et al [18] demonstrated that the most efficient way for converting solar thermal energy into electricity is to withdraw feed water from the heat recovery steam generator (HRSG) downstream of the last economizer, to produce high pressure saturated steam and to return the steam to the HRSG for superheating and reheating. The integrated solar plant concept offers an effective means for the continued development of parabolic trough technology. In a careful plant design, solar thermal to electric conversion efficiencies will exceed, often by a significant amount, those of a solar-only parabolic trough project. An integrated plant bears only the incremental capital cost of a larger Rankine cycle which provides further reductions in the leveled cost of solar energy. He YaLing et al [19] proposed a model for a typical parabolic trough solar thermal power generation system with Organic Rankine Cycle (PT-SEGS–ORC) was built within the transient energy simulation package TRNSYS. They found that the heat loss of the solar collector increases sharply with the increase in Pinter at beginning and then reaches to an approximately constant value. The variation of heat collecting efficiency with v is quite similar to the variation of heat losses.. In addition, it is found that the optimal volume of the thermal storage system is sensitively dependent on the solar radiation intensity. Gang et al.[20]the innovative configuration of low temperature solar thermal electricity generation with regenerative organic Rankine cycle (ORC) mainly consisting of small concentration ratio compound parabolic concentrators (CPC) and the regenerative ORC. The effects of regenerative cycle on the collector, ORC, and overall electricity efficiency are then analyzed. The results indicate that the regenerative cycle has positive effects on the ORC efficiency but negative ones on the collector efficiency due to increment of the average working temperature of the first-stage collectors. And found that there generative cycle optimization of the solar thermal electric generation differs from that of a solo ORC. The system electricity efficiency with regenerative ORC is about 8.6% for irradiance 750 W/m2 and is relatively higher than that without the regenerative cycle by4.9%.Goswami DY [21] proposed co-generation system producing electricity and fresh water by a solar field driven supercritical organic Rankine cycle (SORC) coupled with desalination. The proposed system can use parabolic trough solar collectors (among other options) to produce 700 kW thermal energy with temperatures up to 400°C at peak conditions. Thermal energy is delivered to the SORC which uses hexamethyldisilane (MM) as the working organic fluid and could achieve cycle efficiency close to 21%. The SORC condensation process is undertaken by the feed seawater to reduce thermal pollution. Due to the elevated temperature of the preheated seawater, the RO unit specific energy consumption decreases. Although, lot of literature it is found that the efficiency of the combined cycle is more than the simple individual cycle. Other important conclusion found that the more and more energy going to waste from stack with exhaust flue gases even after passing through HGRC. Almost flue gas around 150-1800C is going to waste from stack.

After reading literature review it is concluded that no

researcher use the energy at temperature 150-1800C from the flue gases. In this research integration of the ORC (organic Rankine cycle) in the preexisting cycle is done for recovery of the low temperature heat from the exhaust gases which are coming from the HRSG after generation of the steam for simple Rankine cycle. It is proposed to examine the effect of the various parameters on the performance of the combined cycle and comparison is done with or without integration of the ORC.

2.2 Organic Rankine Cycle

Organic Rankine cycles have gotten more consideration amid the most recent decade. This cycle takes after the crucial principles of regular Rankine cycles working with steam in like manner plants however has a few points of interest over steam Rankine cycle which made it prevalent. Firstly this cycle can work on low pressures and temperatures in comparison to the conventional Rankine cycle and reveals a better result than steam Rankine cycle especially from low grade heat sources because it has working fluids include such as variety of HCs and other refrigerants what's more, as per scope of open heat source pressure and temperatures, different outputs can be obtained by using useful working fluids, secondly, it can also work without multi-stage turbines and feed-water heaters and that thing makes it simple using. Although this, solar parabolic collectors are a tremendous source of heat energy but these have low grade thermal energy. Because of this, these solar collectors give only some KWs to some megawatts of power generation mainly near factories and rural areas to generate own electricity consumption without the necessity for connection to grid that may be costly as shown in Fig-1.

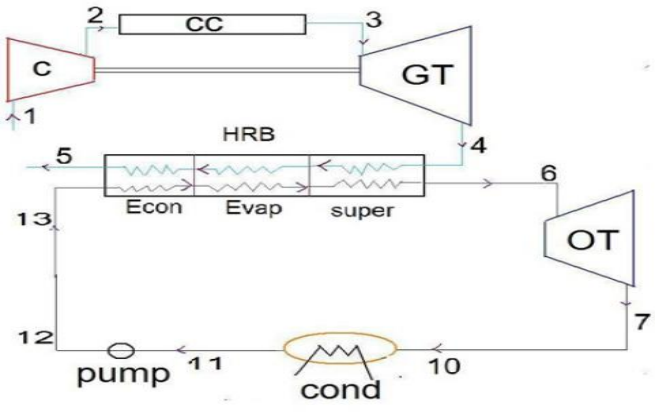

Figure 1: Combined Cycle plant without regeneration

Disadvantages of solar ORCs are comparatively high costs and low thermal efficiency (10 to 25 %) according to working fluids and working conditions) mainly because of low HTF (Heat transfer fluids) temperature in solar collector. As described before, the organic fluid works in ORC cycles are classified into HCs and refrigerants, some of those are dry liquids which mean they have a positive slope T-S graph in the vapour area. This makes it reasonable for some organic liquids to works legitimately without superheating to an extraordinary possibility and make no harm turbine. It has been appeared in this review, an examination of various dry organic liquids with or without superheating and recuperation has been done to reveal the difference in cycle effectiveness and execution of the system that encourages us to settle on a choice to pick the system condition as indicated by our requirements.

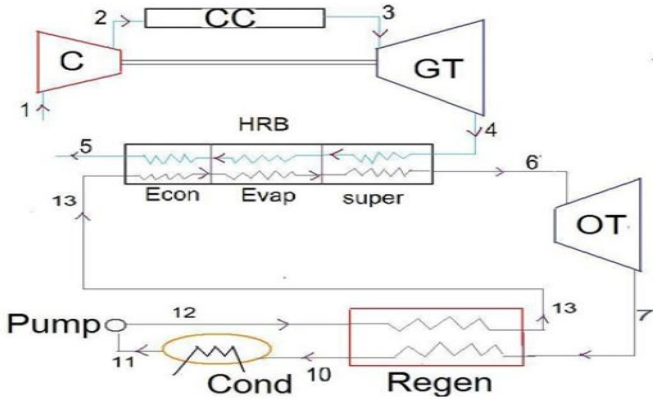

Figure 2: Combined cycle plant with regeneration

2.3 Combined Cycle Principles of Operation

The organic Rankine cycle works on the principle of a turbo generator which works as a simple steam turbine to convert thermal power into mechanical power and then into electrical power by an electrical generator. Besides of using steam of water, orc system evaporates organic fluid, classified by a molecular weight higher than the water that leads to slow rotation of the organic turbine that also leads to the less erosion of metallic parts and the blades. Organic Rankine cycle is normally a Rankine cycle in which besides of using water other organic fluid is used like R134a, R1234ze, R1234a, R245fa etc as shown in Fig-3.

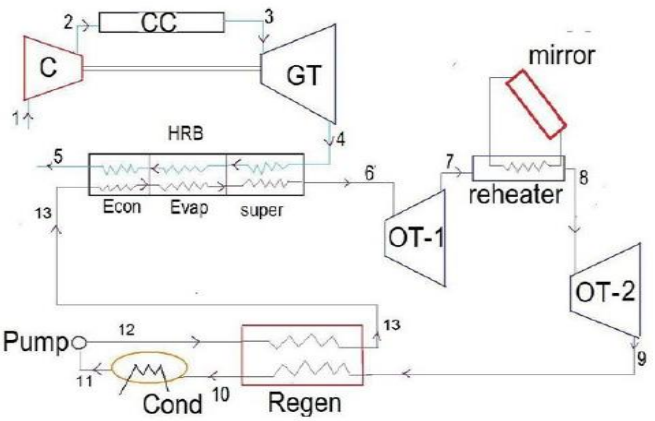

Figure 3: Combined cycle plant with regeneration and solar reheating

The heat recovery boiler (HRB) is nothing but is the simple heat exchanger, or it can be used as a series of heat exchangers. It is also can be called a boiler, because it produces organic vapour for the ORC turbine by passing the hot fumes gas spilling out of a gas turbine or ignition motor through edge of heat exchanger tubes. The HRB can takes a shot at common flow and use constrained dissemination utilizing pumps. As the hot fumes gasses stream past heat exchanger tubes through which boiling water courses, heat is utilized causing the made of vapor in the tubes. The tubes are masterminded in modules or segments, each serving an alternate capacity in the creation of dry superheated vapor. These modules are alluded to as evaporators, super heater and preheaters and economizers. The economizer works as a heat exchanger which preheats the organic fluid (liquid) to get the temperature to the saturation temperature (boiling point), that liquid to be supplied to a thick-walled boiler drum. That drum is installed where finned evaporator tubes is located that circulate heated organic fluid. Hot exhaust gases passing past to the evaporator tubes, and the heat is being absorbed and then the vapor is being created of in the tubes. This vapor-liquid mixture goes to the boiler drum where the vapour is separated from the hot liquid by using moisture cyclones and separators. The separated liquid is again recirculated to the evaporator tube the function of the some boiler drums is also to storage and water treatment functions. There are several other design of steam boiler in which another design is a once-through HRB, where thin-walled components are used in place of boiler drum which are better for handling changes in exhaust gas temperature and vapour pressures during frequently stops and starts. In other designs, duct burners can be used for adding heat to the exhaust gas current and boost vapour manufacturing; it's have been used to generate vapour even if no not sufficient exhaust gas flow is there. Saturated vapour from boiler drums or any once-through boiler system has been sent to super heater to produce dry vapour that is requirement for the organic turbine. And the organic fluids goes to the preheaters, that are placed where very low amount of heat is available and then this fluid takes energy from three and heated by the heat exchanger liquids such as the mixture of glycol water and from there very economic and useful amount of heat is extracted. The superheated organic vapour produced from the HRB is supply to organic turbine where it is expanded by the turbine blades and gives rotation to turbine shaft. The mechanical energy delivered to the generator driving shaft is transformed into high grade energy (electricity). After exiting the organic turbine, the organic vapor goes to the condenser which paths the condensed organic liquid back to HRB Combined-cycle plant works to generate electricity and absorbs waste heat from gas turbine to increase efficiency and the electrical output. Gas turbine plant burns fuel and air is compressed in compressor and then it mixes with the fuel combustion chamber. This mixture of gas and fuel is goes to gas turbine. This hot mixture is rotates the turbine blade and then shaft of turbine is rotated. This rotating turbine gives its mechanical energy to the generator shaft which transformed a part of rotating energy into electrical power. The heat recovery boiler absorbs exhaust gas. This Heat Recovery Boiler (HRB) absorbs heat from the exhaust gas turbine which would otherwise goes through the exhaust stack. The HRB makes organic vapor of organic fluid from the heat of exhaust from the gas turbine and it is supplied to steam turbine. Organic turbine gives additional electricity. The organic turbine sends its mechanical energy to the generator drive shaft, and then the additional electrical power is produced as shown in Fig-4 and 5 respectively.

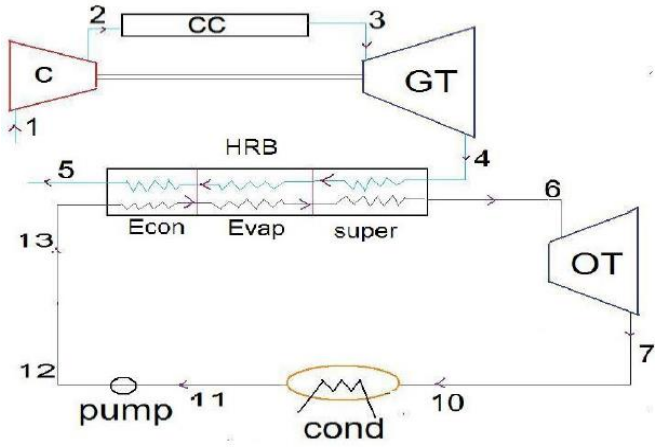

Figure 4: Combined cycle plant without regeneration

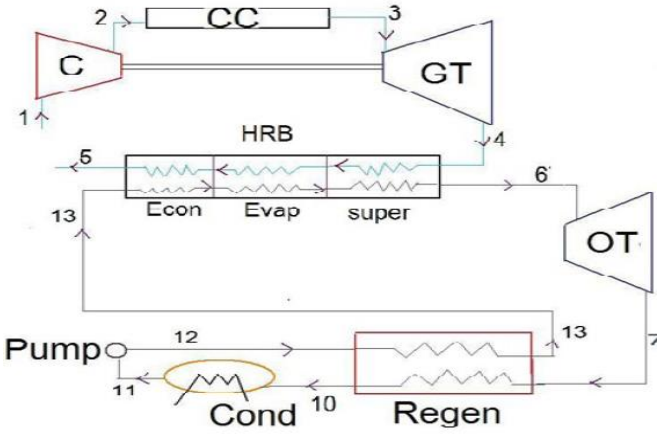

Figure 5: Combined cycle plant with regeneration

2.4 Thermodynamic Analysis

In this paper, a parametric study with various temperature and pressure at organic turbine inlet has been considered to determine efficiency and performance of organic fluid in system. The following assumptions are there to simplify the analysis, also taking energy analysis.

1. Assumed all the components are steady-state process and steady flow.

2. The changes in the kinetic energy and the potential energy are assumed to be negligible.
3. There are negligible heat and pressure loss in pipes that are connecting all the components to each other.
4. All compressor, turbines, and pump work adiabatically.
5. Pressure drops in regenerator, HRB, and condenser neglected.

Considered as control volume.

Mass Balance

$\sum_{in} m_{in} = \sum_{out} m_{out}$

Energy Balance

$Q\text{-}W + \sum_{in} m_{in} - \sum_{out} m_{out} = 0$

2.5 Energy changes in the each component of combined cycle plant

2.5.1 Air Compressor

Compressor is a work absorbing device. Air compressor is used for compressing air from atmospheric condition to high pressure. Isentropic work input to the compressor is expressed as

$W_c = \dot{m}_a * (h_{2s} - h_1)$

Compressor efficiency as,

$\eta_c = \frac{h_{2s}-h_1}{h_2-h_1}$

Actual compressor work is given by

$W_c = \dot{m}_a * (h_2 - h_1)$

2.5.2 Combustion chamber

In combustion chamber fuel is burnt and heat released by combustion is supplied to compressed air in External heat exchanger at constant pressure. Heat supplied in combustion chamber is given by

$Q_{s1} = \dot{m}_a * (h_3 - h_2)$

2.5.3 Gas turbine

Turbine is a work producing component. Air is expanded adiabatically in gas turbine. Isentropic work output of gas turbine is

$W_{GTi} = \dot{m}_a * (h_3 - h_4)$

Gas turbine efficiency as,

$\eta_{GT} = \frac{h_3-h_4}{h_3-h_{4s}}$

Actual gas turbine work is

$W_{GT} = \dot{m}_a * (h_3 - h_4)$

2.5.4 Heat Recovery Boiler

In HRB energy of hot exhaust gas of gas turbine is used for producing superheated vapor of organic fluid. HRB is a heat exchanger in which heat is transferring from hot exhaust gas to organic fluid. Energy balance for HRB is

$\dot{m}_a h_4 + \dot{m}_f h_{13} = \dot{m}_a h_5 + \dot{m}_f h_6$

Heat supplied to organic fluid,

$QHRB = \dot{m}_f * (h_6 - h_{13})$

2.5.5 Organic Rankine Turbine

Organic turbine is a work obtaining device in which organic fluid is expanded from HRB pressure to condenser pressure adiabatically. The isentropic work output of ORT,

$W_{OTi} = m_f * (h_6 - h_{7s})$

Organic turbine efficiency as,

$\eta_{OT} = \frac{h_6-h_7}{h_6-h_{7s}}$

Actual organic turbine work is

$W_{OT} = \dot{m}_f * (h_6 - h_7)$

2.5.6 Condenser

Condenser is a heat exchanger in which heat is rejected to environment is given by

$Q_{cond} = m_f * (h_{10} - h_{11})$

2.5.7 Organic pump

Organic pump is used for increasing pressure of organic fluid from condenser pressure to boiler pressure. Ideal work of organic pump

$W_{OPi} = m_f * v_{11} * (P_{12} - P_{11})$

Organic pump efficiency as,

$\dot{\eta}_{OP} = W_{OPi} / W_{OP}$

Actual organic pump work is given by

$W_{OP} = m_{f} * v_{11} * (P_{12} - P_{11})/\dot{\eta}_{OP}$

2.5.8 Efficiency of the Gas Turbine cycle

The efficiency of gas turbine plant is given by the ratio of net-work output of gas turbine plant to the heat supplied in combustion chamber,

$\dot{\eta}_{GTP} = (W_T - W_C)/ Q_{S1}$

2.5.9 Efficiency of Organic Rankine cycle

It is ratio of net work output of ORC and the total heat supplied in ORC

$\dot{\eta}_{ORC} = (W_{OT} - W_{OP})/ Q_{S2}$

2.5.10 Efficiency of the combined cycle plant

The ratio of the total work output combined cycle plant and total external heat supplied

$\dot{\eta}_{CCP} = \{ (W_T - W_C) + (W_{OT} - W_{OP}) \}/Q_{S1}$

2.6 Energy changes in each component of combined cycle plant with regeneration

2.6.1 Air Compressor

Compressor is a work absorbing component. Air compressor is used for compressing air from the atmospheric condition to the high pressure. Isentropic work input to compressor is expressed as

$W_C = m_a * (h_{2S} - h_1)$

Compressor efficiency as

$\eta_C = \frac{(h2S - h1)}{(h2 - h1)}$

Compressor work is specified by

$W_C = m_a * (h_2 - h_1)$

2.6.2 Combustion chamber

In the combustion chamber fuel is burnt and heat released by the combustion is supplied to compressed air in the External heat exchanger at constant pressure.
Heat supplied in the combustion chamber is given by

$Q_{S1} = m * (h_3 - h_2)$

2.6.3 Gas turbine

Air is expanded adiabatically in gas turbine. Isentropic work output of gas turbine is given by

$W_{GTi} = m_a * (h_3 - h4)$

Gas turbine efficiency as,

$\dot{\eta}_{GT} = (h3 - h_4)/(h_3 - h_{4S})$

Actual gas turbine work is

$W_{GT} = m_a * (h_3 - h_4)$

2.6.4 Heat Recovery Boiler

In HRB heat of the hot exhaust gas of gas turbine is used for producing superheated vapor of organic fluid. HRB is a heat exchanger in which heat is transferring from hot exhaust gas to organic fluid. Energy balance for HRB is

$m_a h_4 + m_f h_{13} = m_a h_5 + m_f h_6$

Heat supplied to organic fluid,

$Q_{HRB} = m_f * (h_6 - h_{13})$

2.6.5 Organic Rankine Turbine

Organic turbine is the work producing component in which expansion of organic fluid takes place from boiler pressure to condenser pressure adiabatically. Isentropic work output of ORT,

$W_{OTi} = m_f * (h_6 - h_{7s})$

Organic turbine efficiency as,

$\dot{\eta} = (h_6 - h_7) /(h_6 - h_{7S})$

Actual organic turbine work is

$W_{OT} = m_f * (h_6 - h_7)$

2.6.6 Regenerator

Regenerator is a liquid-vapor heat exchanger in which feed organic liquid is heated by the superheated vapor leaving from organic turbine.

$\dot{m}_f h_9 + \dot{m}_f h_{12} = \dot{m}_f h_{10} + \dot{m}_f h_{13}$

2.6.7 Condenser

Condenser is a heat exchanger in that heat is rejected to environment is given by

$Q_{cond} = m_f * (h_{10} - h_{11})$

2.6.8 Organic pump

Organic pump is used for increasing the pressure of organic fluid from condenser pressure to boiler pressure. Ideal work of organic pump

$W_{OPi} = m_f * v_{11} * (P_{11} - P_{12})$

Organic pump efficiency as,

$\dot{\eta}_{OP} = W_{OPi} / W_{OP}$

Actual organic pump work is given by

$W_{OP} = \{m_f * v_{11} * (P_{12} - P_{11})\} / \dot{\eta}_{OP}$

2.6.9 Efficiency of the Gas Turbine cycle

The efficiency of the gas turbine plant is given by the ratio of the net work output of gas the turbine plant and heat supplied in combustion chamber,

$\dot{\eta}_{GT} = (W_T - Wc) / Q_{S1}$

2.6.10 Efficiency of Organic Rankine cycle

It is the ratio of the net work output of ORC and total heat supplied in ORC

$\dot{\eta}_{ORC} = (W_{OT} - W_{OP}) / Q_{S2}$

2.6.11 Efficiency of combined cycle plant

It is defined as the ratio of total work output of the combined cycle plant to and total external heat supplied

$\dot{\eta}_{CCP} = \{ (W_T - W_C) + (W_{OT} - W_{OC}) \} / Q_{S1}$

2.7 Energy changes in the each component of combined cycle plant with regeneration and solar reheating

2.8 Air Compressor

Compressor is the work absorbing device. Air compressor is used for compressing the air from atmospheric condition to the high pressure. Isentropic work input to the compressor is expressed as

$W_c = m_a * (h_{2S} - h_1)$

Compressor efficiency as

$\dot{\eta}_c = (h_{2S} - h_1) / (h_2 - h_1)$

Actual compressor work is specified by

$Wc = m_a * (h_2 - h_1)$

2.8.1 Combustion chamber

In combustion chamber fuel is burnt and the heat released by the combustion is supplied to compressed air in External heat exchanger at constant pressure .Heat supplied through combustion chamber is given by

$Q_{S1} = m_a * (h_3 - h_2)$

Gas turbine: turbine is a work producing device. Air is expanded adiabatically in gas turbine. Isentropic work output of gas turbine is

$W_{GTi} = m_a * (h_3 - h4)$

We have gas turbine efficiency as,
Actual gas turbine work is

$\dot{\eta}_{GT} = (h3 - h_4) / (h_3 - h_{4S})$

2.8.2 Heat Recovery Boiler

In the HRB heat of the hot exhaust gas of the gas turbine is used for producing the superheated vapor of organic fluid. HRB is a heat exchanger in which heat is transferring from the hot exhaust gas to organic fluid. Energy balance for HRB is

$m_a h_4 + m_f h_{13} = m_a h_5 + m_f h_6$

Heat supplied to organic fluid,

$Q_{HRB} = m_f * (h_6 - h_{13})$

2.8.3 Organic Rankine Turbine1

Turbine is a work producing component.the expansion is taking place from HRB pressure to intermediate pressure in organic turbin-1 adiabatically. The isentropic work output,

$W_{OTi} = m_f * (h_6 - h_{7s})$

Organic turbine efficiency as,

$\dot{\eta} = (h_6 - h_7) / (h_6 - h_{7S})$

Actual organic turbine work is

$W_{OT} = m_f * (h_6 – h_7)$

2.8.4 Solar reheater

Solar reheater is the concentrated solar plate collector in that solar energy is used for reheating organic fluid. Heat supplied to the solar collector is given by

$Q_{S2} = A_S I_S \dot{\eta}_m$

Heat supplied to organic fluid

$Q_{S2} = m_f * (h_7 – h_8)$

2.8.5 Organic Rankine Turbine2

Turbine is a work producing component. The expansion of organic fluid is takes place from boiler pressure to intermediate pressure in organic turbin-2 adiabatically. The isentropic work output,

$W_{OT2} = m_f * (h_8 – h_{9S})$

Organic turbine efficiency as,

$\dot{\eta}_{OT2} = (h_8 – h_9)/(h_8 – h_{9S})$

Actual organic turbine work is

$W_{OT} = m_f * (h_8 – h_9)$

2.8.6 Regenerator

Regenerator is a liquid-vapour heat exchanger in which feed organic liquid is heated by superheated vapour leaving from organic turbine.

$m_f h_9 + m_f h_{12} = m f h_{10} + m_f h_{13}$

2.8.7 Condenser

Condenser is a heat exchanger in that heat is rejected to environment is given by

$Qcond = mf * (h_{10} – h_{11})$

2.8.8 Organic pump

Pressure of organic fluid is increased from condenser pressure to boiler pressure by pump. Ideal work of organic pump

$W_{OPi} = m_f * v_{11} * (P_{12} – P_{11})$

Organic pump efficiency as,

$\dot{\eta}_{op} = Wopi/ Wop$

Actual organic pump work is given by

$W_{OPi} = \{ m_f * v_{11} * (P_{12} – P_{11})\} \dot{\eta}_{OP}$

2.8.9 Efficiency of the Gas Turbine cycle

The efficiency of the gas turbine plant is given by the ratio of network output of the gas turbine plant and heat supplied in combustion chamber,

$\dot{\eta}_{GT} = (W_T – Wc)/ Q_{S1}$

2.8.10 Efficiency of Organic Rankine cycle

It is ratio of the net-work output of ORC and total heat supplied in ORC

$\dot{\eta}_{ORC} = (W_{OT1} + W_{OT2} – WC)/(Q_{S2} + Q_{HRB})$

2.8.11 Efficiency of combined cycle plant

The ratio of the total work output of the combined cycle plant to the total heat externally supplied

$\dot{\eta}_{CCP} = [(W_{GT} – W_C) + (W_{OT1} + W_{OT2} – W_{OP})]/ (Q_{S1} + Q_{S2})$

3. Exergy analysis of the each component of the combined cycle plant with the regeneration and the solar reheating

"Exergy loss or destruction of the compressor"

$ED_C = \dot{m}_a * T_0 * (S_2 - S_1)$

"Exergy loss or destruction of the gas turbine"

$ED_{GT} = \dot{m}_a * T_0 * (S_4 - S_3)$

"Exergy loss or destruction in HRB"

$ED_{HRBT} = \dot{m}_a * T_0 * (S_5 - S_4) + \dot{m}_f * T_0 * (S_6 - S_{13})$

"Exergy loss or destruction in the organic turbine-1"

$ED_{OT1} = \dot{m}_f * T_0 * (S_7 - S_6)$

"Exergy loss or destruction in the solar reheater"

$ED_{reheater} = \dot{m}_f * T_0 * (S_8 - S_7) – Q_{s2} * (T_0/T_s)$

“Exergy loss or destruction in the organic turbine-2"

$ED_{OT2} = \dot{m}_f * T_0 * (S_9 - S_8)$

"Exergy Destruction in the regenerator"

$ED_{REG} = \dot{m}_f * T_0 * (S_{10}-S_9) + \dot{m}_f * T_0 * (S_{13}-S_{12})$

"Exergy loss or destruction in the condenser"

$ED_{cond} = \dot{m}_f * T_0 * (S_{10}-S_9) + \dot{m}_f * T_0 * (h_{10}-h_{11})$

"Exergy loss or destruction in the organic Rankine cycle pump"

$ED_{OP} = \dot{m}_f * T_0 * (S_{12}-S_{11})$

"Exergy transfer in the gas turbine cycle by combustion chamber"

$ET_{cc} = Q_{s1} - \dot{m}_a * T_0 * (S_3-S_2)$

"Exergy transfer by the HRB to organic fluid"

$ET_{HRB} = Q_{HRB} - \dot{m}_f * T_0 * (S_6-S_{13})$

"Exergy transfer by the solar heater to organic fluid"

$ET_{reheater} = Q_{s2} - \dot{m}_f * T_0 * (S_8-S_7)$

"Second law efficiency of the gas turbine power plant"

$$\eta_{II\ law\ GTP} = \frac{W_{GTP}}{ET_{CC}}$$

"Second law efficiency of the organic Rankine cycle"

$$\eta_{II\ law\ ORC} = \frac{W_{ORC}}{ET_{HRB}}$$

"Second law efficiency of the combined cycle plant"

$$\eta_{II\ law\ CCP} = \frac{W_{ORC}+W_{GTP}}{ET_{CC}}$$

3.1 Input Parameters

The input parameters taken for computation of results are given below:

Table 1: input parameters for numerical computations for three ORC systems

S.No.	Parameters	Numerical Value
1	Air compressor inlet pressure	P_1= 100 kPa
2	Isentropic efficiency of air compressor	$\dot{\eta}_C$= 0.80
3	Air compressor inlet temperature	T_1= 27˚C
4	Pressure ratio of compressor	r_p= 18
5	Isentropic efficiency of Gas turbine	$\dot{\eta}_{GT}$= 0.85
6	Power output of the Gas Turbine Plant	W_{GTP}= 20 MW
7	Pinch point temperature difference	ΔT_{pinch}= 20˚C
8	Organic Rankine turbine inlet pressure	P_1= 2500 to 4200 kPa
9	Solar irradiation on CSP collector	I_S= 750 W/m^2
10	Isentropic efficiency of organic turbine	$\dot{\eta}_{OT}$= 0.85
11	Effectiveness of regenerator LVHE	e = 0.85
12	Mirror efficiency of CSP collector	$\dot{\eta}_m$= 0.65
13	Efficiency of organic Rankine pump	$\dot{\eta}_{ORP}$= 0.85
14	Condenser Temperature	T_{cond} = 40˚C
15	Dead State Temperature	T_o= 25^{0}C
16	Organic fluid used	Acetone. R134a, R227ea,and R1234yf, R1234ze

4. Results and Discussions

A computational model is developed by using Engineering Equation Solver (Klein and Alvarado, 2005) for evaluating Exergy and the energy analysis of combine cycle plant with Solar reheating and Regeneration. The input data for evaluation are mentioned in chapter 4 except the parameter, whose effect is discussed in particular plot, has been varied.

4.1 Comparison of the various organic fluids

Table-1 shows the comparison variation in first law efficiency of three systems (i.e. (i) the organic Rankine cycle using R134a is which is about 13.96%, (ii) Using R134a in ORC with Regeneration system 15.64 %, and (iii) ORC with Regeneration and solar Reheat system and using R134a is 12.37%) as compared to (i) the organic Rankine cycle using R1234yf is which is about 13.1%, (ii) Using R1234yf in ORC with Regeneration system 14.94%, and (iii) ORC with Regeneration and solar Reheat system and using R1234yf is 11.56%) respectively. Similarly using R1234ze in the three systems the results comes out to be (i) the organic Rankine cycle is which is about 13.09% (ii) ORC with Regeneration system 14.95%, and (iii) ORC with Regeneration and solar Reheat system is 10.23%). It was also observed that the efficiency against the organic turbine inlet pressure and temperature. From the table-1, it is obvious that the efficiency of organic Rankine cycle increases with regeneration while the efficiency of combined cycle plant remains constant. By using the regeneration heat supplied to the organic cycle plant decreases hence the rate of evaporation increase which results output increases and hence the organic Rankine cycle efficiency increases. With solar reheating organic Rankine cycle plant shows increase in efficiency while the combined cycle plant shows decrease in efficiency because of decrease in mean temperature of the heat addition in the system with superheating.

4.2 Comparisons of Exergy efficiency with Regeneration without Regeneration and Regeneration with Solar reheat cycle using different ecofriendly organic fluids

Table-2 shows the effect of various ecofriendly organic fluids on second law performance of various ecofriendly organic fluids in the three systems and it was found that second law efficiency becomes to be43.16% using R134a in organic Rankine cycle and 49.97% using R134a in ORC with Regeneration system and 48.51% ORC with Regeneration and solar Reheat system using organic R134a fluid. Respectively. It is was observed that second law efficiency (in terms of exergetic efficiency) of the organic Rankine cycle increases with maximum pressure and maximum temperature. It is seen that efficiency of combined cycle plants decreases with increase in organic Rankine cycle maximum temperature but increases with increase in the maximum pressure.

4.3 Exergy efficiency

Table-3 shows the thermodynamic performances of ORC with Regeneration and solar Reheat system using different ecofriendly refrigerants at 2500kPa maximum pressure and 120 $^{\circ}$C temperature of ORC fluid. It was observed that maximum exergy destruction based on exergy input to be fund using organic R1234ze fluid.

Table-1: Thermal performance (First Law Efficiency) of ORC

System	R134a	R1234yf	R1234ze	R227ea	R407c	R245fa
ORC with Regeneration and solar Reheat system	0.1237	0.1156	0.1023	0.1061	0.1591	0.09879
ORC with Regeneration system	0.1564	0.1494	0..1495	0.1307	0.1940	0.1390
Organic Rankine Cycle	0.1396	0.1310	0.1309	0.1109	0.1532	0.1186

Table-2: Exergetic Efficiency (Second Law Efficiency) of ORC

System	R134a	R1234yf	R-1234ze	R227ea	R245fa
ORC with Regeneration and solar Reheat system	0.4851	0.4833	0.4811	0.4860	0.5038
ORC with Regeneration system	0.4897	0.4910	0.492	0.4908	0.4913
Organic Rankine Cycle(ORC)	0.4316	0.4310	0.4294	0.4290	0.4232

Table-3: Thermal performances of ORC with Regeneration and solar Reheat system

Eco Friendly Heating organic Fluid	R134a	R1234yf	R-1234ze	R-227ea	R245fa
$Eff._{First_Law}$	0.1237	0.1156	0.1023	0.1061	0.1591
$Eff._{Second_Law}$	0.4851	0.4833	0.4811	0.4860	0.5038
$EDR_{Rational}$	0.5149	0.5267	0.5989	0.5240	0.4962

5. Conclusion

In this paper, an extensive first law (energy) and second law (Exergy) analysis of R134a, R245fa, R1234yf, R1234ze, R227ea organic fluids in combined cycle with regeneration and reheating is presented. Some conclusions of this analysis are summarized as follows:

1. Exegetic efficiency (second law efficiency) and Energy efficiency (first law efficiency) of Organic Rankine cycle with Regeneration is higher than without Regeneration for all selected organic fluids.
2. R1234yf have higher first law efficiency and exergetic efficiency (second law efficiency) in Organic Rankine cycle but R1234ze have higher exergetic efficiency (second law efficiency) improvement from basic system.
3. When solar reheating is done in Organic Rankine cycle than efficiency of Rankine cycle is improved but the efficiency of combined cycle is decreased.
4. Efficiency of combined cycle plant remains almost constant with Regeneration.
5. With increase in maximum pressure of Rankine cycle, efficiency of combined cycle shows increasing trend while with increase in maximum temperature of Rankine cycle, efficiency of combined cycle shows decreasing trend.
6. R1234yfis recommended for practical applications due to its highest exergetic efficiency among selected organic fluid but some important problems related to low flammability and explosion risk have to be considered while managing it.
7. R245fa has highest exergetic efficiency and compared to remaining selected organic fluids and it is recommended for practical applications.

References

[1] Jaafar M. N., Kaviri A. G., (2013), Exergy environmental optimization of Heat Recovery Steam Generators in combined cycle power plant through energy and exergy analysis. Energy Conversion and Management, 6 ,pp. 27–33.

[2] Dincer I. Ahmadi P., (2010), Exergo environmental Analysis and Optimization of a Cogeneration Plant System using Multimodal Genetic Algorithm (MGA). Energy, *Vol*-35, pp. 5161-72.

[3] Boyano A., Blanco-Marigorta A. M., Morosuk T., Tsatsaronis G., Exergo-environmental Analysis of a Steam Methane Reforming Process for Hydrogen Production. Energy, 36(2011), pp. 2202-2214.

[4] Cabrera M., Tsatsaronis G., (2011) Exergoeconomic and Exergoenvironmental Analyses of a Combined Cycle Power Plant with Chemical Looping Technology. International Journal of Greenhouse Gas Control, Vol-5, pp. 475-482.

[5] Ibrahim K. T., Rahman M. M., Abdalla N. A., Optimum Gas Turbine Configuration for Improving the Performance of Combined Cycle Power Plant. Procedia Engineering,15(2011), pp.4216-4223.

[6] Ameri M., Hejazi H. S., The Study of Capacity Enhancement of the Chabahar Gas Turbine Installation using an Absorption Chiller. Applied Thermal Engineering, 24(2004), pp.59–68.

[7] Boonnasa S., Namprakai P., Muangnapoh T., Performance Improvement

[8] of the Combined Cycle Power Plant by Intake Air Cooling using an Absorption Chiller, Energy,31(2006), pp. 2036–2046.
[9] Hosseini R., BeshkanI. A., Soltani M., Performance Improvement of Gas Turbines of Fars (Iran) Combined Cycle Power Plant by Intake Air Cooling using a Media Evaporative Cooler. Energy Conversion and Management, 48(2007), pp. 1055–1064.
[10] Ibrahim T. K., Rahman M. M., Effect of Compression Ratio on Performance of Combined Cycle Gas Turbine. International Journal of Energy Engineering,2(2012)1, pp. 9-14.63
[11] Khaliq A., Kaushik S., Thermodynamic Performance Evaluation of Combustion Gas Turbine Cogeneration System with Reheat. Applied Thermal Engineering, 24(2004), pp. 1785–1795.
[12] Mohagheghi M., Shayegan J., (2009), Thermodynamic Optimization of Design Variables and Heat Exchangers Layout in HRSGs for CCGT, using Genetic Algorithm. Applied Thermal Engineering, Vol-29, pp. 290–299.
[13] Bracco S., Silvia S., Exergetic Optimization of Single Level Combined Gas Steam Power Plants Considering Different Objective Functions. Energy, 35(2010), pp. 5365-5373.
[14] Woudstra N., Woudstra T., Thermodynamic Evaluation of Combined Cycle Plants. Energy Conversion and Management, 51(2010)5, pp. 1099–1110.
[15] Mansouri M. T., Ahmadi P., Kaviri A. G.,(2012) Exergetic and Economic Evaluation of the Effect of HRSG Configurations on the Performance of Combined Cycle Power Plants. Energy Conversion and Management, Vol-58, pp. 47–58.
[16] Xiang W., Chen Y., (2007)Performance Improvement of Combined Cycle Power Plant Based on the Optimization of the Bottom Cycle and Heat, Recuperation, Thermal science,Vol-16, pp. 84-89.
[17] Kelly B, Herrmann U, Hale MJ. (2001)"Optimization studies for integrated solar combinedcycle systems" In: Proceedings of solar forum 2001, solar energy: the power to choose; April 21–25,2001 Washington DC, USA.
[18] He Ya-Ling, Mei Dan-Hua, Tao Wen-Quan, Yang Wei-Wei, Liu Huai-Liang.(2012) "Simulationof Parabolic trough solar energy generation system with organic Rankine cycle" Applied Energy,Vol-97 : pp-630–641.
[19] Gang Pei, Li Jing, JieJi. "Analysis of low temperature solar thermal electric generationusing regenerative organic Rankine cycle" Applied ThermalEng 2010; 30:998–1004.
[20] Goswami DY,Manolakos D, Stefanakos E, Papadakis G,Li C, KosmadakisG,(2013) "Performance investigation of concentrating solar collectors coupled with a trans-criticalorganic Rankine cycle for power and seawater desalination cogeneration Desalination";318:107–117.

Nomenclature

Symbols/Subscript

ED	Exergy destruction
Qs1	Heat addition to combustion chamber
Qs2	Heat addition to HRSG
Qs3	Heat transfer to HRB
HRB	Heat recovery boiler
GT	Gas turbine
ST	Steam turbine
OT	Organic turbine
W	work
C	Compressor
P	pump
m	mass flow rate
CC	combustion chamber Efficiency
HRSG	Heat recovery steam generator
ORC	Organic Rankine cycle
a	Air
COND	Condenser

International Journal of Research in Engineering and Innovation (IJREI)
journal home page: http://www.ijrei.com
ISSN (Online): 2456-6934

Thermodynamic performance analysis of two stage vapour compression refrigeration systems with flash-intercooler using eco-friendly new refrigerants (R134a, R1234yf, R1234ze, R227ea and R152a)

R.S. Mishra

Department of Mechanical Engineering, Delhi Technological University, Delhi, India

Abstract

In this paper, comparison between three vapour compression refrigeration systems (i.e.System-1: Three stage compression with multiple expansion valves and water coolers and System-2: Three stage compression with multiple expansion valves and flash inter cooling chambers in parallel and System-3: Three stage compression with multiple expansion valves and flash inter cooling chambers in series)using environmental friendly refrigerants on the basis of energetic and exergetic approach have been made. It has been observed that for all selected new eco-friendly refrigerants, energy and exergetic efficiency of system-2 is lower than system-1 and sytem-3.The best performance using R134a was observed in system-3. For all Vapour compression refrigeration systems R227ea showed lowest thermal performance in terms of COP, second law efficiency whereas performances of R134a is better in comparison of other selected refrigerants 2.Thermodynamic second law performance of R134ze is less than R1234yf . Since R134a is easily available and also gives better thermodynamic performances, therefore R134a may also be used for practical applications without taking of any safety precautions.
© 2018 ijrei.com. All rights reserved
Key words: Irreversibility Computation, VCRS, Energy-Exergy Analysis**,** Thermodynamics of Refrigeration systems

1. Introduction

Nowadays most of the energy utilize in cooling and air conditioning in industrial as well as for domestic applications, in addition to energy consumption, using of refrigerants in cooling and air conditioning having high GWP and ODP which are responsible for increasing global warming and ozone depletion. The primary requirements of ideal refrigerants are having good physical and chemical properties. Due to good physical and chemical properties such as non-corrosiveness, non-toxicity, non- flammability, low boiling point, Chlorofluorocarbons (CFCs) have been used over the last many decades, but hydro-chlorofluorocarbons (HCFCs) and Chlorofluorocarbons (CFCs) having large amount of chlorine content as well as high global warming potential and ozone depletion potential, so after 90s refrigerants under these categories these kinds of refrigerants are almost prohibited [1]. This paper mainly deals with the impact on second law efficiency in terms of exergetic efficiency with change in temperature of low, intermediate and high temperature evaporator of three systems.. It is also observed that second law efficiency decrease with increase in evaporator temperature. R134a and R227ea have maximum and minimum second law efficiency for both systems similar to performance evaluation in terms of energetic efficiency. It was also found that temperature variation in low and intermediate evaporator put great impact on second law efficiency in comparison with temperature evaporator, for all three systems.

2. Literature Review

Most of the study has been carried out for the performance evaluation of vapour compression refrigeration system using energetic analysis, but with the help of first law analysis irreversibility destruction or losses in components of system unable to determined [1], so that second law thermodynamic analysis is the advanced approach for thermodynamic analysis which gives an additional practical view of the processes. The utility of second law analysis on vapour compression refrigeration systems is well defined because it gives the idea

Corresponding author: R.S. Mishra
Email Id: hod.mechanical.rsm@dtu.ac.in

for improvements in efficiency due to modifications in existing design in terms of reducing exergy destructions in the components. The second law exergetic analysis also provides new thought for development in the existing system. Bolaji B.O. et.al.[2] explained the utility of natural refrigerants as the ideal, environmentally friendly refrigerants and suggested ultimate solution for the problems of ozone depletion and global warming and concluded that the HFC refrigerants are currently the leading replacement for CFC and HCFC refrigerants in refrigeration and air-conditioning systems. However, they are equally foreign to nature like CFCs and HCFCs, consequently, strong basis for the need to embrace the use of natural refrigerants as replacement for the halocarbon refrigerants was provided and also analysed the potentials of various natural refrigerants in terms of their areas of application in the field of refrigeration and air-conditioning because natural refrigerants are hydrocarbons and their mixtures are miscible with both mineral oil used in R12 and polyol ester oils used in R134a systems with exception of ammonia and are fully compatible with all materials traditionally used in refrigeration systems and concluded that the natural refrigerants are the most suitable long time alternatives in refrigeration and air-conditioning systems. Nikolaidis and Probert [3] explained the utility of system optimization by using exergy analysis to investigate the behaviour of two stage compound compression cycle with flash intercooling using R-22 as refrigerant by varying the condenser saturation temperature and evaporator saturation temperature from 298 to 308 K and 238 to 228 K respectively and determined the effect of temperature change in condenser and evaporator on plants irreversibility rate and concluded that the changes in the temperatures of condenser and evaporator significantly effecting the plants overall irreversibility. Qureshi and Zubair [4] computed the performance degradation due to fouling occurred in the vapor compression systems for various applications using three ecofriendly refrigerants (i.e.R-134a, R-410A and R-407C. and found that the first law efficiency in terms of COP and second law efficiency in terms of exergetic efficiency using R-134a gives best performances in the all cases. Xuan and Chen [5] presented explained about the replacement of R502 by mixture of HFC-161 and found that mixture of HFC-161 gives same and higher performance than R404a at lower and higher evaporative temperature respectively on the vapour compression refrigeration system designed for R404a.Cabello et al.[6] considered the effect of condensing pressure, evaporating pressure and degree of superheating experimentally on the single stage vapour compression refrigeration system using R22, R134a and R407c and found that the mass flow rate is greatly affected by change in suction conditions of compressor in results on refrigeration capacity because refrigeration capacity depended on mass flow rate through evaporator. It was also found that for higher compression ratio R22 gives lower COP than R407C. similarly Spatz and Motta [7] mainly focused on the replacement of R12 with R410a by conducting experiment on vapour compression refrigeration systems for medium temperature and carried out thermodynamic analysis. The comparison was made of heat transfer and pressure drop characteristics and observed that the R410a gives best thermodynamic performances among R404a. Han et al. [8] carried out experimental studies on vapour compression refrigeration systems under different working conditions and their experimental results revealed that there could be replacement of R407c in vapour compression refrigeration system without any modification in the existing design.

Getu and Bansal [9] had optimized the design and operating parameters of like condensing temperature, subcooling temperature, evaporating temperature, superheating temperature and temperature difference in cascade heat exchanger R744-R717 cascade refrigeration system. A regression analysis was also done to obtain optimum thermodynamic parameters of same system.

Mohanraj et al [10] concluded 3.6% greater thermodynamic performance by using mixture of R290 and R600a in the ratio of 45.2: 54.8 by weight through experimental investigation on same domestic refrigeration system under different environmental temperatures COP of system using R134a. Padilla et al [11] carried out exergy analysis of domestic vapour compression refrigeration system using R134a and concluded that thermal performances in terms of power consumption, irreversibility and exergy efficiency of R134A is better than R12.

3. Energy and exergy analysis

For carrying out energetic and exergetic analysis, computational models of system-1 to system-3 have been developed and impact of chosen refrigerants on these systems has been analyzed on the saving of energy and due to increase of energy crises, global warming and depletion of ozone layer.. The work input required running the vapour compression refrigeration system reduced by using compound compression and further decreased by flash intercooling between compressors. COP of system can also be enhanced by compressing the refrigerant very close to the saturation line this can be achieved by compressing the refrigerants in more stages with intermediate intercoolers. The refrigeration effect can be increase by maintaining the condition of refrigerants in more liquid stage at the entrance of evaporator which can be achieved by expanding the refrigerant very close to the liquid line. The expansion can be brought close to the liquid line by sub cooling the refrigerant and removing the flashed vapours by incorporating the flash chamber in the working cycle. The evaporator size can be reduced because unwanted vapours formed are removed before the liquid refrigerant enters in the evaporator. Multi-stage vapour compression with flash intercooler and individual throttle valves (system-1), three compressors arranged in compound compression, individual

throttle valves, condenser and evaporator (system-2)and Multiple evaporator at constant temperature with compound compression, flash intercooler and multiple throttle valves and system-3 consists of three compressors arranged in compound compression, multiple throttle valves, condenser and evaporator

In this investigation following assumptions are made:

1. Load on the low, intermediate and high temperature evaporator is 10TR,
2. Dead state temperature (T0): 25^0C
3. Difference between evaporator and space temperature is 5 ^{0}C.
4. Adiabatic efficiency of compressor: 80%.
5. Dead state enthalpy (Φ0) and entropy (s0) of the refrigerants have been calculated corresponding to the dead state temperature (T0) of 298K.
6. Variation in kinetic and potential energy is negligible.
7. Expansion process is adiabatic
8. Temperature of evaporator is 0^0C respectively.
9. Condenser temperature : 50^0C
10. Degree of sub cooling : 10^0C

3.1 Thermodynamic Analysis

First law of thermodynamic gives the idea of energy balance of system while concept of exergy was given by second law of thermodynamics, which always decreases due to thermodynamic irreversibility. Exergy is defined as the measure of usefulness, quality or potential of a stream to cause change and an effective measure of the potential of a substance to impact the environment.

Exergy at any state is given as

$$X = (\Phi - \Phi_0) - T_0(s - s_0) \quad (1)$$

Compressors

$$\left(T_o\dot{S}_{gen}\right)_{c1} = \dot{W}_{c1} + \dot{m}_{c1}(X_2 - X_1) \quad (2)$$
$$(T_o\dot{S}_{gen})_{c2} = \dot{W}_{c2} + \dot{m}_{c2}(X_4 - X_3) \quad (3)$$
$$(T_o\dot{S}_{gen})_{c3} = \dot{W}_{c3} + \dot{m}_{c3}(X_6 - X_5 \quad (4)$$
$$\dot{\Psi}_c = (T_o\dot{S}_{gen})_{c1} + (T_o\dot{S}_{gen})_{c2} + (T_o\dot{S}_{gen})_{c3} \quad (5)$$

Evaporators

$$(T_o\dot{S}_{gen})_{e1} = \dot{m}_{e1}(X_1 - X_{10}) - \dot{Q}_{e1}\left(1 - \frac{T_0}{T_{r1}}\right) \quad (6)$$
$$\dot{\Psi}_e = (T_o\dot{S}_{gen})_{e1} \quad (7)$$

Condenser

$$\dot{\Psi}_{cond} = \left(T_o\dot{S}_{gen}\right)_{cond} = \dot{m}_{c3}(X_6 - X_7) - \dot{Q}_e\left(1 - \frac{T_0}{T_r}\right) \quad (8)$$

Throttle Valves

$$(T_o\dot{S}_{gen})_{tv1} = \dot{m}_{e1}(X_{77} - X_{10}) \quad (9)$$
$$\left(T_o\dot{S}_{gen}\right)_{tv2} = (\dot{m}_{e1} + \dot{m}_{f1})(X_{77} - X_9) \quad (10)$$
$$(T_o\dot{S}_{gen})_{tv3} = (\dot{m}_{e1} + \dot{m}_{f2})(X_{77} - X_8) \quad (11)$$
$$\dot{\Psi}_{tv} = (T_o\dot{S}_{gen})_{tv1} + (T_o\dot{S}_{gen})_{tv2} + (T_o\dot{S}_{gen})_{tv3} \quad (12)$$

Liquid subcooler

$$\dot{\Psi}_{lsc} = (T_o\dot{S}_{gen})_{sc} = \dot{m}_{c3}(X_7 - X_{77}) \quad (13)$$

Flash intercoolers

$$(T_o\dot{S}_{gen})_{f1} = \dot{m}_{f1}(X_9 - X_3) + \dot{m}_{c1}(X_2 - X_3) \quad (14)$$
$$(T_o\dot{S}_{gen})_{f2} = \dot{m}_{f2}(X_8 - X_5) + \dot{m}_{c1}(X_4 - X_5) \quad (15)$$
$$\dot{\Psi}_f = (T_o\dot{S}_{gen})_{f1} + (T_o\dot{S}_{gen})_{f2} \quad (16)$$

Total irreversibility destruction in system-1

$$\sum\dot{\Psi}_k = \dot{\Psi}_e + \dot{\Psi}_c + \dot{\Psi}_{cond} + \dot{\Psi}_{tv} + \dot{\Psi}_{lsc} + \dot{\Psi}_f \quad (17)$$
$$\dot{m}_{f1'} = \frac{\dot{m}_{c1'}(\Phi_{2'} - \Phi_{3'})}{(\Phi_{3'} - \Phi_{10'})} \quad (18)$$
$$\dot{m}_{c2'} = \dot{m}_{c1'} + \dot{m}_{f1'} \quad (19)$$
$$\dot{m}_{c2'} = \frac{\dot{Q}_{e1'}}{(\Phi_{5'} - \Phi_{8'})} + \dot{m}_{c2'}\left(\frac{x_{8'}}{1 - x_{8'}}\right) \quad (20)$$
$$\dot{m}_{f2'} = \frac{\dot{m}_{c2'}(\Phi_{4'} - \Phi_{5'})}{(\Phi_{5'} - \Phi_{8'})} \quad (21)$$

Power required for running the compressors

$$P_{c1'} = \frac{\dot{m}_{c1'}(\Phi_{2'} - \Phi_{1'})}{60} \quad (22)$$
$$P_{c2'} = \frac{\dot{m}_{c2'}(\Phi_{4'} - \Phi_{3'})}{60} \quad (23)$$
$$P_{c3'} = \frac{\dot{m}_{c3'}(\Phi_{6'} - \Phi_{5'})}{60} \quad (24)$$
$$\text{Energetic efficiency} = \frac{\dot{Q}_{e'}}{P_{c'} * 60} \quad (25)$$

3.2 Rate of exergy loss due to irreversibilties ($T_o\dot{S}_{gen}$) in various components of system-2

Compressors

$$(T_o\dot{S}_{gen})_{c1'} = \dot{W}_{c1'} + \dot{m}_{c1'}(X_{2'} - X_{1'}) \quad (26)$$
$$(T_o\dot{S}_{gen})_{c2'} = \dot{W}_{c2'} + \dot{m}_{c2'}(X_{4'} - X_{3'}) \quad (27)$$
$$(T_o\dot{S}_{gen})_{c3'} = \dot{W}_{c3'} + \dot{m}_{c3'}(X_{6'} - X_{5'}) \quad (28)$$
$$\dot{\Psi}_{c'} = (T_o\dot{S}_{gen})_{c1'} + (T_o\dot{S}_{gen})_{c2'} + (T_o\dot{S}_{gen})_{c3'} \quad (29)$$

Evaporator

$$\left(T_o\dot{S}_{gen}\right)_{e1'} = \dot{m}_{e1'}(X_{1'} - X_{12'} - \dot{Q}_{e1'}\left(1 - \frac{T_0}{T_{r1'}}\right) \quad (30)$$
$$\dot{\Psi}_{e'} = (T_o\dot{S}_{gen})_{e1'} \quad (31)$$

Condenser

$$\Psi_{cond'} = \left(T_o \dot{S}_{gen}\right)_{cond'} \dot{m}_{c3'}(X_{6'} - X_{7'}) - \dot{Q}_{e'}\left(1 - \frac{T_o}{T_{r'}}\right) \quad (32)$$

Throttle Valves

$$(T_o \dot{S}_{gen})_{tv1'} = \dot{m}_{e1'}(X_{11'} - X_{12'}) \quad (33)$$

$$\left(T_o \dot{S}_{gen}\right)_{tv2'} = \dot{m}_{c2'}(X_{9'} - X_{10'}) \quad (34)$$

$$(T_o \dot{S}_{gen})_{tv3'} = \dot{m}_{c3'}(X_{77'} - X_{8'}) \quad (35)$$

$$\Psi_{tv'} = (T_o \dot{S}_{gen})_{tv1'} + (T_o \dot{S}_{gen})_{tv2'} + (T_o \dot{S}_{gen})_{tv3'} \quad (36)$$

Liquid subcooler

$$\dot{\Psi}_{lsc'} = (T_o \dot{S}_{gen})_{lsc'} = \dot{m}_{c3'}(X_{7'} - X_{77'} \quad (37)$$

Flash intercoolers

$$(T_o \dot{S}_{gen})_{f1'} = \dot{m}_{f1'}(X_{10'} - X_{3'}) + \dot{m}_{c1'}(X_{2'} - X_{3'}) \quad (38)$$

$$(T_o \dot{S}_{gen})_{f2'} = \dot{m}_{f2'}(X_{8'} - X_{5'}) + \dot{m}_{c2'}(X_{4'} - X_{5'}) \quad (39)$$

$$\dot{\Psi}_{f'} = (T_o \dot{S}_{gen})_{f1'} + (T_o \dot{S}_{gen})_{f2'} \quad (40)$$

Total irreversibility destruction in system-1

$$\sum \dot{\Psi}_{k'} = \dot{\Psi}_{e'} + \dot{\Psi}_{c'} + \dot{\Psi}_{cond'} + \dot{\Psi}_{tv'} + \dot{\Psi}_{lsc'} + \dot{\Psi}_{f'} \quad (41)$$

Exergetic efficiency

$$= \frac{\text{Exergy of cooling load of evaporators}}{\text{Compressors work}} = \frac{\dot{E}P}{\dot{W}} \quad (42)$$

Exergetic efficiency of system

$$= \frac{\left(\dot{Q}_{e1}\right) - T_o\left(\frac{\dot{Q}_{e1}}{T_{r1}} + \right)}{P_c * 60} \quad (43)$$

4. Result and Discussions

The effect of various ecofriendly refrigerants with coefficient of performance for considered refrigerants of system-1 to system-3 is shown by Table-1 to Table-8 respectively. The first law efficiency in terms of COP of system-1 using R227ea is higher than HFC-134a, HFO-1234yf & HFO1234ze, However R1234ze gives better COP than using R134a, however lowest first law performance in terms of COP was observed by using R1234yf in the system-1.Similarly in case of system-2, R-1234ze gives higher COP than using all ecofriendly refrigerants. R134a in system-2 has higher COP than R1234yf. Therefore R1234ze is best alternative for replacing R134a in system1 and System-2. For system-3, the COP Using R1234ze is higher than by using R227ea and R134a.

Table-1: First Law efficiency in terms of COP of various Refrigeration Systems of 35 kW cooling capacity

Refrigerant	System-1 Two stage compression with water inter cooler and liquid sub cooler	System-2 Two stage compression with water intercooler, liquid sub cooler and liquid flash chamber	System-3 Two stage vapour compression with water intercooler liquid sub cooler and flash intercooler
R134a	2.866	3.08	3.086
R1234yf	2.551	2.796	2.782
R1234ze	3.078	3.157	3.159
R227ea	3.098	3.134	3.137
R152a	3.016	3.134	3.152

However, and lower first law performance in terms of COP was observed by using HFO-1234yf. Hence HFO-1234ze can be a good 'replacement of HFC-134a at higher value of evaporator temperature and HFO-1234yf can be a good replacement lower value of evaporator temperature after certain modification.

Table-2 shows the comparison between three vapour compression refrigeration systems. It was observed that second law efficiency of system -3 is higher than system -1 however, by using R134a is higher than other ecofriendly refrigerants however first law efficiency in terms of COP and exergetic efficiency of HFC-134a is more than R134yf and HFO1234ze. Hence HFO-1234yf can be a good replacement of HFC-134a at lower value of evaporator temperature and HFO-1234ze can be a good replacement of HFC-134a at lower value of evaporator temperature after certain modification Table-3 &Table-4 show the higher exergy destruction ratio in terms of exergy of fuel in terms of power required for running all systems by using R234zebut lower than by using R-227ea. In case of all (three), systems using R134a, the system -3 gives lowest EDR and system-1 gives higher EDR while second system has lower EDR than system1 and higher than system-3.

Table-2: Second Law efficiency in terms of Exergetic Efficiency of various Refrigeration Systems of 35 kW cooling capacity

Refrigerant	System-1 Two stage compression with water inter cooler and liquid sub cooler	System-2 Two stage compression with water intercooler, liquid sub cooler and liquid flash chamber	System-3 Vapour compression with water intercooler liquid sub cooler and flash intercooler
R134a	0.3833	0.4091	0.4099
R1234yf	0.3686	0.4040	0.4020
R1234ze	0.3095	0.3175	0.3177
R227ea	0.2727	0.2760	0.2762
R152a	0.3676	0.382	0.3841

Table-3: Exergy Destruction Ratio based on exergy input of various Refrigeration Systems of 35 kW cooling capacity

Refrigerant	System-1 Two stage compression with water inter cooler and liquid sub cooler	System-2 Two stage compression with water intercooler, liquid sub cooler and liquid flash chamber	System-3 Two stage vapour compression with water intercooler liquid sub cooler and flash intercooler
R134a	0.6167	0.5909	0.5901
R1234yf	0.6314	0.5960	0.5980
R1234ze	0.6905	0.6825	0.6823
R227ea	0.7273	0.7240	0.7238
R152a	0.6324	0.6180	0.6158

Table-4: Exergy Destruction Ratio based on exergy output of various Refrigeration Systems of 35 kW cooling capacity

Refrigerant	System-1 Two stage compression with water inter cooler and liquid sub cooler	System-2 Two stage compression with water intercooler, liquid sub cooler and liquid flash chamber	System-3 Vapour compression with water intercooler liquid sub cooler and flash intercooler
R134a	1.734	1.373	1.35
R1234yf	2.018	1.391	1.379
R1234ze	3.123	2.133	2.128
R227ea	5.036	2.618	2.615
R152a	1.720	1,580	1.557

Table-5: Exergy input of various Refrigeration Systems

Refrigerant	System-1 Two stage compression with water inter cooler and liquid sub cooler	System-2 Two stage compression with water intercooler, liquid sub cooler and liquid flash chamber	System-3 Vapour compression with water intercooler liquid sub cooler and flash intercooler
R134a	12.13	11.37	17.01
R1234yf	13.72	12.52	18.87
R1234ze	11.37	11.09	16.62
R227ea	11.30	11.17	16.73
R152a	14.51	11.60	16.65

Table-6: Power required (kW) to run the compressor-1for all vapour compression refrigeration systems of 35 kW cooling capacity

Refrigerant	System-1 Two stage compression with water inter cooler and liquid sub cooler	System-2 Two stage Compression with multiple expansion Valves and flash inter cooling Chambers in parallel	System-3 Vapour compression with water intercooler liquid sub cooler and flash intercooler
R134a	5.455	4.816	7.224
R1234yf	6.177	5.218	7.828
R1234ze	5.288	5.043	7.565
R227ea	5.409	5.297	7.946
R245fa	5.251	4.87	7.305

The irreversibility analysis of systems, the exergy destruction Ratio based on exergy of fuel in terms of total power and exergy destruction Ratio based on exergy of products are shown in Table-3 to Table-4 respectively. However the exergy of fuel in terms of total power required to run all system are shown in Table-5 respectively. It was observed that the exergy destruction ratio of system-3 is lower than system-1. Table-6 and Table-7 are showing the power required to run all compressors in all system using five ecofriendly refrigerants.

Table-7: *Power required (kW) to run the compressor-2for all vapour compression refrigeration systems of 35 kWCooling capacity*

Refrigerant	System-1 Two stage compression with water inter cooler and liquid sub cooler	System-2 Two stage compression with water intercooler, liquid sub cooler and liquid flash chamber	System-3 Vapour compression with water intercooler liquid sub cooler and flash intercooler
R134a	6.674	6.65	9.791
R1234yf	7.545	7.302	11.05
R1234ze	6.084	6.044	9.056
R227ea	5.890	5.869	8.789
R152a	6.354	6.299	9.351

5. Conclusions and Recommendations

Thermodynamic energy-exergy analysis of multi-stage vapour compression refrigerator and flash intercooler with individual or multiple throttle valves have been done in terms of COP, second law efficiency and irreversibility destruction ratio based on exergy of fuel and Exergy destruction based on exergy of product and following conclusions have been made

1. The total power required to run sytem using R1234yf is more than using R134a while R134a required more power than using R1234yf in case of all systems. Similarly, the same trends also observed in case of power required to run the second compressor in all systems. However compressor-1 required more power by using R234ze by replacing R134a
2. Three VCR systems (system-1 to system-3) were analyzed analytically and it was observed that COP (energetic efficiency) of system-3 is higher than system-2. The COP of all systems increases with increase in evaporator temperature for chosen refrigerants. It was also observed that R134a shows better thermodynamic performances in terms of COP and exergetic efficiency and R-227ea gives low first law performance in term of COP and second law efficiency in terms of exergetic efficiency for all systems.
3. From the irreversibility point of view, or exergy destruction based on exergy of fuel or exergy of output, the system-1 was found worst Total efficiency defect is more for HFO-1234yf followed by HFO-1234ze and HFC-134a, but the difference is small.
4. Increase in ambient state temperature has a positive effect on exergetic efficiency and EDR, i.e. EDR reduces and exergetic efficiency increases.HFO1234ze gives lesser values of exergetic efficiency whereas HFO-1234yf gives lower values of thermal performances values.
5. First law performance in terms of COP and second law exergetic performance of system-3 is higher than system-2for selected new ecofriendly refrigerants.
6. For all vapour compressor refrigeration systemsR227ea shows minimum thermal performance in terms of COP, second law efficiency.
7. System 1 also gives higher thermodynamic performance than system-2 and lower than system-3.

References

[1] R. Cabello, J. Navarro-Esbrı, R. Llopis, E. Torrella. Analysis of the variation mechanism in the main energetic parameters in a single-stage vapour compression plant. Int J Applied Thermal Engineering.2007; 27:167-176.

[2] Bolaji B.O, Z. Huan (2013) Ozone depletion and global warming: Case for the use of natural refrigerant – a review, Journal of Renewable and Sustainable Energy Reviews, Vol-18, Pages 49-54

[3] Nikolaidis, C. and Probert, D., Exergy method analysis of a two stage vapour compression refrigeration plants performance, Applied Energy, Vol. 60, (1998), pp. 241-256

[4] Qureshi, B.A., Zubair, S.M. (2011), Performance degradation of a vapor compression refrigeration system under fouled conditions, International Journal of Refrigeration, Vol. 34(4), pp. 1016-102

[5] Yongmei Xuan, Guangming Chen. Experimental study on HFC-161 mixture as an alternative refrigerant to R502. Int J Refrigeration. Article in Press

[6] R.Cabello a, E.Torrella b, J.Navarro-Esbr. Experimental evaluation of a vapour compression plant performance using R134a, R407C and R22 as working fluids. Int J Applied Thermal Engineering.2004; 24:1905-1917.

[7] Mark W. Spatz, Samuel F. Yana Motta. An evaluation of options for replacing HCFC-22 in medium temperature refrigeration systems. Int J Refrigeration.2004; 27:475-483.

[8] X.H. Han, G.M. Chen. Cycle performance study on R32/R125/R161 as an alternative refrigerant to R407C. Int J Applied Thermal Engineering.2007; 27:2559-2565.

[9] H.M Getu, P.K Bansal. Thermodynamic analysis of an R744-R717 cascade refrigeration system. Int J Refrigeration.2008; 31:45-54.

[10] M. Mohanraj,et.al .Experimental investigation of R290/R600a mixture as an alternative to R134a in a domestic refrigerator. Int J Thermal Sciences.2009; 48:1036-1042.

[11] M. Padilla, R. Revellin, J. Bonjour. Exergy analysis of R413A as replacement of R12 in a domestic refrigeration system. Int J Energy Conversion and Management.2010; 51:2195-2201.

Methods and Applications in Fluorescence

ACCEPTED MANUSCRIPT

Tunable Single and Double Emission Semiconductor Nanocrystal Quantum Dots: A Multianalyte Sensor

To cite this article before publication: ratneshwar kumar ratnesh *et al* 2018 *Methods Appl. Fluoresc.* in press https://doi.org/10.1088/2050-6120/aaba8a

Manuscript version: Accepted Manuscript

Accepted Manuscript is "the version of the article accepted for publication including all changes made as a result of the peer review process, and which may also include the addition to the article by IOP Publishing of a header, an article ID, a cover sheet and/or an 'Accepted Manuscript' watermark, but excluding any other editing, typesetting or other changes made by IOP Publishing and/or its licensors"

This Accepted Manuscript is **© 2018 IOP Publishing Ltd**.

During the embargo period (the 12 month period from the publication of the Version of Record of this article), the Accepted Manuscript is fully protected by copyright and cannot be reused or reposted elsewhere.
As the Version of Record of this article is going to be / has been published on a subscription basis, this Accepted Manuscript is available for reuse under a CC BY-NC-ND 3.0 licence after the 12 month embargo period.

After the embargo period, everyone is permitted to use copy and redistribute this article for non-commercial purposes only, provided that they adhere to all the terms of the licence https://creativecommons.org/licences/by-nc-nd/3.0

Although reasonable endeavours have been taken to obtain all necessary permissions from third parties to include their copyrighted content within this article, their full citation and copyright line may not be present in this Accepted Manuscript version. Before using any content from this article, please refer to the Version of Record on IOPscience once published for full citation and copyright details, as permissions will likely be required. All third party content is fully copyright protected, unless specifically stated otherwise in the figure caption in the Version of Record.

View the article online for updates and enhancements.

This content was downloaded from IP address 14.139.251.107 on 03/04/2018 at 11:53

Tunable Single and Double Emission Semiconductor Nanocrystal Quantum Dots: A Multianalyte Sensor

R. K. Ratnesh and Mohan Singh Mehata†*

Laser-Spectroscopy Laboratory, Department of Applied Physics, Delhi Technological University, Bawana Road, Delhi-110042, INDIA.

†MSM should also be considered as the first author.

*Corresponding author E-mail: msmehata@gmail.com; msmehata@dtu.ac.in

Accepted Manuscript

Abstract:

We have prepared stable colloidal CdTe and CdTe/ZnS core-shell quantum dots (QDs) using hot injection chemical route. The developed CdTe QDs emit tunable single and dual photoluminescence (PL) bands, originating from the direct band edge and the surface state of QDs, as evident by the steady-state and time-resolved spectroscopy. The developed CdTe and CdTe/ZnS QDs act as optical sensors for the detection of metal ions (e.g., Fe^{2+} and Pb^{2+}) in the feed water. The PL quenching in the presence of analytes has been examined by both the steady-state and time-resolved PL spectroscopy. The linear Stern-Volmer (S-V) plots obtained for PL intensity and lifetime as a function of metal ion concentration demonstrates the diffusion-mediated collisional quenching as a dominant mechanism together with the possibility of fluorescence resonance energy transfer. Thus, the prepared core and core-shell QDs which cover a broad spectral range of white light with high quantum yield (QY) are highly sensitive to the detection of metal ions in feed water and are also important for biological applications [13].

Keywords: Core-Shell Quantum dots, Photoluminescence, Lifetime, Quenching, Optical sensor

Accepted Manuscript

1. Introduction:

The production of CdTe and II-VI QDs has been fascinating in the last few decades due to their novel properties and their wide applications in the various fields of science and technology [1-5]. These QDs exhibit unique optical properties such as small full-width half maxima (FWHM), uniform particle size distribution, broad excitation range, high stability and excellent robustness against photobleaching [6,7].

For the synthesis of II-VI semiconductor QDs such as CdTe, ZnS, CdS, CdSe and CdTe/ZnS, mainly two routes of synthesis were employed. The first one is known as low-temperature synthesis, which is carried out either at room temperature or considered below the 100°C. Such reactions take place in an aqueous environment containing various types of surface capping ligands. This process is simple and cost-effective. On the other hand, hot-injection synthesis process overcame the shortcoming and allowed the growth of QDs with narrow size distribution and different shapes. The resulting magic size semiconductor CdTe and CdTe/ZnS core-shell QDs covers broad emission range, *i.e,* the so-called white light emission. The hot-injection synthesis is carried out at a temperature range of 100 – 350°C. The procedure of synthesis of CdX (X = Te, Se, and S) at high temperatures using coordinating solvent trioctylphosphineoxide (TOPO) is widely accepted [8,9]. The synthesis of magic size QDs can also be done with thermodynamically controlled reaction conditions, which results in the stable electronic structure of these QDs. To reduce the surface defect of bare QDs, a shell layer was prepared on the surface of the core. Preparation of this shell layer was an effective approach in reducing the surface dangling bonds and in improving the spectral properties of QDs [10,11]. The core-shell approach provides another method of modularity and addresses the problems occurring in QDs prepared by high-temperature synthesis and provides higher stability, biocompatibility and sensitivity.

Accepted Manuscript

The QDs are also used in sensing applications and have been quite fascinating in the past. Heavy metal impurities are hazardous to humans because these substances are toxic in nature and are retained by the ecological system [12]. The existence of heavy metals in the ambient environment has increased dramatically during the last few decades [13]. The main sources of heavy metals in the environment include combustion of various fossil fuels, burning of huge amounts of coal and a large amount of industrial heavy metals disposed into the atmosphere and the aquatic environment, which create an adverse effect on ecosystems and on living organisms. Though few of the heavy metals such as copper (Cu), iron (Fe) and zinc (Zn) are biologically essential and required by some organisms, excess concentrations can lead to toxicity [14-17]. Furthermore, very low concentrations of some selective heavy metals such as cadmium (Cd), mercury (Hg) and lead (Pb) produce harmful effects and are not biologically necessary for organisms because they lead to the production of excessive free-radicals [18-21]. This promoted for developing an analytical tool and technique which could detect and minimize the heavy metal pollution and prevent the damaging effects of pollution at the very beginning. In the last few decades, the reliable analytical techniques used for the detection of heavy metals include atomic absorption spectrometry, inductively coupled plasma mass spectrometry [22, 23], fluorescence spectrometry, capillary electrophoresis, X-ray and microprobes [24-26]. All these techniques are highly sensitive, although most of these techniques have disadvantages such as initial installation costs, sophisticated instruments, not being very handy and the requirement of trained operators, which make it difficult for real-time and on-site monitoring of metal ions [27]. Now, researchers are trying to develop highly sensitive, cost-effective and convenient sensors for the detection of toxic heavy metal ions. Semiconductor QDs meet this requirement as they are highly sensitive to metal ions such as Pb^{2+} and Cu^{2+}. Earlier, organic dyes, fluorescent proteins or lanthanide chelates were mostly used as staining agents for metal sensors, but they had several limitations such as

Accepted Manuscript

broad spectrum, poor photochemical stability less fluorescence intensity [28]. On the other hand, QD based metal detection sensors have several features like unique tunable optical properties and good photochemical stability, which strongly recommend the replacement of classical organic dye. QDs represent a new way of fluorescent labels that have more use for biosensing and bioimaging due to their wide range of unique optical properties [29,30]. The PL spectra of QDs mainly depend on the particle size and their surface charge or ligands attached to QDs surface. The tunable size and shape of QDs can be easily produced in contrast to classical organic dye staining agents, by some modification in synthesis techniques and using different surface legends. The nature of PL of QDs entirely depends upon excitons recombination [2,31]. The fluorescence analytes detection technique is extensively used for the detection of transition metals ions, especially copper ions (Cu^{2+}) [31-38]. Cu^{2+} plays a significant role in human health as many prion-type diseases are directly linked to the amount of Cu^{2+} binding and aggregation or folding of proteins. The excess amount of Cu^{2+} significantly affects the cellular physiology. In the human body, an excess amount of Cu^{2+} increases the chances of fibril formation of β-amyloid, which leads to Alzheimer's disease [39], and novel PL based research of QDs can reveal the early steps of fibril formation in animals [40]. Furthermore, Parkinson's disease is also linked to Cu^{2+} binding as Cu^{2+} links to α-synuclein easily and the excess of α-synuclein in animals causes the onset of Parkinson's disease [41,42]. The QD-based sensors show more sensitivity, broader absorption band, longer PL lifetimes (tens and even hundreds of nanoseconds) and higher photostability than organic dyes [43,44]. Their broad absorption spectra provide an option for the selection of excitation energy which also helps in the elimination of scattering of light in the detection system.

In this paper, we synthesize magic-sized CdTe QDs and CdTe/ZnS core-shell QDs following Successive Ion Layer Adsorption and Reaction (SILAR) technique. These QDs provide single and

Accepted Manuscript

dual tunable PL bands, and cover a wide range of visible light. Dual PL band is unusual and reported for the first time for CdTe QDs. Furthermore, both the water-soluble core and core-shell QDs were used for the sensing of various metal ions and it was found that the QDs are sensitive to the selective metal ions. Steady-state and time-resolved PL techniques were used to examine the sensitivity of QDs to the metal ions.

2. Experimental

2.1. Materials

Trioctylphosphine (TOP, 90 %), oleic acid (OA, ≥A95 %, tech grade), tellurium powder (Te, 99.5 %), zinc oxide (ZnO, 99.9 %), sulfur (S, ≥99 %), hexadecyl amine (HDA, 90 %, tech grade), mercaptopropionic acid (MPA, 99 %), cupper (Cu^{2+}, 99.99 %), cobalt (Co^{2+}, 99.9 %), nickel (Ni^{2+}, 99.9 %), iron (Fe^{2+}, 99.9 %)and lead (Pb^{2+}, 99.9 %) perchlorate were purchased from Sigma-Aldrich, cadmium oxide (CdO, > 99 %), toluene (99.5 %), methanol (99.9 %), hexane and 1-octadecene (ODE, ≥ 95.0 %) were purchased from Alfa Aesar, and used without further purification.

2.2 Synthesis

2.2.1 Synthesis of CdTe QDs

The synthesis process was carried out in a moisture and oxygen-free environment by purging the experimental setup with nitrogen (N_2). The flow diagram for the synthesis of QDs is described in Scheme 1**.** In order to prepare the Cd precursor, a mixture of CdO (0.160 gm), OA (1.5 ml) and ODE (20 ml) was taken into 500 ml three-neck round-bottom flask and heated up to 210 °C with continuous stirring until the cadmium precursor becomes transparent. At this temperature, the TOPTe solution was swiftly injected into the Cd reaction mixture. The TOPTe precursor was prepared by dissolving 0.250 gm Te in 0.4 ml TOP, and 2 ml ODE was taken in a glass vial while

Accepted Manuscript

continuously stirring in the oxygen-free environment. After injecting the cool TOPTe precursor solution into the hot Cd precursor, the temperature of the solution was dropped down to about 10°C from the previous value of 210°C. Further, with the addition of TOPTe precursor, the color of reaction solution changes suddenly, which indicates fast nucleation and growth. After every two minutes of TOPTe precursor injection (at a fixed temperature, 200°C) the sample was taken out in intervals for 20 minutes. After 20 minutes, the heating mantle was removed and the temperature of the solution was brought down to 80°C. At this temperature, 30 ml of cool methanol solution was added, and finally the reaction mixture was centrifuged at 6500 rpm for 10 minutes. This process was repeated many times to obtain pure CdTe QDs. The obtained eluent was dispersed into toluene and kept for the synthesis of core-shell QDs.

2.2.2 Synthesis of modified CdTe QDs

Here, we made a slight modification in the synthesis of CdTe QDs from the previously mentioned procedure. A mixture of CdO (0.160 gm), OA (2 ml) and ODE (20 ml) was taken in a three-neck round-bottom flask and heated up to 280°C with continuous stirring for about one hour. At this temperature, a transparent Cd precursor solution was obtained. The temperature of the precursor solution was reduced to 200°C and held for about 10 minutes with continuous stirring. Then, the temperature of the Cd precursor solution was raised up to 220°C and maintained for about 10 minutes. At this temperature, the TOPTe precursor (as discussed above) was swiftly injected and subsequently the color of the solution started changing. During the process, an aliquot was taken out every two minutes till the color of the solution became dark red. This final product/eluent was obtained after 24 minutes; thereafter the heating mantle was removed. When temperature reduces to 80°C, 30 ml methanol was added to the reaction mixture and centrifuged at 6500 rpm for 20 minutes. This process was repeated several times to obtain pure CdTe QDs.

Accepted Manuscript

2.2.3 Synthesis of CdTe/ZnS core-shell QDs

The synthesis of CdTe/ZnS Core-shell QDs was carried out in two steps, followed by SILAR technique (Scheme-2). The first step is used to synthesize CdTe core and the second involves making of the shell of ZnS over the core CdTe QDs [6, 45]. For the preparation of core-shell QDs, a certain amount of CdTe nanocrystals (diameter 4.5 nm) with a concentration of 6.8×10^{-5} mmol (the CdTe core QDs concentration was estimated on the basis of UV-vis spectra) [46,47] was dispersed in a mixture of 6 ml of ODE and 3.0 ml of HDA and slowly heated upto 160°C in a nitrogen atmosphere. Then, Zn and sulfur (S) precursors were injected one by one into the solution of CdTe core QDs. The temperature range adjusted for shell growth was about 180°C - 220°C. For the growth of the first monolayer (ML), the amount of Zn precursor taken was approximately 0.33 ml (discussed in preceding section). This was followed by alternating the addition of equal amounts of ***S*** precursors, respectively. A period of 10 minutes between each such addition was sufficient for the reaction to be completed, i.e., the core-shell formation was completed. The core-shell formed was subsequently examined by measuring the absorption and PL-spectra. Upon completion of one monolayer of ZnS, the solution was kept at 220°C for another 30 minutes and finally cooled to room temperature. To remove the unreacted compounds and by-products from the eluent, we added 20 ml of methanol and centrifuged it at 6500 rpm. This process was repeated 3 - 4 times and finally pure core-shell CdTe/ZnS QDs were obtained.

2.2.4. Preparation of water-soluble CdTe/ZnS QDs

The general approach taken to prepare water-soluble QDs was to exchange the native ligands capped on the QDs surface with other water-soluble ligands using host-guest or electrostatic interactions. For this experiment, thiol-containing molecule mercaptopropionic acid (MPA) was used as a binding group. MPA was used to transfer QDs from oil phase to water phase (Scheme S2). Oleic acid worked as a medium for oil phase reaction, and it helped dissolve the cadmium

Accepted Manuscript

oxide precursor. In the ligand exchange technique, TOP ligands were replaced by the MPA from QDs. During this process, the medium was kept basic because the base concentration affects the ligand displacement and controls the final surface charge. In this process, a calculated amount of OA and TOP coated CdTe/ZnS core-shell QDs was mixed with a calculated amount of deionized (DI) water and MPA, and stirred continuously for about 3 hrs at room temperature [48]. To remove the excess MPA from the supernatant solution, centrifugation and decantation were carried out. Successive redispersion of the particles into water, especially at pH 8.5, produced a clear solution.

2.3 Characterization Technique

Steady-state optical measurements were performed in toluene and water (for water-soluble QDs) at room temperature. Absorption spectra were recorded with the UV/VIS/NIR spectrometer, Lambda-750, Perkin-Elmer. Photoluminescence (PL) spectra were collected by Horiba Jobin Yvon Fluorolog-3 spectrofluorometer equipped with double-grating at excitation as well as at emission monochromators (1200 grooves/mm) and Hamamatsu R928P photomultiplier tube (PMT). The excitation source was a 450 Watt CW xenon lamp. Instrumental corrections were applied to all PL spectra to correct for the wavelength dependent PMT response and variation in output intensity from the lamp and grating efficiencies. Excitation and emission slit widths were selected to be 1.0 nm and were kept the same for all measurements. An excitation wavelength of 450 nm was used. Fluorescence decays were recorded using time-correlated single photon counting (TCSPC) system (DeltaFlex-01-DD, Horiba Jobin Yvon IBH Ltd) coupled with DeltaDiode Laser (450 nm, repetition rate of 100 MHz, Horiba Sci.) and PMT (PPD850). The excitation pulse repetition rate and width were about 1 MHz (or 2 MHz) and 334 ps, respectively and the delay time was 10 ns. The data obtained were analyzed using the least square fitting method. High-resolution transmission electron microscopy (HRTEM) images were recorded by Tecnai G^2-20

Accepted Manuscript

electron microscope operated at accelerating voltage of 200 kV. For HRTEM images, CdSe samples were prepared on 300-mesh carbon-coated Cu grids. This was done by dispersing a very small quantity of QDs in toluene (for a dilute solution) and then putting it onto carbon-coated Cu grids and dried to evaporate the solvent. The energy-dispersive X-ray (EDX) spectra and X-ray diffraction (XRD) pattern were recorded by Hitachi-640, at accelerating voltage of 15 KV, and BRUKER- D8, respectively.

3. Results and discussion

Figure 1 shows HRTEM images (a - c) and size histogram (a' - c') of the CdTe QDs prepared at different reaction time and core-shell CdTe/ZnS QDs. The CdTe/ZnS QDs are composed of CdTe-core and one monolayer of ZnS shell. The coating of the shell monolayer over the core results in the increase of the diameter of the QDs, as shown in Fig 1. The average diameter of CdTe-core QDs is 3.7 nm (obtained at 2 minutes) and 4.5 nm (at 20 minutes). Upon adding ZnS ML, the crystallinity is maintained and shows continuous lattice fringes. However, the core-shell diameter increases upto 4.9 nm. HRTEM images of CdTe and core-shell structures CdTe/ZnS exhibit a narrow size distribution with a standard deviation < 10 %.

Figure 2(a) shows the XRD pattern of CdTe and CdTe/ZnS core-shell QDs. The structure, shape, crystallite size, the interplanar spacing (d) and reflection planes (111), (220), (311) are calculated from the XRD data and are given in Table 1. The reflection angles from CdTe are (23.77°), (40.01°) and (46.72°) and from CdTe/ZnS are (24.60°), (41.46°) and (49.10°), respectively. These values are in agreement with the standard JCPDS file No: 65-0890. The intense peak (2θ = 23.77/24.60) obtained corresponds to the reflection plane (111). The synthesized QDs have face-centered cubic (fcc) structure. The average crystallite size (D) was calculated from the Debye-Scherer formula

Accepted Manuscript

$$D = 0.94\,\lambda/\beta cos\theta \quad (1)$$

where λ is the wavelength of X-ray radiation (1.54 Å), β is the FWHM and θ is the diffraction angle. The lattice parameter ***a*** for the cubic structure was determined using the relation

$$a = d(h^2 + k^2 + l^2)^{\frac{1}{2}} \quad (2)$$

where *d* is the interplanar spacing (Å) and (h, k, l) are the Miller indices of the planes. The lattice parameters are nearly the same from the different orientations of the crystal, which shows that the prepared CdTe and CdTe/ZnS QDs have similar characteristics and are crystalline in nature. From the XRD pattern, it is clear that the QDs with crystallite size 3.92 nm (CdTe) and 4.10 nm (CdTe/ZnS) belong to *fcc* phase with a preferred orientation in (111) direction. Additionally, the broad X-ray bands clearly indicate the formation of polydisperse particles. Furthermore, no additional peak arises which shows the formation of pure and single phase QDs. The interplanar spacing estimated from the peak (111) using Bragg's law is approximately 3.74 Å for CdTe and 3.61 Å for CdTe/ZnS.

The Williamson and Smallman's formula was used for evaluating the dislocation density (δ), as given by [49]

$$\delta = \frac{n}{D^2} \quad (3)$$

where ***n*** is the dislocation density factor, (n = 1, gives minimum dislocation density) and D is the crystallite size. The crystallite size and strain broadening were calculated using Williamson-Hall (W-H) relation [50], as follows

$$\frac{\beta \cos\theta}{\lambda} = \frac{K}{D} + \frac{4\,\varepsilon \sin\theta}{\lambda} \quad (4)$$

where λ represents the wavelength of the X-ray radiation, ***k*** is a shape dependent quantity and taken as unity by assuming the shape of the crystallite to be spherical, and ***ε*** is strain broadening. The strain is estimated from the slope of the linear relation of W-H plot obtained between

Accepted Manuscript

βcosθ/λ and sinθ/λ (Fig. 2b). The negative values of strain for CdTe and CdTe/ZnS QDs show compressive strain. The reciprocal intercepts of W-H plot provide dislocation density (δ). There is no significant variation in dislocation density, however, strain decreases by adding the shell of ZnS over CdTe-core. XRD patterns and their Miller indices of the core and core-shell QDs are identical indicating the similar structure of both core and core-shell QDs and their preferred direction of growth. To identify the chemical composition and elemental analysis of the particles, EDX spectra of the CdTe core and CdTe/ZnS core-shell QDs were measured (Supporting information, Fig. S1). The percentage amount of elements in CdTe and CdTe/ZnS samples are given in Table 2.

Figure 3 (a,b) shows absorption and photoluminescence spectra of magic size CdTe QDs prepared at different time intervals at a fixed reaction temperature of 200 °C. The absorption maxima shifted from 473 nm to 557 nm as time interval increased from 2 - 20 minutes. The clear absorption bands are clearly indicating a uniform distribution of QDs. The strong confinement regime and confinement energy of the first excited electronic state can be approximated by the effective mass approximation equation:

$$E_g = E_g^{bulk} + \frac{h^2\pi^2}{2\,R^2}\left(\frac{1}{m_e^*} + \frac{1}{m_h^*}\right) - \frac{1.8e^2}{4\pi\epsilon\epsilon_o\,R} \qquad (5)$$

where E_g is the optical transition energy of CdTe quantum dots, E_g^{bulk} is the energy gap of the bulk CdTe and m_e^* and m_h^* are the effective mass of conduction band electrons and valence band holes of CdTe, respectively. The value of m_e^* is 0.096 m_0 and m_h^* is 0.40 m_0 [51], where m_0 is the electron rest mass (9.1×10^{-31}kg). The estimated average particle size of CdTe QDs obtained at different time intervals at fixed temperature are given in Table 3. The variation of particle diameter (from 3.94 nm to 4.76 nm), PL wavelength, FWHM and Stokes shift with time is shown in Fig. 3c. The PL peak of CdTe QDs shifted from 534 nm to 588 nm with increasing reaction time.

Accepted Manuscript

The FWHM of the band edge PL is maintained between 29 nm - 37 nm, indicating that the particles are nearly monodispersed. The PL peak shifted to longer wavelengths with increase in the size of QDs as a consequence of decrease in quantum confinement, because the emission peak wavelength strongly depends on the diameter of the QDs. In general, the PL of QDs is affected by their surface state and surface defects, as defects often deteriorate the relation between the band-gap PL and the size of the QDs. The QDs with a large number of surface defects show broad and weak PL spectra, and the PL peak is often redshifted [52,53]. The Stokes shift of CdTe QDs is reduced from 61 nm to 30 nm with respect to time. Thus, the radiative transitions with narrow PL directs towards band edge emission.

Figure 4 (a,b) shows the absorption and PL spectra of CdTe QDs with changing time and at a fixed temperature developed upon modification of the preceding one. The absorption maxima of the CdTe shifted from 525 nm to 568 nm (Fig. 4a). The redshift in absorption spectra affects the confinement energy and size of the QDs. The size of the CdTe QDs varies from 4.3 nm to 4.9 nm with time as calculated using Tauc plots. The PL spectra of CdTe QDs obtained after 2 minutes at a temperature of 220°C shows dual bands at 548 nm and 596 nm (Fig. 4b). By varying the time from 2 to 24 minutes at the same temperature, the first PL band shifted from 548 nm to 601 nm and second PL band shifted from 596 nm to 627 nm, as shown in Fig. 4(a). At the same time, the intensity of both the bands increased significantly. The peak wavelength difference between the two bands, which was initially about 48 nm, became 26 nm which is nearly the same for the longer period. The Stokes shift corresponding to the first band of CdTe QDs increases from 22 nm to 33 nm while decreasing from 71 nm to 59 nm for the second PL band. The variation in the PL maxima and Stokes shift with time is shown in Fig. 4c. The unusual dual PL bands, which cover a broad range of the visible spectrum, are worth mentioning. It is clear that the first PL band with a small Stokes shift corresponds to the band edge PL of the CdTe QDs while the second

Accepted Manuscript

PL band at a longer wavelength with large Stoke shift arises from the surface state, *i.e.,* the defect emission, which may be due to the variation in the temperature during the nucleation process.

Figure 5 shows the absorption and PL spectra of CdTe/ZnS core-shell QDs. The shell material which has higher band gap is coated over the surface of CdTe. Both absorption and PL spectra of core-shell QDs are red-shifted as compared to the core CdTe. The maximum absorption band shifted from 557 nm to 590 nm and PL band shifted from 588 nm to 625 nm after overcoating the CdTe with ZnS. Upon increasing the growth temperature and reaction time, both absorption and PL were further red shifted. This could be due to the fractional leakage of exciton into the ZnS shell from the CdTe core, which further affected the confinement energies of the charge carriers [54]. The PL quantum yield (QY) increased from 10 % to 25 % (calculated as per the supporting information formula S1), which might be due to the surface passivation of bare CdTe with ZnS shell. In smaller CdTe dots, the surface to volume ratio is very high, and the PL of TOP-capped QDs is dominated by band-edge PL because it shows narrow and uniform PL. However, this PL also suffers a small deep trap state or incomplete surface passivation; this problem may be reduced by coating CdTe QDs with ZnS layer. The shell layer suppresses deep trap emission by passivation of most of the surface vacancies and traps, resulting in small FWHM and narrow PL emission [53].

Time-resolved PL spectroscopy of CdTe core and CdTe/ZnS core-shell QDs

The photoluminescence decay curves of CdTe QDs prepared at fixed temperature with varying reaction time are shown in Fig. 6(a,b). The decay of CdTe could not fit with mono-exponential (1 Exp) or bi-exponential (2 Exp) functions (shown with χ^2 value and weighted residual), however, it was fitted with tri-exponential (3 Exp) function as follows:

$$\mathrm{I(t)} = \alpha_1 \exp\left(-t/\tau_1\right) + \alpha_2 \exp\left(-t/\tau_2\right) + \alpha_3 \exp\left(-t/\tau_3\right) \quad (6)$$

Accepted Manuscript

where τ_1, τ_2 and τ_3 represent the lifetimes and α_1, α_2 and α_3 are the corresponding pre-exponential factors, respectively. The fitting parameter, χ^2 is higher for the 2 minute sample even in the three exponential fit. The fitting does not improve much even with four exponential fit. However, in four exponential fit the normalized amplitude of fourth and shortest component (<1 ns) is nearly zero, therefore we have ignored the forth component in the fitting. This reflect that even the 3-exponential fit is likely to be an approximation. The typical reduction in chi-squared goodness of fit for 1, 2 and 3-exponentials for some of the data sets are shown in Fig. 6. All the fitted parameters are shown in Table 4. The decay of CdTe obtained for 2min is fitted with tri-exponential function (Fig. 6a) with a decay time of 1.94, 12.56 and 56.77 ns. The pre-exponential functions corresponding to these time constants are 0.62, 0.36 and 0.02, respectively. The average lifetime, defined by $\tau_{av} = \Sigma_i \alpha_i \tau_i^2 / \Sigma_i \alpha_i \tau_i$ is determined to be 18.04 ns.

Upon increasing reaction time from 2 to 20 minutes the decay time of all the three components decreased gradually. The normalized amplitude corresponding to the shorter lifetime component (0.5 – 3.0 ns) is highest (62%), however, the amplitude of the longest lifetime component is very small (2%) in overall contribution. All the three lifetimes become shorter as the reaction time is increased. At 20 minutes, the shortest component is 0.43 ns and the longest component reduces nearly more than half (Table 4). As the reaction time increases, the PL shifts towards longer wavelength region and hence the size of the QDs increases. At the same time the FWHM increases (about 6 nm), which may be due to less confinement of the electron. The number of lifetime components remains same, which means that the distribution of the particles does not affect. The amplitude of the smallest component increases, indicating more uniformity of the QDs. This indicates that the three-lifetime components of the QDs may represent three different states. The shortest component which contributes the maximum to the PL is assigned to the direct band gap and the slower components may be assigned to the defect states [5]. The

Accepted Manuscript

exciton state of CdTe QDs has a large charge transfer (CT) character and the rate of the nonradiative process from this CT to the nonemissive surface state, *i.e.,* trapped state, may increase in the presence of external field [5]. The average lifetime varies from 18.04 ns to 10.84 ns with increasing reaction time from 2 to 20 minutes. Together with the individual components of lifetime, the decrease of τ_{Av} with reaction time may be due to the increase of the CT character, i.e., the rate of non-radiative processes.

The CdTe prepared with slight modification in synthesis procedure gives a wide range of PL spectra and shows a dual emission band. The decay curves of these QDs were recorded at both the bands are fitted (as an approximation) with 3-exponential function (Table 5) and the fitted decay curves together with the chi-squared values and weighted residuals for the selected data set are shown in Fig. 6b. At 550 nm, the decay shows tri-exponential fit with a lifetime of 1.03, 7.89 and 31.90 ns. Again, the contribution of the smallest lifetime component (1.03 ns) is highest among all. The average lifetime is 12.65 ns. While monitoring the second PL band (600 nm) the decay was fitted again with tri-exponential fit with a time constant of 2.47, 14.55 and 51.54 nm. All the lifetime components are different from the obtained at 550 nm (first band) and became more substantial. However, the contribution of the intermediate time constant (14.55 ns) is highest. Note, that the average lifetime of initially prepared CdTe is 18.75 ns, which is higher than the obtained lifetime for the modified CdTe QDs. Thus, it may be concluded that the lifetimes obtained for two different PL bands are different indicating that the origin of the PL is different. Further, upon increasing the reaction time from 2 to 24 minutes, both the PL bands shifted towards longer wavelength. The fitted decay parameters monitored at each band are given in Table 5. Note that the average lifetimes for the shorter and longer wavelength PL bands are nearly the same, as the average lifetime of shorter wavelength band is between 11 ns to 14 ns and for the longer, 18 ns to 20 ns. From the steady-state results and the lifetime components

Accepted Manuscript

together with the pre-exponential factors it is inferred that the PL arises from the direct band gap, and the slower component comes from the surface state. As the size of the QDs increase with increasing reaction time, both the PL bands come closer, however, the average lifetime is nearly the same as obtained for 2 minutes sample. Thus, the recombination of excited carriers on the surface needs the participation of phonon. As a result, the surface related emission has a longer lifetime [55].

Figure 6c shows the PL decay curve of core-shell CdTe/ZnS QDs dispersed in water. While coating with a shell over the core, the average lifetime increased from 18 ns (CdTe, Table 4) to 30.76 ns (CdTe/ZnS). The increase of the lifetime may be due to the surface passivation of CdTe with the ZnS shell, which may decrease the surface defect and increase the recombination of electron-hole and hence decreases the non-radiative rates.

In addition, the effect of photo-irradiation on absorption and PL were examined in degassed (with N_2) and non-degassed (atmospheric) conditions as a function of time, keeping the experimental conditions same as taken for all other measurements (with similar intensity and silt width). It has been found that the effect of photo-irradiation on the intensity of PL spectrum of CdTe is significant at both the conditions. Initially the PL intensity decreases rapidly and becomes nearly constant after a certain time in the atmospheric condition (supporting information Fig. S2). It should be noted that the peak of the PL does not show a considerable shift following photo-irradiation. After 1 hour, the intensity reduces by approximately 60%. Similarly, the PL intensity of the degassed sample of CdTe (degassed with N_2 for about 30 min) also decreases following photo-irradiation. However, the effect of photo-irradiation was slightly less with the same time period (~50%) (Supporting information Fig. S2). On the other hand, there is no significant effect on absorption with 450 nm photo-irradiation, keeping the same intensity and time period indicating that the photo-induced de-enhancements are not due to the decrease of absorption

Accepted Manuscript

intensity but may be due to the change of surface environment. Ohshima *et al.* [5] have reported the effect of photo-irradiation on the absorption and PL spectra of CdTe doped in polymer films and the observed PL enhancement was explained in terms of decrease of the rate of the nonradiative process from the emitting exciton state to the nonemissive surface state as a result of the modification of surface environment following photoirradiation.

Effect of metal ion on PL intensity and lifetime of QDs

To study the effect of various metal ions on the PL of two different types of QDs, core and core-shell QDs were examined as discussed in the experimental section. The prepared QDs usually are water-soluble MPA-capped CdTe and CdTe/ZnS. The concentration of both the QDs is optimized before carrying out the interaction of QDs with metal ions. As observed, the pH of the QDs solution significantly affects the PL intensity of QDs. The optimized pH is about 8.5, at which the PL intensity is maximum, which may be due to the deprotonation of the alkyl acid group which produces more negative charge and coordinated between the ligands and the semiconductor QDs surface. On the other hand, at relatively lower pH, the protonation of surface binding thiolates occurs resulting in the decrease of PL intensity. Further, to see the role of metal ions, we optimized the concentration of the QDs and kept it low, as at higher concentrations self-quenching may dominate, which may affect the effect of metal ion on the PL intensity and sensitivity of detection. Again, the low concentration of QDs, which gives less PL intensity, also influenced the sensitivity of the fluorescence spectrophotometer. Therefore the selection of the PL intensity of QDs concentration is crucial because it affects not only the PL intensity but also the sensitivity and linear range in the detection of the metal ions. Typically the concentration of QDs taken is in the range of 10^{-4} – 10^{-5} $molL^{-1}$ considering the above factors.

Accepted Manuscript

In the first case, metal ions were added gradually to the solution of CdTe QDs. While adding a small amount (0.2 mM) of Fe^{2+} the PL intensity of CdTe QDs decreases significantly without shifting the PL band position (Fig. 7a). Upon increasing the concentration of Fe^{2+} ions, the PL intensity decreased monotonically and became nearly zero at the highest concentration used. For 2.5 mM of Fe^{2+} concentration, the PL intensity of CdTe QDs decreases by about 95% without shifting the PL band position, as shown in Fig 7a. The decrease in PL intensity in the presence of (0 - 2.5 mM) Fe^{2+} is further examined using well known Stern-Volmer (S-V) relation [56-58].

$$\frac{I_0}{I} = \frac{\tau_0}{\tau} = \{1 + K_q \tau_0 [Q]\} \quad (7)$$

where, $I_0(\tau_0)$ and *I (τ)* are the PL intensity and lifetime of QDs in presence and absence of quencher, respectively, K_q is the bimolecular collisional quenching constant and the K_{sv} is the S-V constant. The S-V plot between the concentration of Fe^{2+} ions and PL intensity is nearly linear (Fig. 7b). From the linear relation (R^2 = 0.98), K_{sv} and limit of detection (LOD) are calculated and come out to be 4.8 ×10^3 LM^{-1} and 4.5 × 10^{-3} ML^{-1}, respectively. The rate of quenching (K_q) is about 0.2 × 10^{12} $LM^{-1}S^{-1}$. Thus, the CdTe QDs is most sensitive for the Fe^{2+} and also covers large concentration range, as the decrease of PL intensity is monitored with 0.0 -2.5 mM concentration at which the quenching is about 95 %.

Secondly, the sensitivity, i.e., fluctuations in PL intensity of MPA-capped CdTe/ZnS core-shell QDs is examined systematically in the presence of metal ions (Fig. 8). With the addition of a small amount (0.25 µM) of Pb^{2+} in a CdTe/ZnS containing a solution in the feed water, the PL intensity of CdTe/ZnS is quenched significantly. Upon further increasing the concentration of Pb^{2+}, the PL intensity monotonically decreases [59]. For maximum amount, i.e., 16.5 µM, the PL intensity decreased about 98 % as shown in Fig. 8 (a). The absorption spectra of CdTe/ZnS is also recorded for various concentration of Pb^{2+} and does not exhibit any considerable change

Accepted Manuscript

(Supporting info. S3) indicating that there is no complex formation. Similar measurements were carried out for the different metal ions. On the other hand, the PL intensity is significantly modified by the presence of the metal ions. Thus, now instead of core CdTe, the core-shell QDs are sensitive for $Pb^{+2}$and also cover the maximum range of concentration. From the S-V plot as shown in Fig. 8 (b), the K_{sv} and LOD were calculated and found to be 3.3 $\times 10^6$ LM^{-1} and 1.9 $\times 10^{-6}$ ML^{-1}. The rate of quenching (K_q) is about 0.1 $\times 10^{15}$ $LM^{-1}S^{-1}$. Thus, we conclude that CdTe and CdTe/ZnS QDs are highly sensitive to the selective metal ions and can detect the metal ions in feed water and comparable solvents. Specially, the ZnS containing QDs even with Cd shows relatively less cytotoxicity and is more biocompatible [13].

To understand deeper the quenching of PL of QDs by metal ions, we measured PL decay profile of CdTe in the presence of varying concentration of Fe^{2+}, as shown Fig. 9. In the absence of Fe^{2+}, the observed decay could be well fitted with the three components similar to that in the absence of quencher, as given in Table 6. Each lifetime components decrease monotonically with increasing the concentration of metal ions in the solution of CdTe. Though the pre-exponential factor does not obey the similar trend. Each component is long enough and is easily measurable for the sensing; however it makes the sensing mechanism complex [36] as compared to the PL probe which has a single lifetime. The average lifetime decreased gradually with increasing the concentration of Fe^{+2} ions from 0.02 mM to till the maximum measured concentration (2.5 mM) of Fe^{2+} at which the average lifetime becomes 5.52 ns. Similar changes were observed in the steady-state PL spectra. The S-V plot is nearly linear (Fig. 9b) and is quite correlated with the steady-state results.

The study is further extended by using the core-shell CdTe/ZnS QDs for the detection of metal ions. The decay parameters were calculated in the presence and absence of Pb^{2+} (Fig. 10). The observed PL decay is well fitted with the three components. Similar to CdTe, each lifetime

Accepted Manuscript

component decreases gradually with increasing the concentration of metal ions. Again the pre-exponential factor does not obey the similar trend. The decay time is 30.76 ns in the absence of Pb^{2+} quencher (Table 7). However, upon adding a small amount of quencher the lifetime decreases significantly. With increasing the quencher concentration the lifetime decreases monotonically and becomes 11.35 ns for maximum concentration (16.5 μM) of the quencher. In both cases, each of the decay components decreases with increasing the concentration of metal ions (Tables 6 and 7). Thus, the change in the lifetime and PL intensity follow nearly linear S-V relation indicating that the quenching is collisional in nature.

Further, the sensitivity, i.e., fluctuations in PL/absorption intensity of CdTe and MPA-capped CdTe/ZnS core-shell QDs were examined systematically in the presence of various metal ions (Pb^{2+}, Cu^{2+}, Fe^{2+}, Co^{2+} and Ni^{2+}) and the parameters obtained from the change in PL intensity with a concentration of different metal ions were recorded. There is no significant effect on absorption, which precluded the ground state complex formation. A comparative bar diagram as shown in Fig. 11 (a,b) demonstrated the relative changes in PL intensity with the maximum concentration of metal ions used. Thus core-shell QDs are most sensitive towards Pb^{+2} and also cover the maximum range of concentration, whereas core CdTe QDs are most sensitive towards Fe^{+2}. Thus the LOD and % of quenching varies for core and core-shell QDs. Further, we conclude that both CdTe and CdTe/ZnS are highly sensitive to the metal ions and can detect the metal ions in feed water and comparable solvents.

The core-shell QDs were also investigated by Sutter *et al.* [36, 37] using steady-state and transient measurement including two-photon absorption. It has been shown that the absorption of Cu^{+2} is nicely overlapped with the PL of CdSe/ZnS. And demonstrated the fluorescence resonance energy transfer (FRET) is a dominant mechanism for PL quenching of CdSe QDs in the presence of metal ions. However, in the present case the overlapped areas between the PL and

Accepted Manuscript

absorption of QDs and metal ions, respectively are very small as given in supporting information S4. Though the energy transfer mechanism cannot be ruled out as a reason for PL quenching, the FRET can be an additional mechanism for the PL quenching due to which exact linear S-V plots could not observe both in the steady-state and time-resolved study. The time evolution of PL for different excitation intensities during two-photon excitation provides information about the kinetics of photo-brightening and photo-darkening, which further leads utilization of QDs as sensors with higher accuracy [37].

4. Conclusions

We have described the synthesis of CdTe and CdTe/ZnS core-shell QDs with varying time. We could prepare CdTe QDs which cover a broad PL range with two well separated PL bands, which has been reported for the first time to the best of our knowledge following single port synthesis. The prepared QDs show uniform particle distribution, small FWHM and enhanced PL QY. The PL of both CdTe and CdTe/ZnS quenched significantly in the presence of metal ions. Both the PL and PL lifetime of these QDs was diminished by the metal ions, however the quenching ability and sensitivity is different for different QDs, e.g., Fe^{2+} ions are for CdTe and Pb^{2+} ions are for CdTe/ZnS QDs. The S-V plots are nearly linear and exhibit that the quenching is dominated by dynamic behavior together with FRET and follow diffusion mediated collision quenching, though the mechanism of PL quenching of QDs with metal ions remain still somewhat unclear. In addition to the sensing of metal ions, these quantum dots could also be used for biological applications.

Acknowledgements

We thank the Science and Engineering Research Board (SERB) (EMR/2016/001110), Department of Science and Technology (DST), Govt. of India for providing financial support.

The authors have declared that no competing interests exist.

Accepted Manuscript

References

1. Henglein A 1989 Small-particle research: Physicochemical properties of extremely small colloidal metal and semiconductor particles Chem. Rev. 89 1861 – 1873.
2. Mehata M S 2015 Enhancement of charge transfer and quenching of photoluminescence of capped CdS quantum dots Sci. Rep. 5 12056.
3. Murray C B, Norris D J and Bawendi M G 1993 Synthesis and characterization of nearly monodisperse CdE (E = S, Se, Te) semiconductor nanocrystallites J. Am. Chem. Soc. 115 8706 – 8715.
4. Alivisatos A P 1996 Perspectives on the physical chemistry of semiconductor nanocrystals J. Phys. Chem. 100 13226 – 13239.
5. Ohshima R, Nakabayashi T, Kobayashi Y, Tamai N and Ohta N 2011 External electric field effects on state energy and photoexcitation dynamics of water-soluble CdTe nanoparticles J. Phys. Chem. C 115 15274-15281.
6. Ratnesh R K and Mehata M S 2017 Synthesis and optical properties of core-multi-shell CdSe/CdS/ZnS quantum dots: Surface modifications Opt Mater. 64 250 - 256.
7. Nirmal M and Brus L 1999 Luminescence photophysics in semiconductor nanocrystals Acc. Chem. Res. 32 407 – 414.
8. Kotresh M G, Adarsh K S, Shivkumar M A and Inamdar S R 2016 Steady state and timeresolved spectroscopy study of CdSe and CdSe/ZnS QDs: FRET approach J Fluoresc 26 1249 – 1259
9. Talapin D V, Rogach A L, Haase M and Weller H 2001 Evolution of an ensemble of nanoparticles in a colloidal solution: Theoretical study J. Phys. Chem. B 105 12278 - 12285.

Accepted Manuscript

10. Chen C Y, Cheng C T, Lai C W, Wu P W, Wu K C, Chou P T, Chou Y H and Chiu H T 2006 Potassium ion recognition by 15-crown-5 functionalized CdSe/ZnS quantum dots in H_2O Chem. Commun. 3 263 - 265.
11. Chen J L, Gao Y C, Xu Z B, Wu G H, Chen Y C and Zhu C Q 2006 A novel fluorescent array for mercury (II) ion in aqueous solution with functionalized cadmium selenide nanoclusters Anal. Chim. Acta 577 77 - 84.
12. Verma N and Singh M 2005 Biosensors for heavy metals BioMetals 18 121 – 129.
13. Ratnesh R K and Mehata M S 2017 Investigation of biocompatible and protein sensitive highly luminescent quantum dots/nanocrystals of CdSe, CdSe/ZnS and CdSe/CdS. Spectrochim. Acta A: Mol Biomol Spectro. 179 201 – 210.
14. Wu C S, Cupps J M and Fan X 2009 Compact quantum dot probes for rapid and sensitive DNA detection using highly efficient fluorescence resonant energy transfer Nanotechnology 20 305502.
15. Brewer G J 2010 Risks of copper and iron toxicity during aging in humans Chem. Res. Toxicol. 23 319 – 326.
16. Bruins M R, Kapil S and Oehme F W 2000 Microbial resistance to metals in the environment Ecotoxicol. Environ. Safety 45 198 – 207.
17. Todd M D, Lee M J, Williams J L, Nalezny J M, Gee P, Benjamin M B and Farr S B 1995 The CAT-Tox (L) assay: A sensitive and specific measure of stress induced transcription in transformed human liver cells Appl. Toxicol. 28 118 – 128.
18. Rogers J T, Richards J G and Wood C M 2003 Lonoregulatory disruption as the acute toxic mechanism for lead in the rainbow trout (Oncorhynchus mykiss), Aquat. Toxicol. 64 215 – 234.

Accepted Manuscript

19. Miyake Y, Togashi H, Tashiro M, Yamaguchi H, Oda S, Kudo M, Tanaka Y, Kondo Y, Sawa R, Fujimoto T, Machinami T and Ono A 2006 Mercury^{II}-mediated formation of thymine-Hg^{II}-thymine base pairs in DNA duplexes J. Am. Chem. Soc. 128 2172 – 2173.
20. Kim H K, Rasnik I, Liu J, Ha T and Lu Y 2007 Dissecting metal ion–dependent folding and catalysis of a single DNAzyme Nat. Chem. Biol. 3 763 – 768.
21. Hussein H, Farag S, Kandil K and Moawad H 2005 Tolerance and uptake of heavy metals by Pseudomonads Process Biochem. 40 955 – 961.
22. Kunkel R and Manahan S E 1973 Atomic absorption analysis of strong heavy metal chelating agents in water and waste water Anal. Chem. 45 1465 – 1468.
23. Bings N H, Bogaerts A and Broekaert J A C 2006 Atomic spectroscopy Anal. Chem. 78 3917 – 3946.
24. Tanyanyiwa J and Hauser P C 2002 High-voltage contactless conductivity detection of metal ions in capillary electrophoresis Electrophoresis 23 3781 – 3786.
25. Lorber K E 1986 Monitoring of heavy metals by energy dispersive X-ray fluorescence spectrometry Waste Manage. Res. 4 3 – 13.
26. Bertsch P M and Hunter D B 2001 Applications of synchrotron-based X-ray microprobes Chem. Rev. 101 1809 – 1842.
27. Czarnik A W 1995 Desperately seeking sensors Chem. Biol. 2 423 – 428.
28. Xia Y S and Zhu C Q 2008 Use of surface-modified CdTe quantum dots as fluorescent probes in sensing mercury (II) Talanta 75 215 – 221.
29. Jr M B, Moronne M, Gin P, Weiss S and Alivisatos A P 1998 Semiconductor nanocrystals as fluorescent biological labels Science 281 2013 – 2016.
30. Chan W C W and Nie S 1998 Quantum dot bioconjugates for ultrasensitive nonisotopic detection Science 281 2016 - 2018.

Accepted Manuscript

31. Wu C S, Oo M K K and Fan X 2010 Highly sensitive multiplexed heavy metal detection using quantum-dot-labeled DNAzymes ACS Nano 10 5897 – 5904.

32. Helal A, Rashid M H O, Ch H C and Kim H S 2011 Chromogenic and fluorogenic sensing of Cu^{2+} based on coumarin Tetrahedron 67 2794 – 802.

33. Tang R, Lei K, Chen K, Zhao H and Chen J A 2011 A rhodamine-based off–on fluorescent chemosensor for selectively sensing Cu (II) in aqueous solution J. Fluoresc. 21 141 – 148.

34. Durgadas C V, Sharma C P and Sreenivasan K 2011 Fluorescent gold clusters as nanosensors for copper ions in live cells Analyst 136 933 – 940.

35. Chan Y H, Jin Y, Ch W and Chiu D T 2011 Copper (II) and iron (II) ion sensing with semiconducting polymer dots Chem. Commun. 47 2820 – 2822.

36. Sutter J U, Birch D J S and Rolinski O J 2012 CdSe/ZnS core/shell quantum dots as luminescence life time sensors for Cu^{2+} Meas. Sci. Technol. 23 055103.

37. Sutter J U, Birch D J S and Rolinski O J 2011 The effect of intensity of excitation on CdSe/ZnS quantum dots: opportunities in luminescence sensing Appl. Phys. Lett. 98 021108.

38. Birch D J S, Rolinski O J and Hatrick D 1996 Fluorescence lifetime sensor of copper ions in water Rev. Sci. Instrum 67 2732 – 2737.

39. Sarell C J, Wilkinson S R and Viles H J 2010 Substoichiometric Levels of Cu^{2+} Ions accelerate the kinetics of fiber formation and promote cell toxicity of amyloid-β from alzheimer disease J. Biol. Chem. 285 41533 – 41540.

40. Amaro M, Birch D J S and Rolinski O J 2011 Beta-amyloid oligomerisation monitored by intrinsic tyrosine fluorescence Phys. Chem. Chem. Phys. 13 6434 – 6441.

41. Dudzik C G, Walter E D and Millhauser G L 2011 Coordination features and affinity of the Cu^{2+} site in the α-synuclein protein of parkinson's disease Biochemistry 50 1771 - 1777.

Accepted Manuscript

42. Spillantini M G, Schmidt M L, Lee V M, Trojanowski J Q, Jakes R and Goedert M 1997 α-Synuclein in lewy bodies Nature 388 839 – 840

43. Parak W J, Pellegrino T and Plank C 2005 Labelling of cells with quantum dots Nanotechnology 16 R9 - R25.

44. Michalet X, Pinaud F F, Bentolila L A, Tsay J M, Doose S, Li J J, Sundaresan G, Wu A M, Gambhir S S and Weiss S 2005 Quantum dots for live cells, in vivo imaging and diagnostics Science 307 538 – 544.

45. Li J J, Wang Y A, Guo W Z, Keay J C, Mishima T D, Johnson M B and Peng X G 2003 Large-scale synthesis of nearly monodisperse CdSe/CdS core/shell nanocrystals using air-stable reagents via successive Ion layer adsorption and reaction J. Am. Chem. Soc. 125 12567 - 12575.

46. Schmelz O, Mews A, Basche T, Herrmann A and Mullen K 2001 Supramolecular complexes from CdSe nanocrystals and organic fluorophors Langmuir 17 2861 - 2865.

47. Yu W W, Qu L H, Guo W Z and Peng X G 2003 Experimental determination of the extinction coefficient of CdTe, CdSe, and CdS nanocrystals Chem. Mater. 15 2854 - 2860.

48. Ratnesh R K and Mehata M S 2015 Controlled synthesis and optical properties of tunable CdSe quantum dots and effect of pH AIP Adv. 5 097114 - 10.

49. Williamson G K and Smallman R E 1954 The use of fourier analysis in the interpretation of X-ray line broadening from cold-workd iron and molybdenum Acta Crystallogr. 7 574 – 581.

50. Singh S, Rath M C, Singh A K, Mukherjee T, Jayakumar O D, Tyagi A K and Sarkar S K 2011 CdSe nanoparticles grown via radiolytic methods in aqueous solutions Radiat. Phys. Chem. 80 736 – 741.

Accepted Manuscript

51. Masumoto Y and Sonobe K 1997 Size-dependent energy levels of CdTe quantum dots Phys. Rev. B 56 9734 – 9737.

52. Hines M A and Sionnest P G 1996 Synthesis and characterization of strongly luminescing ZnS-capped CdSe nanocrystals J. Phys. Chem. 100 468 - 471.

53. Dabbousi B O, Viejo J R, Mikulec F V, Heine J R, Mattoussi H, Ober R, Jensen K F and Bawendi M G 1997 (CdSe)ZnS core-shell quantum dots: Synthesis and characterization of a size series of highly luminescent nanocrystallites J. Phys. Chem. B 101 9463 - 9475.

54. Schoos D, Mews A, Eychmuller A and Weller H 1994 Quantum-dots quantum wells CdS/HgS/CdS: Theory and experiment Phys. Rev. B 49 17072 - 17078.

55. Zhou H, Zhou G, Zhou J, Xu D, Zhang X, Kong P and Yu Z 2014 High luminescent core/shell QDs based on noninjection synthesized CdSe QDs: Observation of magic sized CdSe quantum dots RSC Adv. 4 42316 - 42325.

56. Klostranec J M and Chan W C W 2006 Quantum dots in biological and biomedical research: Recent progress and present challenges Adv. Mater. 18 1953 – 1964.

57. Mehata M S and Tripathi H B 2002 Fluorescence quenching of 6-methoxyquinoline: an indicator for sensing chloride ion in aqueous media J. Lumin. 99 47 – 52.

58. Pal A, Srivastava S, Saini P, Raina S, Ingole P P, Gupta R and Sapra S 2015 Probing the mechanism of fluorescence quenching of QDs by Co (III)-Complexes: Size of QD and nature of the complex both dictate energy and electron transfer processes J. Phys. Chem. C 119 22690 – 22699.

59. Xie H Y, Liang H G, Zhang Z L, Liu Y, He Z K and Pang D W 2004 Luminescent CdSe-ZnS quantum dots as selective Cu^{2+} probe Spectrochim. Acta: Part A 60 2527 – 2530.

Accepted Manuscript

Table 1. Various parameters calculated from XRD of CdTe and CdTe/ZnS core-shell QDs prepared by hot injection and SILAR techniques.

Sample	Planes (hkl)	2θ (degree)	FWHM (degree)	Inter-planar spacing d (Å)	Lattice vector a (Å)	Average crystallite size (nm)	Strain × 10^{-3}	Density Dislocation × 10^{16} lines/m^2	Average size (nm)
CdTe	(111)	23.77	3.10	3.74	6.47	3.92	-4.43	6.50	4.5
	(220)	40.01	2.50	2.25	6.36				
	(311)	46.72	2.37	1.94	6.43				
CdTe/ZnS	(111)	24.60	2.90	3.61	6.25	4.16	-3.71	5.77	4.9
	(220)	41.46	2.23	2.17	6.13				
	(311)	49.10	2.42	1.85	6.13				

Table 2. EDX analysis, the percentage constituents of each identified element in the CdTe and CdTe/ZnS QDs.

QDs	Element	Weight %	Atom %
CdTe	Cd	56.95	60.03
	Te	43.05	39.97
CdTe/ZnS	Cd	42.07	35.52
	Te	41.93	32.41
	Zn	9.19	18.32
	S	6.81	13.75

Table 3. Reaction time dependent optical parameters of CdTe QDs.

CdTe (Time variable)	Max. Absorbance peak (nm)	Energy (Eg) eV	Diameter (nm)
2 Min	473	2.62	3.94
4 Min	516	2.40	4.36
6 Min	522	2.37	4.42
8 Min	529	2.34	4.50
10 Min	536	2.31	4.58
12 Min	539	2.30	4.60
14 Min	541	2.29	4.62
16 Min	543	2.28	4.66
18 Min	544	2.27	4.68
20 Min	557	2.22	4.76

Accepted Manuscript

Table 4. The photoluminescence lifetimes and pre-exponential factors of CdTe QDs in toluene obtained at fixed temperature with varying reaction time.

CdTe	λ_{ex} (nm)	λ_{em} (nm)	τ_1 (ns)	τ_2 (ns)	τ_3 (ns)	α_1	α_2	α_3	τ_{Av} (ns)	τ_{mean} (ns)
2 Min	450	530	1.94 ± 0.06	12.56 ±0.11	56.77 ±0.83	0.62	0.36	0.02	18.04	23.75
10 Min	450	570	0.72 ± 0.01	7.52 ± 0.17	29.82 0.42	0.79	0.19	0.02	11.16	12.68
20 Min	450	582	0.43 ±0.01	7.20 ±0.24	24.53 ±0.33	0.87	0.11	0.02	10.84	10.72

Table 5. The photoluminescence lifetimes and corresponding pre-exponential factors of modified CdTe QDs in toluene obtained at fixed temperature with varying reaction time.

CdTe	λ_{ex} (nm)	λ_{em} (nm)	τ_1 (ns)	τ_2 (ns)	τ_3 (ns)	α_1	α_2	α_3	τ_{Av} (ns)	τ_{mean} (ns)
2 Min	450	550	1.03 ± 0.02	7.89 ± 0.14	31.90 ± 0.30	0.70	0.27	0.03	12.65	13.60
		600	2.45 ± 0.13	14.55 ± 0.09	51.54 ± 0.61	0.40	0.57	0.03	18.75	22.84
6 Min	450	560	1.00 ± 0.02	8.11 ± 0.18	30.63 ± 0.40	0.68	0.29	0.03	12.12	13.24
		610	2.16 ± 0.11	15.03 ± 0.10	48.71 ± 0.55	0.42	0.54	0.04	19.94	21.96
12 Min	450	585	0.90 ± 0.02	7.76 ± 0.20	30.21 ± 0.45	0.74	0.24	0.02	10.63	12.95
		620	1.91 ± 0.09	13.77 ± 0.11	43.52 ± 0.54	0.44	0.52	0.04	18.06	19.73
18 Min	450	590	0.90 ± 0.02	7.51 ± 0.23	27.66 ± 0.41	0.72	0.25	0.03	11.23	12.02
		625	2.21 ± 0.10	14.45 ± 0.10	47.94 ± 0.64	0.43	0.54	0.03	18.03	21.53
24 Min	450	590	1.22 ± 0.02	9.85 ± 0.16	35.79 ± 0.45	0.65	0.32	0.03	14.05	15.62
		630	3.26 ± 0.18	15.90 ± 0.10	55.24 ± 0.85	0.37	0.61	0.02	18.24	24.80

Accepted Manuscript

Table 6. Photoluminescence lifetimes and pre-exponential factors of CdTe QDs with different concentration of Fe^{2+} ions in water. Excitation and PL wavelengths were 450 and 588 nm, respectively.

CdTe/Fe^{2+} (mM)	τ_1 (ns)	τ_2 (ns)	τ_3 (ns)	α_1	α_2	α_3	τ_{Av} (ns)	τ_{mean} (ns)
0.00	0.85	7.97	48.15	0.81	0.17	0.02	19.25	18.99
0.02	0.84	7.74	46.65	0.82	0.16	0.02	18.76	18.41
0.62	0.59	5.31	33.18	0.82	0.16	0.02	13.47	13.03
1.24	0.65	5.84	36.83	0.83	0.15	0.02	15.15	14.44
1.74	0.35	3.88	28.97	0.88	0.11	0.01	9.95	11.06
2.50	0.25	2.67	17.29	0.89	0.10	0.01	5.52	06.73

Table 7. Photoluminescence lifetimes and pre-exponential factors of CdTe/ZnS QDs with different concentration of Pb^{2+} ions in water. Excitation and PL wavelengths were 450 and 625 nm, respectively.

CdTe/ZnS (µM)	τ_1 (ns)	τ_2 (ns)	τ_3 (ns)	α_1	α_2	α_3	τ_{Av} (ns)	τ_{mean} (ns)
0.00	2.85	20.07	96.42	0.62	0.36	0.02	30.76	39.78
0.25	2.69	19.34	94.12	0.63	0.35	0.02	30.23	38.71
2.50	2.43	17.33	78.90	0.65	0.33	0.02	25.64	32.88
5.00	1.68	13.38	61.61	0.71	0.27	0.02	20.93	25.55
7.50	1.24	10.56	49.37	0.73	0.25	0.02	17.16	20.39
10.00	1.04	8.45	39.88	0.78	0.20	0.02	14.26	16.45
16.50	0.73	6.31	31.19	0.78	0.20	0.02	11.35	12.74

Accepted Manuscript

Figure caption:

Scheme 1. Schematic representation of two port synthesis of core and core-shell QDs.

Scheme 2. Schematic representation of core and core-shell QDs (followed by SILAR method) and conversion of hydrophobic QDs into hydrophilic using MPA.

Figure 1. The HRTEM images (a, b, and c) and its size histogram (a', b' and c') of core CdTe QDs (2 min), CdTe (20 min) and CdTe/ZnS core-shell QDs, respectively.

Figure 2. The XRD pattern of (a) CdTe and (b) CdTe/ZnS core-shell QDs and Williamson-Hall plot ($\beta\cos\theta/\lambda$ versus $\sin\theta/\lambda$) for CdTe and CdTe/ZnS QDs. The XRD peaks are identified with the standard JCPDS software.

Figure 3. The absorption (a) and normalized photoluminescence (b) spectra of magic size CdTe QDs dispersed in toluene at room temperature with varying reaction time. (c) The plots of various parameter like diameter (i), PL maximum (ii), FWHM (iii) and Stokes shift (iv) as a function of reaction time. The excitation wavelength was 450 nm.

Figure 4. The absorption (a) and PL spectra (b) of modified CdTe QDs dispersed in toluene at room temperatures with varying reaction time. (c) The plots of PL maximum (i) and Stokes shift (ii) as a function of reaction time. The excitation wavelength was 450 nm.

Figure 5. The absorption and normalized PL spectra of CdTe and CdTe/ZnS core-shell QDs dispersed in toluene at room temperature. The excitation wavelength was 450 nm.

Figure 6. The fitted photoluminescence decay curves of CdTe (a) and modified CdTe QDs (b) in toluene obtained at various reaction times and at a fixed reaction temperature measured at PL maximum, and fitted decay curves of CdTe (2 min sample, in toluene) and CdTe/ZnS QDs in water (c) . The χ^2 values and weighted residuals are shown for 1, 2 and 3 exponential fits; (a') for CdTe (20 minutes), (b') for modified CdTe (550 nm, 2 min) and (c') for CdTe/ZnSe QDs. The excitation wavelength was 450 nm.

Accepted Manuscript

Figure 7. The PL spectra of MPA-CdTe QDs with varying concentration of Fe^{2+} (a) and the corresponding S-V plot (b). The excitation wavelength was 450 nm.

Figure 8. The PL spectra of MPA-CdTe/ZnS QDs with varying concentration of Pb^{2+} (a) and corresponding S-V plot (b). The excitation wavelength was 450 nm.

Figure 9. Fitted decay curves of CdTe QDs with various concentration of Fe^{2+} ions (a) and corresponding S -V plot (b). The excitation wavelength was 450 nm.

Figure 10. Fitted decay curves of CdTe/ZnS QDs with various concentration of Pb^{2+}ions (a) and corresponding S-V plot (b). The excitation wavelength was 450 nm.

Figure 11. The comparative bar diagram of PL intensity of (a) CdTe and (b) CdTe/ZnS QDs in the presence of different amount of metal ions (Pb^{2+}, Cu^{2+}, Fe^{2+}, Co^{2+} and Ni^{2+}). The excitation wavelength was 450 nm.

Accepted Manuscript

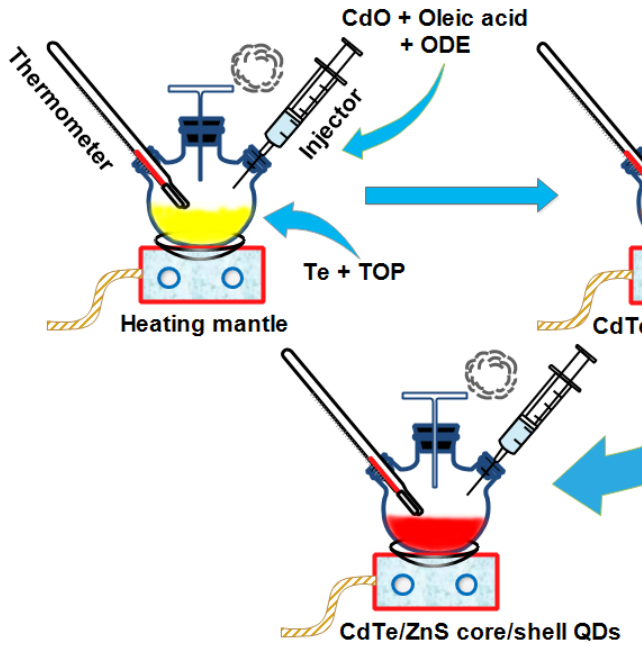

Scheme 1:

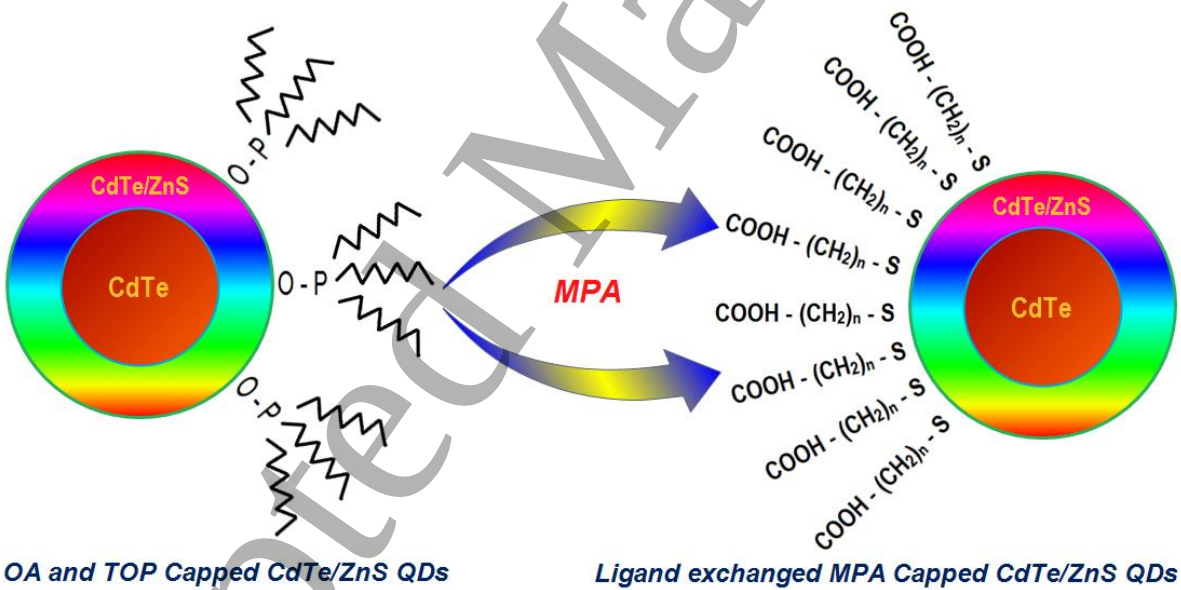

Scheme 2:

Accepted Manuscript

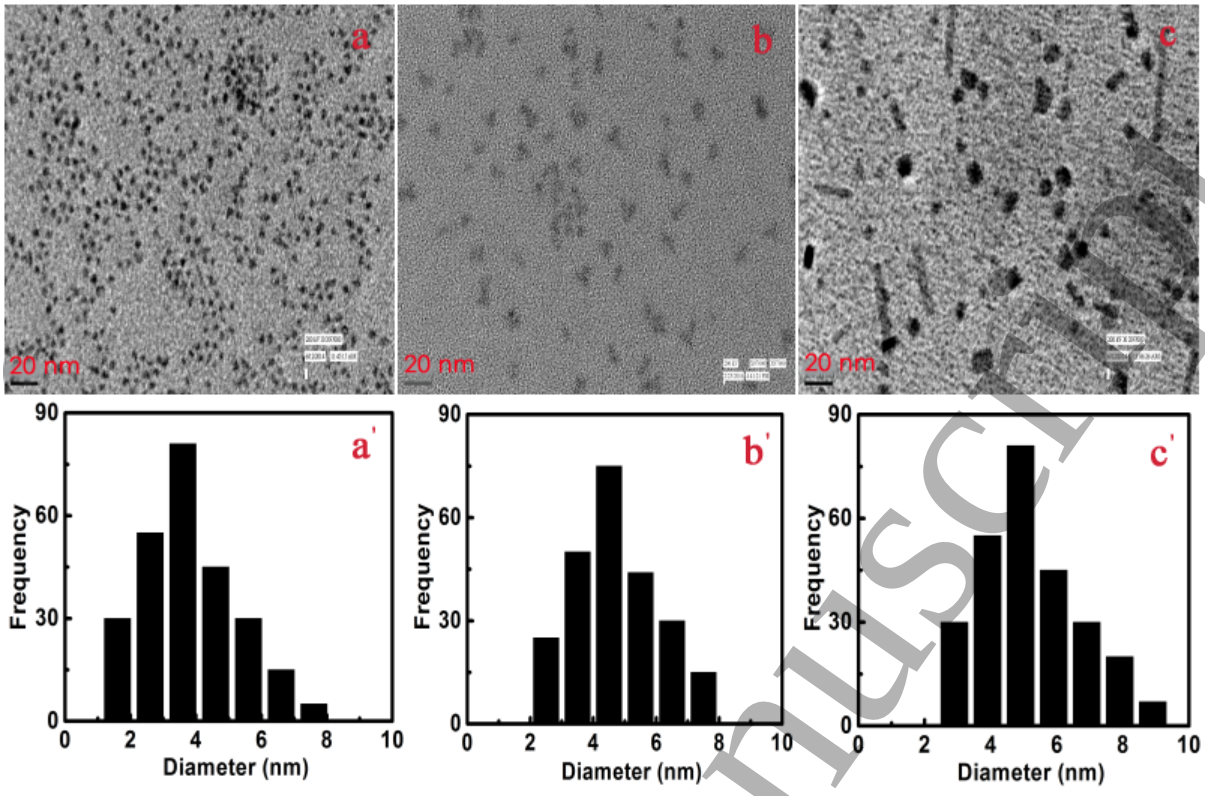

Figure 1:

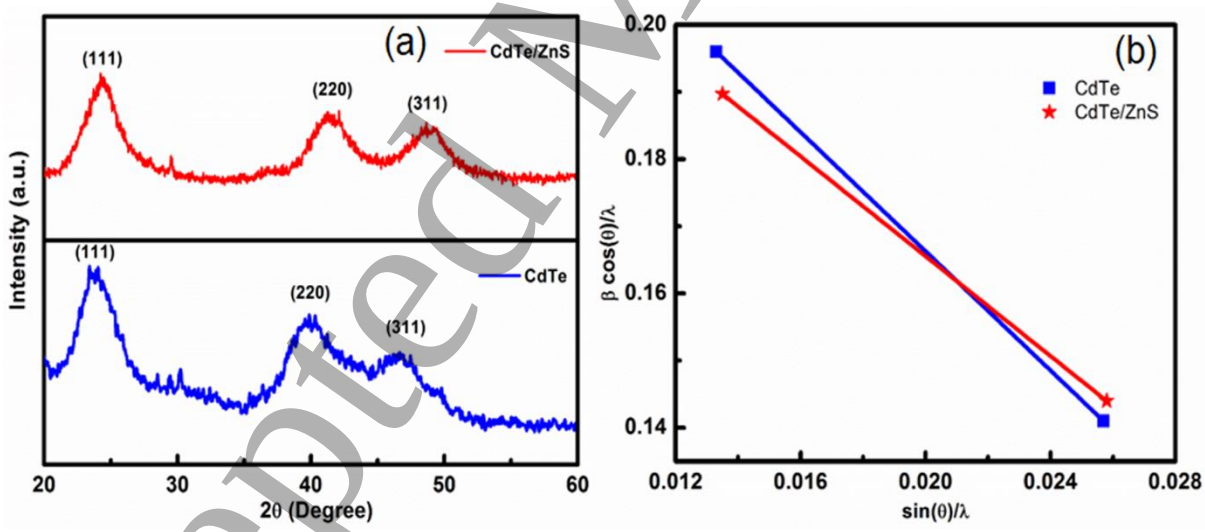

Figure 2:

Accepted Manuscript

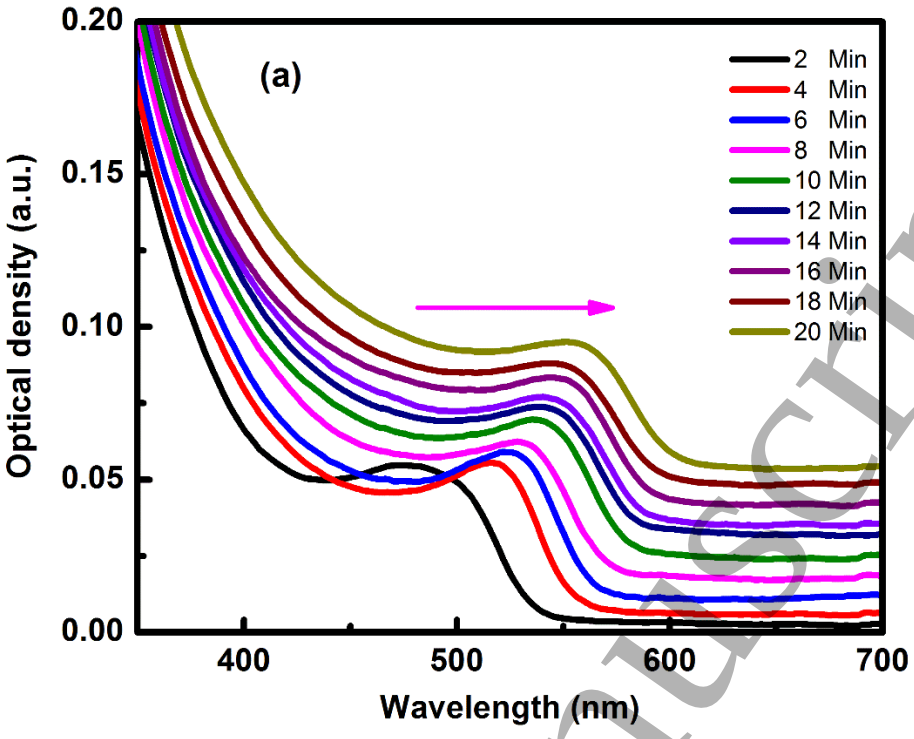

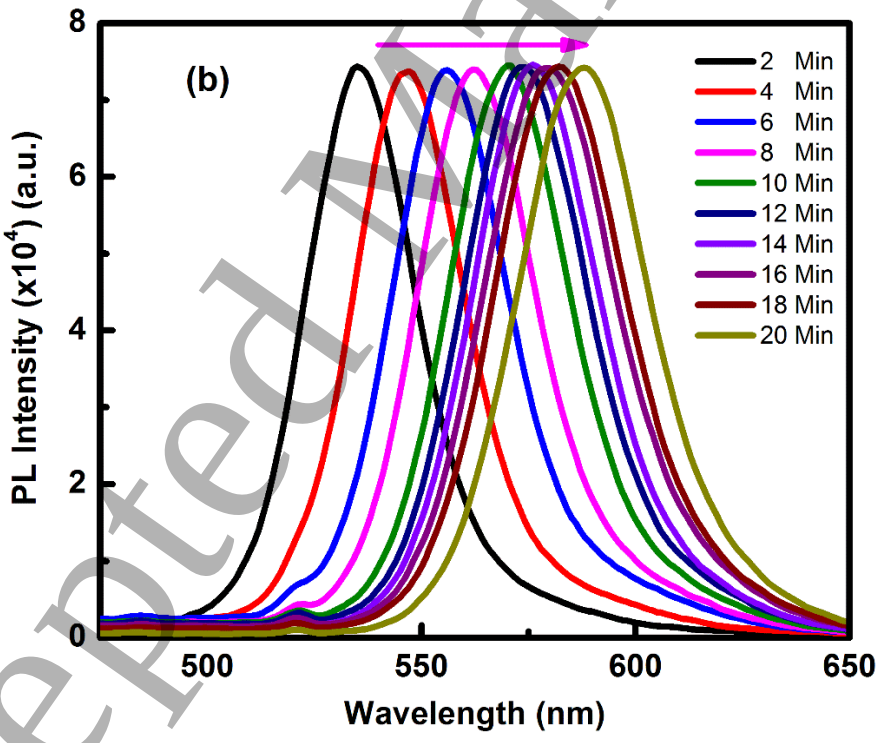

Figure 3 (a,b):

Accepted Manuscript

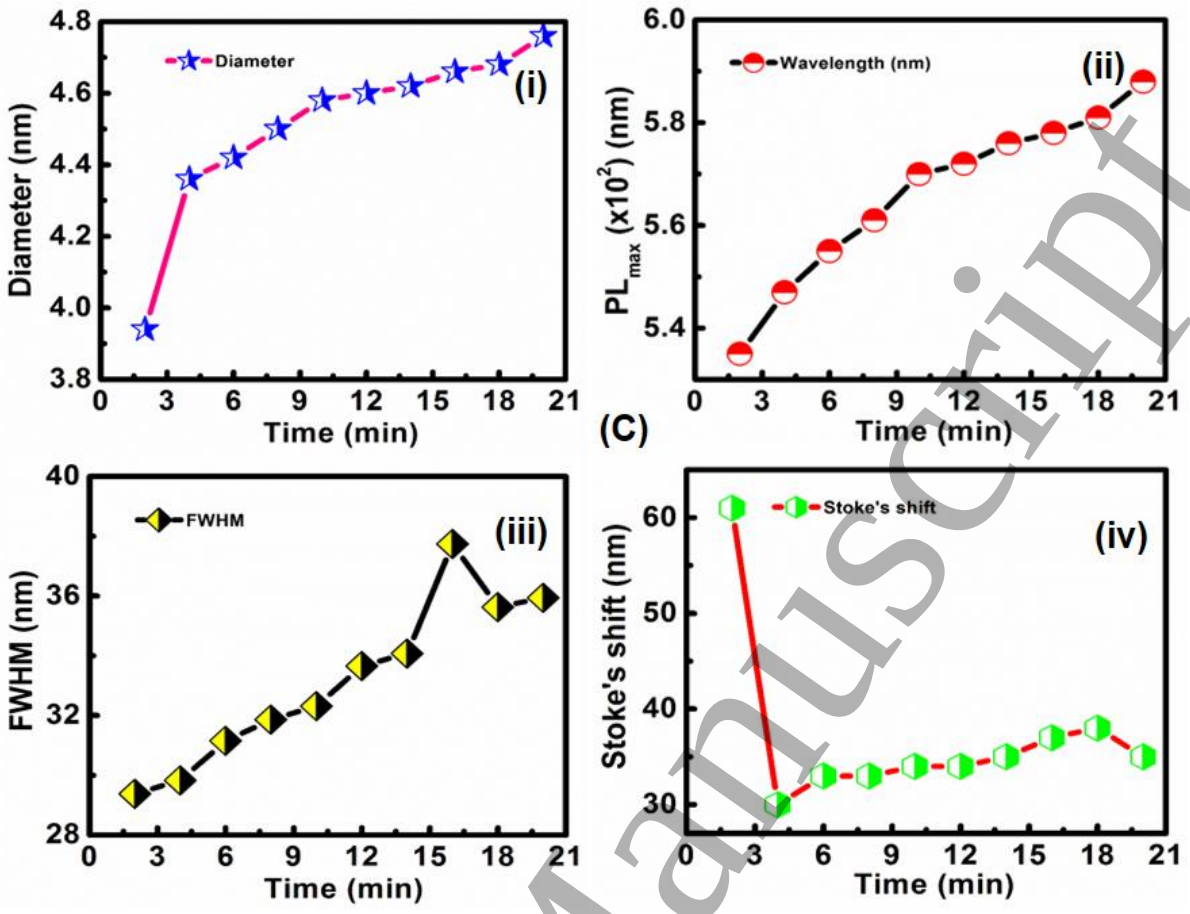

Figure 3(c):

Accepted Manuscript

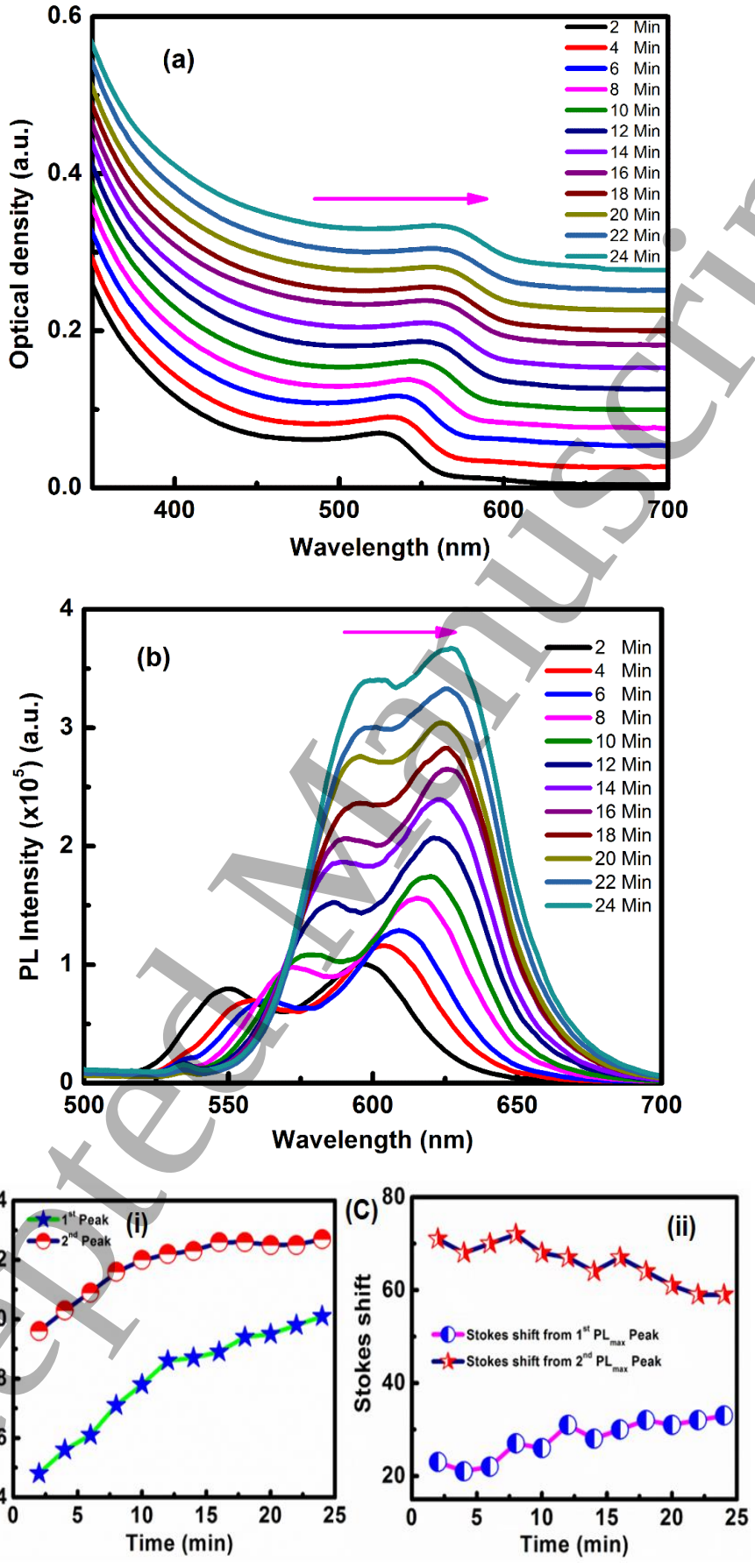

Figure 4:

Accepted Manuscript

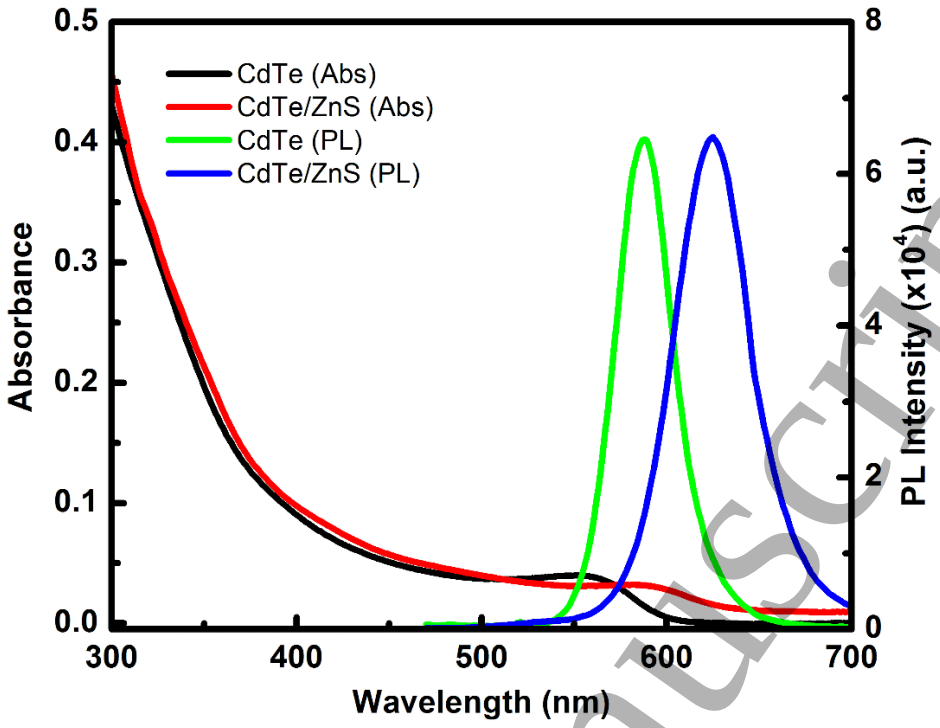

Figure 5:

Accepted Manuscript

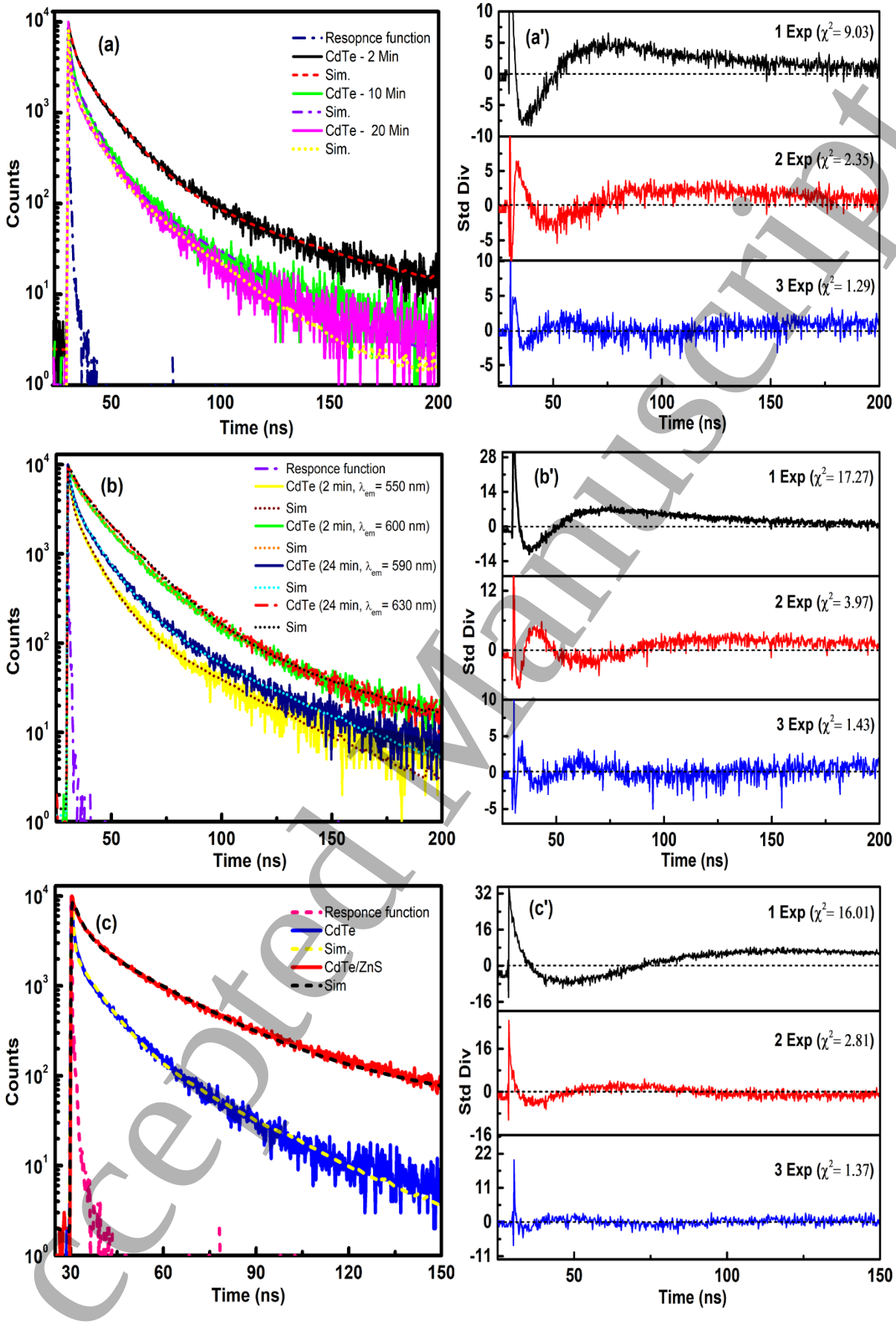

Figure 6:

Accepted Manuscript

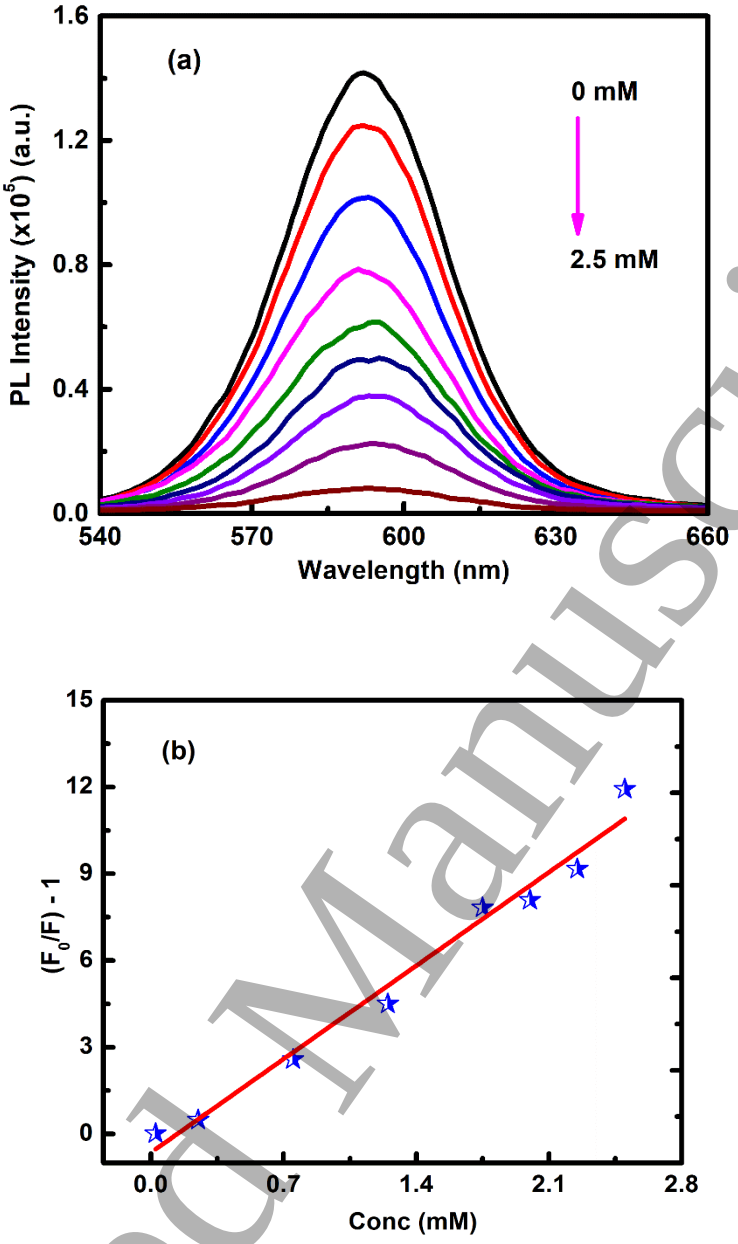

Figure 7:

Accepted Manuscript

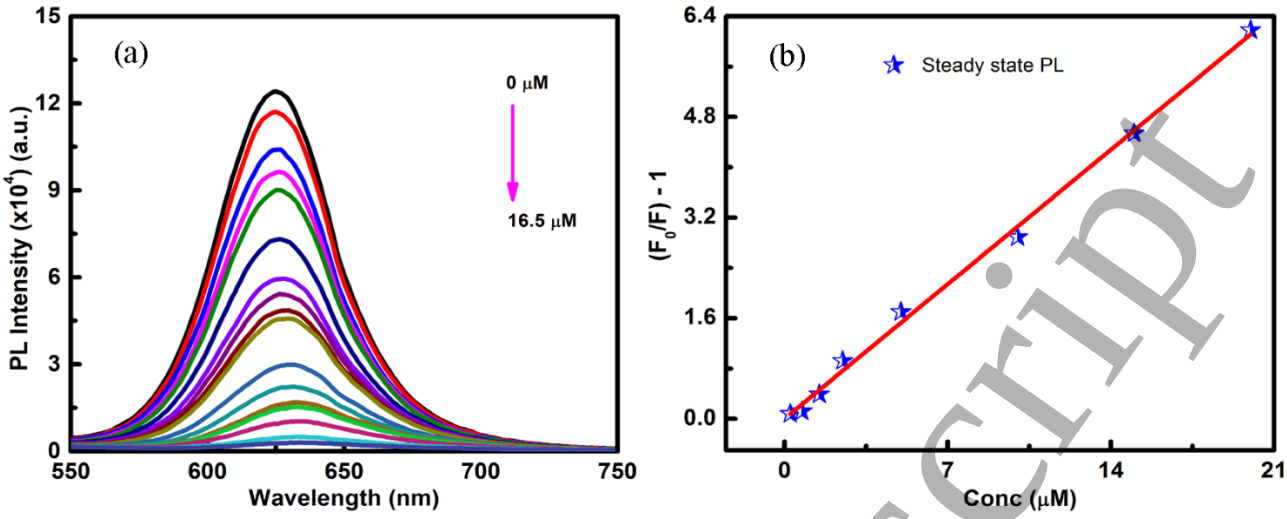

Figure 8:

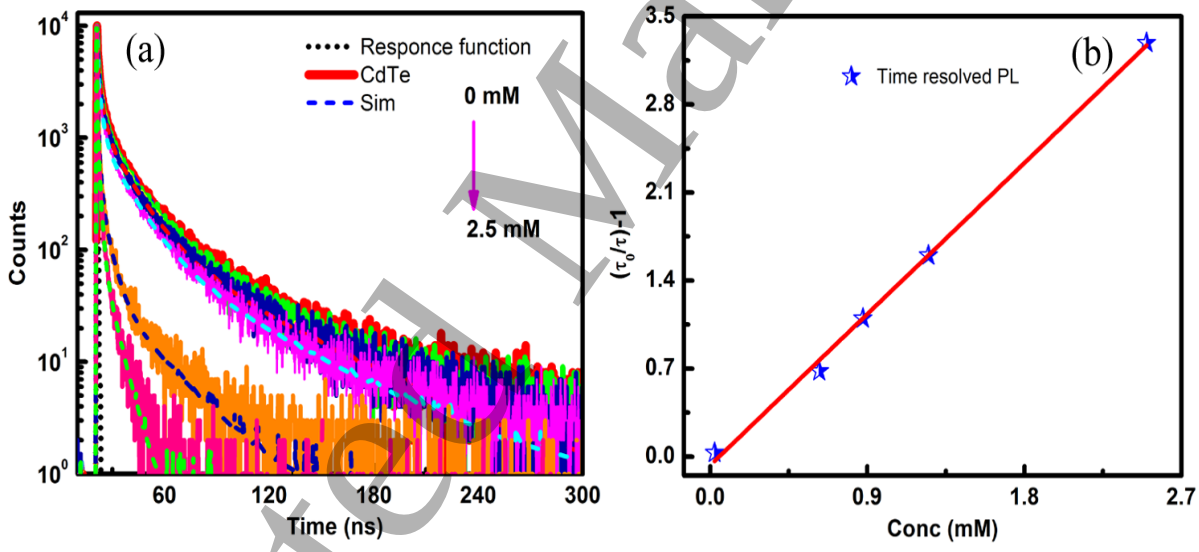

Figure 9:

Accepted Manuscript

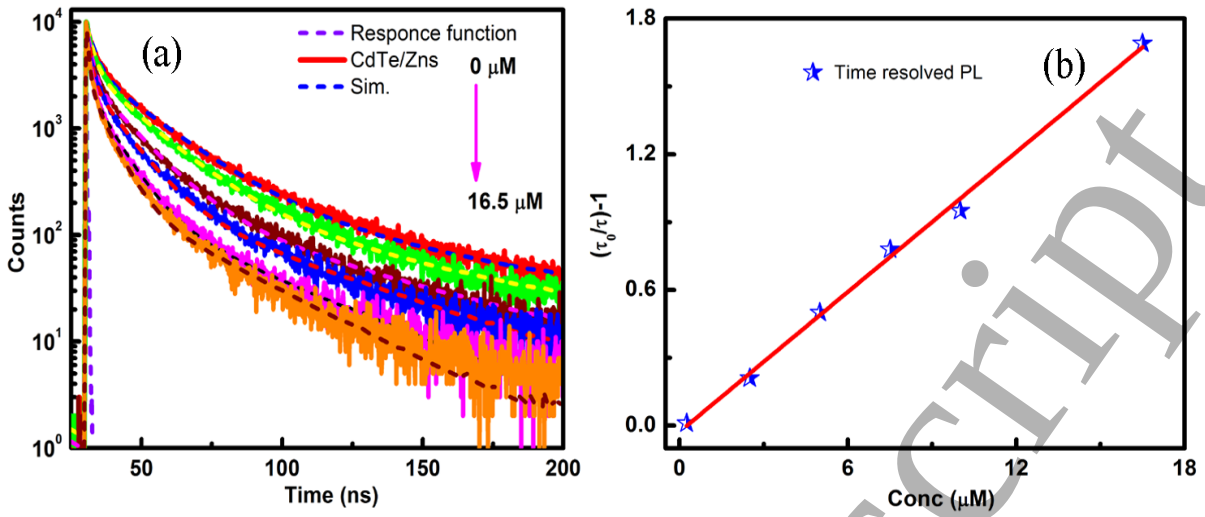

Figure 10:

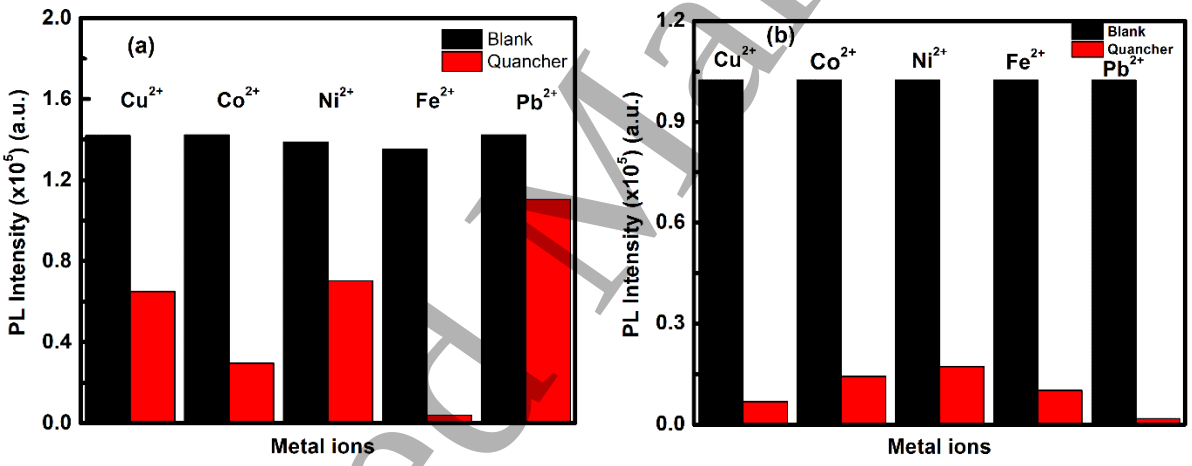

Figure 11:

Accepted Manuscript

Graphic abstract

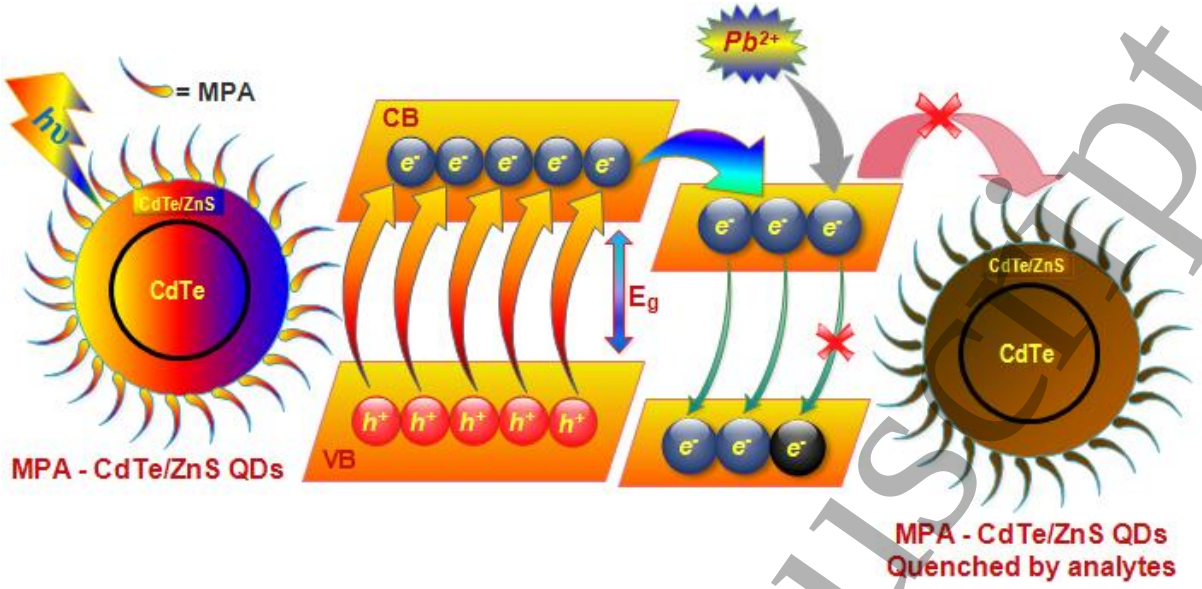

Accepted Manuscript

International Academy of Engineering and Medical Research, **2018**
Volume-3, Issue-3
Published Online March 2018 in IAEMR (http://www.iaemr.com)

TWITTER SENTIMENT ANALYSIS AND TEXT MINING IN R

Rishabh Nigam
Department of IT
Maharaja Agrasen Institute of Technology, Delhi, India
Email- nigamrishabh10@gmail.com

Nidhi Sengar
Department of IT
Maharaja Agrasen Institute of Technology, Delhi, India
Email- raghav_nidhi@yahoo.com

***Abstract*— With the help of Twitter and other social media sites, we can analyze what people think about a particular personality or brand. For a smaller company or personality, it's relatively easier to analyze the public sentiments towards them, but for a medium to large-sized company, the process of analyzing the public sentiments from the large dataset is very difficult and time-consuming, maybe not feasible. This is where Sentiment Analysis comes handy- it can be used to analyze the public opinion towards even a large company easily. Text mining can be used along with sentiment analysis in order to extract meaningful insights from the very large data.**

Keywords— ***Sentiment, Opinion, Mining, Analysis, R language***

I. INTRODUCTION

Twitter is an online micro-blogging as well as a social networking site in which the users of the site can post 280-character text (previously 140) along with an image, video, or a link to another site. The nature of the site is such that it allows the posts to be shared with a large number of people with ease. And also, it can be accessed on any kind of device easily with its web interface or the mobile application. This very nature of Twitter makes it favorable to subject it to analysis for deriving the public sentiment towards any brand name or personality and is better as compared to the rather traditional mediums such as internet news blogs and articles.

But extracting the public sentiment from tweets is a very challenging task as the data that is extracted is highly unstructured. As the length of the text that can be tweeted is limited to 280-characters, the users typically make use of informal language and internet slangs that presents serious challenge. The language used is highly informal, with creative spelling and punctuations, misspellings, slangs, newly invented words, and modern terminology and abbreviations, such as, RT for "re-tweet" and # hash tags, which are used for tagging keywords in the messages. This paper is about how to handle such challenges so as to extract and understand the opinions and sentiments that people are communicating.

The paper shows how methods like lexical analysis can be used to perform sentiment analysis using the R programming language as R is a very popular language and is a preferred choice by many, for performing any kind of analysis. Text mining is also explained in this paper i.e. how intelligent insights can be extracted from an apparently large and seemingly irrelevant data and how the same can be visualized graphically using tools such as word clouds.

II. METHODS

There are many different approaches to solve the problem such as Lexical Analysis (a part of Natural Language Processing), Machine Learning techniques. Supervised Machine Learning, such as Naive Bayes and Support Vector Machine (SVM), can be used but it involves training the data beforehand [1][2]. Unsupervised Machine Learning, such as Latent Dirichlet Allocation (LDA) and word embeddings (Word2Vec) are also used where data need not be labelled [3]. Deep Learning methods such as Convolutional Neural Network (CNN) and Long Short-term Memory (LSTM) can also be applied. I've used Lexical methods, in which we look at the frequency of occurrence of words expressing positive and negative sentiment occurring in the given tweet message and accordingly apply positive and negative scores to the tweets. Overall score is calculated based on the positive and negative scores which dictates the overall polarity of the tweet i.e. whether it is positive, negative or neutral.

Among the different software that can be used to analyze twitter, R offers a wide variety of options to do lots of interesting and fun things. In this paper, I have used RStudio as it makes it pretty much easy to work with the scripts.

International Academy of Engineering and Medical Research, 2018
Volume-3, Issue-3
Published Online March 2018 in IAEMR (http://www.iaemr.com)

III. USING TWITTER API

First step to perform Twitter Analysis is to create a twitter application [6]. This application will allow us to perform analysis by connecting our R console to the twitter using the Twitter API. The application can be created by going to the link: 'https://dev.twitter.com'[6], logging in by using your twitter account and entering the details such as name and description of the application.

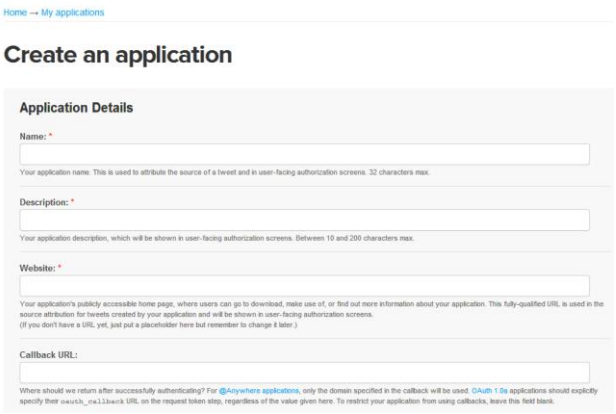

Fig. 1. Creating Twitter Application

Once, all the steps are done, the application will be created as shown below. Please note the Consumer key and Consumer Secret numbers are going to be used in RStudio later.

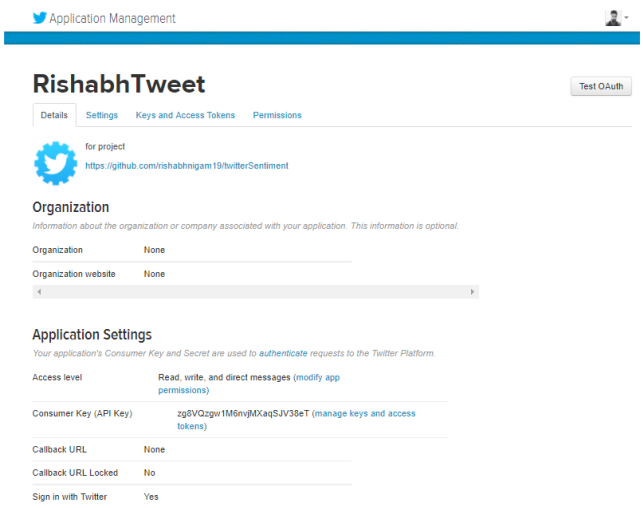

Fig.2 Twitter Application

After creating the twitter application, it is authorized in the RStudio with the help of some packages in R. These are twitter, ROAuth, plyr, among other packages. After this, we can now move on to accessing the twitter API. This step includes the performing handshake using the Consumer Key and Consumer Secret number of the Twitter application.

IV . FETCHING AND CLEANING TWEETS

Once the handshake is done and authorized by twitter, we can fetch most recent tweets related to any keyword by using the searchTwitter() function present in R. The function searchTwitter() is used to download tweets from the timeline which can then be converted into the data frame, so that we can work on it. We can also convert the data frame into .csv file.
A tweet has a lot of raw information in it which we may or may not find useful for our particular application. It comes in the form of the "dictionary" data type with various key-value pairs. [7] A list of some key-value pairs is given below:

- Whether a tweet has been favorited
- User ID
- Screen name of the user
- Original Text of the tweet
- Presence of hashtags
- Whether it is a re-tweet
- Language under which the twitter user has registered their account
- Geo-tag location of the tweet
- Date and time when the tweet was created [7]

Since this is a lot of information we only filter out the information that we need and discard the rest. For our particular application we iterate through all the tweets in our sample and save the actual text content of the tweets in a separate file given that language of the twitter is user's account is specified to be English. The original text content of the tweet is given under the dictionary key "text" and the language of user's account is given under "lang" [7].

V . DATA PREPROCESSING

It is a process to remove the unwanted elements from tweets that do not amount to any sentiments. These include-
1.Emotional Icons- emoticons; identified emotional icons
2.URLs-does not signify any sentiment

International Academy of Engineering and Medical Research, 2018
Volume-3, Issue-3
Published Online March 2018 in IAEMR (http://www.iaemr.com)

3.Stop words- words as “a“, “is”, “the”; does not indicate any sentiment
4.UserNames and HashTags- @ symbol before the username and # for topic
5.Repeated letters-“pleaaase”,“pleaseeee”, “pleaseeeeeeeeee” for the word “please” [4]
6.Slag Words- Non-English words like “lol” for “laugh out loud”, “irl” for “in real life”
These unwanted elements can be removed by replacing them with blank (space) using a string substitute function in R.

VI. SENTIMENT FUNCTION

Once we have the tweets we just need to apply some functions to convert these tweets into some useful information. The main working principle of sentiment analysis is to find the words in the tweets that represent positive sentiments and negative sentiments [8]. For this we need a list or a database of words that contains positive and negative sentiment words. There are a lot of such kind of lists available on the internet that can be downloaded. After downloading the list, the sentiment analysis uses two packages plyr and stringr to manipulate strings. We can also add more words to the already existing database to positive and negative words by using some functions. Following is a snippet of the sentiment function that calculate score for each individual tweet. It first calculates the positive score by comparing words with the positive words list and then calculate negative score by comparing words with negative words list. The final score is calculated as

score= positive score – negative score.

```
#Sentiment function
library (plyr)
library (stringr)

score.sentiment = function(sentences, pos.words, neg.words, .progress='none')
{
  require(plyr)
  require(stringr)
  # we got a vector of sentences. plyr will handle a list
  # or a vector as an "l" for us
  # we want a simple array ("a") of scores back, so we use
  # "l" + "a" + "ply" = "laply":
  scores = laply(sentences, function(sentence, pos.words, neg.words) {
    # clean up sentences with R's regex-driven global substitute, gsub():
    sentence = gsub('[[:punct:]]', '', sentence)
    sentence = gsub('[[:cntrl:]]', '', sentence)
    sentence = gsub('\\d+', '', sentence)
    # and convert to lower case:
    sentence = tolower(sentence)
    # split into words. str_split is in the stringr package
    word.list = str_split(sentence, '\\s+')
    # sometimes a list() is one level of hierarchy too much
    words = unlist(word.list)
    # compare our words to the dictionaries of positive & negative terms
    pos.matches = match(words, pos.words)
    neg.matches = match(words, neg.words)
    # match() returns the position of the matched term or NA
    # we just want a TRUE/FALSE:
    pos.matches = !is.na(pos.matches)
    neg.matches = !is.na(neg.matches)
    # and conveniently enough, TRUE/FALSE will be treated as 1/0 by sum():
    score = sum(pos.matches) - sum(neg.matches)
    return(score)
  }, pos.words, neg.words, .progress=.progress )
  scores.df = data.frame(score=scores, text=sentences)
  return(scores.df)
}
```

Fig. 3. Sentiment Function

After scoring the tweets, we get the positive, negative as well as the overall scores corresponding to the tweets. Below is an example for that (during a real-time analysis).

	Text	Score	Positive	Negative
1	In the Oval Office, however, Trump is still preoccupi...	1	1	0
2	RT @samswey: The people who were so mad at NFL ...	-1	2	3
3	@mcbyrne @donnabrazile I suppose if Trump were 'n...	0	2	2
4	RT @FSU_ATL: trump out here blowing away the hurri...	1	1	0
5	@DAlexanderB @ScottBaio @MrsScottBaio @JoyceM...	0	0	0
6	RT @HoneyDemForce: Trump Alone Can Order a Nucl...	0	1	1
7	RT @thehill: JUST IN: Trump continues attacks on De...	0	1	1
8	RT @RBReich: One of the chemicals under review is ...	0	0	0
9	RT @dcexaminer: Widow releases Trump's call after h...	0	1	1
10	RT @junogsp5: Gregg Jarrett: The Clinton cover-up, b...	1	1	0
11	RT @sassygayrepub: How do you feel Sarah Sanders...	1	1	0
12	RT @frankrichny: Sanders notwithstanding, it is now ...	0	1	1
13	@realDonaldTrump @FoxNews Will she ask you abou...	-1	0	1
14	RT @ImChasingDreamz: my question is HOW THE FUC...	0	1	1
15	RT @kylegriffin1: Per pool, Trump has arrived at Trum...	3	3	0
16	@TheAnaBraga @bigtimecoach248 You and Trump's ...	2	2	0
17	RT @ProudResister: O'Reilly: Settled harassment clai...	0	2	2
18	RT @needmorePMT: /f9tKxiLjxb	0	0	0
19	RT @bethanyshondark: Instead of always interviewin...	2	2	0
20	RT @jrcheneyjohn: Typical Liberal Hypocrite, Congr...	-1	1	2
21	RT @JBCOOKS: A thoughtful op-ed by @alexanderna...	-1	1	2
22	RT @tommyxtopher: @RepWilson Then after everyon...	-2	0	2
23	RT @JoyAnnReid: Shameless. Right wingers are circul...	0	2	2
24	RT @NatashaBertrand: Donald Trump Is Rush-Shippin...	1	1	0

Showing 1 to 24 of 1,500 entries

Fig. 4. Tweets with Scores

VII. VISUALIZING TWEETS

Now that all the work is done. We can create visual histograms and other plots to visualize the sentiments of the user. This can be done by using hist function. A package called RColorBrewer can be used in R to play with colors. Below is an example histogram obtained after the analysis of the word “Kejriwal” (who is the Chief Minister of Delhi, India at the time of writing this paper).

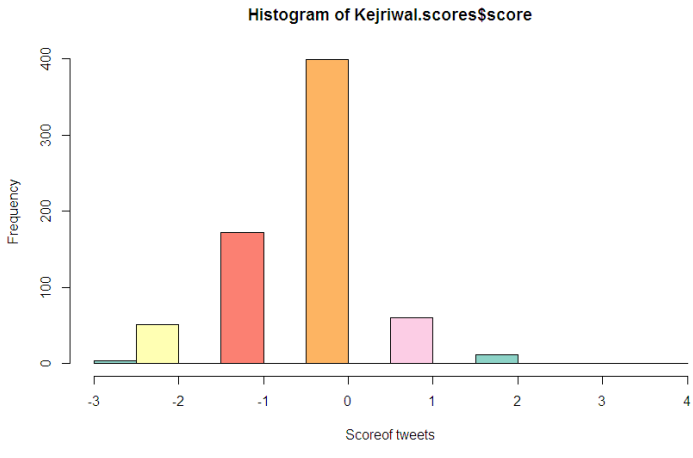

Fig.5. Histogram output

The above histogram shows the frequency of tweets with respect of scores allotted to each tweet. The x-axis shows the score of each tweet as a negative and positive integer or zero. The y-axis shows the frequency. A positive score represents

International Academy of Engineering and Medical Research, 2018
Volume-3, Issue-3
Published Online March 2018 in IAEMR (http://www.iaemr.com)

positive or good sentiments associated with that particular tweet whereas a negative score represents negative or bad sentiments associated with that tweet. A score of zero indicates a neutral sentiment. The higher positive the score, the more positive the sentiments of the person tweeting and vice-versa [9].
The above histogram is skewed towards negative score which shows that the sentiments of people regarding Mr. Kejriwal are negative. This can be justified as in recent days, some of his schemes have backfired.

VIII.TEXT MINING

Text mining, also referred to as text data mining, roughly equivalent to text analytics, refers to the process of deriving high-quality information from text [10]. Applications of text mining are as follows-
● Information Retrieval - Finding keywords in the collection or database
● Natural language processing – Interaction between computer and human. Example- Sentiment analysis
● Information Extraction – Automatically extracting information from machine readable documents

We can do the text mining of the tweets. For this procedure, we need to use 'WordCloud' and 'tm' package for text mining. A WordCloud is best used for visualizing the results of text mining because-
● Word clouds can identify trends and patterns that would otherwise be unclear or difficult to see in a tabular format.
● Frequently used keywords stand out better in a word cloud
● An effective method for analyzing text-data
● Are easy to understand

The following is a WordCloud obtained after performing a text mining for the word "Trump"-

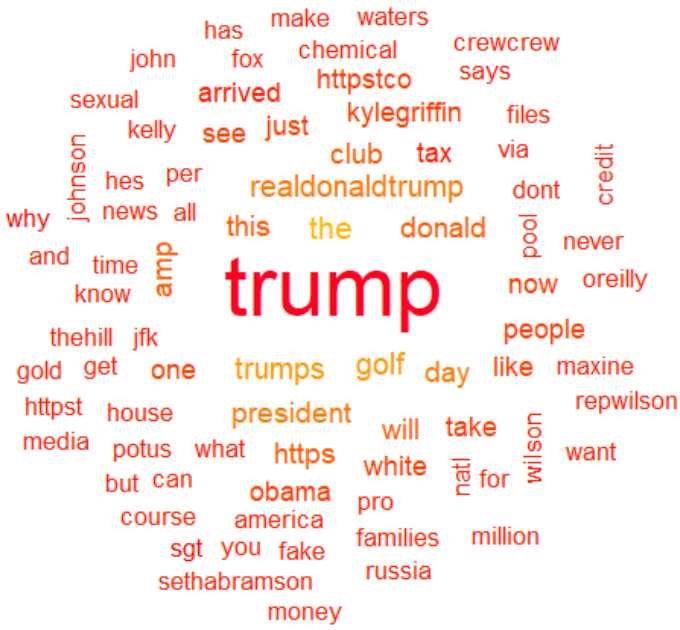

Fig.6. WordCloud after Text Mining

According to this wordcloud, we can see that Trump is the most used term in the tweets followed by president, Obama, money, fake which shows that while tweeting about Trump, the person also connects the term Trump with the words like Obama, fake and money.

IX. CONCLUSION

Sentiment analysis or opinion mining is a hot topic in machine learning. We are still far to detect the sentiments of corpus of texts very accurately because of the complexity in the English language and even more if we consider other languages such as Spanish, French or Chinese.
In this paper we tried to show the basic way of classifying tweets into positive or negative category using Lexical Analysis. We could further improve our efficiency by using Advanced Machine Learning techniques such as Recurrent Neural Networks, Long Short-Term Memory (LSTM) and others.
Some of the future scopes include-
● Data Pre-Processing using more parameters to get best sentiments
● Updating Dictionary for new Synonym and Antonyms of already existing words
● Can be implemented as a Web-Application which can be used to identify top trending topics, top tweets of a particular user, and even location-wise trends

● Advanced Machine Learning techniques such as Recurrent Neural Networks, Long Short-Term Memory (LSTM) and others can be used to increase the efficiency of the analysis.

Moreover, Sentiment Analysis has large number of applications in different verticals. It can be used for-

● Determining the public opinion towards any personality like political leaders and parties

● Predicting the Stock market behavior of a particular company or a group of companies. (This could be done by analyzing overall public sentiment towards that firm with respect to time and using economics tools for finding the correlation between public sentiment and the firm's stock market value)

● Firms can also estimate how well their product is responding in the market, which areas of the market is it having a favorable response and in which a negative response (since twitter allows us to download stream of geo-tagged tweets for particular locations). If firms can get this information they can analyze the reasons behind geographically differentiated response, and so, they can market their product in a more optimized manner by looking for appropriate solutions like creating suitable market segments.

● Predicting the results of popular political elections and polls is also, an emerging application to sentiment analysis. One such study was conducted by Tumasjan et al. in Germany for predicting the outcome of federal elections in which concluded that twitter is a good reflection of offline sentiment [5].

X. REFERENCE

[1] Alexander Pak and Patrick Paroubek. Twitter as a Corpus for Sentiment Analysis and Opinion Mining. In Proceedings of international conference on Language Resources and Evaluation (LREC), 2010.

[2] Luciano Barbosa and Junlan Feng. Robust Sentiment Detection on Twitter from Biased and Noisy Data. In Proceedings of the international conference on Computational Linguistics (COLING), 2010.

[3] Peter D. Turney. Thumbs Up or Thumbs Down? Semantic Orientation Applied to Unsupervised Classification of Reviews. In Proceedings of the Annual Meeting of the Association of Computational Linguistics (ACL), 2002.

[4] Samuel Brody and Nicholas Diakopoulus. Cooooooooooooooollllllllllllll!!!!!!!!!!!!!! Using Word Lengthening to Detect Sentiment in Microblogs. In Proceedings of Empirical Methods on Natural Language Processing (EMNLP), 2011.

[5] Andranik Tumasjan, Timm O. Sprenger, Philipp G. Sandner and Isabell M. Welpe. Predicting Elections with Twitter: What 140 Characters Reveal about Political Sentiment. In Proceedings of AAAI Conference on Weblogs and Social Media (ICWSM), 2010.

[6] Twitter API <https://dev.twitter.com/docs/api>

[7] Twitter Sentiment Analysis; FUNCTIONALITY AND DESIGN by Afroze Ibrahim BaqapuriSSSSS

[8] Analysis of Twitter Data Using R — Part 3: Sentiment Analysis by Rohit Nair

[9] Sentiment Analysis of #MakeInIndia & #Demonetization using by R CH.R.Vinodkumar

[10] Wikipedia, the free encyclopedia <https://en.wikipedia.org/wiki/Text_mining>

Author's Biography

Rishabh Nigam is a final year engineering student at the Maharaja Agrasen Institute of Technology which is affiliated to Guru Gobind Singh Indraprastha University, Delhi, India. His field of study is Information Technology. He is interested in the field of data science, machine learning and data analytics.

Nidhi Sengar is an Assistant Professor in the Information Technology department of Maharaja Agrasen Institute of Technology which is affiliated to Guru Gobind Singh Indraprastha University, Delhi, India. She received her B.Tech degree from MAIT,GGSIPU in 2003 and M.Tech from Delhi College of Engineering, DU inn 2007. She specializes in computer networks and software engineering.